Proceedings

33rd ASPE Annual Meeting

November 4-9, 2018

Red Rock Casino Resort Spa
Las Vegas, Nevada, USA

American Society for
Precision Engineering

P.O. Box 10826, Raleigh, NC 27605-0826
(919) 839-8444 | Fax (919) 839-8039

Proceedings of

The Thirty-Third Annual Meeting of the

American Society for Precision Engineering

November 4-9, 2018
Red Rock Casino Resort Spa
Las Vegas, Nevada USA

All conference activities are on the 5th Floor of the hotel.

The American Society for Precision Engineering (ASPE) is a multidisciplinary professional and technical society concerned with research and development, design, manufacture and measurement of high accuracy components and systems. ASPE activities encompass relevant aspects of mechanical electronic, optical and production engineering, physics, chemistry, and computer and materials science. Membership is open to anyone interested in any aspect of precision engineering.

Founded in 1986, ASPE provides a focus for a diverse but important community. Other professional organizations have covered aspects of precision engineering, always as a sideline to their principal goals. ASPE is based on the core of generic concepts necessary to achieve precision in any application; independent of discipline, ASPE intends to be the focus for precision technology – and to represent all facets from research to application.

The Annual Meeting has evolved into an international forum for the exchange of ideas and presentation of research results relating to precision engineering, metrology, controls and system integration. Precision engineers and scientists from private industry, government laboratories, and universities meet to learn about the latest developments and to exchange ideas about the future directions of these technologies.

ASPE – The American Society for Precision Engineering
301 Glenwood Avenue, Suite 205, Raleigh, NC 27603
919.839.4444
www.aspe.net

Preface

This book comprises the proceedings of the 33rd ASPE Annual Meeting. The contributions reflect the authors' opinions and are published as presented to ASPE, without change. Their inclusion in this publication does not necessarily constitute endorsement by the ASPE, or its editorial staff.

Individual readers of this book and nonprofit libraries acting for them are permitted to make fair use of the material contained in this book to be used in teaching or research; provided they copy said paper in total, as written by the author. Permission is granted to quote excerpts from the scientific or technical works in this book with proper acknowledgment of the source to include: The author's name, the book name, an the ASPE tag line. Reproduction of figures and tables is likewise permitted from the contents of this book, provided that the same acknowledgment of the same source and content is permitted.

Any other type reproduction, systematic copying or multiple reproduction of any material in this book is expressly prohibited except with the written permission of the ASPE editorial staff, addressed to the Society's headquarters.

ISBN 978-1-887706-77-3

2018

American Society for Precision Engineering
301 Glenwood Avenue, Suite 205
Raleigh, NC 27603

Printed in the United States of America

Organizing & Technical Program Committee

Annual Meeting Chairperson

Kate Medicus
Ruda Cardinal, Inc.

Technical Leadership Committee Chairpersons

Chinedum Okwudire, University of Michigan
Controls and Mechatronics TLC Chair

Brandon M. Lane, National Institute of Standards & Technology
Characterization TLC Chair

Jimmie A. Miller, University of North Carolina-Charlotte
Metrology Systems TLC Chair

Robert M. Panas, Lawrence Livermore National Laboratory
Micro and Nano Technologies TLC Chair

Deepak Ravindra, Micro-LAM
Precision Manufacturing TLC Chair

Richard Seugling, Lawrence Livermore National Laboratory
Precision Design TLC Chair

Committee Members

Luis A. Aguirre, 3M Company
David A. Arneson, Professional Instruments Company
Rick Baade, Eindhoven University of Technology
Vivek Badami, Zygo Corporation
Barkin Bakir, Western Michigan University
Michael L. Barkman, Zygo Corporation
Marcin B. Bauza, Carl Zeiss Industrial Metrology
Alex Bean, Corning Tropel Corporation
Eric Belski, Aerotech, Inc.
Michael Binnard, Nikon Research Corporation of America
Niels Bosmans, KU Leuven
Dannis Brouwer, University of Twente
Christopher A. Brown, Worcester Polytechnic Institute
Eric S. Buice, Lawrence Berkeley National Laboratory
Nelson Cardenas, Oculus
Len Chaloux, Moore Nanotechnology Systems
Qunyi Chen, 3M Company
Liam Connolly, The University of Texas at Austin
Michael A. Cullinan, The University of Texas at Austin
Timothy M. Dalrymple, Magic Leap, Inc.
Xin Dong, University of Michigan
John W. Dorsey-Palmateer, Boeing Research & Tech., Retired
Thomas A. Dow, North Carolina State University
Ahment Alper Dumanli, Oregon State University
Nicholas J. Duncan, Aerotech, Inc.
Kevin E. Elliott, Corning, Inc.
Jonathan D. Ellis, University of Arizona
Kenneth Enstrom, Lawrence Livermore National Laboratory
Christopher J. Evans, University of North Carolina-Charlotte
Chunjie Fan, University of North Carolina-Charlotte
Massimiliano Ferrucci, KU Leuven
Ronnie Fesperman, Precision Mindset LLC
Pete J. Fitsos, Lawrence Livermore National Laboratory
Jason Fox, National Institute of Standards & Technology
Stephen Furst, Smart Materials Solutions, Inc.
Steven R. Gillmer, MIT Lincoln Laboratory
Axel Grabowski, Physik Instrumente (PI) GmbH & Co. KG
Robert D. Grejda, Corning Tropel Corporation
Jonathan B. Hopkins, University of California – Los Angeles
Bradley H. Jared, Sandia National Laboratories
Michael R. Johnson, Magic Leap, Inc.
Sajad Kafashi, University of North Carolina-Charlotte
Byron R. Knapp, Professional Instruments Company
Mark T. Kosmowski, Electro Scientific Industries, Inc.
Ian Ladner, Lawrence Livermore National Laboratory
Richard K. Leach, University of Nottingham
ChaBum Lee, Tennessee Technological University
Xingjian Liu, University of Michigan
Stephen J. Ludwick, Aerotech, Inc.
Dan E. Luttrell, Kriterion, LLC
Eric R. Marsh, The Pennsylvania State University
Hossein Mohammadi, Western Michigan University
Joshua D. Montaño, Los Alamos National Laboratory
Darcy Montgomery, Cedarflat Precision Inc.

Bala Muralikrishnan, National Institute of Standards & Technology
Bartosz Nowakowski, Bruker.
Paul R. Parise, Convergent Technologies
Steven R. Patterson, University of North Carolina-Charlotte
Antonius T. Peijnenburg, VDL Enabling Technologies Group
Jon R. Pratt, National Institute of Standards & Technology
Keval Ramani, University of Michigan
Suresh Kumar Ramasamy, Apple Inc.
Theo Ruijl, MI-Partners
Sourabh K. Saha, Lawrence Livermore National Laboratory
Tony Schmitz, University of North Carolina- Charlotte
Burak Sencer, Oregon State University
Deming Shu, Argonne National Laboratory
Robert A. Smythe, Äpre Instruments, LLC
Rongrong Sun, Washington State University
Joshua Tarbutton, University of North Carolina – Charlotte
John Taylor, University of North Carolina-Charlotte
Hy D. Tran, Sandia National Laboratories
David L. Trumper, Massachusetts Institute of Technology
Mario O. Valdez, Los Alamos National Laboratory
Lucas M. Valdez, Los Alamos National Laboratory
Jan van Eijk, MICE Holding bv
Herminso Villarraga-Gómez, Nikon Metrology, Inc.
Deokkyun Yoon, University of Michigan
Xiangzhi Yu, University of Rochester
Bowen Zeng, University of Michigan
Rayne Zheng, Virginia Polytechnic Institute
John C. Ziegert, University of North Carolina-Charlotte

ASPE gratefully acknowledges the time and the effort of the organizing and technical program committee to bring the precision engineering community this program.

Contents

Preface ii

Organizing Committee . . . . . iii-iv

Table of Contents v

ASPE Lifetime Achievement Award vi

ASPE Distinguished Service Award vii

ASPE 2018 Legacy Award. vii

2018 Scholarship Recipients viii

ASPE Student Schlorships viii

Sustaining Corporate Sponsors . . . . . ix-x

Corporate Sponsors xi

Technical Paper Index 1-11

Technical Papers 15-587

Author Index 589

ASPE Lifetime Achievement Award

John C. Ziegert Ph.D.

University of North Carolina-Charlotte

The Lifetime Achievement Award was conceived to honor particularly noteworthy contributions to the advancement of the discipline and/or Society over a career of service in precision engineering, and this year, ASPE is pleased to present this very special award to **John C. Ziegert, Ph.D.,** Emeritus Professor in Mechanical Engineering at UNCC, for leadership in educating the next generation of engineers as well as research within the profession for nearly 30 years.

Dr. Ziegert earned a B.S. in Mechanical Engineering at Purdue University, an M.S. from Northwestern University and a Ph.D. from the University of Rhode Island. He joined the University of Florida faculty in 1990,and was appointed to the Newton C. Ebaugh Chair in Mechanical Engineering in 2004. In 2006, he joined the Mechanical Engineering faculty at Clemson University where he held the Timken Chair in Design. In 2011, he joined the Mechanical Engineering faculty at the University of North Carolina at Charlotte where he participated in the activities of the Center for Precision Metrology and directed the Siemens Large Manufacturing Lab. He is a Fellow of SME and the American Society of Mechanical Engineers, past-President of the American Society for Precision Engineering, and served as Editor-in-Chief for Precision Engineering: Journal of the Joint Societies for Precision Engineering and Nanotechnology, from 2006 to 2015. In 2009, he received the Arnold O. Beckman Founders Award from the Instrument Society of America., and in 2017 he received the SME Frederick W. Taylor Manufacturing Research Medal.

ASPE Distinguished Service Award

Wendy Shearon worked as the ASPE Meetings and Members Manager for 18 years. During her tenure, Wendy served the society in multiple roles, including membership renewals and processes, meeting and conference planning, and committee work. She has provided a legacy of excellent service to ASPE members. In grateful appreciation, we recognize Wendy as co-recipient of the 2018 Distinguished Service Award.

Ilka Lee worked as the Office Manager of ASPE since its incorporation in 1986. She supported the society's journal, Precision Engineering, by working both with the Editors-in-Chief and publisher. Ilka also handled ASPE's accounting tasks and supported the Board activities. She has been a steadfast member of the ASPE staff. For her 32 years of dedicated service, we celebrate Ilka as co-recipient of the 2018 Distinguished Service Award.

2018 Legacy Award

In special recognition of ASPE leadership. This award commemorates the significant leadership and contributions of **Dr. Thomas Dow** to the American Society for Precision Engineering and the international precision engineering community. It celebrates his 32 years of service as the Founding Executive Director of ASPE (1986-2018).

2018 Scholarship Recipients

Graham J. Siddall Student Scholarship

ASPE is pleased to be able to award the first Graham Siddall Student Scholarship to **Martin J. Ward** at the University of Texas at Austin (Advisor: Michael A. Cullinan).

With a 10-year student endowment, Graham Siddall will recognize a student scholar in the field of precision engineering. This prestigious award is valued at $2,500 and will support the student winner in the form of waived conference and tutorial fees and a stipend to cover travel costs to the 33rd Annual Meeting in Las Vegas.

Graham Siddall received his BS degree in Production Engineering and Management with First Class honors from the University of Nottingham in England. He received his M.Sc. and Ph.D. degress in Natural Philosophy (Physics) in 1971 and 1975, respectively, working under the guidance of Professor R.V. Jones at the University of Aberdeen in Scotland. Learn more about Dr. Siddall by visiting http://aspe.net/about-aspe/siddall-scholarship.

ASPE Student Scholarships

ASPE is proud to award 2 student scholarships for the 33rd ASPE Annual Meeting in Las Vegas, Nevada. This year's scholarship recipients are **Liam Connolly**, University of Texas at Austin (Michael Cullinan, Advisor) and **Kumar Arumugam**, University of North Carolina-Charlotte (Stuart Smith, Advisor). The ASPE Student Scholarships include a waiver of the Annual Meeting registration fee and 4 tutorial fees. It also includes an honorarium to cover travel and lodging expenses to the 32nd ASPE Annual Meeting in Charlotte. The ASPE Student Scholarships were made possible by Corning Incorporated, Lion Precision, Moore Nanotechnology and many contributing members.

ASPE 2018 Sustaining Corporate Sponsors

3M Company
St. Paul, MN 55144
Phone: 888-364-3577
www.mmm.com

Aerotech, Inc.
101 Zeta Drive
Pittsburgh, PA 15238-2897
Phone: 412-963-7470
www.aerotech.com

Ametek Precitech, Inc.
44 Blackbrook Road
Keene, NH 03431
603-357-2511
www.precitech.com

Carl Zeiss Industrial Metrology LLC
6250 Sycamore Lane North
Maple Grove, MN, 55369
Phone: 763-744-2400
www.zeiss.com/metrology

Chardon Tool
115 Parker Court
Chardon, OH 44024
440-286-6440
www.ChardonTool.com

Cranfield Precision
Division of Fives Landis Ltd.
Woburn House
3 Adams Close
Kempston, Bedford, MK42 7 JE
United Kingdom
Phone: +44 (0)1234 312820
www.cranfieldprecision.com

Lion Precision
563 Shoreview Park Road
St. Paul, MN 55126-7014
Phone: 651-484-6544
www.lionprecision.com

Mahr Inc.
1144 Eddy Street, Providence, RI 02905
401-782-3168
www.mahr.com

ASPE 2018 Sustaining Corporate Sponsors

Makino
7680 Innovation Way
Mason, OH 45040
Phone: 513-573-7200
www.makino.com

Moore Nanotechnology Systems LLC
230 Old Homestead Highway
Swanzey, NH 03446
Phone: 603-352-3030
www.nanotechsys.com

New Way Air Bearings
50 McDonald Boulevard
Aston, PA 19014
610-494-6700
www.newwayairbearings.com

Physik Instrumente
16 Albert Street
Auburn, MA 01501
508-832-3456
www.pi-usa.us

Specialty Components
14 Village Lane
Wallingford, CT 06492
203-284-9112
www.specialtycomponents.com

VDL Enabling Technologies Group USA
3758 Spinnaker Court
Fremont, CA 94538-1706
510-996-4662
www.vdletg.com

ASM Pacific Technology Ltd.
12/F Watson Centre
16-22 Kung Yip Street
Kwai Chung, N. T. HONG KONG
852-2619-5107
www1.asmpacific.com/en/

ASPE 2018 Corporate Sponsors

ADCOLE Corporation
669 Forest Street
Marlborough, MA 01752
Phone: (508) 485-9100
www.adcole.com

Contour Fine Tooling, Inc.
143 Jaffrey Road
Marlborough, NH 03455
Phone: (603) 876-4908
www.contour-diamonds.com

Corning Inc.
Corning, NY 14831
Phone: (607) 974-3842
www.corning.com

K & Y Diamond
2645 Diab
Laurent, Quebec H4S 1E7
Canada
514-333-5606
www.kydiamond.ca

Philips Innovation Services
High Tech Campus 7
5656 AE Eindhoven
The Netherlands
31-40-27-48060
www.innovationservices.philips.com

Prior Scientific, Inc.
80 Reservoir Park Drive
Rockland, MA 02370
781-878-8442
www.prior-us.com

Professional Instruments Company
7800 Powell Road
Hopkins, MN 55343
952-933-3315
www.airbearings.com

University of North Caroina-Charlotte
Center for Precision Metrology
9201 University City Boulevard
Charlotte, NC 28223-0001
704-687-8499
cpm.uncc.edu

Zygo Corporation
Laurel Brook Road
Middlefield, CT 06455-0448
Phone: (860) 347-8506
Toll-free: (800) ZYGO-NOW
www.zygo.com

ASPE 2018 Annual Meeting
Oral Sessions

Session 1
Characterization
Tuesday, November 6, 2018, 8:30 AM - 10:00 AM
Session Chair: Brandon M. Lane (National Institute of Standards and Technology) and Nelson Cardenas (Oculus)

1. **Infidelity and the Calibration of Surface Topography Measuring Instruments**
   Leach, R. K. (University of Nottingham); de Groot, P. J. (Zygo Corporation); Haitjema, H. (Mitutoyo Research Center Europe B.V.) 15
2. **Experimental Verification and Uncertainty Evaluation of an Error Mapping Technique for Rotary Tables and Rotary Axes**
   Wang, Q.; Miller, J. A.; Goch, F. G. (University of North Carolina-Charlotte). 21
3. **Virtual Optimization of Artifact Based Calibration of Machine Tools**
   Aguirre, G.; Iñigo, B.; Cilla, J.; Urreta, H. (IK4-IDEKO) 26
4. **Calibration of a High-precision Five Degree of Freedom Hybrid Mechanism**
   Karim, S.; Piano, S.; Leach, R. K. (University of Nottingham); Tolley, M. (Science and Technology Facilities Council (STFC)) 32
5. **Achievable Figure and Finish on Infrared Crystal with the Micro-LAM Process**
   Shahinian, H.; Kode, S. K.; Ravindra D.; Zaytsev, D.; Navare, J. A. (Micro-LAM, Inc.). . . . 38

Session 2
Machining Process Improvements
Tuesday, November 6, 2018, 10:30 AM - 12:00 PM
Session Chair: Kevin E. Elliott (Corning, Inc.) andLucas M. Valdez (Los Alamos National Laboratory)

1. **High Performance Turning Assisted by Chip-pulling**
   Sencer, B.; Maulimov, M. (Oregon State University) 43
2. **The Effect of Symmetric and Asymmetric Dynamics on Period-N Bifurcations**
   Honeycutt, A.; Schmitz, T. L. (University of North Carolina-Charlotte) 47
3. **Design Improvement of the Cutting Fluid Supply of a Large 5-axis Machine Tool**
   Hernandez-Becerro, P.; Blaser, P.; Wegener, K. (ETH Zürich); Mayr, J. (inspire AG) 53
4. **PIRest Technology – New Piezo Technology for Active Alignments and Error Corrections in Difficult-to-access Areas and Systems**
   Reiser, J.; Marth, H.; Bach, M. (Physik Instrumente 59

***No Abstract Available**

Session 5

Metrology - Machine Characterization

Wednesday, November 7, 2018, 1:30 PM - 2:10 PM

Session Chair: Robert D. Grejda (Corning Tropel Corporation)
and Richard K. Leach (University of Nottingham)

1. **Limits of Displacement Measure Interferometry on Rough Surfaces Using A Microchip Laser Source**
   Arumugam, K.; Smith, S.; Her, T.-H. (University of North Carolina-Charlotte) 117
2. **Ultra-Precise Motion Error Measurement of Rotation Kinematics for the Integration in Nanomeasuring and Nanofabrication Machines**
   Fern, F.; Füßl, R.; Schienbein, R.; Theska, R. (Ilmenau University of Technology) 122

Student Challenge

Wednesday, November 7, 2018, 2:10PM - 3:00PM

Session Chair: Kate M. Medicus (Optimax Systems, Inc.)

1. **Introduction to the ASPE Student Challenge**
   Aguirre, L. A. (3M Company); Smith, S. (University of North Carolina-Charlotte)
2. **Presentation of the Student Challenge Winners**
   Aguirre, L. A. (3M Company); Smith, S. (University of North Carolina-Charlotte)
3. **Student Presentations**

Session 6
Metrology

Thursday, November 8, 2018, 8:30 AM - 10:00 AM

Session Chair: Jimmie A. Miller (University of North Carolina-Charlotte)
and Jon D. Ellis (University of Arizona)

1. **Representing the Specification of Industrial X-ray Computed Tomography with Amplitude- Wavelength Space**
   Villarraga-Gómez, H. (Nikon Metrology, Inc.); Leach, R. K. (University of Nottingham); Smith, S. T. (University of North Carolina - Charlotte) 127
2. **Real-time in Situ Metrology of the Shape of an X-ray Adaptive Mirror Using an Array of Interferometric Absolute Position Sensors**
   Badami, F. G.; Abruna, E. (Zygo Corporation); Huang, L.; Idir, M. (Brookhaven National Laboratory) 136
3. **High Accuracy Cylindrical Mirror Measurement by Three-dimensional Nano-profiler Based on the Normal Vector Tracing Method**
   Kang, J.; Shiraji, H.; Kizaki, R.; Toyoshi, Y.; Kitayama, T.; Yamamura K.; Endo, K. (Osaka University); Miyawaki, T.; (Nikon Corporation) 142
4. **A Curved Surface-Insensitive Optical Sensing Technique for Precision Spindle Health Monitoring**
   Lee, C-B. (Tennessee Technological University); Kim, G. (Tri-N Co., Ltd.) 146

***No Abstract Available**

Session 7
Precision Design of Instruments
Thursday, November 8, 2018, 10:30 AM - 12:00 PM
Session Chair: Richard M. Seugling (Lawrence Livermore National Laboratory) and Mark T. Kosmowski (Electro Scientific Industries, Inc.)

6. **Advancement of Gas Film Lubrication for High Performance Turbomachinery and How Additive Manufacturing is Playing a Key Role in the Effort ***
   Ertas, B. (GE)
7. **Error Budgeting, Manufacturing and Measurement Considerations for the Development of a High Precision Motion Platform**
   Elliott, K.E..; Brackley, D.; Doig, A. J.; Sheehan, B. (Corning, Inc.) 150
8. **Berkeley Met5: Engineering Precision and Stability for the Highest Resolution EUV Lithography Tool**
   Allezy, A. P. (Lawrence Berkeley National Laboratory) 156
9. **Designing Low Frequency Band Gaps in Additively Manufactured Parts Using Internal Resonators**
   Elmadih, W.; Syam, W. P.; Maskery, I.; Leach, R. K. (University of Nottingham) 162
10. **Design of an Instrument for Characterizing the Embedded Brain issue Cutting Process**
    Ramirez, A. E.; Culpepper, M. L. (Massachusetts Institute of Technology) 168
11. **PZT-Actuated Compliant Locking Device**
    Tschiersky, M.; Brouwer, D. M.; Stramigioli, S. (University of Twente); Berselli, G. (University of Genova); 174

Session 8
Precision Machining
Thursday, November 8, 2018, 1:30 PM - 3:00 PM
Session Chair: Deepak Ravindra Ph.D. (Micro-LAM, Inc.) and Ronnie R Fesperman Jr. (Precision Mindset LLC)

1. **State-of-the-art in Applying Ultrasonic Assisted Diamond Turning to Different Materials**
   Bulla, B.; Robertson, D.; Dicke, C. (son-x GmbH) 180
2. **High Speed Cutting of Monocrystalline Silicon by Off-axis Diamond Turning**
   Berger, D.; Schönemann, L.; Riemer, O.; Brinksmeier, E. (University of Bremen) 184
3. **Suitability of RSA Aluminum for Monolithic DOE in the VIS Range**
   Jagodzinski, M.; Kühne, S.; Malcher, M. (Technische Universität Berlin); Oberschmidt, D. (Fraunhofer Institute for Production Systems and Design Technology (IPK)) 190
4. **Focused Ion Beam Milling of Microscale Features**
   Wong, A. R.; Dow, T. A.; Pankow, M. (North Carolina State University) 196
5. **Bessel Beam Array for High Resolution Wafer Dicing**
   Hiu Hung Lee, Erxuan Zhao, Wrei Lin, Yina Chang and Shih-Chi Chen (The Chinese University of Hong Kong) 201

***No Abstract Available**

Poster Session 1

Tuesday - November 6, 2018 , 3:30 PM - 5:00 PM

Session Chair: Brian O'Connor (Aerotech)

Characterizations, Data Reduction and Applications of Measurement

1. **Pressure Measurement and Uncertainty for Wound Irrigation Devices**
   Pawar, A.; Schmitz, T. L. (University of North Carolina-Charlotte). 209
2. **The Effect of the Micro-LAM Process on the Underlying Structure of the surface of IR Crystals**
   Shahinian, H.; Kode, S. K.; Ravindra D.; Zaytsev, D.;
   Navare, J. A. (Micro-LAM, Inc.) 215
3. **A Novel Positioning Measurement Method Using Polar Microstructure**
   Zhao, C.; Cheung C.-F. (The Hong Kong Polytechnic University). 221
4. **Determination of the Lateral Resolution of an Interference Microscope Using A Micro-Scale Sphere**
   Su, R.; Thomas, M.; Leach, R. K. (University of Nottingham);
   de Groot, P. J. (Zygo Corporation;) Coupland, J. M. (Loughborough University) 225

Micro and Nano Technologies

1. **MEMS-based Graphene Resonant Gas Sensor for Health Monitoring**
   Cayll, D.; Hyung C. J.; Cullinan, M. A. (The University of Texas at Austin);
   Ladner, I. S. (Lawrence Livermore National Laboratory). 230
2. **Finite Element Analysis and Fabrication of a Plate-type Ultrasonic System for Cooling ***
   Kim, H.; Lim, E.; Park, J-K. (Korea Institute of Machinery & Materials (KIMM))
3. **Investigation of Assembly of a Levitation Actuator**
   Nakazato, A.; Takaki, Y.; Torii, A.; Doki, K.;
   Mototani, S. (Aichi Institute of Technology) 235
4. **Improvement of the Trajectory of an Inchworm with a Low-Cost Camera**
   Takaki, Y.; Torii, A. ; Nakazato, A.; Mototani, S.;
   Doki, K. (Aichi Institute of Technology) 239
5. **Multiple-indicators Improvement of Silicon Cylindrical Optics Polishing for High Energy Laser**
   Tian, T.; Shi, F.; Dai, Y.; Peng, X.; Han, K.; Zhong, Y.; Li, F.;
   Luo, C.; (National University of Defense Technology). 243
6. **Ultra-Precise Closed-Loop Piezo Positioning with Interferometry for Nano Manufacturing Machines**
   Schindler, G.; Hirschmann, T. C.; (Attocube Systems AG) 249

Precision Manufacturing Machines and Technologies

1. **Compensating for Film Stress in Thin Mirror Substrates Using Ion Implantation**
   Chalifoux, B.; Yao, Y.; Woller, D. B.; Heilmann, R. K.;
   Schattenburg, M. L. (Massachusetts Institute of Technology). 253

***No Abstract Available**

2. **Design and Manufacture of Angular Variation Pyramid Pattern of Random Arrangement**
Choi, D.-S.; Moon, S.-H.; Lee, J.-R.; Jeong, Ji-Y.;
Je, T.-J. (Korea Institute of Machinery & Materials (KIMM));
Jeon, E.-C. (University of Ulsan) 259

3. **Modulated Tool Path Turning Stability Analysis**
Copenhaver, R.; Schmitz, T. L. (University of North Carolina-Charlotte) 263

4. **Improvement of Multistage Superfinishing of Sapphire with Vitrified-bonded Diamond Superabrasive Stones**
Furushiro, N; Yamaguchi, T.; Hirooka, D. (Kansai University);
Matsumori, N.; Tanada, K. (Mizuho Co., Ltd.) 269

5. **Estimation of Saw Wire Temperature during Machining of Rock in Vacuum**
Furutani, K.; Inukai, R.; Takano, T. (Toyota Technological Institute);|
Okada, T. (Institute of Space and Astronautical Science, JAXA);
Saiki, K. (Osaka University); Ohue, H. (Tokusen Kogyo Co. Ltd.) 273

6. **Flexure-based Cutting Force Dynamometer**
Gomez, M.; Schmitz, T. L. (University of North Carolina-Charlotte) 277

7. **Direction-Dependent Receptances for Anisotropic Nickel Superalloy**
Honeycutt, A.; Schmitz, T. L. (University of North Carolina-Charlotte);
Glavicic, M. (Rolls Royce) 283

8. **Analysis of the Basic Performance of the Hybrid System Using Fluid Jet and Pad Polishing**
Je, T.-J.; Jeong, J.-Y.; Lee, J.-R.; Moon, S.-H.; Choi, D.-S.
(Korea Institute of Machinery & Materials(KIMM)) 288

9. **Microblast-assisted Metal Polymer Hybrid Joining**
Kajihara, Y.; Tamura, Y.; Kimura, F. (The University of Tokyo);
Yamaguchi, E. (Sintokogio Ltd.) 292

10. **Tool Wear and Chip Formation in Turning of Heat-resistant Alloy of Cr-Mo-V Forged Steel**
Kawamura, Y.; Takino, H. (Chiba Institute of Technology) 297

11. **A Study on Circular Test for the Parallel Kinematic Machine Considering Kinematic Errors ***
Lee, H.-H.; Yang, S.-H. (Kyungpook National University)

12. **Development of Digital Manufacturing Platform in Wafer-level Optics**
Lin, C.-T.; Chang, K.-D.; Gu, J.-N.; Lin, H.-Y.;
Chou, T.-H. (Industrial Technology Research Institute) 301

13. **Tool Path Optimization for Slow Tool Servo Assisted Ultra-Precision Diamond Turning of Micro Lens Arrays**
Liu, Y.; Zhang, P. (Harbin Institute of Technology) 307

14. **Develoment of a Surrogate System to Study the Dry Turning of Plutonium**
McNutt, N.; Dow, T. A.; Wong, A. R.; Garrard, K. P. (North Carolina State University) 311

***No Abstract Available**

15. **Tool Path Planning for Ultra-Precision Machining of Interrupted Optical Surfaces Based on NURBS Surfaces**
Morgan, C. J.; Rubeo, M. A. (Moore Nanotechnology Systems 317

17. **Ultra-high Precision Grinding of Optical Glass Using Acoustic Emission Monitoring Technique**
Onwuka, G. R.; Odedeyi, P. B.; Abou-El-Hossein, K.; Abdulkadir, L. N. (Nelson Mandela University) 321

18. **CFD Simulation of Injection Molding Processes**
Schmuetz, J.; Karnatz, L.; Bartsch, P. (Beuth University of Applied Sciences Berlin) 325

19. **Investigating the Self-protective Tool Formation during Cutting of Titanium Alloy**
Song, X.; Takahashi, Y.; Ihara, T. (Chuo University) 329

20. **Preliminary Study on Figuring of Reaction-sintered Silicon Carbide by Plasma Chemical Vaporization Machining**
Sun, R.; Ohkubo, Y.; Kawai, K.; Arima, K.; Yamamura D. K. (Osaka University) 335

21. **Modified Dwell Time for Free-form Optical Elements Polishing**
Sun, X.; Zha, J.; Chen, Y.; Li, Y. (Xi'an Jiaotong University) 339

22. **Fundamental Design Study on High-speed Aerostatic Spindle with Water-Cooling Function**
Yamazaki, S.; Nakao, Y. (Kanagawa University) 344

23. **Numerical Simulation Analysis and Design of Membrane-type Restrictor ***
Yang, Y. L.; Huang, T.-T.; Lin, S. C.; National (Tsing Hua University)

24. **Feasibility Study on Precision Compression Molding of Chalcogenide Glass Micro-Optical Elements**
Zhang, L.; Zhou, W.; Yi, A. Y. (The Ohio State University) 350

25. **Design and Fabrication of Multiple-Folded Compact Imaging System using Freeform Surfaces ***
Zhou, W.; Yi, A. Y. (The Ohio State University)

27. **A Curved Surface-Insensitive Optical Sensing Technique for Precision Spindle Health Monitoring**
Lee, C-B (Texas A&M University); Kim, G. (Tri-N Co. Ltd.) 353

28. **Fabrication of Mirco-Holes Array Through Multiple Electrodes with Distributed μ-pulsed Electrochemical Machining**
Thalkar, M.; Patel, D.S.; (Indian Institute of Technology Kanpur); Jain, V.K. (M.A.N.I.T. Bhopal); Ramkumar, J. (Indian Institute of Technology Kanpur) 357

29. **A Parallel-Axis Grinding Method for Large Aspect Ratio Internal Threads**
Wu, G.; Li, Z.; Wang, G.; (Harbin Institute of Technology). 364

30. **Development of an Automatic Grinding System for Servo Valve Spool Throttling Edge**
Guo, H.; Li, Y.; Yang, Z.; Wang, G.; (Harbin University of Science and Technology) 369

***No Abstract Available**

31. **Statistically Based on-Target Optimization in Micro-Milling of Titanium Alloy for Biomedical Applications**
Zhang, X.; Li, Y.; Wang, G.; (Harbin Institute of Technology) 375

32. **Advanced Vibration Control for Ultra Precision Machining Technology**
Hashimoto, T.; Kamal, A.M.; Jacobs, B.H.;
Roblee, J.W.; (Ametek Precitech, Inc.); Worthey, J.L. (Ametek TMC). 381

33. **Process Chains for the Mass Production of Functional Structured Surfaces**
Schönemann, L.; Holthusen, A.;
Riemer, O.; (LFM Laboratory for Precision Machining of the Leibniz-IWT). 385

34. **Machined Surface Quality Improvement for CFRP Hole Making Process Using Ultrasonically Assisted Drilling**
Kim, T.-G.; Shin, K.; Jeong, A.-M.; An, J.-W.; Kim, H.-Y.;
Kim, C.-H.; Lee, S.-W.; (Korea Institute of Industrial Technology (KITECH) 389

35. **Preparing and Repairing Precision Ground Surfaces Using Flatstones**
Arneson, H. (Professional Instruments Company) 393

36. **Characterizing Chemical Wear of Single Crystal Diamon Tools in Cutting Alloys**
Blum, A.; Venditti, K.; Patel, R.;
Evans, C. (University of North Carolina at Charlotte) 397

37. **Diamond Turning Plastic Optics**
Bodlapati, C.; Dow, T. A.; Wong, A. R. (North Carolina State University);
Sohn, A. (Oculus) 401

***No Abstract Available**

Poster Session 2

Wednesday - November 7, 2018

3:30 PM - 5:00 PM

Session Chair: Brian O'Connor (Aerotech)

Controls and Mechatronics

1. **Compliant Spindle for Robotic Grinding**
   Brown, A. R.; Slocum, A. H. (Massachusetts Institute of Technology). 409
2. **CFRP Drilled Holes Inspection System with Reaction Force Compensation Mechanism**
   Kim, H. Y.; Seo, C. H.; Jo, J. H.; Kim, T.-G.; Kim, C.-H.;
   Lee, S. S. (Korea Institute of Industrial Technology); Lee, M.-G. (Ajou University) 415
3. **Frequency Response Functions for Sliding Friction Contacts**
   Kossack, C. A.; Ziegert, J. C.;
   Schmitz, T. L. (University of North Carolina-Charlotte) 419
4. **Optimally Locating Multiple Tuned-mass-dampers for Vibration Reduction in Machine Tool Structure**
   Lee, J.; Kim, C.-J. (Korea Institute of Machinery & Materials (KIMM));
   Lee, C.; Lee, K. (Doosan Machine Tools Co., Ltd.) 425
5. **Control of Semi-active Suspension in High Speed Capsule Train by Using Hardware-in-the-loop Simulation Experiment**
   Lee, J.-H.; You, W.-H.; Lim, J.-Y.; Lee, K.-S. (Korea Railroad Research Institute) 430
6. **Design of Mobile Machine Tools with Wheels**
   Lee, S.; Kim, H.; Ro, S.-K. (Korea Institute of Machinery & Materials (KIMM)). 434
7. **Development of Dynamic Model for the Special Prototype of Four-axis Machine Using Coordinate Transformation Method**
   Song, C. K.; Pham, V. D.; Lee, C.-H.
   (Korea Institute of Machinery & Materials (KIMM)) 438
8. **Design and Experiment of Noncontact Eddy Current Damper Module in Linear Motion System with Air Bearing ***
   Song, H.; Seo, C.-H.; Sung, E.; Jeon, Y.; Choi, Y.-M.; Lee, M. (Ajou University);
   Kim, K. (Korea Polytechnic University); Jeong, J. (Korea University)
9. **Reference Trajectory Generation of Decouplable Coarse-fine Stage for Point-to- point Positioning Applications**
   Yoon, D.; Okwudire, C. E. (University of Michigan) 442
10. **Energy-efficient Electromagnetic Teeter-totter Actuator with Magnet Flux-biasing and Latching**
    Yoon, J. Y.; Bhushan, B.; Trumper, D. L. (Massachusetts Institute of Technology) 448
11. **Transfer Function Identification Using Controller with Limited Internal Memory**
    Haase, T.; Köhler, R.; (Physik Instrumente (PI) GmbH & Co. KG) 452

***No Abstract Available**

12. **Overview of an Actively Damped Vibration Isolation System for Ultra High Vacuum Optical Experiments**
Fernandez Galiana, A. (Massachusetts Institute of Technology);
Matichard, F. (California Institute of Technology). 456

13. **Energy Optimal Control of a Hybrid Feed Drive Under Variable-Frequency Disturbances ***
Duan, M.; Ramani, K.S.; Okwudire, C.E.; (University of Michigan)

Metrology Systems and Techniques

1. **Surface Metrology Using Extended-Range Partitioned Aperture Wavefront Sensing**
Beaulieu, D. R.; Bifano, T. G. (Boston University) 462

2. **An Investigation of Cosine Error for Scanning Probe Measurements of Freeform Surfaces**
Betters, E.; Copenhaver, R.; Tarbutton, J.;
Schmitz, T. L. (University of North Carolina- Charlotte);
Lee, C-B, (Tennessee Technological University) 466

3. **Precision Non-contact Fiber Optic Displacement Sensor Based on Near-field Specklegram**
Feng, F.; Chen, W.; Lin, W.; Chen, D.;
Chen, S.-C. (The Chinese University of Hong Kong) 471

4. **Geometric Error Measurement of the Linear Axis of CNC Machine Tools by Multilateration Using Four Laser Tracers**
Han, L.; Zha, J.; Chen, Y. (Xi'an Jiaotong University) 476

5. **Direct Measurement of Gauge Block Using Laser Interferometer ***
Jeong, C. Y.; Kim, M. S.; Kim, J. A.; Kang, C.-S.; Eom, T.-B.
(Korea Research Institute of Standards and Science)

6. **New 3D Figure Measurement System by Angle Integration**
Miyawaki, T. (Nikon Corporation). 480

7. **Influence of Rotary Table Error Motions to Cylindrical Gear Measurements ***
Peng, Y.; Wang, Q.; Goch, F. G. (University of North Carolina-Charlotte)

8. **High-resolution Non-fluorescent Imaging with Low-coherence Interference Structured Illumination Microscopy**
Usuki, S.; Shibata, G.; Miura, K. T. (Shizuoka University) 484

9. **CMM Interim Performance Check Part 1: Design Criteria**
Valdez, L. M.; Montaño, J. D.; Valdez, M. O. (Los Alamos National Laboratory). 488

10. **CMM Interim Performance Check Part 2: Case Study**
Valdez, L. M.; Valdez, M. O.; Montaño, J. D. (Los Alamos National Laboratory). 492

11. **Performance Investigation of Large-scale Rotary Tables Under Loads**
Wang, Q.; Goch, F. G.; Groover, J.; (University of North Carolina-Charlotte;)
von Freyberg, A.; Horn, F.; Fischer, A. (University of Bremen);
Steffens, N. (Hexagon Manufacturing Intelligence) 496

***No Abstract Available**

12. **On-machine and In-laboratory Investigation of Errors of Probes for CNC Machine Tools ***
Wozniak A.; Jankowski, M. (Warsaw University of Technology)

14. **The Effect of Suqareness on the Performance of the Ultra-Precision Machine**
Lai, T.; Peng, X.; Tie, G.; Shi, F.; Zhou, L.; Tian, Y.;
(National University of Defense Technology). 501

15. **Using Error Separation to Test Ultra High Accuracy Spindles**
Arneson, D.; Arneson H.; Oss, D.; (Professional Instruments Company) 505

16. **Using Grejda Optimization to Determine the Best Orientation of a Spindle**
Knapp, B.; Oss, D.; (Professional Instruments Company) 508

Precision Design of Instruments and Machines

1. **Development of a Flexure-based Modal Hammer**
Gomez, M.; Betters, E.; Copenhaver, R.; Schmitz, T. L.
(University of North Carolina- Charlotte) 513

2. **Optimal Reaction Wrench Measuring Platform ***
Kumar, R.; Jain, A.; Khatait, J. P. (Indian Institute of Technology Delhi)

3. **A 3-D Nonlinear Analytical Stiffness Model for Deflected Leaf Springs**
Nijenhuis, M.; Meijaard, J. P.;Brouwer, D. M. (University of Twente). 517

4. **Self-alignment of Kinematic Couplings: Effects of Deformations**
Patti, F.; Vogels, J. M. (VDL ETG Technology & Development BV). 521

5. **On the Design of Long Range Multiaxial Nanofabrication Machines Based on Cartesian Nanopositioning Systems with Additional Ultra Precision Rotations**
Schienbein, R.; Fern, F.; Theska, R.; Füßl, R. (Ilmenau University of Technology) 527

6. **On the Efficient Simulation of the Flexible Multibody Dynamics of Flexure Based Precision Mechanisms Using Superelements**
Schilder, J.; Ellenbroek, M.; van den Belt, M.; de Boer, A. (University of Twente). 533

7. **A Three-Dimensional Beam Ray Tracing of Laser Transportation System**
Shi, H.; Lafortune, K. N.; Robinson, J.; Fry, A.; Spiga D.
(Stanford University) 538

8. **Design of Compact Linear Nanopositioning Flexure Stages with Centimeter Travel Range for X-Ray Instrumentation**
Shu, D. (Argonne National Laboratory) 543

9. **Efficient Modelling of Short and Wide Leaf Springs Using a Superelement Formulation**
van den Belt, M.; Schilder, J.; Brouwer, D. M. (University of Twente) 547

***No Abstract Available**

10. **6-DOF Force Measurement Platform Used for Mapping Functions in Magnetic Levitation Systems**
Gloess, R.; Goos, A.; (Physik Instrumente (PI) GmbH & Co.KG) 552

11. **A Novel Semi-Active Joint for Simultaneously Achieving Fast Settling and Excellent In-Position Stability in Point-to-Point Positioning**
Dong, X.; Okwudire, C.E.; (University of Michigan). 557

12. **Design of a Meta-Material for the Torsional Reinforcement of a Leaf Spring**
Andree, D.J.; Nijenhuis, M.; Brouwer, D.M.; (University of Twente) 563

13. **Precision Scanning Onboard the NASA Tropics Mission**
Gillmer, S.; McMenamin, C.; Powers, B.; Racamato, J.; DiLiberto,, M.; Cunningham, A.; Fuhrman, L.; Crompton, D.; Michael, S.; Clark, K.; Blackwell, W.; (Massachusetts Institute of Technology) 569

14. **Compressed Air System for Ultra Precision Air Bearing Spindles**
Arneson, S.; Arneson D.; Knapp, B.; Oss, D.; (Professional Instruments Company) 575

15. **History of the Blockhead Spindle**
Arneson, C.D.; Liebers, M.J.; (Professional Instruments Company). 578

16. **Inverted Curved Flexure Hinge with Torsional Reinforcements in a Printed Prosthetic Finger**
Boers, A.S.; Naves, M.; Garcia Rodriguez, L.A.; Brouwer, D.M.; (University of Twente) 582

17. **Experimental Design of a Small Stroke Nanometer Resolution Displacement Actuator Based on Thermal Expansion ***
Nuij, P. W. J. M.; van den Hoogenhof, P. (Eindhoven University of Technology); Verbaan, K. (NTS-Group)

18. **A Framework for Error Budgeting in Precision Machine Design ***
Duenner, A. (Magic Leap, Inc.); Slocum, A. H. (Massachusetts Institute of Technology)

***No Abstract Available**

Technical Papers

INFIDELITY AND THE CALIBRATION OF OPTICAL SURFACE TOPOGRAPHY MEASURING INSTRUMENTS

Richard Leach[1*], Peter de Groot[2], Han Haitjema[3]
[1]Manufacturing Metrology Team, Faculty of Engineering, University of Nottingham, Nottingham NG8 1BB, UK
[2]Zygo Corporation, Middlefield, CT 06455, USA
[3]KU Leuven, Mechanical Engineering Department, B-3001 Leuven, Belgium

1. INTRODUCTION

The ability to measure and characterise surface topography is vital in advanced manufacturing and to many precision engineering applications [1,2]. Modern advanced applications require surfaces with complex specifications and with a large range of topography structures. Such structures can vary from random to highly deterministic and can be a mixture of both.

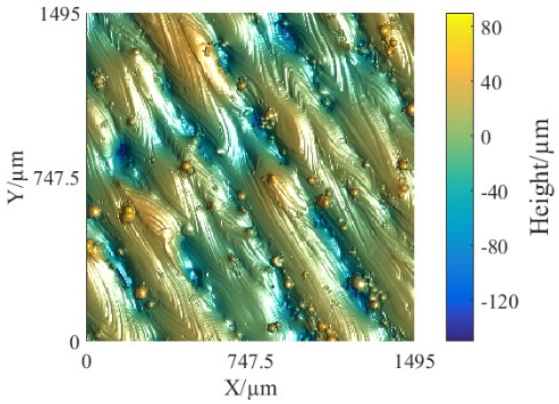

FIGURE 1: Surface manufactured using a laser powder bed fusion process, illustrating the mix of deterministic and random structures, measured with a focus variation microscope

An example of a complex structure that is receiving a lot of attention relates to the metal powder bed fusion processes for additive manufacturing. As shown in FIGURE 1, such surfaces have deterministic features that are the result of the path of the energy source (e.g. weld tracks) and random features that are the result of highly-complex fluid dynamic and high-speed thermal processes (e.g. spatter particles and cracks) [3,4]. High slope angles, both specularly and diffusely reflecting surfaces in the same part, re-entrant features, as well as highly-complex freeform geometries are some of the issues that challenge the use of conventional contact and optical instruments with such surfaces [5,6].

The question we address here is: can an instrument calibration framework be designed that will give a basis for the estimation of the measurement uncertainty when measuring such complex surfaces?

2. THE CURRENT SITUATION

Traditionally, instrument calibration for areal surface topography measurement has relied on a manageable, but arguably incomplete, subset of instrument checks for scale and non-linearity of the measurement axes. Often these use familiar calibration specimens, known as material measures, that carry certifications that provide traceability to the metre.

One well-known material measure for determining the height response of an instrument is the step height [7,8]. Along with grid artefacts for lateral dimensions [9], such material measures are used to calibrate the scales of an instrument. These calibrations, whilst essential, tell us little about how the instrument would respond to complex surface features, such as those shown in FIGURE 1. Material measures that only capture information about the ability of an instrument to measure a series of step-like transitions do not inform us about how the instrument responds to various slope angles [9].

With a few exceptions [10], it is uncommon in manufacturing applications to encounter an uncertainty budget based on calibrations and individual influence factors alone. Instead, quality control engineers perform gauge capability tests directly on the parts that they wish to measure. The results of gauge testing, instrument correlation and demonstrations of control of functional behaviour are the most common ways to qualify an instrument for manufacturing metrology [11]. This leaves a gap in our understanding of the origins of measurement error and how to improve metrological performance in manufacturing applications.

3. EXTENDING THE MEASUREMENT RANGE

Considerable work has gone into improving the quality of non-contact, optical measurements so as to extend the range of applications to surfaces with steep slopes [5,9,12]. At the same time, however, the recognised advances in instrument design and performance have left unanswered the question of calibration for the purpose of a first-principles uncertainty assessment. Pressing the matter further, many optical instruments today take advantage of the scattering from fine roughness on slope angles greater than the classical aperture limit of the objective [13-15].

Calibration for slope effects is integral to some modern interferometry methods, using a purely empirical approach with a wide range of known sample slopes as the source of calibration data. Right-angle vee-groove surfaces can be measured using dual-probe configurations, where measurements from both probes are combined [16]. The slope range can even be extended to microlenses with highly aspheric departures, using field-stitching techniques enabled by correlation of surface roughness detection on the nanometre scale [17]. The measurement geometry of FIGURE 2 requires correction for distortion and field-dependent slope errors for each image tile prior to composition of the final aspheric form measurement of FIGURE 3. This empirical approach serves this application well, but the final performance specification relies on repeatability, reproducibility and tool matching results that are not easily incorporated in an uncertainty budget.

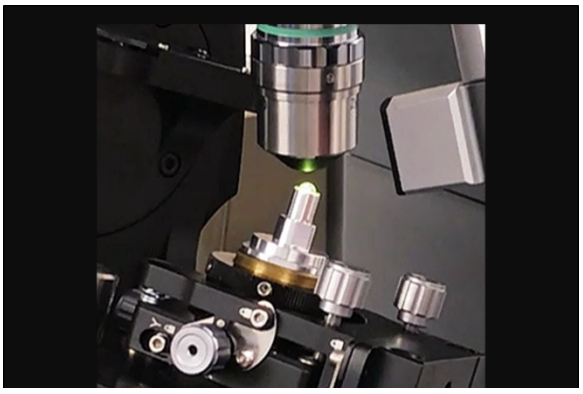

FIGURE 2: Micro-asphere metrology using high-slope measurements at multiple viewing angles in an interference microscopy.

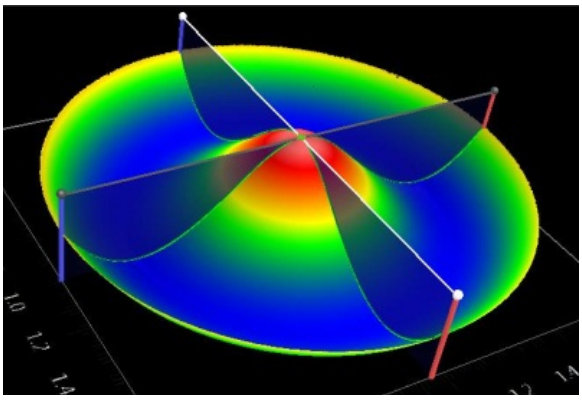

FIGURE 3: Example measurement of a 1.8 mm diameter microlens having 60 µm of aspheric departure. Cross-sections are indicated for illustration.

Focus variation microscopy uses incoherent illumination and detection and can take advantage of the scattering from high slope angles so long as the sloped surface has a certain degree of roughness [13,18] (which is also a basic requirement of FVM due to its use of contrast to detect height differences [18]). Recent advances in focus variation, however, allow high slope measurement even for relatively smooth surfaces, by employing advanced illumination techniques and multi-axis motion systems [19]. However, despite the theory of FVM being well advanced in the conventional Fourier optics regime [20], the combination of specularly reflected light with diffusely reflected light at high slope angles is not yet adequately captured in theoretical models. In the presence of multiple scattering, the spatial frequency response of FVM is not currently known, although there are plans to address this deficit (see section 4). The usual question springs to mind: with complex surfaces, how can we be confident with the resulting topography? FIGURE 4 shows an example of a hole measurement using FVM, where slopes can be seen that are clearly outside the conventional numerical aperture (NA) angle limit [20].

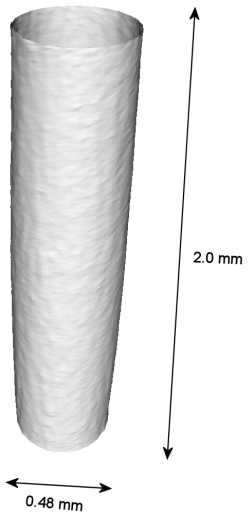

FIGURE 4: Hole measurement using FVM.

Similar arguments to those presented above for FVM apply to imaging confocal microscopy (ICM) [21], and slope measurement capabilities greater than the conventional NA acceptance angle are quoted on some commercial instrument specifications. However, high-slope angles can also cause significant issues for ICM, often resulting in spikes [5]. These sometimes can be avoided by careful tuning of the instrument settings, but this option is not always available when measuring highly variable surface topographies.

4. ADVANCED APPROACHES

It would be more than simply satisfying if the understanding of the fundamental physics of the measurement process could be advanced to the point where the uncertainty of high-slope measurements can be properly estimated from first principles.

In addition to retrace, image distortion and aberration errors that increase with surface slope, fundamental issues arise when light is reflected at angles greater than the NA slope limitation. At some spatial frequencies, there may not even be a useful correlation between the measured texture and the actual surface characteristics. A number of physical effects cause simple measurement models to become invalid and result in a non-linear response of the instrument to surface topography. Examples of such effects are multiple reflection, shadowing and surface plasmon resonance. The only way to model such effects is using rigorous approaches that significantly increases the complexity of the problem while reducing the speed at which solutions can be calculated.

Consider the comprehensive theory developed at the University of Nottingham and Loughborough University, leading to a 3D transfer function for the case of weak scattering [22]. This theory is only valid within the traditional aperture or NA slope limitation. An alternative boundary element method (BEM) promises to allow for predictive response of an instrument from almost any complex surface shapes [23]. With such models, it may be feasible in the future to establish task-specific uncertainty budgets for a wide variety of measurement applications with a common set of material measures. This of course presupposes that these theories can predict measurement values for a known surface topography, and that the inverse problem is soluble without ambiguity.

5. THE ROLE OF THE STANDARDS

ISO Technical Committee 213 Working Group 16 is currently working towards a framework for calibration of surface topography instruments [9]. The proposed framework involves the determination of a number of *metrological characteristics* that are designed to quantify the various influence factors that affect the uncertainty in a measurement carried out with a surface topography instrument [9,24,25]. These characteristics include established concepts such as scale linearity, amplification coefficient, flatness, noise, topographic spatial resolution and *x-y* mapping deviation for the response of an instrument. The corresponding calibration draft document is ISO 25178-700.

A metrological characteristic *Topography fidelity* has been introduced into the ISO framework as a kind of miscellaneous category for all contributions to the uncertainty budget—including surface slope-dependent errors—that are not captured by the more well-known calibrations.

An example calibration for topography fidelity is the determination of the instrument transfer function (ITF), defined as the square root of the ratio of the measured power spectral density (PSD) of a surface structure to its known or independently-determined PSD. In essence, the ITF quantifies the response of a topography-measuring instrument to specific spatial frequencies in the surface structure [26]. The ITF is widely used in the testing of optical components, such as lenses and mirrors, and can be calibrated using a variety of available artefacts, including small step features etched

into glass [26]. However, it is understood that the range of applicability of the ITF is limited, particularly for technical surfaces with rough or complex textures or extreme slope angles. It is also not clear how an ITF evaluation can be incorporated into an uncertainty budget. Consequently, although the ITF concept is defied in the draft ISO 25178-700 document, methods of ITF calibration remain informative rather than normative.

A similar situation exists for other proposed methods of calibrating topography fidelity. A common theme is to use a material measure having a shape that is close to the measurand, and that has been calibrated independently and/or or manufactured in such a way that the real geometry is known. Measuring this specimen using the instrument to be evaluated may give quantitative information about the deviations that can be used in an uncertainty budget.

Artefacts are under development that include a multitude of established difficult-to-measure features such as steep steps and grooves of various spacings and depths. Example artefacts under development include the chirp standard [27] that is comprised of square-waves of varying lengths and depths, and a sample (in fact a collection of samples) [28] that contains a multitude of surface structures on a limited area. Recently a circular chirped specimen with several degrees of randomness in lateral size has been presented to ISO 213 [29]. In addition to these artefacts, there have been proposals for metrics or measures of agreement to allow for reporting and specifying of topography fidelity [30].

It seems, however, unrealistic to suppose that we can design a single artefact that includes all possible surface structures. For less defined structures than the reference specimen, estimates of the uncertainties are not sufficiently reliable. A further issue is that many of these proposed structures have sharp edges or other features that result in measurement outliers, false data or, with interferometry, fringe-order errors that are not easily summarised as statistical variations for the purpose of an uncertainty budget. Finally, for many of these proposed calibration specimens, not much more can be done than taking deviations for granted and trying to quantify these without a solid understanding as to the origins of the errors.

6. THE WAY FORWARD

In the short term, we would argue that it is not yet feasible to establish an instrument calibration framework that would allow for the estimation of uncertainty for general, practical applications in manufacturing metrology. The basic calibrations of scales are a necessity for traceability and verification of instrument function; but they do not replace the traditional gauge capability test on actual parts. Consequently, there is an emerging consensus that it would be premature and perhaps misleading to include in the ISO 25178-700 calibration document specific methods regarding topographical fidelity that go beyond the definition of terms and description of example artefacts.

To advance further, it is clear that additional theoretical work is essential to understanding and reducing the errors resulting from complex surface structures and high slopes. Concurrently, work will continue on the development and proof of the value of material measures, alternative procedures, and quantifiers for calibrating slope-dependent response. These efforts will progressively close the gap between calibration and gauge capability, allowing for a more predictive estimate of instrument performance for diverse applications, and increased confidence in results.

The first but significant step in our current plan is to develop a series of “virtual instruments” that can predict the response of a number of optical instruments (initially CSI, FVM and ICM) for surfaces that have features which cause traditional linear transfer function theories to be invalid. This will be done by developing a 3D implementation of the BEM [23] described above (which is currently only available in 2D) and modelling the source and optics for each instrument modality. Once verified, such virtual instrument models can be used in uncertainty estimations for complex surfaces and perhaps to correct some systematic errors, therefore, improving the response of instruments to complex surface features. As the writer Jonut Díaz says: “Infidelity raises profound questions”. By chipping away the major causes of infidelity in surface topography measurement, we will also gain a deeper understanding of how instruments operate and, potentially, how to improve them.

AKNOWLEDGEMENTS

The authors would like to thank the members of the ISO committee 213 WG 16 for contributing to much of this work. RKL would like to acknowledge funding from EPRSC project EP/M008983/1.

REFERENCES

[1] Whitehouse DJ. Handbook of surfaces and nanometrology, 2nd Edition. CRC Press: 2010.

[2] Leach RK, Smith ST. Basics of precision engineering. CRC Press: 2018.

[3] Senin N, Thompson A, Leach RK. Characterisation of the topography of metal additive surface features with different measurement technologies. Meas. Sci. Technol. 2017;28:095003.

[4] Fox JC, Moylan SP, Lane BM. Preliminary study toward surface texture as a process signature in laser powder bed fusion Additive manufacturing. Proc. ASPE Summer Topical. 2016;168-173.

[5] Thompson A, Senin N, Giusca CL, Leach RK. Topography of selectively laser melted surfaces: a comparison of different measurement methods. Ann. CIRP. 2017; 66:543-546.

[6] Townsend A, Senin N, Blunt LA, Leach RK, Taylor J S. Surface texture metrology for metal additive manufacturing: a review. Prec. Eng. 2016;46:34-47.

[7] Leach RK. Is one step height enough? Proc. ASPE. 2015;110-113.

[8] de Groot D, Fitzgerald D. Measurement, certification and use of step-height calibration specimens in optical metrology. Proc. SPIE. 2016;10329.

[9] Leach RK, Giusca C L, Haitjema H, Evans CJ, Jiang X. Calibration and verification of areal surface texture measuring instruments. Ann. CIRP. 2015;64:797-813.

[10] de Groot, P., Biegen, J., Clark, J. et al. Optical Interferometry for Measurement of the Geometric Dimensions of Industrial Parts. Applied Optics. 2002; 41: 3853-3860.

[11] Montgomery D. Statistical quality control: a modern introduction. Wiley, New York: 2009.

[12] Badami VG, Liesener J, Evans CJ, de Groot P. Evaluation of the measurement performance of a coherence scanning microscope using roughness specimens. Proc. ASPE 2011;23-26.

[13] Hiersemenzel F, Petzing J, Leach RK, Helmli F S, Singh J. Areal texture and angle measurements of tilted surfaces using focus variation methods. Proc. 3rd Int. Conf. Surface Metrology, Annecy, France, Mar. 2012;85-89.

[14] Fay MF, Colonna de Lega X, Schmidt M. Measuring high-slope parts using coherence scanning interferometry. Proc. ASPE. 2014.

[15] Li L, Liu J, Liu Y, Liu C, Zhang H, You X, Gu K, Wang Y, Tan J. A promising solution to the limits of microscopes for smooth surfaces: fluorophore-aided scattering microscopy. Nanoscale. 2018;10:9484-9488.

[16] Zhang T, Feng G, Martin T, Xiangqian J. A method for inspecting near-right-angle V-groove surfaces based on dual-probe wavelength scanning interferometry. Int. J. Adv. Manuf. Technol. 2018:1-7.

[17] Colonna de Lega X, Dresel T, Liesener J, Fay M, Gilfoy N, Delldonna K, de Groot P. Optical form and relational metrology of aspheric micro optics. Proc. ASPE 2017;20-23.

[18] Danzl R, Helmli F, Scherer S. Focus variation – A robust technology for high resolution optical 3D surface metrology. J. Mech. Eng, 2011;57:245-56.

[19] Zangl K, Danzl R, Helmli F, Prantl M. Highly accurate optical µCMM for measurement of micro holes. Proc. CIRP. 2018;In press.

[20] Nikolaev N, Petzing J, Coupland JM. Focus variation microscope: linear theory and surface tilt sensitivity. Appl. Opt. 2016;55:3555.

[21] Artigas R. Imaging confocal microscopy. In: Leach RK. Optical measurement of surface tomography, Spinger, 2011.

[22] Su R, Wang Y, Coupland JM, Leach RK. On tilt and curvature dependent errors and the calibration of coherence scanning interferometers. Opt. Express 2017;25:3297-3310.

[23] Simonsen I. Optics of surface disordered systems. Eur. Phys. J. Special Topics. 2010;181:1-103.

[24] Haitjema H. Uncertainty in measurement of surface topography. Surf. Topog. Met. Prop. 2015;3:035005.

[25] Haitjema H., Leach RK. (2018) Surface texture metrological characteristics. In: The International Academy for Production, Chatti S., Laperrière L., Reinhart G., Tolio T. (eds) CIRP Encyclopaedia of Production Engineering. Springer, Berlin, Heidelberg.

[26] de Groot P, Colonna de Lega X, Sykora DM, Deck L. The meaning and measure of lateral resolution for surface profiling interferometers. Optics and Photonics News. 2012; 23:10-13.

[27] Seewig J, Eifler M, Wiora G. Unambiguous evaluation of a chirp measurement standard. Surf. Topog. Metr. Prop. 2014;2:045003.

[28] Eifler M, Hering J, Freymann GV, Seewig J. Calibration sample for arbitrary metrological characteristics of optical topography measuring instruments. Opt. Express 2018;26:16609-16623.
[29] Dai, G et al, Circular chirp for determination of the instrument transfer function and topographic fidelity, ISO/TC 213, WG 16, London, Feb 7, 2018, Document N771.
[30] Vorburger TV, Song J-F, Chu ML, Bui SH, Zheng A, Renegar TB. Applications of cross-correlation functions. Wear 2011;271:529–533.

EXPERIMENTAL VERIFICATION OF AN ERROR MAPPING TECHNIQUE FOR ROTARY TABLES/AXES

Qichang Wang, Jimmie Miller, Jesse Groover, Gert Goch
Center for Precision Metrology,
University of North Carolina at Charlotte,
Charlotte, NC, USA

1. INTRODUCTION

5-axis machine tools and 4-axis measuring devices are becoming increasingly popular, because the introduced rotary tables/axes facilitate a quick rotational positioning of complicated geometric workpieces, such as gears and freeform optics. However, characterizing the measurement uncertainty due to rotary tables/axes is nontrivial. One conventional calibration method [1] employs three LVDTs, a sphere, a polygon mirror and two auto-collimators for the measurement of the six error motions of a rotary table/axis. The authors proposed a new calibration method with a simpler, quicker and more flexible measurement setup, as well as a fully automated measurement process [2]. This method is able to calibrate the measuring device (3-axis CMM), rotary table and the artifact (a circular ball plate) simultaneously.

This paper compared performance of the proposed calibration method with experimental data from a spindle error analyzer (SEA) [3] on an aerostatic rotary table. Section 2 and Section 3 describe measurement setups and drift tests of two methods. Section 4 reports and discusses the results.

2. SPINDLE ERROR ANALYZER

2.1 Setup of SEA

SEA measures and analyzes a spindle's five error motions, including three translational error motions δ_x,δ_y and δ_z, and two tilt error motions ε_x and ε_y. Lion Precision SEA consists of a 1" dual master ball target, five noncontact capacitive sensors, a nest (sensor holder), seven temperature sensors, a data acquisition (DAQ) device and SEA software. Usually, the target is installed in the spindle's tool holder, and the nest is clamped on the table.

In rotary table calibration, the target was centered and fixed on the rotary table using three toe clamps. Unfortunately, mounting the sensor holder on the probe head of the CMM was not feasible, due to the weight of sensor holder exceeded the load limit for the probe head. As shown in Figure 1, an in-house made metrology frame fixed the sensor holder over the rotary table.

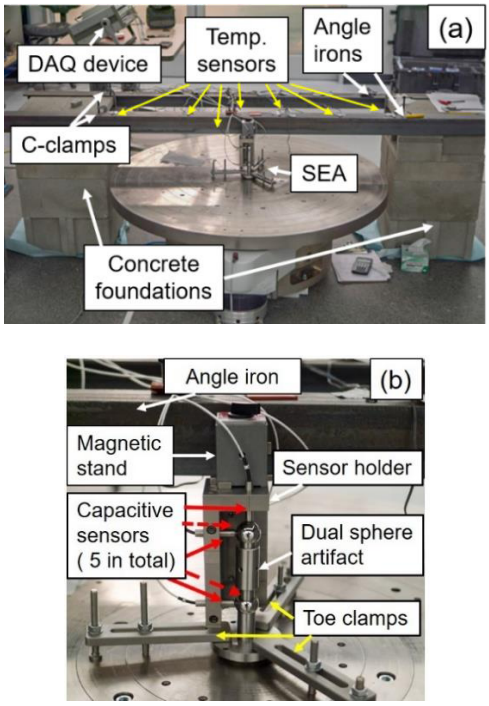

FIGURE 1. Setup of SEA on a Zollern ZART 1200.0390.0 *aerostatic rotary table: (a) illustration of an in-house made metrology frame, which fixed the sensor holder over the rotary table (b) fixture of SEA system on rotary table.*

The beam bridge type metrology frame consisted of two concrete towers and two angle irons. In a four-layer configuration of concrete block towers, each of the 1st, 2nd and 4th layers had two standard cored concrete blocks (0.194 m x 0.194 m x 0.397 m), while the 3rd layer had two cap concrete blocks (0.921 m x 0.194 m x 0.397 m). Blocks in even layers were oriented

perpendicular to the ones in odd layers. Loctite Power Grab Ultimate construction adhesive was applied to bond the blocks. Functioning as horizontal beams across two towers, two 1.500 m x 0.076 m angle irons were fixed at the edges of concrete towers with c-clamps. 0.163 m working space existed between the angle irons and rotary table.

The sensor holder was attached to an angle iron using a magnetic stand. Noncontact capacitive sensors X1 and X2 recorded x displacements of lower and upper spheres, respectively. Sensors Y1 and Y2 measured y displacements of the two spheres. Sensor Z2 measured z displacement of the upper sphere. Alignments of target and sensor holder were completed by trial and error method. In every iteration, the rotary table was rotated by one cycle. Offsets of the target in x and y directions were observed in SEA software. A T-handle hex wrench functioned as a micro-hammer to adjust the initial position of target.

2.2 Drift test of SEA system

An 18-hour drift test was performed to evaluate the stability of the metrology frame, sensor holder, artifact and associated fixtures. The rotary table was held static throughout the test.

The 1st to 6th temperature sensors were attached to the top of the angle iron which held the magnetic stand and nest (Figure 1(a)). Six sensors were evenly distributed between two concrete towers. Less than 0.05°C variation was observed (Figure 2(a)). The 7th sensor reported 0.1°C variation of ambient air temperature near the nest (Figure 2(b)). Less than 0.3 μm drifts were reported by sensors X1, X2, Y1 and Y2 (Figure 2(c)). Sensor Z2 recorded 1.5 μm drift, which may have resulted from the creeping of sensor holder due to gravitational force. Later experiments reflected much less drift.

However, X1, X2 and Z2 displacement sensors, as well as 7 temperature sensors, recorded oscillations with 4-minute periods (Figure 2(d)). X1 and X2 showed stable oscillation, while Z2 was more correlated with ambient temperature. Y1 and Y2 data were consistent throughout the drift test.

Two possible explanations regarding the cause of the oscillation were discussed. The first is that the air temperature of the room oscillates with a period of 4 minutes, caused by cycling of the environment control system. Theoretically, the thermal expansion of the metrology frame, magnetic stand and nest would shift the positions of the capacitive sensors and their readings. A second possible explanation is that the facility regulated the air pressure supplying the aerostatic bearings with a period of 4 minutes. Because the film thickness of axial and radial air bearings of the rotary table varied with the supplied pressure, the positions of rotor and attached double master sphere target were not expected to be consistent. In the mechanical design, there is a belt which causes a net force in the x direction. The recorded temperatures were correlated with the pressure variation and displacement sensors, because the supplied pressure variation also influenced the outlet temperature of air bearings.

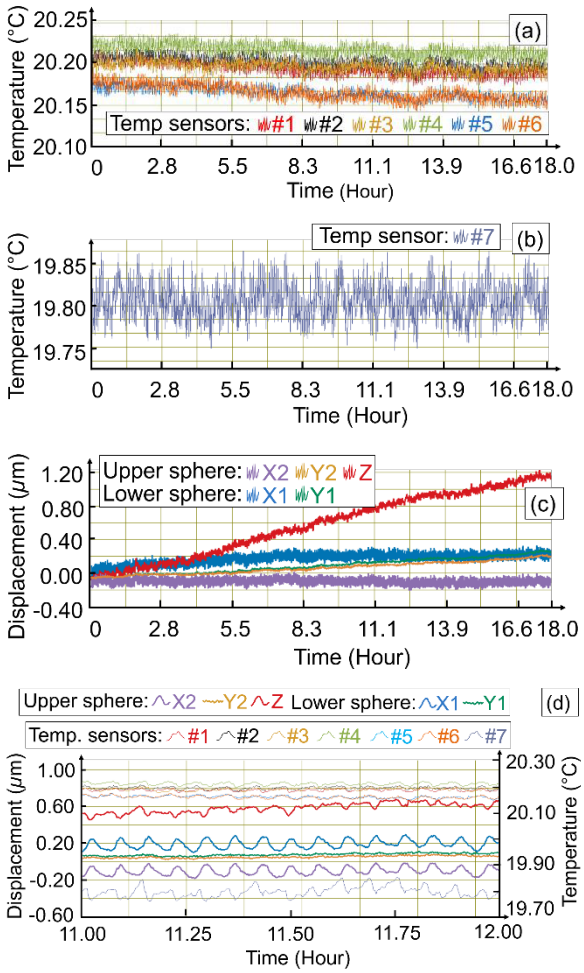

Figure 2. 18-hour drift test of SEA system: (a) temperature data of six sensors attached on an angle iron (b) ambient temperature near ball target (c) displacements data of five capacitive sensors (d) displacements and temperatures from the 11th hour to 12th hour.

Another test was carried out to further study the phenomena. A master sphere was fixed at the center of rotary table. Every two seconds, the CMM probed an equator point of the master sphere, in the -x direction. Displacements of the master sphere along the x-axis were recorded for 30 minutes. A similar test was carried out by repeatly probing the pole of the sphere in the -z direction.

As shown in Figure 3, the displacements had periods of 4-minutes, matching the results from the drift test. X and z displacements of the master sphere had magnitudes of 0.15 μm and 0.08 μm, respectively, which were similar to results from the previous drift test (Figure 2(d)). Because the CMM has higher non-repeatable probing deviations along the x-axis than along the z-axis, Figure 3(a) showed more scatter data than Figure 3(b). It is likely that oscillations with 4-minute periods originated from the oscillations of supplied air pressure. The built metrology frame provided very stable support to the sensor holder of the SEA.

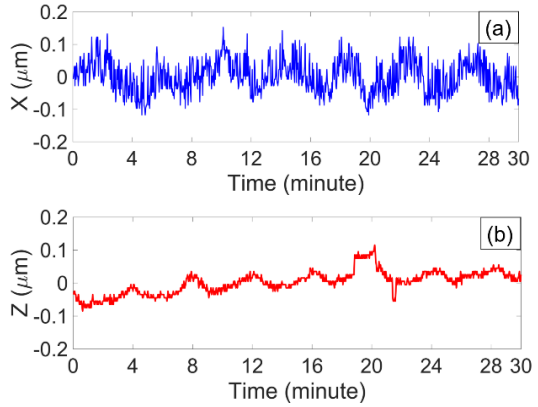

FIGURE 3. Displacements of a master sphere fixed at the center of rotary table, and repeatedly probed at a point in -x and -z directions, respectively: (a) displacement along x-axis (b) displacement along z-axis.

3. CIRCULAR BALL PLATE ARTIFACT

3.1 Design and fabrication of artifact

The designed circular ball plate has 12 spheres evenly distributed in a circular pattern. Using a relatively large diameter of ø400.00 mm helped reduce uncertainties of calculated tilt error motions and angular positioning deviations resulting from the CMM.

In this study, a double layer configuration was adopted (Figure 4). The lower plate functioned as a sacrificing layer to isolate clamping forces away from the primary artifact. Therefore, the upper plate was freed from distortion. A Maxwell style kinematic coupling between the upper and lower plates allowed a full constraint [5]. Instead of adding additional vee blocks, v-grooves were directly machined on the lower plate to reduce the overall height. The outer cylindrical surface assisted the centering of the lower plate.

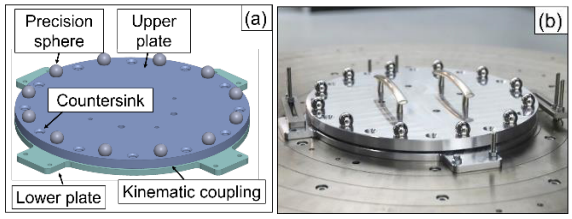

FIGURE 4. Double layer circular ball plate artifact: (a) schematic of artifact configuration (b) assembled artifact.

Countersinks assisted the precise positioning of spheres at installation. 0.3mm gaps were left between the bottom of spheres and the bottom surfaces of countersinks. Proper amount of epoxy glue filled the gap to fix the spheres, so that the circular contact lines between spheres and countersinks remained clean (Figure 5). 1" grade 3 spheres with 1/8" holes were used. By drilling the same size holes at the bottom of the countersinks, the spheres were fixed to the base plate firmly with short pins and epoxy glue.

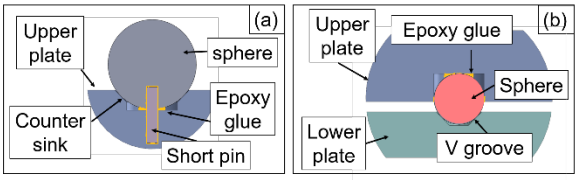

Figure 5. Illustration of ball plate design: (a) fixture of precision spheres (b) Maxwell kinematic coupling.

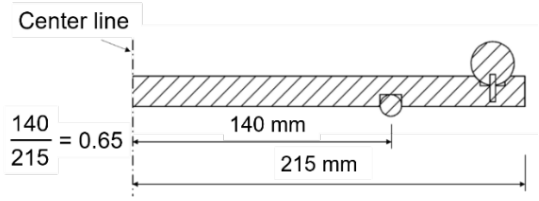

Figure 6. Least deformation of top plate can be achieved by setting the radial position of support points at 65% of the radius of disk [4].

To achieve minimum deflection of the upper plate with three-point support configuration, the radial

position of support points was 65% of the radius of plate [4]. Therefore, the radial positions of the three 0.5" spheres for kinematic mount were set as 140 mm from the center of upper plate (Figure 6).

3.2 Drift test of artifact

One week after assembly, the ball plate artifact was secured on the static rotary table for a drift test. The coordinates of all the spheres were measured continuously for 24 hours.

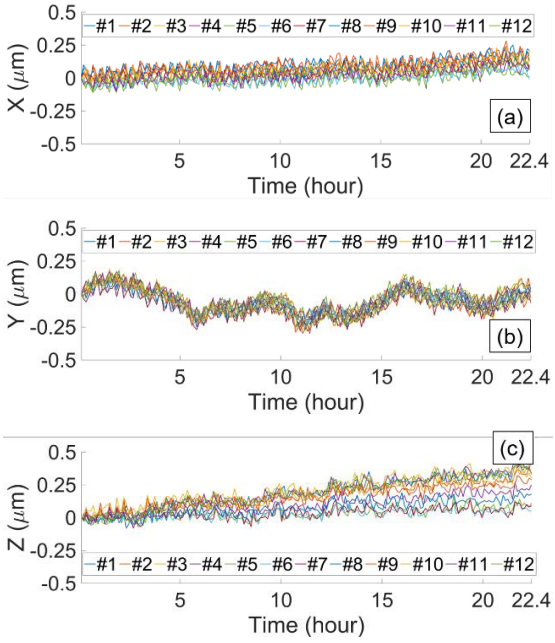

FIGURE 7. 22.4-hour Drift test of ball plate artifact by measuring its 12 spheres continuously: (a) displacements along x-axis (b) displacements along y-axis (c) displacements along z-axis.

In Figure 7(a) and 7(b), 12 spheres had the same trends, which indicated two things: (i) the artifact had high stability along x and y directions (ii) the environmental temperature control effectively limited the thermal expansion of the artifact. In this gantry-type CMM, the x-axis is parallel to the granite foundations (side walls), while the y-axis is parallel to the traveling beam. Although y-axis was not as stable as x-axis, the drift in y-axis was within ±0.25 μm. In Figure 7(c), 12 spheres have different drifting amounts between 0.05 μm and 0.3 μm. It is possible that the epoxy glue for the three lower spheres for kinematic coupling was not fully cured at drift test. The drift of the CMM along z-axis was low. One week after assembly, the ball plate reached an equilibrium state on the rotary table.

4. EXPERIMENTAL COMPARISON

4.1 Calibration results of SEA

The rotary table was rotated through 9 cycles in the counter-clock-wise (CCW) direction in steps of 7.5°. In Figure 8, purple triangles and yellow stars represent sampled error motions at rotary positions of from 2π to 10.08π and 10.08π to 18.16π, respectively. The repeatability periods of all five error motions were around 8.08π.

Differences between the two periods partially originate from the oscillations of the rotary table along x and z axes. Because the maximum rotating speed of the rotary table was several orders lower than that of spindles, SEA software did not detect and record the error motions of the rotary table. Instead, data was manually read and recorded in software's diagnostic mode, which required 30 minutes per cycle. Therefore, 0.2 μm and 0.1 μm oscillations along the x and z axes, respectively, cannot be separated from the corresponding error motions.

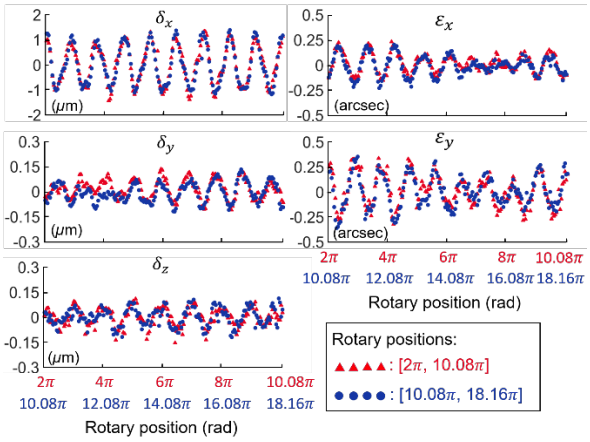

FIGURE 8. Separated error motions of rotary table by SEA.

As showed in Figure 8, δ_x was one order larger then δ_y and δ_z. 0.4 μm magnitude of δ_y was considered small for a heavy-duty rotary table. Amplitude of ε_x and ε_y were less than 0.3", which shows that the rotary table had low tilt error motions in non-load condition.

4.2 Comparison between two methods

For the ball plate test, the rotary table was rotated through 8 cycles in the CCW direction in steps of 7.5°. At every step, 15 points were probed on the #1, #3, #5, #7, #9 and #11 spheres.

Because this ball plate test was completed three months earlier than the SEA test, the two

experiments did not have a common reference rotary position. Therefore, data from the two experiments was aligned laterally for comparison. Error motions in following range of rotary positions were presented (Figure 9): (i) 8.17π to 16.25π for SEA test (ii) 4π to 12.08π for ball plate test.

δ_x separated by two methods were comparable. δ_y from the ball plate test had more scattered data than the SEA test. It may result from the residuals of the CMM and ball plate deviations, as well as the drift of the CMM's y-axis. In future study, iterative calculation might further reduce residuals of the first two sources. δ_z obtained by the ball plate test had smaller magnitude, but two-digit nanometers difference is acceptable.

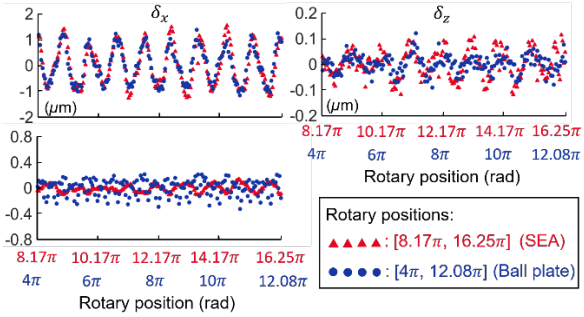

FIGURE 9. Separated error motions of rotary table, obtained by the SEA and the new method, with rotary positions in following ranges: (i) [8.17π, 16.25π] for SEA method (ii) [4π, 12.08π] for new method.

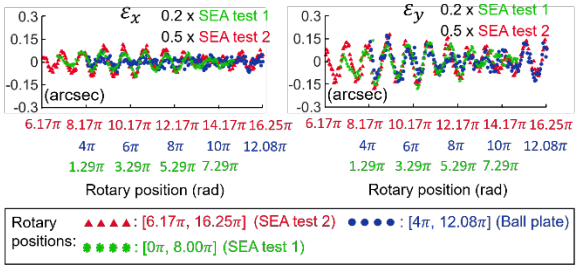

FIGURE 10. Separated error motions of rotary table, obtained by SEA and new method, where amplitudes of two SEA tests were multiplied by 0.2 and 0.5, based on rotary positions in following ranges: (i) [0π, 8π] for SEA test 1 (ii) [6.17π, 16.25π] for SEA test 2 (iii) [4π, 12.08π] for new method.

Although each tilt error motion separated by two methods have similar patterns, the amplitude of SEA results (SEA test 2) is around 100% larger than the new method. Another set of SEA test results (SEA test 1) was provided. The SEA system was removed and reinstalled for the second SEA test.

ε_x and ε_y from the new method and two SEA tests were aligned laterally for comparison (Figure 10). After multiplying the amplitudes of two SEA tests by 0.2 and 0.5, respectively, all three tests results are comparable. Because two SEA test results had similar patterns but different amplitudes, it is likely that a scaling error exists in the SEA test data.

5. SUMMARY

This paper compared performances of the SEA and the new circular ball plate method experimentally on an aerostatic rotary table. Measurement setups and drift tests are explained in detail. Comparable results of δ_x, δ_y and δ_z were obtained. Although each tilt error motion from the two methods has similar patterns, the amplitudes of SEA results were several times larger than the ones of the new method. Another SEA test revealed that a scaling error of SEA method may exist. Further investigation is needed to figure out the reason.

6. ACKNOWLEDGEMENT

The authors gratefully acknowledge the financial support by the Center for Precision Metrology at UNC Charlotte.

7. REFERENCES

[1] Suh, S.H., Lee, E.S., Jung, S.Y., 1998, Error modelling and measurement for the rotary table of five-axis machine tools. *The International Journal of Advanced Manufacturing Technology*, *14*(9) (pp.656-663).

[2] Wang, Q., Miller, J., Von Freyberg, A., Steffens, N., Fischer, A., Goch, G. (2018). Error mapping of rotary tables in 4-axis measuring devices using a ball plate artifact. *CIRP Annals*, *67*(1), 559-562.

[3] Lion Precision, www.lionprecision.com.

[4] Craig, L. D., Boulet, J. A. M. (1999). Deflections of a Uniformly Loaded Circular Plate with Multiple Support Points. 1; Introduction. *NASA Scientific and Technical Report Series*, NASA/TM-1999-209631.

[5] Slocum, A. (2010). Kinematic couplings: A review of design principles and applications. *International journal of machine tools and manufacture*, *50*(4), 310-327.

VIRTUAL OPTIMIZATION OF ARTIFACT BASED CALIBRATION OF MACHINE TOOLS

Gorka Aguirre, Beñat Iñigo, Julen Cilla and Harkaitz Urreta
Design and Precision Engineering
IK4-IDEKO
Elgoibar, Gipuzkoa, Spain

INTRODUCTION

Volumetric accuracy in machine tools was defined as the ability of the machine to produce accurate 3D shapes [1]. The development of volumetric calibration or error mapping strategies, and the compensation of the measured systematic errors, has been the focus of many research projects over the time [2].

The main challenge in this field has been the development of measuring devices and procedures able to map the main errors of the machine in their whole workspace within a reasonable time and with sufficiently low uncertainty. Calibrated artifact-based solutions were developed first, and in the last years laser tracker based solutions have been proposed.

There is a trend towards the integration of verification and self-diagnosis systems in machine tools following “Industry 4.0” principles, and the verification and recalibration of volumetric accuracy is one of the key requirements. Artifact based calibration systems find here an important advantage due to their much lower cost, and there are therefore ongoing developments aiming at the integration of this kind of solutions in machine tools. The use of 1D ball bars will be discussed here.

The optimization of the integration of artifact-based verification and calibration solutions will determine the success of this approach, with aspects such as the design of the artifact, the measurement strategy and the machine occupation time to be considered

FIGURE 1: 1D calibration artifact in machine tool

CALIBRATION OPTIMIZATION SOFTWARE

Given the need for optimization criteria for the design of machine integrated volumetric calibration solutions, a specific software tool has been developed. This tool allows for the simulation of the measurement and compensation process with uncertainty analysis, and includes tools for sensitivity analysis and optimization.

Software architecture

The architecture of the software is presented in FIGURE 2. Four main functional modules and a virtual machine model are described next.

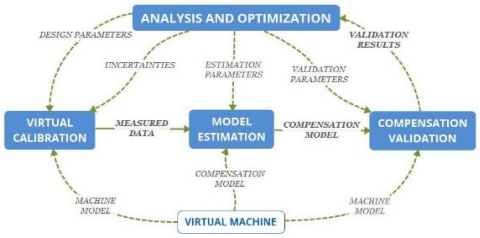

FIGURE 2: Software structure

Virtual machine

A model simulates the volumetric error of the machine at any point in the workspace. Two different models are used, one to simulate the real machine, used in virtual calibration and compensation validation modules, and another one which simulates the compensation model in the model estimation module. Effects such as geometric errors, thermal influences, elasticity, etc. can be considered in the model.

Virtual calibration

This module replaces the calibration test in the machine. The measurement strategy is defined here (artifact, measurement positions, associated uncertainties, etc.) and the measurements are simulated using the virtual machine model.

Model estimation

This module processes the result of the virtual calibration and estimates the parameters of the selected calibration model structure.

Compensation validation

This module evaluates how the volumetric error estimated by the calibration model fits the error of the calibrated machine (the virtual machine model here). Both models are evaluated in a dense cloud of points distributed in the machine workspace. The volumetric error of the machine before and after compensation is the main validation result, while other aspects such as the measurement time can be considered.

Analysis and optimization

This module controls the execution of the calibration-validation process of the previous modules. Since all relevant variables are parameterized, this module can be used to modify these parameters with different goals, from uncertainty analysis to sensitivity analysis and optimization.

The uncertainty of the volumetric compensation is estimated by performing Monte Carlo simulations [3] where the uncertainties of the machine, measurement tools and environment are propagated through the model estimation and validation process.

Implementation

In the following, the use of the virtual optimization tool for artifact-based calibration of machine tools will be demonstrated by applying it to the error mapping of a 3-axis milling machine with a 1D ball array.

A cantilever-type travelling column machine has been selected for the demonstration:

Kinematic chain: Tool-Z-Y-X-Bed-Workpiece

Workspace: X(0-3000), Y(0-1500), Z(0-1300)

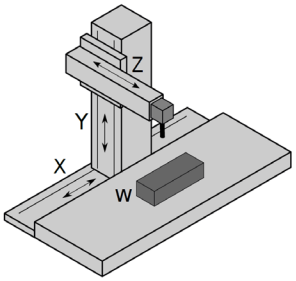

FIGURE 3: Machine kinematic structure

VIRTUAL MACHINE MODEL

Two virtual machine models are required in the implementation of the virtual calibration software. One model is used to simulate the real machine *M*, and can include as many effects as needed to be considered in the analysis. For the calibration model *C*, only the effects that want to be identified as a result of the calibration process are included, since adding effects to it will require more extensive measurement procedures. The same virtual machine module is used for both models, only selecting different parameters in each case.

The virtual machine models *VM* provide the position of the tool center point (TCP) in the machine´s main coordinate system, in function of the programmed axis positions *X(x, y, z)*, the tool offset *t*, and any other effect that may deviate it, such as guiding errors, backlash, thermal effects, etc., which are parameterized in the model by a set of parameters *E*.

The machine model and the compensation model are defined by different sets of parameters, E_M and E_C respectively.

$$\begin{cases} \mathrm{M} = \mathrm{VM}(\mathrm{X}, t, E_M) \\ \mathrm{C} = \mathrm{VM}(\mathrm{X}, t, E_c) \end{cases}$$

The details of the implementation of these models are given in the following.

Machine kinematics

Homogeneous transformation matrices (HTM) are commonly used to model the kinematic chain between the workpiece and the tool tip.

The kinematic model of a 3 axis machine can be expressed as follows, where the TCP coordinates in the machine's coordinate reference system can be calculated in function of the HTMs $({}^{0}\mathrm{T}_X, {}^{X}\mathrm{T}_Y, {}^{Y}\mathrm{T}_Z)$ that define the relative translations and rotations between the three machine axes and the origin of coordinates *0* in the machine. ${}^{Z}\mathrm{t}$ represents the tool offset in the reference system of the *Z* axis.

$$VM = {}^{0}\mathrm{T}_X \cdot {}^{X}\mathrm{T}_Y \cdot {}^{Y}\mathrm{T}_Z \cdot {}^{Z}\mathrm{t}$$

In this implementation, the physical effects to be included in the virtual machine model are modelled as elements contributing to any of the elements of the previous equation. In the following, ${}^{0}\mathrm{T}_X$ will be used here to illustrate the implementation of the model.

Error models

ISO 230 defines six geometric errors for each linear axis, considered as a rigid body: linear position error (EXX), straightness errors (EYX, EZX) and angular errors (EAX, EBX, ECX). These errors are function of the linear position of the axis and can be included in the HTM

representation, together with the commanded position *x* as follows:

$$ {}^{0}\mathrm{T}_{X} = \begin{bmatrix} 1 & -ECX & EBX & x + EXX \\ ECX & 1 & -EAX & EYX \\ -EBX & EAX & 1 & EZX \\ 0 & 0 & 0 & 1 \end{bmatrix} $$

A 3-axis machine can be represented by 21 errors, 6 for each linear axis as above, and three more corresponding angular location errors between the axes (E_{B0X}, E_{C0X} and E_{A0Y}).

Once the machine kinematics is defined, modelling the geometric errors requires the definition of the mathematical functions that represent of each of the 21 errors. Polynomials and Fourier series are typically used to define the errors and different types are available.

Machine model

A key element to the success of the optimization software presented here is the proper definition of the model that represents the machine to be calibrated. The magnitude of each error, their shape, how fast they change within the workspace, the relevance of thermal and flexibility errors determine aspects such as the number of measurements needed or the order of the calibration model. The experience and engineering judgement of the user of the software is thus important for defining a proper machine model.

The geometric errors of the machine have been modelled here based on the following function.

$$ E(x) = a_0 + a_1 x + \sum_n (b_n \sin n\pi x + c_n \cos n\pi x) $$

a_0, a_1, b_n and c_n are the model parameters, and x is the axis position, here normalized to $[-1,1]$ range. The model is defined here by assigning a uniform probability distribution to each parameter variation range (e.g. $[-a_0, a_0]$).

Table 1 shows the parameter values that have been used in the analyses shown in this paper.

In FIGURE 4, some EXX error functions generated with these parameters are shown.

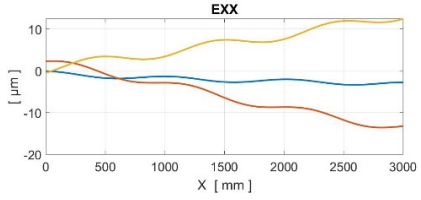

FIGURE 4: EXX error function examples

Table 1: Error parameters for machine model

	a_0	a_1	n_1	b_1	c_1	n_2	b_2	c_2
EXX	0	40	0.5	20	20	3	10	10
EYX	0	0	0.5	30	0	3	3	3
EZX	0	0	0.5	15	0	3	3	3
EAX	10	20	0.5	10	10	3	5	5
EBX	10	20	0.5	10	10	3	5	5
ECX	10	20	0.5	10	10	3	5	5
EB0X	40	-	-	-	-	-	-	-
EXY	0	0	0.5	15	0	1	5	5
EYY	0	20	0.5	5	5	1	3	3
EZY	0	0	0.5	15	0	1	5	5
EAY	10	15	0.5	10	10	1	5	5
EBY	10	15	0.5	10	10	1	5	5
ECY	10	15	0.5	10	10	1	5	5
EA0Z	40	-	-	-	-	-	-	-
EB0Z	40	-	-	-	-	-	-	-
EXZ	0	0	0.5	15	0	1	5	5
EYZ	0	0	0.5	15	0	1	5	5
EZZ	0	20	0.5	15	15	1	3	3
EAZ	10	15	0.5	6	6	1	2	2
EBZ	10	15	0.5	6	6	1	2	2
ECZ	10	15	0.5	6	6	1	2	2

The volumetric error (defined later) evaluated at multiple points in the workspace by the families of machines derived from this definition shows the following probability distribution.

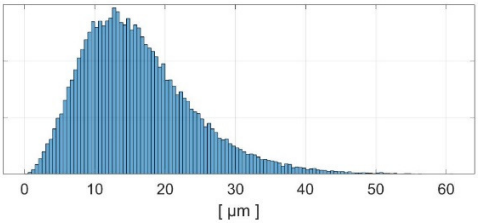

FIGURE 5: Volumetric error distribution

Calibration model

The calibration model must include only the errors that want to be identified. Including too many effects or a high model order requires a more detailed measurement process to be able to separate all effects and identify all the

parameters, and it has the added risk of overfitting, where the model estimation shows very good results (small residuals) but the extrapolation in the workspace is not good.

In this work, the calibration model includes the 21 error functions and in the machine model, represented by Legendre polynomials in this case.

$$E = a_0 + a_1 x + \frac{a_2}{2}(3x^2 - 1) + \frac{a_3}{2}(5x^3 - 3x) + \cdots$$

MODEL OF THE CALIBRATION METHOD

The modelling of the main elements of the calibration process is discussed next.

Error mapping method

The calibration method is based on measuring the position of the spheres of a calibrated artifact with a probe that moves with the machine. Since the true distance between each pair of spheres is known (within calibration uncertainty), it can be compared to the distances as measured by the machine to obtain information about the positioning accuracy of the machine. By repeating this process in several positions of the artifact to cover the working volume of the machine and with a proper mathematical processing, the geometric errors of the machine can be identified. The design of the artifact, the choice of positions in which to make the measurements and the mathematical structure of the calibration model are some of the main aspects that can be optimized with the use of the software proposed in this work.

For each position in the machine of the artifact (indexed k), the control coordinates X_i^k at which the *N* spheres (indexed *i*) have been measured by the machine are obtained. $\frac{N(N-1)}{2}$ distances d_{ij}^k between these spheres can be calculated with the compensation model.

$$d_{ij}^k = \left\| C(X_j^k, t, E_C) - C(X_i^k, t, E_C) \right\|$$

In an ideal machine and measuring system, the distances measured in any position *k* with the errors in the model set to 0 ($d_{ij}^k(E = 0)$) would be identical to the distances calibrated distances (d_{ij}^c). Geometric errors of the machine, thermal variations and errors in the measurement will produce differences ε_{ij}^k between the measured distances and the calibrated ones.

The compensation model *C* is calculated by identifying the error parameters in *E* so that ε_{ij}^k is minimized.

$$\min\left(\sum\left(\varepsilon_{ij}^k\right)^2\right) = \min\left(\sum\left(d_{ij}^k - d_{ij}^c\right)^2\right)$$

Measuring probe

A measuring probe is mounted on the machine spindle to perform the measurement of the spheres. The conventional way to detect the center of the sphere with a machine tool is the use of a touch-trigger probe, but here, in order to reduce the probe uncertainty and the measurement time, a probe with three orthogonal non-contacting distance sensors is used, with a self-centering function that moves the probe to a nominal position with respect to the sphere so that the measurement is read from the machine displacement and not from the distance sensors [4].

With this measuring method, the uncertainty added by the probe is defined by the repeatability of the distance sensors and the accuracy of the linear scales of the machine in measuring small displacements, of up to 1 mm.

The uncertainty of the probe is modelled here with normal distribution and 1 micron standard deviation.

Artifact design and uncertainty

A calibrated ball artifact is used as measuring target in the error mapping process. The design of the artifact is mainly defined by the number of spheres and the relative position between them. 1D artifacts are in principle not optimal for volumetric calibration, because the distances measured in one artifact position will all be aligned in the same direction. 2D or 3D artifacts allow the measurement of distances that are not aligned, and this brings a higher degree of decoupling between how each machine error affects each measured distance. This is of interest for the model estimation, requiring a lower number of measurements, but 2D and 3D artifacts are in general more difficult to handle and can pose limitations due to interferences with the machine.

In this work, a 1500 mm long 1D artifact with 11 balls is taken as a reference for the analysis, and the effects of its design parameters will be discussed. Regarding its design, small variations in the distribution of the spheres are considered here, introducing small offsets in their positions, as shown in the next figure.

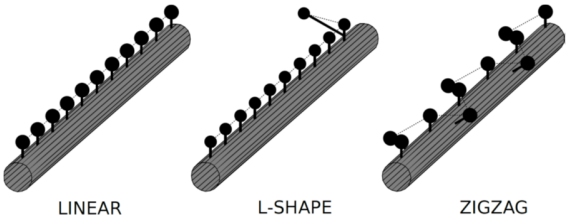

FIGURE 6: Artifact design variations

The calibrated lengths between the spheres will be taken as true references for the comparison with distances measured by the machine. The uncertainty in the true distance between the spheres needs to be considered in the virtual analysis of the error mapping process.

The main contributors to the uncertainty are the uncertainty of the machine where it is calibrated, the thermal effects and the deformation due to the inclination.

As a combination of these effects, the uncertainty in the reference distances between the spheres is modelled here as a normal distribution with 2 micron standard deviation.

Artifact position sets

The calibration process is based on measuring the artifact in several positions to cover the workspace of the machine and provide enough information so that all the parameters of the compensation model can be identified with the expected uncertainty.

Different sets of artifact positions can be considered as base components of the measurement strategy. In the next figure, the position sets considered for analysis in this work are represented.

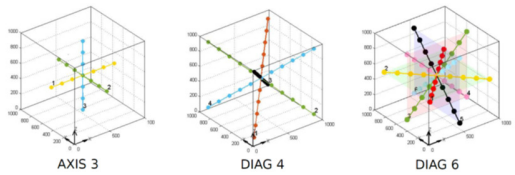

FIGURE 7: Artifact position sets

Distribution in the workspace

The artifact position sets do not cover the whole workspace of the machine, and therefore more than one set needs to be measured. This can be parameterized by indicating how many sets are distributed in each axis direction, as in the next figure.

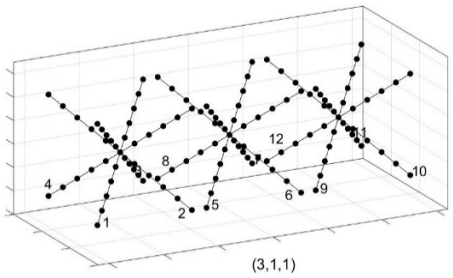

FIGURE 8: (3,1,1) distribution in workspace of artifact position sets

Validation criteria

The estimated calibration model is validated by comparing it to the virtual machine model that represents the machine that has been calibrated. In an ideal error mapping process, both models should provide the same TCP coordinates for any axis positions within the workspace of the machine.

The difference between them defines thus the volumetric error in the calibration process, and it can be evaluated in a set of X_i machine positions (60x20x20 in this work) distributed over the workspace:

$$e_i = \|C(X_i, t, E_C) - M(X_i, t, E_M)\|$$

The maximum value of the volumetric calibration error vector e_i is used here as the quality measure of the calibration process. Secondary quality measures can be defined as validation results, such as the estimated measurement time for example, which need to be considered when looking for the optimal configuration.

OPTIMIZATION OF THE CALIBRATION PROCEDURE

The use of the virtual calibration optimization software presented above is demonstrated here by performing some analysis on the machine and calibration procedure presented in previous sections.

Artifact design

Different variations on the shape of the 1D ball array have been presented above (see FIGURE 6). Their influence on the calibration result has been analyzed by applying the calibration procedure with the three designs, measuring three DIAG 4 artifact position sets distributed along X axis. The reduction in volumetric error and in the probability distribution is shown in the next figures.

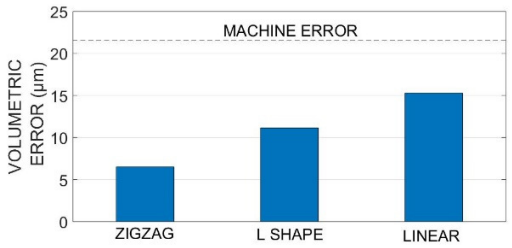

FIGURE 9: Calibration error in function of the design of the linear artifact.

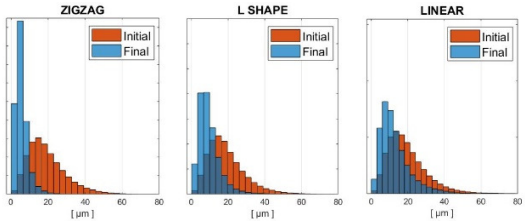

FIGURE 10: Volumetric error probability distribution variation for each design.

As expected, the zigzag shape gives the best result, and it will be used in the analyses presented next.

Artifact position sets

The next step is to find the optimal set of artifact positions. Three basic sets have been analyzed (see FIGURE 7), together with some combinations of them, and the calibration error and the measurement time have been considered for a fair comparison.

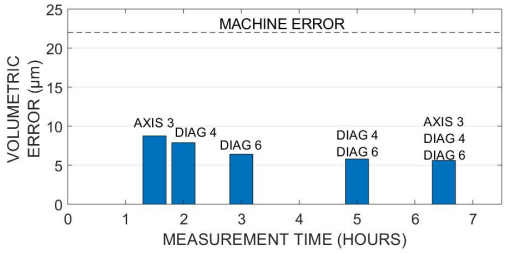

FIGURE 11: Calibration error in function of the artifact position sets.

The benefit of the software presented here is seen most clearly with this result, where results are not so predictable and help in finding the best result between several in principle reasonable approaches, with large differences in measurement time and in the calibration error. DIAG 6 is selected here as optimal strategy and used in the final simulations

Artifact set distribution in the workspace

Finally, the influence of the number of artifact sets measured to cover the workspace of the machine is analyzed, considering one to five sets distributed along X axis. Considering that measurement time is proportional to the number of sets, three sets would normally be selected as the optimal solutions.

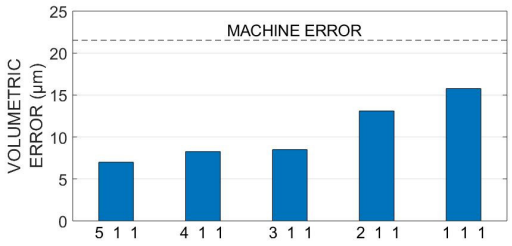

FIGURE 12: Calibration error in function of the artifact set distribution

CONCLUSIONS

The development of a software for the optimization of artifact-based calibration processes has been presented. The implementation on a 3-axis machine tool shows how the software can be of advantage when designing such processes, helping in defining aspects such as artifact design, measurement strategy and others, helping in taking decision where experience or intuition are no sufficient. Experience is however critical in the definition of the expected machine errors.

REFERENCES

[1] McKeown PA, Loxham J. Some aspects of the design of high precision measuring machines. CIRP Annals 1973;22.

[2] Schwenke H, Knapp W, Haitjema H, Weckenmann A, Schmitt R, Delbressine F. Geometric error measurement and compensation of machines–An update. CIRP Annals - Manufacturing Technology 2008;57:660–75.

[3] Evaluation of measurement data — Guide to the expression of uncertainty in measurement. Joint Committee for Guides in Metrology; 2008.

[4] Pérez de Nanclares A, Aguirre G, Urreta H. Calibration method for calibrating the drive axis of a machine tool. EP3101384 A1, 2016.

CALIBRATION AND ADJUSTMENT OF A HIGH-PRECISION FIVE DEGREE-OF-FREEDOM HYBRID MECHANISM

Shah Karim[1*], Samanta Piano[1], Richard Leach[1], David Branson[2], Martin Tolley[3]

[1]Manufacturing Metrology Team, Faculty of Engineering, University of Nottingham, Nottingham, NG8 1BB, UK
[2]Advanced Manufacturing Research Group, Faculty of Engineering, University of Nottingham, Nottingham, NG8 1BB, UK
[3]Central Laser Facility, Science and Technologies Facilities Council, Oxfordshire, OX11 0QX, UK

INTRODUCTION

Positioning and aligning a target at the laser beam focal point to an accuracy of few micrometres represents a significant challenge for laser systems requiring positioning mechanisms with greater than and two degrees of freedom (DOF), and particularly hybrid mechanisms composed of both parallel and serial kinematic components [1]. To meet the accuracy, repeatability and speed requirements of high-power and high-repetition rate laser operations, the Central Laser Facility (CLF) has designed and developed a new high-accuracy microtargetry system (HAMS) for accurate mounting and motion control of targets for the Astra-Gemini laser [2,3]. Kinematically, HAMS uses a hybrid mechanism, in which a tripod (parallel mechanism) is serially connected to a two-axis linear system (serial mechanism), to control all five degrees of freedom (DOF) for positioning and aligning a target at the laser focus (see [3,4] for details). Targets are patterned around the circumference of the target sections, which are then attached to an interface wheel held on the moving platform of the tripod.

As with any other precision machine, a hybrid mechanism's performance can be affected by many sources of error. Thus, the accuracy of the final position of the target is influenced by the kinematic errors of the mechanism (usually the main sources) due to geometric errors, such as manufacturing and assembly errors of the joints, by load deformation due to external forces, and by thermal deformation [5]. These factors should be addressed with an appropriate error compensation method rather than changing the structure or design of the mechanism, which is often expensive. One method to compensate for geometric errors is to carry out kinematic calibration and adjustment (hereafter, just called calibration).

Kinematic calibration of a mechanism (serial or parallel) can be defined as a procedure to estimate the numerical values of the errors, which represent the differences between the actual and nominal values of the kinematic parameters, to better describe the kinematics of the mechanism, and these values are used to improve the mechanism's accuracy by acting on the mechanism's controller [6]. Generally, the calibration process has four steps: development of a model to relate the 3D Cartesian position of the end-effector (or target) to the kinematic parameters of the mechanism; acquisition of the actual end-effector positions and orientations using a measuring instrument; identification of the kinematic error parameters based on the model and measurement; and error compensation by adjusting the parameters of the controller [7].

Although it has been shown that kinematic calibration can be a practical and economical way for enhancing the accuracy of parallel mechanisms, the calibration process is more complex than for a serial mechanism [7,8]. This extra complexity is due to the significant difficulty in identifying the kinematic parameters using a minimum set of error data, which can be easily determined in a time- and cost-effective manner, without compromising the accuracy of the calibration results [7-9]. Although some general strategies for calibration based on minimum set of error data exist for serial mechanisms, for parallel mechanisms only calibration methods for individual mechanisms have been reported [6-11]. Finding general strategies for the cost-effective calibration is an important area of the current research in parallel mechanisms [7-11].

Furthermore, for hybrid mechanisms, despite recent research and considerable utilisation in industrial applications, comprehensive studies of their design, kinematics, error sources and calibration are lacking [12].

In this paper, a practical and cost-effective solution to the kinematic calibration of a hybrid mechanism is outlined to demonstrate the improvement of the accuracy of HAMS based on minimum set of error data.

KEY ISSUES IN CALIBRATING PARALLEL AND HYBRID MECHANISMS

Although the methodology for the calibration of serial, parallel and hybrid mechanisms follows the same procedure, a number of issues must be considered when developing a calibration process for a parallel or hybrid mechanism.

First of all, an effective model for a mechanism's calibration must describe all the possible sources of error. Moreover, each source of error should ideally be represented by one parameter only (no redundant parameters). Some researchers refer to such models as minimum complete and parametrically continuous (MCPC) [6,13]. There are mainly two approaches to develop a valid MCPC model, where [6,8]:

- Errors are described by the variations of a specific set of parameters used to define the mechanism's structure, such as link lengths, joint axes inclination and joint coordinates offsets. In terms of forward kinematics, the model can be represented as [14]
$$S = f(Q, s_n + \Delta)$$
where $S = [x, y, z, \alpha, \beta, \gamma]^T$ represents the end-effector's pose, $Q = [q_1, \dots q_n]^T$is the vector of the joint coordinates, $s = [s_1, \dots s_n]^T$ is the vector of the nominal structure parameters, and Δ is the vector of their errors. In many cases, these parameters are defined by adopting the well-known Denavit-Hartenberg approach [14].
- Errors are represented by a separate set of parameters describing the differences between the nominal and actual geometry of the mechanism. The forward kinematics of the model can be shown as
$$S = f(Q, s_n, \Delta)$$
where $\Delta = [e_1, e_2, e_3, \dots]$, which consists of geometrical error parameters.

Irrespective of which approach is used to develop a model for a calibration, since both have advantages and disadvantages, the number of parameters necessary to describe a parallel or hybrid mechanism (and, hence, their error parameters) can be very high. To give an idea from a literature survey, it is necessary to have up to 138 error parameters for a 6-DOF Stewart-Gough platform, a minimum of 38 parameters to describe a 5-DOF parallel mechanism and 33 parameters to describe the 3-DOF parallel mechanism of a 5-DOF hybrid machine tool [8,10,11]. This represents a significant challenge in the calibration process when developing a suitable representative kinematic model of the mechanism with a minimum number of error parameters.

Furthermore, adopting a suitable measurement scheme to identify the error parameters can be another challenge in calibrating a parallel or hybrid mechanism. Existing calibration methods are usually categorised as external calibration and internal or self-calibration [9,10]. External calibration, in which the geometric error parameters are identified by minimising the residuals between the end-effector's actual pose measured by an external measurement system (such as, laser tracker, camera, interferometer) and the predicted pose of the mechanism's controller, can be carried out by either full pose or partial pose measurements. Internal calibration, in which the identification is implemented by minimising the residuals between the actual values of the active and/or redundant joint sensors and the predicted joint values of the controller, is carried out only by partial pose measurements. Full pose measurements can be effective in identifying all possible error parameters required for the calibration; however, they can be difficult to achieve, requiring the measurement of a high number of poses for a parallel mechanism [9]. On the other hand, partial measurement can be cost- and time-effective, but only a partial set of error parameters are identifiable [10,11]. In some cases, a hybrid calibration method is used to reconcile the advantages of both methods.

This paper proposes a practical calibration method for a hybrid mechanism by taking into consideration the use of the mechanism for the target alignment operation of the CLF. As such, the calibration uses a simple model with a minimum number of error parameters which can be easily measured by selecting the poses relevant to the target alignment, and the compensations are then applied to the

mechanism's controller with limited changes to its parameters.

CALIBRATION APPROACH FOR HAMS

For the convenience of the modelling, the structure of HAMS is briefly reviewed here, while the details can be found elsewhere [4]. HAMS has three sub-structures (see Figure 1). A linear *xz* system, producing two translation motions along *x* and *z* axes, forms sub-structure 1. Sub-structure 2 is the tripod, the parallel part of the hybrid mechanism, providing a rotational motion about the *x* axis (called tip *u*) and a translational motion along the *y* axis. Sub-structure 3 is essentially a rotary motor which actuates the rotating platform mounted on the moving platform, and produces a rotational motion about the *y* axis (called tilt *v*). The parallel structure is called an RPS mechanism, in which each chain is composed of a revolute joint (R), a prismatic join (P) and a spherical joint (S). To calibrate the hybrid mechanism, a step-by-step strategy was adopted in this study, which means the calibration procedure was carried out on the parallel part first. This was done because it was required to know the actual performance of each sub-structure independently for the purpose of the laser target alignment operation. In this paper, the calibration problem will focus on the RPS of the hybrid mechanism.

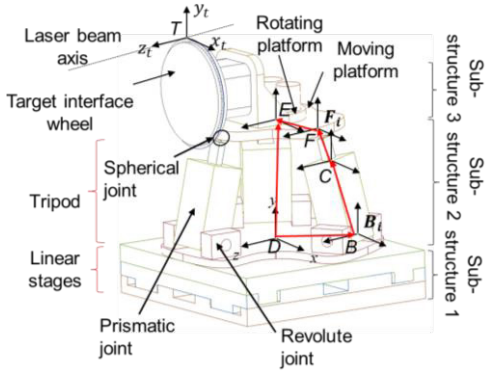

FIGURE 1. Kinematic structure of HAMS.

MODELLING

Figure 1 schematically represents the kinematic structure of HAMS, showing the geometrical relationships among the coordinate systems placed at the points of interest for the analysis, such as point *T*, which indicates the target position, and point *D* and *E*, which indicate the centroids of the fixed platform and the moving platform of the tripod. The origins of the coordinates are also placed at *B*, the centre of the rotational joint, at *C* on the prismatic joint, indicating the home position of the joint, and at *F*, the centre of the spherical joint. The three prismatic joints of the tripod's legs are driven to obtain the nominal pose $q = [\,y, u, v]^T$ of the moving platform through changing the distance ∇ between $\boldsymbol{B_i}$ and $\boldsymbol{F_i}$, where $\boldsymbol{B_i}$ is the position of point *B* with respect to the coordinate at *D*, $\boldsymbol{F_i}$ is position of *F* with respect to the coordinate at *E* and ∇ are the kinematic parameters. A revolute joint can be defined by four structural parameters (two positional and two rotational), since the position of the mechanical hinge is not relevant in its kinematic analysis but only the location (position and direction) of its geometrical axis [13]. For a prismatic joint, only the axis direction is relevant and thus two rotational parameters are enough. A spherical joint needs three parameters to be defined, since only the position of the sphere is relevant. Thus, for calibration purposes, each leg of the parallel mechanism needs 9 error parameters and, therefore, 27 error parameters for the whole mechanism.

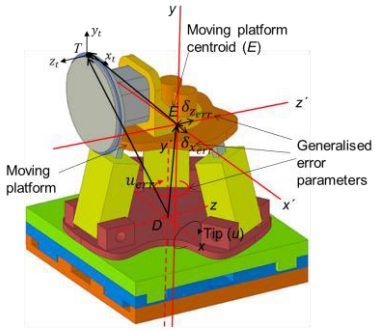

FIGURE 2. Kinematic model of HAMS.

The number of error parameters can be reduced to a minimum by carefully considering the kinematic constraints of the RPS mechanism. Each leg of the RPS is connected to the fixed base by a revolute joint at *F*, and the planes in which the spherical joints are allowed to move should ideally intersect at *E* [4]. In reality, during the rotations of the moving stage (tip *u* in this case), two translational parasitic motions (in the *x* and *z* directions) and one rotational parasitic motion about *y* are generated, which means that point *E* changes its positions in the *x* and *z* directions with respect to point *D* (these three error motions can be defined with a 4×4 matrix with respect to the coordinate at *E*). Since only the positions of the revolute joints are affected if there are kinematic errors generated from any source of a leg (revolute, prismatic or spherical joints), it is logical that the three parasitic motions of the moving platform actually contain the resultant effects of the errors stemming from the legs. These three errors, related to the tip rotation

of the platform, are defined as the generalised error parameters of the tripod. Thus, the kinematic model can be redrawn as shown in Figure 2, in which all the coordinates between *D* and *T* (not all are shown) are placed in a serial manner. The details of the error model development are described elsewhere [4]. The equations used to describe the positional deviations of the target can be derived by writing the necessary transformation matrices for all the coordinates of the mechanism, with and without error conditions. The positional deviation equations of target *T* are in the following form:

$$D_{xt_{tip\,err}} = \delta_{x_{err}} - (d_3 + t_z)(\cos v \sin u_{err} + \sin v \cos u_{err}) + t_x(\cos v \cos u_{err} - \sin v \sin u_{err} - 1), \quad (1)$$

$$D_{yt_{tip\,err}} = (h_5 + h_6 + t_y)(\cos u - 1) + (d_3 + t_z)\sin u\,(\cos v \cos u_{err} - \sin v \sin u_{err}) + t_x \sin u\,(\cos v \sin u_{err} + \sin v \cos u_{err}), \quad (2)$$

$$D_{zt_{tip\,err}} = \delta_{z_{err}} - (h_5 + h_6 + t_y)\sin u + (d_3 + t_z)(\cos u \cos v \cos u_{err} - \cos u \sin v \sin u_{err} - 1) + t_x \cos u\,(\cos v \sin u_{err} + \sin v \cos u_{err}). \quad (3)$$

where, *u* and *v* are the tip and tilt motions; $\delta_{x_{err}}$, $\delta_{z_{err}}$ and u_{err} are the generalised error parameters; h_5, h_6, d_3, t_x, t_y and t_z represent the structural offsets of HAMS.

MEASUREMENTS AND ERROR IDENTIFICATION

The following should be noted.

1. The inverse kinematics in the hybrid system's controller are capable of compensating the motions in the *x* and *z* directions; however, these compensations are based on an inverse kinematic calculation of the controller, may not necessarily be accurate, and, therefore, need to be evaluated in the calibration.

2. Equations (1) to (3) show that four sources are responsible for the positional deviations of the target:

- tip motion, since the target is at an offset in the *x* and *y* directions from the centroid of the moving platform (Abbe offsets),
- structural parameters between the centroid of the platform and the target,
- positional deviations at the centroid of the platform that include the parasitic motions $\delta_{z_{err}}$ and $\delta_{x_{err}}$,
- the rotational parasitic motion u_{err} causing Abbe errors at the target due to the offsets.

The measurement process of the calibration, shown in Figure 3, is explained below.

i. RPS is a 3-DOF mechanism; therefore, if the tip (*u*), tilt (*v*) and *y* (height) values of the platform are specified, the other three parameters ($\delta_{z_{err}}$, $\delta_{x_{err}}$ and u_{err}) can be determined. Because, orientation of a target is adjusted once the target is placed at a certain position (according to the CLF's target alignment process), and also because the tilt (*v*) of the moving platform is not used, only the tip motions of the platform were considered in the calibration process (therefore, *v* = 0 and *y* is fixed). The tip motions were selected such that they are representative of the range of rotational motions normally used in the CLF's target alignment procedure.

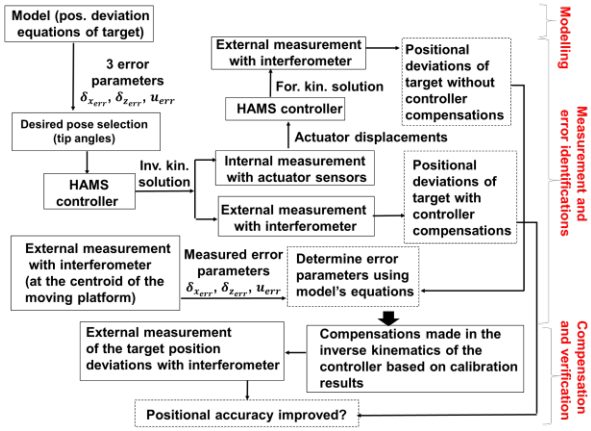
Model (pos. deviation equations of target)
3 error parameters $\delta_{x_{err}}$, $\delta_{z_{err}}$, u_{err}
Desired pose selection (tip angles)
HAMS controller
Inv. kin. solution
External measurement with interferometer
For. kin. solution
HAMS controller
Positional deviations of target without controller compensations
Actuator displacements
Internal measurement with actuator sensors
External measurement with interferometer
Positional deviations of target with controller compensations
External measurement with interferometer (at the centroid of the moving platform)
Measured error parameters $\delta_{x_{err}}$, $\delta_{z_{err}}$, u_{err}
Determine error parameters using model's equations
External measurement of the target position deviations with interferometer
Compensations made in the inverse kinematics of the controller based on calibration results
Positional accuracy improved?
Modelling
Measurement and error identifications
Compensation and verification

FIGURE 3. The calibration process flow diagram of HAMS.

ii. Once the desired tip angles were entered into the controller, the displacements of the target were measured using a displacement interferometer (Renishaw XL-80). The *z* motions were determined from the *z* stage actuator sensor (no *x* displacement observed), meaning that the *z* positional deviation values from the interferometer reading included controller compensation.

iii. Displacements of the three actuators of the tripod, as determined from the sensors for the particular tip motions, were used as the forward kinematics input of the controller. The target's tip angles and positional deviations were measured with the interferometer. It was found that *z* displacements varied from those measured in step ii. No *x* or *z* stage sensor motions were determined in this case, meaning no controller

compensation is included in the measured positional deviations, which represent the actual positional deviations during the tip motions of HAMS.

iv. The positional deviations of the target from step iii could be used in the model equations (1) to (3) to find the error parameters $\delta_{z_{err}}$, $\delta_{x_{err}}$ and u_{err} (for known structural parameters). Alternatively, these were measured directly at the centroid of the moving platform of the tripod using the interferometer (the details are given elsewhere [4]). When using these parameter values in the model equations, the predicted positional deviations agreed with the values measured in step iii.

COMPENSATION AND VERIFICAITON

It was found that the controller compensated for the $\delta_{z_{err}}$ error motion in the *z* direction; however, the relatively smaller error motion $\delta_{x_{err}}$ in the *x* direction remained uncompensated. For small angle rotations, the measured values of $\delta_{z_{err}}$ and $\delta_{x_{err}}$ are found to vary linearly with the tip angles (see [4] for details) and, therefore, it was possible to compensate for these deviations as functions of tip rotations in the inverse kinematic solution of the controller. Alternatively, the values of the target positional deviations were included in the inverse kinematics to generate compensations in the *x* and *z* directions as functions of tip rotations. After compensations, the interferometer was used to measure the positional deviations of the target for various tip rotations. The results were compared with the positional deviations measured in step ii to verify the improvement achieved through this calibration process.

CALIBRATION UNCERTANITIY

The overall measurement uncertainty arising from the repeatability of the measured distances and from the atmospheric effects on the interferometric measurements was estimated to not to exceed 180 nm (at a coverage factor $k = 2$, giving a confidence level of approximately 95%). The values of measurement uncertainty, compared to the positional deviations measured on the micrometre scale, are not shown in the calibration results as they are relatively small.

However, there are a number of influence factors in this calibration that need to be further investigated, for example:

- since the *xz* platform makes *xz* motions for compensations, the stages' accuracy should be considered as an influence factor when measuring the target's position deviations;
- the nominal values of the structural offsets between the centroid of the platform and the target were used; also, the perpendicular errors between any two structural features were ignored;
- the measurements to determine the error values $\delta_{z_{err}}$, $\delta_{x_{err}}$ and u_{err} were taken as close to the centroid of the platform as possible, instead of at the centroid.

RESULTS AND DISCUSSION

The key points of the calibration results are as follows.

1. The controller's compensations for the *x* and *z* positional deviations during tip rotations were evaluated (Figure 4). While the controller is overcompensating for the positional deviation in *z*, there is no compensation in the *x* direction. Although the *z* direction accuracy is the most sensitive to the target alignment, the *x* and *y* direction accuracies are also important; otherwise, the laser will miss the targets.

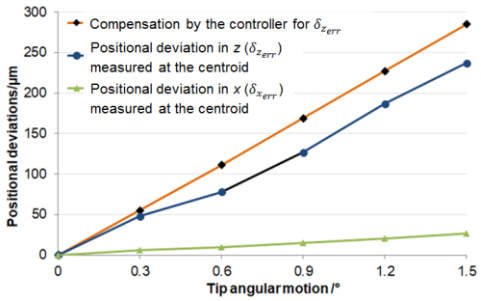

FIGURE 4. Comparison between the actual positional deviations at the centroid of the platform and the compensated values by the controller.

2. The positional deviations of the target predicted by the error model agree with those measured (uncompensated values before calibration) - see Figure 5. This shows the validity of using a simplified kinematic model with generalised error parameters in the calibration of this 5-DOF hybrid mechanism.

3. Figure 6 shows that the position accuracy of the target has improved significantly (more than 85%) in the *x* and *z* directions. However, the calibration of the complete hybrid mechanism will be part of our on-going research.

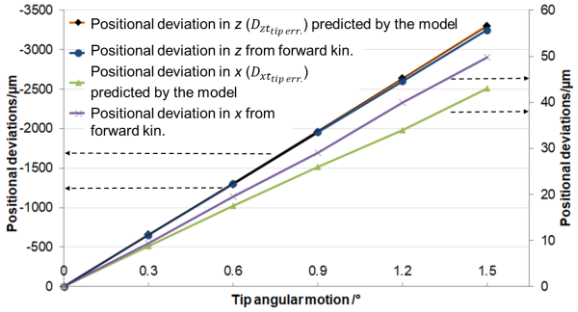
Positional deviation in z ($D_{zt_{tip\,err.}}$) predicted by the model
Positional deviation in z from forward kin.
Positional deviation in x ($D_{xt_{tip\,err.}}$) predicted by the model
Positional deviation in x from forward kin.
Positional deviations/µm
Tip angular motion /°

FIGURE 5. Comparison between the target positional deviations predicted by the model and the measured values.

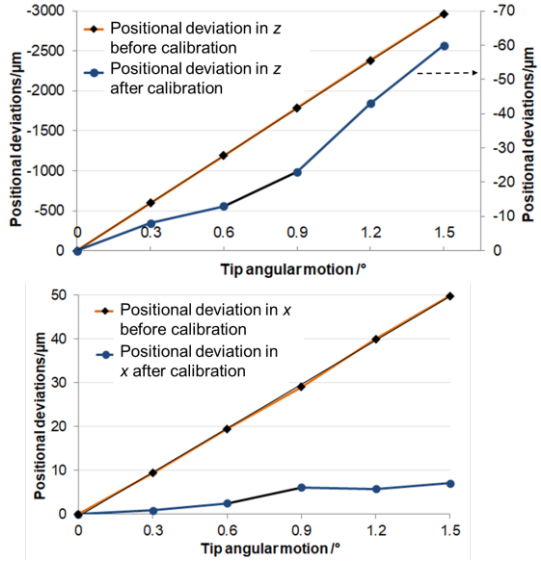
Positional deviation in z before calibration
Positional deviation in z after calibration
Positional deviation in x before calibration
Positional deviation in x after calibration
Positional deviations/µm
Tip angular motion /°

FIGURE 6. Target position accuracy improvement through the calibration process.

CONCLUSION

Calibration of a parallel or hybrid mechanism is a difficult problem in terms of developing a suitable kinematic model, identifying error parameters, adopting cost-effective measurement plans and implementing compensations into the mechanism's controller. This problem is approached in this study in a practical way with the help of a simplified model with minimum error parameters, by carrying out simple measurements and by compensating the errors using effective steps, resulting in a significant improvement in the target positioning accuracy. Future work involves the development of a closed-loop control system for HAMS for automatic alignment of the targets to the laser focus with high-repetition rate.

This work was supported by the Engineering and Physical Sciences Research Council [grant numbers EP/M008983/1, EP/L016567/1] (EPSRC) and the Science and Technologies Facilities Council (Oxfordshire, UK).

REFERENCES

[1] Symes DR, Booth N, Baraclough M, Indorf G, Oliver P, Scott GG, Neely D, Spindloe C, Heathcote RI, Clarke RJP, Foster S, Gregory CD, Rajeev PP. Progress on positioning of solid targets for Gemini. Central Laser Facility Ann. Report 2014; 15.

[2] Spindloe C, Arthur G, Hall F, Tomlinson S, Potter R, Kar S, Green J, Higgingbotham A, Booth N, Tolley MK. High volume fabrication of laser targets using MEMS techniques. J. Phy. Conf. Ser. 2016; 713: 012002.

[3] Karim S, Piano S, Leach RK, Tolley M. Error analysis for a high-precision five degree of freedom hybrid mechanism for high-power high-repetition rate laser system. Proc. ASPE. 2017; 366-372.

[4] Karim S, Piano S, Leach RK, Tolley M. Error modelling and validation of a high-precision five degree of freedom hybrid mechanism for high-power high-repetition rate laser system (in press). Prec. Eng. 2018.

[5] Bosmans N, Reynaerts D. Force loops. In: Leach RK, Smith ST, (ed.). Basics of precision engineering. CRC Press: 2018.

[6] Fassi I, Legnani G, Tosi D, Omodei A. Calibration of serial manipulators: theory and applications. In: Low KH, (ed.). Industrial robotics: programming, simulation and applications. Advanced Robotic Systems International: 2007.

[7] Wu JF, Zhang R, Wang RH, Yao YX. A systematic optimisation approach for the calibration of parallel kinematics machine tools by a laser tracker. Int. J. Mach. Tools & Man. 2014; 86:1-11.

[8] Legnani G, Tosi D, Adamini R, Fassi I. Calibration of parallel kinematic machines: theory and applications. In: Low KH, (ed.). Industrial robotics: programming, simulation and applications. Advanced Robotic Systems International: 2007.

[9] Huang T, Chatwynd DG, Whitehouse DJ, Wang J. A general and novel approach for parameter identification of 6-DOF parallel kinematic machines. J. of Mech. & Mach. Theory. 2005; 40:219-39.

[10] Song Y, Zhang J, Lian B, Sun T. Kinematic calibration of a 5-DOF parallel kinematic machine. Prec. Eng. 2016; 45:242-261.

[11] Huang P, Wang J, Wang L, Yao R. Kinematic calibration of a hybrid machine tool with regularization method. Int. J. of Mach. T. & Man. 2011; 51:210-220.

[12] Harib KH, Sharifullah AMM, Moustafa KAF. Optimal design for improved hybrid kinematic machine tools. Ann. CIRP. 2013; 12:109-14.

[13] Mooring B, Roth Z, Driels M. Fundamentals of manipulator calibration. Wiley: 1991.

[14] Tsai LS. Robot analysis: the mechanics of serial and parallel manipulators. Wiley: 1999.

Effect of laser-assisted diamond turning (Micro-LAM) on form and finish of selected IR crystals

Hossein Shahinian[1], Jayesh Navare[1], Dmytro Zaytsev[1], Sai Kode[1], Farzad Azimi[1], Deepak Ravindra[1]
[1]Micro-LAM , Inc
5960 S Sprinkle Rd
Portage, Michigan, USA

INTRODUCTION

In this paper we investigate the effect of laser-assisted diamond turning, hereafter referred to as μ-LAM (Micro-LAM process), on the form and surface finish of selected infrared (IR) crystals that are fabricated with the process. The μ-LAM process is a technology that enables the simultaneous use of laser emission during single point diamond turning (SPDT) [1]. The laser is passed through the diamond and the irradiance of the laser on the machining zone facilitates the cutting action of the diamond tool due to the local heating and "softening" of the material during the cut [2, 3].

The SPDT process has enabled the easy production of freeform and aspherical optics [4, 5]. These optics have found vast applications in fields of optical imaging [6, 7], illumination, etc. It is imperative for the SPDT process to produce parts with form errors less than quarter of the operating wavelength of the light.

The IR crystals chosen for the purpose of this study are single crystal silicon (Si) and single crystal calcium fluoride (CaF_2). Si has a relatively high index of refraction and low density enabling it to be a great candidate for compact and light IR optical systems [8]. CaF_2 on the other hand is highly transmissive and it's low absorption rates makes the material a good choice for the emission of high power lasers [9].

Several studies have been undertaken to understand the cutting mechanics of SPDT of infrared materials that are inherently brittle in nature [10-12]. Although these studies provide significant insights into fabrication techniques for making optical quality parts made of IR crystals, they don't offer considerably distinctive solutions, for successful machining of the IR optical materials. Indeed, those articles have done a great body of work on optimization of the conventional cutting parameters, i.e. spindle speed, tool feed, tool rake angle, depth of cut (DOC), etc.

The μ-LAM process provides a different solution for enhancing the diamond turning process, i.e. emission of a laser beam. The addition of the laser raises the question that how the presence of the laser-induced heat, would affect the process repeatability, as well as the form and finish tolerances achievable. After all, heat can introduce large temperature variations, thus reducing the precision of the diamond turning process, that usually is performed under highly controlled conditions.

EXPERIMENTAL METHOD

To study the effect of the μ-LAM process on the surface form and finish of Si and CaF_2, an experimental approach was undertaken. Two convex samples with a specific radius of curvature (ROC), were machined. The machining is done on an ultraprecise diamond turning lathe, a Precitech Nanoform® 250. Each sample is cut under identical conditions in the presence and absence of the emission of the laser of the μ-LAM system.

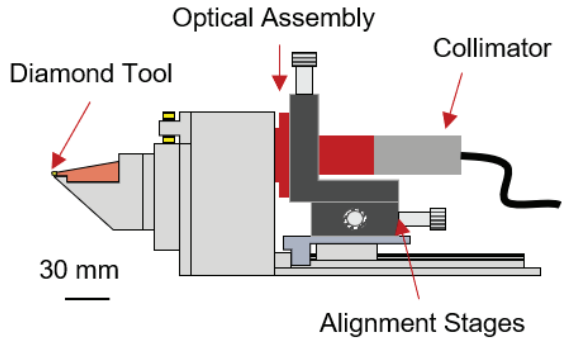

FIGURE 1. Optimus$_{T+1}$ Tool Post

Optimus$_{T+1}$ Tool Post

The Optimus$_{T+1}$ is a tool post that is a proprietary design of the Micro-LAM team. It incorporates an optical assembly that is designed to deliver an IR laser beam (1064nm wavelength) through the diamond cutting tool, see FIGURE 1.

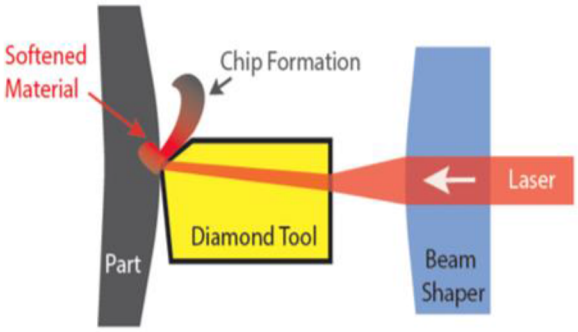

FIGURE 2. The delivery of laser emission at the cutting edge of the diamond tool

The laser delivered by the optical system within the tool post, is focused near the cutting edge of the diamond tool, see FIGURE 2. This highly focused spot of the laser at the cutting edge provides the local heat that enables the material "softening" mentioned in the introduction.

Test Samples

Two convex samples comprised from single crystal Si and CaF_2 were used. Details on the geometry of the samples are given in Table 1.

Table 1. Test sample information

Material	Dimensions	ROC (mm)
Si	∅62 mm × 5 mm	205
CaF_2	∅25.4 mm × 15.5 mm	50

Metrology

The form measurements are done using a Taylor Hobson LuphoScan® 260-420 HD. This instrument is a multi-wavelength scanning interferometer.
The surface finish of the samples was measured using a Taylor Hobson® CCI, a scanning white light interferometer (SWLI).

Table 2. Supporting metrology information

Hardware	Data type and analysis
LuphoScan 260-420 HD	Form measurements Piston, tilt, power removed Total points measured ≈ 10^6 Metric used: Sq or RMS (nm)
Taylor Hobson CCI	Roughness measurements 4th order Chebyshev removed High-pass filter with λ = 80 μm Detector size = 1024 × 1024 pixels Metric used: peak-to-valley (PV)

Details regarding the metrology hardware, the applied processing filters, and quantification metrics used, are outlined in Table 2.

Diamond Cutting Tools

Single crystal synthetic diamond tools manufactured by K&Y Diamond® were used for all the cutting tests. Information regarding the tools used for the cutting tests can be found in Table 3.

Table 3. Tool information

Tool	Rake angle (°)	Nose radius (mm)	Primary clearance (°)
1	-35	0.3	10
2	-35	0.3	10
3	-35	0.5	10

The -35° rake angle provides the necessary compressive stresses during the cutting of the brittle crystals.

Diamond turning conditions

In each of the performed experiments two cuts were done. The first cut used the base tool path for generation of the aimed convex geometry. The second cut was done with a program that was compensated for the surface errors measured after the first cut. It should be noted that both cuts are meant as "finishing" passes.
The machining parameters were selected based on the information available in the public literature [10, 12]. The parameters are listed in Table 4.

Table 4. Machining parameters of the samples

Sample	RPM	Feed (mm/min)	DOC (μm)
Si	2000	3	6
CaF_2	4500	6	2

Four experiments were done. These tests are aimed to establish a direct comparison between the achievable form and finish of the diamond turning process, with and without the μ-LAM system. These tests are listed in Table 5.

Table 5. Cutting tests with μ-LAM and conventional diamond turning

Test	Tool	Laser power (W)
Si-1	1	0
Si-2	2	2.7
CaF_2-1	3	0
CaF_2-2	3	2.7

The Si tests were done using two different tools, i.e. tool 1 and tool 2. The reason for using the two different tools was the expected higher tool wear imposed by cutting the larger Si parts. In contrast, the diamond tool wear during the CaF_2 experiments, are expected to be negligible, due to the sample smaller size and material. To ensure that the conventional cutting experiment, i.e. CaF_2-1, was conducted under conditions with less tool wear, the CaF_2-2 test was done post the CaF_2-1 test.

RESULTS

The cutting tests of Si-1, Si-2, CaF_2-1, and CaF_2-2, (see Table 5 for the testing conditions), were done with a spindle balance of less than 1 nm PV deviations in the spindle position. In each test the surface of the samples were measured using the SWLI and LuphoScan instruments.

Form measurements

FIGURE 3(a), (b) depict the form errors imparted on Si sample cutting with conventional diamond turning and the μ-LAM process, respectively. The interferograms are taken post the application of the corrective tool path. The PV corresponds to the difference between the highest and lowest point on the measurement data. The measurement data of the parts closely match one another, confirming that the heat induced by the laser has minimal effect in introducing additional form errors.

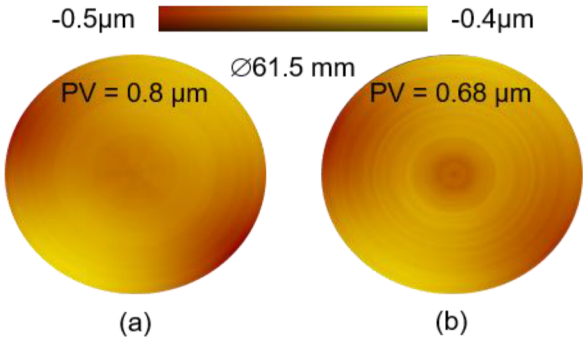

FIGURE 3. Form error measurements for the Si samples; (a) conventional diamond turning (b) μ-LAM process

The form errors imparted during the machining of CaF_2 samples are illustrated in FIGURE 4. The good agreement between the PV values of the measurements of the parts cut in the absence of the laser, i.e. FIGURE 4(a) and the presence of the laser, i.e. FIGURE 4(b), is complemented by the fact that large surface defects near the center are nearly gone on the sample machined with the μ-LAM process. These defects are speculated to be a consequence of the single crystal structure of the CaF_2 sample. Their absence on the CaF_2-2 sample demonstrates how the laser enhances the ductile cutting of the CaF_2 material.

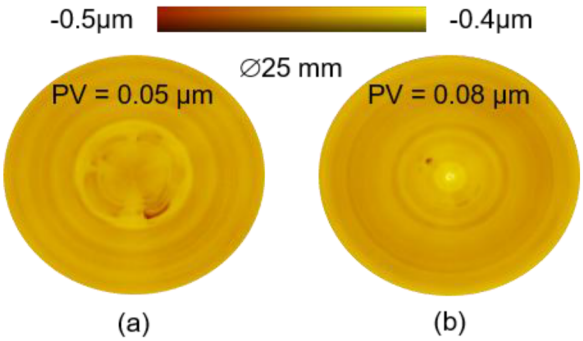

FIGURE 4. Form error measurements for the CaF_2 sample. (a) without μ-LAM (b) with μ-LAM

Roughness measurements

The roughness interferograms for both samples are taken near and off the center of the parts. In single crystal materials, often brittle fracture patterns at the center are observed.

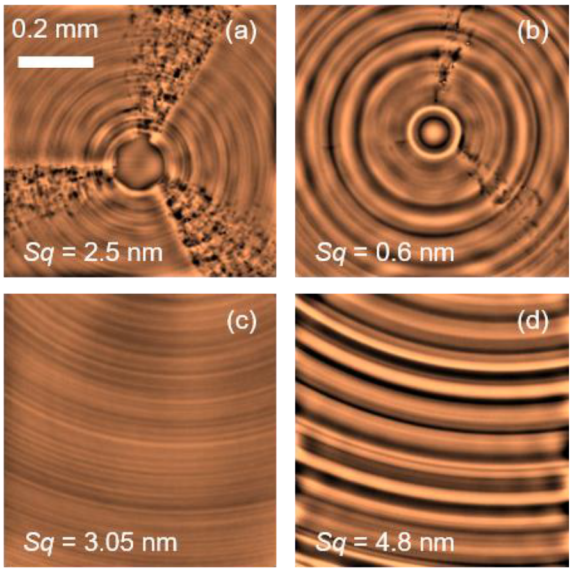

FIGURE 5. SWLI measurements on Si part (a, b) near center with and without μ-LAM respectively (c, d) off-center with and without μ-LAM respectively

For quantification of the surface roughness, the RMS of the height data, i.e. Sq, is used. FIGURE 5 shows the SWLI measurements for the Si parts. Comparing FIGURE 5(a), (b), the brittle fracture pattern near the center is far more severe when the part is machined with conventional diamond turning. FIGURE 5(c), (d), on the other hand, suggest that the waviness of the sample machined with the μ-LAM process is slightly more prominent.

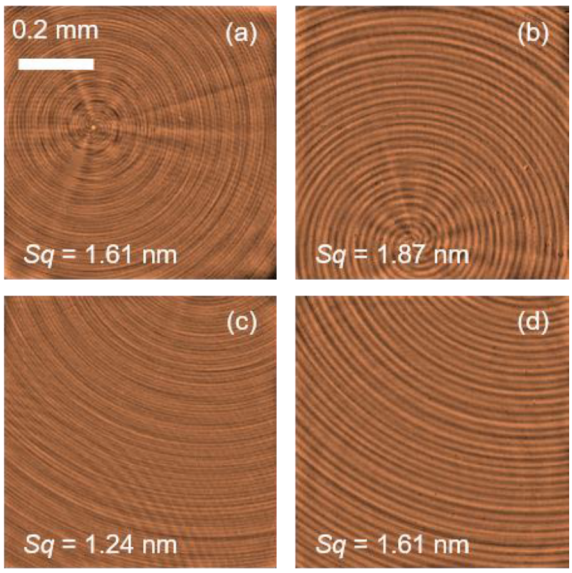

FIGURE 6. SWLI measurements on CaF_2 sample; (a, b) near center with and without μ-LAM respectively (c, d) off-center with and without μ-LAM respectively

The roughness measurements for CaF_2 sample is shown in FIGURE 6. The data suggests an increase in the waviness in the measurement data, similar to what was observed on the Si sample. No additional damage pattern was present near the center of the part.

DISCUSSION

As reported in the previous section, the key conclusion of the results is that the μ-LAM process doesn't add any complexity to the machining of IR crystals in terms of achieving desired form and finish. This result was expected since the heating of the sample during the machining happens in a very localized manner (<200 μm in radius). Furthermore, due to the very shallow depth of cuts during diamond turning, the heating effects of the laser on the part are expected to be quite repeatable. The repeatable nature of the heating effect implies that the correction program can compensate for any variations as a result of the heating.

On both sample materials cut with conventional diamond turning, clear defects and zones exhibiting brittle fractures were seen. The improved surfaces of the materials with the addition of the μ-LAM system, implies that the local heating of the laser, facilitates the ductile cutting of the IR crystals under study. This result confirms the material "softening" effect of the laser, on the workpiece.

Lastly, it should be noted that the μ-LAM process, had a minor negative effect on the extent of the waviness induced by the machining process. This is speculated to be not a significant issue. The reason behind the increase in waviness, is attributed to the absence of a B-axis of the machining center. The tool orientation with respect to the workpiece surface is continuously changing during the machining. As a corollary, the laser spot and its power density will be susceptible to variations as the cutting progresses. These variations are thought to be the main cause of the enhanced waviness on the samples. Many articles do address the importance of the waviness error on visible light optics [13-15]. However, the extent of the added waviness doesn't affect the optical performance of the crystals in the IR wavelength significantly.

CONCLUSION

The capability of machining IR materials that are inherently brittle in nature using the *μ*-LAM process was compared with conventional diamond turning. Even though the laser, a significant heat source, is propagated through the diamond tool, the *μ*-LAM can achieve and maintain the desired form on the machined materials. In addition, while not reported in this paper, the *μ*-LAM process has shown to enhance the tool life in cutting the brittle IR crystals nearly two times.

As future efforts of the R&D team in *μ*-LAM, testing on additional IR crystals will be continued. Furthermore, a deeper study into the effect of the laser on the sample waviness and solutions for the reduction of the waviness, in the absence of a B-axis will be conducted.

ACKNOWLEDGEMENTS

We would like to acknowledge the help and efforts of Ms. Alyson Markos in preparation of this paper.

REFERENCES

1. Ravindra, D., *Ductile mode material removal of ceramics and semiconductors.* 2011.

2. Ravindra, D., M.K. Ghantasala, and J. Patten, *Ductile mode material removal and high-pressure phase transformation in silicon during micro-laser assisted machining.* Precision engineering, 2012. **36**(2): p. 364-367.

3. Ravindra, D. and J. Patten, *Ductile regime single point diamond turning of quartz resulting in an improved and damage-free surface.* Machining Science and Technology, 2011. **15**(4): p. 357-375.

4. Zhang, X., Z. Li, and G. Zhang, *High performance ultra-precision turning of large-aspect-ratio rectangular freeform optics.* CIRP Annals, 2018.

5. Davies, M., J. Owen, J.R. Troutman, D.L. Barnhardt, and T.J. Suleski. *Ultra-Precision Diamond Machining of Freeform Optics for the IR*. in *Freeform Optics*. 2015. Optical Society of America.

6. Yang, T., D. Cheng, and Y. Wang, *Freeform imaging spectrometer design using a point-by-point design method.* Applied optics, 2018. **57**(16): p. 4718-4727.

7. Shahinian, H., T. Noste, N. Sizemore, C. Hovis, P. Shanmugam, N. Horvath, and D. Gurganos. *See-through smart glass with adjustable focus*. in *Digital Optics for Immersive Displays*. 2018. International Society for Optics and Photonics.

8. Frid, H., S. Bhowmik, S. Dudorov, and J. Oberhammer, *Optimization of Micromachined Millimeter-Wave Planar Silicon Lens Antennas with Concentric and Shifted Matching Regions.* Progress In Electromagnetics Research, 2017. **79**: p. 17-29.

9. Martyshkin, D., V. Fedorov, M. Mirov, I. Moskalev, S. Vasilyev, V. Smolski, A. Zakrevskiy, and S. Mirov. *High power (9.2 W) CW 4.15 μm Fe: ZnSe laser*. in *Lasers and Electro-Optics (CLEO), 2017 Conference on*. 2017. IEEE.

10. Abdulkadir, L.N., K. Abou-El-Hossein, A.I. Jumare, P.B. Odedeyi, M.M. Liman, and T.A. Olaniyan, *Ultra-precision diamond turning of optical silicon—a review.* The International Journal of Advanced Manufacturing Technology, 2018: p. 1-36.

11. Mukaida, M. and J. Yan, *Ductile machining of single-crystal silicon for microlens arrays by ultraprecision diamond turning using a slow tool servo.* International Journal of Machine Tools and Manufacture, 2017. **115**: p. 2-14.

12. Komiya, R., T. Kimura, T. Nomura, M. Kubo, and J. Yan, *Ultraprecision cutting of single-crystal calcium fluoride for fabricating micro flow cells.* Journal of Advanced Mechanical Design, Systems, and Manufacturing, 2018. **12**(1): p. JAMDSM0021-JAMDSM0021.

13. Shahinian, H., *Fiber Based Tools for Polishing Optical Materials*. 2018, The University of North Carolina at Charlotte.

14. Shahinian, H., M. Hassan, H. Cherukuri, and B.A. Mullany, *Fiber-based tools: material removal and mid-spatial frequency error reduction.* Applied optics, 2017. **56**(29): p. 8266-8274.

15. Hull, T., M.J. Riso, J.M. Barentine, and A. Magruder. *Mid-spatial frequency matters: examples of the control of the power spectral density and what that means to the performance of imaging systems*. in *Infrared Technology and Applications XXXVIII*. 2012. International Society for Optics and Photonics.

HIGH PERFORMANCE TURNING ASSISTED BY CHIP-PULLING

Burak Sencer and Mukhtar Maulimov
School of Mechanical, Industrial and Manufacturing Engineering
Oregon State University, Corvallis, USA

INTRODUCTION

Friction is one of the key factors limiting the achievable productivity and efficiency in most machining processes. Typically, adverse effects of friction in machining has been addressed through better tool material design and use of coolants [1,2]. This paper presents an innovative technique to significantly increase the efficiency of turning processes by alleviating friction forces using an assistive device. As opposed to breaking the cut chip using chip breakers, in the proposed technique, the chip is not broken but pulled using a system to realize a new turning process so-called the “chip-pulling turning”. By pulling the cut chip externally, the friction force acting along tool’s rake face could be reduced and even cancelled. This, in return, increases the shear angle and leads to efficient material removal with significantly lower process forces and energy. An electro-mechanical chip-pulling device is designed that can pull the guided chip continuously during the turning operation. Design of the chip-pulling system, proposed pulling device and its automatic control are presented. The effect of chip-pulling is validated experimentally through various cutting experiments. Furthermore, orthogonal cutting force models are used to model the effect of chip-pulling on the process.

CANCELLING FRICTION BY CHIP-PULLING

Figure 1 depicts the basic mechanism to cancel friction forces in orthogonal cutting and chip guidance. As shown in Fig.1a, chip pulling force (tension) is applied on the cut chip as it flows on the rake face of the tool. This tension directly cancels the friction force. As a result, shear angle could be increased, and the chip thickness ratio is improved. Fig.1b presents the manual chip-pulling pulling concept and Fig. 1c shows the changes in cutting forces when the cut chip is pulled manually by hand [3,4]. As shown, during turning of low carbon steel(SPCC), cut chip can be pulled robustly and cutting forces can be lowered greatly. Also notice that, when the chip is pulled the chip thickness reduces validating the change in the chip compression ratio, which confirms the shear angle increase.

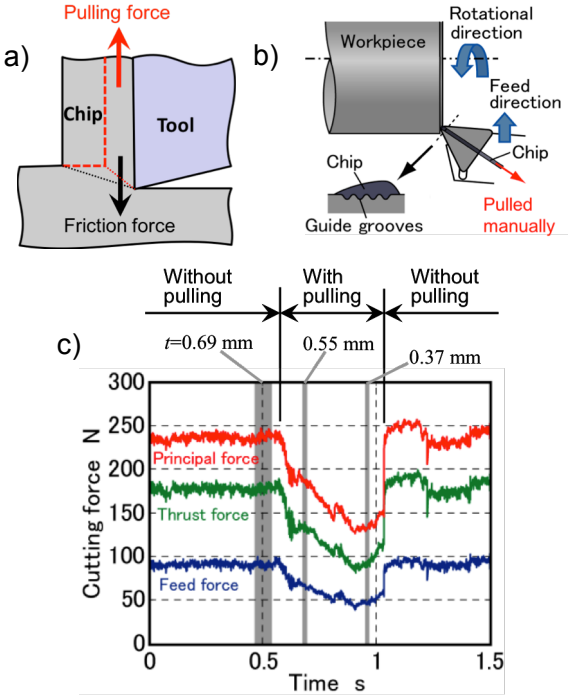

FIGURE 1: Friction cancelling (a) and Chip pulling turning (b) chip pulling turning concept c) Manual chip-pulling results

AUTOMATED CHIP-PULLING SYSTEM

Based on the preliminary results obtained through manual chip pulling. An automated chip pulling turning system is developed. Fig. 2 shows the concept system. As shown, the cut

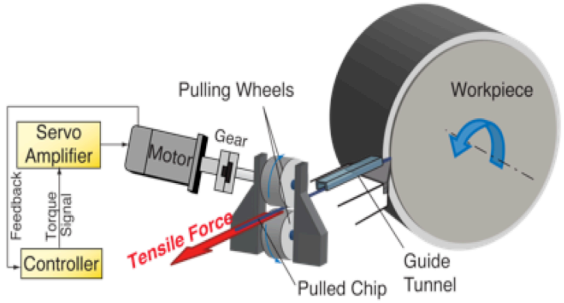

FIGURE 2: Automated chip-pulling turning

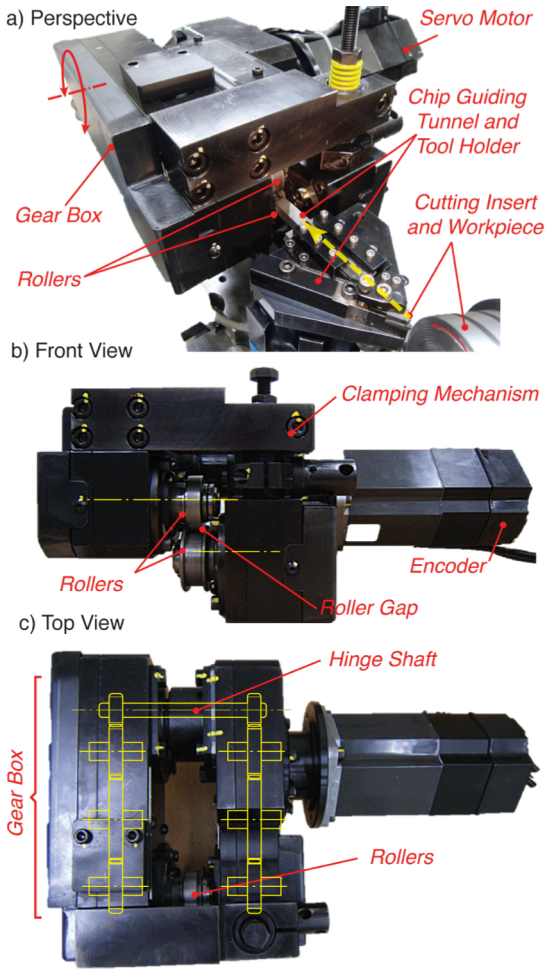

FIGURE 3: Prototyped chip pulling device

chip is guided through a tunnel to a pulling device. The pulling device is designed with a pair of rollers driven by a servo motor. Fig.3 shows the prototyped electromechanical pulling device. The servo motor drives a pair of rollers through a gear box. The pulling speed and force can be controlled by the servo control system [5,6,7]. Tension inserted on the chip is regulated by simply controlling the chip pulling speed, i.e. chip flow velocity. By pulling the chip faster than its original chip flow speed; greater tension is inserted. Overall chip-pulling speed is limited by the maximum tension that the chip can carry.

TURNING ASSISTED BY CHIP-PULLING

The effect of chip pulling in turning process is demonstrated briefly in the previous section. As compared to conventional turning, in chip-pulling turning, process forces can be minimized by applying tension on the cut chip by cancelling the friction forces as experimentally demonstrated in Fig.1. This section models effect of chip pulling on the process based on the orthogonal cutting theory [8,9,10] based on the single thin shear plane model.

Assuming a thin shear plane, a cutting force diagram is drawn for chip pulling cutting in Fig. 4. Firstly, when the chip is pulled, pulling force directly cancels friction force on the rake face by the amount of F_{pull}, which rotates the resultant force direction. Since shear deformation occurs by the resultant force, the shear direction also rotates creating a larger shear angle, ϕ'. The new shear plane has a smaller shear area due to increased chip thickness ratio. Normal and friction forces are reduced to F_n' and f' as depicted in Fig. 4. In contrast, friction angle does not change significantly and is assumed to be constant as a property of the material-tool pair [9]. Since chip pulling force cancels friction force, the deducted friction force f'-F_{pull} defines a new friction angle β' and a resultant force vector, R'. It should be noted that β' is defined as the 'effective friction angle' associated with the chip pulling cutting process, and it can be manipulated by the pulling force.

Thus, the idea of 'effective friction angle', β', allows incorporation of the pulling force to the well-known orthogonal cutting model and facilitate analysis of the process. Firstly, maximum shear stress or minimum energy principle [8],

$$\phi' = 45^0 + \alpha - \beta' \text{ or } \phi' = 45^0 + \alpha/2 - \beta'/2 \quad (1)$$

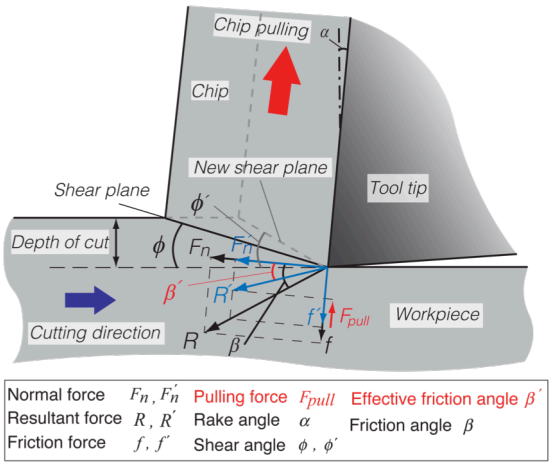

FIGURE 4: Thin shear plane model incorporating chip pulling force effect

can be used to predict the modified shear angle. The resultant force of the new process is calculated from shear strength τ_s and cutting area *A* as:

$$R' = \frac{\tau_s A}{\sin(\phi')\cos(\phi' - \alpha + \beta')} \quad (2)$$

The relationship between normal and friction forces are obtained from the force diagram (see Fig.4) and Eq. (2):

$$\left.\begin{aligned} F_n' &= R'\cos(\beta') \\ f' &= R'\cos(\beta')\tan(\beta) \end{aligned}\right\} \quad (3)$$

Using above relationships, pulling force to achieve the desired effective friction angle is calculated as:

$$F_{pull} = \frac{\tau_s A}{\sin(\phi')\cos(\phi' - \alpha + \beta')} \times \left[\cos(\beta')\tan(\beta) - \sin(\beta')\right] \quad (4)$$

Eq. (4) defines the required chip tension to control the effective friction angle and thus the cutting process. The model is evaluated at various pulling conditions where simulated cutting forces, cutting energy and the required pulling effort are compared to actual measurements. Note that, accuracy of max. shear stress and min. energy principle models depend heavily on cutting conditions. Given the zero-rake angle condition and simplicity of the Merchant's model [10] as shown in Fig. 4, both max. shear stress and min. energy principles actually capture the chip-pulling process mechanics well. Both models validate that introducing controlled tension on the chip; process forces could be reduced almost by half without changing any of the actual cutting parameters. It introduces an opportunity to cut in higher material removal rate and efficiency with lower forces. In particular, for certain processes thrust force can be cancelled completely by the pulling force for precision or chatter-free cutting of flexible work-pieces, which is demonstrated in the following section. As the pulling force is increased, friction energy consumed by cutting is reduced. The advantage obtained in reduction of cutting energy is more than 5 times than that of inputted by pulling. This in return reduces overall energy, heat generation and helps to improve tool life.

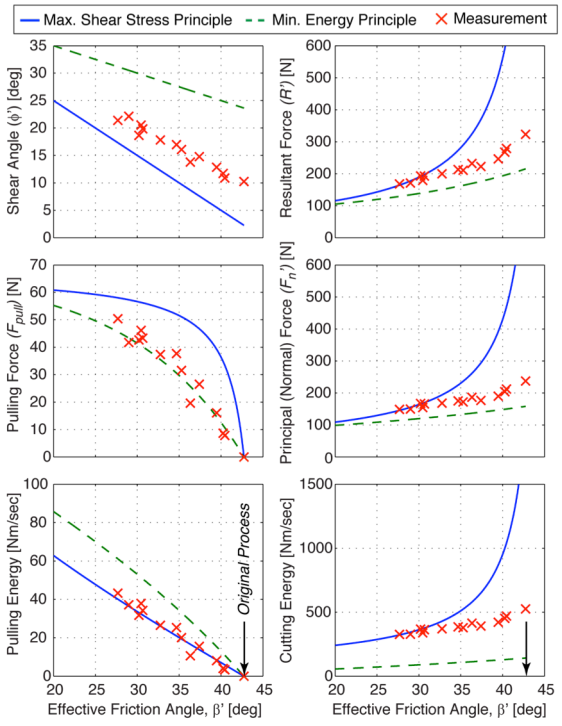

FIGURE 5: Analytical and experimental results. (Workpiece: low-carbon steel (JIS: S10C), Tool: sintered tungsten carbide insert, nose radius of 0.8[mm] and rake angle 0[deg], Feed: 0.12[mm/rev], 215[rpm], Cutting speed: 133 [m/min], Depth of cut: 0.4[mm])

PRECISION TURNING WITH CHIP PULLING

In conventional turning processes the thrust force component acts in the radial direction and therefore causes deflection errors or chatter vibrations on slender/thin compliant workpieces. If adjusted correctly, the chip pulling force can be used to reduce friction force on rake face to achieve zero thrust force cutting as well. Note that if the pulling force is greater than then friction force, workpiece can even be pulled towards the tool generating negative friction force component. This characteristic is actually similar to the mechanics elliptical vibration cutting process [11].

Here, a preliminary application is considered, and results are demonstrated in Fig. 6. In this experiment compliant soft copper workpiece is machined with a PCD tool. As shown, friction force on the tool is cancelled by the pulling force, which is controlled by the developed chip tension control system. This, in return, allows cancellation of the thrust force component and enables precision finish of slender shafts without deflection and circumventing vibration problems [12,13].

CONCLUSIONS

This paper presented a new turning process that is enhanced by pulling the cut chip. An electromechanical pulling system is designed for automatically pulling the chip. It is shown that develop chip pulling system can pull the chip at different speeds and apply controlled tension to cancel friction forces and thereby improve the process efficiency. The system demonstrated that the friction force could be fully cancelled to achieve precision turning of slender work-pieces. Lastly, the thin shear plane model is utilized to model the mechanics of the chip pulling cutting process. The model captures the fundamental effect of chip pulling reasonably well and provides guidance for planning the process.

ACKNOWLEDGEMENTS

This research is supported by NSF's Academic Liaison with Industry (GOALI) Award Number: 1661926. Authors express their deep gratitude to the Ultra-Precision Engineering Laboratories of the Nagoya University, Japan.

REFERENCES

[1] Bailey JA. Friction in metal machining—mechanical aspects. Wear. 1975 Feb 1;31(2):243-75.

[2] Arrazola PJ. Investigations on the effects of friction modeling in finite element simulation of machining. International journal of mechanical sciences. 2010 Jan 1;52(1):31-42.

[3] Shamoto E, Aoki T, Sencer B, Suzuki N, Hino R, Koide T. Control of chip flow with guide grooves for continuous chip disposal and chip-pulling turning. CIRP Annals-Manufacturing Technology. 2011 Jan 1;60(1):125-8.

[4] Aoki T, Sencer B, Shamoto E, Suzuki N, Koide T. Development of a high-performance chip-guiding turning process—tool design and chip flow control. The International Journal of Advanced Manufacturing Technology. 2016 Jul 1;85(1-4):791-805.

[5] Sencer B, Maulimov M. A new turning system assisted by chip-pulling. Journal of Manufacturing Processes. 2018 Jun 28.

[6] Sencer B, Tomoya A, Shamoto E, Hasegawa T, Koide T. Development of a chip pulling system for efficient turning. Procedia CIRP. 2014 Jan 1;14:616-20.

[7] Kalman RE. A new approach to linear filtering and prediction problems. Journal of basic Engineering. 1960 Mar 1;82(1):35-45.

[8] Shamoto E, Altıntas Y. Prediction of shear angle in oblique cutting with maximum shear stress and minimum energy principles. Journal of manufacturing science and engineering. 1999 Aug 1;121(3):399-407.

[9] Altintas Y. Manufacturing automation: metal cutting mechanics, machine tool vibrations, and CNC design. Cambridge university press; 2012 Jan 30.

[10] Merchant ME. Mechanics of the metal cutting process. I. Orthogonal cutting and a type 2 chip. Journal of applied physics. 1945 May;16(5):267-75.

[11] Shamoto E, Moriwaki T. Study on elliptical vibration cutting. CIRP Annals-Manufacturing Technology. 1994 Jan 1;43(1):35-8.

[12] Budak E, Altintas Y. Analytical prediction of chatter stability in milling—part II: application of the general formulation to common milling systems. Journal of Dynamic Systems, Measurement, and Control. 1998 Mar 1;120(1):31-6.

[13] Shamoto E, Fujimaki S, Sencer B, Suzuki N, Kato T, Hino R. A novel tool path/posture optimization concept to avoid chatter vibration in machining–proposed concept and its verification in turning. CIRP Annals-Manufacturing Technology. 2012 Jan 1;61(1):331-4.

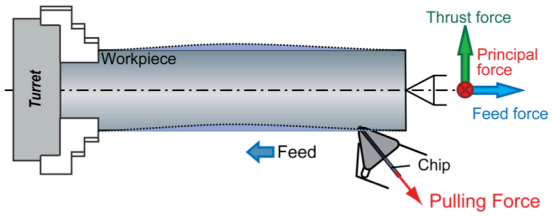

a) *Force relations*

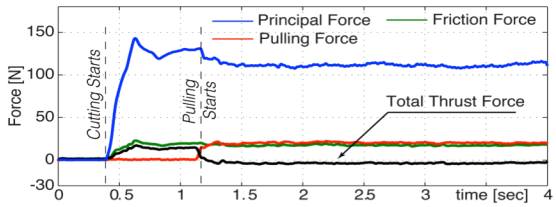

b) *Measured cutting forces*

FIGURE 6: Zero thrust force control. (Workpiece: tough pitch copper, Tool: PCD insert with a guide groove, nose radius of 0.8[mm] and rake angle of 0[deg], Feed: 0.12[mm/rev], Rotational speed: 315[rpm], Depth of cut: 0.6[mm], Cutting speed: 65[m/min])

THE EFFECT OF SYMMETRIC AND ASYMMETRIC DYNAMICS ON PERIOD-N BIFURCATIONS

Andrew Honeycutt and Tony L. Schmitz
Department of Mechanical Engineering and Engineering Science
University of North Carolina at Charlotte, Charlotte, NC

INTRODUCTION

The mean material removal rate (MRR) in milling is calculated from the product of radial depth of cut, *a*, axial depth of cut, *b*, feed per tooth, f_t, and spindle speed, Ω. Because higher MRR reduces machining time, increasing MRR also decreases production cost. It is therefore desirable to increase all four process parameters (*a*, *b*, f_t, and Ω) within the limits of the machining system. Limitations to these increases include: chatter (or unstable machining performance), tool wear, torque/power limits for the selected spindle, and feed rate limits for the selected drive. While all four limits can be imposed individually (or in combination), the focus for this study is chatter.

It is well understood that chatter occurs due to the inherent combination of structural flexibility and the periodic cutting force that excites the structural dynamics. Two primary categories for unstable behavior are: 1) regenerative; and 2) mode coupling chatter. Only regenerative chatter, where the process feedback leads to gain-dependent behavior, is considered here. This feedback occurs because the instantaneous chip thickness depends on both the vibration state of the cutter at the current time and the surface left behind by previous tooth passages (which introduces a time delay, or memory, in the differential equations of motion). Because the cutting force is a function of this instantaneous chip thickness and the current vibration state depends on the instantaneous force, the feedback loop is closed. Traditionally, the system gain is described as the axial depth of cut for a selected radial depth. The spindle speed dictates the time delay so, together, the spindle-speed and axial depth offer the control parameters for milling [1].

Traditionally, regenerative chatter is considered to be a self-excited vibration and can be described as a secondary Hopf bifurcation (a bifurcation is a dramatic change in the dynamic state due to small modifications in the process parameters). The relationship between Ω and the limiting *b* value is typically presented in a stability map, or stability lobe diagram. Figure 1 provides an example.

In recent research, it has been demonstrated that different types of instability can occur in milling. Not only can secondary Hopf bifurcations be observed, it has also been shown that period-n (n = 2, 3, 4, …) bifurcations can exist, where the system response repeats every n tooth periods (rather than every tooth period for the forced vibration that characterize stable milling) [2-3]. Figure 2 displays an example.

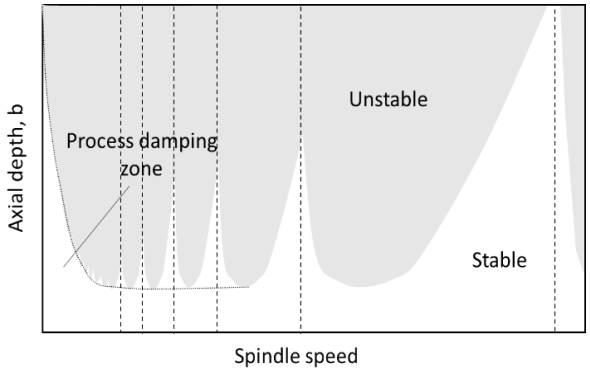

Figure 1. Example stability map for milling.

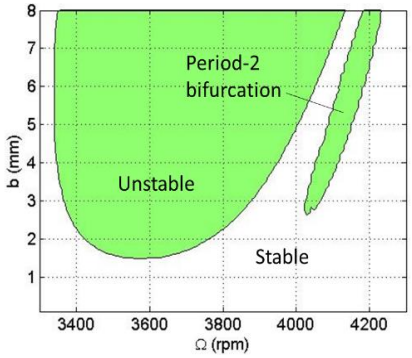

Figure 2. Stability map with period-2 bifurcation zone.

The purpose of this study is to experimentally and numerically (time domain simulation) explore the stability behavior for dynamic systems with both asymmetric and symmetric dynamics. Results are presented for a flexure-based experimental setup that produces significant asymmetry in the dynamic stiffness relative to the cutting direction. Period-n bifurcations are simulated and validated. Systems with symmetric dynamics that apply the same modal parameters as the flexible direction for the flexure-based setup are then simulated. Both period-n and secondary Hopf bifurcations are identified and compared to the asymmetric system behavior. Conclusions are finally presented.

ASYMMETRIC DYNAMICS

Because flexure-based experiments, where the workpiece is mounted on a single degree-of-freedom (SDOF) flexure, provide convenient measurement of the milling process outputs, they are a common choice for model validation. This setup represents the case of strongly asymmetric system dynamics because the SDOF flexure is much more flexible in one Cartesian direction than the other two. Additionally, the tool point dynamics are typically selected so that the tool's lowest dynamic stiffness is much higher than the flexure's lowest dynamic stiffness.

To demonstrate bifurcation behavior for a strongly asymmetric system, the milling response was predicted using time domain simulation and validated using the flexure-based experimental configuration shown in Figure 3. For this setup, the flexure's time dependent displacement, velocity, and acceleration during cutting were measured by a capacitance probe, laser vibrometer, and low mass accelerometer, respectively, to assess milling behavior under various process parameters. The laser tachometer signal was used to synchronously sample the flexure motion data.

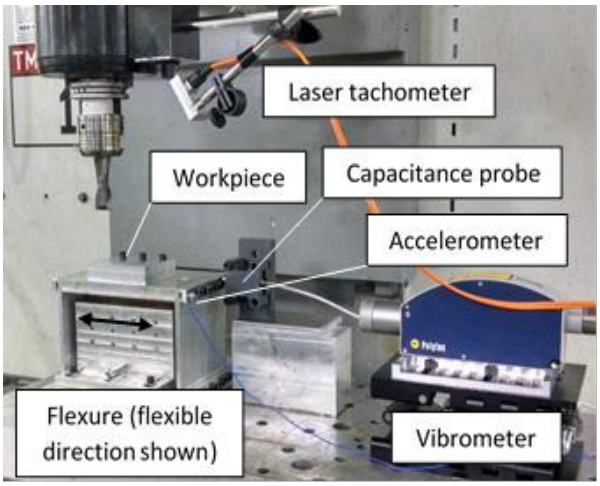

Figure 3. SDOF parallelogram, leaf-type flexure experimental setup.

The flexure and tool point dynamics are listed in Table 2. These modal parameters were extracted from *x* (feed) and *y* direction impact tests completed on both the flexure and single-flute 19.05 mm diameter, 30 deg helix endmill. The mechanistic cutting force coefficients for the 6061-T6 aluminum workpiece were k_{tc} = 792 N/mm^2, k_{nc} = 352 N/mm^2, k_{te} = 26 N/mm, and k_{ne} = 28 N/mm. Time domain simulations were completed for up milling in the flexure's low stiffness direction with a 2 mm radial depth and 0.1 mm/tooth feed. The simulation outputs included the cutting force and flexure motion *x* and *y* components for a range of {spindle speed, axial depth} combinations. The flexure displacement and velocity signals were synchronously sampled at the tooth period (once-per-revolution for the single flute cutter). Figure 4 shows the flexure's time dependent, feed direction displacement, *x*, and velocity, *dx/dt*, as well the periodic sampling result (circles). It is observed that the process behavior repeats each period for the stable {3400 rpm, 6 mm axial depth} cut after the initial transients have attenuated.

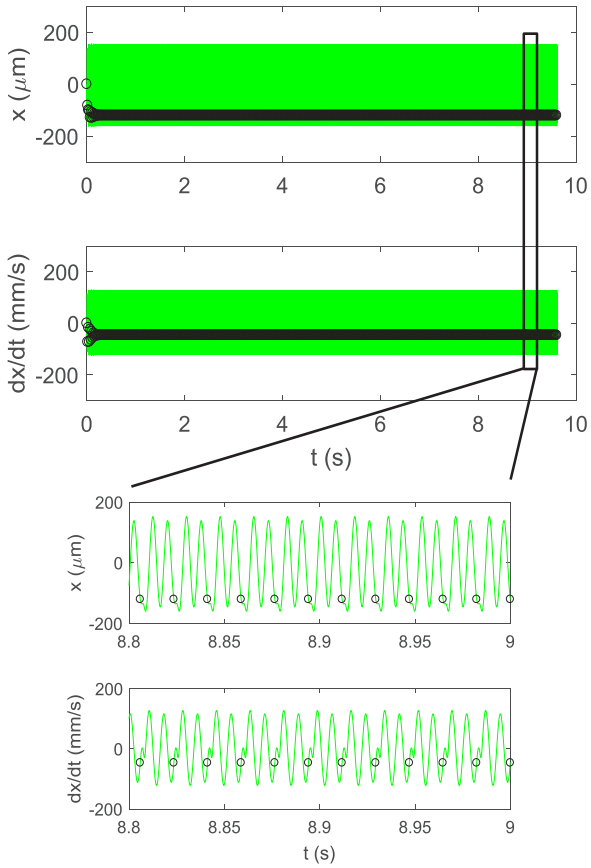

Figure 4. Predictions for stable {3400 rpm, 6 mm axial depth} up milling using the Table 1 dynamics with a 2 mm radial depth and 0.1 mm/tooth feed. (Top) time dependent displacement with periodic samples (circles); (bottom) time dependent velocity with periodic samples. (Inset) higher magnification view to observe individual periodic samples of the displacement (top) and velocity (bottom).

Table 1. Modal parameters (natural frequency, dimensionless viscous damping ratio, and stiffness) for asymmetric flexible feed direction experimental setup.

Flexure			Tool point		
x (feed direction)			*x*		
130.0 Hz	0.0147	2.1×10^6 N/m	1055 Hz	0.045	4.2×10^7 N/m
y			*y*		
756 Hz	0.085	7.7×10^7 N/m	1055 Hz	0.045	4.2×10^7 N/m

To more effectively visualize the process behavior, the displacement is plotted versus the velocity in the Figure 5 Poincaré map. Here, the sampled points all align at a single location because the stable milling process exhibits forced vibration at the tooth period. For this figure, the transient portion (during the cut entry) was excluded to leave only the steady-state behavior.

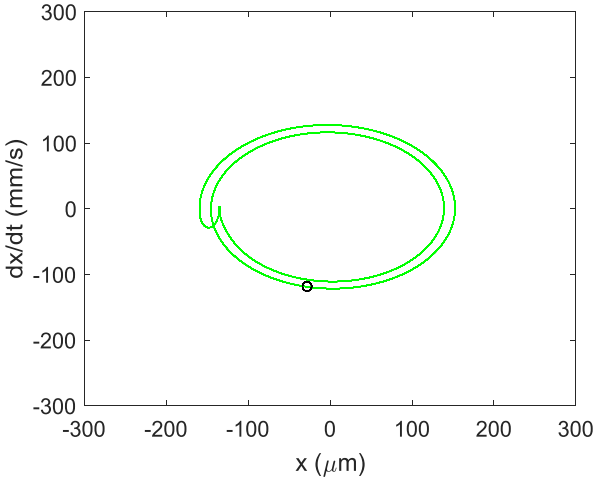

Figure 5. Predicted Poincaré map for stable {3400 rpm, 6 mm axial depth} up milling using the Table 1 dynamics with a 2 mm radial depth and 0.1 mm/tooth feed.

Figures 6 and 7 show the results for {3310 rpm, 6 mm axial depth}. This behavior represents a period-2 bifurcation because the motion repeats every other tooth period, rather than every tooth period. Here, two points are observed in the Poincaré map. Cutting tests were completed on the Figure 3 setup to validate the time domain predictions. The experimental results are presented in Figure 8, where the displacement was measured by the capacitance probe and the velocity by the laser vibrometer. The time dependent signals were sampled once per tooth period using the laser tachometer signal and the transients (from the cut entry) were excluded. Good agreement with Figure 7 is observed and the simulation performance is verified.

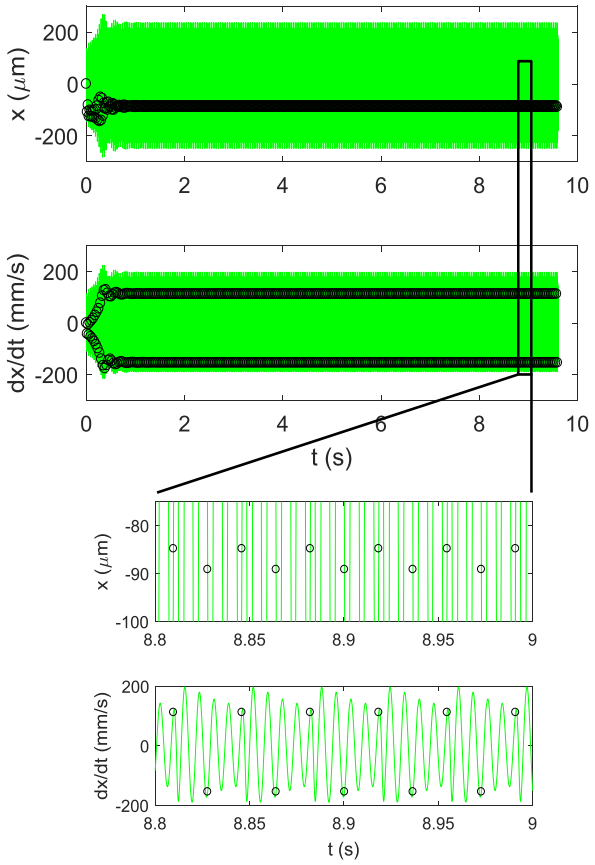

Figure 6. Predictions for period-2 {3310 rpm, 6 mm axial depth} up milling using the Table 1 dynamics with a 2 mm radial depth and 0.1 mm/tooth feed.

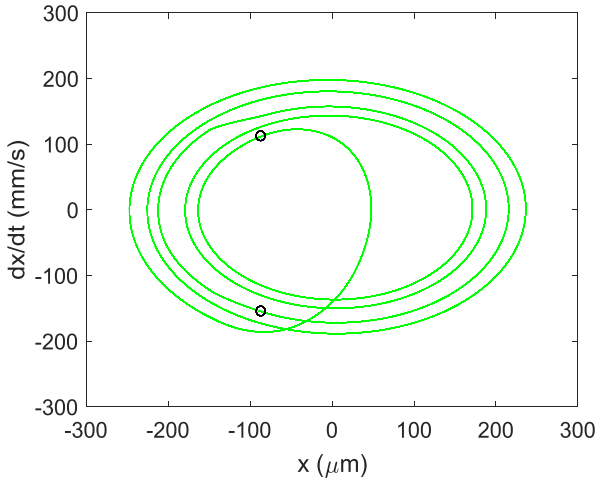

Figure 7. Predicted Poincaré map for period-2 {3310 rpm, 6 mm axial depth} up milling using the Table 1 dynamics with a 2 mm radial depth and 0.1 mm/tooth feed.

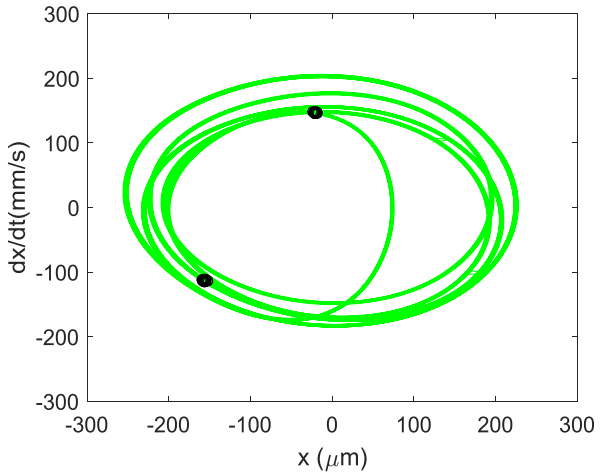

Figure 8. Experimental Poincaré map for period-2 {3310 rpm, 6 mm axial depth} up milling using the Table 1 dynamics with a 2 mm radial depth and 0.1 mm/tooth feed.

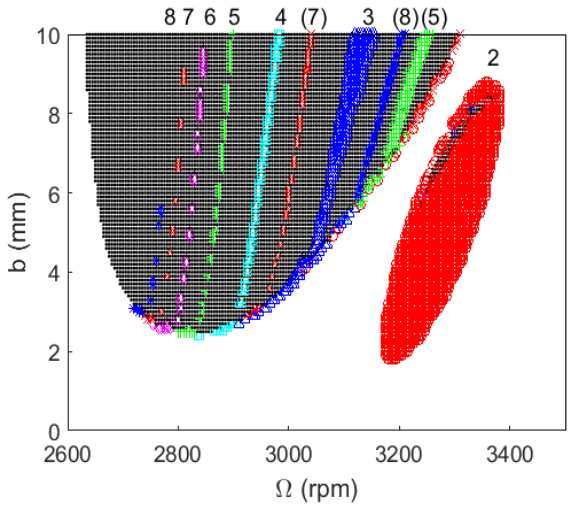

Figure 9. Predicted stability map for up milling using the Table 1 dynamics with a 2 mm radial depth and 0.1 mm/tooth feed. The bifurcation period is identified by the numerals 2-8.

To obtain a global stability map, time domain simulations were completed over a grid of spindle speeds, Ω, from 2600 rpm to 3500 rpm (5 rpm increments) and axial depths, *b*, from 0.1 mm to 10 mm (0.1 mm increments). Periodic sampling was applied to the *x* data to individually identify period-2 through period-8 bifurcations. The results are presented in Figure 9, where the symbols are defined in Table 2. An elliptical, period-2 "island" is seen between 3200 rpm and 3400 rpm within the stable zone; the Figure 7 prediction and Figure 8 experiment were completed at a point inside this island. Period-2 through period-8 bifurcation "bands" are also observed within the secondary Hopf bifurcation zone (i.e., traditional regenerative chatter). In Figure 9, the bifurcation period is identified using the numbers 2-8, which appear at decreasing spindle speeds (i.e., right to left from 2 to 8). Repeated bands at higher speeds are also present; these are indicated with parentheses (e.g., (7) appears between 3 and 4 at a higher spindle speed range than 7).

Table 2: Symbols for period-n stability maps.

Period	Symbol	Color
2	Circle	Red
3	^	Blue
4	Square	Cyan
5	+	Green
6	Diamond	Magenta
7	×	Red
8	*	Blue
Stable	No symbol	(White space)
Secondary Hopf	.	Black

Using Figure 9, various bifurcation behaviors can be identified and then studied individually. For example, a secondary Hopf bifurcation is observed at {2850 rpm, 6 mm axial depth}. This quasi-periodic behavior is displayed in Figure 10 (time domain) and Figure 11 (Poincaré map). In Figure 11, the characteristic elliptical distribution for the periodically sampled points is obtained due to the presence of the new incommensurate chatter frequency (i.e., self-excited vibration).

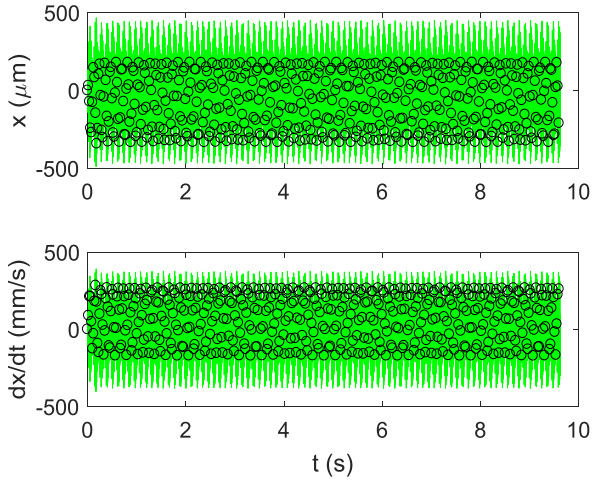

Figure 10. Predictions for unstable {2850 rpm, 6 mm axial depth} up milling using the Table 1 dynamics with a 2 mm radial depth and 0.1 mm/tooth feed.

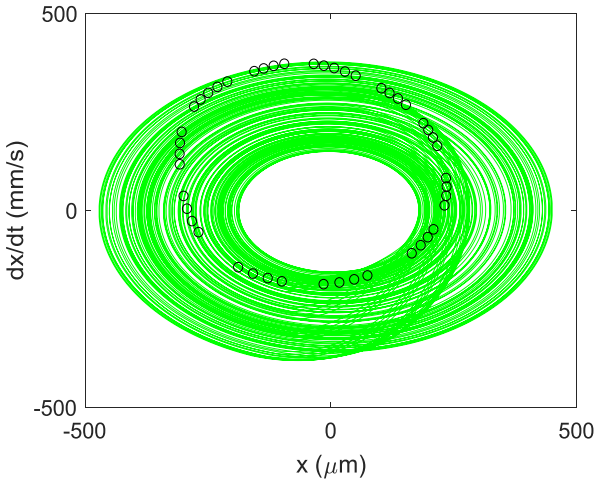

Figure 11. Predicted Poincaré map for unstable {2850 rpm, 6 mm axial depth} up milling using the Table 1 dynamics with a 2 mm radial depth and 0.1 mm/tooth feed.

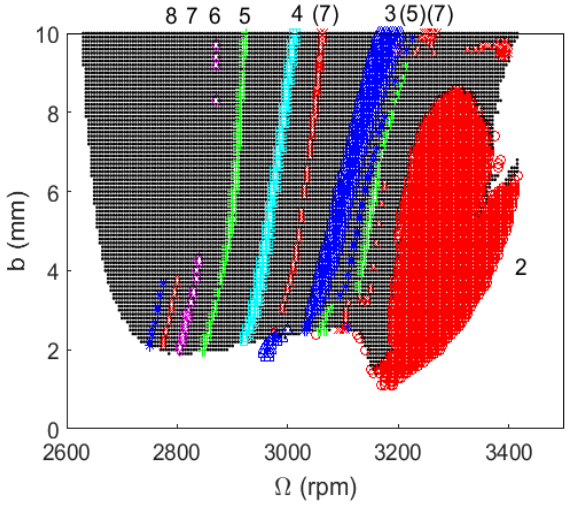

Figure 12. Predicted stability map for up milling using the Table 3 symmetric dynamics with a 2 mm radial depth and 0.1 mm/tooth feed.

SYMMETRIC DYNAMICS

Because tools, holders, and spindles are rotationally symmetric by design, it is common to observe symmetric system dynamics in practice. Therefore, simulations were next completed using the validated time domain solution to see how the process behavior changed with a shift from asymmetric to symmetric dynamics. First, the Table 1 dynamics were modified to match the flexure's stiff *y* direction modal parameters to the flexible *x* direction; see Table 3. The same cutting force model and cutting conditions as used for Figure 9 were applied. The symmetric dynamics stability map is provided in Figure 12 (5 rpm and 0.1 mm increments). It is seen that: 1) the period-2 island has expanded into the original secondary Hopf zone; and 2) a "hump" has appeared in the stability boundary near {3100 rpm, 2 mm axial depth}.

Table 3. Modal parameters (natural frequency, dimensionless viscous damping ratio, and stiffness) for strongly asymmetric flexible feed direction experimental setup.

Flexure			Tool point		
x (feed direction)			*x*		
130.0 Hz	0.0147	2.1×10^6 N/m	1055 Hz	0.045	4.2×10^7 N/m
y			*y*		
130.0 Hz	0.0147	2.1×10^6 N/m	1055 Hz	0.045	4.2×10^7 N/m

WEAKLY ASYMMETRIC DYNAMICS

As a final study, a dynamic system with weak asymmetry was considered. This is seen in practice, for example, when the flexible tool response dominates the system dynamics, but the *x* direction is slightly stiffer than the *y* (or vice versa) due to asymmetry in the spindle-machine dynamics into which the endmill is inserted. For this study, the *y* direction stiffness and natural frequency were set to 90% of the *x* (feed) direction values; see Table 4. The results are displayed in Figures 13 (symmetric) and 14 (asymmetric). It is seen that the Figure 14 stable gap (white space) has shifted, the period-2 island appears within the stable zone, and the stability hump has grown to a local stability peak (near 2900 rpm) with a new period-2 zone immediately to its left. Clearly, the weak asymmetry has added significant complexity to the overall stability behavior.

Table 4. Modal parameters for weakly asymmetric dynamics system (symmetric when no multiplier used for y direction).

Flexure			Tool point		
x (feed direction)			*x*		
125.8 Hz	0.0136	1.75×10^6 N/m	1188 Hz	0.095	4.24×10^7 N/m
y			*y*		
0.9(125.8) Hz	0.0136	0.9 (1.75×10^6) N/m	1188 Hz	0.095	4.24×10^7 N/m

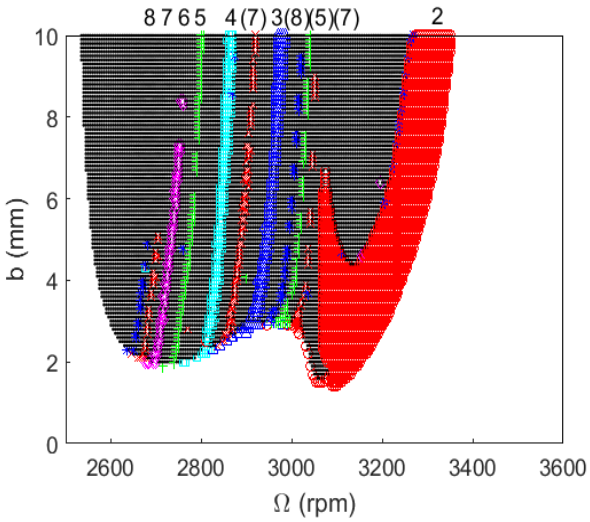

Figure 13. Predicted stability map for up milling using the symmetric Table 4 dynamics with a 2 mm radial depth and 0.35 mm/tooth feed.

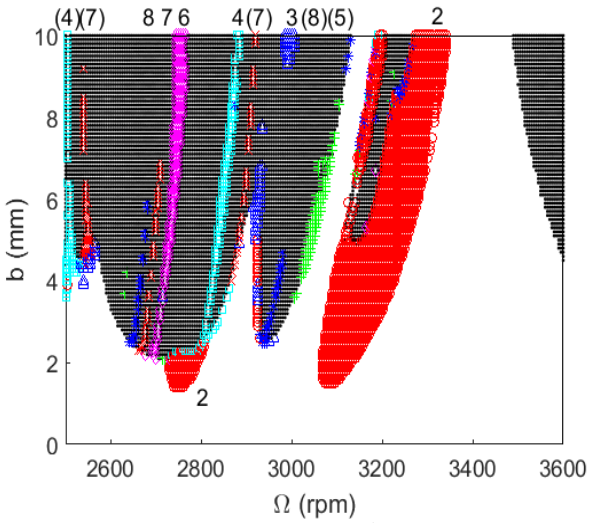

Figure 14. Predicted stability map for up milling using the asymmetric Table 4 dynamics with a 2 mm radial depth and 0.35 mm/tooth feed.

CONCLUSIONS

This paper described the application of time domain simulation to the prediction of milling behavior for asymmetric, symmetric, and weakly asymmetric system dynamics. These choices correspond to three common physical setups: a single degree-of-freedom flexure setup often used to perform validation experiments (asymmetric); long, flexible endmill dynamics (symmetric); and tool or workpiece-dominated dynamics with slight asymmetry in the plane of the cut (weakly asymmetric). The time domain simulation outputs included displacement and velocity, which were synchronously sampled to identify the milling behavior. The two signals were sampled at the tooth period to produce Poincaré maps. Also, subharmonic periodic sampling was completed at integer multiples of the tooth period and then these results were combined with a numerical stability metric to automatically produce a stability map from a grid of time domain simulations. Experimental validation was provided for the flexure-based setups. The following results were observed.

- Asymmetric dynamics

In a flexure-based setup (Table 1), the process behavior was predicted and verified for feed in the flexible direction of the asymmetric flexure. A period-2 island was seen in the stable zone with period-3 and higher bands located within the traditional secondary Hopf bifurcation zone.

- Symmetric dynamics

The dynamics for the flexure-based setup was modified to match both directions to the original flexible direction. Time domain simulations were completed to produce a stability map. It was seen that the period-2 island expanded into the original secondary Hopf zone and a hump appeared in the stability boundary near the new period-2 location in both instances. The period-3 and higher bands persisted.

- Weakly asymmetric dynamics

In this case, the stiff direction was similar to the flexible direction, but not identical (the stiffness and natural frequency were set to 90% of the flexible direction values). It was seen in the stability map that the stable gap shifted in spindle speed, a period-2 island appeared within the stable zone, and a new local stability peak with a corresponding period-2 zone appeared. Generally speaking, the weak asymmetry added significant complexity to the stability map.

ACKNOWLEDGEMENTS

This material is based on work supported by the National Science Foundation under Grant No. CMMI-1561221.

REFERENCES

[1] Schmitz, T. and Smith, K.S., Machining Dynamics: Frequency Response to Improved Productivity, Springer, New York, NY, 2009.

[2] Honeycutt, A. and Schmitz, T., 2016, A Numerical and Experimental Investigation of Period-n Bifurcations in Milling, Journal of Manufacturing Science and Engineering, 139/1: 011003.

[3] Honeycutt, A. and Schmitz, T., 2016, A New Metric for Automated Stability Identification in Time Domain Milling Simulation, Journal of Manufacturing Science and Engineering, 138/7: 074501.

DESIGN IMPROVEMENT OF THE CUTTING FLUID SUPPLY OF A LARGE 5-AXIS MACHINE TOOL

Pablo Hernández-Becerro[1], Philip Blaser[2], Josef Mayr[1] and Konrad Wegener[2]
[1]inspire AG Technoparkstrasse 1, 8005 Zürich, Switzerland
[2]Institute of Machine Tools and Manufacturing (IWF)
ETH Zürich, Switzerland

INTRODUCTION

Thermally induced deviations are the major cause of the lack of repeatability in production and measurement systems (Bryan [1]). Thermal deviations are caused by internal and external influences. Internal influences refer to heat losses in the machine elements, such as drives or bearings. External influences refer to the interaction between the mechanical system and its surroundings. These include effects such as the convective heat exchange with the environment or the process cutting fluid. Schellekens et al. [2] pointed out that the thermal isolation of the machine from external influences is hard to achieve due to the complexity of the heat transfer mechanisms. In order to understand and predict the effect of the internal and external influences thermo-mechanical models can be used. Thermo-mechanical models are based on the finite element (FE) discretization of the physical field equations, i.e. the heat transfer and elasticity equations. Several examples of physical models can be found in the literature. Mian et al. [3] studied the effect of the change of the environmental temperature in a 3-axis machine tool. The authors stated that the initial thermal state of the machine is usually unknown. They defined a settling time as the time required for the machine tool structure to be in equilibrium with the environment. Ess [4] used FE for the simulation of the thermo-mechanical response of machine tool assemblies. The machine elements connecting the different structural parts of the machine tool were represented by macro models accounting for the thermal conductivity, thermal capacity and mechanical stiffness. The effect of the direct measurement system was also included for the calculation of the resulting tool center point (TCP) error.

One application for physical models is the development of a state observer for the online compensation of thermal errors in machine tools. Thiem et al. [5] developed a thermo-mechanical FE model of a parallel kinematic machine. The model aimed at compensating the elongation of the ballscrew of the mechanism in the axial direction. The authors measured the resulting thermal errors by means of laser interferometry. The measured deviations were later used to optimize the most uncertain parameters of the model, enabling the use of the prediction for online thermal error compensation. The authors claimed that the results were comparable to compensation strategies based on empirical models, such as characteristic diagrams.

Another use for thermo-mechanical models takes place during the design phase, contributing to reduce the time required for the development of a new machine tool prototype. Mayr et al. [6] used the Finite Difference Element Method (FDEM) in order to efficiently compute the thermal errors of machine tools. The authors applied this approach to improve the design of a machine tool frame. The proposed design, which was based on a more symmetric construction, was evaluated by computing the position and orientation errors at one point of the working space. Sun et al. [7] used physical models for the improvement of thermal response of a 3-axis ultra-precision grinding machine. The heat losses at the linear motors and the spindle had a major influence on the thermally induced errors. This work redesigned the structural parts close to the heat sources in order to enhance the heat dissipation and reduce the heat transfer from the sources to the guideways. Sun et al. developed a FE model, which they validated exclusively with structural temperatures. The temperature rise for the studied load case was reduced after the design optimization both in the simulation and experimental results. The model showed that the straightness error motions of the Z-axis improved after the structural optimization. These works demonstrate the feasibility to use physical models in the design optimization of the thermal behavior of a machine tool.

DEVELOPMENT OF THE THERMO-MECHANICAL MODEL

This paper focuses on the development of a thermo-mechanical model of a large 5-axis machine depicted in Figure 1. A rotary table is located in the workpiece side and a rotary head on the tool side. The kinematic chain according to ISO 10791-1:2015 [8] is: H [w B X b Z Y A (C) t]. The thermo-mechanical models describe the thermally induced TCP deviations by means of a FE discretization of the machine tool structure. The focus of model developed in this work is the evaluation of the effect of external heat sources, namely the environment and the cutting fluid. For this study the influence of the internal heat losses (e.g. friction in the bearings) is minimized by moving the axes at sufficiently low feed rates.

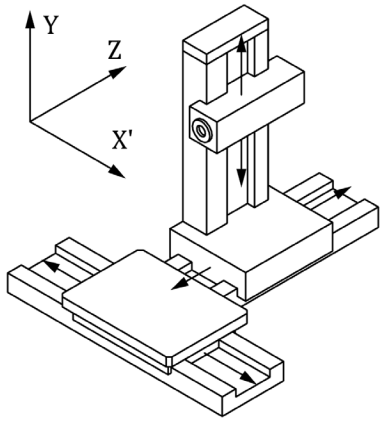

FIGURE 1. Schematic of linear axes of the machine tool adapted from ISO 10791-1:2015 [8]

The main goals of the cutting fluid are removing the chips, reducing tool wear and tempering the structure. The introduction of fluid media on the structure modifies the thermal response of the machine tool, changing the position and orientation errors. The machine tool under investigation supplies cutting fluid in three different ways. The bed cutting fluid delivers the fluid through two nozzles located at the back to the Z-axis. The cutting fluid is supplied also on the spindle head and through a shower located on the upper part of the housing of the working space. Previous measurements, presented by Hernández-Becerro et al. [9] and Blaser et al. [10], showed that the effect of the bed cutting fluid have the largest influence on the thermally induced TCP errors in this machine tool, as it affects a larger part of the structure. The supply of fluid media modifies the heat exchange between the structural parts, where the boundary conditions transition from natural convection with the air to forced convection. This leads to a switch in the boundary conditions, which needs to be correctly handled. The values of the heat transfer coefficients (HTC) are estimated from simplified CFD simulations of the fluid channels. Due to the high pressure of the fluid, required to reach the working space and remove the chips, the fluid does not affect homogeneously the bed. This is represented in the model by considering a spatial distribution of the HTC over the cutting fluid channel. The cutting fluid temperature is controlled by an external unit, whose set temperature is a sensor close to the machine tool bed partially capturing environmental influences.

The convective heat transfer between the environment and the structure is caused by natural convection. The values of the HTC can be estimated by means of empirical formulas, computational fluid dynamic (CFD) simulations or meta modeling techniques, as presented by Pavliček et al. [11]. The environmental temperature in a non-acclimatized workshop varies over time and space. The model considers the different layers in order to accurately describe the stratification of the air temperature. A machine housing covers the working space, altering the convective heat exchange. This enclosure is also considered in the description of the boundary conditions, adjusting the values of the HTC.

In order to capture accurately the resulting TCP deviations, the model includes the effect of the measurement system. The direct measurement system consists of glass scales made of steel fixed to the structure in the middle. The relative TCP deviations are then partly corrected by the measurement systems.

The model evaluates the thermal response of the machine over 12 hours. The machine is exposed to an uncontrolled environmental temperature and a continuous supply of cutting fluid from the back of the Z-axis. Before the cutting fluid is introduced, the model is initialized with 14 hours of environmental temperature. This allows the model to transition from a homogeneous initial temperature to a realistic initial temperature distribution. The validation can be then performed by comparing the outputs of the model to measurements of structural temperatures and thermally induced TCP errors. The temperature is measured with direct-to-digital temperature sensors attached to the surface of the structure, with a resolution of 0.1 K and sampling time of 11

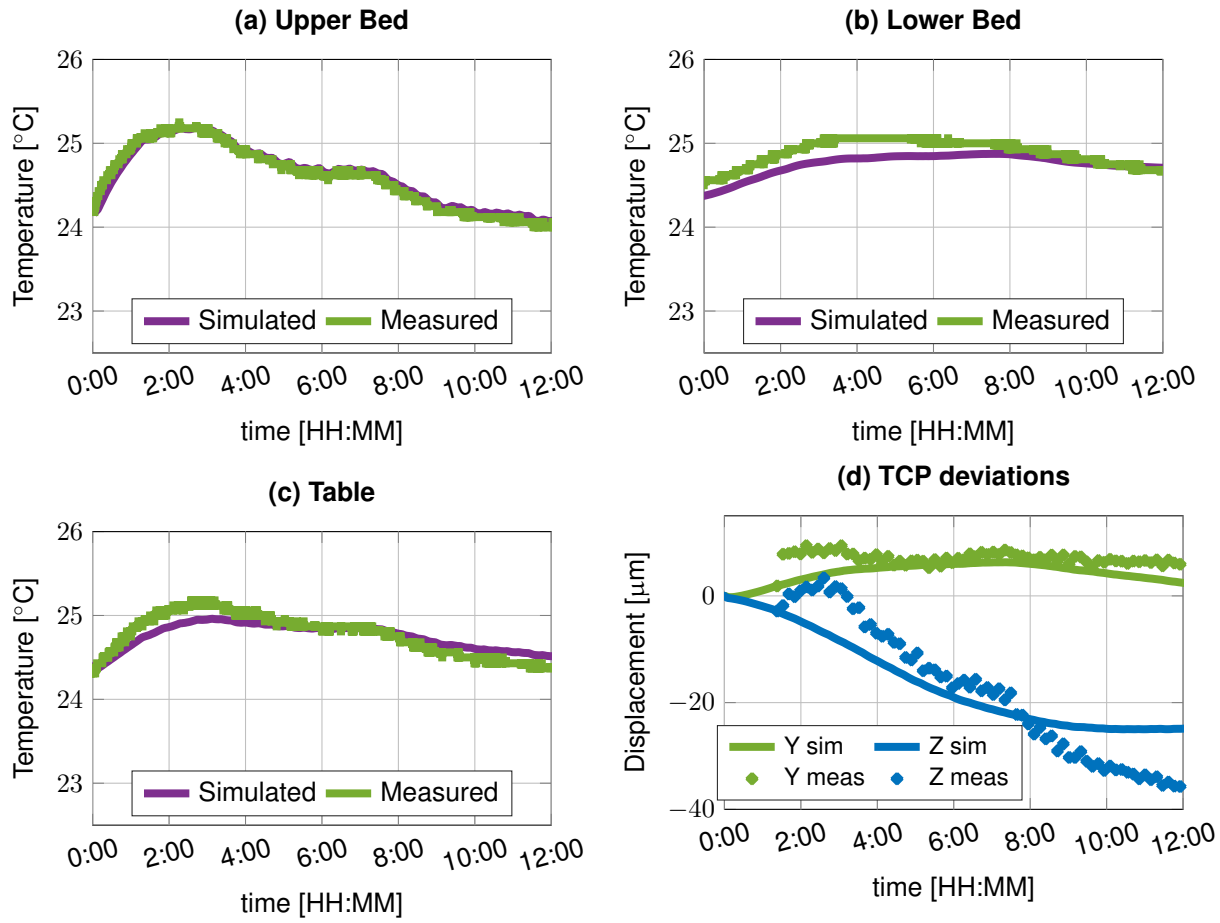

FIGURE 2. Comparison of the outputs of the model and the measurements. (a) Temperature on the upper part of the machine tool bed (b) Temperature on the lower part of the machine tool bed (c) Temperature on the table (d) Thermal errors of the TCP relative to the workpiece

s. Figure 2 compares the model results with the measurements on the machine tool. The model captures accurately the temperature distribution of surfaces closer to the cutting fluid, such as Figure 2(a) and 2(c). For surfaces further away from the influences of the cutting fluid, i.e. where the natural convection plays a major role, the accuracy of the temperature prediction is reduced, as displayed in 2(b).

The model is further validated with measurements of the deviations at the TCP relative to the table. The measurement procedure is based on the R-Test [12]. A precision sphere is placed on the table and a sensor nest mounted on an invar holder is located on the spindle side. The oil resistant LVDT sensors have a resolution of 0.06 µm and a repeatability of 0.01 µm. The TCP deviations are measured every 9 min and are compared to the output of the simulation. Figure 2(d) compares measured TCP displacements relative to the precision sphere with the model output. The first hours of the measurement are missing due to a problem with the data acquisition. The model can represent the trends of the thermal errors at this point of the working space in Y- and Z-direction. The maximum discrepancies between model and simulation are bellow 10 µm. The differences are caused by the uncertain boundary conditions describing the heat exchange with the environment as well as uncertainties in the expansion coefficients coupling the thermal and mechanical model. Due to the symmetry of the machine tool design the thermal errors measured in X-direction are small. The uncertainty of the measurement setup is not sufficiently small to capture

the thermal errors in X-direction. Thus the thermal errors in X-direction are excluded from the model validation.

The validated physical model represents the behavior of the system under investigation and allows the evaluation of the underlying phenomena leading to the TCP deviations. The transient response of the bed after the introduction of the cutting fluid results in a deformation of the tool-sided axes of the machine tool. The machine bed requires a long time for the homogenization of the temperature field. This creates a transient deformation of the positioning error of the Z axis. The column moving along the Z-axis is greatly affected by the environmental temperature fluctuations. When the room temperature increases, the tool-sided axes expand in the negative Z-direction resulting in TCP errors illustrated in Figure 2.

At the position of the axes where the model is evaluated, the thermal growth of the tool-sided axes is comparable to the growth of the workpiece-sided axes. This results in thermal errors below 10 µm in Y-direction. However, evaluating the deformation at other positions of the Y axis, larger thermal errors occur at the TCP. These effects are dominated by the high sensitivity of the machine tool column to the environment.

PROPOSED DESIGN MODIFICATIONS

The introduction of the cutting fluid into the structure of the machine creates a transient thermal response. This transient phase has a negative repercussion on the machine tool repeatability. The cutting fluid contributes in removing the chips from the guideways of the Z-axis. Therefore, supplying the cutting fluid directly to the working space without affecting the structure of the bed is not an option for the machine tool manufacturer. The new design of the cutting fluid supply needs to reduce the transient phase in order to ensure the repeatability of the machine tool. An homogenization of the supply of the cutting fluid with several inlets for the fluid along the guideways of the Z-axis is proposed. The redesigned supply can be included in the model by introducing homogeneous boundary conditions along the channels of the Z-axis, representing the forced convection of the fluid media. Figure 3 depicts the deviations of the guideways of the Z-axis in Y-direction 2 hours 30 min and 6 hours after turning on the cutting fluid. The modified supply ensures a that the thermal deviations in Y-direction are constant along the whole stroke of the Z-axis. This reduces the angular errors, which are more challenging to account for in online compensation strategies.

The cutting fluid temperature is regulated by an external unit. By setting the environmental temperature as reference, it is ensured that the whole machine tool is exposed to the same temperature minimizing internal gradients. In the current machine tool design, the reference temperature for the cutting fluid control is a signal measured on the machine tool. This signal is influenced not only by the workshop environment but also by the structural temperature of the machine tool bed, which results in a negative effect. If the machine tool bed is warming up, the cutting fluid warms up following the set temperature. A new reference sensor for the fluid temperature control is proposed, measuring the unaffected workshop temperature oscillations. This is introduced in the simulation by modifying the cutting fluid temperature for the corresponding boundary conditions. The proposed set temperature leads to a reduction of the resulting TCP errors.

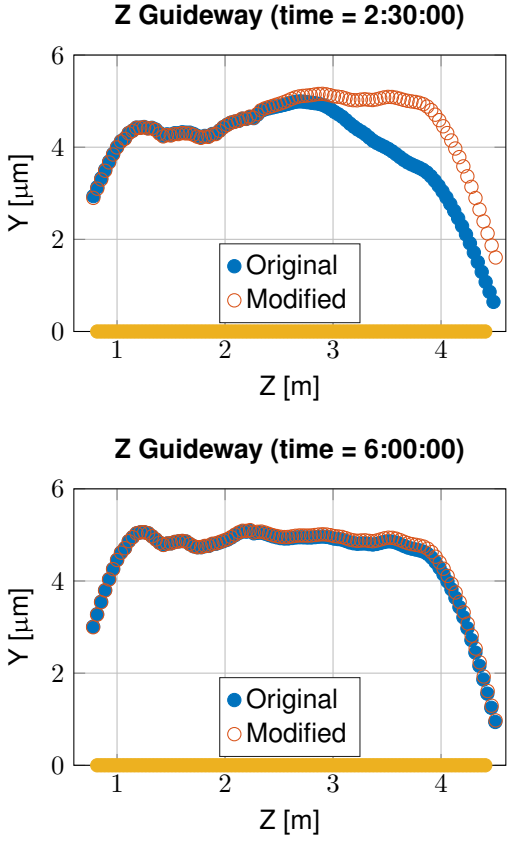

FIGURE 3. Deformation of the Z-guideway in Y-direction of the original design and the modified cutting fluid supply

After modifying the supply of the cutting fluid, the

focus is reducing the sensitivity of the column of the Z-axis to the environment. One design alternative is to introduce cooling fluid along the structural parts exposed to environmental changes. In order to avoid the introduction of a separate external unit, the cooling fluid needs be delivered by the same cooler unit used for the cutting fluid. This structural cooling is introduced in the model by modifying the boundary conditions of the structural parts in contact with the fluid. The simulation shows that tempering the column of the machine tool only enlarges the sensitivity of the structure to the environment, increasing the TCP errors. The option to include coolant into the columns is further investigated when the reference temperature is kept constant. A constant temperature succeeds in damping the oscillation of the thermal errors due to the changes in the room temperature. However, increasing the amount of fluid media implies a higher energetic demand, which is not an optimal solution.

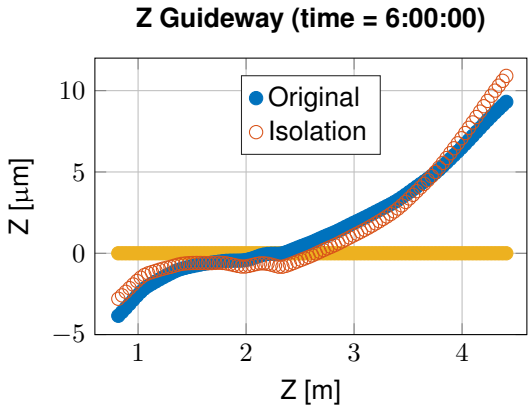

FIGURE 4. Deformation of the Z-guideway in Z-direction of the original design and with the isolation in the Z-axis column

Another alternative for decoupling the column from the environment is the introduction an a thermally isolating material on the surface of the structure. The Z-axis is a large column providing the required stiffness to the structure. Most of the heat sources are located far from this part and heat losses are effectively dissipated by the cooling system. Therefore adding a thermally isolating material only contributes to the decoupling of the structure from the environment without hindering the heat dissipation of the heat sources. This design modification is introduced in the model by reducing the HTC of the affected boundary conditions. The introduction of the cutting fluid and the increasing environmental temperature lead to a thermal expansion of the machine tool bed. This is illustrated in Figure 4, depicting the thermal deformation of the Z guideways 6 hours after the cutting fluid is connected. Figure 4 shows that the back of the Z-axis deforms in positive Z-direction and the front in negative direction, indicating a thermal growth of the bed. In Figure 5 the thermal deformation of the Y-guideways is shown after 6 hours with cutting fluid. In the original design the column expands and tilts leading to a deformation in the negative Z-direction. This deformation is further enhanced by the expansion of the remaining tool-sided axes, leading to a resulting error at the TCP relative to the workpiece depicted in Figure 6. By reducing the convective heat exchange between the Z-axis and the environment, the Z-axis deforms into the positive Z-direction. This displacement is mainly influenced by the expansion and tilting of the machine tool bed. The deformation into the positive direction of the Z-axis has positive effect, counteracting the expansion of the Y-, A- and (C)-axis.

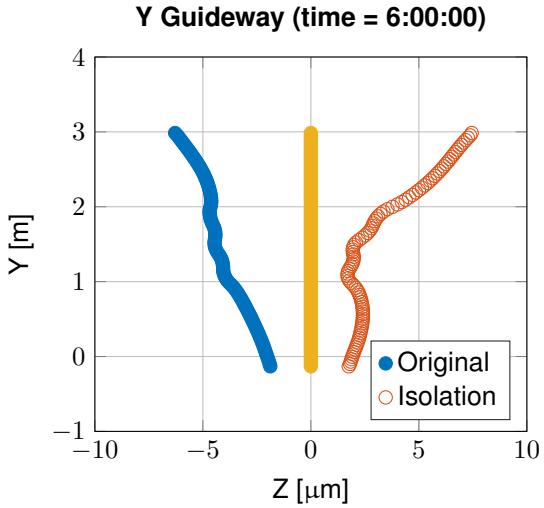

FIGURE 5. Deformation of the Z-guideway in Z-direction of the original design and with the isolation in the Y-axis column

The thermo-mechanical model shows that combination of the modification of the cutting fluid supply, the cutting fluid reference temperature and the isolation of the Z-axis from the environment results in a reduction of the TCP errors, as illustrated in Figure 6.

CONCLUSIONS AND OUTLOOK

This work investigates the external effects influencing the thermal behavior of a large 5-axis-axis machine tool. A thermo-mechanical model of a whole machine tool structure is developed and

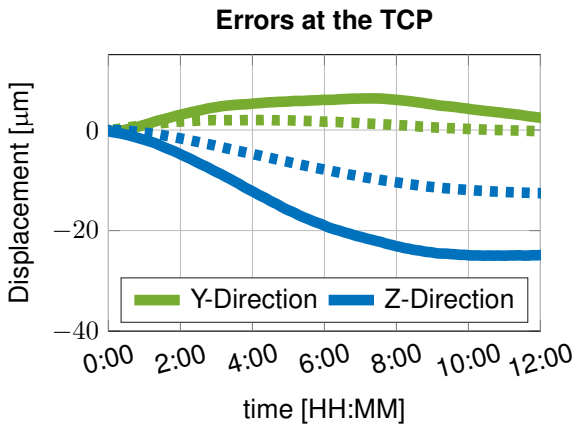

FIGURE 6. Simulated TCP errors relative to the workpiece. Comparison between the original design (solid lines) and the proposed design modification (dashed lines)

validated with experiments. Several design measures for the optimization of the cutting fluid supply and the response of the machine to the environment are proposed and verified by simulation. The thermally induced TCP errors are reduced over 50% in the working space by design modifications.

Future work concentrates on the implementation of the proposed design modifications in the next machine tool prototype. The remaining thermal errors, which are not possible to eliminate by design, will be compensated with models based on online measurements of the TCP deviations.

ACKNOWLEDGMENTS

The authors would like to thank the Swiss Federal Office for Professional Education and Technology (CTI) and the Swiss National Science Foundation (SNSF) for their financial support.

REFERENCES

[1] Bryan J. International Status of Thermal Error Research (1990). CIRP Annals - Manufacturing Technology. 1990;39(2):645 – 656.

[2] Schellekens P, Rosielle N, Vermeulen H, Vermeulen M, Wetzels S, Pril W. Design for Precision: Current Status and Trends. CIRP Annals. 1998;47(2):557 – 586.

[3] Mian NS, Fletcher S, Longstaff AP, Myers A. Efficient estimation by FEA of machine tool distortion due to environmental temperature perturbations. Precision Engineering. 2013;37(2):372 – 379.

[4] Ess M. Simulation and compensation of thermal errors of machine tools. Dissertation ETH Zürich, Nr. 20300; 2012.

[5] Thiem X, Kauschinger B, Ihlenfeldt S. Structure Model Based Correction of Thermally Induced Motion Errors of Machine Tools. Procedia Manufacturing. 2017;14:128 – 135. 17th Machining Innovations Conference for Aerospace Industry, MIC 2017, 6-7 December 2017, Garbsen, Germany.

[6] Mayr J, Weikert S, Wegener K. Comparing the Thermo-Mechanical-Behavior of Machine Tool Frame Designs Using a FDM-FEA Simulation Approach. Proceedings of the 22nd ASPE Annual Meeting. 2007;(1):17–20.

[7] Sun L, Ren M, Hong H, Yin Y. Thermal error reduction based on thermodynamics structure optimization method for an ultra-precision machine tool. The International Journal of Advanced Manufacturing Technology. 2017 Feb;88(5):1267–1277.

[8] ISO 10791-1:2015. Test conditions for machining centres –Part 1: Geometric tests for machines with horizontal spindle (horizontal Z-axis). Geneva, Switzerland; 2015.

[9] Hernández-Becerro P, Blaser P, Mayr J, Weikert S, Wegener K. Measurement of the effect of the cutting fluid on the thermal response of a five-axis machine tool. Proceedings of the Laser Metrology and Machine Performance XII. 2017;(1):17–20.

[10] Blaser P, Hernández-Becerro P, Mayr J, Wegener K. Thermal errors of a large 5-axis machine tool due to cutting fluid influences - Evaluation with thermal test piece. In: 32st ASPE Annual Meeting; 2017. p. 531–536.

[11] Pavliček F, Dietz F, Blaser P, Züst S, Mayr J, Weikert S, et al. An approach for developing meta models out of fluid simulations in enclosures of precision machine tools. In: 31st ASPE Annual Meeting; 2016. p. 456–461.

[12] Weikert S. R-Test, a New Device for Accuracy Measurements on Five Axis Machine Tools. CIRP Annals - Manufacturing Technology. 2004;53(1):429 – 432.

PIREST TECHNOLOGY – NEW PIEZO TECHNOLOGY FOR ACTIVE ALIGNMENTS AND ERROR CORRECTIONS IN DIFFICULT-TO-ACCESS AREAS AND SYSTEMS

Jonas Reiser, Harry Marth and Mathias Bach
RnD Piezo Systems,
Physik Instrumente (PI) GmbH & Co. KG,
Karlsruhe, Germany

INTRODUCTION

There is a large number of high precision machines in the semiconductor industry, astronomy, space instrumentation as well as synchrotron beamlines. The one thing all of these systems have in common is that they have many extremely precise components in difficult-to-access areas. The highly- integrated systems are often used in special environmental conditions, for example, vacuum, X-ray or cryogenic temperatures. Additionally, there is always the risk of misalignment of some high precise components caused by vibration, aging, temperature changes or relaxation of preload.

Conventionally, changes in dimension between two components are compensated by flat washers. They need to be adjusted and inserted mechanically. Adjusting them as precisely as required is not always possible and the predefined dimension can't be changed anymore [1]. Furthermore, it is not always possible to access the components without large efforts.

Consequently, there is the need for error-correction elements, which can be used to adjust such misalignments without the need for mechanical intervention.

Using the piezoelectric actuators' conventional mode for this kind of operation requires a stable, low-noise power supply permanently applied to the actuator. Moreover, the actuators' lifetime is reduced by applying an offset voltage over a long period of time. High DC voltages in high atmospheric humidity environments may damage piezo actuators due to chemical reactions that release hydrogen molecules within the piezo materials [2].

This is different in the case of the here presented piezo- based, semiactive PIRest actuators. They are inserted once and can actively adjust and readjust the gap between two components. The PIRest technology's main advantage is that the last piezo position can be held without an offset voltage. Thus, the lifetime in high atmospheric humidity environments will be increased by this. Moreover, the new technology allows fine alignment in micrometer ranges with nanometer resolution. Alignment tasks within difficult-to-access areas and systems are considerably simplified.

The technology is based on ferroelectric domain switching processes. By controlling the actuator with special electrical signals, its remanent strain can be increased or decreased step-by-step in its specified travel range with nanometer resolution. A phenomenological model emulates this behavior by paying attention to the most important influencing factors.

FUNCTIONAL PRINCIPLE

Ferroelectric domain switching processes occur during polarization and depolarization of soft PZT ceramics.

After sintering PZT ceramics in the manufacturing process, the ferroelectric domains are orientated statistically. This is equal to the point S_0 in the hysteresis loop of a PZT actuator in Figure 1. This point is called the "thermal depolarized state" [4].

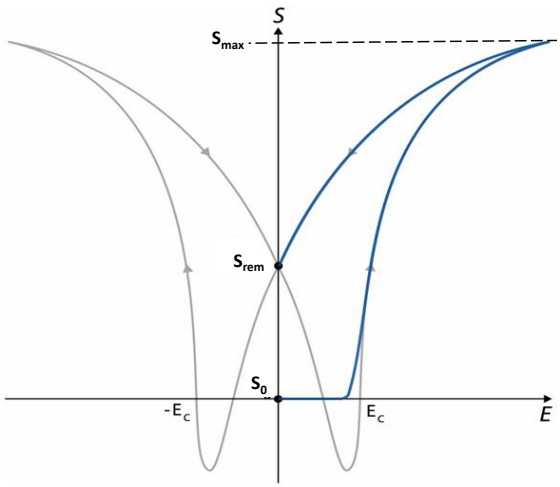

FIGURE 1. S-E hysteresis loop and polarization procedure of a PZT actuator [3] (extended).

In order to use the piezoelectric effect of sintered PZT ceramics, the material needs to be polarized once. This is achieved by applying an electric field with a field strength $E \geq E_c$ for a certain period of time. E_c is the coercive field strength which depends on the ceramic material. The coercive field strength E_c of a soft PZT ceramic is approximately 1 kV/mm [5].

Starting at the S_0 point and increasing the electric field, the mechanical strain S doesn't change initially. This is shown by the horizontal curve in Figure 1. In the vicinity of the coercive field strength E_c, the mechanical strain S increases very quickly because the ferroelectric domains are aligned parallel to the electric field vector (ferroelectric effect). This is shown by the almost vertical curve in Figure 1. Consequently, the domain switching processes result in changes in the length of the actuator. Polarizing the ceramic material causes an increase in length. Additionally, the elementary cells are deformed by the piezoelectric effect, which results in a further increase of the mechanical strain S.
The mechanical strain S can be raised to S_{max} by increasing the electric field strength more and more. The corresponding electric field strength is approximately 2-3 kV/mm [5]. At this point, all domains are aligned parallel to the electric field vector and the piezoelectric effect has reached its maximum. The mechanical strain S saturates.

After applying the polarization voltage to the PZT actuator for a certain period of time, the electric field strength E is reduced to 0 kV/mm again. But as shown in Figure 1, the corresponding mechanical strain S won't be zero. There is still a part left. It is called the remanent strain S_{rem} of the actuator and it is the result of the domain switching processes during the polarization procedure. Usually, the PZT actuators are delivered in that polarized state. At this point, the actuator can be driven unipolar or bipolar (only limited in negative direction). This is shown by the hysteresis loops in Figure 2.

Depending on the used material, the nominal adjustment range is approximately 1000-2000 ppm of the actuator's length. If the electrical field strength E is set to zero in the conventional operating mode, the mechanical strain S will always be reduced to S_{rem}.

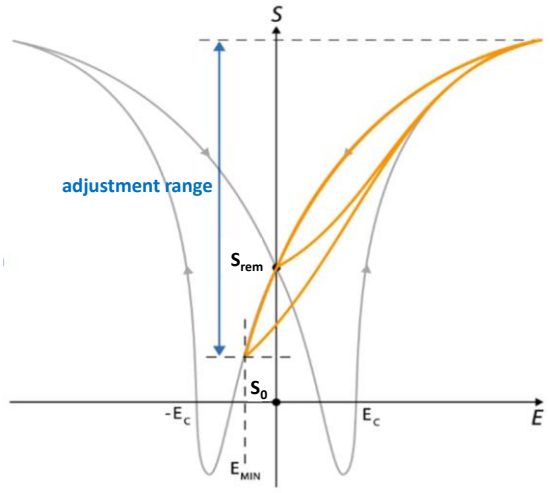

FIGURE 2. S-E hysteresis loop and conventional unipolar and bipolar operation of a PZT actuator [3] (extended).

In contrast to the conventional operating mode of PZT actuators, the new PIRest technology uses the lower part of the hysteresis loop. This part has not been used for positioning purposes before.
Instead of fully polarizing the PZT ceramic by a constant voltage, it is possible to polarize the actuator step-by-step. By controlling a soft PZT actuator based on a specially optimized material with positive voltage pulses, the mechanical strain can be increased step-by-step from the thermal depolarized state S_0. This is shown by the schematic hysteresis loops on the right-hand side in Figure 3.

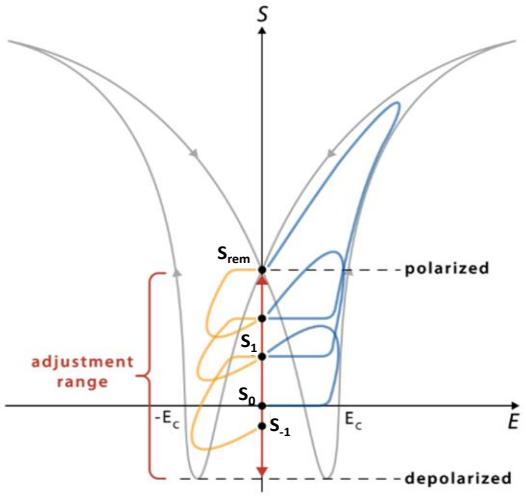

FIGURE 3. S-E hysteresis loop and PIRest operating mode of a PZT actuator [3] (extended).

By controlling multiple voltage pulses, it is possible to stop at any intermediate position < S_{rem}.
After reaching the point S_{rem}, the length can't be increased anymore because all domains are aligned parallel to the electric field vector. The actuator is fully polarized at this point, which corresponds to the standard delivery condition.

The schematic hysteresis loops in Figure 3 show that there is an additional change in length during the voltage pulses.
The actuator's length increases very quickly when the voltage pulse starts. The reason for that is the piezoelectric effect of the domains that are already aligned parallel to the electric field vector (elongation of the elementary cells). This is shown in Figure 4.

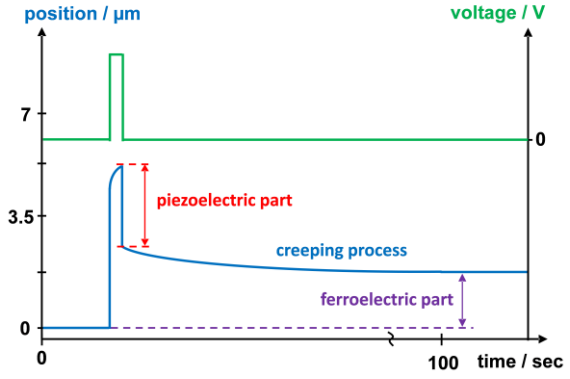

FIGURE 4. Schematic change in length of a PZT actuator during polarization with a positive voltage pulse.

This peak in the position signal can't be avoided. Furthermore, the greater the height of the voltage pulse is, the higher this peak will be.
After the voltage pulse has finished, the length decreases. As it is shown in the figure above, the length doesn't return to the original value. There is still a part left, which is the result of some domains switching from the thermal depolarized orientation to a new orientation. The new orientation is rather parallel to the electric field vector than the initial one. The switching procedure results in a change in length. Since the voltage pulses only last a few milliseconds, not all domains are stimulated to switch to a new orientation. The more domains are aligned, the larger the position step will be.
In addition to that, some domains were aligned by the voltage pulse, but the induced energy was not high enough to hold them steadily in the new orientation. These domains switch back to their initial orientation. The result is a creeping process, which lasts approximately two to four time decades. Afterwards, the length changes only related to temperature.
Controlling the actuator with negative voltage pulses decreases the actuator's length again. This is shown by the schematic hysteresis loops on the left hand side in Figure 3. The length can be reduced to the completely depolarized state, where all domains are probably aligned perpendicular to the electric field vector. This is the minimum length that can be achieved in the PIRest operating mode.

The change of a PZT actuator's remanent strain by step-by-step polarizing and depolarizing is shown in the following Figure 5.

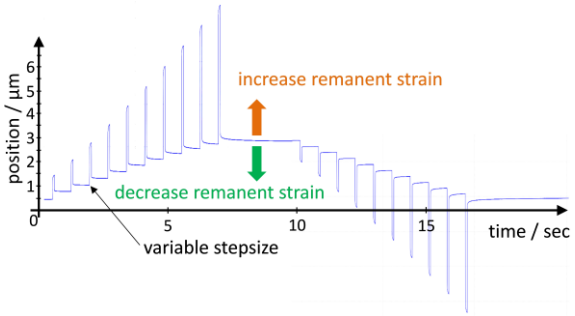

FIGURE 5. Change of a PZT actuator's remanent stain by polarizing and depolarizing step-by-step.

The PIRest technology's adjustment range is approximately 600 ppm of the actuator's length. Moreover, it is possible to reach up to 1000 ppm with specially optimized materials.

PHENOMENOLOGICAL MODEL

The new PIRest technology is based on a phenomenological model that emulates the change of the remanent strain during the polarization and depolarization process. The voltage pulse's height and width, the actuator's temperature and prestress level as well as the time factor are the main influencing factors for this kind of operation. By paying attention to the most important influencing factors, the model calculates the electrical signals to get to the new target position.

In the conventional mode, a creeping process occurs after setting the actuator to a definite position by controlling a constant voltage. This

leads to a logarithmic position change with approximately 1 %/decade.
After controlling the actuator with voltage pulses in the PIRest mode, the length changes in a logarithmic way, too. However, a method was developed and integrated into the phenomenological model, so that it is able to compensate this creeping process. This is realized by controlling the actuator with a combination of voltage pulses in both directions. Figure 6 shows the difference between a polarization pulse with and without creep compensation. The change in length during the transition time is not shown.

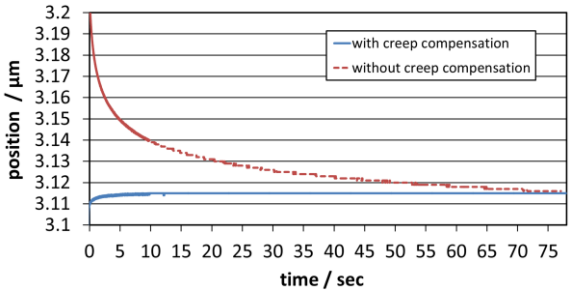

FIGURE 6. Position change of a PZT actuator after a positive polarization pulse with creep compensation ON/OFF.

Consequently, the PIRest technology provides long-term stability over several months without creeping and is therefore predestined for alignment tasks in micrometer ranges [1]. The main difference to the conventional mode is that no offset voltage needs to be supplied for holding the last piezo position. This is a great advantage, especially in high humidity environments.

The position stability of a soft PZT actuator was measured over a period of 16 days (see Figure 7). At the beginning of measuring, the actuator was set to approximately 50 % of the adjustment range. Afterwards, the PIRest actuator was disconnected from the piezo amplifier.

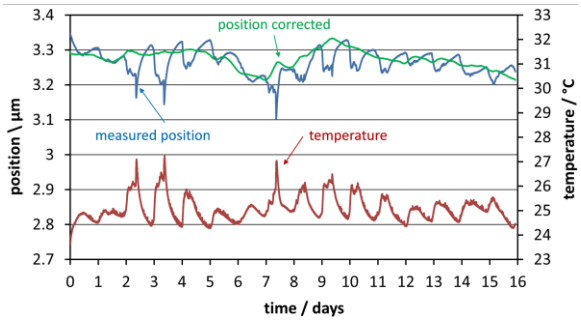

FIGURE 7. Position stability of a PZT actuator at approximately 50 % remanent strain in a non-stable thermal environment.

The position changes are mainly caused by temperature changes with a negative temperature coefficient. After eliminating the temperature influences of the test setup and the actuator, a drift of approximately 100 nm remains. The relative humidity during the measurement was not monitored. Meanwhile, independent measurements with other systems show that the relative humidity influences the capacitive sensor signal. Capacitive sensors were used for the PIRest position stability test as well. Consequently, the remaining drift could be caused by humidity changes. Further tests will provide prove to this hypothesis.
However, the most important conclusion is that no gradual change of the remanent strain can be observed. The partly polarized states were stable during measuring. Current tests show the same behavior over a period of 12 weeks.
Temperature- correlated position changes are widely known from the conventional piezoelectric PZT ceramics. As the conventional PZT actuators are used in a fully polarized state, there is a negative temperature coefficient. This is a material- based phenomenon of PZT ceramics. Because the PIRest actuators' degree of polarization is changed, the temperature coefficient differs. Consequently, there can be positive (fully depolarized state) and negative (fully polarized state) temperature coefficients as well. The temperature coefficient in a partially polarized state will always be smaller than the temperature coefficient in a fully polarized or fully depolarized state. It is in a range of approximately ± 4 ppm/K [5].
In general, the adjustment range in the PIRest mode is reduced by a rising temperature.

The phenomenological model of the PIRest technology provides different operating modes for bidirectional, incremental motion with

adjustable step size (“manual movement”), referencing the fully polarized and fully depolarized state (“limit movement”), and setting the actuator to a definite position within the adjustment range (“target movement”). Tests showed that the model achieves an accuracy of ± 3.5 % of the actuator’s adjustment range in the target movement mode (at room temperature and with activated creep compensation). The results are shown in Figure 8. Different target positions were commanded and the maximum positive and negative position deviations of six PIRest actuators were determined.

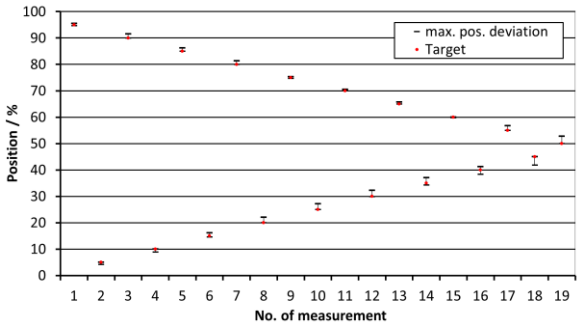

FIGURE 8. Model verification – measurement results.

The positioning step size can be adjusted in the “manual movement” mode. The minimum step size that can be achieved depends on different factors such as, the resolution of the D/A converter and the shape of the voltage pulse.
Figure 9 shows the depolarization of a PZT actuator with a small step size of a few nanometers. Creep compensation was activated and any overshooting during the transition time is not shown for better visibility.

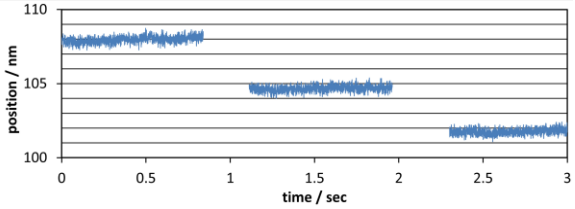

FIGURE 9. Reducing mechanical strain by depolarizing with creep compensation and nanometer resolution
(overshooting during transition time is not shown).

CONTROL UNIT AND PIREST ACTUATOR TYPES

The phenomenological model is stored inside a control unit with an integrated optimized piezo amplifier.
There are different possibilities for implementing such a control unit. For example, it can be implemented as a handheld device that can be used independently for fine alignment of separated machines in the field. Furthermore, it can be a slide-in module for an existing controller chassis or just a desktop device.
No matter how this is realized, the control unit simplifies adjustment in highly- integrated machines and at inaccessible areas. All cables that are required for the adjustment procedure can be considered during the design of the machine [1] or retrofitted into existing machines.

To set the actuator to a new position, it needs to be connected to the control unit only once. Afterwards, the actuator can even be disconnected from the control unit and the new position is held without supplying additional power.
Figure 10 shows three PIRest actuator types with center preload option. All of these actuators have up to 4000 N load capability and high stiffness. The adjustment range depends on the size and is between 2 µm, 5 µm and 10 µm.

FIGURE 10. PIRest actuators P-131.11, P-131.12 and P-131.13 with adjustment ranges 2 µm, 5 µm and 10 µm.

Other actuator types and larger adjustment ranges are also possible. The PIRest technology is not limited to special actuator shapes or sizes.

Moreover, it is possible to drive multi-axis systems in the PIRest mode as well. The E-135.601M control unit developed for PIRest provides up to six channels which can be controlled either in a channel configuration or an axis configuration. Coupled movements in all degrees of freedom can easily be performed by using a coordinate transformation matrix.

Elastic hinges are used for mechanical decoupling and to avoid over- constrained systems. Possible designs for a bipod, tripod or even a hexapod are shown in Figure 11.

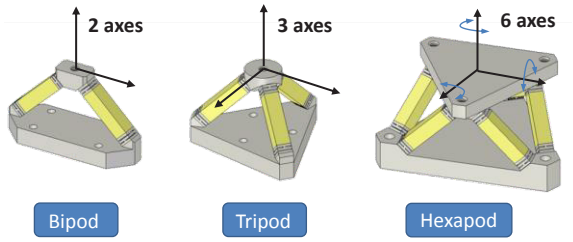

FIGURE 11. Multi-axis PIRest systems with two, three, and six degrees of freedom, decoupled by elastic hinges.

CONCLUSION

The phenomenological model, which the PIRest technology is based on, provides different operating modes allowing bidirectional, incremental motion with an adjustable step size, and setting of the PIRest actuator to maximum and minimum remanent strain or to a definite position within the adjustment range. The developed creep compensation method reduces the position drift after a voltage pulse and therefore offers long-term stability over several months.

It is possible to drive single-axis actuators as well as multi-axis systems in the PIRest mode. The phenomenological model and the PIRest intelligence are stored inside a microcontroller-based control unit.

Main applications are quasistatic fine alignment and error correction in micrometer ranges and with nanometer resolution, especially in difficult-to-access areas and systems.

The classical approach of compensating deltas in the dimensions between two components with passive shims can be simplified and considerably accelerated. Additionally, the PIRest actuators offer flexibility over time for any correction needed within the system. Compared to the conventional operating mode, the piezo actuator's lifetime will be significantly increased in quasistatic applications, because electrical voltage doesn't need to be applied for holding the last piezo position.

REFERENCES

[1] Physik Instrumente (PI) GmbH & Co. KG, Brochure – PIRest Actuators, Karlsruhe, Germany, 2017.

[2] PI Ceramic GmbH, PI_CAT128E_R3_Piezoelectric_Actuators.pdf, Lederhose, Germany, 2016, p. 63.

[3] PI Ceramic GmbH, PI_CAT125E_R3_Piezoelectric_Ceramic_Products.pdf, Lederhose, Germany, 2016, p. 9.

[4] Patrick Pertsch, Dissertation – Das Großsignal-verhalten elektromechanischer Festkörperaktoren, Illmenau, Germany, 2003, p. 19.

[5] Patrick Pertsch, Piezoceramic Basics and Actuator (PICMA®) Application Properties, Lederhose, Germany, 2016.

MAGNETICALLY LEVITATED LINEAR STAGE FOR IN-VACUUM TRANSPORTATION TASKS

Lei Zhou, David L. Trumper
Department of Mechanical Engineering
Massachusetts Institute of Technology, Cambridge, MA, USA

INTRODUCTION

The reticle handling task in photo lithography machines is becoming increasingly challenging in the extreme ultraviolet (EUV) era [1]. In the next generation lithography machines, the reticle needs to be transported through a distance of 2 m between the storage position and the scanning position in high vacuum, and the transportation mechanism needs to satisfy the ultra-tight contamination requirements. In addition, due to the increased system complexity, the allowed height for the reticle transportation mechanism in the machines is constraint within 100 mm. To fulfill these requirements, the use of the traditional robot manipulator is challenging.

In this work, we present a new concept of in-vacuum transportation mechanism using a magnetically levitated linear stage (MLLS). Compared with robot manipulators, linear stages usually require less volume for long distance transportation tasks, and thus can satisfy the tight volume constraint with less challenge. In addition, we introduce magnetic levitation to the linear stage to eliminate particle generation of mechanical bearings. To reduce the system's complexity, we present a linear bearingless slice motor design [2], where the stage's magnetic levitation in several degrees of freedom (DOFs) are achieved passively. This design helps reduce the number of actuators and sensors in the system.

Linear hysteresis motor is selected as the driving principle for the MLLS. Hysteresis motor has the advantages of simple structure and high thermal and mechanical robustness [3]. In addition, the secondary of a hysteresis motor can be made from permanent-magnet-free solid metal material. This is desirable for in-vacuum operation, since permanent magnets (PM) can out-gas in high vacuum when it is not encapsulated. Hysteresis linear motor also allows using the same secondary material for magnetic and structural purposes, thereby beneficial for a compact design. In the past, most of the developed hysteresis motors are in rotary form and operate in open-loop. Our past work [4] studied the position control for rotary hysteresis motors. To our knowledge, this paper presents the first experimental study of linear hysteresis motor.

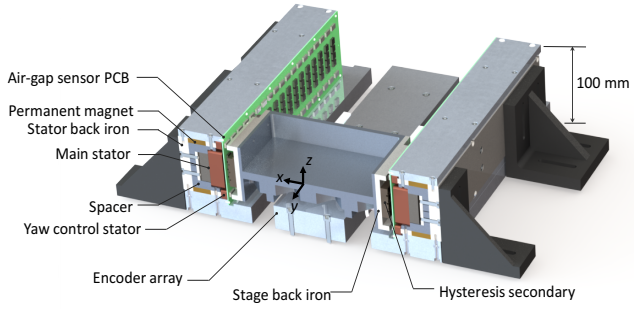

(a) Cross-section view of CAD model.

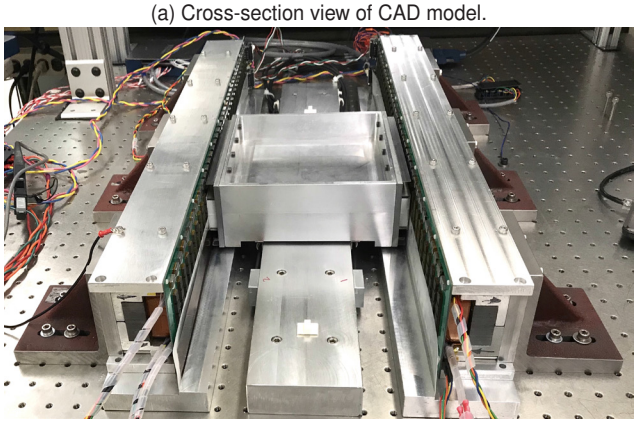

(b) Photograph of linear stage.

FIGURE 1. Cross-section of the magnetically levitated linear motor.

HARDWARE OVERVIEW

Fig. 1 shows the CAD model and the photograph of the magnetically levitated linear stage system, which comprising two stators, one moving stage, and a sensing system. The coordinate system is shown in Fig. 1a. Here the moving stage is driven along the y-axis. The magnetic levitation of the moving stage is active in x- and θ_z-directions, and is passive in z-, θ_x-, and θ_y-directions. In our design, the moving stage is vacuum compatible. When the system is integrated in the lithography machine, a channel with thin walls (not shown in figures) needs to be configured along the motion range of the moving stage, and separates the moving stage and the stators. The moving stage is levitated and transports the reticle inside the channel in clean vacuum, while the stators are configured outside the channel, and are in a rela-

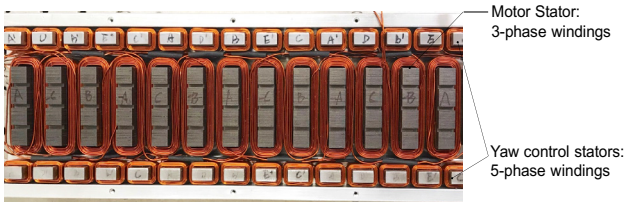

FIGURE 2. Photograph of front view of the stator.

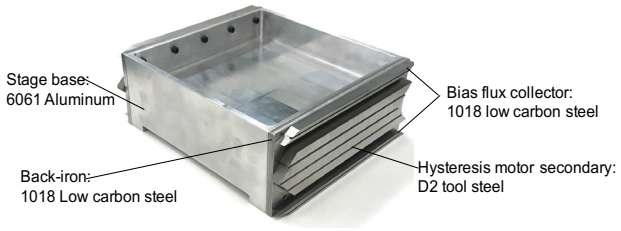

FIGURE 3. Photograph of the moving stage in the magnetically levitated linear stage.

tively dirty vacuum environment. The air-gap of the linear motors is 1.5 mm.

Fig. 2 and Fig. 1 show the photograph of the front and side views of the stator, respectively. The stator assembly mainly consists of a motor stator, two yaw control stators, and a flux-biasing structure comprising two rows of PMs and one stator back-iron. The stators are fixed on the base via three angle plates. Lumped windings are selected for the stators due to volume constraints. The windings on the motor stators are 3-phase, while the windings in the yaw control stators are 5-phase. There are 11 currents independently controlled in the system, including two sets of 3-phase windings in the left and right motor stators, and one set of 5-phase windings in the yaw control stators. The current controlled switching type power amplifiers AMC B30A40 is being used to drive currents in the windings. The DC bus voltage is 300V.

Fig. 3 shows a photograph of the moving stage, which comprising an aluminum stage base, two stage back-irons, two hysteresis motor secondaries, and four bias flux collectors. The hysteresis motor secondaries are made of D2 tool steel. The D2 tool steel has relatively large magnetic hysteresis, which allows it being used for hysteresis motor secondary. It also has large permeability, which is advantageous for reluctance force generation for magnetic suspension purpose. The total mass of the stage is 4.9 kg.

Two kinds of displacement sensors are used to measure the stage's motion in x-, y-, and θ_z-DOFs. To measure the x- and θ_z-directional displacements of the stage at different y-positions, 16 optical displacement sensors are

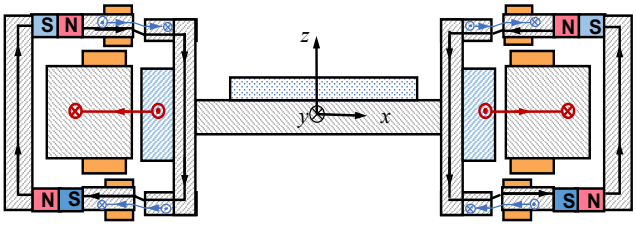

FIGURE 4. Magnetic fluxes in the MLLS system. Black lines: PM fluxes for passive magnetic suspension in z, θ_x, and θ_y-DOFs; red lines: motor fluxes for x-directional suspension force and y-directional thrust force, blue line: yaw control fluxes for θ_z-directional suspension torque.

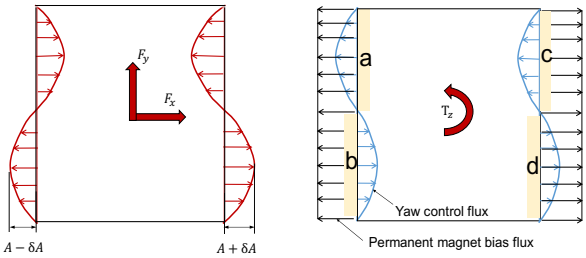

(a) Suspension force generation in x-direction.

(b) Torque generation about z-axis.

FIGURE 5. Top view of air-gap magnetic flux distribution and controlling force/torque generation.

arranged along the stator on the printed circuit boards (PCBs) mounted on the front surface of the stators. The signals from the sensors engaged with the stage are used for feedback control to stabilize the stage's magnetic suspension. In addition, two rows of magnetic encoders are arranged along the motion direction for measuring the y-directional displacement of the stage. Two magnetic encoder scale are attached on the moving stage, and in each row there are 4 encoder read heads configured along the moving direction of the stage. With this sensing system design, there is no cable attached on the moving stage. Note that the magnetic encoders are not vacuum compatible. When the system is operating in vacuum, different displacement sensors are needed, for example laser interferometers.

OPERATING PRINCIPLE

Suspension Force Generation

Fig. 4 shows a cross-section diagram of the MLLS and the magnetic flux distributions in the system, and Fig. 5 shows the top view of the air gap magnetic fluxes. There are three kinds of magnetic fluxes in the system. The black lines in Fig. 4 and Fig. 5b show the PM bias magnetic fluxes, which are used to generate passive magnetic suspension force/torque in z-, θ_x-, and θ_y-DOFs. When the stage is displaced in these directions, the

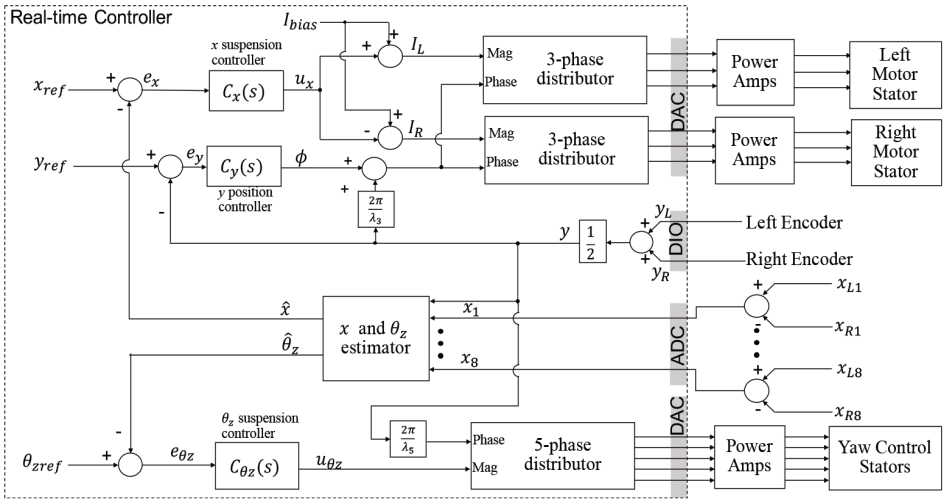

FIGURE 6. Block diagram of the control system for the magnetically levitated linear stage.

PM fluxes in the air gaps provide restoring forces, and therefore stabilize the magnetic suspension passively. Note that the PM bias flux also generates destabilizing force/torque in x- and θ_z-directions, and feedback control is required to stabilize the magnetic suspension in these DOFs. Rotary motors with this magnetic suspension design are often referred as slice bearingless motors, and typical applications of bearingless slice motors include pumps [5], high-speed fans [6], centrifuges [7], etc. To our knowledge, our paper presents the first linear slice bearingless motor design.

The red lines in Fig. 4 and Fig. 5a represents the motor fluxes, which are generated by the windings in the motor stators. The common mode of the left and right motor fluxes is used to generate y-directional thrust force to the stage by interacting with the hysteresis motor secondaries. The differential between the left and right motor fluxes generates x-directional reluctance force, which is used to control the x-directional magnetic suspension.

The blue lines in Fig. 4 and Fig. 5b show the yaw suspension control fluxes, which are generated by the 5-phase windings in the yaw control stators. In the top and bottom air gaps, the yaw suspension control flux is distributed sinusoidally, and is synchronous to the moving stage. This flux steers the PM bias flux to generate θ_z-directional suspension torque. For example, in Fig. 5b, the yaw control flux attenuates the PM bias flux in areas b and c, while intensify the flux in areas a and d, therefore the reluctance forces in the air-gaps generates a torque about z-axis as is shown by the arrow.

Thrust Force Generation

The proposed MLLS uses linear hysteresis motors for the thrust force generation. When the motor windings are excited, the induced magnetization in the secondaries lags behind the external field due to the magnetic hysteresis of the secondary material, and therefore generates thrust forces. The hysteresis motor secondaries are often pre-magnetized using a large current amplitude to improve the force generation capability of the motor. In addition, reluctance thrust forces are existing in linear hysteresis motors at the edges of the motor secondaries. As a result, linear hysteresis motors' characteristics resemble that of hysteresis-reluctance hybrid motors [8].

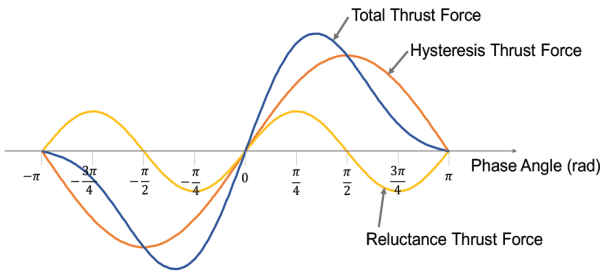

FIGURE 7. Thrust force and phase angle relationships in hysteresis-reluctance hybrid motors.

The linear hysteresis motor in our MLLS system operates in synchronous mode. There are two reasons for this selection. First, the reluctance force in the linear hysteresis motor is oscillatory when the motor is asynchronous, which introduces undesirable vibration to the system. Second, synchronous operation of the motor eliminates secondary hysteresis and eddy current losses. This is highly desirable for the reticle transportation system because cooling the moving stage is extremely challenging since the stage is in vacuum.

TABLE 1. Magnetic levitation stiffnesses and resonance frequencies in the passive levitated DOFs

DOF	Resonance Frequency	Passive Stiffness
z (Vertical)	11 Hz	37 N/mm
θ_x (Pitch)	9 Hz	54 Nm/rad
θ_y (Roll)	9 Hz	163 Nm/rad

Fig. 7 shows the thrust force and phase relationship of linear hysteresis-reluctance hybrid motor in synchronous operation. Here, the horizontal axis shows the phase difference between the stator excitations and the position of the stage. It can be seen that the hysteresis thrust force demonstrates its maximum values at phase angle of $\pm\pi/2$. With the reluctance thrust force added, the peak of the total thrust force shifts toward the center.

CONTROL DESIGN

Fig. 6 shows a block diagram of the control system for the magnetically levitated linear stage. The x- and θ_z-directional displacements of the moving stage are estimated from the encoder and air-gap sensor measurements, and are fedback for suspension control. The x-DOF magnetic suspension control signal u_x is the differential magnitude of the left and right motor current amplitudes, and a bias current I_{bias} added to the motor stator currents for thrust force generation and maintaining magnetic suspension. the θ_z-DOF suspension control effort signal is used to determine the yaw control stator current amplitude. The two stators operates in synchronous mode. The position control loop for the linear stage is closed with the encoder signals being used for feedback, and the control effort signal is used to determine the phase between the motor stator excitation and the position of the linear stage. The signals from the D/A converters of the real-time controllers are send to power amplifiers as current commands.

EXPERIMENTS

Suspension Tests

Table 1 shows the magnetic suspension stiffness in the passive levitated DOFs, which is estimated through measuring the natural frequency of these modes when the stage is levitated. The stage sags below the equilibrium position in the vertical direction by 1.45 mm due to its weight.

Fig. 8 shows the measured plant and loop frequency responses of the x- and Rz-directional magnetic suspension of the moving stage under a bias current of 2.5 A. In the plant frequency responses, the magnitude curves show a notch and peak around 9 Hz, which corresponds to a pair of complex zeros and poles in the x- and θ_z-directional magnetic levitation plants. To our understanding, this is due to the 2nd-order θ_y-directional mode is added to the measured modes. Data show the cross-over frequencies of the x- and θ_z-directional magnetic levitation are 70 Hz and 60 Hz, respectively, and the phase margin of both loops are around 20 degrees.

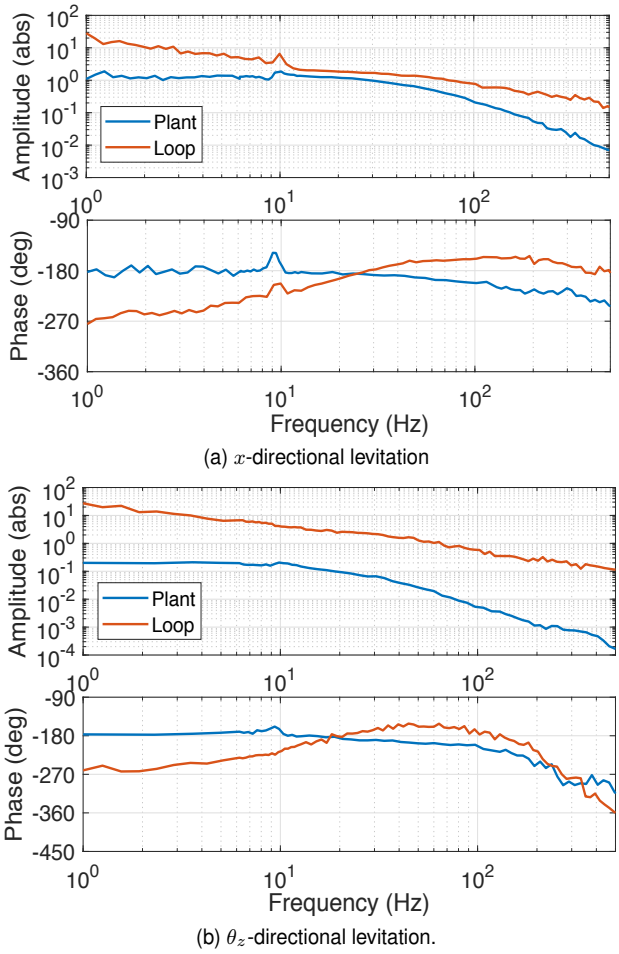

FIGURE 8. Measured plant and loop Bode plots of the x- and θ_z-directional magnetic suspension systems.

Linear Motor Tests

The thrust force and phase relationship for the linear stage is measured under different bias current amplitudes, as shown in Fig. 9. In this measurement, the stage is levitated, and the motor secondaries are pre-magnetized with a zero air-gap and 5A current amplitude. It can be seen that the phase angles of the peak thrust force are between $\pm\pi/4$ and $\pm\pi/2$. This is a result of the combination of hysteresis force and reluctance force. The maximum thrust force that the stage has demonstrated is 3.2 N under 3A bias current amplitude, which corresponds to an acceleration of $650\ \mathrm{mm/s^2}$.

We conducted initial test for the closed-loop position control of linear stage using the method shown in Fig. 6.

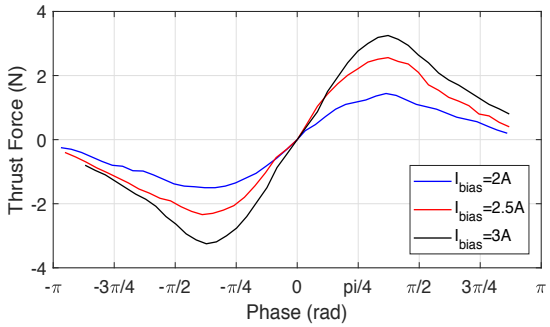

FIGURE 9. Measured thrust force and phase relationship of linear stage under different bias current amplitudes.

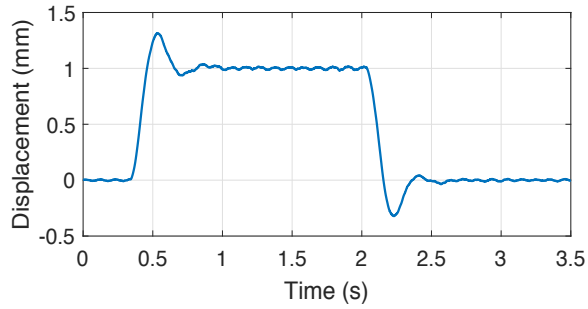

FIGURE 10. Measured position step response of the MLLS.

Fig. 10 shows the measured position step response. Data show that the bandwidth of the position control loop is about 5 Hz. It can be observed that there is a 9 Hz oscillation in the steady-state position signal. This is due to the θ_x-directional (pitch) mode is coupled to the y-directional position control loop. We expect that this oscillatory signal in position can be eliminated if the crossover frequency of the position control loop is above the pitch mode natural frequency. This test shows the availability for the position control for linear hysteresis motors.

CONCLUSIONS AND FUTURE WORK

This work presents a MLLS driven by linear hysteresis motors. Passive magnetic suspension is utilized to reduce actuators and sensors. The prototype system can magnetically levitate the stage and drive its linear motion with a maximum acceleration of $650\ \mathrm{mm/s^2}$.

In the position control tests for the linear stage, we have demonstrated the feasibility of the linear position control, however the bandwidth of the control is relatively low in the presented tests. We are currently working on improving the position control bandwidth of the linear stage. We also plan to test different motor secondary materials with larger magnetic hysteresis to improve the motor's thrust force capability.

ACKNOWLEDGEMENT

We thank ASML for supporting this work. We thank National Instruments Inc. for contributing the real-time controller used in this project.

REFERENCES

[1] Peeters R, Lok S, Mallman J, van Noordenburg M, Harned N, Kuerz P, et al. EUV lithography: NXE platform performance overview. In: Extreme Ultraviolet (EUV) Lithography V. vol. 9048. International Society for Optics and Photonics; 2014. p. 90481J.

[2] Schoeb R, Barletta N. Principle and application of a bearingless slice motor. JSME International Journal Series C Mechanical Systems, Machine Elements and Manufacturing. 1997;40(4):593–598.

[3] Teare BR. Theory of hysteresis-motor torque. Electrical Engineering. 1940;59(12):907–912.

[4] Zhou L, Gruber W, Trumper DL. Position Control for Hysteresis Motors: Transient-time Model and Field-oriented Control. IEEE Trans on Ind Appl. 2018;54(4):3197–3207.

[5] Nussbaumer T, Karutz P, Zurcher F, Kolar JW. Magnetically levitated slice motorsAn overview. IEEE Trans on Ind Appl. 2011;47(2):754–766.

[6] Sugimoto H, Shimura I, Chiba A. Design of SPM and IPM rotors in novel one-axis actively positioned single-drive bearingless motor. In: Energy Conversion Congress and Exposition (ECCE), 2014 IEEE. IEEE; 2014. p. 5858–5863.

[7] Asama J, Kanehara D, Oiwa T, Chiba A. Development of a compact centrifugal pump with a two-axis actively positioned consequent-pole bearingless motor. IEEE Transactions on Industry Applications. 2014;50(1):288–295.

[8] Rahman MA, Osheiba AM. Steady-state performance analysis of polyphase hysteresis-reluctance motors. IEEE Transactions on Industry applications. 1985;(3):659–663.

A MAGNETICALLY SUSPENDED, SPHERICAL PERMANENT MAGNETIC DIPOLE ACTUATOR

Tyler T. Hamer[1], Minkyun Noh[1], Lei Zhou[1], Joshua Chabot[2], and David L. Trumper[1]
[1]Department of Mechanical Engineering
Massachusetts Institute of Technology
Cambridge, MA, USA
[2]MIT Lincoln Laboratory
Lexington, MA, USA

INTRODUCTION

The attitude control system (ACS) of a spacecraft contains a minimum of three reaction wheels to rotate the spacecraft in 3 degrees of freedom (DoF), but typically contains additional reaction wheels for both redundancy and improved pointing accuracy. Each wheel rotates the spacecraft about its axis by imparting an equal-and-opposite torque when the spacecraft accelerates the wheel. Since space, weight, and power (SWaP) are a premium on a spacecraft, reaction spheres, which impart an equal-and-opposite torque about an arbitrary axis when the spacecraft accelerates the sphere about that axis, have been proposed to reduce the ACS down to a single device.

While NASA first proposed reaction spheres over a half century ago, limitations with previous designs have kept the technology from commercialization [1]. These designs can be generalized into two categories: asynchronous, induction-type actuators and synchronous actuators similar to DC and hysteresis motors. The induction-type designs are difficult to model and suffer from eddy current losses in the rotor while the synchronous designs often have rotors constructed from multiple magnets which presents fabrication, strength, and balance issues. To incorporate the best of both worlds, the mechanical simplicity of an induction motor with the efficiency and simple model of a brushless DC motor, a spherical permanent magnetic dipole rotor actuated by a stator of surrounding coils has been considered [2, 3]. This paper presents the modeling, design, and vertical suspension of a prototype permanent magnetic dipole reaction sphere depicted in Figure 1.

OPERATING PRINCIPLE

Torque and force on the dipole rotor arise from the interaction of the rotor's external magnetic field with the current passing through each coil. Since the rotor is a magnetic dipole, the torque ${}^{\mathrm{c}}\boldsymbol{T}_{\mathrm{r}}$ and force ${}^{\mathrm{c}}\boldsymbol{F}_{\mathrm{r}}$ on the rotor by a single coil can be found by approximating the coil as a magnetic dipole as well.

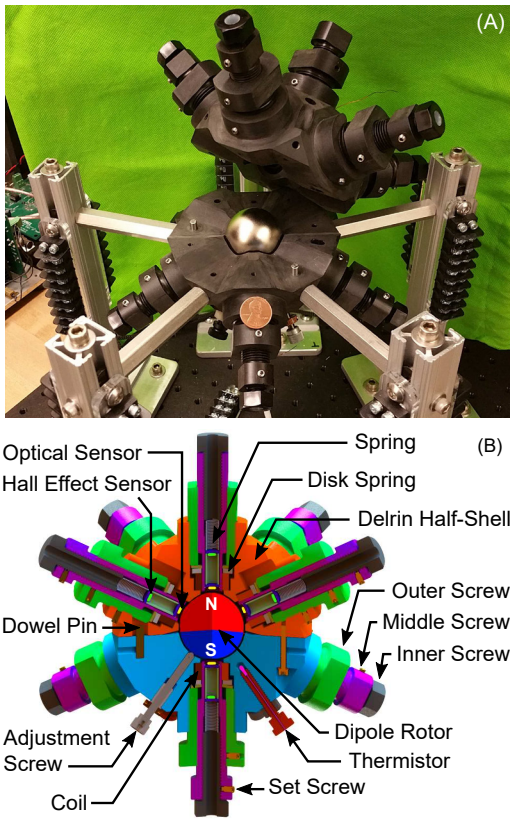

FIGURE 1. Permanent magnetic dipole reaction sphere (a) bench-level prototype with (b) label cross section.

The torque and force between these two magnetic dipoles are

$$ {}^{\mathrm{c}}\boldsymbol{T}_{\mathrm{r}} = -\left(\boldsymbol{m}_{\mathrm{c}} \times \boldsymbol{B}_{\mathrm{r}}\right) \tag{1a} $$

$$ {}^{\mathrm{c}}\boldsymbol{F}_{\mathrm{r}} = -\bigtriangledown\left(\boldsymbol{m}_{\mathrm{c}} \cdot \boldsymbol{B}_{\mathrm{r}}\right), \tag{1b} $$

where $\boldsymbol{B}_{\mathrm{r}}$ is the external magnetic flux density of the rotor and and $\boldsymbol{m}_{\mathrm{c}}$ is the approximated magnetic dipole moment of the coil.

The external magnetic flux density of the rotor is the magnetic flux density of a dipole $\boldsymbol{B}_{\mathrm{dipole}}$:

$$ \boldsymbol{B}_{\mathrm{dipole}}(\boldsymbol{r}) = \frac{\mu_0}{4\pi}\left[\frac{3\boldsymbol{r}\left(\boldsymbol{m}_{\mathrm{dipole}} \cdot \boldsymbol{r}\right)}{|\boldsymbol{r}|^5} - \frac{\boldsymbol{m}_{\mathrm{dipole}}}{|\boldsymbol{r}|^3}\right], \tag{2} $$

which in spherical coordinates is

$$\boldsymbol{B}_{\text{dipole}}(\boldsymbol{r}) = \frac{\mu_0}{4\pi}\frac{|\boldsymbol{m}_{\text{dipole}}|}{|\boldsymbol{r}|^3}\left(2\cos\theta\hat{\boldsymbol{i}}_{\boldsymbol{r}} + \sin\theta\hat{\boldsymbol{i}}_{\boldsymbol{\theta}}\right), \quad (3)$$

where μ_0 is the permeability of free space and $\boldsymbol{m}_{\text{dipole}}$ is the magnetic dipole moment. $\boldsymbol{r}$ is the position of the point of interest with respect to the center of the magnetic dipole, which in this case will be the position of the center of the coil's approximated dipole with respect to the rotor's center ${}^{\text{r}}\boldsymbol{r}_{\text{c}}$.

The magnetic dipole moment of the rotor $\boldsymbol{m}_{\text{r}}$ is

$$\boldsymbol{m}_{\text{r}} = \not{V}_{\text{r}}\frac{B_{\text{rem}}}{\mu_0}\boldsymbol{n}_{\text{r}}, \quad \not{V}_{\text{r}} = \frac{4}{3}\pi R_{\text{r}}^3, \quad (4)$$

where $\not{V}_{\text{r}}$, R_{r}, and B_{rem}, are the rotor's volume, radius, and remanence respectively, and $\boldsymbol{n}_{\text{r}}$ is a unit vector along the rotor's axis of magnetization. The approximated magnetic dipole moment of the coil is

$$\boldsymbol{m}_{\text{c}} = N i_{\text{c}} A_{\text{ave}} \boldsymbol{n}_{\text{c}}, \quad (5)$$

where N is the coil's number of turns, i_{c} is the current through the coil, A_{ave} is the average area enclosed by each turn, and $\boldsymbol{n}_{\text{c}}$ is a unit vector along the coil's axis.

Substituting Equations (2), (4) and (5) into Equation (1) for when the rotor's center lies along the coil's axis (${}^{\text{r}}\boldsymbol{r}_{\text{c}}/|{}^{\text{r}}\boldsymbol{r}_{\text{c}}| = \boldsymbol{n}_{\text{c}}$), the torque and force on the rotor by a single coil are

$${}^{\text{c}}\boldsymbol{T}_{\text{r}} = K_{\text{T}} i_{\text{c}}(\boldsymbol{n}_{\text{c}} \times \boldsymbol{n}_{\text{r}}) \quad (6a)$$

$${}^{\text{c}}\boldsymbol{F}_{\text{r}} = \frac{1}{2}K_{\text{F}} i_{\text{c}}[3(\boldsymbol{n}_{\text{r}} \cdot \boldsymbol{n}_{\text{c}})\boldsymbol{n}_c - \boldsymbol{n}_{\text{r}}], \quad (6b)$$

where K_{T} and K_{F} are respectively the reaction sphere's torque and force constants for a single coil while the rotor's center lies along that coil's axis:

$$K_{\text{T}} = \frac{\mu_0 |\boldsymbol{m}_{\text{r}}| |\boldsymbol{m}_{\text{c}}|}{4\pi |{}^{\text{r}}\boldsymbol{r}_{\text{c}}|^3 i_{\text{c}}} = \frac{1}{3}N A_{\text{ave}} B_{\text{rem}}\left(\frac{R_{\text{r}}}{|{}^{\text{r}}\boldsymbol{r}_{\text{c}}|}\right)^3 \quad (7a)$$

$$K_{\text{F}} = \frac{3\mu_0 |\boldsymbol{m}_{\text{r}}| |\boldsymbol{m}_{\text{c}}|}{2\pi |{}^{\text{r}}\boldsymbol{r}_{\text{c}}|^4 i_{\text{c}}} = \frac{2N A_{\text{ave}} B_{\text{rem}}}{R_{\text{r}}}\left(\frac{R_{\text{r}}}{|{}^{\text{r}}\boldsymbol{r}_{\text{c}}|}\right)^4. \quad (7b)$$

The overall torque ${}^{\text{c}_{\text{tot}}}\boldsymbol{T}_{\text{r}}$ and force ${}^{\text{c}_{\text{tot}}}\boldsymbol{F}_{\text{r}}$ on the rotor are the superposition of the individual torques and forces from each coil. For a rotor centered within a radial array of identical surrounding coils (thus the rotor's center lies along each coil's axis), these are

$${}^{\text{c}_{\text{tot}}}\boldsymbol{T}_{\text{r}} = \sum_{a=1}^{b} {}^{\text{c}_b}\boldsymbol{T}_{\text{r}} = K_{\text{T}} \sum_{a=1}^{b} i_{\text{c}_b}(\boldsymbol{n}_{\text{c}_b} \times \boldsymbol{n}_{\text{r}}) \quad (8a)$$

$${}^{\text{c}_{\text{tot}}}\boldsymbol{F}_{\text{r}} = \sum_{a=1}^{b} {}^{\text{c}_b}\boldsymbol{F}_{\text{r}} = \frac{1}{2}K_{\text{F}} \sum_{a=1}^{b} i_{\text{c}_b}\left[3(\boldsymbol{n}_{\text{r}} \cdot \boldsymbol{n}_{\text{c}_b})\boldsymbol{n}_{\text{c}_b} - \boldsymbol{n}_{\text{r}}\right]. \quad (8b)$$

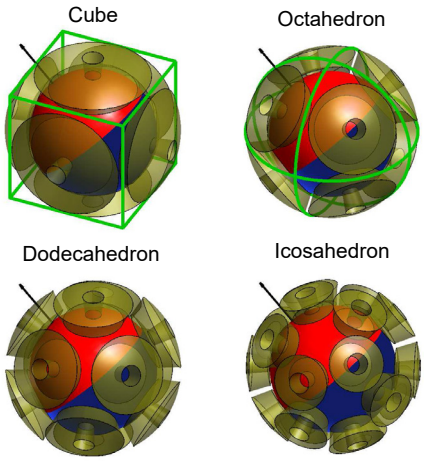

FIGURE 2. Distributions of coils centered on faces of platonic solids. Green lines represent singular dipole orientations (3 DoF suspension of dipole rotor is lost) for cube and octahedron configurations.

In order to maintain symmetry, radial arrays corresponding to the coils centered on the faces of platonic solids are considered. Applying Equation (8) over these distributions, a minimum of 12 equidistant coils is needed for full 3 DoF magnetic suspension of the dipole rotor independent of the rotor's orientation as visualized in Figure 2.

BENCH-LEVEL PROTOTYPE DESIGN

Figure 1 depicts the reaction sphere bench level prototype with a labeled cross section. Twelve equidistantly distributed coils levitate and rotate the dipole rotor while 12 optical sensors and 12 Hall effect sensor, coaxially placed within each coil, measure the rotor's position and the orientation of the rotor's dipole respectively. These position and rotation measurements are fed back to a real-time controller which drives 12 transconductance power amplifiers, each which drive a coil. The design of the actuation, sensing, mechanical structure, power electronics, and controller are described below.

Actuation

The dipole rotor is a 38.1 mm (1.5 in) diameter, permanently axially magnetized, NdFeB (Grade 42) sphere (K&J Magnetics SX8) with a mass of M_{r} = 0.22 kg and remanence of B_{rem} = 1.31 T. The stator consists of two mating, symmetric Delrin half-shells, which together form a dodecahedron with a 40.1 mm diameter spherical pocket that the rotor is contained in. Twelve equidistantly distributed cylindrical coils, one centered on each face of the dodecahedron stator at a diameter of 42.1 mm, levitate and rotate the rotor. Thus when the rotor is centered within the spherical pocket, the prototype has a 1 mm mechanical air gap and 2 mm magnetic air gap and the rotor can translate up to $\pm$1 mm in 3 DoF.

TABLE 1. Actuation Key Parameters.

Symbol	Parameter	Value
M_{r}	rotor mass	0.22 kg
B_{rem}	rotor remanence	1.31 T
R_{r}	rotor radius	19.05 mm
$\lvert{}^{\mathrm{r}}\boldsymbol{r}_{\mathrm{c}}\rvert$	rotor-coil center distance	26.6 mm
N	coil turns	348
A_{ave}	turn average enclosed area	201 mm^2
K_{T}	single-coil torque constant	11.2 mN·m/A
K_{F}	single-coil force constant	2.52 N/A

Each cylindrical coil is wound from N = 348 turns of 0.3 mm diameter (AWG 28) magnet wire making a footprint of 20 mm outer-diameter $\times$ 12 mm inner-diameter $\times$ 10 mm long. The average area enclosed by a turn of each coil is A_{ave} = 201 mm^2. Additionally, each coil has a series self-inductance of L_{s} = 1.6 mH and a series resistance of R_{s} = 4.1 Ω as measured at 100 Hz by an Agilent 4284A LCR meter. When the rotor is centered, FEMM simulation determined an effective distance between the rotor's center and the center of each coil's effective dipole is $\lvert{}^{\mathrm{r}}\boldsymbol{r}_{\mathrm{c}}\rvert$ = 26.6 mm. Substituting these values into Equation (7), the torque constant and force constant of each coil are estimated to be K_{T} = 11.2 mN·m/A and K_{F} = 2.52 N/A respectively, requiring a predicted 0.84 A for 1 DoF suspension by a single coil directly above the rotor. The key parameters for actuation are summarized in Table 1.

Sensing

The stator contains 12 equidistantly distributed sensing modules, one coaxially placed within each of the coils, for feedback. Each sensing module consists of a reflective optical sensor (Fairchild QRE1113GR) for measuring the translational position of the rotor and a Hall effect sensor (Allegro A1308KUA-1-T) for measuring the orientation of the rotor's dipole (rotational position). Within each sensing module, each sensor is mounted on its own printed circuit board (PCB) spaced 15 mm apart. This allows the optical sensor to be positioned about 1 mm from the rotor when closest for highest sensitivity and the Hall effect sensor to be positioned at least 15 mm from the rotor when closest to avoid saturation. When the rotor is centered, the prototype has an optical sensing air gap of 2 mm and a Hall effect sensing air gap of 17 mm.

The sensitivity of the optical sensor and the Hall effect sensor with respect to the rotor's position and orientation of its dipole are provided in Figure 3. To measure these sensitivities, a sensor module is mounted to an aluminum spacer above a steel XY linear stage (Newport 461-XY-M) and a steel Z linear stage (by Oriel Corporation) with the rotor

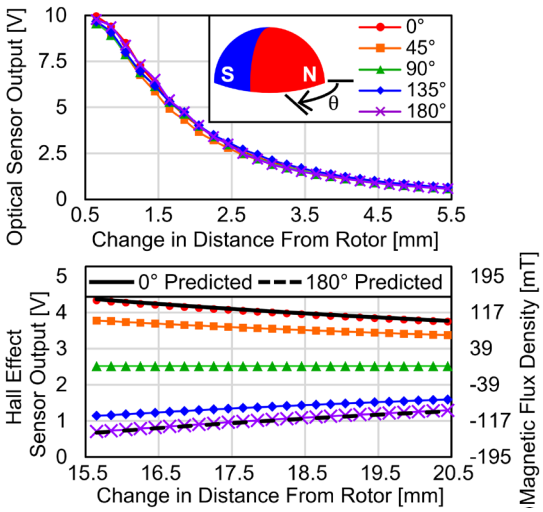

FIGURE 3. Measured sensor module (optical sensor and Hall effect sensor) voltage as functions of the rotor's translation and rotation of its dipole.

mounted on an aluminum spacer above a steel rotary stage (Melles Griot 98 mm dia. stage) across from it. The aluminum spacers keep the rotor at least 50 mm from the stages to ensure the stages' steel does not distort the rotor's dipole magnetic field. The Y-and Z-axes orient the sensor module radially with the rotor. Then the rotary stage sets the dipole's orientation and the X-axis moves the sensor module radially.

With the 0° orientation denoting the rotor's north pole facing the sensor module, the rotary stage indexes the rotor in 45° increments. For each orientation of the rotor's dipole, the X-axis steps the sensor module from 0.65 mm to 20.5 mm from the rotor's surface in 20 μm increments. At each position, the voltage of both sensors are acquired with a sampling rate of 10 kHz using a National Instruments (NI) PXI-6289 M-Series analog input card of 750 kHz bandwidth, 18 bit resolution, and an input range of $\pm$10 V for the optical sensor and $\pm$5 V for the Hall effect sensor.

The optical sensor's voltage did not vary with the dipole's orientation, but varied as a cubic polynomial with its distance from the rotor. Linearized about the optical sensor's distance from a centered rotor (2 mm), the optical sensor has a sensitivity of H_{opt} = 2.75 V/mm. The Hall effect sensor's voltage varied sinusoidally with the dipole's orientation and as a cubic inverse with its distance from the rotor just like the radial component of the rotor's magnetic flux density in Equation (3). Thus the Hall effect sensor's voltage varied linearly with the radial component of the rotor's magnetic flux density with a sensitivity of H_{Hall} = 12.8 V/T.

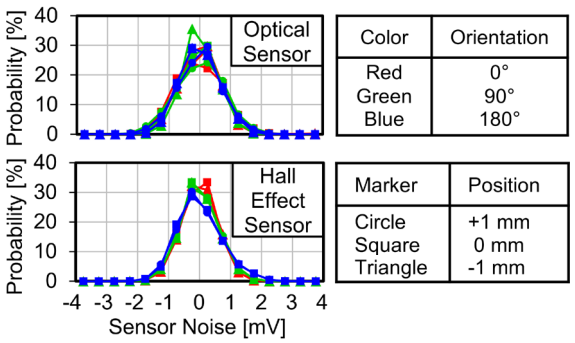

FIGURE 4. Histograms of senor module noise.

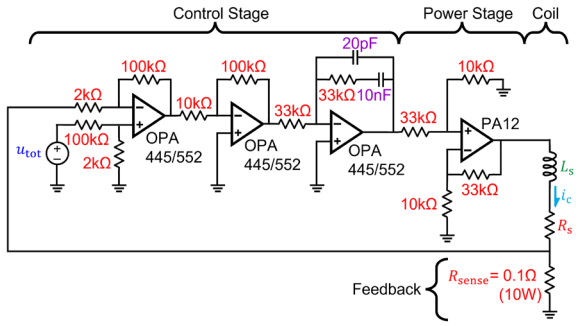

FIGURE 5. Circuit diagram for power amplifier with a DC gain of 0.2 A/V and 5 kHz bandwidth [4].

Using the same setup, each sensor's noise level is measured over a period of 10 sec for the 0°, 90°, and 180° orientations of the rotor's dipole at distances from the rotor corresponding to the rotor's -1 mm, 0 mm, and +1 mm positions. Figure 4 shows histograms for these 9 stationary configurations. Both sensor's noise levels are Gaussian distributed and independent of the dipole's orientation and distance from the rotor. The optical sensor's voltage noise has a standard deviation of 0.67 mV, 9 times larger than the quantization error, corresponding to a position noise standard deviation of 0.24 μm. The Hall effect sensor's voltage noise has a standard deviation of 0.61 mV, 16 times larger than quantization error, corresponding to a magnetic flux density noise standard deviation of 48 μT.

Mechanical Design

The stator consists of two mating, symmetric Delrin half-shells. The bottom half-shell is held up by 5 standoffs running to 80-20 pillars mounted to an optical breadboard. These half-shells are made from Delrin as eddy currents formed from the rotor rotating in metal half-shells would shield the Hall effect sensors. Further, the surface of spherical pocket can then be used as a touch down bearing. To ensure the Delrin does not overheat, four embedded thermistors monitor the stator's temperature.

The rotor can be easily placed within or removed from the stator by separating the two half-shells. To ensure the half-shells mate in a repeatable fashion, the mating surfaces use two dowel pins, one in a slot and the other in a hole. The position of the rotor within the stator's spherical pocket can be manually adjusted externally using 3 adjustment screws within the stator. This allows the rotor's rotation to be tested separately from its suspension if needed.

To coaxially place each sensing module within its accompanying coil, but allow for radial adjustment if needed, a series of three hollow screws is used. The inner screw provides clearance for the sensing module's wires and with a spring, preloads the sensing module against a retaining ring in the middle screw. The outer screw with a plastic disk spring, preloads the coil into a radial pocket centered on one of the stator's 12 outer faces. The middle screw translates along the coil's inner bore and outer screw, positioning the sensing module radially while keeping the module in coaxial alignment with the coil. Set screws in the stator and two outer screws later lock each hollow screw into place.

Power Electronics

Each coil is driven by its own transconductance linear power amplifier, whose circuit is provided in Figure 5. These amplifiers were previously used to drive a bearingless hysteresis motor [4] and later adjusted for use with these coils. A sense resistor of R_s = 0.1 Ω feeds back the current through the coil i_c to a control stage containing of 3 high-voltage op amps (Texas Instruments OPA 445 or OPA 552) to provide PI compensation. The control stage drives a power stage containing a linear power amplifier (Apex Microtechnology PA12) with a gain in the feedback path below 0.25 for stability. The entire circuit drives current through the coil with a DC transconductance gain of G_p = 0.2 A/V and a bandwidth of 5 kHz.

Controller

Signals from the 12 sensing modules are acquired using two NI PXI-6289 M-Series analog input cards. These are fed back to a control algorithm implemented in LabVIEW on a NI PXIe-8135 embedded controller and used to drive the 12 power amplifiers, and in turn their corresponding coils, via an NI PXIe-6739 dedicated analog output card. For initial testing, a control algorithm running at 2 kHz levitates the rotor using a single coil directly above the rotor via feedback from the optical sensor in that coil's coaxial sensing module. The coil above the rotor is used as the other DoF besides rotation about the dipole are passively stable. Figure 6 shows the block diagram for this control system.

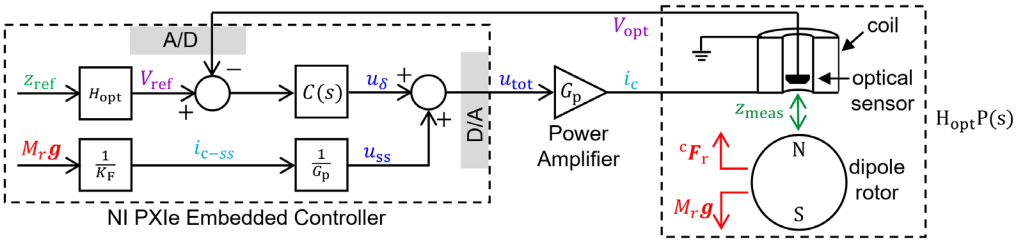

FIGURE 6. Block diagram for vertical suspension of the dipole rotor by the coil and optical sensor above it.

The rotor's weight passes through the inverse of the single-coil motor constant for a centered rotor to generate the single-coil steady state bias current, a predicted $i_{\text{c-ss}}$ = 0.84A. The bias current then passes through the inverse of the power amplifier's DC gain to generate the steady state bias control effort u_{ss} to compensate for the rotor's weight. This control effort is added to the small displacement control effort u_δ responsible for compensating for rotor's small vertical deviations from the center.

The small displacement control effort is generated by a lead compensator $C(s)$ from the difference between the rotor's desired vertical position z_{ref} (0 mm corresponding to a centered rotor) and the rotor's vertical position measured by the optical sensor z_{meas}. To design the lead compensator, a linearized dynamic model $P(s)$ for the rotor's vertical position from the center z with respect to small changes in the current through the coil $i_{\text{c-}\delta}$ is built. It is represented by the following transfer function:

$$P(s) = \frac{z}{i_{\text{c-}\delta}} = \frac{K_{\text{F}}}{k}\left(\frac{k/M_{\text{r}}}{s^2 - k/M_{\text{r}}}\right), \qquad (9)$$

where k is the negative stiffness of the centered rotor's vertical suspension given by

$$k = 4K_{\text{F}} i_{\text{c-ss}} / \left|{}^{\text{r}}\boldsymbol{r}_{\text{c}}\right|. \qquad (10)$$

Substituting in the actuation key values, the rotor's suspension instability has a predicted break frequency of $\sqrt{k/M_{\text{r}}}$ = 6.1 Hz.

Using this model, the DC gain of the transconductance amplifier, and the sensitivity of the optical sensor, the following lead compensation is used to crossover at a predicted ω_{c} = 60 Hz with a predicted phase margin of ϕ_{M} = 25°:

$$C(s) = K_{\text{p}}\frac{\alpha\tau_{\text{d}}s + 1}{\tau_{\text{d}}s + 1}, \qquad (11)$$

where K_{p} = 14.8, α = 3, and τ_{d} = 0.0015 sec.

INITIAL EXPERIMENTATION & RESULTS

Using the controller above, the rotor is successfully levitated in the center of the stator's spherical pocket by the coil above it. The single-coil steady state bias current is measured to be $i_{\text{c-ss}}$ = 0.86A corresponding to a single-coil motor force constant of K_{F} = 2.45 N/A. Both of these values are within 3% of their predicted values. The performance of the rotor's vertical suspension is evaluated in both the frequency and time domain. Table 2 summarizes the overall performance.

TABLE 2. Vertical Suspension Performance.

Symbol	Parameter	Predicted	Measured
$i_{\text{c-ss}}$	bias current	0.84 A	0.86 A
K_{F}	force constant	2.52 N/A	2.45 N/A
$\sqrt{k/M_{\text{r}}}$	instability freq.	6.1 Hz	6.7 Hz
ω_{c}	crossover freq.	60 Hz	50-64 Hz
ϕ_{M}	phase margin	25°	10-22°

Frequency Response

To evaluate the rotor's vertical suspension in the frequency domain, the rotor's desired vertical position is varied sinusoidally with an amplitude of 50 μm over 170 frequencies from 1 Hz to 1 kHz. At each of these frequencies, the frequency response of the rotor's linearized dynamic model $P(s)$, the loop return ratio $RR(s) = C(s)G_{\text{p}}P(s)H_{\text{opt}}$, and the closed loop $RR(s)/[1 + RR(s)]$ is measured. Each of these measured frequency responses along with their corresponding predicted frequency responses are displayed as Bode plots in Figure 7.

The measured frequency response of the rotor's dynamics has a break frequency for its instability of $\sqrt{k/M_{\text{r}}}$ = 6.7 Hz. Additionally, its magnitude unexpectedly drops at 50 Hz until 250 Hz where it recovers after passing through a notch-and-peak pair. This pair implies a pair of complex-zeros and-poles so it is hypothesized that this magnitude drop-then-recover occurs from the stator's mass coupling to and then decoupling from the rotor's mass. This magnitude drop has two effects: (1) It causes the return ratio to crossover through unity magnitude at a measured ω_{c} = 50 Hz with a measured phase margin of ϕ_{M} = 10°, both lower than expected. (2) Since the drop is near crossover, it distorts the closed loop magnitude's resonance peak.

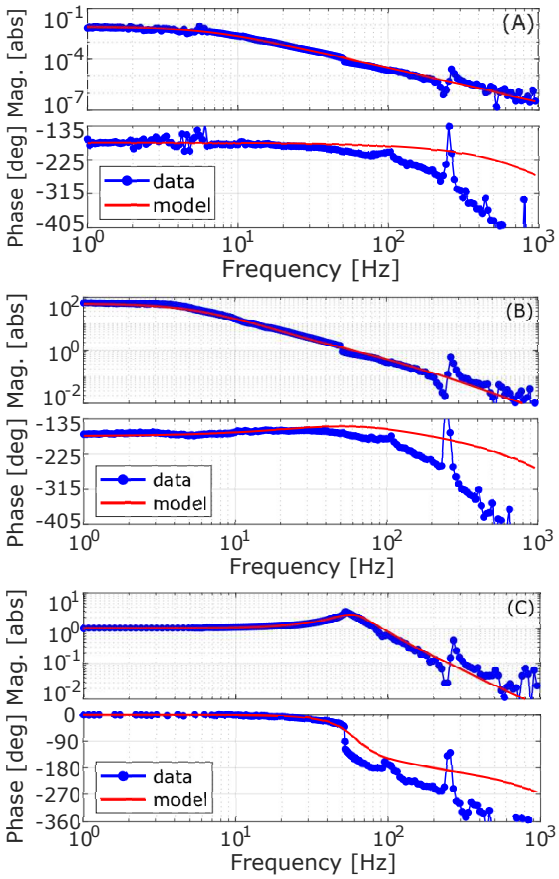

FIGURE 7. Frequency response of (a) the rotor dynamics, (b) return ratio, and (c) closed loop during vertical suspension of the rotor by the coil above it.

Time Response

To evaluate the rotor's vertical suspension in the time domain, the rotor's desired position is stepped 100 μm from -50 μm to 50 μm. Figure 8 shows the rotor's response to this step. The rotor steps 104 μm, peaking in 8.0 ms with 49% overshoot and settling in 51.7 ms. These correspond to a measured ω_c = 64 Hz with a measured phase margin of ϕ_M = 22°, similar to the frequency domain evaluation.

CONCLUSION

Reducing space, weight, and power (SWAP) is essential in the design of spacecraft. One possible way to reduce SWAP is to replace the three reaction wheels of a spacecraft's ACS with a single reaction sphere. This paper presents a spherical permanent magnetic dipole rotor driven by 12 surrounding equidistant coils for consideration as a reaction sphere. Such a design has a mechanically simple rotor like induction motors with the model simplicity of hysteresis-and brushless DC-motors. In fact, it was shown that the torque and force on the rotor can be modeled as the superposition of the torque and force generated by 12 sets of two dipoles.

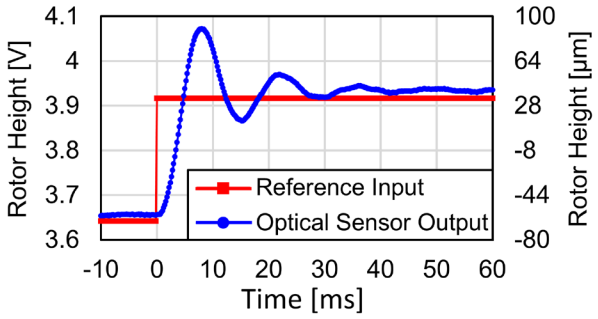

FIGURE 8. Step response of sphere's height for a 100 μm input step.

After presenting the reaction sphere's actuation, the sensing, mechanical structure, power electronics, and controller were presented. The design uses 12 sets of optical sensors and Hall effects sensors, placed coaxially with in each coil, to provide position and rotation feedback respectively. This design was physically constructed. Using a lead compensator, the coil above the rotor successfully levitated the rotor by itself with position feedback from the coil's coaxial optical sensor. The rotor required 0.86 A to levitate corresponding to a force constant per coil of 2.45 N/A while the rotor is centered. The frequency response and the step response of the rotor were measured to evaluate the suspension. The suspension was found to crossover just below 60 Hz, well above the 6.7 Hz instability of the rotor's dynamics, with a phase margin around 16°. Next steps involve testing 1 DoF rotation and then 3 DoF-suspension and-rotation separately, then together.

ACKNOWLEDGMENTS

This work is performed in collaboration with and supported by MIT Lincoln Laboratory.

REFERENCES

[1] Zhu L, Guo J, Gill E. Review of reaction spheres for spacecraft attitude control. Progress in Aerospace Sciences. 2017 May;91:67–86.

[2] Wang J, Jewell GW, Howe D. Analysis, design and control of a novel spherical permanent-magnet actuator. IEE Proceedings - Electric Power Applications. 1998 January;145(1):61–71.

[3] Chabot J. A Spherical Magnetic Dipole Actuator for Spacecraft Attitude Control [Master's Thesis]. Aerospace Engineering Sciences, University of Colorado. Boulder, CO; 2015.

[4] Noh M, Gruber W, Trumper DL. Hysteresis Bearingless Slice Motors With Homopolar Flux-Biasing. IEEE/ASME Transactions on Mechatronics. 2017;22(5):2308–2318.

A NOVEL SEMI-ACTIVE JOINT FOR SIMULTANEOUSLY ACHIEVING FAST SETTLING AND EXCELLENT IN-POSITION STABILITY IN POINT-TO-POINT POSITIONING

Xin Dong[1], Chinedum E. Okwudire[1]
[1]Smart and Sustainable Automation Research Lab
Department of Mechanical Engineering, University of Michigan
Ann Arbor, MI, USA

OVERVIEW

The design of a novel semi-active joint for connecting mechanical bearings to a precision motion stage is presented. The semi-active joint enables the benefits of bearing friction on in-position stability to be achieved while avoiding its adverse effects on settling time in point-to-point positioning. To achieve this goal, the joint is equipped with solenoid actuators that switch its stiffness from low, during settling, to high once the stage gets into position. Simulation results, using the semi-active joint, show 51% and 55% improvements in settling time and in-position stability, compared to the case with rigid joint and compliant joint, respectively. Preliminary experiments on an in-house built motion stage equipped with the designed semi-active joint show that the proposed method has excellent in-position stability, while potentially achieving large reductions of settling time. However, the associated impact force, when the semi-active joint switches its stiffness, excites high frequency dynamics of the system, severely jeopardizing the settling performance. Ongoing work is focused on mitigating the adverse effects of switching using both mechanical design and control methods.

BACKGROUND AND MOTIVATION

Mechanical bearings (i.e., sliding, and especially rolling bearings) are used for motion guidance in most precision and some ultra-precision motion stages due to their low cost, large motion range, high off-axis stiffness and vacuum compatibility [1]. They are also preferable over other bearing types for their excellent in-position stability due to the presence of pre-motion (i.e., 'static') friction caused by mechanical contact. However, the presence of pre-motion friction causes the stages to take a long time to settle into position during point-to-point motions [2]-[4]. To address this issue, model-based compensation methods are most commonly used to predict and cancel out the friction experienced by the stage [2][3]. However, accurate compensation of pre-motion friction often requires the use of complex models which are not robust to changes in on-machine friction [4]-[6].

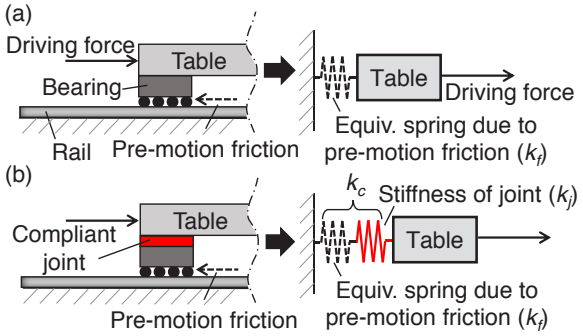

Fig. 1 Schematic and spring model of motion stage with mechanical bearing attached to the table: (a) rigidly, and (b) using the compliant joint.

Prior work [4][5] done by the present authors has demonstrated that undesirable effects of pre-motion friction can be effectively mitigated by attaching the bearing to the moving table of the stage using a joint that is very compliant in the motion direction. Fig. 1(a) shows a typical mechanical-bearing-guided stage in which pre-motion friction is modeled as an equivalent nonlinear spring of stiffness k_f connecting the table to the ground [4][5][7]. At the start of the motion, k_f is very large; but as more driving force is applied to counteract friction, k_f rapidly reduces and eventually becomes zero. Standard feedback controllers often encounter difficulties when trying to overcome the high initial stiffness of pre-motion friction, resulting sluggish settling during point-to-point positioning. Fig. 1(b) illustrates the concept of the compliant joint method [4][5]: rather than being rigidly attached to the moving table, the bearing is attached using a joint of stiffness k_j in the motion direction. Accordingly, the stage with the compliant joint is modeled as a series combination of k_f and k_j, with combined stiffness $k_c = k_f k_j/(k_f + k_j)$. A very small k_j dominates the combined stiffness felt by the stage when k_f is very large in the pre-motion regime. Using the compliant joint, accurate and robust compensation of pre-motion friction, and

large reductions in settling time have been experimentally demonstrated [4][5].

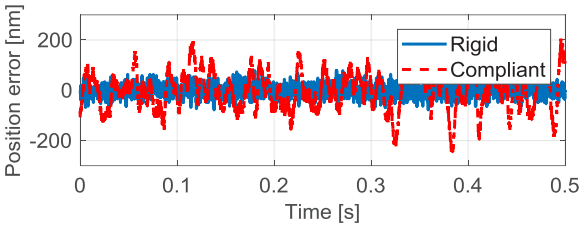

Fig. 2 Measured in-position error of rigid and compliant stages presented in [4][5] when a PWM amplifier is used.

While the adverse effects of pre-motion friction during motion transients (e.g., settling) are mitigated by introducing the compliant joint, the benefits of friction during in-position are also diminished. Due to the initially very large k_f, mechanical-bearing-guided stages often have excellent in-position stability compared to, e.g., air bearing stages (which have zero stiffness in the motion direction). The compliant joint replaces the stiff k_f with a much softer stiffness k_c (since $k_j << k_f$), leading to increased susceptibility of stage's position to disturbances. As a result, the stage with the compliant joint (i.e., compliant stage) has significantly larger errors during in-position, compared to that of the stage without it (i.e., rigid stage), when a PWM amplifier (which is known to have relatively large noise) is used to drive the motor – see Fig. 2. This issue can be mitigated by switching to a linear amplifier which has much less noise level; however, this causes increased cost and reduced energy efficiency.

SEMI-ACTIVE JOINT

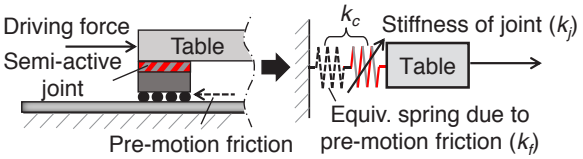

Fig. 3 Schematic and spring model of a mechanical-bearing-guided stage equipped with the semi-active joint.

Fig. 3 shows the proposed method for mitigating the undesirable effects of pre-motion friction during motion transients while maintaining excellent in-position performance. The bearing is attached to the table using a joint that can be switched between two modes (stiff or compliant). The joint is very stiff ($k_j >> k_f$) when the stage is at rest (e.g., while it is in position) such that the combined stiffness approaches the high frictional stiffness (i.e., $k_c \rightarrow k_f$); the joint becomes compliant ($k_j << k_f$) during motion transients such that the combined stiffness is dominated by the much softer k_j (i.e., $k_c \rightarrow k_j$).

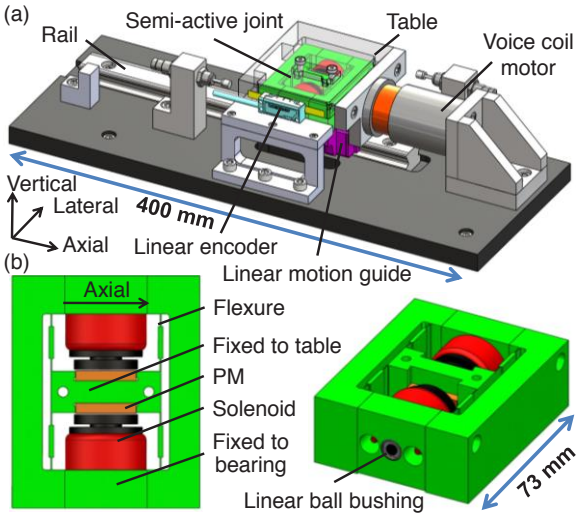

Fig. 4 CAD model of (a) a motion stage equipped with (b) the designed semi-active joint prototype.

Table 1. Stiffness values of flexure, bearing and their combination [N/m].

	Axial	Vertical	Lateral
Flexure	5×10^4	5×10^7	1×10^8
Bearing	$\sim 10^6$	3×10^7	4×10^7
Combined	$\sim 5 \times 10^4$	2×10^7	3×10^7

Fig. 4(a) shows the CAD model of a single-axis mechanical-bearing-guided motion stage equipped with the proposed semi-active joint. The stage has 1.35 kg moving mass and 25 mm travel range. It is guided by a high-rigidity pre-loaded linear motion guide with end seals (THK, SR-25TB), riding on a super-precision grade rail, lubricated using grease (THK, AFB-LF). A voice coil motor (Moticont, LVCM-044) is used to drive the stage. The table's position is measured using a linear encoder system (Renishaw, T1000 read head and RGSZ20 scale) with post interpolation resolution of 4.88 nm.

A semi-active joint prototype (see Fig. 4(b)) is used to attach the bearing to the table. A flexure (made of Aluminum 7075-T6) with four leaf springs is adopted in the semi-active joint design due to its non-contact and friction-free nature. The outer platform of it is connected to the bearing and the center platform is connected to the moving table. Table 1 summarizes the stiffness values of the designed flexure (obtained via finite element analysis using SolidWorks®). Note that the flexure achieves orders of

magnitude less stiffness (in the axial direction) than the initial stiffness of pre-motion friction experienced by the bearing. It also maintains the same order of magnitude of off-axis stiffness as the bearing, so as not to unduly compromise the rigidity in lateral and vertical directions. The stiffness of the semi-active joint is switched through two solenoid actuators and permanent magnets (PMs) which are attached to the outer and center platforms of the flexure, respectively. When no power is applied, the PMs attract the armatures of solenoids such that the center platform of flexure is locked (through contact friction) to the outer platform (i.e., the joint is stiff); when power is applied, the solenoid actuators pull the armatures away from the PMs to allow relative motion between the bearing and the table (i.e., the joint is compliant). Note that linear ball bushings are added between armatures and coils of the solenoid actuators to increase the axial stiffness of the semi-active joint when it is switched to stiff mode.

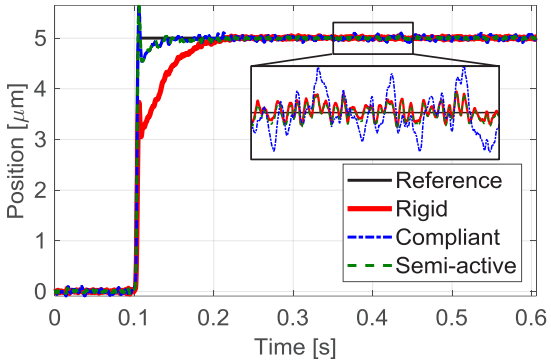

Fig. 5 Simulated settling performance of the stage with rigid joint, compliant joint and semi-active joint (which is switched to compliant mode only from 0.1 s to 0.15 s).

Table 2. Simulated settling time and in-position error (RMS).

	Settling time	In-position error
Rigid	91 [ms]	17 [nm]
Compliant	45 [ms]	38 [nm]
Semi-active	45 [ms]	17 [nm]

Fig. 5 shows the simulated settling performance using the stage of Fig. 4(a) equipped with the rigid joint, compliant joint [4][5] and proposed semi-active joint during a 5 μm point-to-point motion. As seen from Table 2, the compliant stage reduces the settling time by 51%, however, at a cost of more than doubling the root-mean-square (RMS) error during in-position, compared to the rigid stage. Using the proposed semi-active joint (which is switched to compliant mode from 0.1 s to 0.15 s), the stage achieves the same settling time as the compliant stage while maintaining the same in-position performance as the rigid stage.

POINT-TO-POINT POSITIONING TESTS

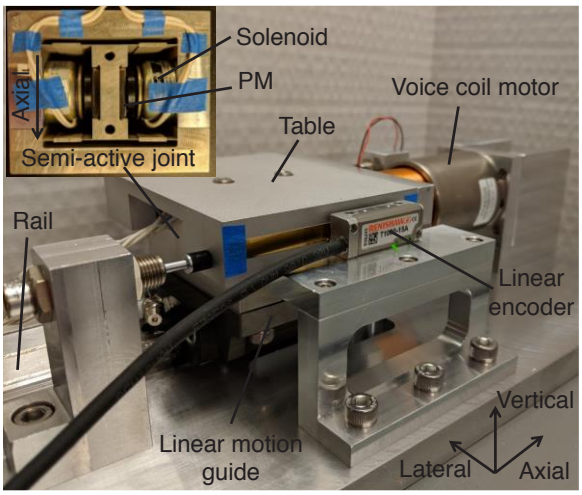

Fig. 6 Assembled in-house built stage equipped with the designed semi-active joint prototype.

Fig. 6 shows the in-house built mechanical-bearing-guided motion stage equipped with the designed semi-active joint prototype. A cascaded P/PI controller with velocity and acceleration feedforward is used for feedback control of the stage. It is tuned to 150 Hz closed loop bandwidth based on the identified dynamics of the rigid stage using loop shaping; the exact same controller gains are used for controlling the stage with compliant joint and semi-active joint. The controller is implemented using a real-time control board (dSPACE, DS1007), running at 10 kHz sampling frequency. A linear amplifier (Trust Automation, TA-115) is used to power the voice coil motor. The solenoid actuators are controlled through two relay modules for switching the semi-active joint between its two modes.

Experiments are carried out using the in-house built stage shown in Fig. 6 for evaluating the settling performance of the proposed method. Point-to-point motion profiles with step sizes of 5 μm and 5 mm are used as the reference trajectory [4]. The time taken for the stage to settle into a ±25 nm window after each step is evaluated. Fig. 7(a) compares the typical settling performance of the stage with rigid joint, compliant joint and semi-active joint during point-to-point motions with 5 μm step size. The rigid stage takes 150 ms to settle while the compliant stage settles within 14 ms, i.e., 91% faster. However, the in-position

error of the compliant stage is 5.4 nm, which is more than two times larger than that of the rigid stage (i.e., 2.3 nm). Using the proposed semi-active joint, which is switched to compliant mode before the start of the motion and switched back to stiff mode when the reference command reaches the target position, the stage is able to achieve an in-position error of 2.3 nm. However, switching of the joint introduces large motion errors during settling, followed by severe oscillations. As a result, the stage with the semi-active joint takes 110 ms to settle which is faster than the rigid stage, but significantly slower than the compliant stage. As seen from the frequency spectrum of position error signal after switching (see Fig. 7(b)), several high frequency modes are excited due to the impact force; since the feedback controller has limited bandwidth, the oscillation takes a very long time to settle. However, observe that the transient dynamics of the stage with semi-active joint is very similar to that of the compliant stage. Therefore, the proposed method can potentially achieve similar settling performance as the compliant stage if the adverse effects of switching are mitigated.

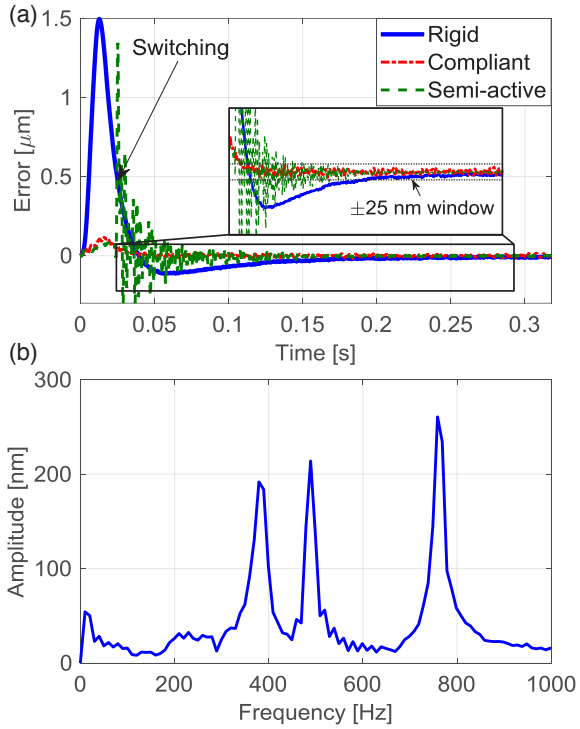

Fig. 7 (a) Typical positioning performance of the stage into the ±25 nm window during point-to-point motions with 5 μm step size; (b) frequency spectrum of position error signal for the semi-active joint case after switching.

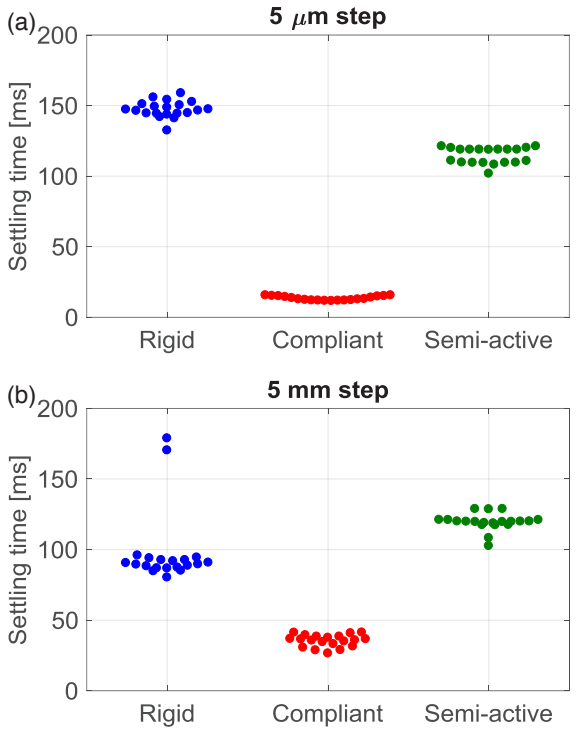

Fig. 8 Comparison of settling times into the ±25 nm window during point-to-point motions with (a) 5 μm and (b) 5 mm step size.

Table 3. Mean settling time and in-position error (RMS) during point-to-point positioning tests.

	Settling time	In-position error
5 μm step		
Rigid	147 [ms]	2.4 [nm]
Compliant	13 [ms]	5.5 [nm]
Semi-active	115 [ms]	2.4 [nm]
5 mm step		
Rigid	98 [ms]	2.7 [nm]
Compliant	35 [ms]	5.9 [nm]
Semi-active	119 [ms]	2.8 [nm]

Fig. 8 compares the settling performance during point-to-point positioning tests with 5 μm and 5 mm step size, based on 20 trials at random positions of the table and Table 3 summarizes the mean settling time and RMS errors during in-position. Note that mean settling times of the rigid stage are 147 ms and 98 ms for the 5 μm and 5 mm cases, respectively. The compliant stage is able to achieve 91% and 64% reductions in the mean settling times (i.e.,13 ms and 35 ms), at a cost of more than doubling the in-position errors compared to the rigid stage. Using the proposed semi-active joint, the stage is able to achieve almost the same in-position stability as the rigid stage. However, due to the large motion errors and the associated residual vibrations (that are

caused by the impact force during switching), the stage with the semi-active joint only achieves slightly faster (22% improvement) settling time during the 5 μm step motion, and has even worse performance during the 5 mm case, compared to the rigid stage. In order to improve the settling performance of the proposed method to similar levels as the compliant stage, ongoing work is focused on mitigating the undesirable effects of switching dynamics using both mechanical design and control methods. For example, damping materials will be implemented to prevent the excitation of high frequency modes. Similarly, electrical low-pass filter (through RC circuits) will be added to slow down the solenoid actuators during switching which will consequently reduce the impact force. From the control side, advanced control techniques, such as disturbance observer and harmonic cancelling controller, will be investigated.

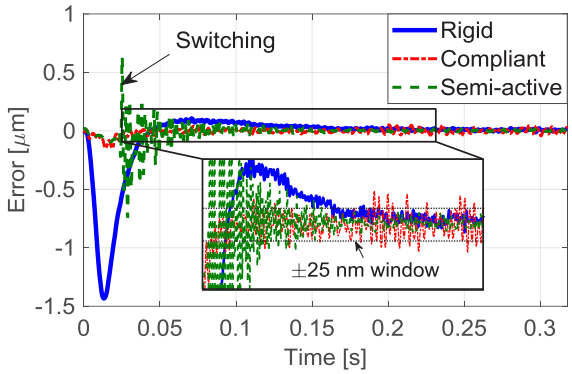

Fig. 9 Typical positioning performance of the stage into the ±25 nm window during point-to-point motion with 5 μm step size. (Note: current noise of 0.0025 A RMS value is added to the current outputted by the amplifier)

Note that the linear amplifier used to drive the motor has very small noise level. To simulate the case when a PWM amplifier is used (for its higher force, better energy efficiency and lower cost), normally distributed current noise with 0.0025 A standard deviation (i.e., RMS value) is added to the control command during point-to-point positioning tests. Fig. 9 shows the typical settling performance during the 5 μm step motion. The rigid stage takes 188 ms to settle within the ±25 nm window, with an in-position error of 6 nm. For the compliant stage, the RMS error during in-position increases significantly to 15.8 nm, making it unable to settle into the desired window. Using the proposed semi-active joint, the stage is able to settle within 127 ms with very similar in-position stability (i.e., 6.4 nm) as the rigid stage.

CONCLUSIONS AND FUTURE WORK

In this paper, a novel semi-active joint for simultaneously improving the settling performance of mechanical-bearing-guided motion stages while maintaining excellent in-position stability in point-to-point positioning has been presented. The proposed semi-active joint actively switches its stiffness between two modes: compliant or stiff; the joint is compliant during motion transients such that the undesirable effects of pre-motion friction on the settling time is mitigated through the compliant joint method; the joint becomes very stiff once the stage gets into position such that the benefits of bearing friction on in-position stability is preserved. It has been shown through simulation that the semi-active joint achieves 51% and 55% improvements in settling time and in-position stability, compared to cases with rigid joint and compliant joint, respectively. A semi-active joint prototype has been designed which integrates two solenoid actuators and permanent magnets into a flexure design to realize the switching mechanism. Preliminary experiments on an in-house built mechanical-bearing-guided motion stage equipped with the designed semi-active joint have demonstrated similar transient dynamics as the compliant stage and almost the same in-position stability as the rigid stage. However, the impact force caused by switching introduces large motion errors and excites high frequency modes of the system during settling, significantly increasing the settling time of the stage. Ongoing work is focused on mitigating the adverse effects of switching on the proposed semi-active joint using both mechanical design and control techniques in order to achieve similar settling performance as the compliant joint method.

REFERENCES

[1] Altintas Y, Verl A, Brecher C, Uriarte L, Pritschow G. Machine Tool Feed Drives. Annals of the CIRP 2011; 60(2):779–96.
[2] Maeda Y, Iwasaki M. Rolling friction model-based analyses and compensation for slow settling response in precise positioning. IEEE Trans Ind Electron 2013; 60(12):5841–53.
[3] Bucci B, Vipperman J, Cole D, Ludwick S. Evaluation of a servo settling algorithm. Precis Eng 2013; 37(1):10–22.
[4] Dong X, Okwudire CE. An experimental investigation of the effects of the compliant joint method on feedback compensation of pre-sliding/pre-rolling friction. Prec. Eng. Article in press.

[5] Dong X, Liu X, Yoon D, Okwudire CE. Simple and robust feedforward compensation of quadrant glitches using a compliant joint. Annals of the CIRP 2017; 66(1):353-6.
[6] Reuss M, Dadalau A, Verl A. Friction Variances of Linear Machine Tool Axes. Procedia CIRP 2012; 4:115–9.
[7] Yoon JY, Trumper DL. Friction Modeling, Identification, and Compensation Based on Friction Hysteresis and Dahl Resonance. Mechatronics 2014; 24(6):734–41.

OVERVIEW OF AN ACTIVELY DAMPED VIBRATION ISOLATION SYSTEM FOR ULTRA-HIGH VACUUM OPTICAL EXPERIMENTS

Álvaro Fernández Galiana[1], and Fabrice Matichard[1,2]
[1]LIGO Laboratory
Massachusetts Institute of Technology
Cambridge, Massachusetts, USA
[2]LIGO Laboratory
California Institute of Technology
Pasadena, California, USA

INTRODUCTION

We present a tabletop six-axis vibration isolation system, Ultra-High Vacuum (UHV) compatible, actively damped, providing 25 dB of isolation at 10 Hz and 65 dB at 100 Hz. While this isolation platform has been preliminary designed to support optics in the LIGO detectors [1], it features characteristics that make it suitable for a variety of applications. The system has been engineered to facilitate the construction and assembly process, while minimizing the production cost. The platform provides six degrees of freedom of passive isolation using a combination of vertical springs and horizontal pendulums. It is instrumented with voice-coil actuators and optical shadow sensors to damp the resonances. All materials are compatible with stringent vacuum requirements [2]. The architecture of the system maximizes the optical table dimensions with respect of the available space. Three units are currently operating for LIGO. The paper presents the system design, controls principles, and experimental results.

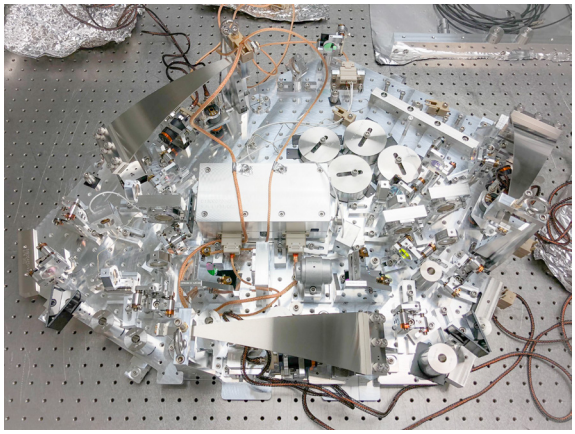

FIGURE 1. ***UHV COMPATIBILITY.*** *Picture of the isolation platform at the LIGO Livingston Observatory. All the materials have been selected to fulfill UHV requirements [2].*

MECHANICAL DESIGN

The system provides seismic isolation and active damping control in all six degrees of freedom. The suspended stage (stage 1) is mechanically isolated from the support base (stage 0) (see Figure 2).

Stage 1 is suspended with three independent blade assemblies (see Figure 3) bolted to stage 0. This approach, based on low-height posts, reduces the cost, weight, and dimensions compared to the welded support frames used in previous LIGO suspensions. It permits to maximize

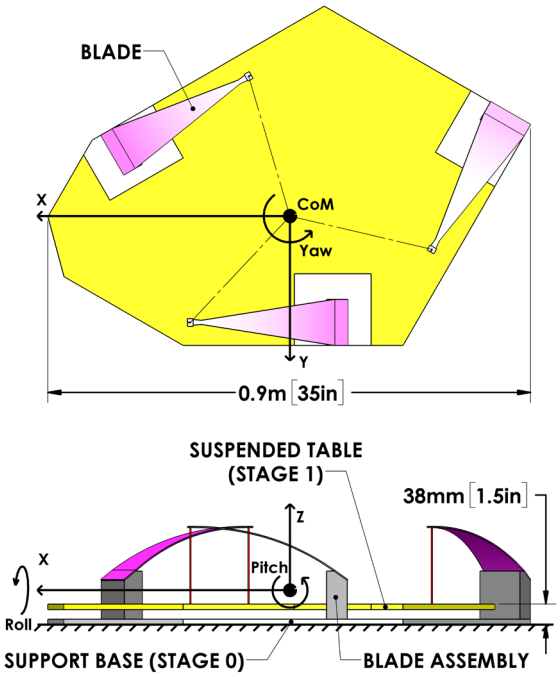

FIGURE 2. ***COMPACTNESS.*** *Schematics of the isolation platform. The optical table is suspended from three blade assemblies, 38 mm (1.5 in) above the reference plane. The footprint matches the space available in the LIGO chambers.*

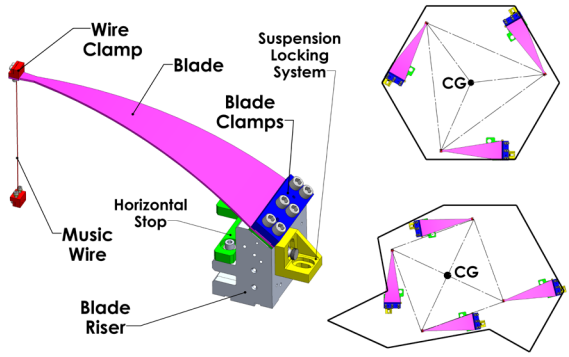

FIGURE 3. ***SHAPE ADAPTABILITY.*** *Blade assembly (left), including the riser clamped to the base, the blade clamped at a specific angle, and the pendulum wire clamped to the tip of the blade. The blade assembly includes built-in hard stops that limit the range of motion of the optical table. Using independent blade assemblies to suspend the optical table makes the design adaptable to different requirements. As an illustration, two optical table shapes that could be isolated using this concept (right).*

the optical table dimensions with respect of the space available (see Figure 1) and makes the system adaptable to different optical table shapes (see Figure 3). The number, position, and characteristic features of the blade assemblies can easily be adapted to various table shapes, payloads, and performance requirements.

There are two types of resonances that are critical to the design of this type of seismic isolator: the suspension modes and the structural modes. The first are the rigid-body modes associated with each of the six degrees of freedom The structural modes are related to the flexible modes of the sub-assemblies, such as the blade assemblies or blade guards (see Figure 4). The isolation bandwidth can be defined as the range between the highest suspension mode frequency and the lowest structural mode frequency.

TABLE 1. Platform parameters.

Parameter	Value
Overall dimensions	0.94 x 0.67 m
Overall height	0.21 m
Total mass	45 kg
Suspended stage	
Table surface	0.34 m^2
Table height	0.38 $\times 10^{-3}$ m
Mass	36 kg

For the isolation platform to meet LIGO requirements [1], the highest suspension mode frequency is ≈2.5 Hz, and the lowest structural mode frequency is ≈220 Hz. At 100 Hz, the suspension provides 65 dB of seismic isolation. The quality factors of the suspension modes are actively damped to values of about 15. The main parameters of the platform are specified in Table 1.

Ultra-high vacuum compatibility

All the materials of the isolation platform are approved for ultra-high vacuum applications and fulfill LIGO vacuum chambers specific requirements [2]. Before the final assembly, all the components are precision cleaned and vacuum baked. In addition, a residual gas analysis is performed after baking to measure the outgasing rate and detect possible residual contaminant.

Suspended stage

The suspended stage consists of an optical table (≈0.34 m^2, ≈18 kg), the optical components (≈11 kg), and balancing masses (≈7 kg) used to level the platform. The table shape is adapted to the available space in the LIGO vacuum chamber [3], resulting in the heptagonal shape shown in Figure 1.

The first structural mode is a bending resonance of the suspended table (Figure 5). To raise this

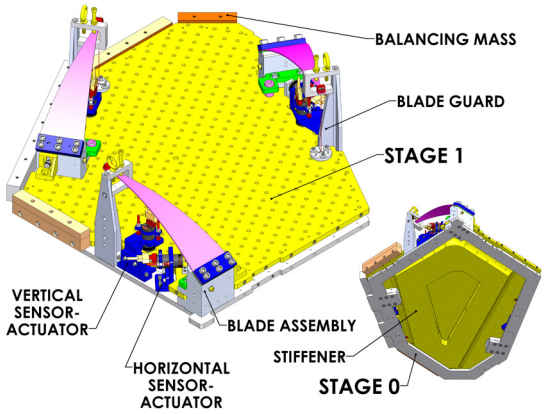

FIGURE 4. ***EFFECTIVE FOOTPRINT.*** *Most of the footprint corresponds to the optical table. The isolation platform is instrumented with six sensor-actuators positioned in vertical-horizontal pairs. The blade guards provide safety during assembly. The optical table features a stiffener underneath to increase the stiffness to mass ratio.*

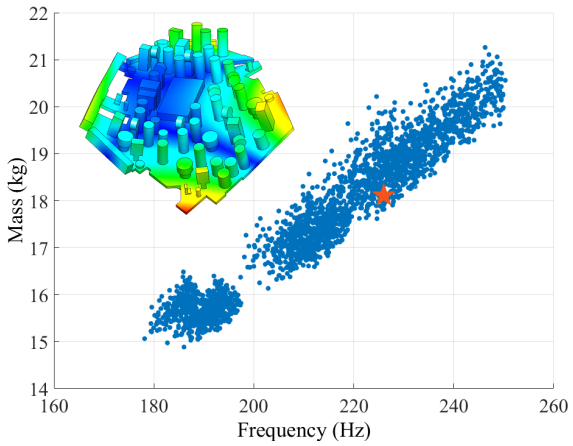

FIGURE 5. ***TABLE STIFFNESS.*** *Results of the table stiffener optimization. Using iterative finite element analysis on the optical table for different stiffener shapes and sizes. The selected dimension (star) was chosen to meet requirements on total mass and center of mass position.*

frequency, a stiffener is incorporated into the optical table (see Figure 4). The shape of the stiffener has been designed to optimize the stiffness to mass ratio. This optimization is done iteratively using Finite Element Analysis (FEA) of the loaded optical table. Figure 5 shows the results of this optimization. The table weights ≈18 kg and has its first resonance at ≈225 Hz.

Horizontal isolation

Horizontal isolation (X-Y-Yaw axis in Figure 2) is achieved by suspending stage 1 from three wires. The pendulum is a simple and effective way to provide passive horizontal isolation. The wires are attached using metallic clamps designed to reduce friction loss. The horizontal modes frequencies can be approximated using Equation 3.

$$z_z = \sqrt{\frac{EI}{mg}}\ \tanh\frac{mgl}{2EI} \tag{1}$$

$$k_{xx}(=k_{zz}) = \frac{mg}{l-2z_z} \tag{2}$$

$$f_{xx}(=f_{yy}) = \frac{1}{2\pi}\sqrt{\frac{k_{xx}}{m}} \tag{3}$$

where E is the wire Young's modulus, I, d and l are, respectively, the area moment of inertia, diameter and length of the wires, m is the mass supported by each wire, and z_z is the vertical distance from the wire tip to the Zero Moment Point (ZMP).

The suspension wires are made of stainless steel, and they are 146 mm long and 0.61 mm in diameter. The small wire diameter places the violin modes at high frequencies (∼750 Hz). The horizontal suspension frequency (1.27 Hz) and the factor of safety (>3) can be approximated using the following equations:

$$\tau_{max} = \frac{mg\delta}{A(l-2z_z)};\ \sigma_{max} = \frac{mg}{A} + \frac{mgz_z d\delta}{2I(l-2z_z)} \tag{4}$$

$$\sigma_{VM} = \sqrt{\sigma_{max}^2 + \tau_{max}^2} \qquad FoS = \frac{\sigma_{VM}}{\sigma_{yield}} \tag{5}$$

where δ is the maximum lateral displacement of the wire ends (1 mm for this platform), A is the cross section area of the wire, τ_{max} and σ_{max} are, respectively, the maximum shear and normal stress at the wire for the displacement δ, σ_{VM} is the equivalent Von Mises stress, and σ_{yield} is the yield strength of the wire. These formulas account for the normal axial stress, shear stress, and bending stress, the latter being predominant in this design.

The rotational stiffness of the isolation system can be estimated using the translation stiffness and the geometrical location of the blade tips as shown in Equations 6 and 7 for an equilateral triangular distribution.

$$k_{roll}(=k_{pitch}) = \frac{3}{2}k_{zz}R^2 + 3k_{yy}h_z^2 - 3mgh_z \tag{6}$$

$$k_{yaw} = \frac{3}{2}(k_{xx}+k_{yy})R^2 + 3\frac{GI}{l} \tag{7}$$

where h_z is the vertical offset between the center of gravity and the ZMP, R is the horizontal distance between the center of gravity and the tip of the blades, and G and I correspond, respectively, to the shear modulus and the moment of inertia of the music wire.

Vertical isolation

The vertical isolation is provided by three triangular stainless steel cantilever blade springs. This shape guarantees an homogeneous stress distribution (assuming small deformation), approximated by equation 11.

$$k_{zz} = \sqrt{\frac{Eah^3}{6l^3}} \tag{8}$$

TABLE 2. Basic isolation platform mechanical parameters.

Parameter	Value
Design paramenters	
Blade base width a	85 $\times 10^{-3}$ m
Blade thickness h	2.11 $\times 10^{-3}$ m
Blade length l	280 $\times 10^{-3}$ m
Young's modullus E	2.1 $\times 10^{11}$ Pa
Vertical resonance f_z	1.64 Hz
Spring constant k_{zz}	1273.1 $\frac{N}{m}$
Tip deflection	92.5 $\times 10^{-3}$ m
Tip rotation	0.66 rad
FoS	3.44

$$f_z = \frac{1}{2\pi}\sqrt{\frac{k_{zz}}{m}} \tag{9}$$

$$\omega_{tip} = \frac{6mgl^3}{Eah^3} \qquad \omega'_{tip} = \frac{12mgl^2}{Eah^3} \tag{10}$$

$$\sigma^{blade}_{xx_{max}} = \frac{6mgl}{ah^2} \qquad FoS = \frac{\sigma_{XX_{max}}}{\sigma_{yield}} \tag{11}$$

where E is the blade Young's modulus, a is the width of the blade at the base, h is the blade thickness, m is the mass supported by each blade, and l is the length of the blade. Since there are three design parameters (a, l, and h) and only two constraints (f_z and $\sigma^{blade}_{xx_{max}}$ from equations 9 and 11), the design has one degree of freedom. For our suspension we defined the length l such that it was well suited to the overall dimensions of the platform. Steel (grade 440C stainless steel) has been used for the blades. Values are given in Table 2.

The preliminary design is performed using equations 9 to 11, which assumes classical infinitesimal strain beam theory. The blade stiffness and peak stress estimates are verified with finite element analysis. The relative error between the two calculations is around 1 % in deflection and 7 % in stress.

Due to its annular shape, stage 0 has low torsional stiffness and relies on being well clamped to the support structure. FEA was used to evaluate the number of clamping elements necessary to establish good contact, and results were verified by experiment.

ACTIVE DAMPING CONTROL

We use low noise ultra-high vacuum compatible sensor-actuators called AOSEM, to damp the high-Q ($\sim$250) suspension modes without compromising the passive isolation. These devices use a coil-magnet pair to generate an actuation strength of 31 mN/A and a shadow sensor to measure the relative motion between stage 0 and stage 1.

Noise budget

The goal is to minimize the output motion of the optical table (X_1). The main input noise is the seismic motion (X_0). The other noise sources, introduced by the active control, are the AOSEM sensor noise (N_s)[4], the analog-to-digital (ADC), and digital-to-analog (DAC) converters noises (N_{dac}, N_{adc})[5, 6]. Each source of noise N_i contributes to the motion of the suspended stage (X_{N_i}). The motion of the optical table (X_1) is the sum of the seismic noise and the control noise contributions. Assuming that they are all incoherent, the motion of the optical table can be estimated as:

$$|X_1|^2 \sim |X_{N_{ELEC}}|^2 + |X_{X_0}|^2 \tag{12}$$

where,

$$|X_{N_{ELEC}}|^2 \sim |X_{N_{DAC}}|^2 + |X_{N_{ADC}}|^2 + |X_{N_S}|^2 \tag{13}$$

PERFORMANCE

A proptotype of the platform was tested at the MIT LIGO facilities and two units have been installed at the LIGO observatories in Livingston, LA (LLO) and Hanford, WA (LHO). The results presented in this section are from the testing of these three units.

Transfer functions

The transfer functions were obtained by driving the coils and reading out the shadow sensors of the AOSEMs. Figure 6 shows an example of transfer function of the suspension. The rigid body mode frequencies are summarized in Table 3.

TABLE 3. Rigid body modes.

Degree-of-freedom	Measured (Model)
Longitudinal-X	1.27 (1.26) Hz
Transverse-Y	1.27 (1.28) Hz
Vertical-Z	1.74 (1.64) Hz
Roll	2.39 (2.23) Hz
Pitch	1.63 (1.56) Hz
Yaw	1.44 (1.44) Hz

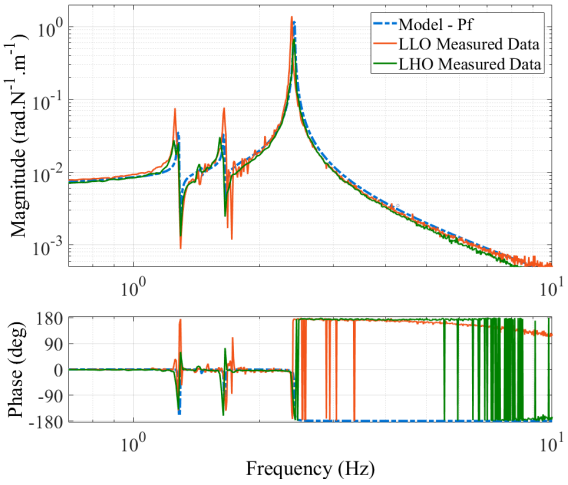

FIGURE 6. ***TRANSFER FUNCTIONS*** *Example of transfer functions measured at LLO and LHO, DC calibrated to match the dynamical model. The data shows f^2 isolation above the resonance.*

Structural modes

The light and low-profile supporting structure reduces the impact of the system onto neighboring elements. The experimental modal analysis of the optical table was performed and gave results consistent with the FEA predictions, as shown in Figure 7. Passive dampers made of Viton have been added to damp the structural modes.

Active Damping

The active damping is performed with feedback control band-pass filters of the form:

$$C(s) = K \frac{s}{\left(\frac{s}{2\pi f_1} + 1\right)\left(\frac{s}{2\pi f_2} + 1\right)} \qquad (14)$$

with one zero and two poles at frequencies f_1 and

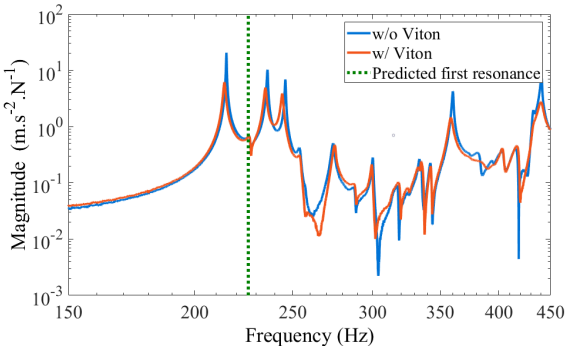

FIGURE 7. ***EXPERIMENTAL MODAL ANALYSIS.*** *The Viton reduces the mode Qs by a factor of 2-3.*

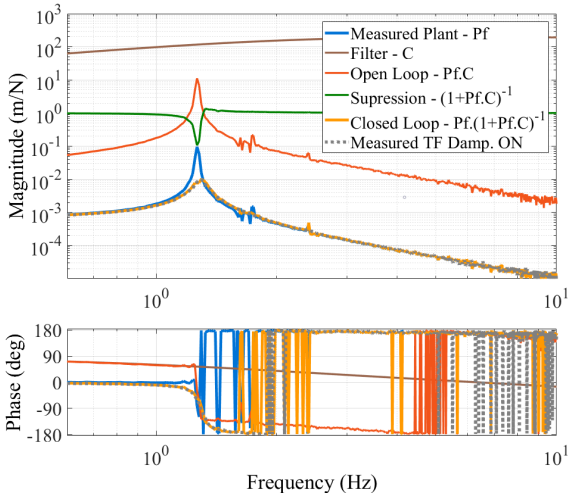

FIGURE 8. ***LOOP SHAPES.*** *Damping control for the longitudinal (X) degree of freedom. Using a band-pass filter (brown), the Q is reduced from ≈260 (blue) to ≈15 (orange) without degradation of the isolation. The phase margin of the controller is ≈53 deg (red). The damped transfer function was measured (grey) and matches the model.*

f_2. This simple controller is sufficient to reduces the Q factors to ≈15 with minimum degradation the passive isolation (see Figure 8).

An example of noise budget is shown in Figure 9. In this example, the input motion is particularly

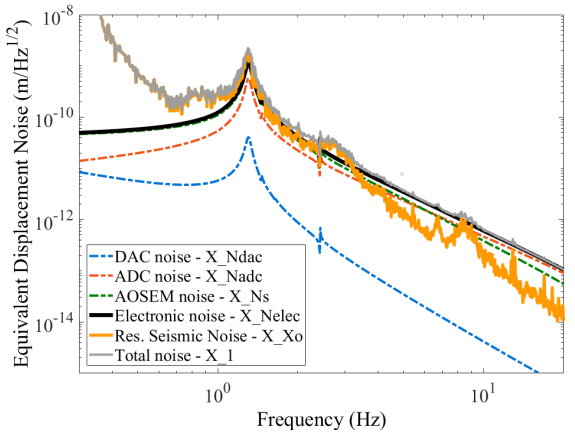

FIGURE 9. ***CONTROL NOISE.*** *Noise budget for the transverse (Y) degree of freedom. The total electronic noise produced by the damping control electronics (dashed black) is compared to the estimated residual seismic noise (orange). In this example, the electronic noise is the predominant source of noise above 3 Hz.*

low, since stage 0 is mounted on a pre-isolator. Consequently, the electronics noise dominates the output motion at frequencies above 3 Hz. Depending on input motion amplitude and applications, the controller can be tuned for a different compromise over the frequency range.

CONCLUSION

A compact isolation platform designed to support LIGO auxiliary optics was presented. The presentation of the design emphasized the compactness, simplicity, and UHV carateristics of the system. The paper descibed the active damping implemented to preserve the passive isolation. Experimental measurements show good agreement between predicted and measured performance. Thanks to its adaptable design and low production cost, this isolation system was easily procured and deployed at the LIGO sites, and can be easily adapted to other applications.

ACKNOWLEDGMENTS

We wish to thank Lee McCuller, Lisa Barsotti, Matthew Evans, Maggie Tse, Peter Fritschel, and Nergis Mavalvala from LIGO-MIT, as well as Norna Robertson and Calum Torrie from LIGO-Caltech for their help in designing this isolation platform. Also thank Stuart M. Aston, Jeff Kissel, Arnaud Pele, TJ Shaffer, Janeen H. Romie, and Betsy Weaver from the LIGO observatories for their contribution during the testing and installation.

LIGO was constructed by the California Institute of Technology and Massachusetts Institute of Technology with funding from the National Science Foundation, and operates under cooperative agreement PHY0757058. Advanced LIGO was built under award PHY0823459. This paper was assigned LIGO Document Number LIGO-P1800182.

REFERENCES

[1] Aasi J, Abbott B, Abbott R, Abbott T, Abernathy M, Ackley K, et al. Advanced LIGO. Classical and quantum gravity. 2015;32(7):074001.

[2] Coyne D, et al. LIGO vacuum compatible materials list. LIGO Laboratory; 2013. LIGO-E960050-v12.

[3] Matichard F, Lantz B, Mason K, Mittleman R, Abbott B, Abbott S, et al. Advanced LIGO two-stage twelve-axis vibration isolation and positioning platform. Part 1: Design and production overview. Precision Engineering. 2015;40:273–286.

[4] Aston S. Advanced LIGO BOSEM Noise Measurement Report. LIGO Laboratory; 2011. LIGO-T0900496-v4.

[5] Heefner J. Preliminary Noise Measurements of the General Standards PCI66-16AI64SSA-64-50M ADCs. LIGO Laboratory; 2006. LIGO-T060158-x0.

[6] Mittleman R. 16 Bit Low Frequency DAC noise measurement. LIGO Laboratory; 2015. LIGO-T1500007-v1.

DESIGN AND MODELING APPROACH FOR A LIFTING AND ACTUATING UNIT FOR THE APPLICATION IN NANO-PRECISION MACHINES

Stephan Gorges[1] **and Steffen Hesse**[1]
[1]**Department of Mechatronics**
IMMS Institut für Mikroelektronik- und Mechatronik-Systeme gemeinnützige GmbH
Ilmenau, Thuringia, Germany

INTRODUCTION

Micro and nano systems play an important role in todays society. But the production facilities for the next generation of such systems become increasingly complex and expensive. New fabrication methods need to be developed to further improve and miniaturize these systems and to make the production accessible to new markets. One key device in the fabrication process is the nano positioning machine (NPM), which moves either the tool or the sample. Furthermore large travel ranges are needed i.e. to structure large wafers or optical parts. Thereby, the vertical motion is a big challenge since it needs to permanently counteract against the gravitational force. The vertical drive system needs to be designed in a way that it induces a minimum amount of heat into the system to avoid any thermal expansion.

The paper at hand presents the design and modeling approach for a lifting and actuating unit (LAU) for the application in the nano positioning machine NPPS100.

There are different ways to address the problem of large vertical travel ranges with nanometer precision.
One popular method is to combine a coarse and a fine stage. Usually two different physical drive methods are used, i.e. a servo spindle drive combined with a piezoelectric stage. In [1] two different vertical drive systems have been extensively investigated under the aspect of NPM application. Single axis stages are already commercially available [2].
The second method utilizes two drive system in parallel: One as a weight force compensation (WFC) and the other one generating dynamic forces for the precision motion. This approach has been realized i.e. in [3] using adjustable springs as WFC combined with voice coil drives and in [4] using pneumatic pressure chambers and direct electromagnetic drives.

The NPPS100 (see Fig. 1) is a planar NPM, which means that x,y and ϕ_z are currently controlled. The slider is mounted on planar air bearing pads. These pads slide on a very smooth natural stone surface. Furthermore, flat drive coils are fixed to this base. When the coils are energized they interact with the permanent magnets, which are mounted on the underside of the slider thereby creating forces and moving it. Interferometers on the base measure the distance to plane mirrors on top of the slider, enabling the measurement of x,y and ϕ_z.

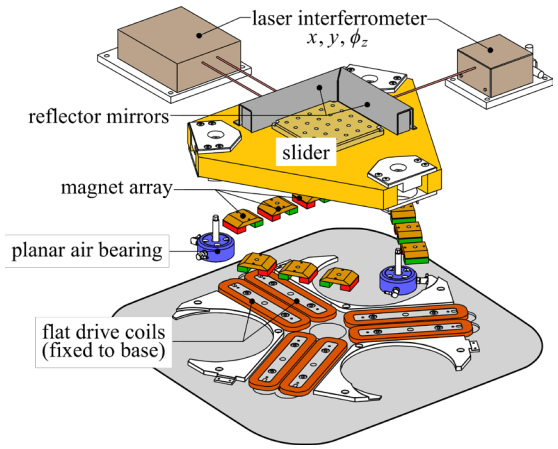

FIGURE 1. Explosional view of the NPPS100 planar drive system

The natural stone surface is not perfectly flat. The surface flatness of about 1 µm is the economic limit. Therefore, a vertical position error is introduced into the bearing pads and the slider. Furthermore, the error is different for all three pads. This results in a slider error in z and also in the occurrence of the two tilting angle errors in ϕ_x and ϕ_y. Additionally, the errors change as a function of the sliders xy-position.

To address these errors and also to give the NPPS100 the ability to travel a macroscopic vertical distance, a new drive system will be integrated.

One approach is, to add three identical Lifting and Actuating Units (LAUs), where each should be integrated between the slider and a bearing pad.

FUNCTIONAL PARTS OF A LIFTING AND ACTUATING UNIT

By lifting the slider, the gap between permanent magnets and the xy-drive coils increases, therefore decreasing the effectiveness of the planar drive. Hence, the design goal was set to a vertical travel of 10 mm, where the planar drive can still control the x- and y-position of the slider.

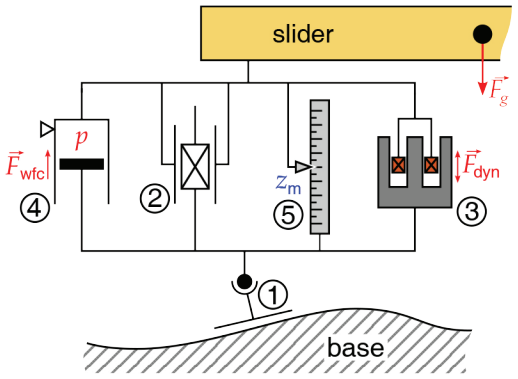

FIGURE 2. Technical principle of one LAU mounted on the slider.

Fig. 2 shows the functional parts which are needed in one LAU.
The base component will be the planar air bearing pad (① in Fig. 2), which will sit at the bottom.

Further a vertical guiding ② is needed, to allow vertical motion. This guiding will be an aerostatic guiding, since it is frictionless and does not wear. Pressurized air is also already available on the slider.
As a precision drive a voice coil motor will be designed ③. These kind of drives have proven to be precise and can be designed very well for the positioning task.
The key component will be the WFC ④. It will be layed out as a pneumatic cylinder. The benefits are the simple mechanics and it can be adjusted to a wide payload range. Further, it can be integrated into the control loop to not only counter the weight force but also create driving forces. Thereby, taking workload from the precision drive. The model equations of this pneumatic WFC will be presented in the next section.
The design of the needed internal vertical measurement system ⑤ and the control system (not displayed) have not been specified yet.

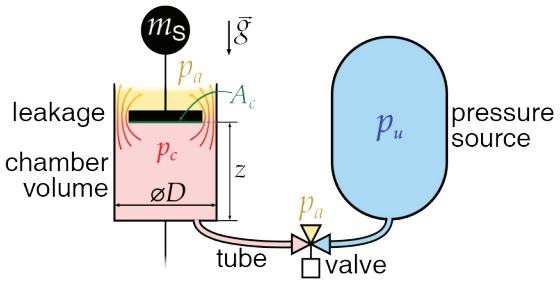

FIGURE 3. The model components of the pneumatic WFC with the main parameters

MODELING OF THE PNEUMATIC WEIGHT FORCE COMPENSATION

The WFC components are shown in Fig. 3. The central element is the pressure chamber, for which the ideal gas law applies

$$p_c = \varrho_c R_S T_c \tag{1}$$

with the specific gas constant R_S, the gas temperature T_c and gas density:

$$\varrho_c = \frac{m_c}{V_c} \tag{2}$$

The chamber volume V_c is composed of the variable chamber volume $V_{cv} = zA_c$ (z : current height of the chamber, A_c : piston surface) and a permanent volume V_{c0}. This permanent volume is an open design parameter and can be incorporated into the cylinder or piston. Further, a isothermal change in state is assumed, since pressure changes in the planed operation are small.

The following forces act on the piston:
F_i : force of inertia
F_g : gravitational force
F_{p_c} : force of inside chamber pressure
F_{p_a} : force of the outside atmospheric pressure

From these forces the force equilibrium is set up:

$$\begin{aligned} F_i + F_g &= F_{p_c} - F_{p_a} \\ m_S\ddot{z} + m_S g &= p_c A_c - p_a A_c \end{aligned}$$

with m_S being the supported mass of the load, g the gravitational acceleration, $\ddot{z}$ as the piston acceleration and p_a as the atmospheric pressure. Assuming the chamber is subjected to supply pressure p_u (maximum possible pressure) and $\ddot{z} = 0$, the minimal feasible cylinder diameter for a working WFC can be calculated via:

$$D_{\min} = \sqrt{\frac{4}{\pi}\frac{m_S g}{p_u - p_a}} \tag{3}$$

The inlet of the chamber is controlled via a pneumatic valve. The governing pneumatic effect is the flow through an orifice. The mass-flow $\dot{m}_{\mathsf{V}}$ is given by the model [5, 6]:

$$\dot{m}_{\mathsf{V}} = C u_v \varrho_0 p_u \sqrt{\frac{T_0}{T_u}} f_p(p_c) \text{ with} \tag{4}$$

$$f_p(p_c) = \begin{cases} \sqrt{1 - \left(\frac{\frac{p_c}{p_u} - b}{1-b}\right)^2} & \text{for } \frac{p_c}{p_u} > b \\ 1 & \text{for } \frac{p_c}{p_u} \leq b \end{cases} \tag{5}$$

with the following parameters:

- C : sonic conductance of the valve
- u_v : value for the valve opening (between 1 and 0)
- ϱ_0 : reference density
- p_u : upstream/supply pressure
- T_0 : reference temperature
- T_u : upstream/supply air temperature
- p_c : downstream/chamber pressure
- b : critical pressure ratio of the valve

C and b depend on the orifice geometry and are given in the data-sheets of some valves. The u_v controls the valve opening. A $u_v = 1$ means that the valve is completely open, for $u_v = 0$ the mass-flow is zero meaning the valve is closed. In [7] the model has been modified for better numerical convergence. This model was later implemented.

Since the pneumatic cylinder should move frictionless, a conventional rubber sealing can not be used. Therefore, a gap between the moving parts has to be accepted, resulting in a leakage air flow $\dot{m}_{\mathsf{L}}$. This gap will act as a throttle bushing, for which the mass-flow model is given in [8] (in this case: non-excentric with constant gap-height):

$$\dot{m}_{\mathsf{L}} = \frac{\varrho_a}{24\eta} \frac{A_{\mathsf{L}} {h_{\mathsf{L}}}^2}{l_{\mathsf{L}}} \left(\frac{{p_c}^2}{p_a} - p_a \right) \tag{6}$$

The gap geometry is defined via the cross-section in flow-direction A_{L}, the length l_{L} and the height h_{L}. The dynamic viscosity of air is represented with η.

Many different models can be applied for the transient behavior of a pneumatic line [9, 6]. A simplified representation is just a delay in the mass-flow:

$$\dot{m}_{\mathsf{T}}(t) = \dot{m}_{\mathsf{V}} \left(t - \frac{l_{\mathsf{T}}}{c} \right) \tag{7}$$

where l_{T} is the length of the tube and c the sonic velocity in air.

Now all inlet and outlet mass-flows have been described. So the first time derivative of the continuity equation can be set up:

$$\dot{m}_c = \dot{m}_{\mathsf{T}} - \dot{m}_{\mathsf{L}} \tag{8}$$

The previously described formulas and parameters have been implemented in a Modelica model. The model has two variants: The first covers the case for the loading of the chamber with Eqs. (4) and (5). The second variant simulates the unloading of the chamber, where p_c becomes the upstream pressure and p_a the downstream pressure.
These model variants can be controlled via a Python script to run different parameter studies.
Furthermore, the model was implemented in a symbolic Python script to simulate the linearized steady state behavior at the quasi-static operation point ($\dot{z} = \ddot{z} = 0, \dot{m}_c \approx 0$) with C being the input and z as the output.

RESULTS

One goal in the design of the pneumatic WFC is a very fine force resolution. This is needed to minimize deviations between the actual weight force (of the slider and the sample) and the compensation force.

The WFC is only the steady component in the positioning process. Utilizing the pneumatic drive in the positioning process to compensate higher frequencies can reduce the load on the dynamic drive and thereby reducing the heat emissions. Therefore, a dynamic pneumatic drive is beneficial. To characterize the dynamics of the drive the maximum acceleration is not significantly important in this nano-positioning use-case. The drive will not reach the maximum possible acceleration in the relatively short projected travel of 10 mm. A better suited indicator in nano positioning is the jerk ($\dddot{z} = j_z$). It indicates how fast a needed force can be created.

Additionally, the first eigen-frequency of the drive is important to see the bandwidth of the WFC. Frequency components above need to be generated by the dynamic drive in the LAU, resulting in the discussed heat emissions.

The available absolute supply pressure p_u is about 5 bar and the worst-case load-mass $m_{\mathsf{S}} = 4.67$ kg, resulting in a minimal feasible piston diameter from Eq. (3) of $D_{\mathsf{min}} \approx 12.1$ mm for the steady state. The design space allows a maximal diameter of 50 mm.

Two effects act against each other when comparing small and large chambers: One effect is, that a larger chamber diameter results in a larger volume, which takes more time to be pressurized (scaling volume).
But to change the force by a certain amount, the larger chamber needs a smaller pressure change (scaling pressure) because of the larger piston area.

Fig. 4 shows the initial jerk j_{zI}, which is available after the tube induced delay. The jerk is displayed for different chamber diameters D. Further it is distinguished between the loading and unloading process for two chamber heights.

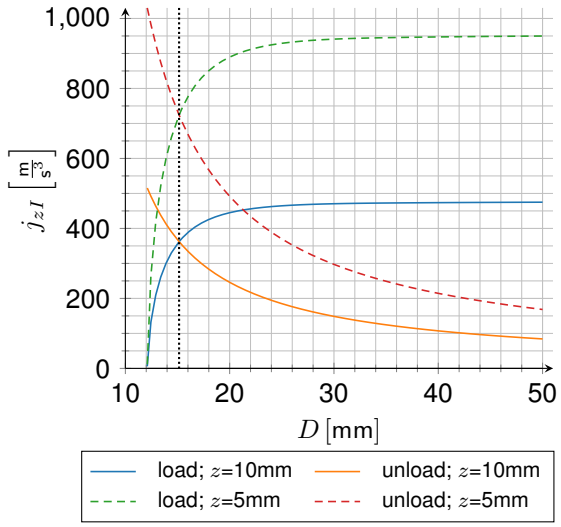

FIGURE 4. Absolute initial jerk at the start of the motion. The pressure chamber starts in the steady state. At $t = 0$ the valve is opened completely.

It can be seen, that for the loading process (solid blue and dashed green line), larger cylinder diameters result in a larger jerk. So the scaling pressure dominates over the scaling of the volume. Chambers with a diameter above $\approx 25\,\mathrm{mm}$ do not benefit much from the increase of the piston area.
For small diameters the jerk goes to zero. This is plausible, since a chamber with D_{min} is not capable of creating any positive motion for the given supply pressure.

For the unloading (solid orange and dashed red line), the smaller diameters result in the highest jerk, which means, that the scaling-volume effect dominates over the scaling-pressure effect.

Comparing the results for different chamber heights z it can be seen, that smaller chambers have much higher jerks. Through further simulations it was found, that the relation of j_{zI} to z is approximately inversely proportional. From this it can also be concluded, that V_{c0} should be kept as small as possible.

The best compromise results in the crossing of the loading and unloading graphs. Interestingly the cross-point is the same for all z (dotted black line), namely $D \approx 15\,\mathrm{mm}$ (further simulations are not displayed). At this diameter the pneumatic drive can create 76 % of the maximum possible positive and 70 % of the maximum possible negative jerk.

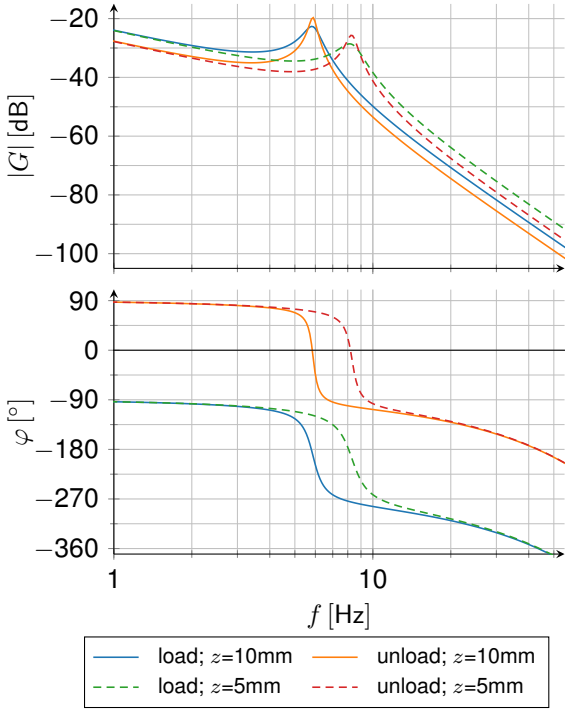

FIGURE 5. State space transfer function G of the pneumatic drive plotted over the frequency f. The input is u_v and the output z.

Fig. 5 shows the bode plots of the state space transfer function $G(j\omega)$ of the model with $D = 15\,\mathrm{mm}$. Both the loading and unloading process models are displayed.
It can be seen, that positive and negative motion have different gains, most likely due to the very different pressure gradient for both processes. Further, the unloading (solid orange and dashed red line) is less damped then the loading (solid blue and dashed green line). This is due to the leakage mass-flow always exiting the pressure chamber. During loading this is a negative effect because it reduces the overall mass-flow into the chamber. For the unloading it is beneficial, since it further in-

creases the outflow. For smaller chamber heights the natural frequency increases, resulting in better possible dynamics, as it was also conducted from Fig. 4. The drop in the phase φ at the end of the frequency range is due to the dead time element of the pneumatic tube.

CONCLUSION AND OUTLOOK

In this paper the problem of the vertical motion in NPMs was investigated. Further the functional design approach was presented with emphasizing the components of the weight force compensation system. The model equations for a pneumatic WFC were presented and were composed to a transient and a steady space model.
With these models the dynamic behavior of the system was simulated to make statements about its behavior. Further the impact of different design and process parameters was discussed.
For the given parameters, mainly load and supply pressure, a best cylinder diameter of about 15 mm was found.

In further studies the other components of the lifting and actuating unit, such as the dynamic drive, will be modeled, designed and dimensioned. It is planned to integrate all component models into a overall model to simulate the system behavior. Further, all components need to be integrated together into the available design space of the unit.

ACKNOWLEDGMENTS

The authors gratefully acknowledge the support by the Deutsche Forschungsgemeinschaft (DFG) in the framework of Research Training Group “Tip- and laser-based 3D-Nanofabrication in extended macroscopic working areas” (GRK 2182) at the Technische Universität Ilmenau, Germany.

REFERENCES

[1] Hackel T. Grundlegende Untersuchungen zu vertikalen Positioniersystemen für Nanopräzisionsmaschinen. PhD thesis, Ilmenau, Germany; 2010.

[2] Physik Instrumente (PI) GmbH & Co. KG. M-511.HD Linear Slide. data sheet, Karlsruhe, Germany: http://www.pi-usa.us/products/PDF_Data/M511_HD_Precision_Positioning_Stage.pdf; 2007.

[3] Jäger G et al. Nanopositioning and nanomeasuring machine NPMM-200—a new powerful tool for large-range micro- and nanotechnology. Surface Topography: Metrology and Properties. 2016; 4: 034004.

[4] Spaan H et al. ISARA 400: Development of an Ultra-Precision CMM for 3D Measurement of Large Parts. Proceedings to the ASPE Spring Meeting, 2009.

[5] International Organization for Standardization. ISO 6358: Pneumatic fluid power—Determination of flow-rate characteristics of components using compressible fluids. 2013.

[6] Richter E et al. A High Performance Pneumatic Force Actuator System Part 1 - Nonlinear Mathematical Model. Dallas, USA: ASME Journal of Dynamic Systems Measurement and Control, 2000; 122, 3: 416-425.

[7] Beater P. Pneumatic Drives - System Design, Modelling and Control. Springer-Verlag Berlin Heidelberg, Berlin: 2007.

[8] Müller K, Nau B. Fluid Sealing Technology, Principles and Applications. M.Dekker Inc. New York, USA: 1998.

[9] Kern R. Physical modelling of a long pneumatic transmission line: models of successively decreasing complexity and their experimental validation. Taylor & Francis Group. 2017.

SUB-SYSTEM LEVEL OVERVIEW OF A MICRO-SCALE SELECTIVE LASER SINTERING TOOL

Nilabh K. Roy[1], Dipankar Behera[1], and Michael A. Cullinan[1]
[1]Department of Mechanical Engineering
The University of Texas Austin
Austin, TX, United States of America

INTRODUCTION

Most of the conventional metal additive manufacturing (AM) processes today are becoming increasingly applicable the aerospace, biomedical and electronics industry because of their ability to handle complex macroscale architectures. However, the commecially available AM tools have resolutions to the order of 100s of microns which is higher to the required feature sizes in several microscale applications. Consequently, there is a gradual shift towards developing metal AM techniques with micron and sub-micron level accuracies to replace multi-step and expensive subtractive manufacturing processes[1].

In a powder fusion processes like SLS, a focused laser beam is applied on selective regions in the layers of particles to produce a sintered 3D part. There are, however, some significant challenges while producing 3D microcomponents like electronic interconnects, precision microtools, and microfluidic arrays etc. Limited laser focus, uneven agglomeration of finer particles and higher susceptibility to oxidation, largely undermine the fidelity of the microscale sintering process.

The proposed tool design seeks to address the these challenges at a subsystem level. Figure 1 shows a schematic of the Microscale Selective Laser Sintering (μ-SLS) system. The current design consists of the following subsytems: micron-level accuracy global translation system,

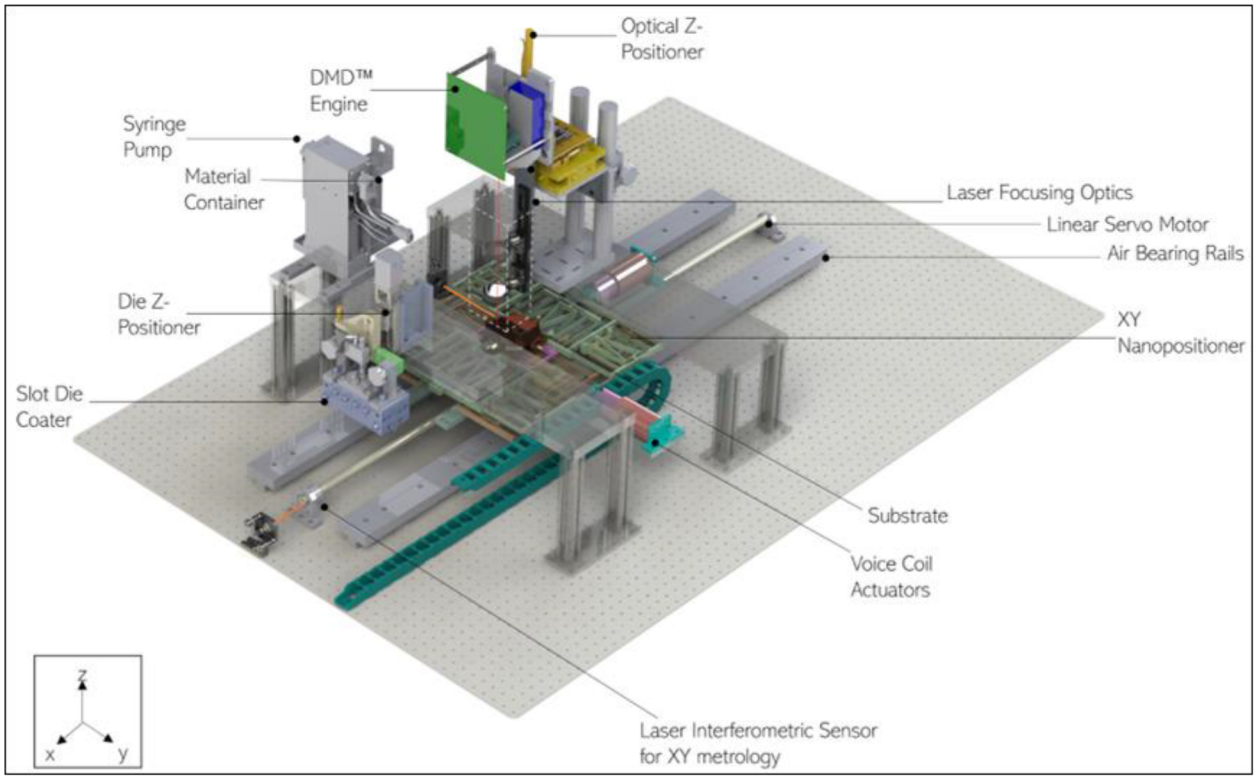

FIGURE 1: Rendered model of the μ-SLS system showing different subassemblies

XY-nanopositioning flexure stage, powder-bed dispense system, and the optical sub-system. The sintering process starts with the positioning of the substrate under the dispense system, followed by the translation of the dispensed bed under the optical system for sintering. The process is then repeated to fabricate layer-by-layer 3D parts. A critical auxiliary step includes the alignment of the sample under the dispense and optical subsytems to achieve submicron accuracy and repeatability in the positioning which is achieved by the long-range XY-nanopositioning stage.

NANOPARTICLE SPREADING SUBSYSTEM

The μ-SLS system uses metallic nanoparticle (NP) inks to achieve the target feature size resolution. Previous studies have shown that using NP inks reduces the agglomeration in during the powder spreading process [2]. In order to achieve high packing efficiencies in the sintered features and a uniform layer-by-layer deposition, a slot-die coating process is used. It consists of a precision machined aluminum die and a syringe pump for controlled and premetered dispense of copper nanoparticle inks. The syringe pump uses a UHMW-based zero dead volume syringe actuated by a BLDC servo motor to provide a non-pulsating fluid flow into the die. The coating gap between the die and the sample is controlled by using a stepper motor actuated lead screw linear guide. Figure 2 shows the different components in the slot die coating setup.

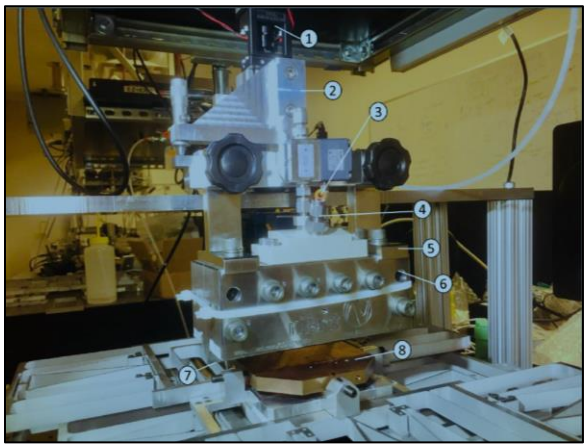

FIGURE 2. Components in the assembly of the slot die coating system- 1. z-direction motor coupled with 100mm travel leadscrew 2. Pivoting bracket 3. Input for air pilot valve 4. Slot die input 5. Die support Arms 6. Die head 7. Die lips 8. Substrate

During the coating process, a liquid bead is formed between the slot die lips and the substrate, bounded by the upstream and downstream menisci. When the substrate starts moving, the downstream menisci enables the coating of the liquid on the substrate. The stability of the coating process is largely determined by the forces acting on the coating bead. Coating defects such as ribbing, rivulets, and air engulfment affect the uniformity of the film. The minimum wet film thickness is a function of coating gap, coating speed and the upstream and downstream pressures.

The sample is translated under the coating station, and the coating gap is set using a laser triangulation sensor. After priming the slot die coater for steady state flow of liquid inside the die, the coating process is done for the first layer. The subsequent layers are coated after the previous layers have been sintered. The coating operability window significantly affects the throughput of the μ-SLS system. The dried film thickness is measured using an optical profilometer. Figure 3 shows the coating uniformity along the length (denoted by equispaced lines L1, L2, L3) and width of a sample, which was coated at 2.5mL/min with a coating gap of 100μm. The average dried film thickness is 520nm±50nm.

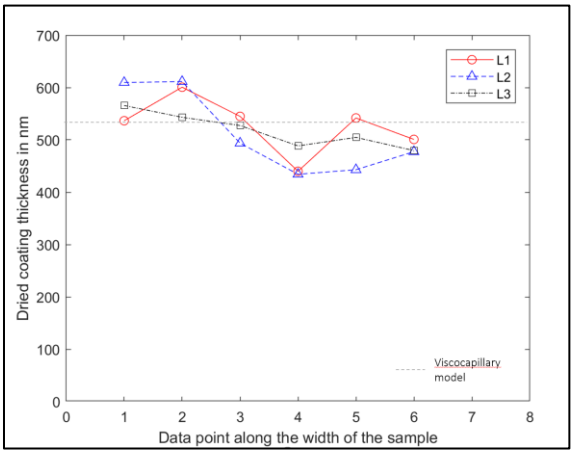

FIGURE 3. Dried coating thickness of Ag NP ink along the length and width of the sample

XY NANOPOSITIONING STAGE

A novel double parallelogram flexure (DPF) mechanism with nested linkages having a 50 mm travel range and sub-100 nm accuracy is designed to facilitate the movement and alignment of the sample under the optical system. The stage is a two level decoupled XY

motion stage and is modular in nature. It employs DPF units with underconstraint eliminators to reduce the additional degrees of freedom of the intermediate stages, commonly associated with DPF units. This design change improves the positioning bandwidth of the stage and the stage has been shown to achieve operating frequencies of upto 20 Hz with sub-micron accuracy which is similar to the sintering times for good sintering of Cu nanoparticles [3]. This reduces any downtime between the sintering and stepping actions and thus, aiding in realizing a high throughput sintering system with micron sized feature resolution. The tracking performance of the XY nanopositioner with the controller has been shown in figures 4 and 5. The detailed design of the XY stage can be found in [3].

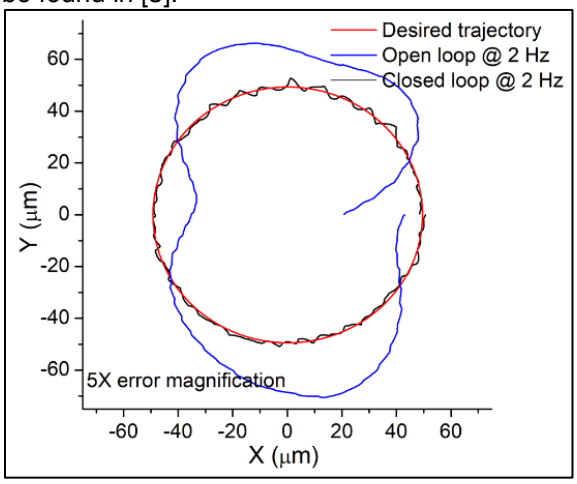

FIGURE 4. XY stage tracking of a 2D 100μm circle at 2Hz in open loop and closed loop (with 5X error magnification

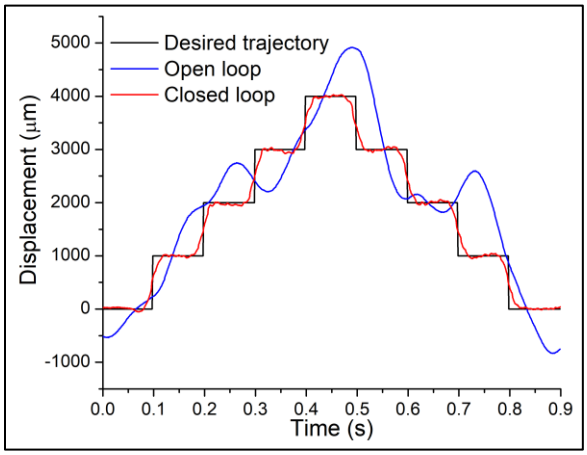

FIGURE 5. Tracking 1 μm steps in open loop and closed loop at 10 Hz

GLOBAL TRANSLATION SUBSYSTEM

In order to limit the errors to ±0.5 μm and to achieve a 1μm feature size during the repeated sintering and layer deposition steps, near frictionless motion is desired. Air bearing linear guides actuated by a direct-drive linear servo motor are used to toggle the sample between the optical station and the nanoparticle dispense system with minimal friction and hysteresis. Although the XY nanopositioning stage is designed as a stepper mechanism for fine positioning of the sample within a 100 nm, the coarse positioning accuracy of the global travel system must be investigated in situ. Apart from translating the sample between the coating and the optical stations, an important requirement of the translation mechanism is to provide a smooth motion of the substrate during the coating process. Table 1 shows positioning accuracy of the linear motor measured in open loop using laser interferometer. The internal encoder of the linear motor is used to measure the positioning accuracy and repeatabilty. Figure 6 shows the average position error during moving in forward and backward directions under the coating area (240mm-360mm from homing position), for a fixed PID value. The errors decrease with an increase in the motor speed. The PID parameters of the motor controller were varied for different sets of experiments. The positioning experiments showed that <100μm repeatability and <50μm accuracy can be obtained using the current setup.

Table 1: Accuracy in positioning the substrate using a laser interferometer in open loop

Target Position (in mm)	Accuracy (in μm)
5	-48.826
10	-25.374
15	57.908
20	6.9685
25	-29.873
30	40.574

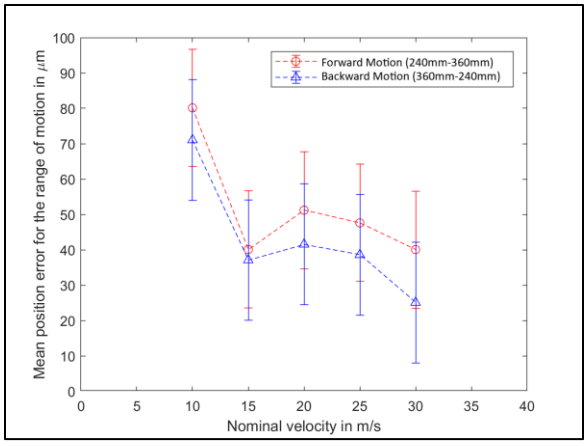

FIGURE 6. Mean position bidirectional errors at varying nominal velocity of the system measured using the internal encoder of the linear motor

OPTICAL SUBSYSTEM

The optical subsystem is designed to address the challenges in achieving the target resolution as well as the throughput of the system. A vertically incident 808 nm wavelength 50W power diode laser is used to sinter the copper nanoparticles. Typical laser spot sizes range between 50-300 μm [4]. To produce one micron features, the focused laser spot size should be reduced significantly, which comes at the cost of process speed. This issue was address by using a digital micromirror device (DMD) which allows each 7 μm by 7 μm pixel in the micro-mirror array to be focused down to a spot size of approximately 1μm. The DMD chipset consists of an array of 1920 by 1080 individually accessible micro-mirrors with a binary pattern update rate of up to 9.5 kHz. A custom optical setup for focusing the laser on the sample plane was designed to maximize the collection of light at the sample plane, achieve a minimum feature size resolution of 1µm and enable large area patterning (>2mm^2) with a single shot exposure of laser. The optical system consists of a collimating lens and an aspheric lens with a theoretical demagnfication of 6.66 times. With a diffraction limited resolution of the optical setup of 1.18µm, it effectively means that every 7µm mirror can be focused down to ~1.2µm at the sample plane. If all the mirrors of the DMD array are activated simultaneously a maximum number of ~2 million spots can be sintered with a 1µm laser spot after demagnification. The optical subsystem is shown in figure 8.

A beam profiler is used to experimentally determine the resolution of the optical system. A monochromatic bitmap pattern with 1920 x 1080 pixels was projected through the DMD on the sample plane. The measured profile of the image at the sample plane, as shown in figure 7 showed that the effective reduction in size of the pattern exiting the micromirror array is 6.23 times, which is close to the predicted demagnification.

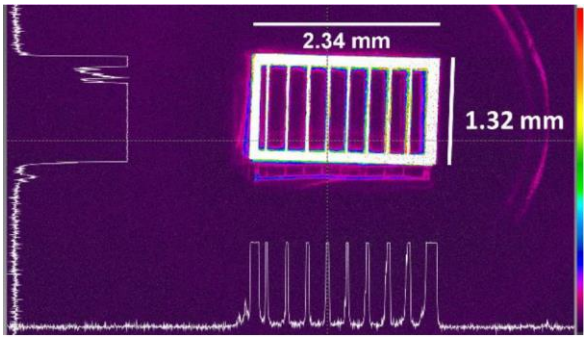

FIGURE 7. Beam profiler image showing the reduced size of the pattern at the sample plane

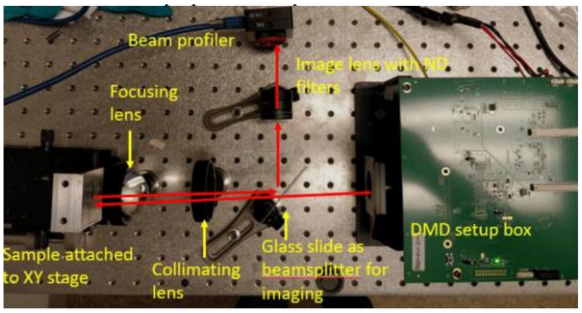

FIGURE 8. Optical subsystem for μ-SLS system

CONTROL SYSTEM

Currently, all the subsystems are controlled by their respective drivers and controllers. Further development work is needed to integrate the subsystems with each other and completely automate the sintering process.

SINTERING TEST RESULTS

The current sintering tests are done by horizontally setting up the optical subsystem on an optical table. Some single layer sintering results with spin coated and slot die coated samples are shown in figure 9. After the first layer was coated and sintered, the excess ink was removed from the sample using an ultrasonication process. The ultrasonication parameters depend on the amount of ink present on the sample. Then, the samples were annealed for improving the structural and electrical properties.

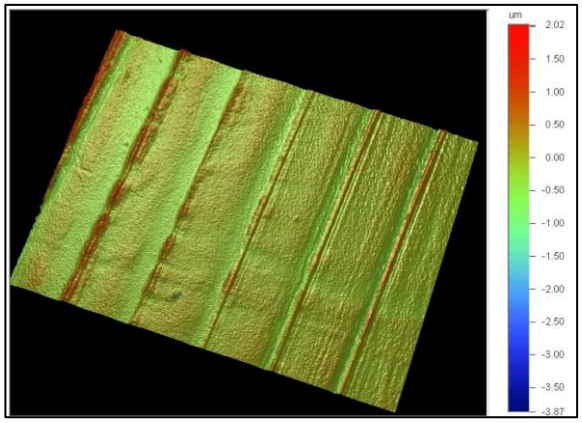

(a)

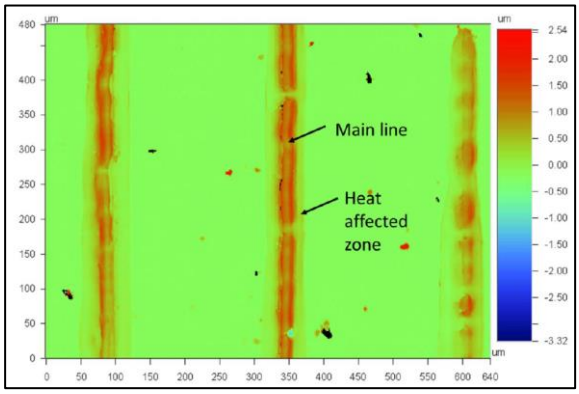

(b)

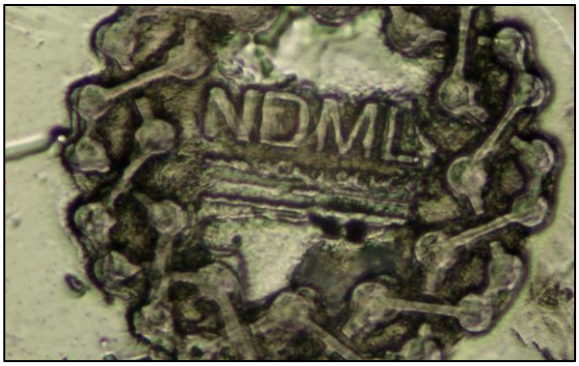

(c)

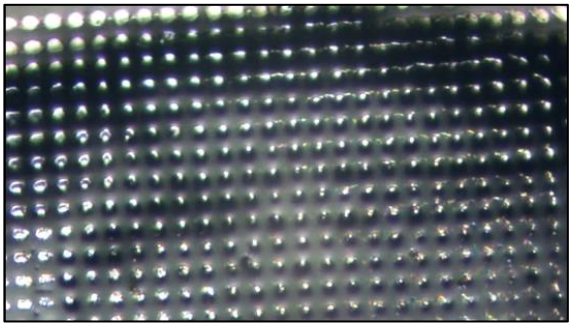

(d)

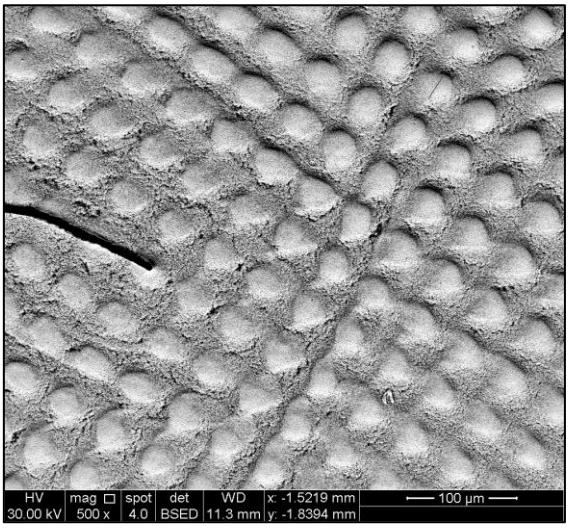

(e)

FIGURE 9: Sintered regions a) Surface topography of 10µm line width and 200µm line spacing b) 2D profile of Figure 9a showing the heat affected zones c) Sintered logo of authors' lab at University of Texas, Austin d) Post-sintering, pre-ultrasonication image of circular array with 30 µm diameter and 40 µm pitch e) Post-annealing scanning electron micrograph of Figure 9d.

MULTIPLE LAYER SINTERING

For the initial multilayer sintering experiment, a 500μm circle was sintered. The first layer of the coated substrate (100 μm coating gap) was partially dried to remove excess solvent at 85ºC for 5-7 minutes and then sintered at 50W, 4 seconds exposure duration. The average height of the sintered circle measured using optical profilometry was 2.37μm. Another sample was coated and sintered at the same parameters. The sintered sample was coated again at a 100 μm coating gap and then dried. After the second layer was dispensed on the top of the first layer, the same circular pattern was sintered at an exposure duration of 6 seconds. The average height of the 2 layers was around 5.26 μm. Excess NP ink was removed from both the samples by ultrasonicating them. The bilayer sintered sample was found to be 2.34 times higher than the single layer sample. Figure 10 shows a 3D rendering of the surface topography of single layer and two-layer sintered samples.

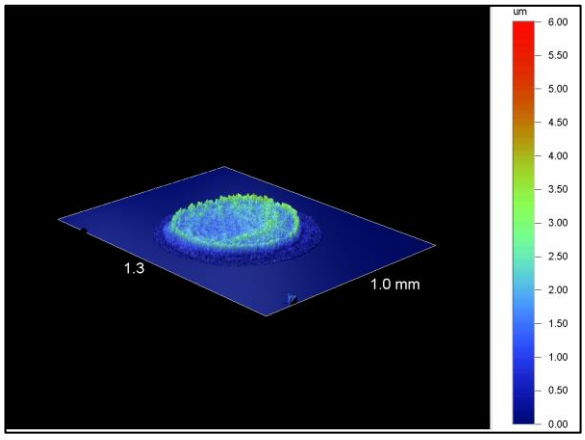

(a)

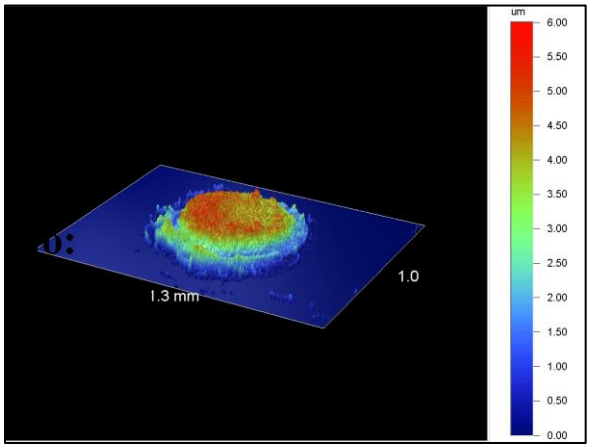

(b)

FIGURE 10. a) Single layer sintering of a 500μm circle b) Two layer sintering of a 500μm circle

REFERENCES

[1] L. Hirt, A. Reiser, R. Spolenak, and T. Zambelli, “Additive Manufacturing of Metal Structures at the Micrometer Scale,” *Adv. Mater.*, vol. 29, no. 17, 2017.

[2] N. K. Roy *et al.*, “A Comprehensive Study of the Sintering of Copper Nanoparticles Using Femtosecond, Nanosecond, and Continuous Wave Lasers,” *J. Micro Nano-Manufacturing*, vol. 6, no. 1, p. 010903, 2017.

[3] N. K. Roy and M. A. Cullinan, “Design and characterization of a two-axis, flexure-based nanopositioning stage with 50 mm travel and reduced higher order modes,” *Precis. Eng.*, vol. 53, no. September 2017, pp. 236–247, 2018.

[4] M. Vaezi, H. Seitz, and S. Yang, “A review on 3D micro-additive manufacturing technologies,” *Int. J. Adv. Manuf. Technol.*, vol. 67, no. 5–8, pp. 1721–1754, 2013.

A ROLL-TO-ROLL SYSTEM FOR IN-LINE, TIP BASED NANOMETROLOGY OF PATTERNED MATERIALS AND DEVICES

Liam G. Connolly, Andrew Cheng, James Garcia, and Michael A. Cullinan
Department of Mechanical Engineering
The University of Texas at Austin
Austin, Texas, United States of America

ABSTRACT

This paper presents the development of a proof-of-concept tool to preform nanoscale metrology for process control in the roll-to-roll manufacturing of nanopatterened materials, films, and flexible electronic devices. The system leverages a uniquely compact single-chip atomic force microscope (sc-AFM) positioned with nanoscale precision over a stainless-steel, air bearing supported idler roller and dynamically actuated to compensate for curvature, eccentricity and surface topology of the roller to perform a single, 15 μm x 17 μm rectangular scan on the flexible substrate with nanometer resolution every 60 seconds.

INTRODUCTION

The promise of roll-to-roll (R2R) manufactured electronic devices is to bring a unique combination of low unit cost, high-performance and extremely desirable mechanical properties. However, developing both the devices and manufacturing techniques to achieve this goal has proven difficult and time consuming, especially when moving beyond lab-scale fabrication. In-line inspection techniques which provide real-time process feedback can vastly improve the yield and cost-efficiency of a nanofabricated device, particularly in the challenging dynamic environment of R2R manufacturing. Moreover, access to larger amounts of metrology data, at a lower cost to manufacturing productivity, can accelerate the development and installation process for new fabrication methods. However, optical methods for direct inspection fail at the critical dimension levels desired for optimal performance and packaging of this new class of materials. Further, electron-beam inspection techniques are much too slow for any sort of in-line operation, most especially in the high-speed R2R environment. A new methodology for high-speed, in-line R2R inspection of nanoscale features is needed to effectively develop the new fabrication processes and flexible hybrid electronic devices required to realize this goal [1]–[3].

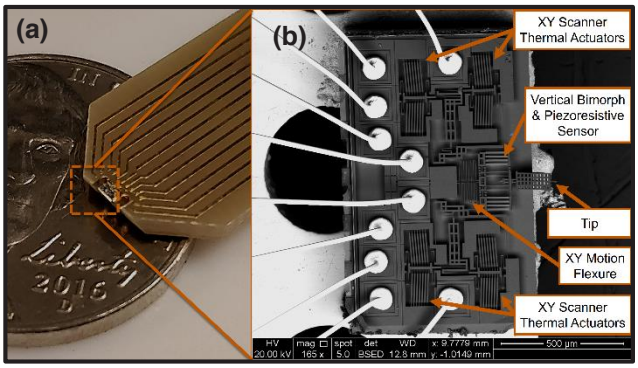

FIGURE 1. (*a) Photograph of ICSPI sc-AFM attached to a wire-bond PCB on a US Nickel. (b) Microscope picture showing major components of MEMS AFM [5].*

Through the application of extraordinarily compact MEMS-based single chip atomic force microscopes (sc-AFMs, ICSPI Corp.) with high scanning speeds and total volume less than 0.25 mm^3, the R2R metrology tool greatly increases the throughput and modularity of direct, nanometer-scale measurement on flexible substrates [4]–[6]. This sc-AFM consists of a vertical bimorph and piezoresistive cantilever sensor for vertical tip movements and integrated X/Y actuators and flexure bearings as shown in Figure 1.

SYSTEM METHODOLOGY

The metrology system is designed to operate at a speed relatively commiserate with in-line process control for an Imprio 80 Jet-and-Flash Nanoimprint Lithography tool (Molecular Imprints) for R2R nanomanufacturing at UT's NASCENT NSF Engineering Research Center. In order to validate the tool concept, the system will begin by operating in a step-and-scan mode similar to the web flow in the Imprio 80 tool, with

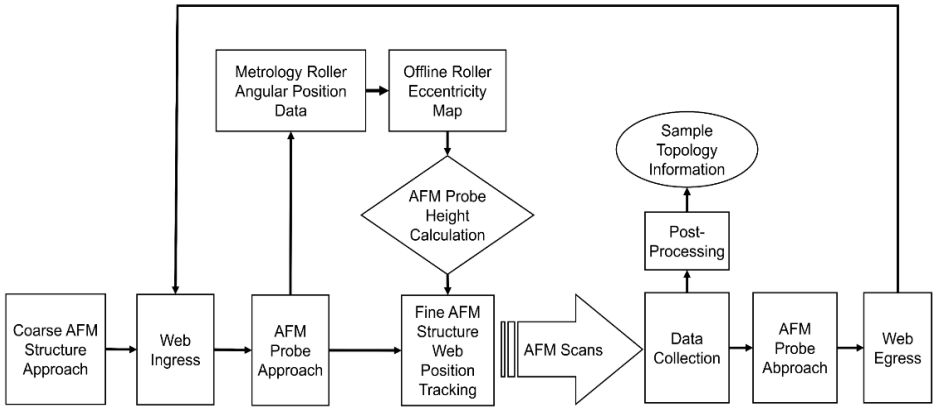

FIGURE 2. *System Operational Flow for Nanometrology Data Acquisition in Step-n-Scan Operation*

an AFM scan occurring once every ~60 seconds. Figure 2 illustrates the basic system operation.

The system must be able to:

(1) control position of the AFM probe with nanometer-scale accuracy
(2) achieve a large enough maximum range and high enough disturbance rejection to prevent destructive tip-sample interaction under all operational conditions
(3) rapidly perform AFM approach movements
(4) Track web velocity and roller topology at high speed.

Positioning of the AFM probe is split into three coupled positioning sub-systems during system operation. First, the gantry structure over the web to which the AFM is mounted is positioned in both the vertical and lateral (machine) directions to within 200 μm of the web by means of the dual-monolith flexure bearing based positioner with feedforward control, after which a feedback control mode is utilized. The fine approach mechanism then brings the sc-AFM within 10 μm of the substrate in closed loop operation using the piezoresistive cantilever sensor as feedback. Once at optimal scanning height, the fine approach system is held at a constant height while the discrete sc-AFM controller begins the scan.

After scanning is complete, the sc-AFM is returned to a safe height to prevent any destructive tip-sample interference. It is kept roughly 150 μm from the substrate during web travel using an offline mapping of the metrology roller topology to compensate for changes in height as the metrology idler roller rotates. Once the next desired "hotspot" for process control reaches the plane of the AFM tip, web movement is halted, and the AFM is once again approached to within 10 μm of the web and scans another 255 μm^2 imaging area once more. The described prototype tool is shown in Figure 3.

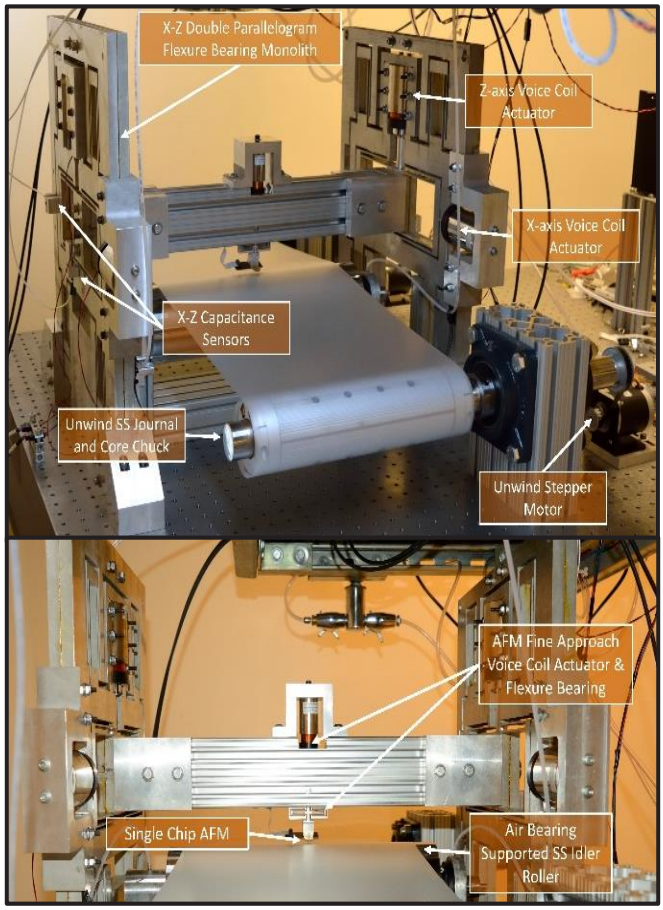
X-Z Double Parallelogram Flexure Bearing Monolith
Z-axis Voice Coil Actuator
X-axis Voice Coil Actuator
X-Z Capacitance Sensors
Unwind SS Journal and Core Chuck
Unwind Stepper Motor
AFM Fine Approach Voice Coil Actuator & Flexure Bearing
Single Chip AFM
Air Bearing Supported SS Idler Roller

FIGURE 3. *R2R Nanometrology proof-of-concept prototype tool with major sub-systems and components labeled*

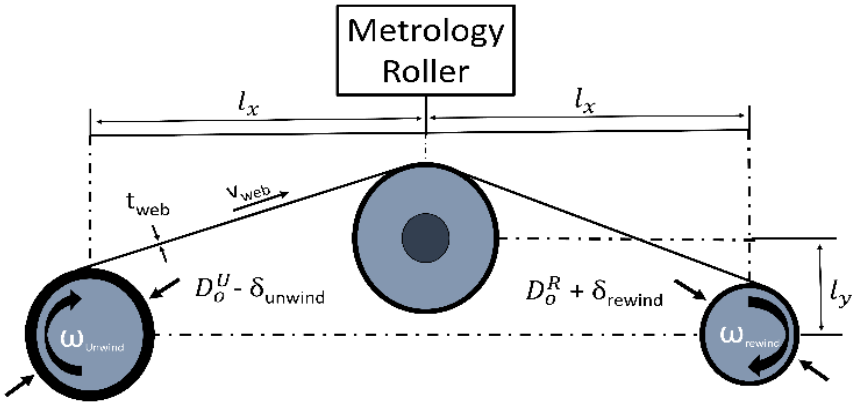

FIGURE 4. Web Handling System Diagram

EXPERIMENTAL SETUP

Web Handling and Tension Control

The web handling subsystem provides a dual benefit to the tool; unwind/rewind operations for material flow are accomplished concurrently with an open-loop web tension control. The basic layout of the subsystem is shown in Figure 4. This is necessary as, due to the nature of the nanoimprinted substrates for measurement, the top side of the material cannot come into hard contact with any rollers. This constraint renders typical load cell or "dancer" feedback tension control systems infeasible. Moreover, as minimization of web disturbances is of importance to the acquisition of high-quality metrology data, stiffness and alignment of the cantilevered winding stands ensures minimal lateral movement of the substrate over the short web span, eliminating the need for a noisy and expensive pivot table web-guide module in such a short web.

Each winding stand in the subsystem consists of an extruded aluminum structure rigidly bolted to an air isolated optical table (Newport) and two, four-bolt flange-type self-aligning roller bearings (UCF208-24) on either side of the structure together supporting a turned 304SS journal. Rolls of material are held to the journal through a standard 3-inch core diameter air-bladder expansion chuck which is attached to journal with a c-style clamp (PARA Co.). The journal is then rotated by stepper motor (Anaheim Automation, 23W209S-LW8) driving the journal via a timing belt and pulley. The motors are driven by an open source, Arduino based open loop controller (Syntheos, grbl).

The subsystem moves the web of material at a constant rate, v_{web}, and, by leveraging model-based control using tracked total angular rotation since system startup, initial roll diameters, D_o^U and D_o^R, and known mechanical properties of the polycarbonate web to apply a tensive force of approximately 10N through a modulated difference in angular velocities ω_{unwind} and ω_{rewind}. This controller performs all required web handling functions.

Gantry Positioner

The AFM gantry is rigidly attached to two, dual-axis double parallelogram flexure mechanism monoliths with a degree of freedom in each the *x* and *z* axis as can be seen in Figure 5 [7]–[9]. The monoliths consist of two 0.5 in thick 6061-T651 aluminum waterjet cut plates rigidly bolted together. The stiffness of the DPFMs is designed by choice of beam thickness and DPFM geometry to allow a roughly 2.5 mm and 4 mm range in the *X* and *Z* axis respectively. Each axis is actuated by a 65 N linear voice coil actuator (MotiCont. LCVM 051-064-02). These actuators are driven by a custom linear current amplifier (based on Apex Microtech., PA02A). The position of the motion stage relative to each axis is measured by capacitance probes (LION Precision, CPL290, C5 Probe) for each axis on each of the two monoliths. The gantry positioning

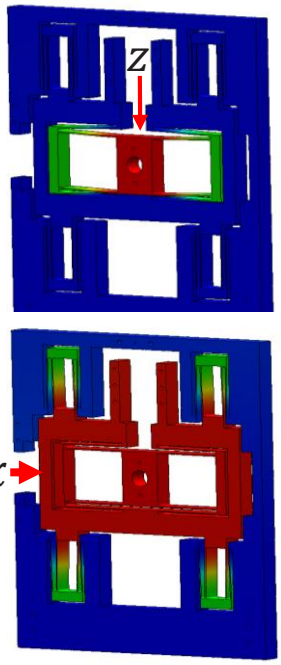

FIGURE 5. Double Parallelogram Flexure Mechanism Positioning Axis

system is controlled by a cRIO Virtex-5 LX50 FPGA controller (NI cRio-9022, 9114) with both 24-bit ADC and 16-bit DAC modules (NI 9039, 9269) for real-time voice coil actuation and position sensing [10].

Probe Fine Approach and sc-AFM Imaging

Final approach of the sc-AFM is accomplished through a small, water-jet cut, 0.5 in thick 7075-T651 aluminum DPFM coupled with a 10 N voice coil actuator (MotiCont LVCM 25-0-38-01). The sc-AFM contains onboard actuators for X, Y, and Z positioning and a piezoresistive sensor for nanometer accurate measurement of tip height. The probe tip is controlled for frequency modulation, non-contact scanning of a 15 μm by 17 μm area by a discrete PI controller (ICSPI Corp.). The number of pixels per scan and tip dwell time at each point can be varied from 64 x 64 to 1024 x 1024 and from 500 μs to 1000 μs respectively through software to balance the tradeoff between scan speed and resolution.

PRELIMINARY RESULTS

The AFM gantry positioning system was operated in feedforward mode and its noise in position measured. The ± 3σ envelope for the z-axis monoliths was vary between ± 2.33 – 3.60 nm and x-axis monoliths between ± 3.54 - 9.16 nm at 10 kHz sampling. Sensor accuracy at this frequency is expected to be ± 2 nm. Moving mass (e.g. gantry mass) for these tests was calculated to be 2.7 kg. Histograms of this noise are shown in Figure 6a and 6b.

Further, an AFM scan of a 92.5 ± 3 nm step height by 3 μm period calibration grating attached to a 150 μm thick, 80 mm wide polycarbonate web was carried out using the proof-of-concept tool. Average scan time for the probe settings used in Figure 7 was found to be 31.9 s. For this scan, X and Y pixel sizes are calculated to be 117 nm and 132 nm respectively given total scan area and number of pixels recorded. The calculation of average step height and standard deviation of the grating was 93.9 ± 2.9 nm. It should be noted that the scan was carried out using a sc-AFM with a tip that has yet to be focused ion beam (FIB) sharpened for cost reasons. As the unsharpened tip is roughly the same size as the period of the test grating, edge detection methods were used to calculate step height.

CONCLUSION

A prototype tool for high-speed metrology of nanoscale features on a flexible substrate was demonstrated, be it for eventual use with photonic films, metamaterials, or flexible hybrid electronics. Unlike wavelength-limited or indirect measurement optical methods, or time-consuming electron beam inspection, the nanometrology system presented can achieve the high scan speeds, nanometer-scale

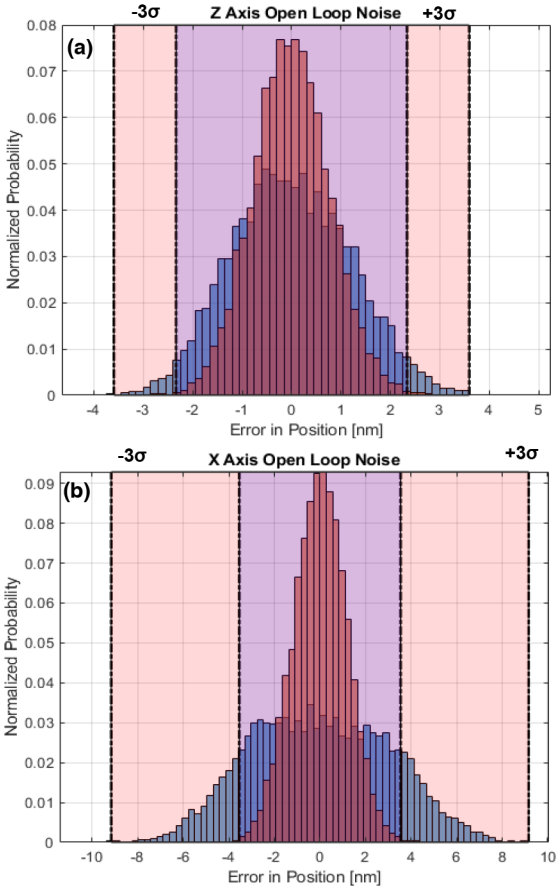

FIGURE 6. Open Loop Noise Histograms for Z (a) & X (b) Axis of Both Vertical Flexure Bearing Monoliths

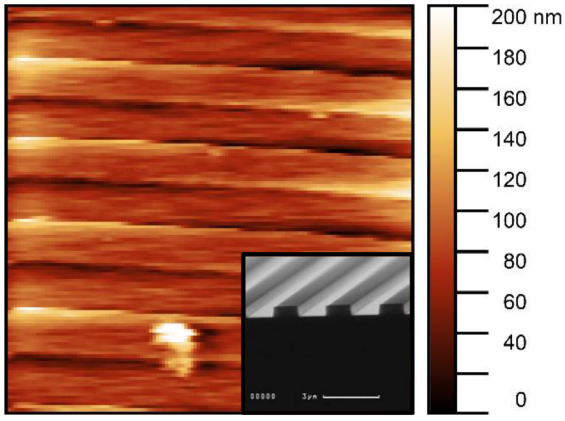

FIGURE 7. 31.9 second AFM Scan of TGZ2 Calibration Grating on a 150 µm Polycarbonate Web (Ted Pella Inc).

resolution, and uniquely compact in-line design necessary to optimize and implement real time process control in the challenging environment of roll-to-roll nanofabrication.

ACKNOWLEDGEMENTS

The authors would like to thank Nilabh Roy, Martin Ward, Dipankar Behera and Tsung-Fu Yao for the many helpful and informative discussions. This research is based upon work supported primarily by the National Science Foundation under Cooperative Agreement No. EEC-1160494 and the National Science Foundation Graduate Research Fellowship program under Grant No. 2017251210.

REFERENCES

[1] A. Nathan *et al.*, "Flexible electronics: The next ubiquitous platform," *Proc. IEEE*, vol. 100, no. SPL CONTENT, pp. 1486–1517, 2012.

[2] S. Bauer, "Flexible electronics: Sophisticated skin.," *Nat. Mater.*, vol. 12, no. 10, pp. 871–2, 2013.

[3] H. Subbaraman, X. Lin, X. Xu, A. Dodabalapur, L. J. Guo, and R. T. Chen, "Metrology and Instrumentation Challenges with High-rate, Roll-to-Roll Manufacturing of Flexible Electronic Systems," *Instrumentation, Metrol. Stand. Nanomanufacturing, Opt. Semicond. VI*, vol. 8466, p. 846603, 2012.

[4] N. Sarkar, G. Lee, and R. R. Mansour, "CMOS-MEMS dynamic FM atomic force microscope," in *Transducers 2013*, 2013, no. June, pp. 916–919.

[5] D. Strathearn, N. Sarkar, G. Lee, M. Olfat, and R. R. Mansour, "The benefits of miniaturization of an atomic force microscope," *Proc. IEEE Int. Conf. Micro Electro Mech. Syst.*, pp. 1363–1366, 2017.

[6] T.-F. Yao, A. Duenner, and M. Cullinan, "In-line metrology of nanoscale features in semiconductor manufacturing systems," *Precis. Eng.*, 2016.

[7] C. Li, J. Wang, and S. C. Chen, "Flexure-based dynamic-tunable five-axis nanopositioner for parallel nanomanufacturing," *Precis. Eng.*, vol. 45, pp. 423–434, 2016.

[8] X. Zhou, D. Wang, J. Wang, and S. C. Chen, "Precision design and control of a flexure-based roll-to-roll printing system," *Precis. Eng.*, vol. 45, pp. 332–341, 2015.

[9] X. Zhou, H. Xu, J. Cheng, N. Zhao, and S.-C. Chen, "Flexure-based Roll-to-roll Platform: A Practical Solution for Realizing Large-area Microcontact Printing.," *Sci. Rep.*, vol. 5, no. April, p. 10402, 2015.

[10] N. K. Roy and M. A. Cullinan, "Design and characterization of a two-axis, flexure-based nanopositioning stage with 50 mm travel and reduced higher order modes," *Precis. Eng.*, vol. 53, no. April, pp. 236–247, 2018.

SENSORLESS WAVEFRONT CORRECTION FOR DMD-BASED FAST 3D IMAGING AND NANOFABRICATION

Mindan Ren, Qiang Geng, Wenqi Ouyang and Shih-Chi Chen*
Department of Mechanical and Automation Engineering
The Chinese University of Hong Kong
Shatin, N.T., Hong Kong SAR, China
*Email: scchen@mae.cuhk.edu.hk

In this paper, we present a method to simultaneously perform wavefront correction and random-access scanning based on a digital micromirror device (DMD) and binary holography. Previously, we reported an ultrafast DMD-scanner [1, 2] that operates at the DMD pattern rate, i.e., 22.7 kHz, for two-photon excitation (TPE) imaging and two-photon polymerization (TPP) applications. To enhance the imaging and fabrication resolution, e.g., imaging through turbid tissues, point spread function of the laser focus is engineered and optimized via superposing the scanning and wavefront correction holograms. Mathematical models have been derived; imaging and fabrication experiments are performed to verify the predicted performance.

PRINCIPLE OF WAVEFRONT CORRECTION

TPE microscopy has been widely implemented and used for in vivo biological studies. Although according to the Rayleigh criterion, the resolution of a TPE microscope is limited by the diffraction of light, in practical imaging studies, the resolution is much worse than the predicted diffraction limit due to inhomogeneous optical properties of specimens, e.g., varying refractive index and scattering effect, leading to aberration and blurry images. To address the issue, active wavefront correction methods have been developed, i.e., adaptive optics, based on deformable micromirror arrays [3], which allows light to go deeper into the specimen with improved imaging quality.

Zernike method has been widely used to model distorted wavefronts. The Zernike polynomials are presented in Eq. (1), which consist of orthogonal polynomials. The first few terms of the Zernike polynomials represent the classical aberrations. For example, the 1st and 2nd terms are tilt and tip respectively; and the 7th and 8th terms represent coma. In the field of telescope, Zernike polynomials can be used to model any atmospheric turbulence by linear combination of the polynomials. The optimal coefficients can be determined by the gradient descent method [4].

$$Z_n^m = \begin{cases} \sqrt{n+1}R_n^m(r)\sqrt{2}\cos m\theta\,, & m>0 \\ \sqrt{n+1}R_n^{-m}(r)\sqrt{2}\sin(-m\theta)\,, & m<0 \\ \sqrt{n+1}R_n^0(r), & m=0 \end{cases} \quad (1)$$

where

$$R_n^m(r) = \sum_{k=0}^{\frac{n-m}{2}} \frac{(-1)^k(n-k)!}{k!\left(\frac{n+m}{2}-k\right)!\left(\frac{n-m}{2}-k\right)!} r^{n-2k}$$

n and *m* are integral and satisfy

$|m| \le n$, $n-|m| = even$.

DMD-BASED WAVEFRONT CORRECTION

To realize wavefront correction and 3D scanning simultaneously with a single DMD, the Zernike polynomials must first be superposed to the scanning wavefront and converted to binary holograms. As reported in [1, 2], Lee holography [5] may be used to control the laser focal point in space in a discrete fashion, and each calculated hologram corresponds to a specific point in space. In brief, binary holograms can be calculated as

$$h(i,j) = \begin{cases} 1, & -\frac{q}{2} \le \frac{R(x,y)}{T} + \frac{\phi(x,y)}{2\pi} + n \le \frac{q}{2} \\ 0, & otherwise \end{cases} \quad (2)$$

where $h(i,j) \in \{0,1\}$ represents the pixels on the DMD; 1 and 0 refer to the "on" and "off" states, respectively. *T* is the grating period of the hologram; *n* is an integer; and *q* is a constant that determines the width of the fringes.

To combine wavefront correction and random-access scanning, taking axial scanning as an example, we may superpose the spherical wavefront and any linear combination of the Zernike terms, as described in Eq. (3),

$$\phi(x,y) = \sum_{j=1}^{N} \alpha_j Z_j + \frac{\pi(x^2+y^2)}{\lambda f} \quad (3)$$

where $\phi(x,y)$ represent the superposed wavefront; z_j is the j^{th} Zernike mode, α_j is the coefficient of the j^{th} Zernike mode, λ is the wavelength; and f is the focal length of the spherical wavefront. Substituting Eq. (3) into Eq. (2), one can find the binary hologram for simultaneous scanning and wavefront correction. Figure 1 presents examples of a calculated Zernike wavefront superposed to a spherical wavefront of a radius of 20 mm.

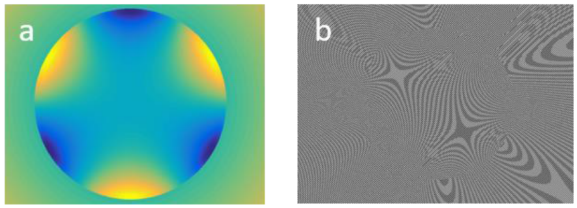

FIGURE 1. (a) Phase; and (b) DMD pattern of a spherical wavefront superposed with calculated Zernike modes

Hill-Climbing Algorithm

As every term of the Zernike polynomial is orthogonal to each other on the unit disk, one can search for the optimal coefficients of every Zernike mode sequentially. For example, the hill-climbing algorithm is a widely used optimization method to obtain the local optimal solutions [6]; and there exists a unique local optimal value (or coefficient) for each Zernike mode, which is also the global optimal solution. To apply the hill-climbing algorithm to the DMD system, we first determine the quality of the images via the evaluation function (f) as presented in Eq. (4). This function is related to the derivative of the image brightness (i.e., $I(x, y)$).

$$f = \left\{ \sum_x \sum_y \begin{bmatrix} |I(x,y) - I(x-1,y)|^2 + |I(x,y) - I(x-1,y-1)|^2 \\ +|I(x,y) - I(x-1,y+1)|^2 + |I(x,y) - I(x,y-1)|^2 \\ +|I(x,y) - I(x,y+1)|^2 + |I(x,y) - I(x+1,y-1)|^2 \\ +|I(x,y) - I(x+1,y)|^2 + |I(x,y) - I(x+1,y+1)|^2 \end{bmatrix}^{\frac{1}{2}} \right\} \quad (4)$$

Figure 2 presents the flow chart of the hill-climbing algorithm applied to the DMD scanning system. First, the DMD is programmed only with tip/tilt phases and spherical wavefront, i.e., lateral and axial scanning. Next, for the i^{th} Zernike mode, the hill-climbing algorithm is applied to find the optimal coefficient. To achieve this, we set the initial search center to be 0 and search gap to be b (Note b = 0.4 in the experiments.). In the first round, three images are taken with coefficients of -b, 0, and b, respectively. For each image, the evaluation function is calculated to determine the best image. If the center coefficient has the maximum evaluation function value, the search gap is reduced by half in the next iteration. If not, the search center shifts to the coefficient where the maximum value is obtained. This process is repeated until the search gap is small enough such that the differences among the three images become negligible. The same procedure is applied to identify coefficients of all selected Zernike modes.

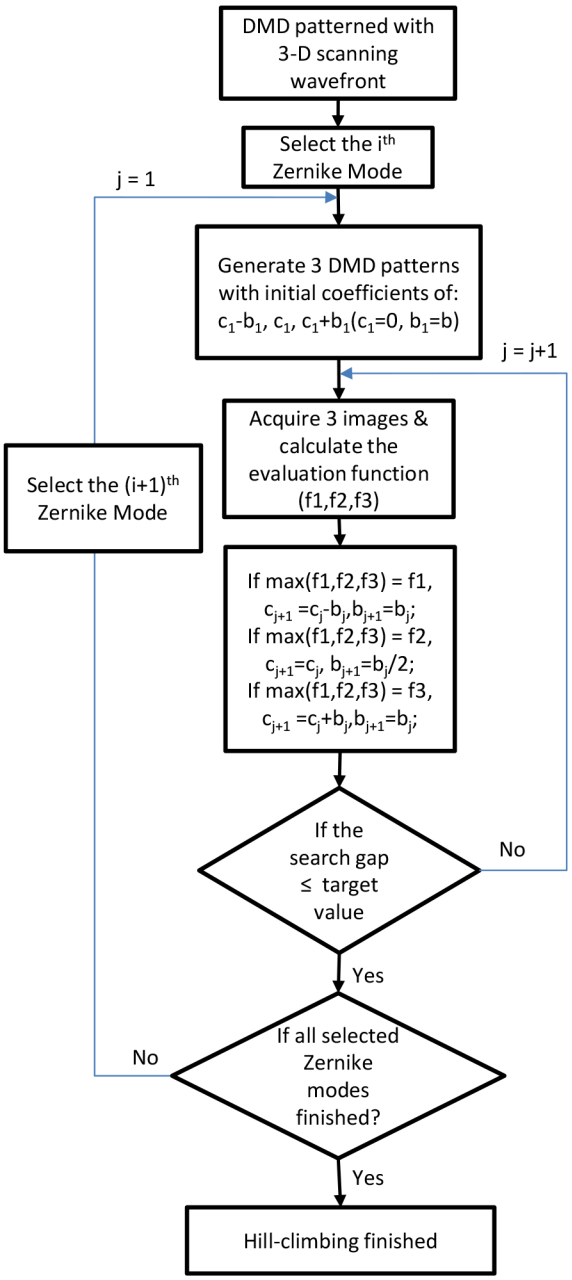
DMD patterned with 3-D scanning wavefront
Select the i^{th} Zernike Mode
j = 1
Generate 3 DMD patterns with initial coefficients of: c_1-b_1, c_1, c_1+b_1(c_1=0, b_1=b)
j = j+1
Acquire 3 images & calculate the evaluation function (f1,f2,f3)
Select the $(i+1)^{th}$ Zernike Mode
If max(f1,f2,f3) = f1, c_{j+1} =c_j-b_j,b_{j+1}=b_j;
If max(f1,f2,f3) = f2, c_{j+1}=c_j, b_{j+1}=b_j/2;
If max(f1,f2,f3) = f3, c_{j+1} =c_j+b_j,b_{j+1}=b_j;
If the search gap ≤ target value
No
Yes
If all selected Zernike modes finished?
No
Yes
Hill-climbing finished

FIGURE 2. Flow chart of the hill-climbing algorithm applied to the DMD system

SYSTEM CONFIGURATION

Figure 3 presents the optical configuration of the DMD-based laser scanning system for both imaging and nanofabrication applications [1, 2]. The laser source is a tunable Ti: sapphire femtosecond laser of 3.4 W (Chameleon Vision S, Coherent). Firstly, the input laser beam is expanded to ensure the DMD aperture (DLP 4100, Texas Instrument) is fully filled. As the DMD functions both as a programmable binary hologram and a blazed grating, it introduces negative angular dispersion to the laser beam. A blazed transmission grating and a mirror (M1) are included in the light path to compensate the angular dispersion generated by the DMD. After the DMD, the dispersion-free laser beam is guided to an infinity-corrected objective lens via a 1:1 telescope, i.e., L3 and L4. An iris diaphragm is placed at the back focal plane of L3 to spatially reject all diffracted beams except the -1st order diffraction of the hologram. A detector (PMT/CCD) is placed after the dichroic mirror for TPE imaging applications or TPP fabrication respectively.

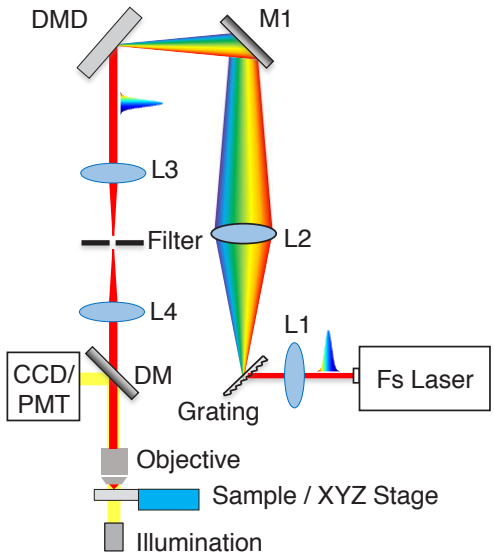

FIGURE 3. Optical configuration of the TPP fabrication/TPE imaging system, enabled by DMD scanner; M1: high-reflectivity mirrors; DM: dichroic mirror; L1, L2, L3, and L4: lenses

IMAGING EXPERIMENTS

To verify the performance of the hill-climbing algorithm, we performed imaging experiments on a pollen grain sample (~25 μm, Sunflower Pollen, Vision Scientific) with a water dipping objective lens (CFI75 Apo LWD 25XW, Nikon). First, we purposely introduced some aberration to the system by inserting a layer of agarose of 1 mm thick between the pollen slide and objective lens, as illustrated in Fig. 4.

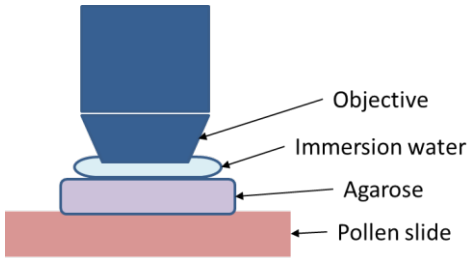

FIGURE 4. A layer of agarose is introduced between the the pollen sample and the objective

To remove the aberration introduced by the agarose layer, the 5^{th},6^{th},7^{th},8^{th} and 11^{th} terms of the Zernike modes are selected to perform the hill-climbing algorithm. (Note that the first four terms of the Zernike modes contribute to the piston, tilt, tip and defocus effect respectively; and thus are not used.) Table 1 presents the optimal coefficients for each mode calculated based on the process described in Fig. 2. Figure 5 presents the calculated correction wavefront, and the corresponding DMD pattern.

TABLE 1. 5 Zernike modes and the optimal coefficients measured in the correction.

Zernike Mode(n,m)	Optimal Coefficient	Description
(2,-2)	0.1	Oblique astigmatism
(2,2)	0.8	Vertical astigmatism
(3-1)	-0.4	Vertical coma
(3,1)	-0.4	Horizontal coma
(4,0)	0.05	Primary spherical

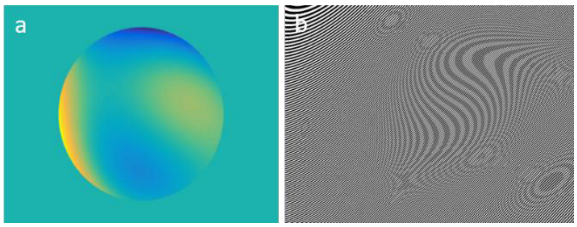

FIGURE 5. (a) Phase of the correction wavefront; and (b) the corresponding DMD pattern

Figure 6 presents the imaging results of the pollen sample. Figure 6(a) and 6(b) present the imaging results “without” and “with” the agarose layer respectively, where one may observe the spikes on the pollen becomes slightly blurred in Fig. 6(b). Figure 6(c) presents the imaging result with the agarose layer as well as the wavefront

correction phase (Fig. 5), i.e., the wavefront correction phase is superposed to the scanning hologram during the image acquisition process. From the result, one may find the spikes on the pollen are sharper than both Fig. 6(a) and 6(b). This is becuase for Fig. 6(c) the aberration from other sources are also corrected.

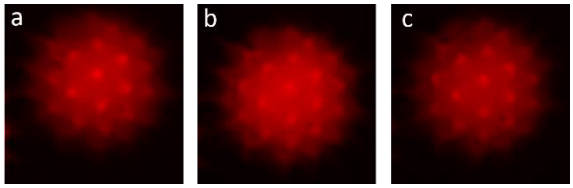

FIGURE 6. Pollen imaging results (a) without and (b) with a layer of agarose; (c) with both a layer of agarose and wavefront correction phase

PSF ENGINEERING FOR NANOFABRICATION

Although aberration is usually not an issue for nanofabrication or TPP processes (The resin is clear.), the size and shape of the laser focus, i.e., point spread function (PSF), may vary at different locations in the DMD work space, which may negatively affect the fabrication results, i.e., non-uniform voxel size or fabricated structures at different regions in the workspace. To address the issue, we first measure the PSF at different regions in the workspace; next, the holograms of the correction wavefront (obtained via the hill-climbing algorithm) are superposed to all scanning points to ensure that the PSF (or voxels) at different regions in the work space are uniform. 200 nm fluorescent beads (F8809, Thermo Fisher Scientific) were prepared to measure the PSF. Figure 7 presents measured PSF "without" and "with" wavefront correction hologram in the corner of the DMD work space. The corresponding maximum PMT signals are 0.18V and 0.24V respectively, indicating that the fluorescent intensity increased by ~33% after the wavefront correction hologram is applied to the scanning hologram.

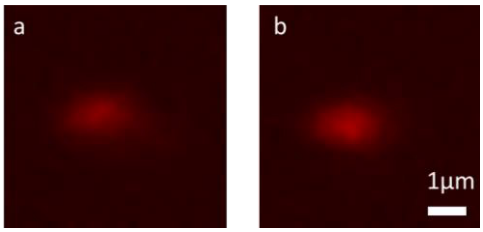

FIGURE 7. (a) PSF without correction; and (b) corrected PSF in the corner of the work space

Table 2 presents the optimal coefficients used in the correction wavefront

TABLE 2. Seven Zernike modes and coefficients used in the correction wavefront

Zernike Mode(n,m)	Optimal Coefficient	Description
(2,-2)	-0.5	Oblique astigmatism
(2,2)	0.6	Vertical astigmatism
(3-1)	-0.2	Vertical coma
(3,1)	-0.1	Horizontal coma
(3,-3)	0.5	Vertical trefoil
(3,3)	0.6	Vertical coma
(4,0)	-0.1	Primary spherical

CONCLUSION

In this work, we present the application of a sensorless wavefront correction method (i.e., hill-climbing algorithm) to the DMD-based TPE microscope and TPP fabrication system, realizing ultrafast random-access scanning and simultaneous wavefront correction (or PSF engineering) using a single DMD. Zernike polynomials are used to model arbitrary wavefronts introduced by the specimen and the optical system. The hill-climbing algorithm is applied to search for the optimal coefficients of the selected Zernike modes. Experiments have been performed to verify the effectiveness of the sensorless wavefront correction method in both TPE imaging and PSF engineering. The results may find important applications in biomedical imaging and nanofabrication.

REFERENCES

[1] Geng Q, Gu C, Cheng J, and Chen S. DMD-based Two-photon Microscopy for Three-dimensional and Random-access Imaging. Optica. 2017, 4(6): 674-677.

[2] Geng Q, Wang D, and Chen S. DMD-based Random-access Scanner for Fast 3-D Imaging and Fabrication, Proc. of the Annual Meeting of the ASPE, Charlotte, NC, USA, Oct. 2017, pp. 99 - 102.

[3] Débarre D, Botcherby EJ, Watanabe T, Srinivas S, Booth MJ, Wilson T. Image-based Adaptive Optics for Two-photon Microscopy. Opt. Lett. 2009, 34: 2495-2497.

[4] Noll RJ. Zernike Polynomials and Atmospheric Turbulence. J. Opt. Soc. Am. 1976, 66: 207-211.

[5] Lee WH. Binary Synthetic Holograms. Applied Optics. 1974, 13(7): 1677-1682.

[6] Wright AJ, Burns D, Patterson BA, Poland SP, Valentine GJ, Girkin JM. Exploration of the Optimisation Algorithms Used in the Implementation of Adaptive Optics in Confocal and Multiphoton Microscopy. Microsc. Res. Tech. 2005, 67: 36-44.

RECENT ADVANCES IN ULTRASONIC NANOCOINING TO CREATE LARGE ARRAYS OF SUB-WAVELENGTH FEATURES

STEPHEN J. FURST, NICHOLE C. MILLER, AND TIMOTHY J. MCDONALD

Smart Material Solutions, Inc.

Raleigh, NC, USA

NANOPATTERNING

Motivation

Nanopatterning can be used to create 3D surface textures comprised of large arrays of features, each smaller than the wavelength of visible light. Such a surface suppresses Fresnel reflections, creating a broadband anti-reflective effect. The decreased reflections increases light transmission through the surface [1]. The surface area enhancement of a textured surface exhibits super-hydrophobicity, giving the surface self-cleaning properties [2]. Features located at a spacing less than the diffraction limit, about 200 nm for visible light, are effectively invisible; therefore, an undistorted image can be passed through a transparent material.

These surfaces have been proposed for use in a wide array of commercial applications, such as anti-reflective and self-cleaning coatings for electronics displays, solar panels, or windows [3]. More broadly, nanopatterns can be used to create structured color, surface plasmon effects for bio-sensing [4], or high-transmission, broadband linear polarizers [5]. They form a critical component in augmented reality headsets or can be used to inhibit the growth of bacterial colonies on a surface [6].

Methods

The values of these surfaces have been documented in academia for decades; however, large-scale patterning remains a challenge. Scale up often involves first making a small area master then replicating it using a soft imprinting process. Ideally, the master mold can be used in a roll-to-roll process to enable the pattern to be replicated seamlessly [10]. However, step-and-repeat batch processes are easier to implement on small area masters. A nanopattern master is typically generated initially by slow methods such as focused ion beam machining [7], UV interference lithography, electron beam lithography [8], or some sort of chemical self-assembly process [9].

Challenges

Both the initial pattern formation and scale up by imprinting have significant challenges. The initial patterning is typically done in a vacuum and on wafer scale. The sheer number of features – more than a trillion at a 250 nm pitch to coat a laptop screen – makes serial fabrication extremely time consuming. Even if a robust master is made, replicating it seamlessly using a step-and-repeat process is impossible. A roll-to-roll process can be used, but in that case a seamless master is needed on the OD of a large metal drum.

ULTRASONIC NANOCOINING

Nanocoining is a mechanical indenting process invented at the North Carolina State Precision Engineering Consortium to seamlessly nanopattern large-area drum molds for roll-to-roll manufacturing [11][12]. Nanocoining is hundreds of times faster than competing technologies, thus enabling cutting-edge technologies from academia to be applied to commercial products like wire-grid polarizers, displays, OLEDs, biosensors, solar panels, and windows.

This work describes the design and fabrication of the nanocoining pilot system developed at Smart Material Solutions, Inc. (SMS). The system is a multifunctional diamond-turning lathe and diamond-indenting machine. SMS will also discuss recent improvements to the nanopatterning of its diamond dies, including the fabrication of nanopillars and linear gratings with pitches below 200 nm. Finally, SMS will present prototype molds and nanostructured films created with these molds.

Process Overview

Nanocoining is an ultra-precision indenting process that seamlessly nanopatterns drum molds for roll-to-roll manufacturing. The process uses an ultrasonic resonant actuator to indent a nanopatterned diamond die into a diamond-turned metal surface 50,000 times per second, with each indent precisely registered side-by-side (Figure 1). The patented process can cover up to 2 in^2 of metal every minute, which is hundreds of times faster than competing technologies like electron-beam lithography.

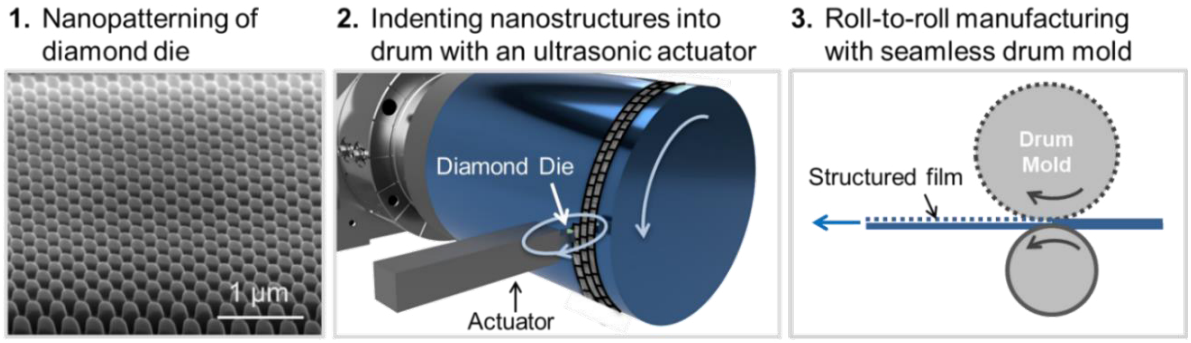

Figure 1: The nanocoining process.

Pilot System Design

The pilot system shown in Figure 2 is a multifunctional diamond-turning lathe and indenting system built on a CMM base. The system, designed by SMS and fabricated in partnership with Aerotech, Inc. and Professional Instruments, Inc., is capable of producing cylindrical drum molds up to 6 inches in diameter and 6 inches long. Thus far, it has been used to diamond turn 2 inch diameter cylinders with less than 5 nm RMS surface finish and subsequently indent nanofeatures into the diamond-turned cylinder (Figure 4). The cross-roller axes have a variable stiffness, which makes sub-100 nm form error difficult to achieve. However, the flexibility of the Aerotech A3200 controller provides the ability to integrate external sensor data and compensate for repeatable errors.

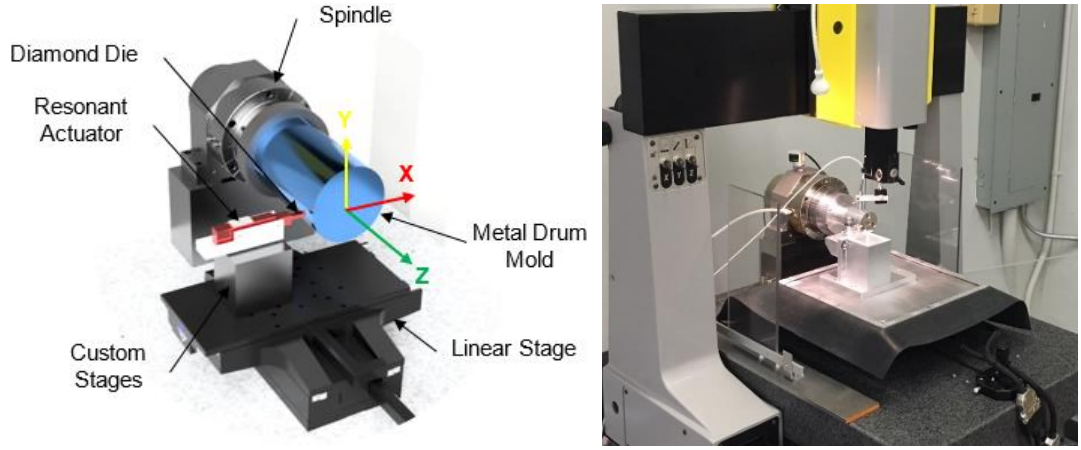

Figure 2: CAD drawing (left) and photo (right) of the nanocoining pilot line.

PROCESS VALIDATION

Nanopatterning of Diamond Die

SMS has developed new methods to nanopattern the diamond dies that are used as indenting tools in the nanocoining process using focused ion beam (FIB) milling. These improved methods reduce the processing time, mitigate stage drift that can smear features, and enable the fabrication of smaller features over larger areas (up to 20x20 μm currently). The improved nanofabrication has resulted in several new feature sizes, lattices, and shapes like those summarized in Figure 3. For example, SMS has fabricated nanopillars with pitches below 200 nm and gratings with spacings below 140 nm, microfeatures up to a few microns in pitch, and hierarchical features comprised of nanofeatures on top of microfeatures. Periodic features on

square and hexagonal lattices as well as stochastic and arbitrary features have been fabricated. Figure 3 also shows a variety of additional shapes including linear gratings, nanohole arrays, and more complicated structures.

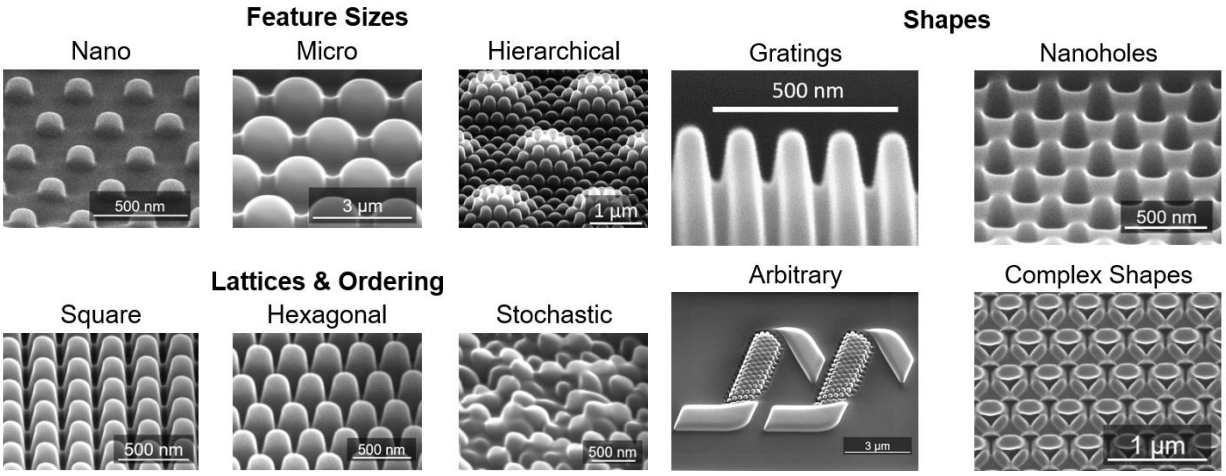

Figure 3: SEM images of nanostructured diamond using FIB milling with a variety of length scales (<150 nm to several microns), lattices, and shapes.

Prototype Molds

SMS has successfully indented a prototype 2 inch diameter molds with its pilot system using improved diamond dies with nanofeatures on a 250 nm pitch. Figure 4 shows a photo an example of the system diamond-turning (left) then indenting (right) prototype electrolytic high-phosphorous Nickel mold. The pilot system is capable of creating molds up to 6 inches (152 mm) in diameter and 6 inches (152mm) long, a size that is compatible with many of our partners' roll-to-roll setups. SMS will scale up to these larger drum molds over the next several months.

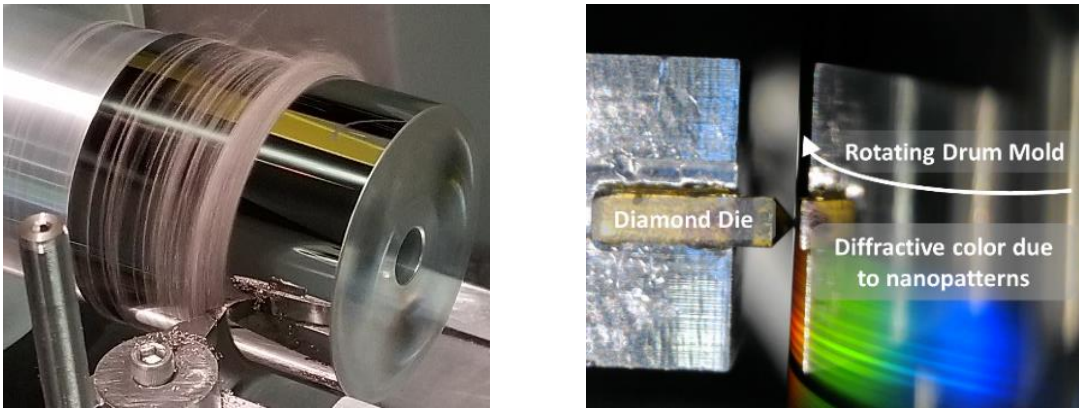

Figure 4: Pilot system in diamond-turning (left) and indenting (right) mode.

Optical Properties of Replicated Films

Prototype molds have been used to nanopattern UV-curable polymers on a variety of plastic substrate to create films with structural color due to diffraction and anti-reflective properties (Figure 5). UV-Vis spectroscopy measurements of a film patterned on one side with square lattice features on a 320 nm pitch show broadband increase in transmission (reduction in reflection) of 1.5-2% over most of the visible range. Since Fresnel reflections occur on both sides of the film, patterning one side can only eliminate about half of the total (~8%) reflection. This means by reducing 2% of reflection, our film is operating at 50% efficiency. The photo on the left in Figure 5 is patterned on both side and shows a significant reduction in glare as a result. Taller features will reduce reflections across all wavelengths while reducing feature pitch can shift the anti-reflective region to the left on the plot [13].

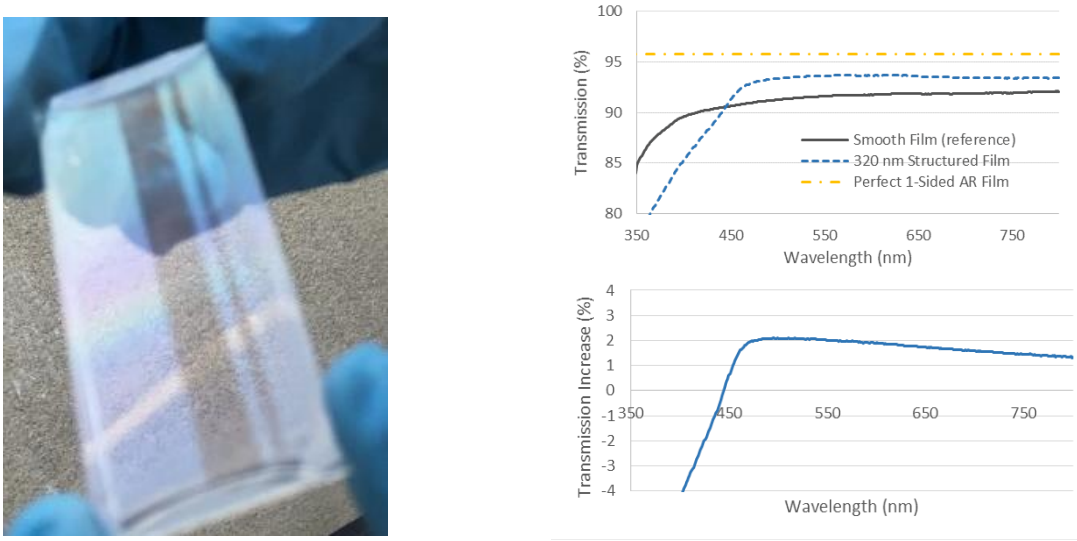

Figure 5: Photos of a nanostructure film demonstrating an anti-reflective strip (left), and a UV-Vis spectroscopy measurement demonstrating the performance of the anti-reflective strip relative to a smooth polymer strip (right).

FUTURE WORK

In the next 3-4 months, work will continue to focus on improving indent depth control and registration and then scaling to 6 inch diameter molds. During scaling, the durability of the diamond die will be assessed through before and after AFM and side-angle SEM measurements.

Further, SMS has begun developing methods to diamond turn then indent thin foils and sleeves. These foils are thin enough to be pressed flat after indenting to make small-area molds for batch imprinting. Once these methods are finished SMS will begin roll-to-roll imprinting with its partner at UMass Amherst and resist imprinting at NC State University.

Over the long term, SMS will begin indenting with new diamond die patterns to prove their use for a broad array of commercial applications.

REFERENCES

[1] G. Tan *et al.*, "Broadband antireflection film with moth-eye-like structure for flexible display applications," *Optica*, vol. 4, no. 7, p. 678, 2017.

[2] Y. T. Cheng, D. E. Rodak, C. A. Wong, and C. A. Hayden, "Effects of micro- and nano-structures on the self-cleaning behaviour of lotus leaves," *Nanotechnology*, vol. 17, no. 5, pp. 1359–1362, 2006.

[3] B. Materials and T. Note, "BMTN-01 : Anti-reflective Coatings in Solar Energy Devices," pp. 1–3, 2011.

[4] T. Chung, S. Y. Lee, E. Y. Song, H. Chun, and B. Lee, "Plasmonic nanostructures for nano-scale bio-sensing," *Sensors*, vol. 11, no. 11, pp. 10907–10929, 2011.

[5] S. H. Ahn, J.-S. Kim, and L. J. Guo, "Bilayer metal wire-grid polarizer fabricated by roll-to-roll nanoimprint lithography on flexible plastic substrate," *J. Vac. Sci. Technol. B Microelectron. Nanom. Struct.*, vol. 25, no. 6, p. 2388, 2007.

[6] M. Michalska *et al.*, "Tuning antimicrobial properties of biomimetic nanopatterned surfaces," *Nanoscale*, vol. 10, no. 14, pp. 6639–6650, 2018.

[7] D. P. Adams, M. J. Vasile, and T. M. Mayer, "Focused ion beam sculpting curved shape cavities in crystalline and amorphous targets Sputtering rate of micromilling on water ice with focused ion beam in a cryogenic environment Focused ion beam sculpting curved shape cavities in crystalline and amorphous targets," *J. Vac. Sci. Technol. B J. Appl. Phys. Appl. Phys. Lett. J. Vac. Sci. Technol. A J. Vac. Sci. Technol. B*, vol. 24, no. 21, pp. 1766–927, 2006.

[8] J. G. Hartley *et al.*, "Quantifying throughput improvements for electron-beam lithography using a suite of benchmark patterns," no. March 2013, p. 86800P, 2013.

[9] T. Nakanishi *et al.*, "Large Area fabrication of moth-eye antireflection structures using self-assembled nanoparticles in combination with nanoimprinting," *Jpn. J. Appl. Phys.*, vol. 49, no. 7 PART 1, pp. 0750011–0750017, 2010.

[10] N. Kooy, K. Mohamed, L. Pin, and O. Guan, "A review of roll-to-roll nanoimprint lithography," *Nanoscale Res. Lett.*, vol. 9, no. 1, p. 320, 2014.

[11] E. Zdanowicz, T. A. Dow, and R. O. Scattergood, "Rapid fabrication of nanostructured surfaces using nanocoining," *Nanotechnology*, vol. 23, no. 41, p. 415303, 2012.

[12] E. Zdanowicz, T. A. Dow, R. O. Scattergood, and K. Youssef, "Nanostructure fabrication on germanium and silicon by nanocoining imprint technique," *Precis. Eng.*, vol. 37, no. 4, pp. 871–879, 2013.

[13] M. Burghoorn *et al.*, "Single layer broadband anti-reflective coatings for plastic substrates produced by full wafer and roll-to-roll step-and-flash nano-imprint lithography," *Materials (Basel).*, vol. 6, no. 9, pp. 3710–3726, 2013.

WAFER SCALE EXFOLIATION OF MONOCRYSTALLINE MICRO-SCALE SILICON FILMS

Martin J. Ward and Michael A. Cullinan
Department of Mechanical Engineering
The University of Texas at Austin
Austin, Texas, United States of America

ABSTRACT

This paper presents the development and simulation of a wafer scale exfoliation process and tool. The method uses an electroplated nickel tensile layer to propagate a crack across a wafer and produce cost-effective single-crystal silicon thin-films with a thickness of between 5 µm and 35 µm across a 4 inch wafer.

INTRODUCTION

Combing highly desirable mechanical properties with CMOS compatibility and high performance, monocrystalline thin-film silicon devices such as flexible solar cells or wearable electronics hold extraordinary promise but have yet to be manufactured in any sort of cost-feasible manner. The process described here is particularly cost-effective compared to other methods of creating thin-film Si, such as etching or mechanical grinding, which further increases the envelope of applications, including flexible solar cells and wearable electronics [1], [2]. Silicon exfoliation involves peeling the top layer off a wafer, including any device built into the surface. This approach has the advantage of leveraging existing semi-conductor fabrication techniques to produce flexible devices while other flexible device manufacturing methods require the development of completely new manufacturing procedures.

The exfoliation process flow developed is shown in Fig. 1. First, seed and adhesion layers are evaporated onto a wafer, on top of any previously fabricated devices. A 10-35 µm layer of nickel is then electrodeposited before a heat treatment process designed to induce a residual tensile stress in the nickel. This stress is just below the threshold for spontaneous exfoliation. Then a specific external load is applied to exfoliate the film while maintaining uniformity and regulating thickness.

PROTOTYPE EXFOLIATION TOOL

Previous versions of this process used a wedge-shaped tool to apply extra stress near the crack front [3]. This produced both friction and vibrations which introduced roughness in the exfoliated surface. Other groups used a tape handle layer to apply a peeling force by hand [4]. When tested, this produced inconsistencies in the load and exfoliation results, but also final surface reduced roughness. To overcome these limitations, a tool that could create controlled peeling loads was proposed.

Design

A prototype, as shown in Fig. 2, that could maintain a constant exfoliation load and displacement constraint was fabricated. The tool was designed to be quickly manufactured and widely configurable to rapidly test different production concepts to aid in the design of a more advanced prototype tool to optimize manufacturing process parameters. The tool features a simple adjustable roller design attached to a linear actuator.

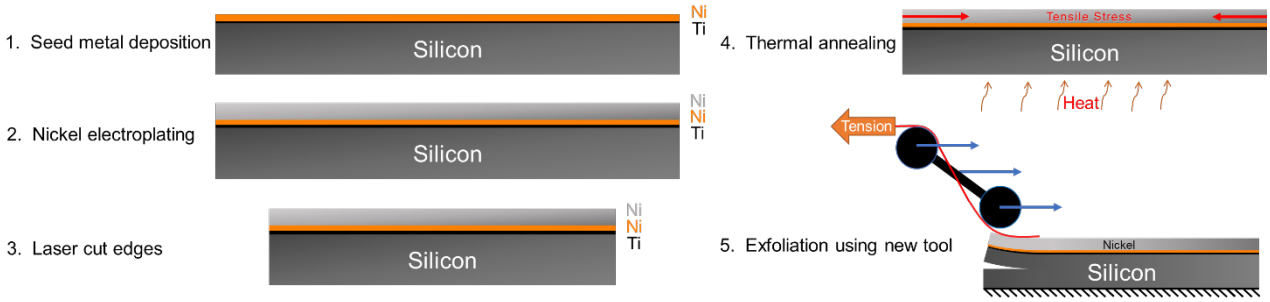

FIGURE 1. Exfoliation process flow

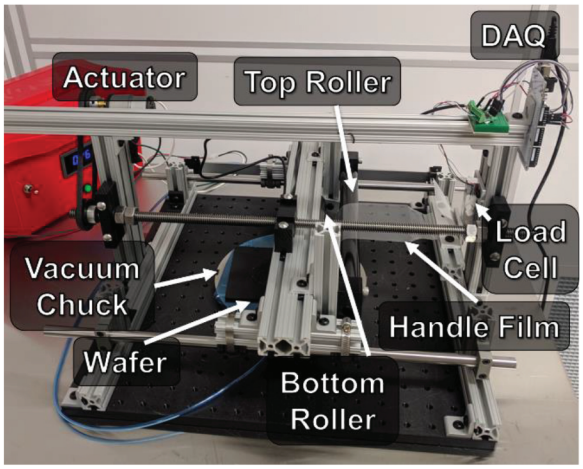

FIGURE 2. Exfoliation tool prototype

The wafer is flattened and adhered to a glass slide with double-sided adhesive polyimide tape and then secured with a vacuum chuck. The glass and tape are necessary because atmospheric air pressure is not sufficient to flatten the wafer which has been bowed by the tensile stress in the nickel. The flattened state creates a repeatable fixturing and helps define the stresses in the system for accurate modeling. A handle film is then attached to the nickel surface with adhesive tape and the two-roller design moves the film across the wafer while maintaining a constant peeling angle and force to propagate the crack front. See Fig. 1 for a side view of the roller configuration. The exfoliation force is controlled by tensioning and clamping the handle film at a set preload which is monitored by a load cell. A linear encoder and edge detection sensor are used to sync load data with profile data measured after exfoliation. A system for actively controlling the handle tension is currently being investigated. Exfoliation speed can be adjusted via the PWM controller of the DC motor driving the leadscrew of the linear actuator. The results shown were performed at a relatively slow speed of approximately 8 mm/min, but a range of speeds is achievable with the tool and are being examined.

Modeling

To better understand the ideal load for the tool to apply, a 2D fracture mechanics model was created. Previous work in the field of thin-film interfacial fracture mechanics indicates that a stable crack path in the substrate, parallel to the wafer surface occurs when the shear mode stress intensity, K_{II}, is equal to zero, and the opening mode stress intensity, K_I, is equal to a critical value, K_{Ic} [5]. It also indicates that there is a characteristic crack depth for a given elastic system. The theoretical system is defined by the material properties of the Si and Ni, the crack length, the film thickness, and the film stress. Analytical solutions from [6], [7] suggest that changing the applied load can skew the mode mix ratio and therefore the characteristic crack depth. An analytical solution to the loading conditions created by the tool was not feasible, so a parametric FEA model was created using ANSYS Fracture Tools that can be run iteratively to solve for the characteristic crack depth. Variation of the inputs was done using adaptive sampling to produce a Kriging metamodel with increased accuracy around the solution. Figure 3 shows response of the crack depth to various system parameters and external loading.

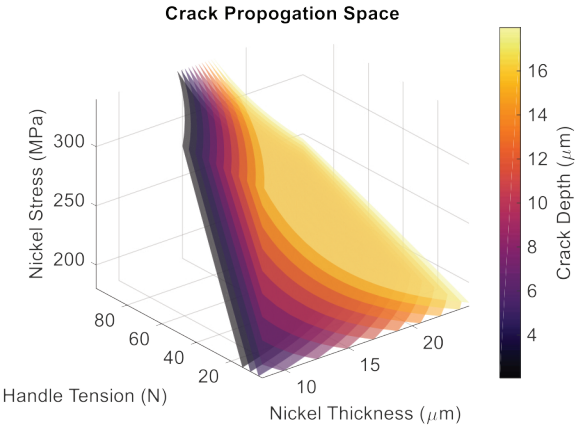

FIGURE 3. Crack propagation space metamodel

The solution reveals some trends in the effect of each input. For example, increasing the tension tends to decrease the crack depth, which compares well to basic fracture theory as increasing tension essentially reduces the edge load created by the nickel. Increasing nickel thickness and nickel stress both drive the crack downward into the wafer. This model can be used to predict the crack depth for a given system.

Metrology

The ability to measure and quantify the produced films is critical to improving the exfoliation processes. Fully characterizing this process requires thickness profile measurements for both the exfoliated film and the electro-deposited nickel across as large an area as possible. A curvature profile is also necessary to define the initial stress state. These measurement requirements present significant challenges due to the necessary vertical resolution, a few microns, and horizontal range spanning the entire 100 mm wafer. The unsupported silicon film is

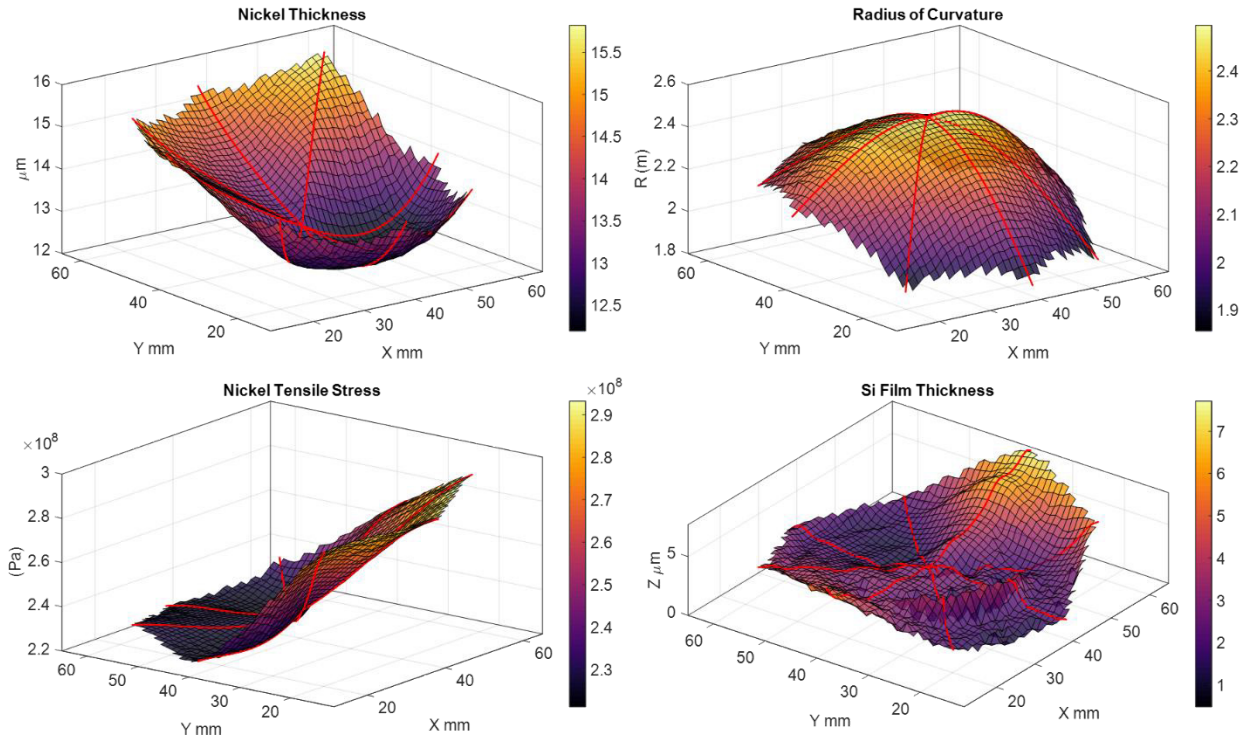

FIGURE 4. Metrology Surface Mapping. Red lines represent actual data, surface gird is a basic interpolation to aid visualization.

also very brittle and can only be handled with a backing layer, thus eliminating all available direct measurement methods. The solution was to use a combination of dual KEYENCE LK-H207K laser displacement sensors for point thickness measurements and an Olympus OLS-4100 confocal microscope for long profile scans to build a complete metrology map. Data processing and synthesis was performed in MATLAB. Confocal line scans were taken between each stage of the process in a radial pattern and then leveled and subtracted from each other to find the film profiles. Point thickness measurements were also taken in a defined grid pattern between stages and combined with the lines scans to create thickness profiles of the Ni and Si films. After the wafer has been processed by thermal annealing another set of lines scans are taken to define the curvature of wafer. The film thickness data, together with the post-anneal curvature profile can be used to estimate the stress state in the nickel using a modified Stoney's equation for (100) silicon wafers [8]. The results for a low crack depth wafer are shown in Fig 4. Correlations between the nickel thickness and nickel stress and the resulting silicon film thickness can be observed in the plots and the broad picture provided by the data will help build the relationship between the film thicknesses and stress state.

RESULTS

Trials using the tool to exfoliate silicon thin-films using four and six inch wafers showed promising results for film thicknesses ranging from 5 to 35 μm. Compared to earlier tests with wedge-style crack propagation tool, usable fabrication area and surface roughness are both improved. Typical film thickness uniformity for a 12 μm thick film exfoliated from a four-inch wafer showed a standard deviation of 2 μm. Table 1 shows an average of 10, 2 x 2 mm roughness measurements taken on one wafer for each type of exfoliation method.

TABLE 1. Average roughness measurements for different exfoliation methods.

	Wedge Tool	Hand Peel	Roller Tool
Ra (nm)	151	107	75.5
Rz (μm)	3.46	1.99	1.15

The exfoliation process is repeatable, but more testing and measurements need to be performed to validate the modeled relationship between inputs and crack depth. Fig. 5 shows an example of a thin-film exfoliated using the prototype tool.

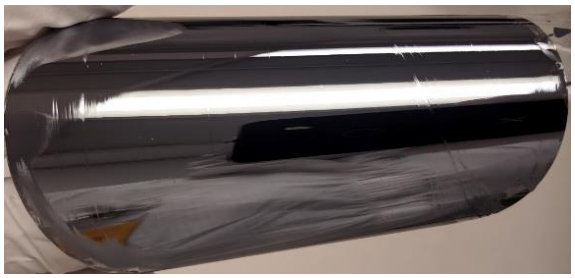

FIGURE 5. Exfoliated film sample. Silicon side up with nickel backing.

Results demonstrating the capabilities of the tool for crack depth control and the model for crack depth prediction are shown in Fig. 6, which compares the predicted crack depth with the measured depth and provides the loading in the form of nickel thickness and stress and handle tension as context.

The model appears to overestimate the effect of the handle tension but follows the nickel thickness and stress trends well. Variation in the actual exfoliated thickness that is not explained by measurements of the nickel thickness or stress maybe caused by imperfections in the tool construction.

Future Work

In the future, a high-performance version of the tool will be designed and built, including an active tension control system. Using this tool an array of experiments will be performed to validate the model throughout the design space. Information from those tests will be used to design and build an optimal tool with precision control over the external loads applied during exfoliation.

CONCLUSION

We have successfully demonstrated an exfoliation process to produce micron-scale single crystal silicon films over a wafer scale area. The construction of the exfoliation tool and model provides the basis for scalable, large-area, monocrystalline thin-film devices.

ACKNOWLEDGMENTS

The authors acknowledge and thank Miaomiao Yang for her experience, effort, insight, and support in accomplishing this work. The authors thank Kirsten Cole Christopherson for her effort in completing these experiments. The authors would also like to thank Liam Conolly, Dipankar Behera, and Cheng Zhao for the informative discussions and technical expertise. This work is based upon work supported primarily by the National Science Foundation under Cooperative Agreement No. EEC-1160494. Any opinions, findings and conclusions or recommendations expressed in this material are those of the author(s) and do not necessarily reflect the views of the National Science Foundation.

REFERENCES

[1] J. Ahn, H. Chou, and S. K. Banerjee, “Graphene-Al2O3-silicon heterojunction solar cells on flexible silicon substrates,” *J. Appl. Phys.*, vol. 121, no. 16, p. 163105, Apr. 2017.

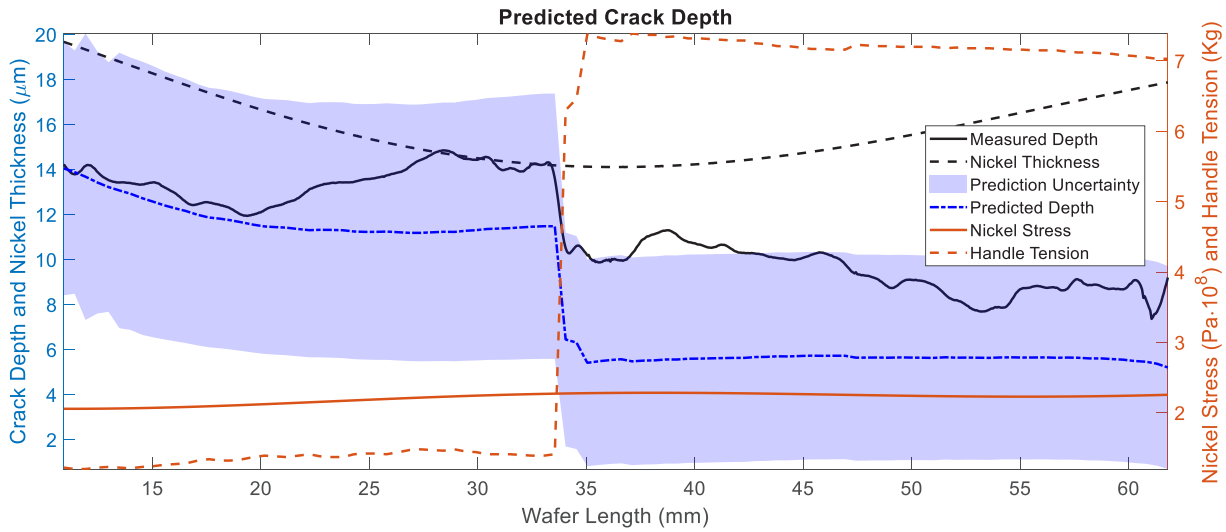

FIGURE 6. Crack depth control and prediction with a step input to the handle tension.

[2] C. Pang, C. Lee, and K.-Y. Suh, “Recent advances in flexible sensors for wearable and implantable devices,” *J. Appl. Polym. Sci.*, vol. 130, no. 3, pp. 1429–1441, Nov. 2013.
[3] R. A. Rao *et al.*, “A novel low cost 25µm thin exfoliated monocrystalline si solar cell technology,” in *Photovoltaic Specialists Conference (PVSC), 2011 37th IEEE*, 2011, pp. 001504–001507.
[4] S. W. Bedell *et al.*, “Advanced flexible electronics: challenges and opportunities,” 2014, p. 90831G.
[5] M. D. Thouless, A. G. Evans, M. F. Ashby, and J. W. Hutchinson, “The edge cracking and spalling of brittle plates,” *Acta Metall.*, vol. 35, no. 6, pp. 1333–1341, Jun. 1987.
[6] Z. Suo and J. W. Hutchinson, “Steady-state cracking in brittle substrates beneath adherent films,” *Int. J. Solids Struct.*, vol. 25, no. 11, pp. 1337–1353, Jan. 1989.
[7] M. D. Drory, M. D. Thouless, and A. G. Evans, “On the decohesion of residually stressed thin films,” *Acta Metall.*, vol. 36, no. 8, pp. 2019–2028, 1988.
[8] G. C. A. M. Janssen, M. M. Abdalla, F. van Keulen, B. R. Pujada, and B. van Venrooy, “Celebrating the 100th anniversary of the Stoney equation for film stress: Developments from polycrystalline steel strips to single crystal silicon wafers,” *Thin Solid Films*, vol. 517, no. 6, pp. 1858–1867, Jan. 2009.

LIMITATIONS CAUSED BY ROUGH SURFACES WHEN USED AS THE MIRROR IN DISPLACEMENT MEASUREMENT INTERFEROMETRY USING A MICROCHIP LASER SOURCE

Kumar Arumugam, Stuart T Smith, and Tsing-Hua Her
University of North Carolina at Charlotte
Charlotte, North Carolina, USA

INTRODUCTION

Microchip lasers (MCL) have potential to provide single frequency, single polarization, and short line-width lasers operating in fundamental transverse mode [1]. If this potential can be realized, these laser sources might be used as the source for an economic displacement interferometer.

The motivation for this study is to investigate limits of the MCL for displacement interferometry involving a moving mirror, flat or cylindrical, that has a substantial surface roughness. The MCL used in this study is Thorlabs CPS532. A Homodyne Quadrature Laser Interferometer [2] (HQLI) (*Figure 1*) was used for this test. Both Bennett and Porteus [3] and Davies [4] have developed theories to assess the reflectance from rough surfaces as a function of surface roughness rms (σ) and wavelength (λ) of the light source used. The theory is applicable to measurements with ratio, $\sigma / \lambda << 1$.

Figure 1 (a) shows a block diagram of the experimental apparatus used in this study. The mirror of the moving arm was either flat or cylindrical, with roughness parameters Sq ranging from 17 to 660 nm, and $S\Delta q$ from 5 to 155 µm·mm^{-1}. To increase the fringe contrast, a telescope lens (Melles Griot 09 LBX 001) was used to focus the laser on to a small spot on the rough surface.

The quadrature signals illustrated in *Figure 2*, are obtained by using a polarizing beam splitter (PBS) to separate the S and P polarization intensities (I_s and I_p), which are measured by the two photodetectors. The locus of the two quadrature signals shown in *Figure 2*, correspond to the phase shift due to the displacement of the moving arm. Ideally this locus should follow a circular path, but due to offsets, amplitude, and phase variations the locus follows an elliptical path.

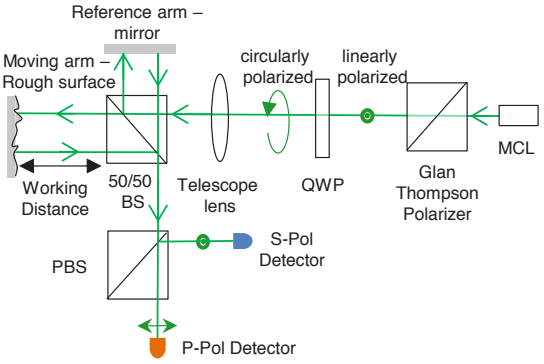

(a)

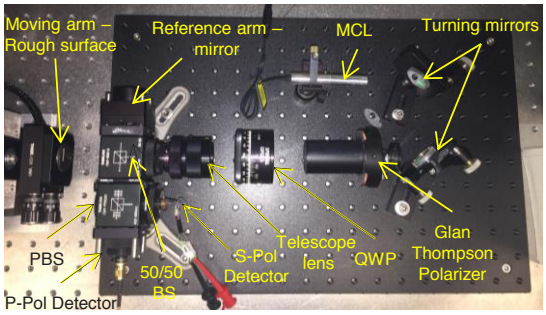

(b)

Figure 1: The homodyne quadrature laser interferometer used in this study: (a) schematic representation, and (b) experimental setup. QWP- quarter wave plate; BS- beam splitter, PBS- polarized beam splitter

These variations are compensated using a real-time nonlinear fit. The phase obtained using the corrected quadrature is unwrapped in real-time to compute the displacement Δz of the target surface given by

$$\Delta z = \frac{\lambda_0}{4\pi}\left[\tan^{-1}\left(\frac{I_S}{I_P}\right) + 2\pi n\right], \qquad (1)$$

where n is the number of complete rotations around the locus and λ_0 is the wavelength of the laser (532 nm).

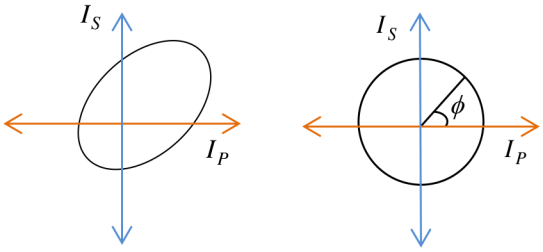

Figure 2: Illustration of Lissajous plots of I_s and I_p as a function of displacement; (a) measured signal, (b) ideal signal after correction

RESULTS

An initial study of microchip laser performance indicated that, under controlled laboratory conditions and using a plane mirror, it is feasible to measure displacements corresponding to pathlength differences of about 20 mm, with noise and stability of few tens of nanometers.

The folowing sections present results of a study to evaluate the effects of roughness and form of the moving mirror on displacement measurement. Both flat and cylindrical surfaces were used for the moving mirror.

Flat Surfaces

To evaluate the influence of surface roughness of the moving arm of a displacement interferometer, the plane mirror (or cube-corner reflector) was replaced by flat, surface-finish comparator blocks or cylinders with known Sq and $S\Delta q$ values. As an example, *Figure 3* shows fringes detected by the photodetectors during a displacement of 5 mm for a flat surface having an Sq = 168 nm and $S\Delta q$ = 40 µm·mm^{-1}.

There are four sets of data in this figure:

1. The two rapidly varying signals were directly acquired from the two detectors. Tens of millions of data points are needed to determine displacements. However, for the purpose of plotting, a large number of data points have been skipped. The apparent beating in this signal is due to the multiple modes in the lasing source with each mode having a wavelength difference of $\Delta\lambda$ = 0.1 nm, see *Figure 4*.

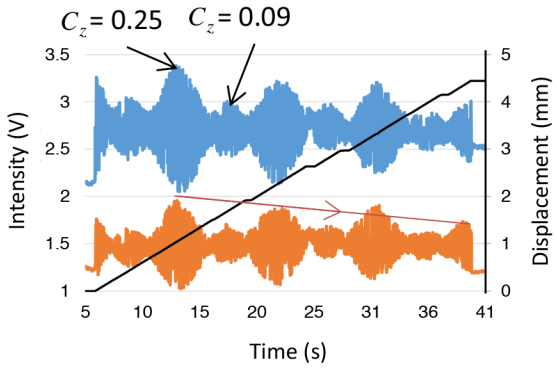

Figure 3: Fringes produced for a displacement of 5 mm (flat surface: Sq = 168 nm and *$S\Delta q$ = 40* µm·mm^{-1})

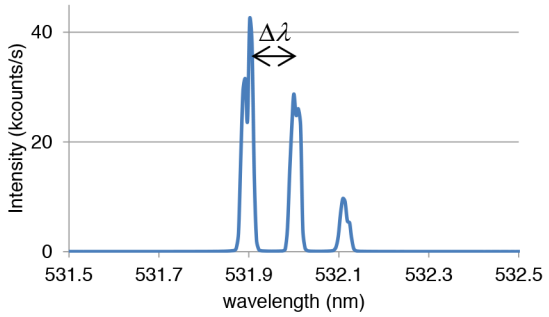

Figure 4: The optical spectrum of the green laser CPS532 measured with LabRam HR800 showing three distinct wavelengths with an approximate difference of $\Delta\lambda$ = 0.1 nm

2. The beating caused by the multiple modes produces local maxiumum contrast (C_z), which varies as a function of the mirror displacement z. This contrast reduces as the roughness of the mirror increases, see *Figure 5*.

3. As the mirror moves away from the focal location of the telescope lens, the contrast of the measured intensity reduces. The envolope of this reducing contrast is shown by the red line.

4. Also shown in *Figure 3* is the measured displacement which indicates 4.61 mm of travel (secondary axis). The actual

displacement of the moving mirror was 5 mm ± 1 μm. This descrepancy is due to loss of contrast caused by the combined effect of multimode beating and scattering from the rough surface.

The loss of contrast occurs when the signal amplitudes are at the minima in the beats. Away from these mimima, for the surfaces evaluated in these studies, the contrast is always sufficient to distinguish the fringes and the measurement errors are considerably reduced in these regions. Consequently by measuring in the higher contrast regions, it is possible to determine displacement with errors within the HQLI and experimental test performance, rather than being dominated by lost fringes. Restricting measurements to within the high contrast regions correspondingly limits displacement ranges to around 0.7 mm to 1 mm. Another influence is the speed of the moving mirror, in this case additional errors occur due to sampling rate limitations of the data acquistion process.

The displacement results are compared with an encoder of 4 nm resolution (Aerotech Npaq A3200 w/ ANT-(25/50)L Stage). The difference in measured displacement between the HQLI and encoder is listed in *Table 1.* The results correspond to four different velocities of the moving mirror, shown as different colors (see key at the bottom of the table).

Table 1: Measured Displacement comparison of the HQLI and the encoder for a single mirror over different displacement ranges and velocities (moving arm mirror Sq *= 168* nm, $S\Delta q$ *= 40.28* μm·mm^{-1}*)*

Disp. (mm)	Difference (μm)			
1	0.49	0.9	2.9	1.98
2	1.33	3.73	7.77	11.48
5	5.63	38.93	63.79	40.33

0.03 mm.s^{-1} 0.1 mm.s^{-1} 0.15 mm.s^{-1} 0.2 mm.s^{-1}

For displacement up to 1 mm and speeds below 0.1 mm·s^{-1}, the deviations are within the experimental uncertainties. At higher speeds the sampling rate effects reduce the resolution. Additionally, for the longer displacements (5 mm) the fringes lost their contrast due to beating of the laser source.

Reduction of Wokring Range of Displacement with Increased Roughness

Figure 4 shows the measured signals for a surface with higher roughness parameters of Sq = 660 nm and $S\Delta q$ = 155 μm·mm^{-1}. The measured displacment is 1.93 mm, whereas the true displacemnt with the encoder is 2 mm ± 1 μm. The high contrast region of signals persist for about 0.7 mm. After this, the contrast becomes so low that the phase information cannot be retrieved.

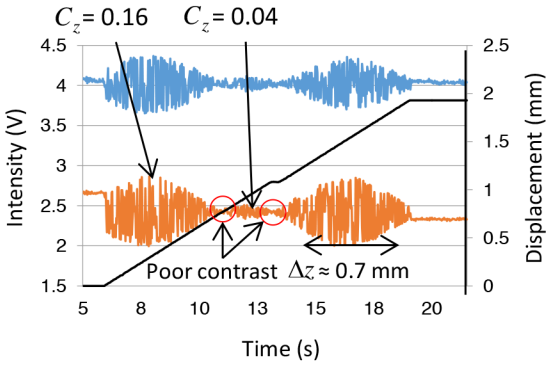

Figure 5: Fringes produced during the displacement of 2 mm (flat surface: Sq *= 660* nm and $S\Delta q$ *= 155* μm·mm^{-1}*)*

Cylindrical Surfaces

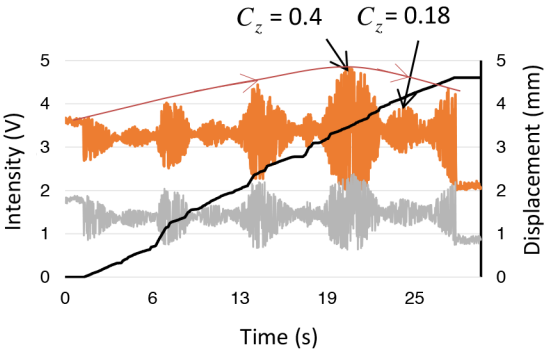

Figure 6: Fringes produced during the displacement of 5 mm (cylindrical surface: Sq *=* 100 nm *and* $S\Delta q$ *=* 52 μm·mm^{-1}*)*

To assess the performance of HQLI with cylindrical surfaces, a polished cylinder of diameter 12.7 mm, Sq = *100* nm, $S\Delta q$ = *52* μm·mm^{-1} was attached to the moving arm.

Figure 6 shows the detected fringes during a displacement of 5 mm. The contrast reduction

(shown in red) due to the focus effect of telescope lens becomes more pronounced by the curved surface from which light is reflected. The highest contrast of C = 0.4 occurs when the spot on the curved surface is at the focal point of the lens. The displacement curve shown in black loses its linearity at the locations where the contrast is not substantial enough to compute the displacement.

Table 2 lists the difference between the displacement measurement of the HQLI and the encoder.

Table 2: Displacement measurement comparison of HQLI and the encoder for a single mirror over various displacement ranges and velocities (moving arm mirror Sq = 100 nm *and $S\Delta q$ = 52* µm·mm-1*)*

Disp. (mm)	Difference (µm)			
1	0.66	1.64	6.9	11.3
2	2.01	5.11	13.6	23.5
5	205.7	176.2	245.7	510.5

0.03 mm.s^{-1} 0.1 mm.s^{-1} 0.15 mm.s^{-1} 0.2 mm.s^{-1}

Difference In Measured Displacement Between HQLI And an Encoder Of All Surfaces Studied

Table 3 summarizes the difference in displacement measurements between the HQLI and the encoder. In these experiments, to explore performance of HQLI in its high contrast regions, flat and cylindrical surfaces of various roughness values were displaced to 0.7 mm or 1 mm with a common velocity of 0.03 mm·s^{-1}. For surfaces with $Sq \geq$ 168 nm, it was necessary to use a telescope lens to overcome the loss of contrast. Without the lens, interference fringes were not visible.

CONCLUSION

This study used a microchip laser as a source to perform displacement measurements on rough surfaces up to Sq = 654 nm and $S\Delta q$ = 204.79 µm·mm^{-1}.

For all the flat surfaces considered, the difference in displacement measured with HQLI and encoder stays below 1.2 µm, for up to a displacement of 1 mm. However, without using the telescope lens, the measurement is limited to a rough surface of Sq = 65 nm and $S\Delta q$ = 11.36 µm·mm^{-1}.

Currently, the displacement measurements were conducted for cylindrical mirrors of diameter ≥ 12.7 mm and surface roughness Sq ≤ 112 nm and $S\Delta q$ ≤ 94 µm·mm^{-1}. The difference in measurement with the HQLI and the encoder is below 1 µm for both these surfaces.

Table 3: Difference in d*isplacement (1* mm *or 0.7* mm*) measurement between HQLI and encoder, moving arm being surfaces with different roughness values*

Sq (RMS)	$S\Delta q$ (µm·mm-1)	Machining process	Form	Range of displacement (mm)	Difference (µm)	Telescope lens used?
NA	NA	Plane mirror	flat	1	0.8	No
17	5	Lapping	flat	1	0.8	No
64	11	Lapping	flat	1	1.2	No
168	40	Lapping	flat	1	0.49	Yes
468	126	Lapping	flat	1	0.70	Yes
660	155	Grinding	flat	0.7	0.32	Yes
100*	52*	Polishing	Cylinder (Dia. 12.7 mm)	1	0.66	Yes
112*	94*	Lapping	Cylinder (Dia. 18 mm)	0.7	0.42	Yes

NA- Not applicable

* Values obtained after removing the cylindricity in the measurement data from Zygo Nexview- SWLI (Scanning White light Interferometer). Software used for cylindricity removal is MX-Zygo.

ACKNOWLEDGMENTSs
We would like to thank Kristen Venditti and Dr. Fan Zhang for their help with surface roughness parameter measurements, and laser spectral measurements repectively.

REFERENCES
[1] J.J. Zayhowski , Microchip lasers, The Lincoln Laboratory journal, 1990; 3: 427-446.

[2] T. Požar , P Gregor˘ci˘c and J Možina, A precise and wide-dynamic-range displacement-measuring homodyne quadrature laser interferometer, Appl Phys B, 2011; 105:575–582.

[3] H. E. Bennett and J. O. Porteus, Relation between surface roughness and specular reflectance at normal incidence, Opt.Soc.Am., 1961; 51: 123- 129.

[4] H. Davies, The reflection of electromagnetic waves from a rough surface, Proc. IEE-Part IV: Institution monographs, 1954; 101(7): 209 – 214.

ULTRA PRECISE MOTION ERROR MEASUREMENT OF ROTATION KINEMATICS FOR THE INTEGRATION IN NANOMEASURING AND NANOFABRICATION MACHINES

Florian Fern[1], Roland Füßl[1], Ralf Schienbein[2], and René Theska[2]
[1]Institute of Process Measurement and Sensor Technology
Technische Universität Ilmenau
Ilmenau, Germany
[2]Department of Precision Engineering
Technische Universität Ilmenau
Ilmenau, Germany

INTRODUCTION

The semiconductor industry has been done an incomparable progress during the last 60 years. With the ongoing reduction of the structure size by new fabrication techniques the nanomeasurement systems have also increased their performance [1]. Besides this development the measurement and fabrication of freeform surfaces, aspheric lenses or high aspect ratio structures are still highly challenging. There are different commercial and scientific approaches to measure on freeform surfaces [2, 3, 4, 5].

NMM-1

The nanomeasuring and nanopositioning machine (NMM-1) with a working volume of $25 \times 25 \times 5\,\text{mm}^3$ and a resolution of 0.1 nm [6], developed at the TU Ilmenau together with SIOS Meßtechnik GmbH, follows the rules of the Abbe comparator principle in all three linear measurement axes of the cartesian coordinate system. Therefore the measuring apparatus has to be arranged in such a way that the distance that should be measured is in a straight-line extension of the used scale. To perform 3D freeform measurement and fabrication techniques without affecting the working volume the NMM-1 is extended by additional rotation kinematics. Those kinematics increase the degree of freedom to five by adding two independent rotational movements whose rotation axes intersect in the so called Abbe point. In a comparison of rotation systems the tool rotation shows the best properties [7] and provides the possibility to orientate the tool in its optimal working angle to the local surface (see figure 1). It consists of a goniometric stage mounted on a rotary stage and is able to address the whole upper hemisphere. The used tools for measurement and fabrication (focus sensor, AFM [8], 2PP[9], FE-SPL[10]) have a punctual interaction with the sample. The point of interaction is called Tool Centre Point (TCP). The system is designed in such way that the TCP is in the Abbe point of the rotation axes and the linear measuring axes. An angular actuation of the ideal system only changes the tool orientation but the TCP does not change its position.

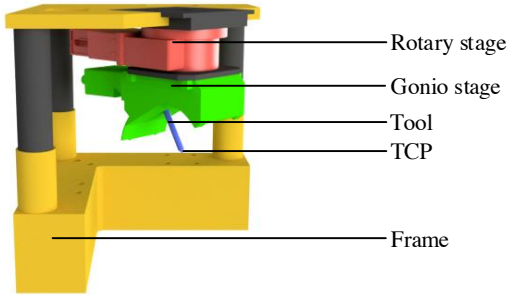

FIGURE 1. Extended nanomeasuring, nanomeasurement and nanofabrication machine with removed corner mirror and linear scanning stage

ERROR MEASUREMENT

The TCP position is directly affected by the motion error of the used rotation stages. Their insufficient movement leads to an additional translational error which has to be known to maintain low uncertainties in measurement and an optimal fabrication result. In the final setup there will be no measurement system which allows to measure the position of the interaction point of the tool directly. With a mounted sensing tool the error motion can not be measured directly and can only be determined by performing a measurement on a well know artefact.

To test the properties of the rotation system like thermal influence, long term stability and other quantities a direct measurement of the TCP shall be done. To provide a metrological traceable measurement result an interferometric measurement is

done. The existing machine infrastructure is used to provide comparable environment conditions.

Plane mirror interferometer
State of the art plane mirror interferometers are used for high precise position and movement measurements. They are based on the original interferometer principle by Michelson. The laser beam is divided by a polarized beam splitter in a reference and a measurement beam. Both beams pass a $\lambda/4$ plate which changes the linear polarization to a circular polarization and are reflected on the reference resp. measurement mirror. After passing the $\lambda/4$ plate again the polarisation has turned by 90°. Since the beams are orthogonal polarized they do not interfer. A third $\lambda/4$ plate polarizes both beams circular. In an evaluation unit the beam is divided again and with additional polarization filters 2 $90°$ phase shifted signals can be used to interpolate and to perform forward backward measurement [11].

Reflectors
For the plane mirror interferometer various reflectors are usable. Since the orientation of the TCP varies, a plane mirror can not be used to measure the distance. Figure 2 shows possible retro reflectors which reflect the incident beam in opposite direction.

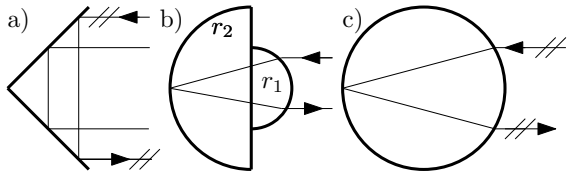

FIGURE 2. Three types of wide range interferometer retro reflectors; a) Corner mirror b) cat's eye reflector c) high index ball

Corner mirror
A corner mirror reflects the measurement beam parallel to the incident beam (see figure 2). The reflection angle is tilt invariant but it provides the smallest acceptance angle of $\pm 45°$.[12] Furthermore a parallel movement of the corner mirror leads to a parallel shift of the reflected beam which is twice the parallel movement. With an reflectance on the mirrors surface of $R_r = 96\%$ the total reflectance R_{tot} is about 88.5%.

Cat's eye reflector
A cat's eye reflector consist of two hemispheres (plane convex lens) with a different radius $r_1 < r_2$. The focal length of the first lens must be equal to the radius of the second lens if both lens have the same refractive index $n_1 = n_2 = n$(see figure 2b).

$$f' = \frac{r_1}{n-1} = r_2 \tag{1}$$

In the paraxial region the light is reflected parallel to the incident light. The achievable acceptance angle is $\pm 60°$. Both hemispheres are contacted by using glue or processes like optical bonding. For most of the applications the hemisphere with r_2 has a reflective coating. Therewith the total reflectance can be calculated with $n = 1.5$.

$$R_{total} = R_T\, R_R\, R_T = 80\%$$

With an anti-reflective coating on the smaller hemisphere the total reflectance can be further increased.

HIGH INDEX BALL
The geometric parameters of a cat's eyes reflector are directly influenced by the refractive index. With an refractive index of $n = 2$ equation 1 leads to $r_1 = r_2$. A sphere can be used as a reflector which can be manufactured more precisely. So called high index balls are already used as interferometer reflector in different ways. For a HE-NE laser based interferometer OHARA S-LAH79 glas with an n=1.99613 refractive index can be used.

TABLE 1. Material properties for OHARA S-LAH79 Glas

Material Properties	
Refractive index (HE-NE)	1.99613
Diameter	10 mm
Thermal expansion	$6 \cdot 10^{-6} m/m\,K$
Transmission (650 nm)	0.998

For most of the interferometric measurements (e.g. laser tracer) one hemisphere of the ball is coated to increase the reflected light. However, with limiting the acceptance angle of the reflector. The acceptance angle can be increased by using an uncoated high index ball to $\varphi_z = 360°$ and $\varphi_x = 360°$. With a reflectance of $R = 11\%$ the total reflectance is reduced to:

$$R_{tot} = R\,(1-R)^2 = 8.7\%$$

An optimal theoretical coating with $R = 0.33\%$ would lead to a maximal $R_{tot} = 14.3\%$. Due to high manufacturing issues coating a sphere uniformal this solution is not further examined. Based on the wide range the high index ball is further examined to perform the measurement[13].

Parallel shift

A parallel shift of the reflector s leads to shift of $2\,s$ of the reflected beam. Additionally, the intensity profile of the laser is Gaussian distributed. A shift of $1/4$ of the beam diameter decreases the intensity to 50% of the reflected intensity of R_{tot}. The intensity of the reflected beam decreases drastically between $1/4\,D$ and $1/2\,D$.

Optical Path

Since the high index ball is used for an interferometric measurement, the optical path must be taken into account. Since the sphere is rotationally symmetric the calculation are simplified to a two dimensional problem. In the par axial area the distance h between the optical axis does not have an influence on the measured optical length. For

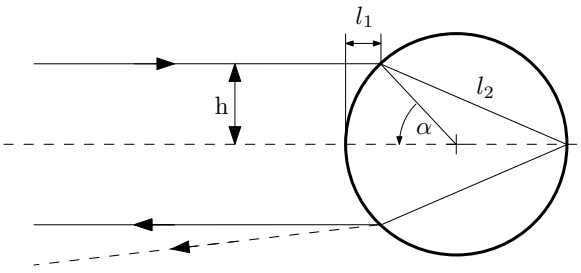

FIGURE 3. Optical path of a ray in the distance h to the optical axis; - - - reflected divergent beam —— ideal reflected beam; l_1

a beam diameter of 1 mm and a sphere radius of 5 mm the optical path length L is directly affected by the distance to the optical axis.

$$\begin{aligned} L_{path} &= 2\,l_1 n_2 + 2\,l_1 n_1 \\ l_1 &= r - \cos(\alpha) r \\ l_2 &= \sqrt{(2r - l_1)^2 + (\sin(\alpha) r)^2} \end{aligned} \tag{2}$$

The difference in the optical path length leads to deformation of the wavefront, which influences the interferometer.Beside this difference , the reflected beam is not perfectly parallel to the incident beam and shows a divergence γ, which can be expressed analytically[14] (see equation 3).

$$\gamma = 4 \arcsin\left(\frac{h}{r\,n}\right) - 2 \arcsin\left(\frac{h}{r}\right) \tag{3}$$

For a distance $h = 0.5\,\text{mm}$ the divergence $\gamma = 0.2\,\text{mrad}$. That would lead to a difference in the path length difference of 2.5 nm at a distance of 150 mm. So the wavefront changes with the diameter of the beam, the distance between interferometer and sphere.

Interferometer

To improve fringe counting the plane wave interferometers have an aperture ($D = 1\,\text{mm}$) before the evaluation unit. The aperture allows for evaluate the fringe pattern up to the point where a whole period, (minimum and maximum) passes the aperture. At this point the interferometer contrast theoretically (see equation 4) drops to zero[15] and leads to an interrupt of the measurement.

$$C = \frac{I_{max} - I_{min}}{I_{max} + I_{min}} \tag{4}$$

Since there is even under best conditions just a reflectance of 8.7% the contrast is already low. The amplitude controller of the interferometer corrects the offset and the amplitude difference to perform a demodulation for slow changes. As explained above the wavefront returned from reflector is not plane any more. That leads to a complex interference pattern which has to be interpreted. Using equation 2 for a perfect perpendicular reflected beam the path length difference L_{path} is about 30 nm. A parallel shift of the reflector increases the distance h and increases the path difference. For shift of 300 µm the path difference is about 300 nm. That leads, combined with the incomplete illumination, to an break down in the fringe counting. The high index ball retro reflector can therewith be used to perform high resolution interferometric measurements if the parallel shift is kept low.

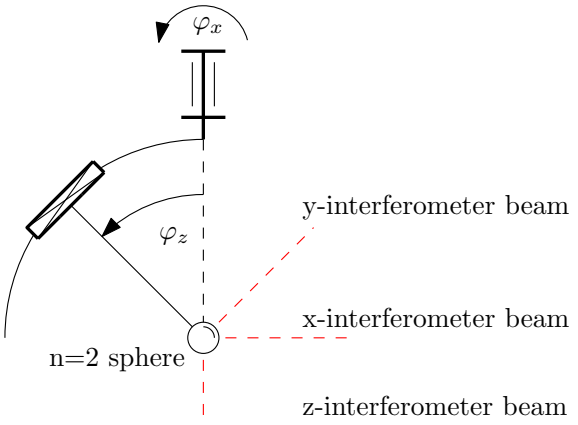

FIGURE 4. Experimental setup for the high index ball measurement. With the actuation angles φ_x and φ_z

MEASUREMENT SETUP

As explained, the TCP of the utilized tool is affected by the bearings error motion. Those effects

are charcterized by ameasurement which is done under the same measurement conditions as they occur in the machine. Therefore the measurement stage of the NMM-1 with the mirror corner is removed so that the measurement beams cross in the TCP. The tool is replaced with a reflector tool for interferometric measurement. It consists mainly of the described high index ball on a shaft. So the change of the position of the sphere caused by an actuation can be measured directly. Since the roundness deviation of the sphere is much higher then the needed accuracy of the DOF=5 extended NMM-1 a measurement of the repeatability of the single positions is performed. The index tool can be moved relative to the goniometer stage in x-, y-, z-direction to bring the sphere centre to the intersection point of the rotation axes. The distance between the rotation axis of the rotational stage and the rotation axis of the goniometer d is fixed and can not be changed.

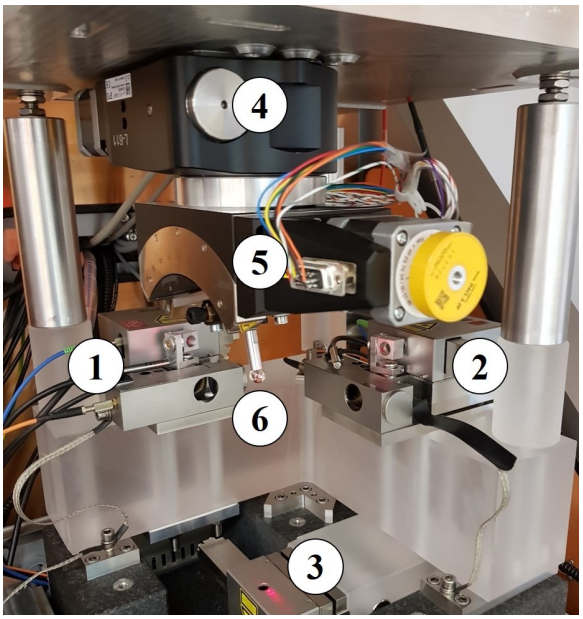

*FIGURE 5. Experimental setup for the high index ball measurement - NMM-1 with an additional rotation unit and removed 3D- mirror corner; **1** x-interferometer, **2** y-interferometer, **3** z-interferometer, **4** rotary stage, **5** goniometer stage, **6** index tool*

measurement results

The repeatability of the kinematic system has been observed with a long time measurement of ten repetitions over ten hours. Thereby the goniometer stage angle is changed between 30° and 60° in steps of 5° and the rotation stage turns between 0° and 360° in steps of 30°. At each step the measurement take one 60 s.To avoid reverse play and therewith increasing uncertainty each position is reached every time from the same direction of actuation. Figure 6 shows, the x-y-z- position of the sphere. The sphere is adjusted in the 45° position of the goniometer in such way that the roundness deviation for a 360° rotation of the rotation stage is minimal. An actuation of the goniometer leads therewith to additional excentricity with $e = d\cos(\alpha_{gon} - 45°)$. Which can be seen in the increasing diameter of the error motion in figure 6. The temperature has been controlled to fixed value with two level system. The laboratory is at 22.0 °C and the climate chamber is stabilized to 22.4 °C with an circulation cooling system. The

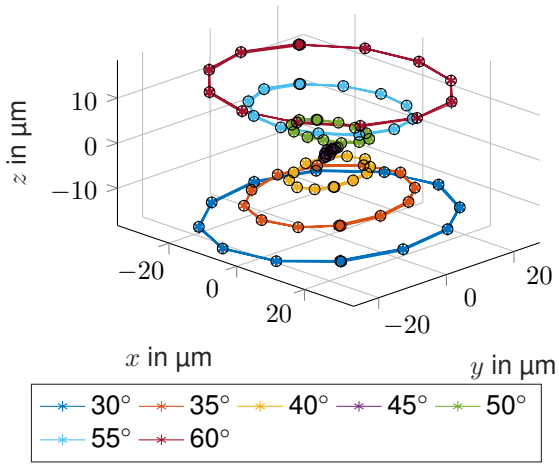

FIGURE 6. Measurement results of the x-y-z position of the TCP for ten repetitions. Seven different actuation angles of the goniometer stage.

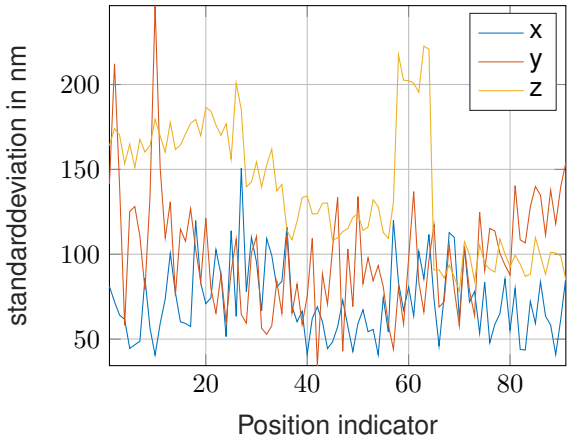

FIGURE 7. Measurement results of the x-y-z position of the TCP for ten repetitions

standard deviation of all 91 different position is calculated for the ten measured repetitions in x, y and z-direction separately (see figure 7). In the

the x- and y- direction the standard deviation is between 50 nm and 100 nm. For the z-direction it is slightly higher between 100 nm and 150 nm for certain positions. This might depend different thermal expansion coefficients for the directions or a load dependent behaviour of the complete system.

CONCLUSION AND OUTLOOK

A new method for high precise position measurement using a high index retroreflector has been succsessfully developed, implemented and used to characterize a high precision rotation system used in a new DOF=5 nanomeasuring system. The repeatability of the TCP position is determined with a standard deviation of maximal 100 nm. Based on those principle the influence of the actuation speed and other quantities can be examined.To improve the ability for an absolute measurement the sphere topology must be further examined, or a second interferometer for a differential measurement must be used.

ACKNOWLEDGEMENTS

The authors gratefully acknowledge the support by the Deutsche Forschungsgemeinschaft (DFG) in the framework of Research Training Group “Tip- and laser-based 3D-Nanofabrication in extended macroscopic working areas” (GRK 2182) at the Technische Universiät Ilmenau, Germany.

REFERENCES

[1] Manske E, Füßl R, Mastylo R, Vorbringer-Dorozhovets N, Birli O, Jäger G. Ongoing trends in precision metrology, particularly in nanopositioning and nanomeasuring technology. tm - Technisches Messen. 2015;82(7-8).

[2] Cho SJ, Ahn BW, Kim J, Lee JM, Hua Y, Yoo YK, et al. Three-dimensional imaging of undercut and sidewall structures by atomic force microscopy. The Review of scientific instruments. 2011;82(2):023707.

[3] Hopkins JB. The Effect of Probe Tilt Angle on the Quality of Scanning Tunneling Microscope Measurements [Bachelor Thesis]. Massachusetts Institute of Technology. Boston; 2005.

[4] Schuler A, Weckenmann A, Hausotte T. Setup and evaluation of a sensor tilting system for dimensional micro- and nanometrology. Measurement Science and Technology. 2014;25(6).

[5] Petter J, Berger G. Non-contact profiling for high precision fast asphere topology measurement. In: Lehmann PH, editor. Optical Measurement Systems for Industrial Inspection VII. Proceedings of SPIE;. p. 878819.

[6] Manske E, Hausotte T, Mastylo R, Machleidt T, Franke KH, Jäger G. New applications of the nanopositioning and nanomeasuring machine by using advanced tactile and non-tactile probes. Measurement Science and Technology. 2007;18(2):520–527.

[7] Schienbein R, Theska R, Weigert F. A contribution to the implementation of ultraprecision rotations to multiaxial nanopositioning machines. Ilmenau; 12.09.2017.

[8] Manske E, Jäger G. Multi-sensor Approach for Multivalent Applications in Nanometrology. International Journal of Automation and Smart Technology. 2012;2(2):141–145.

[9] Weidenfeller L, Schienbein R, Reinhardt C, Kirchner J, Manske E. Development of laser positioning system of high accuracy in the nanometer range. In: Proc. SPIE 10544, Advanced Fabrication Technologies for Micro/Nano Optics and Photonics XI; 2018. .

[10] Rangelow IW, Ahmad A, Ivanov T, Kaestner M, Krivoshapkina Y, Angelov T, et al. Pattern-generation and pattern-transfer for single-digit nano devices. Journal of Vacuum Science & Technology B, Nanotechnology and Microelectronics: Materials, Processing, Measurement, and Phenomena. 2016;34(6):06K202.

[11] Büchner HJ, Jäger G. A novel plane mirror interferometer without using corner cube reflectors. Measurement Science and Technology. 2006;17(4):746–752.

[12] Franziska Bernhart. Weitwinkelreflektorsysteme; 14.10.2010.

[13] Nakamura O, Goto M, Toyoda K, Takai N, Kurosawa T, Nakamata T. A laser tracking robot–performance calibration system using ball–seated bearing mechanisms and a spherically shaped cat's–eye retroreflector. Review of Scientific Instruments. 1994;65(4):1006–1011.

[14] Miroslav Sulc. High index glass spherical targets for laser interferometry;.

[15] John K, Theska R, Manske E, Büchner HJ. The influence of polarisation changes introduced by deflecting elements to interferometric measurements. Shaping the future by engineering : 58th IWK, Ilmenau Scientific Colloquium, Technische Universität Ilmenau, 8 - 12 September 2014 ; proceedings. 2014;.

REPRESENTING THE SPECIFICATION OF INDUSTRIAL X-RAY COMPUTED TOMOGRAPHY WITH AMPLITUDE–WAVELENGTH SPACE

Herminso Villarraga-Gómez[1, 3], Lars Körner[2], Richard Leach[2], and Stuart T. Smith[1]
[1]Center for Precision Metrology, University of North Carolina at Charlotte, NC, USA
[2]Manufacturing Metrology Team, University of Nottingham, Nottingham, UK
[3]Nikon Metrology, Inc., Brighton, MI, USA

INTRODUCTION

With its main advantage being the ability to perform nondestructive measurement of parts' internal features, X-ray computed tomography (CT) is becoming established in the field of dimensional metrology [1-5]. The current approach being applied by ISO working group 213, to allow comparison of CT with other traditional measuring systems, such as tactile coordinate measuring machines (CMMs) or optical measuring instruments, is that its metrological performance should be quantified using verification tests that resemble some common features of the current standardized techniques, such as those in ISO 10360 part 2 [6-7]. The VDI/VDE 2630-1.2 guidelines [10] are an example of an approach that is designed to extend the ISO 10360 series to the field of X-ray CT metrology. But trying to implement CT verification tests as an extension of the ISO 10360-2 series, which were originally developed for tactile CMMs, presents several challenges, particularly because the physical principles of CT operation differ substantially from those of CMMs. Depending on the different types of interaction between the measuring sensor and the surfaces of the workpiece being measured, each technique has its own distinctive attributes that impact their capabilities and range of applications.

It is also necessary to compare the performance of instruments that have similar measuring capabilities but different operating principles. This has been achieved for CT systems by performing inter-laboratory comparisons [11-13], and additionally by testing a variety of calibrated workpiece artifacts and performing comparisons against CMM measurements, e.g., see [2, 8, 14-21]. It would be useful to have a single method that compares X-ray CT against the performance of other measurement technologies. Having such a method would also ease the choice of which instrument type to use in given situations. Fortunately there is a method to create such a comparison devised in the 1970s. The performance limits associated with each technique, in terms of their ability to measure surfaces, can be illustrated by using an amplitude-wavelength (AW) map or 'Stedman diagram' [22-26], a technique that creates a polygonal area enclosing the working capabilities of a measurement instrument for surfaces modeled as ideal sinusoids of varying amplitude A and wavelength W. Following the framework developed by Stedman, this paper proposes to map X-ray CT instrument performance to AW space. The general process is illustrated in Figure 4. To build the AW space, four key parameters are needed, which describe the maximum component size and the achievable resolution in all axes of operation. Due to the historic link to surface metrology, the range and resolution are evaluated in two directions. The naming for those two directions are amplitude and wavelength, i.e., A and W. Based on the naming convention of Stedman, those two directions have further associated names: horizontal for the wavelength direction and vertical for the amplitude. While this separation is often needed for other surface and dimensional metrology systems, in X-ray CT this separation of the principal directions can essentially be ignored. This assumption relies on the feature sizes being representative of a cubic volume that is isotropic in all aspects. Thus, for derivation of the AW space, the value for the parameters describing the horizontal and vertical directions are equal.

RANGE LIMITS, R_{v} AND R_{h}

The range limits of the maximum component size (R_{v} and R_{h} for the vertical and horizontal directions respectively) are set by estimating the maximum measuring range that can be covered by industrial X-ray CT instruments operating at source voltages ranging from 20 kV up to 450 kV, which is typically the range covered by current microfocus CT technologies. Although the energy spectra emitted by X-ray tube sources are inherently polychromatic, the penetration depth of the X-ray beam into a material can be estimated in terms of its effective energy E_{eff} [27]. Assuming

a narrow and quasi-monochromatic beam of energy E_{eff} passing through a slab of homogeneous material of density ρ, the attenuation of intensity in the X-ray beam can be described by the Beer-Lambert law:

$$I(x) = I_0 \cdot e^{-\mu \cdot x}, \qquad (1)$$

where I_0 denotes the intensity of the incident X-ray beam, $I(x)$ the intensity of the beam after passing through a length x within the slab, and μ the linear attenuation coefficient of the slab's material. The linear attenuation coefficient is expressed in inverse length units (cm^{-1}), but instead of μ, the mass attenuation coefficient $\mu_m = \mu/\rho$, with ρ the density of the absorber material, is more commonly found in current databases. The mass attenuation coefficient is energy and material dependent, i.e., $\mu_m = \mu_m(E, Z_{eff})$, where E represents the energy of the incident radiation and Z_{eff} the effective atomic number of the material. Therefore, for a given material of density ρ, the attenuation coefficient $\mu = \rho \cdot \mu_m(E, Z_{eff})$ is also dependent on the X-ray beam energy that passes through it and the material composition.

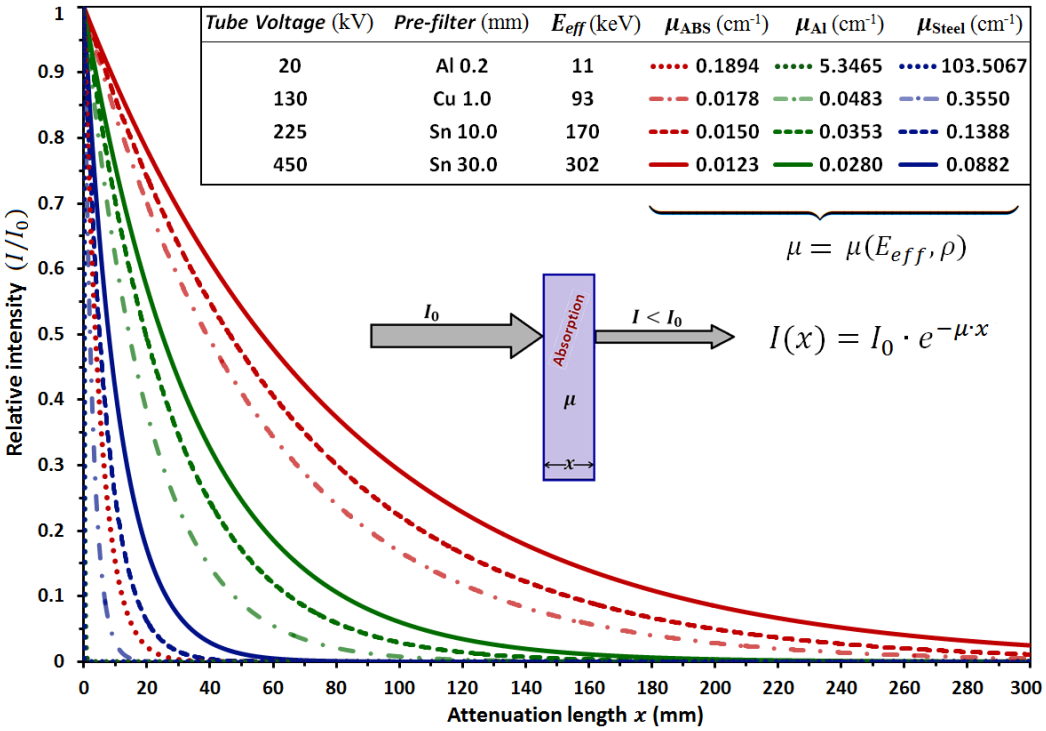
Tube Voltage (kV) | Pre-filter (mm) | E_{eff} (keV) | μ_{ABS} (cm^{-1}) | μ_{Al} (cm^{-1}) | μ_{Steel} (cm^{-1})
20 | Al 0.2 | 11 | 0.1894 | 5.3465 | 103.5067
130 | Cu 1.0 | 93 | 0.0178 | 0.0483 | 0.3550
225 | Sn 10.0 | 170 | 0.0150 | 0.0353 | 0.1388
450 | Sn 30.0 | 302 | 0.0123 | 0.0280 | 0.0882
$\mu = \mu(E_{eff}, \rho)$
I_0
Absorption
μ
x
$I < I_0$
$I(x) = I_0 \cdot e^{-\mu \cdot x}$
Relative intensity (I/I_0)
Attenuation length x (mm)

FIGURE 1. Attenuation curves for X-ray beams of different energies (as listed in the inset box), under the assumption of monochromaticity, when they pass through a length x in homogeneous materials of different types: ABS (acrylonitrile butadiene styrene), aluminum (Al), and steel 316L.

Figure 1 shows the attenuation curves associated with X-ray beams of different energies E_{eff} passing through a length x in homogeneous materials of different types. For simplicity, in lieu of using a polychromatic simulation, a monochromatic computation is presented here. The full spectrum of the incident photons from the tungsten X-ray tube is simplified to a beam of photons all having the same energy. The effective energies E_{eff} used for the computations of the attenuation curves are shown in Figure 1, and were calculated by using a recently developed simulation tool that, based on interpolating cubic spline polynomials, computes the spectra generated by tungsten target X-ray tubes [27]. The input quantities required to run the simulation are tube voltage, pre-filtration thickness, and the type of filter material. The third column of the inset table of Figure 1 shows four effective energy results E_{eff} that correspond to tube voltages of 20 kV, 130 kV, 225 kV, and 450 kV, with different combinations of hardware pre-filtration. Using these energy values E_{eff}, the attenuation coefficients μ of acrylonitrile butadiene styrene

(ABS), aluminum (Al), and steel were computed using data for the mass attenuation coefficient μ_m from the NIST database XCOM [28]. With these attenuation coefficients μ, the curves shown in Figure 1 were computed by using Eq. (1). Based on these results, the limits R_v and R_h fall into the 300 mm range for polymer materials. But as can also be seen in Figure 1, this range is smaller for workpieces made of metals, such as aluminum, and would be much smaller for heavy metals, such as steel alloys, nickel compounds, and cast iron materials. Thus, depending on the material composition and the maximum material thickness of the part, the maximum component size can be significantly smaller. An important feature of this assumption is that the penetration depth of X-rays is the limiting dimension of the CT technique, whereas the bounding dimensions of the component are often limited by the detector size. Therefore, it is also worth noting that the limits of R_v and R_h may be further restricted by the physical size of X-ray detectors, which in cone-beam acquisition setups—considered as an efficient configuration for volumetric CT—correspond to a flat planar detector.

RESOLUTION LIMITS, r_v AND r_h

The notion of the different resolutions is a heavily debated topic in X-ray CT, e.g., see [7, 29-38]. Thus, the selection of the figure of merit for the resolution limits (r_v and r_h for the vertical and horizontal directions respectively) is critical. Part of the ongoing debate on resolution, is the differentiation between measurable (metrological) 'structural resolution' and 'spatial resolution'. The spatial resolution, also named high-contrast resolution, is concerned with the resolving power on the grey-scale image/volume. It is defined by the modulation transfer function (MTF), which is a measure of how a system attenuates the amplitude of different spatial frequencies of the captured object during the imaging process. The left side of Figure 2 pictorially models the point spread function (PSF) response for a single pixel during the CT imaging process. The absolute value of the Fourier transform of the PSF gives the MTF, which is a direct and quantitative measure of the CT system's ability to transfer contrast at a particular spatial resolution through the imaging chain from the object to the image. There are a variety of CT configurations that can be used to achieve different spatial resolutions—in ranges from millimeters to nanometers (i.e., sub-micron level)—and fit different applications, e.g., see [4, 39]. In general, although the spatial resolution of CT scanning is limited by the size of the focal spot emanating the X-rays, nanometer resolutions can be achieved in the lower energy range with synchrotron X-ray sources or with the help of focusing elements, such as Fresnel zone plates or Kirkpatrick-Baez mirrors (e.g., see [39-42]).

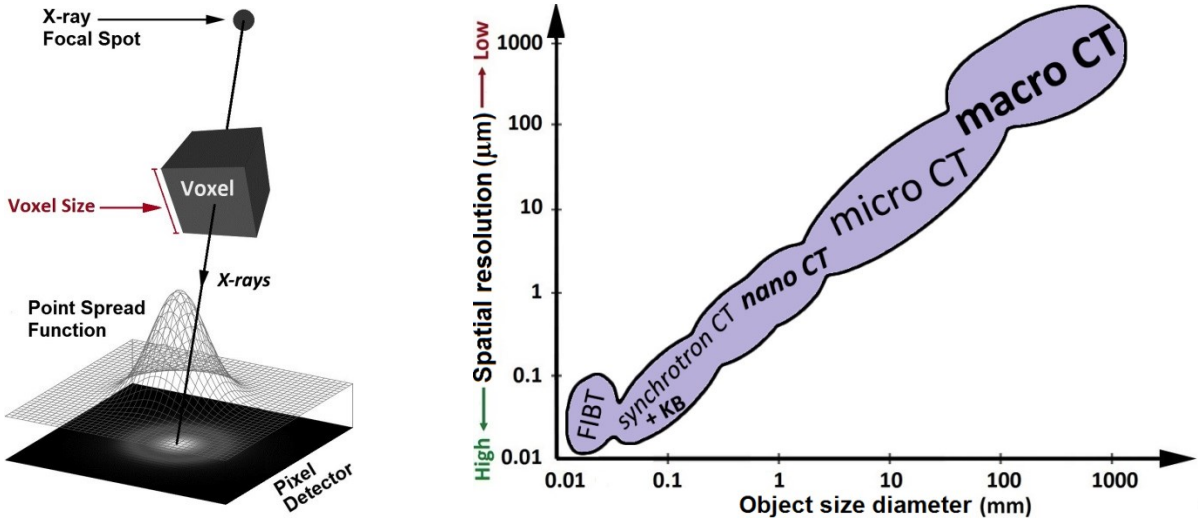

FIGURE 2. Left: Schematic representation of the point spread function (PSF) response for a voxel/pixel detection during CT aqcuisition. The Fourier transform of the PSF gives the MTF. Right: Typical spatial resolutions that are achievable by multi-scale CT as a function of sample size (based on [1, 4, 42]): conventional CT or macro CT (>10 µm), micro CT (currently >3 µm), nano CT (currently >0.4 µm), synchrotron CT (currently >0.2 µm), synchrotron CT with Kirkpatrick–Baez mirrors (currently >0.04 µm), and focused ion beam tomography (FIBT, currently >0.01 µm).

The right side of Figure 2, for example, depicts the typical spatial resolutions (as a function of sample size) achievable by current technologies of multi-scale CT. However, this high-contrast resolution does not capture the entirety of a measurement process for metrology tasks that involve high dimensional accuracy. In the current state of the art of dimensional metrology, the uncertainties associated with measurements of length are typically in the range of a few to several tenths of micrometers [1, 11-13]. It is actually the concept of 'structural resolution' that defines the size of the smallest structures that can be measured dimensionally. The concept of structural resolution necessarily includes the entire measurement chain—including the surface determination stage [1]. Approaches to measure the structural resolution of X-ray CT metrology systems have been proposed by several institutions. All proposed methods require a dedicated artifact. Some artifacts aiming to create a surface texture of known spatial frequency spectrum have been investigated elsewhere [32, 34-37, 43]. While these methods can help with understanding how spatial frequencies will be transmitted through the measurement chain, different figures of merit can be obtained from those transfer characteristics. Other artifacts are based on obtaining a value for the smallest radius/diameter that can be measured. Here, concepts include the use of sharp edges, and evaluate how the measurement chain will approximate it as a radius, or to study the smallest sphere for which a diameter can be computed. The two-spheres (or 'Hourglass') method is another way to determine structural resolution [7, 31], see Figure 3. In this method, the interface of two spheres is measured using CT. If the interface is measured using a measurement system of infinite resolution, the contact area measured should be equal to the Hertzian contact area. However, the measurement chain will degrade this interface, and the contact area can be approximated by knowing its diameter and height values. Given that the theoretical Hertzian contact area can be shown to be less than a nanometer [31], length of the interface diameter can be considered an appropriate estimation of the metrological structural resolution, i.e., the smallest measurable feature. Several values with different levels of error margin in each resolution assessment are reported elsewhere [31], showing that, by using a modern microfocus CT system with an acceleration voltage of 210 kV, the limiting structural resolution (the CT interface of two spheres)—at the highest magnification—can be considered to be around 10 µm.

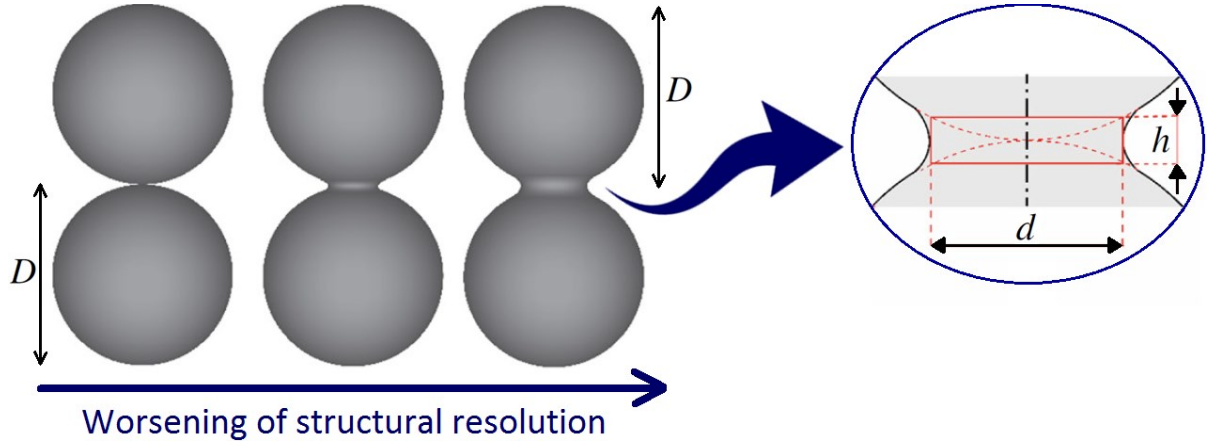

FIGURE 3. The two-spheres (or 'Hourglass') *method for evaluating the metrological structural resolution in dimensional CT [7, 31]. A worsening of the structural resolution will affect the measured interface of the two interfacing spheres with diameter D. The approximated interface region can be described by two parameters, the height of the interface region h and the apparent diameter of the interface d. Hence, when the resolution of the measurement system worsens, the measured interface diameter will increase.*

In the calculations in this work, the metrological structural resolution has been used as the resolution limits (r_v and r_h)—as opposed to the high-contrast resolution, as the structural resolution represents the entire measurement chain. While the resolution is affected by many system and operator variables, this paper uses numerical values for r_v and r_h that approach the most ambitious values of structural resolution for X-ray CT dimensional metrology that are reported in recent literature [31], i.e., 10 µm. However, the authors of this paper are aware that these are

optimistic values, which might not be achievable for all combinations of materials, component size, and resolution and system setups. With these considerations, this paper proposes to use the smallest and most optimistic interface radius of the hourglass approach ($R_{\min}$) as the resolution limit of X-ray CT in AW space to cover a large-range of metrology inspection applications that could be performed with X-ray CT. Since the smallest achievable interface diameter that can be measured in the hourglass artifact, according to recent literature [31], is of the order of 10 μm, the proposed value of $R_{\min}$ for the calculations of the AW space presented in this paper equates to 5 μm. The calculations following Stedman also require a largest radius measurable by the instrument. The authors assume that there are no limitations on the ability of measuring flat surfaces when using CT, except, perhaps, by the presence of cone-beam (or Feldkamp) artifacts, which generally can be minimized by tilting the measuring object with respect to the CT rotating axis [1]. Therefore, in the derivation of the AW space presented below, $R_{\max}$ was set to an arbitrary large value.

THE AMPLITUDE–WAVELENGTH MAP

Based on Fourier analysis, and for mathematical convenience, surface profiles can be modeled as a superposition of ideal sinusoids of the form,

$$y_n = A_n \cdot \sin(2\pi x/W_n), \quad (2)$$

where A_n and W_n are their amplitudes and wavelengths respectively. Surface slopes and curvatures can be derived by first and second order derivatives, respectively, i.e.,

$$S = \frac{dy_n}{dx} = \left(\frac{2\pi A_n}{W_n}\right) \cdot \cos(2\pi x/W_n), \quad (3)$$

$$C = \frac{d^2 y_n}{d^2 x} = -\left(\frac{4\pi^2 A_n}{W_n^2}\right) \cdot \sin(2\pi x/W_n). \quad (4)$$

In equations (3) and (4) the maximum slope $S_{\max}$ and minimum radius of curvature $R_{\min}$ occur at

$$S_{\max} = 2\pi A_n/W_n, \quad (5)$$

$$1/R_{\min} = 4\pi^2 A_n/W_n^2. \quad (6)$$

To cover a wide-range of values of A_n and W_n, the AW mapping [22-25] was originally designed to be a log-log plot. Therefore, by taking the logarithms of Eqs. (5) and (6), the straight lines of constant maximum slope $S_{\max}$ and constant minimum radius $R_{\min}$ that restrict the operating envelope of the AW space can be created. More specifically,

$$\log A_n = \log(S_{\max}/2\pi) + \log W_n, \quad (7)$$

$$\log A_n = \log(1/4\pi^2 R_{\min}) + 2 \cdot \log W_n, \quad (8)$$

are restricting boundaries of the AW polygonal area enclosing the working capabilities of a measurement instrument that is presumed to measure surfaces modeled by Eq. (2), and subject to the additional restrictions $R_v > 2A_n > r_v$ and $R_h > W_n > 2r_h$, see Figure 4. In Figure 4 (left), for the case of X-ray CT metrology instruments, $R_v = R_h \approx 300$ mm and $r_v = r_h = R_{\min} \approx 5$ μm, as explained in the preceding sections. The maximum slope limit $S_{\max}$ of the sinusoidal surface (that could be measured by X-ray CT) was set to ~90° (i.e., $S_{\max} \approx 1.5708$ rad). Given the volumetric nature of the imaging process of X-rays, slope angle limitations are assumed to be negligible. Hence the slope angle of 90° used for the calculations of the AW map is justified. In addition, as discussed in the previous section, $R_{\max}$ was set to an arbitrary large value given that, in principle, there are no limitations for X-ray CT to measure flat surfaces of constant (or mean) zero curvature.

As a last remark, it is worth noting that the values of R_v, R_h, r_v, r_h, $R_{\min}$, and $S_{\max}$, hypothetically (or tentatively) identified in this paper for X-ray CT technologies, are the limits currently observed in metrological practice and reported in the literature (including the optimistic values that may apply to the metrological structural resolution). In general, these limits may be further restricted by other considerations, such as the focal spot size of the X-ray source, degree of beam collimation, projection geometry, sample size, the physical size of X-ray detector, and the details of the reconstruction algorithms used for a particular CT application. In particular, in the context of metrology applications, it is of crucial importance to account for the measurement uncertainties typically observed in the current literature [1, 11-13] when setting the aforementioned limiting values (R_v, R_h, r_v, r_h, $R_{\min}$, and $S_{\max}$). At the same time, these boundaries could be extended—and their limiting values be pushed up or down—by new developments in technology, as long as metrological performance can be demonstrated for dimensional measurement tasks, in a way that is more comprehensive than simple optical image visualization (e.g., high contrast resolutions are

currently achievable by multi-scale CT imaging technologies, see Figure 2, but these 'resolutions' cannot currently be tied to a one-to-one relationship for structural resolutions of metrological performance). The limiting factors for the other measurement technologies, as featured in Figure 4, were selected from published references [44-50]. However, the polygonal limiting boundaries in the figure are drawn only for illustration and will likely evolve with more comprehensive models of limiting factors in CT metrology.

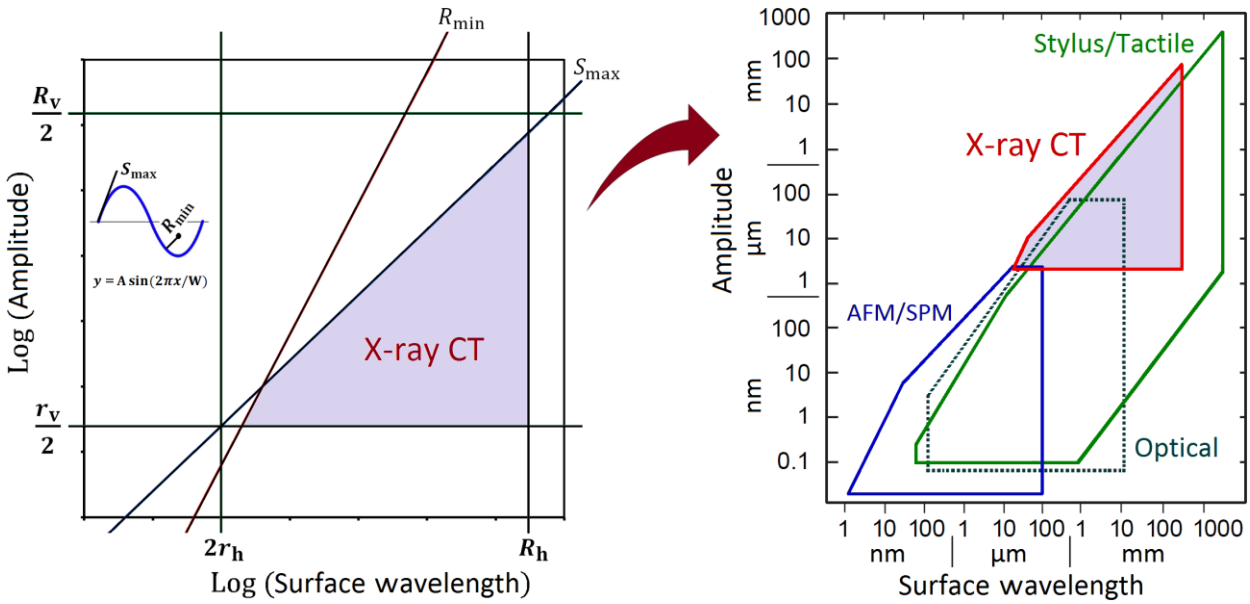

FIGURE 4. X-ray CT metrology performance represented in the Stedman (amplitude–wavelength) space. Left: Setting the parameter constraints. Right: Comparison of CT's performance in amplitude–wavelength space with other dimensional metrology techniques that include mechanical stylus/tactile methods (from nanoscale stylus profilometry to large-scale CMMs), optical methods (optical profilometry, confocal microscopy, and interferometry), atomic force microscopy (AFM), and scanning probe microscopy (SPM).

CONCLUSIONS

This paper is an elaboration upon previously published work [1], which introduced a plot of industrial X-ray CT's performance in amplitude-wavelength space for the first time (to the authors' knowledge). This plot facilitates the comparison of X-ray CT competence with other traditional measuring techniques (e.g., tactile and optical methods), in terms of resolution and measuring range and, therefore, provides a quick overview of the limitations and capabilities of CT in the field of dimensional surface metrology. Such a comparison can be carried out without the study of often complex instrument specifications or lengthy performance comparisons. An AW plot (or AW map) provides only a generalized measure of performance for comparisons with other instruments. In a more comprehensive comparison, considerations of cost, measurement time (dynamics) [48], conformance with standards, and other unique characteristics that differentiate the different measuring processes should also be included. In particular, the CT technique is known to be susceptible to unwanted effects, namely CT artifacts, that emerge from discrepancies between the absorption values used for computing the CT data and the actual absorption (or attenuation) of the measuring object. CT artifacts can occur from influences like the component's geometry and its orientation within the CT machine [1]. Such errors can be mapped in the Fourier domain and can affect metrological performance. These unwanted effects are not encapsulated in the AW map.

RKL and LK would like to acknowledge funding from the following grants of the EPSRC: EP/101534X/1 and EP/M008983/1.

REFERENCES

[1] H. Villarraga-Gómez, PhD Dissertation: Studies of Dimensional Metrology with X-ray CAT Scan, Department of Physics and Optical Science: The University of North Carolina at Charlotte, 2018.

[2] H. Villarraga-Gómez, C. Lee and S. T. Smith, "Dimensional metrology with X-ray CT: a comparison with CMM measurements on internal features and compliant structures," *Precision Engineering,* vol. 51, pp. 291-307, 2018.

[3] J. P. Kruth, M. Bartscher, S. Carmignato, R. Schmitt, L. De Chiffre and A. Weckenmann, "Computed tomography for dimensional metrology," *CIRP Annals - Manufacturing Technology,* vol. 60, no. 2, pp. 821-842, 2011.

[4] L. De Chiffre, S. Carmignato, J. P. Kruth, R. Schmitt and A. Weckenmann, "Industrial applications of computed tomography," *CIRP Annals - Manufacturing Technology,* vol. 63, no. 2, pp. 655-677, 2014.

[5] A. Buratti, J. Bredemann, M. Pavan, R. Schmitt and S. Carmignato, "Applications of CT for Dimensional Metrology," in *In Industrial X-Ray Computed Tomography (Eds: Carmignato S., Dewulf W., and Leach R.)*, Cham, Switzerland, Springer, 2018, pp. 333-369.

[6] M. Bartscher, M. Neukamm, U. Hilpert, U. Neuschaefer-Rube, F. Hartig, K. Kniel, K. Ehrig, A. Staude and J. Goebbels, "Achieving Traceability of Industrial Computed Tomography," *Key engineering Materials,* vol. 437, pp. 79-83, 2010.

[7] S. Carmignato, A. Pierobon, P. Rampazzo, M. Parisatto and E. Savio, "CT for Industrial Metrology - Accuracy and Structural Resolution of CT Dimensional Measurements," in *4th Conference on Industrial Computed Tomography (iCT)*, Wels, Austria, 2012.

[8] M. Bartscher, U. Hilpert, J. Goebbels and G. Weidemann, "Enhancement and proof of accuracy of industrial computed tomography (CT) measurements," *CIRP Annals - Manufacturing Technology,* vol. 56, no. 1, pp. 495-498, 2007.

[9] ISO 10360-2, Geometrical Product Specifications (GPS) - Acceptance and reverification tests for coordinate measuring machines (CMM) - Part 2: CMMs used for measuring linear dimensions, Geneva: ISO copyright office, 2009.

[10] VDI/VDE 2630-1.2, Computed Tomography on Dimensional Measurement - Influencing variables on measurement results and recommendations for computed-tomography dimensional measurements, Berlin: Beuth Verlag GmbH, 2010.

[11] S. Carmignato, A. Pierobon and E. Savio, "CT Audit: Interlaboratory Comparison of Computed Tomography Systems for Dimensional Metrology, Final Report," Laboratory of Industrial and Geometrical Metrology, University of Padova, Padova (Italy), 2012.

[12] J. Angel and L. De Chiffre, "Inter laboratory comparison on Industrial Computed Tomography: CIA-CT comparison - Final report," DTU Mechanical Engineering, Technical University of Denmark, Kongens Lyngby (Denmark), 2013.

[13] A. Stolfi and L. De Chiffre, "InteraqCT Comparison on Assemblies - Final Report," DTU Mechanical Engineering, Technical University of Denmark, Kongens Lyngby (Denmark), 2016.

[14] S. Carmignato, D. Dreossi, L. Mancini, F. Marinello, G. Tromba and E. Savio, "Testing of x-ray microtomography systems using a traceable geometrical standard," *Measurement Science and Technology,* vol. 20, no. 8, p. 084021 (7pp), 2009.

[15] K. Kiekens, F. Welkenhuyzen, Y. Tan, P. Bleys, A. Voet, J. Kruth and W. Dewulf, "A test object with parallel grooves for calibration and accuracy assessment of industrial computed tomography (CT) metrology," *Measurement Science and Technology,* vol. 22, no. 11, p. 115502 (7pp), 2011.

[16] M. Bartscher, M. Neukamm, M. Koch, U. Neuschaefer-Rube, A. Staude, J. Goebbels, K. Ehrig, C. Kuhn, A. Deffner and A. Knoch, "Performance assessment of geometry measurements with micro-CT using a dismountable work-piece-near reference standard," in *10th European Conference on Non-Destructive testing*, Moscow, Russia, 10pp, 2010.

[17] A. Voet, K. Kiekens, F. Welkenhuyzen, Y. Tan, W. Dewulf and J. P. Kruth, "A test object for calibration and accuracy assessment in X-ray CT metrology," in *10th International Symposium on Measurement and Quality Control*, Osaka (Japan), 4pp, 2010.

[18] A. Staude, J. Goebbels, K. Ehrig, M. Bartscher, M. Koch and U. Neuschaefer-Rube, "A new test piece for geometry and defect measurements with micro-CT," in *10th European Conference on Non-Destructive testing*, Moscow, Russia, 8pp, 2010.

[19] S. Carmignato, A. Pierobon, F. Marinello and E. Savio, "Olympic Gauge: A New Reference Standard for Testing X-ray Microtomography Systems," in *10th Euspen international conference*, Delft (Netherlands), pp. 217-220, 2010.

[20] F. Léonard, S. B. Brown, P. J. Withers, P. M. Mummery and M. B. McCarthy, "A new method of performance verification for x-ray computed tomography measurements," *Measurement Science and Technology,* vol. 25, no. 6, p. 065401 (10pp), 2014.

[21] P. Müller, J. Hiller, A. Cantatore, G. Tosello and L. De Chiffre, "New reference object for metrological performance testing of industrial CT systems," in *12th Euspen International Conference*, Stockholm (Sweden), 4pp, 2012.

[22] M. Stedman, "Basis for comparing the performance of surface-measuring machines," *Precision Engineering,* vol. 9, no. 3, pp. 149-152, 1987.

[23] M. Stedman, "Mapping the performance of surface-measuring instruments," in *Proc. SPIE Vol. 803, Proc. of Micromachining of Elements with Optical and Other Submicrometer Dimensional and Surface Specifications*, The Hague (Netherlands), pp. 138-142, 1987.

[24] A. Franks, "Nanometric surface metrology at the national physical laboratory," *Metrologia,* vol. 28, no. 6, pp. 471-482, 1991.

[25] S. Rosén, T. R. Thomas and B.-G. Thomas, "The Stedman diagram revisited," *Surface Topography: Metrology and Properties,* vol. 2, p. 014005 (5pp), 2013.

[26] A. Blum and C. Evans, "The history and future of the Stedman diagram," in *Proc. of ASPE - Spring Topical Meeting*, Tucson, Arizona (USA), pp. 26-31, 2017.

[27] A. M. Hernandez and J. M. Boone, "Tungsten anode spectral model using interpolating cubic splines: unfiltered x-ray spectra from 20 kV to 640 kV," *Medical Physics,* vol. 41, no. 4, p. 042101 (15p), 2014.

[28] M. J. Berger, J. H. Hubbell, S. M. Seltzer, J. Chang, J. S. Coursey, R. Sukumar, D. S. Zucker and K. Olsen, "XCOM: Photon Cross Section Database (version 1.5)," National Institute of Standards and Technology, Gaithersburg, MD, 2010. [Online]. Available: http://physics.nist.gov/xcom. [Accessed March 2018].

[29] M. Bartscher, H. Bremer, T. Birth, A. Staude and K. Ehrig, "The resolution of dimensional CT - An edge-based analysis," in *4th Conference on Industrial Computed Tomography* , Wels - Austria, 2012.

[30] VDI/VDE 2630-1.3, Computed Tomography in Dimensional Measurement - Guideline for the application of DIN EN ISO 10360 for coordinate measuring machines with CT sensors, Berlin (Germany): Beuth Verlag GmbH, 2011.

[31] F. Zanini and S. Carmignato, "Two-spheres method for evaluating the metrological structural resolution in dimensional computed tomography," *Measurement Science and Technology,* vol. 28, p. 114002 (9pp), 2017.

[32] F. A. Arenhart, V. C. Nardelli, G. D. Donatelli, M. C. Porath, C. Isenberg and R. Schmitt, "Design of a Multi-Wave Standard for Evaluating the Frequency Response of CT Measuring Systems," in *11th ISMQC*, Cracow-Kielce, Poland, 2013.

[33] J. Illemann, M. Bartscher, O. Jusko, F. Härtig, U. Neuschaefer-Rube and K. Wendt, "Procedure and reference standard to determine the structural resolution in coordinate metrology," *Meas. Sci. Technol.,* vol. 25, no. 6, 2014.

[34] M. Flessner, N. Vujaklija, E. Helmecke and T. Hausotte, "Determination of metrological structural resolution of a CT system using the frequency response on surface structures," in *MacroScale*, Vienna, Austria, 2014.

[35] F. A. Arenhart, V. C. Nardelli and G. D. Donatelli, " Characterization of the surface content transfer function of CT measuring systems," in *Conference on Industrial Computed Tomography*, Wels, Austria, 2014.

[36] F. A. Arenhart, V. C. Nardelli and G. D. Donatelli, "Characterization of the metrological structural resolution of CT systems using a multi-wave standard," in *XXI IMEKO World Congress "Measurement in Research and Industry"*, Prague, Czech Republic, 2015.

[37] F. A. Arenhart, C. R. Baldo, T. L. Fernandes and G. D. Donatelli, "Experimental Investigation of the Influencing Factors on the Structural Resolution for Dimensional Measurements with CT Systems," in *6th Conference on Industrial Computed Tomography*, Wels - Austria, 2016.

[38] M. Bartscher, O. Sato and F. U. Härtig, "Current state of standardization in the field of

dimensional computed tomography," *Measurement Science and Technology,* vol. 25, no. 6, p. 064013 (14pp), 2014.

[39] E. Maire and P. J. Withers, "Quantitative X-ray tomography," *International Materials Reviews,* vol. 59, no. 1, pp. 1-43, 2014.

[40] P. J. Withers, "X-ray nanotomography," *Materials Today,* vol. 10, no. 12, pp. 26-34, 2007.

[41] G. E. Ice, J. D. Budai and J. W. L. Pang, "The race to X-ray microbeam and nanobeam science," *Science,* vol. 334, no. 6060, pp. 1234-1239, 2011.

[42] J. Kastner and C. Heinzl, "X-ray Computed Tomography for Non-destructive Testing and Materials Characterization," in *Integrated Imaging and Vision Techniques for Industrial Inspection (Liu Z., Ukida H., Ramuhalli P., Niel K., editors)*, London, England (UK), Springer, 2015, pp. 227-250.

[43] F. A. Arenhart, V. C. Nardelli and G. D. Donatelli, "Comparison of surface-based and image-based quality metrics for the analysis of dimensional computed tomography data," *Case Studies in Nondestructive Testing and Evaluation,* vol. 6, pp. 111-121, 2016.

[44] S. Stedman and K. Lindsey, "Limits of surface measurement by stylus instruments," in *Proc. SPIE Vol. 1009, Surface Measurement and Characterization*, Hambur (Germany), pp. 56-61, 1988.

[45] M. Stedman, "Limits of topographic measurement by the scanning tunnelling and atomic force microscopes," *Journal of Microscopy,* vol. 152, no. 3, pp. 611-617, 1988.

[46] J. E. Griffith and D. A. Grigg, "Dimensional metrology with scanning probe microscopes," *Journal of Applied Physics,* vol. 74, no. 9, pp. R83-R109, 1993.

[47] T. R. Thomas, "Trends in surface roughness," *International Journal of Machine Tools and Manufacture,* vol. 38, no. 5-6, pp. 405-411, 1998.

[48] C. W. Jones and R. K. Leach, "Adding a dynamic aspect to amplitude–wavelength space," *Measurement Science and Technology,* vol. 9, no. 5, p. 055105 (7pp), 2008.

[49] S. H. R. Ali, "Advanced Nanomeasuring Techniques for Surface Characterization," *International Scholarly Research Notices (ISRN) Optics,* p. 859353 (pp23), 2012.

[50] R. K. Leach, C. L. Giusca, H. Haitjema, C. Evans and X. Jiang, "Calibration and verification of areal surface texture measuring instruments," *CIRP Annals,* vol. 64, no. 2, pp. 797-813, 2015.

REAL-TIME *IN SITU* METROLOGY OF THE SHAPE OF AN X-RAY ADAPTIVE MIRROR USING AN ARRAY OF INTERFEROMETRIC ABSOLUTE POSITION SENSORS

Vivek G. Badami[1], Ernesto Abruña[1], Lei Huang[2] and Mourad Idir[2]

[1]Zygo Corporation, Middlefield, CT
[2]Brookhaven National Laboratory – NSLS II, Upton, NY

BACKGROUND

The demand for higher resolution X-ray imaging in scientific applications is driving the need for smaller and more stable focal spot sizes in x-ray beamlines for the next generation of brighter and more coherent x-ray sources [1,2]. Adaptive x-ray mirrors are one avenue to meet the stringent requirements on the location and size stability while producing smaller spots. Equipped with closed-loop feedback, these mirrors would be capable of compensating for deviations in the beamline optics due to effects such as the heat distortion caused by the x-ray beam, environmental changes, hysteresis in the actuators, micro-creep in the mirror material and the actuators, distortion due to mounting and other disturbances.

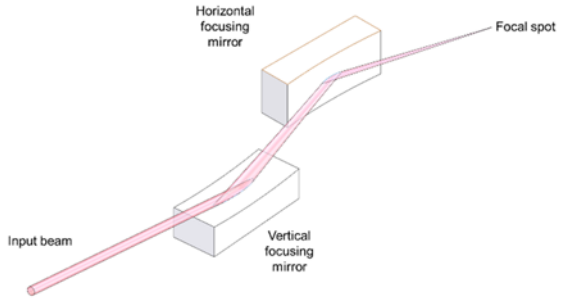

FIGURE 1. Schematic of Kirkpatrick-Baez (KB) mirror system.

A common configuration for these types of x-ray mirrors is the Kirkpatrick-Baez (KB) configuration wherein a horizontal and vertical mirror are used at grazing incidence together to control focusing of the beam in the verticaland horizontal direction respectively as shown in FIGURE 1 [3]. These mirrors can vary in length from a few centimeters to ~1.5 m. Coatings of parallel "stripes" of different heavy metals, e.g., platinum or rhodium, on the mirror surface enable the use of these mirrors with x-rays of different energies. Lateral translation of the mirror perpendicular to the direction of the x-ray beam selects the stripe in a process known as a "stripe swap." Similarly, in a mirror swap lateral translation can also exchange entire mirrors mounted side-by-side into the x-ray beam to obtain a completely different set of beam parameters.

These mirrors need to meet very challenging figure specifications at the nm PV level and adaptive x-ray mirrors are the way forward to meet these requirements. Built-in actuators, most commonly piezoelectric, control surfaces of both mirrors in the KB configuration.

These mirrors are currently operated open loop, i.e., without direct feedback on the mirror shape. Invasive metrology techniques that directly measure the actual x-ray spot size or wavefront are used to initially set the mirror shape. These techniques typically require interruption of the beam, reducing the available time for actual experiments. Further, once the beam is set and the experiment is in process, the operator is blind to changes in spot size and position. Experimenters are forced to rely on the stability of the adjusted mirror for maintaining the beam parameters.

Maintaining the mirror shape at the sub-nm level is challenging and to address this issue while mitigating beamline interruption, we propose and demonstrate an *in situ* real-time metrology system for the active monitoring of an adaptive x-ray mirror using an array of interferometric absolute position sensors [4-6].

FIGURE 2. Compact fiber sensor, 3 mm in diameter and 27 mm long.

SENSOR TECHNOLOGY

The sensor is a compact fiber-based device (Zygo ZPS™), which has several unique features that enable this type of measurement [6]. The compact size of the sensor (see FIGURE 2) allows for the packing of sensors into dense arrays for addressing short spatial frequencies on the target. The sensor operates in a Fizeau configuration wherein interference between the reflections from the sensor reference surface R_R and the target R_T generate the measurement signal as shown in FIGURE 3. The well-defined measurement reference (the sensor reference surface) is physically accessible permitting the direct referencing of the sensor reference surface to the metrology frame without any additional materials, e.g. adhesives, in the metrology loop which can compromise the stability. This design feature enables the sub-nm stability levels required for demanding measurements.

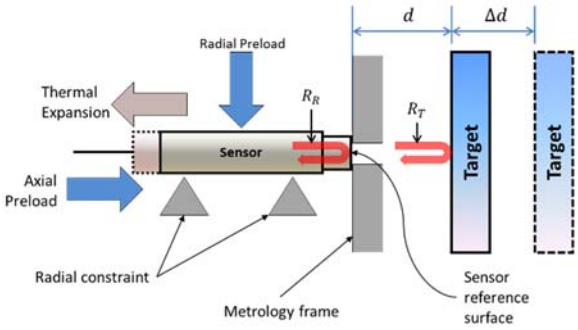

FIGURE 3. Sensor optical schematic with an accessible reference surface which directly references the metrology frame.

A properly designed constraint system, also shown in FIGURE 3, minimizes contributions from the thermal expansion of the sensor as the reference surface of the sensor remains in contact with the metrology frame under the influence of an axial preload even as the sensor body changes length.

The absolute capability of these sensors distinguishes it from other interferometric based fiber sensors. Whereas other sensors can only measure the *displacement* Δd from some arbitrary origin, ZPS sensors can measure the actual *distance* d to the target from the sensor reference surface. In practice, this means that the position of the target can be reestablished even if after the target removal and replacement.

The high sensor bandwidth (maximum bandwidth of 104 kHz) and the low noise performance of (5 pm $Hz^{-1/2}$ 3σ over central ±100 µm of the operating range) can enable the real-time control of the mirror shape under closed-loop feedback control to sub-nm levels at the relatively low bandwidth required for maintaining mirror figure.

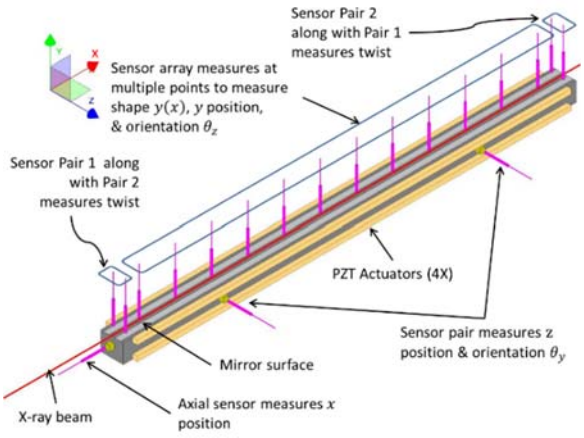
Sensor Pair 2 along with Pair 1 measures twist
Sensor array measures at multiple points to measure shape $y(x)$, y position, & orientation θ_z
Sensor Pair 1 along with Pair 2 measures twist
PZT Actuators (4X)
Sensor pair measures z position & orientation θ_y
Mirror surface
Axial sensor measures x position
X-ray beam

FIGURE 4. Measurement principle showing measurement of rigid body motions and deformations.

METROLOGY PRINCIPLE

FIGURE 4 shows the basic principle - an array of sensors measuring the shape of the reflecting surface of the mirror. Additional sensors in the array, e.g., a sensor pair at either end, can measure mirror twist or other deformation modes. Sensors can also be added to measure the position and orientation of the mirror in six degrees-of-freedom (DOF).

The high repeatability (<0.5 nm 3σ) of the absolute measurement capability combined with the high stability (<1 nm/day) can enable other unique functionalities:

1) The restoration of a previously optimized mirror shape after an event such as a mirror or stripe swap, greatly reducing the time taken to reoptimize the mirror shape.
2) *In situ* measurement of the absolute shape of the mirror, through calibration of the sensor array against a known shape. This has significant advantages over the current practice of *ex situ* (laboratory based) measurements of the mirror which are blind to the significant perturbations of the mirror shape due to clamping forces and thermal changes that result when moving the mirror from the pristine laboratory environment to the less forgiving operating environment of the beamline.

This initial proof-of-principle demonstration will focus exclusively on the measurement of

changes in the mirror shape using an array of sensors similar to FIGURE 4. The performance of the sensor array is compared to a Fizeau interferometer by simultaneous measurements of the shape change a ~450 mm long piezo-actuated deformable mirror.

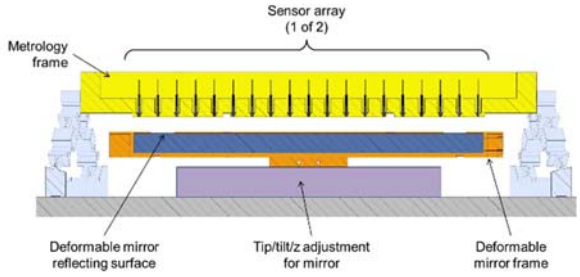

FIGURE 5. Sectioned view showing one of two sensor arrays mounted in metrology frame with sensors monitoring reflecting surface of mirror.

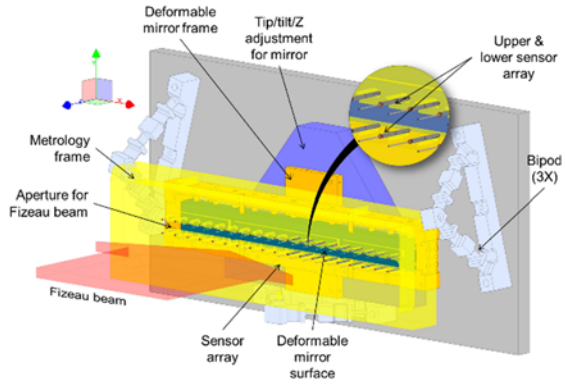

FIGURE 6. Schematic of full measurement setup showing Fizeau measurement through the metrology frame.

METROLOGY SETUP

The setup implemented for this experiment shown in FIGURE 5 is based on the conceptual depiction of FIGURE 4 and is designed to only measure shape changes. The setup consists of an array of sensors mounted in an independent stable metrology frame located adjacent to the reflecting surface of the mirror. This arrangement is unique in that the sensor array directly monitors the *reflecting* surface of the mirror in contrast to other approaches which monitor the rear side of the mirror [7].

Two rows of 19 sensors (of which only the central 17 are used) spaced ~24 mm apart straddle a central rectangular aperture in the metrology frame which provides access to the mirror surface for a simultaneous Fizeau measurement as shown in FIGURE 6. While the two rows of sensors in this setup enable comparison with the Fizeau interferometer in compliance with the Abbe principle, in actual service a single row of sensors positioned directly over the x-ray beam footprint on the mirror may be envisaged. FIGURE 7 shows the setup juxtaposed with the 18" Fizeau interferometer used for the comparison.

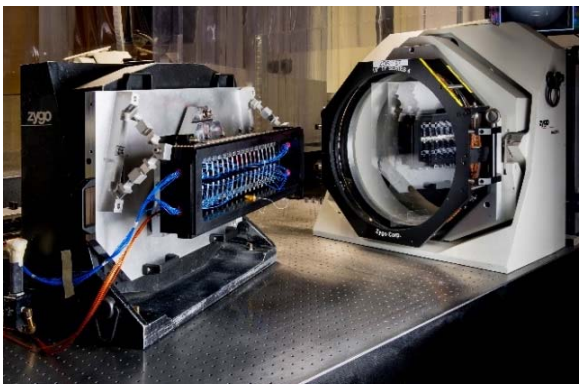

FIGURE 7. Measurement setup shown in front of an 18" Fizeau interferometer. Setup rotated away from measurement position to show details of metrology frame.

The ~450 mm long piezo-bimorph style mirror has 12 piezo actuators sandwiched between two glass face sheets. The mirror mounts to the common baseplate through a tip/tilt/z mount (as shown in FIGURE 5 and FIGURE 6). These adjustments allow positioning of the mirror surface at the 3.5 mm standoff of the sensor while also allowing alignment of the mirror to within the angular acceptance of the sensors. The mirror adjustment is based on a three-vee/three-ball arrangement with linear adjustment of the three balls providing the required adjustment DOF. The preload forces and the contact stiffnesses at the vee-ball interface provide a first resonance of over 200 Hz.

A cost-efficient Aluminum 6061-T6 metrology frame provides nm-level thermal shape stability by exploiting the high thermal conductivity of the material which prevents the formation of gradients and the associated shape deformation despite the relatively high coefficient of thermal expansion (CTE). The frame mounts to the common baseplate through three bipods each of which constrains 2 DOF, exactly constraining the frame with the flexure equivalent of a three-ball/three-vee kinematic mount. The mirror mount has all the adjustment DOF while the frame is fixed. Tailoring the stiffnesses of the bipods

decouples the metrology frame from external deformations, e.g., structural deformations of the mirror frame during mirror shape changes, differential expansion of the various components of the setup and other structural deformations. The constraint system also ensures a first resonance of ~200 Hz to ensure sub-nm vibration contributions based on the characteristics of the vibration isolation system and the ambient seismic vibration levels.

The mounting of the sensors exploits the accessibility of the sensor reference surface by preloading a chamfer along the edge of the face of the sensor into a ring-contact with spherical cup within the frame as shown in FIGURE 8, providing both axial and radial constraint. The preload mechanism at the rear end of the sensor provides an axial preload force while simultaneously providing radial constraint. The ring-contact allows adjustment of the sensor pointing by manipulating the radial constraints of the preload mechanism.

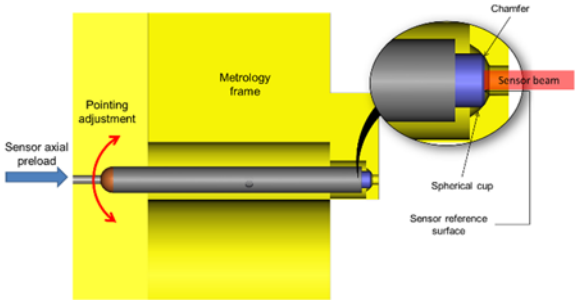

FIGURE 8. Sensor mounting detail.

MEASUREMENT PROCEDURE

The entire setup is placed on a tip-tilt mount (see FIGURE 7) and aligned to an 18" Zygo Fizeau interferometer. The setup was allowed to thermalize for over 24 hours before starting data acquisition from both instruments. Each measurement of a mirror shape is comprised of five data sets collected serially. Each data set consists of 10k data points for each sensor in the array (at a sampling rate of 2 kHz) and 32 phase averages for the Fizeau interferometer. The latter minimizes the effects of air turbulence and vibration. The first measurement is of the undeformed mirror, which corresponds to a cylinder with a radius of curvature (R_C) of ~3.2 km. Application of voltages to the pie zo-actuators generates the deformed mirror shape. A second set of measurements after allowing the mirror to settle into its new shape over a few minutes, records the post-deformation shape.

Two fiducials on the metrology frame, which are visible in the field-of-view of the Fizeau interferometer, establish the location and orientation of the sensor array in the coordinate system of the Fizeau interferometer. The sensor locations were previously determined relative to the fiducials using a coordinate measuring machine (CMM) measurement. Together, this information establishes the measurement locations of the displacement measured by each of the sensors relative to the Fizeau data. The calibrated distance between the two fiducials also determines the lateral calibration constant for the interferometer which in turn provides the lateral scaling for the Fizeau data.

A dedicated refractometer mounts to the metrology frame and continuously measures the refractive index of air. The index values are used to correct the ZPS sensor data automatically and in real-time.

DATA PROCESSING

Agreement between the two instruments is based on evaluating the difference between each instrument's measurement of the mirror shape changes. A mirror shape change measurement constitutes the difference between an initial shape (R_C = 3.2 km) and an actuated shape as generated by a set of piezo actuator voltages. Perfect agreement between the instruments would result in the difference being identically zero at each sensor location in the array.

The resulting array measurement is composed of the pairwise average between sensors in the two arrays, i.e., the average of readings from a sensor in one linear array with the corresponding sensor from the other array. The average produces an effective measurement along a line midway between the two sensor arrays. The Abbe principle is satisfied by choosing Fizeau data for the comparison from a region centered about this line. The Fizeau data is the pointwise average of ten rows of pixel about the centerline.

The locations of the measurement points of the sensor array are transformed into the coordinate system of the Fizeau interferometer by referencing the fiducials, whose locations are determined by centroiding the intensity images in the Fizeau data.

RESULTS

The measurand is the pointwise difference between the shape changes measured by the two techniques at each of the sensor locations. FIGURE 9 shows one example of the

~0.4 nm (1σ) short-term repeatability based on five measurements made in quick su ccession over a typi cal measurement period while the holding the all actuators at a fixed voltage. Thi s repeatability captures the contributions of relatively fast error sources such as air turbulence, vibration, and short-term deformations of the metrology frame.

Varying both the voltage s and the choice of actuators generates a variety of deforme d shapes. The data shown below in FIGURE 10 - FIGURE 12 represent three examples of the shapes generated and the associated difference between the two measurements.

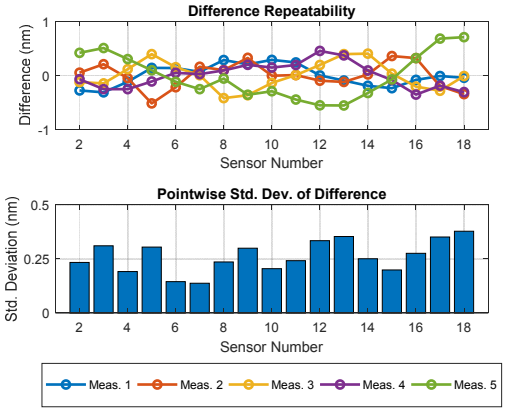

FIGURE 9. Pointwise measurement repeatability of the differen ce evaluated over five measurements. Differences are from the mean.

The graphic at the top of each figure shows the state of the actuators during the when the mirror is deformed. The red boxes indicate actuators which were energized to produce the deformation state, while the light gray boxes repre sent actuators held at zero volts. The upper grap h shows the deformed mirror shape as measured by the Fizeau interferometer, while the lower one shows the average difference between the Fizeau and the sensor array at the sensor locations, indicated by the open circles, over five data sets. The lines in the lower graph are an aid to the eye and do not represent actual data in the regions between the open circles.

In each data set, the starting configuration of the mirror is its undeformed shape, i.e., all actuators set to zero volts. Variation of the voltage applied to the energized actuators varies the magnitud e of the generated sha pe. TABLE 1 summari zes the RMS difference between the two measurements for each mirror deformation.

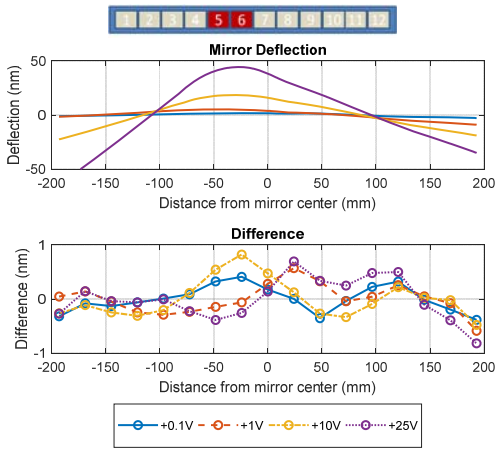

FIGURE 10. Deformation and diffe rence with actuators 5 & 6 energized.

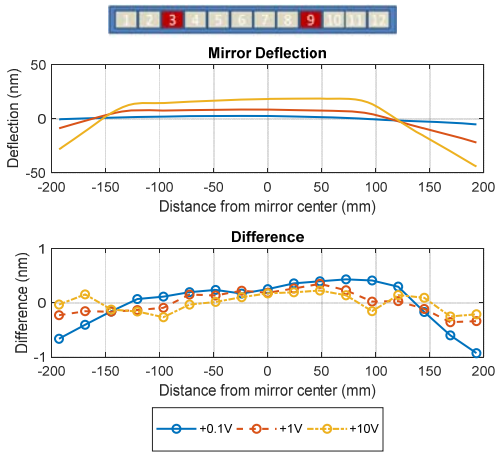

FIGURE 11. Deform ation difference with actuators 3 & 9 energized.

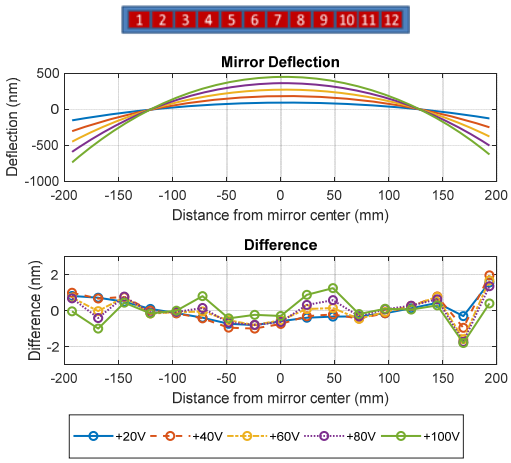

FIGURE 12. Deformation and difference with all actuators energized.

TABLE 1. Summary of differences between sensor array and Fizeau interferometer.

Actuators Energized	Applied Voltage (V)	Difference (nm RMS)
5 & 6	+0.1	0.23
	+1	0.26
	+10	0.34
	+25	0.37
3 & 9	+1	0.41
	+10	0.21
	+25	0.17
1-12	+20	0.61
	+40	0.79
	+60	0.72
	+80	0.72
	+100	0.69

MEASUREMENT UNCERTAINTY

Several factors contribute to the uncertainty in the measurand, i.e., the pointwise difference between the two techniques. The uncertainty is a function of position along the mirror, with some terms being constant while others vary along the length. An example of the former are the contributions due to vibration and air turbulence, while terms dependent on mirror slope are examples of the latter. The overall average measurement uncertainty (k=2) over the length of the mirror is ~1.6 nm with a maximum value of ~3.3 nm for the sensors located at the extreme ends of the mirror. The main contributor to the uncertainty is a local slope dependent term resulting from the uncertainty associated with focusing the interferometer on the mirror surface. These uncertainties depend on the shape of the deformation and the values reported above are for the largest deformation, i.e., the +100V case when all actuators are energized. The uncertainty contributions from the sensor array alone and metrology frame are significantly smaller and estimated to be ~0.6 nm (k=2) on average. The largest contributor to this uncertainty is the contribution of the flexing of the metrology frame due to thermal gradients of ~0.5 nm (k=2) for the measurements shown.

SUMMARY & CONCLUSIONS

The challenges of meeting the stringent spot size requirements of the next generation of synchrotrons requires the use of adaptive mirrors in combination with a new approach to the measurement and control of the shape of these mirrors.

We have demonstrated a technique for real-time *in situ* mirror metrology of synchrotron mirrors that shows sub-nm agreement with a Fizeau interferometer in the measurement of shape changes over a variety of deformation shapes and magnitudes. The two techniques agree to within the uncertainty of the difference.

An uncertainty analysis of the measurement shows that the dominant uncertainty contributors are from the Fizeau interferometer due to uncertainties associated with focusing. The dominant contributor from the sensor array is the flexion of the metrology frame due to thermal gradients across the frame. The use of a material with a lower coefficient of thermal expansion can further reduce this sub-nm contribution further by an order of magnitude.

This approach has the potential to provide feedback for closed-loop control of the mirrors to enhance their functionality leading to increased ease-of-use and increased beamline uptime for science.

ACKNOWLEDGEMENTS

The authors gratefully acknowledge the extensive help and support received from Rich Boland, Dave Schenarts, Mike Holmes, Lars Selberg, Ned Bennett, Bruce Elder, Thomas Dresel, Bruce Truax and Les Deck at Zygo.

REFERENCES

[1] Mimura H et al, 2010. Breaking the 10nm barrier in hard-X-ray focusing, Nature Physics, Vol. 10, pp. 122-125.

[2] Mills D, Padmore H and Lessner E, 2013. "X-ray Optics for BES Light Source Facilities". United States, pp 108-117. https://www.osti.gov/servlets/purl/1287448.

[3] Kirkpatrick P and Baez AV, 1948. Formation of optical images by x-rays, Jour. Optical. Soc. America. 38 (9): 766-774.

[4] Badami VG and Abruña E, 2018. Absolutely: Small Sensor, Big Performance, Mikroniek, Nr. 1, pp. 5-9.

[5] Abruña E, 2017. Multiwavelength - interferometry-based sensor redefines precision position metrology, Laser Focus World, 53(7), pp. 38-41.

[6] www.zygo.com/?/met/absolutepositionmeasurement/zps.htm

[7] Vannoni M et al, 2016. Calibration and optimization of an x-ray bendable mirror using displacement measuring sensors, Optics Express 24(15), pp 17292-17302.

HIGH ACCURACY CYLINDRICAL MIRROR MEASUREMENT BY THREE-DIMENSIONAL NANO-PROFILER BASED ON THE NORMAL VECTOR TRACING METHOD

Jungmin Kang[1], Hiroki Shiraji[2], Ryo Kizaki[2], Yui Toyoshi[2], Takao Kitayama[2], Kazuya Yamamura[2], Takashi Miyawaki[3] and Katsuyoshi Endo[1]
[1]Research Center for Ultra-precision Science and Technology, Osaka University, Osaka, Japan
[2]Department of Precision Science and Technology, Graduate School of Engineering, Osaka University, Osaka, Japan
[3]Department of Processing Technology Development, Production Headquarter, Nikon Corporation, Kanagawa, Japan

INTRODUCTION

The demands of high-precision free-form optical elements has increased obviously in numerous fields of science, technology and industry [1]. For example, Hard and soft X-ray synchrotron radiation facilities and X-ray Free Electron Laser (XFEL) use high precision ellipsoidal and paraboloidal mirrors which have figure errors of 1 nm or less Peak-and-Valley (PV), in order to concentrate X-ray within nanoscale range [2]. Also Extreme UltraViolet light Lithography (EUVL) uses Mo/Si multilayers of off-axial and aspherical mirrors, which have figure error of 1 nm PV or less, due to control 13.5 nm-wavelength ultraviolet light and manufacture Very Large Scale Integrations (VLSI) within design rule of 5 nm or less [3][4]. In astronomy, projects of large reflecting telescope such as the Thirty Meter Telescope Plan introduces hyperboloidal huge mirrors composed by hundreds of hexagonal segments that of figure errors are 40 nm or less [5].

In order to manufacture these high precision optical elements, the measurement technology of three-dimensional absolute figure should be achieved nanometer-scale accuracy and sub-nanometer-scale precision. Nowadays, in the case of single millimeter spatial wavelength measurement, Phase Shift Fizeau Interferometry (PSI), Stitching Interferometry, Computer Generated Hologram (CGH) Fizeau Interferometry, Coordinate Measuring Machines (CMMs) and so on, are introduced for the three-dimensional free-form measurement of dozen-nanometer-scale uncertainty [1][6][7]. However, all the interferometry methods have to require the reference elements, that of figure errors are not absolutely zero nor uncontrolable. Since CMMs contacts the sample surface during measurement, it has a large dependence of contact angle and contains the possibility of deforming sample figure. Thus, there are no methods to achieve the accuracy of single nanometer-scale for the three-dimensional free-form measurement.

Therefore, we have developed a new non-contact three-dimensional nano-profiler which is based on the normal vector tracing method [8][9][10]. The laser beam which propagates linearly in space, the high measurement accuracy rotary encoders, and high rotational motion accuracy air spindles were introduced to the new nano-profiler as core concepts. In this study, a cylindrical mirror, which is a typical free-form surface, was measured and the results were compared to CGH interferometer.

NON-CONTACT THREE DIMENSIONAL NANO-PROFILER

The Concepts of Nano-profiler

FIGURE 1 shows the schematic view of non-contact three-dimensional nano-profiler which is based on normal vector tracing method. It is divided two units which correspond to the optical and sample units, and have two-pairs of two orthogonal goniometers rotating around the x- and z-axes of each units, which are φ and θ for optical unit, and β and α for sample unit. There is also a linear motion stage that moves along the y-axis. The resolution of four-goniometers and a linear motion stage are 35 nrad and 1 nm, respectively. The optical unit has an optical head on the side of φ-axis goniometer, which have a laser beam source of 670 nm wavelength and a quadrant photodiode (QPD). QPD center is mounted on the center of two rotation axes, φ and θ, and is aligned horizontally and vertically. The emitted laser beam is focused to be incident

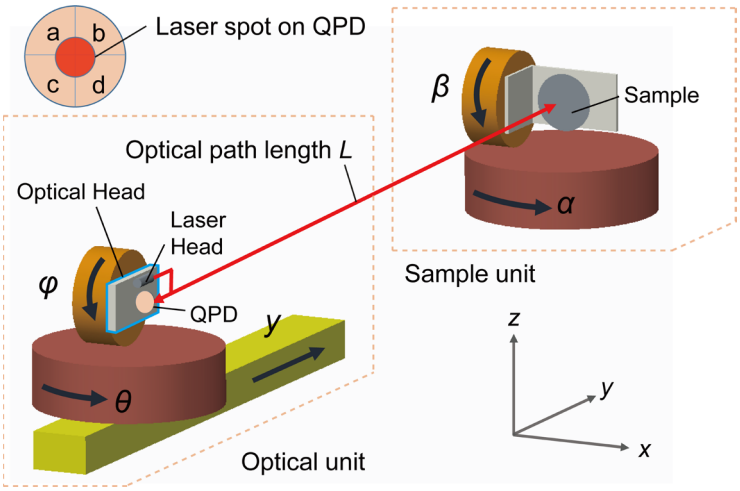

FIGURE 1. The schematic view of the three-dimensional nano-profiler based on the normal vector tracing method.

on the sample surface and is reflected to QPD surface. The distance between QPD and sample is the optical path length (OPL) *L*. The length of *L* is 400 mm and always is kept constantly by the simultaneous numerical control of four-goniometers and a linear motion stage with encoder.

Optical Head

FIGURE 2 shows the optical head design of nano-profiler. A laser beam is initially emitted from the collimator, focused and 90º turned toward the beam splitter (BS) by the semi-focusing lens and mirror. After transmits the BS, a split beam is turned 90º and propagates through λ/4 plate, and is focused toward sample surface by the main focusing lens within the diameter of 300 μm. Then, the beam is reflected toward the lens and transmits through the λ/4 plate and BS again, and propagates through the Neutral Density (ND) filter and finally reaches to the QPD within the diameter of 50 μm. Here, if the sample surface had a difference figure slope

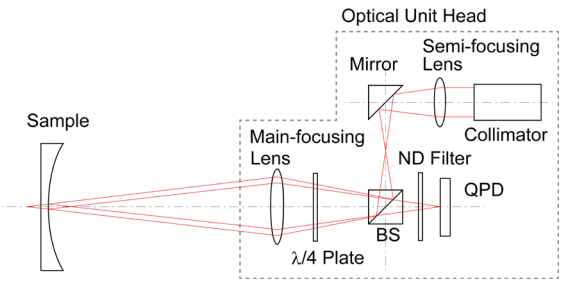

FIGURE 2. The optical unit head design diagram of nano-profiler.

with the ideal one, the reached beam position would move from the center of QPD, and the difference would be measured as a function of *φ*, *θ*, *β*, *α*, and *y*, during keep *L* constantly. Then the normal vector ***n*** would be obtained at each positions of *xz* coordinates and the figure slope would be derived from ***n***. Finally, the figure errors would be calculated from the slopes by the function-fitting-algorithms like integral.

RESULT

A Cylindrical Mirror

A cylindrical mirror is one of the typical aspheric optical element that has two-folded symmetry surface, and has a curvature only along one direction. In this study, an ultra-precision polished cylindrical mirror with 100.6 mm-curvature radius was measured as a sample. FIGURE 3 shows schematic diagram of sample status. The measurement area was 25 × 25 mm^2 and three-fiducial marks were provided inside of the area, due to the comparison with other measuring method of CGH Interferometry. The area was raster scanned with 0.1 mm-pitch, running time was about 50 minutes. Ten-time of measurements were totally held consecutively and the average figure error was obtained as a two-dimensional mapping plot data.

Figure error and Repeatability

FIGURE 4 shows the result of measurement. The PV value was 297 nm. Nine-row striped patterns were shown in the result, which were considered that caused by the polishing process of sample surface. The three blue spots on the corners were corresponding to the position of

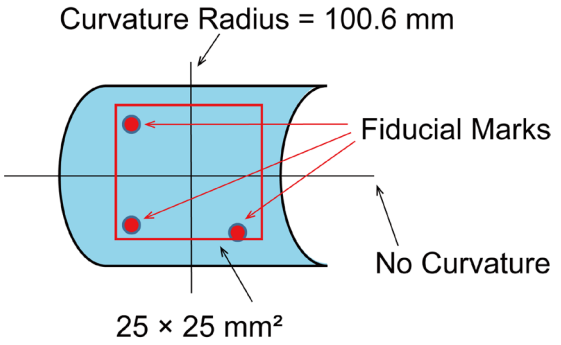

FIGURE 3. The schematic view of cylindrical mirror.

three fiducial marks, which were prepared in order to index the correct positions for the comparison with CGH interferometry result. However, it was considered that the marks caused QPD output to zero voltage because they were designed not to reflect the light beam, and nano-profiler was derived to recognize incorrect information of normal vectors at the spotted areas. To remove these additional errors, the measurement area was trimmed to 19 × 19 mm^2 and the PV value marked under 200 nm.

Also the repeatability of figure error was derived from the standard deviations (SD) of ten-time measurements average. The whole SD average value marked sub-nanometer height, which achieved the purposed repeatability of 1 nm or less.

Comparison with Computer Generated Hologram Interferometry

The cylindrical mirror was measured by CGH interferometer. Same area of 19 × 19 mm^2 with nano-profiler measurement result was trimmed for convenience of comparison. The nine-striped patterns shown in FIGURE 4 also observed in the CGH interferometer result.

The profile of center-line, zero position of x-axis, of the two figure errors were compared. The peak-and-valley structures and periods of each profiles were matched well. The difference of two figure-error profiles were also obtained 50 nm PV or less. Thus, the nano-profiler achieved higher measurement uncertainty than that of CGH interferometry which is λ/10 at 632.8 nm-wavelength light source. It is determined by the accuracy of reference wavefront and the patterns of curved lines prepared onto glass substrates for holograms, and so on. The comparison result revealed that our newly

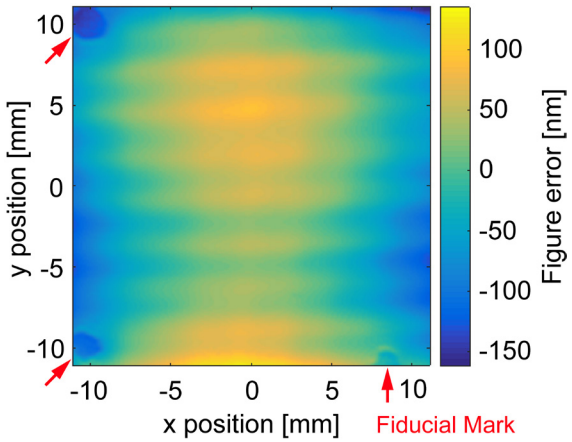

FIGURE 4. The two-dimension mapping plot of three-dimensional figure errors. Ten-time measurements was prepared consecutively and the average was plotted.

developed measurement method reached at the higher accuracy beyond the evaluable range of CGH interferometry, as a three-dimensional free-form measurement way.

CONCLUSION

In this study, a result comparison between the nano-profiler and CGH interferometer was prepared with a same sample of cylindrical mirror, in order to evaluate the properties of new-developed non-contact three-dimensional nano-profiler based on normal vector tracing method. The figure errors were measured ten times, and the average value were obtained below 200 nm PV with sub-nanometer repeatability. The results of two methods were well agreed within the range of 50 nm PV or less and it shows that our newly developed nano-profiler is succeeded to measure a typical free-form optics of cylindrical mirror with same or higher uncertainty than that of common interferometry methods. Furthermore, the new nano-profiler is possible to improve the measurement uncertainty higher than λ/10, because it does not require any reference optics for figure measurement, and is able to measure its systematic and motion errors independently by other methods.

REFERENCES

[1] Fang F.Z, Zhang X.D, Weckenmann A, Zhang G.X, Evans C. Manufacturing and measurement of freeform optics. CIRP Annals – Manufacturing Technology. 2013; 62: 823-846

[2] Siewert F, Buchheim J, Zeschke T, Brenner G, Kapitzki S, Tiedtke K. Sub-nm accuracy metrology for ultra-precise reflective X-ray optics. Nuclear Instruments and Methods in Physics Research A. 2011; 635: S52-S57.
[3] Wu B, Kumar A. Extreme ultraviolet lithography and three dimensional integrated circuit – A review. Appiled Physics Review. 2014; 1: 011104.
[4] Li L, Liu X, Pal S, Wang S, Ober C.K, Giannelis E.P. Extreme ultraviolet resist materials for sub-7 nm patterning. Chemical Society Review. 2017; 46: 4855.
[5] Nelson J, Sanders G.H. The Status of the Thirty Meter Telescope Project. Proceedings of SPIE. 2008; 7012: 70121A-1.
[6] Burge J.H. Applications of computer-generated holograms for interferometric measurement of large aspheric optics. Proceedings of SPIE. 1995; 2576: 258-269.
[7] Henselmans R, Cacace L.A, Kramer G.F.Y, Rosielle P.C.J.N, Steinbuch M. The NANOMEFOS non-contact measurement machine for freeform optics. 2011; 35: 607-624.
[8] Kudo R, Kitayama T, Tokuta Y, Shiraji H, Nakano M, Yamamura K, Endo K. High-accuracy three-dimensional aspheric mirror measurement with nanoprofiler based on normal vector tracing method. Optics and Lasers in Engineering. 2017; 98: 159-162.
[9] Kudo R, Okita K, Okuda K, Tokuta Y, Nakano M, Yamamura K, Endo K. Simulation-based systematic error compensation for nanoprofiler using normal vector tracing method. Measurement. 2015; 73:473-479.
[10] Kudo R, Okuda K, Usuki K, Nakano M, Yamamura K, Endo K. Three-dimensional surface figure measurement of high-accuracy spherical mirror with nanoprofiler using normal vector tracing method. Review of Scientific Instruments. 2014; 85: 045101.

A CURVED SURFACE-INSENSITIVE OPTICAL SENSING TECHNIQUE FOR PRECISION SPINDLE HEALTH MONITORING

ChaBum Lee[1] and Gyu Ha Kim[2]
[1]Department of Mechanical Engineering
Texas A&M University
College Station, Texas, USA
[2]R&D Department
Tri-N Co. Ltd.
Daegu, South Korea

ABSTRACT

The dimensional measurement technique utilizing curved-edge diffraction is applied for the dynamic system identification of precision spindle system. Both static and dynamic behavior including stiffness, damping ratio, and parasitic motion of a precision ball bearing spindle system is characterized by impact response, while the spindle displacement is measured with the curved-edge-type sensors (CES). The CES effects of spindle radius and surface quality were theoretically and empirically investigated. The capacitive-type sensors (CS) were used for a baseline comparison with the CES outputs. Unlike CS, CES is not sensitive to the spindle radius, surface quality, and coupling motions, shows high bandwidth and low noise, and allows for the dimensional measurement at a localized area. These results indicate that CES can be a good alternative to CS for spindle metrology. In the experiment, natural frequency (56 Hz (linear) and 680 Hz (angular)), stiffness (460~790 N/μm) and damping ratio (0.04~0.08) of precision spindle system were measured by CS and CES at the same time. The dynamic model of ball bearing spindle system was also discussed.

INTRODUCTION

Precision ball bearing, hydrostatic or aerostatic spindles represent a key part of machine tools because they determine the quality of the final product produced and the overall manufacturing productivity and efficiency. Therefore, dynamic system identification and condition monitoring of precision spindles is a key factor in increasing the availability of the machine tool and achieving a more robust machining process [1-4]. Precision spindle metrology, i.e., utilizing a cylindrical or spherical target artifact with non-contact sensors to measure a machine tool spindle's "axis of rotation" errors, including radial, axial, and tilt errors, is basic science and technology for sustainable manufacturing [5,6].

Significant research has been devoted to the development of measurement and analysis techniques of precision spindles. Currently, a few approaches in measuring and evaluating precision spindle systems by using capacitive-type sensors (CS) or eddy current-type sensors (ECS) exist [7,8]. However, these sensors are typically designed for flat target surface measurement. CS and ECS are the most commonly used in spindle measurements. It is standard practice for commercial CS and ECS to be factory calibrated with flat-target surfaces. Because the probe will measure the average distance to the target, the gap at zero volts will be different than when the system was calibrated [9,10]. As depicted in Figure 1, errors will also be introduced because of the different behavior of the electric fields between sensing electrode and the curved surface and between guard electrode and the curved surface. In cases where a non-flat target must be measured, the system can be factory calibrated to the final target shape or the probe has to be custom-made for a certain shape.

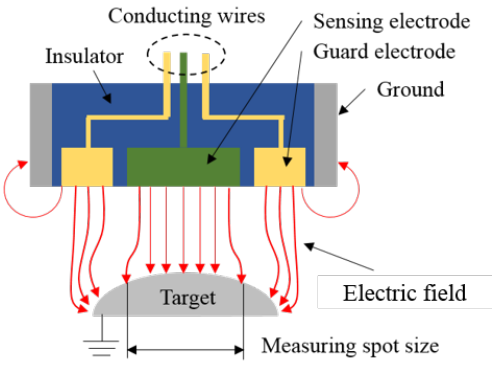

FIGURE 1. A schematic of dimensional measurement from the curved target surface by using capacitive-type sensor.

In this study, a curved-edge sensor (CES) is adapted for dynamic system identification of precision ball bearing spindle system. In the previous work [13-15], knife-edge sensors (KES) was firstly introduced, and the result indicates that the KES can be a good alternative to CS in nanopositioning applications, *e.g.*, microscopy, surface profilers, or coordinate measuring machines. In addition to KES, CES was introduced [11,12]. CES was compared with CS in terms of linearity, measuring range, bandwidth and long-term stability. As a result, it is expected that CES can be one of alternative sensors applicable to spindle metrology. Here a CES model that can describe curved-edge diffraction phenomenon on a curved surface is established by using electromagnetic wave propagation theory. The curved-edge diffraction effects according to surface quality, shaft radius, and materials are empirically characterized, and dynamic system identification of ball bearing spindle system is discussed.

MEASUREMENT PRINCIPLE

Diffraction is the bending of wavefronts around obstacles, and its effects are typically only noticeable for waves where the wavelength similar to the size of the diffracting obstacle. Diffraction occurs with all propagating waves, including sound waves, water waves, electromagnetic (EM) wave. Diffraction over a knife-edge, so-called knife-edge diffraction, can be understood through using Huygens construction. This effect is initially an oscillation then as the direct path is cut off, a signal loss. Unlike knife-edge diffraction, an analytical approach to diffraction by a curved edge is very difficult because curved edge diffraction must be understood from the asymptotic solution of several canonical problems, which involve the illumination of the edge by different wave fronts.

As illustrated in Figure 2, an EM wave incident on the curved edge gives rise to an incident wave (E_i), reflected wave (E_r), and edge diffracted wave (E_d), and those electric fields can be mathematically expressed. The regions, RB, SB and DSB, indicate reflection boundary, shadow boundary, and deep shadow boundary, and R indicates the radius of spindle shaft. Such waves that propagate along a surface ray may be excited at the curved edge shadow boundaries similar to knife edge diffraction. Such surface ray fields may also be excited at the transition region and can be separated into three different regions.

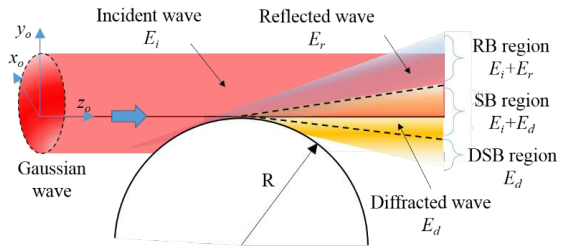

FIGURE 2. A schematic of curved-edge diffraction.

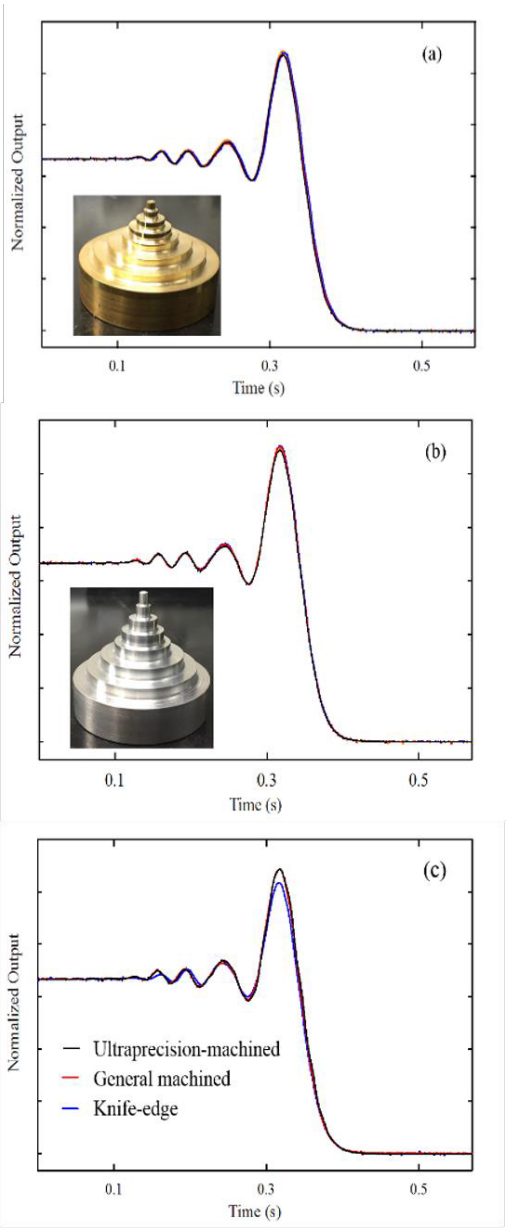

FIGURE 3. Curved-edge diffraction effects of materials, radius and surface quality: (a) ultraprecision-machined Cu, (b) generally-machined Al and (c) comparison (ϕ20 mm).

EXPERIMENTS

Curved edge diffraction fringes of two test samples with different radius (ϕ3, 5, 10, 20, 30, 40 and 50 mm) conditions, surface conditions and different material (Cu, Al) conditions were measured as shown in Figure 3. The Cu sample was machined by ultraprecision machine tool (Nanoform 200) that is used for optical component machining, and the Al sample was machined by general machine tool that can be found in any machine shop. The He-Ne laser (633 nm wavelength) was incident on the edge of the sample, the fringes that can be collected from RB, SB and DSB regions were obtained by scanning the curved edges of each sample as illustrated in Figure 2. The distance between the curved edge and the detector was kept 150 mm. As a result, any significant changes according to materials, radius curvature were not found in given experiment conditions. However, a slight difference in fringe amplitude between curved edge and knife edge was observed.

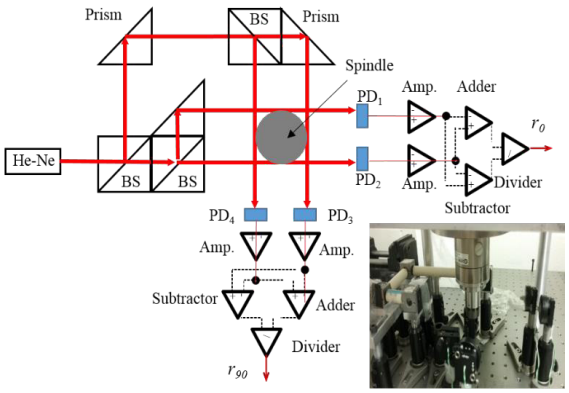

FIGURE 4. Experiment setup.

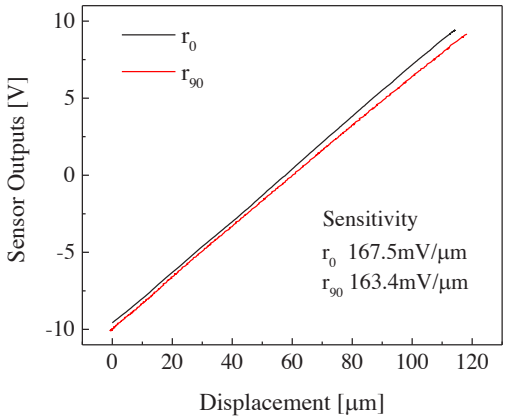

FIGURE 5. Calibration results: linearity errors (calculated as standard deviation of residual errors) were 0.10% and 0.14% for r_0 and r_{90} in full scale (95% confidence).

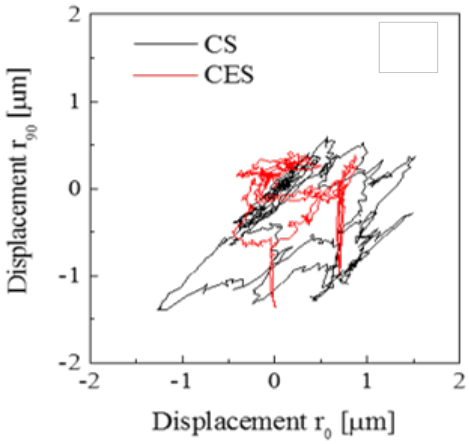

FIGURE 6. Spindle runout at 1,000 rpm.

In the experiment, the precision ball bearing spindle system was chosen. Dynamic system identification of the spindle system was investigated by the curved edge sensor as illustrated in Figure 4. The CS was used for a baseline comparison with the outputs of the CES as shown in Figure 5. This result indicates that the CES is highly linear. The CS and CES outputs were compared with respect to spindle velocity up to 8700 rpm (maximum rpm). The two CS was placed around spindle shaft (ϕ34 mm) along the r_0 and r_{90} directions. As seen in Figure 6, two sensor outputs were compared.

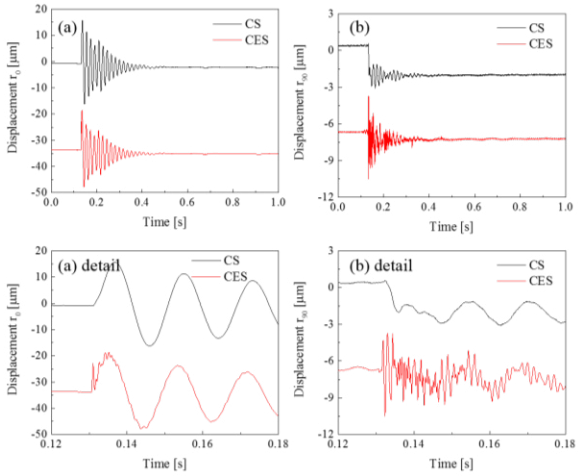

FIGURE 7. Impact response at spindle velocity 0 rpm (stationary) condition: (a) r_0 and (b) r_{90}.

The impact test using hammer with force sensor along the radial direction was performed. The CS and CES measured the displacement along the r_0 and r_{90} directions and the applied force was measured at the same time, while the

impact was applied to the r_0 direction under stationary condition (Figure 7). Two frequencies, 56 Hz and 680 Hz, are presented in the oscillation curves measured by CES in all conditions, and 680Hz oscillations are only observed for approximately 40 ms after impact.

CONCLUSION

A novel sensing method based on edge diffraction technique applicable to spindle metrology and spindle dynamic system identification was investigated. The precision ball bearing spindle system was characterized by impact test, and its dynamic model was established based on the experiment. Thus, this technique can be used to five degree-of-freedom spindle error measurements, spindle health monitoring, and dynamic characterization of the spindle system in a near future. The curved edge diffraction model will be in-depth studied to fundamentally understand edge diffraction behavior in reflection boundary, shadow boundary, and deep shadow boundary and to characterize how this behavior affects CES performance.

ACKNOWLEDGEMENTS

The research was supported by National Science Foundation (Award Number: CMMI 1463502) through the Texas A&M University. Similarly, this work was supported by the Center for Manufacturing Research at the Tennessee Technological University.

REFERENCES

[1] W. Gao, Precision nanometrology: Sensors and measuring systems for nanomanufacturing, Springer (2010).

[2] K. Liu, M. Sun, T. Zhu, Y. Wu, Y. Liu, Modeling and compensation for spindle's radial thermal drift error on a vertical machining center, Int. J. Mach. Tools Manuf., 105, 58-67 (2016).

[3] J. Kim, S. Zhao, G. Kim and S-K. Lee, Rolling bearing-suspended spindle run-out control using repetitive control and adaptive feedforward cancelation, Int. J. Prec. Eng. Manuf., 14(12), 2171-2178 (2013).

[4] J. Kim and S-K. Lee, Micro-patterning technique using a rotating cutting tool controlled by an electromagnetic actuator, Int. J. Mach. Tools Manuf., 101, 52-64 (2016).

[5] M. Madden, M. Aketagawa, T. Kumagai, Y. Maeda and E. Okuyama, Concurrent measurement method of spindle radial, axial and angular motions using concentric circle grating and phase modulation interferometers, Meas. Sci. Technol. 25, 094005 (2014).

[6] Eric R. Marsh, Precision spindle metrology, DEStech Publications, Inc., 2017.

[7] J. Fleming, A review of nanometer resolution position sensors: Operation and Performance, Sens. Actuators A: Physical, 190, 106-126 (2013).

[8] K. Liu, M. Sun, T. Zhu, Y. Wu, Y. Liu, Modeling and compensation for spindle's radial thermal drift error on a vertical machining center, Int. J. Mach. Tools Manuf., 105, 58-67 (2016).

[9] Philip T. Smith, R. Ryan Vallance and Eric R. Marsh, Correcting capacitive displacement measurements in metrology applications with cylindrical artifacts, Precision Engineering, Vol. 29, No. 3, pp. 324-335 (2005).

[10] R. Ryan Vallance, Eric R. Marsh and Philip T. Smith, Effects of targeting spherical surfaces with capacitive displacement sensors, Proceeding of American Society for Precision Engineering Annual Meeting (2004).

[11] C. Lee, S. M. Mahajan, R. Zhao, and S Jeon, A curved edge diffraction-utilized displacement sensor for spindle metrology, Rev. Sci. Instrum. 87, 075113 (2016).

[12] C. Lee, R. Zhao, S. Jeon, A simple optical system for miniature spindle runout monitoring, Measurement, 102, 42-46 (2017).

Error Budgeting, Manufacturing and Measurement Considerations for the Development of a High Precision Motion Platform

Kevin E. Elliott[1], Scott L. Adriaansen[2], Douglas E. Brackley[1], Allan J. Doig[1], Brian C. Sheehan[1]
[1]Advanced Machine Systems, Corning Inc., Painted Post, NY
[2]Machine and Automation Systems Engineering, Corning Inc., Corning, NY

Introduction

As part of a manufacturing process for a specialty material a Large Scale Optical System (LSOS), which was comprised of an Optical Source and an Optics Box, is required be positioned 60 inches (1.5 meters) from the material under process. This LSOS must be able to track within the process window of 200 um which is moving in one axis at a speed of 250 in/min (6.35 m/min). The LSOS weighs approximately 2000 lbs. (~910 kg) and must travel approximately 26 inches (0.66 m) in the vertical direction. In addition, the entire motion platform which houses the LSOS, must be relocated twice a day (to and away from the process position) a total distance of 4-6 feet (1.2-1.8 meters) to enable "normal" operations to continue. Due to facility limitations, weight of the system was constrained at a maximum of 16,000 lbs. (~7,250 kg).

A quick calculation showed that approximately 30 arcsec of error in the pitch of this vertical axis would result in the LSOS operating outside of the specified process window. As a result, the team developed a detailed error budget to quantify the errors and highlight areas of concern. The team then used the error budget to drive the design of the system and to incorporate the required precision into the translation slides for the vertical axis and the system frame. This was a time constrained development effort which required success in a single iteration, thus the team owned every aspect of the precision including design, assembly and measurement.

Error Budget

The initial error budget for this system was modeled after what would be expected for a machine tool. Errors for displacement, angular and thermal errors were calculated or estimated based on the current initial design (all errors were calculated even if the errors were determined to be second order or in a direction which would not affect the function of the LSOS). The original concept was configured such that the optical source was mounted to the frame of the system. Only the focusing and adjustment optics assembly, referred to here as the Optical Box, was mounted to the motion platform vertical axis. It was quickly determined that the largest driver of error was deviation of the optical source as it propagated through the Optics Box. (The details of the optics box and optical source will not be discussed in this paper)

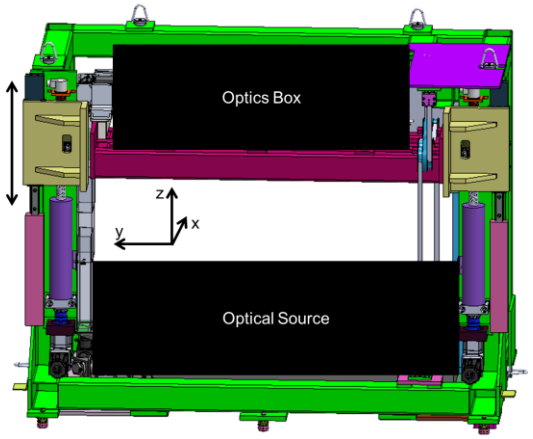

FIGURE 1. Initial concept for motion platform illustrating only the Optics Box moves

Small error motions due to pitch or yaw resulted in amplified errors of the optical source in the process area when propagating through the Optics Box. This was largely due to the long optical path distance between the source and the process window, (~70 inches from Optical Source to the Optics Box, ~72 inches inside the Optics Box, ~60 inches from the Optics Box to the process, this is at total of 202 inches, ~1.78, 1.83, 1.52 and 5.13 meters respectively, See *FIGURE 2*). The predicted errors are based off of yaw and pitch errors (6.4 and 3.2 arcsec respectively, based off calculations using horizontal/vertical straightness estimates of 0.0005 inches, 12.7 um) and were 110 um and 63 um respectively at the point of process. These values are a substantial fraction of the

total process window of 200 um. By moving the optics box and optical source together the total distance for the angular errors to propagate will be reduced from 202 inches to 60 inches (30% of the original) and any horizontal straightness errors will be eliminated as they are a result of the location of the optical source projecting off of the turning mirror into the optics box.

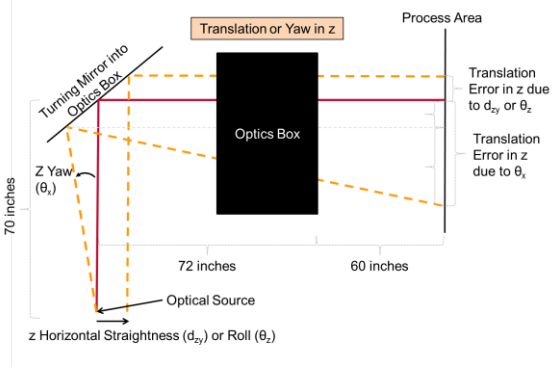
Translation or Yaw in z
Process Area
Turning Mirror into Optics Box
Optics Box
Translation Error in z due to d_{zy} or θ_z
Translation Error in z due to θ_x
Z Yaw (θ_x)
70 inches
72 inches
60 inches
Optical Source
z Horizontal Straightness (d_{zy}) or Roll (θ_z)

FIGURE 2. Schematic of yaw and horizontal straightness errors (not drawn to scale)

Driven by the error budget and reasoning above, the team elected to select a design where the Optics Box and the Optical Source move together on the same carriage. The negative impacts of this decision increased the size and weight of the total system as now the payload was ~2000 lbs. total (approximately double that of just the Optics Box).

Other error terms inherent to the Optics Box were also considered but will not be discussed here. The Optics Box was a purchased component and little could be done to mitigate these errors. Conversely, one item of note was the focusing optic at the exit of the optics box. It was expected that this focusing optic would either amplify or cancel errors due to rotational or translational shifts from pitch and yaw motions. To quantify this value, the transfer function for the focusing optic was derived, using the equations for field of view [1]. The error was added to the other terms in the error budget but was found to be small in comparison. The resulting shift due to the focusing optic was less than 5 um for both angular and translational deviations.

The total error in the system was calculated by a root sum square analysis of all the calculated terms [2]. For perspective, all of the errors were also summed. It was found that the total error of the system root sum square and sum value were 142 um and 354 um respectively. As an input to the error budget a value of 5 arcsec for pitch, roll and yaw for the slide assemblies were assumed (roll was not critical but included for consistency with the understanding, if needed, the value could be relaxed). Using the new values/configurations defined by the error budget the system went through several iterations. The final system is shown below in *FIGURE 3.*

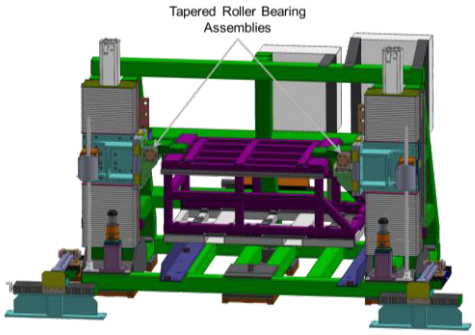

FIGURE 3. Final design of the motion platform, Optics box and Optical Source (not shown) move together

Design

The general design of the system was comprised of two vertical slide assemblies which were mounted to a frame and each connected to a carriage which housed the LSOS. The design was approached from the inside-out, starting with the moving carriage and working out toward the machine frame. Doubling the payload of the moving axis resulted in upsizing several components, which will be described below in the sections for the motion platform major components. Where possible, the system was built using principles of Airy points and kinematics to minimize any effects of system deflection due to gravity [2][3].

Carriage and Mounting Assemblies

The carriage was designed to rigidly hold the Optical Source and the Optics Box in a manner such that there was no movement between the two during system translation. As described above, this eliminates the largest contributors to the total system error budget. The structure was a weldment, to reduce weight, and FEA was used to ensure no part of the carriage sagged more than 0.001 inches (0.0254 mm), with respect to the mounting points. In addition, the components of the LSOS were mounted such that the supports were located as near to mounting points of the carriage as possible to minimize errors due to gravity sag. The carriage was mounted to the motion stages at two points

(one on each stage). The carriage was decoupled from the yaw of the stages through preloaded tapered roller bearing assemblies on both sides and horizontally on one side using a linear guide assembly. The decoupling was designed in to minimize errors transferred by the system stages, avoid over-constraint and offer adequate compliance in the event the two stages were not synchronized, such as during homing. The carriage was designed such that the center of gravity was as close to the center of the mounting points as possible (x direction from *FIGURE 1*) to minimize any moments which would cause deflection changes due to accelerations [2].

Vertical Slide Assemblies

Each vertical slide assembly was comprised of a slide base, two linear guides (with two trucks per guide, total of four per vertical slide assembly), a ball screw and a slide carriage/bracket to connect the four linear guide trucks to the carriage (this carriage/bracket is where the tapered roller bearing and horizontal linear guide assemblies were mounted to the carriage).

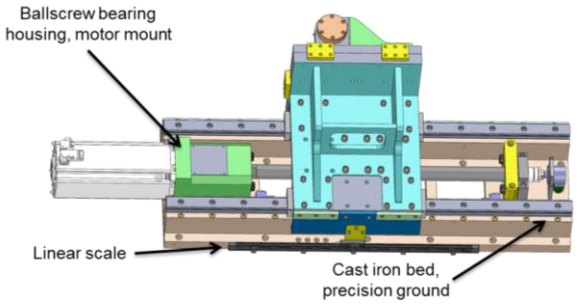

FIGURE 4. Vertical Slide Assembly

Using the L10 life and load calculations [4], size 55 ballscrews and linear guides were selected. The guides and ballscrews dictated the design and size of the slide bed assemblies. These assemblies were constructed onto three piece slide bases. The bases were cast iron and the bolt interfaces were machined flat to 0.0002 inches (5 um) or better. Final machining was completed after the bases were permanently bolted together. Reference edges were included in conjunction with cam locking fixture clamps to align both sets of linear guides during assembly. This is inherently over constrained but due to the ability to maintain straightness between the reference edges, discussed in more detail below, this did not cause any issues. Also, it is believed that the averaging effect of the over-constraint increased the total system precision [5]. The carriage brackets also included reference edges and clamps for the trucks on one of the linear guides. The mounting holes for the slave linear guide trucks were oversized so that those trucks could be floated into position.

The tapered roller bearing assemblies were aligned to the vertical slide carriage using Kerf shims which were ground at assembly to reduce any misalignment in the pitch direction.

Motion Platform Base

Similar to the carriage, the base for the motion platform was a tubular structure. Given the tight tolerances on the motion platform, a more traditional machine tool type frame would have been preferred, such as cast iron [2], but due to the weight and system mobility requirements along with the tight timeline the team elected to use a welded tubular frame. In order to ensure required precision and stiffness, the team performed extensive FEA to understand system response under operation and to analyze sag in critical areas. The design change which required translation of the entire LSOS resulted in the system growing substantially, as discussed earlier, with the total width increasing by 15% (y direction from *FIGURE 1*). When considering stiffness and precision of the frame, staying below the required 16,000 lbs. system weight requirement became a challenge.

The frame contained two pads on the front where the vertical slide assembles were to be mounted. These pads were specified to be flat and parallel to within 0.002 inches (51 um) when in the vertical orientation, as shown below.

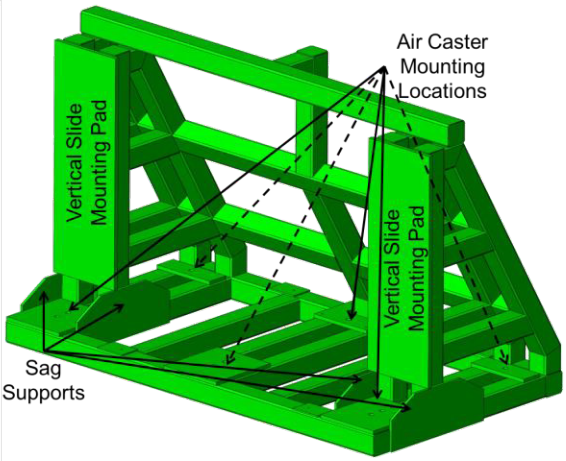

FIGURE 5. Motion Platform Frame, dashed lines indicate backup air caster mounting locations

The base rests on six air caster feet. In practice, only three feet are used (the two under the large pads and one in the middle of the rear of the machine) to keep from over-constraining the frame. The additional air casters are present for use in emergency situations, so that the machine can be moved if one of the primary three was to malfunction. The air caster feet have pads built in which act as feet so regardless of the inflation state the system is always supported on the same points at all times. This was believed to be critical in maintain precision as the motion platform was moved in and out of position every day. This consistent support strategy was chosen to minimize any bending or twisting of the frame.

With the large weight of the carriage and the vertical slides near the front of the machine, tipping was a large concern as well as deflection of the carriage in the pitch direction as the carriage traversed. There was a tradeoff between placing the front feet directly below the main support columns of the motion platform and comfortably placing the center of gravity inside the feet of the platform. Safety and risk of tipping were the higher priority and thus the feet were placed in front of the main support column with three mounting options for the feet. The drawback to this approach is that the frame will sag due to gravity load in this region even with the extra support brackets seen in Figure 5 above.

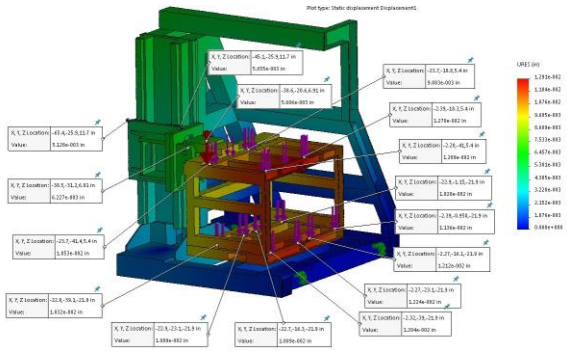

FIGURE 6. FEA of Carriage Deflection between top and Bottom Positions

Extensive FEA was performed around the frame concentrating primarily on the highest and lowest positions to predict the pitch of the carriage as it moves along the vertical axis. It was found in the final design that the largest deformation of any single point on the carriage (between top and bottom positions) was 0.0002 inches (5 um) but in general deflection was negligible throughout the carriage (specifically at the mounting locations for the LSOS components). It was assumed that averaging would aid in minimizing pitch errors.

Manufacture, Assembly and Measurement

The team worked closely with the machine shops which were manufacturing the precision components. In many cases, the team visited the shops to measure parts both on the machine and on surface plates after removal from the machines. For particular components, such as the slide beds, the team dictated how the parts were to be machined and clamped. As before, during machining Airy points or exact simulations of assembled part clamping/bolting configurations were considered. In general, higher precision parts were machined with a spec of 0.0002 inches (5 um), this was typically the tightest tolerance local shops would agree over the length of the components, and hand lapped or scrapped where needed.

As noted previously the slide bed bases were final machined after permanent assembly. The critical aspect of these bases was the relationship between the back surface and the rail mounting surfaces (both horizontal and vertical). These were all toleranced to be flat and parallel (or perpendicular depending on the surface) to 0.0002 inches (5 um) the full length, approximately 30 inches (0.76 meters). Given that this was a high profile project and delivering absolute precision was the highest priority, the team planned to hand lap or scrape the slides into an even tighter specification of 0.0001 inches (2.5 um). In all aspects of this assembly, the team erred on the side of precision with the tradeoff of addition time and cost.

The back surface was first ground and then the slide bed base assembly was flipped. All four rail surfaces were ground in one set up. The base assemblies were removed from the machine and placed on a surface plate to be measured. An autocollimator and precision levels were used to verify straightness of the ground surfaces, the surface plate was used as a reference. Given the tight tolerances, vendors were not able achieve all specified tolerances after initial attempts. In the interest of time, the team elected to accept the slide bed bases as measured after initial attempt. Achieving the specified tolerances would have been preferred but given that the team had planned to hand lab

and scrape the slide bed bases, the time saved would have been marginal.

The team then hand lapped and scraped the rail mounting surfaces until the 0.0001 inch (2.5 um) specification was met on all four rail surfaces. The surfaces were measured again using an autocollimator and precision levels. In addition, a master straightedge and bluing was used to identify high and low regions. During the process the attitude and parallelism was constantly monitored and, if needed, adjustments were made to the areas being lapped or scrapped. To verify the attitude of the horizontal surfaces precision levels were used. Fixtures were developed which used precision levels and precision indicators to monitor non-parallelism between the sides as well as deviations which would result in roll in the final system. All of the errors described above were measured in the single arcsec range over the entire length of the slide after lapping.

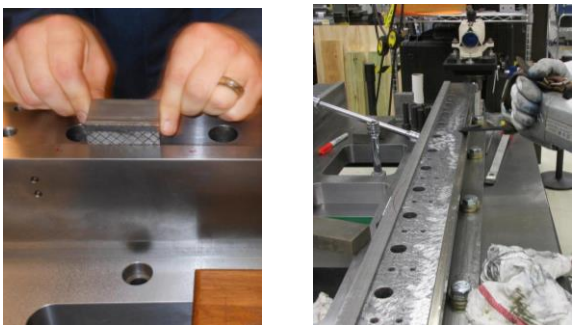

FIGURE 7. Hand lapping and scraping of the rail surfaces

For the remainder of the vertical slide assembly every component which was added was measured and in many cases adjustment made repeatedly until the team was confident in the results. Various equipment was used throughout the process to verify specifications. These included precision levels, autocollimator, laser interferometers and precision levels. For the final slide assembly, all measurement were taken at the point where the LSOS carriage was to be mounted (location of the tapered roller bearing assemblies), i.e. the effective point of process.

The entire assembly was dependent on the stiffness and precision of the base. It was difficult to find a machine shop willing to agree to machine the pads flat and parallel on the large 149 inch long base to within 0.002 inches (51um). The chosen machine shop required multiple iterations to finally achieve the specified tolerance. Originally, the frame was laid on its back, slide mounting pads were facing upward, to be measured even though it was known that the vertical and horizontal orientations would not be loaded the same and may result in addition errors. This was done because the precision levels could be used to easily correlate the two pad measurements while the frame was lying on its back. Unfortunately, as suspected, the errors in the horizontal state were much larger than that in the vertical state. Thus, the base frame was placed back in the vertical state for measurements. To measure and verify the flatness and parallelism of the pads, a commercially available measurement system which uses a spinning laser to establish a plane and a position sensitive detector (PSD) was used.

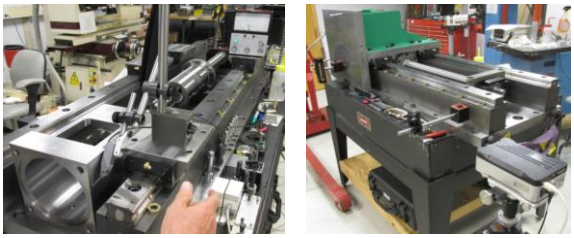

FIGURE 8. Servo housing alignment and final slide assembly measurement

The pads were verified in the above measurement to be within specification. As a contingency plan if the pads were not able to be manufactured within specification, the team had planned to lay the system on its back and shim the slide assemblies in place and fill the gap with a filler such as Moglice [6]. This still would encounter the problem of the variations in the deformation of the frame in the horizontal versus vertical orientation, for which the team would have had to compensate.

The vertical slides were mounted to the base frame using an overhead crane. The mounting pads on the Base had a single pin for alignment. The vertical slide assembles were set to be parallel using a precision box level against the rail surfaces and rotating about the pin.

Once the entire assembly was completed the frame was roughly leveled and the carriage was leveled using a precision level on a reference pad built into the top of the carriage. The carriage leveling was achieved in the software

by adjusting the servo positions. At this point, two axis precision bubble levels were bonded to the frame. They were attached to a plate with three jacking screws so that the plates could be leveled prior to bonding. These served as leveling masters so that the system could be quickly leveled after the moving it into position.

Final System Performance

FIGURE 9. Images of the completed Motion Platform

Each slide assembly was measured and software corrected after final assembly for linear displacement errors. These measurements were performed at the location of the tapered roller bearings with a laser interferometer.

Criteria	Value	Units
Useable Stroke	26	in
Payload/slide	4000	lbs.
Maximum Velocity	500	in/min
Acceleration/Deceleration	1	g
Positioning Accuracy	0.00005	in
Velocity Control	0.01	%
Horizontal Straightness	0.0002	in
Vertical Straightness	0.0002	in
Pitch	1.7	Arc sec
Yaw	1.3	Arc sec

TABLE 1. Final Results for Motion Platform

The final check of the system was to dynamically measure pitch and yaw of the system while traversing at max speed. To accomplish this, a three axis laser interferometer was purchased and integrated into the frame. This was a fiber based Fabry-Perot interferometer. The fibers and optics were mounted to the frame using adjustable five axis mounts for alignment. The retro-reflectors were mounted to bottom of the LSOS carriage. The fibers and retro-reflector were mounted in three of the four corners of the LSOS carriage area. Using software which was purchased with the interferometer, the dynamic errors were measured and it was found that pitch and yaw were both less than 2 arcsec full travel. It was found that dynamically measured (three axis interferometer) and statically measured (precision levels at intervals along the travel) pitch and yaw of the system were in agreement within the measurement error. The table above summarized the performance of the system as measured after full assembly.

REFERENCES

[1] Grievenkamp J. Field Guide to Geometrical Optics. SPIE Press. 2004.
[2] Slocum A. Precision Machine Design. Prentice Hall. New Jersey: 1992.
[3] Smith S, Chetwynd D. Foundations of Ultraprecision Mechanism Design. CRC Press. 1992.
[4] THK Linear Motion Systems Support Book. No. 507E.
[5] Teo T, Slocum A. Principle of Elastic Averaging for Rapid Precision Design. Precision Engineering. 2017; 49: 146-159.
[6] In-Place Machining of Large Bed Ways. American Machinist. 1998

BERKELEY MET5: ENGINEERING PRECISION AND STABILITY FOR 8 NM RESOLUTION EUV LITHOGRAPHY

Arnaud Allézy[1], Christopher Anderson[1], Carl Cork[1], Michael Dickinson[1], Geoffrey Gaines[1], Gideon Jones[1], Ryan Miyakawa[1], Patrick Naulleau[1], and Senajith Rekawa[1]
[1]Center for X-Ray Optics
Lawrence Berkeley National Laboratory
Berkeley, California, United States of America

INTRODUCTION

Semiconductor industry growth is enabled by Moore's Law (number of transistors in an integrated circuit doubles about every two years). Transistor scaling enables lower leakage and higher switching speed. Since scaling is driven by wavelength shrink, switching from visible light to EUV brings significant benefits, it will also stop the increase of number of lithography steps and masks needed. The first generation of EUV is now being deployed by various chip suppliers [1] and research and development effort is transitioning to the extension of EUV lithography to high numerical aperture (NA), which also drives the scaling. To this end the EUREKA research program was launched at Lawrence Berkeley National Laboratory (LBNL) to develop next generation EUV patterning materials & processes.

A cornerstone activity of the EUREKA program is the development of a 0.5 NA microfield exposure tool referred to as MET5 [2]. With a depth of focus of 30 nm, the 0.5 NA tool requires 1 nm resolution metrology in the three linear directions and 100 nrad in tip/tilt. Wavefront errors need to be smaller than 0.5 nm RMS [3]. Including variable illumination capabilities, MET5 has an ultimate optical resolution of 8 nm [4] and calls for stringent stability specifications (less than 1 nm drift over exposure times as long as 1 min).

MET5 includes a two mirror objective with nanometer resolution precision stage systems, and a support/metrology system engineered for high stability. The mechatronics systems are designed to ensure stability against drifts and allow nearly arbitrarily slow experimental resist materials to be characterized.

PROPOSED LAYOUT

In MET5, the EUV light is reflected on the reticle, then through the PO, and expose the resist at the surface of the wafer. The optical column is comprised of three major subsystems:

- the reticle stage assembly (RSA),
- the metrology frame assembly (MFA), which supports the projection optic box (POB), the displacement measurement interferometer (DMI) measuring the lateral motion of the reticle and wafer with respect to the POB, and the wafer height sensor (HS),
- wafer stage assembly (WSA).

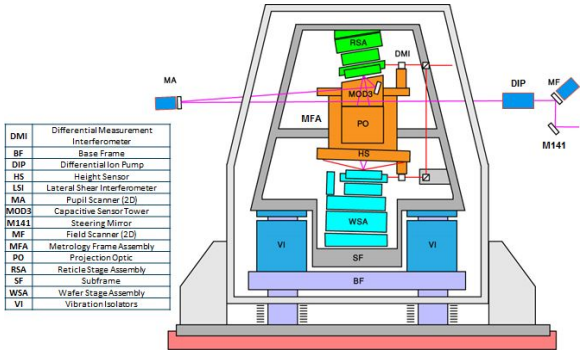

FIGURE 1. MET5 system layout.

The optical column is supported by a subframe (SF) that is floating on in-vacuum vibration isolators. The vacuum vessel is mounted separately to the ground and decoupled from the inside components with bellows.

REQUIREMENTS AND APPROACH

The 'aerial image' is the EUV print illumination, at the diffraction limit it is sinusoidal with a 16 nm period, (e.g. 8 nm lines). Any motion between aerial image and wafer during the exposure will reduce image contrast. A 10% reduction in contrast was chosen as the acceptable limit. This resulted in an in-plane

stability requirement that the aerial image must be stable with respect to the wafer to within 1.5 nm RMS over 60 s.

This specification is then subdivided across four main contributions: the reticle, the optic, the metrology frame, and the wafer. See equation below. The error budget assumes a 1.2X multiplier to any 'anti-correlated' motion, and a 5X magnification.

$$\sqrt{(\sigma_{WSA})^2 + (0.2\sigma_{RSA})^2 + (1.2\sigma_{MF})^2 + (1.2\sigma_{PO})^2} \leq 1.5\ nm\ RMS$$

The respective impacts of elementary disturbances (jumps, drifts, vibration) is then folded into the stability of each component, as shown below.

		Gauss factor	Corrected value	Multiplier*	Aerial Image Error
RETICLE/SF:					
linear drift	0.4 [nm PP]	0.577	0.23	0.2	0.05
jump	0.8 [nm PP]	0.707	0.55	0.2	0.11
vibration	2.0 [nm RMS]	1.000	2.00	0.2	0.40
metrology	0.6 [nm RMS]	1.000	0.60	0.2	0.12
fine stage	0.3 [nm RMS]	1.000	0.30	0.2	0.06
	TOTAL Stability [nm RMS]		**2.41**		**0.48**
WAFER/SF:					
linear drift	0.4 [nm PP]	0.577	0.23	1.0	0.23
jump	0.8 [nm PP]	0.707	0.55	1.0	0.55
vibration	0.7 [nm RMS]	1.000	0.70	1.0	0.70
metrology	0.6 [nm RMS]	1.000	0.60	1.2	0.72
fine stage	(not included here, accounted for at RETICLE)				
	TOTAL Stability [nm RMS]		**1.31**		**1.38**
PROJECTION OPTICS/SF:					
vibration	0.0 [nm RMS]	1.000	0.02	1.2	0.02
	TOTAL Stability [nm RMS]		**0.02**		**0.02**
METROLOGY FRAME/SF					
vibration	0.0 [nm RMS]	1.000	0.01	1.2	0.01
	TOTAL Stability [nm RMS]		**0.01**		**0.01**
			TOTAL SYSTEM STABILITY [nm RMS]		**1.50**

FIGURE 2. Stability error budget.

A multi-degree-of-freedom (MDOF) analytical model fed by the measured ground motion power spectral density predicted the vibrational internal position errors.

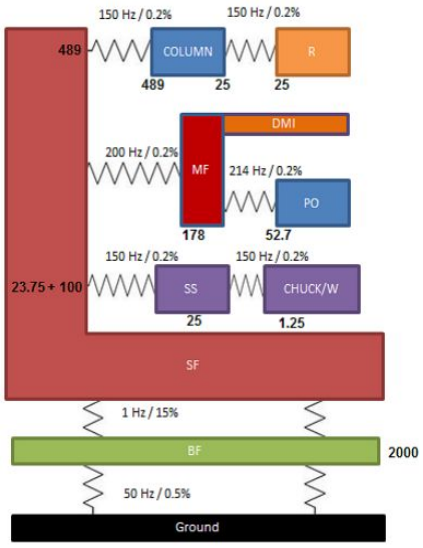

FIGURE 3. Analytical MDOF model.

Finally, natural frequency requirement and thermo-structural stability were verified using finite Element Analysis to optimize the architecture of the system.

INSTALLATION SITE

MET5 is installed at the LBNL Advanced Light Source (ALS). With more than 40 beamlines installed around the 200 m diameter storage ring, the cultural noise levels are high and many vibration sources are close by (cooling water pumps, cooling towers, air handling units, neighboring beamlines, users). Acceleration levels are typically a few $mm.s^{-2}$ RMS but can reach up to 50 $mm.s^{-2}$ during localized activity (doors opening and closing, people walking, dewars being rolled). Velocity wise, the site is below VC-F [5]. Displacement wise, in terms of RMS above 10 Hz, the ALS floor is typically 10 to 30 nm in the vertical direction and 2-10 nm in the lateral directions. This is three times noisier than MAX-IV in Sweden but two to three times quieter than ESRF in France or NSLS-II in the USA [6]. Peak displacement of around 100 nm can be measured during localized activity.

A series of major improvements to the building thermo-structural stability (isolating major cooling pumps and towers, addition of more cooling power to the building and upgrade of the obsolete building controls) has not yet been completed so high thermal fluctuations (up to 2 C/hour) are still observed.

The ALS building has been well characterized over the years though, and valuable data is continuously collected (pumps and fans frequencies, air temperature, settlement).

CLEAN ROOM

For environmental stability and particle control, MET5 is installed in a class 1000 clean room, providing temperature (21°C +/-0.01°C) and humidity (50% +/-1%) stability. Significant heat sources were relocated outside the clean room and the tool is equipped with thermally controlled footers to mitigate the impact of floor temperature fluctuations.

STAGE CONFIGURATION, DRIFT CONTROL

To address drifts, due to transient heat from the stage motors for example, a control feedback loop is implemented. The piezo controller bandwidth is about 50 Hz for the X, Y and Z directions, such that a 1 Hz bandwidth integrator can be achieved. The wafer needs to remain stable with respect to aerial image, not the optic itself, and thus corrections to a given axis can be applied either on the reticle or the wafer side, assuming a 5X magnification between them. Therefore, only 3 total axes of fine short stroke motion are required.

The drift control feedback signal is provided by the HS system in the vertical direction and the DMI system in the lateral directions. Lateral corrective motion is applied at the reticle stage and vertical correction at the wafer stage. The stage configuration is as shown below.

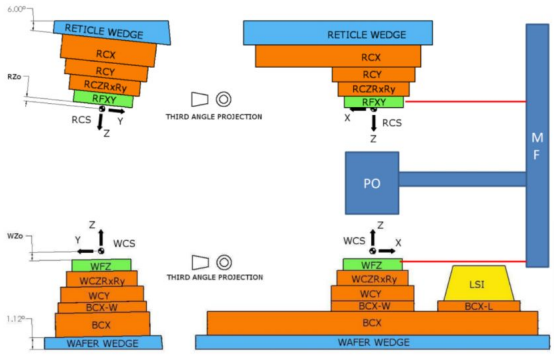

FIGURE 4. Stage configuration.

The 7-axes RSA is shown below. Its first natural frequency was measured at 170 Hz.

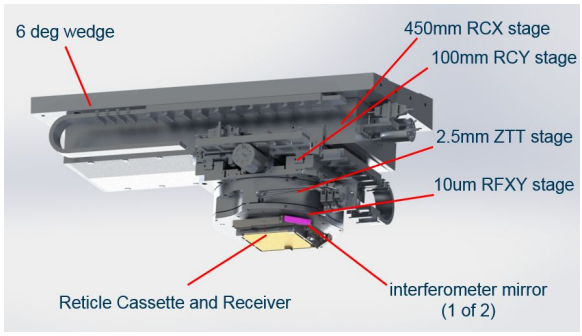

FIGURE 5. RSA 3D model view.

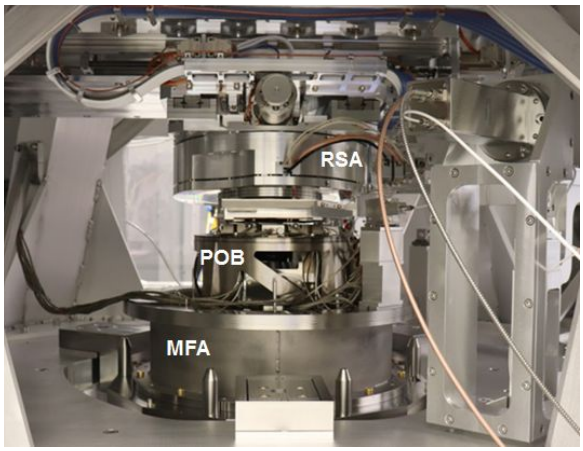

FIGURE 6. Upper SF view, RSA above the POB.

The wafer stage has two carriages, one for printing (5-axes), and one for in-situ interferometry (6-axes) [7], as shown below. Its first natural frequency was measured at 142 Hz.

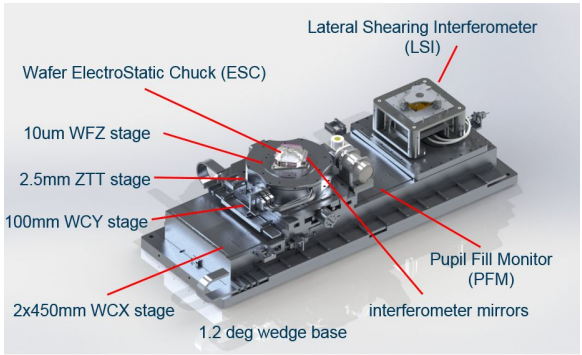

FIGURE 7. WSA 3D model view, with the shearing interferometer alongside the wafer.

The integrated lateral shearing interferometer (LSI) operates side-by-side with the wafer chuck to characterize the optical performance in-situ. The LSI assembly consists of a nanofabricated diffraction grating manufactured at the Center for

X-ray Optics (CXRO) nanofabrication lab, mounted on a 6-axis hexapod stage, which sits over an in-vacuum CCD camera.

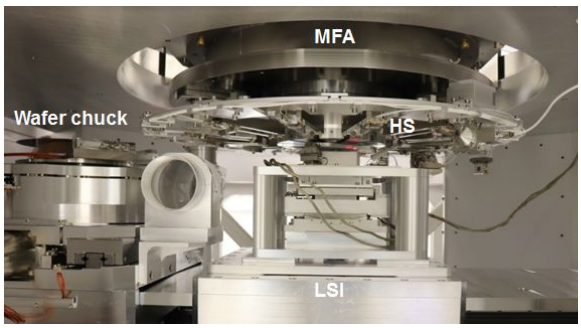

FIGURE 8. Lower SF view, LSI below HS (wafer chuck parked on the left).

SUBFRAME, METROLOGY FRAME

The aluminum subframe with steel cross beams floats on in-vacuum passive vibration isolators. It supports the RSA (160 kg), the MFA (250 kg) and WSA (210 kg). It has a first natural frequency of 140 Hz (see below).

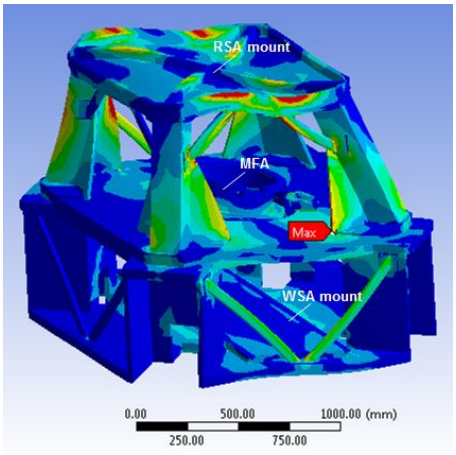

FIGURE 9. First natural frequency of the subframe at 143 Hz.

The Invar metrology frame holds the 5X magnification optics and the MET5 custom wafer height sensor (HS), as shown below. Three custom flexures were developped to maximize the first natural frequency of the MF (250 Hz), while being radially compliant for the differential expansion of the Invar MFA and the aluminum SF.

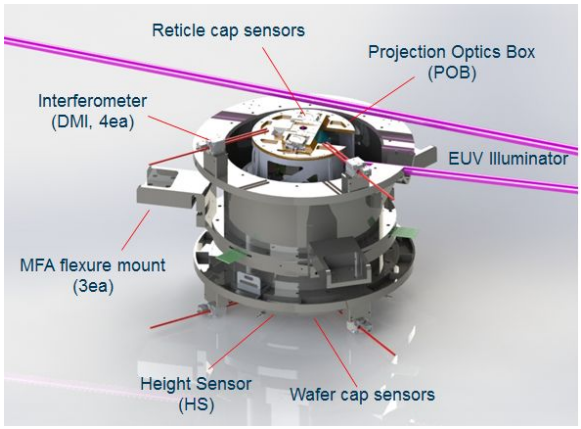

FIGURE 10. MFA 3D model view.

The projection optics is a two-mirror Schwarzschild objective fabricated by Zygo (PO) and includes an integrated illuminator module fabricated by Zeiss (MOD3).

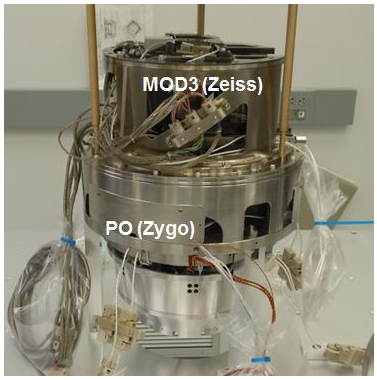

FIGURE 11. POB about to be lifted in the tool.

The HS measures the absolute distance from the MFA to the wafer at three overlapping locations, and three other locations forming a triangle, allowing for the measurement of tip and tilt. Each of the six channels of the height sensor is composed of two 3° Invar wedges, a source module (holding fiber-coupled focusing optics, 200 um pinhole, input lens) and a detector module (holding output lens, dual diode).

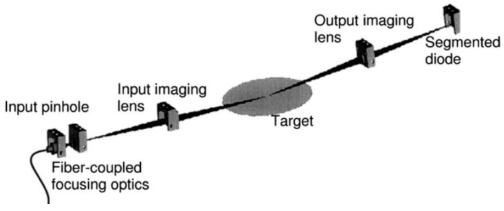

FIGURE 12. HS optical design.

The pinholes and the dual diodes are mounted on vertical flexures to ease alignment (see below).

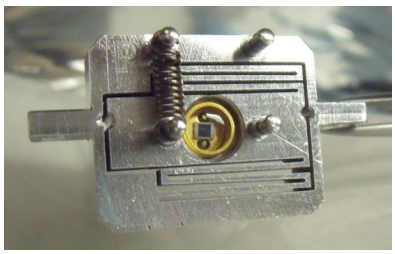

FIGURE 14. Flexure mount for dual diode.

The HS is made of Invar and has been weight relieved in order to increase the natural frequency of the MFA on its flexures.

FIGURE 15. Bottom view of the MET5 HS.

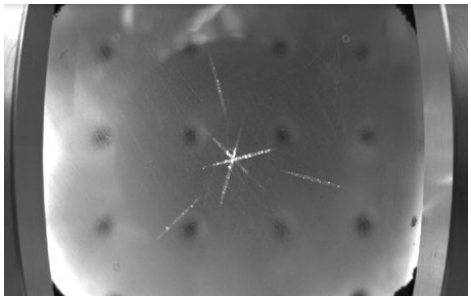

FIGURE 16. The 6 laser beams of the HS create 6 spots on the wafer for Z-Tip-Tilt measurement.

The ratio of the signals on the dual diode gives absolute distance to the wafer to 1 nm accuracy. Tip and tilt is evaluated to 100 nrad. The MET5 HS achieves 0.4 nm RMS shot noise [8].

The metrology frame also supports the beamsplitters of the Displacement Measuring Interferometer (DMI) that measures the lateral displacements of the mask and wafer. The four beams (Wafer X,Y and Reticle X,Y) are produced from a single laser source via the beam delivery frame (BDF). The BDF employs beamsplitters and folding mirrors to position and orient the 4 DMI beams in front of their respective mirrors installed on the reticle cassette and the wafer electrostatic chuck (see below).

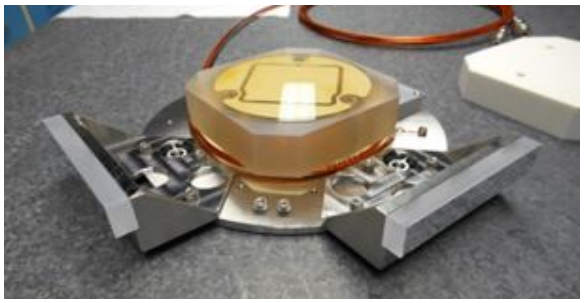

FIGURE 18. DMI mirror on the wafer chuck.

VIBRATION ISOLATION

The VIS is built around 4ea vacuum compatible MinusK SM-1 passive isolators. The isolators frequency is 1 Hz vertical, 0.5 Hz lateral. For maximum performance, the center of gravity of the isolated payload, or subframe, is coincident with the point of interested (focus on the wafer) and in the plane defined by the top of the isolators. Because of the compliance of the system, the isolators were retrofitted with motorized levelers and encoders, in order to keep the payload level when the large masses of the RSA and WSA are shifting around.

RESULTS/SUMMARY

Current vibration metrology on the commissioned MET5 indicates less than 1 nm RMS at the wafer and less than 2 nm at the reticle. With this high degree of stability for the MET5 subframe and stages, preliminary LSI measurements yielded an optical wavefront error of less than 1 nm RMS, prior to performing any optical alignment. This measurement represents the world's first at-wavelength wavefront measurement of a high NA EUV lithography optic. Print-based alignment and optimization of the system is now underway with patterning already observed at the 12 nm level.

ACKNOWLEDGMENTS

This work was performed at the LBNL CXRO. The authors would like to thank the entire team at CXRO that helped make this work possible.

The authors would also like to acknowledge MI-PARTNERS for its support in the preliminary phase of the project, PI|MiCoS for the stages, ZYGO and ZEISS for the optics. This work was performed at Lawrence Berkeley National Laboratory with support from Intel, Samsung, EUV Tech, Inpria, and JSR through the U.S. Department of Energy under Contract No. DE-AC02-05CH11231. Support for the projection optics was also provided by the Department of Energy, Advanced Manufacturing Office.

REFERENCES

[1] van Schoot J, Others. EUV high-NA scanner to extend EUV single exposure. In: *The EUVL Workshop*. 2016.

[2] Naulleau P, Allézy A, Anderson C, Cork C, Denham P, Dickinson M, Gaines G, Gullikson R, Miyakawa R, Rekawa S, Thur W, Zehm D, Soufli R, Bremer M, Girard L, Kestner B, Kincade J, Marchetti L, Hudyma R. Status of high numerical aperture EUV lithography development: The Berkeley MET5. In: *2016 International Symposium on Extreme Ultraviolet Lithography*.

[3] Girard L, Marchetti L, Bremer M, et al. Fabrication of EUVL micro-field exposure tools with 0.5 NA. In: *Optifab 2015*. Epub ahead of print 2015. DOI: 10.1117/12.2203138.

[4] Naulleau P, Anderson C, Benk M, et al. EUV extendibility research at Berkeley Lab. In: *2017 International Symposium on VLSI Technology, Systems and Application (VLSI-TSA)*. 2017, pp. 1–2.

[5] Amick H, Gendreau M, Busch T, et al. Evolving criteria for research facilities: vibration. In: *Buildings for Nanoscale Research and Beyond*. International Society for Optics and Photonics, 2005, p. 593303.

[6] Compilation of ground motion measurements - Overview of Measured Sites, http://vibration.desy.de/overview (accessed 30 March 2018).

[7] Naulleau P. EUREKA: A Industry EUV Research Center at LBNL. In: *2016 International Workshop on EUV Lithography*. Center for X-ray Optics, Lawrence Berkeley National Laboratory.

[8] Miyakawa R, Anderson C, Naulleau P. High-NA metrology and sensing on Berkeley MET5. In: *Extreme Ultraviolet (EUV) Lithography VIII*. Epub ahead of print 2017. DOI: 10.1117/12.2261893.

[8] Miyakawa R, Anderson C, Naulleau P. High-NA metrology and sensing on Berkeley MET5. In: *Extreme Ultraviolet (EUV) Lithography VIII*. Epub ahead of print 2017. DOI: 10.1117/12.2261893.

DESIGNING LOW FREQUENCY BAND GAPS IN ADDITIVELY MANUFACTURED PARTS USING INTERNAL RESONATORS

Waiel Elmadih[1], Wahyudin P. Syam[1], Ian Maskery[2], Richard Leach[1]
[1]Manufacturing Metrology Team
[2]Centre for Additive Manufacturing
University of Nottingham
Nottingham, NG8 1BB, UK

INTRODUCTION

Additive manufacturing technologies provide a high degree of design freedom to exploit complex structures with tailorable mechanical properties. Within these properties lies vibration isolation, which depends mainly on the mass and stiffness of the structure. Traditional techniques for providing vibration isolation promote shifting the resonant frequency above or below the frequency of interest [1–3]. There has been little focus on methods to completely eliminate vibration waves from a precision engineering component. One promising method to do this is to design the structure to have a phononic band gap (BG) spanning the frequency of the undesirable incident waves [4]. A BG is a frequency region in which there is no propagation of elastic waves [5].

BGs can be formed by Bragg scattering or through the use of internal resonators. A Bragg scattering BG is formed by the destructive superposition of reflected waves, and occurs at frequencies of the order of the wave speed divided by the size of the unit cell of which the structure is composed [6]. Several applications of Bragg BGs have been reported successful as can be seen in the work of Ampatzids et al. [7] who presented and experimentally verified a 1D BG at sub-7 kHz in composite material. Hsu et al. [8] presented a silicon-based metametrial with several BGs between 60 MHz and 100 MHz, and Wang et al. [9] proposed a 3D periodic structure with a BG between 35 MHz and 36 MHz. Bragg induced BGs can also be seen in the work of Martin et al. [10]. The main difference between internal resonator band gaps (IRBs) and Bragg scattering BGs is that IRBs can be tuned to much lower frequencies, by hindering the wave propagation around the resonance of the structure. Liu et al. [11] presented a 3D structure including lead spheres embedded in a soft rubber coating; that structure provided an IRB with a response lower by two orders of magnitude than the reference structure of no IRB mechanism. Matlack et al. [12] designed additively manufactured lattice structures with embedded resonators and recorded IRBs in frequency ranges between 2.4 kHz and 8.3 kHz [12].

In this paper, we report on the design, modelling and experimental verification of a repeating lattice structure with a tuneable low frequency BG based on internal resonators. We present relationships between the BG properties and the geometrical parameters of the proposed IRB structure. An optimised IRB structure is then used in a case study in which a vibration isolation platform is designed to provide isolation for an all-optical dimensional measuring system (AODMS) [13]. The control of IRBs will serve as a future design tool for machines and structures with elimination of vibration waves in multiple degrees of freedom.

THE IRB UNIT CELL

The general IRB unit cell of this study is shown in FIGURE 1. The outer frame is a scaffold providing structural integrity, whilst a resonator occupies the centre of the cell and connects to the scaffold walls with six thin struts.

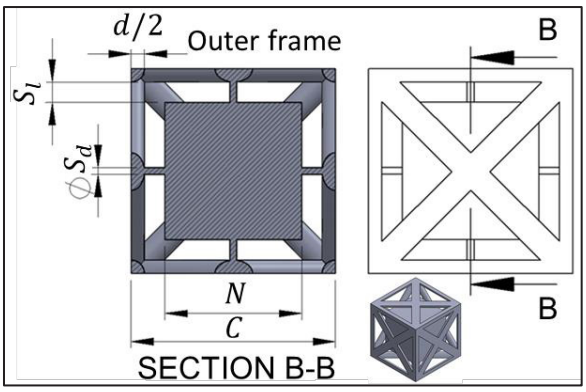

FIGURE 1. IRB unit cell. The outer frame supports structural loads, while the lower stiffness struts (with thickness S_d and length S_l) and resonator (of dimension N) hinder wave propagation and provide a tunable BG.

The various cell dimensions are related by

$$C = N + 2S_l + d \quad (1)$$

where C is the cell size, S_l is the length of an internal strut, N is the length of the resonator and d is the diameter of the struts making up the supporting scaffold. The reader is referred to the design tool in reference [2] for information on designing strut-based lattices of different volume fractions and sizes.

METHODOLOGY

The IRB unit cell of this study can be tessellated in 3D using the linear lattice vectors $n_1e_1 + n_2e_2 + n_3e_3$. The periodicity of the lattice structure can be defined in the spatial coordinates as

$$\begin{aligned} e_x &= C_x i_x, \\ e_y &= C_y i_y, \\ e_z &= C_z i_z, \end{aligned} \quad (2)$$

where $e_{x,y,z}$ are the lattice basic vectors, $C_{x,y,z}$ are the unit cell sizes and $i_{x,y,z}$ are the lattice periodicity numbers. For a cubic lattice, C_x, C_y and C_z are all equal to C.

This work uses a finite element (FE) method which can predict BGs with higher accuracy and efficiency [12,14] than the wavelet method [15], plane wave expansion method [16] and finite difference time domain method [17]. The FE method also allows the calculation of the dispersion curves (DCs) of complex structures, such as the IRB unit cell of this study. For modelling the elastic wave propagation, the reciprocal lattice vectors (k_x, k_y and k_z) for the cubic IRB lattice of study can be expressed by

$$\begin{aligned} k_x &= \frac{2\pi}{C_x} i_1, \\ k_y &= \frac{2\pi}{C_y} i_2, \\ \text{and} \quad k_z &= \frac{2\pi}{C_z} i_3. \end{aligned} \quad (3)$$

Bloch theorem dictates that the propagation of waves in a periodic structure can be understood by the harmonic displacement of a single unit cell [6]. In our case, we have

$$\boldsymbol{q_1} = e^{-i\omega k}\boldsymbol{q_2} \quad (4)$$

where $\boldsymbol{q_1}$ and $\boldsymbol{q_2}$ represent the displacements of the nodes at one edge or face of the unit cell, and ω is their angular frequency. The vectors k are bounded by a single reciprocal lattice unit cell [6]. Within this reciprocal cell, k values are further restricted to only part of the reciprocal cell called the irreducible Brillouin zone (IBZ), as shown in FIGURE 2. The IBZ contains sufficient wavevectors to describe wave propagation throughout the whole structure.

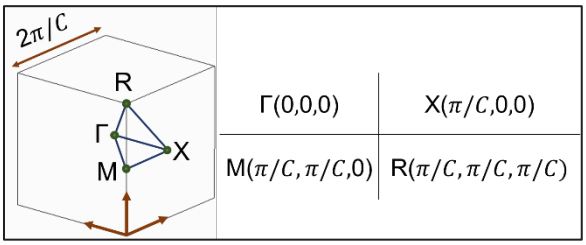

FIGURE 2. The IBZ of a cubic lattice. On the right are the reciprocal space coordinates (k_x, k_y, k_z) for a set of commonly examined wavevectors.

For a cubic lattice, we identify three types of nodes (see FIGURE 3) in the 1D case and thus three vectors containing the displacements of the cell are considered: the leftmost nodes, rightmost nodes and all inner nodes. The number of nodes expands to nine in 2D, and nineteen in 3D, which is the focus of this work.

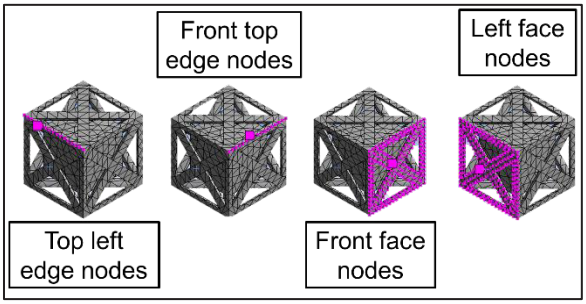

FIGURE 3. Examples of the types of nodes in the proposed IRB cell.

A generalised eigenvalue problem

$$\boldsymbol{K} - \omega^2\boldsymbol{M} = 0 \quad (5)$$

is constructed for each wavevector in the IBZ, based on stiffness and mass matrices obtained from the commercial software ANSYS (after ensuring mesh convergence). The scan for the eigenvalues is carried out in four runs along the Γ-X, X-M, M-R, and R- Γ directions, and the total count of wavevectors representing the IBZ is set to 360. Frequency regions with no solution for the eigenvalue problem indicate BGs.

In this investigation, the ratio S_d/c is varied, taking values between 0.005 and 0.033, and the wavevector DCs are calculated at each value. The same commercial software (ANSYS) is used to model the attenuation profile of a structure with a finite number of IRB cells. Experimental verification is provided by additively manufacturing a structure of similar number of unit cells from Nylon-12 with laser powder bed fusion (LPBF), then performing a vibration test.

RESULTS AND DISCUSSION

We present the calculated DCs of an IRB cell with the parameters S_l/c = 0.1, S_d/c = 0.033, and C= 30 mm. The material properties for Nylon-12 parts manufactured with LPBF are presented in TABLE 1 and the DCs are shown in FIGURE 4.

TABLE 1. Properties of L-PBF Nylon-12 [18].

Density	Young's modulus	Poisson's ratio
0.95 g/cm^3	1500 MPa	0.35

Wavebands which start to propagate at 0 Hz are interrupted with a BG caused by the internal resonator at 1620 Hz. The BG spans across the four selected boundaries of the IBZ, Γ-X-M-R-Γ and thus it is a 3D BG. The BG continues up to 2700 Hz where new wavebands start propagating.

The ability of this unit cell to provide vibration isolation between 1620 Hz to 2700 Hz is confirmed by examining a structure of the same unit cell in 9×9×9 tessellations. According to Chen et al. [19], any number of unit cells higher than seven is enough to identify a BG with harmonic response analysis. The leftmost nodes are excited with a harmonic force of 1 N between 0.1 Hz to 3500 Hz with a sample spacing of 1 Hz. The average displacement of all rightmost nodes of the structure under the aforementioned settings are depicted in FIGURE 4 (inset). It is observed that the displacement is attenuated in the BG region between 1620 Hz to 2700 Hz. The frequency can be normalised with the speed of the wave in the medium *v* and the cell size C to provide more generalised results. This gives the advantage of adding the material and the cell size to the BG tuning mechanism. Thus, the right ordinate of FIGURE 4 and the abscissa of FIGURE 4 (inset) show the normalised frequency for the unit cell under study. The normalised frequency of the BG is calculated to be from 0.039 to 0.065.

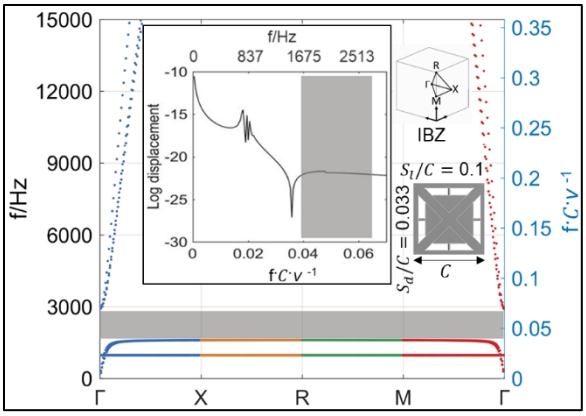

FIGURE 4. DCs of a cubic IRB lattice cell and harmonic response analysis of the same cell in 9×9×9 tessellations (inset). Wave propagation is shown along selected reciprocal vectors in the IBZ. The shaded frequency region represents a 3D BG.

Bandgap tuning parameter

For control of the BG in FIGURE 4, a structural parameter identified as the ratio between the diameter of the resonator strut to the cell size S_d/C is selected because it is expected to have a direct control on the stiffness of the resonator. Having control over the stiffness of the resonator is the first step towards tuning the stiffness/mass ratio (K/m) and tuning the ability of the cell to provide a BG. S_d/C takes values in the range of 0 to $1-d/C$. The parameter d/C takes a value of 0.13 for a 30% volume fraction cell [2]. Thus, the identified parameter S_d/C takes values between 0 and 0.87.

Since our interest is low frequency BGs (see Case study section), we choose S_d/C values in the lower range, as can be seen in TABLE 2. Values in this lower range are expected to provide a low K/m ratio of the resonator mechanism and ultimately a low resonance frequency.

The starting value S_d/C = 0.033 is selected with the aim of designing an IRB cell with unit cell size of 30 mm and a resonator strut of a diameter equal to the minimum LPBF manufacturing size (1 mm). To ensure that the mass of the IRB cell is kept constant, the study is carried at a constant S_l/C value of 0.1. This value is aimed at having a high value of m for the resonator to ensure a lower resonant frequency while ensuring low overhang of the struts to avoid lamination during LPBF.

TABLE 2. The parameters of five unit cells used in the BG tuning study.

S_d/C \ S_l/C	0.1
0.033	Start and end normalised frequencies of the BG formed by any combination of these values are calculated and are shown in FIGURE 4.
0.025	
0.02	
0.01	
0.005	

It is assumed that at $S_d/C = 0$, the resonator has no diameter, and thus no IRB mechanism is available. The normalised start and end frequencies as calculated for the five IRB cell types are given in FIGURE 5. All the cells provided BGs.

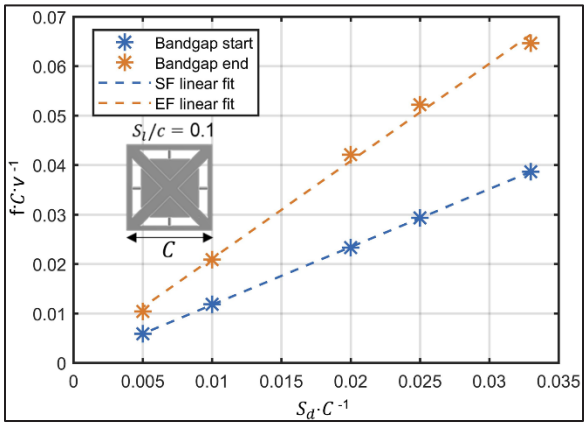

FIGURE 5. The lower and upper normalised BG frequencies for various configurations of IRB cell (see TABLE 2).

The lowest recorded BG spanned a normalised frequency range from 0.005 to 0.01. This was for the cell of S_d/C=0.005. This BG was the narrowest compared to those of the other examined cells. The start and end frequencies of the BG increase linearly with the increase in S_d/C. The equation that correlates the parameter S_d/C to the normalised BG start frequency (SF) is

$$SF = (1.17 \pm 0.013)\frac{S_d}{C} + 3.7 \times 10^{-5} \pm 0.001, \quad (6)$$

which is a linear fit to the numerical data of SF with an adjusted *R*-squared value of 0.9999. The equation that correlates the parameter S_d/C to the normalised BG end frequency (EF) is

$$EF = (1.97 \pm 0.205)\frac{S_d}{C} + 13.97 \times 10^{-4} \pm 0.004, \quad (7)$$

which is a linear fit to the numerical data of EF with an adjusted *R*-squared value of 0.9947.

Experimental verification

Using LPBF, a 3×3×3 Nylon-12 sample with a cell size of 30 mm was fabricated. Due to the 1 mm manufacturing limitation of the employed LPBF system, the nominal strut diameter was designed to be 1 mm, and the strut length was 3 mm. The strut diameter was manufactured with a deviation of -10% from the nominal value. The targeted mass was 297 g, while the measured mass was 350 g. This deviation is expected to be due to changes in material density related to the laser scanning speed, powder quality and laser power of LPBF system. The experiment set up is shown in FIGURE 6.

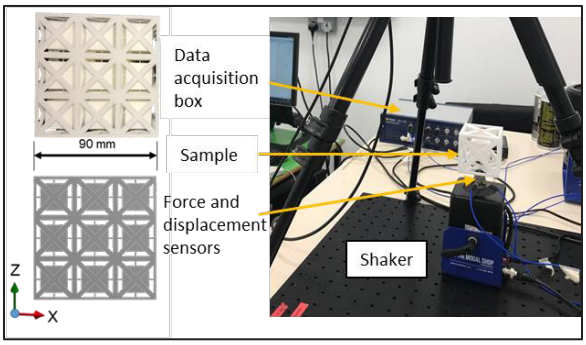

FIGURE 6. 3×3×3 *Nylon-12 sample as modelled (bottom left) and fabricated (top left). The experimental setup is shown on the right.*

A periodic chirp excitation signal is send through the data acquisition box to the Modal Shop K2007E01 shaker. The signal bandwidth was 0 kHz to 3.5 kHz. The sample is attached to force and displacement sensors which are in turn attached to the shaker. The experiment was controlled using proprietary software which controls a data acquisition box, to which the shaker and oscillation sensors are attached. The experimental result, shown in FIGURE 7, is produced with multiple sweeps of the frequency range with a sample spacing of 0.39 Hz.

The experiment is in good agreement with the simulation of similar settings in terms of resonant frequencies, general attenuation profile and lack of resonance peaks in the BG frequency region.

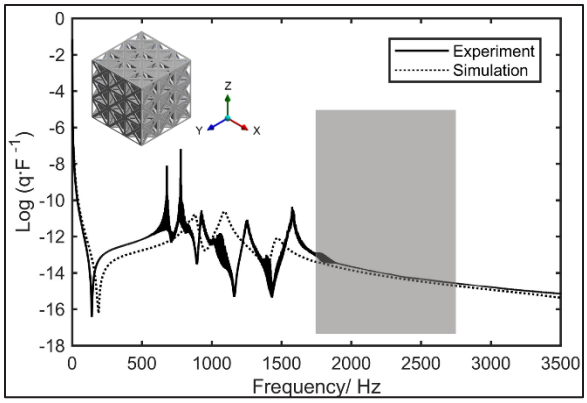

FIGURE 7. Harmonic response analysis of 3×3×3 Nylon-12 sample as simulated (dotted line) and experimentally tested (solid line). The ordinate shows the logarithm of the displacement q per unit input force F.

CASE STUDY

A metrology platform is to be designed using IRB lattice structures to provide 3D vibration isolation in the range between 50 Hz to 100 Hz. The dimensions of the required platform are: min. (150×150×150) mm, max. (200×200×200) mm for an AODMS sensor of 10 kg mass. The aim of the study is to determine whether IRB structures are suitable for providing the isolation in the specified range.

Results and discussion

The first step was to select the IRB cell that can provide the BG within the specified frequency region. The selection was made by searching for the BG by the input of the material properties and cell size to FIGURE 5. The ability of a specific cell of certain dimensions and material composition to provide a suitable BG was then explored. Unit cells that can provide the BG within the sought frequency region were identified. Two unit cells of different size and material composition that can provide the BG between 50 Hz to 100 Hz are highlighted and the cells' specifications are summarised in TABLE 3.

TABLE 3. IRB cells that can provide vibration isolation between 50 Hz to 100 Hz.

Option	(1) S_d = 0.75 mm, S_l = 15 mm, 150 mm	(2) S_d = 1 mm, S_l = 5 mm, 50 mm
Material	Nylon-12	TPE-210-s
Cell mass	1.37 kg	53.8 g
Young's modulus	1.5 GPa	8 MPa

Of these two cells, option-2 is more suitable for manufacturing the platform due to:

- The compact cell size of 50 mm that allows higher number of tessellation in a confined space of (200×200×200) mm and thus better realisation of the BG.
- Larger minimum feature size of 1 mm compared to 0.75 mm for option-1, and thus better suitability for LPBF.
- Higher number of cells, and thus a more defect tolerant design.

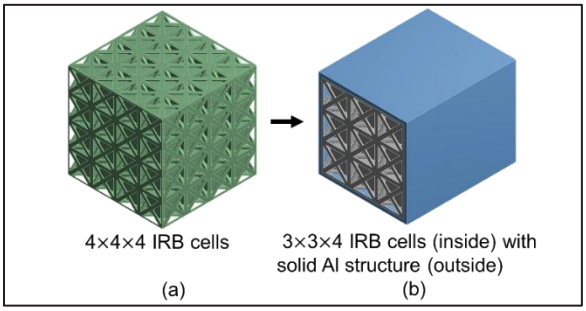

FIGURE 8. Improvements made on the IRB platform design: (b) higher structural stiffness.

The low Young's modulus of option-2 allows the realisation of BGs at low frequencies and with achievable cell dimensions. However, the material suffers from two limitations: low structural stiffness and high thermal expansion coefficient. To address these two issues, the design of FIGURE 8 (b) proposes the use of 3×3×4 IRB cells embedded in solid aluminium casing of 3 mm thickness. The design is modelled to withstand double the mass of the sensor for safety. The simulated responses of the described structure are shown in FIGURE 9 and depict attenuation of the excitation signal between 50 Hz to 100 Hz in 3D.

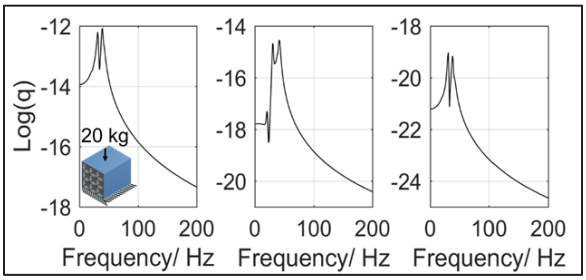

FIGURE 9. Simulated harmonic response of IRB cells with solid Al host in longitudinal (left), x- (middle) and y- (right) directions under 20 kg load.

CONCLUSIONS

We have shown that strut-based lattices can be designed to have low frequency 3D BGs when

resonators are embedded within the structure. The strut diameter of the resonator is found to be a direct means for tuning the BG. BGs in frequency regions as low as 50 Hz are predicted to be achievable using a low-stiffness 50 mm lattice cell embedded in an Al casing. Verification of the BG simulation method was carried using a 30 mm Nylon-12 specimen fabricated with LPBF. Good agreement with the simulated results was found. This work is a promising step forward for eliminating vibrations in precision engineering applications. Future work will examine more IRB lattices with more BG tuning parameters, and will study the design and manufacturability of a metrology frame for an AODMS. This work was supported by the Engineering and Physical Sciences Research Council (grant number EP/M008983/1). The authors would like to thank Joseph White from University of Nottingham for helping with this work.

REFERENCES

[1] Syam WP, Jianwei W, Zhao B, Maskery I, Elmadih W, Leach RK. Design and analysis of strut-based lattice structures for vibration isolation. Precis. Eng. 2017; 52: 494-506.

[2] Elmadih W, Syam WP, Maskery I, Leach RK. Additively manufactured lattice structures for precision engineering applications. Proc. 32nd ASPE. Charlotte: 2018.

[3] Schmitz TL, Smith KS. Mechanical vibrations: modeling and measurement. Springer. New York: 2011.

[4] Panesar A, Abdi M, Hickman D, Ashcroft I. Strategies for functionally graded lattice structures derived using topology optimisation for additive manufacturing. Additive Manufacturing. 2018; 19: 81-94.

[5] Elmadih W, Syam WP, Maskery I, Chronopoulos D, Leach RK, Mechanical vibration bandgaps in surface-based lattices. Additive Manufacturing. Under review (2018).

[6] Phani AS. Elastodynamics of lattice materials, in: Phani AS, Hussein M I. Dynamice of lattice material. John Wiley and Sons. 2017; 53–59.

[7] Ampatzidis T, Leach RK, Tuck CJ, Chronopoulos D. Band gap behaviour of optimal one-dimensional composite structures with an additive manufactured stiffener. J. Compos. Part B Eng. 2018; 153: 26–35.

[8] Hsu FC, Lee C I, Hsu JC, Huang TC, Wang CH, Chang P. Acoustic band gaps in phononic crystal strip waveguides. Appl. Phys. Lett.. 2010; 96: 3-6.

[9] Wang L, Bertoldi K. Mechanically tunable phononic band gaps in three-dimensional periodic elastomeric structures. Int. J. Solids Struc. 2012; 49: 2881-2885.

[10] Martin A, Kadic M, Schittny R, Bückmann T, Wegenerz M. Phonon band structures of three-dimensional pentamode metamaterials. Phys. Rev. B. 2017; 025309:1-7

[11] Liu Z, Zhang X, Zhu YY, Yang Z, Chan C T, Sheng P. Locally resonant sonic materials. Science. 2000; 289:1734-1736.

[12] Matlack KH, Bauhofer A, Krödel S, Palermo A, Daraio C. Composite 3D-printed meta-structures for low frequency and broadband vibration absorption. 2016; 113: 8386-8390.

[13] Leach RK, Elmadih W, Piano S, Senin N, Sims-Waterhouse D, Syam WP, Su R, Thomas M. Enriching micro-scale metrology with an all- optical dimensional measuring system. Proc. euspen Micro/Nano Manufacturing Workshop. Strathclyde: 2017.

[14] Khelif A, Hsiao FL, Choujaa A, Benchabane S, Laude V. Octave omnidirectional band gap in a three-dimensional phononic crystal. IEEE Trans. Ultrason. Ferroelectr. Freq. Control. 2010; 57: 1621–1625.

[15] Yan Z, Wang Y, Zhang C. Wavelet method for calculating the defect states of two-dimensional phononic crystals. Acta Mech. Solida Sin. 2008; 21: 104–109.

[16] Zhou XZ, Wang YS, Zhang CS. Three-Dimensional sonic band gaps tunned by material parameters. Appl. Mech. Mater. 2010; 29: 1797–1802.

[17] Sigalas MM, García N. Theoretical study of three dimensional elastic band gaps with the finite-difference time-domain method. J. Appl. Phys. 2000; 87: 3122–3125.

[18] Materialise. PA 12 (SLS): Datasheet. 2018; http://www.materialise.com/en/manufacturing/materials/pa-12-sls (accessed January 31, 2018).

[19] Chen Y, Yao H, Wang L. Acoustic band gaps of three-dimensional periodic polymer cellular solids with cubic symmetry. J. Appl. Phys. 2013; 114: 043521-043528.

DESIGN OF AN INSTRUMENT FOR CHARACTERIZING THE EMBEDDED BRAIN TISSUE CUTTING PROCESS

Aaron E. Ramirez and Martin L. Culpepper
Department of Mechanical Engineering
Massachusetts Institute of Technology
Cambridge, MA

INTRODUCTION AND MOTIVATION

The overarching goal of this research is to identify, understand, and ultimately to predict the drivers that dominate and limit cutting performance in embedded brain tissue cutting. Achieving this will enable mapping of larger brain volumes, which in turn enables greater understanding of mammalian neural structure and pathology. Such understanding would be valuable in understanding the physical basis of diseases such as Alzheimer's, as well as contributing to a better understanding of brain-based capacities such as learning and memory. In this work, an instrumented cutting machine (FIGURE 1) to record video and force data was developed to observe and characterize the embedded tissue cutting process.

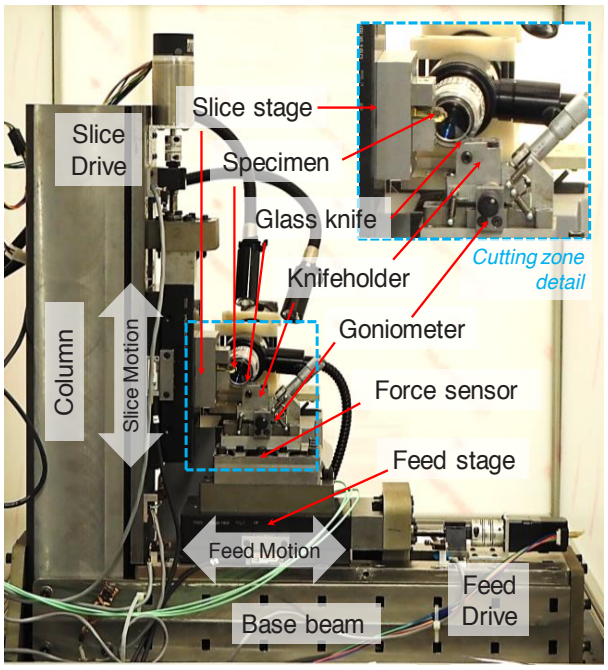

FIGURE 1: Annotated image of instrumented cutting setup. The machine has two primary motion axes, a video microscope, and a 3-axis force sensor.

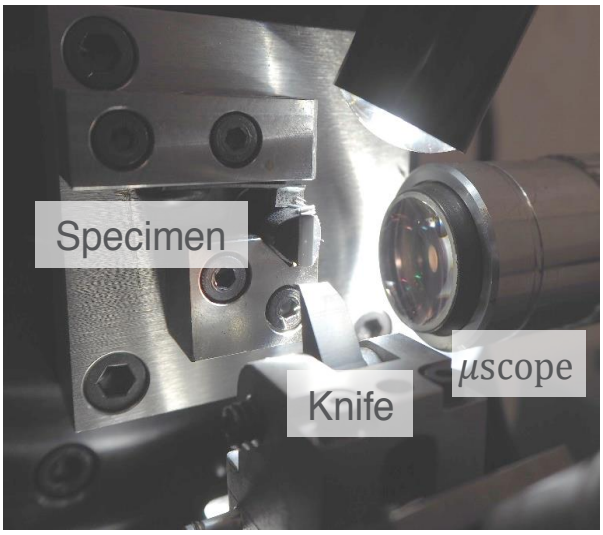

FIGURE 2: Close-up of cutting zone, cutting a Delrin beveled specimen. The width of cut increases with depth.

BACKGROUND: BRAIN MAPPING

In order to map neuron networks with synaptic resolution, *post-mortem* brain tissue embedded in epoxy resin is sliced into 'sections' (identical to the 'chip' in machining) of thicknesses between 20 nm to 1 um. Sequences of slices are subsequently imaged on an electron microscope and a 3D map of the neuronal network is constructed by stacking the images while tracing neurons through the images. The lateral dimensions of the sections typically do not exceed 1 mm due to onset of chatter. Difficulties are generally encountered when attempting to cut wider sections, thinner sections (below around 30 nm), or thin and wide sections [1-3]. These cutting difficulties present a limit on the volume of tissue that can be mapped; with current techniques it is possible to reliably cut volumes of about 1 mm^3, but there is considerable scientific interest in sectioning and mapping increasingly larger volumes such as an entire mouse brain of volume ~1 cm^3, about a 1000-fold increase in current capabilities, as well as improving the reliability and predictability of sectioning smaller tissue volumes.

The sectioning process very closely resembles orthogonal cutting, which is a foundational model originally developed for studying metal cutting and machining [4]. A captured frame (FIGURE 3) from a machine prototype shows the resemblance. There exists an opportunity to draw from the extensive machining and cutting literature to aid understanding of the embedded tissue cutting process, and apply this knowledge to process and equipment design to improve size limits in sectioning.

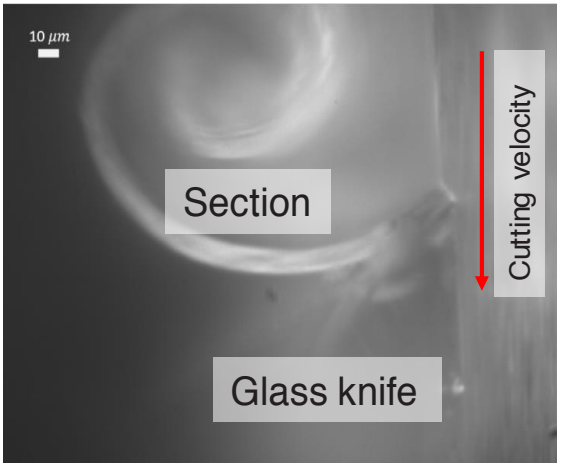

FIGURE 3: A section being cut from an Embed-812 epoxy blank sample, with shear angle visible under illumination.

DETERMINISTIC DESIGN METHODOLOGY

The general design strategy was to work backwards from the functional requirements to generate target specifications for the instrument's major subassemblies and structural elements.

The expected cutting loads and requirements for force sensing were selected according to cutting data from [5]. A spreadsheet-based analytical error model utilizing a kinematic model of the machine described using homogeneous transformation matrices (HTMs), as described in [6], was used to monitor expected load-induced errors and their propagation throughout the structural loop; the model was most useful for keeping track of sine errors. The model was used iteratively during the design process to aid in the selection of concepts, materials, and components.

The functional requirements used to design the cutting instrument are summarized in TABLE 1. Cutting speed was selected based on current sectioning equipment capabilities, to reproduce poor sectioning behavior.

TABLE 1. Functional requirements for the instrumented cutting visualizer.

Requirement	Value	Unit
Feed travel range	6.35	mm
Slice travel range	8	mm
Cutting speed	0.1 - 10	mm/s
Force resolution	~1	mN
Force accuracy	~1-10	mN
Maximum force	~10	N
Slice velocity accuracy	1%	
Section thickness accuracy	0.1	um
Feed position accuracy	0.1	um

The overall stiffness target for the machine was determined based on limiting variations in section thickness to no more than 10% of the minimum section thickness, which was determined by the microscope resolution. The 100 nm deflection limit to meet the section thickness accuracy specification required the load-induced error contributions of several subassemblies to be kept to no more than tens of nanometers, likewise for thermal drifts during a cut (which typically lasts for less than a minute). The use of an error model was essential for this, as it allowed an assessment of the impact on error at the tool point. Special attention was paid to avoiding any backlash or slop on moving components or interfaces, and ensuring all motion interfaces were preloaded. The machine was also designed such that the need for precision alignment between the drive components was minimized by utilizing a decoupling flexure stage between the driving screw and the crossed-roller bearing stage.

SYSTEM COMPONENTS

Machine structure

The machine utilizes an open-frame design, which is easier to operate and simplifies mounting and positioning of auxiliary hardware for characterization and calibration, as it leaves room around the machine with access to the work zone. The base of the machine is a built-up box beam made of Invar 36 plate to mitigate thermal expansions in the sensitive feed direction, with other components being made mostly of mild steel. The column is a 101.6 mm square tube of 7.94 mm wall thickness A36 steel.

Motion control

Crossed-roller bearing stages (THK VRU6160) provide high-stiffness linear motion guidance for the feed and slice axes. THK BNK-series ballscrews with preloaded nuts and 1 mm pitch are used to drive both axes, with decoupling leadscrew flexures

to mitigate the effects of misalignment. The slice axis, due to the need for slow speeds, is driven by a brushless motor with sine encoder feedback; the feed axis is driven by a stepper motor with a harmonic gear reduction (Oriental Motor CRK series and driver). Both stages are able to step with finer resolution than the linear feedback sensors can measure; further characterization to find ultimate performance limits using capacitive probes is ongoing.

Software

The instrument is controlled via a single LabVIEW program running on a Dell Precision 7510 laptop running Microsoft Windows 7. The LabVIEW control loop runs five parallel loops which communicate via message queues. The loops are for handling the GUI, camera control, DAQ I/O, communication with slice stage motion controller, and feed stage control. Force sensor and video data are processed in MATLAB.

Electrical and sensing

The electrical panel is powered with a 24V 600W power supply (Delta Electronics PMC-24V600W1BA).

Three Kistler 9215 single-axis piezo sensors are arranged to provide a three-axis force measurement. The charge output from these sensors is conditioned by a Kistler Type 5073 3-channel Charge Amplifier into +- 10V signals, which is read into a National Instruments 9239 24-bit ADC.

Rotary position feedback for the brushless motor's sine commutation is provided by a Heidenhain ERO 1480 sine encoder, currently configured for 4,000,000 counts per revolution. This feedback is used by a Galil DMC31012 motion controller with 16-bit encoder interpolator to control a Maxon EC-Max 283867 brushless motor. Linear position feedback for both the slice and the feed stage is from Renishaw T1001 linear encoders with TI2000A interfaces, which give a 40 nm signal period and a max resolution of 10 nm (4X counting).

Optics

For flexibility in choosing depth of field, field of view, and resolution, a modular zoom lens system was selected (Navitar 12x Ultrazoom), and to adjust the microscope position it is mounted on a Physik Instrumente F206 hexapod. The objective lenses used are a Mitutoyo 50x and Motic 20x both with long working distances of ~10 mm; currently the 20x objective is in use for its larger depth of field. For recording video, a Lumenera LT225 monochrome CMOS camera shoots 170 fps at full HD.

Force sensor design and modeling

The ability to sense cutting force without significantly altering the cutting process is critical to gain an improved understanding of the cutting mechanics. A high-stiffness, high resolution, high-bandwidth force sensor measuring in at least two directions (cut and thrust forces) built up of relatively inexpensive single-axis sensors is described here

In this design, three single-axis force sensors are mounted to a platform to sense forces in three directions (FIGURE 4) and the entire assembly is calibrated after being mounted on the machine. A thin sheet flexure absorbs shear loads, and shunts some of the force intended to be measured by the single-axis sensors (pressing the need for in-situ calibration).

This sensor must be loaded at the same location at which it was calibrated (point *P* in the figure), otherwise the sensor gain will be different and error will be introduced. Such a design was more economical than a pre-calibrated multi-axis piezo-based sensor and allows for introducing gain via the moment arms, at the cost of larger size and requiring calibration and associated hardware.

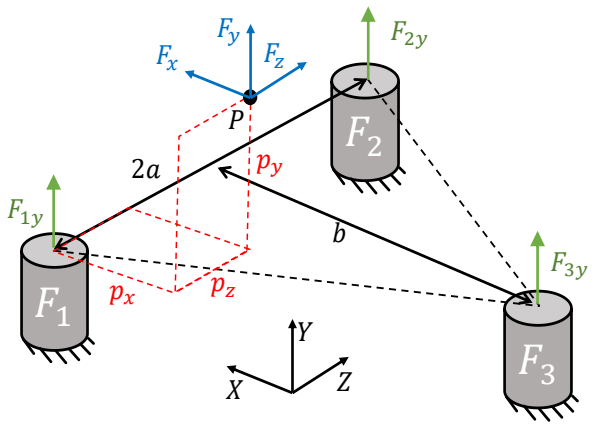

FIGURE 4: Schematic of force sensor built up from three single-axis piezo force sensors – the tops of the cylinders are rigidly mounted to a sensing platform, and a sheet flexure that shunts shear loads to ground (not shown). Each sensor can measure in the Y *direction only.* F_x F_y *and* F_z *are the applied loads at* P*, which in use will correspond to the knife edge.*

Using static equilibrium, an analytical formula for the gain of the sensor can be arrived at:

$$\begin{bmatrix} F_x \\ F_y \\ F_z \end{bmatrix} = \begin{bmatrix} \frac{p_x}{p_y} & \frac{p_x}{p_y} & \frac{p_x}{p_y} - \frac{b}{p_y} \\ -1 & -1 & -1 \\ -\frac{p_z}{p_y} & \frac{2a}{p_y} - \frac{p_z}{p_y} & \frac{a}{p_y} - \frac{p_z}{p_y} \end{bmatrix} \begin{bmatrix} F_{1y} \\ F_{2y} \\ F_{3y} \end{bmatrix} \quad (1)$$

In principle, the force sensor could be used using this calibration matrix computed from the part geometry, individual sensor gains, and loading point lever arms, but errors in each of these would erode the accuracy of the sensor; thus, the sensor should be calibrated before use. The analytical model was used during the design process to trade off force sensor sensitivity, with increases in deflection-related pitching errors due to the increasing moment arms, with the intention of *in-situ* calibration.

Knifeholder and goniometer

An exactly-constrained kinematic goniometer design is used to adjust the clearance angle of the knife while keeping the knife point at a particular point; this gives the designer flexibility to choose the physical layout of the goniometer, and to ensure backlash-free operation via preloaded kinematic contacts. The design also allows adjusting the knife to use a fresh portion of the edge. A 2D schematic of the angle adjustment concept is shown in FIGURE 5.

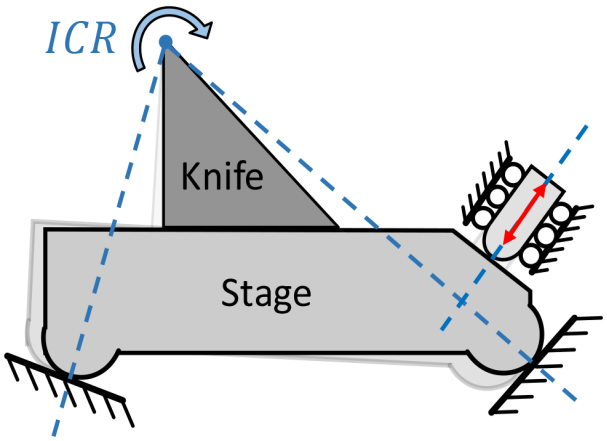

FIGURE 5: Kinematic goniometer concept. Instant center of rotation lies at intersection of surface normals; a third contact rotates the rigid body. Valid for small displacements. Friction is the main performance limiter for such a mechanism.

The module has 4 ball-on-flat contacts and one cylinder-on-flat contact. A CAD model of the implementation is shown in FIGURE 6. Different knifeholders can be mounted on the goniometer stage, and the current knifeholder is designed to hold glass knives, which are 25.4 mm x 25.4 mm 45 degree wedges. Steel knives cut, ground, and sharpened to the same form factor as the glass knives are also used. A holder was also designed to use off-the-shelf microtome blades cut to 6 mm width on a custom sacrificial waterjetting fixture.

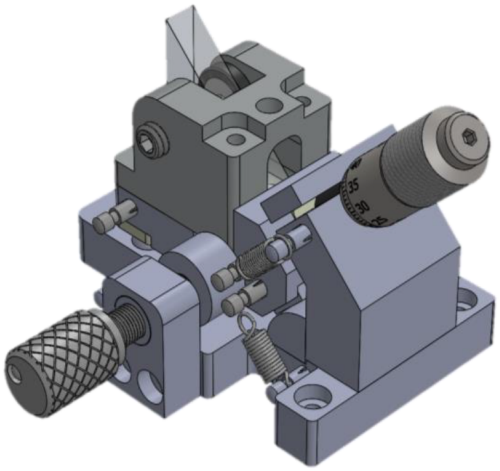

FIGURE 6: Kinematic goniometer and knifeholder. A magnetically-preloaded screw allows for edge translation to use different parts of the cutting edge. The other contacts are preloaded with extension springs. This design is good for a range of approximately 10 deg and is primarily limited by friction.

CALIBRATION AND COMMISSIONING

Force sensor calibration

A calibration frame using pulleys and dead weights was designed to aid in calibrating the force sensor (FIGURE 7). The calibration frame registers to the instrument with three kinematic contacts, and to the optical table via four kinematic contacts (this set of four contacts is potted in place with epoxy due to the overconstraint). These kinematic contacts allow the frame to be removed when calibration is complete so as not to interfere with normal operation, and to apply loads at the same location if recalibration is later deemed necessary. The frame is designed with one kinematic contact against the feed stage, so that the calibration results do not depend on the feed stage position. The frame is designed so that calibration can be carried out from the front of the instrument.

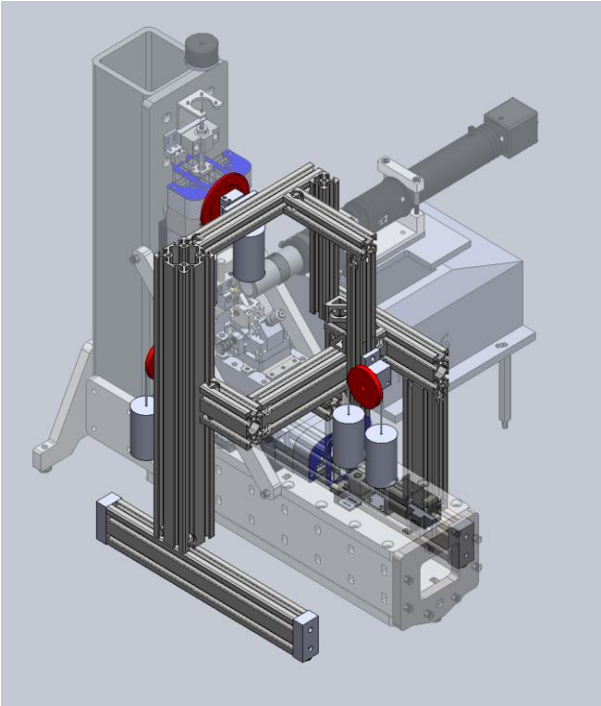

FIGURE 7: Force sensor calibration frame, in place against machine. Dead weights and pulleys allow for loads to be placed on the force sensor, at the frame's center

The primary difficulty in calibrating the 3-axis force sensor is to repeatably apply known loads, in known directions. For the known loads, it was desirable to use dead weights between 20-200g, however gravity loads can only be applied in one direction – a mechanism was needed to change the direction of the load vector. To accomplish this, pulleys acting as levers (FIGURE 8) or bell-crank linkages (FIGURE 9) were designed. A schematic of their use in conjunction with a calibration knife (FIGURE 11) is shown in FIGURE 10. Music wire of 0.762 mm (0.030") diameter (selected to avoid buckling for the loads used) is used to transfer both tensile and compressive loads from the pulley to the sensor's loading point. Both flexure pulley designs were 3D-printed from PLA material on a Sindoh 3DWox.

Ball-bearing, knife-edge, and flexure pulleys were evaluated for accuracy and precision in a test setup which transferred the pulley's output via a load wire to an LSM300 strain gauge force sensor, which itself was calibrated with dead weights. Flexure pulleys were ultimately chosen due to their superior precision (the only pulleys with precision higher than the test sensor's), with the potential tradeoff of low accuracy if the output stiffness is too low (e.g., if the torsional stiffness of the pulley entirely reacts the dead weight load). The stiffness of the force sensor is much higher than that of the flexure pulley, and the expected error due to this is approximately half a percent.

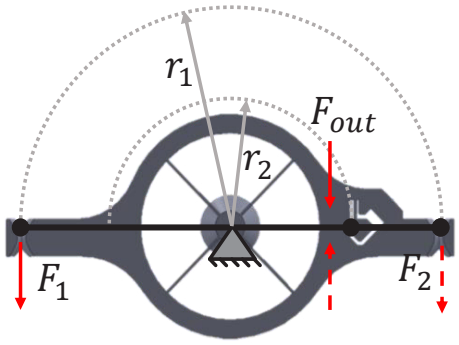

FIGURE 8: Schematic of Y-direction (parallel and anti-parallel to gravity) loader, overlaid on CAD model of implementation via flexure pivot. This implementation has a gain of (r_2/r_1), currently 1.5.

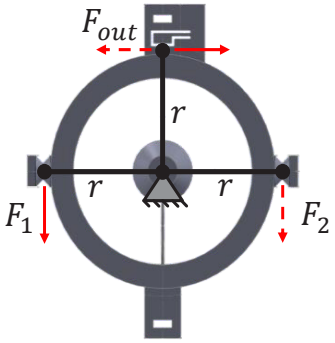

FIGURE 9: Bell-crank converts a gravity dead-weight load (F_1 or F_2) into a load at the output rotated 90 degrees. This implementation has unity gain and is used to apply X and Z direction loads.

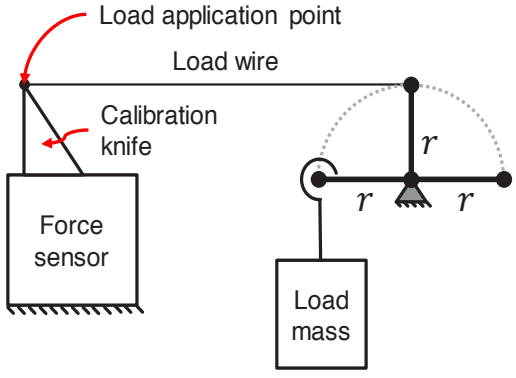

FIGURE 10: Schematic of calibration load application, bell crank type. The load can be applied on the left or right loading arm for bidirectional loading.

A calibration dummy knife (FIGURE 11) was designed to clamp the load wire and transfer load to the force sensor.

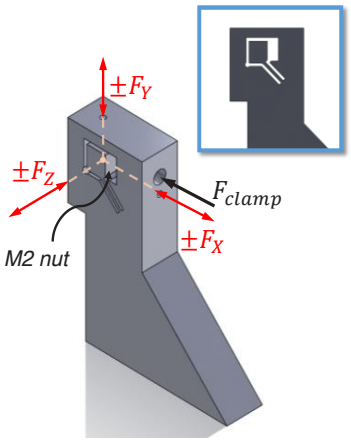

FIGURE 11: CAD model of calibration load-transferring dummy knife. The clamping force is applied via an M2 screw which threads into an M2 nut inserted into a pocket. INSET: side view showing the clamping pad guided by a simple flexure bearing

Cutting polymer specimens

For commissioning and software debugging, the cutting instrument is currently in use cutting polymer specimens (including Delrin, epoxies, polycarbonate, and PMMA) to study cutting forces; thereafter the cutting instrument will be used to study cutting behavior in embedded tissues. FIGURE 12 shows a set of cutting traces acquired on the instrument.

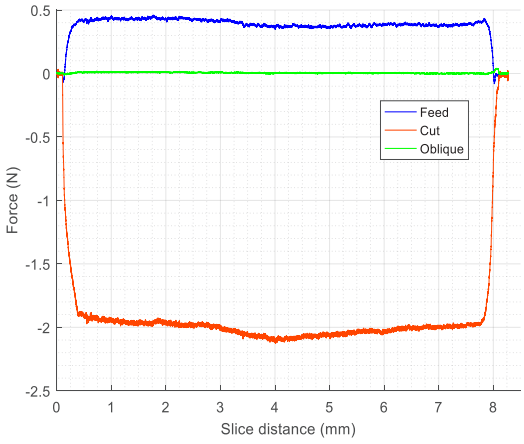

FIGURE 12: Cutting forces vs cut distance in Delrin. 10 um feed, 45 deg S30V steel knife, cut speed 0.2 mm/s, 43 deg rake, 2 mm width of cut. Force sensors sampled at 5 kHz.

The positive feed force indicates that the cutting tool is being pulled into the specimen rather than pushed out – this is known to happen in polymer specimens at high rake angles [7].

FUTURE AND ONGOING WORK

Dynamic characterization via modal hammer impact testing is underway, although difficulties are encountered with obtaining meaningful characterization at the cutting zone – applying an impact force and measuring displacement at the cutting zone has proven difficult due to small size. Efforts are underway to understand and reduce force sensor noise and improve force sensor accuracy via improved calibration procedures. Experiments with compliant knives and their effect on chatter onset stability limits in polymer specimens are also currently underway.

ACKNOWLEDGEMENTS

The authors gratefully acknowledge UChicago Argonne, LLC for sponsoring this work with award 6F-31461.

REFERENCES

[1] R. Schalek, D. Lee, N. Kasthuri, A. Peleg, T. Jones, V. Kaynig, *et al.*, "Imaging a 1 mm 3 volume of rat cortex using a MultiBeam SEM," *Microscopy and Microanalysis,* vol. 22, p. 582, 2016.

[2] D. G. C. Hildebrand, M. Cicconet, R. M. Torres, W. Choi, T. M. Quan, J. Moon, *et al.*, "Whole-brain serial-section electron microscopy in larval zebrafish," *Nature,* vol. 545, p. 345, 2017.

[3] C. J. Peddie and L. M. Collinson, "Exploring the third dimension: volume electron microscopy comes of age," *Micron,* vol. 61, pp. 9-19, 2014.

[4] Y. Altintas, *Manufacturing automation: metal cutting mechanics, machine tool vibrations, and CNC design*: Cambridge university press, 2012.

[5] M. L. Ericson and H. Lindberg, "Design and potential of instrumented ultramicrotomy," *Polymer,* vol. 38, pp. 4485-4489, 1997.

[6] A. H. Slocum, *Precision machine design*: Society of Manufacturing Engineers, 1992.

[7] A. Kobayashi, *Machining of plastics*: R.E. Krieger Pub. Co., 1981.

PZT-ACTUATED COMPLIANT LOCKING DEVICE

Martin Tschiersky[1], Giovanni Berselli[2], Just L. Herder[3], Dannis M. Brouwer[1] and Stefano Stramigioli[4]

[1]Chair of Precision Engineering
University of Twente
Enschede, The Netherlands

[2]Department of Mechanics, Energetics, Management and Transportations
University of Genoa
Genova, Italy

[3]Department of Precision and Microsystems Engineering
Delft University of Technology
Delft, The Netherlands

[4]Department of Robotics and Mechatronics
University of Twente
Enschede, The Netherlands

Abstract

In this paper, a novel design of a fully compliant locking device is presented, for possible application in robotic actuation systems. The synthesis method based on a rigid linkage mechanism is explained, a parametrization scheme is proposed, and an optimization procedure is conducted using kinetostatic flexible multi-body analysis in conjunction with global optimization techniques. The performance of the optimized locking device design is validated via numerical simulations.

INTRODUCTION

Locking devices can be subdivided into several subclasses, such as clutches and brakes. Commonly, these machine elements rely on the contact between friction surfaces for their functioning.

Friction-based Locking Devices (FLDs), along with other types of mechanical and singularity-based lockers [1], have been applied in robotics and mechatronics applications with the aim of increasing energy efficiency, improving safety or to reconfigure modular assemblies.
With respect to energy management, the FLDs main function is either to reduce the actuators energy consumption during standstill by disconnecting the load (e.g. normally-closed brakes installed on industrial robots) or to control the power flow of elastic energy buffers employed in advanced actuation systems, such as series-elastic [2], parallel-elastic [3] or variable stiffness actuators [4]. A structured method to analyze clutched elastic actuator designs is presented in [5].

A large number of FDL designs have been presented and commercialized, which can be compared on the basis of a set of desirable technical characteristics [6]. In particular, FLDs should be compact, lightweight and guarantee a short switching time between the locked and unlocked state, while simultaneously providing a high maximum locking torque.

One potential means of achieving these properties in a FDL for rotary applications is the use of piezoceramics, namely lead zirconate titanate (PZT), for actuation. PZT-stack actuators offer a large bandwidth as well as a high specific power. Furthermore, their capacitive nature results in lower energy consumption in comparison to other actuation principles. The idea of a piezoelectric actuated brake was first patented in 1989 by Yamatoh et al. [7] and was also used in the patented actuator of Hanley et al. [8].
The main challenge associated with the use of piezoelectic materials for applications beyond the micrometer scale lies in their low-displacement and high-force characteristic. Therefore, generally a transmission mechanism for displacement amplification is necessary.

The goal of our research is to leverage the advantages while overcoming the challenges of piezoelectric actuation in a novel compliant locking mechanism, to be used for both clutch and brake applications. While many linear single-stage PZT motion amplifiers have been conceived in the past [9], this paper presents a novel inherently radially coupled multistage concept.
First, the design synthesis is presented. In the following sections the design topology is parameterized and the geometry is optimized. The performance of the optimized result is validated via numerical simulations across different software packages. Lastly, the results are discussed and conclusions elaborate on the main findings.

CONCEPT

The proposed mechanism, though different in its technical nature, is inspired by the functional principle of the planar Hoberman linkage [10]. A small radial stroke at the outside of the mechanism is converted into a largely amplified radial stroke at its inside. Thus, a small actuator displacement at the outer perimeter can be used to clamp a shaft which is located at the center of the mechanism. In contrast to a mechanism with the same mechanical advantage but only one point of engagement, the proposed mechanism, similarly to the Hoberman linkage, engages to the shaft at symmetrically spaced points around the rotation axis. Thus, the reaction forces due to the normal forces at the contact are contained within the mechanism itself.

Still, when using PZT-actuators, the input displacements are typically at an order of magnitude at which any backlash in the system leads to a rapid functional degradation. Therefore, a monolithic flexure mechanism is proposed, in which the desired kinematics are achieved purely by elastic deformation, that is mainly by bending of its compliant members. The design topology is obtained by conceptually converting a linkage system, that is solely comprised of rigid members and revolute joints, into a corresponding fully compliant mechanism, which is suitable for parameter optimization. The three-step synthesis process is illustrated in Figure 1.

Rigid link concept

In the basic concept, shown in Figure 1 a), a number of output nodes $n_n \geq 3$ is equally distributed on an inner pitch circle with radius r. Radially adjacent output nodes connect to each other via two rigid links of equal length l that are connected to another by a second set of revolute joints. Thereby, the loop of the first amplification stage is closed. Based on the terminology of Hoberman [10], we will refer to the inner nodes of a stage as central nodes and to the outer ones as terminal nodes. Radial lines passing through the central node of the first stage will be referred to as unit lines and the ones passing through the terminal points as normal-lines. The angle between two normal-lines will be referred to as the normal angle $\alpha = {}^{2\pi}/_{n_n}$. The sections between two normal-lines constitute the unit cells of the mechanism.

The terminal nodes of the amplification stage again form a concentric circle and in turn constitute either the input of the entire mechanism or the output, i.e. the central nodes, of a consecutive amplification stage. The total number of consecutive stages n_s can be any positive integer. The normal angle α of the mechanism is preserved as long as the mechanism input displacement at the outer perimeter is radially symmetric.

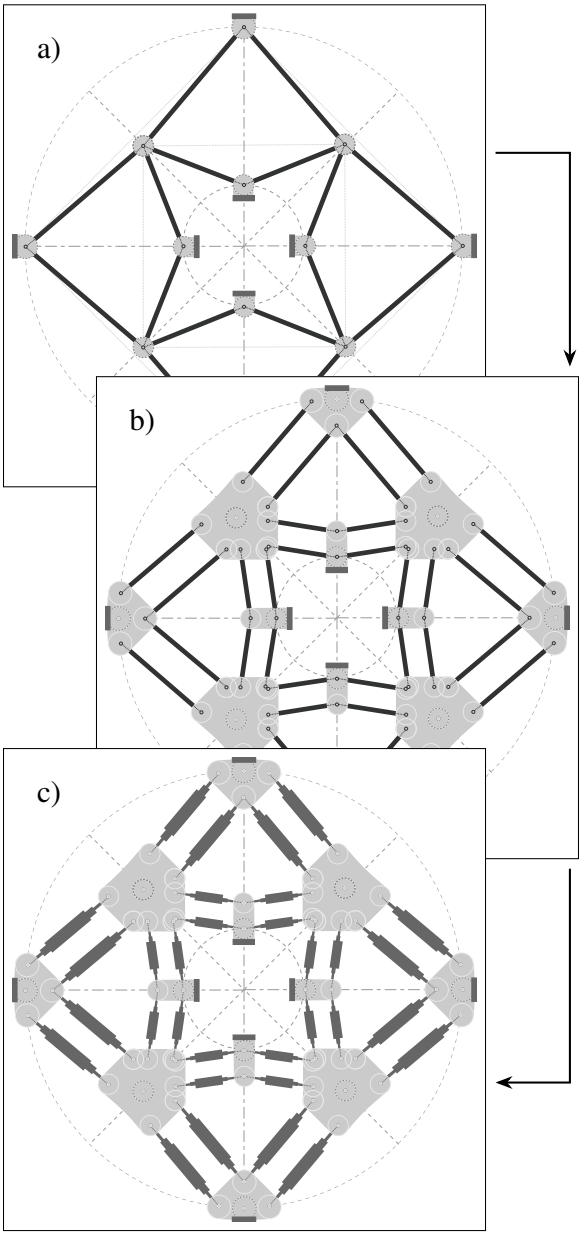

FIGURE 1. Synthesis of the mechanism topology for $n_n = 4$ and $n_s = 2$. Pitch circles and normal-lines are depicted by light gray dashed lines, the unit lines by dash-dotted lines and the singularity lines by dotted lines. Rigid bodies are illustrated by gray areas, rigid links by dark gray thick lines and the compliant links by medium dark gray lines with changing thickness.

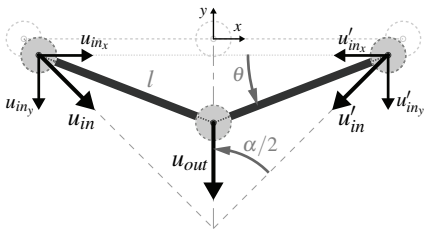

FIGURE 2. Unit cell kinematics.

Unit cell

The function principle of each unit cell is similar to that of a toggle lever. Assuming a symmetric translational input u_{in} along the normal-lines at both terminal nodes, the central node will travel along the unit line. In order to avoid a singular configuration of the mechanism, the central nodes and terminal nodes must not lie in a straight line. Thus, an angle θ between the links and the straight line is formed. An example of a single unit cell is illustrated in Figure 2. The output displacement u_{out} is given by:

$$u_{out} = lsin\theta + u_{in}cos\frac{\alpha}{2} \tag{1}$$

From Equation 1 it can be seen that the output motion is a superposition of the linear motion $u_{in}cos\frac{\alpha}{2}$ and the non-linear motion $lsin\theta$. The latter being the characteristic motion, which is leveraged in order to obtain a very high initial ratio (infinite at $\theta = 0$) to travel from the initial position to the contact position and to produce a lower ratio for transmitting normal forces to the shaft, when in contact. Plots of the output displacement u_{out}, as well as for the transmission ratio in relation to the input displacement u_{in} and to the normal angle α are shown in Figure 3.

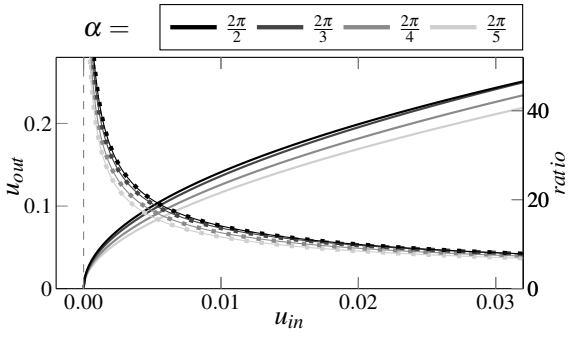

FIGURE 3. Transmission behavior of a unit cell. Output displacement, represented by thick lines, and transmission ratio, represented by thin lines with square markers. Input and output displacements shown as fractions of link length l.

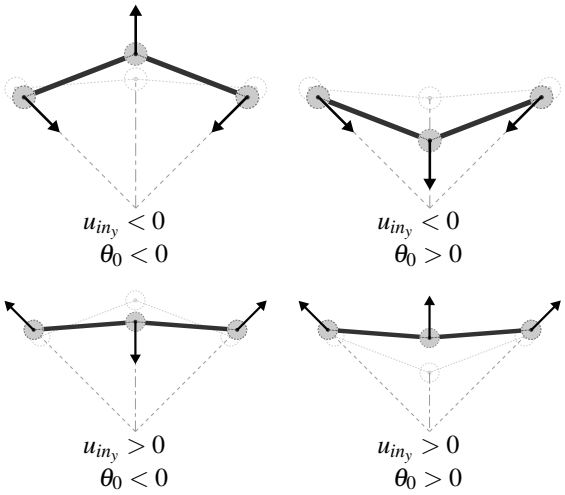

FIGURE 4. Input/output modalities of a single amplification stage.

It can be seen that for small strokes, in the lower percentage regime of the link length, smaller normal angles yield higher transmission ratios.

Depending on the initial angle θ_0 of the links and the direction of u_{in}, different input/output modalities can be achieved. The set of possible configurations is shown in Figure 4. Unit cells with pushing input nodes ($u_{in_y} < 0$) possess decreasing transmission ratios while unit cells with pulling input nodes ($u_{in_y} > 0$) possess increasing transmission ratios. By combining multiple amplification stages with different modalities in series, 4^{n_s} mechanism configurations can be achieved which exhibit complex transmission behaviors.

Constrained rigid link concept

Intermediate hubs are added at the interface to the mechanism input and output, as well as between amplification stages. In order to fix the relative rotations between the hubs, the single links of the basic concept are substituted by parallelogram linkages. This is shown in Figure 1 b).

Compliant concept

In the last step, the constrained rigid link mechanism is approximated by a compliant mechanism, in which the rotational degrees of freedom are obtained by bending of compliant links, that substitute both the rigid links and the revolute joints. This step is shown in Figure 1 c).

PARAMETRIZATION

The parametrization of the mechanism is done on the basis of the unit cells, representing each amplification stage, as shown in Figure 5.

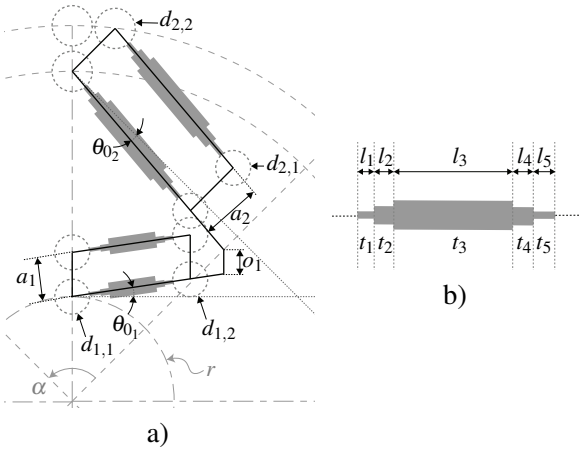

FIGURE 5. Mechanism parametrization.

Due to the mirror symmetry along the unit line, only one side is considered. Each unit cell is defined by four parameters. Its layout is described by the neutral axes of the compliant links, as is illustrated in Figure 5 a).
A parallelogram is given by the inner radius r, the normal angle α, the angle θ_0, and by the offset a between the two parallel lines. The total length of the compliant links is determined by this parallelogram description and the connector diameters d that define the margin for the intermediate hubs at each end. Two adjacent stages are separated by an offset o that determines the distance between the inner beams of both stages, such that their end nodes do not coincide. This distance is defined orthogonally to the singularity line of the inner stage.
The compliant links of each stage, are modeled by a chain of rigidly interconnected beam elements, each of which has a parameter defining its relative length l and its thickness t. This is shown in Figure 5 b). All stages and beams are indexed from output to input of the mechanism.

OPTIMIZATION

In order to obtain a feasible mechanism with an optimal transmission ratio, an optimization routine is conducted to find the ideal parameters.
The full parameter set $\mathbf{x}$ is given by:

$$\begin{aligned}\mathbf{x} = [\quad & [\Psi],\ [n_n], \\ & [\theta_1, \ldots, \theta_{n_s}], \\ & [s_1, \ldots, s_{n_s}],\ [a_1, \ldots, a_{n_s}], \\ & [o_1, \ldots, o_{n_s-1}],\ [d_{1,1}, \ldots, d_{n_s,2}], \\ & [t_{1,1}, \ldots, t_{n_s,n_b}],\ [l_{1,1}, \ldots, l_{n_s,n_b}] \quad]\end{aligned} \tag{2}$$

The parameter Ψ is a binary value and controls the actuation direction at the input, while n_b marks the number of beam elements that form one compliant link. In the scope of this investigation, only mechanisms that are composed of two stages are considered ($n_s = 2$). Each compliant link is discretized by five beam elements, thus $n_b = 5$. Hence, the total number of parameters is 33.

The objective $\boldsymbol{\delta}$ of the optimization is to maximize the output force F_{out} for a given input force F_{in} and input stroke Δu_{in}. Thus, $\boldsymbol{\delta}$ becomes the inverse of the output force.

$$\boldsymbol{\delta} = {F_{out}}^{-1} \tag{3}$$

Geometric constants for the shaft diameter, brake shoe thickness and initial air gap between the aforementioned are prescribed, determining the inner radius r and the output stroke Δu_{out} before contact. A soft constraint on the maximum stress σ_{max} is given in the form of a penalty $\mathbf{p}$, which is multiplied by a penalty factor k_p and added to the objective. The minimization problem becomes:

$$f(\mathbf{x}) = \boldsymbol{\delta} + k_p \mathbf{p} \tag{4}$$

All parameters in $\mathbf{x}$ are subject to upper bounds $\mathbf{b_u}$ and lower bounds $\mathbf{b_l}$. Furthermore, sets of linear inequality constraints $\mathbf{c_l}$ and non-linear inequality constraints $\mathbf{c_{nl}}$ are used to ensure the geometrical feasibility of candidate geometries.

Optimization Model

The flexible multibody dynamics software package SPACAR [11] is used to simulate one unit cell of the fully parametrized mechanism, as is shown in Figure 6. The compliant links are modeled using flexible finite two-node planar beam elements. Intermediate bodies, such as the hubs and the brake shoe, are modeled using rigid beam elements. The shaft is modeled using a beam element with stiffness properties corresponding to the shaft diameter. These beam elements include geometric nonlinearities and their flexibility is formulated in the form of discrete deformation modes. Symmetry conditions are applied to the two nodes intersecting with each normal-line, respectively. Thereby, their radial and circumferential translations as well as their rotations are positively and rigidly coupled.

Optimization Procedure

For each candidate parameter set, a two-step kinetostatic simulation is executed. First, the normal force F_n acting on the shaft is evaluated,

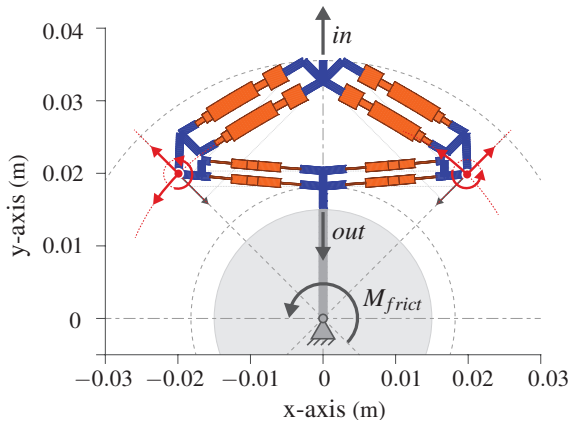

FIGURE 6. Optimized unit cell geometry. Flexible beams drawn in orange, rigid beams in blue and the shaft beam in gray. The gray field indicates the shaft diameter. Gray arrow symbols show load directions. Red arrow symbols show symmetry conditions.

considering the contact between brake shoe and shaft. Consecutively, a moment M_{frict} is applied at the shaft's central rotation axis, which represents the maximum static moment that the mechanism can hold based on F_n and assuming a friction coefficient μ. This results in an added tangential force component F_t at the brake shoe, leading to a small decrease of the applied normal force F_n. This reduced normal force between brake shoe and shaft yields the operational output force F_{out}, which determines the objective value $\boldsymbol{\delta}$. Further, the maximum stress σ_{max} in the compliant beams is determined for this combined load case, yielding the penalty value $\mathbf{p}$. The Genetic Algorithm function ga() from the MATLAB Global Optimization Toolbox is used, for solving the minimization problem.

RESULTS

For an input force $F_{in} = 1750$ N, and input displacement $\Delta u_{in} = 20$ µm, a shaft diameter of 30 mm, a brake shoe thickness of 3 mm, an initial air gap (Δu_{out}) of 200 µm, a friction coefficient of $\mu = 0.5$, and using a AISI 420 tool steel ($E = 200$ GPa, $G = 80$ GPa, $\sigma_{yield} = 1280$ MPa) a design is obtained that can provide a holding torque of up to 1.9 Nm. The resulting unit cell geometry is the one shown in Figure 6. The kinetostatic transmission behavior from input to output regarding radial position and forces can be seen in Figure 7 and Figure 8, respectively. The graphs show that the transmission behavior can be roughly described as piecewise linear, having straight segments for the non-contact and the

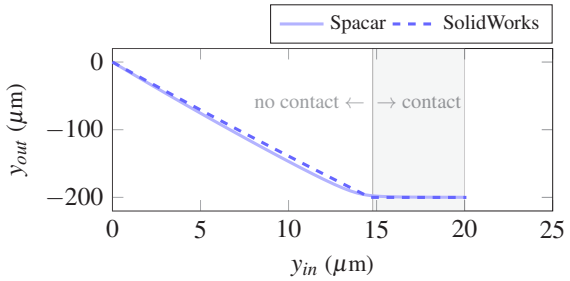

FIGURE 7. Displacements of the unit cell.

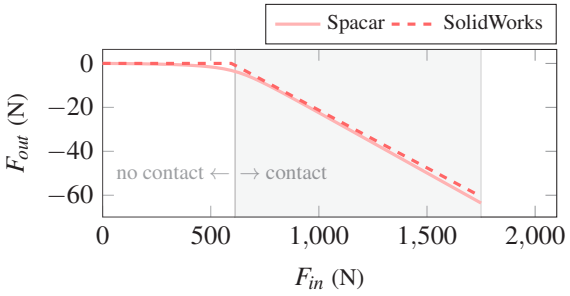

FIGURE 8. Force transmission of the unit cell.

contact region. The transmission ratio before contact as determined by the displacements is -14.1, the ratio after contact as determined by the forces is -18.7. The entire mechanism has an outer diameter of 69.96 mm and is 10 mm in height.

Validation

The mechanism was modeled, as is shown in Figure 9, and analyzed using a non-linear static contact analysis in the SolidWorks Simulation toolbox. The results are shown along with the SPACAR results in Figure 7 and Figure 8. Both, the displacements and the forces show good agreement. The maximum stress is found to be 313 MPa in SolidWorks and 338 MPa in SPACAR.

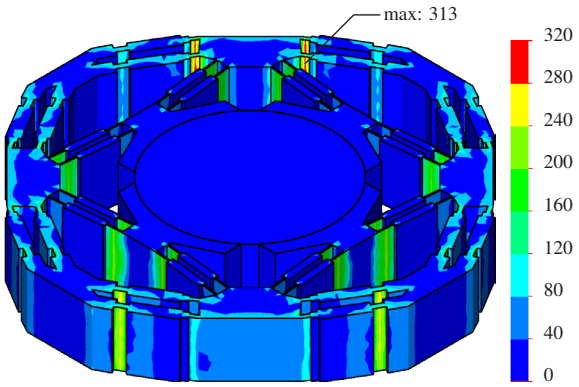

FIGURE 9. SolidWorks simulation stress plot. Stresses shown in MPa.

DISCUSSION

The concept investigated in this paper is limited to polygon shaped node arrangements with $n_n \geq 3$ inputs. However, given a different mechanism layout, designs with $n_n = 2$ inputs are also feasible, allowing a normal angle of $\alpha = \pi$.

In order to eliminate any under-constraints, the input nodes are required to be translationally and rotationally constrained in all planar directions.

The proposed actuation via PZT-stacks can be done in various manners. Two possible methods are direct actuation in which each input is actuated by a separate, dedicated PZT-stack, and actuation by an out-of-plane flexure mechanism which transforms a single axial displacement into a distributed radial displacement at the inputs. Also integrating piezo-stacks into the planar mechanisms rigid sections appears feasible.

The presented mechanism can be converted into a normally closed version, by using its fully deflected shape at full input displacement, not considering the contact, as the initial shape and inverting the input direction.

The small deviation between the force profiles of the SPACAR model and the SolidWorks model may be caused by the deformation of the intermediate bodies, which were assumed perfectly rigid in the SPACAR model.

CONCLUSION

This paper presents a synthesis method to obtain compliant planar mechanisms, which can be used to clamp a centrally located shaft. The distinctive features are the monolithic design and the achievable high motion amplification ratio, making the use of PZT-stack actuators with micrometer scale input strokes feasible. The proposed optimization routine is applied and yields a compact mechanism design, that can transform a 1750 N and 20 µm actuator input into a 1.9 Nm braking torque, after traveling across an air gap of 200 µm. The results are successfully validated across different software packages.

ACKNOWLEDGMENTS

This project has received funding from the European Union's Horizon 2020 research and innovation programme under grant agreement No. 688857 (SoftPro).

REFERENCES

[1] Plooij M, Mathijssen G, Cherelle P, Lefeber D, Vanderborght B. Lock Your Robot: A Review of Locking Devices in Robotics. IEEE Robotics Automation Magazine. 2015;22.

[2] Leal Jr AG, de Andrade RM, Filho AB. Series Elastic Actuator: Design, Analysis and Comparison. Recent Advances in Robotic Systems. 2016;.

[3] Haeufle DFB, Taylor MD, Schmitt S, Geyer H. A clutched parallel elastic actuator concept: Towards energy efficient powered legs in prosthetics and robotics. In: 4th IEEE RAS EMBS International Conference on Biomedical Robotics and Biomechatronics (BioRob); 2012. p. 1614–1619.

[4] Wolf S, Grioli G, Eiberger O, Friedl W, Grebenstein M, Hppner H, et al. Variable Stiffness Actuators: Review on Design and Components. IEEE/ASME Transactions on Mechatronics. 2016 Oct;21(5):2418–2430.

[5] Plooij M, Wolfslag W, Wisse M. Clutched Elastic Actuators. IEEE/ASME Transactions on Mechatronics. 2017 April;22(2):739–750.

[6] Schmid SR, Hamrock BJ, Jacobson BO. Fundamentals of Machine Elements. CRC Press; 2014.

[7] Yamatoh K, Ogura M, Kanbe K, Isogai Y. Piezoelectric brake device. Google Patents; 1987. Patent US07182964.

[8] Hanley MG, Caliendo GP, Anderson DB. Actuator having piezoelectric braking element. Google Patents; 1997. Patent US5986369.

[9] Ling M, Cao J, Zeng M, Lin J, Inman DJ. Enhanced mathematical modeling of the displacement amplification ratio for piezoelectric compliant mechanisms. Smart Materials and Structures. 2016;25(7):075022.

[10] Hoberman C. Radial expansion/retraction truss structures. Google Patents; 1988. Patent US5024031A.

[11] Jonker JB, Meijaard JP. In: Schiehlen W, editor. SPACAR — Computer Program for Dynamic Analysis of Flexible Spatial Mechanisms and Manipulators. Springer Berlin Heidelberg; 1990. p. 123–143.

STATE-OF-THE-ART IN APPLYING ULTRASONIC ASSISTED DIAMOND TURNING TO DIFFERENT MATERIALS

Benjamin Bulla, David Robertson and Clemens Dicke
son-x GmbH
Aachen, Germany

BACKGROUND AND MOTIVATION

Ultra precision diamond machining is a well known technology for the manufacturing of optical components made of non ferrous, plastic and crystalline IR materials. The application of this process to ferrous materials, glass or even tungsten carbide is conventionally extremely limited. This presentation will highlight the possibilities that are given through the application of an ultrasonic assistance to the conventional process. The limits in steel machining and the machining of other difficult to cut materials will be discussed.

THE PROCESS

The affinity between the carbon (diamond) and the iron (work piece) leads to excessive tool wear in conventional diamond machining of steel even at very small cutting distances [1]. For that reason, the ultrasonic assisted technology was invented. It enables direct cutting of hardened steel components with single crystal diamond tools. The unique system (UTS2 Fig. 1) used in these experiments works with an almost linear oscillation of 100 kHz, which allows a better cooling of the tool and a suppression of the chemical interactions, which results in a significant increase of the tool life and the possibility to generate optical quality surfaces in hardened steel. It also creates a higher impact into the machined material by the tool, which might have a positive effect when machining hard and brittle material.

FIGURE 1. Ultrasonic Tooling System UTS2

This technology has been investigated over years and has proven its potential for the manufacturing of optical mould inserts. A surface roughness in the range of Ra < 5 nm and a form accuracy of PV<200nm can be achieved on steel [2]. The application of this process to other materials can also have different positive effects that shall be investigated.

Fig. 2 illustrates the tool motion in this process. An oscillation with 100.000 cycles per second parallel to the cutting direction leads to a separation of the tool and the machined material, which leads to the described positive effects. Due to the bending motion of the resonant tool holder body, the tool separates slightly from the machined surface, so there is not damage to the diamond tool edge, while the back motion occurs.

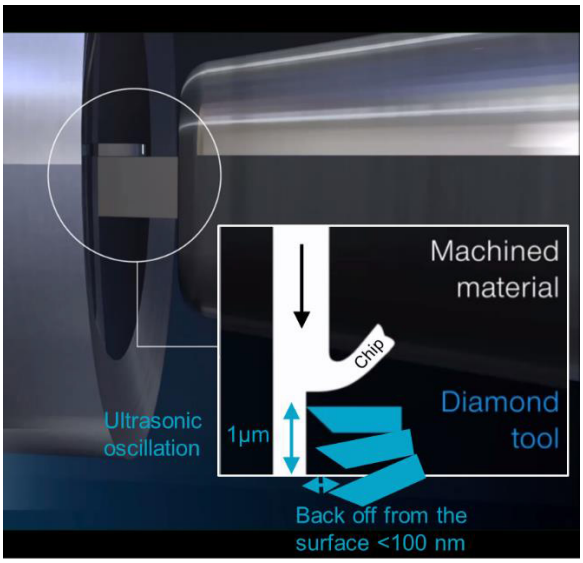

FIGURE 2. Ultrasonic assisted machining

FREEFORMS IN STEEL

The most prominent application of ultrasonic assisted diamond turning is the machining of stainless steel. In this case the process is already

applied on an industrial level, hence a large variety of geometries, including freeforms and microstructures are possible. In order to machine freeform/non symmetric surfaces, the C-axis machining mode (Slow-Tool-Servo) is applied, where the tool position is modified according to the angular position of the machined sample. This way the cutting operation follows a non symmetric path, creating a freeform surface.

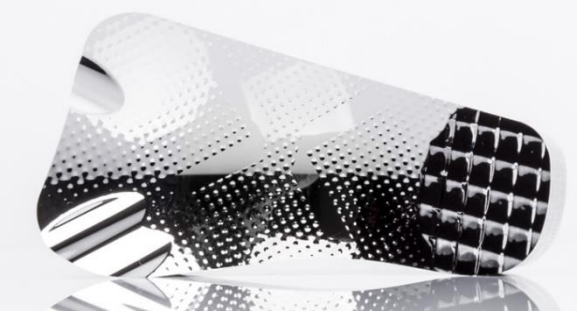

FIGURE 3. Freeform steel part

Fig. 3 demonstrates a stainless steel insert with freeform surface. The diagonal of this sample is approximately 70 mm. The hardness of the X40Cr14 ESR steel is 52 HRC. A surface quality below Ra < 5 nm could be achieved, which can be measured by white light interferometry, Fig. 4. The semi finish is typically machined with a feed of 20 μm/rev and a depth of cut of 20 μm as well. In the finish cut especially the feed is reduce to 5 μm/rev, in order to achieve smooth optical surface without visible cutting marks.

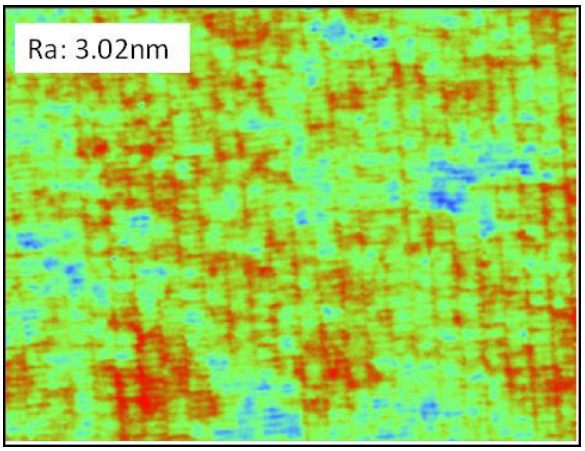

FIGURE 4. Surface roughness of steel after ultrasonic assisted diamond turning

In the case of steel machining the surface roughness is not only influenced by the process parameters and the ultrasonic vibration of the tool, also the inhomogeneity of the steel material has a strong impact. The material properties can even become predominant in cases where the roughness is lower than 5 nm Ra. For some application it is desirable to reach a surface finish in the range of 1 nm Ra. It is an ongoing investigation with different steel types in order to see if such a low roughness is possible.

GLASS MACHINING

Glass is a general definition for a large variety of materials and properties. In this particular experiment the machining tests were conducted on N-BK7, a common glass type. A convex glass sample with a diameter of D = 40 mm and a radius of 80 mm was machined.

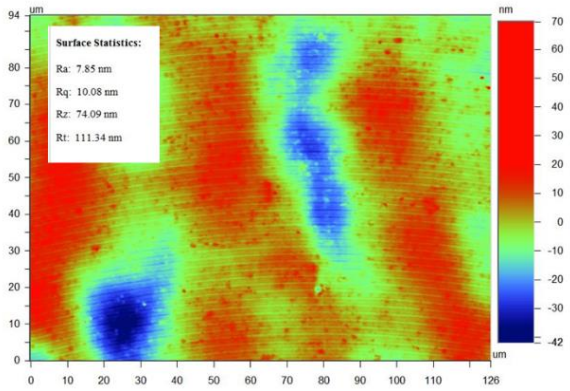

FIGURE 5. Surface roughness of N-BK7 after ultrasonic assisted diamond turning

Cutting marks are clearly visible (Fig. 5) which demonstrates that a ductile cutting process has taken place at the bottom of the chipping process, where the surface is created. One theory that explains the machinability of hard and brittle materials through diamond machining is by the critical chip thickness described by Bifano et al. in 1991 for the first time [3]. While the actual chip thickness is below the material specific value of the critical chip thickness, a ductile material behavior is predominant, and the cutting process takes place. When the critical chip thickness is exceeded, then the cracking of the material is predominant, and the surface will have a high amount of fractures.

Additionally to the material specific behavior, the process can also have an impact on the ductile behavior of the material and over its strength while it is machined. Through the impact of the ultrasonic motion, the diamond tool hits the material and induced a higher amount of micro cracks into the material where there is a non ductile regime. These micro cracks weaken the

material and make it more gentle to machine for the tool, reducing the tool wear and increasing tool life.

Furthermore, the impact of the tool by the ultrasonic motion induces a mechanical stress into the cutting zone. This type of stress is beneficial for the ductility of the material, which improves the surface quality that can be generated by the process. In summary two positive effects can be added by the ultrasonic assisted process, when it machines hard and brittle material, the material weakening by micro cracks and the improvement of the ductility through induced compressive stress in the cutting zone.

The stability of the process as well as the ductile behavior of the material are key for a successful process.

TUNGSTEN CARBIDE MACHINING

A material that has been a challenge for years in ultra precision machining is tungsten carbide, which is in fact much harder than glass with a hardness of approximately 2800 HV10 for binderless tungsten carbide. Its application as a mould material for glass moulding is unbeaten due to its mechanical properties and temperature resistance.

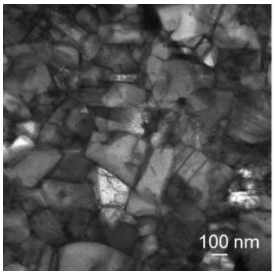

Young's-Modulus	680 GPa
Hardness	2811 HV 10
Fracture toughness	6 MPa√m
Density	15,41 g/cm³
Grain size	~ 200 nm

Calculated theo. krit. DOC:
$h_{cu,krit}$ = 165 nm

FIGURE 6. Mechanical properties of binderless nanograin tungsten carbide

Machining of this materials is usually performed through ultra precision grinding and hand polishing. This process is non deterministic and time consuming, and also limited when it comes to challenging geometry features. This is where the potential lies for ultrasonic assisted diamond turning.

There are two major challenges when it comes to diamond machining tungsten carbide, at first a ductile behavior of the material needs to be achieved in order to be able to generate an optical surface. The possibility to machine brittle materials in a ductile mode has been discussed. Furthermore the local process load, mechanical and thermal, should not exceed the critical values for single crystal diamonds. Otherwise the tool will fail quickly.

A critical chip thickness of 165 nm was calculated for binderless nanograin tungsten carbide based on the properties shown in Fig. 6. Therefore the machining parameters need to be set in a way, that the chip thickness during the process does not exceed the value of 165 nm. The feed and depth of cut (DOC) can be calculated under this requirement depending on the tool radius. All parameter combinations below the graphs shown in Fig. 7, depending on the tool radius, will therefore allow a ductile machining mode.

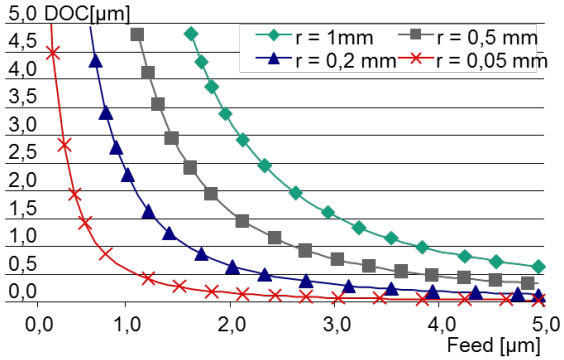

FIGURE 7. Parameter limits for ductile machining

Further experiments that were conducted before this publication have shown, that the process forces are too high for the tool, when the actual limits of the ductile regime are reached. In fact, the parameters need to be set much more gentle in order to keep a sharp cutting edge and avoid tool chipping. Besides these parameters, the dynamic parameter of the cutting speed has an influence as well. Low cutting speeds, much lower as used in steel machining, show better results. All parameters used for this experiment are shown in Table 1.

Parameter	Unit	Value
Cutting speed	[m/min]	1.6
Cutting depth a_p	[µm]	1.0
Feedrate	[µm/rev.]	1.0
Tool radius	[mm]	1.0
Tool rake angle	[°]	0
Ultrasonic frequency	[kHz]	103.88
Ultrasonic amplitude	[µm]	2

TABLE 1. Parameters for tungsten carbide machining

When these parameters were set, an optical surface could be generated on a sample with a diameter of 10 mm and a convex radius of 15 mm. In total an amount of 6 passes were conducted during the machining operation with the same tool. The sample is shown in Fig. 8.

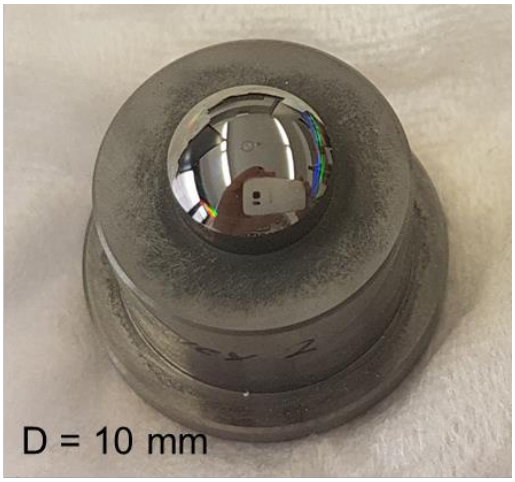

FIGURE 8. Machined tungsten carbide sample

On the machined sample, a roughness of Ra ~ 2-3 nm was achieved (Fig. 9). Such a roughness is only possible, if a ductile material behavior takes place, which indicates that the assumptions were correct.

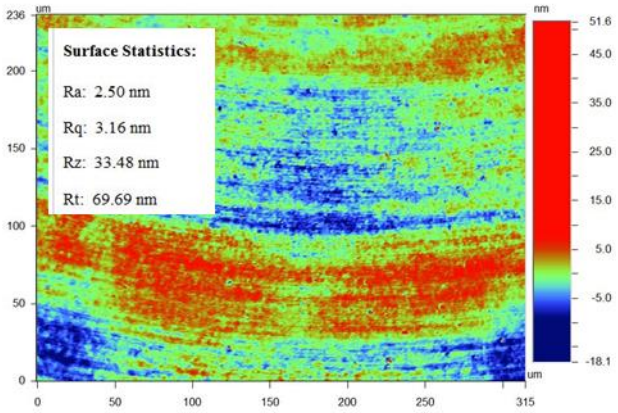

FIGURE 9. Surface roughness of tungsten carbide after ultrasonic assisted diamond turning

Furthermore the tool sharpness was not lost, even though six cycles were conducted with the same tool within the same setup. In the image of the tool in Fig. 10 after these operations, some micro chipping can be identified. The tool wear is already starting and probably not more than one of these samples can be machined with one tool within these specifications. Nevertheless the quality that was achieved is very high and reaches the optical standards that are also reached in grinding and polishing.

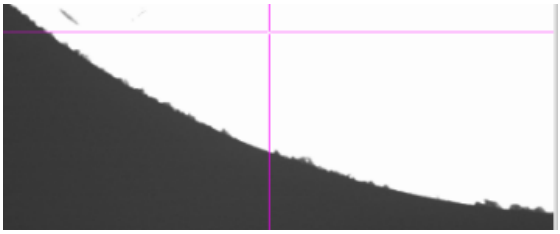

FIGURE 10. Tool wear after ultrasonic assisted diamond turning of tungsten carbide

As a last parameter the form accuracy of the spherical surface was measured. The total PV was below 500 nm (Fig. 11). In these experiments the machinability itself was the focus and the form accuracy was not corrected after the measurement. It demonstrates that a high quality can be achieved and the optical standards are met with regards to the form error as well.

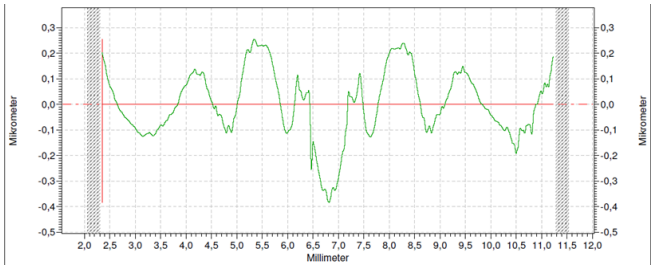

FIGURE 11. Form error of tungsten carbide sample after ultrasonic assisted diamond turning

The potential of the ultrasonic assisted diamond machining process is high for the machining of hard and brittle materials. Further investigations are required in order to identify the actual limits and to better understand the phenomena that take place.

REFERENCES

[1] Moriwaki, T.; Shamoto, E.: Ultraprecision Diamond Turning of Stainless Steel by Applying Ultrasonic Vibration, Annals of the CIRP Volume 40/1/1991, Page 559-562

[2] Klocke, F.; Dambon, O.; Bulla, B., Hünten, M., Influence of different steel alloys on the machining results in ultrasonic assisted diamond turning, Key Engineering Materials Vols. 523-524 pp 203-208, 2012

[3] T. G. Bifano, T. A. Dow and R. O. Scattergood, Ductile-Regime Grinding: A New Technology for Machining Brittle Materials, J. Eng. Ind 113(2), 184-189 (May 01, 1991)

HIGH SPEED CUTTING OF MONOCRYSTALLINE SILICON BY OFF-AXIS DIAMOND TURNING

Daniel Berger[1], Lars Schönemann[1,2], Oltmann Riemer[1] and Ekkard Brinksmeier[1,2]
[1]LFM Laboratory for Precision Machining
Leibniz Institute for Materials Engineering
[2] MAPEX Center for Materials and Processes
University of Bremen
Germany

INTRODUCTION

The research unit "Ultra-Precision High Performance Cutting" (UP-HPC) aims at reducing primary and secondary process times, inter alia by high speed cutting (HSC) [1]. The results on high speed cutting of metallic materials have already been presented in 2015 and 2017 at the ASPE Annual Meeting [2, 3].

Besides ductile materials, the class of brittle-hard materials, like monocrystalline silicon, is currently under investigation within this research unit. The fracture-free machining of these materials has attracted numerous research in the past [4]. Both, undefined and defined cutting edges can be applied for achieving a negative rake angle, which is one of the prerequisites for enabling a ductile material removal. In case of defined cutting edges, diamond machining is the process of choice [5]. Especially for the generation of complex freeforms, as needed for e.g. infrared (IR) applications, diamond milling ("fly-cutting") and off-axis turning are frequently applied. In most cases, moderate cutting speeds (200-600 m/min) are set to avoid high thermal loads or high frequency excitation of structural loops [6]. As the final product is high-end equipment, long primary and secondary process times are acceptable. The added value still exceeds the production costs by far. However, the reduction of primary and secondary process times is naturally desirable when manufacturing higher batch numbers [7]. Consequently, the influence of high ($v_c \geq 4{,}000$ m/min) and conventional cutting speeds ($v_c \geq 400$ m/min) on the material removal mechanism of monocrystalline silicon was investigated in this study by off-axis diamond turning experiments with an interrupted cut.

EXPERIMENTAL PROCEDURE

Experiments were conducted on a Moore Nanotech 350FG. The workpiece mounting fixture on the work spindle was designed to adapt three square workpieces (10 x 10 mm^2). The radius of the workpiece's center was set at 110 mm, which resulted in a work spindle speed of 531 min^{-1} for low cutting speed (400 m/min) and 5310 min^{-1} for high cutting speed (4,000 m/min). The two axis mode was utilized (Y-Z) for machining, where the Y-axis generated the v_c-dependent feed speed and the Z-axis was used for plunging into the material with a certain depth of cut (a_p).

A single-crystal diamond radius tool was applied for turning. For each set of cutting speeds a tool in fresh condition was applied. The specifications for tool and workpiece are shown in Table 1 and the experimental setup is illustrated in Figure 1.

TABLE 1. Tool and workpiece specifications

	Specification	Value
Tool	Cutting material	Single-crystal diamond
	Corner radius	r_ε = 0.76 mm
	Cutting edge radius	r_β = 150 nm
Workpiece	Material	Monocrystalline silicon
	Crystal Orientation	(100)/(110)/(111)
	Geometry	10x10x0.5 mm^3

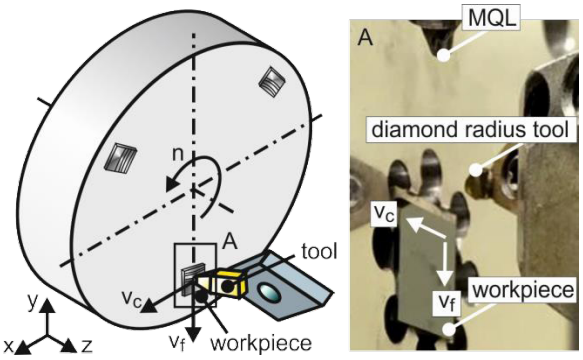

FIGURE 1. Experimental setup for off-axis turning of monocrystalline silicon with $v_c \perp v_f$.

Whereas the focus in [2] was laid on ductile materials, in this study the influence of cutting speed on the material removal mechanism of brittle-hard materials is of interest. It is expected that high cutting speeds will increase the pressure within the contact zone, which is beneficial for ductile machining. This, however, has to be confirmed by fundamental investigations. Thus, the above mentioned parameters were set for two process strategies, one for the machining of isolated single cuts (Figure 2, left side) and one for the machining of flats by overlapping single cuts (Figure 2, right side).

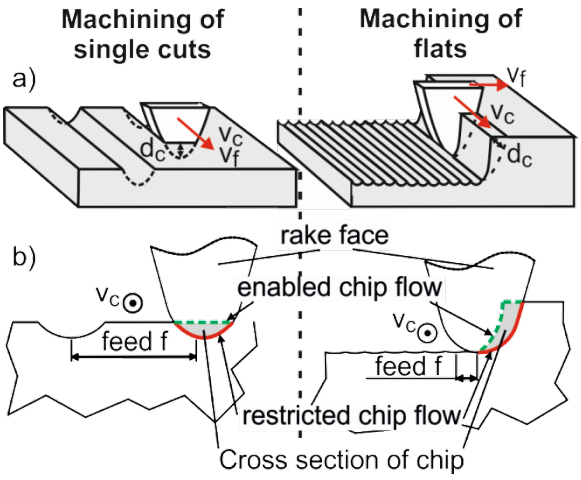

FIGURE 2. Process strategies for high speed off-axis diamond turning

Subsequently to the experiments, surface roughness and subsurface damage (only for machining of flats) were determined in order to evaluate the influence of cutting speed on the machined surface layer. Roughness was measured by a Taylor Hobson CCI HD white-light interferometer. Subsurface damage was investigated by polishing a wedge with a certain slope into the workpiece. Polishing was followed by an etching process with diluted hydrofluoric acid (0.1% HF), which exposes possible cracks.

RESULTS

Analysis of single cuts

The machining of single cuts aimed at investigating the dependence of the critical depth of cut (a_p) on the process parameters. The feed rates were set to 160 mm/min when machining with a cutting speed of 400 m/min, while it was 1,600 mm/min for 4,000 m/min, resulting in equidistant cuts on each of the specimens. The depth of cut was varied by continuously plunging the tool deeper into the material. All relevant machining parameters are listed in Table 2.

TABLE 2. Parameters for turning single cuts

Parameter	Value
Cutting speed v_c	400 / 4,000 m/min
Feed speed v_f	160 / 1,600 mm/min
Rake angle γ	0° / -20° / -30°
Depth of cut a_p	Var. (0 to > 500 nm)

The determination of a critical a_p, which is the value where a transition from ductile to brittle machining takes place, was performed by analyzing the maximum height Sz in the center of the machined single cuts. Sz describes the difference between the highest peak and the deepest valley of the surface topography and is therefore a suitable parameter for describing the nature of the material removal mechanism (ductile/brittle). With increasing depth of cut, Sz also increases and the single cuts can be separated in ductile (a), ductile-brittle (b) and brittle (c) areas, as explained in Figure 3 and applied in Figures 4-6. These areas can be separated by means of the Sz distribution. In ductile mode, Sz linearly increases. This trend continues in ductile-brittle mode, but scatter is present. Brittle mode starts when Sz spreads widely and no linear trend is apparent anymore. The analysis has been performed by a MATLAB script, which runs through the single cuts and determines Sz on a 40 x 30 pixel area in intervals of 40 pixels. Pixel area and intervals have been chosen to maximize the covered area and minimize the offset of linearized area of curvature. 100 µm in X- and Y-direction corresponds to 306 pixels.

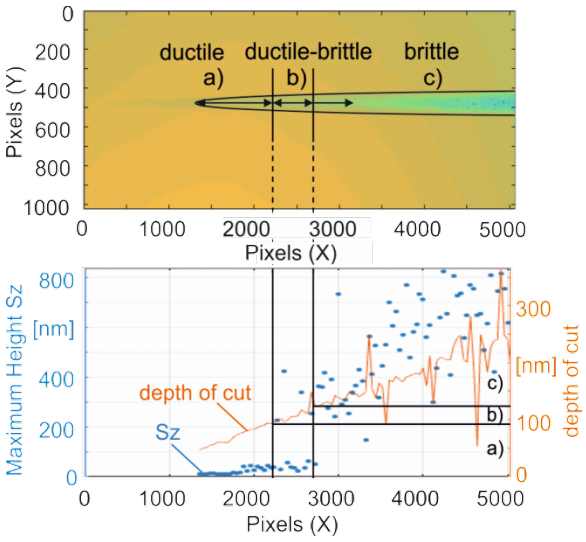

FIGURE 3. Analysis of single cuts

The strong variation of a_p, especially at higher depths of cut, results from brittle damages (outbreaks and burrs).
Figures 4 to 6 show the analysis of the maximum height Sz depending on the actual depth of cut for the rake angles 0°, -20° and -30° and crystal orientation (110), respectively. For the sake of clarity, the single values are not shown in the figures, but instead the blue and red areas enclose all values (three specimens for each parameter setting) for the different cutting speeds. While the triangles occur through the scattering values for Sz at higher depths of cut, the elliptical areas show the linear rise of Sz at low depths of cut. The derived values at the bottom of the figures indicate the transition between ductile and brittle machining.

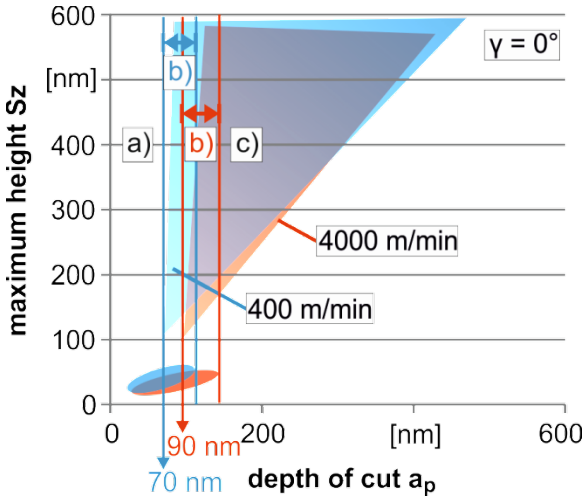

FIGURE 4. Sz for single cuts over a_p for γ of 0°

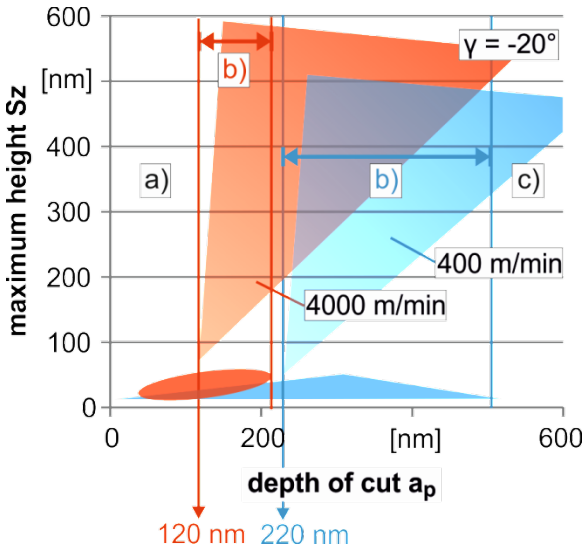

FIGURE 5. Sz for single cuts over a_p for γ of -20°

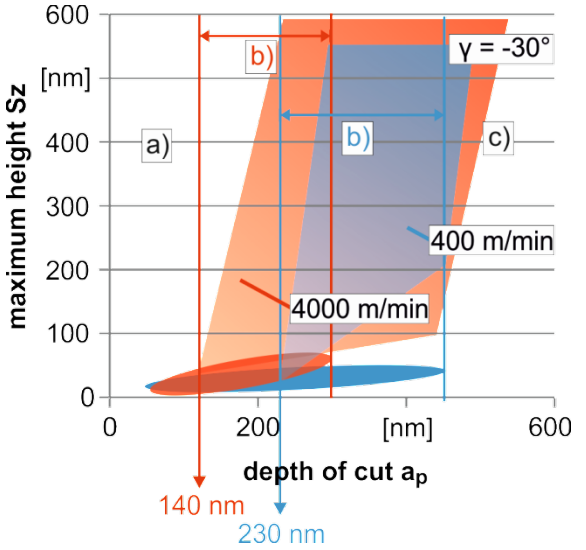

FIGURE 6. Sz for single cuts over a_p for γ of -30°

For both cutting speeds, the critical a_p increased with rising negative rake angles. But in fact, the usual rake angles of -20° and -30° show a different behavior than expected, as the higher cutting speeds lead to minor values of the critical a_p than the lower cutting speeds. Only for a rake angle of 0°, which is not common for the machining of brittle-hard materials, a higher cutting speed lead to a marginally higher critical depth of cut. A possible explanation for this could be derived from the machining kinematics (Figure 2a). The chip can only flow to the upside

during the machining of single cuts, while the machining of flats enables a chip flow to different directions, leading to a rapid decrease of pressure (Figure 2b). Machining with negative rake angles and high cutting speed supports the formation of high pressures, avoiding a controlled chip removal (chips pile up in front of the tool until the pressure reaches a maximum value) and brittle damage already occurs at low critical depths of cut. Meanwhile, the increasing pressure for low cutting speed does not exceed a critical value for maintaining a ductile material removal. All values for the critical a_p at different crystal orientations, cutting speeds and rake angles are finally shown in Figure 7.

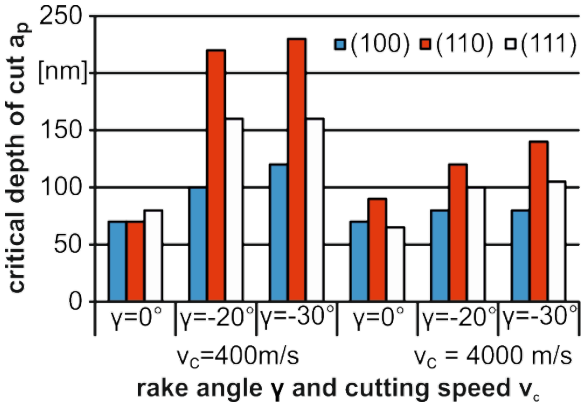

FIGURE 7. Critical a_p for different cutting speeds and rake angles

Analysis of flats

According to the preliminary results from the machining of single cuts, a rake angle of -30° was chosen for the machining of flats by adding a feed movement in Y. The parameters applied in these experiments are shown in Table 3.

TABLE 3. Parameters for turning of flats

Parameter	Value
Cutting speed v_c	400 / 4,000 m/min
Feed speed v_f	5 / 7.5 / 10 µm/rev
Rake angle γ	-30°
Depth of cut a_p	5 µm

As Figure 8 shows, higher cutting speeds lead to lower surface roughness in most cases. For the machining of flats, the measurement of arithmetic mean height Sa is more common than Sz, which is why this parameter was used for analysis of the machined flats in contrast to the single cuts.

Only for workpieces with a crystal orientation of (111), a cutting speed of 400 m/min lead to superior surface quality compared to a cutting speed of 4,000 m/min, although the differences between roughness values are marginal, at least for feed rates of 5 and 7.5 µm. When (100)-workpieces were machined, the arithmetic mean height for 7.5 µm feed per revolution differed between 10 nm (v_c = 4,000 m/min) and 30 nm (v_c = 400 m/min). By implication, ductile machining of this material is not possible when applying the parameters from above (Table 3) with low cutting speeds, while high cutting speed at feeds per revolution of 5 and 7.5 µm leads to a surface roughness below 10 nm.

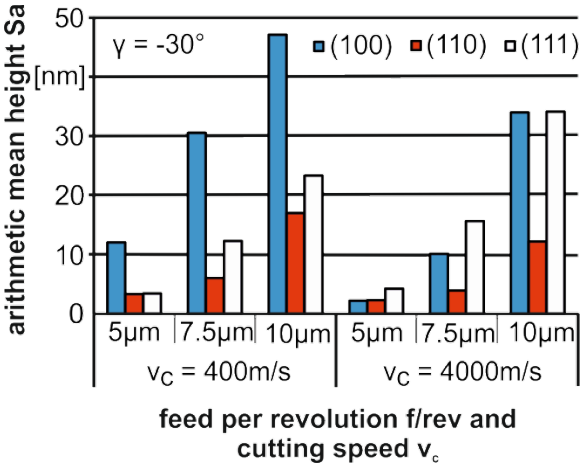

FIGURE 8. Sa for flats over f/rev and v_c for γ of -30°

By turning flats with overlapping cuts, the chip can be deflected not only to the upside, but also sidewise. The higher pressure in the contact zone, induced by negative rake angles at high cutting speeds, does not override the prerequisites for ductile machining, but enhances them instead.

Subsurface damage of machined flats

The analysis of subsurface damage on the machined surfaces was performed by wedge polishing and etching. The wedge has an angle of 0.08°, which means that the depth is linearly increasing up to 6 µm over a length of 4.5 mm. The subsequent etching with diluted hydrofluoric acid (0.1% HF) is necessary to expose possible cracks, which can then be detected and assigned to a certain depth. The measured subsurface damages are shown in Figure 9.

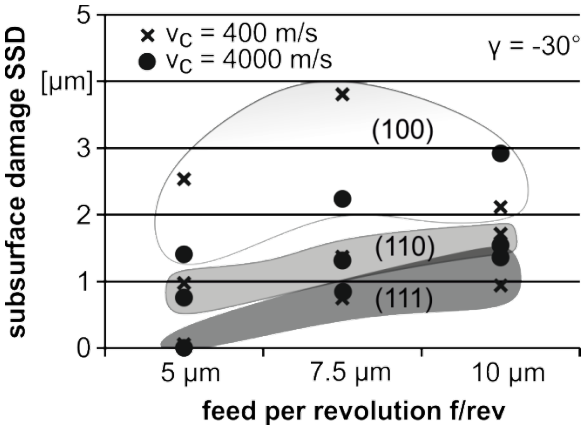

FIGURE 9. SSD for flats over f/rev for γ of -30°

A correlation between the crack depth and surface roughness (Fig. 7) can be recognized. This relationship has also been reported earlier in several investigations [8, 9]. For crystal orientations (110) and (111), the influence of cutting speed on crack depth was low, while it is pronounced for (100) specimens. In general, deeper cracks occur at this crystal orientation. For lower feed rates (5 and 7.5 μm), higher cutting speeds are advantageous regarding crack depth, while this changes to the opposite for the high feed rate (10 μm). The crack depth varies strongly and does not follow the trend of the lower feed rates anymore. This could be explained by the brittle material removal, which occurred at such high feed rates when machining (100) specimens (see Figure 8).

CONCLUSION

This study has shown the dependence of cutting speed on the material removal mechanism when machining monocrystalline silicon by off-axis diamond turning. It was found that a tenfold increase in cutting speed not only reduces the machining time, but also leads to equal or even superior surface quality, which was proven also by surface roughness and subsurface damage measurements. These findings are valid for the machining of flats with overlapping cuts. Interestingly, the machining of separated single cuts revealed that the critical depth of cut is smaller for high cutting speeds compared to low cutting speeds. This was explained by the machining kinematics. Since the chip's cross section differs significantly from turning of flats (feed speed orthogonal to cutting speed), the chip can only flow to the upside. The high pressure, induced by high cutting speeds and negative rake angles, leads to brittle fracture at low depths of cut, no matter which negative rake angle was used. This hypothesis was supported by the results from experiments conducted with 0° rake angle, where higher cutting speeds had a positive influence (lower pressure leads to unrestricted flow of the chip).

The results for the subsurface damage analysis correlate with the surface roughness, so that equal or even lower crack depths occur when machining with high cutting speeds. Measured crack depths varied between 1 and 4 μm, depending on crystal orientation and feed rate.

In future experiments, these findings will be examined for fly-cutting process to exclude a systematic influence from the process itself. Additionally, the influence of tool wear on the preservation of ductile machining will be investigated.

REFERENCES

[1] Brinksmeier E, Riemer O, Schönemann L. High performance cutting for ultra-precision machining. International Journal of Nanomanufacturing. 2015; 11; 245-260.

[2] Schönemann L, Riemer O, Brinksmeier E. Recent Advances in Ultra-precision Milling with Multiple-Cutting Edges. 32nd ASPE Annual Meeting. 2017; 175-179.

[3] Brinksmeier E, Preuss W, Riemer O, Rentsch R. Ultraprecision High Speed Cutting. 30th ASPE Annual Meeting. 2015; 58-63.

[4] Neo W K, Kumar A S, Rahman M A. A review on the current research trends in ductile regime machining. International Journal of Advanced Manufacturing Technologies. 2012; 63; 465-480.

[5] Brinksmeier E, Preuss W. Micro-machining. Philosophical transactions. Series A, Mathematical, physical, and engineering sciences. 2012; 370; 3973-3992.

[6] Owen J D, Troutman J R, Harriman T A, Zare A, Wang Y Q, Lucca D A, Davies M A. The mechanics of milling of germanium for IR applications. CIRP Annals 2016; 65; 109-112.

[7] Brinksmeier E, Preuss W, Riemer O, Rentsch R. Cutting forces, tool wear and surface finish in high speed diamond machining. Precision Engineering 2017; 49; 293-304.

[8] Hed P P, Edwards D F. Relationship between subsurface damage depth and

surface roughness during grinding of optical glass with diamond tools. Applied Optics 1987; 26; 2491.
[9] Esmaeilzare A, Rahimi A, Rezaei S M. Investigation of subsurface damages and surface roughness in grinding process of Zerodur® glass–ceramic. Applied Surface Science 2013; 313; 67–75.

Suitability of RSA Aluminum for monolithic DOE in the VIS Range

Marco Jagodzinski[1], Stefan Kühne[1], Markus Malcher[1], Dirk Oberschmidt[1]

[1]Institute for Machine Tools and Factory Management IWF
Department Micro- and Precision Devices
Technische Universität Berlin
Germany

INTRODUCTION

Imaging diffractive optical elements (iDOE's) with strong curvature enable the development of compact concentric spectrometer designs [1,2].
Production can be lithographic or mechanical. Both methods coexist on the basis of specific advantages, which are comprehensively described in the literature [3,4].
The choice of the manufacturing process and the benefits of the respective advantages depend very much on the application, the optical design, the quantity, the production time and the resulting costs [3,4].
However, the successful production of diffraction gratings is a very sensitive process that depends on various technological parameters regarding both technologies.
In addition, the material is crucial. Focused on mechanical technologies only few special materials are suitable for the production of nanoscale structures. Within this material spectrum, the choice is defined by the wavelength-dependent reflectivity. Aluminum for example is the most suitable material for VIS, whereas gold is most suitable for IR.
The reflectance could be adjusted to a certain wavelength, for example, by means of functional coatings [5]. However, in some cases, e. g. applications for vacuum or large temperature variation, coatings cause problems due to adhesion issues. Therefore, monolithic elements without coating are preferred for these applications.
Fine-grained RSA aluminum alloys have shown their suitability for the production of continuous optical elements. For the manufacturing of discontinuous structures, a deviant behavior is documented [4, 6]. Machined surfaces show finely dispersed damages which reduce the functionality of the optical element.
In the presented study, the RSA types 905, 6061, 443, and 501 are examined with regard to their suitability for the production of monolithic iDOE's.

EXPERIMENTS

The machine tool used in this case is a modified 3-axis ultra-precision machining center LT-ULTRA MMC1100 (Figure 1). A tilt and turn module with two additional rotational hydrostatic axes (A and C) is mounted to enable 5 axes machining. The positional reproducibility of all linear axes is < 40 nm, the angular resolution of the rotatory axis is < 5''.
The machine was modified with regard to the production of diffraction optics. As shown in Figure 1 those modifications include active and passive measures for the reduction of thermal and mechanical disturbances. Regarding long-term stabilization of temperature in the range of ϑ = 20°C ± 0.015°C, the machine is located in a specially developed temperature chamber. A reduction of vibration was achieved by active vibration decoupling and stiffening of the machine. In addition, all pulsation sources are removed and the machine is placed on a foundation which is decoupled from the building.

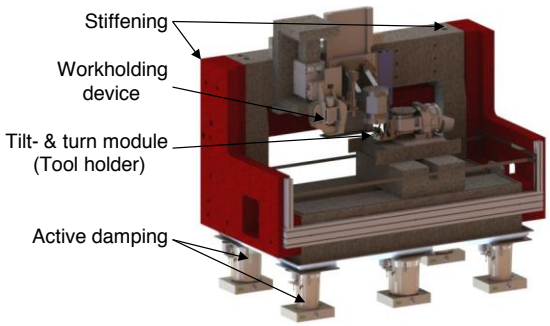

FIGURE 1. Machine tool that has been used within the experiments

During tool setup procedure [7] a BRUKER NEOS N8 AFM has been used to ensure the required measurement accuracy. The AFM lateral and vertical resolution is < 1 nm. Figure 2 shows an exemplary profile of a blaze grating.

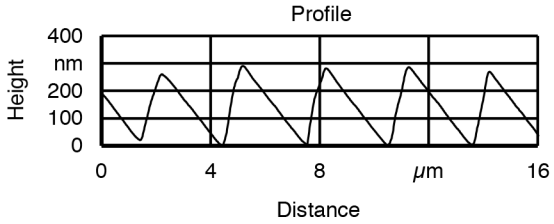

FIGURE 2. Grating profile measured by AFM

The diffraction efficiency of optical elements is measured by using a laser setup. The surfaces are redundantly evaluated using AFM and a white-light interferometer Zygo NewView 5010. Using the WLI, additional microscope images of the surfaces with precisely adjustable illumination intensity can be captured. Exemplary microscope images of the examined alloys are given in Figure 3.

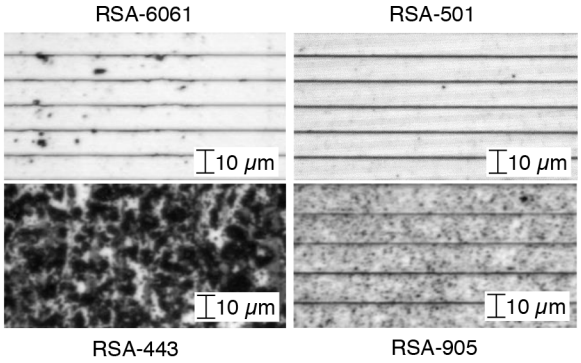

FIGURE 3. Microscope images of blaze gratings machined in RSA-6061 and RSA-501

Methodology

The machining is done by an ultra-precision shaping process.

To ensure that there is no nanoscale pre-damage, the used tools were exclusively selected synthetic rectangular shaped monocrystalline diamonds. The selection is done by test production of a few single lines and AFM examination of the results.

All examined RSA-Alloys showed more or less fine disperse damages when being cut by rectangular shaped tools. The amount of damage depends on the selected material and process parameters. The surface damages increase the stray light which cause lower gray-level values in the defective areas. For an objective, qualitative comparison gray level densities were determined from microscope images.

The defect ratio is defined by the proportion of damaged surface from whole examined area. It can be calculated by integrating the relative gray level density function in the area of the surface defect gray levels. With identical measuring field size and illumination intensity, the defect ratio allows a comparison and optimization of the process parameters based on the density of the gray levels. The image processing and calculations were conducted by means of a self-developed Matlab-script which calculates the gray-level densities of the microscope images and marks all pixels below a determined threshold-value. The darker grey tones from the steep anti-blaze facets are discarded from defect ratio calculation.

The determined gray level density functions of two test gratings, the corresponding microscope images to the density functions and images with red-marked defects are depicted in Figure 4.

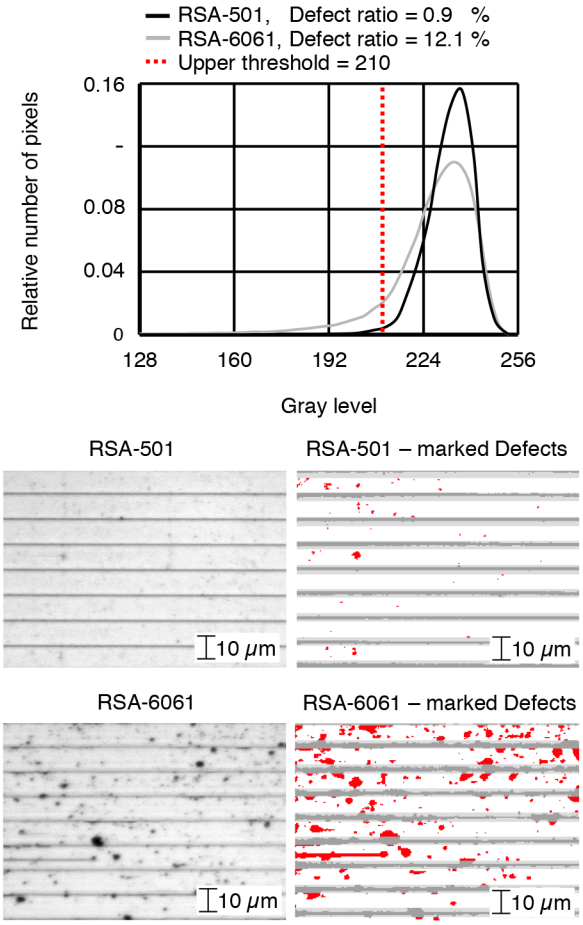

FIGURE 4. Gray level density functions of two test gratings in RSA 501 and 6061 and corresponding surface images with marked defect areas

It clearly can be seen that a higher proportion of darker grey tones correspond to a higher defect ratio and the method enables the identification of defective areas.
The Roughness R_q has been determined from WLI-measured topographic data. The structure waviness resulting from machine oscillations [8] has been filtered by application of a high-pass cut-off filter.

RESULTS
Within the experiments the aluminum alloys RSA-905, RSA-443, RSA-6061 and RSA-501 have been examined.
The mentioned finely dispersed surface damages have mostly been detected on surfaces of machined RSA types 905, 443, and 6061. This is in contradiction to the excellent suitability of these materials concerning the production of continuous optical surfaces.
The dimension of damage depends on the alloy, the process parameters, the cooling lubricant media and the material batch. In addition, this varies locally with very clear transitions, which suggest material inhomogeneities. It is assumed that damages are torn out colloids or exposed inclusions that are plastically closed in the production of continuous optics by falling below the minimum chip thickness in the edge area of the used radius tools. The nearly perfect rectangular chip geometry in grating production prevents this enclosure.
The results with regard to the respective materials are described as follows.

RSA-443
Despite its associated applicability for optical mirrors [9], it was neither possible to measure periodic structures nor to obtain roughness values by usage of WLI. As displayed in Figure 3, the surface is severely damaged. Due to the depicted damages the material is considered unsuitable for the production of diffractive VIS optics. Therefore, RSA-443 has been discarded from extensive / further investigation.

RSA-905
Due to its hardness, strength and diamond turnability, RSA-905 is applied for optical mirrors and injection moulds [9]. During the experiments blaze-grooves without major damages have been machined but a significant amount of fine disperse defects remains on the surface (see Figure 3). The defect ratio varies from 80 % to 90 % and is independent of the examined process parameters sagittal angle α_s, cutting depth h_z and cutting speed v_x. The surface roughness R_q is strongly dependent on cutting angle, which correspondents to the sagittal angle of the optical element, and the cutting depth [4,10].
Due to the strong surface damages RSA-905 is considered unsuitable for the production of diffractive optics.

RSA-6061
RSA-6061 is used for optical mirrors and due to its long term stability it is suitable for aerospace applications [11]. Compared to RSA-905 and RSA-443, machining RSA-6061 led to lowest achieved defect ratio (2.2 %) and roughness value (2 nm). It was presumed, that the extrusion direction of the material might have an influence on the experimental results. Therefore, the experiments have been conducted along orthogonal cutting directions.
A comparison of experimental results of the two cutting directions with lowest achieved roughness and defect ratio in RSA-6061 and the results for RSA-501 is depicted in Figure 5.

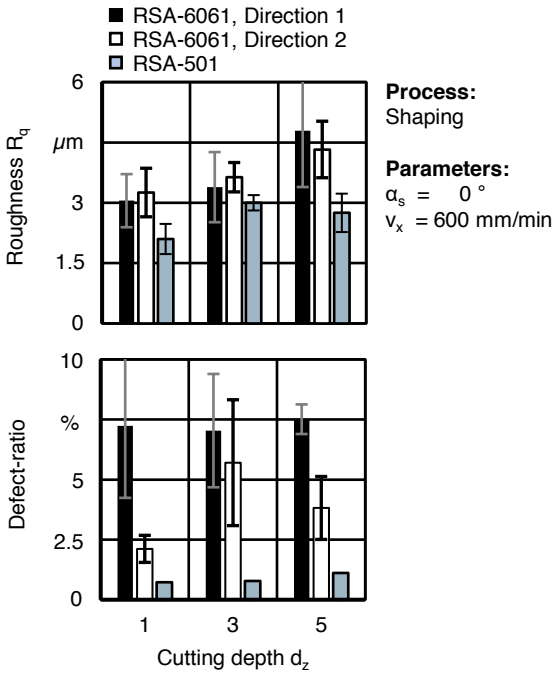

FIGURE 5. Comparison of determined defect ratios and roughness values of RSA-6061 and RSA-501

There is no significant influence of the cutting direction on the Roughness R_q but regarding the defect ratio much lower values have been

achieved along cutting direction 2. The proportion of the defective surface can be further reduced by lowering the infeed. It was not possible to eliminate it completely so far. For cutting depths of 1 μm an average defect ratio of 2.2 % has been achieved. Defect ratios of 1.5 % have been measured occasionally.
Unfortunately, the orientation of the RSA-6061 samples with regard to previous treatment could not be determined. Therefore, the extrusion direction cannot be associated with the cutting directions.
Nevertheless, it is recommended to consider this effect because surface defects can be reduced by selecting a suitable cutting direction. However, regarding high-efficient optical elements, the achievable defect ratio is still considered too large.

RSA-501

RSA-501's application field is not dedicated for optics. Nevertheless, it was examined here for the production of the diffraction structures. While investigating RSA-501, significant differences in roughness R_q and defect ratio of machined optical elements became apparent compared to the other RSA materials.
As depicted in Figure 5 much lower defect ratios (0.7 % - 0.8 %) have been achieved compared to RSA-6061. As depicted in Figure 6, the cutting depths have a slight influence on defect ratio and roughness R_q.

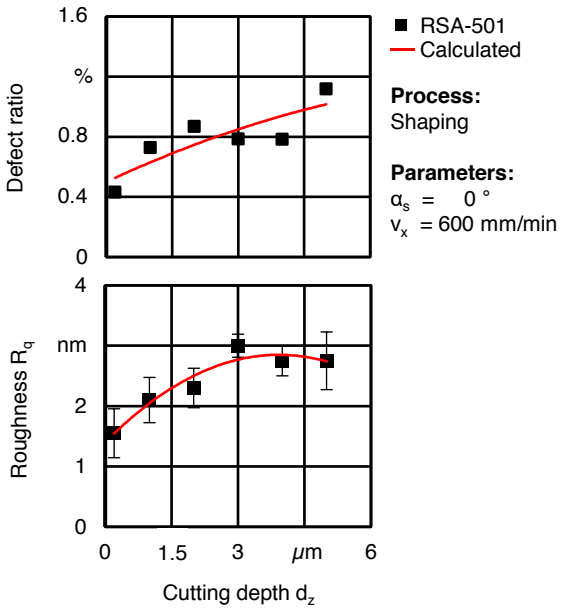

FIGURE 6. Defect ratio and roughness of RSA-501 in dependence of cutting depth

The roughness and defect ratio can be reduced by lowering the cutting depth. The lowest values of average roughness (R_q = 1.5 nm) and defect ratio (0.5 %) have been achieved at cutting depths h_z = 0.2 μm. The surface damage and roughness R_q (~ 2.3 nm) are almost unaffected by varying sagittal angles (Figure 7). This benefits the production of curved optics, as a rotational axis for sagittal realignment of the tool is not necessary.

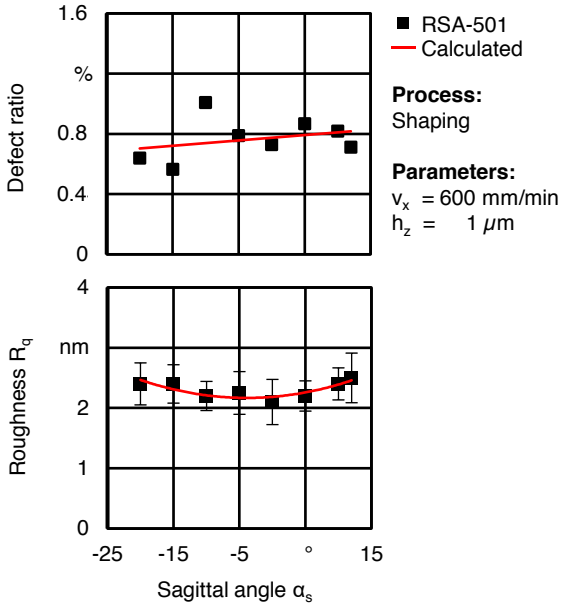

FIGURE 7. Defect ratio and roughness of RSA-501 in dependence of sagittal angle

Due to the lowest achieved values for roughness and defect ratio RSA-501 is by far the most suitable material. A summarization of the achieved results can be seen in Table 1.

TABLE 1. Achievable values of roughness and defect ratio for cutting depths of 1 μm

RSA type	905	6061	501
R_q	4 nm	3 nm	2 nm
Defect ratio	80 %	2.2 %	0.7 %

APPLICATION

Due to the possibility to manufacture high-efficient monolithic VIS-optics from RSA-501, a test grating with a grating period of g = 4 μm and a blaze angle α = 5.32° has been manufactured in RSA-501. An AFM-Profile of the examined plane test grating is displayed in Figure 8.

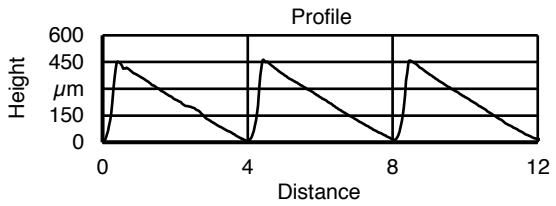

FIGURE 8. AFM-Profile of plane test grating

The grating has a maximum calculated diffraction efficiency of 90 % in Littrow-configuration at a wavelength of 690 nm in TM-mode. With a value of 85 %, the measured maximum diffraction efficiency amounts 94.4 % of the calculated diffraction efficiency.
The measured and calculated wavelength-dependent efficiencies of the TM and TE mode are shown in Figure 9.

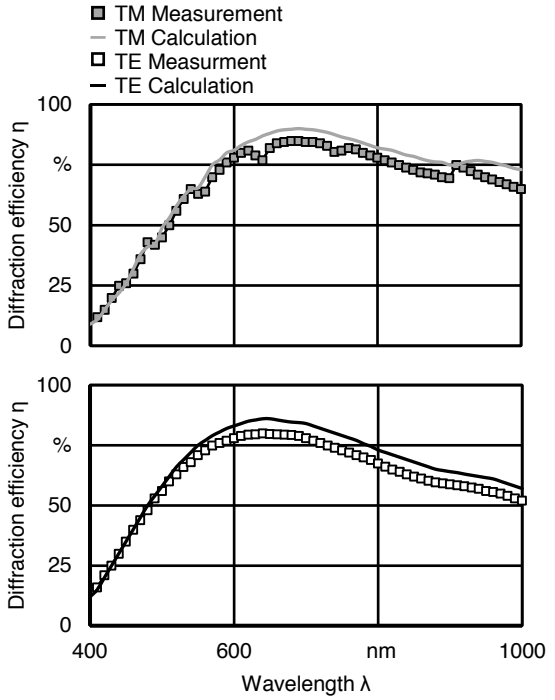

FIGURE 9. Measured and calculated diffraction efficiencies of the plane test grating

Additionally, a spherical DOE for an Offner-Spectrometer has been manufactured (Figure 10).
The Offner assembly is a frequently used configuration for telescopes [8] und spectrometers [13, 14, 15]. It was developed by Offner [16] to minimize spherical aberrations in mirror optics. In the simplest configuration, 3 mirror elements are arranged concentrically. One convex element and two concave elements.
Due to the deviation from purely spherical elements, further aberrations can be minimized [17]. However, the basic arrangement remains unchanged. In the corresponding spectrometer construction, the convex element is replaced by a convex diffraction grating.
A strong miniaturization of this construction requires strong curvatures of all optical elements.
The sphere's radius of curvature and diameter are R = 20 mm and D = 8 mm. The blaze facets are individually adjusted to orientate the blaze angle of 5.32° to the local surface slope. The positional accuracy of the grooves is in the range of 100 nm which is enabled by the compensation of tool displacement with AFM-measurements of dedicated test structures [6].

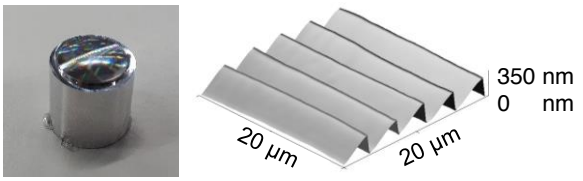

FIGURE 10. Spherical DOE and Topography of the structured sphere that has been measured by WLI

CONCLUSION

In the presented study the suitability of different RSA aluminum types for the production of efficient diffraction gratings by means of ultra-precision shaping was examined.
The results clearly show that the materials RSA-443, RSA-905 and RSA-6061, in contrary to their repeatedly confirmed excellent suitability for the production of continuous optics, are partly unsuitable with regard to discontinuous optical structures. The efficiency of monolithic diffractive optical elements produced by ultra-precision machining is thus clearly limited.
RSA-6061 showed an existing but limited suitability. The materials RSA-443 and RSA-905 were discarded for further investigation. The material RSA-501, which is not widely used in the production of optics, showed very good properties and was included in the test procedure.
By varying parameters, the results for RSA6061 can be optimized, but significantly better results can be achieved by using RSA-501.
While the defect rate of RSA-6061 was optimized from 7 % to 2.2 %, RSA-501 could be optimized to 0.7 % for cutting depths of 1 µm.

Due to the unexpectedly good suitability of RSA-501, diffractive test optics were manufactured and investigated.
The realized monolithic optics have a significantly reduced roughness and defect ratio and therefore less surface-induced scattered light (TIS) than the alternative materials.

ACKNOWLEDGEMENT
The results are an integral part of the project 3D BLAZE, which is part of the initiative KMU Innovative: Photonics. We thank the Federal Ministry of Education and Research for the funding.
In addition, we would like to thank the students of the TU-Berlin, who always diligently and inquisitively support our investigations. In this context we would like to thank Felix Weiß in particular.
Furthermore, we would also like to thank DIOS GmbH for their support in evaluating the DOE and LT-Ultra precision GmbH as well as Carl Zeiss Jena GmbH for the good cooperation in the course of this project.

REFERENCES
[1] Last, A.: Fehllicht in LIGA-Mikro-spektrometern: Berichte // Forschungszentrum Karlsruhe, Technik und Umwelt FZKA 6885, Karlsruhe, 2002.
[2] Mertz, L.: Concentric spectrographs. Applied optics 16 (1977) 12, S. 3122–3124.
[3] Glaser, T.: High-end spectroscopic diffraction gratings. Design and manufacturing. Advanced Optical Technologies 4 (2015) (1), S. 25–46
[4] Kühne S. Ultrapräzisionsverfahren zur Erhöhung der Güte abbildender Beugungsgitter, Fraunhofer Verlag 2018
[5] Gebhardt, A.; Steinkopf, R.; Scheiding, S.; Risse, S.; Damm, C.; Zeh, T.; Kaiser, S.; Strojnik, M.; Paez, G.; MERTIS: Optics manufacturing an verifi-cation, in: SPIE Optical Engineering, San Diego 2010
[6] Meier A. Diamantdrehen komplexer diffraktiver Mikrostrukturen, Shaker 2016
[7] Uhlmann, E.; Kühne, S.; Jagodzinski, M.; Widemann, R.; Haskic, K.: Precision enhancement technologies for multi-axis ultra-precision machining of freeform optical elements with variable micro/nano structures. ASPE/ASPEN (2017)
[8] Uhlmann, E.; Kühne, S.; Jagodzinski, M.; Malcher: CHARACTERIZATION AND OPTIMIZATION OF ULTRA-PRECISION MACHINE TOOLS AND PROCESSES BY TIME RESOLVED PSD SIGNATURE OF MICRO/NANO STRUCTURED OPTICAL SURFACES. ASPE Topical Meeting (2017)
[9] RSP Technology. Available online: http://www.rsp-technology.com/ (accessed on 13 July 2018).
[10] Uhlmann, E.; Kühne, S.; Jagodzinski, M.: Influence of the rake angle on the surface formation during micro shaping of submicron optical structures in Au-layers. euspen's 16th International Conference & Exhibition, 2016
[11] Guido P. H. Gubbels, Bart W. H. van Venrooy, Albert J. Bosch, Roger Senden, "Rapidly solidified aluminium for optical applications", Proc. SPIE 7018, Advanced Optical and Mechanical Technologies in Telescopes and Instrumentation, 70183A (23 July 2008)
[12] J Blommaert, J.; Delauré,B.; Livens, S.; Nuyts, D.; Tack,k.; Lambrechts, A.; Morau, V.; Callut, E.; Habay, G.; andenbussche,J.; Minoglou, K.; Deep, A.: CHIEM: a versatile compactT hypersprectral imager, The 4S Symposium 2018
[13] Peter, G.; Helbert, J.; Hiesinger, H.;Weber, I.;Walter, I.; und Arnold, G.; Säuberlich, T.: Developing of MERTIS as an advanced process from the study up to the flight model. SPIE Optics + Photonics, San Diego 27.08.2013
[14] Battistelli, E.; Coradini, A.; Mugnuolo, R.; Capanni, A.; Paolinetti; R., Re; E.; Magnani, P.: Challenging design and development of Ma_Miss, a miniatur-ized spectrometric instrument for Mars sub-soil analysis: SPIE Optics + Optoelectronics, Prague. 18.04.2011
[15] Guldimann, B.; Deep, A.; Vink, R.; Harnisch, B.; Kraft, S.; Sierk, B.; Bazalgette, G.: OVERVIEW ON GRATING DEVELOPMENTS AT ESA. Deep A. & Vink, R. CEAS Space J (2015) 7, S. 433.
[16] Offner, A.: New Concepts in Projection mask Aligners. Opt. Eng 14 (1975)
[17] Prieto-Blanco, X.; González-Nuñez, H.; de la Fuente, R.: Off-plane anastig-matic imaging in Offner spectrometers. Journal of the Optical Society of America. A, Optics, image science, and vision 28 (2011) 11, S. 2332–2339.

FOCUSED ION BEAM MILLING OF MICROSCALE FEATURES

Anthony Wong, Thomas Dow, Mark Pankow
Department of Mechanical and Aerospace Engineering
North Carolina State University
Raleigh, NC

INTRODUCTION

As modern electronics have continued to shrink in size, the need for smaller and smaller optics has increased. For instance, a typical smartphone display can have pixels tens of micrometers in size. Some digital camera sensors now have pixels with single digit micrometer dimensions. Matching microscale optics are needed for each pixel to collimate light from a display or focus light onto a sensor. For a display, such optics would produce higher output intensity, while lowering the power consumption. In this day and age of portable, high-volume electronic devices, low-cost and light-weight microscale lens arrays need to be developed for applications such as this.

This research is part of the development of a novel process for manufacturing microlens arrays. In this process, a die with 4 to 9 convex features, 20-30 μm in lateral size will be manufactured from a hard material. Next this die will be rapidly indented multiple times to create a mold with millions of concave features. Creating the mold through plastic deformation using an indenter compared to more traditional means such as milling can greatly reduce the fabrication time because larger areas are made during each indent. This concept is similar to a previous project at NC State in which nanoscale features were replicated through an indenting process [1]. The mold will be used with a conventional plastic manufacturing process, such as compression molding or injection molding, to make a microlens array with millions of convex features. This work focuses on the first step of making the indenting die with convex features.

In the previous work at NC State, nanoscale features were milled into an indenting die with a focused ion beam (FIB). A FIB is able to precisely accelerate gallium ions at a target with spot sizes as small as tens of nanometers in diameter. When the gallium ions impact the target, molecules from the target will sputter off leaving a new shape. The FIB milling process is controlled by only a handful of parameters. First, the beam current determines the shape of the ion intensity distribution. In literature, the beam intensity distribution is often modeled with a Gaussian profile [2]. As the beam current increases, the width of the distribution increases. The beam current does not change after the milling process begins, as it is related to the optics in the FIB. The focus and stigmation would need be adjusted for a new beam current setting. The maximum dwell time, map of relative dwell times and number of passes are the parameters used to setup the equivalent of a toolpath in conventional milling. The maximum dwell time is the longest amount of time an area would be exposed to the ion beam. The longer the dwell time, the more material will be sputtered. A map of locations and relative dwell times for each (x, y) coordinate tells the machine where to turn the beam on and what percentage of the maxium dwell time to expose that area. The number of passes is the number of times the “toolpath” will be repeated.

Many researchers have examined the fabrication of concave molds with a focused ion beam. Yoshida et al. [3] made a press mold out of glassy carbon for an array of 20 μm diameter lenses by machining the form with a Nd-YAG, 300 mW laser, followed by FIB milling to improve the surface finish and to remove debris from the laser machining process. Langridge et al. [4] explored fabricating 1 to 10 μm diameter parabolic concave features in silicon with the FIB for molding glass. Youn et al. [5] used a FIB to mill glassy carbon molds for microfluidic devices.

In addition to optical mold fabrication, there is a significant body of research on milling arbitrary 3D shapes with the FIB. In particular, Adams et al. [2] describe a method of combining the beam intensity distribution with the sputtering yield to predict the material removal and final shape.

In this paper, FIB milling of glassy carbon is investigated for the purpose of producing an indenting die. Glassy carbon has high hardness and compressive strength, which are needed for

the die which will be plastically deforming the mold. It also is amorphous, which means it will FIB mill more uniformly than a material with grain structure. Finally, it has a relatively high material removal rate, about 5 times that of diamond.

MATERIAL REMOVAL RATE

To determine the material removal rate of the FIB with glassy carbon, a simple experiment was devised. The ion beam of a FEI Quanta 3D FEG executed a square milling pattern on a 25 x 25 x 3 mm glassy carbon sample (SPI-Glas 11). Based on Adams' work [2], it was recommended to keep the depth of the feature less than half the width of the feature to minimize redeposition. This means that as the material sputters, it can land back on the material and redeposit, reducing the effective sputtering rate and shape fidelity. This effect can be significant, particularly for deep narrow features where the sputtered material cannot escape. The depressed surface was measured with a Zygo New View 5000, so that the volume of removed material could be calculated. This volume was divided by the machining time to yield a material removal rate.

For a 15 nA current, the volume removed was calculated to be 73 μm^3 for a 24 second milling operation. This yields a material removal rate of 3 $\mu m^3/s$. When the experiment was repeated for a 65 nA current, it removed 165 μm^3 of material over 6 seconds and achieved a material removal rate of 27 $\mu m^3/s$.

The material removal rate allows the time to mill a single feature to be estimated. The volume that must be removed to achieve the desired shape is estimated to be on the order of 2,500 μm^3. Removal rates of 3 $\mu m^3/s$ and 27 $\mu m^3/s$ correspond to machining times for a single feature of 14 minutes and 1.5 minutes respectively. This material removal rate study indicates that the FIB can mill glassy carbon fast enough to make a die with 4 features in a reasonable amount of time, as in minutes or hours, as opposed to days.

FEASIBILITY TRIAL

A Matlab script was developed to generate a command file for the FIB in the form of a bitmap where each pixel specifies an (x, y) coordinate. The color of each pixel is interpreted by the FIB as the relative dwell time of the ion beam. A plot of the relative dwell times is shown in Figure 1. A bitmap was generated which contained a dwell time distribution to create a 2 by 2 array of convex, smooth features, as well as a 5 µm border around the array. Each pixel represents a 40 x 40 µm area. A parabolic distribution of dwell times was used to command the FIB to mill the bumps. The dwell time goes to zero at the center of the feature where little material should be removed. At the base of the feature, the dwell time is 100% where the maximum amount of material is to be removed. Figure 2 shows the results of this pattern of dwell times. The recessed area is approximately 50 x 50 µm and 6 µm at its deepest point.

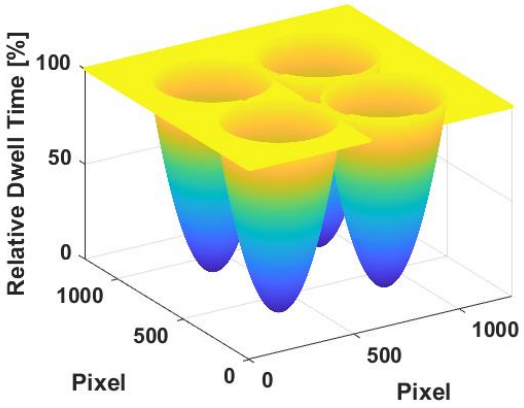

FIGURE 1. Representation of the relative dwell times assigned to each pixel (Zero values were removed for clarity.)

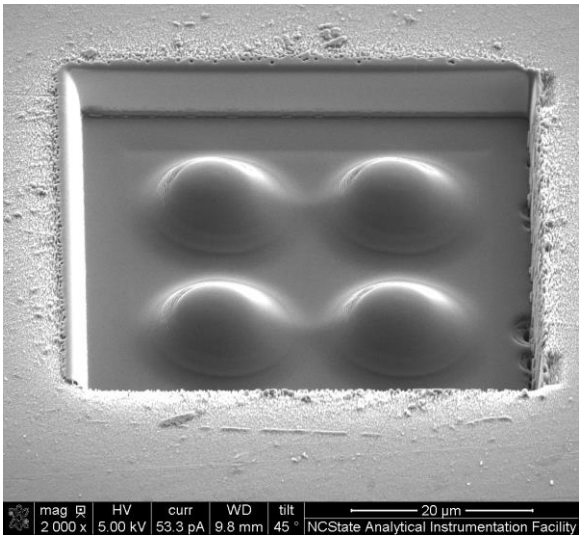

FIGURE 2. SEM image of FIB milled bumps in glassy carbon

ERROR CORRECTION

The FIB sputtering yield is dependent on the angle of incidence of the beam on the surface, so the previous pass influences the current pass. A simulation tool has been developed using Adam's

model [2], but it has not yet proven useful for planning the command file for the FIB.

Rather, a rudimentary method of correcting an initial guess was used to FIB mill the desired shape. An initial relative dwell time map was created based on parabolically distributed dwell times used in the feasibility trial, but the features were more tightly spaced. No border was included, and the features were enlarged slightly to meet the project goals. The modified pattern is shown in Figure 3, where each pixel is 50 µm. A glassy carbon surface was FIB milled with this pattern to approach the correct depth. An SEM image of the surface is shown in Figure 4.

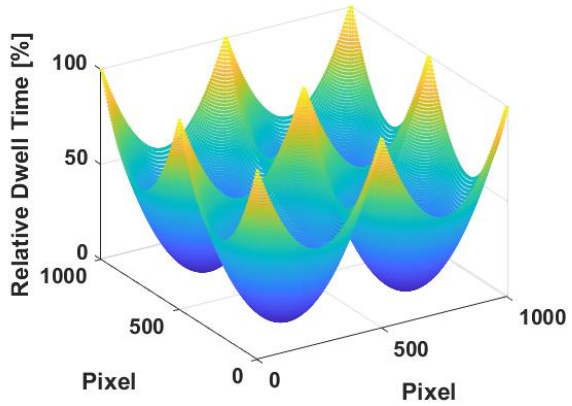

FIGURE 3. Modified relative dwell time map (Zero values were removed for clarity)

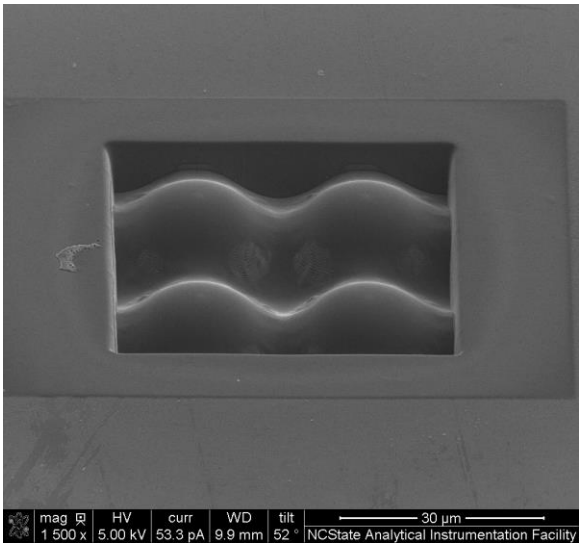

FIGURE 4. SEM image of the convex features FIB milled into glassy carbon

The surface topography was measured with a Keyence VK-X1100 laser confocal microscope. The measured surface was then compared to the desired shape, which in this case was a hemisphere over a circular aperture. Representative data is shown in Figure 5, where the measured data is the colored surface and the faceted surface is the desired spherical surface. The error of the surface was calculated with respect to the beam direction and converted to a percentage of the maximum FIB milled depth. An example of this error map is shown in Figure 6. The command file was then adjusted by this percentage. For instance if a location were 5% too tall, the beam would be commanded to dwell 5% longer and remove more material there.

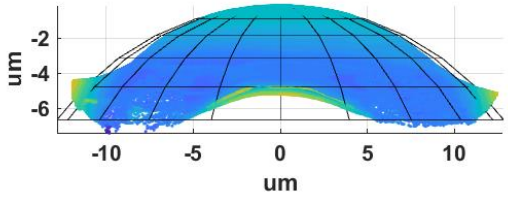

FIGURE 5. Measured surface data with the desired spherical shape overlaid (Colormap is the same as Figure 6.)

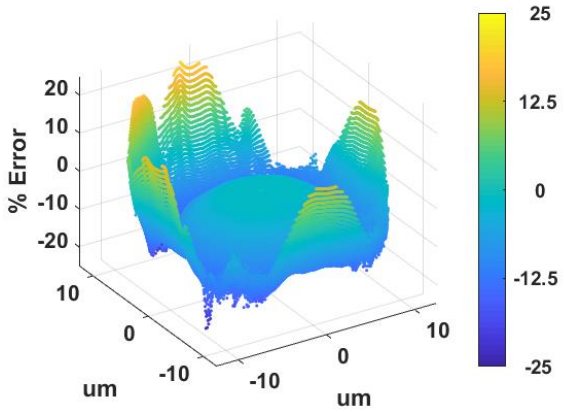

FIGURE 6. The deviation from the desired spherical surface converted to a percentage of the maximum FIB milled depth

This method was able to correct some of the error in the features. Figure 7 shows the average height error of the horizontal and vertical meridians of four bumps. In this visualization, a perfect surface would be a flat line representing zero error. The “original” four features were made with the parabolically distributed dwell times. Four more features were made with the dwell times adjusted by the previously described error compensation scheme. Within a 15 µm diameter aperture, the measured surface is within 250 nm of the desired shape. However, this method was

not able to correct the errors outside the 15 µm aperture. Further investigation needs to be conducted to determine the reason for this.

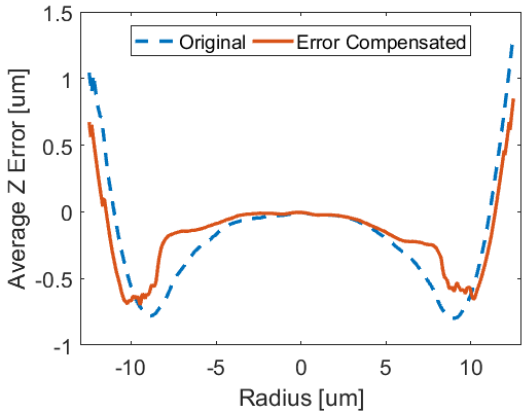

FIGURE 7. Comparison of the average error of 4 features FIB milled with and without error compensation

INDENTATION

A 1 mm diameter glassy carbon rod (SPI-11) was cut to about a 2 mm length with a low speed diamond wheel saw. A holder was made of 0.25 inch diameter 6061 aluminum round stock. One end of the aluminum rod was turned to a 90º cone on a manual lathe. A hole was drilled into the tip of the cone to hold the glassy carbon piece. The glassy carbon was glued into the aluminum with a cyanoacrylate based adhesive (Gorilla Super Glue).

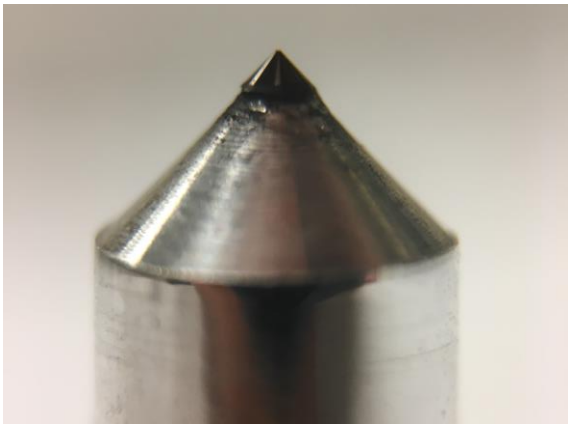

FIGURE 8. Diamond turned glassy carbon blank potted in an aluminum holder

The face of the glassy carbon rod was turned with a -30º rake, 3 mm nose radius diamond tool in a Nanoform 600 diamond turning machine. Surfaces finishes of 4-8 nm RMS were achieved. Next the cylindrical glassy carbon was turned with a 0º rake, 1 mm nose radius diamond tool to form a frustum with a 90º cone angle leaving a circular flat on the tip. Figure 8 shows an example of one of the glassy carbon blanks manufactured in this manner.

A 2 by 2 array of convex features were FIB milled into the tip of the glassy carbon frustum. After FIB milling the features, a border was also FIB milled so the bumps would be higher than the surface around it. The final glassy carbon tip is shown in Figure 9.

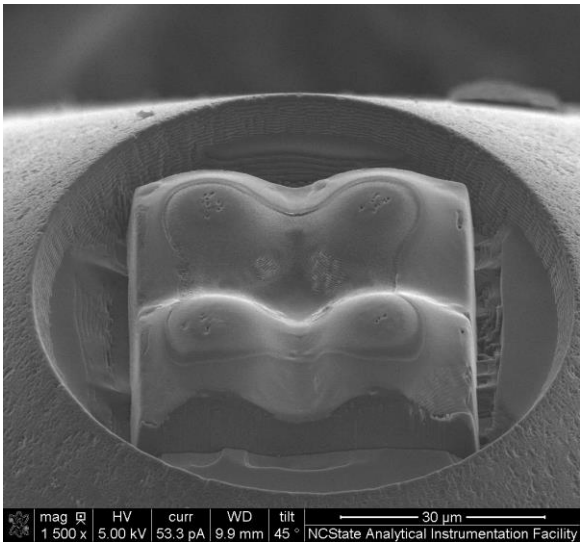

FIGURE 9. SEM image of the glassy carbon tip after FIB milling convex features and border

An 1100 aluminum sample was prepared to be indented by diamond turning the face to 6 nm RMS. The glassy carbon and its aluminum holder were mounted in the tool post of the diamond turning machine. The axes of the diamond turning machine were then used to press the glassy carbon into the aluminum sample. 1100 aluminum was chosen because it is soft, diamond turnable and is well characterized in literature. Figure 10 shows a measurement of aluminum indentation from the laser confocal microscope. The aluminum appears to have replicated the glassy carbon features quite well.

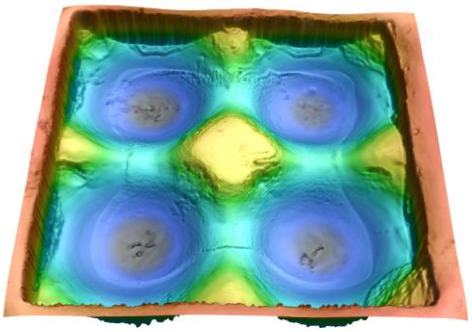

FIGURE 10. Laser confocal microscope measurement of an 1100 aluminum sample after it has been indented with the FIB milled glassy carbon.

CONCLUSIONS

This work demonstrates the feasibility of creating a glassy carbon die with microscale features with focused ion beam milling. These features were then replicated in an aluminum workpiece which could be used as a mold. Future work will focus on the fidelity and speed of the replication of the glassy carbon features.

REFERENCES

[1] Dow T, Zdanowicz E, Sohn A, Scattergood R, Nowak W, inventors; North Carolina State University, assignee. Methods and systems for fast imprinting of nanometer scale features in a workpiece. United States patent application US 14/431,348. 2015 Aug 27.

[2] Adams D, Vasile M, Mayer T. Focused ion beam sculpting curved shape cavities in crystalline and amorphous targets. J Vac Sci & Technol B. 2006 Jul;24(4):1766-75.

[3] Yoshida Y, Okazaki W, Uchida T. Laser and focused ion beam combined machining for micro dies. Rev Sci Instrum. 2012 Feb;83(2):02B901.

[4] Langridge M, Cox D, Webb R, Stolojan V. The fabrication of aspherical microlenses using focused ion-beam techniques. Micron. 2014 Feb 1;57:56-66.

[5] Youn S, Takahashi M, Goto H, Maeda R. A study on focused ion beam milling of glassy carbon molds for the thermal imprinting of quartz and borosilicate glasses. J Micromech and Microeng. 2006 Oct 20;16(12):2576.

BESSEL BEAM ARRAY FOR HIGH RESOLUTION WAFER DICING

Hiu Hung Lee, Erxuan Zhao, Wei Lin, Yina Chang and Shih-Chi Chen*
Department of Mechanical and Automation Engineering
The Chinese University of Hong Kong
Shatin, N.T., Hong Kong
*Email: scchen@mae.cuhk.edu.hk

In this paper, we present a new parallel micro-machining method based on the generation and control of multiple Bessel beams. The new method may realize ultrafast high-resolution (1000 mm/s; < 3 μm kerf) stealth laser dicing on glass or semiconductor wafers. In our study, a spatial light modulator (SLM) is used to generate multiple Bessel beams from a femtosecond laser; each Bessel beam's characteristics (e.g., aspect ratio and intensity distribution) and location can be controlled directly through the SLM. Mathematical models as well as experimental results are presented to demonstrate the improved dicing speed and resolution.

INTRODUCTION

New wafer dicing technologies play a crucial role in semiconductor industry as the quality of the final product highly depends on the cut quality. In addition, less material loss during dicing also means more silicon real estate becomes available for making devices. Conventionally, wafer dicing is performed by blade dicing or laser ablation dicing, where materials are mechanically removed or pulverized in the cutting path, i.e., kerf, causing issues such as debris, contaminations, or damage to the devices etc. More recently, a new laser technique, i.e., stealth laser dicing, was introduced to overcome these problems. Stealth laser dicing refers to a process that utilizes a laser beam to introduce defects inside a glass or semiconductor wafer for separating it into many small pieces with high precision and speed [1-3]. State-of-the-art stealth laser dicing systems introduce defects to materials with Gaussian beam-based nanosecond lasers with a wavelength of 1064 nm. To separate a thick wafer, the laser must scan at different depths inside the wafer for a dozen times to ensure quality separation, achieving a kerf width of ~10 μm.

BESSEL BEAM vs. GAUSSIAN BEAM

Gaussian beam has been the most extensively used beam mode in both engineering and scientific research. However, in many laser fabrication applications, the short Rayleigh range of the Gaussian beam often limits the penetration depth into a workpiece and imposes additional requirements on the sample. In this work, we apply Bessel beams to improve dicing results.

Comparing with a Gaussian beam, a Bessel beam has a more localized (narrower) lateral intensity profile and an extremely long focal region, i.e., tens to hundreds of microns, as shown in Fig. 1. As such, it may be used to enhance the imaging or laser fabrication resolution. Bessel beam was first predicted by Durnin in 1986 [4] as a "nondiffracting" beam, which does not change its transverse intensity profile as it propagates. In addition to the unique intensity profile, the "self-healing" property of a Bessel beam, i.e., restoring its intensity profile even it is partially obstructed at one point, may further increase the penetration depth in scattering or semi-transparent media. These unique characteristics make Bessel beam one of the best candidates to be implemented in a stealth laser dicing system to process thick wafers and to achieve minimal kerf width.

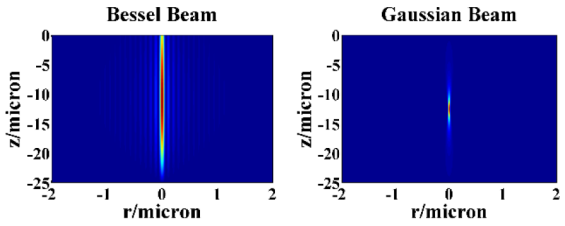

FIGURE 1. Simulated intensity profiles of a Bessel beam (left) and Gaussian beam (right)

To fully exploit Bessel beams for wafer dicing, a few issues must be addressed: (1) control and optimize the Bessel beam intensity profile; and (2) suppress the side lobes (rings). In terms of intensity profile, the length of the focal region must be appropriately adjusted to fit inside a wafer of any thickness (e.g., 50 – 700 microns); as the laser will be partially absorbed as it passes through the wafer, the intensity needs to be

higher at deeper wafer regions to achieve optimal dicing results. These issues may be addressed by optimizing the phase correction pattern on the SLM.

MODEL & CONTROL OF BESSEL BEAMS

Bessel beams are solutions to the Helmholtz equation in cylindrical coordinates. To model a Bessel beam, we first consider the Fourier transform of a field $U(x,y)$ defined in a plane traverse to the optical axis (i.e., z-axis) . In an orthogonal system of coordinates [x, y, z], each plane wave component is defined by a wave-vector $k = [k_x, k_y, k_z]$. For azimuthally independent optical fields such as $f(r, z)$, the Fourier transform of the plane wave becomes a zero-order Hankel transform [5], as expressed in Eq. (1).

$$S(k_r, z=0) = \int_0^\infty U(r, z=0) J_0(k_r r) r dr \quad (1)$$

where $k_r = \sqrt{k_x^2 + k_y^2}$; $r = \sqrt{x^2 + y^2}$; and J_0 is the zero-order Bessel function. The inverse Fourier transform is given by

$$U(r, z=0) = \int_0^\infty S(k_r, z=0) J_0(k_r r) k_r dk_r \quad (2)$$

Any azimuthal independent field can be considered as a zero-order Bessel beam $J_0(k_r r)e^{ik_z z}$ that propagates in the free space, where $k_z = \sqrt{k^2 - k_r^2}$ is the axial wave-vector component. Different Bessel beam components have different axial wave vectors. These components will interfere on the optical axis, resulting in the unique intensity distribution of the Bessel beam that is azimuthally independent. The axial field distribution can be mathematically expressed as:

$$U(r=0, z) = \int_0^k k_z S(\sqrt{k^2 - k_z^2}, z=0) e^{ik_z z} dk_z \quad (3)$$

Eq. (3) shows that the axial intensity of the azimuthally independent field is a one-dimensional Fourier transform of the product of the axial wave vector and the spatial spectrum. Thus, off-axis shift can be achieved by multiplying the spatial spectrum with the phase of an oblique plane wave.

In addition, the axial intensity distribution of a Bessel beam can be arbitrarily controlled by programming the spatial spectrum of the Bessel beam. Here, we define a quasi-Bessel beam with arbitrary axial intensity distribution of a finite envelop of $A(z)$. The spatial spectrum can be mathematically expressed as:

$$S\left(\sqrt{k^2 - k_z^2}\right)_{z=0} = \frac{1}{2\pi k_z} \int_{-\infty}^{\infty} A(z)\, e^{ik_{z0}z} e^{-ik_z z} dz \quad (4)$$

As the Bessel beam has a sparse spatial spectrum, multiple Bessel beams can be obtained by multiplexing their spatial spectra with different oblique plane wave phase patterns. Note that the multiplexed spatial spectra cannot overlap with each other in order to prevent interference among the generated Bessel beams. Each Bessel beam can be individually controlled by projecting the corresponding spatial spectrum. In our system, a phase-only LC-SLM is used to generate multiple Bessel beams, forming a Bessel beam array, where individual Bessel beams are adjustable. The phase pattern is calculated by modified mixed-region amplitude freedom method [8]. Figure 2 presents the block diagram of the Bessel beam generation algorithm.

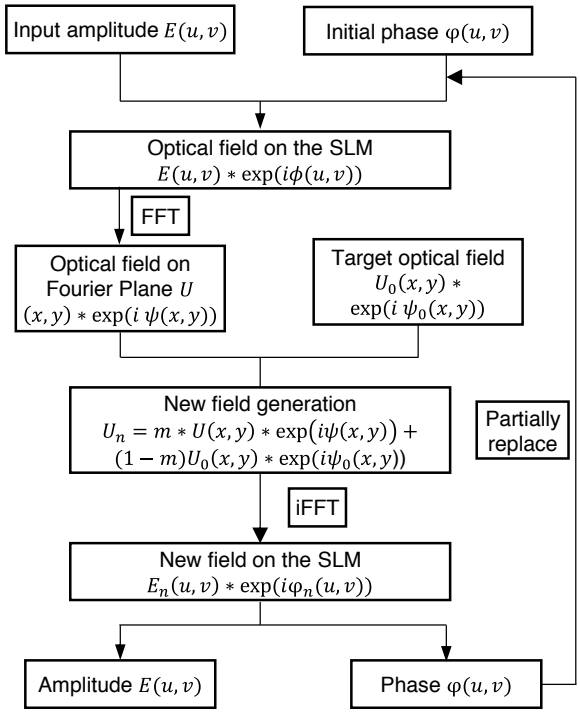

FIGURE 2. Block diagram of the algorithm for generating the Bessel beam array

SYSTEM CONFIGURATION

Figure 3 presents the optical configuration of the Bessel beam wafer dicing system. The laser source is a Ti-Sapphire regenerative amplifier (Spitfire Pro, Spectra-Physics) and an optical parametric amplifier (OPA, TOPAS-Prime, Spectra-Physics) with a tunable wavelength from

290 nm to 2600 nm, pulse width of 100 fs, and repetition rate of 1 kHz. First, the laser beam is expanded to fully fill the aperture of the LC-SLM, which convert the Gaussian beam into one or multiple Bessel beams. The Bessel beams then pass through a pinhole (i.e., spatial filter) to remove the 0th order diffraction. Lens 2 and Lens 3 form a 4-f system, and lastly the Bessel beams are focused inside the wafer. The wafer is mounted on a precision XYZ stage for positioning. To observe the fabrication process, an imaging system is built in conjunction with the fabrication system, as shown in Fig. 3.

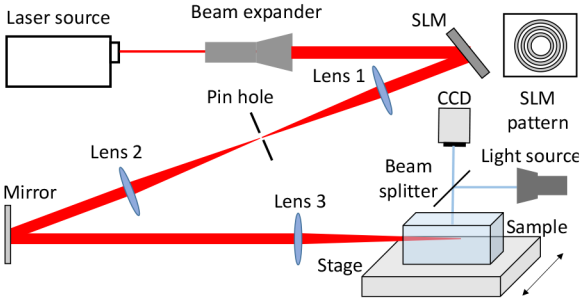

FIGURE 3. Optical configuration of the multi-Bessel beam laser dicing system

CONTROL OF BESSEL BEAM ARRAY

In this section, we experimentally generate and characterize the Bessel beam array. The Bessel beams with normal intensity distribution can be generated via annular apertures with different off-axis shifts [6, 7]. The number of generated Bessel beams depends on the number of annular apertures on the SLM. Figure 4 shows the spatial spectrum and the calculated phase pattern on the SLM for generating four (quasi-) Bessel beams. It should be noted that an initial oblique plane wave phase pattern is added to the background to minimize the influence of the 0th order diffraction on the SLM.

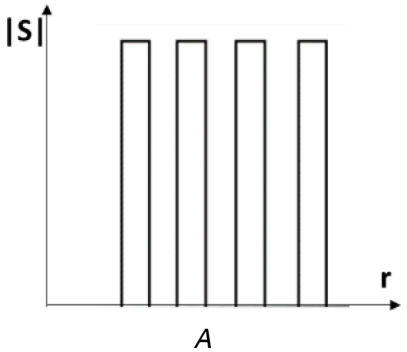

A

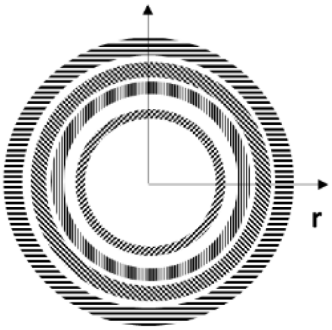

B

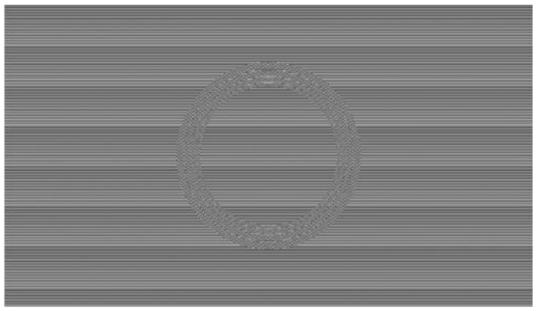

C

FIGURE 4. (A) Spatial spectral of four Bessel beams with normal intensity distribution. (B) Oblique plane wave phase pattern for Bessel beam separation; (C) pattern displayed on the LC-SLM

As discussed before, the position of each Bessel beam can be independently controlled by adding different oblique plane wave phase patterns to the corresponding annular aperture. By adjusting the phase with different oblique angle, the position and separation of each Bessel beam can be precisely controlled. In Fig. 5, we experimentally demonstrate the generation and position control of four Bessel beams with normal axial intensity distribution. Figure 5A and 5B present the recorded four Bessel beam profiles that have a 5-mm and 10-mm spacing in both X and Y directions respectively. Figure 5C and 5D presents the four Bessel beam profiles of 8-mm / 5-mm spacing as well as 5-mm / 8-mm spacing in the X and Y directions respectively. Figure 5E and 5F present zoom-in views of the two Bessel beams boxed in Fig. 5B. From the results in Fig. 5, one may observe that all generated Bessel beams in the array achieve good quality. Accordingly, we can conclude that the number and position of the Bessel beam can be individually controlled by adjusting the number of the annular apertures as well as the added phase pattern respectively.

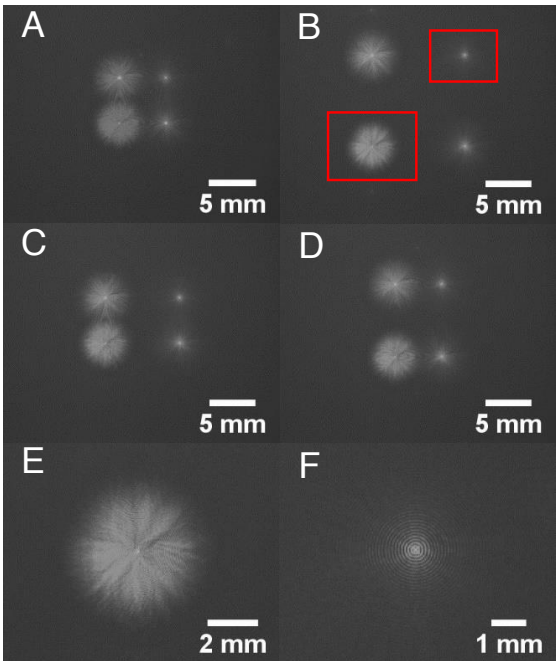

FIGURE 5 A-D. Multiple Bessel beams with different separation distances in the X and Y directions; E and F. Zoom-in view of the Bessel beams boxed in 5B

Next, we demonstrate how to control the axial intensity distribution of multiple Bessel beams simultaneously. Figure 6A presents the SLM pattern that generates two Bessel beams with different intensity distribution modification. The inner ring induces an increasing axial intensity while the outer ring induces a decreasing axial intensity. The experimental results are shown on Fig. 6B, where the vertical axis represents the normalized intensity and the horizontal axis represents the axial position (Δz). Considering the laser beam may be partially absorbed by the wafer at different depths, Bessel beams of increasing intensity profile (with increasing depth) are desired to achieve optimal dicing results.

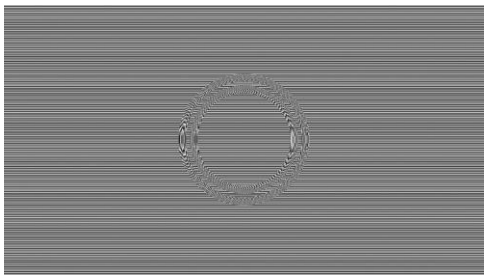

A

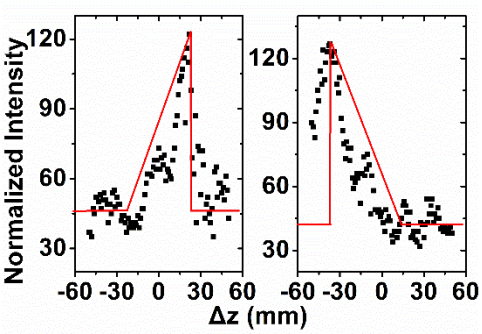

B

FIGURE 6 Simultaneous control of two Bessel beams' axial intensity distribution. A: Pattern on the SLM; and B: individually control intensity profile of the two Bessel beams

In the last experiment, we compare the laser dicing results between a conventional Gaussian beam and a Bessel beam. The results are presented in Fig. 7. From the results, we can find that the application of Bessel beams has effectively reduces the 12 required Gaussian beam passes to a single Bessel beam pass with a smaller kerf, measured to be ~3 μm after wafer separation. By controlling the intensity distribution of the Bessel beam, highly uniform and consistent cut paths in the axial direction can be achieved. The application of multiple Bessel beam may further improve the dicing throughput.

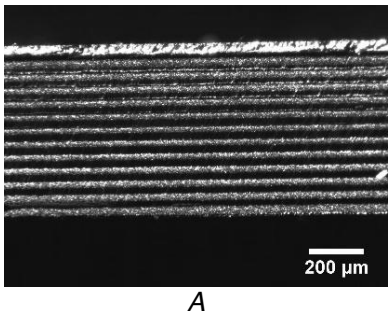

A

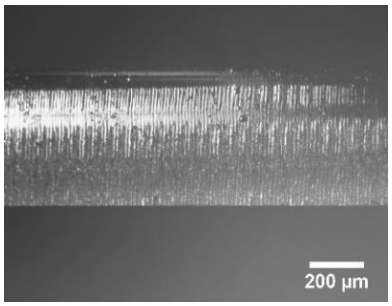

B

FIGURE 7. Comparison between a (A) Gaussian beam and (B) Bessel beam for wafer dicing

CONCLUSION

We have presented models and experimental results of a new wafer dicing method that employs multiple Bessel beams to achieve fast and high-resolution wafer dicing (1000 mm/s; < 3 μm kerf). The Bessel beam array is generated by an LC-SLM which controls individual Bessel beam's characteristics, i.e., location and intensity distribution in the axial direction. The superior dicing results have confirmed the practicality of fast wafer dicing with Bessel beam arrays.

REFERENCES

[1] Ohmura E, Kumagai M, Nakano M, Kuno K, Fukumitsu K, Morita H. Analysis of Processing Mechanism in Stealth Dicing of Ultra-Thin Silicon Wafer. Journal of Advanced Mechanical Design, Systems, and Manufacturing. 2008, 2(4): 540-549.

[2] Fukuyo F, Fukumitsu K, Uchiyama N. Stealth Dicing Technology and Applications. In Proc. 6th Int. Symp. on Laser Precision Microfabrication, 2005.

[3] Kumagai M, Uchiyama N, Ohmura E, Sugiura R, Atsumi K, Fukumitsu K. Advanced Dicing Technology for Semiconductor Wafer Stealth Dicing. 2006. ISSM IEEE International Symposium on Semiconductor Manufacturing, pp. 215-218.

[4] Durnin J. Exact Solutions for Nondiffracting Beams. I. The scalar theory. JOSA A. 1987, 4(4): 651-654.

[5] Čižmár T and Dholakia K. Tunable Bessel Light Modes: Engineering the Axial Propagation. Optics Express. 2009, 17: 15558-70.

[6] Čižmár, T. et al. Generation of Multiple Bessel Beams for a Biophotonics Workstation. Optics Express. 2008, 16: 14024-35.

[7] Bowman R, Muller N, Zambrana-Puyalto X, Jedrkiewicz O, di Trapani P, and Padgett M. Efficient Generation of Bessel Beam Arrays by Means of an SLM," Eur. Phys. J. Special Topics. 2011, 199:159–166.

[8] Pasienski M, and Demarco B. A High-Accuracy Algorithm for Designing Arbitrary Holographic Atom Traps. Optics Express. 2008, 16:2176-90.

Poster Sessions

ANALYSIS OF WOUND IRRIGATION DEVICES

Amogh Pawar and Tony L. Schmitz
Department of Mechanical Engineering and Engineering Science
University of North Carolina at Charlotte, Charlotte, NC

INTRODUCTION

Wound irrigation is defined as the steady flow of a fluid across an open wound for removal of bacteria, necrotic tissue, and deeper debris [1]. In a wound irrigation process, the surface pressure obtained at the wound is critical. Correct pressure determination ensures that the pressure at the wound due to an irrigation device is enough for the removal of bacteria and foreign debris, but not so high that it causes further tissue damage.

Surface pressure measurements were performed for three irrigation devices, including a 500-ml bottle with four holes in the pouring cap, a 60 ml Monoject™ COVIDIEN™ syringe, and an IRIG-8™ Wound Irrigation System from CENTURION™. The irrigation trials were performed by a total of 20 participants consisting of doctors and nurses using the three devices (60 trials) at the Carolina Medical Center Emergency Department, Charlotte, NC. The current literature does not contain a standard pressure measurement method for wound irrigation. It is anticipated that this study will help to standardize irrigation pressure measurement within the medical community.

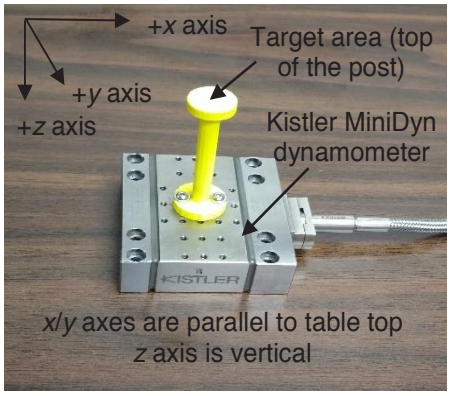

Figure 1. Target and dynamometer setup.

METHODOLOGY

A setup was designed to perform the measurements and subsequent data analysis. This setup included a 3D printed target (a post that represented the wound area), containers (to catch the fluid after impact), a force Kistler MiniDyn force dynamometer, and a digital single-lens reflex (DSLR) camera to photograph the stream image during fluid application. See Figs. 1 and 2.

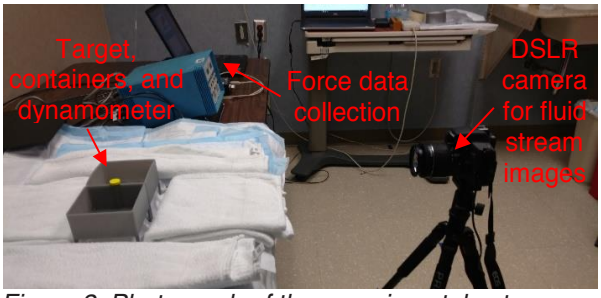

Figure 2. Photograph of the experimental setup.

Surface wound pressure was calculated from measurements of: 1) the fluid stream force at the point of impact; and 2) the cross-sectional area of the fluid at the same location. The impact force was measured by the dynamometer, while the impact area was determined from the camera images and subsequent image processing in MATLAB® R2017a.

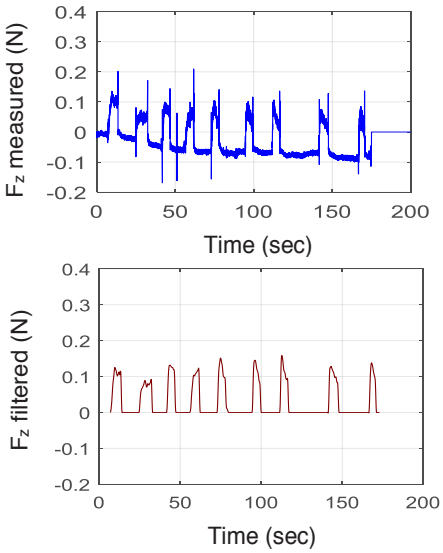

Figure 3. Time domain force data (F_z) for participant 13. (Top) measured, (bottom) filtered.

Time domain force data for all 60 trials was also analyzed in MATLAB. Measured *z* direction force data for a single trial using the 60 ml syringe is shown in Fig. 3 (top panel). Electrical noise was present in the measured data as well as drift and a DC offset. A 3rd

order low pass Butterworth filter with a cut off frequency of 1 Hz was used to attenuate high frequency noise. Drift compensation was completed by finding the slope of the line passing through the fluid impact start time and end time and then subtracting that line from the force data set. Noise filtering, slope removal, and DC offset removal was completed for the measured force in all three directions separately (F_x, F_y, and F_z). The components were then combined vectorially to obtain the resultant force (F). The same process was followed for all 60 trials.

The cross-sectional impact area of the fluid stream was estimated by locating the edges of the stream close to the point of impact from its digital image captured during fluid application. The distance between the edges provided the diameter of the impact area which, in turn, was converted into the cross-sectional area of the fluid. The Canny edge detection algorithm was applied in this study. An edge detection example using the 60 ml syringe is shown in Fig. 4.

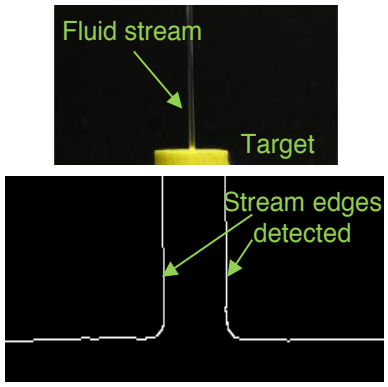

Figure 4. Edge detection for participant 13 using the 60 ml syringe. (Top) image, (bottom) result.

The time-dependent fluid stream pressure was calculated by dividing the time-dependent force by the total stream impact area. This was done for each participant using all three irrigation devices. Also, an uncertainty analysis was completed to evaluate the measured pressure uncertainty for each trial.

UNCERTAINTY ANALYSIS

Every measurement result has an associated uncertainty. It is essential to evaluate this uncertainty to fully describe the measurement result. By the law of propagation of uncertainty, the combined standard uncertainty of the dependent variable, or measurand (fluid stream pressure in this case), can be determined by combining the uncertainties in the independent variables (force due to fluid impact and total stream impact area). Equations 1-3 show the pressure equations for the three irrigation devices.

$$P_1 = \frac{F_1}{A_1} = \frac{F_1}{2\pi\left(\frac{Dp_{d1}}{2p_D}\right)^2} = \frac{2F_1 {p_D}^2}{\pi D^2 {p_{d1}}^2} \quad (1)$$

$$P_2 = \frac{F_2}{A_2} = \frac{F_2}{\pi\left(\frac{Dp_{d2}}{2p_D}\right)^2} = \frac{4F_2 {p_D}^2}{\pi D^2 {p_{d2}}^2} \quad (2)$$

$$P_3 = \frac{F_3}{A_3} = \frac{F_3}{5\pi\left(\frac{Dp_{d3}}{2p_D}\right)^2} = \frac{4F_3 {p_D}^2}{5\pi D^2 {p_{d3}}^2} \quad (3)$$

where,

$P_{1, 2, 3}$ = time-dependent fluid stream pressure

$A_{1, 2, 3}$ = total impact area of fluid streams

$F_{1, 2, 3}$ = time-dependent force

$p_{D1, 2, 3}$= average pixel count of the post top between edges

$p_{d1, 2, 3}$ = average pixel count of the impact stream

D = diameter of the post top/target area

As per GUM [2-3], the combined standard uncertainty of a measurand (which is influenced by input variable uncertainties) is described as the square root of the sum of the products of squares of the input uncertainties and the squares of the sensitivity coefficients (i.e., partial derivative of the measurand with respect to the selected input); see Eq. 4, where the correlation between input variables has been taken to be zero. Therefore, to find the combined standard uncertainty the sensitivity coefficients and the standard uncertainties needed to be determined.

$$u_c = \sqrt{\sum_i {c_i}^2 {u_i}^2} \quad (4)$$

where,

u_c = combined standard uncertainty

c_i = sensitivity coefficient

u_i = input standard uncertainty

The sensitivity coefficients were evaluated at the mean pressure for each measurement. The method for calculating the mean values of the input quantities (F, D, p_D, p_d) is described in the following paragraphs.

For *F*, the following steps were used. First, the time interval for the applied pressure was determined. For the pressurized device there is single interval per trial. For the bottle and syringe, however, there were multiple intervals. In all cases, the interval was identified by two points based on the start and end points (Fig. 5 shows an example for the bottle with four holes). The force data for the interval was truncated to contain only force data between these start and end points. The mean force value of the trial was then calculated by taking the mean value of the truncated force data. Equation 5 shows the mean force calculation.

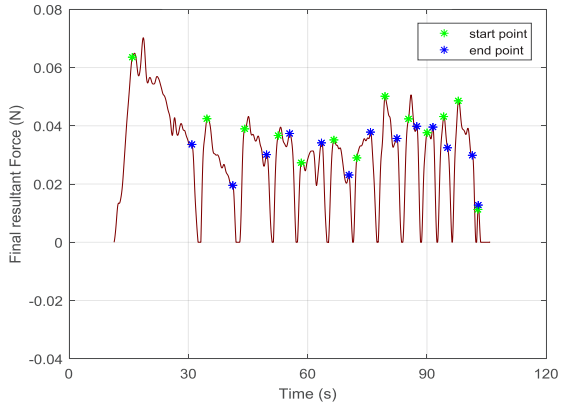

Figure 5. Force for bottle with four holes in pouring cap.

$$F_{m1,2,3} = \bar{x}\left(\bar{x}(F_{t1}), \bar{x}(F_{t2}) .... \bar{x}(F_{tn})\right) \quad (5)$$

where,

$F_{m1,2,3}$ = mean force value from all intervals

$F_{t1}, F_{t2} .... F_{tn}$ = truncated force data from n intervals

The diameter of the post top (*D*) was measured using a digital Vernier caliper (Mitutoyo CD-6 ASX). This was taken as the mean value. From the post diameter image, the number of pixels between the edges of the post top diameter, p_D, was taken as the mean value.

The mean value of p_d was found by counting the number of pixels between the edges of the fluid stream or by calculating the average number of pixels in the case of multiple fluid streams.

Sensitivity coefficients (c_i) were determined by taking the partial derivatives of the measurand (*P* in this case) with respect to the input quantities (*F, D,* p_D, p_d). For the bottle with four holes in the pouring cap, the sensitivity coefficients were calculated using Eqs. 6-9.

$$\frac{\partial P_1}{\partial F_1} = \frac{2 p_D{}^2}{\pi D^2 p_{d1}{}^2} \quad (6)$$

$$\frac{\partial P_1}{\partial D} = -\frac{4 F_1 p_D{}^2}{\pi D^3 p_{d1}{}^2} \quad (7)$$

$$\frac{\partial P_1}{\partial p_D} = -\frac{4 F_1 p_D}{\pi D^2 p_{d1}{}^2} \quad (8)$$

$$\frac{\partial P_1}{\partial p_{d1}} = -\frac{4 F_1 p_D{}^2}{\pi D^2 p_{d1}{}^3} \quad (9)$$

Similarly, the sensitivity coefficients were calculated for the syringe device and the pressurized irrigation device by taking the partial derivatives of *P* with respect to the corresponding input quantities (*F, D,* p_D, p_d).

The standard uncertainties (u_i) were set equal to the standard deviations of the corresponding inputs: *F*, *D*, p_D, and p_d. The uncertainty in *F* was calculated form the noise floor of the force data. The force data was truncated between the start of the sampling time and the start of the force interval. The standard deviation of these values was calculated and taken to be the uncertainty in *F*.

The uncertainty in *D* was obtained from the specifications for the digital Vernier caliper (Mitutoyo CD-6 ASX) since it was used for the measurement of the diameter of the post top (target area). The value represented as “accuracy” was taken to be the standard uncertainty in *D*.

The uncertainty in p_D was determined by first calculating the pixel count of 10 rows of values between post top edges at the impact point of the stream. The standard deviation of this range in pixel count values was taken as the standard uncertainty.

The uncertainty in p_d was determined by first calculating the pixel count of a range of values as close as possible to the impact point of the stream. The standard deviation of this range of pixel count values was taken as the standard uncertainty.

Substituting the sensitivity coefficient expressions and the standard uncertainties, the combined standard uncertainty can be written as shown in Eq. 10. The expanded uncertainty (*U*) was obtained by multiplying the combined standard uncertainty (u_c) by a coverage factor (*k*). A coverage factor of 2 was selected here; see Eq. 11. Using Eq. 11, the expanded uncertainty values for the 20 participants using the three irrigation devices was calculated.

$$u_c(P) = \sqrt{\left(\frac{\partial P}{\partial F}\right)^2 u^2(F) + \left(\frac{\partial P}{\partial D}\right)^2 u^2(D) + \left(\frac{\partial P}{\partial p_D}\right)^2 u^2(p_D) + \left(\frac{\partial P}{\partial p_d}\right)^2 u^2(p_d)} \quad (10)$$

where,

$\frac{\partial P}{\partial F}, \frac{\partial P}{\partial D}, \frac{\partial P}{\partial p_D}, \frac{\partial P}{\partial p_d}$ = sensitivity coefficient associated with F, D, p_D, p_d

$u(F, D, p_D, p_d)$ = standard uncertainty in F, D, p_D, p_d

$$U(P) = k u_c(P) \quad (11)$$

where,

$U(P)$ = Expanded uncertainty of mean fluid pressure

k = coverage factor

$u_c(P)$ = combined standard uncertainty of mean fluid pressure

RESULTS

Figure 6 shows the mean pressure obtained for all 20 participants using the three irrigation devices. The error bars represent the expanded uncertainty ($k = 2$) associated with each measurement. It is observed that the mean pressure obtained from all participants is the highest for the 60 ml syringe. The bottle with four holes in the pouring cap had the lowest mean pressure. However, the pressure uncertainty for the syringe was also the highest.

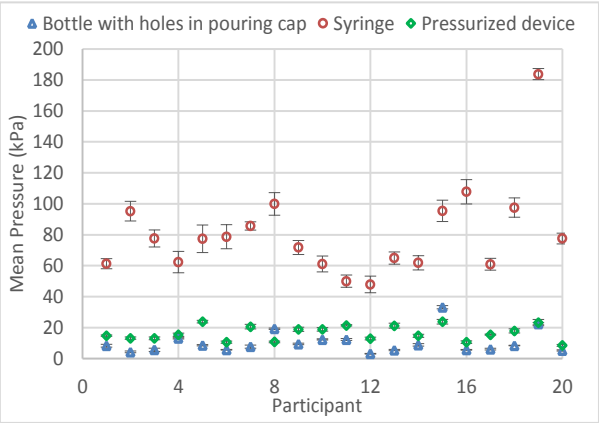

Figure 6. Mean pressure for all participants with expanded uncertainty (k = 2) error bars.

Figure 7 displays the mean of all the mean pressures obtained using each irrigation device. It was calculated by taking the mean of the mean pressure for each participant using the selected irrigation device. The error bars represent the mean of the expanded uncertainties.

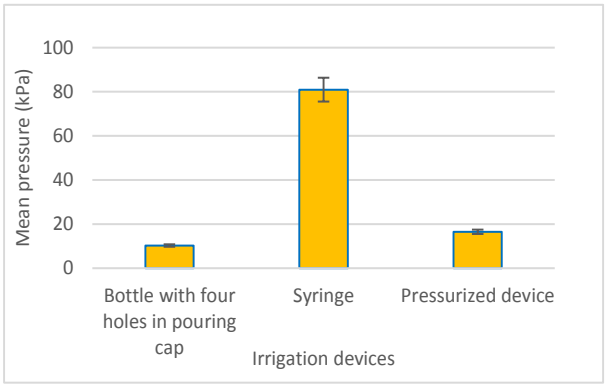

Figure 7. Mean pressure of all participants with mean expanded uncertainty for the three irrigation devices.

From Figure 7, the mean pressure of all the participants using an irrigation device were:

- bottle with four holes in the pouring cap: 10.28 kPa
- syringe: 80.95 kPa
- pressurized device: 15.50 kPa.

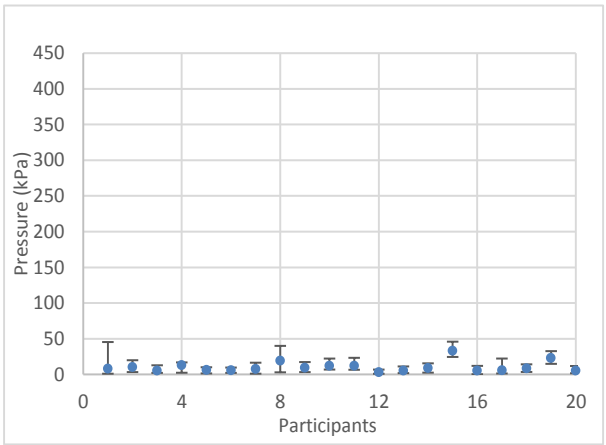

Figure 8. Mean, maximum, and minimum pressures for all participants using the bottle with four holes in the pouring cap.

Figures 8-10 show the mean, maximum, and minimum pressures obtained by the participants using the three irrigation devices. The upper and lower endpoints of the error bars represent the maximum and minimum calculated pressure for the selected participant over all intervals in the trial. For the bottle and syringe, there were multiple intervals, so these maximum and minimum values were selected from all intervals in a single trial. For the pressurized device these values were obtained from the single interval in the trial.

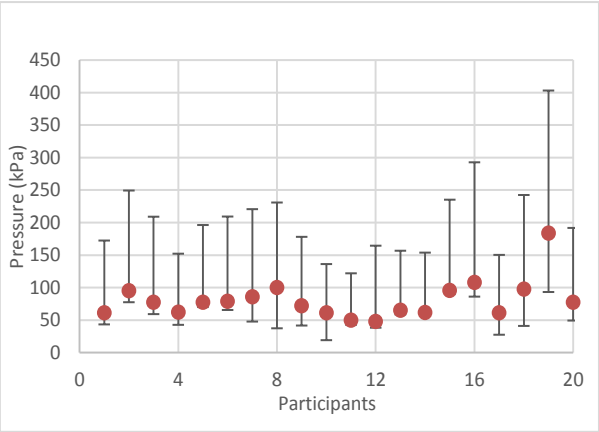

Figure 9. Mean, maximum, and minimum pressures for all participants using the 60 ml syringe.

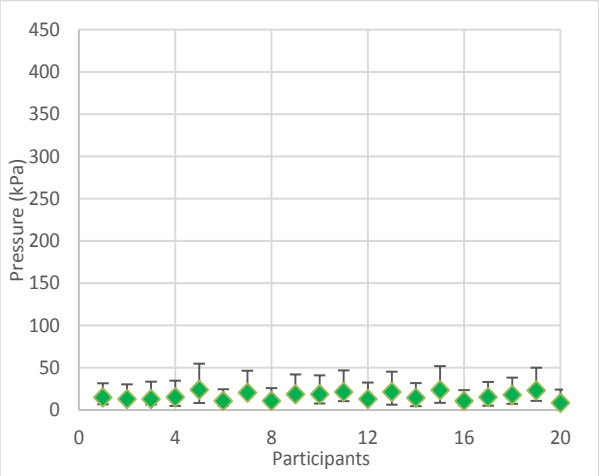

Figure 10. Mean, maximum, and minimum pressures for all participants using the pressurized device.

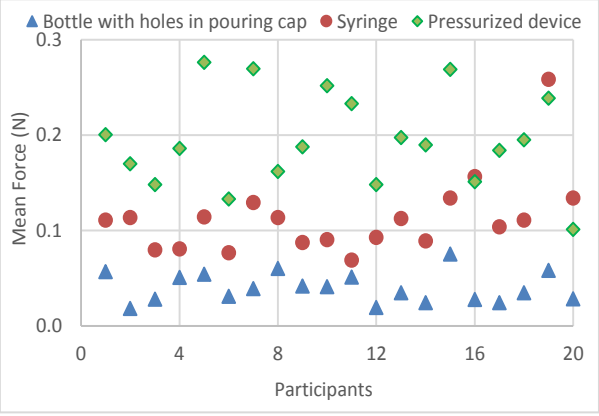

Figure 11. Mean force for all trials using the three irrigation devices.

Figure 11 displays the mean force obtained for all 20 participants using the three irrigation devices. For this result, the total stream area was not considered. Rather, the total impact force was considered only.

Figure 12 displays the duration of each trial for all 20 participants using the three irrigation devices. The trial started when the fluid impacted the target area and ended when the full 500 ml of irrigation fluid was dispensed. The mean duration of a single trial was the highest for the 60 ml syringe. The pressurized irrigation device required the least time and was most consistent.

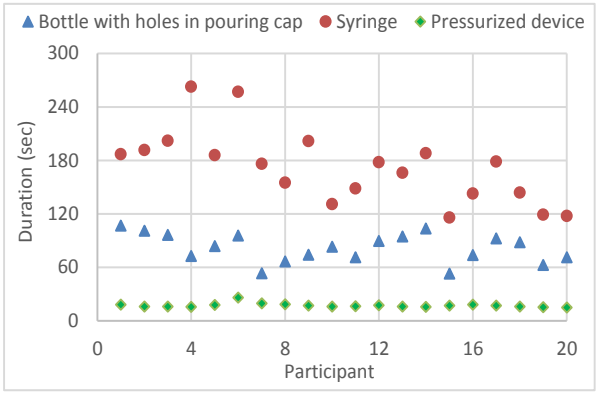

Figure 12. Duration of each trial for all participants using the three irrigation devices.

The mean durations of the trials (i.e., the time taken for a participant to dispense 500 ml using an irrigation device) were:

- bottle with four holes in the pouring cap: 81 s
- syringe: 172 s
- pressurized device: 17 s.

CONCLUSIONS

The purpose of this study was to serve the medical community by studying the pressure imposed on wounds by three common irrigation devices, reporting the experimental techniques, and evaluating the measurement uncertainty. To collect data for the study, 20 doctors and nurses conducted wound irrigation trials using: 1) a bottle with four holes in the pouring cap; 2) a syringe; and 3) a pressurized irrigation device. The motivation for the study was based on a literature review. The current literature does not contain a standard pressure measurement method for wound irrigation. Further, there is no consensus on what pressure is required for proper irrigation. It is anticipated that this study will help to standardize irrigation pressure measurement within the community.

The study results are summarized here. From Fig. 6 it can be observed that the mean pressure obtained from all participants was highest for the 60 ml syringe. The bottle with four holes in the pouring cap had the lowest mean pressure. However, the pressure uncertainty for the syringe was also the highest. Further, the standard deviation of mean pressures

from all participants (as shown in Fig. 7) was the highest for the syringe. The pressurized irrigation device had the lowest standard deviation of mean pressures from all participants.

Observing Fig. 12, the mean duration of a single trial (500 ml dispensation of fluid) was the highest for the 60 ml syringe. The pressurized irrigation device required the lowest time. It was also observed that the standard deviation of trial durations is maximum for the 60 ml syringe and minimum for the pressurized irrigation device.

REFERENCES

[1] Ennis, W.J., Valdes, W., Salzman, S., Fishman, D., and Meneses, P. (2004) Trauma and wound care (Chapter 17). In: Morison, M.J., Ovington, L.G., and Wilkie, K., Eds. Chronic Wound Care. A Problem-Based Learning Approach. London: Mosby Elsevier Limited, pp. 291-307.

[2] Evaluation of Measurement Data – Guide to the Expression of Uncertainty in Measurement JCGM 100:2008 (GUM 1995 with minor corrections).

[3] Taylor, B.N. and Kuyatt, C.E. (1994) Guidelines for Evaluating and Expressing the Uncertainty of NIST Measurement Results. NIST Technical Note 1297.

The effect of laser-assisted diamond turning (Micro-LAM) on the underlying surface structure of selected IR crystals

Hossein Shahinian[1], Jayesh Navare[1], Dmytro Zaytsev[1], Sai Kode[1], Deepak Ravindra[1]
[1]Micro-LAM Inc
5960 S Sprinkle Rd
Portage, Michigan, USA

INTRODUCTION

In this paper we present the influence of, laser assisted diamond turning, i.e., μ-LAM process on the subsurface residual stresses of infrared (IR) crystals. The μ-LAM process uses the emission of laser light during single point diamond turning (SPDT) of optical components [1]. Conventional diamond machining centers can produce surfaces with low roughness values (<5 nm RMS), and form accuracy of 100 nm – 200 nm peak to valley (PV) [2, 3]. They key principle behind the fabrication of parts with such tight tolerances, is the use of ultra-precise and rigid machines that use single crystal diamond as their cutting tools. The μ-LAM process, leverages the laser light propagated through the single crystal diamond tool and on the cutting edge of the tool. The laser effectively induces heat "softening" to the material being cut, thus facilitating the cutting process [4, 5].

The SPDT has been an enabling technology in production for freeform and aspherical optics [6, 7]. Freeform optics have received a wide traction for several optical applications, such as imaging optics [8, 9], illumination optics [10], etc. The optics generated by SPDT would require additional post finishing step, for having acceptable performance in the visible light regime [11-14]. However, those restriction are much looser when dealing with IR optics. Thus, the SPDT process is of great value for such optics.

Many articles, published previously by the Micro-LAM team, have demonstrated the positive effect of the laser on the cutting process in improving the surface finish of the parts produced as such. To better understand the key reasons behind the enhanced performance of a diamond tool using the μ-LAM system, an investigation on the underlaying surface residual stresses of the cut materials with and without the μ-LAM system, is proposed.

Studying the residual stresses of metallic and non-metallic components have been undertaken by different methods in the past [15, 16]. One of the most common approaches in doing so is the use of the X-ray diffractometer (XRD). The application of XRD in measuring residual stresses has been shown in several articles [17-20]. In this article the focus is not on the calculation of the residual stresses of the parts per se, but the goal is to compare the extent to which the residual stresses on the optics fabricated with and without the μ-LAM process differ.

The comparison is done for two different IR crystals that have wide applications within the optics community. The first sample is made of single crystal silicon (Si), and the second is a polycrystalline zinc sulfide (ZnS). Both materials can be cut in a ductile manner with single crystalline diamond tools [21].

EXPERIMENTAL METHOD

To compare the residual stresses induced during fabrication of ZnS and Si, planar samples were used. The testing includes diamond turning of the surface of the samples with and without the μ-LAM system. The experiments are conducted under identical spindle RPM and feedrates for the respective materials. The cuts are performed on a 2-axis ultraprecision lathe, a Precitech Nanoform 250. The machined samples are then measured on an XRD instrument post the cutting.

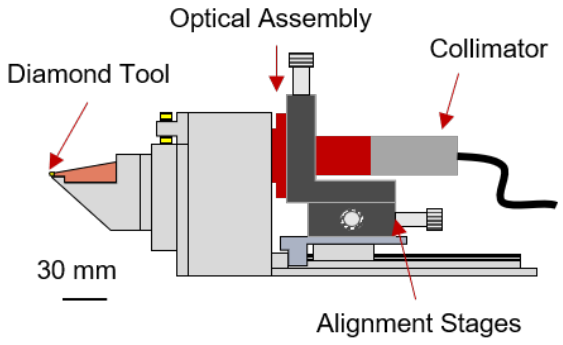

FIGURE 1. The Optimus$_{T+1}$ tool post

Optimus$_{T+1}$ tool post

The tool post is a proprietary product of the Micro-LAM team, whereby the laser is delivered to the cutting zone. **Error! Reference source not found.** depicts a sketch of the Optimus$_{T+1}$. The laser used has a wavelength of 1064 nm, and the beam is focused near the cutting edge of the diamond tool. The diamond material has a transmission of 70% for the 1064 nm wavelength. This implies that most of the laser power is transmitted through the tool towards the cutting edge. The laser light is then guided such that the beam exits the diamond at the cutting edge of the tool. The transmitted laser through the tool "softens" the workpiece material as a result of the heat produced from the absorption of the laser radiation in a very localized fashion. This softening of the material facilitates the cutting process, thereby reducing the amount of tool wear induced during diamond turning. The schematics of the μ-LAM process in action is depicted in FIGURE 2.

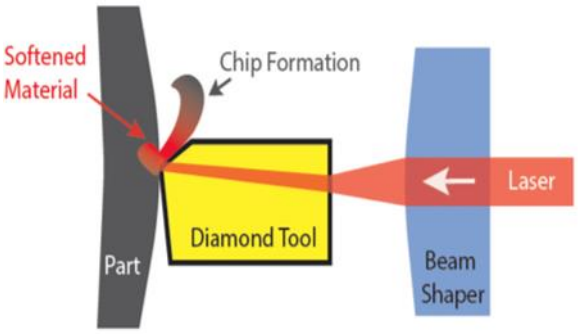

FIGURE 2. The transmission of the laser through the diamond too and the material "softening"

Test samples

The planar Si and ZnS, samples were diamond turned prior to the testing to ensure both samples had similar surface texture before the experiments. Table 1 outlines the dimensions of the used samples.

Table 1. Test sample information

Material	Dimension	Initial surface
Si	∅28 mm × 5 mm	Diamond turned
ZnS	∅25 mm × 5 mm	Diamond turned

Diamond cutting tools

The cutting tools used were made of single crystal synthetic diamonds. The tools were designed in such way that a path for the transmission of the laser was available. The tools were fabricated by K&Y Diamond®. The negative rake angle of the tool was necessary. As investigated by many researchers the negative rake angle provides a better opportunity for the ductile cutting of brittle materials [22].

Table 2. Diamond tool information

Tool	Rake angle (°)	Nose radius (mm)	Cutting height (mm)
1	-35	0.3	1.05
2	-35	0.3	1.17
3	-35	0.5	1.11
4	-35	0.5	1.09

Diamond turning conditions

The testing conditions for the samples were opted based on the information available in the literature [23]. The diamond cutting conditions for Si and ZnS can be found in tables 3, 4 respectively.

Table 3. Cutting conditions for Si samples

Cut	RPM	Feed (μm/rev)	DOC (μm)
a	2000	3	6
b	2000	2	6
c	2000	1.5	6

Table 4. Cutting conditions for ZnS

Cut	RPM	Feed (μm/rev)	DOC (μm)
α	4000	0.75	6
β	4000	0.5	4
δ	4000	0.375	2

Four tests on the samples were conducted. Each sample underwent the cutting sequences outlined in table 3 and table 4 for their respective materials. Table 5 lists the four conducted experiments.

Table 5. Cutting tests with and without the μ-LAM system

Test	Cuts	Tool	Laser power (W)
Si-1	a, b, c	1	0
Si-2	a, b, c	2	2.7
ZnS-1	α, β, δ	3	0
ZnS-2	α, β, δ	4	2.7

The emission of the laser through the diamond is measured with an Ophir Optronics® F150A-BB-26-PPS power meter. FIGURE 3(a) shows the scattered footprint of the laser on a digital camera. FIGURE 3(b) shows the transmitted laser power measured with the power meter.

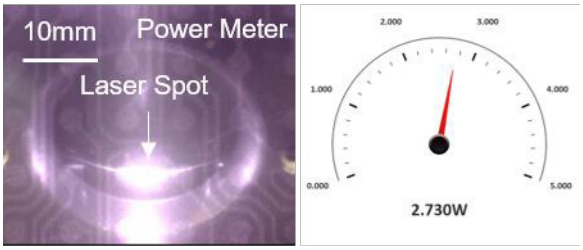

(a) (b)

FIGURE 3. (a) scattered laser footprint 8 mm away from the tool tip (b) measured laser power at that location

Metrology

Each workpiece was examined in two ways. The surfaces of the samples were measured under a scanning white light interferometer (SWLI), Taylor Hobson® Talysurf CCI. The instrument specifics as well as the processing operations applied to the raw data can be found in Table 6.

Table 6. SWLI instrument information

Hardware	Processing
Taylor Hobson Talysurf (CCI)	Best fit 4th order Chebyshev removed
20× Mirau objective 1024 × 1024 detector	Metric: RMS of the data i.e. Sq

The XRD measurements of the parts were acquired on a third generation Empyrean® diffractometer. The measurement was done using the gonio axis, and the instrument information can be found in Table 7.

Table 7. XRD measurement information

Diffractometer parameter	value
$K_{\alpha 1}$ wavelength	1.540598 Å
$K_{\alpha 2}$ wavelength	1.544426 Å
Generator voltage	45 V
Tube current	40 A
Gonio scan step size	0.002°

RESULTS

The cutting tests of Si-1, Si-2, ZnS-1, and ZnS-2, (see Table 5 for the tests), were done on four different samples. The spindle was balanced in each test to less than 1 nm PV deviations in the spindle position. In each test the surface of the samples were measured using the SWLI and XRD instruments.

Interferometric measurements

FIGURE 4(a), (b) depict the SWLI interferogram of the Si parts cut with and without the μ-LAM system. The RMS roughness (Sq) values were measured to be nearly the same. However, it should be noted that the surface cut with conventional diamond turning, showed minute traces of brittle fracture near the center of the part. These brittle fracture zones are very common in cutting single crystal materials [21].
The measurement interferograms for the ZnS samples are depicted in FIGURE 5 (a), (b). Evident in the figure both surfaces show signs of pits and damage zones. Nevertheless, these damaged zones appear to be of higher severity on the sample produced with conventional diamond turning. This is confirmed by the higher surface roughness RMS value of the ZnS sample machined with conventional diamond turning.

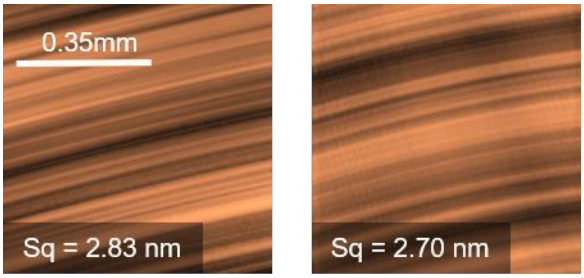

(a) (b)

FIGURE 4. interferometric imaging of Si samples (a) conventional (b) μ-LAM

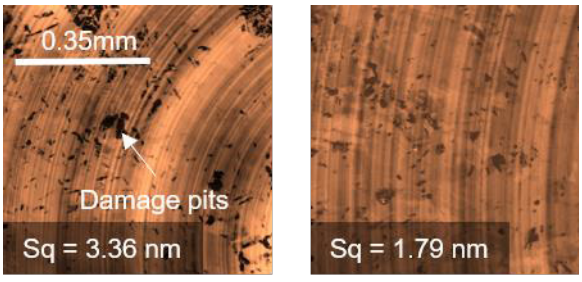

(a) (b)

FIGURE 5. Interferometric imaging of ZnS samples (a) conventional (b) μ-LAM

XRD measurements

To evaluate the relative residual stresses for the machined samples, XRD measurements were taken. To quantify the relative residual stresses, the full width at half maximum (FWHM), of the

diffraction peaks were calculated from the FWHM of the best fit Gaussian curves to the diffraction peaks. A narrower peak implies the presence of less residual stresses underneath the surface of the part. FIGURE 6 depicts the XRD measured data for the Si samples. The figure suggests a very distinct difference between the peaks of the samples at 68°. The FWHM for the Si-1 and Si-2 samples are 7.46°, and 0.05° respectively. These numbers suggest that the Si sample machined using the μ-LAM process has nearly 150 times smaller residual stresses than that processed with conventional diamond turning. The splitting of the peaks on the measurement for the surface made with the μ-LAM process is attributed to the slight difference of the $K_{\alpha 1}$ and $K_{\alpha 2}$ wavelengths of the diffractometer.

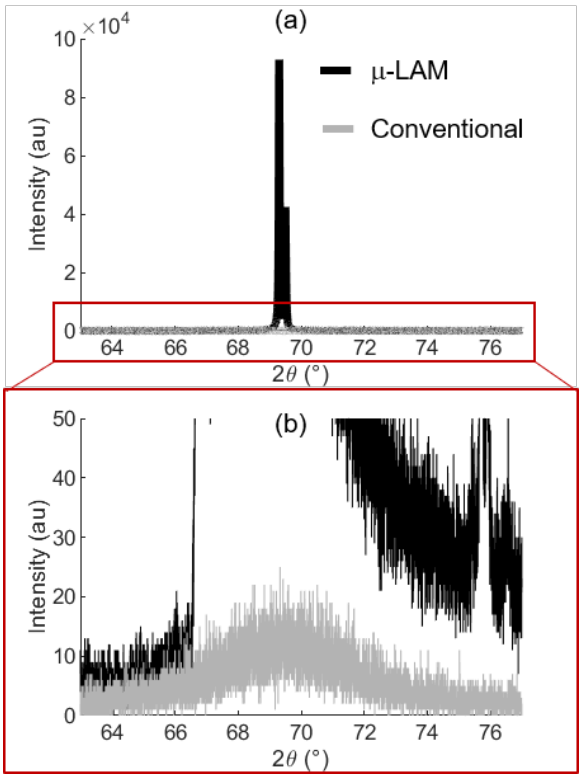

FIGURE 6. XRD peaks of single crystal Si diamond turned with and without μ-LAM; (a) Clear peak for the surface made with μ-LAM (b) zoomed on the peak of the Si made with conventional diamond turning

The same XRD measurements were done on the ZnS samples. Since the ZnS samples were made of a polycrystalline material, more than one diffraction peaks were scrutinized. FIGURE 7 shows the peaks that were studied. FIGURE 8 shows the FWHM of the peaks of ZnS-1 and ZnS-2 sample.

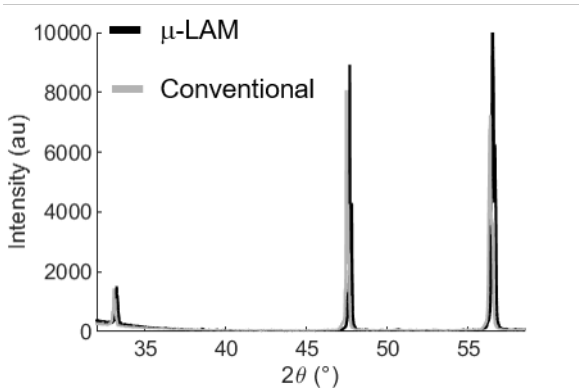

FIGURE 7. XRD measurements of the ZnS samples cut with and without the μ-LAM process

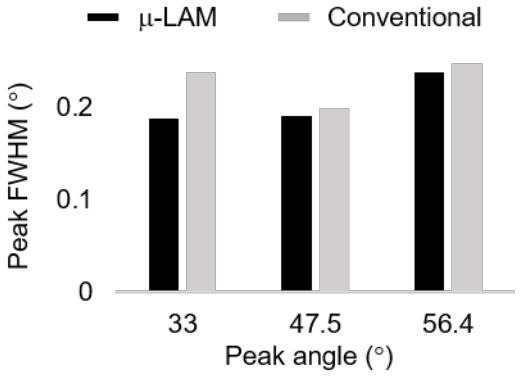

FIGURE 8. FWHM of diffraction peaks measured on ZnS samples

The FWHM of the peaks in FIGURE 8 suggests that the residual stresses are marginally lower for the sample machined with the μ-LAM process. That said, this data is inconclusive as the differences are within the uncertainty of the measurement of the XRD machine.

DISCUSSION

The results presented in the previous section are proof that the μ-LAM process does not deteriorate the mechanical integrity of the IR crystals with the addition of the laser to the diamond turning process. In case of Si, the laser has indeed greatly reduced the residual stresses of the part. From the lower residual stresses measured on the Si sample turned with the μ-LAM, it can be inferred that the surface and subsurface integrity of the Si can be greatly

improved using the μ-LAM process. A damage free surface and subsurface would intuitively require a cutting that happens in a more ductile fashion. Smaller residual stresses and therefore damage free sub surface, provides the opportunity to use those optics for high power IR lasers. A surface with high residual stresses is susceptible to fatigue fracture due to the extreme thermal gradients introduced by the lasers used.

The XRD measurement on the ZnS sample, doesn't show the significant reduction of the residual stresses within the ZnS material using the μ-LAM process. This could be attributed mainly to the much lower absorption rates of ZnS, compared to Si, in the 1064 nm wavelength regime. The absorption percentage of the laser power for the 1064 nm wavelength are 60% and 4%, for Si and ZnS respectively.

In addition, although the XRD data of the ZnS samples doesn't show a significant reduction in the residual stresses of the material, the SWLI interferograms clearly show a reduction in the pits and digs induced on the surface of the parts. This decrease in the surface defects, is speculated to be mainly due to a more ductile cutting of the ZnS using the μ-LAM process.

CONCLUSION AND FUTURE WORK

In summary of this paper, it was shown that the μ-LAM process enhances the ability of conventional diamond turning of IR crystals by producing mechanically more robust and damage free surfaces. While not reported here, our experimental evidence shows that the process can increase the diamond tool life at least twice as much as what is achievable in conventional diamond turning of Si.

As part of the future research efforts in the Micro-LAM team, this study approach will be pursued on additional IR crystals, as well as other hard and brittle materials to further understand and investigate the physics of the μ-LAM process.

ACKNOWLEDGEMENTS

We would like to acknowledge Dr. Pnina Ari-Gur for the XRD measurements of the samples. We would also like to thank Ms. Alyson Markos for her help in preparing the figures of the paper.

REFERENCES

1. Ravindra, D., *Ductile mode material removal of ceramics and semiconductors.* 2011.
2. Rhorer, R.L. and C.J. Evans, *Fabrication of optics by diamond turning.* Handbook of optics, 1995. **1**: p. 41.1-41.3.
3. To, S.S., V.H. Wang, and W.B. Lee, *Single Point Diamond Turning Technology*, in *Materials Characterisation and Mechanism of Micro-Cutting in Ultra-Precision Diamond Turning*. 2018, Springer. p. 3-6.
4. Ravindra, D., M.K. Ghantasala, and J. Patten, *Ductile mode material removal and high-pressure phase transformation in silicon during micro-laser assisted machining.* Precision engineering, 2012. **36**(2): p. 364-367.
5. Ravindra, D. and J. Patten, *Ductile regime single point diamond turning of quartz resulting in an improved and damage-free surface.* Machining Science and Technology, 2011. **15**(4): p. 357-375.
6. Zhang, X., Z. Li, and G. Zhang, *High performance ultra-precision turning of large-aspect-ratio rectangular freeform optics.* CIRP Annals, 2018.
7. Cheng, Y.-C., W.-J. Peng, H.-Y. Chou, and F.-Z. Chen. *Fabrication and measurement of freeform mirror for head-up display system*. in *Optical Fabrication, Testing, and Metrology VI*. 2018. International Society for Optics and Photonics.
8. Shahinian, H., T. Noste, N. Sizemore, C. Hovis, P. Shanmugam, N. Horvath, and D. Gurganos. *See-through smart glass with adjustable focus*. in *Digital Optics for Immersive Displays*. 2018. International Society for Optics and Photonics.
9. Huang, H. and H. Hua, *High-performance integral-imaging-based light field augmented reality display using freeform optics.* Optics Express, 2018. **26**(13): p. 17578-17590.
10. Wu, R., Z. Feng, Z. Zheng, R. Liang, P. Benítez, J.C. Miñano, and F. Duerr, *Design of Freeform Illumination Optics.* Laser & Photonics Reviews, 2018: p. 1700310.
11. Hull, T., M.J. Riso, J.M. Barentine, and A. Magruder. *Mid-spatial frequency matters: examples of the control of the power spectral density and what that means to the performance of imaging systems*. in *Infrared Technology and Applications XXXVIII*. 2012.

International Society for Optics and Photonics.
12. Chen, G., Y. Sun, F. Zhang, C. An, W. Chen, and H. Su, *Influence of ultra-precision flycutting spindle error on surface frequency domain error formation.* The International Journal of Advanced Manufacturing Technology, 2017. **88**(9-12): p. 3233-3241.
13. Shahinian, H., *Fiber Based Tools for Polishing Optical Materials*. 2018, The University of North Carolina at Charlotte.
14. Shahinian, H., M. Hassan, H. Cherukuri, and B.A. Mullany, *Fiber-based tools: material removal and mid-spatial frequency error reduction.* Applied optics, 2017. **56**(29): p. 8266-8274.
15. Almen, J.O. and P.H. Black, *Residual stresses and fatigue in metals*. 1963: McGraw-Hill.
16. Lu, J., *Handbook of measurement of residual stresses*. 1996: Fairmont Press.
17. Fitzpatrick, M., A. Fry, P. Holdway, F. Kandil, J. Shackleton, and L. Suominen, *Determination of residual stresses by X-ray diffraction.* 2005.
18. Klug, H.P. and L.E. Alexander, *X-ray diffraction procedures: for polycrystalline and amorphous materials.* X-Ray Diffraction Procedures: For Polycrystalline and Amorphous Materials, 2nd Edition, by Harold P. Klug, Leroy E. Alexander, pp. 992. ISBN 0-471-49369-4. Wiley-VCH, May 1974., 1974: p. 992.
19. Prevey, P.S., *X-ray diffraction residual stress techniques.* ASM International, ASM Handbook., 1986. **10**: p. 380-392.
20. Dufrenoy, S., T. Chauveau, I. Lemaire-Caron, R. Brenner, and B. Bacroix, *Comparison of 2 methodologies developed for the determination of residual stresses through X-ray diffraction: application to a textured hcp titanium alloy.* International Journal of Material Forming, 2018. **11**(3): p. 341-355.
21. Liu, H., W. Xie, Y. Sun, X. Zhu, and M. Wang, *Investigations on brittle-ductile cutting transition and crack formation in diamond cutting of mono-crystalline silicon.* The International Journal of Advanced Manufacturing Technology, 2018. **95**(1-4): p. 317-326.
22. Mir, A., X. Luo, K. Cheng, and A. Cox, *Investigation of influence of tool rake angle in single point diamond turning of silicon.* The International Journal of Advanced Manufacturing Technology, 2018. **94**(5-8): p. 2343-2355.
23. Abdulkadir, L.N., K. Abou-El-Hossein, A.I. Jumare, P.B. Odedeyi, M.M. Liman, and T.A. Olaniyan, *Ultra-precision diamond turning of optical silicon—a review.* The International Journal of Advanced Manufacturing Technology, 2018: p. 1-36.

A NOVEL POSITIONING MEASUREMENT METHOD USING POLAR MICROSTRUCTURE

Chenyang Zhao[1], Chi Fai Cheung[1]
[1]Partner State Key Laboratory of Ultra-precision Machining Technology
Department of Industrial and Systems Engineering
The Hong Kong Polytechnic University
Hong Kong, China

INSTRUCTIONS

Although there are many fundamental optical sensor technologies applied in precision measurement [1,2], air refractive index error and wavelengths errors are their main uncertainty sources. A stringent environment such us vacuum is needed to control the above uncertainty sources. This paper presents a novel method which attempts to integrate ultra-precision machining and computer vision technologies is found to be feasible and promising for the precision measurement because of its simple device, space-saving, low-cost, high-robust features.

In this paper, a unique texture surface named polar microstructure was proposed in this paper. Polar microstructure aims to serve a unique global map for the subsequent matching measurement, the template matching algorithm was used for image processing and determine the absolute position of the selected image in the global map. The relevant experiment was conducted to test the uniaxial uncertainty of the proposed method.

POLAR MICROSTRUCTURE

As shown in Figure 1, the polar microstructure is designed based on the concept of polar coordinate system. The surface feature of the polar microstructure is composed of concentric circles and straight lines whose spacing is equal to 50 micrometers, respectively. It is fabricated by a process chain of ultra-precision machining technology combining single point diamond turning (SPDT) and single point diamond broaching (SPDB). It can be fabricated by using Nanoform 350G ultra-precision machining system from Nanotechnology Inc., USA [3].

It is found that the polar microstructure possesses high discrimination rate even the form accuracy of polar microstructures is in micrometer range. Due to the unique characteristics of polar microstructure not only for the geometric patterns but also the sorting of intensity values of pixels, its grey-scale intensity distribution is unique which guarantees the reliability and the robustness.

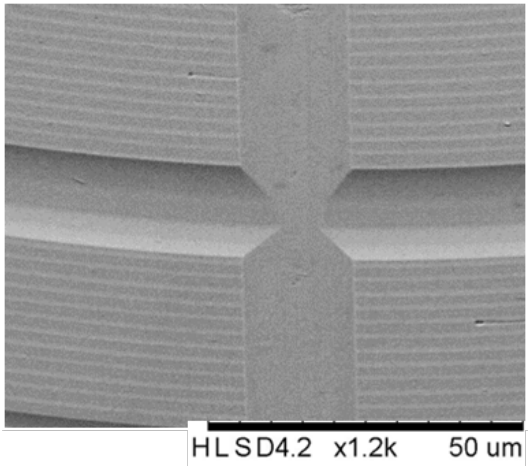

FIGURE 1. Polar microstructure surface

This paper makes use of template matching method as the method for the precision positioning t through image registration of template image and reference image [4]. The Normalized Cross-Correlation (NCC) method has been proven to be one of the most effective and robust methods that supports the measurement of the resemblance between template image and its coincident region at the reference. The NCC value is given by Eq. (1):

$$NCC_{(u,v)} = \frac{\sum_{i=1}^{m}\sum_{j=1}^{n}[R(u+i,v+j)-\bar{R}(u,v)]\cdot[T(i,j)-\bar{T}]}{\left[\sum_{i=1}^{m}\sum_{j=1}^{n}(R(u+i,v+j)-\bar{R}(u,v))^2\right]^{\frac{1}{2}}\cdot\left[\sum_{i=1}^{m}\sum_{j=1}^{n}(T(i,j)-\bar{T})^2\right]^{\frac{1}{2}}} \quad (1)$$

Where $\bar{R}(u,v)$ is the grey-scale average intensity of reference image $R(u,v)$, whereas $\bar{T}$ is the grey-scale average intensity of the template image T. These values are defined as Eq. (2) and Eq. (3):

$$\bar{R}(u,v) = \frac{1}{m \cdot n} \sum_{i=1}^{m} \sum_{j=1}^{n} R(u+i, v+j) \quad (2)$$

$$\bar{T} = \frac{1}{m \cdot n} \sum_{i=1}^{m} \sum_{j=1}^{n} T(i, j) \quad (3)$$

The NCC values delivers between the interval [-1, 1], it means that if NCC = 1, the similarity is the best possible whereas if NCC = -1, the template and the corresponding image are completely different. As a result, the point (u,v) which presents the best possible resemblance between R and T is derived as Eq. (4) and Eq. (5):

$$(u,v) = \arg \max_{(\hat{u},\hat{v}) \in A} NCC(\hat{u},\hat{v}) \quad (4)$$

Where,

$$A = \{(u,v) \mid 1 \le \hat{u} \le M - m, 1 \le \hat{v} \le N - n\} \quad (5)$$

To evaluate the machining quality of polar microstructure, a comparison between the simulation result and the machining results are shown in Figure 2 and Figure 3.

The iterative closest point (ICP) method is used to register the two simulations and the measurement results so as to locate the same area. Figure 4 shows the contrasting profiles of the simulation and measurement results. The results show that the UPM is feasible to obtain a high-precision and reliable polar microstructure surface.

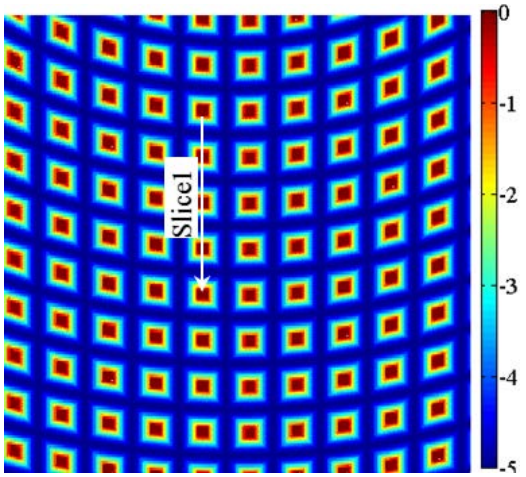

FIGURE 2. Simulated result of surface profile of Polar Microstructure

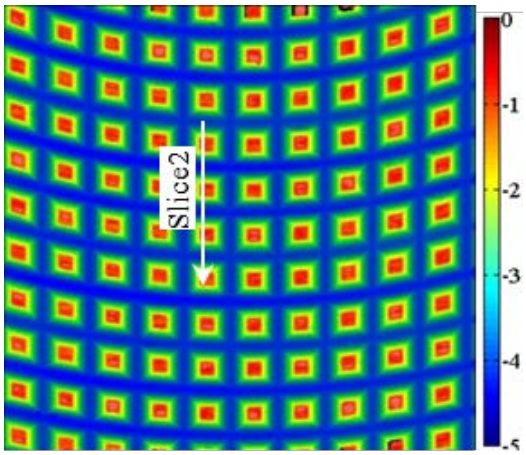

FIGURE 3. Measured result of surface profile of Polar Microstructure

.

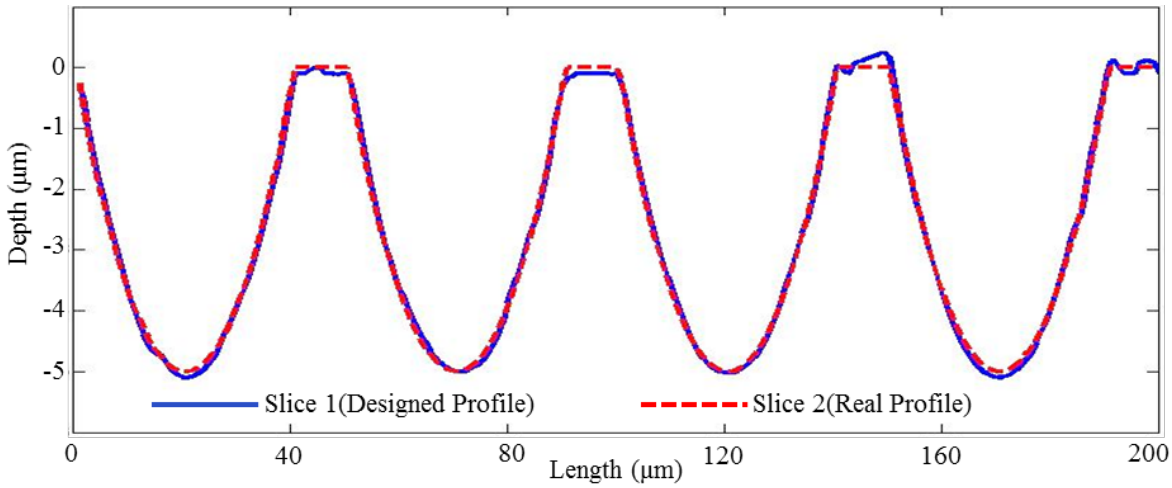

FIGURE 4. Contrasting profiles

EXPERIMENTS AND RESULTS

In this experiment, a nanometer level piezoelectronic drive stage is used to test the uniaxial uncertainty of the proposed method. The experimental setup is shown in Fig. 5 while the polar microstructure and its fixture are mounted on the drive stage. A microscope is used to observe the surface of polar microstructure while the image is captured by CMOS sensor as shown in Figure 6.

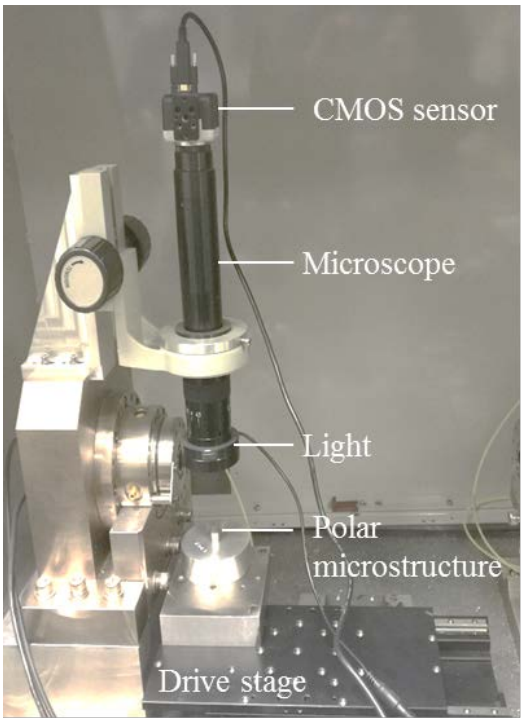

FIGURE 5. Experimental setup

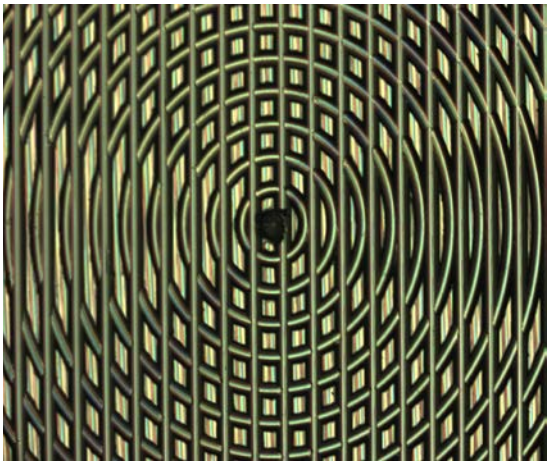

FIGURE 6. Polar microstructure observed with CMOS sensor

To test the position performance of the integrated polar microstructure and template matching method, the experiment is conducted to drive a 500 μm-distance reciprocating for 50 times each along x and y axis, images are captured during each reciprocating cycle. Hence, the integrated polar microstructure and template matching method is used to determine the position of each image which is captured by camera at each step.

It should be illustrated that considering the calculation amount in Eq. (3) as well as to prevent there are some areas which are actually outside the area of global image (G), the top left corner (100 pixels x 100 pixels) of each image captured by camera is chosen as template image (T). When the reference image ($R_{\max}$) which has the most similarity with template image (T) is calculated, the pixel (u, v) which is on the top left corner of $R_{\max}$ is defined as the "result pixel". The actual distance between the "result pixel" with the pixel on the top left corner on the global image (G) is defined as position. After calculation, all the calculated position points are compared to the actual position points.

To illustrate the measurement performance of the integrated polar microstructure and template matching method clearly, the distance ($D_{(i,j)}$) of each measurement point between actual position coordinate value ($x_{werth(i,j)}$, $y_{werth(i,j)}$) and the calculation position coordinate value ($x_{TM(i,j)}$, $y_{TM(i,j)}$) is determined, which can be expressed as Eq. (6):

$$D_{(i,j)} = \sqrt{(x_{werth(i,j)} - x_{TM(i,j)})^2 - (y_{werth(i,j)} - y_{TM(i,j)})^2} \quad (6)$$

The difference $D_{(i,j)}$ between the calculated positions and the displayed positions by the drive stage is acquired and the results are shown in Fig. 7(a) and Fig. 7(b) in X and Y axis respectively. The standard deviations of positioning errors are found to be 198.6 nm and 222.8 nm in x and y axis, respectively.

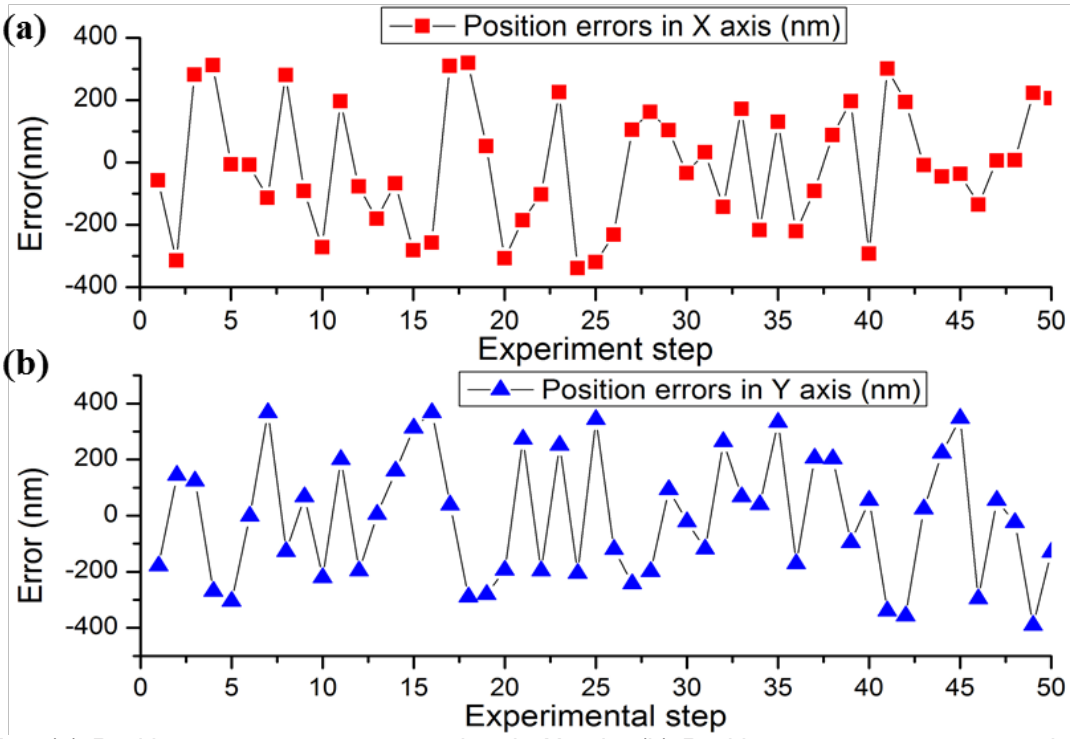

FIGURE 7. (a) Position measurement uncertainty in X axis. (b) Position measurement uncertainty in Y axis.

CONCLUSIONS

A novel method integrating ultra-precision machining and computer vision technologies is found to be feasible and promising for the precision measurement. The polar microstructure surface has been machined by single point diamond turning and single point diamond broaching processes which ensure the machining errors which can be controlled in high precision level. A series of experiments have been conducted to evaluate the positioning measurement accuracy. The experimental results show that the proposed measurement method is able to achieve 200 nm level of uncertainty. It is hopefully to be applied in workpiece positioning and machine tool repeatability in the future.

ACKNOWLEDGEMENTS

The work described in this paper was mainly supported by PhD studentship (project account code: RU7J) from The Hong Kong Polytechnic University. The authors would also like to express their sincerely thanks to the financial support from the Research Office of The Hong Kong Polytechnic University (Project code: BBX7).

REFERENCES

[1] Gao W, Kim SW, Bosse H, Haitjema H, Chen YL, Lu XD, Knapp W, Weckenmann A, Estler WT, Kunzmann H. Measurement technologies for precision positioning. CIRP Annals. 2015 Jan 1;64(2):773-96.

[2] Solecky E, Patterson OD, Stamper A, McLellan E, Buengener R, Vaid A, Hartig C, Bunday B, Arceo A, Cepler A. In-line E-beam wafer metrology and defect inspection: the end of an era for image-based critical dimensional metrology? New life for defect inspection. InMetrology, Inspection, and Process Control for Microlithography XXVII 2013 Apr 10 (Vol. 8681, p. 86810D). International Society for Optics and Photonics.

[3] Zhao C, Cheung CF, Liu M. Modeling and simulation of a machining process chain for the precision manufacture of polar microstructure. Micromachines. 2017 Nov 27;8(12):345.

[4] Zhao C, Cheung C, Liu M. Integrated polar microstructure and template-matching method for optical position measurement. Optics express. 2018 Feb 19;26(4):4330-45.

DETERMINATION OF THE LATERAL RESOLUTION OF AN INTERFERENCE MICROSCOPE USING A MICRO-SCALE SPHERE

Rong Su[1], Matthew Thomas[1], Peter de Groot[2], Jeremy Coupland[3], Richard Leach[1]
[1]Manufacturing Metrology Team, Faculty of Engineering, University of Nottingham, Nottingham NG8 1BB, UK
[2]Zygo Corporation, Middlefield, Connecticut, USA
[3]Wolfson School of Mechanical, Electrical and Manufacturing Engineering, Loughborough University, Loughborough LE11 3TU, UK

INSTRUCTION

The lateral resolution of a surface topography measuring instrument refers to the ability to clearly distinguish surface heights between two closely spaced features. Specifications for lateral resolution often include the traditional Rayleigh and Sparrow criteria inherited from optical imaging systems [1], and there are more definitions that include a measure of the height transmission listed in the draft ISO specification standard, ISO 25178 part 600 [2].

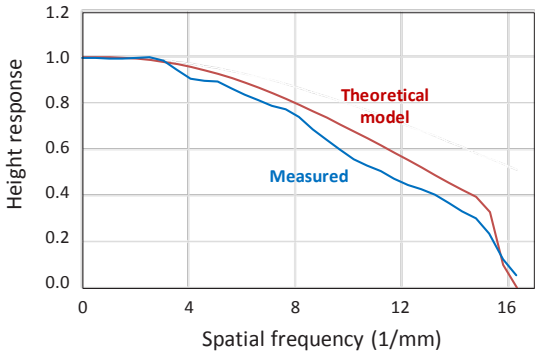

FIGURE 1 Example instrument transfer function of a laser Fizeau interferometer showing a spatial frequency limit of 16 cycles/mm over a 100 mm aperture [3].

A more complete characterisation of lateral resolution is the linear height-response instrument transfer function (ITF). The linear ITF represents the measured amplitudes relative to the true amplitudes of surface sine waves as a function of spatial frequency. In the limit of low-amplitude sine waves ($<<\lambda/4$), we can predict the instrument response by mapping the Fourier components of the surface, weighted by the ITF, to the surface topography. The small height limitation in the ITF representation follows from the need to avoid nonlinear effects and to keep the spatial frequencies separable [1].

FIGURE 1 shows the measured ITF for a laser Fizeau interferometer [3]. Data of this kind are valuable when using optical metrology to quantify the power spectral density of a surface – an important parameter in optics fabrication.

There are a variety of calibration artefacts for lateral resolution, such as a line pairs, star patterns, a series of sinusoids with a chirped pitch and pseudo-random binary structures [4]. The measurement results in FIGURE 1 correspond to a line-spread function test, using a 30 nm step feature [3].

An alternative to directly measuring the ITF over a range of surface frequencies is to calculate the ITF using modelling. The theoretical curve in FIGURE 1, for example, follows from a Fourier optics analysis of a coherent system, including apertures and known aberrations, with the object represented as a distribution of phase shifts proportional to surface heights [5]. Once this model is in place, for the purpose of generating a height-response ITF, it is easy enough to generate virtual sinusoidal surfaces in software at the small ($<\lambda/4$) surface height limit.

The modelling approach to the ITF presupposes that we have an effective means of calibrating for the optical properties of the instrument. This becomes increasingly cumbersome for techniques such as coherence scanning interferometry (CSI), which employs a spatially-extended, spectrally-broadband light source [6]. Modelling of such systems traditionally involves diffraction calculations followed by numerical integration over an area of pupil positions, illumination directions and optical path lengths for each point in the field of view, under the assumption of ideal optics [7,8].

A compelling modelling framework for surface topography measurement using CSI relies on the

definition of a 3D transfer function (3D TF) for the optical system [9-11]. In this framework, the object surface is a weakly-scattering structure or "foil", and under reasonable physical conditions, we can compactly model the CSI imaging process as a 3D linear shift-invariant filtering operation. This linear systems theory is valid provided two assumptions are satisfied: 1) the first Born approximation is assumed, which means the total electromagnetic field on the surface is only determined by the incident field [12]. This approximation is accurate if the scattered field is small compared to the incident field on the surface. The weak scattering case can be considered when the refractive index contrast is small or if the object consists of sparse point-like objects. 2) Alternatively, the foil model of the surface must be valid, where the surface can be strongly scattering but must be slowly varying on a wavelength scale, i.e. the radius of the local curvature of the surface is much greater than a wavelength, such that the multiple scattering effect is negligible and the Kirchhoff approximation is assumed. Moreover, the reflection coefficient is assumed constant and polarisation independent over the range of incident/reflected angles accepted by the numerical aperture (NA) [13]. The Kirchhoff approximation is required if the refractive index contrast is large between the air and the material.

Importantly, based on the foil model of the surface, it is possible to fully characterise the transfer properties and the resolutions of a CSI system by measuring a precision sphere [14-16]. This follows from the observation that a sphere, which is smaller than the field of view, reflects light through all possible angles within the NA limits of the optics. Once this calibration is completed, it is straightforward to calculate what the response would be to a sequence of sinusoids of small amplitudes, providing the height-response ITF.

In this paper, we will demonstrate calculation of the linear height-response ITF of a CSI system using the foil model, calibrated using a precision sphere. This approach provides an alternative to calibration by the more familiar specimens, such as star patterns and chirped sinusoids, while enabling a more complete system characterisation than the traditional ITF specification.

METHOD

CSI is a well-established technique for surface topography measurement [17,18]. The major advantage of CSI is that it can estimate the phase information of the light back-reflected/scattered from the sample surface and the spectrum of broadband light source modulates the interferometric fringes in order to make it easier to determine the fringe order than in traditional phase shifting interferometry. CSI overcomes the 2π ambiguity that can be present when the surface topography or a sharp step feature interrupts the imaging of continuous interference fringes.

The detailed theoretical derivation of the foil model and the characterisation of the 3D TF of CSI can be found elsewhere [10,14,19]. Here, we will briefly describe the characterisation procedure. As shown in FIGURE 2, we first acquire the 3D fringe data of the spherical cap by CSI data acquisition and storing the intensity image stack in the usual way. Given that the sphere diameter is known, the foil function of the spherical cap, described as

$$o(x, y, z) = 4\pi jRw(x, y)\delta[z - s(x, y)], \quad (1)$$

where $j = \sqrt{-1}$, R is the Fresnel amplitude reflection coefficient and is assumed to be a complex constant for simplicity, corresponding to the limit case of normal incidence reflection [10], and $w(x,y)$ is a window function with smooth cut-off for defining the space-limited surface region under illumination. The 'foil' is defined by the 1D Dirac delta function $\delta(z)$ based on the surface topography of the object $s(x,y)$. The foil function can be generated numerically. Taking the Fourier transform of the fringe data and the foil function gives us the spectra of the spatial frequency components. Then the 3D TF for the specific optical instrument at the time of calibration can be calculated by dividing the fringe by the foil in the spatial frequency domain. From the 3D TF, the point spread function (PSF) can be derived through its inverse Fourier transform, and the 2D TF is calculated as the projection of the 3D TF onto the *x-y* plane by summing the 3D TF along the axial direction for each lateral spatial frequency. The 1D ITF plot, similar to FIGURE 1, can then be extracted from the 2D TF. In other words, the traditional ITF can be obtained by dimension reduction of the 3D TF.

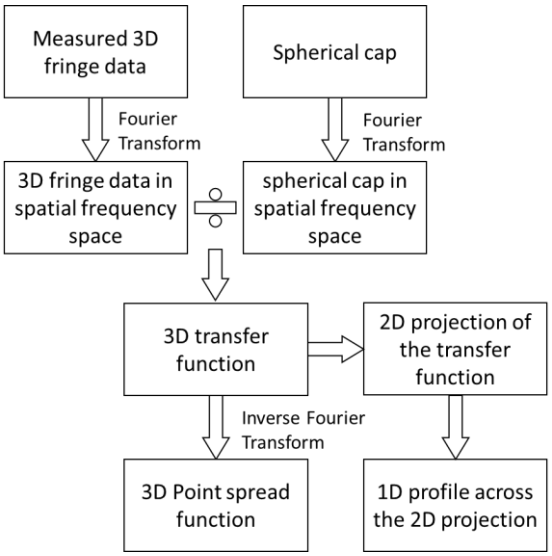
Measured 3D fringe data
Spherical cap
Fourier Transform
Fourier Transform
3D fringe data in spatial frequency space
spherical cap in spatial frequency space
3D transfer function
2D projection of the transfer function
Inverse Fourier Transform
3D Point spread function
1D profile across the 2D projection

FIGURE 2 Characterisation procedure of 3D TF of CSI.

In this work, we use a ZYGO NewView™ 8300 CSI system with a 0.55 NA objective lens, 167 µm field of view and 0.163 μm lateral sampling distance. The three microspheres used here are made of silica and have different diameters, 44 μm, 57 μm and 59 μm. The spheres are checked for surface quality and sphericity under scanning electron microscope (SEM) as shown in FIGURE 3, and we assume the sphericity error is negligible, i.e. the sphere can be described solely by its diameter. More information about the necessary microsphere tolerance is given elsewhere [15].

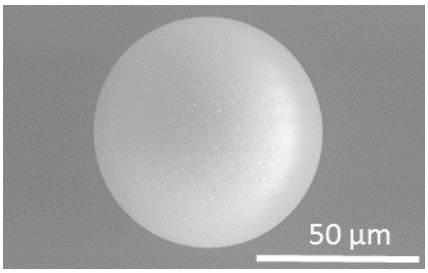

FIGURE 3 SEM image of a microsphere.

RESULTS

The three microspheres of different diameters were measured with CSI, and the 3D fringe data for each obtained. As previously mentioned, we compute a 3D TF from each measurement, where each sphere's diameter determines the form of each modelled surface. For each sphere, measurements are taken at four orientations (0°, 90°, 180°, 270°). The resulting TFs from each orientation are averaged to reduce the effect of any directional bias, such as those caused by asphericity of the microsphere or the influence of randomly located dust particles on the spherical surface. This averaging is performed by taking the arithmetic mean of the magnitude of differently orientated 3D TFs. The result of this can be seen in FIGURE 4.

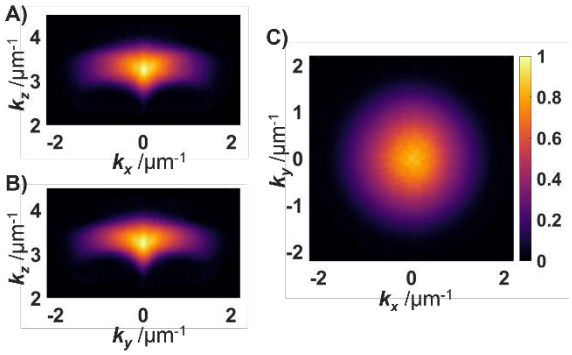

FIGURE 4 Magnitude of the 3D TF associated with the 44 μm sphere after averaging and normalisation to one. Slices are shown at spatial frequencies A) $k_y = 0$, B) $k_x = 0$, and C) $k_z = 2/\lambda = 3.45\ \mu m^{-1}$ ($\lambda = 0.58\ \mu$m). The colour bar and colour map used are shared between the three slices.

A 3D PSF is acquired by the inverse Fourier transform of the 3D TF, and is displayed in FIGURE 5. It is interesting to note that the 3D PSF of CSI contains fringes along the axial direction, which would not be seen in an ordinary widefield microscope.

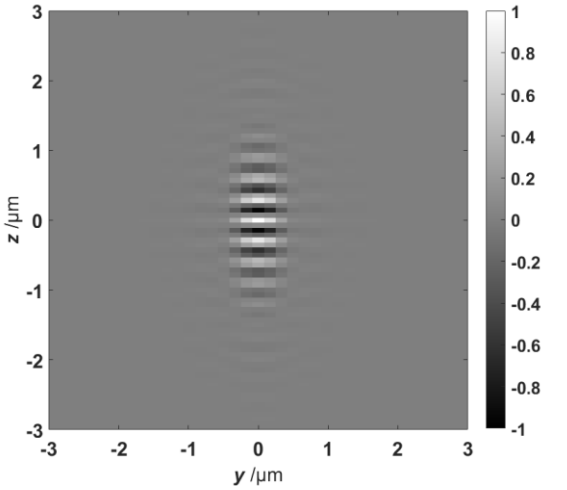

FIGURE 5 A slice of the 3D PSF, computed by inverse Fourier transform of the 3D TF shown in FIGURE 4. Magnitude normalised to one for plotting.

The averaged 3D TF of each sphere is projected onto the lateral spatial frequency (k_x-k_y) plane to produce a 2D projection of the 3D TF. This process is done by summing the 3D TF along the k_z direction at each k_x and k_y, followed by

normalising the magnitude of the resulting 2D projection to one. This projection characterises at each lateral spatial frequency coordinate (k_x,k_y) the instrument's ability to transfer the surface function (equation (1)) to the measured optical field (i.e. the 3D fringe data). From the fringe data, the surface topographic information is retrieved using a surface reconstruction algorithm, e.g. the frequency domain analysis method [20].

From each of the averaged 3D TFs we obtain an approximately circularly-symmetric 2D projection (which is what we would expect from an optical imaging system with a circular aperture). The one shown in FIGURE 6 is obtained from the 44 μm sphere. The 3D TFs and the corresponding 2D projections obtained from the measurements of the three spheres are almost completely identical to each other, despite the differences in diameter between the three spheres, providing evidence that the transfer function of a CSI can be obtained solely via measurement of a microsphere based on the linear theory of CSI.

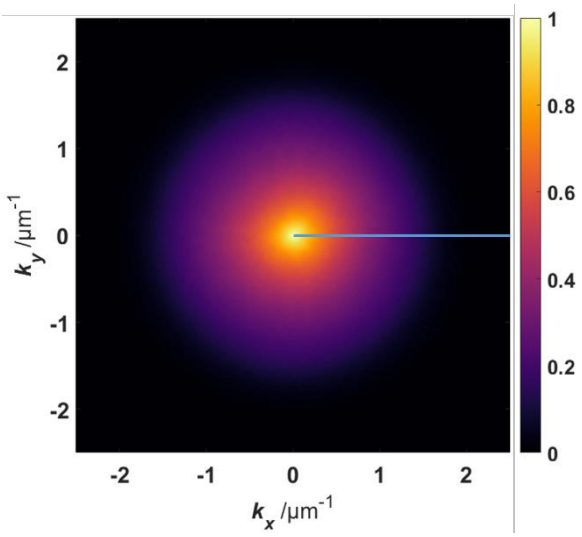

FIGURE 6 The 2D projection of the 3D TF shown in FIGURE 4. Since the other two projections associated with the other two spheres are nearly identical, only one is displayed. The blue lines are the lines along which profiles are taken for FIGURE 7.

Profiles of the three projections are taken radially from the origin of the axes, in this case arbitrarily along the positive k_x axis (marked in FIGURE 6), and compared to both each other and the theoretical model in FIGURE 7. This theoretical model is produced using equation (32) in reference [10]. Given the system has a 0.55 NA, the central wavelength of 0.58 μm and full-width-at-half-maximum bandwidth of 0.08 μm, the theoretical cut-off frequency is approximately 2 μm^{-1}.

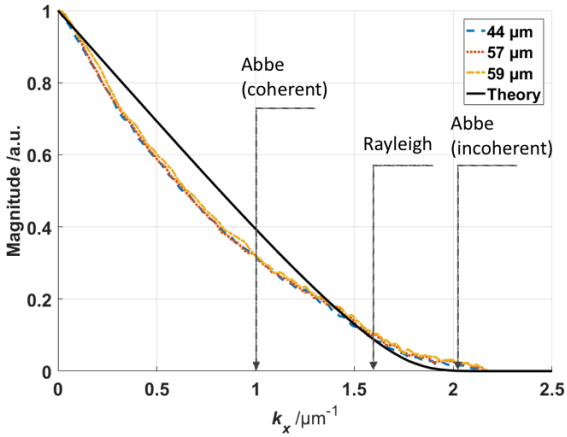

FIGURE 7 Profiles of the 2D projections from each sphere measurement taken along the positive k_x axis as marked on FIGURE 6. The projection associated with the 44 μm diameter sphere is the blue dashed line, the 57 μm is the red dotted line, the 59 μm is the yellow dash-dot line, and the theoretical model is given by the black solid line. Cut-off frequencies corresponding to the Rayleigh and Abbe criteria of resolution limit are shown.

The measured TFs are in general very close to the theoretical one. The discrepancy is highly likely caused by slight defocus of the CSI system. The reader may consult [16] for more detailed explanation and discussion on this. Assuming the surface reconstruction algorithm is a linear operation applied to the measured optical field and the digital sampling frequency of the camera is higher than 2 μm^{-1} (which is true for high magnification objective lens), the traditional ITF defined in [1] can be estimated from the 3D TF.

CONCLUSION

The linear height-response instrument transfer function (ITF) offers a more complete characterisation of the lateral resolution of an optical surface topography measuring instrument. We demonstrate in this paper, the ITF can be estimated from measuring a microsphere based on the linear theory of 3D imaging, particularly in this case, the foil model in CSI. This approach provides an alternative to calibration by the more familiar specimens such as star patterns and chirped sinusoids.

Importantly, an optical model such as the 3D TF presented here is not limited to recreating the linear ITF, which is known to have limitations based on the assumption of linear response of the

instrument [1]. The foil model provides a means of predicting the response to more challenging surface topographies and shapes that often give rise to anomalous or unexpected results that are inconsistent with the linear response. The sphere calibration, therefore, enables a more complete system characterisation than the traditional ITF specification, potentially leading to software correction methods to extend the linear range of the instrument [14,19]. For future work, the authors will provide a rigorous experimental verification of the foil model and investigate the validity regimes of the ITF and 3D TF, and their relationship.

ACKNOWLEDGEMENT
This work was supported by the Engineering and Physical Sciences Research Council (EPSRC) (EP/M008983/1) and the European Metrology Programme for Innovation and Research (EMPIR) project FreeFORM (15SIB01).

REFERENCES

1. Colonna de Lega X, de Groot P. Lateral resolution and instrument transfer function as criteria for selecting surface metrology instruments. OSA Proc. Optical Fabrication and Testing 2012; OTu1D.
2. ISO 25178-600:2017 Geometrical product specifications (GPS) – surface texture: areal – part 600: Metrological characteristics for areal-topography measuring methods.
3. Deck LL and de Groot P. Using the instrument transfer function to evaluate Fizeau interferometer performance. OSA Technical Digest 2017; OM2B.7.
4. Leach RK, Giusca CL, Haitjema H, Evans C, Jiang X. Calibration and verification of areal surface texture measuring instruments Ann. CIRP 2015; 64: 797-813.
5. Goodman JW. Introduction to Fourier Optics, 3rd edition. Roberts & Company: 2005.
6. de Groot P. Principles of interference microscopy for the measurement of surface topography. Advances in Optics and Photonics 2015; 7: 1-65.
7. Totzeck M. Numerical simulation of high-NA quantitative polarization microscopy and corresponding near-fields. Optik 2001; 112: 399-406.
8. de Groot P, Colonna de Lega X, Liesener J et al. Metrology of optically-unresolved features using interferometric surface profiling and RCWA modelling. Opt. Express 2008; 16: 3970.
9. Coupland JM and Lobera J. Holography, tomography and 3D microscopy as linear filtering operations. Meas. Sci. Technol. 2018; 19: 07010.
10. Coupland JM, Mandal R, Palodhi K, Leach RK. Coherence scanning interferometry: linear theory of surface measurement. Appl. Opt. 2013; 52: 3662-3670.
11. Kou SS and Sheppard CJR. Imaging in digital holographic microscopy. Opt. Express 2007; 15: 13640-13648.
12. Born M and Wolf E. Principles of Optics: Electromagnetic Theory of Propagation, Interference and Diffraction of Light, 7th edition. Cambridge: Cambridge University Press: 1999.
13. Beckmann P and Spizzichino A. The Scattering of Electromagnetic Waves from Rough Surfaces. Pergamon: 1963.
14. Su R, Wang Y, Coupland JM, Leach RK. On tilt and curvature dependent errors and the calibration of coherence scanning interferometry. Opt. Express 2017; 25: 3297-3301.
15. Su R, Coupland JM, Wang Y, Leach RK. Tolerance on sphere radius for the calibration of the transfer function of coherence scanning interferometry. Proc. SPIE 2017; 10329.
16. Su R, Thomas M, Leach RK, Coupland JM. Effects of defocus on the transfer function of coherence scanning interferometry. Opt. Lett. 2018; 43: 82-85.
17. de Groot P. Chapter 9. Coherence scanning interferometry, in Optical Measurement of Surface Topography. Leach RK. Springer: 2011.
18. ISO 25178-604:2013 Geometrical product specifications (GPS) – surface texture: areal – part 604: Nominal characteristics of non-contact (coherence scanning interferometry) instruments.
19. Mandal R, Coupland J, Leach RK, Mansfield D. Coherence scanning interferometry: measurement and correction of three-dimensional transfer and point-spread characteristics. Appl. Opt. 2014; 53: 1554-1563.
20. de Groot P, Deck L. Surface profiling by analysis of white-light interferograms in the spatial frequency domain. J. Mod. Opt. 1995; 42: 389-401.

MEMS-BASED GRAPHENE RESONANT GAS SENSOR FOR HEALTH MONITORING

David R. Cayll[1], Ian S. Ladner[1], Joon Hyong Cho[1], and Michael A. Cullinan[1]
[1]Department of Mechanical Engineering
The University of Texas at Austin
Austin, Texas, United States of America

ABSTRACT

This paper introduces the design of a MEMS-based resonator with the ability to detect single gas molecules in air. Graphene doped with nanoparticles will be used as a doubly clamped beam resonating at its natural frequency. As specific gas molecules selectively bond to the dopants in the graphene sheet, the system's mass increases, therefore decreasing its natural frequency. For example, a shift in resonant frequency of up to 37 Hz is expected in this device when one atom of acetone is bonded to the graphene surface.

INTRODUCTION

The development of a cheap, selective, and ultrasensitive gas sensor has applications in the biomedical industry as a diagnostic tool. Many current sensors use catalytic reactions to sense gas concentration. These catalysts are often expensive and are not selective or responsive enough to be used as a reliable diagnostic tool. Using graphene doped with nanocrystal catalysts allows for cheaper, more sensitive sensors due to higher surface to volume ratios than conventional catalysts [1].

A large roadblock in this technology is the reprudicibility of measurements from device to device. This is due to intrinsic strain variance in the different graphene sheets since they are grown on imperfect copper foil and have grain boundaries [2]. By implementing the geometry shown in Fig.1, the inherent strain variances from processing can be removed by adding a preload force to the graphene via thermal actuator (Fig 1d). This preload is calibrated via capacitive force and displacement sensors shown in Fig.1a & 1c.

MEMS DESIGN

To be able to place a precise, repeatable preload on the graphene sheet, the stress and strain in the sheet must be known. The capacitive load and displacement sensors have a resolution of 44 nN and 0.25 nm respectively for this reason. These resolution limits are set by photolithography constraints as well as the stray capacitance in the signal processing circuit. Actuator travel sensitivity was determined by the preload required and max displacement was determined by the yield strength of graphene.

Since the preload is known, Eq. 1 can be used to predict the resonant frequency of a doubly clamped membrane [3]

$$f_{res}(T_{TA}) = \frac{1}{2L}\sqrt{\frac{T_0+T_{TA}}{\rho_0 * \alpha * w}} \quad (1)$$

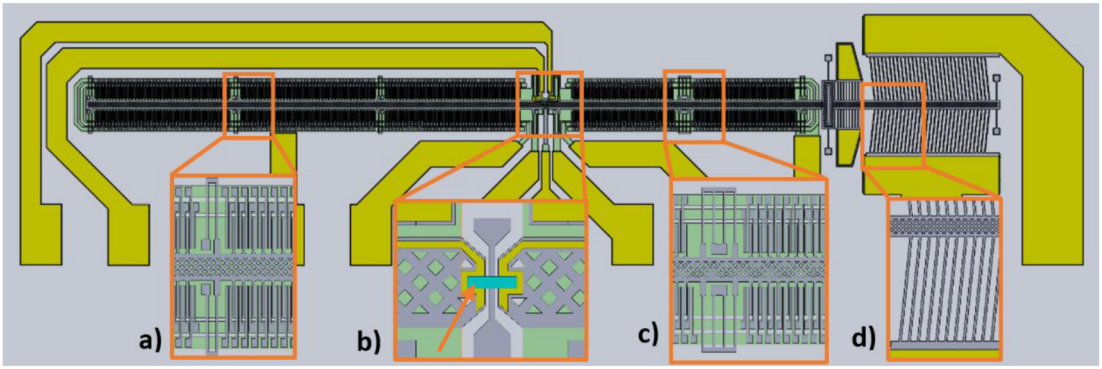

FIGURE 1. MEMS resonator geometry. 1a) Capacitive load sensor 1b) Graphene resonator 1c) Capacitive displacement sensor 1d) Thermal actuator

Where T_0 is built-in tension, T_{TA} is the preload tension created by the thermal actuator, ρ_0 is the density of graphene, α is the adsorbed mass coefficient, and w is the width of the resonator. This relation allows us to create devices with comparable resonant frequencies across the wafer and accounts for manufacturing defects.

SENSING MECHANISM

Graphene is an ideal material for this mechanical sensor system because of its high strength and its very low mass per unit surface area since it is a single atomic layer thick. The graphene resonators can be chemically functionalized using catalytic nanoparticles to preferentially attract specific gas molecules [1]. Once bonded, these gas molecules will increase the adsorbed mass coefficient, α, in Eq. 1. This will cause a shift in resonant frequency proportional to gas concentration.

The circuit shown in Figure 2 will be used to test the resonator and measure this small shift in resonant frequency.

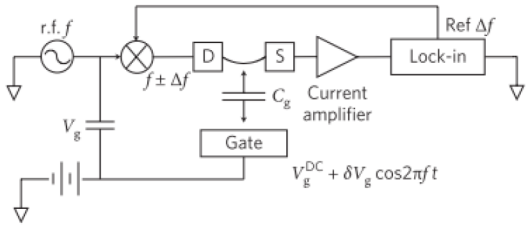

FIGURE 2. Resonance sensing circuit

MODELING

In order to sense small shifts in resonance, the quality factor, or bandwidth relative to center frequency, of the resonator must be maximized. There are 3 major types of damping in MEMS resonators: viscous, free molecular flow (FMF), and thermoelastic. Knudsen number [4], shown in Eq. 2, is used to determine whether statistical or continuum mechanics is a valid model in a given system.

$$K_n = \frac{l_{mfp}}{w} \quad (2)$$

Where l_{mfp} is the mean free path of the particles in the medium, and w is the width of the resonator. When K_n<0.01 viscous flow is dominant, when K_n>10 FMF is dominant, and between 0.01 and 10 is a transition regime where the two Q-factors add inversely [5]. Q-factor can never be larger than the smallest damping component, therefore the damping of a system can be approximated by the dominant mechanism in the region.

Viscous damping is modeled with Navier-Stokes equation [5] to find its effect on the q-factor of the resonator. This form of damping is highly dependent on pressure as well as resonator width. The relationship between width, pressure, and Q-factor is shown in figure 3. As expected, the Q-factor increases as the beam gets narrower and as pressure decreases. In order to minimize damping losses due to the viscous effect, the gas sensor will operate in a modest vacuum of 10 torr with a resonator width of 200 nm.

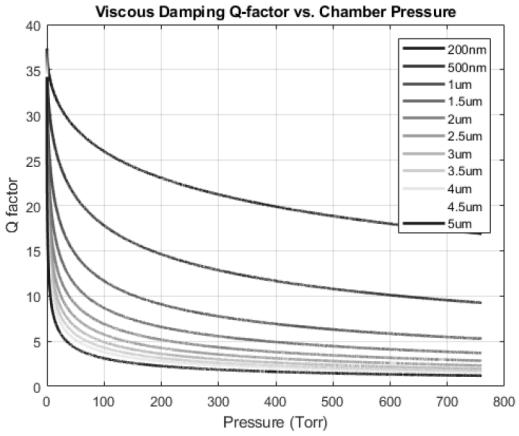

FIGURE 3. Q-factor due to viscous damping vs. chamber pressure

The second damping regime is free molecular flow, which is when the width of the resonator is on the order of the mean free path of the gas and below. This regime is dominated by the kinetic effects of the collisions between noninteracting gas molecules and the resonant graphene beam [5]. Figure 4 shows the relationship between FMF damping and chamber pressure. At 10 Torr, the FMF Q-factor is about 150, which is almost 5 times the corresponding Q for the viscous flow regime, therefore viscous flow is dominant, and efforts to increase efficiency should be concentrated on the viscous regime.

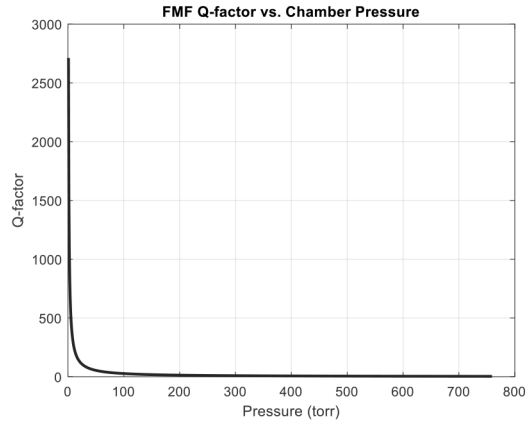

FIGURE 4. FMF Q-factor vs. chamber pressure for 200 nm width resonator

The final regime is thermoelastic damping. This type of damping is thermodynamic in nature and arises from internal friction due to strain gradients. Nonuniform expansion and contraction in the resonator release energy in the form of heat [6]. This damping mechanism has been observed in systems operating in low vacuums where viscous and FMF damping are virtually eliminated [7]. The system proposed in this paper calls for a relatively lower vacuum level, therefore thermoelastic damping will be dwarfed by the aforementioned mechanisms.

In order to increase the overall Q-factor, viscous damping must be minimized since it is the dominant mechanism. To do this, the underlying MEMS device will be used to put strain on the graphene as it resonates in an effort to increase its resonant frequency. Equation 3 describes how the viscous Q is dependent on resonant frequency [5].

$$Q_{visc} = \frac{\omega_{res} t_g l_g w_g \sqrt{\frac{\rho_g E}{12}}}{6\pi\mu R \sqrt{\frac{E}{12\rho_g}}\left(1+\frac{R}{\delta}\right)} \quad (3)$$

Where ω_{res} is resonant frequency in rad, t_g is thickness of graphene, l_g is length of graphene, w_g is width of graphene, ρ_g is mass density of graphene, E is young's modulus of graphene, μ is the dynamic viscosity of air, R is width of the harmonically vibrating sphere used to analyze this system [5], and δ is boundary layer thickness.

The trend described in equation 3 is plotted in figure 5. As resonant frequency increases, so does Q. To understand the amount of strain necessary to shift resonance, equation 1 and 3 are combined in figure 6 to show the relationship between strain and Q factor in graphene resonators of different sizes. It is worth noting that the thinner the beam, the more of an effect increasing resonant frequency has on Q.

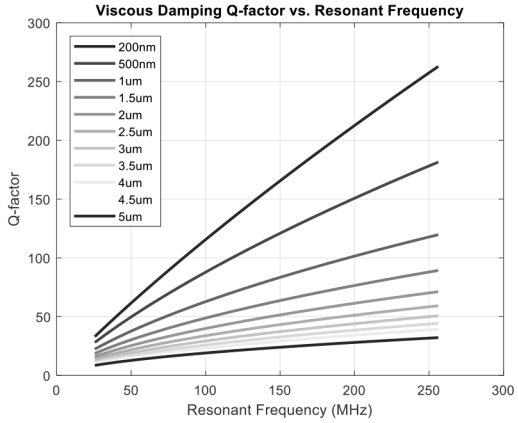

FIGURE 5. Viscous Q-factor vs. graphene resonant frequency for select beam widths

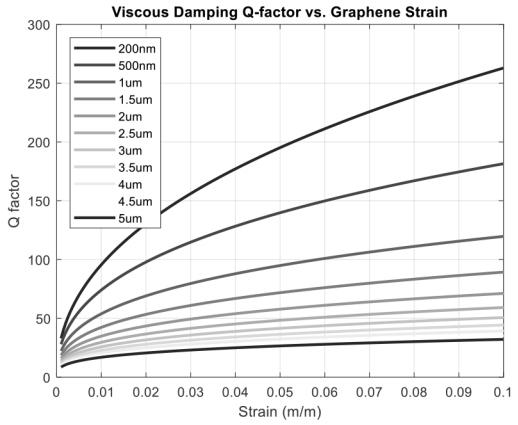

FIGURE 6. Viscous Q vs. strain in graphene beam for select beam widths

Shifts in resonant frequency also affect the FMF damping shown in Eq. 4 [5].

$$Q_{FMF} = \frac{\omega_{res} t_g \sqrt{\frac{\rho_g E}{12}}}{K_m p \sqrt{\frac{E}{12\rho_g}}} \quad (4)$$

Where K_m is $3.6*10^{-3}$ s/m and p is chamber pressure. The relationship is shown graphically in figure 7. FMF damping follows the same trend as viscous damping and is, therefore, still a secondary source of damping. At 10% strain, Viscous Q is 262.9 and FMF Q is 2925.0. When added inversely and assuming thermoelastic

damping is many orders of magnitude higher [7] and can be ignored, the overall Q factor of the system is 241.2 which is greater than our goal of 200 and should simplify sensing large shifts in resonance.

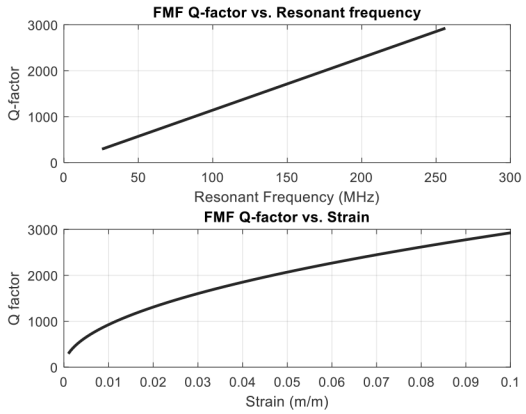

FIGURE 7. FMF Q-factor vs. resonant frequency and strain in graphene given 200 nm beam width

MANUFACTURING

The MEMS device is fabricated using a modified PolyMUMPs approach [8]. The device includes a polysilicon electrode routing layer, a thicker polysilicon device layer, a sacrificial oxide layer to suspend the device layer, silicon nitride insulation layer, and a gold electrode layer. Figure 8 describes shows the process flow for the MEMS device.

A polymeric stamp method [9] is employed to pick up graphene from an arbitrary substrate to be placed onto the suspended stages. The process flow in figure 9 shows the modified transfer method used.

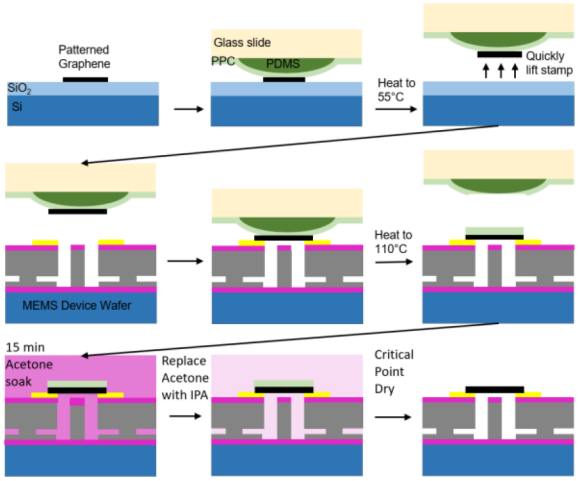

FIGURE 9. Process flow for stamp transfer of graphene onto MEMS device.

To dope the graphene with nanocrystals, a solution-based procedure will be used [10]. The doping will be done before transfer for manufacturing feasibility purposes.

RESULTS

The MEMS architecture is designed to measure displacements in the graphene of as little as 0.25 nm and forces as small as 44 nN. Currently, devices are being manufactured while the transfer process is being validated. Initial transfers onto suspended MEMS stages look promising as shown in Figure 10.

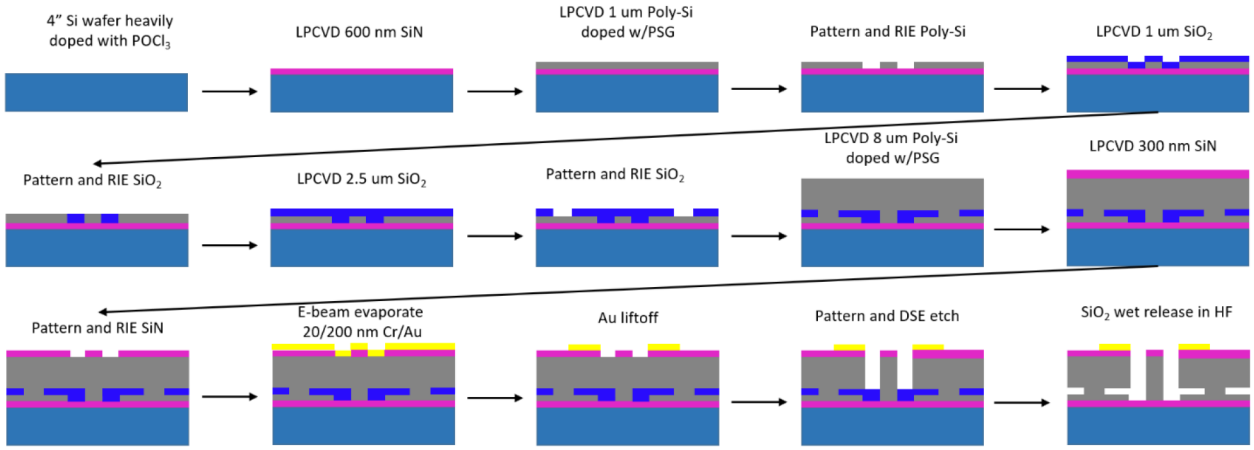
4" Si wafer heavily doped with POCl3
LPCVD 600 nm SiN
LPCVD 1 um Poly-Si doped w/PSG
Pattern and RIE Poly-Si
LPCVD 1 um SiO2
Pattern and RIE SiO2
LPCVD 2.5 um SiO2
Pattern and RIE SiO2
LPCVD 8 um Poly-Si doped w/PSG
LPCVD 300 nm SiN
Pattern and RIE SiN
E-beam evaporate 20/200 nm Cr/Au
Au liftoff
Pattern and DSE etch
SiO2 wet release in HF

FIGURE 8. Modified PolvMUMPs MEMS Process flow

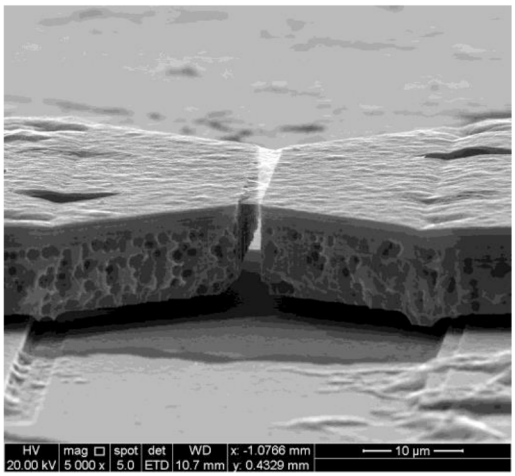

FIGURE 10. Transferred and suspended graphene

CONCLUSION AND FUTURE WORK

The resonator designed in this work has proven to be manufacturable to perform within our specifications. It has also been designed to be sensitive enough to detect very small changes in adsorbed mass at relatively high quality factors. The final 3 steps of the polymetric stamp transfer process in figure 9 are being tuned to be more repeatable and precise. MEMS processing is underway, and circuitry for reading the capacitive sensors is under development as well.

REFERENCES

[1] Mao, S., Cui, S., Lu, G., Yu, K., Wen, Z., & Chen, J. (2012). Tuning gas-sensing properties of reduced graphene oxide using tin oxide nanocrystals. Journal of Materials Chemistry, 22(22), 11009. https://doi.org/10.1039/c2jm30378g

[2] Van Der Zande, A. M., Barton, R. A., Alden, J. S., Ruiz-Vargas, C. S., Whitney, W. S., Pham, P. H. Q., … McEuen, P. L. (2010). Large-scale arrays of single-layer graphene resonators. Nano Letters, 10(12), 4869–4873. https://doi.org/10.1021/nl102713c

[3] Chen, C., Rosenblatt, S., Bolotin, K. I., Kalb, W., Kim, P., Kymissis, I., … Hone, J. (2009). Performance of monolayer graphene nanomechanical resonators with electrical readout. Nature Nanotechnology, 4(12), 861–867. https://doi.org/10.1038/nnano.2009.267

[4] Bhiladvala, R. B., & Wang, Z. J. (2004). Effect of fluids on the Q factor and resonance frequency of oscillating micrometer and nanometer scale beams. Physical Review E - Statistical, Nonlinear, and Soft Matter Physics, 69(3 2), 1–5. https://doi.org/10.1103/PhysRevE.69.036307

[5] Blom, F. R., Bouwstra, S., Elwenspoek, M., & Fluitman, J. H. J. (2014). Dependence of the quality factor of micromachined silicon beam resonators on pressure and geometry, 19(1992). https://doi.org/10.1116/1.586300

[6] Zener, C. (1937). Internal Friction in Solids. Physical Review Letters, 206(1932).

[7] Bianco, S., Cocuzza, M., Ferrero, S., Giuri, E., Piacenza, G., Pirri, C. F., … Correale, R. (2006). Silicon resonant microcantilevers for absolute pressure measurement. Journal of Vacuum Science & Technology B: Microelectronics and Nanometer Structures, 24(4), 1803. https://doi.org/10.1116/1.2214698

[8] Chapter 2 PolyMUMPs Design Guidelines and Rules, Rev. 13.0., vol. 1.

[9] Kim, K., Yankowitz, M., Fallahazad, B., Kang, S., Movva, H. C. P., Huang, S., … Tutuc, E. (2016). Van der Waals Heterostructures with High Accuracy Rotational Alignment. Nano Letters, 16(3), 1989–1995. https://doi.org/10.1021/acs.nanolett.5b05263

[10] Gutés, A., Hsia, B., Sussman, A., Mickelson, W., Zettl, A., Carraro, C., & Maboudian, R. (2012). Graphene decoration with metal nanoparticles: Towards easy integration for sensing applications. Nanoscale, 4(2), 438–440. https://doi.org/10.1039/C1NR11537E

INVESTIGATION OF ASSEMBLY OF A LEVITATION ACTUATOR

Ayaka Nakazato[1], Akihiro Torii[1], Yushi Takaki[1], Kae Doki[1] and Suguru Mototani[1]
[1]Department or Electrical Engineering and Electronics
Aichi Institute of Technology
Toyota, Aichi, Japan

INTRODUCTION

In recent years, the miniaturization of products is progressing. There are various kinds of machines in a factory where products are produced, causing problems of space in the factory. Piezoelectric elements are used in moving actuators. By using the piezoelectric element, a general-purpose and compact moving mechanism can be realized. By adding a floating function to the moving mechanism, an energy loss and positioning error due to a friction during the movement can be reduced.

A levitation actuator composed of laminated piezoelectric elements was fabricated. In the conventional levitation actuator, the piezoelectric element was fixed by using an adhesive between the counterweight and the metal plate [1]. The fixed condition of the adhesive affected the levitation characteristics such as the levitation height and the levitation frequencies.

In this paper, a levitation actuator using a hinge is constructed. The hinge connects a counterweight and plate, a piezoelectric element was inserted and fixed in the space. The frequency characteristics of the levitation height of the mechanism is obtained by changing the voltage applied to the piezo. The possibility of the levitation height control is described.

LEVITATION ACTUATOR

Levitation principle

Figure 1 shows the operating principle of the levitation actuator. By applying a sinusoidal voltage at an appropriate frequency to the piezoelectric element of the levitation actuator, the piezoelectric element expands and contracts. At the same time, the plate vibrates at high speed. Since the plate vibrates at high speed, an air gap is formed between the plate and the floor surface. As a result, the air film generated by the squeeze film effect is produced. The actuator levitates itself, realizes non-contact mechanism, and eliminates the friction.

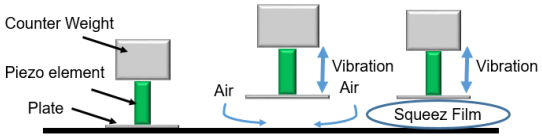

Figure 1 Principle of Levitation

Construction

Figure 2 shows a conventional levitation mechanism. The piezo element is fixed using an adhesive between the counterweight and the plate. The levitation actuator newly created in this study is shown in Figure 3. The plate is 30 mm in diameter, 3 mm in thick and 5.7 g in weight. The counter weight is 20 mm in diameter, 15 mm in height, and 34.9 g in weight. A stacked-type piezo (NEC-Tokin, AD0505D16, 20 mm long) is used. The piezoelectric element is sandwiched between semicircular metals with an outer diameter of 21 mm and is fixed in its longitudinal direction. As shown in Figure 3, the semicircular metals are fixed between the weight and the plate. The total weight is 63.6 g, and the total length is 43 mm.

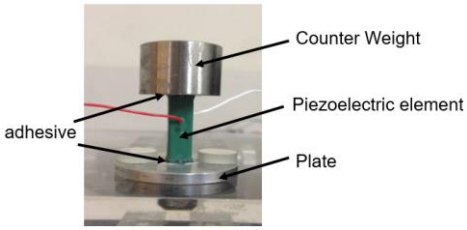

Figure 2 Levitation actuator using adhesive

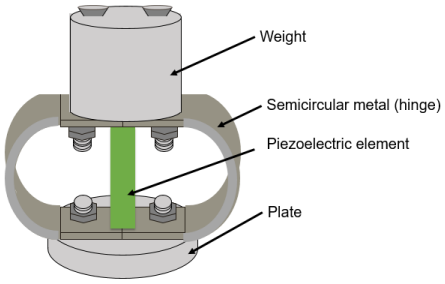

Figure 3 Illustration of the developed mechanism

As shown in Figure 4, the semicircular metals are fixed between the weight and the plate. The weight, semicircular metals, and plate are fixed with screws. A torque screwdriver is used to maintain a predetermined tightening torque. Figure 5 is a top view. A groove fixing the piezoelectric element was dug in the elastic hinge. The elastic hinge is shown in Figure 6. The hinge with a groove is made of stainless steel. The groove with 1 mm depth and 1 mm by 3 mm area is formed to fix the piezoelectric element.

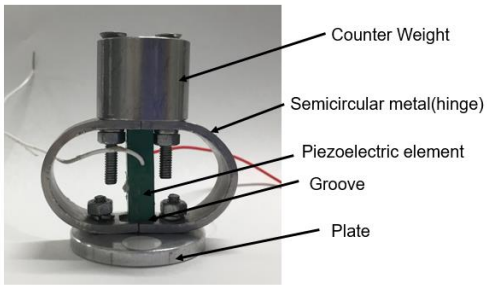

Figure 4 Developed levitation actuator with hinge

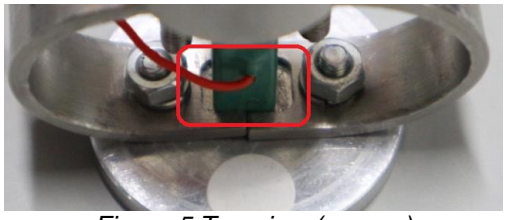

Figure 5 Top view (groove)

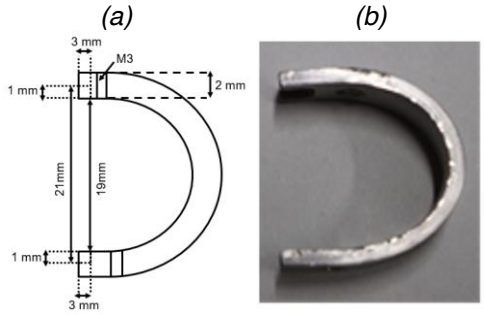

Figure 6 Hinge

MEASUREMENT OF LEVITATION HEIGHT

To confirm the frequency characteristics of the levitation height, the following experiment is conducted. The signal output from a function generator is amplified. The sinusoidal wave of 40 Vpp is applied to the piezoelectric actuator. The levitation height is measured with a laser displacement meter. The frequency varies in the range of 1 kHz to 10 kHz every 0.1 kHz. The displacement is measured three times. After each measurement, the levitation actuator is disassembled. The reproducibility is confirmed by reassembling the levitation actuator. Tightening torque of the screw fixing the counter weight and the plate is 18 cNm.

Figure 7 shows the levitation displacement according to the frequency. In Figure 7, horizontal axis denotes the frequency and the vertical axis denotes the average value of the displacement measured at every frequency. The highest levitation is obtained with the frequency of 4.5 kHz. There is a difference in the displacement between three trials. The displacements are 2.7 μm, 6.1 μm, 7.7 μm. The reassembling causes the difference in levitation height of the mechanism. In addition, it is considered that the groove where the piezoelectric element is fitted is too deep.

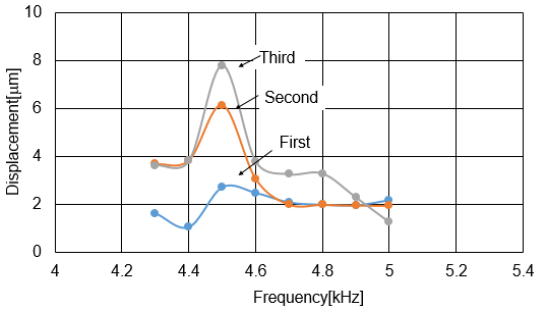

Figure 7 Frequency characteristic of the levitation actuator

IMPROVED LEVITATION ACTUATOR

In the previous chapter, the levitation height varies in respect to three trials. In order to solve the problem, we propose an improved levitation actuator.

Levitation actuator without grooves

In the levitation actuator of the previous chapter, there was a groove for fixing the piezoelectric actuator. In this chapter, a levitation actuator without groove is produced. A levitation actuator newly manufactured is shown in Figure 8. The new levitation actuator consists of a plate, counterweight, elastic hinge, and piezo element. The similar experiments described in the previous chapter are conducted.

Experimental results

Figure 9 shows the levitation displacement according to the frequency. In Figure 9, horizontal axis denotes the frequency and the

vertical axis denotes the average value of the displacement measured at every frequency. The highest levitation is obtained with the frequency of 6.1 kHz. Figure 10 shows the levitation heights measured three times at 6.1 kHz. There is a little difference in the displacement between three trials. The displacements are 38.8 μm, 38.5 μm and 23.3 μm.

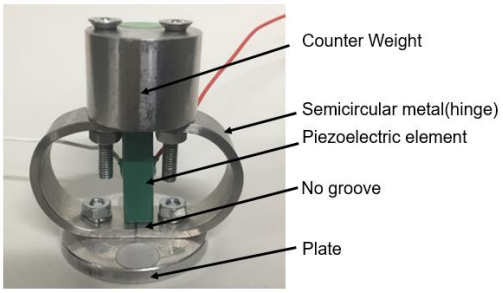

Figure 8 Levitation actuator produced

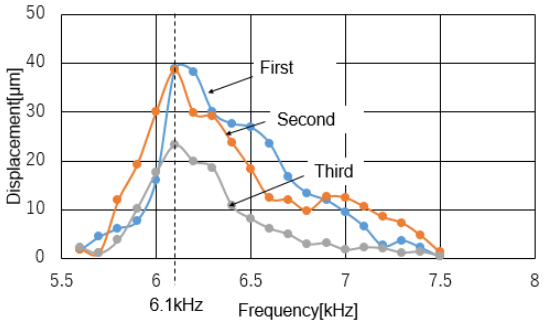

Figure 9 Frequency characteristic

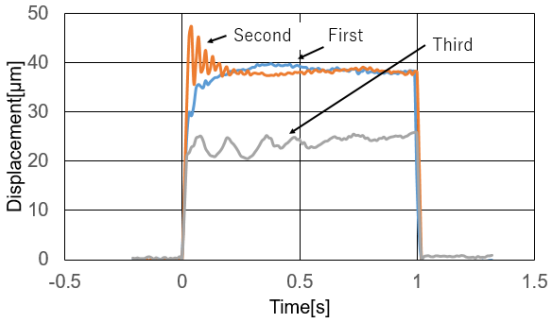

Figure 10 Displacement at 6.1 kHz

Voltage dependence of levitation height

The measurement method is the same. The applied voltage is 20 Vpp, 30 Vpp, 40 Vpp. The frequency varies from 1 kHz to 10 kHz every 0.1 kHz. The average value of the three measurement results of the levitation height at every frequency is obtained. Tightening torque of the screw fixing the counter weight and the plate is 18 cNm.

Figure 11 shows the levitation characteristics when the applied voltage is changed to 20 Vpp, 30 Vpp, 40 Vpp. The frequency range from 1 kHz to 10 kHz was measured every 0.1 kHz. The levitation was not seen in the part which was not plotted. The maximum levitation height was 7.8 μm, 10 μm, and 34 μm, respectively. The frequencies at that time were 6.3 kHz, 6.1 kHz, 6.0 kHz, respectively. These results show the similar trend[2]. Therefore, the maximum levitation height increases as the applied voltage increases. Also, the frequency at maximum levitation decreases

.

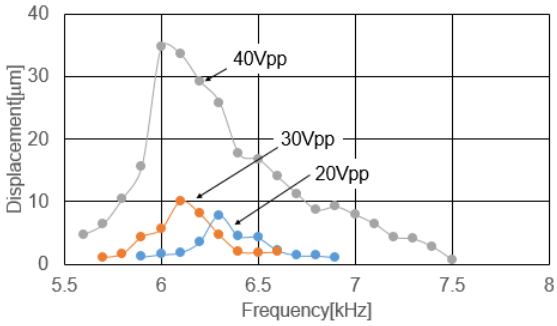

Figure 11 Voltage-frequency characteristics

CONFIRMATION OF PIEZO POSITION

We confirm the levitation height in terms of the piezo position due to the assembly of the levitation actuator. Measurement is performed by the change of the position of the piezoelectric element without disassembling the levitation actuator. The input voltage to the piezoelectric actuator is the same as before, and the frequency is set to 6.1 kHz at which the maximum levitation is obtained. A control signal is applied for one second.

Figure 12 shows positions of the piezoelectric actuator and the displacement. As shown in Figure 12 (a), the piezo is placed at the center of the semicircle metal. Figure 12 (b) shows the measurement results. The levitation displacements of three trials are between 8 μm and 9 μm.

As shown in Figure 13 (a), the piezo is placed at the edge of the semicircle metal. Figure 13 (b) shows the measurement results. The levitation displacements of three trials are between 4 μm and 10 μm.

The levitation height shown in Figure 12 is larger than that in Figure 13. Therefore, the

displacement changes according to the position of the piezoelectric element. It is because that the position of the center of gravity is shifted by changing the position of the piezo element. To increase the levitation height, it is necessary to fix the piezoelectric element to the center of the semicircular plate.

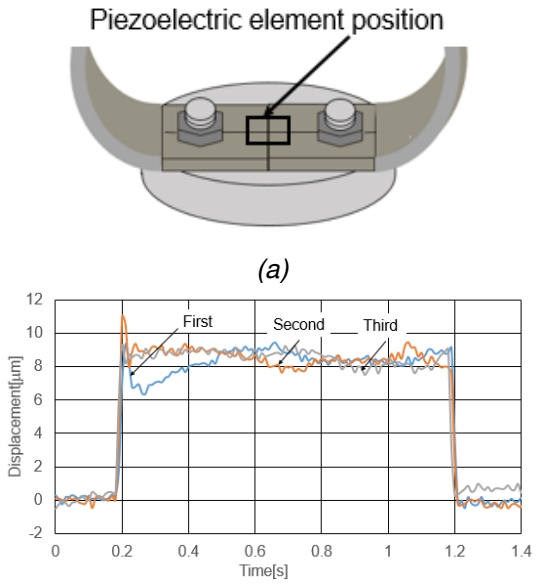

Figure 12 Displacement obtained with the piezo at the center

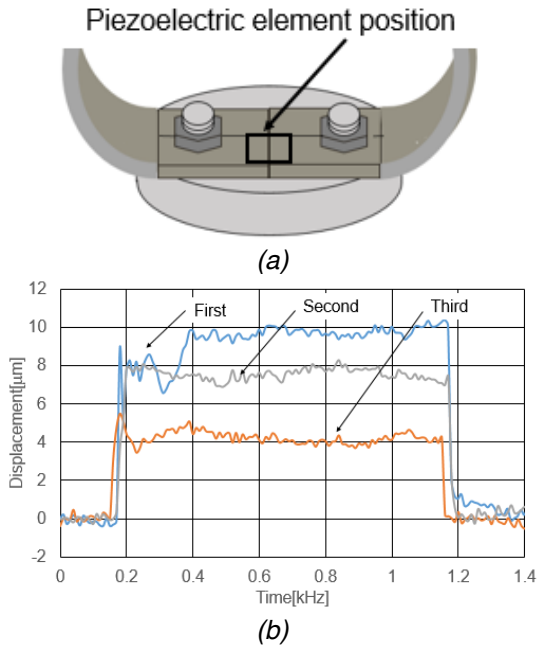

Figure 13 Displacement obtained with the piezo at the edge

SUMMARY

We developed a levitation actuator using a hinge. A groove is formed to fix a piezoelectric element. There were differences in the levitation height in three trials. The reason for this is considered that the vibration of the piezoelectric element was not well transferred to the elastic hinge due to the deep groove. Therefore, it is necessary to shallow the groove of the hinge. Subsequently, the model without the groove is manufactured. The levitation height is measured by changing the position of the piezo element. The levitation with the piezo at the center of the hinge is the largest in the experiments. The results obtained in this paper is used to realize the levitation height control of the levitation actuator.

REFERENCES

[1] Akihiro Torii, Shori Sone, Kae Doki, Suguru Mototani, Levitation caused by vertical viblation of a piezoelectric actuator, euspen's 15th International Conference, Leuven, Belgium, June 2015, pp. 273-274.

[2] Akihiro Torii, Kento Tanaka, Suguru Mototani, Kae Doki, Levitation characteristics of an actuator in a non-contact mechatronic system, euspen's 17th International Conference, Hanover, DE, May 2017, pp. 451-452.

[3] Priya S, Viehland D, Carazo AV, Ryu J and Uchino K, Non-Linear behaviour of piezoelectric ceramics, 2001 J. of Appl. Phys. 90, 1469-1479

[4] Sone S, Torii A, Doki K and Mototani S, Levitation energy of piezoelectric actuator using a levitation mechanism 2014 International Symposium on Micro-NanoMechatronics and Human Science 49-52

[5] Akihiro Torii, Shori Sone, Kae Doki and Suguru Mototani, Input signal for levitation caused by vertical vibration of a piezoelectric actuator 2015. Proceeding of the ASPE, pp. 299-302

IMPROVEMENT OF THE TRAJECTORY OF AN INCHWORM WITH A LOW COST CAMERA

Yushi Takaki[1], Akihiro Torii[1], Ayaka Nakazato[1],
Suguru Mototani[1] and Kae Doki[1]
Department or Electrical Engineering and Electronics
[1] Aichi Institute of Technology
Aichi, Japan

INTRODUCTION

In recent years, the miniaturization and improvement of various devices such as mobile phones and home appliances are progressing. Many precision parts are used for these products, but each part is manufactured with the equipment for each process, which uses much energy and space. If an actuator with a multi-degree of freedom operation is used in a production system, the number of manufacturing equipment can be reduced. So, the installation space and energy consumption can be reduced as compared with the conventional large-scale production equipment.

In our laboratory we have developed the inchworms using piezoelectric elements and electromagnets [1][2]. For inchworm operation, the micro deformation of the piezoelectric element was used. It is suitable for positioning. However, the deformation of the piezoelectric element is very small, and it is impossible to realize a wide operating range. By repeating the micro motion generated by the piezoelectric element, a wide operating range was obtained. The electromagnet is used to hold the position of an inchworm. The electromagnet in the excited state holds the position, and the electromagnet in the non-excited state moves by the deformation of the piezoelectric element. This inchworm is aimed at application as a positioning device and is characterized as a no guide mechanism.

The inchworm using the electromagnetic force adheres to a magnetic substance such as iron. The position of the electromagnet in contact with the floor is moved by expansion and contraction of the piezoelectric element. While the electromagnet moves, it slides on the moving surface. The friction force generated on the contact surface is not known, and the inchworm, therefore, moves out of the given trajectory. We previously reported the method of measuring the position of an inchworm with an USB web camera, adjusting the amount of the expansion and contraction of the piezoelectric element, and correcting the position and orientation of the inchworm [3].

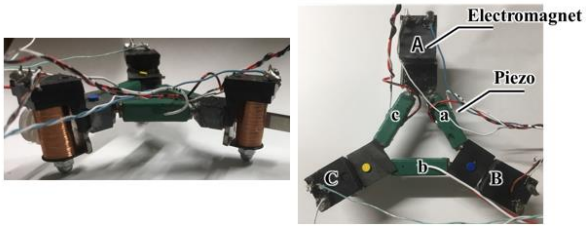

FIGURE 1. Inchworm

In this paper, we describe the control signal for correcting the movement locus of the inchworm, and discuss the constant of the position and orientation feedback control system.

INCHWORM

Figure 1 shows the fabricated inchworm. Three electromagnets and three piezoelectric elements are combined in an equilateral triangle shape. The inchworm has a delta structure, and three piezoelectric elements are attached to each side, and an electromagnet is attached to the connection point of the piezoelectric element. The electromagnets are A, B, C in the clockwise direction, and the piezoelectric elements are a, b, c. The electromagnet is in contact with the metal floor surface. The inchworm can move linearly and rotationally in a plane. The piezoelectric element used is AD0505D16F manufactured by NEC TOKIN Co. and extends by 17.4 μm (catalog value) against the applied voltage of 150 VDC. The electromagnet is an internal resistance of 300 Ω and an inductance of 800 mH. The size of the inchworm is 77 mm in width, 28 mm in height, and 67 g in weight. The size depends on the length (20 mm) of the piezoelectric element and the height depends on the length (25 mm) of the core of the electromagnet. A hemispherical metal

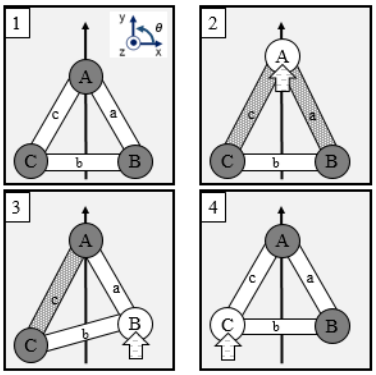

FIGURE 2: Principle of displacement in y-direction

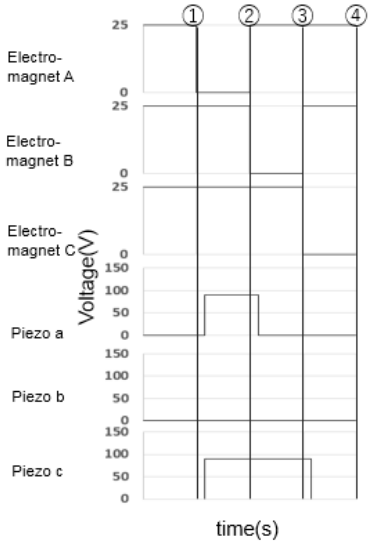

FIGURE 3: Control signals for y-displacement

is attached to the bottom part of the electromagnet.

The inchworm moves according to the principle of an inchworm. As an example, the movement in the y-direction is described. Figure 2 shows the principle of operation in the y direction, and Figure 3 shows the control signal. First, the piezoelectric element is contracted, the electromagnet A is in a non-excited state, the electromagnets B and C are in an excited state, and the piezoelectric elements a and c are extended. Next, the electromagnet A is in an excitation state and the electromagnet B the non-excitation state, and the piezoelectric element a is contracted. Finally, the electromagnet B is in an excitation state and the electromagnet C the non-excitation state, and the piezoelectric element c is contracted. By repeating this cycle, it is possible for the inchworm to move in the y

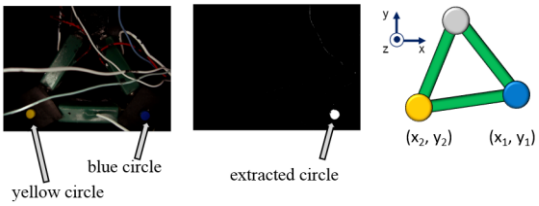

(a) Original image (b) processed image (c) coordinate

FIGURE 4: Image and coordinate of vision system

direction. It is also possible to move in x direction and rotate by replacing signal.

The environment during the operation and the position of an inchworm is detected by the USB web camera (3264 x 2448). In the measurement, light from outside is blocked, and a ring light is used as a light source. The frame rate of the camera is 15 fps (frames per second), but the image of the inchworm is captured every 0.35 s. Area of the image is 48.3 mm x 36.2 mm, the resolution of one pixel is approximately 14.8 μm. The captured image is processed by a computer (CPU: i7 - 7700, clock: 3.60 GHz, memory: 16 GB).

DISPLACEMENT MEASUREMENT

Figure 4 shows an example of a position detection. The circles (blue and yellow) shown in Figure 4a are attached to the electromagnet, and the position of the circle is detected. The circles are found by using circular Hough transform of Matlab. The radius and the x,y coordinate of the circles are calculated. The processing time is approximately 0.3 s. The blue circle in Figure 4a is extracted as shown in Figure 4b, and the center position is determined. Next, the position of the yellow circle is detected in the same process. As shown in Figure 4c, the positions of the circles are (x1, y1) and (x2, y2). The position of the inchworm is measured after one cycle is completed. Position detection accuracy was about 1 pixel from the previous research. [3]

POSITION AND ORIENTATION CORRECTION

This section describes the displacement when the inchworm is moved in the y direction. The voltage applied to the piezoelectric element is 90 V and the voltage applied to the electromagnet is 25 V. The control cycle was set to 2 s (control frequency 0.5 Hz).

The error when the inchworm moves in the y direction is classified into the following four cases. (1) $x>0$, $\theta>0$, (2) $x>0$, $\theta<0$, (3) $x<0$, $\theta>0$, (4) $x<0$,

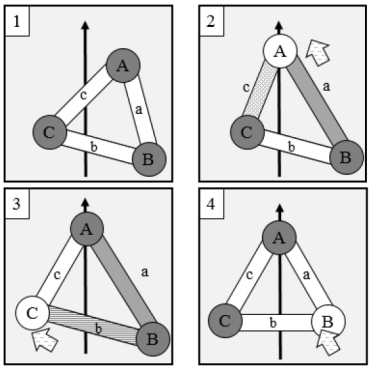

FIGURE 5: Compensation

θ<0. Figure 5 shows the case (2) where an error of the angle of rightward (θ< 0) and of the right side (x >0) with respect to the target moving direction in the positive direction of the y axis. The image measured by the USB camera is captured by the computer to detect the position and generates the control signal of the next cycle.

Figure 6 shows the flowchart of the control signal generation. The USB camera is used to measure the position of the electromagnets B and C, and the position of the inchworm is calculated by equations (1) - (3).

$$x = \frac{x_1 + x_2}{2} \quad (1)$$

$$y = \frac{y_1 + y_2}{2} \quad (2)$$

$$\theta = \tan^{-1}\frac{y_1 - y_2}{x_1 + x_2} \quad (3)$$

The position is measured, after the state 4 in Figure 3 is completed. Next, the applied voltage V_b of the piezoelectric element b for position correction of the inchworm is determined. For correcting in the x-axis direction, voltage is applied to the piezoelectric element b, and the extension and contraction of the piezoelectric element b is used. The voltage applied to the piezoelectric element b is an absolute value of a value proportional to the error x in the x-axis direction and the time integration of the error in x. Let the former the constant K_{xP} and the latter the constant K_{xI}. Furthermore, the applied voltage V_a of the piezoelectric element a and V_c of the piezoelectric element c for orientation correcting of the inchworm are determined. In Figure 5, the inchworm is wrongly turned to right (θ< 0). Therefore, in order to correct the inchworm to the left, the position of the electromagnet A is directed to left. For this purpose, the extension of the piezoelectric element a for moving the electromagnet A in the non-excited state is larger

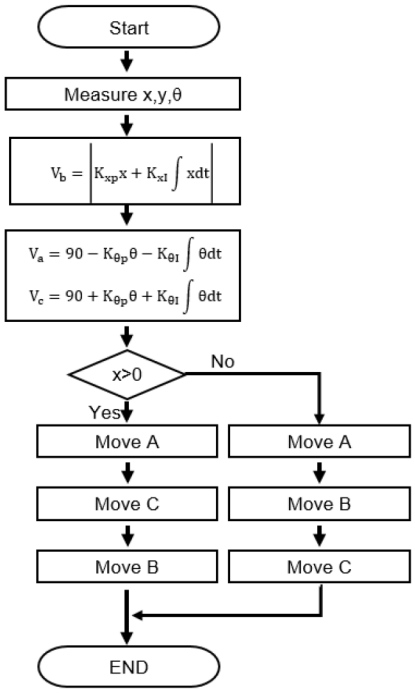

FIGURE 6: Flowchart of compensation of control signal

than that of the piezoelectric element c, and the electromagnet A is moved in the left direction. In the original control signal, the applied voltage to the piezoelectric element a and the piezoelectric element c is a square wave of 0 V or 90 V. When an error occurs in the path of the inchworm, the applied voltage is adjusted. The voltage applied to the piezoelectric element a and the piezoelectric element c increases or decreases according to the error angle θ and the integration of angle θ. Let the former the constant $K_{\theta P}$ and the latter the constant $K_{\theta I}$.

CONTROL PARAMETERS

Equations (4)-(6) shows the determination the applied voltages of the piezoelectric elements a, b, and c.

$$V_b = \left|K_{xp}X + K_{XI}\int Xdt\right| \quad (4)$$

$$V_a = 90 - K_{\theta p}\theta - K_{\theta p}\int \theta \quad (5)$$

$$V_c = 90 + K_{\theta p}\theta + K_{\theta p}\int \theta \quad (6)$$

X: error in x-direction θ:error attitude angle

The maximum applied voltage of each piezoelectric element is 150 V. The optimum values of the proportional constants K_{xP}, K_{xI}, $K_{\theta p}$, $K_{\theta I}$ in the equations (4)-(6) are examined. The constants K_{xP} and K_{xI} affect the error in x direction. The constants $K_{\theta p}$ and $K_{\theta I}$ affect the angle θ.

The inchworm repeats the displacement 100 times in the flowchart shown in Figure 8 in the y direction. During the displacement, the average of the error in x-direction and that in the angle θ, the movement is evaluated. The smaller the average is, the higher the performance of the inchworm realized. From the preliminary experimental results, the constants are determined as follows; $K_{xP} = 2$, $K_{xI} = 0.2$ $K_{\theta p} = 2$ $K_{\theta I} = 0.2$.

Figure 7 shows the experimental results obtained by $K_{xI} = 0.2$, $K_{\theta p} = 2$, $K_{\theta I} = 0.2$. The constant K_{xP} varied from 0 to 5. Figure 8 shows the experimental results obtained by $K_{xP} = 2$, $K_{\theta p} = 2$, $K_{\theta I} = 0.2$. The constant K_{xI} varied from 0 to 0.5. From Figures 7 and 8, the smallest average of the error in x-direction is 10.4 μm, which is obtained by $K_{xP} = 2$, $K_{xI} = 0.2$, $K_{\theta p} = 2$, $K_{\theta I} = 0.2$.

Figure 9 shows the experimental results obtained by $K_{xP} = 2$, $K_{xI} = 0.2$, $K_{\theta I} = 0.2$. The constant $K_{\theta p}$ varied from 0 to 5. Figure 10 shows the experimental results obtained by $K_{xP} = 2$, $K_{xI} = 0.2$, $K_{\theta p} = 2$. The constant $K_{\theta I}$ varied from 0 to 0.5. From Figures 9 and 10, the smallest average of the angle θ is 0.0007 deg, which is obtained by $K_{xP} = 2$, $K_{xI} = 0.2$, $K_{\theta p} = 1$, $K_{\theta I} = 0.2$.

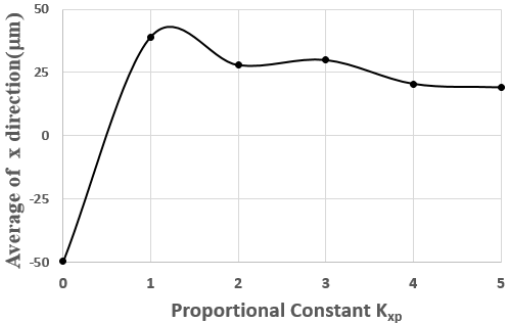

FIGURE 7. Average of error x-direction when K_{xP} is varied

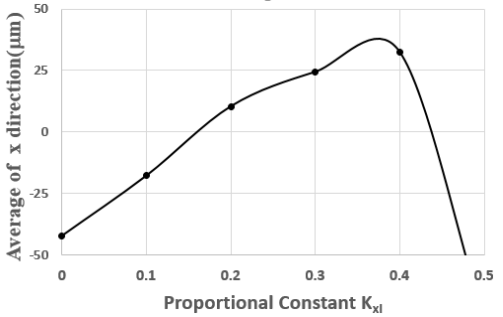

FIGURE 8. Average of error x-direction when K_{xI} is varied

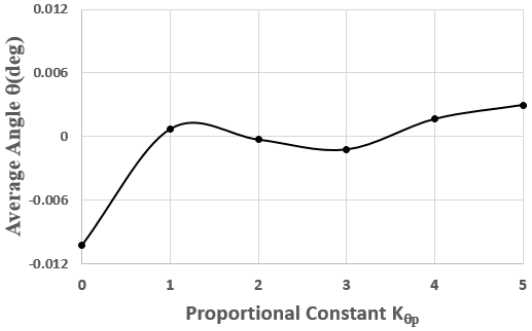

FIGURE 9. Average of error θ *when* $K_{\theta p}$ *is varied*

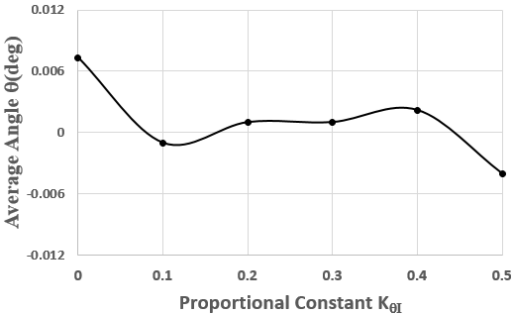

FIGURE 10. Average of error θ *when* $K_{\theta I}$ *is varied*

Summary

In this paper, we described the control signal for correcting the movement path of the inchworm and examined the proportional constants used in the position and orientation correction feedback.

REFERENCES

[1] Akihiro Torii, Masaaki Banno, Akiteru Ueda, and Kae Doki : "A study on the small-size self-proppeled stewart-platform", IEEJ Trans. EIS, Vol. 130, No. 4, pp. 660-667 (2010) (in Japanese)

[2] Akihiro Torii, Yuta Mitsuyoshi, Suguru Mototani, Kae Doki, "Improvement of Linear Displacement of an Inchworm", IEEJ Trans. EIS, Vol. 137, No. 12, pp.1600-1606 (2017) (in Japanese) DOI:

[3] Akihiro Torii, Yushi Takaki, Suguru Mototani, and Kae Doki "Position measurement of a 3-DOF inchworm using a vision system", euspen's 18th International Conference & Exhibition IT June 2018 pp.203-204

Multiple-indicators improvement of silicon cylindrical optics polishing for high energy laser

Ye Tian[1,2,4], Feng Shi[1,2,4,*], Yifan Dai[1,2,4], Xiaoqiang Peng[1,2,4], Kai Han[3], Yaoyu Zhong[1,2,4], Furen Li[1,2,4], Chi Luo[1,2,4]

[1]College of Intelligence Science, National University of Defense Technology, Changsha, China

[2]Ultra-precision engineering key laboratory of Hunan province, Changsha, China

[3]College of Advanced Interdisciplinary Studies, National University of Defense Technology, Changsha, China

[4]Laboratory of Science and Technology on Integrated Logistics Support, National University of Defense Technology, Changsha, China

INTRODUCTION

The high energy laser(HEL) system is one of the best unifications of scientific research and engineering application. They are widely utilized in our society and becoming increasingly significant in some representative national strategic and tactical applications[1].

In HEL applications, fabrication quality of optical elements significantly influences the performance of total system in several aspects. For instance, the output beam quality is dictated by element precision[2]. The highest output energy and working thermal stability are limited by the laser energy absorption coefficient[3, 4]. Even the laser systems size and capital cost are closely related to the effective aperture ratio. Especially for those cutting-edge physical programs, the progress of optical element performance significantly accelerates the technique development [5, 6]. With the laser energy climbing, much stricter requirements of element precision and performance are brought.
In this paper, we will discuss three main aspects of application performance: A. Element precision, which is evaluated by power spectrum density (PSD) of spatial error; B. Laser performance, which is usually evaluated by laser energy absorption coefficient; C. Aperture ratio, which is the ratio of effective to physical aperture.

However, in practical engineering, these aspects need to be exactly further divided as many fabrication indicators, shown in Table 1. Only if all the indicators would be raised to a high level, the requirement of HEL systems could be fulfilled.

Table 1. The relationship between system performance and fabrication indicators

Performance of laser system	Requirement of optics	Fabrication indicators
Statistic beam quality	PSD	1. Low-spatial frequency error 2. Mid-spatial frequency error (MSFR) [7, 8] 3. High frequency error (Roughness) [9]
Upper limit of laser energy, Thermal stability, Dynamic beam quality	Exogenous energy absorption coefficient	1. surface/subsurface defects(scratches, pits, etc.) [10,11] 2. Micro-structures [12, 13] 3. Mid&high-spatial frequency error [14] 4. Impurities
Size and Aperture	Effective aperture ratio	Edge effect range [15]

Utilizing modern optical fabrication technology, it is easy to pursue a single indicator to an ultra high level. But it becomes a tough task to achieve all the indicators in high level for one single element. Processes combination is the most possible solution. But in this way, due to conflicts between processes, the ceiling of each indicator is inevitably decreased.

The problem becomes more challenging when the multiple-indicators fabrication need to be realized on a silicon cylindrical element substrate. Firstly, it is a hot issue to realize scratch-less and ultra-smooth surface on silicon substrate.[16] Secondly, cylinder is a non-rotationally symmetric surface for which current

pad-rotating smoothing process cannot be adapted. Since in a micro zone of cylinder, the curvature radius is changing dramatically(from surface radius to infinity) during a rotation period. MSFR cannot be restrained and will limit the final precision of the computer-controlled optical surfacing (CCOS) process.

To fabricate a high level multiple-indicators required silicon cylindrical optic, we make combination, promotion and optimization of several processes and achieve this goal.

Improvement of MSFR by cylinder smoothing
Traditional cylinder polishing is based on the combination of reciprocate motion along the section curve and the generator. The figuring effect is indeterminable and largely depends on the experience of the operator. Although precise cylinder smoothing and polishing can also be realized in traditional ways, modern CCOS method can be better expanded to parabolic, elliptic and hyperbolic cylinders.

However, small tool CCOS generates more serious MSFR residual.[17] MSFR worsens beam quality and limits the improvement of low-spatial frequency error. To restrain it, pad-rotating smoothing technology has been applied[18]. But the current smoothing cannot be applied to non-rotational symmetrical surface, such as cylinders.

We propose a pad cylinder smoothing solution, which is based on the research in Ref. [19]. Smoothing has two principles: 1. The ability of reducing existing MSFR. It requires stable pressure difference in the corresponding mid-spatial micro zone during material removing process. 2. The ability of generating no new MSFR. This depends on the wide frequency range of removal function and high entropy tool path.

To fit the principle 1 on cylinder surface, firstly, we apply a cylinder pad and change its motion from planetary motion to revolution only. Then, the pad-hinge-spindle system is modified to keep the pad generatrix being always parallel to the work piece generatrix. Thirdly, Semi-rigid pad is utilized to obtain stable pressure difference in the micro zone. To fit the principle 2, we apply several polishing pads in different size and use pseudo random tool path.

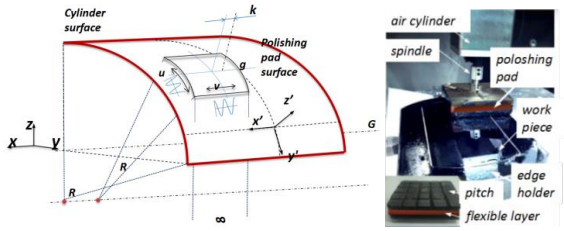

Fig. 1. (a)Cylindrical pad polishing motion (b) The practical equipment

As shown in Fig. 1(a), the pad motion is resolved into three parts: u(a sine reciprocating along the circumference), v (a sine reciprocating along the cylinder generatrix) and scanning. The modified pad motion is realized by a 5-axis machine tool. The separate control of those three motions can realize deterministic material removal in various styles.

A convex silicon cylindrical substrate is polished by this smoothing way, shown in Fig. 1(b). The surface error is measured by CGH-based subaperture stitching method, shown in Fig.2. The cylinder smoothing decreases Zernike residual from 161nm to 55.6nm. Correspondingly, the 2-division PSD curve shrinks obviously in the mid-frequency range from 0.3mm-1 to 2mm-1, shown in Fig. 3.

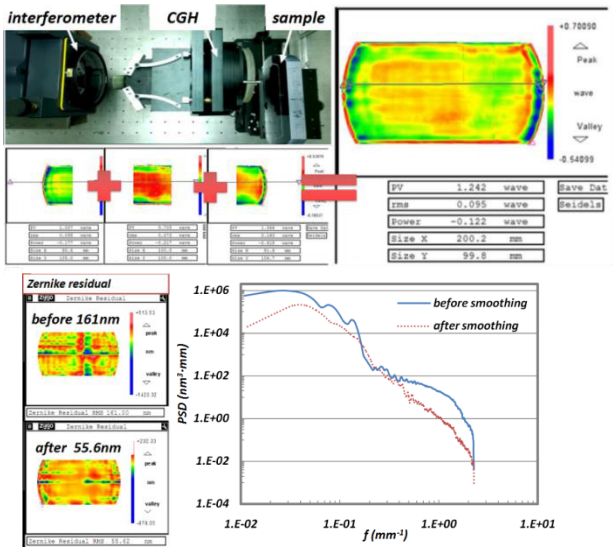

Fig. 3. Fig. 2. CGH-based subaperture stitching measurement [20]
Improvement of MSFR by smoothing

Improvement of surface quality (high-spatial frequency error and surface defect)
The silicon elements are usually polished using silicon dioxide colloid polishing fluid (particle size is 50nm). Any particle in micrometer scale is

possible to generate scratches and ruin the surface quality[21].

Since optical pitch is harder than other polishing pad materials, it is often utilized in the smoothing process.[18, 19] When the ambient large particles have same concentration, pitch pad is much more easier to generate scratches than other pad materials.

To obtain scratch-less surface, we reference bowl feed polishing[22] and combine work piece immersing polishing with cylinder smoothing. The work piece is submersed under polishing fluid, shown in Fig. 4.

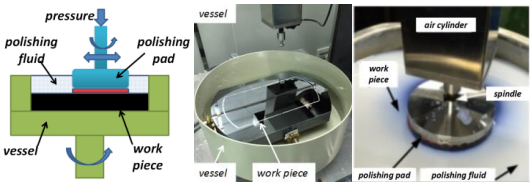

Fig. 4. Immersion polishing equipment

In this way, on one hand, the large particles in fluid are isolated from the polishing interface. Because the surface energy of nano silicon dioxide particles is higher than that of micrometer particles. To be the lowest surface energy status, the solid-colloid interface is tend to absorb nano particles rather than those in micrometer scale.[23] Besides, the nano particles are also agglomerated on the surface of micrometer particles and wrap them, illustrated in Fig. 5(a). Meanwhile, the polishing fluid also isolates the work piece from the outer atmosphere, especially from large particles in air. Thus, scratches induced by large particles are effectively restrained.

We combine this immersion solution with cylinder smoothing and obtain high level surface quality on the convex cylinder surface. In a dark room observation, no scratch is found on the immersion polished surface. Another observation is also conducted after a 30 seconds HF etching, to ensure no subsurface defect is buried under the oxidation layer of SiO_2. The comparison of scratches between two process status is shown in Fig. 5(b).

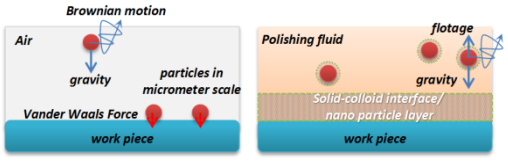

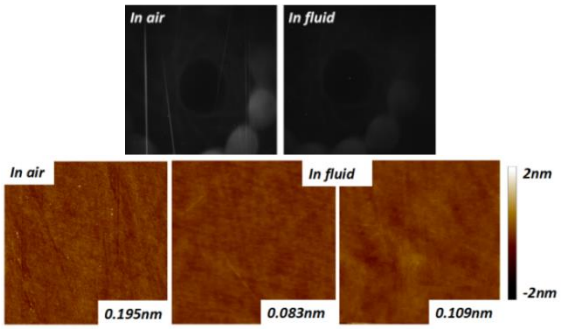

Fig. 5. Improvement of scratches by immersion polishing(a) Particles are excluded from polishing interface;(b) Surface defect contrast between polishing in air and fluid Fig. 6. HSFE(roughness) results

One the other hand, the environment parameters, such as temperature and pH value, of polishing interface can be controlled elaborately as well as repeatedly. On the same convex cylinder surface, the roughness maintains around RMS 0.1nm (Bruker®, AFM, AnsysScan, 10μm×10μm zone), shown in Fig. 6.

Besides, with the recycling and filter, the consumption of fluid is similar with common jet polishing processes.

Improvement of full frequency range spatial error

We apply the combined process of immersed deterministic cylinder polishing and ion beam figuring (IBF) to improve the full frequency range spatial error. Silicon surface morphology transformation is sensitive to parameters of ion beam, especially to incident angle and beam energy[24]. A self-established 5-axies IBF machine tool is utilized to figure the surface error, shown in Fig. 7.

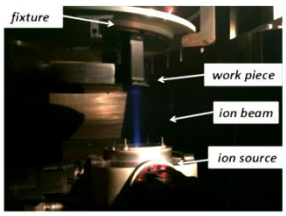

Fig. 7. IBF process

The iteration of smoothing and IBF improves low&mid-spatial frequency error of the silicon cylindrical substrate. The final measurement results are shown in Fig. 8.

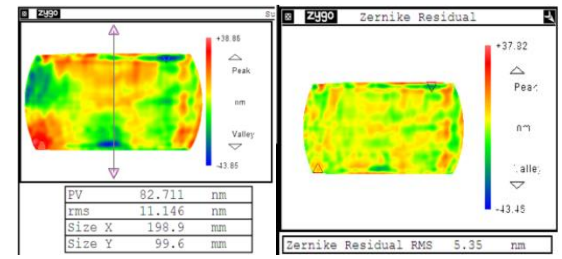

(a)Reflection wave front (b)Zernike residual

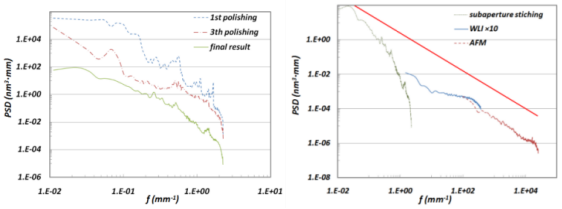

(c)PSD evolution

Fig. 8. Final precision results

And the full range PSD curve is shown in Fig. 9. The red line is the PSD requirement of cylindrical surfaces for a certain high energy laser system.

Fig. 9. PSD result of full range spatial error (The blue line is measured by a Zygo® Newview 700 white light interferometer, 10x.)

Improvement of laser energy absorption coefficient

Exogenous absorption precursors, listed in Table 1, are induced by fabrication processes and environment. Since they generate unwanted additional energy absorption, precursors need to be restrained before coating[25]. The improvement of mid&high-spatial frequency error decreases the absorption. Besides, scratch is also controlled during polishing.

Aiming at reducing micro-structures and impurities, HF+IBE is chosen as the post process. According to our previous research, in the subsurface of polished mono-crystalline silicon substrate, exists convex micro-structures. Those micro structures worsen laser performance of optics by raising laser energy absorption. As the result of that, the final IBE process (should be kept in a relatively lower ion energy) needs to remove surface material as deep as 1.5μm[12].

Infrared laser irradiation and calorimeter test[26] are conducted on three Φ50mm silicon samples, S1, S2 and S3. S1 and S2 are immersion polished, while S3 is polished in air (AFM roughness RMS value is around 0.2nm, a few scratches). S1 is also post-processed by HF+IBE. They are all high reflection coated in a same deposition process. The temperature evolution during laser test is shown in Fig. 10.

After calculation, absorption coefficients are 30ppm, 106ppm and 127ppm, for S1, S2 and S3, respectively. The improvements of immersion polishing and post-process are both distinct.

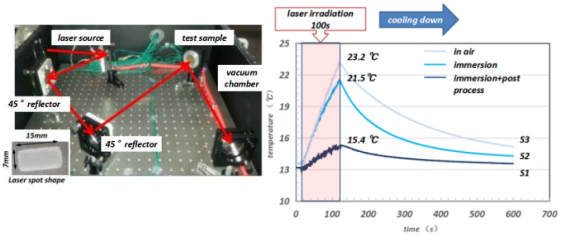

Fig. 10. Laser test system (left) and temperature curve (right).

For instance, in a certain high energy laser application, 100ppm absorption coefficient leads to thermal deformation 0.2μm per single element in 10 seconds. However, once the coefficient fall down to 30ppm, the deformation will decrease to less than 0.1μm per element. The deformation of the entire system wave front can reduce to less than 1μm.

The realization of full aperture

The optical effective aperture ratio partly decides the size of entire system and auxiliaries. Its importance is much more evident for the optics in high energy laser systems, since they are normally fixed in vacuum or special atmosphere chambers.

However, the edge effect in polishing shrinks the effective aperture by few millimeters. It is clearly shown in Fig. 2, the surface figure is surrounded by a circle of steep valley-peak structure. The circle is as wide as 8-15mm and contributes the highest peak-valley error value of the total surface. The upper limit of allowed system laser beam width is only 85-92% of the element physical size.

We solve this problem by two optimization. In the theoretical way, removal function compensation[27] is utilized to obtain accurate dwell time distribution in edge area. In the engineered way, edge supporting assistant is skilled applied to enlarge the scanning zone of polishing pad and, meanwhile, to increase the stability of pad motion in the edge area. As the

result, almost no width is effected by the edge effect each side. The effective aperture of this Φ200mm cylindrical element reaches 198.9mm (the actual physical surface is Φ199mm, excluding a 0.5mm chamfering each side). The ratio of effective aperture reaches 99.4%.

Full aperture fabrication has great engineering significance. It gives researchers more room in the innovation of lightweight and miniaturization design of systems.

In this paper, a combined process is proposed, which is based on cylinder smoothing, immersion polishing, and IBF. To appropriate the non-rotational symmetrical cylindrical surface, we modify pad motion of smoothing. The spatial error is controlled in the full frequency range. For a Φ200/R962.3mm convex cylinder, the surface error RMS value is 12nm, Zernike residual is better than 6nm, roughness RMS value is around 0.1nm @10×10μm. By introducing fluid immersion method, the mono-crystalline silicon cylindrical surface is scratch-less and ultra smooth. Besides, the post-process, which is combined by IBE and HF acid etching, decreases laser energy absorption coefficient from 127ppm to 30ppm in the working wavelength. Last but not least, all the indicators are realized in the full physical aperture, Φ198.9mm/Φ200mm.

Utilizing higher level elements will effectively optimize beam quality, laser resistance, thermal stability and life time of the entire system. Meanwhile, this progress of fabrication also gives more room for designers and helps pushing the high energy laser technology to a higher peak.

Funding
National Natural Science Foundation of China (NSFC) (51675526, 91323302, 91523101);

Acknowledgment
We firstly appreciate J. M. Linghua Zhang and Miss. Xia Tian for their help and support. We thank Engineer Jianghua Qian, Jie Ding, Shun Song, Jumei Cao and Xu Liu for their help in sample preparation. And we appreciate Dr. Baozhu Yan and Dr. Xiaoting Fang for their help in experiment.

REFERENCES

[1] Directed-energy weapon, https://en.wikipedia.org/wiki/Directed-energy_weapon.
[2] E. L. Church and P. Z. Takacs, Appl. Opt. 32, 3344 (1993).
[3] Y. Y. Du, J. Z. An, X. J. Shu, Hi. Pow. Las. & Part. Bea., 20, 1333-1338 (2008).
[4] Q. S. Lu, Z. J. Liu, Hi. Pow. Las. & Part. Bea. 2, 303-308 (1993).
[5] S. Du, Doctor thesis (Changsha, China, National University of Defense Technology, 2011), p. 1,p. 96.
[6] Sparks M. J. Appl. Phys. 42, 5029-5046 (1971).
[7] R. N. Youngworth, B. D. Stone, App. Opt., 39, 2198-2209 (2000).
[8] J. M. Tamkin, T. D. Milster, Appl. Opt., 49, 6522-6536 (2010).
[9] J. E. Harvey, A. Kotha, Proc. of SPIE, 2576, 155-174 (1995).
[10] [10]. N. Bloembergen, Appl. Opt. 12, 661 (1973).
[11] F Shi, Y Tian, X Q Peng, and Y F Dai, Appl. Opt. 53, 598 (2014).
[12] Y Tian,F Shi, Y F Dai, X Q Peng, and Y Y Zhong , Appl. Opt. 56, 598 (2017).
[13] F. Shi, Y. Zhong, Y. Dai, X. Peng, M. Xu, T. Sui, Opti. Exp. 24, 20842-20854 (2016).
[14] J. M. Elson and C. C. Sung, Appl. Opt. 21, 1496 (1982).
[15] D. W. Kim, W. H. Park, S. Kim, and J. H. Burge, Opt.Exp. 17, 5656-5665 (2009).
[16] Feng X, Al E A E. Scie. 37, 1504 (2006).
[17] R. A. Jones, and W. J. Rupp, Opti. Engi., 30, 1962-1968 (1991).
[18] D. W. Kim, W. H. Park, H. K. An, J. H. Burge, Opt. Exp., 18, 22515-22526 (2010).
[19] X. Nie, S. Li, F. Shi, and H. Hu, Appl. Opt. 53, 1020-1027 (2014).
[20] S. Chen, S. Xue, G. Wang and Y. Tian, Opti. Comm. 390 61 (2017).
[21] T. Suratwala, R. Steele, M. D. Feit, L. Wong, P. Miller, J. Menapace,. J. Non-Crys. Soli., 354, 2023-2037 (2008).
[22] R. W. Dietz and J. M. Bennett, Appl. Opt. 5, 881 (1966).
[23] K. Y. Li, (Harbin Institute of Technology press), 1998, p. 194.
[24] W. L. Liao, Doctor thesis (Changsha, China, National University of Defense Technology, 2016), p.78.
[25] M. Trost,S. Schröder,T. Feigl, A. Duparré, and A. Tünnermann, Appl. Opt. 50, C148–C153 (2011).

[26] M. Hass, J. W. Davisson, H. B. Rosenstock, and J. Babiskin, Appl. Opt. 14, 1128-30 (1975).
[27] H. Hu, Y. Dai, X. Peng, J. Wang, Appl. Opt. 50, 1220 (2011).

Ultra-Precise Closed-Loop Piezo Positioning with Interferometry for Nano Manufacturing Machines

Gregor Schindler[1] and Thomas Ch. Hirschmann[1]
[1]attocube systems AG, Munich, Germany

MOTIVATION

The downscaling reaches nearly every area in our life. Actual technologies are limited and for further improvements in precision new dimensions have to be made available. This trend is visible in multiple industries from microfabrication to precision semiconductor manufacturing machines. Requirements to metrology and drive engineering increases rapidly. attocube develops and produces ultra-precise sensors, drive technologies and combine these technologies together.

Positioners with closed-loop optoelectronic encoders have typically a resolution of 1 nm and a repeatability of around 50 nm. The optoelectronic encoders cannot be utilized in low temperature environment.

In this publication, we present a room temperature close-loop positioning system consisting of piezo-based positioners in combination with a Fabry-Pérot interferometer. The interferometer has a resolution of 1 pm and makes precise nano-positioning over 1 μm, up to 5 meter, with a repeatability of few nanometers possible.

STATE OF THE ART

For the measurements, shown in this publication an attocube standard positioner and interferometer are used.

Piezo-Based Positioner

attocube provides piezo based x-, y- and z-positioners as well as goniometers and rotators for different environments from ultra-high vacuum to low temperature environments. The positioners use the slip-stick principle to realize working ranges up to 50 mm with a minimum step size of 10 nm.

The slip-stick principle, shown in Figure 1, is distinguished by an applied a sawtooth shaped pulse is applied to the piezo. During the phase of the slow flank, the movable table sticks to the drive element and is moved over a distance Δx. By applying a steep flank of the voltage pulse to the piezo, the drive element is accelerated very rapidly over a short period of time, so that the inertia of the movable table overcomes friction. This way, the table disengages from the accelerated drive element and remains nearly non-displaced. The typical minimum step size for positioners is 50 nm at room temperature and about 10 nm at cryogenic temperatures. By applying a DC voltage, it is possible to obtain a sub-step-size resolution of 10 nm. This sub-step-size is limited by the resolution of the reference system.

The positioners be can used with included resistive or optoelectronic reference systems for closed-loop positioning. The repeatability of such the optoelectronic sensors achieves 50 nm with a resolution of 1 nm.

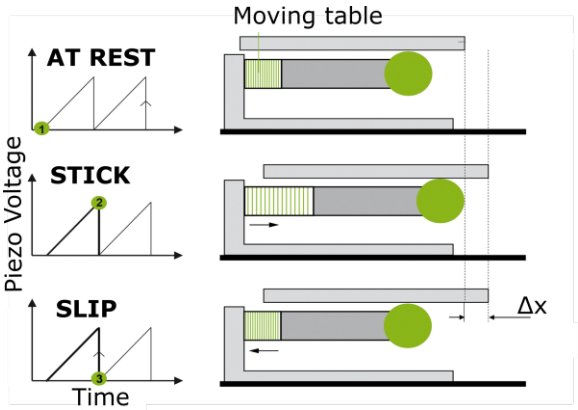

FIGURE 1. Function of the slip-stick piezo positioner for high working ranges with also high precision with nanometer repeatability. During the phase of the slow flank the movable table sticks to the drive element and is moved over a distance Δx. By applying a steep flank of the voltage pulse to the piezo, the drive element is accelerated very rapidly over a short period of time, so that the inertia of the movable table overcomes friction. With this method, the table disengages from the accelerated drive element and remains nearly non-displaced.

Industrial Displacement Sensor

attocube's Industrial Displacement Sensor (IDS) is a Fabry-Pérot interferometer-based sensor [1]. To measure displacements down to the picometer regime and up to velocities of 2 m/s. Moreover, it is also possible to measure on target materials with reflectivity from 4 % like glass to high reflectivity materials like aluminum or gold. Working distances and angular tolerances depend on the reflectivity as well as the used sensor head. With a corner cube working distances up to 5 meter can be realized.

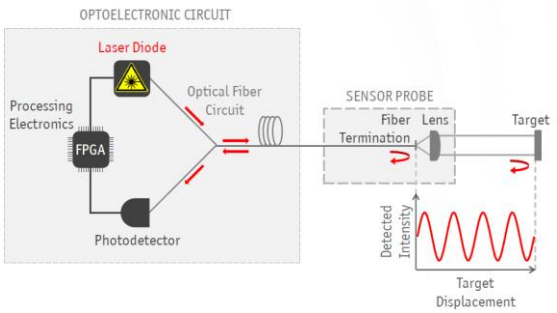

FIGURE 2. Working principle of the Industrial Displacement Sensor. Using the back reflection of the fiber as reference signal, simplifies alignment and reduces measurement errors.

Figure 2 shows the working principle of the IDS. The back reflection of the fiber is used as reference, thus only the alignment of the measurement signal is necessary.

To avoid long term drifts of ambient conditions an Environmental Compensation Unit (ECU) measures temperature, pressure and humidity and calculates the actual refractive index.

ULTRA HIGH-ACCURACY CLOSED-LOOP POSITIONING

The above presented positioner and IDS are combined to a closed-loop system. First the setup and then the measurement results are presented, completed with two application examples.

Measurement Setup

Closed-loop positioners exist with different encoders. The optoelectronic encoder with a position resolution of 1 nm and a repeatability of 50 nm is used at attocube systems. The IDS additionally offers the possibility to measure on the true position of the sample (point of interest) and not on the individual linear stage.

The setup consists of attocube's ECSx3030 positioner operated with the AMC100 position controller and the IDS with a D4/F17 sensor head measuring on a mirror target on the positioner. Figure 3 shows a schema of the used setup, which is realized on an optical table to reduce environmental influences.

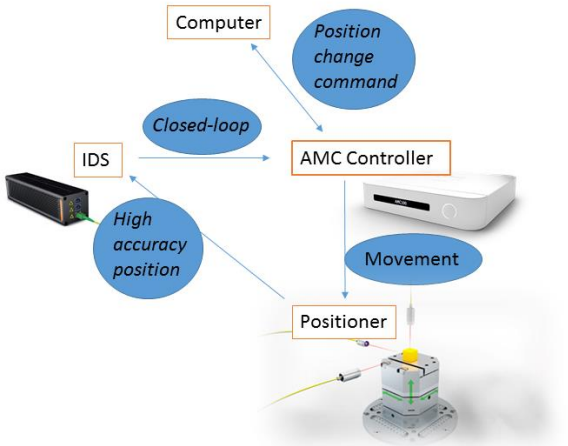

FIGURE 3. Setup for real-time positioning tracking of a x-positioner system and extendable with y- and z-direction. The yellow cube presents the point of interest, where the sample is placed.

The position of the positioner stage is updated with 1.63 kHz and the data was recorded with 50 kHz bandwidth. For high bandwidths the noise at room temperature due to environmental influences is the limitation for precise sensing. Reducing the environmental influences by isolating the system, the noise can be further minimized. The measured data are sampled down to 625 Hz by average. The following measurement results show both signals, the 50 kHz and the 625 Hz.

Measurement Results

The measurement starts at a reference point set to zero. Then 1 μm steps are executed every 10 seconds. Figure 4 depicts all position steps as well as the zoom-in of each relatively constant position. The averaged data shows that a repeatability of 2 nm at room temperature is possible.

Next, we present a measurement with about 1 nm steps. In Figure 5, are ten 1 nm steps given by command and 9 nm are recorded by the IDS. Position steps with 0.9 nm in

average are visible in the 50 kHz signal and additionally highlighted in the 625 Hz averaged signal.

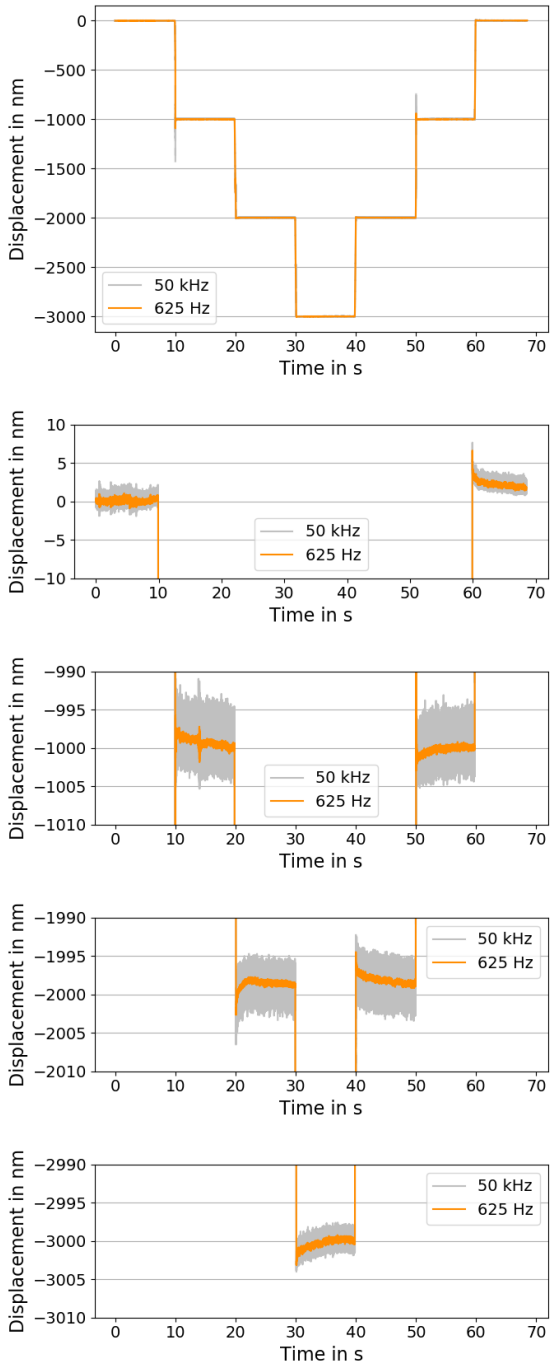

FIGURE 4. Measurement with 1 µm steps and a repeatability of 2 nm. The data was recorded with 50 kHz and then sampled to 625 Hz by an average function. The zoomed pictures show the 2 nm repeatability of the positioner.

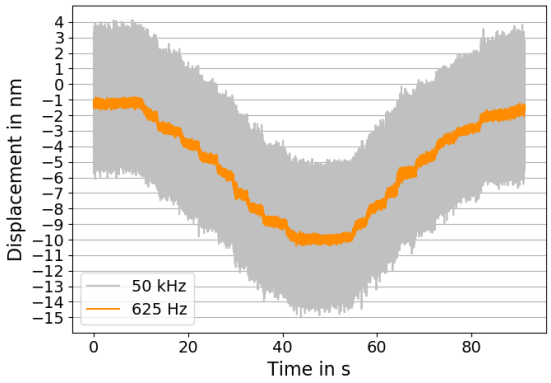

FIGURE 5. Measurement result of given 1 nm steps with the closed-loop system at room temperature.

In Summary

With the external closed-loop interferometer, it is possible to positioning targets with 2 nm repeatability and to realize about 1 nm steps at ambient lab conditions. The presented systems can also be used in environments like ultra-high vacuum and low temperature. Changing the environment to ultra-high vacuum even smaller steps are possible. E. Nazaretski [4] presented 0.5 nm steps in a hard X-ray microscope.

Further Applications

The closed-loop positioning system offers the possibility of high accuracy target positioning. This can be used in precision engineering as well as microscopes like Atomic-Force Microscope (AFM) or Confocal-Microscope (CFM).

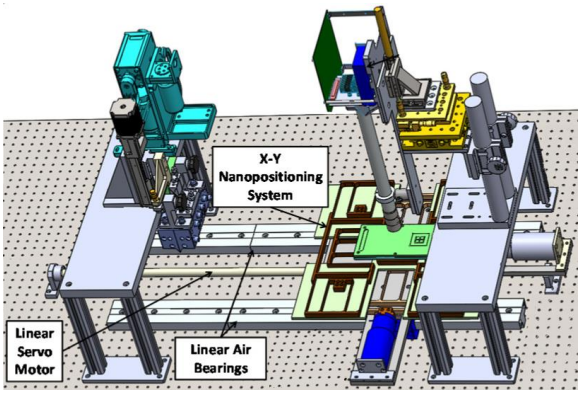

FIGURE 6. Application of a closed-loop positioning system realized by Roy et al. The Micro-scale Selective Laser Sintering Tool very small tolerances are needed in this application.

In the ASPE talk “Sub-system Level Overview of Micro-scale Selective Laser Sintering Tool” presented by Roy *et al.* [2] presents the innovative method for manufacturing integrated circuit package building blocks (*e.g.* microcontrollers) is the so-called micro-scale selective laser sintering (*μ*-SLS). Additive manufacturing is state-of-the art in many engineering applications requiring accuracy in the micrometer range. However, the production of integrated circuit packages is in dimensions on the order of a few micrometers and need smaller tolerances than conventional additive manufacturing methods can provide.

Another possible application for closed-loop positioners is demonstrated by Hirschmann [3] for surface morphology or quality control. A cylinder with 200 *μ*m diameter is rastered in x- and y-direction by a closed-loop position system. Measuring the displacement in z-direction it is possible to reconstruct the surface of the cylinder, which is shown in Figure 7 as an example.

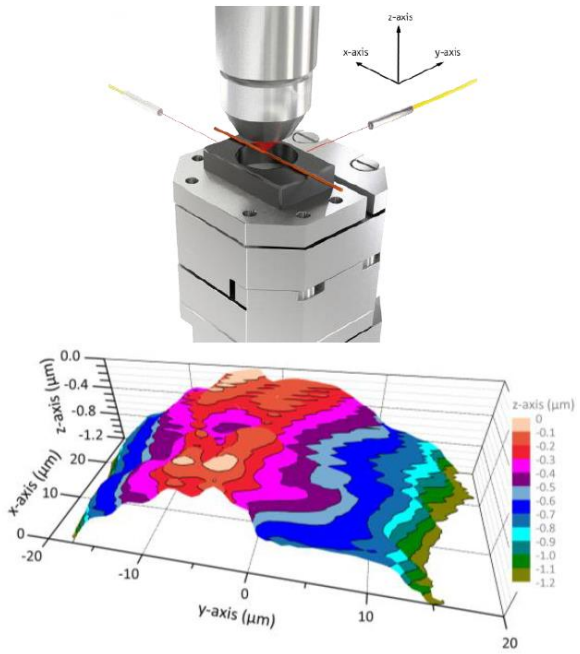

FIGURE 7. A metal cylinder was mounted on a 3D stack consisting of positioners and precision scanners. The cylinder’s surface was measured from above (z-axis), all while its position (x- and y-axes) was simultaneously tracked. 3D color plot showing the surface morphology of a 200 µm diameter cylinder. Each color represents a 100 nm height step in z-direction [3].

CONCLUSION

Measuring on the target itself or the target holder gives the advantage of knowing the exact position of the target up to picometer resolution depending on the environment.
Using three sensors instead of one per axis allows to additionally determine angular changes of the target.

QUESTIONS

Please direct any questions to Gregor Schindler at attocube system AG headquarters. His contact information is listed below.

- Telephone: +49-89-420 797-0
- Email: info@attocube.com

REFERENCES

[1] Thurner K, Quacqarelli F P, Braun P-F, Dal Savio C and Karrai K. Fiber based distance sensing interferometry, Applied Optics 2015; 54: 3051-3063.
[2] Nilabh K Roy, Chee S Foong, Michael A Cullinan. Design of a Micro-scale Selective Laser Sintering System, 27th Annual International Solid Freeform Fabrication Symposium, Austin, Texas, USA, 2016.
[3] Hirschmann T Ch. Ultra-precise position and vibration analyses using Fabry-Pérot interferometry, euspen’s 17th International Conference & Exhibition, Hannover, 2017.
[4] Nazaretski E, Lauer K, Yan H, Bouet N, Zhou J, Conley R et al. Pushing the limits: an instrument for hard X-ray imaging below 20 nm, Journal of Synchrotron Radiation, March 2015; 2: 336-341.

COMPENSATING FILM STRESS IN THIN MIRRORS USING ION IMPLANTATION

Brandon D. Chalifoux[1], Youwei Yao[2], Kevin B. Woller[3], Ralf K. Heilmann[2], and Mark L. Schattenburg[2]
[1]Department of Mechanical Engineering
[2]Kavli Institute for Astrophysics and Space Science
[3]Plasma Science and Fusion Center,
Massachusetts Institute of Technology, Cambridge, MA USA

INTRODUCTION

For optical applications where mass is constrained, such as in space telescopes, the use of thin mirrors may allow larger collecting area or lower cost than thick mirrors. In addition to benefiting from mass reduction, X-ray telescope mirrors have a nested architecture as shown in Figure 1, in which thin mirrors allow larger collecting area. The Lynx X-ray Observatory, which is being studied as a concept for the 2020 NASA Decadal Survey [1], will require thin accurately-figured mirrors with a high-reflectivity X-ray coating, in order to provide the large collecting area and high angular resolution requirements that enable the mission to achieve its science objectives. The required mirrors will be approximately 0.5 mm thick and have axial slope errors close to 0.1 arc-second RMS.

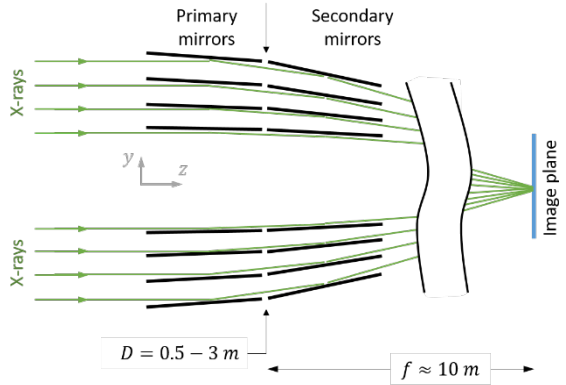

FIGURE 1. Diagram of an X-ray telescope, showing nested shells (primary and secondary mirrors). Thin mirrors are critical for building large-aperture X-ray telescopes.

Thin mirrors are more difficult to fabricate than thick mirrors, but recent advances, such as magneto-rheological finishing (MRF) and ion-beam figuring (IBF), have made figuring thin mirrors possible. For example, Zhang, *et al.* [2] have successfully fabricated thin silicon mirrors using polishing [3] and IBF [4] that are rapidly approaching the accuracy requirements of Lynx. However, the mirrors must be coated with thin high-Z metal films to meet reflectivity requirements, and thin films typically have significant intrinsic stress.

For X-ray telescope mirrors, after the mirror substrate meets the optical requirements, a thin reflective film, such as 20 nm iridium, must be deposited on the mirror surface to achieve the desired X-ray reflectivity. Such films often have large intrinsic stress, which can deform thin mirror substrates by hundreds of nanometers or more. In addition, this intrinsic stress is often neither sufficiently uniform nor repeatable. While magneto-rheological finishing (MRF) and ion-beam figuring (IBF) are effective methods of fine figuring of thin mirrors, both must be applied before the reflective films are deposited.

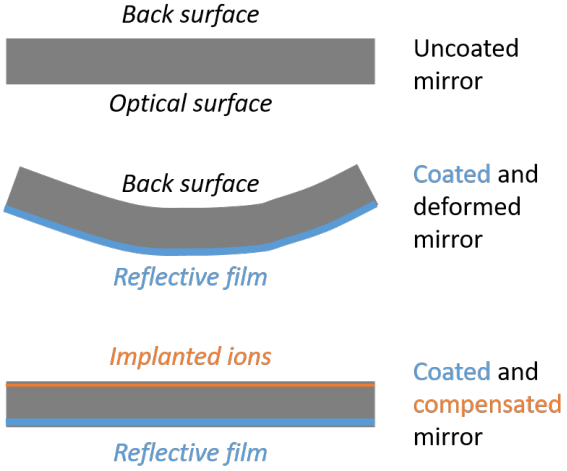

FIGURE 2. Film stress compensation concept. A mirror with excellent figure must be coated, which causes deformation. Compensation allows restoration of the excellent figure, decoupling coating optical quality from stress.

There are numerous methods under development to address the film stress issue. The simplest approach would be to adjust deposition process parameters to achieve stress-free coatings, but low-stress coatings usually have higher film roughness or reduced film density [5] [6], neither of which are desirable for high reflectivity. Film stress compensation, illustrated in Figure 2, is a process where another stressed film is used to balance the reflective film stress. This allows the optical properties of the film to be decoupled from the film stress. For thin mirrors especially, this significantly enhances the possibility of developing a recipe that allows mirrors to meet both reflectivity and figure requirements.

Balancing tensile films with compressive films [7], or balancing front-back coatings [8] are under development, but non-repeatability and non-uniformity of the film stress may limit these approaches. Spatially-varying film stress compensation may be achieved by varying substrate bias during deposition of a back-side coating [9], patterning a stressed back-side coating [10], or by ion implantation stress generation [11] or ultrafast laser pulse stress generation [12] on the back of the mirror substrate.

Ion implantation is a technique for imparting controllable and stable stress into the surface of a substrate, which can be used to compensate for film stress after the reflective film is deposited. In this work, we demonstrate the use of ion implantation for film stress compensation, using flat silicon wafers. Ion implantation causes damage to the crystal lattice within the first several microns of the surface, which results in a reduced density in the implanted region, and a compressive stress [13]. Stress can also be generated in other materials such as various glasses [14].

EXPERIMENTAL OVERVIEW

In this work, we demonstrate this film stress compensation technique using five flat silicon wafers (0.52 mm thick, 100 mm diameter, <100> orientation, double-side polished). We measure a wafer's surface topography, then sputter about 30 nm of compressively-stressed chromium onto the front surface (chrome is a low-cost surrogate for iridium in these experiments). After re-measuring the wafer surface and calculating the film stress distribution, we use ion implantation on the back surface to restore the wafer surface to its original shape. We demonstrate restoration of the wafer surface shape close to our metrology repeatability of around 20 nm RMS.

For cost reasons, we chose to demonstrate compensation of chromium film stress, since chromium can easily be deposited at MIT with compressive stress comparable to that of iridium, a common X-ray mirror coating.

The coating and compensation process is outlined in Table 1. Some of these process steps are already required for making a mirror, so the three process steps that are specific to film stress compensation are highlighted in bold. The simplicity of this process may be beneficial for production of a large number of mirrors.

TABLE 1. Film stress compensation process. The process steps that are not otherwise required for making a mirror are in bold.

	Process step	Details
1	Measure	Shack-Hartmann
2	Coat	Sputter 30 nm Cr
3	Anneal	2 hr, 200 °C
4	Measure	Shack-Hartmann
5	**Implant**	**2 MeV Si^{++} ions**
6	**Anneal**	**4 hr, 120 °C**
7	**Measure**	**Shack-Hartmann**

METROLOGY AND STRESS CALCULATION

We use a Shack-Hartmann surface topology metrology system, developed by Forest, *et al.* [15], with a 635 nm diode laser source. The measurement repeatability of a flat reference, as calculated by comparing measurements on sequential days over the course of two weeks, is 14.1 nm RMS. The metrology system is enclosed in a box to reduce air turbulence (which introduces noise into the measured wave front), but precision temperature control is not implemented. Room temperature variations are around ±2 °C. There is no vibration isolation.

The wafers are held in a low-stress mount developed by Akilian, *et al.* [16]. A careful procedure was developed to repeatably align wafers and to minimize distortion imposed by the mount. A reference silicon wafer, 0.4 mm thick, was measured daily over two weeks. The measurement repeatability of this wafer, as calculated by comparing measurements from sequential days (with one outlying measurement removed), is 18.4 nm RMS. The spectrum of this variation, in terms of normalized Zernike

polynomial coefficients[1], is included in Figures 3 and 4. The mount causes a small amount of deformation, especially astigmatism (Z_2^2).

The non-uniform stress distribution in a coating is calculated from the deformation caused by that coating. The integrated stress, which is the film stress integrated over the film thickness, is the only measurable quantity from the deformation field. We calculate the integrated stress in the chrome film and implanted layer using an analytical method [17]. Metrology noise makes the stress-distribution non-unique for a given measured deformation, and there are other sources of uncertainty in the stress distribution (such as substrate thickness variation). However, these errors are below our current metrology noise level.

COATING AND ANNEALING

The purpose of the coating, for this demonstration, is to provide a stable compressive stress that we can compensate with ion implantation. We did not measure reflectivity of the coating, but aside from annealing cycles, there is no reason ion implantation (applied to the back surface) would affect the coating (deposited on the front surface). Since the purpose of stress compensation is to decouple the optical properties of the film with the intrinsic stress, we are only concerned here with the stress.

Prior to coating, we removed any surface damage (i.e., residual damage from grinding and polishing) by growing 1.2 µm of wet thermal silicon dioxide at 1050 °C on each side of the wafers. This oxide grows partially into the silicon, and we then strip the oxide film using dilute hydrofluoric acid. This process caused an average of 34 nm RMS change in the wafer surface, dominated by astigmatism (Z_2^2) and spherical deformation (Z_2^0).

The five wafers were cleaned, then coated with chromium using a RF magnetron sputtering source. The background pressure was 1.5 x 10^{-5} Torr, the sputtering gas was Argon at 3 mTorr, and the sputter gun power was 150 W, resulting in a 0.095 nm/sec deposition rate. The wafers were RF biased with negative voltage during coating to ensure a compressive film stress (this occurs due to the atomic peening effect [5] [9]). A compressive stress is necessary for ion implantation since ion implantation in silicon also generates compressive stress. For reflective coatings, compressive stress is often associated with higher reflectivity [6] [18].

The coated wafers were annealed at 200 °C for 2 hours in a tube furnace with nitrogen flow, to stabilize the coatings [10]. This also tends to reduce the stress in the coatings, which others have used to reduce iridium film stress without affecting reflectivity [19]. The large variation in the mean integrated stress in the coatings, summarized in Table 2, was due to coating chamber calibration errors. This resulted in large run-to-run coating thickness variation. The Zernike spectrum of each wafer after annealing (excluding Z_2^0 since it is so large) is shown in Figure 3. Z_2^0 is included in Table 2. The Z_3^1 and Z_4^0 terms result from non-uniform integrated stress on the wafer [17].

TABLE 2. Coating spherical deformation and mean integrated stress.

Wafer	Coating Z_2^0 deformation [nm RMS]	Coating mean integrated stress [N/m]
1	383.5	-8.0
2	1623.3	-35.4
3	1269.6	-26.9
4	1029.0	-21.4
5	804.9	-16.4

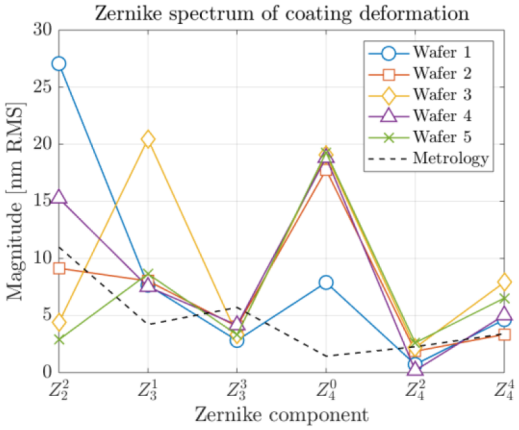

FIGURE 3. Zernike spectrum of difference between pre-coating and post-coating surface

[1] Note that Zernike polynomials, labeled Z_n^m, of the same radial degree (n) and frequency (m), but different phase, were added in quadrature to condense the figures.

measurements. The metrology data are the repeatability measurement of a reference wafer.

After coating and annealing, the coated wafers were again annealed, at 120 °C for 4 hours, to determine whether changes would occur during the post-implant annealing cycle. We measured no significant deformation from this annealing.

IMPLANT

The ion implantation was performed at the MIT Plasma Science and Fusion Center, using a tandem linear ion accelerator. Silicon anions are generated from a sputter source, accelerated to a high potential terminal (660 kV), where they lose electrons to nitrogen gas bled into the terminal region, and are finally accelerated away from the high potential terminal. The final ion beam charge state is selected using a magnetic field and aperture, and in this demonstration the ion beam is composed of 2 MeV Si^{++} ions. The ion beam is then electrostatically steered to different positions on the wafer.

The wafer is fixed in position, normal to the ion beam, and is held on an electrostatic chuck. The ion beam current is continuously monitored using a pico-ammeter. To ensure accurate ion dose measurement, secondary electron ejection from the surface is suppressed by floating the wafer at a +1.0 kV potential, which also provides the electrostatic force to chuck the wafer.

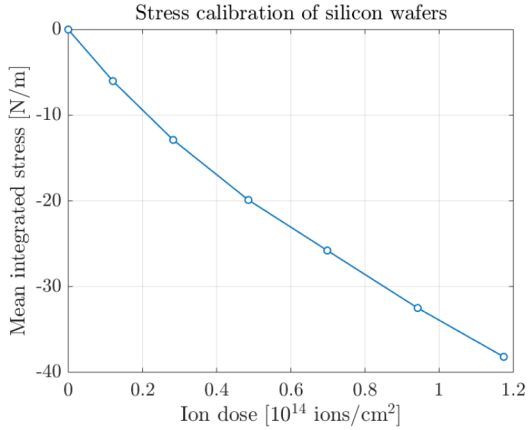

FIGURE 4. Stress generated by 2 MeV Si^{++} ions into <100> silicon wafers. All data are from wafers annealed at 120 °C for 4 hours.

The wafers were implanted on the back-side with a spatially-varying dose, which was determined using a stress-dose calibration (Figure 4) and stress maps calculated as described above. The total implanted dose was in the range of 0.4-1.0 x 10^{14} ions/cm^2. During the implant, the ion current was held at 1.5 ± 0.1 µA. Using computer control, the ion beam was steered to a point on the wafer and held until the desired dose at that point was accumulated, then moved to the next point.

The ion beam generates about 1.5 W of heat in the wafer, and we have found that wafer temperature during the implant can strongly affect the final stress. The electrostatic chuck keeps the wafer near room temperature, relying on the chuck thermal mass during the implant time, which was less than 30 minutes.

POST-IMPLANT ANNEALING

Annealing after ion implantation is critical for stabilizing the implant stress. Ion implantation causes damage to the silicon crystal lattice, which generates the observed stress. In the semiconductor industry, this damage is often undesirable, so implanted wafers are annealed to heal this damage. In our case, we require that the damage remains and that it is stable.

Figure 5 shows the effect of annealing ion stress over time. Annealing at higher temperatures reduces the mean integrated stress, but also reduces the drift in stress over time. Annealing at both 100 °C and 120 °C show no significant drift over about 1 week, so we chose to anneal all implanted wafers at 120 °C for 4 hours in a tube furnace with nitrogen gas flow.

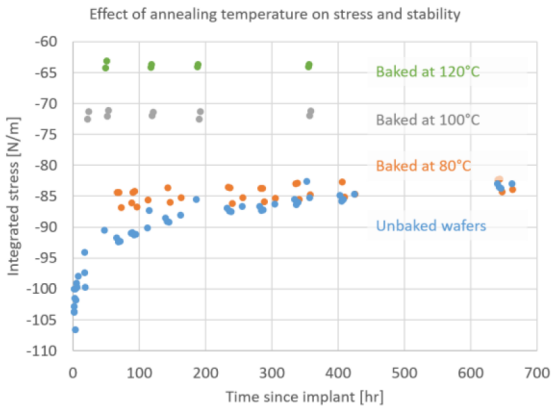

FIGURE 5. Effect of annealing for 4 hours at different temperatures on implanted stress. Annealing at higher temperature reduces stress but improves stability.

We then monitored 5 wafers, which were implanted and then annealed at 120 °C for 4 hours. The integrated stress after annealing was -20 to -30 N/m (compressive). The wafers were

then held at room temperature over four months. We found no measureable drift, with errors consistent with metrology noise. We also found no effect of baking two of these wafers for 12 hours at 70 °C.

STRESS COMPENSATION RESULTS

Ideally, after ion implantation and annealing, the wafer shape would be identical to the pre-coating shape, to within the metrology noise. The Zernike spectrum of the residual error for each wafer is shown in Figure 6. For all but one wafer, the residual error spectrum is dominated by spherical curvature error (Z_2^0). Note that wafer 1 and wafer 2 were not oxidized, which may explain the astigmatism (Z_2^2) observed in these wafers. Table 4 summarizes the results from the five wafers used for this demonstration. Figure 7 shows the height maps for one wafer, indicating wafer deformation from the coating as well as the comparison of the final measurement to the original measurement.

TABLE 4. Coating deformation and post-compensation residual height error for five coated and compensated wafers.

Wafer	Coating deformation [nm RMS]	Residual error [nm RMS]	Error reduction factor
1	384.7	33.7	11
2	1623.4	58.5	28
3	1270.0	57.8	22
4	1029.4	45.7	23
5	805.2	36.3	22

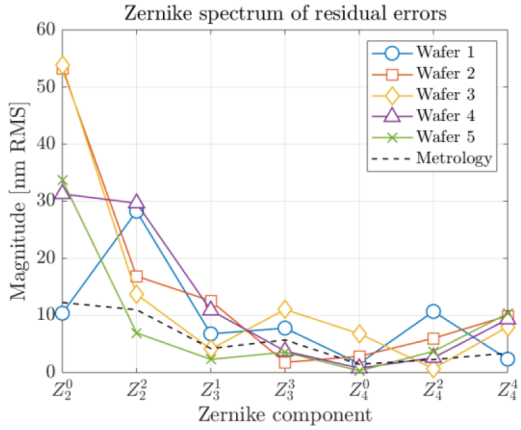

FIGURE 6. Zernike spectrum of difference between pre-coating and post-compensation surface measurements. The metrology data are the repeatability measurement of a reference wafer.

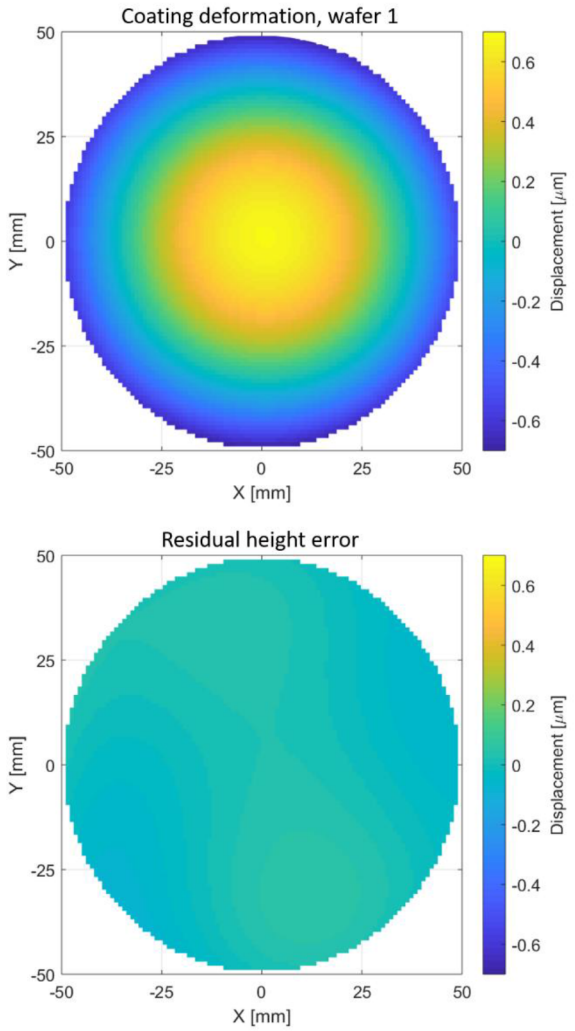

FIGURE 7. Measured height map of coating deformation (top) and difference between pre-coating and post-compensation surface measurements (bottom).

CONCLUSION

Ion implantation is a useful method of compensating for compressive film stress in silicon mirrors. The process is simple, since only three process steps beyond the normal mirror production process are required. We demonstrated reduction of coating stress deformation using ion implantation by a factor of over 20, nearly as effective as patterning stressed films [10], but requiring far fewer process steps. We demonstrated that the film stress to be compensated can be variable from run-to-run with no significant effect on our ability to compensate. In addition, we have demonstrated stability of implanted wafers with the chosen annealing process, to within our metrology repeatability.

FUTURE WORK

The stress compensation accuracy might be improved in numerous ways. For example, the annealing could be split into two parts, adding one measurement step. A second, shorter annealing step could allow trimming to achieve a more precise stress closer to the desired stress. Multiple implant cycles may also enable better compensation, but determining a proper annealing cycle would be critical, to avoid annealing implant damage from the first cycle.

When a metal film is deposited onto a silicon substrate, the difference in coefficient of thermal expansion will cause temperature-dependent deformation, which may be important. The depth of the ion implantation (around 2 μm for this work) is far larger than typical metal film thicknesses (typically around 20 nm). A double-side coated mirror would start with lower stress [8], so a smaller correction would be necessary. Initial testing suggests that the effect of implanting 2 MeV Si^{++} ions through a 30 nm Cr film has a small effect on the Cr stress, so calibration would be necessary.

ACKNOWLEDGEMENTS

The authors would like to thank Marty Culpepper, Brian Wardle, Will Zhang, and Lester Cohen for helpful discussions and advice.

This work was funded by NASA APRA grants NNX14AE76G and NNX17AE47G.

REFERENCES

[1] Gaskin, et al. The Lynx X-ray Observatory: concept study overview and status. Proc. SPIE 106990N (2018).

[2] Zhang, et al. Astronomical x-ray optics using mono-crystalline silicon: high resolution, light weight, and low cost. Proc. SPIE 106990O (2018).

[3] Riveros, et al. Fabrication of lightweight silicon x-ray mirrors for high-resolution x-ray optics. Proc. SPIE 106990P (2018).

[4] Ghigo, et al. Final correction by Ion Beam Figuring of thin shells for X-ray telescopes. Proc. SPIE 107063I (2018).

[5] Windischmann, H. Intrinsic stress in sputter-deposited thin films. Critical Reviews in Solid State and Materials Sciences, 17:6, 547-596 (1992).

[6] Broadway, et al. Achieving zero stress in iridium, chromium, and nickel thin films. Proc. SPIE 95100E (2015).

[7] Broadway, et al. In-situ stress measurement of single and multilayer thin-films used in x-ray astronomy optics applications. Proc. SPIE 103991B (2017).

[8] Mori, et al. Reflective coatings for the future x-ray mirror substrates. Proc. SPIE 1069941 (2018).

[9] Yao, et al. Stress manipulated coating for fabricating lightweight X-ray telescope mirrors. Opt. Express 23:22, 28605-28618 (2015).

[10] Yao, et al. Thermal oxide patterning method for compensating coating stress in silicon x-ray telescope mirrors. Proc. SPIE 1069942 (2018).

[11] Chalifoux, et al. Compensating film stress in silicon substrates for the Lynx X-ray telescope mission concept using ion implantation. Proc. SPIE 1069959 (2018).

[12] Zuo, et al. Ultrafast laser micro-stressing for correction of thin fused silica optics for the Lynx X-Ray Telescope Mission. Proc. SPIE 1069954 (2018).

[12] Volkert, C. Stress and plastic flow in silicon during amorphization by ion bombardment. J. Appl. Phys., 70:7, 3521-3527 (1991).

[13] Chalifoux, et al. Using ion implantation for figure correction in glass and silicon mirror substrates for x-ray telescopes. Proc. SPIE 103991D (2017).

[14] Forest, et al. Metrology of thin transparent optics using Shack-Hartmann wavefront sensing, Opt. Eng., 43:3, 742-753 (2004).

[15] Akilian, et al. Thin optic constraint, Precision Engineering, 31:2, 130-138 (2007).

[16] Chalifoux, et al. Correcting flat mirrors with surface stress: analytical stress fields. J. Opt. Soc. Amer. A, *accepted for publication.*

[17] Thornton and Hoffman. Stress-related effects in thin films. Thin Solid Films, 171:1, 5-31 (1989).

[18] Chan, et al. Reflective coatings for lightweight x-ray optics. Proc. SPIE 84433S (2012).

DESIGN AND MANUFACTURE OF ANGULAR VARIATION PYRAMID PATTERN IN RANDOM ARRANGEMENT

Doo-Sun Choi[1], Seung Hwan Moon[1,2], Je-Ryung Lee[1], Ji-Young Jeong[1,3], Eun-chae Jeon[4], Seong-Dae Choi[2], Tae-Jin Je[1,3]
[1]Department of Nano Manufacturing Technology, Korea Institute of Machinery and Materials Daejeon, 34103, Korea
[2]Department of Mechanical System Engineering Kumoh National Institute of Technology, Gumi, 39177, Korea
[3]Department of Nano Mechatronics University of Science and Technology Daejeon, 34113, Korea
[4]School of Materials Science and Engineering, University of Ulsan, Ulsan 44610, Korea

INTRODUCTION

Recently, in the display industry, studies have been conducted using a hemispherical micro lens array as a method for uniformly distributing the light emitted from a light source and improving light extraction efficiency [1-3]. However, the hemispherical patterns have the disadvantage that the front luminance is low because the light is emitted in all directions. To resolve these disadvantages, patterns with the shape of a square pyramid, which can diffuse light and emit a large amount of light to the front, have been researched [4-5]. In order to distribute the light evenly, it is necessary to rotate pyramids within the pattern at various angles with respect to their center point. In this study, at coordinate position system for the angular rotation pyramid pattern was designed and a method studied to correct the position error that occurs when each pyramid pattern is processed by the indentation processor. In addition, it was confirmed that the angular rotation micro pyramid array pattern can be manufactured with almost the same precision as intended in the design positions through such an indentation process.

DESIGN OF ANGULAR VARIATION PYRAMID PATTERNS IN RANDOM ARRANGEMENT

In this research, two design rules were applied to uniformly distribute the fine pyramid patterns in random arrangement. First, the pyramid forms could not overlap. When the pyramid forms overlap, the pyramid shape is damaged and transformed. Therefore, each pyramid must be arranged so that its edges do not overlap with another pyramid. Second, all the pyramid shapes had to be created within the design domain. This is because the fill factor is different. The fill factor is the ratio of the area occupied by the pattern to the total area, and the fill factor has great influence on the optical characteristics of a pyramid.

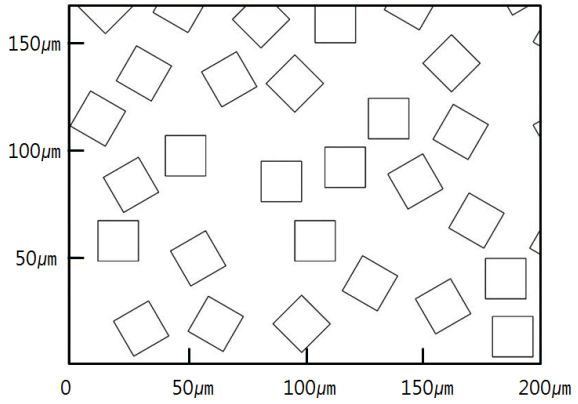

FIGURE 1. Design pattern of pyramids with randomly distributed angles of rotation

Figure 1. shows the result from simulation of the positional coordinates of the pattern designed using MATLAB. It was confirmed that the angular rotation square cross-section pyramid patterns in the irregular arrangement were distributed without overlapping. The size of the pyramid pattern was designed based on a diagonal length of 25 μm and a fill factor of 25%.

In order to uniformly distribute the light, the pattern was rotated randomly at an angle of 0 °, 30 °, 45 °, or 60 ° with respect to the center point of the pattern. The number of pyramids at for each angle was the same in the design area.

EXPERIMENTAL SYSTEM CONFIGURATION

Ultra-precise indentation machining techniques were used to produce pyramid patterns in random arrays. The indentation machining technology is a technique or transferring the shape of the tool to the surface of the material by indentation of the surface of the material with the tool. Figure 2. shows the indentation machining system used in this research. This is a 4-axis machining device in which the X, Y, and Z axes are driven with 1 μm feed precision and the C axis is driven with a rotation accuracy of 0.01°. When a voltage is applied, the solenoid device that is actuated is equipped with a tool that indents the material. The applied voltage of the solenoid can be controlled with a precision of 0.01V. It can also be driven at speeds up to 5 Hz to manufacture pyramid patterns quickly. Figure 3. shows a square pyramid diamond indentation tool with a face angle of 136°, which was used in the research.

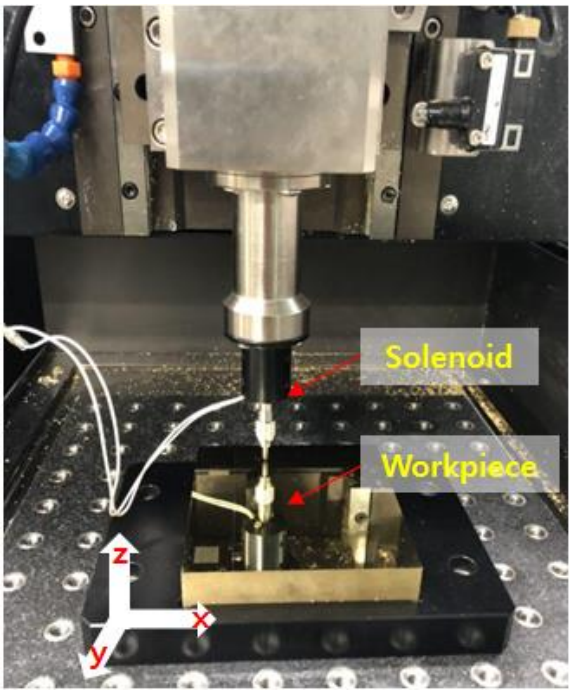

FIGURE 2. The experimental indentation system

FIGURE 3. Diamond tool shape for indentation machining of a pyramid pattern

ANALYSIS OF PATTERN SIZE ACCORDING TO CHANGE IN THE APPLIED VOLTAGE

The push-in drive distance of the tool mounted on the solenoid varies with the intensity of the applied voltage. The depth and size of the pyramid pattern formed by tool indentation also changes. Therefore, in order to fabricate a design pattern of the desired size, it is necessary to analyze and set the proper applied voltage. Figure 4. shows the result from analyzing the size of the machined pyramid form according to the voltage applied to the solenoid. The voltage applied was varied from 1.7 to 2.3 V by 0.05 V. Through this experiment, it was confirmed that when the solenoid applied voltage was set to 1.95 V, a pyramid pattern with a diagonal length of 25 μm was produced. Based on these results, the coordinates of the entire random pattern were determined and processed.

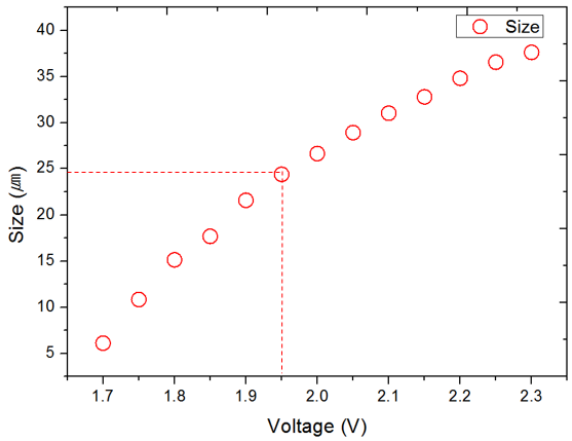

FIGURE 4. Variation of pattern size with increasing voltage

COMPENSATION OF POSITION ERROR IN ANGULAR ROTATED MACHINING

Figure 5. shows the result of indentation according to the design coordinates. The size of the processed pattern was about 25 μm on average, and it was processed to be similar to the design value. However, the position of each pattern processed was different from the design. It was confirmed that the cause of the difference in position coordinates was inconsistency between the rotation center of the tool and the rotation center of the machine. Accordingly, to process the randomly distributed angular rotation pyramid pattern so that it coincided with the design coordinates, it was necessary to correct the position error generated from the rotation center mismatch between the machine and the tool.

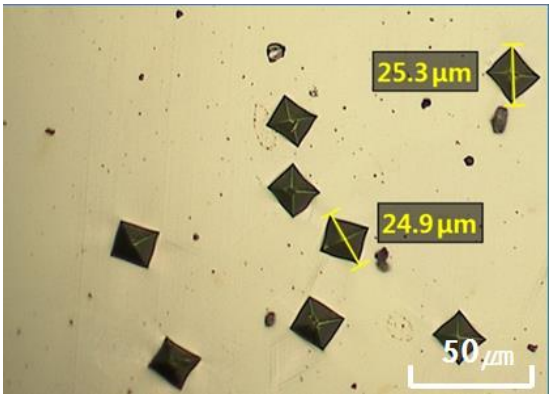

FIGURE 5. A machined pyramid pattern with randomly distributed angle of rotation

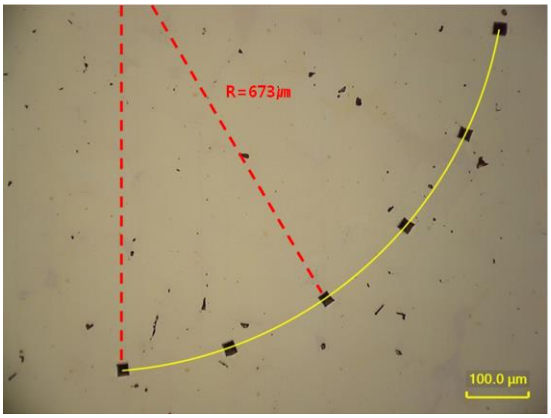

FIGURE 6. The result of machining in the same position by a tool of which the angle is rotated

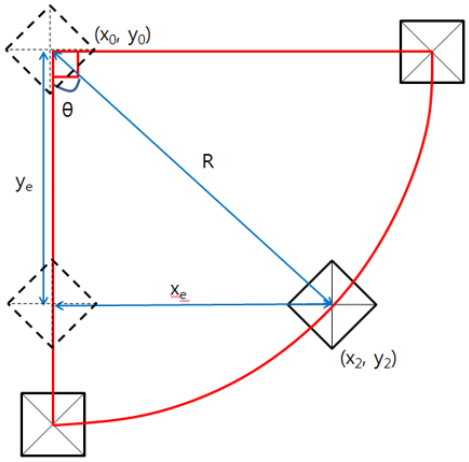

FIGURE 7. Model of position error due to center axis misalignment of tool for indentation machining of rotated pyramid pattern (R: Radius, θ: Tool tilting angle, X_e: Error of the x axis, Y_e: Error of the y axis)

Figure 6. shows the results obtained by rotating only the tool angle from the same position to analyze the distance between the center point of the machine and the center points of the tool. When connecting the center points of the rotated pyramid pattern, an arc was generated, and the result from measuring the radius showed it to be 673 μm. Figure 7. is a schematic diagram showing the position error of the rotating pyramid pattern generated by the center axis mismatch between the tool and the machine. When the tool was rotated from 0° to 90°, the center point of each pattern was drawn to form a circular arc relative to the specific coordinates. At this time, the specific point X_0, Y_0 is the ideal indentation machining coordinate, R is the radius error generated from the ideal coordinates. By using the rotation angle θ and the radial distance, it was possible to obtain X_e and Y_e, which are the X and Y coordinate position error, respectively. Accordingly, by making corrections using the position errors X_e and Y_e obtained through the above process, the positions of the design coordinates and the actual machining pattern could be matched.

ANGULAR ROTATED PYRAMID PATTERN MACHINING WITH POSITION ERROR CORRECTION METHOD

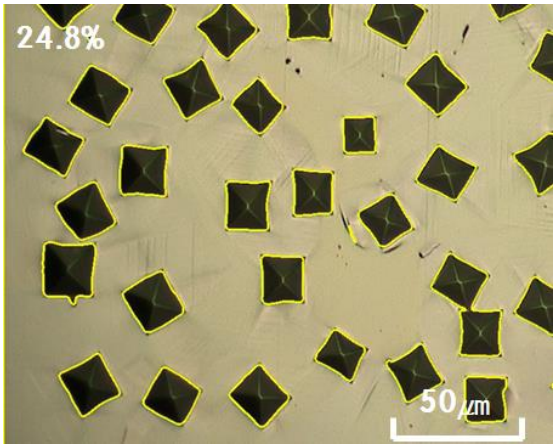

FIGURE 8. Machined result of angular rotation pyramid pattern with position correction method

Figure 8. shows the shape of the pyramid pattern angle-change of the random array reworked after applying the position-error correction method. The average size of the processed pattern was about 24.7 μm and the fill factor was about 24.8%. It was confirmed that the machined results almost coincided with the initially designed coordinates.
With the use of this position correction method, it was confirmed that a fine pyramid pattern of irregular arrangement evenly distributed according to size and filling ratio could be manufactured precisely and efficiently.

CONCLUSIONS

1. Research was done to improve light diffusion and luminance effect by the design and indentation manufacturing of at micro random pattern of square pyramid shapes.
2. The coordinate generation method was designed so that no pyramid patterns overlapped according to the pattern size and the fill factor, and that all the patterns were generated within the processing region.
3. The size of the pyramid pattern was analyzed according to the variation of the solenoid voltage of the indentation device and based on this, at pyramid pattern of the same size as the design was manufactured.
4. In the machining of random pyramid patterns, the position error due to the angular rotation of the tool was analyzed and at correction method was determined.
5. As a result of indentation machining of the random pyramid patterns while applying the position correction result, the position result was almost the same as that in the initial design.

REFERENCES

[1] E-c Jeon, J-R Lee, D-H Choi, H-J Choi, T-J Je. Micro-machining and Optical Characterization of Randomly Distribute Micro-Lens Array. Euspen, Proceedings of the 16th International Confrence of the Euspen Society for Precision Engineering and Nanotechnology. 2016; 16: 507-508.

[2] X-H Li, R Song, Y-K Ee, P K, J F Gilchrist, N Tansu. Light extraction efficiency and radiation patterns of III-nitride light-emitting diodes with colloidal microlens arrays with various aspect ratios: IEEE Photonics Journal. 2011; 3: 489-499

[3] Sang-Hyun Eom, Edward Wrzesniewski, Jiangeng Xue. Close-packed hemispherical microlens arrays for light extraction enhancement in organic light-emitting devices. ELSEVIER. Organic Electronics. 2010; 12: 472-476

[4] N Skoulidis, H M Polatoglou. Modeling the optical properties of Si-capped germanium quantum dots. ELSEVIER. Computational Materials Science.` 2008; 41: 245-253

[5] M Karl, D Rulke, T beck, D Z Hu, D M Schaadt, H Kalt, M Hetterich. Reversed pyramids as novel optical micro-cavities. ELSEVIER. Superlattices and Microstructures. 2010; 47: 83-86

MODULATED TOOL PATH TURNING STABILITY ANALYSIS

Ryan W. Copenhaver and Tony L. Schmitz
Department of Mechanical Engineering and Engineering Science
University of North Carolina at Charlotte, Charlotte, NC

INTRODUCTION

Unlike milling operations where the rotating tool constantly engages and disengages the workpiece to produce intermittent cutting conditions, conventional turning, boring, and threading operations typically exhibit continuous cutting. Once the cutting edge is engaged with the workpiece, it remains in contact at a specified feed rate until the cut concludes. This tends to produce a continuous chip that can wrap and collect near the cutting edge when machining ductile materials; see Fig. 1. The local buildup of this continuous chip can result in one or more of several undesirable outcomes including workpiece scratching, tool damage, machinist injury, and increased cycle time to clear the chip(s) from the tool/workpiece.

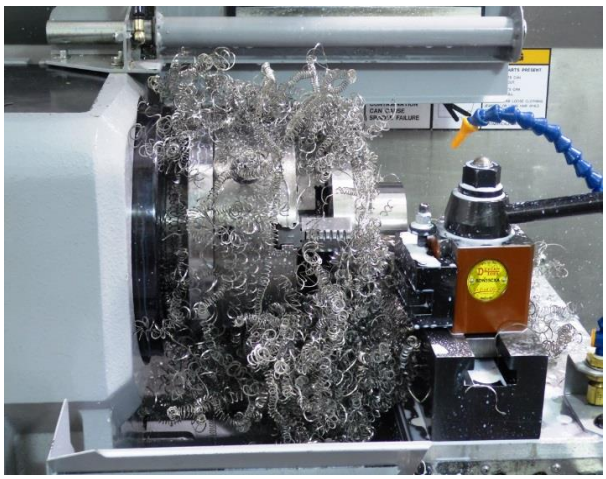

Figure 1. Chip buildup observed in a turning operation.

In this study, stability testing is reported for MTP turning with a flexible tool using two different stability metrics. These metrics are: 1) the traditional frequency-domain analysis, where the frequency content of a process signal is analyzed to identify the chatter frequency (should it exist); and 2) a periodic sampling approach, where the synchronicity of the sampled signal is evaluated numerically.

Existing chip management strategies include the use of specialized rake face geometries (i.e., chip breakers) and high pressure coolant directed at the rake face-chip interface to intentionally fracture the otherwise continuous chip. The performance of these strategies depends on the chip thickness, chip radius of curvature, and workpiece material [1], as well as the coolant pressure, direction, and location when high pressure coolant is applied.

An alternative approach to these techniques is modulated tool path (MTP) turning, where discrete chips are formed by repeatedly interrupting the continuous chip formation by using the machine axes to superimpose low frequency tool oscillations on the nominal tool feed motion. In this case, successful chip separation is based on the oscillation frequency relative to the spindle speed and the oscillation amplitude relative to the global feed per revolution.

Prior MTP efforts have demonstrated its effectiveness for controlling broken chip length in turning [2-5] and threading [6]. An experimental setup used to measure feed motion, force, temperature, and chip formation data using both constant feed and MTP cutting conditions was described [7-8]. Here, stability is reported for MTP turning with a flexible tool. The stability is established using: 1) the traditional frequency-domain analysis, where the frequency content of a process signal is analyzed to identify the chatter frequency magnitude (should it exist); and 2) a new periodic sampling approach, where the synchronicity of the sampled signal is evaluated numerically. The two methods are demonstrated using force, acceleration, and velocity data in a tube turning (orthogonal cutting) setup. Potential advantages of the new approach are: 1) a generic threshold for instability is defined in the absence of noise ($M > 0$); and 2) a smaller number of samples may be required to evaluate stability relative to the frequency spectrum analysis since a higher number of samples is not required to increase frequency resolution.

INTERRUPTED CUTTING

An exaggerated depiction of an MTP turning operation is displayed in Fig. 2. The broken chip length is dependent on two, user-defined MTP parameters: 1) the tool oscillation frequency relative to the spindle speed, or Oscillations Per Revolution (*OPR*); and 2) the oscillation amplitude relative to the global feed per revolution, or the Ratio of the Amplitude to the Feed rate (*RAF*). The MTP parameters are defined as:

$$OPR = \frac{60 \cdot f}{\Omega} \tag{1}$$

$$RAF = \frac{A}{f_r} \quad (2)$$

where f is the tool oscillation frequency (Hz) in the feed direction, Ω is the spindle speed (rpm), A is the tool oscillation amplitude, and f_r is the global feed per revolution for a traditional, constant feed turning operation. The time-dependent feed motion of the tool relative to the work, z_f, is then described using these two parameters.

$$z_f = \left(\frac{\Omega}{60} f_r\right) t + RAF \cdot f_r \cdot \sin\left(\frac{\Omega}{60} 2\pi \cdot OPR \cdot t\right) \quad (3)$$

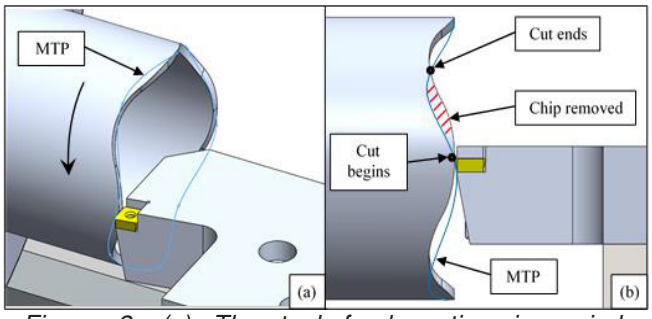

Figure 2. (a) The tool feed motion is varied sinusoidally to produce a wavy surface in the feed direction. (b) By selecting appropriate OPR and RAF values, broken chips are periodically produced.

STABILITY ANALYSIS

In interrupted cutting operations, two types of system response may exist. These are forced vibrations and self-excited vibrations (chatter). In forced vibrations, the response occurs at the excitation frequency [9]. In milling, this is the tooth passing frequency, which is defined by the product of the spindle speed and number of teeth on the rotating cutter. The tooth passing frequency describes the number of cutting edge contacts with the work per unit time. For example, the tooth passing frequency for a spindle speed of 6000 rpm using a four tooth endmill is 6000(4)/60 = 400 Hz. In MTP, the excitation frequency is the product of the spindle speed and *OPR*. For a 600 rpm spindle speed and an *OPR* of 0.5, the excitation frequency is 600(0.5)/60 = 5 Hz. The limit on this excitation frequency is the bandwidth for the computer numerically-controlled (CNC) lathe's axis control.

In self-excited vibration, on the other hand, the periodic forcing function is modulated by some physical mechanism into oscillation near the system's natural frequency that corresponds to the most flexible mode [10]. For machining operations, this physical mechanism is the feedback provided by the overcutting of the previous surface in the current pass. This yields a time delay because the current chip thickness depends on the commanded chip thickness, the current tool vibration state, and the tool's vibration state when leaving the previous surface.

Because the response frequencies differ between forced and self-excited vibrations, periodic sampling of machining signals at the forcing frequency enables stable (forced) and unstable (self-excited) behavior to be distinguished. When sampled at the forcing frequency, forced vibrations repeat. For self-excited vibration, the sampled points do not repeat because both the forcing frequency and the chatter frequency are present.

STABILITY METRIC

The variation in the periodically sampled points enables a numerical value to be assigned that indicates stable or unstable performance. The MTP stability metric is:

$$M = \frac{\sum_{i=2}^{N} |x_s(i) - x_s(i-1)|}{N} \quad (4)$$

where x_s is a vector of periodically sampled x values and N is the length of the x_s vector. The x values can be any process signal, including displacement, velocity, or acceleration of the tool or workpiece; cutting force; or sound [11]. With this stability metric, the absolute value of the differences in successive sampled points is summed and then normalized. For stable cuts (forced vibration), the sampled points repeat, so the M value is close to zero. For unstable cuts, however, $M > 0$ [12-13].

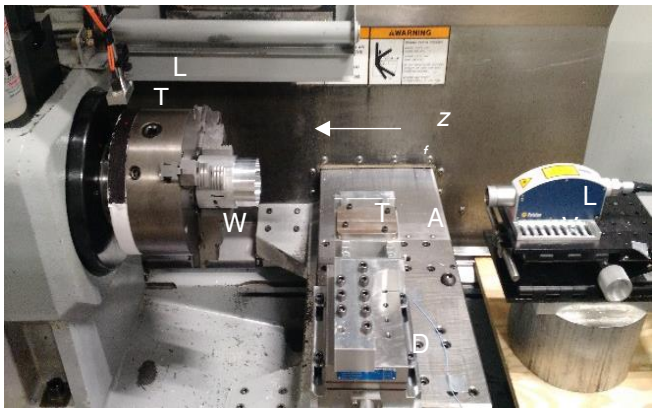

Figure 3. Photograph of tube turning setup including: workpiece (W), dynamometer (D), flexure-based cutting tool (T), laser tachometer (LT), accelerometer (A), and laser vibrometer (LV).

EXPERIMENTAL SETUP

The testbed for the turning experiments was a Haas TL-1 CNC lathe (8.9 kW, 2000 rpm spindle). Tubular workpieces were machined from ASM 6061-T6

aluminum. The outside diameter of the workpieces was 72 mm and the wall thicknesses were {1, 1.5, and 2} mm, corresponding to stable, marginally stable, and unstable conditions for this setup. Concentricity and cylindricity of the outside and inside diameters with the rotational axis of the lathe spindle was assured by performing a finishing cut prior to conducting the experiments. Type C, 80° parallelogram carbide inserts with a zero rake angle, 7° relief angle, and a flat rake face were used (ANSI catalog number CCMW3252, Kennametal part number 3757916). Tube turning was selected so that the cutting speed would not vary with a fixed spindle speed [14]. Experiments were conducted at a cutting speed of 206 m/min (911 rpm) with a nominal feed rate of 0.102 mm/rev. The commanded *OPR* and *RAF* values for all tests were 0.5 and 0.8, respectively. The tests were then repeated using a constant feed rate so that MTP performance could be compared to traditional turning. Stability of the cut was controlled by varying the tube wall thickness (i.e., the chip width).

Dynamic cutting forces were measured using a three-axis dynamometer (Kistler 9257B) mounted to the cross slide. A notch-type flexure was mounted to the top of the three-axis dynamometer [15]. This flexure carried the carbide insert and acted as the cutting tool. This configuration provided a flexible response in the sensitive direction (z_f). A laser vibrometer (Polytec OFV-534/OFV-5000) was used to measure the feed (z_f) direction velocity of the cutting tool. An accelerometer was fixed to the free end of the tool to measure the tool acceleration in the thrust direction. A laser tachometer was used to determine the actual spindle speed for periodic sampling at the MTP forcing frequency. A photograph of the setup is provided in Fig. 3. The thrust direction is aligned with the spindle axis, while the cutting direction is tangent to the cut surface. The tool's frequency response function was measured using impact testing [9]. Primary vibration modes occurred at: {298, 395, and 1464} Hz.

RESULTS

The traditional approach for examining and quantifying unstable cutting is to convert the time-domain data to the frequency-domain using the Fast Fourier Transform (FFT) and then analyze the frequency content for a chatter frequency (i.e., content at a frequency other than the forcing frequency and its harmonics). The alternative approach presented here uses periodic sampling to determine the synchronicity of the MTP process signal with respect to the forcing frequency defined by the spindle speed and *OPR*. The two techniques were applied to MTP cutting test signals and compared. Results are presented for force, acceleration, and velocity signals at three chip widths (i.e., tube wall thicknesses), b = {1, 1.5, and 2} mm.

Frequency-domain results

The FFT-based analyses are provided in this section. For brevity, results are presented in Figs. 4 and 5 for thrust direction force only at 1 mm and 2 mm chip widths. Similar results were obtained for the acceleration and velocity signals. For the stable 1 mm chip width, the forcing frequency (911(0.5)/60 = 7.6 Hz) appears, but no appreciable chatter frequency content is observed. For the unstable 2 mm chip width, a 406 Hz chatter frequency is seen (corresponds to the 395 Hz cutting tool mode).

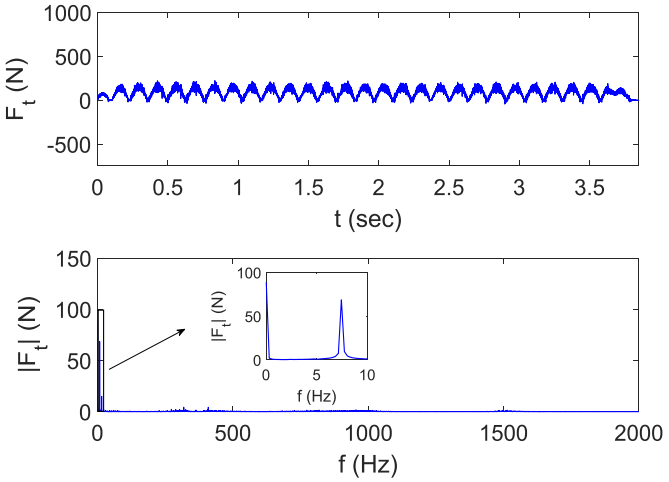

Figure 4. (Top) Thrust direction force for 1 mm chip width. (Bottom) Frequency content.

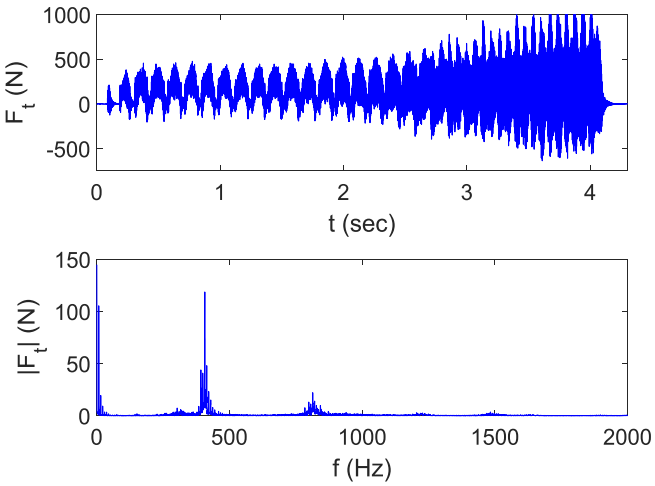

Figure 5. (Top) Thrust direction force for 2 mm chip width. (Bottom) Frequency content.

Periodic sampling results

The periodic sampling analyses are provided in this section. Results are again presented for thrust direction force at 1 mm and 2 mm chip widths. However, the signals are now sampled at the forcing frequency of 7.6 Hz. The samples are superimposed on the time-domain signals as circles in Figs. 6 and 7. It is observed that the sampled points repeat for the 1 mm chip width, which indicates stable behaviour. For the unstable 2 mm chip width, on the other hand, the points do not repeat (the quasi-periodic behaviour indicates a secondary Hopf bifurcation).

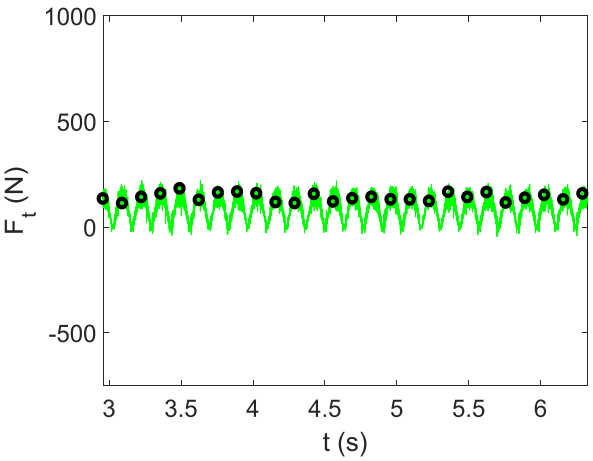

Figure 6. Periodic sampling of the thrust direction force for 1 mm chip width. The time-domain signal is represented by the solid line and the sampled points by the circles.

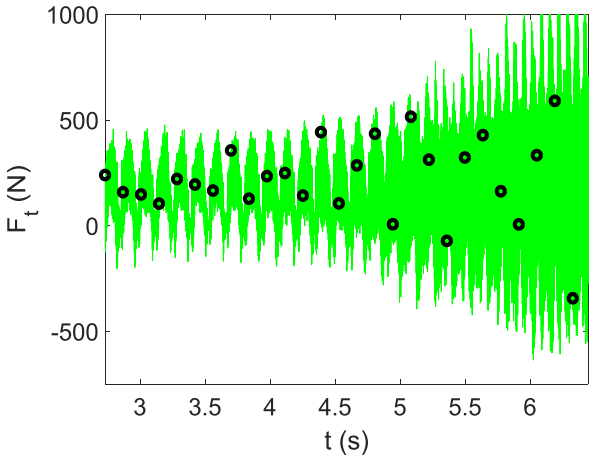

Figure 7. Periodic sampling of the thrust direction force for 2 mm chip width.

The stability metric from Eq. 4 was next calculated for all three process signals at the three chip widths, b = {1, 1.5, and 2} mm. The results are summarized in Table 1. It is seen that the metric value, M, changes dramatically between stable (b = 1 mm and 1.5 mm) and unstable cutting conditions (b = 2 mm).

Table 1. Stability metric values for force, acceleration, and velocity signals from MTP cuts.

Signal type	b (mm)	M
Force	1	18.1 N
Force	1.5	23.1 N
Force	2	109.0 N
Acceleration	1	137.3 m/s^2
Acceleration	1.5	141.6 m/s^2
Acceleration	2	272.0 m/s^2
Velocity	1	0.014 m/s
Velocity	1.5	0.014 m/s
Velocity	2	0.056 m/s

COMPARISON

In this section the FFT and periodic sampling results are compared for the MTP cuts. Additionally, machining trials were completed at a constant feed rate (with all other conditions remaining the same) to compare the stability behavior between the constant feed and MTP cases. These results are presented in Figs. 8-10. It is observed that the FFT and periodic sampling (PS) approaches demonstrate the same trends, i.e., the b = 1 mm and 1.5 mm cuts are stable with small values, while the b = 2 mm cut is unstable with a much larger value.

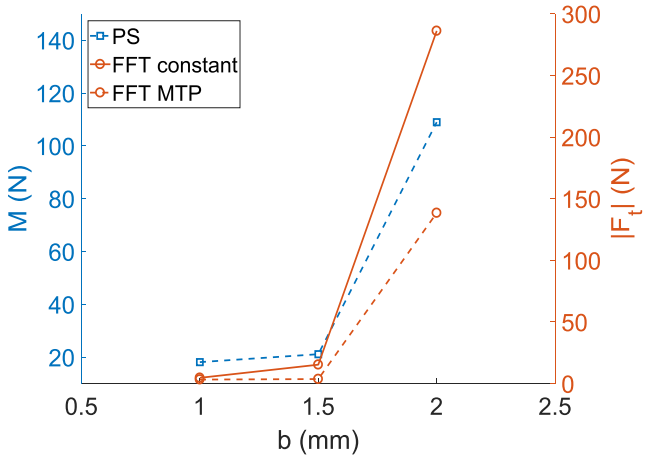

Figure 8. Comparison of FFT (chatter frequency peak magnitude) and periodic sampling (metric value) results for thrust direction force.

One interesting difference is that the constant feed cut with a chip width of 1.5 mm is only marginally stable as indicated by the elevated FFT amplitude at the chatter frequency, while the MTP cut is stable. This difference in stability between constant feed and MTP cutting conditions and will be the focus of follow-

on studies. Note that no periodic sampling results are presented for the constant feed cut since there is no external forcing frequency in this case.

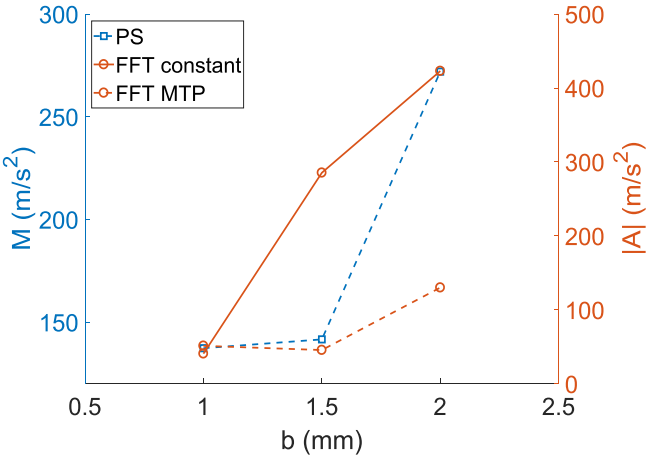

Figure 9. Comparison of FFT (chatter frequency peak magnitude) and periodic sampling (metric value) results for thrust direction acceleration.

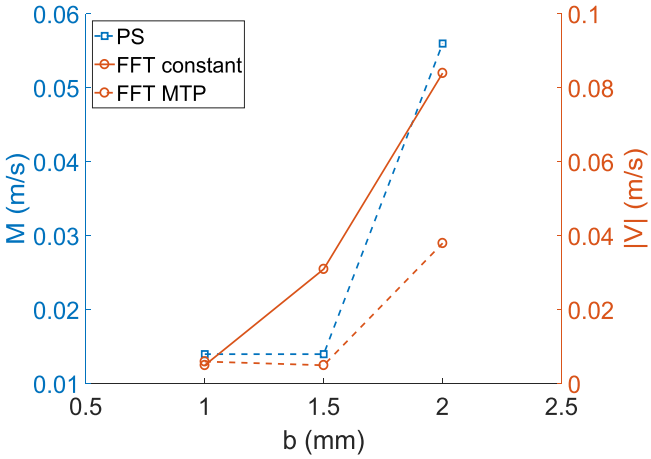

Figure 10. Comparison of FFT (chatter frequency peak magnitude) and periodic sampling (metric value) results for thrust direction velocity.

CONCLUSIONS

This paper described a new stability metric for modulated tool path (MTP) turning, where discontinuous chips are obtained by superimposing a sinusoidal oscillation on the feed direction motion. The new metric was based on periodic sampling of the MTP process signals (such as force, acceleration, velocity, displacement, or sound). The sampling frequency was selected to match the forcing frequency, which was determined from the product of the spindle speed and the number of oscillations per revolution for the MTP motion. Potential advantages of the new approach are: 1) a generic threshold for instability (in the absence of noise) is defined; and 2) a smaller number of samples may be required to evaluate the process stability relative to the frequency spectrum analysis since a higher number of samples is not required to increase frequency resolution. Tube turning experiments were completed and the periodic sampling-based stability metric results were compared to the traditional frequency-domain approach, where content near a system natural frequency indicates unstable cutting conditions (self-excited vibration). Both approaches identified unstable cutting conditions at the same chip width using force, acceleration, and velocity signals collected during cutting trials.

ACKNOWLEDGEMENTS

The authors gratefully acknowledge financial support from the UNC Charlotte Center for Precision Metrology Affiliates.

REFERENCES

[1] Zhang, Y.Z, 1980, Chip Curl, Chip Breaking, and Chip Control of Difficult-to-cut Materials, Annals of the CIRP, 29/1: 79-83.

[2] Adams, D., 2008, Chip Breaking in Turning Operations Using CNC Toolpaths, MS Thesis, UNC Charlotte, Charlotte, NC.

[3] Assaid, T.S., 2010, Generation, Measurement, and Assessment of Modulated Tool-Path Chip Breaking in CNC Turning Processes. MS Thesis, UNC Charlotte, Charlotte, NC.

[4] Tursky, D., 2010, Chip Breaking Through Oscillating CNC Toolpaths and its Effect on Chip Length, Tool Wear and Machine Dynamics, MS Thesis, UNC Charlotte, Charlotte, NC.

[5] Berglind, L., Zeigert, J., 2013, Chip Breaking Parameter Selection for Constant Surface Speed Machining, ASME 2013 International Mechanical Engineering Congress and Exposition Volume 2B: Advanced Manufacturing, San Diego, CA.

[6] Berglind, L., Zeigert, J., 2015, Modulated tool path (MTP) machining for threading applications, Procedia Manufacturing, 1: 546-555.

[7] Copenhaver, R., Rubeo, M., Guzorek, S., Landge, S., Smith, K.S., Ziegert, J., Schmitz, T., 2017, A Fundamental Investigation of Modulated Tool Path Turning Mechanics, Procedia Manufacturing, 10: 159-170.

[8] Rubeo, M., Copenhaver, R., Landge, S., Schmitz, T., 2016, Experimental Platform for In-process Metrology during Orthogonal Turning, American Society for Precision Engineering Annual Meeting, October 23-28, Portland, OR.

[9] Schmitz, T., Smith, K.S., 2012, Mechanical Vibrations: Modeling and Measurement, Springer, New York, NY.
[10] Schmitz, T., Smith, K.S., 2009, Machining Dynamics: Frequency Response to Improved Productivity, Springer, New York, NY.
[11] Delio, T., Tlusty, J., Smith, S., 1992, Use of Audio Signals for Chatter Detection and Control, Journal of Engineering for Industry, 114:146-157.
[12] Honeycutt, A., Schmitz, T., 2016, A New Metric for Automated Stability Identification in Time Domain Milling Simulation, Journal of Manufacturing Science and Engineering, 138/7: 074501.
[13] Honeycutt, A., Schmitz, T., 2017, Milling Stability Interrogation by Subharmonic Sampling, Journal of Manufacturing Science and Engineering, 139/4: 041009.
[14] Ivester, R., Whitenton, E., Heigel, J., Marusich, T., Arthur, C., 2007, In: 10th CIRP International Workshop on Modeling of Machining Operations, Reggio Calabria, IT.
[15] Smith, S.T., 2000, Flexures: Elements of Elastic Mechanisms, CRC Press, Boca Raton, FL.

IMPROVEMENT OF MULTISTAGE SUPERFINISHING OF SAPPHIRE WITH VITRIFIED-BONDED DIAMOND SUPERABRASIVE STONES

Naomichi FURUSHIRO[1], Tomomi YAMAGUCHI[1], Daisuke HIROOKA[1], Noboru MATSUMORI[2] and Kenichi TANADA[2]
[1]Kansai University, Suita, Osaka, Japan
[2]Mizuho Co., Ltd., Kizugawa, Kyoto, Japan

ABSTRACT

Recently sapphire is widely used for LED substrate. In the planarization process of sapphire, lapping is used before polishing. However, machining time of lapping takes more than 30 minutes because sapphire is hard material. Superfinishing process can be substitute for the lapping. Superfinishing uses fixed abrasive stones, and it is possible to process sapphire in shorter time.

Surface roughness of the lapping process is 2nmRa. Therefore, superabrasive stones are suitable for superfinishing. Then, vitrified-bonded diamond superabrasive stones with different grain diameter were developed. Superfinishing performances of those stones were compared. Subsequently multistage superfinishing was examined by combining diamond stones in descending order of grain diameter. The target roughness 2nmRa was achieved in 8 minutes of 4-stage superfinishing.

In this study, we have examined three different combinations to improve multistage superfinishing of sapphire.

MATERIALS AND METHODS

In previous study, we used 4-stage superfinishing to achieve 2nmRa in 8 minutes [1]. In this study, we compared three different combinations of multistage superfinishing. TABLE 1 and 2 show multistage superfinishing process and superfinishing time in each process. FIGURE 1 shows appearance of superfinishing . FIGURE 2 (b), (c), (d), and (e) show the result of Process A [1].

TABLE 1. Multistage superfinishing processes.

	Stage 1	Stage 2	Stage 3	Stage 4
A	SD 2000	SD 4000	SD 6000	SD 20000
B	SD 3000	SD 6000	SD 20000	
C	SD 2000	SD 4000	SD 8000	SD 20000
D	SD 2000	SD 4000	SD 12000	SD 20000

TABLE 2. Multistage superfinishing time.

	Stage 1	Stage 2	Stage 3	Stage 4
A	1 min	1 min	1 min	5 min
B	2 min	1 min	5 min	
C	1 min	1 min	N/A	N/A
D	1 min	1 min	2 min	2.5 min

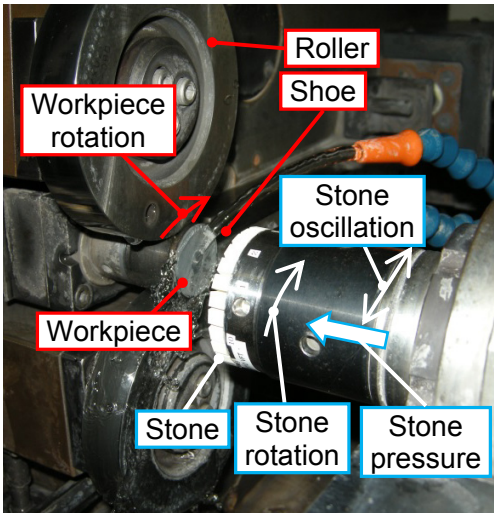

FIGURE 1. Centerless flat superfinishing of sapphire.

IMPROVEMENT OF ROUGH FINISHING

In Process A, the amount of removal and stone wear in Stage 1, SD 2000 stone, which is rough finishing, were excessive [1]. Therefore, in Process B, SD 3000 stone was chosen as Stage 1. TABLE 3 shows stone specification and superfinishing conditions.

TABLE 3. Stone specification and superfinishing conditions.

Stone specification	SD 3000 I 110 V
Superfinishing pressure	0.22-0.66 MPa
Stone speed	452 m/min
Workpiece speed	115 m/min
Oscillation	16.7 Hz
Amplitude	0.5 mm
Superfinishing time	1-3 min
Superfinishing fluid	Water (rust inhibitor 1%)
Workpiece	Sapphire (100nmRa)

Superfinishing pressure and superfinishing time were varied and the amount of removal, stone wear and surface roughness was measured.

FIGURE 3 shows the comparison of the amount of removal in each superfinishing pressure. The amount of removal was large enough (dashed line in FIGURE 3) in superfinishing pressure of 0.22 and 0.44 MPa.

FIGURE 4 and 5 show the comparison of stone wear and stone working area ratio in superfinishing pressure of 0.22 and 0.44 MPa, respectively. Stone wear of 0.22 MPa was larger than that of 0.44 MPa and therefore stone working area ratio was smaller than that of 0.44 MPa.

FIGURE 6 and 7 show laser microscopic image and SEM micrograph of stone surface at 2 min and 3 min in superfinishing pressure of 0.22 MPa, respectively. Highest grain at 2 min dropped after 1-minute superfinishing (FIGURE 7 (c)) and then stone working area ratio decreased.

FIGURE 8 shows the comparison of surface roughness in each superfinishing pressure. SD 3000 stone achieved surface roughness of 20nmRa in 2-minute superfinishing.

Results indicate that SD 3000 can generate sufficient surface roughness and the amount of removal and stone wear are appropriate in superfinishing pressure of 0.44 MPa and superfinishing time of 2 minutes.

Subsequently Stage 2, SD 6000 stone, and Stage 3, SD 20000 were applied in Process B. TABLE 4 shows stone specification and superfinishing conditions of SD 20000 stone. The target roughness 2nmRa was achieved in 8 minutes of 3-stage superfinishing.

FIGURE 2 (f), (g), and (h) show the result of Process B.

TABLE 4. Stone specification and superfinishing conditions.

Stone specification	SD 20000 L 105 V
Superfinishing pressure	0.90 MPa
Stone speed	18 m/min
Workpiece speed	129 m/min
Oscillation	16.7 Hz
Amplitude	0.5 mm
Superfinishing time	2.5, 5 min
Superfinishing fluid	Water (rust inhibitor 1%)
Workpiece	Sapphire (8nmRa)

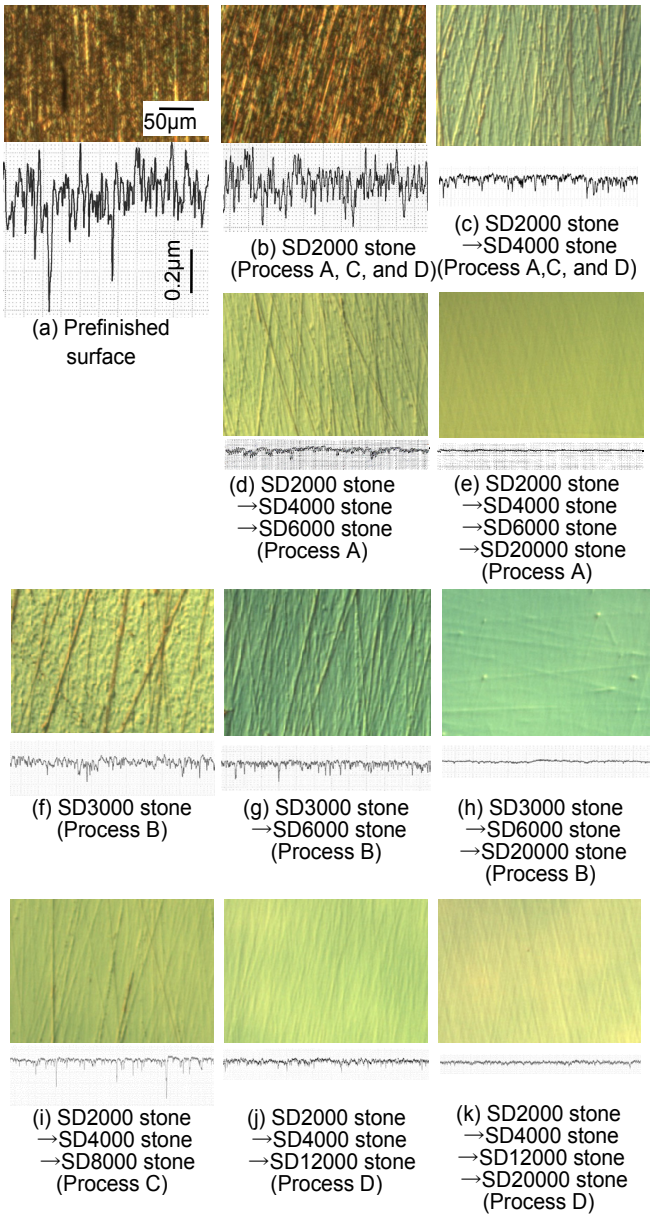
50μm
0.2μm
(a) Prefinished surface
(b) SD2000 stone (Process A, C, and D)
(c) SD2000 stone →SD4000 stone (Process A,C, and D)
(d) SD2000 stone →SD4000 stone →SD6000 stone (Process A)
(e) SD2000 stone →SD4000 stone →SD6000 stone →SD20000 stone (Process A)
(f) SD3000 stone (Process B)
(g) SD3000 stone →SD6000 stone (Process B)
(h) SD3000 stone →SD6000 stone →SD20000 stone (Process B)
(i) SD2000 stone →SD4000 stone →SD8000 stone (Process C)
(j) SD2000 stone →SD4000 stone →SD12000 stone (Process D)
(k) SD2000 stone →SD4000 stone →SD12000 stone →SD20000 stone (Process D)

FIGURE 2. Superfinished surface of sapphire in each process of multistage superfinishing.

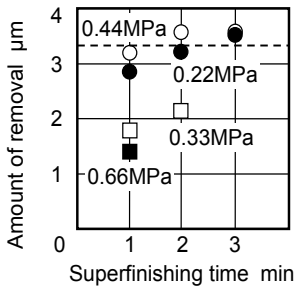

FIGURE 3. Comparison of the amount of removal as a function of superfinishing time.

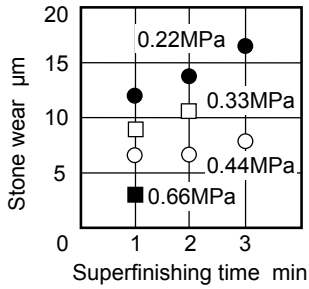

FIGURE 4. Comparison of stone wear as a function of superfinishing time.

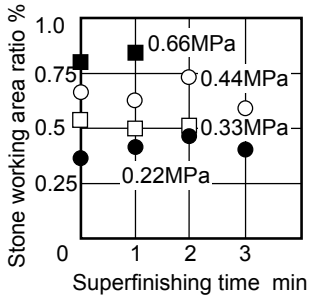

FIGURE 5. Comparison of stone working area ratio as a function of superfinishing time.

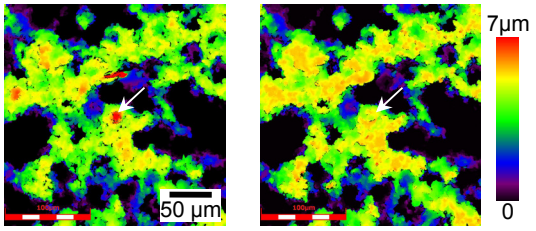

(a) 2 min (b) 3 min

FIGURE 6. Laser microscopic image of SD 3000 stone in superfinishing pressure of 0.22 MPa.

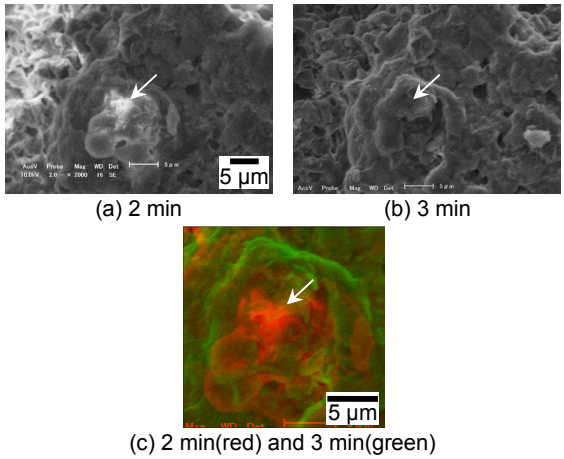

(a) 2 min (b) 3 min

(c) 2 min(red) and 3 min(green)

FIGURE 7. SEM micrograph of SD 3000 stone in superfinishing pressure of 0.22 MPa.

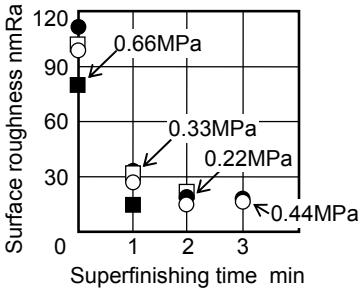

FIGURE 8. Comparison of surface roughness as a function of superfinishing time.

IMPROVEMENT OF FINE FINISHING

Next, in Process C and D, SD 8000 and SD 12000 stones were used in Stage 3 to reduce superfinishing time of Stage 4, SD 20000 stone. TABLE 5 shows stone specification and superfinishing conditions of SD 8000 and SD 12000 stones

In Process C, SD 8000 stone could not remove sufficient amount in a minute and remained deep scratches. FIGURE 2 (i) shows the result of SD 8000 stone.

FIGURE 9 shows the comparison of the amount of removal in each stone. The amount of removal was large enough in superfinishing with SD 12000 stone. In Process D, SD 12000 stone can remove almost sufficient amount of sapphire (dashed line in FIGURE 9) in a minute. Since few scratches remained after 1-minute superfinishing, 1-minute superfinishing was added and removed the scratches. FIGURE 2 (j) shows the result of SD 12000 stone.

FIGURE 10 and 11 show the comparison of stone wear and stone working area ratio in superfinishing with SD 8000 and SD 12000 stones, respectively.

FIGURE 12 shows the comparison of surface roughness in each stone. SD 12000 stone achieved surface roughness of 3nmRa in 2-minute superfinishing.

Subsequently Stage 4, SD 20000 stone were applied in shorter time, 2.5 minutes. The target roughness 2nmRa was achieved in 6.5 minutes of 4-stage superfinishing. FIGURE 2 (k) shows the result of SD 20000 stone.

FIGURE 13 shows the comparison of surface roughness in each process.

Those results indicate various process can achieve the target roughness 2nmRa. To optimize multistage superfinishing process, the removal amount estimation method based on the real contact pressure presumption [1] is necessary.

TABLE 5. Stone specification and superfinishing conditions.

Stone specification	SD 8000 I 110 V SD 12000 L 105 V
Superfinishing pressure	0.90 MPa
Stone speed	452 m/min
Workpiece speed	115 m/min
Oscillation	16.7 Hz
Amplitude	0.5 mm
Superfinishing time	1-2 min
Superfinishing fluid	Water (rust inhibitor 1%)
Workpiece	Sapphire (11nmRa)

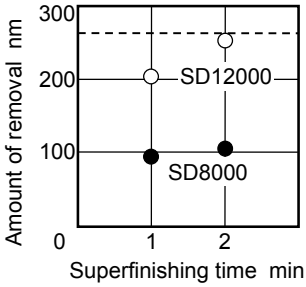

FIGURE 9. Comparison of the amount of removal as a function of superfinishing time.

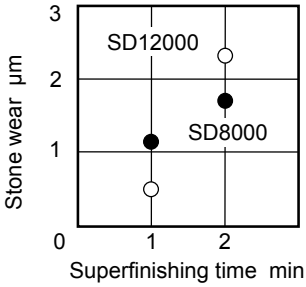

FIGURE 10. Comparison of stone wear as a function of superfinishing time.

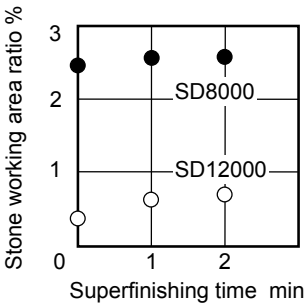

FIGURE 11. Comparison of stone working area ratio as a function of superfinishing time.

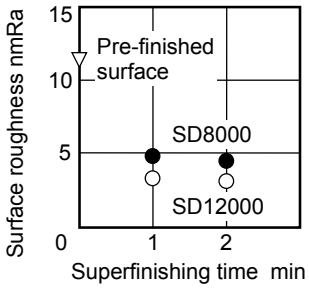

FIGURE 12. Comparison of surface roughness as a function of superfinishing time.

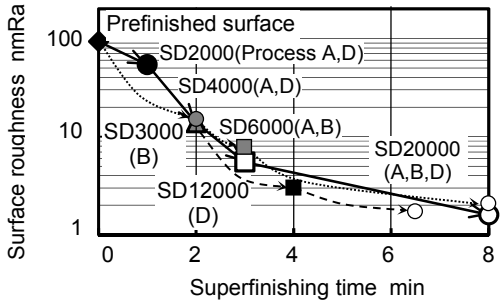

FIGURE 13. Comparison of improvement of surface roughness in Process A, B, and D as a function of superfinishing time.

CONCLUSINOS

In this study, three different combinations of multistage superfinishing process of sapphire were examined.

We have achieved the target roughness with fewer stage process and in less time process.

ACKNOWLEDGEMENT

This work was partially supported by JSPS Grant-in-Aid for Scientific Research Number JP18K03886.

REFERECES

[1] N. Furushiro, T. Yamaguchi, D. Hirooka, M. Yamaguchi, N. Matsumori, K. Tanada, “Development of Removal Amount Estimation Method based on Calculation of Elastic Deformation of Superabrasive Stones during Multistage Superfinishing of Sapphire”, International Journal of Automation Technology. 2017, 11 (6): 883-894.

ESTIMATION OF SAW WIRE TEMPERATURE DURING MACHINING OF ROCK IN VACUUM

Katsushi Furutani[1], Ryota Inukai[1], Takayoshi Takano[1], Tatsuaki Okada[2], Kazuto Saiki[3], and Hiroyuki Ohue[4]
[1]Toyota Technological Institute
Nagoya 468-8511 Japan
[2]Institute of Space and Astronautical Science (ISAS/ JAXA)
Sagamihara 252-5210 Japan
[3]Graduate School of Science, Osaka University
Toyonaka, Osaka 560-0043 Japan
[4]R&D Department, Tokusen Kogyo
Ono, Hyogo 675-1361 Japan

INTRODUCTION

In future planetary or asteroid explorations, *In-situ* analysis is demanded. The authors have proposed a wire-sawing machine to observe the interior of a rock sample with the compensation for the tool wear [1]. While a rock sample was cut with a saw wire, electroplated nickel which fixes diamond grains on a core wire was adhered on the rock. Consequently, the grains slipped on the nickel layer and the rock was little removed. Factors are possibly the hardness difference between the rock and nickel, and the softening of nickel due to the generated heat during machining.

The authors have measured the average temperature of a saw wire by observing its electric resistance in air and vacuum [2]. Figure 1 shows the experimental setup. While a saw wire was reciprocally fed by a slider-crank mechanism, its electrical resistance was measured by flowing current pulses to avoid the noise. After the relationship between the temperature and resistance was calibrated, the temperature was estimated. The temperature rose 3 and 23°C at an average velocity of 0.24 m/s after 270 reciprocations in air and vacuum, respectively. Although the average temperature of the saw wire was measured, the temperature at grains is still unknown.

In this paper, the temperature of abrasive grains during machining was estimated by simulation.

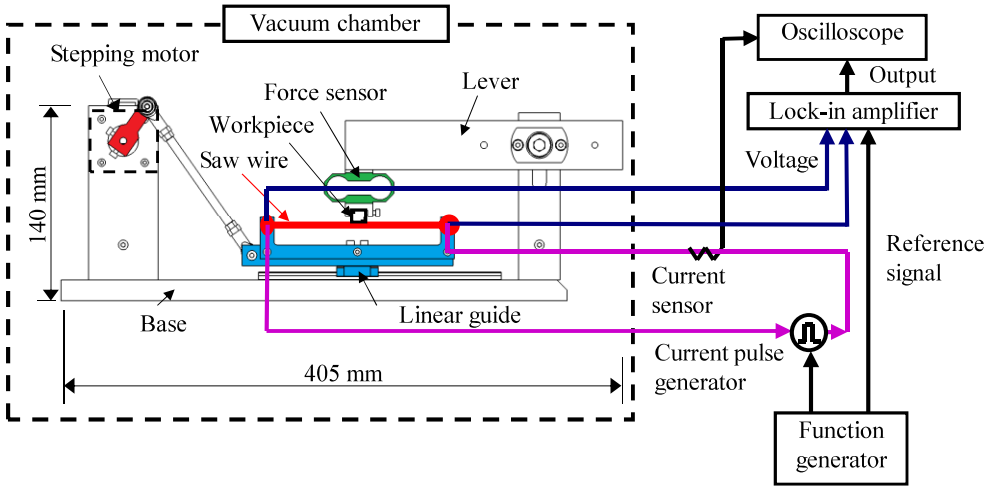

FIGURE1. Wire-sawing machine with slider-crank mechanism.

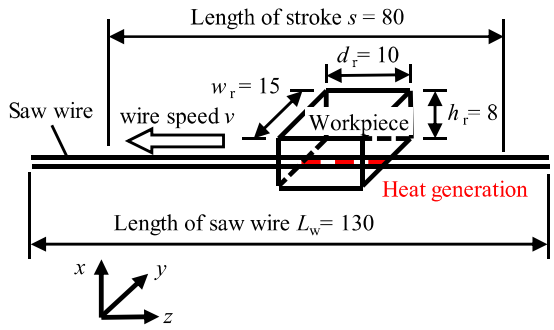

FIGURE 2. Schematic of wire saw cutting (unit: mm).

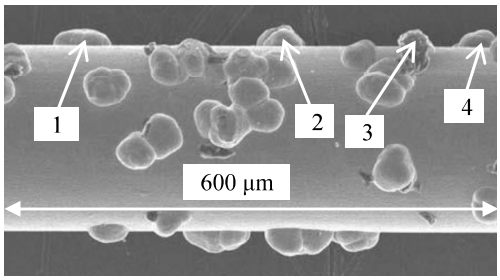

FIGURE 3. Appearance of saw wire.

SIMULATION MODEL

Figure 2 shows a schematic of the basalt rock wire-sawing. A saw wire with a length of 130 mm was reciprocally fed at a velocity of *v* for a stroke of 80 mm in the *z*-direction. The heat was generated at the contact part of the saw wire. Figure 3 shows a photo of the saw-wire. There are 4 abrasive grains with a diameter of 40 µm at the top surface within 600 µm. In this paper, it is assumed that only the abrasives on the top surface contribute the removal process though ones on the side surfaces also work in an actual process.

The temperature distribution is represented by the following partial differential equation:

$$\frac{\partial T(\boldsymbol{r},t)}{\partial t} = \frac{\lambda_{\mathrm{m}}}{\rho_{\mathrm{m}} C_{\mathrm{pm}}} \nabla^2 T(\boldsymbol{r},t) + \frac{q(\boldsymbol{r},t)}{\rho_{\mathrm{m}} C_{\mathrm{pm}}} \qquad (1)$$

where $\boldsymbol{r}$ is the position, t is the time, T is the time dependent temperature at any position, ρ_m is each material density, C_{pm} is the specific heat of each material, λ_m is the thermal conductivity of each material, and q is the time dependent heat energy generation rate at any position. It was assumed that the specific heat and thermal conductivity are independent from the temperature. The heat is not transferred by convection in vacuum. Because the heat capacity of debris and radiation from the wire were negligible, the generated heat was conducted into the rock or wire.

Figure 4 illustrates an expanded view of a finite difference model around the contact part. A half of the system was modelled due to its symmetry. To simplify the model, all elements were represented with cuboids. The mesh size around grains was the same as the grain size. It was assumed that the heat was generated at grains contacting the basalt. The heat energy was equally divided into contacting abrasive grains

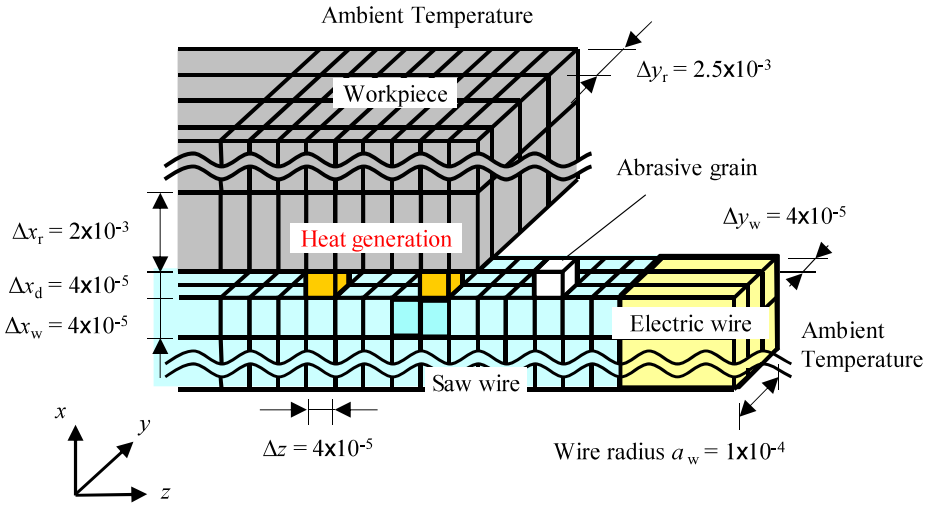

FIGURE 4. Schematic for 3D mesh (unit: m).

TABLE 1. Analysis conditions.

Saw wire (SWP-A)	Density ρ_w	7.85×10^3 kg/m^3
	Specific heat C_w	450 J/(kg•K)
	Thermal conductivity λ_w	60 W/(m•K)
Workpiece (Basalt)	Density ρ_r	2.68×10^3 kg/m^3
	Specific heat C_r	841 J/(kg•K)
	Thermal conductivity λ_r	1.37 W/(m•K)
Abrasive grain (Diamond)	Density ρ_d	3.52×10^3 kg/m^3
	Specific heat C_d	513 J/(kg•K)
	Thermal conductivity λ_d	2000 W/(m•K)
Time mesh Δt		2.0×10^{-5} s
Length of stroke s		8.0×10^{-2} m
Average wire speed v		0.08, 0.16, 0.32, 16 m/s
Number of strokes n_s		100
Average cutting power P		0.133 W (at v = 0.16 m/s)
Ambient temperature		31 °C

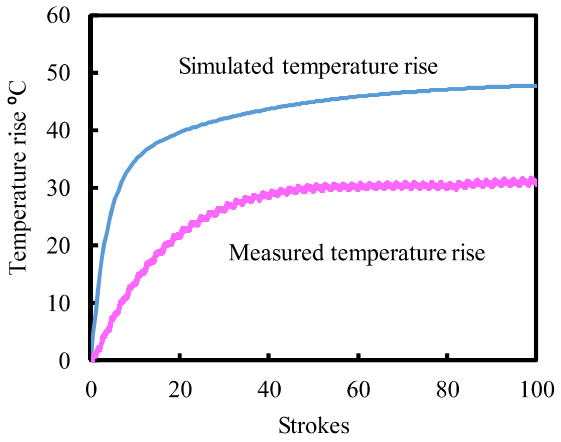

FIGURE 5. Simulated and measured temperature rise (v=0.16 m/s).

with the basalt. With an increase the number of grains, the temperature at the grains decrease under the same total energy. The temperature at the ends of the electrical wire to measure the resistance and on the top surface of the basalt mounted on a holder was fixed at the ambient temperature because of their larger heat capacity than the saw wire.

Equation (1) was discretized based on the model. Then it was solved by the alternating direction implicit (ADI) method [3], which is unconditionally stable. The time step is divided into 3 steps for three-dimensional analysis. The temperature distribution in each direction was calculated and then alternated the directions for each divided time step.

SIMULATION RESULTS

Table 1 shows analysis conditions. Because the average power can be calculated as:

$$P = \frac{1}{T_m}\int_0^{T_m} |F_p v| dt \quad (2)$$

where F_p, v and T_m are the principal force, the feeding velocity of the saw wire and the machining time, respectively [2], it is proportional to the velocity and one used in the simulation was estimated from an experimental result such as 0.133 W at 0.16 m/s. The heat conductivities of the saw wire, diamond and basalt are 60, 2000 and 2 W/m·K [4].

Figure 5 shows a comparison of simulated and measured temperature rise at a velocity of 0.16 m/s. Because their trends coincided each other, the model is adequate. The distribution of grains and heat conduction through the grains on the sides may cause the error.

Figure 6 shows examples of temperature rise profile after the first stroke. In both cases, the temperature rose within z = 20-110 mm where the rock was actually cut. The basalt was located within z = 20-30 mm at the end of the stroke. Because the heat was generated at the grains contacting the basalt, the temperature locally rose over 100°C at v = 16 m/s. The local temperature rise was small at v = 0.16 m/s because the generated heat was small and the heat was fully conducted due to long machining time.

Figure 7 shows the temperature distribution on top surface after 100 strokes. Each distribution

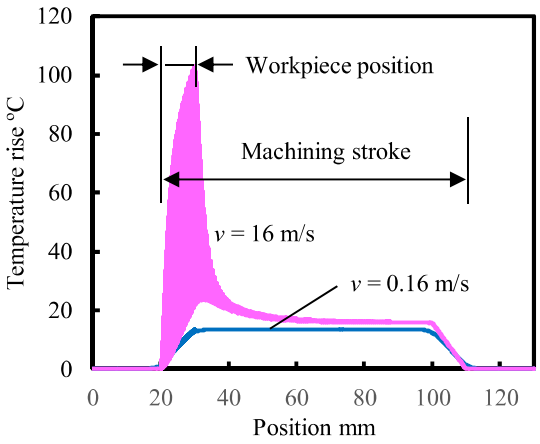

FIGURE 6. Temperature rise profile at end of first stroke (v=0.16, 16 m/s).

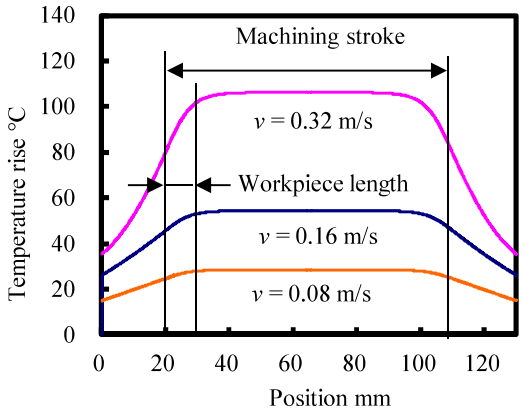

FIGURE 7. Temperature distribution on top surface after 100 strokes.

at the middle was flat by accumulating the heat. The heat mainly leaked out from the ends of the saw wire into the electric wires. The temperature at the center of the stroke reached 55°C at v = 0.16 m.

Figure 8 shows the relationship between the highest temperature rise after 100 strokes and wire velocity. The temperature rise was proportional to the velocity.

The temperature at 0.16 m/s rose 55°C at which nickel does not soften. However, nickel actually adhered on the machined groove of basalt in the experiments. Therefore, the temperature rise did not affect the adhesion of the nickel.

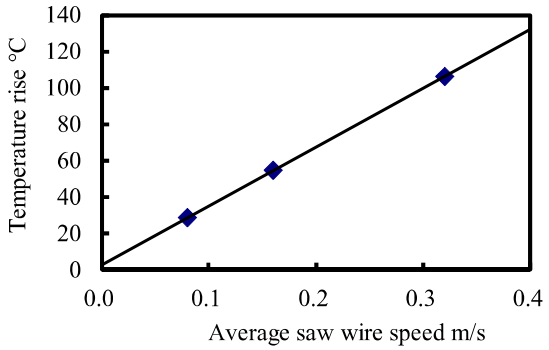

FIGURE 8. Relationship between highest temperature rise and wire velocity.

CONCLUSIONS

In this paper, the temperature of the saw wire during machining in vacuum was estimated especially at the grains. The trend of the temperature in the simulation coincided with the experiment. The highest temperature was much lower than softening temperature of nickel at the velocity that nickel was adhered on the basalt in an actual process. Therefore, the temperature rise did not affect the adhesion of the nickel.

Friction tests will be done to investigate other factors for a future work.

REFERENCES

[1] Furutani K, Fukunaga S, Okada T, Saiki K, Ohue H. Effect of Vacuum on Wire-sawing as Preliminary Experiment to Lunar Exploration. Proceedings of 2011 Annual Meeting of American Society for Precision Engineering, Denver, CO. 2011; 349-352.

[2] Furutani K, Inukai R, Takano T, Okada T, Saiki K, Ohue H. Measurement of Saw Wire Temperature during Cutting of Rock in Vacuum. Proceedings of 2014 Annual Meeting of American Society for Precision Engineering, Boston, MA. 2014; 508-511.

[3] Wang TY, Chen C CP. 3-D Thermal-ADI: A Linear-Time Chip Level Transient Thermal Simulator, IEEE Trans. Comput. Aided Des. Integrated Circuits Syst. (TCAD), 2002; 21(12): 1434-1445.

[4] Guéguen Y, Palciauskas V. Introduction to the Physics of Rocks. Princeton University Press. Princeton, NJ: 1994.

DETERMINATION OF CUTTING FORCES USING A FLEXURE-BASED DYNAMOMETER: DECONVOLUTION OF STRUCTURAL DYNAMICS USING THE FREQUENCY RESPONSE FUNCTION

Michael F. Gomez and Tony L. Schmitz
Department of Mechanical Engineering and Engineering Science
University of North Carolina at Charlotte
Charlotte, NC

INTRODUCTION

Accurate measurement of cutting forces is fundamental to the understanding and modeling of machining processes. Traditionally, cutting force measurements are performed using a multi-axis piezoelectric-based cutting force dynamometer. A workpiece is mounted on the dynamometer, which is mounted to the machine table and aligned with the feed direction [1]. However, the dynamic properties of the dynamometer must be considered when operating at or near the dynamometer's natural frequencies. At the natural frequencies there is an artificial amplification of force signals which can lead to inaccurate force readings. The cutting force measurements can be corrected by filtering the measured forces using the dynamometer force-to-input force transmissibility [2-4]. In doing so, there is a structural deconvolution of the unwanted dynamometer dynamics from the measured force signals.

This paper presents a novel method for cutting force measurement using displacement of a flexure-based dynamometer. In this case, the structural deconvolution is carried out by applying a filter to measured vibration signals based on the flexure's inverted frequency response function (FRF).

STRUCTURAL DECONVOLUTION

A simulation was programmed in MATLAB® to demonstrate the deconvolution of the structural dynamics for a single degree of freedom (SDOF) system. The first step in performing the deconvolution is to measure the structure's FRF. This was completed by impact testing, where an instrumented hammer is used to excite the structure and a measurement transducer is used to record the resulting vibration [1]. Using the system's FRF (see Fig. 1) the differential equation of motion in response to a harmonic forcing function takes the form:

$$m\ddot{x} + c\dot{x} + kx = A\sin(\omega t) \quad (1)$$

where, m, c, and k are the modal mass, damping, and stiffness parameters obtained from the FRF, A is force magnitude, and ω is the forcing frequency. The solution to the differential equation was obtained in this study by time-domain simulation; example results are displayed in Fig. 2.

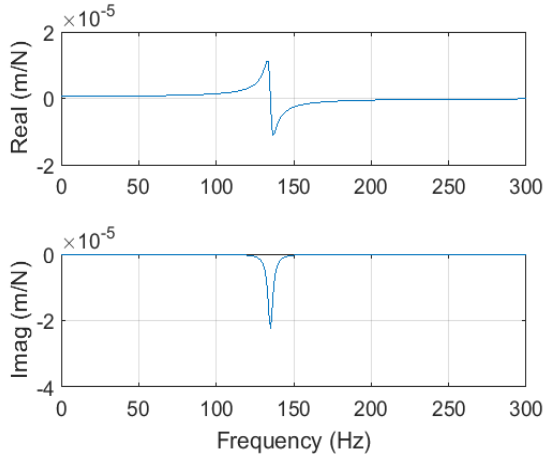

Figure 1: Real and imaginary parts of the FRF for the simulated SDOF system. The natural frequency, f_n, of the system is 135 Hz.

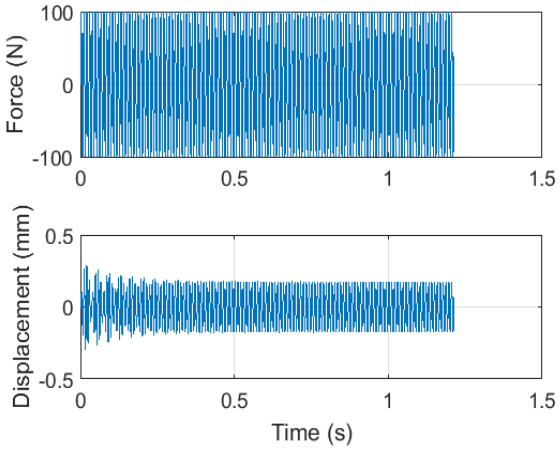

Figure 2: Time-domain response of a SDOF system (bottom) to the force profile (top). The displacement was calculated using Euler integration.

The inverted FRF is used to generate a filter which is applied to the frequency-domain displacement to

determine the frequency-domain force; see Fig. 3. The force is then transformed back into the time-domain. As a result, the force is based on displacement, rather than the traditional piezoelectric signal.

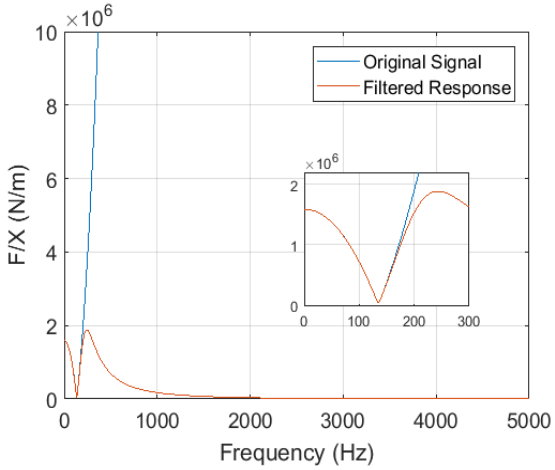

Figure 3: Frequency-domain response of the inverse filter used to remove the influence of the SDOF system dynamics. A low-pass 4th order Butterworth filter is applied to remove the effects of high-frequency content.

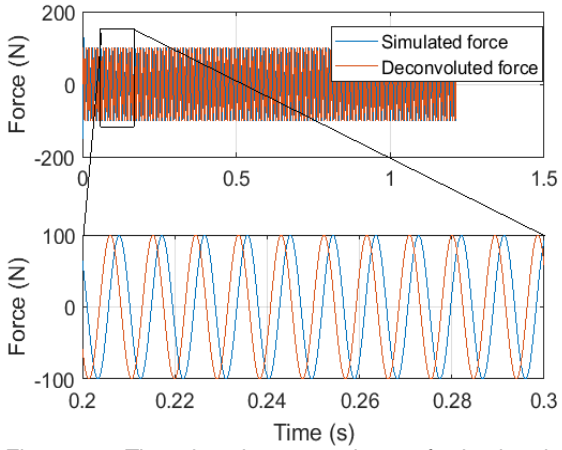

Figure 4: Time-domain comparison of simulated and calculated forces obtained by structural deconvolution.

Figure 4 demonstrates the technique for an ideal displacement signal. The results closely agree. To investigate the effects of noise, a 5% noise level was added to the force and displacement signals. The results are shown in Fig. 5. The structural deconvolution method is adversely affected by noise levels. Therefore, a high signal-to-noise ratio is necessary in order to obtain accurate results.

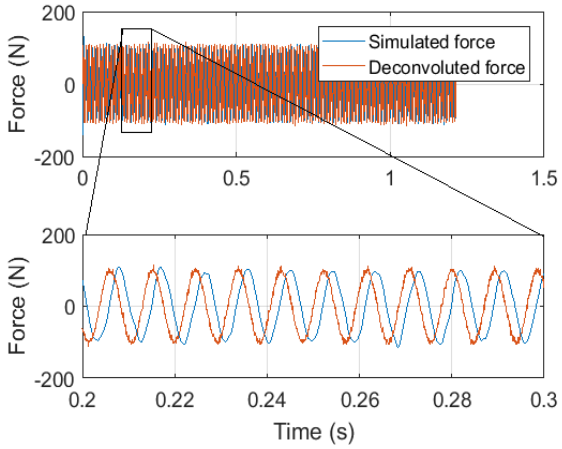

Figure 5 : Time-domain response of a SDOF system. A 5% noise level was added to the force and displacement signals.

EXCITATION FORCE MEASUREMENT

A series of tests were performed in order to compare measured and calculated forces. The SDOF flexure dynamics are provided in Table 1.

Table 1: SDOF Flexure dynamics.

f_n [Hz]	Damping ratio	k [N/m]
134.0	0.029	1.66×10^6

A function generator (Tektronix AFG 3022B) was used to command a waveform input for a modal shaker (TV 51075-M), which then excited the SDOF flexure system through a stinger (the stinger supports axial tension and compression, but not bending or shear [5]). A piezoelectric load cell (PCB 086C04) was affixed to the flexure end of the stinger to measure the excitation force applied to the system. The flexure vibrations were measured using a capacitance probe (LION Precision C-18-13-2.0). The experimental setup is illustrated in Fig. 6.

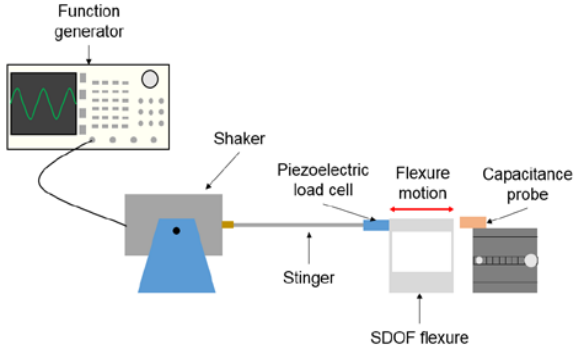

Figure 6: Flexure-based dynamometer experimental setup with a capacitance probe and modal shaker. Note that the excitation direction is in-line with the flexible direction of the flexure.

A series of waveforms were used to illustrate the ability to reproduce excitation forces via structural deconvolution. The commanded waveforms are described in Table 2.

Table 2: Commanded waveforms produced by the function generator and shaker.

Waveform	Forcing frequency [Hz]
Sine	5
Ramp	5
Square	20
Gaussian	50

While the sine and ramp waves contain only the fundamental forcing frequency, the square and Gaussian waves contain additional frequency content at integer multiples of the forcing frequency. The results of this experiment are shown in Figs. 7-10.

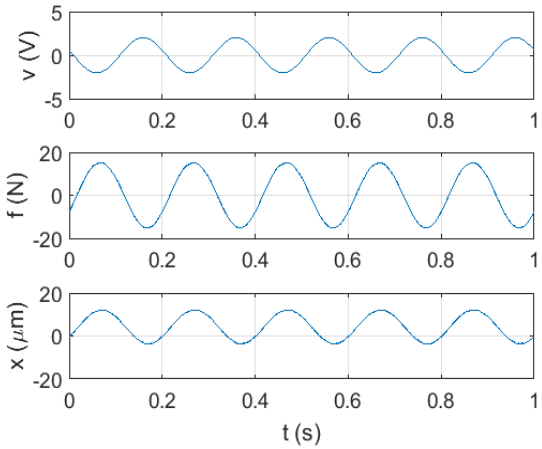

Figure 7: Time domain signals for a commanded sine wave at 5Hz. The commanded sine wave (top), the measured force by the piezoelectric load cell (middle), and the measured displacement by the capacitance probe (bottom).

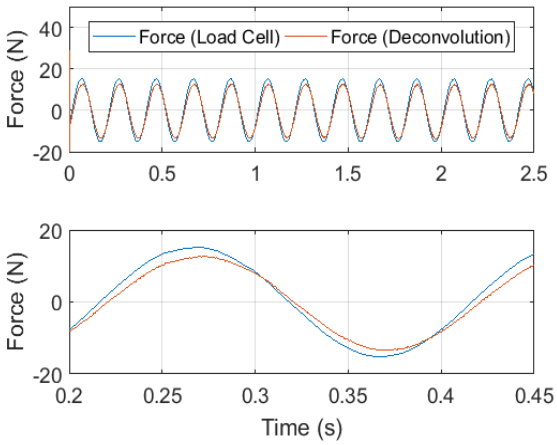

Figure 8: Time-domain comparison of measured and calculated forces for a sine wave with a forcing frequency of 5 Hz.

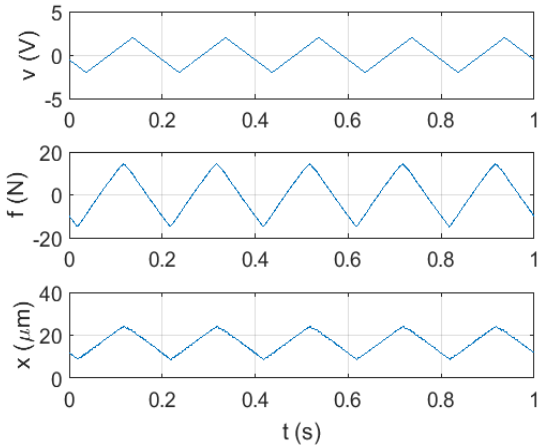

Figure 9: Time-domain signals for a commanded ramp wave at 5 Hz.

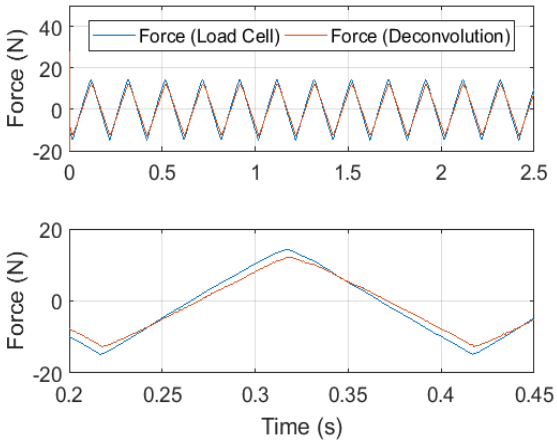

Figure 10: Time-domain comparison of measured and calculated forces for a ramp wave with a forcing frequency of 5 Hz

Frequently, partial radial immersion cutting forces resemble trains of periodic impulses [5]. Therefore, square and Gaussian waves were used to simulate the forces that may be encountered during milling experiments; see Figs. 11 and 13. A 4th order low-pass Butterworth filter was applied to the inverse flexure FRF with a cut-off frequency equal to the 10th harmonic (multiple) of the forcing frequency.

The forces were successfully reconstructed with minor discrepancies in the amplitude, as shown by Figs. 12 and 14. The differences in amplitude can be attributed to the low-pass filter which attenuates higher-order frequencies which may be present in the forcing function.

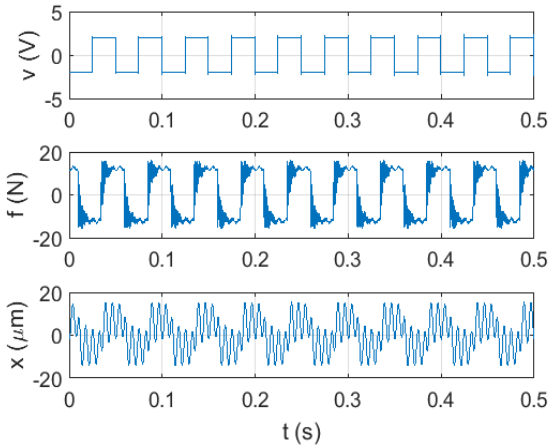

Figure 11: Time-domain signals for a commanded square wave at 20 Hz and a 50% duty cycle.

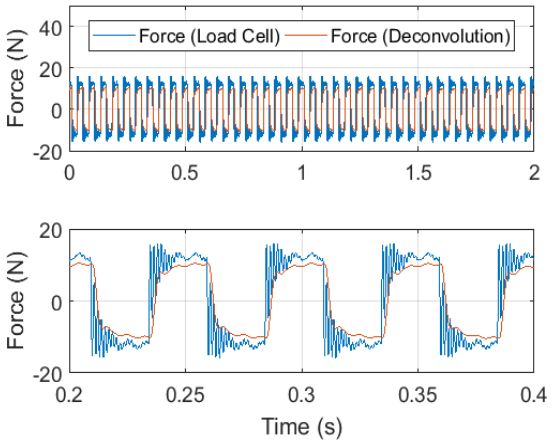

Figure 12: Time-domain comparison of measured and calculated forces for a square wave with a forcing frequency of 20 Hz.

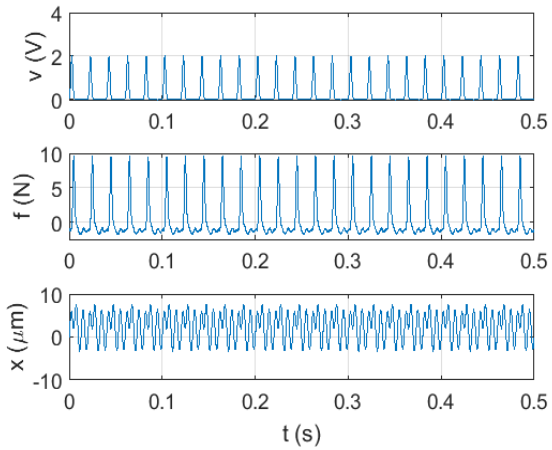

Figure 13: Time-domain signals for a commanded Gaussian wave at 50 Hz.

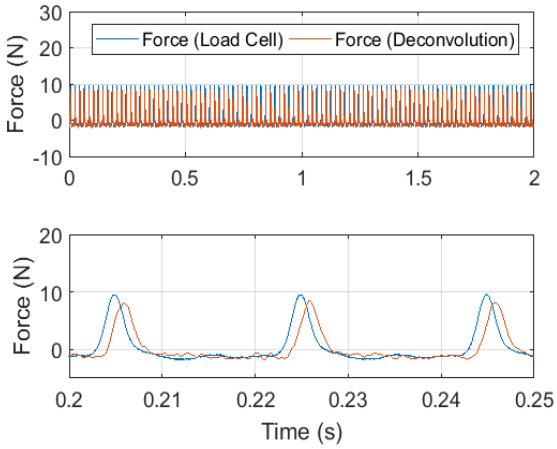

Figure 14: Time-domain comparison of measured and calculated forces through structural deconvolution. There is good agreement between the measured and calculated forces.

The measured and calculated force frequency content for the Gaussian waveform is shown in Fig. 15. It can be observed that the structural deconvolution replicates the fundamental frequency and its harmonics until the relative amplitudes are substantially dissipated. Further, the frequency-domain is useful in observing any added effects from the piezoelectric load cell.

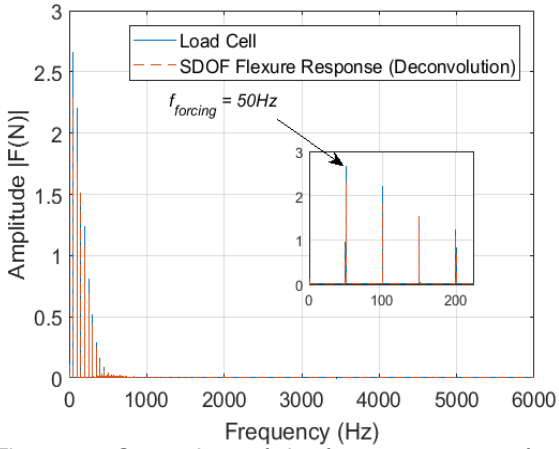

Figure 15: Comparison of the frequency content for the measured and calculated forces.

CUTTING FORCE MEASUREMNT

The first set of cutting tests were carried out by mounting an aluminum workpiece on a multi-axis dynamometer (Kistler Type 9257B). The second set of cutting tests were performed by mounting the workpiece on the SDOF flexure, where the flexure displacement was measured using a capacitance probe (LION Precision C-18-13-2.0); see Fig. 16. It is important to note that the measurement transducer

was aligned with the flexible direction of the SDOF flexure.

Stable down-milling machining conditions were selected for all trials at a spindle speed of 2550 rpm. The radial and axial depths of cut were both 2 mm. A set of three feed rates were chosen for this study: {25, 75, and 125} μm/tooth.

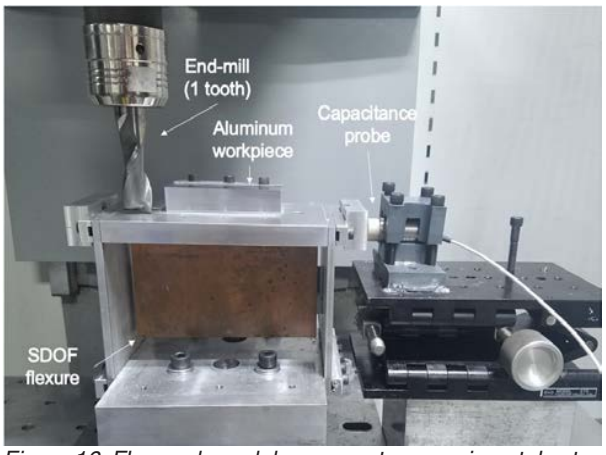

Figure 16: Flexure-based dynamometer experimental setup with a capacitance probe. Note that the feed direction is in-line with the flexible direction of the flexure.

RESULTS

The magnitude and coherence of the FRF for the SDOF flexure-dynamometer is shown by Fig. 17. The FRF was generated by an impact test using a modally tuned hammer (PCB 086C04 SN29958) and its displacement response was measured using the capacitance probe.

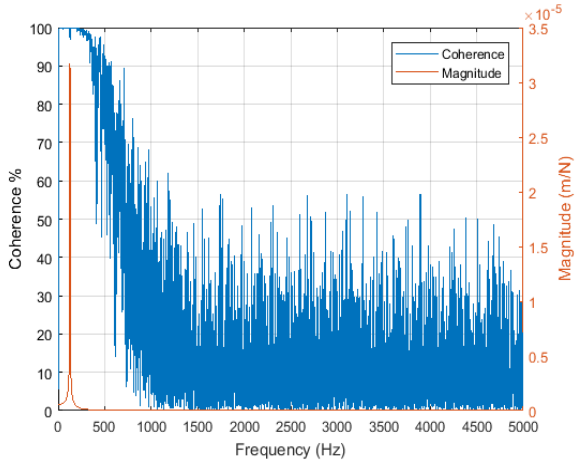

Figure 17: Magnitude and coherence measurements for the single degree of freedom flexure system used for the generation of cutting forces.

A comparison of the force signals is shown in Figs. 18-20. The displacement signal of the SDOF flexure was used to calculate cutting forces. Further, a low-pass filter was applied to the measured cutting forces to attenuate the high frequency content introduced by the dynamometer. These initial results show good agreement between the flexure-based dynamometer and the piezoelectric-based dynamometer.

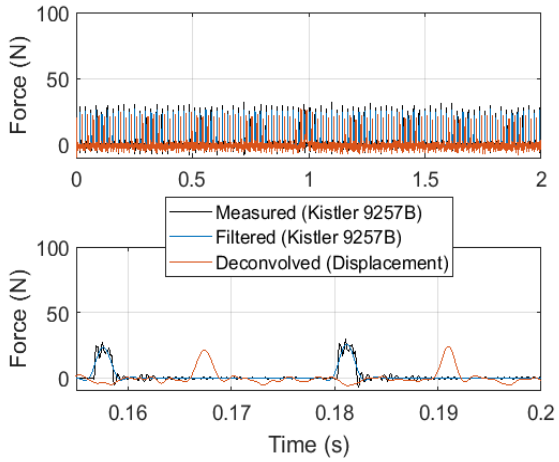

Figure 18: Measured, filtered, and calculated cutting forces for the 25 μm/tooth test.

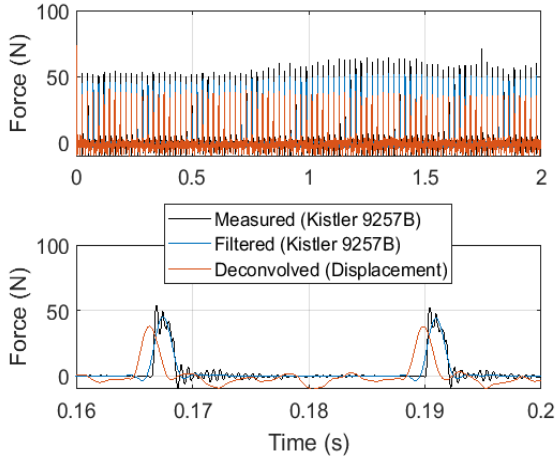

Figure 19: Measured, filtered, and calculated cutting forces for the 75 μm/tooth test.

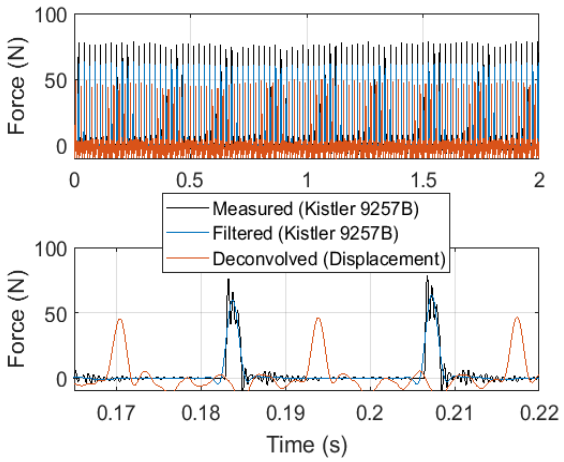

Figure 20: Measured, filtered, and calculated cutting forces for the 125 µm/tooth test.

The frequency content for the measured and calculated cutting forces is shown in Fig. 21. The additional frequency content introduced by the dynamometer structural response serves to artificially amplify the measured cutting forces at higher frequencies.

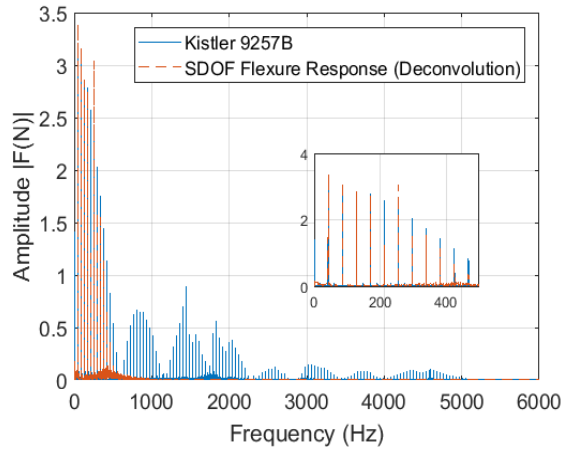

Figure 21: Cutting force frequency content for the Kistler 9257B dynamometer and the SDOF flexure-based dynamometer.

CONCLUSIONS

The purpose of this paper was to demonstrate the ability to measure cutting forces using the displacement of a flexure-based dynamometer. In this case, the structural deconvolution was carried out by applying a filter to a measured displacement signal based on the flexure's inverted frequency response function. It was shown that, for a variety of excitation forces, the measured displacement can be used to reconstruct the force profile.

It was found that it is important to consider the signal-to-noise ratio for the displacement transducer because the displacement-to-force frequency domain analysis is sensitive to noise. A low-noise displacement sensor is therefore necessary to accurately reconstruct the excitation force.

REFERENCES

[1] Schmitz T. L. and Smith K. S. (2009). Machining Dynamics: Frequency Response to Improved Productivity. Springer, New York, NY

[2] Korkmaz E., Gozen B. A., Bediz B., Ozdoganlar O. B. (2015). High-Frequency Compensation of Dynamic Distortions in Micromachining Force Measurements. Procedia Manufacturing 127: 673-678.

[3] Castro L. R., Vieville P., Lipinski P. (2006). Correction of dynamic effects on force measurements made with piezoelectric dynamometers. International Journal of Machine Tools and Manufacture 46: 1707-1715.

[4] Rubeo, M. A. and Schmitz T. L. (2016). Mechanistic force model coefficients: A comparison of linear regression and nonlinear optimization. Precision Engineering 45: 311-321.

[5] Schmitz T. L. and Smith K. S. (2012). Mechanical Vibrations: Modeling and Measurement. Springer, New York, NY

DIRECTION-DEPENDENT RECEPTANCES FOR ANISOTROPIC NICKEL SUPERALLOY

Andrew Honeycutt[1], Mike Glavicic[2], and Tony L. Schmitz[1]
[1]Department of Mechanical Engineering and Engineering Science
University of North Carolina at Charlotte, Charlotte, NC
[2]Rolls Royce Corporation, Indianapolis, IN

INTRODUCTION

It is common practice to produce monolithic metallic components with thin ribs from solid billets by machining. This enables complex parts with high strength-to-weight ratio to be produced without significant assembly time and cost. For high material cost situations, it is often preferred to apply near net shape strategies, where an initially thin feature (produced by forging or additive processes, for example) is machined to produce a thinner feature with the required dimensions and surface integrity. Application domains range from aerospace components to laptop cases.

A significant challenge in near net shape applications is that the low dynamic stiffness of the thin rib features limits both machining stability (i.e., chatter can occur) and part accuracy (via the surface location errors that can arise from forced vibrations) [1]. If the dynamic response of the workpiece is modeled, however, machining parameters and tool paths can be selected to produce acceptable parts. This process is complicated when machining anisotropic materials. In this case, the dynamics are direction-dependent due to the variation in elastic modulus with crystal orientation.

In this research, the single crystal superalloy CMSX-4 was selected for machining trials and dynamics prediction. This alloy was developed for gas turbine engine airfoil, seal, and combustor components to provide high temperature creep strength, fatigue resistance, oxidation resistance, and performance retention in thin-walled configurations. Its nominal composition is provided in Table 1 [2].

Table 1. CMSX-4 nominal composition.

Element	Wt.%	Element	Wt.%
Cr	6.5	Al	5.6
Co	9.6	Ti	1.0
W	6.4	Ta	6.5
Re	3.0	Hf	0.1
Mo	0.6	Ni	Balance

An analytical approach is presented here to describe the natural frequency of fixed-free beams, as well as the change in natural frequency as material is removed by milling. Fixed-free beams with stepped profiles are used to represent the thin ribs geometries and subsequent material removal. Due to the CMSX-4 anisotropy, results are presented for two material directions with corresponding differences in elastic modulus.

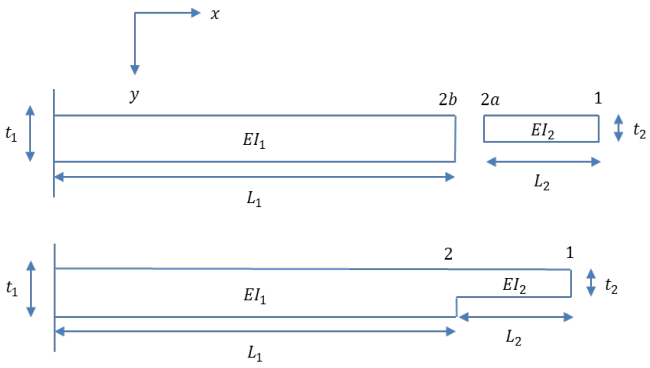

Figure 1. Beam model for RCSA. (Top) The two components and associated coordinates (1 and $2a$ for the free-free component and $2b$ for the fixed-free component) are identified. (Bottom) The assembly and associated coordinates (1 and 2) are shown.

ANALYTICAL MODEL

Receptance coupling substructure analysis (RCSA) is a frequency domain, analytical procedure used to couple component receptances (or frequency response functions) in order to predict the assembly receptances [3-4]. In this work, the free-free receptances for the machined section of a beam were rigidly coupled to the remaining (unmachined) fixed-free section; see Fig. 1. Using rigid compatibility and equilibrium conditions, the assembly direct receptances, $H_{11} = \frac{Y_1}{F_1}$ and $H_{22} = \frac{Y_2}{F_2}$, at assembly coordinates Y_1 and Y_2 are written as a function of the component receptances at coordinates 1, $2a$, and $2b$; see [3] for the derivation. The required direct and cross receptances for the free-free (coordinates 1 and $2a$) and fixed-free (coordinate $2b$) components are:

- $h_{11} = \frac{y_1}{f_1}$, $h_{12a} = \frac{y_1}{f_{2a}}$, $h_{2a1} = \frac{y_{2a}}{f_1}$, $h_{2a2a} = \frac{y_{2a}}{f_{2a}}$, and $h_{2b2b} = \frac{y_{2b}}{f_{2b}}$, where y_i is the component

displacement and f_j is the (internal) component force

- $l_{11} = \frac{y_1}{m_1}$, $l_{12a} = \frac{y_1}{m_{2a}}$, $l_{2a1} = \frac{y_{2a}}{m_1}$, $l_{2a2a} = \frac{y_{2a}}{m_{2a}}$, and $l_{2b2b} = \frac{y_{2b}}{m_{2b}}$, where m_j is the (internal) component moment
- $n_{11} = \frac{\theta_1}{f_1}$, $n_{12a} = \frac{\theta_1}{f_{2a}}$, $n_{2a1} = \frac{\theta_{2a}}{f_1}$, $n_{2a2a} = \frac{\theta_{2a}}{f_{2a}}$, and $n_{2b2b} = \frac{\theta_{2b}}{f_{2b}}$, where θ_i is the component rotation
- $p_{11} = \frac{\theta_1}{m_1}$, $p_{12a} = \frac{\theta_1}{m_{2a}}$, $p_{2a1} = \frac{\theta_{2a}}{m_1}$, $h_{2a2a} = \frac{\theta_{2a}}{m_{2a}}$, and $p_{2b2b} = \frac{\theta_{2b}}{m_{2b}}$.

The assembly receptances are provided in Eqs. 1 and 2 [3].

$$\begin{bmatrix} H_{11} & L_{11} \\ N_{11} & P_{11} \end{bmatrix} = \begin{bmatrix} h_{11} & l_{11} \\ n_{11} & p_{11} \end{bmatrix} - \begin{bmatrix} h_{12a} & l_{12a} \\ n_{12a} & p_{12a} \end{bmatrix} \left(\begin{bmatrix} h_{2a2a} & l_{2a2a} \\ n_{2a2a} & p_{2a2a} \end{bmatrix} + \begin{bmatrix} h_{2b2b} & l_{2b2b} \\ n_{2b2b} & p_{2b2b} \end{bmatrix} \right)^{-1} \begin{bmatrix} h_{2a1} & l_{2a1} \\ n_{2a1} & p_{2a1} \end{bmatrix} \quad (1)$$

$$\begin{bmatrix} H_{22} & L_{22} \\ N_{22} & P_{22} \end{bmatrix} = \begin{bmatrix} h_{2a2a} & l_{2a2a} \\ n_{2a2a} & p_{2a2a} \end{bmatrix} - \begin{bmatrix} h_{2a2a} & l_{2a2a} \\ n_{2a2a} & p_{2a2a} \end{bmatrix} \left(\begin{bmatrix} h_{2a2a} & l_{2a2a} \\ n_{2a2a} & p_{2a2a} \end{bmatrix} + \begin{bmatrix} h_{2b2b} & l_{2b2b} \\ n_{2b2b} & p_{2b2b} \end{bmatrix} \right)^{-1} \begin{bmatrix} h_{2a2a} & l_{2a2a} \\ n_{2a2a} & p_{2a2a} \end{bmatrix} \quad (2)$$

The component receptances can be obtained from measurements or models. In this work, the Timoshenko beam model was implemented to find the free-free receptances. This requires a numerical solution of the partial differential equation displayed in Eq. 3 [5-6], where E is the elastic modulus, I is the second moment of area, ρ is the density, A is the cross-sectional area, G is the shear modulus, and $\hat{k}$ is a shape factor that depends on the beam's cross section [7].

To determine the required fixed-free ($2b2b$) receptances for the L_1 section component, the free-free receptances for this component (obtained from Eq. 3) were rigidly coupled to a rigid boundary (i.e., zero receptances). Equation 1 was also applied for this sub-step, where the $2b$ coordinate was assigned to the rigid boundary and the 1 and $2a$ coordinates to the L_1 section component. The RCSA method reported here builds on prior finite element-based models used to predict the thin rib dynamics and, in many cases, the change in the rib dynamics as material is removed [8-26].

$$\left(\frac{\partial^2 y}{\partial t^2} + \frac{EI}{\rho A}\frac{\partial^4 y}{\partial x^4}\right) + \left(\frac{\rho I}{\hat{k}AG}\frac{\partial^4 y}{\partial t^4} + \frac{EI}{\hat{k}AG}\frac{\partial^4 y}{\partial x^2 \partial t^2}\right) - \left(\frac{I}{A}\frac{\partial^4 y}{\partial x^2 \partial t^2}\right) = 0 \quad (3)$$

EXPERIMENTAL RESULTS

The test sample geometry shown in Fig. 2 was sectioned from cast CMSX-4 76×152×12 mm plates using wire EDM. The solidification <001> direction for the plates was nominally along the 152 mm dimension. This is the direction of lowest modulus. Two orientations within the cast plate were selected to interrogate the effect of modulus on the sample receptances. The orientations are displayed in Fig. 3. The 0 deg samples were collected from one plate and the 90 deg samples from a second plate. These samples were then finish machined as shown in Fig. 1 to measure the change in fixed-free natural frequency as material was removed. The measured natural frequency variation was then compared to RCSA predictions.

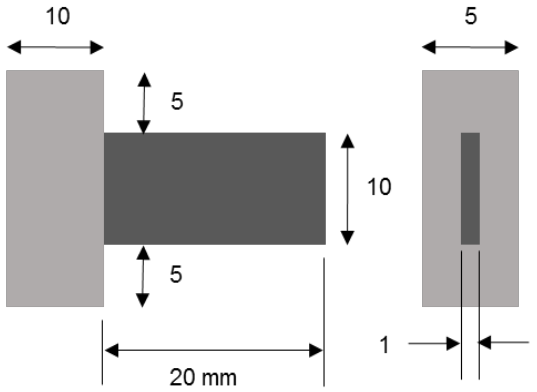

Figure 2. Sample geometry.

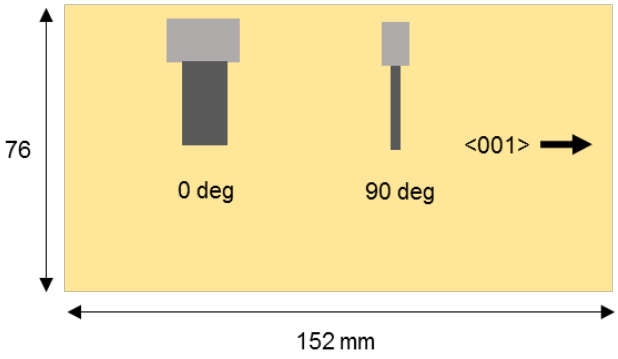

Figure 3. Sample orientations within the cast CMSX-4 plates.

The sample densities and elastic moduli were measured to obtain the values required for the RCSA analyses. Archimedes' water displacement method

was used to determine the density. The following steps were completed.

- A container of water was placed on a scale and the mass was recorded.
- The sample was submerged in the water with a thin wire so that it was fully submerged, but not touching the bottom of the container.
- The mass was again recorded.
- Since the buoyant force is equal to the weight of the displaced water, the volume of the sampled was estimated using the measured force and water density.
- The sample mass was measured.
- The density was calculated using the sample mass and volume.

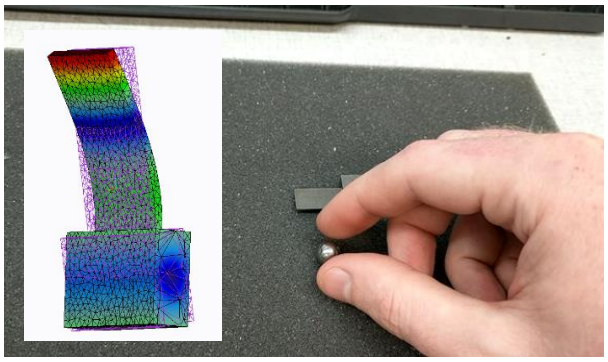

Figure 4. Elastic modulus determination. The free-free boundary condition impact testing setup and finite element model (inset) are shown.

The elastic modulus was measured by free-free boundary condition impact testing. The samples were placed on a soft foam foundation and excited by dropping a steel sphere at the top free edge of the thin rib. The corresponding sound signal was measured and converted to the frequency domain to determine the fundamental natural frequency. A finite element model of the sample (with free-free boundary conditions) was then generated and the elastic modulus was varied until the fundamental natural frequency matched the measured value; the measured density values were used as input to the finite element model. See Fig. 4 for the setup. The density and modulus measurement were repeated for both sample directions from Fig. 3 (0 deg and 90 deg). The results are provided in Table 2.

Table 2. Measured sample density and modulus.

Orientation	Density (kg/m^3)	Elastic modulus (GPa)
0 deg	8797	188
90 deg	8695	166

Receptance measurements were completed using a modal hammer (PCB 086C04) to excite the beam and a laser vibrometer (Polytec OFV 5000 controller/OFV 534 laser head) to measure the velocity; see Fig. 5, which shows the sample clamped in a vise to approximate fixed-free boundary conditions.

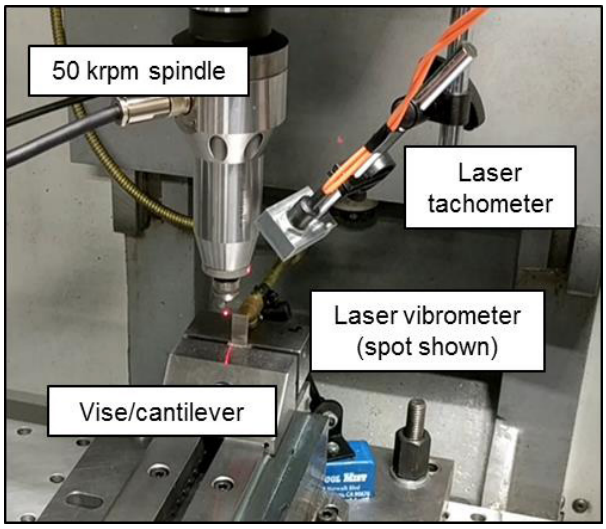

Figure 5. Experimental setup. The rib was machined to reduce the thickness and the receptance was measured for multiple L_2 values.

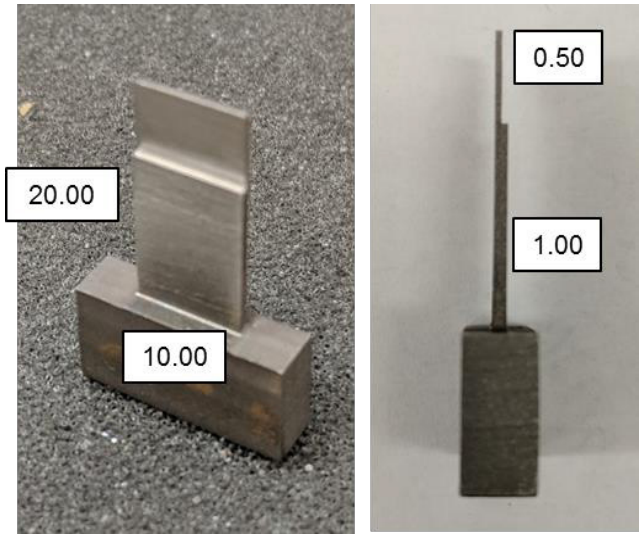

Figure 6. Photograph of machined sample (dimensions in mm).

Direct receptance measurements were performed at the sample's free end. The length of the reduced thickness section, L_2, was changed by machining, where a 1.50 mm diameter two-flute solid carbide endmill (approximately 10 mm stickout length) was

used (0.010 mm/tooth, 11000 rpm). The cutting flutes were ground away above the selected axial depth to avoid contact between the vibrating tool and machined surface. The beam thickness was reduced from 1 mm (t_1 from Fig. 1) to 0.5 mm (t_2) in 0.025 mm axial steps with a radial depth of 0.50 mm. Measurements were performed after the desired reduced thickness length was obtained. A photograph of a machined sample is displayed in Fig. 6.

The variation in natural frequency, f_n, with L_2 is provided in Table 3 for the two sample orientations. Note that the natural frequencies differ; the higher values are associated with the 0 deg sample that had the higher modulus in the flexible bending direction.

Table 3. Variation in measured natural frequencies with L_2 for both sample orientations.

0 deg		90 deg	
L_2 (mm)	f_n (Hz)	L_2 (mm)	f_n (Hz)
0	1874	0	1777
1.27	1970	1.27	1879
2.54	2074	2.54	1989
3.81	2163	3.81	2109
5.08	2240	5.08	2114
6.35	2296	6.35	2289

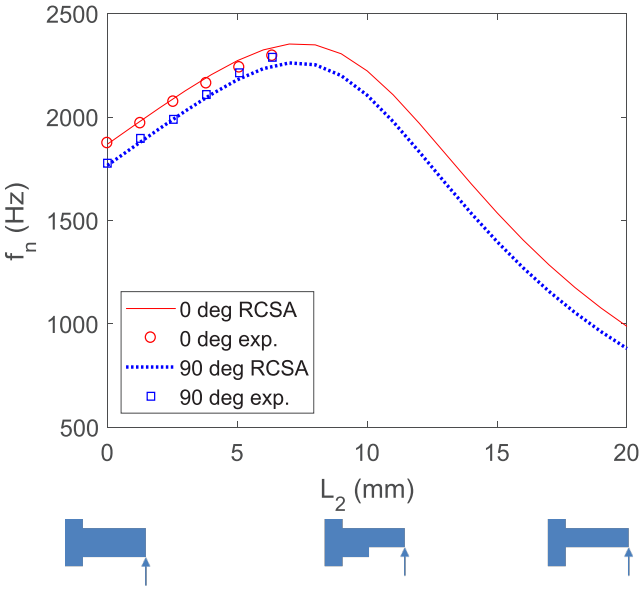

Figure 7. Comparison of measured and predicted natural frequencies. The variation in natural frequencies with L_2 is provided for both sample orientations.

A comparison between measured natural frequencies and RCSA predictions is displayed in Fig. 7, where the RCSA natural frequencies were identified from the predicted receptances using peak-picking [3]. An interesting trend is revealed by the simulation. It is observed that the natural frequencies first increase and then decrease as additional material is removed. The initial increase is obtained due to the mass removal without significant change in the fixed-free beam stiffness. With additional material removal, however, the beam stiffness decreases dramatically and the natural frequency decreases despite further mass removal.

CONCLUSIONS

An analytical approach was presented for predicting thin rib, fixed-free beam dynamics with varying geometries. The method was based on receptance coupling substructure analysis (RCSA). The effect of workpiece material anisotropy on receptance was investigated by choosing two different sample orientations within two CMSX-4 nickel superalloy plates. Separate free-free impact testing measurements verified the difference in elastic moduli between the two directions.

The outcome of both predictions and experiments was that the receptances differed between the two orientations (0 deg – flexible bending direction perpendicular to the solidification direction and 90 deg – parallel). The implications for machining are that the operating parameters may need to be changed depending on the orientation of the rib's flexible direction. For example, the preferred spindle speed to avoid chatter for one direction may be different than another. The best speeds for chatter avoidance are proportional to the natural frequency [1]. If the natural frequencies differ, then a stable speed for one orientation may be unstable for another. Given the RCSA model, however, the receptances can be predicted and optimal machining parameters may be selected in a pre-process manner.

ACKNOWLEDGEMENTS

The authors gratefully acknowledge financial support from MAI BA-21 (USAF contract number FA8650-17-2-5246).

REFERENCES

[1] Schmitz, T. and Smith, K.S., 2009, Machining Dynamics: Frequency Response to Improved Productivity, Springer, New York, NY.

[2] Harris, K. and Wahl, J.B., 2004, Improved single crystal superalloys CMSX-4 (SLS) [La+Y] and CMSX-486, Superalloys 2004, K.A. Green, T.M. Pollock, and H. Harada, Eds., TMS (The Minerals, Metals & Materials Society).

[3] Schmitz, T. and Smith, K.S., 2012, Mechanical Vibrations: Modeling and Measurement, Springer, New York, NY.
[4] Bishop, R.E.D., and Johnson, D.C., 1960, The Mechanics of Vibration, Cambridge University Press, Cambridge, UK.
[5] Weaver, Jr., W., Timoshenko, P., and Young, D., 1990, Vibration Problems in Engineering, 5th Ed., John Wiley and Sons, New York, NY.
[6] Schmitz, T. and Duncan, G.S., 2005, Three-component receptance coupling substructure analysis for tool point dynamics prediction, Journal of Manufacturing Science and Engineering, 127/4: 781-790.
[7] Hutchinson, J., 2001, Shear coefficients for Timoshenko beam theory, Journal of Applied Mechanics, 68: 87-92.
[8] Budak, E., Altintas, Y., 1995, Modeling and avoidance of static form errors in peripheral milling of plates, International Journal of Machine Tools & Manufacture, 35: 459-476.
[9] Tlusty, J., Smith, S., and Winfough, W., 1996, Techniques for the use of long slender end mills in high-speed milling, Annals of the CIRP, 45/1: 393-396.
[10] Smith, S. and Dvorak, D., 1998, Tool path strategies for high speed milling aluminum workpieces with thin webs, Mechatronics, 8: 291-300.
[11] Ning, H., Zhigang, W., Chengyu, J., and Bing, Z., 2003, Finite element method analysis and control stratagem for machining deformation of thin-walled components, Journal of Materials Processing Technology, 139: 332-336.
[12] Ratchev, S., Nikov, S., and Moualek, I., 2004, Material removal simulation of peripheral milling of thin wall low-rigidity structures using FEA, Advances in Engineering Software, 35: 481-491.
[13] Ratchev, S., Liu, S., Huang, W., and Becker, A.A., 2004, Milling error prediction and compensation in machining of low-rigidity parts, International Journal of Machine Tools & Manufacture, 44: 1629-1641.
[14] Bravo, U., Altuzarra, O., López de Lacalle, L.N., Sánchez, J.A., and Campa, F.J., 2005, Stability limits of milling considering the flexibility of the workpiece and the machine, International Journal of Machine Tools & Manufacture, 45: 1669-1680.
[15] Ratchev, S., Liu, S., and Becker, A.A., 2005, Error compensation strategy in milling flexible thin-wall parts, Journal of Materials Processing Technology, 162-163: 673-681.
[16] Thevenot, V., Arnaud, L., Dessein, G., and Cazenave-Larroche, G., 2006, Influence of material removal on the dynamic behavior of thin-walled structures in peripheral milling, Machining Science and Technology, 10/3: 275-287.
[17] Mañé, I., Gagnol, V., Bouzgarrou, B.C., and Ray, P., 2008, Stability-based spindle speed control during flexible workpiece high-speed milling, International Journal of Machine Tools & Manufacture, 48: 184-194.
[18] Rai, J.K. and Xirouchakis, P., 2008, Finite element method based machining simulation environment for analyzing part errors induced during milling of thin-walled components, International Journal of Machine Tools & Manufacture, 48: 629-643.
[19] Seguy, S., Dessein, G., and Arnaud, L., 2008, Surface roughness variation of thin wall milling, related to modal interactions, International Journal of Machine Tools & Manufacture, 48: 261-274.
[20] Adetoro, O.B., Wen, P.H., Sim, W.M., and Vepa, R., 2009, Stability lobes prediction in thin wall machining, Proceedings of the World Congress on Engineering 2009 Vol I, WCE 2009, July 1-3, 2009, London, UK.
[21] Chen, W., Xue, J., Tang, D., Chen, H., and Qu, S., 2009, Deformation prediction and error compensation in multilayer milling processes for thin-walled parts, International Journal of Machine Tools & Manufacture, 49: 859-864.
[22] Gang, L., 2009, Journal of Materials Processing Technology, Study on deformation of titanium thin-walled part in milling process, 209: 2788-2793.
[23] Arnaud, L., Gonzalo, O., Seguy, S., Jauregi, H., and Peigné, G., 2011, Simulation of low rigidity part machining applied to thin-walled structures, International Journal of Advanced Manufacturing Technology, 54: 479-488.
[24] Izamshah, R., Mo, J.P.T, and Ding, S., 2011, Hybrid deflection prediction on machining thin-wall monolithic aerospace components, Proc. IMechE Part B: Journal of Engineering Manufacture, 226: 592-605.
[25] Smith, S., Wilhelm, R., Dutterer, B., Cherukuri, H., and Goel, G., 2012, Sacrificial structure preforms for thin part machining, CIRP Annals - Manufacturing Technology, 61: 379-382.
[26] Polishetty, A., Goldberg, M., Littlefair, G., Puttaraju, M., and Patil, P., 2014, A preliminary assessment of machinability of titanium allow Ti 6Al 4V during thin wall machining using trochoidal milling, Procedia Engineering, 97: 357-364.

EFFECT OF DISTANCE OF POLISHING PAD AND NOZZLE FROM SURFACE OF ROLL MOLD IN HYBRID POLISHING PROCESS

Tae-Jin Je[1,2], Ji-Young Jeong[1,2], Je-Ryung Lee[1], Seung Hwan Moon[1], Doo-Sun Choi[1]
[1]Department of Nano Manufacturing Technology
Korea Institute of Machinery and Materials
Daejeon 34103, Korea
[2]Department of Nano Mechatronics,
University of Science and Technology
Daejeon 34113, Korea

INTRODUCTIONS

The BLU (Back Light Unit), the core component of display products, requires optical films in order to increase the optical functions such as uniformity and high brightness. These films are mainly produced by a roll to roll process using a roll mold with optical micro patterns, and most of these molds are fabricated by ultra-precision cutting machining. However, sharp and regular feed marks are generated by the cutting tool in the cutting process of roll molds having a mirror surface. These marks act as optical defects that are easily seen by the user in the display products. As one method to solving this problem, a FJP (Fluid Jet Polishing) process using abrasive particles and a fluid jet has been widely studied.[1-2] The FJP process using a discharging nozzle is known to have advantages of a fast material removal rate, wide polishing area, and the absence of feed marks.[3-4] However, in non-ferrous metal materials such as copper, nickel, etc., which are widely applied to roll molds with a mirror surface, there are problems such as damage to the mirror surface by the high speed of fluid jet, and quality deterioration by adhesion of the micro abrasive. Furthermore, the machined surface and surrounding environment can be contaminated by the scattered polishing liquid.

In a previous study aimed at solving these problems, a hybrid polishing system was designed to apply a rotating elastic pad to the FJP process, and the basic performance was analyzed.[5] In the polishing process using this hybrid system, machining results can be complexly affected by varying conditions of FJP and rotary pad polishing.

In this paper, effects on the polished surface of a brass roll mold were analyzed according to varying contact force depending on the compression distance of the polishing pad and v-

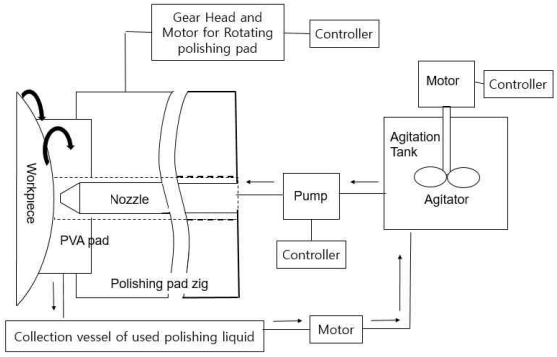

FIGURE 1. Schematic diagram of hybrid polishing system design composed of FJP part and rotary pad polishing part.

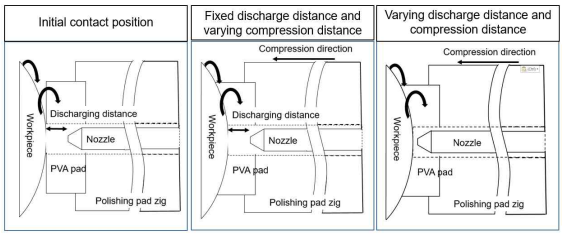

(a) (b) (c)

FIGURE 2. Movement methods of PVA pad and nozzle; (a) shows initial state at contact position, (b) shows fixed discharging distance and varying compression distance, and (c) shows varying discharging distance and compression distance.

-arying discharging distance of the fluid jet.

EXPERIMENTAL SYSTEM AND METHODS

Figure 1 shows a schematic diagram of the hybrid polishing system used in this study. The hybrid polishing system was composed of the FJP part and pad polishing part. In the FJP process, the surface of the mold is machined by a discharging fluid jet containing abrasives at a high pressure and a high speed. In the pad polishing process,

the polishing liquid ejected from the FJP process is prevented from scattering and absorbs a part of the abrasive contained in the polishing liquid. it then rotates the pad to process the surface of the mold. The nozzle for discharging the fluid jet was made of a carbide material with a diameter of 1 mm and it is located at the center of the hollow part of the polishing pad. The polishing pad had a hollow shape with an outer diameter of 30 mm and an inner diameter of 10 mm. PVA (polyvinyl alcohol) having pores on more than 90% of its surface that can effectively adsorb and can be smoothly deformed according to the state of the mold surface was used for the pad material. Figure 2 presents a schematic diagram showing two working methods of the hybrid polishing system. (a) shows the initial contact state and (b) shows a method of changing the position of the polishing pad in a state where the position of the nozzle was fixed. (c) shows another working method where the distances of the nozzle and the polishing pad from the mold surface were simultaneously reduced.

SURFACE CONDITION OF THE TURNED ROLL MOLD

Figure 3 shows the surface condition of a turning machined roll mold of brass material. On the surface of the mold, regular feed marks and tear marks generated by the cutting tool are observed. The measured surface roughness was about 0.2 μm Ra (1 μm Rz).

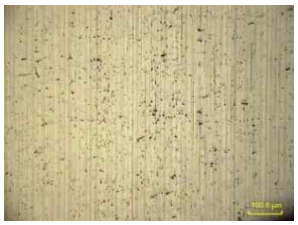

FIGURE 3. Micrograph image of machined surface of brass roll mold by CBN cutting tool

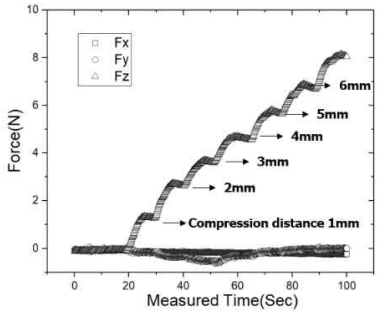

FIGURE 4. Contact force of the PVA polishing pad according to varying compression distance

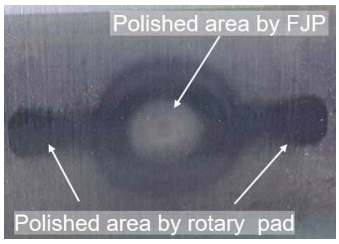

(a)

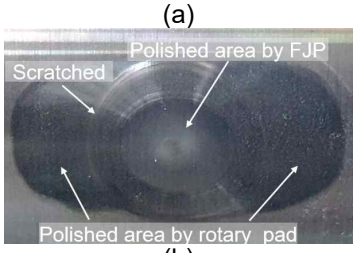

(b)

FIGURE 5. Camera images of polished brass roll mold by hybrid polishing process; (a) is the polished surface at a contact force of 1 N, (b) is the polished surface at 6 N

MEASUREMENT OF CONTACT FORCE ACCORDING TO PAD COMPRESSION DISTANCE

Depending on the compression distance of the elastic polishing pad, the contact force acting on the surface of the roll mold is changed. Figure 4 shows a graph of the contact forces at each compression distance measured by a dynamometer. The contact forces were measured to be about 1 N at a compression distance of 1 mm, and about 6 N at 5 mm.

INFLUENCE ACCORDING TO FIXED NOZZLE DISTANCE AND VARYING CONTACT FORCE

In order to analyze the effect according to compression of the PVA polishing pad, the discharging distance of the nozzle was fixed at 10 mm and the contact force of the pad set was at 1 N and 6 N. The rotational speed of the pad was 300 rpm and the discharging pressure was 10 bar. The polishing liquid is a mixture of white aluminum oxide #1500 with Isopar-H solution at a concentration of 5%.

Figure 5 shows camera images of the polished surface of the roll mold by the hybrid polishing process for 3 min at contact force of 1 N and 6 N. As shown in Figure 5 (a) where the surface was machined by contact force of 1 N, the polished area by the PVA pad is dimly visible whereas the polished shape by FJP is clearly. However, as shown in Figure 5 (b), the polished shape by FJP at a contact force of 6 N is dimly observable and the polishing area by the pad was wider and more glossy than in (a).

For a detailed analysis, polished surfaces were observed by using a microscope, as shown in Figure 6. Figures 6 (a) and (b) respectively show the polishing surface by the fluid jet and the pad at a compression distance of 1 mm. Collision marks and flow marks by the fluid jet were confirmed on the area subjected to FJP, as shown in (a). The feed marks on the roll mold surface were removed by the polishing effect. However, the feed marks remain on the surface polished by PVA due to insufficient contact force, as shown in (b). Figures 6 (c) and (d) shows the polishing surfaces at a compression distance of 5 mm. At this condition, the flow marks by the fluid jet were difficult to see on the machined surface, as presented in Figure 6 (c), whereas many collision marks were generated. These machined results were ascribed to a reduction of the FJP effect due to the flow of the fluid jet by being disturbed by fluid that filled the hollow part of the pad because of the decreased amount of pores of the PVA pad according to increasing contact force. Figure 6 (d) shows the surface polished with the PVA pad with contact force of 6 N. The feed marks were eliminated and polished marks were generated on this surface by the rotating pad, which absorbs the polishing liquid. Figures 7 (a) and (b) show profile graphs measured along the center line of each area in Figure 6. At a contact force of 1 N and a discharging distance of 10 mm, because FJP has a prominent effect on the roll surface, the profile has as 'W' shape with

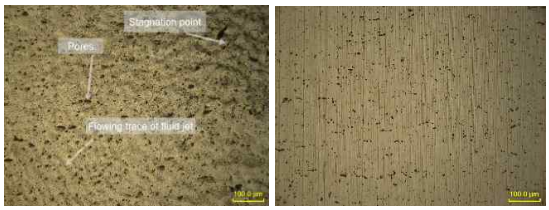

(a) (b)

(c) (d)

FIGURE 7. Micrograph image of surfaces polished by fluid jet((a) and (c)) and pad polishing((b) and (c); (a) and (c) are surfaces polished at discharge distance of 10 mm and contact force of 1 N, (c) and (d) are polished at contact force of 6 N

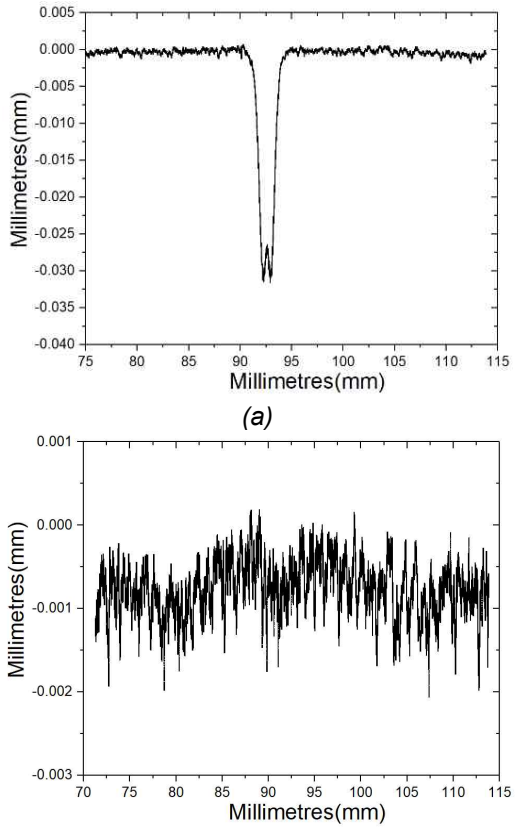

FIGURE 7. Cross-section profile graphs of polished area by hybrid polishing process; (a) is the profile of the surface polished at a contact force of 1 N, (b) is the profile of the surface polished at 6 N

a depth of 30 μm, as shown in Figure 8 (a). Where the vertical fluid jet collides with surface of the roll mold, it is known that the flowing speed of the fluid jet is stagnated, and less material removal occurs compared to the surrounding area that fluid jet flow along the surface of the roll. For this reason, the cross-section of the polished surface was formed the 'W' shape. However, because the flow of the fluid jet was hindered by the polishing liquid that filled in the hollow part of the pad, the measured profile of the polished surface by a contact force of 6 N does not show the 'W' shape, as shown in Figure 7 (b). In addition, the depth of the removed material was drastically decreased to a level of 1 μm.

INFLUENCE ACCORDING TO SIMULTANEOUSLY CONTROLLED NOZZLE DISTANCE AND CONTACT FORCE

In order to analyze the change of the surface of the roll mold when the contact force of the

polishing pad and the spraying distance of the nozzle were simultaneously controlled, an abrasion test was performed by applying a pad contact force of 6 N and a nozzle distance of 5 mm, as shown in FIG. 2 (c).

Figure 8 (a) shows a camera image of the polished surface under the above conditions, and (b) shows a profile graph of the cross-section of the polishing area. The polished depth was about 3 μm that was deeper that compared to present in Figure 7 (b). Unlike the result of the previous section, a 'U' shape profile was formed by FJP. However, the material removal rate is very low compared to the polishing time of 3 min at one point. Therefore, in the process of applying the rotation of the roll mold and feed motion of the hybrid polishing system, it is necessary to increase the discharging pressure within a range that does not damage the surface of the roll mold for raising the efficiency of FJP the process.

CONCLUSIONS

In this paper, effects on the polishing surface according to variation of the compression distance of the polishing pad and nozzle from the roll mold were studied. The following conclusions were drawn.

1. The contact force of the PVA polishing pad increased from 1 N to 6 N as the compression distance increased from 1 mm to 5 mm.
2. In the case of fixing the discharging distance of the fluid jet and controlling the compression distance of the PVA pad, a machined profile having deep depth and a 'W' shape is clearly shown at low contact force.
3. When the pad contact force is increased, the polished area is widened and more glossy. However, the efficiency of the FJP process was decreased, because the flow of the fluid jet on the roll mold is disturbed by polishing liquid that filled the hollow part of the PVA pad.
4. In the case where polishing conditions were controlled to increase the pad contact force and shorten the nozzle discharging distance at the same time, the amount of material removal increased slightly compared to the polishing time. In addition, the profile of the polished shape was formed in a slightly different 'U' shape from that of the normal FJP.

Based on the results of this study, future studies will be conducted to analyze the effects of different polishing conditions such as kinds of workpieces, pads, and abrasive particles, and nozzle discharge pressure.

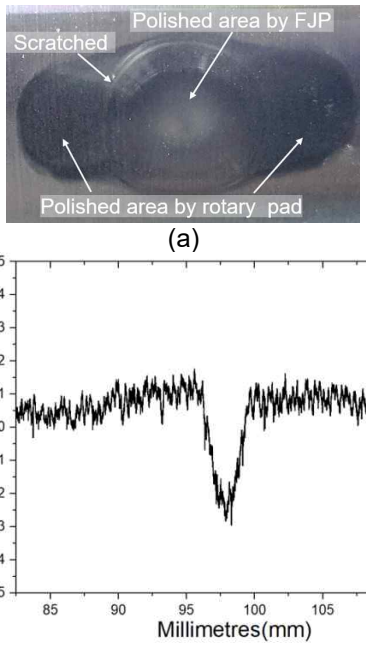

FIGURE 8. (a) is a camera image of a surface polished at a discharging distance of 5 mm and a contact force of 6 N and (b) is a profile graph of this surface.

REFERENCES

[1] Cao Z C, Cheung B CF and Kong LB, Computational Fluid Dynamics-Based Analysis of Material Removal Characteristics in Fluid Jet Polishing. Proc IMechE Part B:J Engineering Manufacture, 2015; 230; 1036-1048

[2] Cao Z C, Cheung C F, Theoretical modelling And Analysis of The Material Removal Characteristic in Fluid Jet Polishing. International Journal of Mechanical Sciences. 2014; 89; 158-166

[3] Peng W, Grun C, and Li S, Material Removal Mode Affected by The Particle Size in Fluid Jet Polishing, Applied Optics, 2013; 33; 7727-7933

[4] Jeong J Y, Je T J, Jeon E c, Kim G H and Choi H J. Set-up of The Fluid Jet Polishing System and Basic Machining Test. Proceedings International Conference of Manufacturing Technology Engineers. 2016; 60

[5] Je T J, Jeong J Y, Lee J R, Moon S H, Jeon E c, Choi D S. Hybrid Polishing System And Basic Process Experiment Using Fluid Jet and Rotary Pad Device. Euspen's 18th International Conference. 2018; 235-236

MICROBLAST-ASSISTED METAL POLYMER HYBRID JOINING

Yusuke Kajihara [1], Yuta Tamura[1], Fuminobu Kimura[1], and Eiji Yamaguchi[2]
[1]Institute of Industrial Science
The University of Tokyo
Komaba 4-6-1, Meguro-ku, Tokyo, Japan
[2]SINTOKOGIO. LTD
Honohara 3-1, Toyokawa-City, Aichi, Japan

INSTRUCTIONS

Joining metals and polymers is an essential manufacturing technique since many metal parts are replaced by polymers to save weight in automobiles, mobile phones, and other industrial devices. Although metals and polymers have been joined with bolts or adhesives, a metal-polymer direct joining technique is strongly required to reduce the cost and number of processes. In this study, we focus on the injection-molded direct joining (IMDJ), utilizing micro-patterned metal surface. Figure1 shows a schematic of the IMDJ process. In this process, small textures with sizes ranging from 10 nm to 100 μm are formed on the metal surface. Then molten polymer flows over the surface, penetrating the textures during the injection molding process. Finally, a strong joint between the metal and polymer is obtained mainly due to mechanical interlocking [1]. Small textures are usually formed via chemical etching [2] and laser machining [3]. Although the IMDJ process can achieve strong joints, it is not widely applied to industrial products mainly due to the lack of its reliability. This is ascribed to the fact that joining conditions are not optimized and that the joining mechanism is not well interpreted. To overcome these issues, it is indispensable to investigate the relationships between injection molding conditions and surface textures, and joining strength. Consequently, the surface forming technique requires quantitative control of the size and density of surface textures.

In this study, we propose to introduce microblasting technique to form surface textures on a metal surface [4]. We used a direct pressure-type micro-blasting equipment, in which abrasive grains, blasted by compressed air through a nozzle, which can be laterally scanned, hit a workpiece surface to plastically form small textures as shown in Fig. 2. The main advantage of this technique is that surface textures with various sizes and densities can be formed by changing the grain material, grain size, blasting pressure, and scanning speed. In addition, since the process does not need a special equipment for chemicals and its cost is much lower than that of the laser process, abrasive blasting is considerably more compatible with industry. One objective of this study is to develop the blast-assisted metal polymer direct joining technique, which realizes strong joining strengths greater than 15 MPa without preheating workpieces. Another objective is to investigate relationships between surface textures and joining strength.

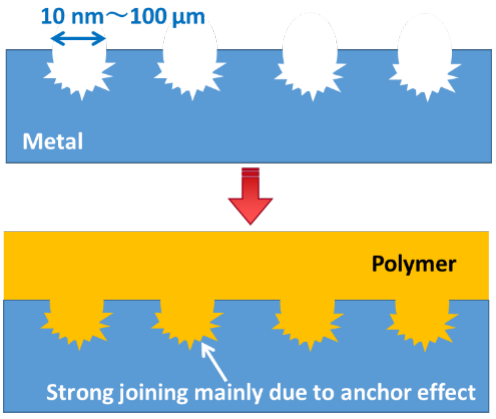

FIGURE 1. Schematic of the IMDJ process.

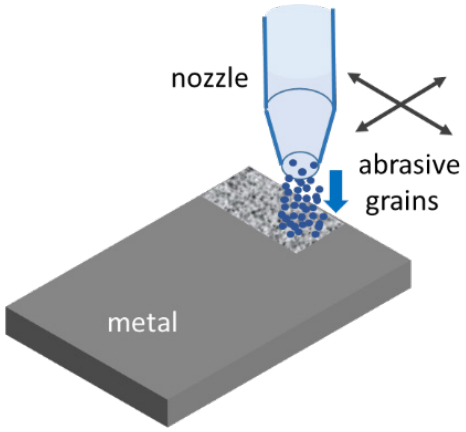

FIGURE 2. Microblasting technique.

BASIC EXPERIMENT

First we developed the blast-assisted metal polymer direct joining technique with much higher blasting pressure and suitable abrasive grains.

Specimen and apparatus

We used a direct pressure-type MICROBLASTER (SINTOKOGIO, LTD) to form textures. It can apply much higher air pressure than general blasting machines. Here we used glass beads and alumina particles as abrasive grains. Grain average sizes are shown in Table 1. Micro textures were formed at 1.0 MPa air pressure, 10 mm nozzle distance, and 200 mm/s scanning speed. The pressure is much higher and the distance is much smaller than usual blasting conditions. Figure 3 shows the specimen geometry based on ISO 19095-2 [5]. We manufactured lop joints with aluminum alloy A5052 and polybutylene terephthalate (PBT, 1101G-X54, Toray Industries, Inc.).

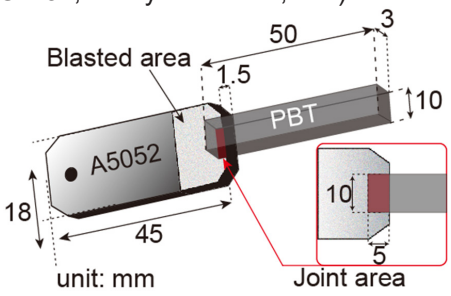

FIGURE 3. Specimen geometry to be joined.

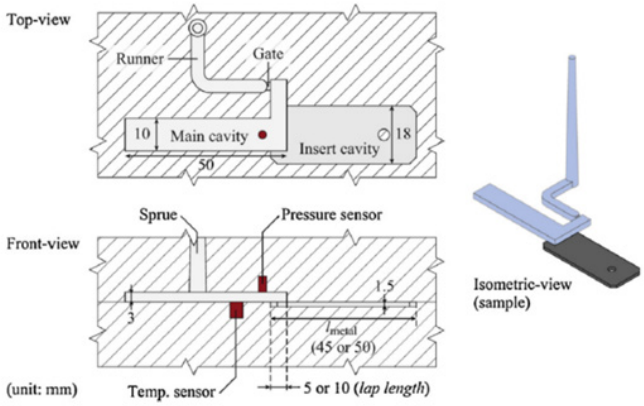

FIGURE 4. Schematic view of the mold cavity.

TABLE 1. Used media for micro blasting.

Grain	Glass bead		Alumina particle				
Name	G1	G2	A1	A2	A3	A4	A5
Average size(μm)	67.5	256	47.5	71.5	84.5	107.5	181

TABLE 2. Injection molding conditions.

Mold Temp.	Injection speed	Packing pressure	Holding pressure	Polymer Temp.
140 °C	300 mm/s	90 MPa	60 MPa, 8 s	270 °C

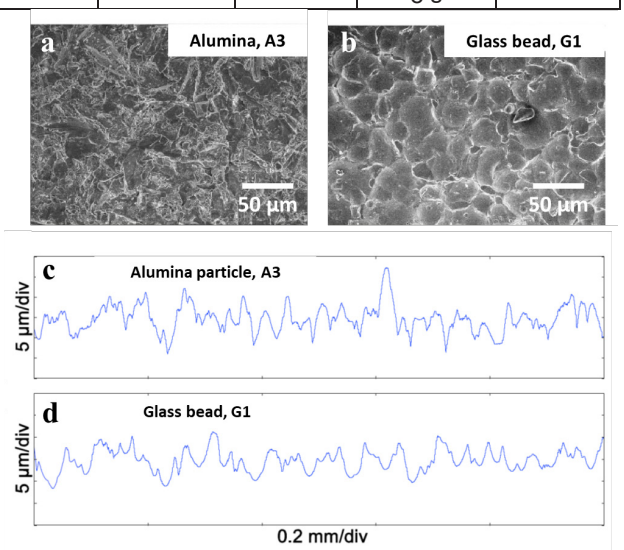

FIGURE 5. SEM images of treated surface with (a) Alumia A3 and (b) Glass bead G1 and surface profiles with (a) Alumia A3 and (b) Glass bead G1.

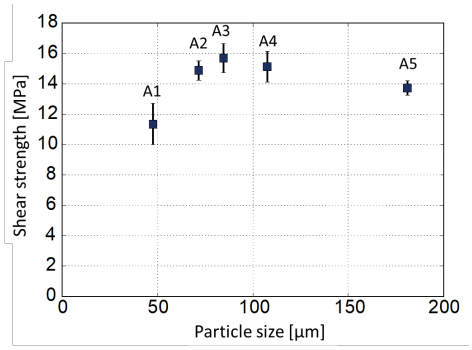

FIGURE 6. Shear strength with various alumina particle sizes.

Figure 4 illustrates a schematic view of the mold cavity [6]. Pressure and temperature sensors are installed near the joining area to monitor the values in real time. The injection molding was carried out on ROBOSHOT α100iA Linear (Fanuc corp.) with a 22 mm diameter screw. Injection molding conditions are listed in Table 2. Packing pressure is the cavity pressure just after the cavity is fully packed with molten polymer. Note that the metal workpiece was not pre-heated before injection molding. We manufactured 6 specimens with each grain. After the manufacture, we performed tensile shear test with our original tensile tester [7].

Results and discussion

Any workpiece blasted with glass beads did not join the polymer. On the other hand, all workpieces blasted with alumina particles joined polymer strongly. Surprising finding is that the shear strength reaches more than 15 MPa with alumina A3 without pre-heating the workpiece. It is a little difficult to interpret the difference from previous studies. Most possible reasons are that the blasting pressure (1.0 MPa) was much higher and more suitable grains were adopted in this study. Figures 5(a) and (b) show SEM images on treated surface with alumina particles A3 and glass beads G1. Figures 5(c) and (d) represent surface profiles studied with a roughness meter (SE 300, Kosaka Laboratory, Ltd) on treated surface with A3 and G1. In Figs. 5(c) and (d), arithmetic average roughness *Ra* are both about 2 μm. Thus it is impossible to judge the joining strength just with *Ra*. As shown in Figs 5(b) and (d), surface textures formed with glass beads are more rounded, which leads to weak interlocking. Though not shown here, it was confirmed with finite element analysis.

Figure 6 shows the shear strengths with various alumina particles listed in Table 1. Particle A3 gives the best strength. Since smaller particles have lower kinetic energy, A1 and A2 provide lower strengths. When we use larger particles, a smaller amount of particles is blasted in a unit of time. For the reasons stated above, alumina particle A3 showed the best performance. In this study, A3 is basically used as abrasive grains hereafter.

CORRELATION WITH SURFACE TEXTURES

We then studied the correlation between surface textures and joining strength. Extracting parameters of surface textures which are highly correlated with joining strength should contribute to understanding of joining mechanism.

Study with same size particles

First we used workpieces formed with the same size alumina particles. The abrasive grain was alumina particle A3 (Table 1) and workpieces were blasted with various air pressures. Other blasting conditions are same as the basice experiment. Higher pressure yields higher roughness, which leads to larger *Ra*. Here we focus on *Ra* and average length of roughness curve element *RSm*. The former is correlated with the structure depth and the latter with structure density. Surface profiles (ISO 4287:1997 [8]) are measured with the roughness tester before the injection molding and then the relationships between joining strength and the profile is estimated. The molding conditions are same as Table 2. Figures 7 show the relationships between joining strength and *Ra*, *RSm*. Each color represents air pressure. *RSm* has no correlation with shear strength partially because *RSm* does not change so much depending on air pressure. On the other hand, *Ra* has strong correlation with shear strength (correlation coefficient R = 0.74). We conclude that *Ra* is strongly correlated with joining strength when we use the same abrasive grains. In other words, when the texture density is same, higher roughness is more effective to achieve strong joints.

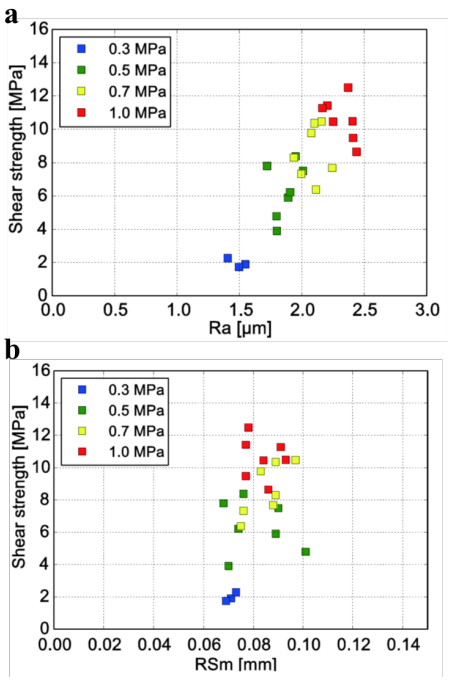

FIGURE 7. Relationship between joining strength and (a) Ra, (b) RSm.

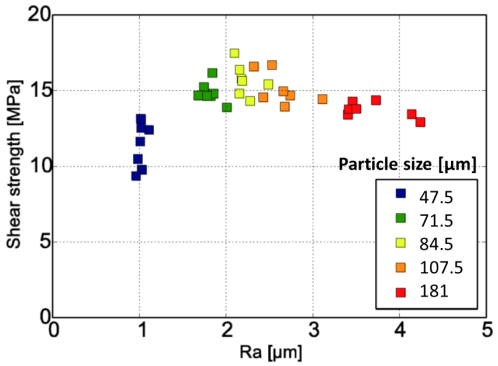

FIGURE 8. Shear strength with various particle sizes.

Study with various size particles

Next we form textures on workpieces with various alumina particle sizes listed in Table 1 (A1~A5). Blasting conditions are same as the basic experiment. In this case, both *Ra* and *RSm* have strong correlation with particle sizes (*R* = 0.95 and 0.92, respectively). Though not shown here, *RSm* increases from 0.05 to 0.15 mm with increasing particle size. The molding conditions are same as Table 2. Figure 8 plots the shear strengths with various particle sizes. The important finding here is that *Ra* shows almost no correlation with shear strength, which is different from the prior study with same size particles. We also compared the shear strength with maximum height roughness *Rz*, arithmetic mean slope *Δa*, skewness *Rsk*, and kurtosis *Rku* to find no correlation. It means that it is impossible to estimate the joining strength just by measuring *Ra* or other roughness parameters from an arbitrary surface texture.

In this analysis, the difficulty is that *Ra* and *RSm* does not change independently with particle sizes. In addition, surface profile parameters have just the averaged information. We hence focus on aspect ratios of all small structures since aspect ratio (depth/diameter) has independent information of each structure and contains the related information of both *Ra* and *RSm.* We calculated aspect ratios of all picked-up pores from surface profiles (length = 4 mm). Figure 9 is a histogram of aspect ratios of holes on two workpieces. The numbers of pores with the same aspect ratio are counted. One workpiece was blasted with alumina particles at 0.3 MPa and did not join with polymer. The other piece was blasted at 1.0 MPa and strongly joined polymer. In Fig. 9, the difference is very clear. Almost all the aspect ratios on the not-joined metal piece are less than 0.1, whereas a lot of aspect ratios indicate more than 0.1 on the joined metal piece. Other results confirmed the reproducibility. These results strongly suggest that only the pores with aspect ratios of more than 0.1 should contribute to joining. Here we counted the number of such effective pores on treated metals blasted with alumina particle A1~A5 and investigated the relationship between the number and the shear strength. Figure 10 plots the result, where correlation coefficient *R* is estimated to be 0.94. It should be noted that the number of "all" pores does not have any correlation with the shear strength. Though further analyses remain to perform, this study confirms that we could estimate the joining strength before injection molding by counting the number of effective pores on the treated surface.

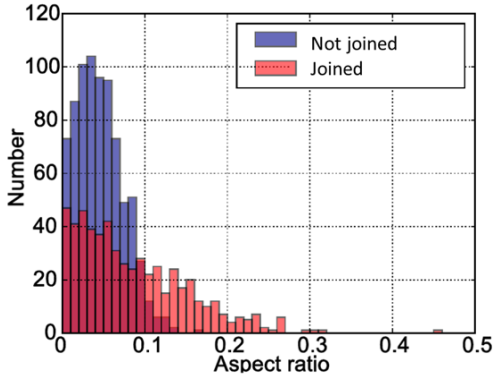

FIGURE 9. Histogram of aspect ratios of pores.

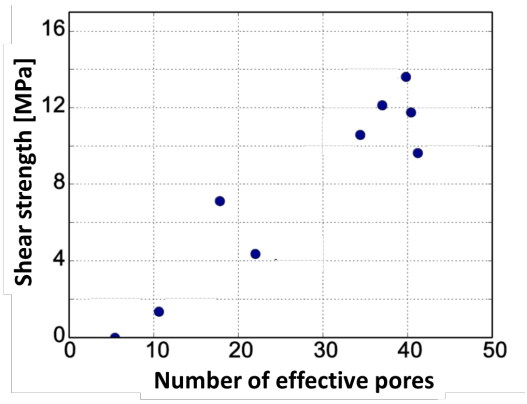

FIGURE 10. Relationship between effective pore numbers and shear strength.

SUMMARY AND FUTURE WORKS

We have developed the blast-assisted metal polymer direct joining technique and have investigated correlations of molding conditions and surface textures to joining strength. We achieved strong metal-polymer lap joints without pre-heating the metal pieces with alumina particles and much higher blasting pressure. Then we studied the joining strength correlation with surface textures and confirmed that the number of effective holes (aspect ratio > 0.1) on the treated surface should have the strong correlation with shear strength. Future works are further analyses for the correlation between surface textures and joining strength, numerical analysis with FEM, and observing the joining section via SEM/TEM to further understand the joining mechanism.

ACKNOWLEDGMENT

This study was partially supported by The Foundation for the Promotion of Industrial Science.

REFERENCES

[1] Ramani K, Moriarty B, Thermoplastic bonding to metals via injection molding for macro-composite manufacture, Polymer Engineering and Science 1998; 38: 870-877.

[2] Okumura A, Asami Y, Method of manufacturing composite molded article, US Patent app. 2013; 13/990,927.

[3] Taki K, Nakamura S, Takayama T, Nemoto A, Ito H, Direct joining of a laser-ablated metal surface and polymers by precise injection molding, Microsystem Technologies 2016; 22:31-38.

[4] Kajihara Y., Tamura Y., Kimura, F., Suzuki, G., Nakura, N., Yamaguchi, E., Joining strength dependence on molding conditions and surface textures in blast-assisted metal-polymer direct joining, CIRP Annals, 2018; 67 591-594.

[5] ISO 19095-2:2015, Plastics -- Evaluation of the adhesion interface performance in plastic-metal assemblies -- Part 2: Test specimens.

[6] Kimura F, Kadoya S, Kajihara Y, Effects of molding conditions on injection molded direct joining using a metal with nano-structured surface, Precision Engineering 2016; 45:203-208.

[7] Kadoya S, Kimura F, Kajihara Y, Tester for tensile shear evaluation of metal–polymer single lap joint, Precision Engineering 2018; in press.

[8] ISO 4287:1997, Primary, Waviness and Roughness Profiles.

TOOL WEAR AND CHIP FORMATION IN TURNING OF HEAT-RESISTANT ALLOY OF Cr-Mo-V FORGED STEEL

You Kawamura[1] and Hideo Takino[1]
[1]Department of Mechanical Science and Engineering, Faculty of Engineering
Chiba Institute of Technology
Narashino, Chiba, Japan

INTRODUCTION

Cr-Mo-V forged steel is a material suitable for mechanical parts used in high-temperature and high-pressure environments, such as turbine rotors and turbine valves in power plants [1, 2]. In general, parts made of Cr-Mo-V forged steel are manufactured by cutting in the final stage of the manufacturing process. Thus, it is important to understand the cutting characteristics of Cr-Mo-V forged steel to efficiently produce these parts with high accuracy. However, few studies have been carried out to investigate the cutting characteristics of Cr-Mo-V forged steel [3, 4].

In our previous study [3], cylinders made of Cr-Mo-V forged steel were turned by a numerically controlled turning machine with various cutting tools of different materials, such as cermet and tungsten carbide. The wear on a flank face was observed, the length of which was measured to find the most suitable tool material for cutting Cr-Mo-V forged steel. We also experimentally investigated the characteristics of chip formation. It was found that the length of chips for Cr-Mo-V forged steel was longer than that for stainless steels.

The characteristics of chip formation are an important factor in turning. The formation of continuous chips may obstruct the operation of a turning machine. Thus, the length of the chips generated during turning should be shortened to improve workability. In the present study, we turned Cr-Mo-V forged steel cylinders with various tools having a chip breaker of different shapes, and investigated the chip formation and tool wear for each tool. From the experimental results, we found the most appropriate tool for turning Cr-Mo-V forged steel in terms of workability and tool life.

WORKPIECE MATERIALS

The workpieces used in this study were cut out from the blank of a turbine rotor made from Cr-Mo-V steel. The blank was made by casting followed by forging by Pacific Steel Mfg. Co., Ltd., Japan. Figure 1 shows a schematic drawing of the blank. The unhatched area of the blank was used as an actual turbine rotor. The workpieces were produced from the hatched area on the left. It was thus assumed that the material properties of the workpieces used in our experiment were the same as those of the actual turbine rotor.

The chemical components and the physical and mechanical properties of the Cr-Mo-V forged steel are shown in Tables 1 and 2, respectively. In Table 2, the properties of the stainless steels are also shown for comparison.

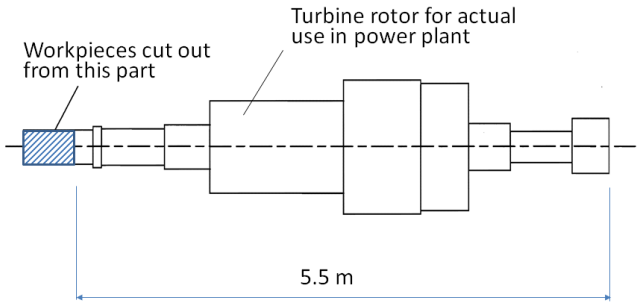

FIGURE 1. Blank of turbine rotor for actual use in power plant, from which workpieces in this study were cut out.

TABLE 1. Chemical components of Cr-Mo-V forged steel [wt %].

C	Si	Mn	P	S	Ni	Cr	Mo	V
0.31	0.08	0.78	0.007	0.002	0.41	1.10	1.13	0.22

TABLE 2. Physical and mechanical properties of workpieces.

	Hardness HV	Tensile strength	Elongation	Density	Thermal conductivity	Specific heat
	[-]	[N/mm^2]	[%]	[g/mm^3]	[W/m deg]	[x10^3 J/kg deg]
Cr-Mo-V steel	200	795	19	7.8	45 (100 °C)	
					46 (200 °C)	0.55 (260 °C)
					35 (600 °C)	0.63 (570 °C)
Stainless steel SUS304	200	520	40	7.9	17 (200 °C)	0.53 (200 °C)
					24 (600 °C)	0.65 (600 °C)
Stainless steel SUS303	200	520	40	7.9	16 (100 °C)	0.50 (100 °C)

EXPERIMENTAL METHOD

The cutting tools used in this study were commercially available tools made of cermet. The radius of the tool tip was 0.4 mm. Each tool had a chip breaker with a different shape, as shown in Fig. 2(a). The cross-sectional profiles of the chip breakers are shown in Fig. 2(b); tool types A, B, and C have chip breakers with angles of 13º, 14º, and 15º at the rank face, respectively. Figure 2(c) shows photographs of the tool edges looking from the direction of the arrows in Fig. 2(a). As shown in Fig. 2(c), tool type A has no slope at its edge, tool type B has a gentle slope, and type C has a sharp slope.

The workpieces were cylinders with 50 mm diameter and 20 mm thickness, whose side surface was cut by a manual lathe (TSL-800, Takisawa Machine Tool Co., Ltd.). The depth of cut and feed rate were 0.3 mm and 0.08 mm/rev, respectively, and the cutting distance was 400 m. To achieve this cutting distance, the side surface was repeatedly cut eleven times. No coolant was used during cutting. After the cutting, the chip length was measured, and the tool wear of the flank face was evaluated with an optical microscope.

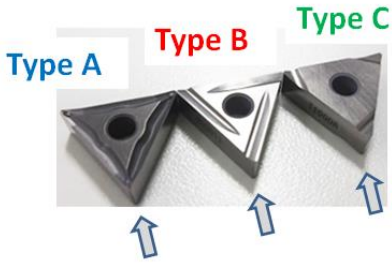

(a) Photograph of outlook

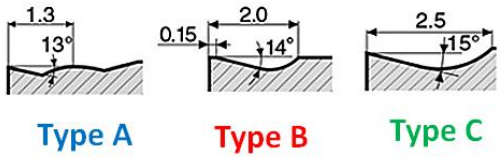

(b) Cross-sectional profiles of the chip breakers

(C) Photographs of tool edges looking from the direction of the arrows in Fig. 2(a)

FIGURE 2. Cutting tools used in this study.

CHIP FORMATION AND TOOL WEAR

Figure 3 shows the experimental results for the length of the chips generated at various cutting speeds. The shape of the chips was helical in every case. In this experiment, the turning operation was not obstructed by the chips. As shown in Fig. 3, the chip length increased with increasing cutting speed for every tool. Moreover, tool type C generated the longest chip among the three types of tool.

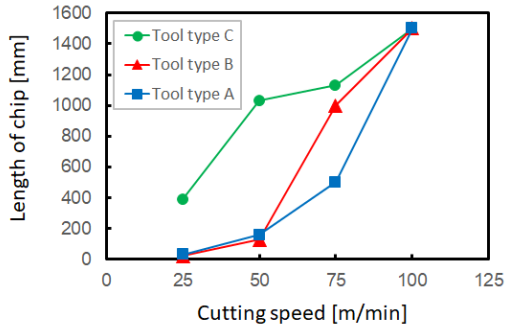

FIGURE 3. Lengths of the chips generated at various cutting speeds for each tool.

Figure 4 shows the relationship between the cutting speed and the tool wear for each tool. In Fig. 4, the tool wear includes the fracture of the tool, which was quantified by measuring its length on the flank face. As shown in Fig. 4, the tool wear decreased with increasing cutting speed, in contrast to the length of the chips. Observation with an optical microscope showed that a fracture appeared at the tool edge for every tool when the cutting speed was 25 m/min. For tool types A and B, the edge was worn without a fracture when the cutting speed was 50 m/min and above. For tool type C, the edge

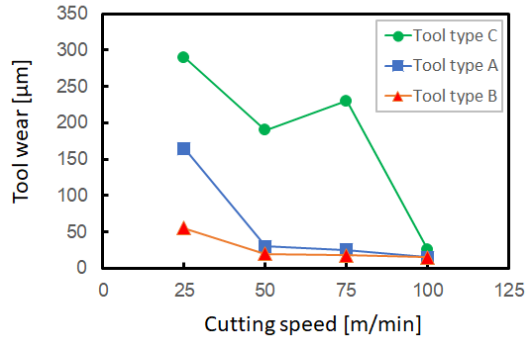

FIGURE 4. Relationship between the cutting speed and the tool wear for each tool.

fractured when the cutting speed was up to 75 m/min, and it was worn without a fracture when the cutting speed was 100 m/min. In other words, every tool tended to fracture when the cutting speed was low. Moreover, tool type C was more easily fractured than tool types A and B. This is considered to be due to the relatively large angle of 15° at the rank face of type C, as shown in Fig. 2(b), and the sharp edge, as shown in Fig. 2(c).

Consequently, in terms of the chip formation and tool wear, a tool having a chip breaker with an angle of 14° or less (tool type B or C) is suitable for turning Cr-Mo-V forged steel, as shown in Figs. 3 and 4. Moreover, the turning using tool type B or C should be conducted at a cutting speed of 50 m/min to achieve low tool wear and short chips.

MEASUREMENT OF CUTTING FORCE

We measured the cutting force in three perpendicular axial directions during turning by a cutting dynamometer (TD-300A, Kyowa Electronic Instruments Co., Ltd.). The measurement of the cutting force was conducted for the first cutting in the eleven repetitions of the side cutting.

Figure 5 shows the time variation of the cutting forces for tool types B and C, as examples for the cutting speeds of 25 and 100 m/min in the three axial directions, i.e., the main force, thrust force, and feed force. As shown in Fig. 5, the cutting force fluctuated at the low cutting speed of 25 m/min. From Figs. 4 and 5, it was found that when the cutting force fluctuated, the tool wear, i.e., fracture, was large. Thus, one possible reason for the generation of the fracture is the deposition then breaking off of a build-up edge on the tool edge, which also causes the fluctuation of the cutting force.

Figure 6 shows the time average of the resulting cutting force for each tool. The resulting cutting forces were calculated from the measured cutting forces in the three axial directions. As shown in Fig. 6, the cutting force for tool type C was the lowest among the three tools. This is considered to be due to type C having the sharpest edge with an angle of 15° at the rank face. Moreover, the cutting force hardly change with the cutting speed, although the tool wear was large when the cutting speed was low. Thus, to detect the failure of the tool, the measurement of the time variation of the cutting force was important rather than that of its time average.

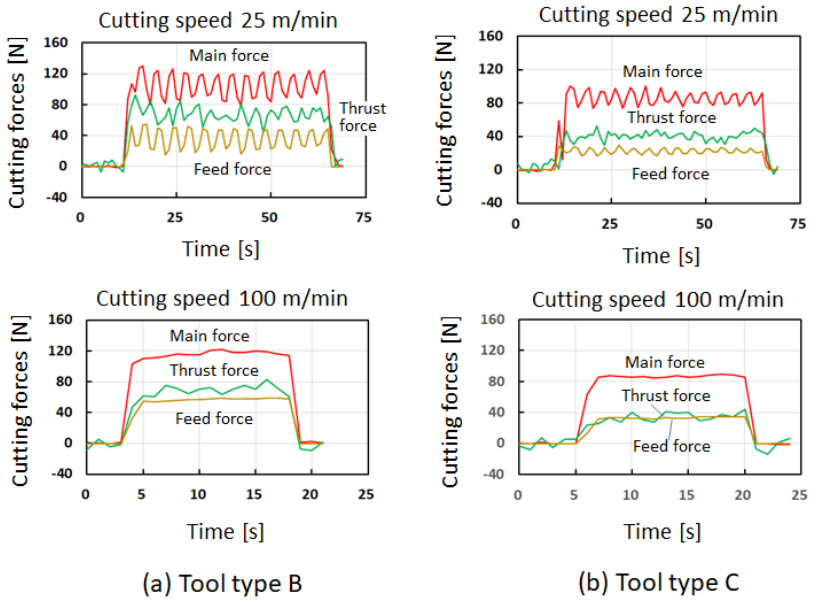

FIGURE 5. Time variation of the cutting forces for the first cutting in eleven repetitions of the side cutting.

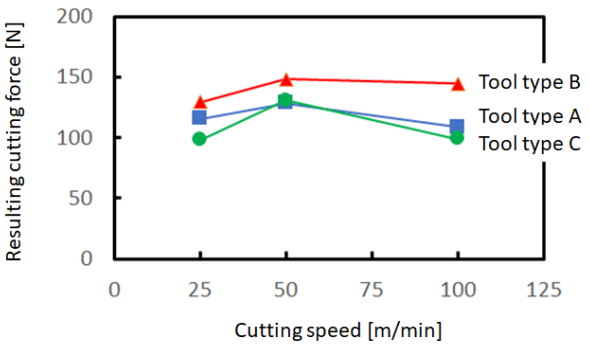

FIGURE 6. Change in time average of the resulting cutting force with cutting speed.

CONCLUSIONS

Cr-Mo-V forged steel cylinders were turned with various tools having a chip breaker of different shapes, and the chip formation and tool wear were investigated for each tool. As a result, in terms of chip formation and tool wear, a tool having a chip breaker with an angle of 14° or less (tool type B or C) is suitable for turning Cr-Mo-V forged steel. Moreover, turning using tool type B or C should be conducted at a cutting speed of 50 m/min to achieve low tool wear and short chips.

The cutting force was measured by a cutting dynamometer. It was found that fluctuation of the cutting force occurred during the cutting process when the cutting speed was low. When the cutting force fluctuated, the tool wear, i.e., fracture, was large. One possible reason for the generation of the fracture was the formation then removal of a build-up edge on the tool edge. Moreover, the time average of the cutting force hardly changed with cutting speed, although the tool wear was large when the cutting speed was low. Thus, the measurement of the time variation of the cutting force was important rather than that of its time average to detect the failure of the tool.

ACKNOWLEDGEMENT

This work was performed as part of the Ministry of Education, Culture, Sports, Science and Technology (MEXT)-supported program for the Strategic Research Foundation at Private Universities.

REFERENCES

[1] Viswanathan R, Jaffee R I. Toughness of Cr-Mo-V Steels for Steam Turbine Rotors. J Eng Mater Technol. 1983; 105: 286-294.
[2] Masuyama F. History of Power Plants and Progress in Heat Resistant Steels. ISIJ International, 2001; 41: 612–625.
[3] Takino H, Ota M, and Yamanaka A. Cutting characteristics in turning of Cr-Mo-V forged steel. Proc. ASPE. 2016; 56: 562-565.
[4] Tran T V, Takino H, and Ogata T. Relationship between Fatigue Strength and Surface Characteristics for Machined Parts of Heat-resistant Alloy of Cr-Mo-V steel. Proc. euspen. 2018; 337-338.

DEVELOPMENT OF DIGITAL MANUFACTURING PLATFORM IN WAFER-LEVEL OPTICS

Chun-Ting Lin, Kao-Der Chang, Jhen-Nan Gu, Hung-Yi Lin, and Ta-Hsin Chou
Mechanical and Mechatronics Systems Research Laboratories
Industrial Technology Research Institute
Hsinchu, Taiwan, R.O.C.

INSTRUCTIONS

The demands for food, clothing housing, transportation, education are a necessary element in people's daily life. Among them, the demand for transportation has been dramatically changed. The automotive industry is a century industry. However, the latest development has transferred from the power machinery system to the electronic system, energy system, and smart system. In the development of the technologies, autonomous cars, also known as self-driving cars, are one of the hottest topics of the year. The main driving force for autonomous cars is that it can sense the surrounding environment by using technologies such as radar, LiDAR, GPS and machine vision[1-2] and convert the sensing data into appropriate navigation information to achieve the purposes of the navigation, the obstacle avoidance and the automation. The concept of the autonomous car can be traced back to the 1930s However, the first autonomous car which really works was introduced in the 1980s and was developed by Carnegie Mellon University for the Navlab and ALV projects. In 1987, Eureka PROMETHEUS programs at the Federal Defense University in Munich, Germany, have also begun to introduce related technology research with Mercedes-Benz. In recent years, Google releases its own autonomous car in the specific environment and expects to solve all the unresolved problems of the autonomous car in 2020.

For the autonomous cars mentioned above, the Advanced Driver Assistance Systems (ADAS)[3-4] is the best solution currently available[5]. The main function of ADAS is providing drivers to recognize the current condition of the car and the environment and giving a warning of the possible dangers and accidents in advance. It enables the drivers to take an early response before the danger occurs. The image recognition system is one of the major development technologies that various manufacturers are paying attention to. In the future, an intelligent car will carry more than 10 camera modules. In the image recognition system, optical lens is the most important key component. The optical lens needs to operate in a temperature of -40°C to 125°C. In addition, the verification tests of the acid rain, water proof, and air proof which may take a long time (about 3 to 5 years) makes the optical lens manufacturers difficult to cut into the markets of Original Equipment Manufacturing (OEM) and Original Design Manufacturing (ODM). For the current situation, most optical lens manufacturers focus on the aftermarket (AM) products, such as the dashboard cameras and reversing cameras.

SIMULATION AND MEASUREMENT

For the multiple camera modules, the calibration of the image centers of the different cameras is difficult and the cost is high. The wafer-level lens array camera provides an alternative solution to solve the problems of the calibration and the cost. The lens array camera is the coplanar design and forms the images on the same image sensor. The coplanar design can reduce the complexity of the alignment of multiple camera modules and the problem of the calibration can be solved. For the lens array camera design, the depth information of the object can be obtained by using the parallax principle. For the wafer-level optics manufacturing process, the manufacturing cost can be further reduced. The wafer-level optics has its drawbacks. The first is the limitation of the number of the lens stack for the mass production. The number of the lens stack is about 2 to 3 for the mass production due to the severe fabrication error tolerance. The second is the low-resolution imaging quality. For three-lens stack, the resolution of the image is about 0.75 mega pixels[7]. Finally, the materials of the wafer-level optics mostly use the material of UV glue. The biggest challenge of the UV glue used for the automotive lens is the pass of the verification tests of the operating temperature and reliability.

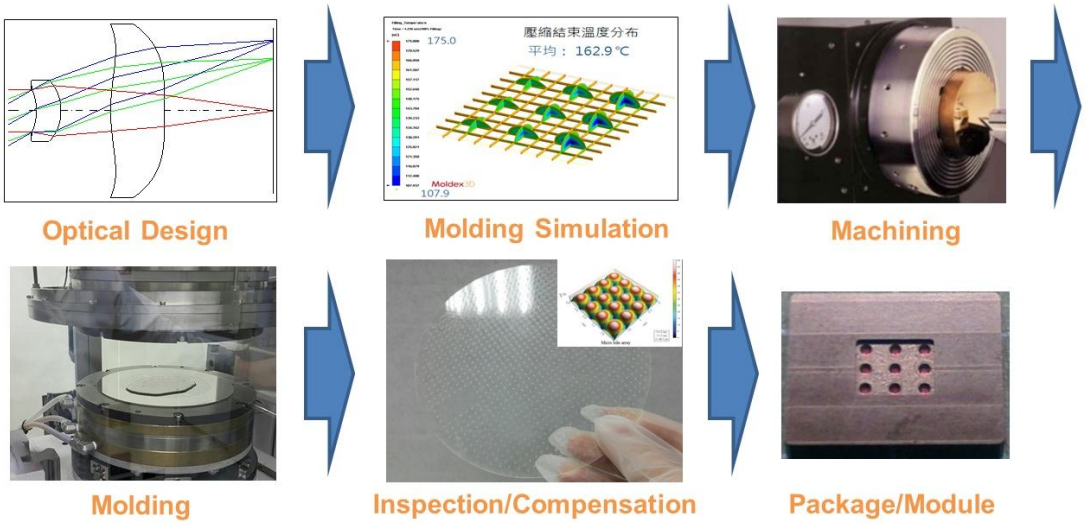

FIGURE 1. Steps of the wafer-level optics manufacturing process.

In view of the above drawbacks, the current improvement methods are the configuration of array camera segment imaging and the technology of image fusion so as to achieve high-resolution imaging quality. For example, for the 4×4 lens array camera module published by Pelican Imaging[6], the resolution of the fused image is about 8 mega pixels and the depth information of the object can be calculated. Currently, there are related material manufacturers such as Daicel and AJI, which have been developed thermosetting materials. The glass transition temperature T_g of the Daicel and AJI thermosetting materials is higher than 180°C. Therefore, the Daicel and AJI thermosetting materials have the opportunity to pass the verification tests of the operating temperature and reliability.

We has developed the wafer-level optics manufacturing process in recent years. The thermosetting material OTH107 produced by Japan Daicel is chosen for lens material. The glass transition temperature T_g is up to 185°C, which meets the demands of the operating temperature for the automotive lens. The steps of the wafer-level optics manufacturing process steps shown in Figure 1. At first, the camera with large-size imaging sensor is chosen and the lens is optical designed by optical software Code V. The industrial camera EO-18112 of Edmund Optics with the resolution and pixel size of 18 mega pixels and 1.25 μm is chosen as the camera. A 3×3 lens array is designed for imaging on the same image sensor. The imaging of each lens has a resolution of 0.2M pixels (520×390 pixels). The f-number of the lens is 3.5. The arrangement of the 3×3 lens array is shown in Figure 2. The refractive index and Abbe number of the lens material OTH107 are 1.51756 and 54.2, respectively. Each lens is composed of an aspherical lens and an infrared filter as shown in Figure 3. The thickness of the infrared filter is 0.3 mm and the glass material is Schott D263T with the refractive index and Abbe number of 1.5231 and 54.49, respectively. The optimized aspherical coefficients of the lens is shown in Figure 4 and the fabrication error tolerances of the lens are also analyzed as shown in Figure 5.

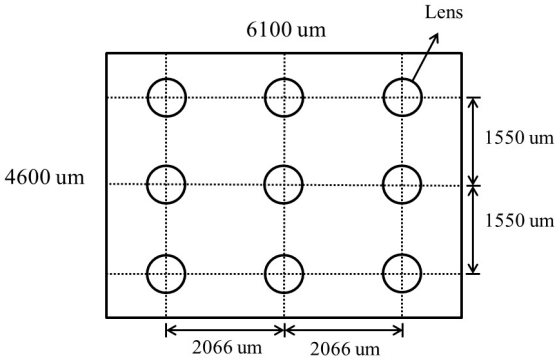

FIGURE 2. Arrangement of 3×3 lens array.

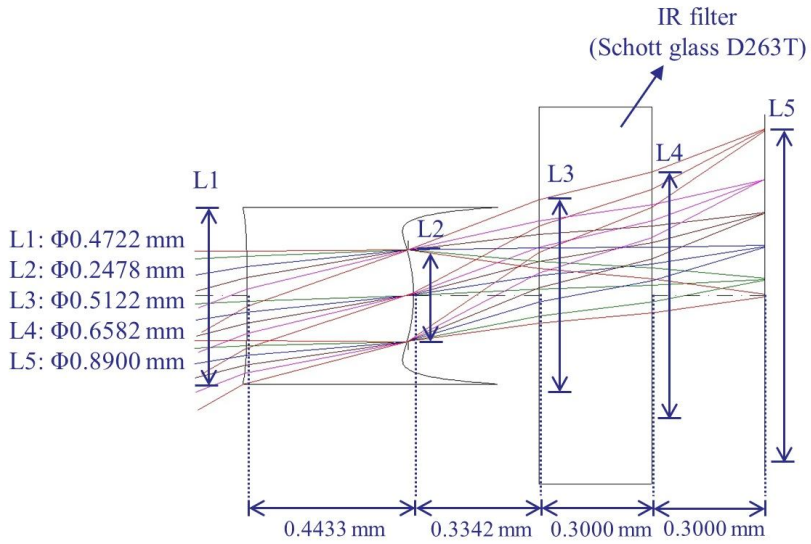

FIGURE 3. Schematic figure of each lens.

Aspherical surface 1

Parameter	value
Radius	28.266944
Conic Constant (K)	-11323.636392
4th Order Coefficient	-3.174018
6th Order Coefficient	-25.691524
8th Order Coefficient	623.037929
10th Order Coefficient	-5785.830964

Aspherical surface 2

Parameter	value
Radius	-0.436843
Conic Constant (K)	0.034196
4th Order Coefficient	0.208331
6th Order Coefficient	359.493291
8th Order Coefficient	-36249.964906
10th Order Coefficient	1080970.842998

FIGURE 4. Optimized aspherical coefficients of the lens.

Item	Tolerance
Shape accuracy	< 1 μm
Roughness	< 55 nm
Eccentric distance	±2 μm

FIGURE 5. Fabrication error tolerances of the lens.

The molding results of the 3×3 lens array are simulated by the mold flow software Moldex3D. Then the technology of the ultra-precision machining is used to fabricate a 4-inch lens array mold whose lens shape is aspherical. The 4-inch mold is preheated to 140°C, and then the thermosetting material is dispensed onto the mold. Due to the double-sided surfaces of the lens, the upper and lower molds need to be aligned precisely. After the mold clamp step, the molds start to heat up. The thermosetting resin material is cured into a lens and the entire molding time is about 30 minutes. When the hot press process is finished, the desired lens is obtained by cooling the molds and released from the molds. The shape accuracy of the lens is measured by 3D measuring instrument. At last, the 3×3 lens array is cut from the 4-inch lens array substrate and

assembled to lens module. The exploded view of 3×3 lens array module is shown in Figure 6. The comparison of the mold, product, and molding simulation on the shape accuracy, roughness, and eccentric distance of surface 1 and 2 in the central region of the lens substrate is shown in Figure 7. The image of 3×3 lens array captured by the industrial camera EO-18112 is shown in Figure 8.

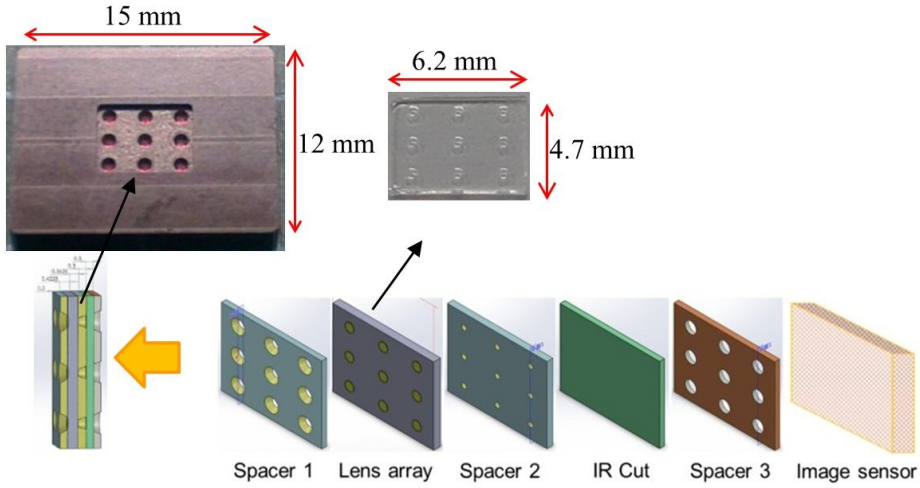

FIGURE 6. Exploded view of 3×3 lens array module.

Item	Tolerance	Mold	Product	Molding simulation
Shape accuracy	<1 μm	1.073 μm 0.097 μm	1.471 μm 0.111 μm	1.483 μm 0.112 μm
Roughness	< 55 nm	29.1 nm 24.8 nm	34.9 nm 18.9 nm	N/A
Eccentric distance	±2 μm	0.79 μm	4.26 μm	4.27 μm

FIGURE 7. Comparison of the mold, product, and molding simulation in the central region of the lens substrate.

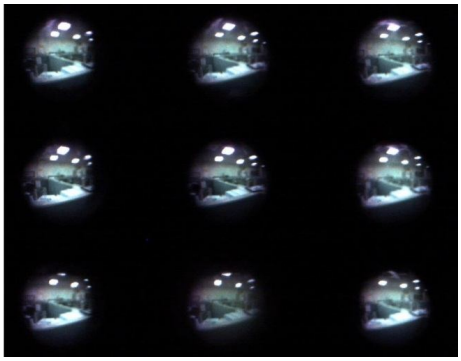

FIGURE 8. Image of 3×3 lens array captured by the industrial camera EO-18112.

RESULTS AND DISSCUSSION

We want to establish the digital manufacturing platform which integrate with the optical software Code V, mold flow software Moldex3D and cloud database system to reduce product development cycle time and increase the yield rate. The flow chart of the digital manufacturing platform is shown in Figure 9. First of all, the project goal is confirmed. The lens is optical designed by optical software Code V and the fabrication error tolerances are also analyzed. Then the molding results are simulated by the mold flow analysis software Moldex 3D and the lens molding process is proceeding at the same time. The simulated molding results and initial actual molding results are compared. The simulated molding results are tried to approach to the initial actual molding

results by adjusting the simulation parameters and models. After the simulated molding results can closely or precisely predict the actual molding results, the molding simulation are added with the compensation design. At last, the final actual molding results are expected to be able to meet the demands of the optical design.

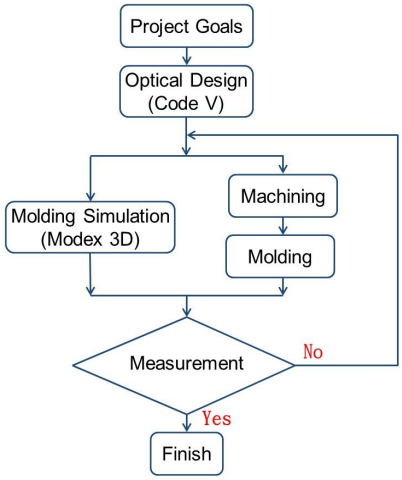

FIGURE 9. Flow chart of the digital manufacturing platform.

Due to the shrinkage of the material during the lens molding process, it will result in the deviation of the shape accuracy, roughness, and eccentric distance of surface 1 and 2. Take the eccentricity, the deviation of the central position of surface 1 and 2, as an example. The farther the lens away from the center of the wafer-level lens substrate, the greater the eccentric distance as shown in Figure 10. In the machining process, the distance between the central position of the surface and the center of the lens substrate is increased for the pre-compensation. After the shrinkage of the material during the lens molding process, the distance between the central position of the surface and the center of the lens substrate will be decreased. The surface will be back to the right position and the eccentricity will be reduced. The digital manufacturing platform is needed to reduce the number of trial and error and the cost of the modification of the mold. The data of the simulation analysis can be uploaded to the cloud database system. If there is a similar design in the future, the data analyzed in the past may be referred to.

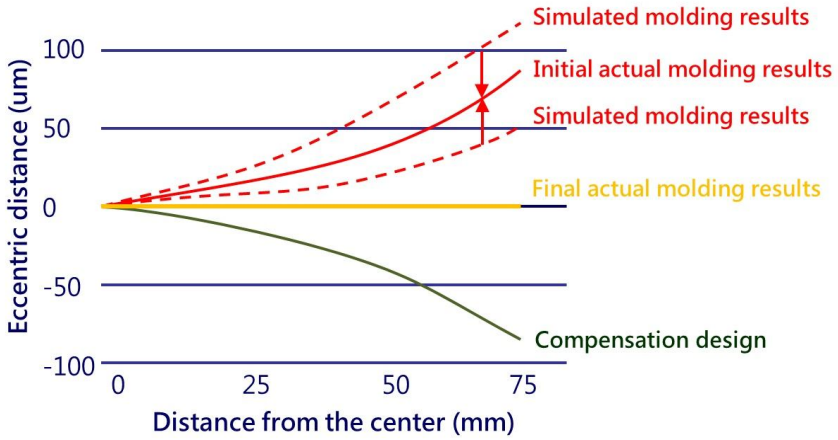

FIGURE 10. Operating procedure of the digital manufacturing platform.

CONCLUSION

In this paper, the 3×3 lens array camera is used for automotive lenses to solve the problems of the calibration and the cost of the multiple camera modules. For the use of thermosetting materials and wafer-level optics manufacturing process, the problem of the non-heat-resistance of the materials can also be solved. The digital manufacturing platform is introduced to reduce the product development time and increase production yield. In the future, the automotive lens products will be small volumes and large varieties and the digital manufacturing platform can meet the demands of the development of automotive lens products.

ACKNOWLEDGEMENT

Thanks to the support of Mechanical and Mechatronics Systems Research Laboratories (MMSL), Industrial Technology Research Institute (ITRI) (Project No. H301AA712P) and the support

of the wafer-level optics facilities from Kinik company, this project was carried out well.

REFERENCES

[1] Todd L. The Beginning of the end of driving. Motor Trend. 2012 Nov 27.

[2] Jadranka D, Beate M, Gereon M. European roadmap smart systems for automated driving. European Technology Platform on Smart Systems Integration; 2015.

[3] David G, Antonio ML, Angel DS, Thorsten G. Survey of pedestrian detection for advanced driver assistance systems. IEEE transactions on pattern analysis and machine intelligence 2010 Jul; 32(7): 1239-58.

[4] Sanket B, Manthan S, Pravin J, Digvijay R, Aniket B. Advanced driver assistance system. 2012 Sixth International Conference on Sensing Technology (ICST) 2012; 718-22.

[5] National Highway Traffic Safety Administration. U.S. Department of Transportation Releases Policy on Automated Vehicle Development: 2013.

[6] Kartik V, Dan L, Jacques D, Andrew M, Gabriel M, Priyam C, Robert M. Picam: An ultra-thin high performance monolithic camera array. ACM Transactions on Graphics (TOG) 2013 Nov; 32(6): 166:1-166:13.

Tool path optimization for slow tool servo assisted ultra-precision diamond turning of micro lens arrays

Yutao Liu, Zheng Qiao, Yangong Wu, Jiadai Xue, Bo Wang and Peng Zhang
Center for Precision Engineering, Harbin Institute of Technology, Harbin, Heilongjiang, P.R. China

STS DIAMOND TURNING OF MLAs

The micro lens arrays (MLAs) containing a mass of micro lenses has already been obtained widespread use in the optical systems [1, 2]. Its optical properties are decided directly by its surface quality after machined. Therefore, how to fabricate efficiently the MLAs has always been the focus in the current research. Up to now, slow tool servo (STS) assisted ultra-precision diamond turning is regarded as a promising machining approach with high accuracy to generate the MLAs on the flat or roller mold.

In this study, a series of machining experiments were carried out on the electroplated copper roller mold using STS diamond turning approach based on the self-developed ultra-precision horizontal drum roll lathe, as shown in Figure 1. This machine tool includes 3-axis, i.e. the linear X-, Z- and the rotatory C-axes. When the MLAs is generated using this drum roll lathe on the roller mold, the motion relation of each axis is illustrated detailedly in Figure 2.

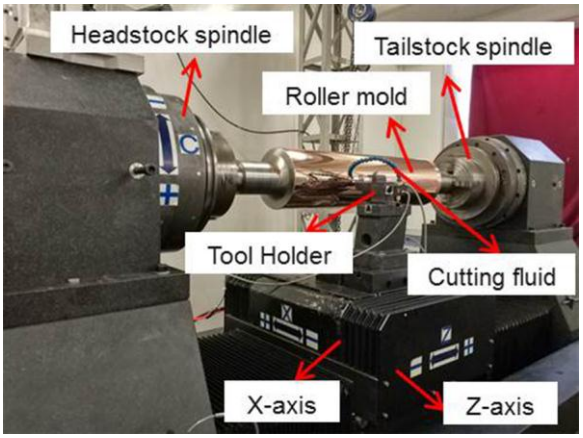

FIGURE 1. Machine tool for the MLAs machining process.

In addition, the dimension of roller mold is too large, so the micro lenses on its surface can not be measured directly. A transfer printing method [3] is commonly adopted to solve this problem in the industry. The MLAs is transferred to polyethylene terephthalate (PET) optical film using ultra-violet (UV) curable resin and UV light. Subquently, surface quality of the transferred MLAs can be measured using optical microscope.

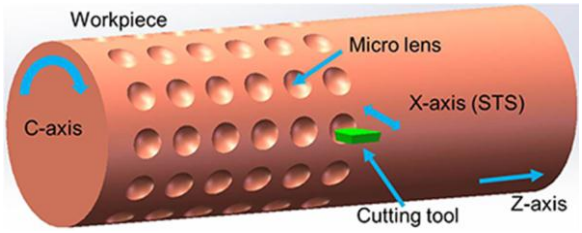

FIGURE 2. Schematic of STS assisted ultra-precision diamond turning of MLAs.

CHATTER MARK

The surface quality of machined MLAs was acquired by a 3D super depth digital microscope, i.e. VHX-1000 supplied by KEYENCE Co. Ltd. As highlighted with red circle in Figure 3, the obvious chatter mark on the surface of micro lens occurs at the initial position of the machined profile along the cutting direction. It is noted that black circles as highlighted in Figure 3 are merely the dusts, which still adhere on the

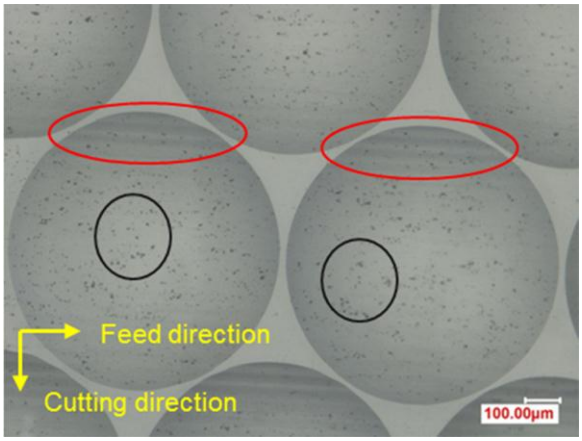

FIGURE 3. Microscopic images of transferred MLAs before optimizing tool path.

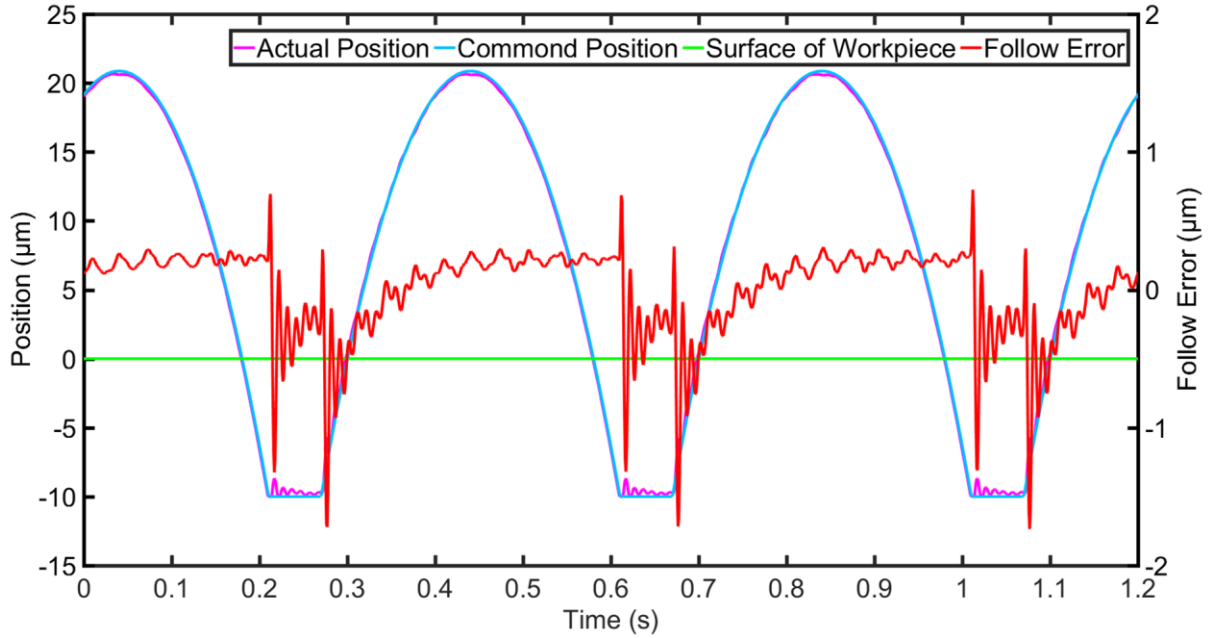

FIGURE 4. The collected kinematic information of the cutting axis： follow error, actual and command position. (before optimizing tool path)

surface of the MLAs after cleaning using ethyl alcohol. Based on previous research, the chatter mark is a general problem for the generation of MLAs using STS diamond turning [4]. And the defect will degrade the optical properties of MLAs. Therefore, the generation of MLAs without the chatter mark has been a key issue at present.

Figure 4 shows the real-time kinematic data of the the cutting axis (X-axis) before optimizing tool path, which were collected via the UMAC controller in the course of machinig. The plot was drawn using a post-process software (MATLAB). It can be seen from Figure 4 that fluctuations of follow error are serious at the begining position of the machined micro lens, i.e. the region of intersection of the green line and the blue line. The maximun amplitude of follow error is up to hundreds of nanometers. Therefore, the chatter mark is generated in this place, as shown in Figure 3. With the progress of processing along the cutting direction, the fluctuations of follow error decrease gradually. Then the chatter mark is also disappearing. According to analysis and experimental result, the chatter mark can be attributed to the overlarge instantaneous follow error of the cutting axis of machine tool during processing.

OPTIMIZED TOOL PATH

In order to overcome generation of the chatter mark, an optimal tool path was proposed to fabricate MLAs with a fine surface quality by means of enlarging machining path in this study. As shown in Figure 5, upper part of the red line represents the cutting region in the tool path, i.e. the profile of micro lens; lower part of the red line denotes the uncut region in the tool path, i.e. idle stroke. During processing, h denotes the distance between the tool tip and the surface of workpiece before optimizing tool path; H represents the distance between the tool tip and

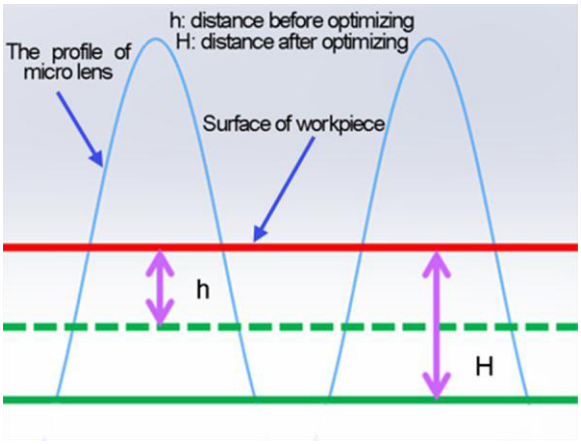

FIGURE 5. Schematic of tool path optimization for enlarging machining path.

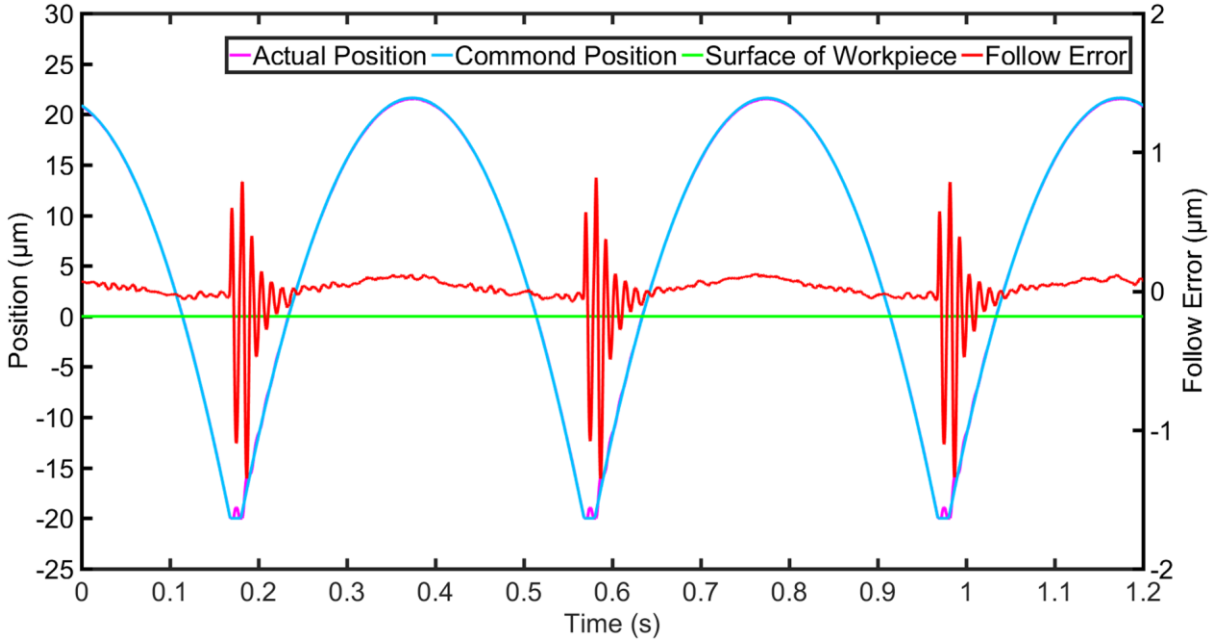

FIGURE 6. The collected kinematic information of the cutting axis： follow error, actual and command position. (after enlarging machining path)

the surface of workpiece after enlarging machining path. In this manner, although machining efficiency wil be reduced slightly due to increased idle stroke, the overlarge fluctuations of follow error of the X- axis will also occur at the uncut region rather than the cutting region. Therefore, the chatter mark on the surface of micro lens at the initial position will be avoided effectively.

EXPERIMENT

To verify the effectiveness of enlarging machining path on chatter mark, a range of cutting experiments were conducted on the above ultra-precision drum roll lathe using same cutting parameters as well as same workpiece. A round-shaped natural diamond (ND) tool with a nose radius of 2.995 mm, 0º rake angle and 8º clearance angle was used in the experimwnt. As a cutting fluid, ISOPAR H (Exxon Mobil Co. Ltd.) was used for lubrication and chip removal.

The typical MLAs with 20.52-μm height and 700-μm aperture on the roller mold was carried out with enlarging machining path, i.e. H=2h=20 μm. Figure 6 shows the real-time kinematic data of the cutting axis after optimizing tool path. As analyzed above, the large fluctuations of follow error of the cutting axis appear at the uncut region. And fluctuations of follow error at the cutting region are relatively gentle. The surface quality of machined MLAs after enlarging machining path was measured using the above microscope as well as same magnification, as shown in Figure 7. It can be seen that no chatter mark at the begining position occurs along the cutting direction of the processed micro lens. The experimental result shows the method of enlarging machining path can restrain the generation of the chatter mark efficiently, when the MLAs is fabricated using STS diamond turning.

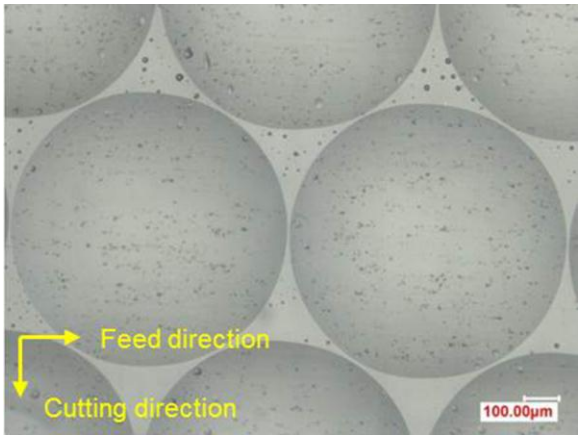

FIGURE 7. Microscopic images of transferred MLAs after enlarging machining path.

CONCLUSION

In this study, the enlarging machining path is presented to eliminate the chatter mark at the beginning position of machined micro lens.Then the micro lenses with 20.52-μm height and 700-μm aperture are acquired with a fine surface topography on the electroplated copper roller mold, which validates the effectiveness of enlarging machining path.

FUTURE WORK

In the current study, changing where the large fluctuations of follow error happen is just a compromised way. Although enlarging machining path can be used for generating the MLAs with a good surface finish on the roller mold, this method can not eliminate the large fluctuations of follow error in nature. In the future research, the reasons of generation for the overlarge fluctuations of follow error during processing will become the focus.

ACKNOWLEDGEMENTS

This work was performed under the auspices of the National Science and Technology Major Project of High-end CNC Machine Tools and Basic Manufacturing Equipment of China (grant number 2011ZX04004–021) and the Chinese National Natural Science Foundation (grant number 51605119).

REFERENCES

[1] Zhu W L, Duan F, Zhang X. A new diamond machining approach for extendable fabrication of micro-freeform lens array. Int J Mach Tool Manuf 2018; 124: 134-148.

[2] Gao P, Liang Z, Wang X. Fabrication of a Micro-Lens Array Mold by Micro Ball End-Milling and Its Hot Embossing. Micromachines 2018; 9(3): 96.

[3] Oh J S, Song C K, Hwang J. An ultra-precision lathe for large-area micro-structured roll molds. J Korean Soc Precis Eng 2013; 30(12): 1303-1312.

[4] Huang P, To S, Zhu Z. Diamond turning of micro-lens array on the roller featuring high aspect ratio. Int J Adv Manuf Technol 2018; 1-7.

DEVELOPMENT OF A SURROGATE SYSTEM TO STUDY THE DRY TURNING OF PLUTONIUM

Noa M. McNutt, Thomas A. Dow
Department of Mechanical and Aerospace Engineering
North Carolina State University
Raleigh, NC, USA

INTRODUCTION

In the last 20 years, there has been a spike in research on dry machining, how to remove cutting fluids from the machining process. This is part of a greater effort to make many manufacturing processes more sustainable, environmentally friendly, and safer for workers [5]. Cutting fluids, while effective at removing heat and lowering friction at the cutting zone, are often harmful to humans and the environment [5]. While much research has been focused on dry machining of common engineering metals, more research is required to investigate possible dry machining techniques for more difficult to machine materials, such as fissile materials used in nuclear fuels and explosives.

When cutting fluids are used on fissile materials such as plutonium, there is a significant cost associated with the disposal of cutting fluids. After a part is machined, the slurry of the cutting fluid and radioactive chips must be separated and safely disposed of. Balog[4] claims that proper disposal of cutting fluid used on plutonium can cost up to $300,000 per cubic foot. Unfortunately, due to its limited stock and radioactive nature, plutonium itself cannot be used in machining experiments to optimize dry cutting parameters. Therefore, in order to study how to best dry machine plutonium, this project aims to find a proper surrogate metal and study it in place of plutonium.

Due to its atomic stability at room temperature, low yield strength and hardness, the gallium δ-stabilized allotrope of plutonium is often used in metal forming and machining operations to manufacture nuclear fuel rods and warhead “hemishells” [6],[2]. This ductile, soft allotrope is very difficult to dry machine. It is known for chip adhesion issues that result in smearing, built up edge (BUE), and generally poor surface quality [3]. Figure 1(A) displays a turned surface marred by smearing due to chip adhesion to the tool [3]. Figure 1(B) shows how surface finish can be improved by reducing the effects of chip adhesion to the tool.

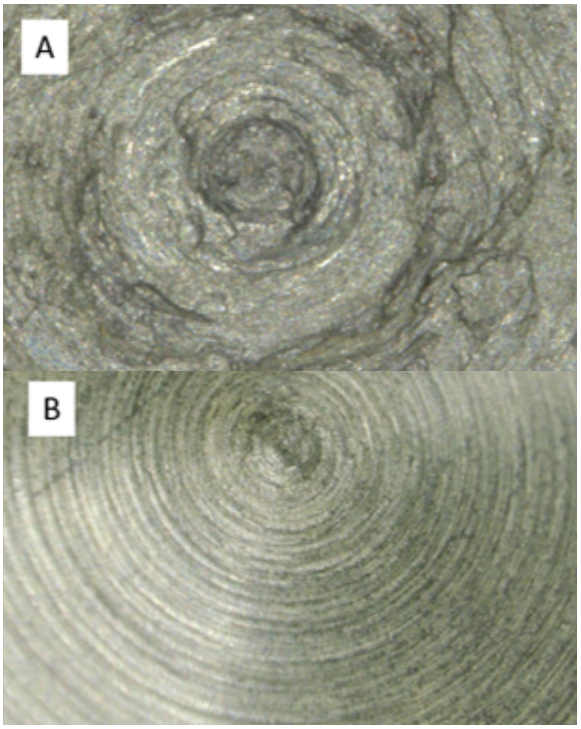

FIGURE 1. Turned plutonium surface A) marred by smearing due to chip adhesion B) void of smearing [3]

An example of what the tool that produced the surface in Figure 1(A) might look like is shown in Figure 2.

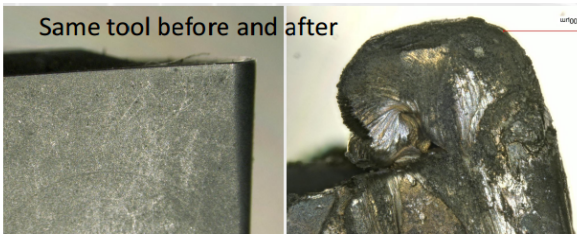

FIGURE 2. Carbide tool tip before (Left) and after (Right) turning plutonium [3]

The image in Figure 2(Right) is of a BUE that is a result of chip adhesion to the rake face of the tool.

POTENTIAL SURROGATE IDENTIFICATION AND TESTING

First, before any machining takes place, a proper surrogate needs to be identified. An ideal surrogate material for plutonium would display similar machinability challenges in the absence of cutting fluid, namely issues pertaining to chip adhesion to the tool. These issues include BUE and chip seizure. In order to identify this optimal surrogate, several material properties were considered: hardness, crystal structure, yield strength and thermal diffusivity. A proper surrogate should be a soft, FCC metal, with low thermal diffusivity and similar yield strength to the plutonium metal. Four potential surrogates were considered: OFHC partially annealed copper, lead babbitt, and 2 grades of commercially pure aluminum: 1100 and 1199. Copper was recommended by Gilmore et al. , while pure aluminums were recommended by Hecker[6]. Babbitt was selected for its high density and FCC crystal structure. Material properties of interest are shown in Table 1.

TABLE 1. Material properties of potential surrogate metals compared to plutonium

	Crystal Structure	Yield Strength (MPa)
Plutonium	FCC	100
Copper	FCC	195
Babbitt	FCC	42
1100 Aluminum	FCC	103
1199 Aluminum	FCC	110
	Hardness (Hv)	Thermal Diffusivity (m^2/s)
Plutonium	45	4E-6
Copper	75	110E-6
Babbitt	22	140E-6
1100 Aluminum	34	89E-6
1199 Aluminum	31	95E-6

It can be seen in Table 1 that the yield strength, hardness and crystal structure of plutonium can be matched by the two species of aluminum. Unfortunately, due to its low thermal diffusivity, plutonium is unlike most metals. In an effort to predict overall machining performance, a scoring system was developed. This machining surrogate score (MS score) attempts to predict a particular metal's similarity to plutonium in a dry machining environment. Equation 1 describes the relationship between a material's properties and its MS score.

$$MS\ Score = \left| \frac{\sigma_{ypu} - \sigma_{yx}}{\sigma_{ypu}} * \frac{\alpha_{pu} - \alpha_x}{\alpha_{pu}} \right| \qquad (1)$$

Where σ_{ypu} and α_{pu} are yield strength and thermal diffusivity of plutonium, respectively. σ_{yx} and α_x are yield strength and thermal diffusivity of the potential surrogate material, respectively. The MS scores of the 4 potential surrogates is shown in Figure 3. Note that a perfect score of zero would indicate that a surrogate has identical yield strength and thermal diffusivity to plutonium.

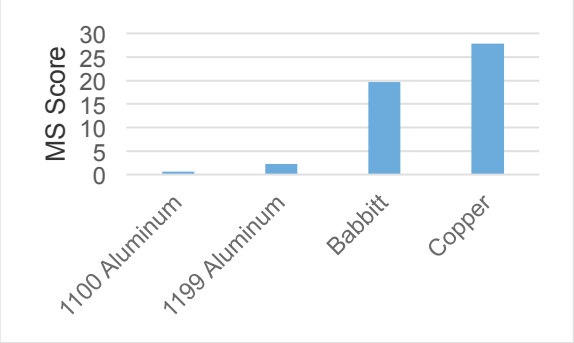

FIGURE 3. MS Scores of the four potential surrogate metals

Notice that the two aluminums score much better (lower value) than the Babbitt or copper. This is due to their smaller thermal diffusivities compared to Babbitt or copper and similar yield strengths to plutonium. This suggests that the aluminums will machine more similarly to plutonium in a dry machining environment. Now that some potential surrogates have been identified, machining tests must be conducted to qualitatively determine if any of these metals behave like plutonium in a dry machining environment. Babbitt was not futher studied due to potential health hazards associated with its lead content. While this measure likely won't be a perfect indicator of machining similarity to plutonium, hopefully it can serve as a method to disqualify metals with little similarity to plutonium going forward.

Surrogate Machining Experiments

Now that some potential surrogates have been identified, some initial machining experiments were conducted to verify if they were good surrogates to plutonium.

First, copper was tested by way of a non-overlapping feed rate facing cut on the Nanoform 600 diamond turning machine. Non-overlapping cuts provide insight on BUE and chip adhesion, since each groove can be isolated and compared to the ideal case [1]. Figure 4 shows the machine tool setup used in this experiment. Non-overlapping cuts were done at a 20 µm depth of cut, 573 rpm, on a 100 mm diameter disc. This set cutting speed to be a maximum of 3 m/s at the outside of the face. This cutting speed is similar to those used for machining plutonium at Los Alamos National Laboratory.

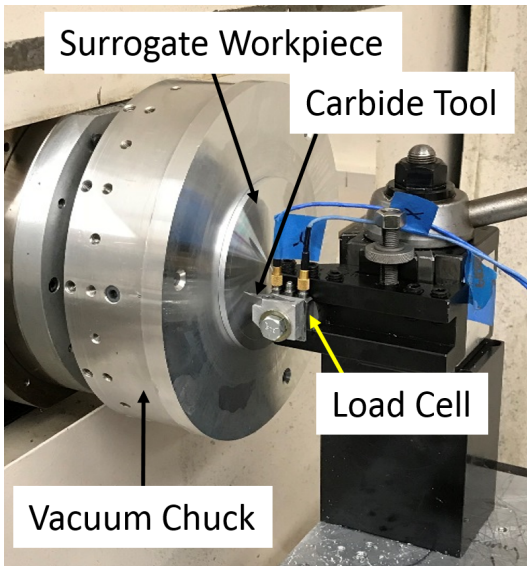

FIGURE 4. Nanoform 600 diamond turning station, set up with an 1199 aluminum workpiece and Kennametal carbide tool

Non-overlapping cuts with copper showed little evidence of significant BUE. Figure 5 displays a 2-d profile of two of the grooves cut into the copper.

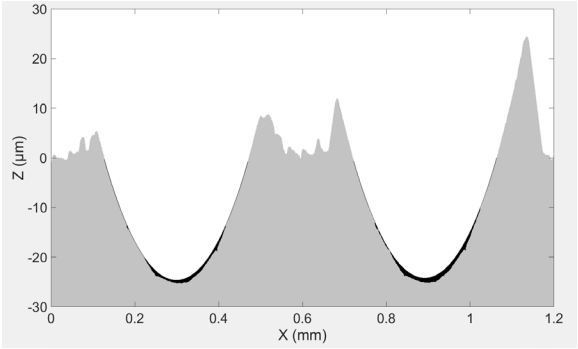

FIGURE 5. Two grooves cut into copper with a 0.4 mm nose radius tool.

Gray area in Figure 5 represents the copper workpiece, the small dark area at the bottom of the grooves is material removed from the uncut chip area that is not accounted for by the advertised tool radius. This dark area can either be accounted for by BUE or by tool edge imperfections. Post mortem micrographs of the tool indicate that the dark areas in Figure 5 are likely due to tool imperfections rather than BUE.

The peaks seen on the edges of the grooves are the result of a phenomena called plowing, where some of the uncut chip is displaced to the side of the groove by the tool, rather than removed entirely from the workpiece. Plowing can be caused by a worn, dull tool edge, or by a seized chip that inhibits material flow over the rake face fo the tool. Post-mortem micrographs of the tool indicate that chip seizure was likely the cause of the plowing. This is a good indicator of machinability traits similar to those of plutonium.

Next, 1100 aluminum was tested using the same non-overlapping facing operation. Figure 6 shows the 2-d profile of the grooves.

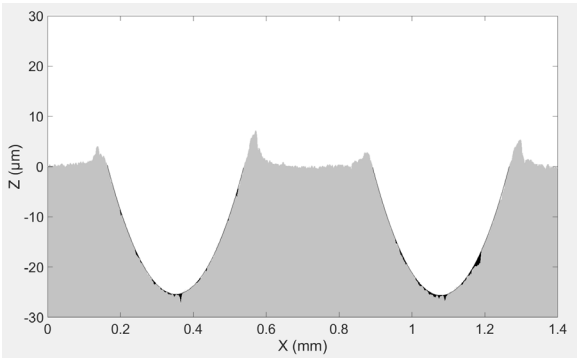

FIGURE 6. Two grooves cut into 1100 aluminum with a 0.4 mm nose radius tool.

Due to the small amount of dark area and little evidence of plowing, it can be concluded that little BUE or chip seizure occurred with this 1100 aluminum, suggesting that this is not a viable machining surrogate to plutonium. Micrographs of the tool corroborate that no significant BUE or seizure occurred on the tool.

Finally, 1199 aluminum was tested using the same non-overlapping facing operation as was used on copper and 1100 aluminum. Figure 7 shows the 2-d profile of the grooves.

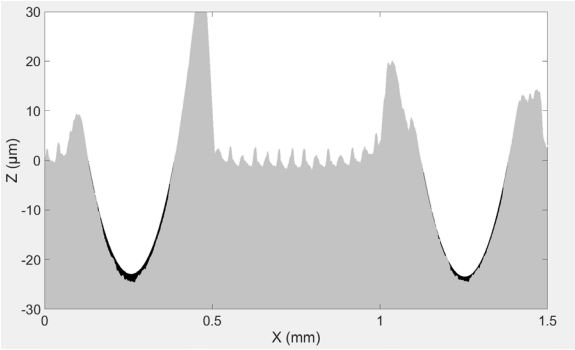

FIGURE 7. Two grooves cut into 1199 aluminum with a 0.4mm nose radius tool.

While dark area due to BUE was limited, large peaks indicate that plowing due to chip seizure was a major factor when turning these grooves. When the cut concluded, a large chip seizure was still present on the tool. Figure 8 is a photograph of the chip seized to the tool.

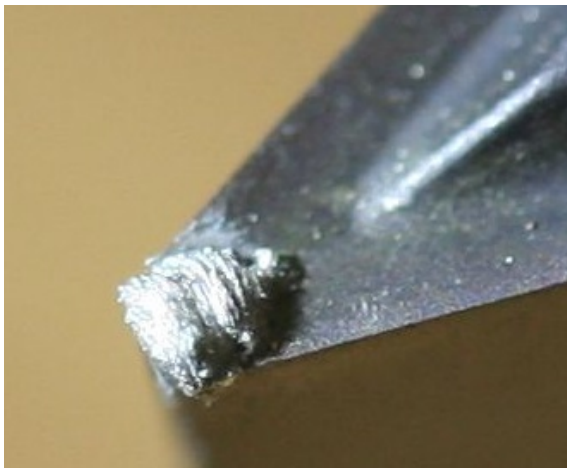

FIGURE 8. A ball of 1199 aluminum adhered to the rake face of the tool.

Surrogate Testing Conclusions

Compare the aluminum chip adhesion in Figure 8 to the plutonium chip adhesion in Figure 2 (right). Both pictures show significant ability of the work piece material to adhere to the rake face of the tool. This ability to adhere to the tool causing chip flow issues indicated that 1199 aluminum was the best of the four potential surrogates considered.

Differences between 1199 and 1100 aluminum were likely due to crystallographic orientation and grain size of the particular species, rather than slight differences in chemical makeup. The copper tested was classified as partially annealed, quarter hard copper. Fully annealed copper should be tested in the future, since it should have more similar strength and strain hardening characteristics to plutonium.

1199 ALUMINUM PARAMETER STUDY

After concluding in the previous section that 1199 aluminum was the most suitable surrogate metal to study the dry machining of plutonium, experiments were commenced in order to understand how machining parameters affect chip adhesions and surface roughness of the dry machined part.

The 1199 aluminum was then tested by way of an overlapping feed rate facing cut on the Nanoform 600 diamond turning machine. Figure 4 shows the machine tool setup used in this experiment. Cutting and thrust forces were measured during these operations. Overlapping cuts were done at a 120 µm depth of cut, 573 rpm, on a 100 mm diameter disc. This set cutting speed to be a maximum of 3 m/s at the outside of the face. With the 0.4 mm nose radius tool used, these parameters will result in a theoretical surface roughness of 150 nm RMS. This value cannot be achieved in reality since it assumes no machine-tool vibration, a perfect tool cutting edge, and perfect chip formation. This value is strictly dependent on tool nose radius and cross feed, and is invariant of parameters such as cutting speed, rake angle and depth of cut.

Rake Angle Study

Rake angle was the first machining parameter to be tested with 1199 aluminum. As mentioned above, rake angle does not affect theoretical surface roughness.

Rake angles tested varied between +3° and +15° in increments of 3°. During each experiment, chips were collected at three points in time: at the onset of the cut, halfway through the cut, and at the very end of the cut. These chips provided insight about the geometry of the cutting process. After each experiment concluded, the Rq surface roughness of each workpiece was measured. Depth of cut was set at 120 µm, about 0.005". Cutting (surface) speed ranged from 3 m/s at the outer radius of the disc, down to 0 m/s at the center of the disc. Figure 9 shows the surface roughness of the disc as a function of tool rake angle.

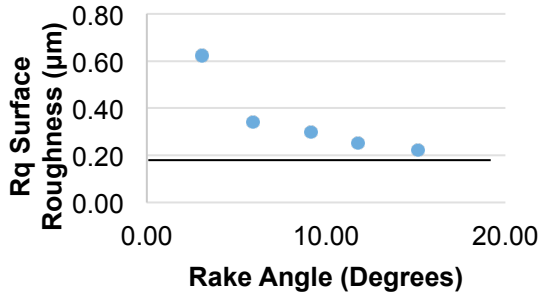

FIGURE 9. Rq surface roughness of 1199 aluminum as a function of tool rake angle, the black line represents theoretical surface roughness.

Surface finish improved as rake angle increased. The best finish of 0.22 µm was achieved at +15° rake angle. The surface finish approaches the theoretical roughness at high rake angles, but does not achieve it. This asymptotic behavior is expected, since theoretical roughness cannot be achieved due to machine-tool vibration, spindle errors, axis errors, tool edge form error and environmental factors.

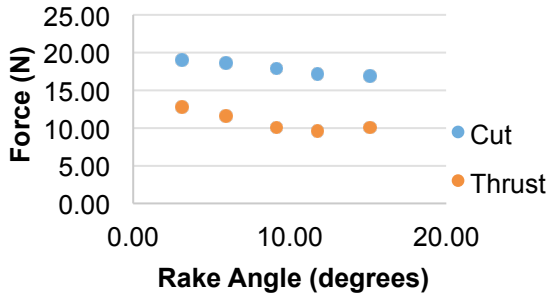

FIGURE 10. Machining forces measured was a function of rake angle while machining 1199 aluminum

Figure 10 shows that cut and thrust forces decreased as rake angle increased. Lower forces will result in less machine vibration, and often result in better surface finish.

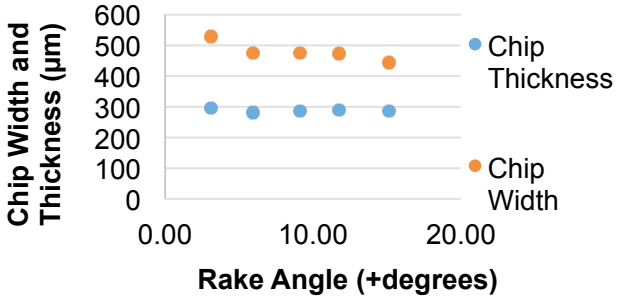

FIGURE 11. Chip thickness and width as a function of tool rake angle, 1199 aluminum

Figure 11 shows that chip was invariant with rake angle, while chip thickness decreases as rake angle is increased. By assuming that density of the aluminum is constant, this indicates that chip velocity increases as rake angle is increased. Faster chip flow is often correlated with lower friction at the chip-tool interface.

CONCLUSIONS

After testing partially annealed OFHC copper, 1100 aluminum and 1199 aluminum, it was determined that 1199 aluminum showed the best ability to serve as a surrogate material for machining plutonium. This is due to its similar ability to adhere to the tool, causing chip flow stoppages and subsequent surface fidelity issues.

After 1199 aluminum was determined to be the best surrogate tested, a study of how rake angle affects the surface finish of the material was conducted. Rake angles tested varied from +3° to +15° in increments of 3°. It was found that as rake angle increased, surface finish improved. Chip velocity, shear plane angle, and machining forces also increased with rake angle. According to [3] and [4], this result also occurs on plutonium.

FUTURE WORK

While the partially annealed OFHC copper didn't show as much potential to serve as a plutonium surrogate in this study, large grain, fully annealed OFHC copper should be tested in the same manner as the other potential surrogates.

Other parameters such as cutting speed, depth of cut, cross feed, tool nose radius, tool coatings and depth of cut need to be studied for 1199 aluminum.

REFERENCES

[1] Suit B. Analysis of Accelerated Tool Wear and Built Up Edge When Diamond Turning Ferrous Metals. Master's Thesis, Precision Engineering Center, North Carolina State University. 2016; 136-138.

[2] Wick O. Plutonium Handbook: A Guide to the Technology, Volumes I and II. American Nuclear Society. 1980; 82.

[3] Balog J, Gonzales T, Harwood S, Stout S, Lopez O, Lucero R. Dry Machining of Plutonium Metal: Insert Selection for Machinability and Meeting Surface Finish Criteria. LANL Engineering Week Poster. 2013.

[4] Stephan E, Balog J. Process Engineering Workshop- PT2 Machining. Los Alamos National Laboratory Presentation. 2018.

[5] Gyanendra S, Prabir S. Dry Machining: A Step Towards Sustainable Machining-Challenges and Future Directions. Journal of Cleaner Production. 2017, 165:1560.

[6] Hecker S. Plutonium and Its Alloys, From Atoms to Microstructure. Los Alamos Science. 2000, 321.

[7] Gilmore R, Robbins B, Anderson J. Threading and Assembly of Soft Delta-Stabilized Plutonium Parts. Los Alamos National Laboratory. 1967, 3.

Tool Path Planning for Ultra-Precision Machining of NURBS Surfaces

Christopher Morgan, Ph.D.[1]
Mark Rubeo, Ph.D.[1]
[1]Moore Nanotechnology Systems, LLC
Swanzey, NH

ABSTRACT
Freeform optical designs are being widely adopted in the optics industry. Applications include automotive heads-up display [1], AR/VR and short-throw projectors [2]. These applications require freeform surfaces with non-circular apertures and opto-mechanical features. Also, the optics must have high form accuracy and surface finish for acceptable performance. Consequently, successful fabrication of freeform optics is a key technology for wide adoption of these systems. See Figure 1 for a typical freeform lens.

One common fabrication technique of freeform optics is single point diamond machining by slow slide servo (SSS), where the linear axes of a lathe are synchronized with a rotary axis to profile the freeform surface geometry. The tool path trajectory for SSS requires high accuracy and high-density data for CNC controller interpolation. Historically tool paths have been based on analytical calculation derived from the optical equation [3]. While this technique yields high accuracy results, it suffers from the flexibility needed by optical system designers. For instance, surfaces may be part of an opto-mechanical system containing locating and mounting features. Also, the surfaces may be mounted to fixturing that limits access to the surface by a tool. Interrupted surfaces create an even bigger challenge for tool path planning in non-cutting areas.

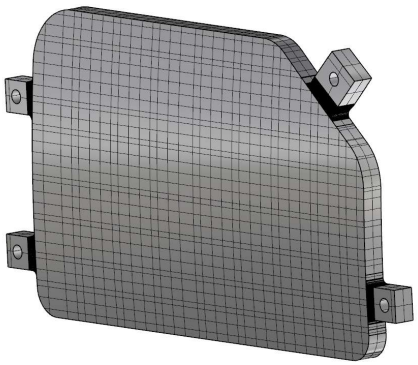

FIGURE 1. CAD rendering of a freeform lens.

A typical workflow for fabrication of freeform surfaces is shown in Figure 2. Many of the steps require testing, or dry running, the program on the machine controller. Dry running a program is time consuming and it takes place when the machine is ready to fabricate the part, wasting valuable production time. Also, locating the fixture and workpiece with respect to the machine coordinate system can be especially challenging because the tool path has been created without awareness of the fixture size and location.

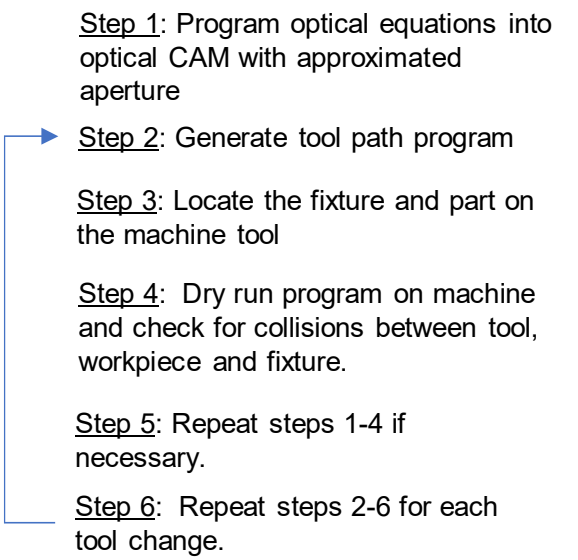
Step 1: Program optical equations into optical CAM with approximated aperture
Step 2: Generate tool path program
Step 3: Locate the fixture and part on the machine tool
Step 4: Dry run program on machine and check for collisions between tool, workpiece and fixture.
Step 5: Repeat steps 1-4 if necessary.
Step 6: Repeat steps 2-6 for each tool change.

FIGURE 2. Workflow for generating tool paths for freeform surfaces using conventional optical CAM software.

An alternative to analytical calculation of the tool path is to utilize native cad data, or NURBS surfaces, for tool path generation [4]. Freeform optical surfaces may be defined by an equation in cartesian or polar space, but they may also be designed by ultraprecision NURBS surfaces. Given the complexity of CAD designs it is beneficial to have CAM software that can generate toolpaths on any CAD design and use the same toolpath algorithm for all surfaces, even mechanical features.

This paper will discuss the development of CAM software, NanoCAM 4, based on NURBS surfaces. Topics include surface generation, tool path design and machine controller integration.

SURFACE GENERATION

While a direct import of optical surfaces is ideal, most optical design software does not provide NURBS surfaces to adequate precision. Therefore, an algorithm has been developed for NanoCAM 4 to take optical equations and convert them to NURBS surfaces of better than 1e-6 precision. NURBS surfaces are defined as follows:

$$\boldsymbol{S}(u,v) = \sum_{i=0}^{n}\sum_{j=0}^{m} R_{i,j}(u,v)\boldsymbol{P}_{i,j} \qquad (1)$$

The rational basis functions

$$R_{i,j}(u,v) = \frac{N_{i,p}(u)N_{j,q}(v)w_{i,j}}{\sum_{k=0}^{n}\sum_{l=0}^{m} N_{k,p}(u)N_{l,q}(v)w_{k,l}} \qquad (2)$$

are weighted p-th and q-th degree B-spline basis functions $N_{i,p}$ with the parameters u and v. The algorithm utilizes the first and second derivative of Eq. (1) to minimize surface complexity while maintaining desired precision.

Surfaces may consist of multiple equations in different domains summed together. For instance, Figure 1 is a power polynomial equation overlaid with an asphere equation. The power polynomial equation is defined in cartesian space and the asphere is defined in polar space. The algorithm was, therefore, extended so that that NURBS surfaces may be morphed or summed.

Once the NURBS surfaces have been created they can be used to facilitate fixture design and positioning. Fixturing of freeform surfaces is critical to maintain proper reference point. Figure 3 describes a new workflow enabled by NURBS based CAM software. After the NURBS surfaces have been created they are exported to IGES file format for importing into CAD software. The surfaces can be trimmed to the desired profile and opto-mechanical features can be added.

Once the lens design is complete it can be imported into NanoCAM 4 for optimized positioning based on the desired fabrication approach. For this example, the part is centered on the spindle axis about the physical aperture and tilted to orient the surface normal at the center of the part parallel to the Z-axis.

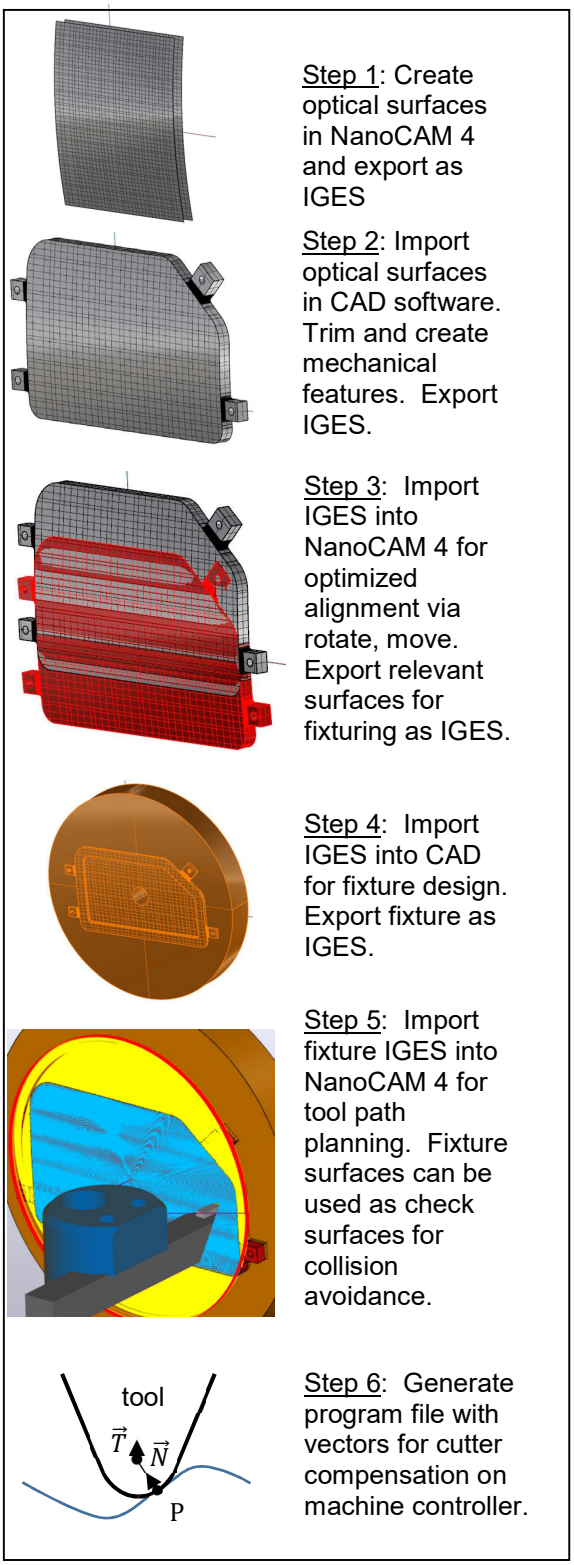
Step 1: Create optical surfaces in NanoCAM 4 and export as IGES
Step 2: Import optical surfaces in CAD software. Trim and create mechanical features. Export IGES.
Step 3: Import IGES into NanoCAM 4 for optimized alignment via rotate, move. Export relevant surfaces for fixturing as IGES.
Step 4: Import IGES into CAD for fixture design. Export fixture as IGES.
Step 5: Import fixture IGES into NanoCAM 4 for tool path planning. Fixture surfaces can be used as check surfaces for collision avoidance.
tool
$\vec{T}$
$\vec{N}$
P
Step 6: Generate program file with vectors for cutter compensation on machine controller.

FIGURE 3. Workflow for generating tool paths for freeform surfaces using NURBS based CAM software.

Next, the relevant surfaces can be exported from NanoCAM 4 and imported into CAD for fixture design. Once fixture design is complete, it can be imported back into NanoCAM 4. The fixture and workpiece CAD models create a reference frame for accurate positioning on the machine tool. For instance, the flat area on the outside of the fixture can be used as a datum for establishing the position of the cutting tool with respect to the freeform surface.

Finally, the tool path program file can be generated with vector information for on-controller cutter compensation. This topic is discussed in a later section.

TOOL PATH DESIGN

There are three aspects of tool path design critical to successful SSS of freeform surfaces; acceleration optimization, link design and tool clearance modeling.

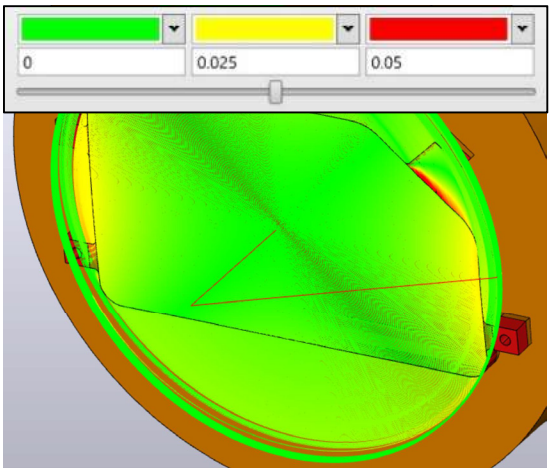

FIGURE 4. Plot of z-axis acceleration in g's during synchronized slide servo machining of freeform optical mold.

Acceleration Optimization

The tool path accelerations should be sufficiently small to not exceed machine tool capabilities. During SSS machining, high accelerations of the linear axes are required to maintain synchronization to the rotary axis. The accelerations can be reduced by slowing the rotary axis speed, but cycle time is increased. Therefore, modeling the acceleration of the linear axis is import for cycle time optimization. Figure 4 is a plot of acceleration during machining of the freeform lens shown in Figure 1. Typical machine axis acceleration capability is 0.05 g's to maintain optical quality form accuracy requirements.

Link Design

The non-cutting area of the tool path, or links, are as important as the tool path points on the freeform surface. The link should be as smooth as possible to prevent high accelerations and jerk of the linear axes. NanoCAM 4 has the ability to control the link for slope or curvature continuity to the tool path points on the optical surface. As seen in Figure 4 the accelerations transition smoothly on and off the optical surface. Higher acceleration, near 0.05 g's, can be observed in the upper right portion of the plot. These accelerations are due to the toolpath avoidance of the opto-mechanical locating "tab". The toolpath algorithm can utilize check surfaces for avoidance during link trajectory calculation. This can be critical to prevent gouging of non-cutting areas of the workpiece and fixture.

Tool Clearance Modeling

The rake face of the diamond cutting tool and the surface normal vector do not stay parallel during SSS machining and therefore tool clearance issues can occur. Tool path visualization like the one shown in Figure 5 can assist in determining the correct tool for a given part geometry. Also, material removal simulation can be utilized to report interference between a stock material model and the diamond tool. While these features have been standard in the CAM industry for many years, optical CAM packages have not supported advanced toolpath simulations. NanoCAM 4 utilizes a parametric model of the diamond tool tip to check for collision between the surfaces and the non-cutting portion of the diamond tool. Also, mesh files can be imported that represent the tool arbor and holder for interference detection.

FIGURE 5. Tool path simulation of workpiece and tool interference analysis.

MACHINE CONTROL TOOL COMPENSATION

After tool path design is complete the calculated points are posted to a program file for interpolation by the machine tool controller. Historically the points in the tool path for SSS are

tool radius compensated. Therefore, a new program is required each time the tool radius changes. The program file size can be more than 1 GB due to the data density required for SSS. Regenerating program for each new tool is time consuming and tool path programs cannot be version controlled. To overcome this limitation tool radius compensation can be performed on the controller. Rather than generating a program file with the tool centered data, the file is written with contact point vector, normal vector, and tool reference vector. The three vectors are utilized by the machine controller to create the proper tool centered reference point based on the tool radius saved on the controller. One important aspect of this approach is generation of a simulated contact point for links. The contact point on the tool is interpolated between during the link to create a smooth and continuous contact point. Therefore, 3D cutter compensation can be performed on and off the surface.

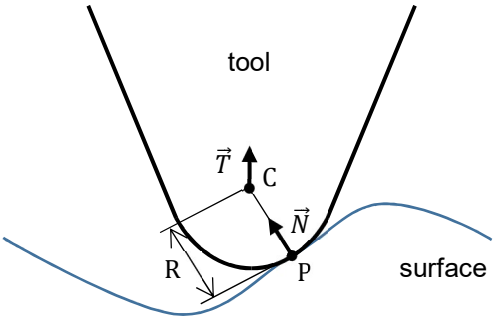

FIGURE 6. Line art diagram describing three-dimensional cutter compensation implemented in control.

SUMMARY

A new optical CAM software package has been developed, NanoCAM 4, which is based on NURBS surface for toolpath planning. The new approach provides flexibility and efficiency over conventional optical CAM algorithms. An algorithm has been developed to create NURBS surfaces with 1e-6 precision with respect to optical equations. The NURBS surfaces facilitate surface positioning and fixture design. The toolpaths generated by this approach maintain smooth trajectories, even outside non-round and irregular apertures. Finally, an on-controller tool radius compensation approach has been introduced to increase productivity.

REFERENCES

[1] Nicolaus Hettler, Robert Hutchins, “Novel Optics: Plastic micro-optics cater to automotive HUD design”, Laser Focus World, 2014.

[2] ricoh.com, "Free-Form Mirror and Deflection Technology for Ultra-Close-Range Projection", 2016. [Online]. Available: https://www.ricoh.com/technology/tech/040_projection.html. [Accessed: 13- Sep- 2016].

[3] Brinksmeier, E., Riemer, O. and Osmer, J., 2008. Tool path generation for ultra-precision machining of free-form surfaces. *Production Engineering*, *2*(3), pp.241-246.

[4] Brecher, C., Lange, S., Merz, M., Niehaus, F., Wenzel, C., Winterschladen, M. and Weck, M., 2006. NURBS based ultra-precision free-form machining. CIRP Annals-Manufacturing Technology, 55(1), pp.547-550.

ULTRA-HIGH PRECISION GRINDING OF OPTICAL GLASS USING ACOUSTIC EMISSION MONITORING TECHNIQUE

Goodness Raluchukwu Onwuka[1], Peter Babatunde Odedeyi[1], Khaled Abou-El-Hossein[1], Lukman Niyi Abdulkadir[1]

Precision Engineering Laboratory,
Mechatronics Department, North Campus
Nelson Mandela University,
Port Elizabeth, Eastern Cape,
South Africa.

INTRODUCTION

Ultra-high precision grinding (UHPG) is a fore front technology that has fast replaced conventional grinding techniques. There is a current increase in the demand for ductile machined brittle engineering materials like silicon, tungsten carbide, borosilicate-crown glass (BK7), borosilicate 9 glass and other optical glasses. The reason being that these materials are widely used in the semiconductor, telecommunications, micro-electronics, automotive and defense industries to manufacture silicon chips, optical lens for night vision and Micro-Electro- Mechanical systems (MEMS). These materials are machined to tight stringent requirements involving mirror surface finishes, nanometric surface roughness values and very low form deviations to be used in the above-mentioned applications [1].

These stringent requirements can be met by applying ultra-precision grinding techniques. One of the major drawbacks in UHPG is insufficient data on process monitoring and optimization of the process.

Furthermore, the mechanical properties and the required part quality of the workpiece are yardsticks for deciding machining process to be used on the work piece [2]. Glass which is brittle and hard is usually machined through ultra-precision grinding process. Ultra-precision grinding of glass is an abrasive process which requires the use of fine grain wheels, wear-resistant abrasives, low run-out spindles and machine tools with high loop stiffness[2]. Grinding of hard and brittle materials such as glass, ceramic and semiconductors by an abrasive process is more complex because high precision parts are required, unlike cutting of ferrous metals which is highly predictable [2].

Due to the nature of glass, grinding initiates micro cracks which deteriorate surface quality hence glass was previously ground conventionally at a hundred percent brittle fracture with subsequent rounds of polishing. The focus is now to initiate the process in such a way that little or no further polishing and finishing processes are required to realize the best surface roughness with minimum machining time [3]. This paper presents a surface roughness monitoring approach with contribution to the unique ultrahigh precision grinding of BK7 glass.

LITERATURE

Acoustic Emission Monitoring in Machining

Since ultra-precision grinding of optical glass takes place at the submicron to Nano-scale dimensions, it becomes a herculean task to obtain essential process monitoring features which are challenging to obtain at the submicron and nanoscale level [4]. Depending on the parameters to be monitored such as: surface roughness, grinding wheel wear, wheel and bond performance, grinding and burn, different monitoring techniques have been applied to the grinding operation [4]. It should be recalled that modelling is not feasible without data on the different cause and effect parameters at play. Hence, the relevance of effective process monitoring.

Acoustic Emission (AE) sensing technique became popular in scientific research by the second half of the 20th century [5]. AE signals are known to possess high-frequency bandwidth ranging from infrasound to ultrasound frequency of 10Hz to 50MHz with low amplitude [5]. AE is a physical phenomenon which entails the formation of transient elastic waves within or on the surface of a parent physical center and is generated by atomic level disturbances[5]. Under the influence of localized dynamic modification in the structure of a material, elastic waves are generated and spread out from the

source of the change[5]. The elastic waves propagate through the structure of the material where its energy is primarily used for local mechanical work and generation of heat while a major part of this energy radiates towards the edge of the structure. On exiting, they are captured by a sensing device as AE [6].

Glass has low acoustic impedance compared to materials like wood and plastic, hence, it is good for AE monitoring technique. Piezoelectric sensors adaptable for AE sensing in machining process monitoring [7]. The incorporation of an in-process sensor requires a high level of guaranty in the ability of the sensor to detect the desired process characteristic and reliably detect the quantity being measured [4]. With an efficient data acquisition system and effective signal processing, AE sensors can detect most of the changes in machining conditions because of its very broad sensor bandwidth from 100 to 900 KHz [7].

Acoustic Emission signals are also suitable for very fast events hence its sensitivity is applicable to ultra-precision grinding process monitoring [8]. Since sensor feedback information is critical for higher yield and process throughput, the selected sensor in UHPG processes should have the necessary qualities to account for process conditions at sub-micrometer to nanoscale dimensions. At a very high level of precision, AE sensors have the capability for this range of applications compared to displacement and force sensors which are suitable for conventional grinding [4].

Another uniqueness of AE sensing technique is that its frequency of propagation is from 100 KHz to 1MHz which is well above most structural natural frequencies, hence its immunity to the interference of machine vibration. Theoretically, each grit from the grinding wheel generates a transient AE signal. Therefore, numerous grits cutting through a workpiece almost simultaneously generates a situation where the interval of consecutive cuts is shorter than the decay time of each burst. This situation generates continuous AE signals [9]. Furthermore, for the initial spark in and spark out stages in conventional grinding, AE is seen as burst signals, sometimes this is because the cutting edges of the grits are not at a uniform circumferential height [9].

SURFACE ROUGHNESS

The Surface roughness is a measure of the inherent, fine, closely-spaced surface irregularities created by a production process. It is usually regarded as surface finish in engineering and is normally expressed in its root mean square value or average surface roughness. Though several surface roughness parameters are measured during a grinding operation, the average surface roughness parameter is the most commonly measured. Masuzawa and Tonshoff in their keynote paper noted that the conditions to actualizing the precision grinding of brittle materials are a low depth of cut, slow feed rate, high wheel rotation, and small grain size [10].

DESIGN OF EXPERIMENT

Experimental designs are broadly applied in controlling the effect of parameters in the precision machining process since it helps to reduce the number of experiments to save time and resources. In addition, it simplifies the generation of result, analysis and reduction in experimental errors [11]. For this research, the Box Behnken Design (BBD) was selected to determine the relationship between surface roughness and machining parameters. It is a spherical revolving second order design based on 3-level incomplete factorial designs or 3 interlocking 2^2 design and a center point [11]. The major advantage of the Box-Behnken design over other designs is that it is less expensive because it utilizes fewer design points. Although, BBD is not best suited for sequential designs [11]. For this research, the selected factors in the BBD were: low depths of cut, feed rate and high wheel speed. Hence, a lower limit of 15000rpm and an upper limit of 45000 rpm were selected respectively with feed rates 1 mm/min, 3 mm/min and 5 mm/min and cutting depths of 2 μm, 5 μm, and 8 μm as shown in Table 1.

TABLE 1: Machining Parameters

Factors	MEANING	-1	0	1
A	Depth of cut (μm)	2	5	8
B	Feed (mm/min)	1	3	5
C	Speed (rpm)	15000	30000	45000

The experimental tests were carried out on a flood coolant, compatible 4 axes Nanoform ultra-grind 250 CNC machines manufactured by Precitech which is designed for diamond turning, milling and grinding for the most demanding applications including glass grinding for plane

and aspheric lenses as shown in Fig. 1. The Nanoform 250 ultra grind comes standardized with Precitech's UPx CNC machine control that provides a user-friendly interface. It is also equipped with a 16 picometer feedback resolution and an operating system with 0.01 nanometer programming resolution. Its sealed natural granite base provides exceptional stability and immunity to external vibration.

FIGURE 1. Nanoform 250 Precision lathe machine

WORKPIECE

Ultrahigh precision grinding was carried out on 30mm diameter Bk7 glass. Bk7 glass possesses outstanding mechanical, optical and physical characteristics which include its resistance to chemical and environmental damage, excellent transmission range in the visible and infrared spectra down to 50nm, low coefficient of thermal expansion and good scratch resistance. Some the physical parameters listed in Table2.

FIGURE 2. *30mm diameter BK7 Glass.*

TABLE 2. *Mechanical Properties*

Parameter	Value
Knoop hardness	610 pascals
Young modulus	82Gpa
Fracture toughness	0.85
Acoustic impedance	Low
Abbe number	64.2
Refractive index	1.157
Thermal expansion	$7.1x\ 10^{-6}K^{-1}$
Thermal conductivity	$1.114Wm^{-1}K^{-1}$

MACHINE SETUP

The work spindle was balanced with help of the on board Precitech DIFFYS software which is also used to position the vacuum chuck to avoid unwanted oscillation patterns on the surface of the workpiece. The oscillation pattern which occur because of uneven contact with workpiece and wheel tip could damage the surface of the workpiece.

The AE sensing unit consists of the 8152B piezoelectric sensor which can detect continuous and burst AE signals within a wide frequency range. The sensor is connected to NI PXI data acquisition module via a BNC 2110 signal board. For the acquisition, a Graphical User Interface programming was created on NI LabVIEW software. Kistler AE sensor-coupler connection comes with inbuilt configurable gain of x10 and x100 for 20dB and 40dB amplification respectively while filtering and RMS conversion of the acquired AE signals were made possible through the inbuilt high pass filter range of 50 kHz to 700 kHz, low pass filter range of 100 kHz to 1MHz. AE samples were acquired and filtered during each run then stored in a text file with the different combination of parameters. After each a pass, the average surface roughness parameter was measured thrice using a Taylor Hobson optical profiler while the average of the three measurements was calculated and recorded.

RESULT AND CONCLUSION

The surface roughness values varied according to the different machining parameter combination. Overall, the increase in feed played a significant role in increasing the surface roughness compared to the depth of cut and wheel speed.

The lowest value observed during the experimental runs was 130nm while the highest value is 320nm. AE amplitude levels showed significant variations with the variation in surface roughness values. Some AE results were further segmented in a window time frame of a fraction of a second to highlight the amplitudes of the raw and rms AE signals using Matlab software. Table 3 shows the variation in peak to peak raw AE signal voltage levels with the surface roughness while figure 2 shows the different AE rms amplitude variation for some of the surface roughness values.

TABLE 3. *Surface roughness and peak to peak voltage values*

Ra (nm)	130	150	220
AE p-p (v)	0.5273	0.7031	0.9277

Figure 2 shows the AErms amplitude levels increasing with increase in surface roughness values in the order 130nm, 260nm, 300nm.
Finally, acoustic emission monitoring technique has been efficiently applied to monitor the UHPG of precision optics with a noticeable increase in amplitude levels of raw and rms signals with the surface roughness. This monitoring technique provides a step to optimizing the UHPG of precision glasses.

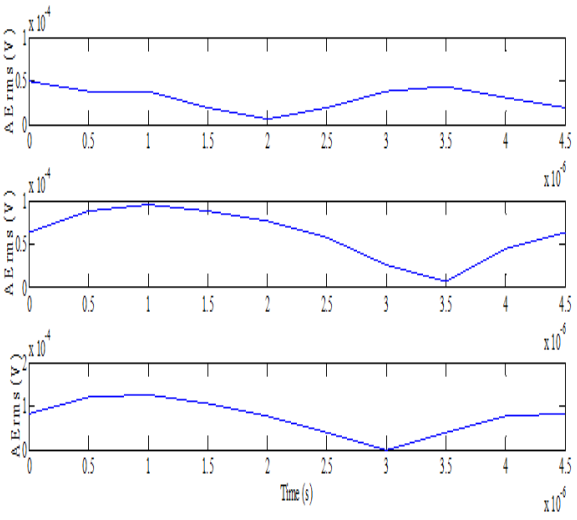

Figure 2*: Surface roughness and AE rms signal voltage levels (top to bottom: 130nm, 260nm, 300nm).*

ACKNOWLEDGMENT
The authors would like to acknowledge the Department of Science and Technology (DST) and the Nelson Mandela University for the assistance and support towards this research.

REFERENCES
[1] Zhong, Z.W., Ductile or Partial Ductile Mode Machining of Brittle Materials. The International Journal of Advanced Manufacturing Technology, 2003. 21(8): p. 579-585.
[2] Brinksmeier, E., et al., Ultra-precision grinding. CIRP Annals-Manufacturing Technology, 2010. 59(2): p. 652-671.
[3] Gu, W., Z. Yao, and H. Li, Investigation of grinding modes in horizontal surface grinding of optical glass BK7. Journal of materials processing technology, 2011. 211(10): p. 1629-1636.
[4] Dornfeld, D.A., Y. Lee, and A. Chang, Monitoring of Ultraprecision Machining Processes. The International Journal of Advanced Manufacturing Technology, 2003. 21(8): p. 571-578.
[5] Bhaskaran, J., et al., Monitoring of hard turning using acoustic emission signal. Journal of Mechanical Science and Technology, 2012. 26(2): p. 609-615.
[6] Sutowski, P., K. Nadolny, and W. Kaplonek, Monitoring of cylindrical grinding processes by use of a non-contact AE system. International Journal of Precision Engineering and Manufacturing, 2012. 13(10): p. 1737-1743.
[7] Teti, R., et al., Advanced monitoring of machining operations. CIRP Annals-Manufacturing Technology, 2010. 59(2): p. 717-739.
[8] Stephenson, D., X. Sun, and C. Zervos, A study on ELID ultra precision grinding of optical glass with acoustic emission. International Journal of Machine Tools and Manufacture, 2006. 46(10): p. 1053-1063.
[9] Webster, J., W. Dong, and R. Lindsay, Raw acoustic emission signal analysis of grinding process. CIRP Annals-Manufacturing Technology, 1996. 45(1): p. 335-340.
[10] Masuzawa, T. and H.K. Tönshoff, Three-Dimensional Micromachining by Machine Tools. CIRP Annals, 1997. 46(2): p. 621-628.
[11] Aslan, N. and Y. Cebeci, Application of Box–Behnken design and response surface methodology for modeling of some Turkish coals. Fuel, 2007. 86(1): p. 90-97

CFD Simulation of Precision Injection Molding Processes

Jörg Schmütz; Leonard Halbeisen; Peter Bartsch
Department VIII, Mechanical Engineering
Beuth University of Applied Sciences
Berlin, Germany

INTRODUCTION

A large variety of optical and microfluidic products is reproduced efficiently by injection molding techniques. However, Fresnel grooves in molds for lenses or other three-dimensional structures in a cavity represent obstacles, which change flow-speed and internal shearing within the molten polymer.

Under certain circumstances, the melt streaming into a cavity from a single gate may split and reunite, forming unwanted weld-lines in the part or trap air instead of filling functional areas (cf. Fig. 1) [1].

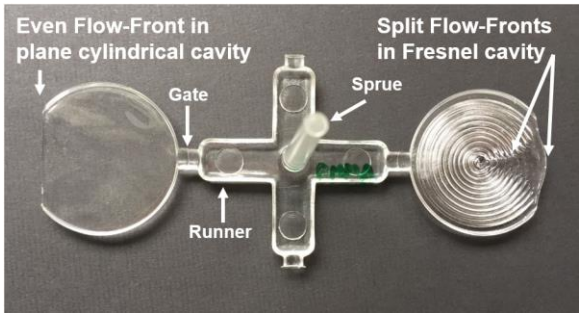

FIGURE 1. PMMA-Parts molded to approx. 80% full in a double-cavity tool [1]

Splitting flow-fronts are observed when injecting different thermoplastic materials with a large variance in viscosity such as Cyclo-Olefin-Copolymer (COC), Cyclo-Olefin-Polymer (COP) and Polymethyl Methacrylate (PMMA) [1].

Eventually, the flow fronts reunite in one particular spot. This may lead to deviations from the desired geometry, such as imperfectly filled Fresnel structures and air enclosures (Fig. 2) [1].

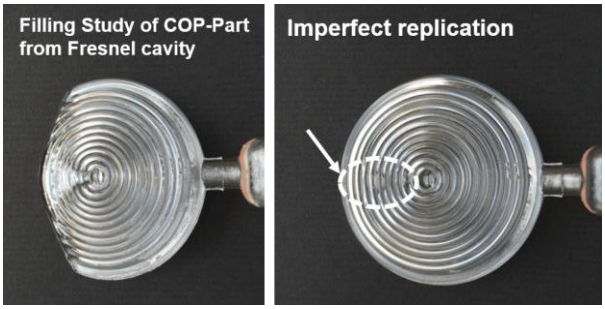

FIGURE 2. . Filling study with split flow-fronts in COP (left) and imperfect replication in COP (right). Both parts on runner and slightly tilted for better visibility. *[1]*

Commercially available simulation tools based on the method of finite elements are not well suited to predict melt-flow and solidification in mold cavities with microscopic features. This also applies for structures of millimeter-size, which are often found in the molding of Fresnel lenses, diffusing screens and other optical components.

SIMULATION SETUP AND MESH DESIGN

When injecting a polymer melt into a mold cavity, the air is pressed out. Since one fluid is replaced by another, a numerical model is required, which models both phases coherently.

The influence of the air however is assumed to be minor as compared to the melt-flow. Therefore, a Volume of Fluids (VoF-) model is chosen to simulate both phases.

In a comparison of different commercially available Computational Fluid Dynamics (CFD) software tools, ANSYS Fluent 17.3 with the Pressure Implicit Splitting of Operators (PISO) scheme is found to provide the best solving algorithm for this particular task.

The molding process is simulated in two geometric halves of the actual molding cavity with sprue, runner, gate and air outlet. One half of the model resembles the cavity for a cylindrical disc (cf. Fig. 1, left) and the other half is used to simulate the cavity for a Fresnel lens with a plane backside (cf. Fig. 3). The mesh consists of layered prims with 869.539 elements and 194.962 nodes with included angles ranging from 20,4° to 140,8°.

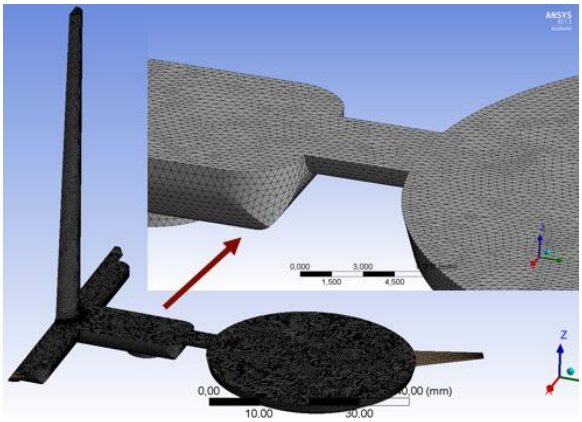

FIGURE 3. Detail of the mesh around the gate of the plane cylindrical mold [2]

The simulation is carried out for the Cyclic Olefin Copolymer (COC) TOPAS 5013. A model for the dynamic viscosity is derived from previous measurements of Mass Flow Indices at different temperatures [3].

VISCOSITY MODEL

The Reynolds-Number for the examined polymer materials (COC, COP, PMMA) is well under 1. Therefore, a laminar flow is assumed and no turbulence model is used.

The viscosity model is based on earlier measurements of Mass-Flow Indices [3] and partly backed up with data derived from the viscosity model for COC used in Moldflow by Autodesk, USA [2]. The dynamic viscosity with respect to the shear velocity is given in Fig. 4 for different melt temperatures.

While dependence on temperature is accounted for in the numeric model, the influence of pressure on the density is neglected. Other important parameters are the temperature transportation capability and the thermal capacity, respectively, which are comprised in the simulation.

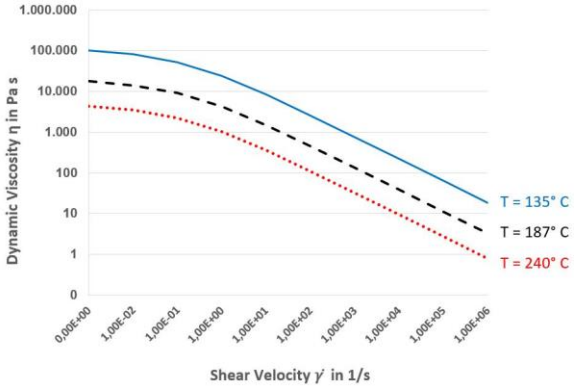

FIGURE 4. Viscosity Model for COC as applied in the numeric simulation [2]

GOVERNING EQUATIONS

Three basic equations have to be solved simultaneously in the numerical simulation of compressible and non-compressible fluids: The first couple of equations accounts for the conservation of mass and momentum, while the third equation expresses the conservation of energy.

The conservation of momentum in a fluid is expressed by the Navier-Stokes Equation, which comprises all governing forces, pressures, velocities and the density.

Since heat convection and conduction play an important role in this model, the energy conservation has to be solved correspondingly. In order to obtain a discrete boundary of the two phases melt and air, the level-set function is applied as described by Moguedet [4].

RESULTS

Simulation results comply well with molding experiments. Figures 5 and 6 show stages of the experimental filling study as compared to the simulation with the COC TOPAS 5013 under identical conditions. The filled volume elements in the simulation are colored in dark orange, while the transparent area within the borders of the cavity is still filled with air. The phase boundary is clearly visible without numerical blurring.

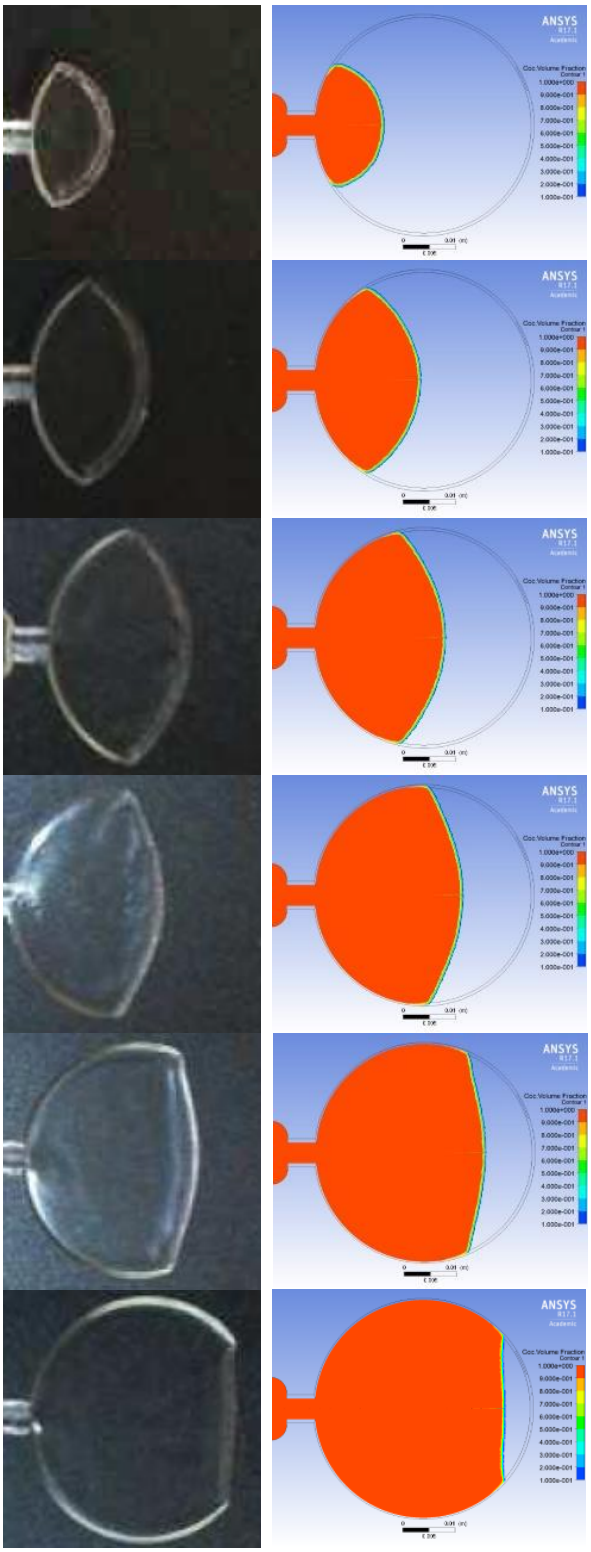

FIGURE 5. Molded plane cylindrical disc (COC) and CFD simulation until appr. 90% full [2]

The mold filling sequence for the plane cylindrical cavity is shown in the left column in Fig. 5. The mold is filled by a uniform source flow originating from the inlet. In top view, the flow front has a crescentic shape which later develops into an almost straight line as mold filling proceeds from 10% to approximately 90% full.

The very same mold filling sequence is shown in the right column in Fig. 5 as observed in the numerical simulation. The propagation and shape of the flow front agree very well with the experimental results.

Both the experiment and the simulation are conducted at a melt temperature of 240° C while applying 800 bar injection pressure and 1.200 bar packing pressure at the nozzle. The mold is preheated to 90° C, but not temperature controlled. No additional spray is used to assist demolding in the experiments.

The CFD simulation results for the molding of the Fresnel lens also agree well with reality. The splitting of the flow fronts can be observed, where one part of the melt propagates along the plane back of the mold, while another part of the melt advances concentrically through the Fresnel grooves.

Longitudinal sections of the flow front indicate, that the foremost melt adheres to the walls of the cavity rather than slipping along, which has been observed in the molding of microscopic structures at excessive shear stresses [5].

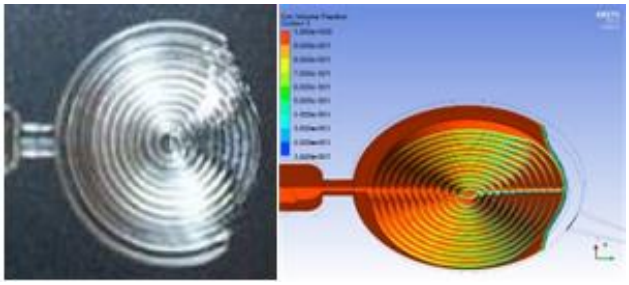

FIGURE 6. Molded COC Fresnel lens and CFD simulation at approximately 70% full [2]

All the practical disadvantages of this mold filling process can be predicted by the simulation. This includes air being trapped in the tip of the grooves.

Simulation of the air outflow is a particular challenge in the CFD simulation. In reality, the air is squeezed out through the separation plane of the tool plates and through the shallow air outlet opposite to the gate.

If the displacement of the air in the mold is not simulated adequately, larger bubbles of compressed air remain in the runner and in the mold, which lead to unrealistic simulation results. If - on the other hand - the air outlet in the CFD model is simply open to both air and melt, the polymer streams out through the air outlet, which has a height of about 0,2 mm. This kind of overfilling is not observed in reality. Therefore, the CFD model must include a mechanism to withhold the melt while letting the air pass through.

TEMPERATURE AND SOLIDIFICATION

In contrast to reality, the CFD simulation allows to switch certain rheological laws on or off. One prior question is the influence of solidification in the filling of the mold. Solidification is generally induced at melt temperatures below the glass transition temperature (134°C for the observed COC TOPAS 5013).

The temperature distribution in the melt after complete filling of the cavity is shown in Fig. 7 as derived from the CFD simulation. Here, only a very fine outer layer of the melt has cooled down to 373 K (100°C, indicated in blue), while the much larger core of the melt is still maintaining the injection temperature (513K or 240°C).

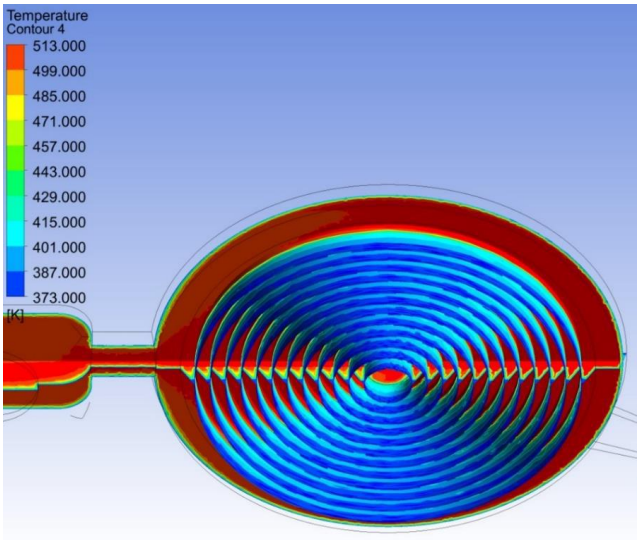

FIGURE 7. Temperature distribution in the filled mold after at 0,39s [2]

As was to be expected, solidification begins in the outer layers of the melt, where heat is withdrawn by conduction to the tool. However, solidification does not influence the melt flow perceptibly, because the injection cycle is too short (0.39 seconds). Accordingly, when the solidification mechanism is switched off in the CFD model, the overall flow pattern of the melt does not change visibly.

CONCLUSIONS

The progression and shape of the flow-fronts in two different cavities can be simulated very truthfully. All the practical challenges in molding are also evident in the CFD simulation. Mass flow, temperature gradients, pressure within the mold and geometric deviations of the molded parts are predictable by this simulation approach.

Future research will be dedicated to the fundamental understanding of micro-molding processes by means of the CFD simulation. Geometries such as periodic gratings, diffractive microstructures and lab-on-a-chip features will be considered.

REFERENCES

[1] Schmütz, Jörg; Heinrich, T.: „Influence of polymer melt properties in precision injection-molding of microfluidical and optical parts “. Proceedings ASPE 2015 Annual Meeting in Austin, Texas, USA, 2015. pp. 591-594.

[2] Karnatz, L.: „CFD-Simulation von Formfüllung und Erstarrung beim Spritzgießen strukturierter Oberflächen“ Master-Thesis, Beuth University for Applied Sciences, Berlin, 2017.

[3] Münch, P.: „Grundlegende Untersuchung des Formfüllverhaltens optischer Kunststoffe beim Spritzgießen mikrostrukturierter Bauteile“. Master-Thesis, Beuth University for Applied Sciences, Berlin, 2013.

[4] Moguedet, M.; Le Goff, R.; Namy, P.; Bereaux, Y.: “Level Set Method for Fully Thermal-Mechanical Coupled Simulations of Filling in Injection and Micro-Injection Molding Process”. Proc. of the COMSOL Conference, Milan, 2009.

[5] Tofteberg, T.R.; Andreassen, E.: “Multiscale Simulation of Injection Molding of Parts with Low Aspect Ratio Micro-features”. International Polymer Processing Journal, Vol. 25, Issue 1, pp. 63-74.

INVESTIGATING THE SELF-PROTECTIVE TOOL FORMATION DURING CUTTING OF TITANIUM ALLOY

SONG Xiaoqi[1], Yukio TAKAHASHI[1], and Tohru IHARA[1]
[1] Department of Precision Mechanics,
Chuo University,
Tokyo, 112-8551, Japan

INTRODUCTION

Titanium alloys are one of metals showing a very high strength-weight ratio, which are widely and commonly applied in the aerospace, automotive and biomedical field. Due to their low thermal conductivity, low elastic modulus, high chemical reactivity and superior mechanical properties at high temperature, titanium alloys are very difficult to cut, and have been classified as "difficult-to-cut" materials [1,2]. During the cutting process, the interaction between tool and workpiece causes the severe contact conditions at the chip/tool and tool/workpiece interface which increase tool wear rate, reduce tool life and lower the productivity. It was confirmed that built-up layer (BUL), which produced by accumulating workpiece material on rake face, has protective effects during cutting of "difficult-to-cut" materials such as hardened steel [3-5], Ni based super alloys [6], so we may also realize the self-protective tool (SPT) by actively and purposely making use of BUL during cutting of titanium alloys. It has been confirmed that BUL or BUE (Built-up edge), can easily form on tool surface [7-9] which can reduce tool wear [7-8] and improve tool life during machining of titanium alloy. It also has been proposed that chemical reaction plays the important role in BUL formation [9]. However, until now BUL formation mechanism is still not fully understood and the usefulness of BUL during cutting of titanium alloy has never been clearly studied.

The main objective of this study is to clarify the SPT formation during cutting of titanium alloy. In this paper, BUL formation conditions, the time-evolution of BUL formation, BUL formation mechanism and the influences of BUL on cutting process (cutting forces, surface quality, tool wear) during cutting of titanium alloy Ti-6Al-4V have been investigated in detail. Firstly, uncoated cemented carbide cutting tools with different tool rake angles and various cutting conditions (cutting speed, feed rate) were selected for dry cutting of Ti-6Al-4V. Secondly, BUL formation conditions were investigated by observing the morphology of worn cutting tools. Moreover, from detailed observation and analysis of the results of short time turning tests, BUL formation process was examined and its formation mechanism was proposed. Finally, cutting forces, surface quality and tool wear were measured to acquire a further understanding of the influences of BUL on them. Then, the usefulness of SPT was discussed.

EXPERIMENTAL PROCEDURE

Workpiece And Cutting Tools

Workpiece is a Ti-6AL-4V alloy bar (annealed 740℃, air cooled) with a diameter of 40mm and a length of 250mm. The chemical compositions and physical properties of Ti-6AL-4V are listed in **Table 1** and **Table 2,** respectively. To study the influences of tool rake angles on BUL formation process, three commercial uncoated cemented carbide tools without chip breaker were used as cutting tools (**Table 3**). All cutting tools have the same cutting angle 91° and the same tip radius 0.4mm. The actual rake angles after mounting for three cutting tools are -5°, 5°, 25°, respectively.

Experimental Set-up

Dry turning tests were carried out in a CNC lathe machine (MULTUS B200, Okuma) equipped with a 3 components piezoelectric dynamometer (9129A, Kistler) for cutting forces measurement (**Fig.1**). Cutting conditions are listed in **Table 4**. After cutting, the finished surface was measured four times along the circumference by surface roughness tester (SJ-201, Mitutoyo). The worn cutting tools after cutting were examined by scanning electron microscope (SEM, Quanta250, FEI) to observe the tools' morphology and to evaluate flank wear. The maximum height above

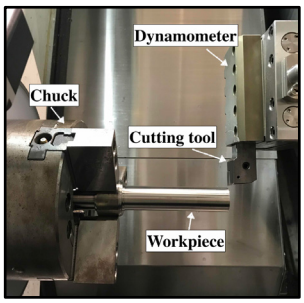

FIGURE 1. Experimental set-up of turning tests

Table 1. *Chemical compositions of workpiece material Ti-6AL-4V (wt%)*

C	N	H	Fe	O	Al	V	Ti
1	0.01	0.001	0.13	0.15	6.18	3.93	bal

Table 2. *Physical properties of Ti-6AL-4V*

Tensile strength (MPa)	0.2% yield strength (MPa)	Elongation (%)	Reduction of area(%)	Density (g/cm^3)	Melting point(℃)	Thermal conductivity at 20℃ (W/(m/K)
952	919	18	46	4.5[10]	1650[10]	6.6[10]

Table 3. *Geometry and properties of the investigated cutting tools*

Tool mark	Tool geometry (Insert number/ holder number)	Rake angle (°)	Roundness of cutting edge (μm)	Hardness (HRA)	T. R. S. (GPa)
WC(-5)	TNGA160404/ CTGNR2020	-5	~2.5	92	2.4
WC(5)	TPGN160304/CTGPR2020K3	5	~2.5	92	2.4
WC(25)	TNGG160404R-P/CTGNR2020	25	~2.5	92	2.4

Table 4. *Cutting conditions*

Cutting speed *V* (m/min)	5, 10, 30, 50, 70, 90, 110, 130
Feed rate *f* (mm/rev)	0.05, 0.1, 0.2
Depth of cut *tu* (mm)	1.0
Cutting time *t* (s)	1, 10, 30, 60, 120, 180, 240, 300
Cutting fluid	Dry

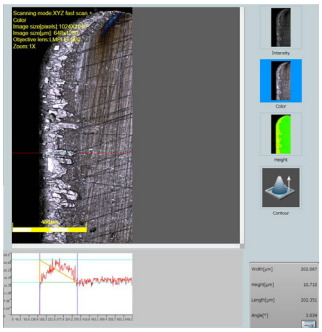

FIGURE 2. Typical LSM observation result on tool rake face for cutting tool WC(5) at V30m /min, f0.1mm/rev, tu1mm after cutting t60s.

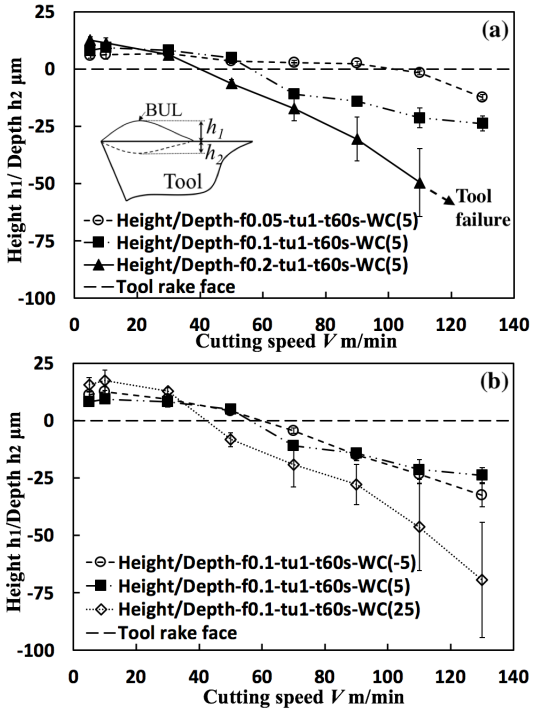

FIGURE 3. Variation of max height h_1 and max depth h_2 with cutting speed (a) for various feed rate with cutting tool WC(5), (b) for various tool rake angle at f0.1mm/rev after cutting t60s.

tool rake face h_1 and the maximum depth below tool rake face h_2 were also measured by laser scanning microscopy (LSM, OIS4100, Olympus). A representative result is shown in **Fig.2**. It can be confirmed that only BUL, liking a coating layer, forms on tool rake face. In addition, the chemical composition of BUL was investigated by electron probe micro analyzer (EPMA, 1610, Shimadzu). From the EPMA analysis, it is confirmed that the composition of BUL is very close to Ti-6Al-4V.

RESULTS AND DISCUSSION

Built-up Layer Formation Conditions

Figure 3(a) shows the variation of h_1 and h_2 with cutting speed for three feed rates with cutting tool WC(5) after cutting *t*60s. The positive value of h_1 means that BUL is higher than the unused tool rake face, which can protect tool. Crater wear (the negative value of h_2), occurs quickly at low cutting speed with larger feed rate than with small feed rate. It is also confirmed that the tool lifespan is less than 60s as cutting speed increase above *V*110m/min at *f*0.2mm/rev. **Figure 3(b)** shows the variation of h_1 and h_2 with cutting speed for three tool rake angles at *f*0.1mm/rev after cutting *t*60s. Contrary to feed rate, tool rake angle has a minor effect on BUL formation cutting speed range. BUL can form on rake face at low cutting speed range *V*5~50m/min. Above this cutting speed range, crate wear happens quickly. It can be observed

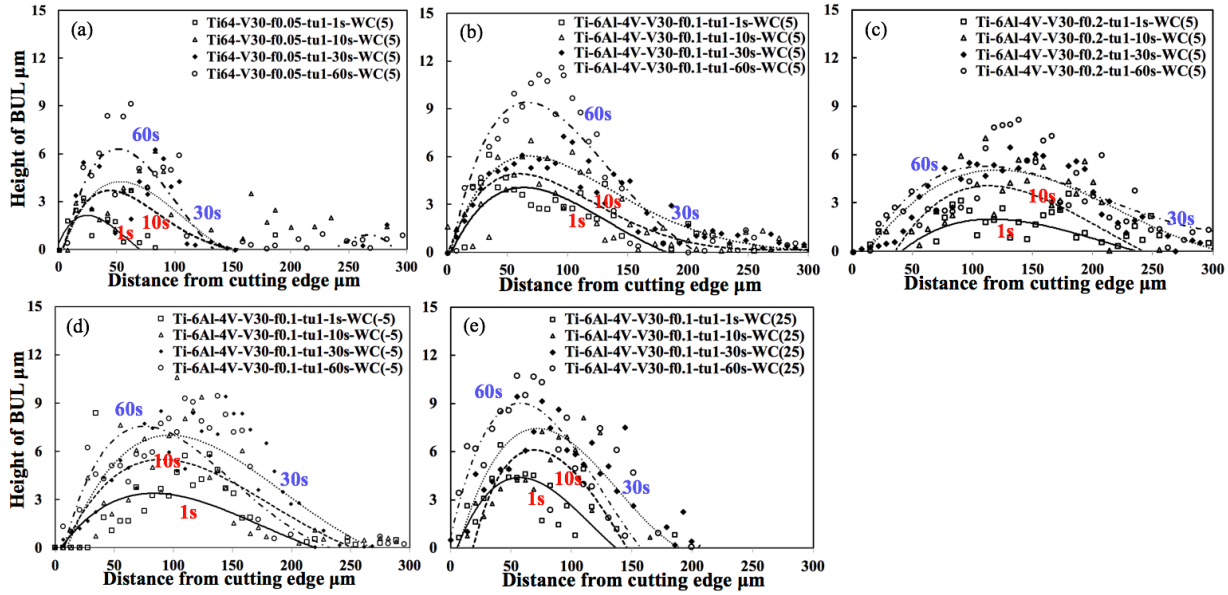

FIGURE 4. Variation of BUL's profiles with cutting time at V30m/min, (a) f0.05mm/rev for WC(5), (b) f0.1 mm/rev for WC(5), (c) f0.2mm/rev for WC(5), (d) f0.1mm/ rev for WC(-5) and (e) f0.1mm/ rev for WC(25).

that crater wear advances slower with cutting tool WC(5) than with cutting tool WC(-5) as the cutting speed increases above *V*90m/min. The reason is that the thin BUL can forms on the surface of crater wear even at high cutting speed for WC(5).

BUL Formation Process and BUL Formation Mechanism

To further understand the characteristics of BUL formation process, the evolution of BUL's profiles with cutting time were measured. The results at *V*30m/min are illustrated in **Fig.4**. For the various feed rate, the contact length is close to constant after cutting *t*10s in all cases and its value increases as feed rate increases. However, the height of BUL firstly has an increasing trend, then become on an almost constant level after cutting *t*10s (**Fig.5(a)**), which suggests that the height of BUL increases with increasing cutting time as the result of the accumulation of workpiece material on rake face and the area of BUL shows no time relevance. Hence, it can be expected that the stable BUL accumulates on rake face and it can be used to realize the SPT during cutting. The same BUL formation process can be observed for various tool rake angles (Fig.4(b), (d), (e)). The contact length decreases as tool rake angle increases. Meanwhile, the contact length and the height of BUL (**Fig.5(b)**) are close to constant after cutting *t*10s, with similar observation for the various feed rate. From these results, it can be concluded that, during dry cutting of Ti-6Al-4V, BUL formation is a time dependent phenomenon and BUL formation has two processes: the

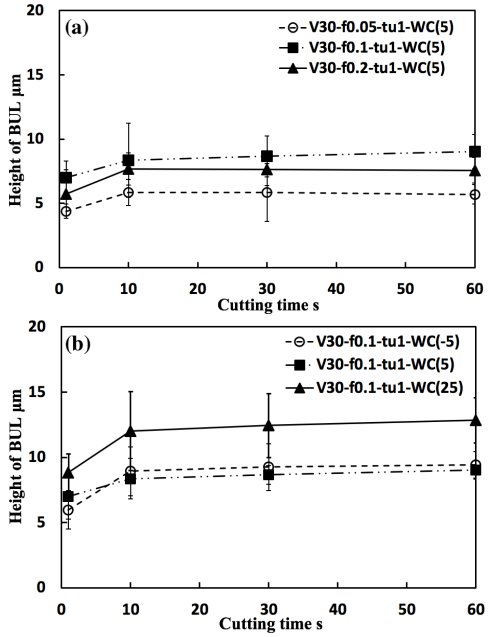

FIGURE 5. Variation of the height of BUL with cutting time (a) for various feed rate with cutting tool WC(5), (b) for various tool rake angle at f0.1mm/rev.

nucleus formation process and the forward growing process, which have also been found during cutting of hardened steel and Ni based supper alloy [4,6]. As a result, BUL formation can be considered as a process of accumulating workpiece material to form the layer structure on rake face. After the stable BUL forms on rake face, it can work as a protecting layer and replace tool rake face to perform actual cutting.

According to the proposed BUL formation mechanism [4,6,11] and the experimental results in this study, BUL formation mechanism during cutting of Ti-6Al-4V can be proposed as follow. During the chip slides along tool surface, adhesion junctions commonly occur at the tool and chip interface. Meanwhile, due to the large plastic deformation, metal contact zone occurs [4,11-13]. In metal contact zone, as the total potential energy between tool clusters and chip clusters is strong enough, lattices relax into cluster sets. And the movement of cluster sets can be described as a quasi-dislocation movement [4,13]. Over a large amount of time and space, if the energy barriers in cluster sets cannot be overcome, cluster sets become stable and chip stops moving. At this point, if fracture happens in chip, the relative motion happens in chip and adhesion occurs on tool rake face. Then, adhesion accumulates and grows to form the nucleus of initial BUL at the middle of contact length through the repeated transfer and growth process (about *t*1~10s as shown in Fig.4). Finally, the initial BUL grows from the middle of contact length to the cutting edge and BUL is formed (after *t*30~60s). This is the BUL formation mechanism during cutting of Ti-6Al-4V. Because energy is spent on BUL formation rather than on tool wear, so once BUL has been formed, system can transfer energy almost without any tool wear. Therefore, we can realize the SPT during cutting of Ti-6Al-4V by actively and purposely making use of BUL.

Cutting Forces and Surface Roughness

Cutting forces measured during cutting tests are summarized in **Fig.6**. It can be observed that feed rate and tool rake angle have the strong effects on cutting forces. And *Fc* exhibits a decreasing trend as feed rate decreases or tool rake angle increases. From the results, it is also confirmed that as cutting speed increases static force has a decreasing trend, while the dynamic force has an increasing trend. The influence of BUL on cutting force could be considered negligible: the value of static force is approximately the same and the dynamic force is smaller in BUL formation cutting speed range than in high cutting speed range.

The influence of BUL formation on the finished surface roughness *Ra* is also an important factor to evaluate whether BUL can be used as the SPT or not. **Figure 7** shows the variation of *Ra* with cutting speed. Small differences in *Ra* under various cutting speed are observed in all cases, except at *V*30~90 m/min, f0.2mm/rev. However, it is found that feed rate has a great effect on *Ra*. Meanwhile, no or few influences of tool rake

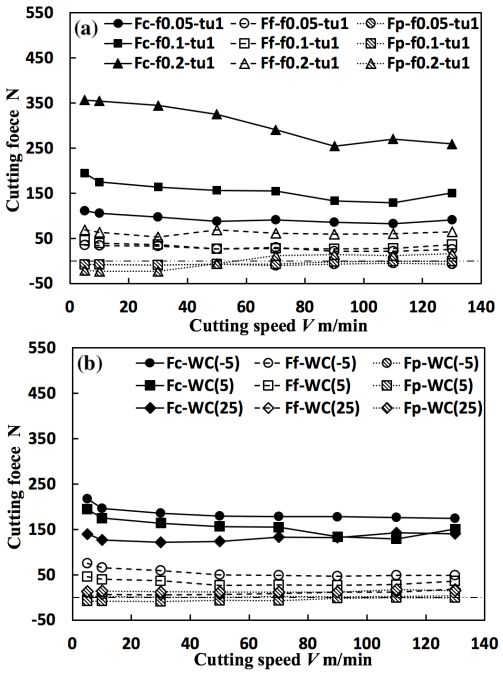

FIGURE 6. Variation of cutting forces with cutting speed (average value during the steady cutting stage) for (a) various feed rate with cutting tool WC(5), (b) various tool rake angle at f0.1mm/rev after cutting t60s (Fc: main cutting force, Ff: feed force, Fp: passive force).

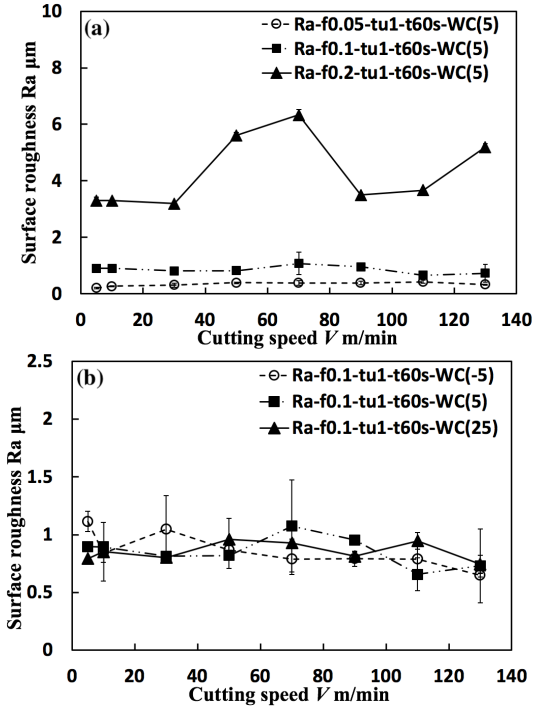

FIGURE 7. Variation of surface roughness Ra with cutting speed for (a) various feed rate with cutting tool WC(5), (b) various tool rake angle at f0.1mm/rev, after cutting t60s

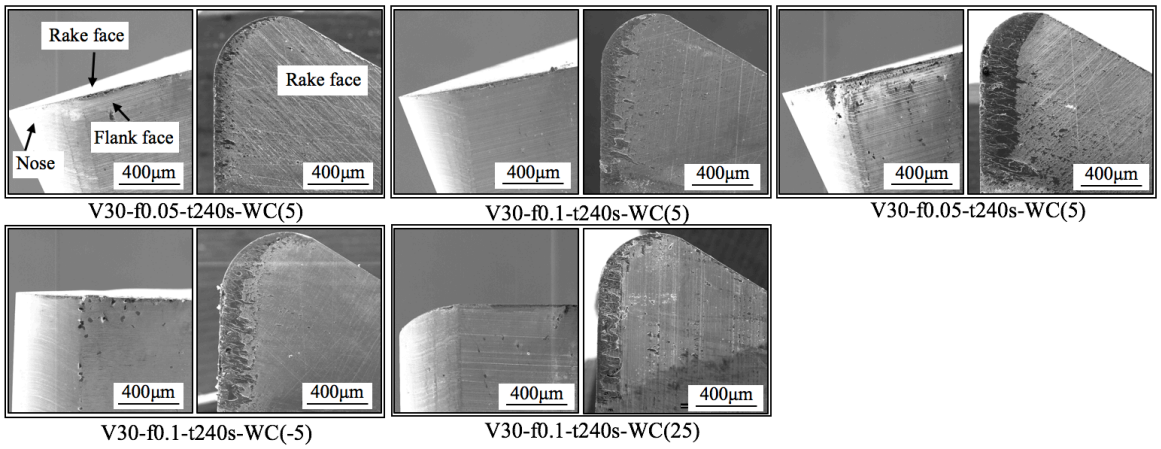

FIGURE 8. SEM images of tool wear during cutting of Ti-6Al-4V alloy at V30m/min

angle on *Ra* is confirmed. These results support that BUL has few influences on *Ra*.

Tool Wear

To give an overview of tool wear during cutting of Ti-6AL-4V, SEM images of tool wear at *V*30m/min after cutting *t*240s are shown in **Fig.8**. It can be observed that there is a significant reduction in contact length as feed rate decreases or tool rake angle increases. BUL, just likes a coating layer, forms on the over all of contact zone. No crater wear forms on rake face. Flank wear is evenly distributed along the cutting edge and notch wear is equal to or smaller than flank wear.

Crater Wear

The evolution of h_1 and h_2 with cutting time for various cutting conditions are shown in **Fig.9**. As expected, BUL has the protective effect and no crater wear occurs at *V*10, *V*30m/min. For case *V*70-f0.05-WC(5), *V*110-f0.05-WC(5), *V*70-f0.1-WC(25), due to severe cutting conditions, crater wear occurs quickly within even a short period of time (t60s). However, the increase of crater wear stops and rake face is protected by the thin BUL after cutting *t*120s. It also can be observed that at the end of tool life for all cases, a significant crater wear occurs, which suggests that crater wear plays a great role on tool life. These results are in good accordance with the results in Ref. [14]. An interesting conclusion is that if we can actively and purposely make use of BUL, we can reduce crate wear and finally improve tool life during dry cutting of Ti-6Al-4V.

Flank Wear

Figure 10 shows the propagation of flank wear under various cutting conditions. It can be seen that in all cases, there is a larger wear rate at the beginning of cutting, and the dependence of flank

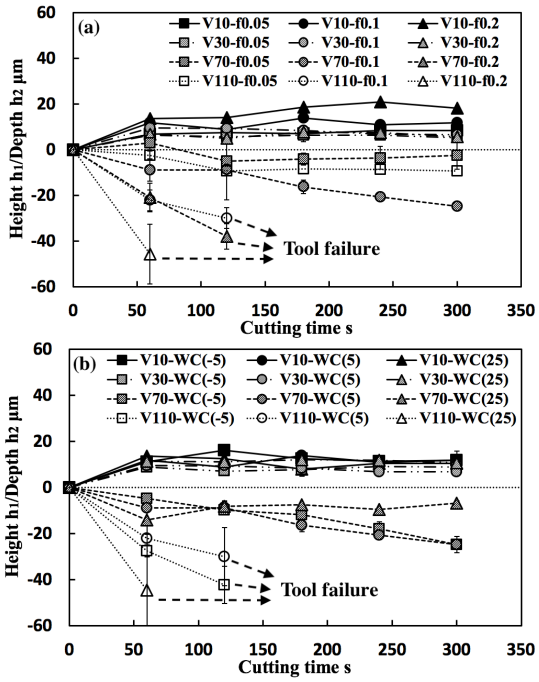

FIGURE 9. Variation of h_1/h_2 with cutting time for (a) various feed rate with cutting tool WC(5), (b) various tool rake angle at f0.1mm/rev

wear on cutting time has a linear character after cutting *t*120s. As shown in Fig.10(a), (b), (c), flank wear increases as cutting speed increases at larger feed rate, however the difference between flank wear diminishes at small feed rate. This is attributed to BUL formation, leading to a more mitigatory contact conditions near cutting edge. It is also confirmed that it is very difficult to cut Ti-6Al-4V at cutting speed over *V*110m/min with large feed rate above *f*0.1mm/rev. From the results shown in Fig.11(b), (d), (e), it can be observed that flank wear rate at *V*30m/min is very similar to flank wear rate at *V*70m/min in all cases. This phenomenon is believed to be responsible

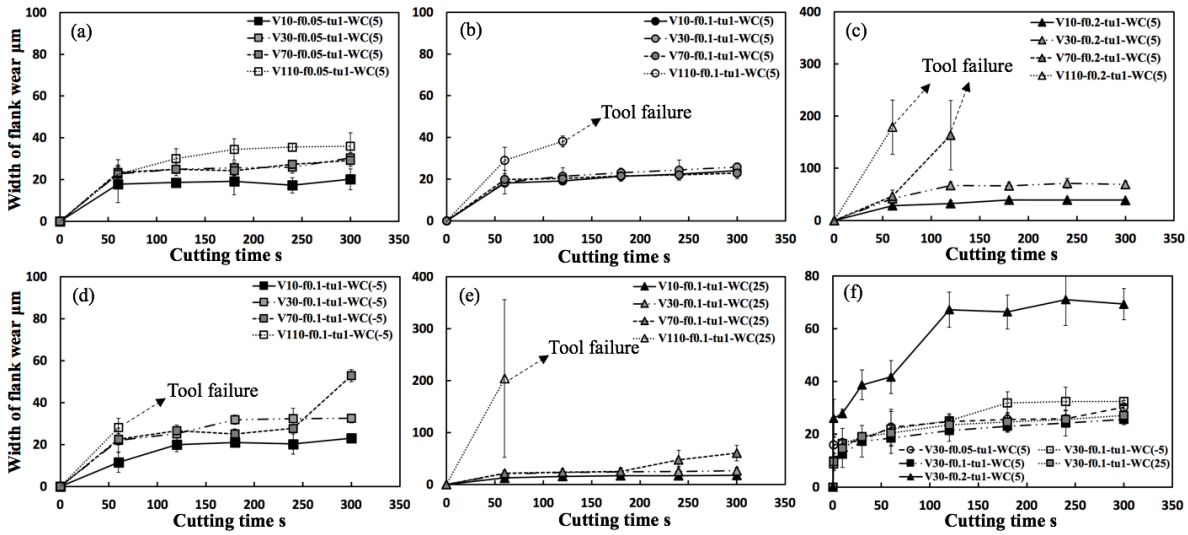

FIGURE 10. Average flank wear during cutting of Ti-6Al-4V alloy under various cutting conditions: (a) f0.05mm/rev for cutting tool WC(5), (b) f0.1mm/ rev for cutting tool WC(5), (c) f0.2mm/rev for cutting tool WC(5), (d) f0.1mm/ rev for cutting tool WC(-5), (e) f0.1mm/ rev for cutting tool WC(25), (e) at V30m/min .

for the protecting effects of BUL or the adhering layer. The reason is that, for all cases, BUL or the adhering layer, accumulated on the worn surface, can be observed. However, there is a significant increase in flank wear at *V*70m/min after cutting *t*300s for WC(-5) and *t*240s for WC(25). These results indicate that the protective effect of BUL decreases as flank wear increases at high cutting speed. Results at *V*30m/min are shown in Fig.10(e). Comparing the variation of flank wear with the height of BUL (Fig.5), it can be confirmed that the height of BUL plays a great role on flank wear development. Considering these results, it can be concluded that the SPT can be used to reduce tool wear during cutting of Ti-6Al-4V.

CONCLUSIONS

The following conclusions can be drawn:

1. The stable BUL can accumulates on rake face in a certain cutting speed range.
2. BUL formation has two processes: the nucleus process and forward growing process.
3. BUL has few influences on cutting forces and surface roughness, therefore, BUL can be used to realize the SPT.
4. It is confirmed that the SPT can be used to reduce tool wear during cutting of Ti-6Al-4V.

ACKNOWLEDGEMENTS

This research was partially supported by the Japan Society for the Promotion Science [Grant-in-Aid for Scientific Research (C), 16K06021]. The authors would also like to gratefully acknowledge for the financial support from Machine Tool Engineering Foundation (Japan).

REFERENCES

[1] Rahman M., Wang Z. and Wong, Y., JSME Inter. Jou.. 2006; 49(1): 11-20.
[2] Veiga C., Davim, J.P. and Loureiro A.J.R., Rev. Adv. Mater. Sci.. 2013; 34: 148-164.
[3] Song X.Q., Takahashi Y., He W.M., and Ihara T., Jou. Jap. Soc. Prec. Eng.. 2016; 82(9): 814-820 (In Japanese).
[4] Song X.Q., Takahashi Y., He W.M., and Ihara T., Jou. Jap. Soc. Prec. Eng.. 2017; 83(5): 445-452 (In Japanese).
[5] Song X.Q., Takahashi Y., He W.M., and Ihara T., Key Eng. Mat.. 2017; 749: 39-45.
[6] Song X.Q., Takahasi Y. and Ihara, T., LEM21 proceedings. 2017; 56: 1-6.
[7] Oliaei S. and Karpat Y., Jou. Mat. Proc. Tech.. 2016; 235: 28-40
[8] Chowdhury M.S.I., Chowdhury S., et al., Surf. Coat. Tech.. 2017; 313: 319-327.
[9] Salguero J., Batista M., Sanchez J.A. and Marcos M., Adv. Mater. Res.. 2011; 223: 564-572.
[10] Silva R., Machado A., Ezugwu E., Bonney J. and Sales W., Jou. Mater. Proc. Tech.. 2013; 213: 1459-1464.
[11] Song X.Q., Takahasi Y. and Ihara, T., Proceedings of 32nd ASPE annual meeting. 2017; 67: 630-635.
[12] Obikawa, T., Asano, Y., Kamata, Y., Int. Jou. Mach. Tools Manu.. 2009; 49: 971-978.
[13] Ihara, T., Science of machine, 2014; 66(10): 825-832. (In Japanese)
[14] Nandy A.K., Gowrishankar M.C. and Paul S., Inter. Jou. Mach. Tools Manu..2009; 49: 182-198.

PRELIMINARY STUDY ON FIGURING OF REACTION-SINTERED SILICON CARBIDE BY PLASMA CHEMICAL VAPORIZATION MACHINING

Rongyan Sun[1], Yuji Ohkubo[2], Kentaro Kawai[1], Kenta Arima[1], Kazuya Yamamura[1]
[1]Division of Precision Science & Technology and Applied Physics, Graduate School of Engineering, Osaka University Suita, Osaka, Japan
[2]Research Center for Ultra-precision Science and Technology, Graduate School of Engineering, Osaka University Suita, Osaka, Japan

INTRODUCTION

In recent years, aspherical lenses are widely demanded in many fields. The most notable benefit of aspheric lenses is their ability to correct for spherical aberration, an optical effect which causes incident light rays to focus at different points when forming an image, creating a blur. However, since it is difficult to process materials with different curvatures, the aspherical lenses produced by precision grinding are costly when they are mass-produced. To overcome this problem, currently the production of aspherical lenses by glass mold press molding is widely used. In this production, the accuracy of the mold determines the precision of the aspheric lenses. So the shape accuracy and surface roughness of molds is the key element. As the material for mold, because of the excellent properties, such as its light weight, high rigidity, high heat conductance and low coefficient of thermal expansion, reaction-sintered silicon carbide (RS-SiC) is noted. However, RS-SiC is difficult to machine owing to its high hardness and chemical inertness and because it contains multiple components [1,2]. As conventional method such as grinding using diamond tools, since the mechanical load is applied on the substrates, scratches and subsurface damage (SSD) layer, which reduce the service life, are inevitably generated on the machined surface.

To overcome the problem of the poor machinability of RS-SiC in conventional machining, the application of atmospheric-pressure plasma chemical vaporization machining (AP-PCVM) to RS-SiC was proposed. AP-PCVM is an ultraprecision figuring technique that uses F radicals to change the surface of substrates to a volatile reaction product to form an objective shape. Since AP-PCVM is a noncontact chemical figuring technique which does not apply a mechanical load to substrates, a subsurface damage layer is not formed in the removal process [3,4]. As a highly efficient and damage-free figuring technique, AP-PCVM has been widely applied for the figuring of single-component materials, such as Si, SiC, quartz crystal wafers, and so forth. However, since there are SiC and Si two component in RS-SiC, the etching rate of SiC and Si is different, it is difficult to obtain etched surface of RS-SiC with low surface roughness.

In this paper, we investigated the reason of large surface roughness of RS-SiC using AP-PCVM. By optimizing the gas composition used in AP-PCVM, surface roughness of etched surface was improved. Then the shape figuring experiment was conducted on RS-SiC using the optimization gas composition obtained.

EXPERIMENTAL SETUP

Fig. 1 shows a schematic view of the plasma generator, which was installed on a computer numerical control (CNC) x-y-z-table. Argon gas was supplied as a carrier gas into the ceramic tube installed at the center of the plasma generator, which was surrounded by a cavity resonator. A microwave electric field with a frequency of 2.45 GHz was applied to generate

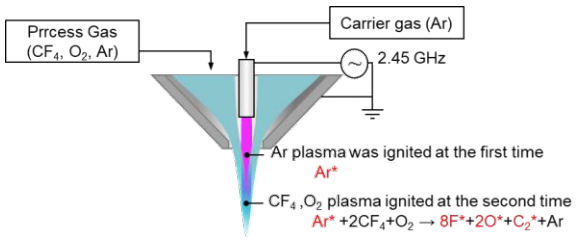

FIGURE 1. Schematic view of the plasma generator.

an electric field whose maximum intensity was near the tip of the ceramic tube, where the argon atoms were ionized and atomic radicals were generated. The argon plasma was ignited at the first time. Simultaneously, argon, CF4 and O2 were supplied as the process gases from another gas inlet offset from the center. At this time, collisions occurred between argon in the active state originating from the center of the plasma generator and argon, CF4 and O2 in the ground state. As a result of the collisions, F radicals and O radicals, which contributed to etching, were generated at the second time. The reason why the CF4 was ionized at the second time but not ionized directly by the microwave electric field is that the F radicals are very reactive, and would have corroded the ceramic tube, decreasing its lifetime, and contamination due to the precipitation of substances originating from the etched ceramic tube would have interfered with the etching process.

RESULTS AND DISCUSSION

Fig. 2 shows the scanning electron microscope (SEM) image of the RS-SiC surface prepared by diamond lapping and energy dispersive X-ray spectrometry (EDX) spectra of point A, B and C. The EDX spectra shows that RS-SiC contains multiple components such as SiC and Si. Owing to the difference in the chemical and mechanical properties of SiC and Si grains, it is difficult to obtain RS-SiC with a smoothly surface.

To investigate the etching characteristics of RS-SiC using AP-PCVM. The carrier gas was Ar (500 sccm) and the process gases were Ar (1000 sccm), CF_4 (50 sccm) and O_2 (50 sccm).

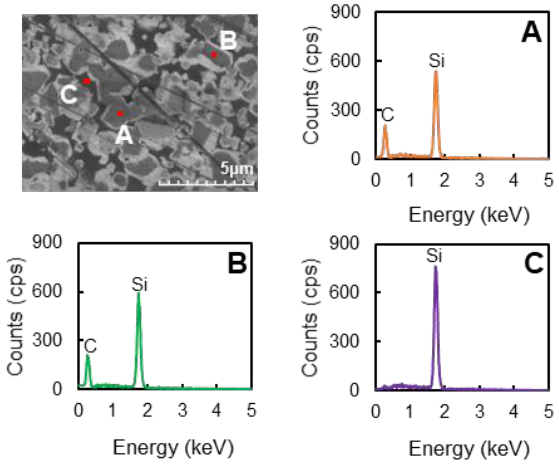

FIGURE 2. SEM image of the surface prepared by diamond lapping and EDX spectra of point A, B and C.

Fig. 3 shows a scanning white-light interferometer (SWLI) image of a removal spot formed by AP-PCVM as well as its cross section and the SEM image of the center of the removal spot. It was found that near the center of the removal spot, the roughness of the surface became large. Comparing with the SEM image of RS-SiC before AP-PCVM, the surface morphology was changed after AP-PCVM. It can be seen that the regions between SiC grains have been etched away. It is assumed that the difference between the etching rates of Si and SiC led to the large surface roughness. Thus, to obtain RS-SiC with a smoothly etched surface, it is essential to optimize the gas composition to make the etching rate of SiC equal to that of Si.

Through our previous research, we found that the etching rate of Si was significant changed when the oxygen fraction in process gas

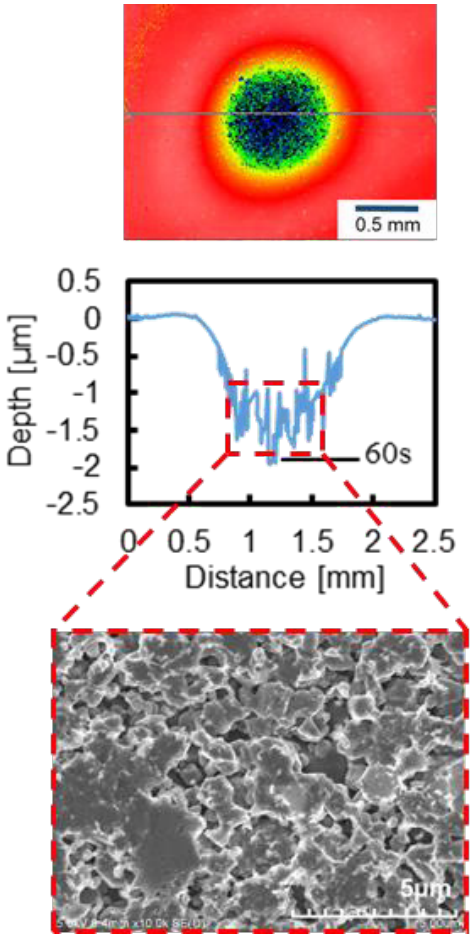

FIGURE 3. SWLI image and cross section of a removal spot formed by AP-PCVM (oxygen fraction 50%) and SEM image of the center of the removal spot.

Changed [5]. Since RS-SiC consists SiC and Si two component. So we investigated the etching characteristic of single crystal 4H-SiC (0001) and Si (100) using different [O_2/(O_2+CF_4)] ratios. We found the etching rate of Si (100) generally increased at low oxygen fractions and the maximum etching rate was obtained at an O_2 concentration of about 10%. Then the etching rate decreased as the oxygen fraction further increased. However, the effect of oxygen addition on the etching rate of 4H-SiC (0001) was not as significant as that on Si (100). With an oxygen fraction of 90%, the etching rate of SiC equal to that of Si. Fig. 4 shows SWLI image and the cross sections of removal spots etched with an oxygen fraction of 90% for 60 and 120 s and the SEM image of the center of the removal spot. This result showed that as the etching rate of SiC was equal to that of Si, the surface roughness of the removal spot etched with an O_2 fraction of 90% was improved comparing with the surface etched with an O_2 fraction of 50% even for the same removal depth.

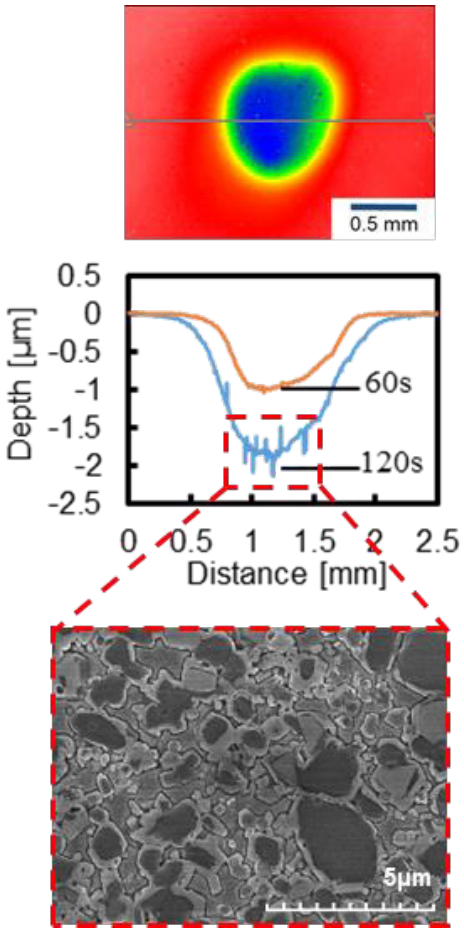

FIGURE 4. SWLI image and cross section of a removal spot formed by AP-PCVM (oxygen fraction 90%) and SEM image of the center of the removal spot.

To investigate the possible surface reactions, X-ray photoelectron spectroscopy (XPS) measurement of the surfaces etched by AP-PCVM with different [O_2/(O_2 + CF_4)] ratios was conducted. Since oxygen is present in the atmosphere, although no oxygen was initially added to the process gases, an oxide layer was formed on the surface as shown in Fig. 5. With increasing oxygen fraction in the process gases, the thickness of the residual oxide layer on Si (100) also increased. This means that the actual AP-PCVM process is not simple an etching process but also involves competition between oxidation and etching processes. As the oxygen fraction increased, the competition between the adsorption of oxygen and the etching by active species inhibited the etching process and led to a decrease in the etching rate at a high oxygen fraction. Since the bond dissociation energy of Si-Si (310 kJ/mol) is lower than that of Si-C (447 kJ/mol) [6], it is considered that the lower bond dissociation energy of Si-Si led to a higher etching rate and oxidation rate of Si (100) than that of 4H-SiC (0001) under the same conditions. So the influence of oxygen of Si (100) is greater than that of 4H-SiC (0001).

A surface etching experiment was conducted to evaluate the roughness of surfaces etched by AP-PCVM with oxygen fractions of 50%, 90% and 95%. Figure 2a shows the initial surface

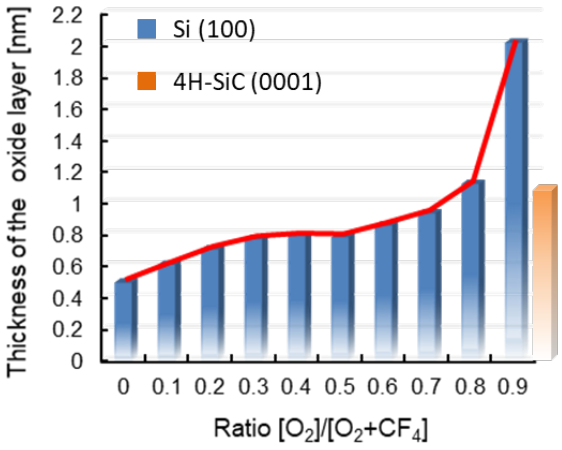

FIGURE 5. Thickness of oxide layer on Si (100) surface and 4H-SiC (0001) surface for different oxygen fractions.

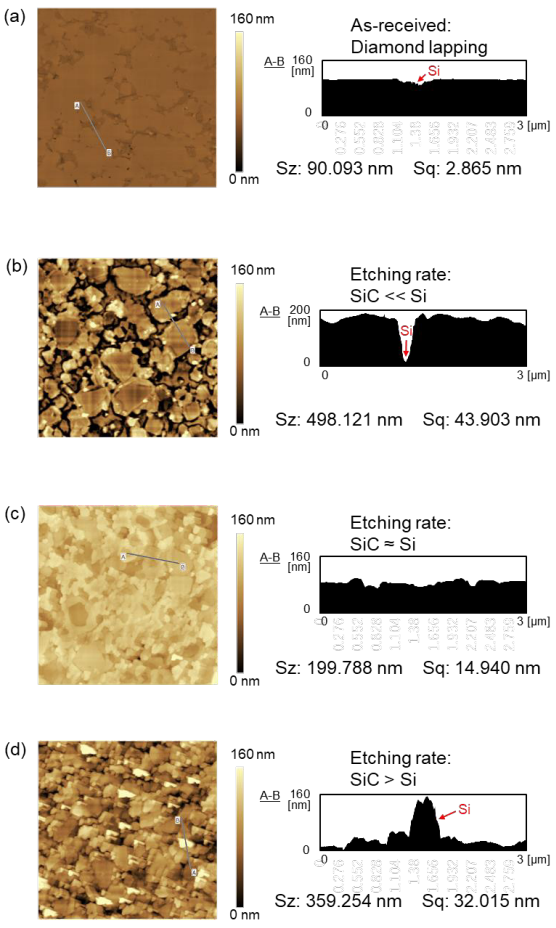

Figure2. (a) AFM image of original surface etched by diamond lapping before AP-PCVM, (b) AFM image of surface etched by AP-PCVM with oxygen fraction of 50%, (c) AFM image of surface etched by AP-PCVM with oxygen fraction of 90%, (d) AFM image of surface etched by AP-PCVM with oxygen fraction of 95%.

before AP-PCVM, which was prepared by diamond lapping. Although the surface roughness was excellent, an SSD layer and scratches were formed. Figure 2b,2c, and 2d show the etched surface by AP-PCVM at the oxygen fraction of 50%, 90% and 95% measured by atomic force microscopy (AFM). With an oxygen fraction of 50%, since the etching rate of Si was greater than that of SiC at this oxygen fraction, the regions between SiC were concave. With an oxygen fraction of 90%, since the etching rates of Si and SiC coincided at this oxygen fraction, a smooth surface was obtained. With an oxygen fraction of 95%, since the etching rate of Si was less than that of SiC, the regions between the SiC grains protruded. As AP-PCVM is an isotropic etching process, the surface roughness after AP-PCVM became slightly rougher than the surface processed by diamond lapping. The surface roughness will be further increased in the finishing stage.

CONCLUSIONS

As a highly efficient and damage-free figuring technique, AP-PCVM has already been successfully applied to figuring single-component materials. Through this study, we have confirmed that for a multicomponent material such as RS-SiC, AP-PCVM with the optimum gas composition can also be used to obtain a smooth surface without forming SSD. In the future work, we will figure an aspherical lens shape using the optimization gas composition obtained in this study.

ACKNOWLEDGEMENTS

This research was partially supported by a research grant from the Adaptable and Seamless Technology Transfer Program through Target-Driven R & D (Industry needs response type, No. AS282I010e) from JST.

REFERENCES

[1] Suyama, S, Kameda, K, Itoh, Y. Development of high-strength reaction-sintered silicon carbide. Diamond and Related Materials. 2003; 12: 1201-1204.

[2] Suyama S and Itoh Y 2007 NTSIC (New-Technology Silicon Carbide): evaluation of microstructure of high-strength reaction-sintered silicon carbide for optical mirror Proc. of SPIE 6666 66660K

[3] Yamamura, K. et al. Fabrication of elliptical mirror at nanometer-level accuracy for hard x-ray focusing by numerically controlled plasma chemical vaporization machining. Rev. Sci. Instrum. 2003; 74: 4549-4553.

[4] Yamamura, K, Shimada, S, Mori, Y. Damage-free improvement of thickness uniformity of quartz crystal wafer by plasma chemical vaporization machining. Ann. CIRP. 2008; 57: 567-570.

[5] Mogab, C. J, Adamas, A C, Flamm, D. L. Plasma etching of Si and SiO2 – The effect of oxygen additions to CF4 plasmas. J. Appl. Phys. 1978; 49: 3796-3803.

[6] Luo, Y. R. Bond Dissociation Energies. In CRC Handbook of Chemistry and Physics, (89th ed.) 65–69.

Modified Dwell Time for Free-form Optical Elements Polishing

Xinyao Sun[1], Jun Zha[1], YaolongChen[1], Yipeng Li[1]
1Xi'an Jiaotong University State Key Laboratory for Manufacturing System Engineering
Xi'an, Shaanxi, China

MODELING AND OPTIMIZATION OF REMOVAL FUNCTION

In this paper, a planetary small grinding head is used to compensate the surface error of free-form optical elements. According to the Preston equation, the amount of material removal is expressed as:

$$\Delta Z(x,y) = C\int_0^t V(x,y)P(x,y)dt$$

P(x,y) and V(x,y) denote the pressure and relative velocity of the polishing tool to the workpiece respectively, and △Z(x, y) denote the amount of material removal at a certain point. Because of the polishing characteristics of the small grinding head, the pressure P in the polishing contact area can be regarded as uniform distribution, so the mathematical modeling is mainly for solving the velocity V (x, y) of the grinding head relative to the workpiece. The kinematic decomposition of the grinding head in the form of planetary motion is shown in fig 1. O_1 is the center of rotation, O_2 is the center of rotation, g is the eccentricity, r_0 is the radius of the polishing plate, so the radius of the effective polishing area is g + r_0. A indicates any point where the discs are in contact with the workpiece. When the Preston coefficient K and the pressure P are constant, the material removal of any contact point between the planetary grinding head and the material can be obtained as follows:

$$Z(r) = \frac{KP\omega_1}{2\pi}\int_0^{\theta_1} [r^2(1+n)^2 + r_1{}^2n^2e^2 - 2rr_1ne(1+n)\cos\theta]^{\frac{1}{2}}d\theta$$

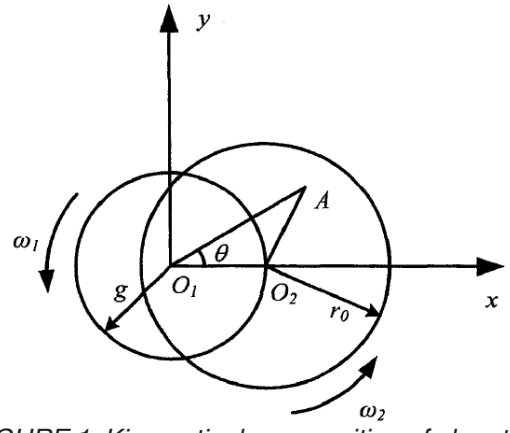

FIGURE 1. Kinematic decomposition of planetary polishing

In the form, n is speed ratio, e is eccentricity. n and e are the key parameters determining the shape of the removal function. The shape of the removal function without parameter optimization does not conform to Gaussian distribution. In CCOS process, the premise of the convergence of surface error is that the distribution of the removal function of small grinding head tends to Gaussian distribution[1]. Therefore, two key parameters need to be optimized, the method is to carry out a comprehensive simulation of the two parameters, and the range is: speed ratio n from - 5 to 5, step size is 0.1; eccentricity from - 1 to 1, step size is 0.1. The removal function under different parameters is tested by R-S to find out whether it meets Gauss distribution. Results as shown in fig 2, the red part is a parameter combination which does not conform to Gaussian distribution, and the blue part is a parameter combination which conforms to Gaussian distribution. Finally, when e=0.8, n=-1, the shape of the removal function is most consistent with the Gauss distribution. Fig 3 is a 3D image for removing function, the amount of material removal has been normalized.

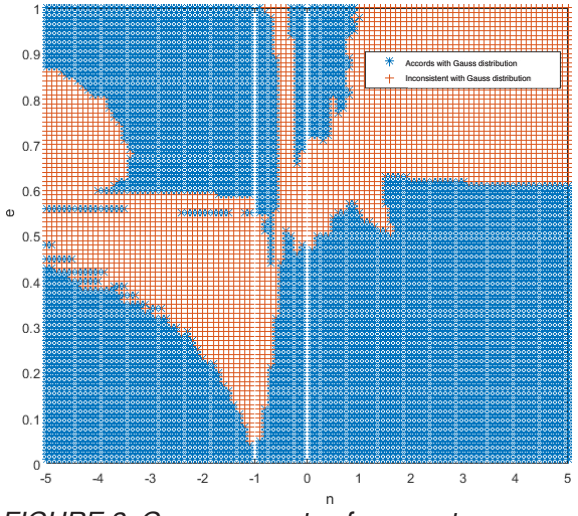

FIGURE 2. Gauss property of parameters

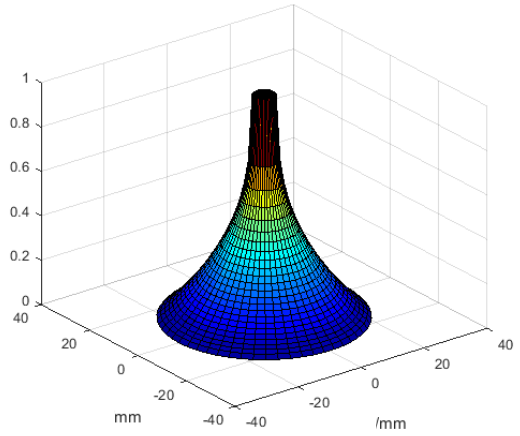

FIGURE 3. Three dimensional distribution of removal function

ESTABLISHMENT OF ERROR MODEL FOR FREEFORM SURFACE

When calculating dwell time, the deconvolution result of surface removal and removal function is actually calculated. Therefore, it is necessary to get accurate surface error data. In this paper, the surface error data of free form surface are obtained by using high precision CMM. After optimization by matlab, the surface error results are shown in fig 4. Using the error data of the three coordinate measurement directly, the edge effect of convolution calculation will appear.

For this reason, the error data is processed by two dimensional outward interpolation, and the Beizer equation is used in the process. The effective area error distribution after extrapolation has not changed. In fact, the PV and RMS of the effective region are 14.856μm and 3.7755μm respectively, which are the same as before interpolation. In addition, the value of 14μm is raised because of the trend continuation of the interpolation point. In the residence time calculation, the point will be removed later, and the accuracy of calculation will not be affected. The error distribution matrix after extrapolation is shown in fig 5.

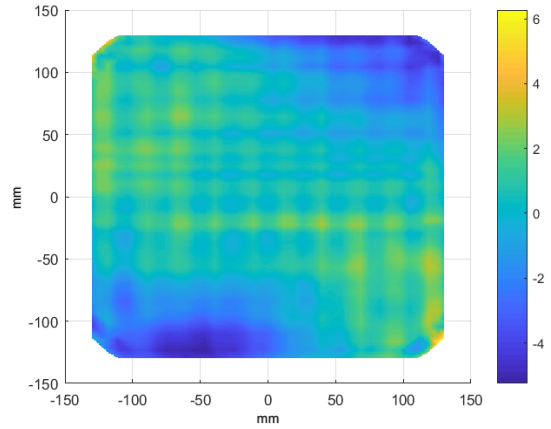

FIGURE 4. Surface error distribution matrix

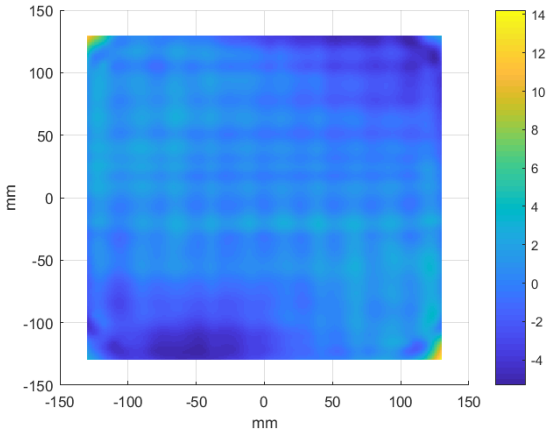

FIGURE 5. Surface error distribution matrix after extrapolation

MODIFIED DWELL ALGORITHM AND ITS OPTIMIZATION METHOD

In this section, a new method for calculating the residence time of free form surface polishing is proposed. This algorithm solves the shortcomings of the traditional method of calculating dwell time and guarantees the non-negative, accuracy and smoothness of the dwell time.

Dwell time algorithm based on machining simulation

The algorithm developed in this paper belongs to one kind of iterative solution. At present, the classical iterative algorithm of dwell time is Jasson-Van-Cittert method[2]. This algorithm initializes the dwell time matrix with random initial value (generally set to 1), normalizes the error distribution matrix and the removal function matrix, and then simulate material removal process. In the process of work, the dwell time is

modified iteratively. Finally, when the error converges to the acceptable range, the algorithm is finished.

In this paper, a similar method is used to refer to the normalization operation in Jensen algorithm, and the error matrix is divided into 256 parts, that is, the normalized minimum value is 0, the maximum value is 256. This value can be adjusted according to the accuracy. The algorithm flow is as follows:
(1). Using the removal function to traverse the error distribution matrix, and the error distribution matrix H_1 is obtained.
(2). For the point that is not equal to 0 in H_n, the dwell time matrix of the corresponding position $D_{n+1}(x, y) = D_n(x, y) + 1$
(3). Check all errors in H_n to meet the requirements, if not satisfied, then n=n+1, return (1); if satisfied, (4)
(4). K=27's sliding average processing for the obtained D_n
(5). Output dwell time matrix D_n

There are several parameters in the algorithm, which need to be set up before the algorithm starts. In the traversal process, each feed step n, the parameter needs to be set according to the interpolation mesh subdivision degree of the error matrix and the algorithm time settings, n is generally set as the minimum unit length of the tool path to achieve precision matching. The moving window size k is set to l/n, where l is the normalized removal function diameter and n is the step size. The following fig6 and fig7 show the error distribution matrix after normalization and interpolation and the corresponding dwell time matrix (the useless information of extrapolation points has been removed).

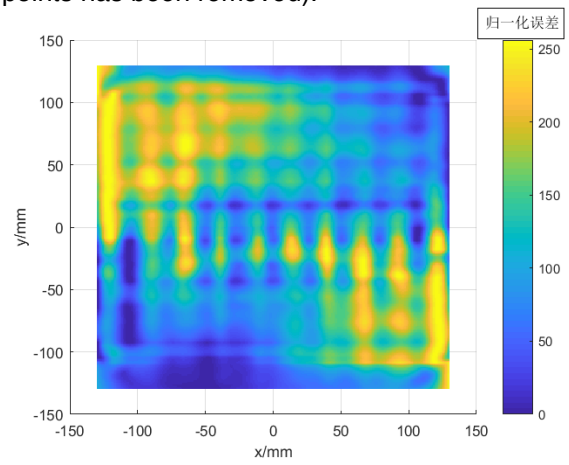

FIGURE 6. Normalized error distribution matrix

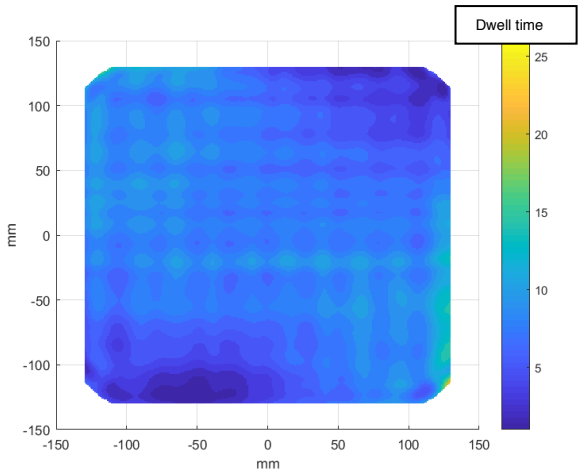

FIGURE 7. Normalized dwell time distribution matrix

The algorithm adopted in this paper is based on eliminating all the errors at the highest surface error, so it can maximize the efficiency of error compensation, while taking into account the requirement of non-negative dwell time. In matlab, simulated removal experiments were carried out. After simulated machining, the normalized PV value of the surface was converged from 256 to 18. The maximum surface error is 12 and the minimum is -6. However, new negative errors appear, which is necessary to avoid in processing.

Dwell time algorithm based on correction of surface error gradient weight

In the previous section, an iterative algorithm for computing dwell time is obtained, and the problem of introducing new negative errors in the solution of dwell time is finally obtained. In this section, we introduce a solution to the image boundary extraction problem commonly used in CNN convolution neural network to correct the results of dwell time algorithm.

The gradient is calculated by second-order difference and applied to matrix data. Laplace operator is used to calculate the gradient of the error distribution matrix of free-form surface. The Laplace operator in image processing is represented by the convolution kernel of 3X3.

1	1	1
1	-8	1
1	1	1

FIGURE 8. Laplace operator

The calculated gradient distribution of surface error is shown below in fig9.

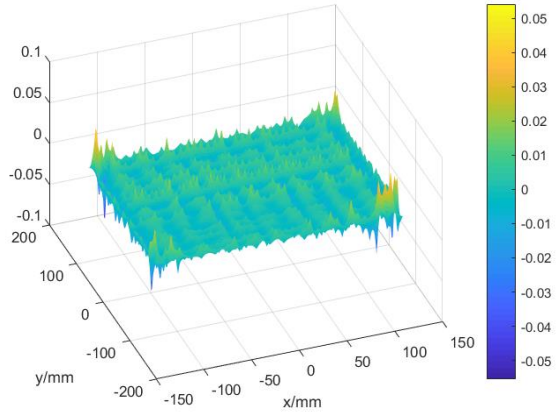

FIGURE 9. Gradient distribution of surface error

The normalized gradient distribution data is processed between [0,1]. Modifying dwell time distribution matrix by using gradient information corresponding to error matrix, and the method is:

$$D_{re}(X_i, Y_i) = \begin{cases} \dfrac{D(X_i, Y_i)}{G(X_i, Y_i)}, & G(X_i, Y_i) \geq HOLD \\ D(X_i, Y_i), & G(X_i, Y_i) < HOLD \end{cases}$$

In the formula, the normalized gradient distribution matrix is expressed by *G(x,y)*. The purpose of this paper is to modify the positive gradient (that is, the peak of surface error), so the threshold of gradient correction is defined as HOLD in advance. The comparison of dwell time distribution after correction is shown in the following fig10. The extreme value of the four sides is caused by the insertion point, which does not affect the actual processing.

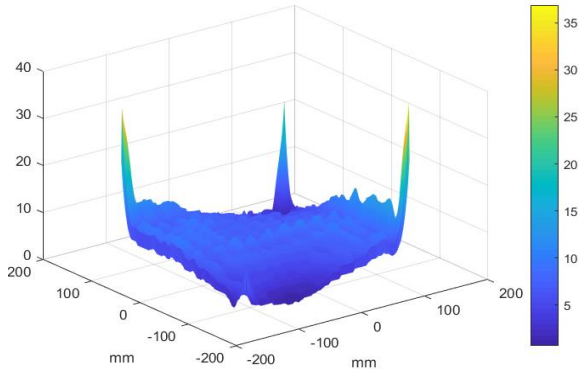

FIGURE 10. Modified dwell time distribution

MACHINING VERIFICATION OF DWELL ALGORITHM

An aluminum alloy material is used for machining verification. The process and measurement process are shown below in fig11,12. During the processing, the step length n=3 and HOLD value of dwell time is set to 0.7.

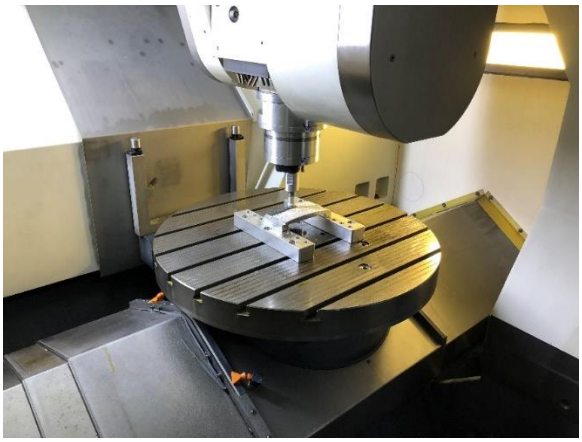

FIGURE 11. Machining of aluminum alloy free-form optical elements by CNC machining center

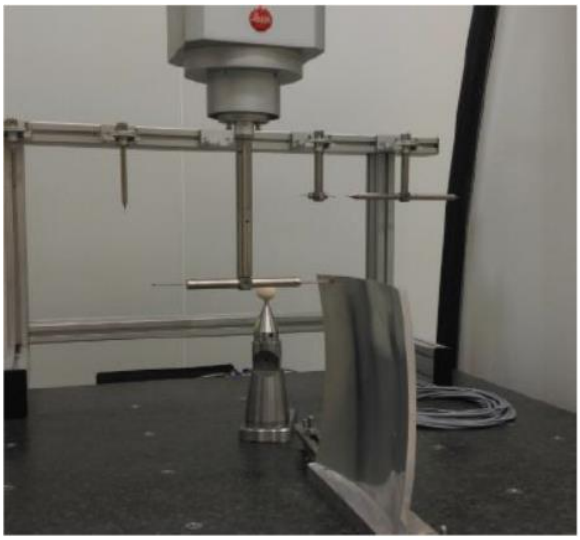

FIGURE 11. Error testing of aluminum alloy free-form optical elements by CMM

After testing, the measurement results indicated the surface error shape converges from 10 μm to 1.8 μm, and the peak of surface error is effectively reduced, as shown in fig12. The validity of the dwell time algorithm was proved.

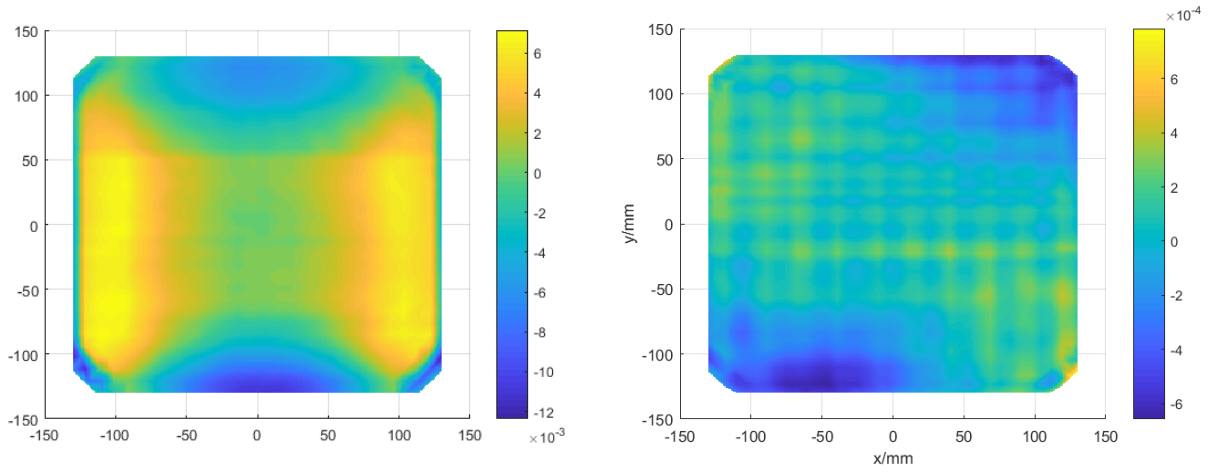

FIGURE 12. Comparison of free form surface error before and after machining

REFERENCES

[1] Wagner R E, Shannon R R. Fabrication of aspheric using a mathematical model for material removal. Applied Optics, 1974, (13)7:1683~1689

[2] Mersereau R, Schafer R. Comparative study of iterative deconvolution algorithms[C]// Acoustics, Speech, and Signal Processing, IEEE International Conference on ICASSP. 2003:192-195.

Fundamental design study on high-speed aerostatic spindle with water-cooling function

Satsuki Yamazaki[1], Dmytro Fedorynenko[2] and Yohichi Nakao[2]
[1]Graduate School of Mechanical Engineering
Kanagawa University
Yokohama, Kanagawa, JAPAN
[2]Department of Mechanical Engineering
Kanagawa University
Yokohama, Kanagawa, JAPAN

INTRODUCTIONS

Further improvement of the machining accuracy by the ultra-precision machine tools is highly desired for producing the high-tech components such as used for the medical, and the optical industries. In the ultra-precision machining, aerostatic spindles are commonly used.

Recently, the demands for manufacturing the parts with the micro structure are increasing. In the micro cutting using the end milling cutter with small diameter, the faster spindle rotations such as 100,000 min^{-1} are required in order to achieve desired cutting speeds and higher productivity. In the range of the higher spindle speeds, the influence of the air viscosity on the heat generation cannot be neglected, because the power losses causing the heat, due to the viscosity is proportional to the square of spindle speed.

In many cases, the high-speed spindle uses air turbine driven mechanism[1,2]. However, a disadvantage of the driven mechanism is that the spindle speed is affected significantly by the cutting forces.

To cope with the problem, an electric built-in motor is desired. However, the motor can be a major heat source, degrading the thermal stability of the high-speed spindle as a result. Accordingly, an effective design of the spindle structure must be demanded.

Final objective of this study is to design and develop the high-speed aerostatic spindle with built-in motor equipped with a shaft center cooling structure for water cooling. In the paper, thermal stability of the spindle is considered via simulation studies based on the introduced mathematical model.

The spindle shaft is supported by the aerostatic pressure. If the water cooling structure for the rotor is made, the air flow and the water flow have to be separate completely. This makes the spindle structure complex. The design issue regarding the structure is not considered in this paper.

In the paper, the aerostatic spindle with a built-in motor is considered in terms of the thermal stability of the spindle. In particular, the center shaft cooling for the water cooling improving thermal stability of the spindle is investigated.

In the rest of the paper, the fundamental structure of spindle to be considered is presented. The mathematical model based on the lumped parameter models is introduced. Considerations regarding the thermal stability of the spindle are carried out via simulations using the introduced mathematical model. For instance, the influence of the heat generations due to the spindle rotation, the motor power on the temperature change of the spindle are presented. Furthermore, the water cooling using the shaft center cooling of the spindle on the thermal stability is discussed as well[3].

STRUCTURE OF AEROSTATIC SPINDLE

A schematic drawing of aerostatic spindle considered in the study is presented in Fig. 1. The spindle has two radial bearings and thrust bearings. A built-in motor is fabricated in the middle of the spindle between two radial bearings. The cooling structures supplied for temperature controlled water flow are made in the spindle including the cooling jackets for the built-in motor and the casing and the shaft-cooling as shown in Fig. 1. In the spindle, the cooling jackets for the motor and the casing can be used separately.

HEAT SOURCES OF SPINDLE

Heat sources of the spindle are the power loss of built-in motor denoted by P_{mo}, the pressure loss of pressurized air given by P_{re} and the power loss P_{ab} due to the air viscosity by the spindle rotation. The heat sources are discussed as follows.

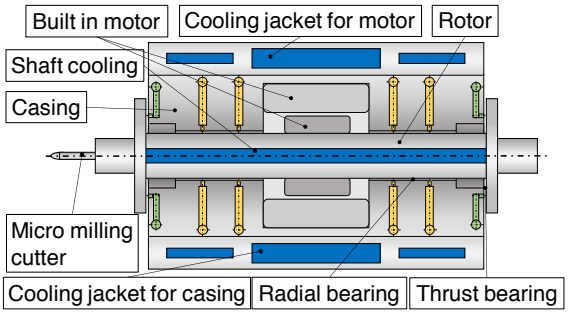

FIGURE 1. Structure of aerostatic spindle

NOMENCLATURE
c : specific heat
e : acceptable error
h : bearing gap
L : length
m : mass of part of spindle
N : rotational speed
P : power loss
Q : flowrate
R : radius
S : heat transfer area
T : temperature
α : coefficient of heat transfer
β : coefficient of liner expansion
μ : viscosity
ρ : density
ω : angular speed of spindle shaft
SUBSCRIPTION
a : air
ab : aerostatic bearing
c : casing
cj : cooling jacket
i : inner
m : motor
n : about nanometor
o : outer
op : output
re : restrictor
rd : radial
ro : rotor
s : supply
sc : shaft cooling
st : stator
th : thrust

Power Loss of Built-in Motor

The power loss of the built-in motor P_m can be represented by the output of motor P_{m_op} and its efficiency η as given by Eq. (1).

$$P_m = P_{m\_op}(1-\eta) \tag{1}$$

In addition, the power loss P_m is divided into the power loss of the stator P_{m_st} and the power loss of the rotor P_{m_ro}. If the ratio between P_{m_st} and P_{m_ro} is presented as R_m and R_r, P_{m_st} and P_{m_ro} can be given as Eq. (2) and Eq. (3).

$$P_{m\_st} = R_{st}P_m \tag{2}$$

$$P_{m\_ro} = R_{ro}P_m \tag{3}$$

Power Loss due to Pressure Drop

In aerostatic bearings, the pressurized air supplied to the bearing surfaces is released into the atmospheric pressure from the spindle. As a result, large pressure drop generated in the spindle results in the power loss of the air. The power loss due to the pressure drop of the pressurized air is represented Eq. (4).

$$P_{re} = p_s \times (Q_{th} + Q_{rd}) \tag{4}$$

In Eq. (4), the flowrate through the thrust and radial bearings are presented as Q_{th} and Q_{rd}.

Power Loss due to Viscous Friction

Influence of viscous friction of the air at the bearing surfaces on the power loss is not necessarily significant in the normal spindle speed in the common aerostatic spindles used in the commercialized machine tools. However, it becomes remarkable with increase of the spindle speed. The power losses due to the viscous friction in the radial and the thrust bearings, P_{rd} and P_{th} becomes extremely high if spindle speed reaches 100,000 min^{-1}. More specifically, P_{rd} and P_{th} is in proportion to the square of the angular velocity ω of the spindle rotation as represented by Eq. (5) and Eq. (6), respectively. Fundamental structure of aerostatic bearings is shown Figure 2.

$$P_{rd} = \frac{2\pi\mu {R_{rd}}^3 L_{rd}}{h_{rd}}\omega^2 \tag{5}$$

$$P_{th} = \frac{\pi\mu({R_{th\_o}}^4 - {R_{th\_i}}^4)}{h_{th}}\omega^2 \tag{6}$$

Total power loss that can be the heat source to increase temperature of air flow can be represented by the sum of P_{re}, P_{rd} and P_{th} as given by Eq. (7).

$$P_{ab} = P_{re} + 2P_{rd} + P_{th} \tag{7}$$

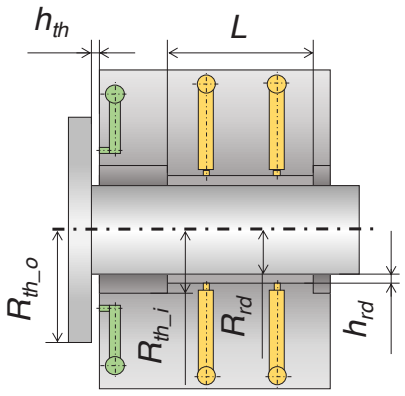

FIGURE 2. Basic structure of aerostatic bearing

The total power loss is obtained for various spindle speeds as in Fig. 3. The influence of the fluids, air and water, on the total power loss P_{ab} given in Eq. (7) is calculated as depicted in Fig. 3. In Fig. 3, the influence of air and water on the temperature is presented. As presented in Fig. 3, the power loss due to the water is approximately 55 times of that of air.

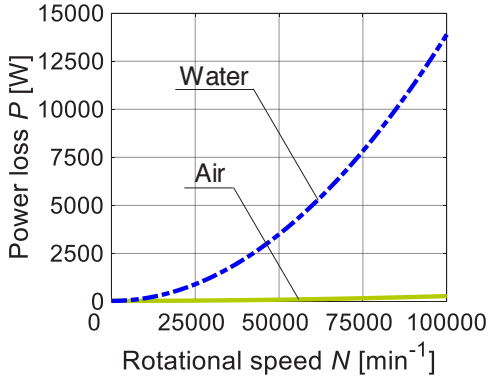

FIGURE 3. Comparison of power losses due to air and water

SIMULATION OF TEMPERATURE CHANGE OF SPINDLE

This study focuses on the fundamental characteristics on the temperature change of the spindle for the first design trial of the high-speed spindle. For the objective, a detail information including change in the temperature distribution of the spindle is not necessarily required. Rater, fundamental characteristics is needed. Thus, a mathematical model based on the lumped parameter model is introduced to predict the temperature change of the spindle.

The basic structure of the spindle to be considered in the simulation study is depicted in Fig. 4. In Fig. 4, the heat transfer taken place in the spindle is illustrated. For example, the air flow through the bearing gaps is heated by P_{ab}. The heat is then transferred from the air flow to the rotor and the casing. The temperature of the rotor and the casing are increased by P_{mo_ro} and P_{mo_st}. The rotor is cooled by the cooling water through the channel of the shaft cooling. Similarly, the casing temperature is increased due to the heat transferred from the air. At the same time, the casing is cooled by the water flow through the cooling jackets for the casing and the motor, as well. Now, the temperature of air flow is given by Eq. (8).

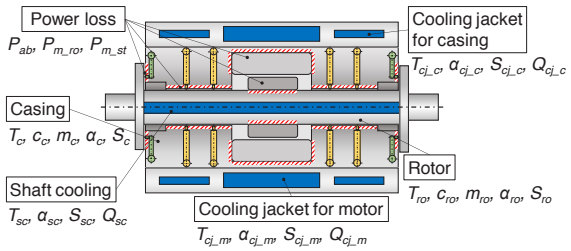

FIGURE 4. Simulation model of spindle

$$T_a = T_{a0} + \frac{1}{c_a \rho_a q_a} \left\{ P_{ab} - \alpha_{ro} S_{ro} \left(T_a - T_{ro} \right) - \alpha_c S_c \left(T_a - T_c \right) \right\} \quad (8)$$

Furthermore, the temperature of the spindle rotor T_{ro} is represented by Eq. (9).

$$c_{ro} m_{ro} \frac{dT_{ro}}{dt} = P_{m\_ro} + \alpha_{ro} S_{ro} \left(T_a - T_{ro} \right) - \alpha_{sc} S_{sc} \left(T_{ro} - T_{sc} \right) \quad (9)$$

Similarly, the temperature of spindle casing T_c is also given by Eq. (10).

$$c_c m_c \frac{dT_c}{dt} = P_{m\_st} + \alpha_c S_c \left(T_a - T_c \right) - \alpha_{cj\_c} S_{cj\_c} \left(T_c - T_{cj\_c} \right) - \alpha_{cj\_m} S_{cj\_m} \left(T_c - T_{cj\_m} \right) \quad (10)$$

The Nusselt numbers that is essential to determine the coefficients of the heat transfer are introduced using Reynolds numbers for each part of the spindle.

Considerations on Cooling Performance

Temperature increases from the initial temperature are evaluated via simulation studies. In Fig. 5, the temperature increases of the spindle rotor, the casing and the air flow against the spindle speed are presented. In the simulation, the temperature of the supplied air was given to be 20 degrees of Celsius as well as the initial temperature of the spindle. In addition, the temperature of the supplied cooling water was set to 15 degrees of Celsius if water cooling is used.

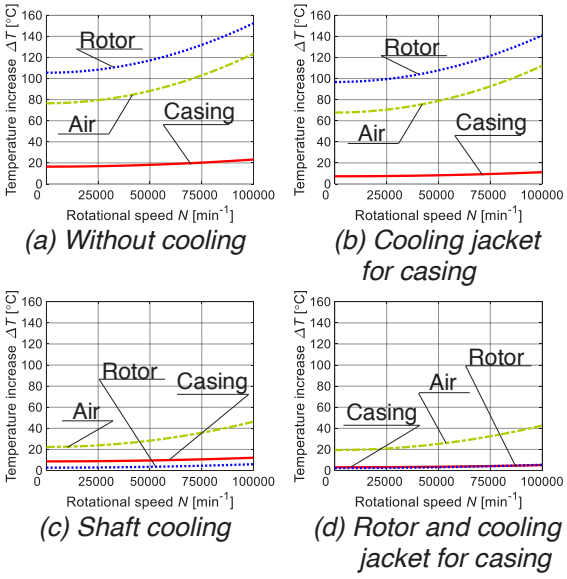

FIGURE 5. Effects of cooling condition on temperature increase

Influences of the cooling conditions, namely the cooling of casing and the cooling of rotor by the water flow, on the temperature change are investigated as shown in Fig. 5. For instance, the temperature changes if no cooling condition was used is depicted in Fig. 5(a). The result indicates that the significant increases in the spindle and the air flow are observed. In contrast, the temperature increase of the casing can be reduced if the cooling of casing by the water flow of 15 degrees of Celsius was used. If the shaft center cooling of the rotor was used, the temperature of the rotor is significantly decreased as presented in Fig. 5(c). In addition, it is observed that the cooling of the rotor reduces not only the temperature of the rotor but also that of the casing, as well. Finally, if the cooling water is supplied into the casing as well as the rotor, the temperature increases of the rotor, the casing and the air flow can be remarkably reduced as presented in Fig. 5(d).

Consideration on Influence of Flowrate on Temperature Change

The effect of the water cooling of the casing and the rotor on the thermal stability is investigated. Thus, influences of the flowrates of the water flow into the casing and the rotor on the temperature changes are evaluated. Now, the water flowrates for the shaft cooling, the cooling jackets for the casing and the motor are denoted as Q_{sc}, Q_{cj_c} and Q_{cj_m}, respectively. In the simulation studies, initial temperature conditions are given as previous considerations given in Fig. 5. Simulation results are presented in Figs. 6 (a)-(d).

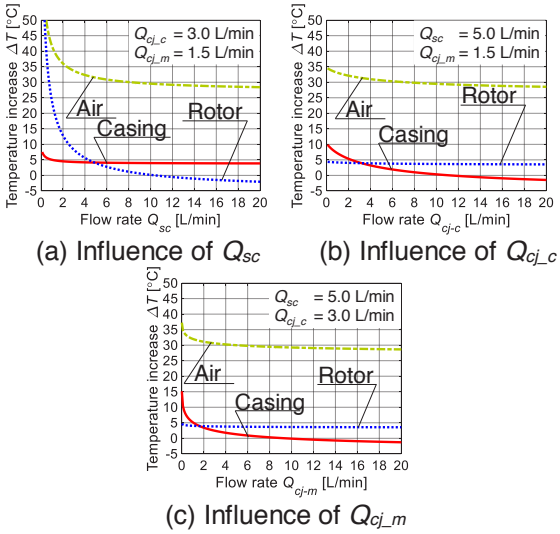

FIGURE 6. Effects of flow rate on temperature increase

The influence of the water flowrate into the rotor on the temperatures of the spindle is given in Fig. 6(a). This result indicates that the flowrate supplied into the shaft-cooling decrease significantly the rotor temperatures. In addition, the casing temperature is influenced by the flowrate of water flow through the shaft-cooling. If the flowrate is set to 12 L/min, the temperature increase of the rotor can be zero. Influences of the flowrate of Q_{cj_c} and Q_{cj_m} on the temperatures are presented in Figs. 6(b) and (c), respectively. The flowrates for each cooling channels in the spindle can be determined based on the results so that the required thermal deformations of the spindle can be obtained.

OPTIMUM CONDITION OF COOLING FLOW RATE

In the ultra-precision machining, the thermal deformation of spindle must be minimized to the acceptable level, for instance, such as orders of the tens of nanometers. Accordingly, the acceptable temperature change can be determined based on the spindle length in the axial direction, the coefficient of linear expansion of the material of the spindle and the required machining accuracy. Acceptable temperature change is represented by Eq. (11).

$$\Delta T = \frac{\Delta L}{\beta \cdot L} \tag{11}$$

If the material of the spindle is the X5CrNi18-10, the coefficient of linear expansion is β = 17.3 x 10^{-6}/K. Then, the relationship between the length of spindle rotor and the acceptable temperature change is calculated as Fig. 8. If the length of the spindle rotor is chosen to be 140 mm, the acceptable temperature change of rotor is ΔT_{ro} = 0.41x10^{-3} degrees of Celsius.

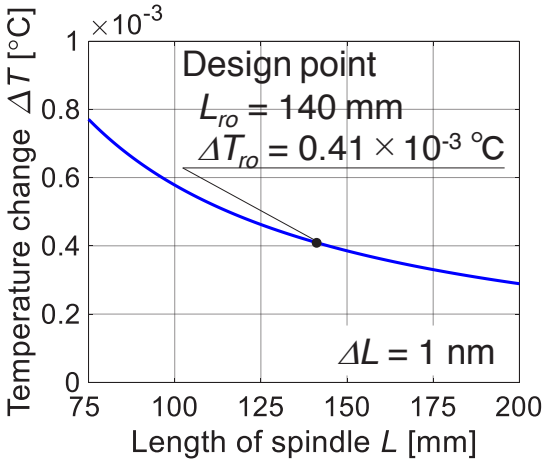

FIGURE 8. Acceptable temperature change

Similarly, the temperature change and the resultant thermal deformation of the casing are considered. If acceptable thermal deformation of casing, in which the casing of length L_c is 108 mm, is 10 μm. The acceptable temperature change of the casing becomes 5.4 degrees of Celsius from Eq. (11). From the simulation results, the flowrates Q_{sc}, Q_{cj_c} and Q_{cj_m} for water cooling for each cooling channel can be determined. For instance, the water temperature is 15 degrees of Celsius. The total flowrate of the cooling water is about 20 L/min as the sum of Q_{sc} =12.81 L/min, Q_{cj_c} =3.0 L/min and Q_{cj_m} =5.15 L/min. Consequently, the temperature change of the rotor can be minimized to be 0.1x10^{-3} degrees of Celsius for the rotor and 1.84 degrees of Celsius for the casing.

Finally, the transient characteristics of the spindle temperature are evaluated via simulations as well. In the simulation, the optimum conditions of the water cooling were used. The temperature changes of the air, the rotor and the casing are represented by Fig. 9. From the simulation, the settling time regarding the temperature of casing is about 120 sec. In contrast, the settling time of temperature of the rotor is 10 sec.

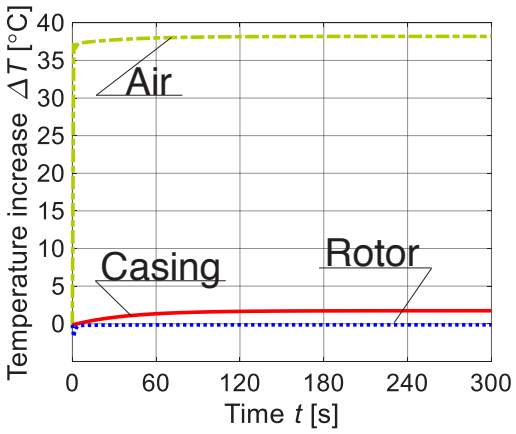

FIGURE 9. Transient temperature changes with introduced optimum cooling condition

CONCLUSION

In the paper, the aerostatic spindle with a built-in motor equipped water shaft-cooling structure was discussed, in particular in terms of the thermal stability. The study focused on the design of aerostatic spindle with higher spindle speed such as 100,000 min^{-1}.

In order to improve thermal stability of the spindle , the water shaft-cooling was considered. Then suitable cooling conditions were determined. It was then verified that it achieves higher thermal stability even in the high-speed rotation of the spindle.

Based on the considerations discussed in the paper, an aerostatic spindle for high spindle speed and the higher thermal stability will be developed in the future our projects.

This project is financially supported by the NSK Foundation for Advancement of Mechatronics. Their supports are gratefully acknowledged.

REFERENCES

[1] Yuuki T., Hiroshi S., Hayato Y., Hidenori S., A thermally stable aerostatic spindle system

equipped with self-cooling function, Journal of Advanced Mechanical Design, Systems, and Manufacturing 2014. 8(6), JAMDSM0079-JAMDSM0079
[2] Yohichi N., Tomohiro., Design of Air Drive Spindle, Proc. of JSME Annual meeting. 2006. 4(0), 49-50 (in Japanese)
[3] Tsubasa Y., Akio H,. Yohichi N., Fundamental study on thermal stability of micro milling spindle supported by water hydrostatic bearing under non-spindle rotation, Proc. of International Conference on Leading Edge Manufacturing in 21st century, LEM21 2017. 9(0), 075

FEASIBILITY STUDY ON PRECISION COMPRESSION MOLDING OF CHALCOGENIDE GLASS MICRO-OPTICAL ELEMENTS

Lin Zhang, Wenchen Zhou, Neil. J. Naples, and Allen Y. Yi
Industrial and Systems Engineering
The Ohio State University, Columbus, OH 43210, USA

ABSTRACT

Chalcogenide glasses are emerging as low-cost alternatives for infrared applications. These materials have promising characteristics that can improve both manufacturing processes and device performance. In this paper, we aim to develop a complete manufacturing process based on precision compression molding of chalcogenide glass. The entire process chain includes mold fabrication, compression molding and profile measurement. A set of mold inserts was designed and fabricated by high-speed single-point diamond milling. The structure of the lower mold insert was semi-closed, which helps both molding and de-molding. Molding experiment was conducted on a commercial precision molding machine with optimized processing parameters. After the molded element was released, the profile of the replicated infrared element was measured using interferometer, which closely matched the dimensions of the curvature of lenslet on the mold. An optical setup was used to validate the optical performance of the molded microlenses. This study demonstrated the feasibility of the proposed manufacturing method, which will greatly improve fabrication efficiency of infrared elements and allow low-cost high-precision infrared micro-optics to be manufactured in high volume.

BACKGROUND

Most recently, chalcogenide glasses are widely used to fabricate infrared optics in civil thermal imaging devices, such as night-vision systems and thermal projectors [1]. These materials are made of chalcogen elements (S, Se, Te) instead of oxygen to bond with heavy metals and metalloids by covalent bonds [2]. Chalcogenide glasses are regarded as important alternative materials to conventional infrared materials not only by virtue of their transparency in the key short-wave infrared (SWIR) to long-wave infrared (LWIR) bands, but the ability to be mass produced and molded into near-net shape lenses as well. These optics provided photonics industry with material candidates for low-cost and high-performance infrared devices.

Precision glass molding is considered as an important manufacturing method in glass forming process, which is a high-volume, low-cost method suitable for molding intricate and precise optical components. In this process, glass is first placed in an open mold cavity. After the glass preform is heated up, the mold is closed with a fixed load applied to force the material into contact with the entire mold areas, while heat and pressure are maintained until the molding material matches well with the cavity of the mold. Chalcogenide glasses are ideal candidates for precision glass molding process because of its low transition temperature (Tg) and steady physical & chemical property at elevated temperature. For high-volume production of infrared optics, precision glass molding is preferred over more traditional methods for its shortened production cycle and reusable tooling.

SINGLE-POIND DIAMOND MILLING

Toolpath Generation Arithmetic

As a key part of a precision glass molding tool, the mold insert is fabricated by high-speed single-point diamond milling. In comparison, high-speed diamond milling does not require other processes and offers a wider fabrication window with more flexibility and high accuracy. Our previous work demonstrated that the typical microlens arrays were fabricated by combining compression molding and the ultraprecision diamond milling process [3].

The mold insert is first rough machined on a Haas VF-3 3-axis vertical machine center (Haas Automation, Inc., USA) from an aluminum 6061 alloy rod. Then the microlens array is fabricated by high-speed diamond ball-end milling using a five-axis CNC ultraprecision machine (Nanotech 350FG, Moore Nanotechnology Systems, USA). The milling process is performed at an extremely high rotation speed of 50,000 rpm, where a fluid cooled air bearing spindle was implemented. The diamond milling tool (K&Y Diamond, Ltd., Diab St-Laurent, CA) has a 0.503 mm tool nose

radius that was compensated in the generation for spiral tool path trajectory. The hardware configuration of the experiment setup is shown in Fig. 1, where the fixture with the mold insert was clamped on the air bearing spindle by a vacuum chuck.

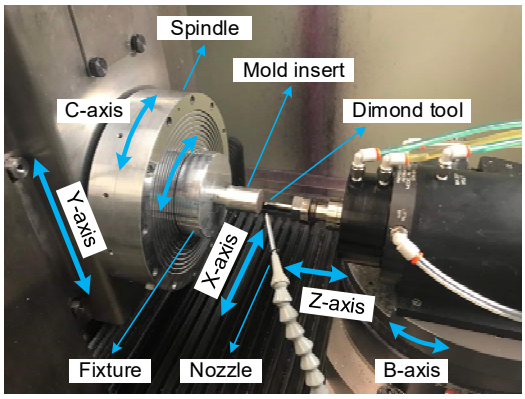

FIGURE 1. High-speed diamond milling hard-ware configuration for mold insert manufacturing

Finish Geometry Measurement

After machining, the micro-structure of the microlens array is obtained by optical surface profiler, white-light interferometer (Wyko NT9100, Bruckner., USA). The microscope photo-graph of the microlens array is illustrated in Fig. 2 (a), which shows that the machined microlens array has good uniformity. An arbitrary region is further captured and stitched, shown in Fig. 2 (b). Each lenslet in these regions shared almost the same features with no structure and position distortions. An arbitrary lenslet from Fig. 2 (b) is extracted and illustrated in Fig. 2 (c). The 3D surface profile further proved that the finished surface is smooth with really sharp lines at the interaction edge boundaries. Besides, the surface roughness of the lenslet was around 15.6 nm, adequate for requirements of infrared optics. Moreover, the micro-topological structures are presented in Fig. 2 (d) by removing base surface profile. The surface quality near the center is slightly worse than the other region. It might be due to slower cutting speed and dynamics error near the center in the mold fabrication.

Surface Profile Measurement

Compression molding process is conducted to replicate the geometry from the mold inserts to the infrared glass at elevated temperature. The glass molding process is carried out on a commercial molding machine Model GP-10000HT (Dyna Technologies, Inc., USA). A piece of chalcogenide glass (As_2S_3) disk with both sides polished is placed between the mold inserts.

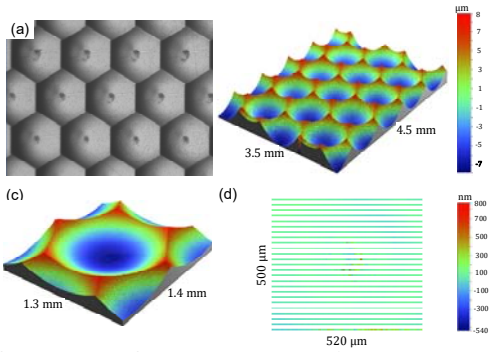

FIGURE 2. Characteristics of the machined mold, (a) the micro-photo of an arbitrary area of microlens array, (b) the 3-D structure of a large area, (c) an extracted lenslet, and (d) the surface micro-topological structures after removing base surface profile.

COMPRESSION MOLDING PROCESS

After three cycles of purge with nitrogen, the chamber temperature reaches 220 °C and the upper mold begins to apply pressure onto the chalcogenide glass disk. To ensure the cavity is fully filled, the applied pressure is maintained for ~10 min. Then an external fan is turned on and the temperature drops to ~40 °C. The molded microlens array is removed from the insert. The entire process and temperature variation during the molding process are shown in Fig. 3.

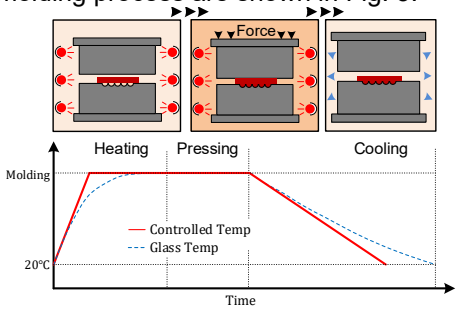

FIGURE 3. Schematics diagram of compression molding process and temperature variation.

Further measurement is conducted to obtain the surface profile and quality of the molded sample. Fig. 4 illustrates the 3D and 2D micro-structures of the molded microlens array. The 3D micro-structures of the molded surface with large area presented the uniformity and homogeneous of microlens array, as shown in Fig. 4 (a). To evaluate the form accuracy of the molded lenslet, an arbitrary lenslet was extracted and illustrated in Fig. 4 (b). The 2D cross-section profiles passing through the axis were compared with

the designed profile, the obtained profile and geometry error presented in Fig. 4 (c). The obtained profile agrees well with the design and the error is limited within 100 nm.

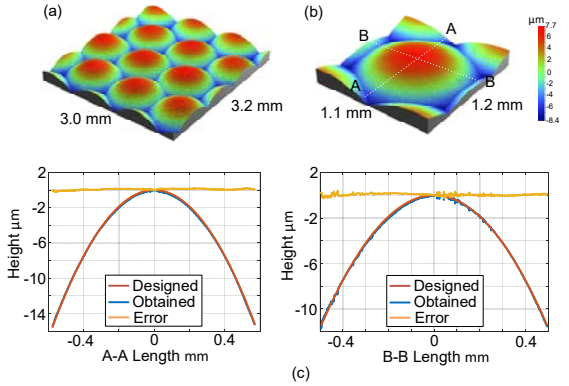

FIGURE 4. Characteristics of the molded microlens array, (a) the 3-D structure of a large area, (b) an extracted lenslet, and (c) the profiles and the machining errors.

Optical Setup and Performance

A simple optical setup is built and employed to verify the optical property of the microlens array. The hardware configuration of the optical setup, shown in Fig. 5 (a), consists of a thermal light source, the molded microlens array and an IR detector. The thermal light source is a wideband IR source (HawkEye Technologies, USA) with a parabolic reflector to collimate the light beam. After that, the microlens array was mounted on a 3D positioning stage. The distance between the microlens array and the IR detector (Sofradir EC, Inc., USA) can be precisely adjusted. Raw data frame captured by the camera were shown in Fig. 5 (b). The uniform bright focal points imaging results demonstrated good profile quality.

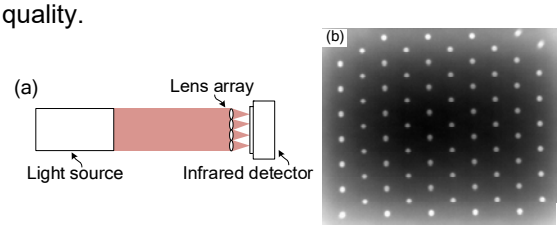

FIGURE 5. Schematic diagram of the (a) hardware configuration of the optical setup, and (b) raw data obtain by IR detector.

CONCLUSION

In summary, this research presents a feasibility study on precision glass molding of chalcogenide glass for infrared micro-optics fabrication. A mold insert with uniform concave spherical dimples is fabricated by high-speed diamond milling. Uniform microlens array is successfully molded by adjusting the compression molding process parameters. Finally, the molded microlens array is assembled in an optical setup to evaluate the optical performance. Experiments show that the molded microlens array can achieve accurate profile and great optical property. The same manufacturing strategy, combining high-speed diamond milling and compression molding, can be easily applied to other micro- and nano-scale optics to improve production efficiency and product quality.

REFERENCES

[1] Lin Zhang, Wenchen Zhou, Neil J Naples, Allen Y. Yi. Investigation of index change in compression molding of $As_{40}Se_{50}S_{10}$ chalcogenide glass. Applied Optics. 2018; 15: 4245-4252.

[2] Andrea Ravagli, Christopher Craig, John Lincoln, Daniel W. Hewak, Ga-La-S-Se glass for visible and thermal imaging. Advanced Optical Technologies. 2017; 6: 1-6.

[3] Lin Zhang, Wenchen Zhou, Neil J Naples, Allen Y. Yi. Fabrication of an infrared Shack–Hartmann sensor by combining high-speed single-point diamond milling and precision compression molding processes. Applied Optics. 2018; 13: 3598-3605.

A CURVED SURFACE-INSENSITIVE OPTICAL SENSING TECHNIQUE FOR PRECISION SPINDLE HEALTH MONITORING

ChaBum Lee[1] and Gyu Ha Kim[2]
[1]Department of Mechanical Engineering
Texas A&M University
College Station, Texas, USA
[2]R&D Department
Tri-N Co. Ltd.
Daegu, South Korea

ABSTRACT

The dimensional measurement technique utilizing curved-edge diffraction is applied for the dynamic system identification of precision spindle system. Both static and dynamic behavior including stiffness, damping ratio, and parasitic motion of a precision ball bearing spindle system is characterized by impact response, while the spindle displacement is measured with the curved-edge-type sensors (CES). The CES effects of spindle radius and surface quality were theoretically and empirically investigated. The capacitive-type sensors (CS) were used for a baseline comparison with the CES outputs. Unlike CS, CES is not sensitive to the spindle radius, surface quality, and coupling motions, shows high bandwidth and low noise, and allows for the dimensional measurement at a localized area. These results indicate that CES can be a good alternative to CS for spindle metrology. In the experiment, natural frequency (56 Hz (linear) and 680 Hz (angular)), stiffness (460~790 N/μm) and damping ratio (0.04~0.08) of precision spindle system were measured by CS and CES at the same time. The dynamic model of ball bearing spindle system was also discussed.

INTRODUCTION

Precision ball bearing, hydrostatic or aerostatic spindles represent a key part of machine tools because they determine the quality of the final product produced and the overall manufacturing productivity and efficiency. Therefore, dynamic system identification and condition monitoring of precision spindles is a key factor in increasing the availability of the machine tool and achieving a more robust machining process [1-4]. Precision spindle metrology, i.e., utilizing a cylindrical or spherical target artifact with non-contact sensors to measure a machine tool spindle's "axis of rotation" errors, including radial, axial, and tilt errors, is basic science and technology for sustainable manufacturing [5,6].

Significant research has been devoted to the development of measurement and analysis techniques of precision spindles. Currently, a few approaches in measuring and evaluating precision spindle systems by using capacitive-type sensors (CS) or eddy current-type sensors (ECS) exist [7,8]. However, these sensors are typically designed for flat target surface measurement. CS and ECS are the most commonly used in spindle measurements. It is standard practice for commercial CS and ECS to be factory calibrated with flat-target surfaces. Because the probe will measure the average distance to the target, the gap at zero volts will be different than when the system was calibrated [9,10]. As depicted in Figure 1, errors will also be introduced because of the different behavior of the electric fields between sensing electrode and the curved surface and between guard electrode and the curved surface. In cases where a non-flat target must be measured, the system can be factory calibrated to the final target shape or the probe has to be custom-made for a certain shape.

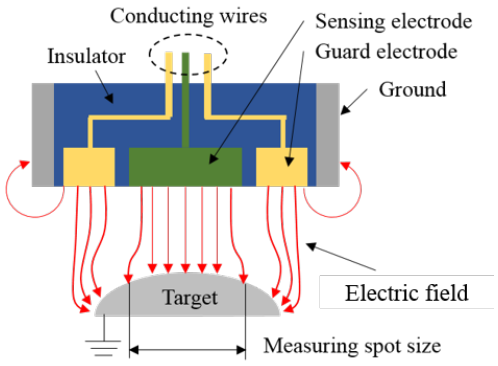

FIGURE 1. A schematic of dimensional measurement from the curved target surface by using capacitive-type sensor.

In this study, a curved-edge sensor (CES) is adapted for dynamic system identification of precision ball bearing spindle system. In the previous work [13-15], knife-edge sensors (KES) was firstly introduced, and the result indicates that the KES can be a good alternative to CS in nanopositioning applications, *e.g.*, microscopy, surface profilers, or coordinate measuring machines. In addition to KES, CES was introduced [11,12]. CES was compared with CS in terms of linearity, measuring range, bandwidth and long-term stability. As a result, it is expected that CES can be one of alternative sensors applicable to spindle metrology. Here a CES model that can describe curved-edge diffraction phenomenon on a curved surface is established by using electromagnetic wave propagation theory. The curved-edge diffraction effects according to surface quality, shaft radius, and materials are empirically characterized, and dynamic system identification of ball bearing spindle system is discussed.

MEASUREMENT PRINCIPLE

Diffraction is the bending of wavefronts around obstacles, and its effects are typically only noticeable for waves where the wavelength similar to the size of the diffracting obstacle. Diffraction occurs with all propagating waves, including sound waves, water waves, electromagnetic (EM) wave. Diffraction over a knife-edge, so-called knife-edge diffraction, can be understood through using Huygens construction. This effect is initially an oscillation then as the direct path is cut off, a signal loss. Unlike knife-edge diffraction, an analytical approach to diffraction by a curved edge is very difficult because curved edge diffraction must be understood from the asymptotic solution of several canonical problems, which involve the illumination of the edge by different wave fronts.

As illustrated in Figure 2, an EM wave incident on the curved edge gives rise to an incident wave (E_i), reflected wave (E_r), and edge diffracted wave (E_d), and those electric fields can be mathematically expressed. The regions, RB, SB and DSB, indicate reflection boundary, shadow boundary, and deep shadow boundary, and R indicates the radius of spindle shaft. Such waves that propagate along a surface ray may be excited at the curved edge shadow boundaries similar to knife edge diffraction. Such surface ray fields may also be excited at the transition region and can be separated into three different regions.

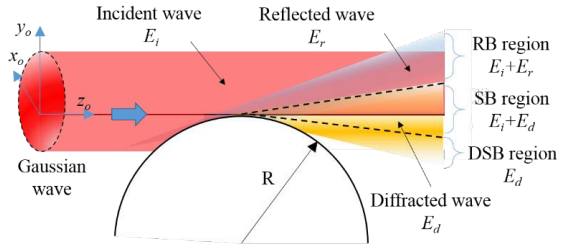

FIGURE 2. A schematic of curved-edge diffraction.

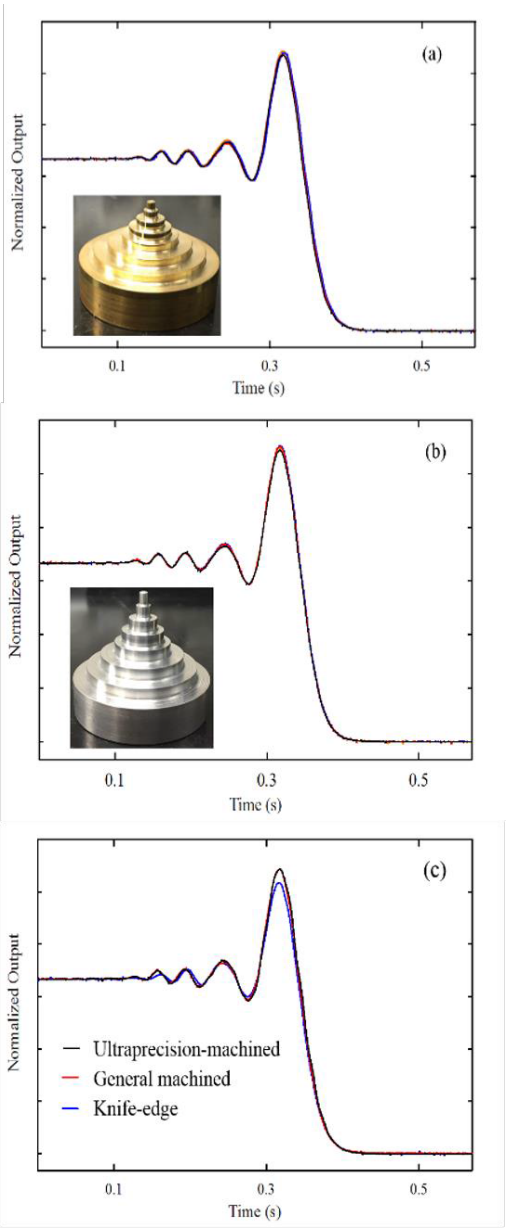

FIGURE 3. Curved-edge diffraction effects of materials, radius and surface quality: (a) ultraprecision-machined Cu, (b) generally-machined Al and (c) comparison (ϕ20 mm).

EXPERIMENTS

Curved edge diffraction fringes of two test samples with different radius (ϕ3, 5, 10, 20, 30, 40 and 50 mm) conditions, surface conditions and different material (Cu, Al) conditions were measured as shown in Figure 3. The Cu sample was machined by ultraprecision machine tool (Nanoform 200) that is used for optical component machining, and the Al sample was machined by general machine tool that can be found in any machine shop. The He-Ne laser (633 nm wavelength) was incident on the edge of the sample, the fringes that can be collected from RB, SB and DSB regions were obtained by scanning the curved edges of each sample as illustrated in Figure 2. The distance between the curved edge and the detector was kept 150 mm. As a result, any significant changes according to materials, radius curvature were not found in given experiment conditions. However, a slight difference in fringe amplitude between curved edge and knife edge was observed.

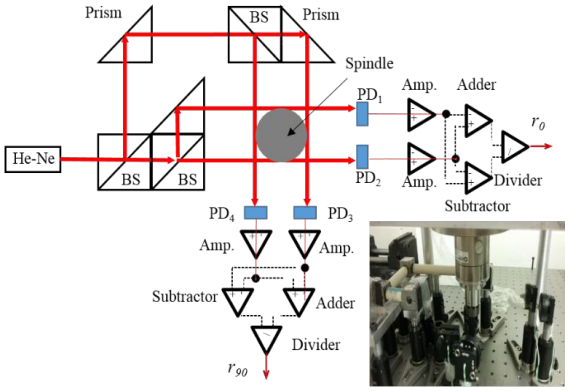

FIGURE 4. Experiment setup.

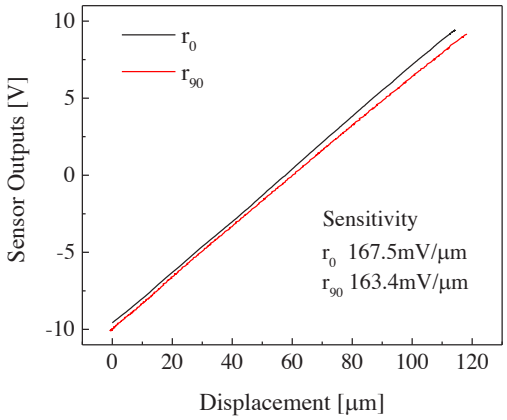

FIGURE 5. Calibration results: linearity errors (calculated as standard deviation of residual errors) were 0.10% and 0.14% for r_0 and r_{90} in full scale (95% confidence).

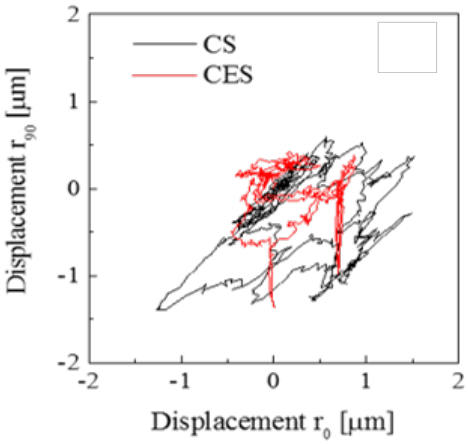

FIGURE 6. Spindle runout at 1,000 rpm.

In the experiment, the precision ball bearing spindle system was chosen. Dynamic system identification of the spindle system was investigated by the curved edge sensor as illustrated in Figure 4. The CS was used for a baseline comparison with the outputs of the CES as shown in Figure 5. This result indicates that the CES is highly linear. The CS and CES outputs were compared with respect to spindle velocity up to 8700 rpm (maximum rpm). The two CS was placed around spindle shaft (ϕ34 mm) along the r_0 and r_{90} directions. As seen in Figure 6, two sensor outputs were compared.

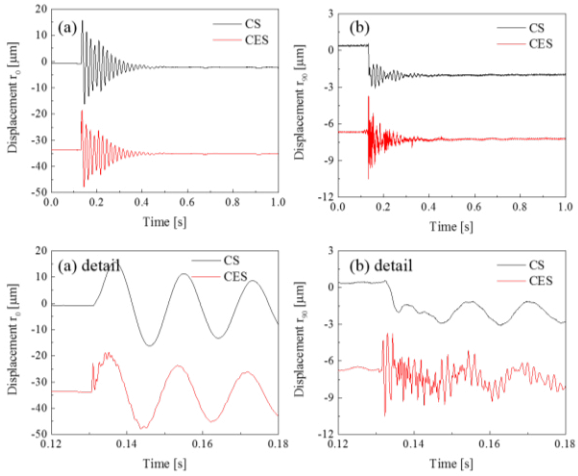

FIGURE 7. Impact response at spindle velocity 0 rpm (stationary) condition: (a) r_0 and (b) r_{90}.

The impact test using hammer with force sensor along the radial direction was performed. The CS and CES measured the displacement along the r_0 and r_{90} directions and the applied force was measured at the same time, while the

impact was applied to the r_0 direction under stationary condition (Figure 7). Two frequencies, 56 Hz and 680 Hz, are presented in the oscillation curves measured by CES in all conditions, and 680Hz oscillations are only observed for approximately 40 ms after impact.

CONCLUSION

A novel sensing method based on edge diffraction technique applicable to spindle metrology and spindle dynamic system identification was investigated. The precision ball bearing spindle system was characterized by impact test, and its dynamic model was established based on the experiment. Thus, this technique can be used to five degree-of-freedom spindle error measurements, spindle health monitoring, and dynamic characterization of the spindle system in a near future. The curved edge diffraction model will be in-depth studied to fundamentally understand edge diffraction behavior in reflection boundary, shadow boundary, and deep shadow boundary and to characterize how this behavior affects CES performance.

ACKNOWLEDGEMENTS

The research was supported by National Science Foundation (Award Number: CMMI 1463502) through the Texas A&M University. Similarly, this work was supported by the Center for Manufacturing Research at the Tennessee Technological University.

REFERENCES

[1] W. Gao, Precision nanometrology: Sensors and measuring systems for nanomanufacturing, Springer (2010).

[2] K. Liu, M. Sun, T. Zhu, Y. Wu, Y. Liu, Modeling and compensation for spindle's radial thermal drift error on a vertical machining center, Int. J. Mach. Tools Manuf., 105, 58-67 (2016).

[3] J. Kim, S. Zhao, G. Kim and S-K. Lee, Rolling bearing-suspended spindle run-out control using repetitive control and adaptive feedforward cancelation, Int. J. Prec. Eng. Manuf., 14(12), 2171-2178 (2013).

[4] J. Kim and S-K. Lee, Micro-patterning technique using a rotating cutting tool controlled by an electromagnetic actuator, Int. J. Mach. Tools Manuf., 101, 52-64 (2016).

[5] M. Madden, M. Aketagawa, T. Kumagai, Y. Maeda and E. Okuyama, Concurrent measurement method of spindle radial, axial and angular motions using concentric circle grating and phase modulation interferometers, Meas. Sci. Technol. 25, 094005 (2014).

[6] Eric R. Marsh, Precision spindle metrology, DEStech Publications, Inc., 2017.

[7] J. Fleming, A review of nanometer resolution position sensors: Operation and Performance, Sens. Actuators A: Physical, 190, 106-126 (2013).

[8] K. Liu, M. Sun, T. Zhu, Y. Wu, Y. Liu, Modeling and compensation for spindle's radial thermal drift error on a vertical machining center, Int. J. Mach. Tools Manuf., 105, 58-67 (2016).

[9] Philip T. Smith, R. Ryan Vallance and Eric R. Marsh, Correcting capacitive displacement measurements in metrology applications with cylindrical artifacts, Precision Engineering, Vol. 29, No. 3, pp. 324-335 (2005).

[10] R. Ryan Vallance, Eric R. Marsh and Philip T. Smith, Effects of targeting spherical surfaces with capacitive displacement sensors, Proceeding of American Society for Precision Engineering Annual Meeting (2004).

[11] C. Lee, S. M. Mahajan, R. Zhao, and S Jeon, A curved edge diffraction-utilized displacement sensor for spindle metrology, Rev. Sci. Instrum. 87, 075113 (2016).

[12] C. Lee, R. Zhao, S. Jeon, A simple optical system for miniature spindle runout monitoring, Measurement, 102, 42-46 (2017).

Fabrication of micro-holes array through multiple electrodes with distributed µ-pulsed electrochemical machining

Mahesh Thalkar[1], Divyansh S. Patel[1], V. K. Jain[1,2], and J. Ramkumar[1]
[1]Department of Mechanical Engineering
Indian Institute of Technology Kanpur,
Kanpur - 208016 (U.P.), India
[2]Department of Mechanical Engineering,
M. A. N. I. T. Bhopal,
Bhopal – 462003 (M.P.), India

INTRODUCTION

ECM is an advanced machining process used for machining of electrically conducting materials where the process is unaffected by the hardness and thermal conductivity of the workpiece material. Electrochemical micro-machining has tremendous potential on account of versatility of its applications in different domains of engineering. It is expected that it will be a promising, successful and economically viable machining process in the micro-manufacturing industries. But micro-machining of large surface area by ECM process is one of the challenging task to the cur-rent date. Such as production of perforated sheets for filtering specific dimensioned micro-particles needs to generate millions of identical micro-holes in small area. As in the case of electrochemical micro-machining (ECMM), high resolution micro-featuring is achieved when a low duty cycle pulsed voltage is employed. When a low duty cycle, pulsed voltage is supplied for machining millions of micro-holes the pulse-off time will increase the effective machining time by significant amount. To minimize the machining time of large number of micro-features, we hypothesize multiple electrodes EC drilling with sequentially distributed micro-second pulses. By providing the sequential firing order based pulse distribution pulse-off time is zero because it at any instant at least one or a number of electrodes would be in pulse-on mode.

This study outlines a numerical and experimental study of perforating micro-holes array through multiple electrodes in ECM process. A novel approach of sequential pulse distribution to each electrode is studied to improve the machining efficiency by reducing the machining time. Simultaneous 4 electrodes of 65 µm tip diameter are used to pierce micro-holes in stainless steel sheet of 100 µm thickness. Micro holes of 121 µm diameters with spacing of 200 μm and 300 μm are machined and optical microscope is used to analyze the geometrical parameters. Numerical simulation is performed in COMSOL Multiphysics to simulate EC perforation process. Electric double layer theory is used to calculate potential in electrochemical reaction. Study shows there is close fit between the simulated and experimental diameters of machined holes.

BACKGROUND

Over the past several years in response to the demand of miniature products, various industries are developing advanced technologies to fulfil the requirements of customer of society in order to sustain their growth. The demand of miniature products is not new for today's micro-engineering field. Without affecting performance capability of product or with increased number of functions its size is decreased to a much smaller scale, mostly in mechatronics, biomedical and robotics industries. Most products of this industries are manufactured to the micron, sub-micron or up to nano level. Endoscopy, micro-neurography, these are examples of visualizing techniques used in bio-medical field where micro products are used [1]. The biggest advantage of ECM process over all other non-conventional process is the process is unaffected by the hardness and thermal conductivity of the workpiece material and surface proper-ties of base material remain unchanged [2].

Many key structural components in the field of aerospace industries such as tur-bine engine blades, optical fibre connectors in electronics industry, printer nozzles, high density flexible printed circuit boards, gratings for electronic microscopes, and chemical fibre spinneret structures contains array of micro-holes with progressively smaller sizes. Ink ejector nozzle used in digital printers is typical examples of components that require array of micro-holes made with a high machining accuracy [3]. Micro-filters with hole ranging from 1-100 um, are used

in filtration or separation, also for sieving of powder in predefined size [4]. Micro-holes with high precision are used in nozzle plates for the conversion of liquid into mist or in the form of finely divided droplets [4]. Interference or resonance effect of light is one of the immensely studied field in optical science, aperture of micro-holes is used to eliminate stray light or to correct light beam micro-hole structures are mostly used. But conventional machining produces some burrs on the edge of the hole which creates obstruction to the light path therefore non-conventional machining processes can be effectively used for the production of micro apertures with highest quality [5]. In PVD and CVD process shallow masks are used on the substrate for the selective deposition of required material. These deposition masks can be made by ECM in required dimensions. In ink jet printing devices, highly corrosive ink is used for printing purposes. Therefore highly corrosion resistant material is needed for nozzle plate of printhead, the print-head or nozzle usually consists of an array of micro-holes with diameters smaller in size [2]. Typical material includes stainless steel and Bronze. Therefore in this work stainless steel used as primary workpiece material for the machining of micro holes.

Many researchers have used different methods to fabricate micro-holes. Among all, micro-EDM is the mostly used process for micro-hole drilling but this process have problem of taper and roundness of edged [1]. Use of kerosene and deionized water shows good results over the processing capability of EDM [6]. Fang et al. used new method of optimized electrolyte dividing manifolds for electrochemical drilling of micro-holes (≈ 1 mm diameter). Flushing efficiency of electrolyte can be improved by this method in case of multiple hole drilling [7]. Precision filled wax deposition meth-od is another hybrid process of micro hole drilling, in this process initially holes are made on SU8 substrate then the holes are filled with wax and extruded, after extrusion the mold is deposited with required material to make micro holes at wax filled bars which are later removed by heating [3]. Kim et al. [8] fabricated multiple electrode of tungsten carbide (WC) material by using reverse EDM process up to 35 μm diameter and used that electrodes as a tool in micro ECM process to drill holes and to make grooves. Productivity of machining process can be increased by this process. Wang and Zhu [9] also fabricated array of square shaped tools by using wire EDM process, after fabrication of square shaped electrodes they processed through electro-chemical bath to make circular in cross section. After making circular in section used to make micro holes on SS304 steel.

In this work multiple electrodes are used to fabricate the micro-holes by the electrochemical drilling process. Electro-chemical drilling process uses micro tool with side wall insulted by insulating material and fed against workpiece in vertical direction. Micro-tools are fabricated by electrochemical etching process where initial diameter of shaft used 800 μm to obtain micro tool-tip diameters ranging from 50-90 μm.

In the present work time-dependent distribution of the micro-pulse is employed to avoid impedance and pulse-off effects. An essential pulsed power supply is designed and developed for of individual pulse distribution to the four electrodes such only one electrode is switched-on by individual distribution of pulses.

NUMERICAL SIMULATIONS

COMSOL Multiphysics 5.2 is used for numerical simulation of electrochemical drilling. 3-D model is studied by using the electric current sub-module under its AC/DC module; deformed mesh sub-module is used to check deformed shape of hole. Electric current and deformed geometry physics are solved simultaneously in this simulation process. Electric current physics is applied to all three domains. Local charge density in electrolyte varies with divergence of current density given by

$$\nabla \cdot J = Q_j \quad (1)$$

Vector of current density results is given by,

$$J = (\sigma + \varepsilon_0 \varepsilon_r \cdot \partial/\partial t)E + J_e \quad (2)$$

Where σ is the electrical conductivity, ε0εrE is electric displacement field and Je the externally supplied vector of current density.

E in above equation is the electrical field is defined by the negative gradient of electric voltage

$$E = -\nabla v \quad (3)$$

Water as a material for electrolyte is chosen with conductivity equal to 70 mS/cm, SS304 for workpiece and copper for tools.

The primary text heading should be 10-point Arial bold, all capital letters, flush left with the margin. If the heading is more than one line, the following lines should also be flush left. The spacing to the next heading should be one line.

TABLE 1: Constants and their values utilized in the analysis.

SN	Para.	Description	Value

1	σ	Electrical Conductivity	70 mS/cm
2	k	Dissolution constant	3.35×10^{-11} $m^3/A{\cdot}s$
3	ρ_w	Density of anode	8000 kg/m^3
4	v	Applied potential	9 V
5	IEG	Inter Electrode Gap	10 µm
6	z	Valency number of ions	2
7	F	Faraday's constant	96500 C/m
8	ε_0	Electrical field constant	1
9	ε_r	Relative permittivity	48

Faraday's equation ($V_n=A{\cdot}J/z{\cdot}F{\cdot}\rho w$) is used to find normal dissolution rate i.e. Vn in. In above equation A is the atomic weight, z is valency, F is Faraday's constant equal to 96500 C/mol, ρ is the density of work piece material and J is current density vector in the normal direction at tool surface, it can be obtained from Eq. (2).

$$V_n=(A{\cdot}J)/(z{\cdot}F{\cdot}\rho\_w) \quad (4)$$

In above expression, current density J is variable parameter, all other parameters are constants and can be expressed as

$$V_n= -(k){\cdot}J \quad (5)$$

Where $k = (A/z{\cdot}F{\cdot}\rho w)$ dissolution constant for Anode material. We know that most commercial materials in use are alloys. Thus, the expression of Vn modified for alloy material is

$$V_n=-1/F\ (\sum i((W_i/100)A_i)/\rho\ (w_i{\cdot}Z_i)\ ) \quad (6)$$

Where i is the summation index denoting number of elements in the alloy and W_i is the weight percentage of a particular element in the alloy. Spacing between two electrodes is fixed to 200 µm. Diameter of tool used in geometry is 90 µm. Boundary conditions are given as follows (see Figure 1),

At workpiece surface

$$v\big|\,\Gamma_{16} = 0\ V \quad (7)$$

At tool surface,

$$v\big|\,\Gamma_{9,10,11,12} = \text{-Ve pulses} \quad (8)$$

Mesh velocity in x direction,

$$V_x\big|\,\Gamma_{1,2,3,4,5,6,7,8,14,15,17,18}= 0 \quad (9)$$

Mesh velocity in y direction

$$V_y\big|\,\Gamma_{9,10,11,12,13,19} = 0 \quad (10)$$

All the outer surfaces are insulated

$$n.J\big|\,\Gamma_{1,2,3,4,5,6,7,8,17,18} = 0 \quad (11)$$

Feed is given to tool surface,

$$V_y\big|\,\Gamma_{(20,21,22,23,)}=7\ \mu m/sec \quad (12)$$

Mesh degradation velocity is given by faradays law

$$V_n\big|\,\Gamma_{16} = -k.(ec.nJ) \quad (13)$$

For SS304 material dissolution constant value i.e. k is equal to 3.35 x 10-11 $m^3/A{\cdot}s$

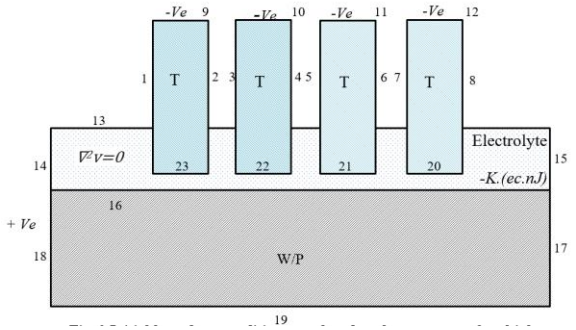

Fig. 1 Initial boundary conditions employed to the geometry of multiple electrodes, electrolyte and the workpiece

Individual pulses of 10 µs pulse width and 25 % duty ratio is applied at each electrode. Workpiece potential is kept to zero and negative pulses are applied at each electrode. Figure 2 shows time dependent current density plot at each electrode, Current density is different at electrodes because of distributed pulse at each electrode.

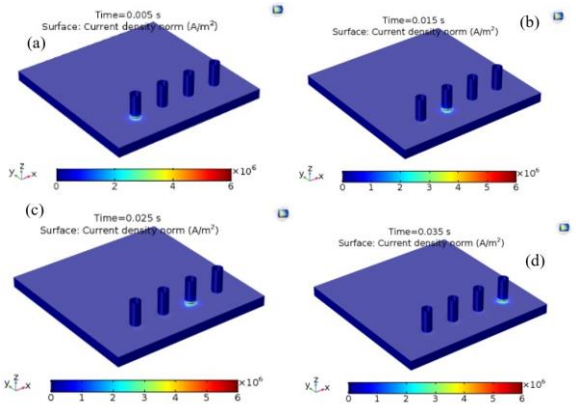

Figure 2: Current density on sequentially distributed pulses to four electrodes during EC drilling

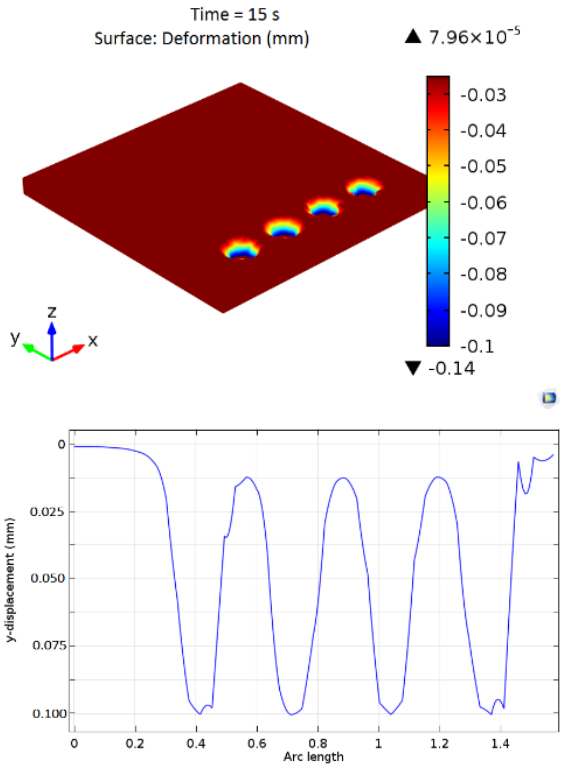

Figure 3 Final simulated profile of holes drilled by 4 electrodes in 15s.

Distribution of current density is Gaussian; maximum at center of electrode and gradually decreasing along the radial direction. Observed maximum current density is 2.5 x 106 A/m2 at the center of tool. Fig. 3 shows the final machining profile of holes. Average diameter of holes obtained is 158.58 µm with the tool of 90 µm at input voltage of 9V and at other parameters as shown in Table 1.

EXPERIMENTAL INVESTIGATIONS

Figure 4 shows the experimental setup and parts employed in fabricating the setup of sequentially distributed pulsed multiple electrode electrochemical micromachining center. Setup has been built by modifying a 3-axis CNC stage by mounting a cantilever tool arm, electrolyte feed tube and an acrylic tank for collecting the electrolyte. Experiments are per-formed on SS304 foil of thickness 100 µm. Four parallel tool of tip diameter 90 µm is used for the drilling process. NaNO3 is used as electrolyte of conductivity 70 mS/cm. Initial spacing between two electrodes used is 1.8 mm. These socket connectors are fabricated with isolated electrical contacts; which are used to supply pulse voltage, detail image of tool holder is shown in Fig. 5(a) and (b).

Development of the power supply

IRFP150N MOSFET is used to generate output pulses. MOSFET is driven by high frequency pulse output of Arduino UNO microcontroller through MOSFET driver TC4429. ATMEGA 328 microcontroller is used to generate switching pulses. Buck converter is used to power up microcontroller with 5V DC supply. Detailed circuit diagram of power supply is shown in Fig. 6.

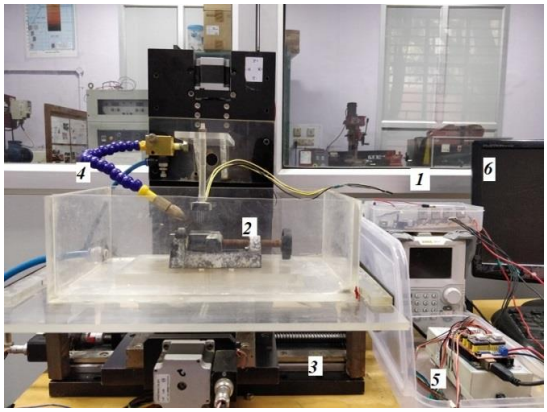

Figure 4: Experimental setup used in machining, 1 Pulse power unit, 2 Electrolyte tank, 3 Linear slides, 4 Electrolyte nozzle, 5 Controller for slides, 6 GUI.

Figure 10 shows the distribution of microsecond pulses to the four electrodes. As it can be seen from the image, at the instant where pulse is being off in first electrode after 5 µs, another pulse is sent to electrode 2. In the same sequentially pulses are distributed in all four electrodes continuously. Where there is no pulse-off time since at least one electrode is machining at any instant. The distribution of pulses can be modified as the number of electrodes increases such as two alternative electrodes can get the same pulse in case of large number of tools.

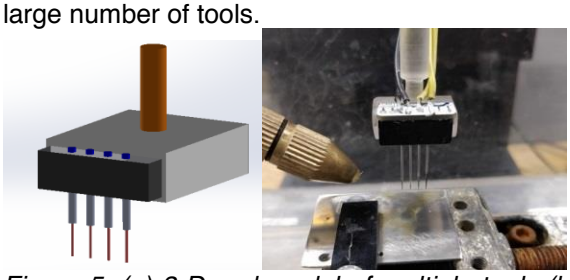

Figure 5: (a) 3-D cad model of multiple tools (b) Multiple tools used in experiments pulses.

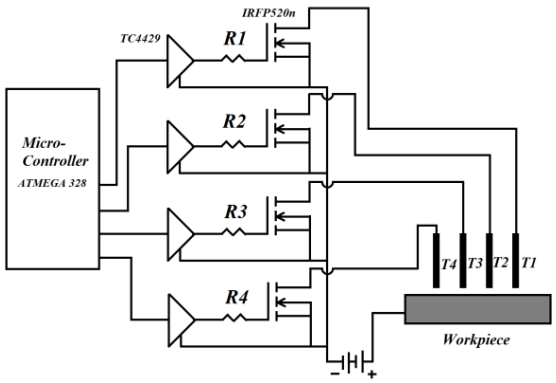

Figure 6: Circuit diagram of power supply for distribution of four pulses.

Figure 7: Screenshot of sequential distribution of pulses at 54 KHz frequency.

Distributed pulses as shown in Figure 7 through a screenshot of oscilloscope during machining.

Parametric Analysis

Table 2 shows entrance and exit diameters of holes at increasing feed rate and voltage.

TABLE 1 Experimental results at increasing feed and input voltage.

Feed	Diameters at varying input voltage		
	9V	10V	11V
Entrance at F = 0.3 mm/min	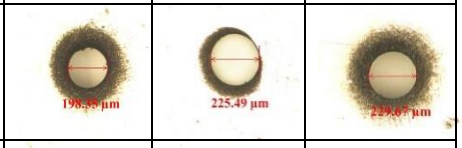		
Exit diameter at F= 0.3 mm/min	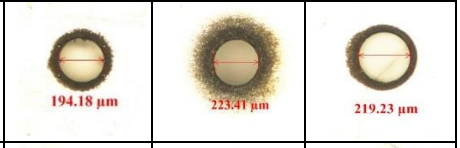		
Entrance Diameter at F = 0.4 mm/min	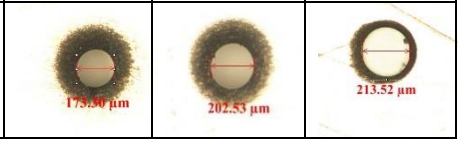		
Exit diameter at F = 0.4 mm/min	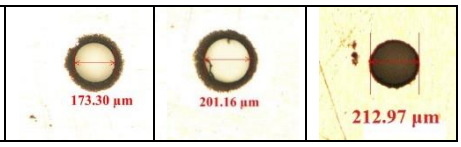		

Figure 8 shows average entrance diameter of drilled hole for different feed rate. Maximum overcut value observed is 139 µm at 11 V and 0.3 mm/min feed and minimum value of overcut is 81 µm; observed at 9 V and 0.5 mm/min feed. For minimum hole diameter, machining condition of 9 V and 0.5 mm/min feed was opted and array of holes are drilled in SS304 foil with spacing of 200 µm. Micro-holes of 121 µm diameters are machined by using 65 µm tool tip diameter (overcut of 56 µm is obtained). Figure 9 shows the entrance and exit diameters of holes. From Figure 9(a) and 9(b), it can be seen that entrance diameter and exit diameter of drilled holes are almost same.

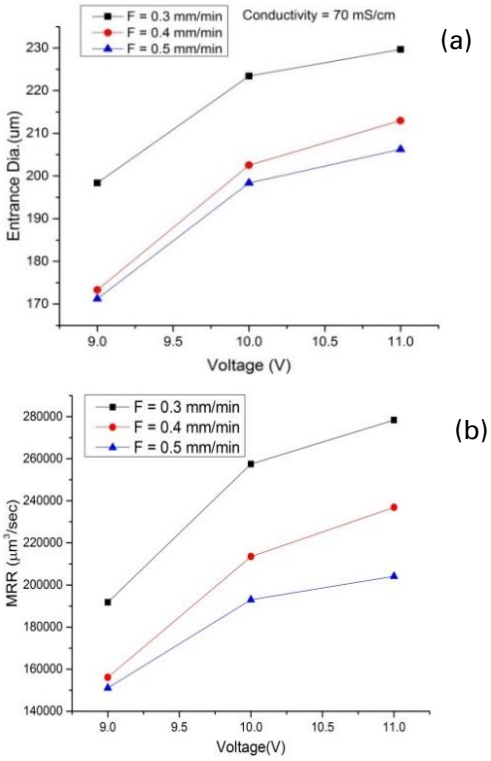

Figure 8: Variation in diameters of holes and average (a), and MRR at different feed rates and voltages (b).

Fabrication of micro mesh sieve

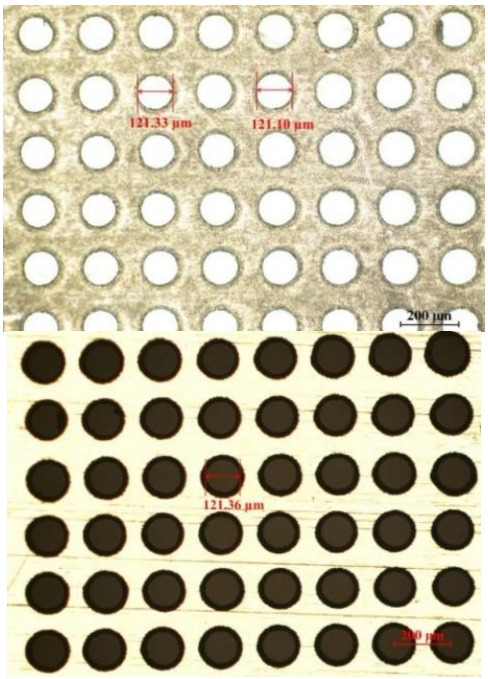

Figure 9: Optical microscopy images of micro-holes drilled at entrance (left) and exit (right).

Holes are exact concentric to the centre point. Burrs around the edges of drilled hole is absent. Stray current effect is more if the side walls of tool are non-insulated, pitting of area nearby to holes can be seen from Figure 9(a). Pitting due to stray current at the back side can be seen from Figure 9 (b). This is due to; as tool comes out of foil, stray current from tip starts to machine nearby area.

Table 3 demonstrates the comparison of simulated and experimental results. The deviation from the predicted diameters ranges from 8 to 11 %, which shows a close fit between the analytical prediction and experimental results. Figure 10 shows an image of sieve fabricated through piercing micro-holes of 150 µm diameter and 200 µm pitch.

Table 3: Comparison of simulated and experimental results

Machining Voltage	Simulated Dia.	Experimental Dia.	% Deviation
9	158.56	173.3	8.505482
10	179.56	202.53	11.34153
11	195.18	212.97	8.353289

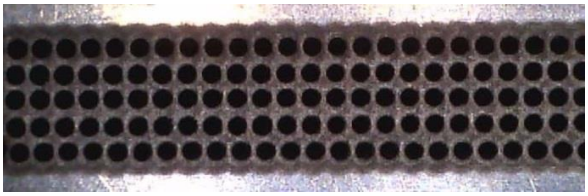

Figure 10: Micrographic image of micro-hole array with diameter of 150 µm and spacing between two holes of 200 µm.

CONCLUSION

Simulations and experiments were conducted on the electrochemical drilling by multiple electrodes. The simulated results of holes drilling was fits closely with experimental drilled holes. The deviation in simulation and experiments observed was 8-11 %. The difference in overcut is significantly high due the assumptions made in the simulations do not consider the effect of electrochemical by-products such as gas bubbles, temperature and sludge. Due to distribution of voltage pulses, load on power supply is found to be decreased to one fourth of original. By using optimum voltage and feed rate, micro hole with precision is machined by the process. By use of 4 electrodes; machining time is reduced by 75% and productivity is increased by 300%. Different sized array of micro-holes with high circularity index are successfully drilled by ECM process. Micro-sieves of 120 µm and 153 µm are fabricated with standard deviation of 0.453 µm from mean. This accuracy confirms the use of process for industrial applications where micro-holes are required.

REFERENCES

[1] D. M. Allen, H. J. A. Almond, J. S. Bhogal, A. E. Green, P. M. Logan, and X. X. Huang, "Typical metrology of micro-hole arrays made in stainless steel foils by two-stage micro-EDM," *CIRP Ann. - Manuf. Technol.*, vol. 48, no. 1, pp. 127–130, 1999.

[2] D. Patel, V. Jain, and J. Ramkumar, "Micro texturing on metallic surfaces: State of the art," *Proc. Inst. Mech. Eng. Part B J. Eng. Manuf.*, 2016.

[3] S. T. Chen and T. S. Luo, "Fabrication of micro-hole arrays using precision filled

wax metal deposition," *J. Mater. Process. Technol.*, vol. 210, no. 3, pp. 504–509, 2010.
[4] "ECM Technologies:Product and showcase." [Online]. Available: http://electrochemicalmachining.com/showcase/micro-reactor. [Accessed: 20-May-2018].
[5] and J. L. Huan Huang, Lih-Mei Yang, "Micro-hole drilling and cutting using femtosecond fiber laser," *Opt. Eng. 53(5), 051513 (May 2014)*.
[6] G. Zhu, J. Bai, Y. Guo, Y. Cao, and Y. Huang, "A study of the effects of working fluids on micro-hole arrays in micro-electrical discharge machining," *Proc. Inst. Mech. Eng. Part B J. Eng. Manuf.*, vol. 228, no. 11, pp. 1381–1392, 2014.
[7] F. Xiaolong, W. Xindi, W. Wei, Q. Ningsong, and L. Hansong, "Electrochemical drilling of multiple small holes with optimized electrolyte dividing manifolds," *J. Mater. Process. Technol.*, vol. 247, no. April, pp. 40–47, 2017.
[8] B. H. Kim, B. J. Park, and C. N. Chu, "Fabrication of multiple electrodes by reverse EDM and their application in micro ECM," *J. Micromechanics Microengineering*, vol. 16, no. 4, pp. 843–850, 2006.
[9] M. H. Wang and D. Zhu, "Fabrication of multiple electrodes and their application for micro-holes array in ECM," *Int. J. Adv. Manuf. Technol.*, vol. 41, no. 1–2, pp. 42–47, 2009.

A PARALLEL-AXIS GRINDING METHOD FOR LARGE ASPECT RATIO INTERNAL THREADS

Guicheng Wu[1], Yuefeng Li[1], Zenghui Yang[2], Zhongyu An[1], Guanglin Wang[1]
[1]School of Mechatronics Engineering
Harbin Institute of Technology
Harbin, Heilongjiang, China
[2]Beijing Research Institute of Precise Mechatronics and Controls
Beijing, China
Corresponding Author: Yuefeng Li, Guanglin Wang
E-mail: yuefengli@hit.edu.cn, glwang@hit.edu.cn

INSTRUCTIONS

Threaded connection is an important mechanical fastening method，which is widely used in the fields of aerospace, automated processing equipment, instrumentation, etc. The precision of thread affects the joint strength directly, which makes thread processing particularly important. The machining method of internal threads can be divided into tapping, extrusion, milling, turning, grinding and other methods [1-4]. Among them, thread grinding is a high-precision machining method, and it is an effective choice for internal threads with strict tolerance requirements. The grinding of internal threads is generally carried out on a special grinding machine. In addition, during the grinding process, the grinding wheel can be accurately shaped, and it can be quickly reshaped as needed after the wheel is formed [5-6].

In order to make the internal thread have a precise tooth shape, the grinding wheel is generally grounded at a certain angle to the central axis of the internal thread, so the mounting position of grinding wheel must be inclined at a corresponding angle according to the helix angle of the thread. The main difficulty in grinding the internal threads with deep holes is the mutual restriction of the helix angle and the bore diameter. In general, the ratio of the length to the diameter of the grinding wheel shaft does not exceed 7:1 [7-8]. As the length of the thread increases or the diameter of the hole decreases, the grinding wheel and the workpiece will collide with the deepening of grinding. Therefore, it is difficult to grind the internal thread with a large length to diameter ratio. In recent years, with the integration of electric steering gear and the increase of power density, the aspect ratio index of the inverted planetary roller screw nut integrated in the long-stroke linear electric steering gear is continuously improved. The ordinary inclined angle grinding can not meet the processing requirements of its internal thread.

In the field of internal thread grinding, most of the research is about the calculation of the minimum interference tilt angle and the simulation of the tilt grinding process, which are not suitable for the machining of large length to diameter internal threads [9-10]. Hang Gao et al. [11] studied the internal thread grinding method for micro-brittle materials, which used parallel-axis grinding method. They establish the mathematical model of the principle error. The parameters of the grinding wheel were optimized and corrected according to the simulation analysis results. Finally, the experimental verification was carried out. The thread pitch diameter precision reaches the H4 level. However, the grinding process and theoretical analysis are complicated, and it cannot be widely applied.

This article presents a parallel-axis grinding method for large length to diameter internal threads. First, a parallel-axis grinding model was established to describe the characteristic parameters of the grinding process. Then, a grinding wheel dressing calculation method is given to avoid the formation of interference. Finally, the feasibility of parallel shaft grinding is verified by an example calculation.

PARALLE-AXIS GRIDING METHOD OF INTERNAL THREADS

The grinding of internal threads is a process for machining internal thread, which uses a forming wheel with helical feed. The movement process is shown in Figure 1. The center axis of the internal thread of the nut is parallel to the center

axis of the grinding wheel, and the eccentricity is *e*. The eccentricity *e* is half the difference between the major diameter of the internal thread and the maximum diameter of the grinding wheel. On one hand, the nut makes a slow rotary motion around its center axis, and the grinding wheel makes a linear feed motion along its own center axis. On the other hand, the grinding wheel performs a high-speed rotational motion along its own axis to complete the grinding task. The process parameters of the grinding are as follows: the rotation speed of the nut is *n* (r/min), the rotation speed of the grinding wheel is *g* (r/min), the linear feed speed of the grinding wheel is *f* (mm/min). The pitch of the internal thread is *P* (mm), the screw number is *h*. The relationship of *f*, *n*, *P*, *h* is given as:

$$f = nPh \tag{1}$$

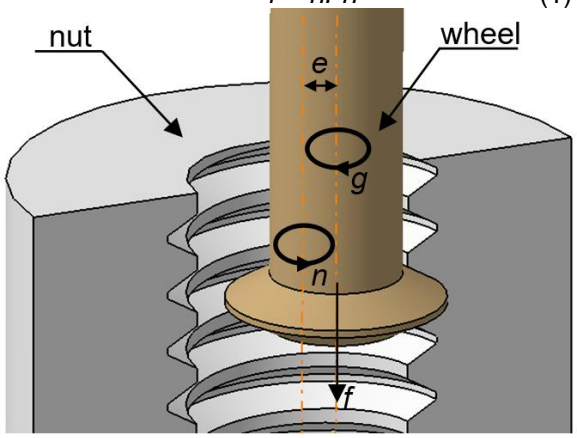

FIGURE 1. Schematic diagram of movement process of grinding

The parametric equation of the thread face is as follows:

$$\begin{aligned} X &= R \cdot \cos(2\pi t) \\ Y &= R \cdot \sin(2\pi t) \\ Z &= Pht + R - D_1 / 2 \end{aligned} \tag{2}$$

In the formula, *R* is a variable, *R* is continuously changing between $D_1/2$ and $D/2$. D_1 is the minor diameter of the internal thread, and *D* is the major diameter of the internal thread. *Ph* is the lead of the internal thread, *t* is a parameter variable, the value of *t* is (0,1).

The initial cross-sectional shape of the grinding wheel is the same as the internal thread profile, which is a diamond shape, and the angle α is consistent with the thread profile angle, as shown in Figure 2. In order to ensure that the grinding wheel can be deeply ground, the maximum diameter of the grinding wheel should be smaller than the minor diameter; at the same time, to ensure the grinding of the entire tooth surface, the minimum diameter of the grinding wheel should be greater than twice the depth of the thread; the difference between the diameter of the grinding wheel and the diameter of the wheel rod should be greater than twice the tooth depth of the thread, all these are given as: $D\text{-}D_1 < D_{wheel} < D$, $D_{wheel}\text{-}d_0 > D\text{-}D_1$. The D_{wheel} is the largest diameter of the grinding wheel, and d_0 is the diameter of the grinding wheel rod. In order to ensure the rigidity of the grinding wheel and reduce the vibration of the grinding wheel during deep grinding, d_0 should be as large as possible.

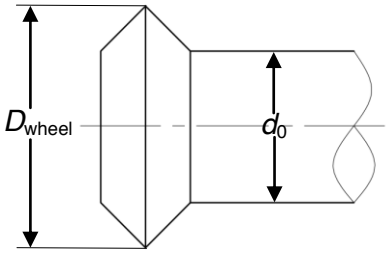

FIGURE 2. Schematic diagram of grinding wheel

When the form-grinding wheel whose profile is consistent with thread profile, there can be difference between the actual enveloping surface generated from the wheel motion and the hypothetical metric thread. Due to this error, the thread dimension may exceed the tolerance and reduce the thread precision. On the condition that the relative motion of the grinding wheel and the workpiece is constant, changing the shape of the wheel contour is a feasible method.

THE DRESSING CALCULATION METHOD OF GRINDING WHEEL

To avoid undercutting, the diameter or angle of the grinding wheel needs to be trimmed. In this paper, the method of minor dressing along the radial direction of the grinding wheel is selected to ensure the normal grinding. The trimming section is shown in Figure 3.

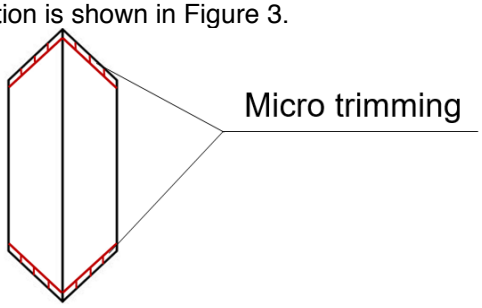

FIGURE 3. Schematic diagram of trimming section of grinding wheel

Before the dressing is performed, the amount of interference between the wheel and the internal thread needs to be calculated. Since the grinding wheel is symmetrical, it is only necessary to calculate the amount of interference on one side. The specific calculation method is as follows:

1. According to the internal thread parameters and machining precision of the nut, the spatial position of the helicoid in each lead is calculated on the basic of the thread surface equation, which is used to calculate interference distance in the following steps;

2. The diamond grinding wheel is divided into several circular sections at equal intervals along the axial direction, and the interval should be as small as possible, which is shown in Figure 4.

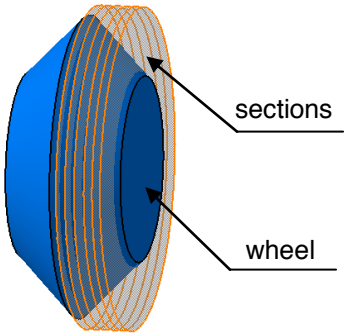

FIGURE 4. Schematic diagram of grinding wheel section

3. On each circular section, find all the points on the thread surface corresponding to the section. Calculate the distance between each point and the center of the section thread according to the two-point space distance formula, and subtract the outer circle radius value of the grinding wheel section. This is the interference distance;

4. Repeat the above steps to calculate the interference distance for each circular section.

5. The original grinding wheel is subtracted from the interference distance value in the radial direction and fitted into a curve, which is the final shape of the grinding wheel.

Because the amount of interference per section of the grinding wheel is different in the radial direction, the amount of calculation is large and needs to be achieved by a specific procedure. The flow chart of program is shown in Figure 5.

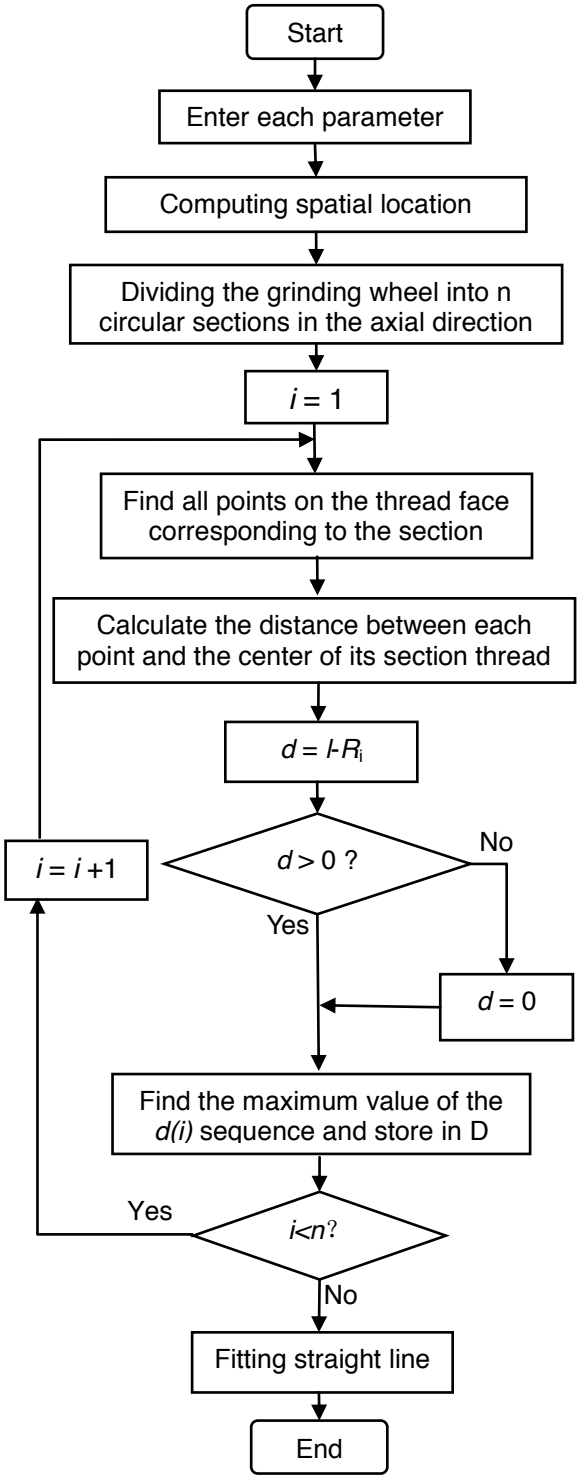
Start
Enter each parameter
Computing spatial location
Dividing the grinding wheel into n circular sections in the axial direction
i = 1
Find all points on the thread face corresponding to the section
Calculate the distance between each point and the center of its section thread
d = l-Ri
d > 0 ?
No
Yes
i = i +1
d = 0
Find the maximum value of the d(i) sequence and store in D
Yes
i<n?
No
Fitting straight line
End

FIGURE 5. The flow chart of program

CALCULATION AND ANALYSIS OF SPECIFIC EXAMPLKES

Take an internal thread as an example, the major diameter is 20.68mm, the minor diameter is 19.68mm, the pitch is 1mm, and the screw number is 3. The maximum diameter of the grinding wheel is 15mm. Using the CATIA software, draw a thread within one lead and assemble with the wheel. The result is shown in Figure 6. As can be seen from the figure, the interference exists in all radial directions of the grinding wheel.

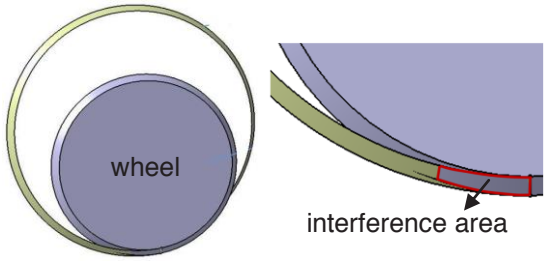

(a) Assemble (b) Partial enlargement

FIGURE 6. Schematic diagram of interference area

The maximum interference distance is calculated by the program in different wheel diameters. The diameter of the grinding wheel varies from 2 to 16 mm, and the curve of the maximum interference distance as a function of the diameter of the grinding wheel is shown in Figure 7.

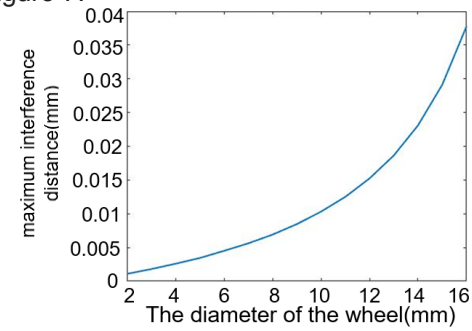

FIGURE 7. *The curve of the maximum interference distance*

As can be seen from the above figure, the maximum interference distance increases as the diameter of the grinding wheel increases. When the diameter of the grinding wheel is 2 mm, the interference distance is 1.1 μm; when the diameter of the grinding wheel is 16 mm, the interference distance is 37.8 μm. It can also be seen that the curvature of the curve gradually increases, indicating that the magnitude of the interference distance increases as the diameter of the grinding wheel increases.

When the maximum diameter of the grinding wheel is 16mm, the diameter of the grinding part varies from 15 to 16mm. The interference of the distance section is calculated by the program, and the interference distance is subtracted from the radius of the original grinding wheel, which is the final shape of the grinding wheel. This is shown in Figure 8, the red segment is the edge shape of the wheel after trimming.

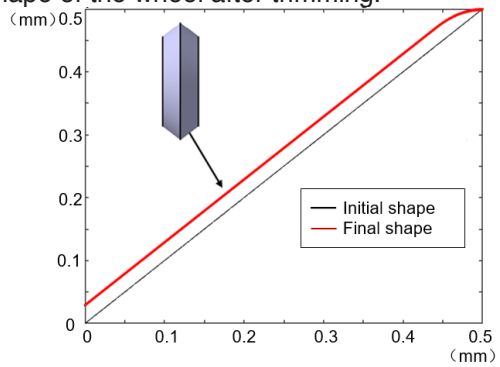

FIGURE 8. Final shape of the grinding wheel

It can be seen that except for the end part, the interference distance of the grinding wheel on each section does not change much and can be regarded as equal. Since the boundary area portion is not applicable when searching for a point corresponding to the section in the program, the interference distance is suddenly reduced to zero at the end portion. It can be seen from the trend that the interference distance does not change much over the entire range, so the interference distance of the entire segment can be simplified into a straight line, which is convenient for processing.

CONCLUSIONS

For the grinding of large diameter to internal thread, this paper proposes a suitable parallel-axis grinding method. Firstly, the movement model of grinding wheel and workpiece in the parallel-axis grinding process was established, and the shape of the grinding wheel was explained. Then, the grinding wheel dressing calculation method is described in detail. Finally, the calculation and analysis of the specific internal thread is carried out. This method has high applicability to internal thread grinding and can be widely used. The theoretical analysis has been completed and the experiment will be

carried out in the follow-up to verified the correctness and universality of the theory.

REFERENCES

[1] Khoshdarregi MR, Altintas Y. Generalized modeling of chip geometry and cutting forces in multi-point thread turning[J]. Int J Machine Tools Manuf ,2015, (98):21–32.

[2] Fromentin G, Poulachon G . Modeling of interferences during thread milling operation[J]. Int J Adv Manuf Technol , 2010, 49(1):41–51.

[3] Lee SW, Kasten A, Nestler A. Analytic mechanistic cutting force model for thread milling operations. [J] Procedia Cirp, 2013, 8(8):546–551.

[4] Chiang CJ, Fong ZH, Tseng JT. Computerized simulation of thread form grinding process[J]. Mech Mach Theory ,2009,44(4):685–696.

[5] Lee SW, Nestler A.Simulation-aided design of thread milling cutter[J]. Procedia CIRP,2012, 1(1):120–125.

[6] Chiang CJ, Fong ZH. Undercutting and interference forthread form grinding with a tilt angle[J]. Mech Mach Theory,2009, 44(11):2066–2078

[7] Wu YR, Hsu WH.A general mathematical model for continuous generating machining of screw rotors with worm-shaped tools[J]. Appl Math Model,2014, 38(1):28–37

[8] Araujo AC, Silveira JL , Jun MBG, Kapoor SG, DeVor R. A model for thread milling cutting forces[J]. Int J Machine Tools Manuf ,2006,46(15):2057–2065

[9] Chiang C J, Fong Z H,Tseng J T. Computerized simulation of thread form grinding process[J]. Mechanism & Machine Theory, 2009, 44(4):685-696.

[10] Chiang C J, Fong Z H. Undercutting and interference for thread form grinding with a tilt angle[J]. Mechanism & Machine Theory, 2009, 44(11):2066-2078.

[11] Gao H, Lu S, Yang A, et al. A methodology for helical mill-grinding of tiny internal threads made of hard brittle materials[J]. International Journal of Advanced Manufacturing Technology, 2016, 91 (1-4):1-13.

DEVELOPMENT OF AN AUTOMATIC GRINDING SYSTEM FOR SERVO VALVE SPOOL THROTTLING EDGE

Hua Guo[1], Zenghui Yang[2], Yuefeng Li[3], Guanglin Wang[3]
[1]School of Mechanical & Power Engineering
Harbin University of Science and Technology
Harbin, Heilongjiang, China
[2]Beijing Research Institute of Precise Mechatronics and Controls
Beijing, China
[3]School of Mechatronics Engineering
Harbin Institute of Technology
Harbin, Heilongjiang, China
Corresponding Author: Yuefeng Li
E-mail: yuefengli@hit.edu.cn

INSTRUCTIONS

The electro-hydraulic servo control system is the executive component of the launch vehicle and other rocket control systems, which controls the attitude and trajectory of the rocket. The electro-hydraulic servo valve is the core of the servo system. It transforms the low-power electrical signal from the pre-stage to the power stage spool movement. Then the direction and magnitude of the high-pressure fluid flow to the hydraulic actuator are controlled by the movement of the spool. Finally, the piston rod of the actuator pushes the engine to swing, so that the precise control of the rocket's attitude and trajectory can be realized [1-4]. The typical structure of the servo valve is the slide valve structure, which has the advantages of simple structure, high power output, high reliability and stable dynamic performance.

The spool valve is the core component which is generally composed of a valve core and a valve sleeve. Under the pressure difference generated by the two control nozzle chamber, the valve core moves to form an opening and output high pressure oil. At the same time, the torque which is proportional to the valve core displacement acts on the armature assembly through the feedback rod. When the torque is balanced with the electromagnetic torque and others, the valve core will stop moving so that the displacement of the valve core can be proportional to the input current. Thus the function of electro-hydraulic conversion is achieved.

The structure of spool valve is shown in Figure 1, when the left displacement of the spool core exceeds the overlap value, the valve ports A and C are opened, and conversely, the valve ports B and D are opened. Therefore, the control action of the servo valve is finally reflected in the axial relative position [5-6].

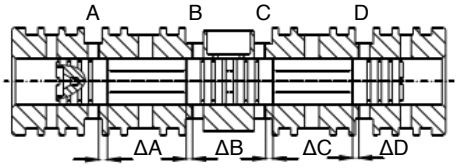

FIGURE 1. Schematic diagram of spool valve.

The overlap amount of spool valve is the key characteristic of the servo valve which means that the performance of the servo valve will be affected whether the overlap is too small or too much. Accordingly, the grinding of overlap is the crucial process in the servo valve manufacturing process. At present, the common method is to grind the working edge of the valve core with a precision cylindrical grinder, and the lap measurement test bench is applied to detect the actual value of the overlap. Then grinding the spool valve according to the test result until the overlap amount meets the requirements [7]. The precision grinding tool setting is divided into two types, the contact tool setting and the non-contact tool setting, and the non-contact tool setting method is widely used because of its mature technology.

At present, the commonly used micro-feed system utilizes the principle of linear motor, mechanical transmission, physical elastic deformation and piezoelectric ceramic electrostrictive to achieve micro-feeding. The mechanical transmission micro-feed technology is mainly applied to the machine tool, and the common mechanisms mainly include precision screw, turbine rod and rack and pinion [8-9]. The micro feed technology of piezoelectric ceramics is to use the strain of material to generate micro-feed which is proportional to the strength of electric field. This technology has been widely used in ultra-precision machining, robotics, microelectronics and aerospace [10-13].In this paper, the axial grinding technology of spool core is mainly studied to solve the difference in the axial dimension of the spool core, improve the grinding precision and efficiency.

DESIGN OF AUTOMATIC GRINDING SYSTEM FOR SERVO VALVE SPOOL THROTTLING EDGE

At present, it is common to use the Swiss precision cylindrical grinding machine, the grinding wheel contact tool setting and the micro -feed of the machine tool table to realize the working edge grinding of the valve core which will result in low axial feed accuracy and poor dimensional consistency. An automatic grinding system for servo valve spool throttling edge is designed to solve those problems.

Non-contact measurement scheme based on acoustic emission sensor

The principle of acoustic emission measurement is to utilize the acoustic emission sensor as the medium to collect the acoustic emission signal during the grinding process and then calculate the signal through the control system to obtain the measurement result. The sensor detects the change in the vibration frequency when the grinding wheel and the spool are in contact with each other, and transmits the detection signal to the control system. According to the readings of the screen, the starting point of the grinding is determined, the grinding amount is measured by the machine scale and the processing is judged by the reading which is shown in Figure 2.

This scheme combines the original feed device of the machine with the newly added micro-feed device to expand the automation level of grinding. In addition, it has good adaptability to the machine tool and simple operation, which can reduce the tool setting error and improve the tool setting precision as well as axial grinding precision.

Theoretical basis of acoustic emission tool setting

The source of acoustic emission signals during grinding is shown in Figure 3, (a) shear deformation of the parts during grinding; (b) friction between the sand grains of the grinding wheel and the surface of the parts; (c) breakage of the grinding wheel abrasive; and (d) the noise produced by the grinding wheel. And the shear deformation of parts is the main cause of acoustic emission [14].

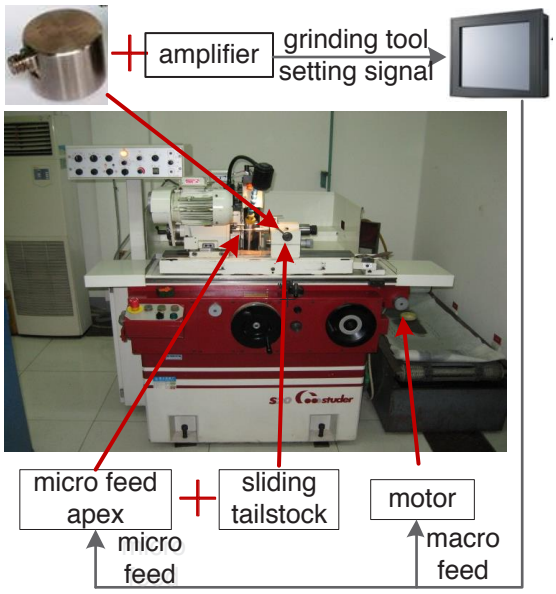

FIGURE 2. Schematic diagram of acoustic emission scheme.

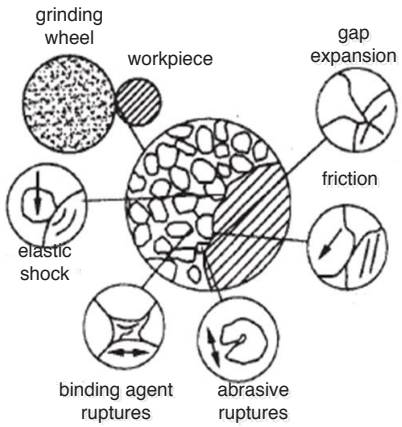

FIGURE 3. Source of acoustic emission signals during grinding.

The relationship between the RMS of acoustic emission signal and the plastic deformation power is,

$$RMS^2 = k\omega = k\sigma V\varepsilon \quad (1)$$

where k is the conversion coefficient between the plastic deformation power and the RMS of acoustic emission signal, σ is the grinding force, ε is the constant strain, V is the volume of plastic deformation.

According to the Merchant two-dimensional model and related calculations, the power Ws of the first deformation zone can be calculated,

$$W_S = \tau b a_c \frac{\cos\gamma}{\sin\phi\cos(\phi-\gamma)} V \quad (2)$$

where τ is the workpiece strength, b is the grinding width, a_c is the grinding feed, γ is the normal angle between the front and the machined surface, φ is the shear angle.

The power Wc of the second deformation zone can be calculated,

$$W_C = k\tau b a_c \frac{\sin\phi}{\cos(\phi-\gamma)} V \quad (3)$$

The RMS formula of acoustic emission signal can be obtained by combining equation (2) and equation (3),

$$RMS = \sqrt{\tau b a_c \left(k\frac{\sin\phi}{\cos(\phi-\gamma)} + \frac{\cos\gamma}{\sin\phi\cos(\phi-\gamma)} \right) v} \quad (4)$$

As a complex waveform signal, the acoustic emission signal is mixed with various information of the transmission source, such as the size of the sound, the position of the sound source and the frequency. The schematic diagram of the acoustic emission signals at various stages of grinding is shown in Figure 4. The grinding tool setting points can be judged based on the characteristic parameters of the acoustic emission signals.

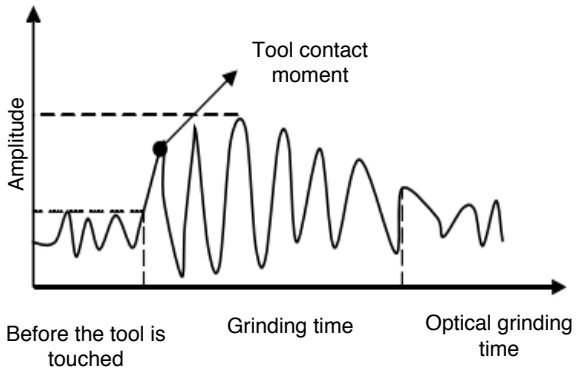

FIGURE 4. Acoustic emission signals at various stages of grinding.

DESIGN AND MANUFACTURE OF MICOR-FEED APEX

The mechanical structure of the precision micro-feed apex as the feed device is shown in Figure 5.

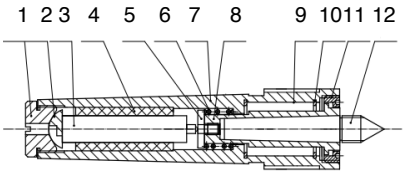

FIGURE 5. Mechanical structure of the micro-feed apex. 1- Pre-tightening nut; 2-Hemisphere pad; 3-Piezoelectric ceramic actuator; 4-Sleeve; 5-Plane screw; 6-Pretighten spring; 7-outer cylinder; 8-Inner cylinder; 9-Linear sliding bearing; 10-Inner ring; 11-End cap; 12-Front apex.

The principle of the micro-feed apex is to make the piezoelectric ceramic drive with different strength of power supply, so that the deformation can be shortened or elongated to push the sleeve and the apex to achieve the propose of microfeed. The micro-feed apex requires a maximum elongation of 40μm, a minimum displacement of 0.5μm, and sufficient stiffness, less damping and less creep. The key parts of the micro-feed apex are the outer cylinder, the inner cylinder and the front apex. These components require high precision and complex processing technology, and the manufacturing accuracy will affect the precision of the entire micro-feed device. The parts and assembly drawing of the micro-feed apex is shown in Figure 6.

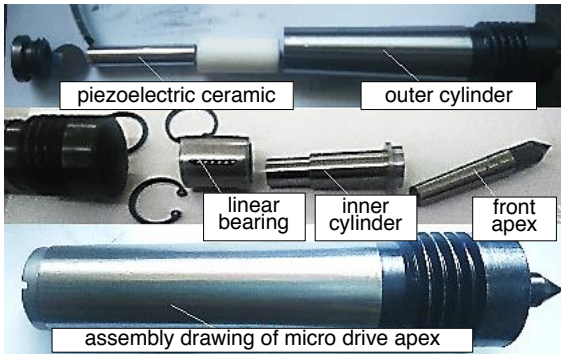

FIGURE 6. Parts and assembly drawing of the micro-feed apex.

EXPERIMENTS

Characteristic experiments of piezoelectric ceramic actuator

Under the condition of open-loop control, there are two kinds of characteristics of piezoelectric ceramic actuator which are hysteresis and creep characteristics. The hysteresis characteristic means that the boost curve and the buck curve of the actuator are nonlinear and do not strictly coincide with each other. Due to the existence of hysteresis characteristic, the output displacement of the piezoelectric ceramic after compression is deviated from the ideal value [15, 16]. The hysteresis curve of selected piezoelectric ceramic actuators under experimental conditions is shown in Figure 7.

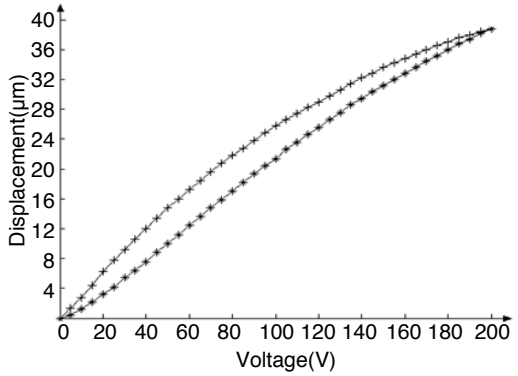

FIGURE 7. Hysteresis loop of the piezoelectric ceramic actuator.

The creep characteristic means that under a certain voltage input, the output displacement of the piezoelectric ceramic reaches an initial value and then starts to slow down with a long time until reaches a stable value. The creep characteristic reflects the hysteresis of output displacement of the piezoelectric ceramic to the input voltage. The displacement error curve of the chosen piezoelectric ceramic is shown in Figure 8.

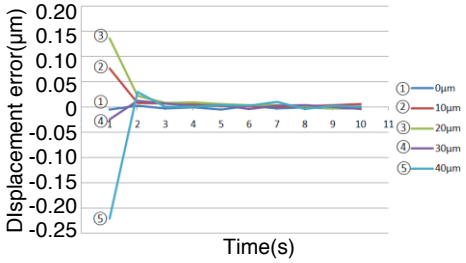

FIGURE 8. Displacement error curve of the chosen piezoelectric ceramic.

Automatic grinding experiments of servo valve spool throttling edge

The system which includes industrial control machine, motor drive mechanism, preamplifier, acoustic emission sensor, piezoelectric actuated micro-feed apex and data acquisition card is shown in Figure 9.

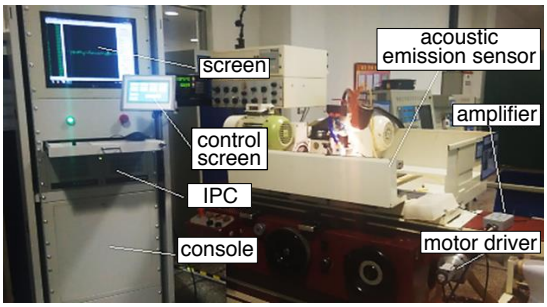

FIGURE 9. Automatic grinding system.

The test procedure is as follows, firstly, the system is installed on the S20 Swiss precision cylindrical grinding machine. Then, 20 pieces of valve cores are selected for the grinding test. After grinding, the amount of overlap and the grinding time are recorded. Finally, the experimental data are analyzed and are shown in Figure 10.

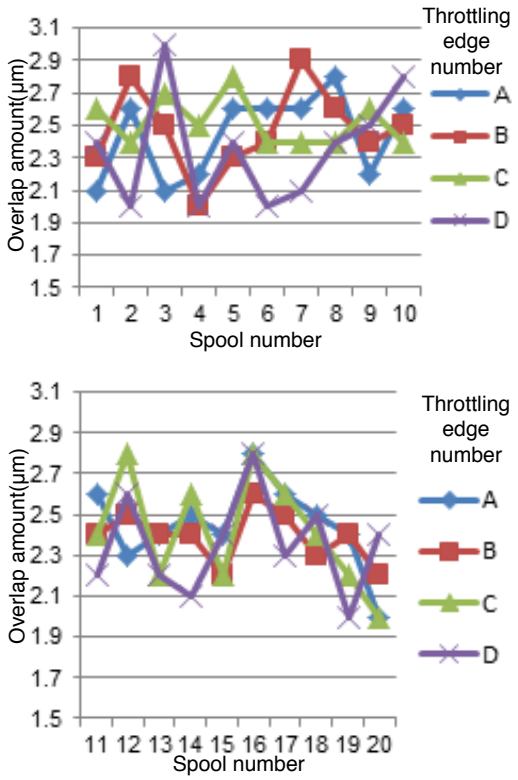

FIGURE 10. Test results of grinding experiment.

According to the above diagram, it can be seen that the overlap amount of working edges of the 20-piece cores all meets the requirements of 2-4μm. In addition, it can be found that the number of grinding operations of the valve core working side is reduced from 3-4 times to 2 times, which makes the efficiency raises by at least 30%.

CONCLUSIONS

A set of grinding system for the servo valve core with acoustic emission tool setting technology, piezoelectric ceramic micro-feed and on-line axial displacement detection is designed in order to solve the problems of artificial tool setting error, low grinding efficiency and low precision of axial trace feed in the grinding process of servo valve core. Subsequently, the valve core overlap grinding test was carried out to verify the processing indicators of this system. The experimental results showed that the system met the design and application requirements.

REFERENCES

[1] Jones J C. Developments in design of electrohydraulic control valves[J]. Moog Technical Paper, 1997.

[2] Wang JZ，Zhao JB，Wang SK. The Development and Future Trends of Electro-hydraulic Servo Technology[J]. Hydraulics & Pneumatics，2014，(5)：1-12.

[3] Wos P, Dindorf R. Adaptive control of the electro‐hydraulic servo‐system with external disturbances[J]. Asian Journal of control, 2013, 15(4): 1065-1080.

[4] Zhao Y, Cong D C, Han J W. An integrated approach for the realization of the real-time control in electro-hydraulic servo system[C]//Applied Mechanics and Materials. Trans Tech Publications, 2008, 10: 513-517.

[5] Kilic E，Dolen M，Koku AB，et al. Accurate pressure prediction of a servo-valve controlled hydraulic system[J]. Mechatronics，2012，22(7)：997-1014.

[6] Card G，Parker D. Servo Valve Design Considerations[J]. Hydraulic Pneumatic Mechanical Power，1985，31(6)：95-98.

[7] Su DH，Ren DL，Yang JL. Comparison of Electro-hydraulic Proportional Valve and Electro-hydraulic Servo Valve on Performances[J]. Hydraulics Pneumatics & Seals，2008，(4)：1-4.

[8] Lin HB. Study on a three-dimension nanometer precision machining[J]. Advanced Materials Research Digital Design and Manufacturing Technology，2010，(3)：686-689.

[9] Niu J，Chen D. Current Development and Counter measure of Ultra-precision Machine Tools[J]. Key Engineering Materials，2011，(5)：632-636.

[10] Xu JJ，Liu WN. Compensation capacitor fault detection method injointless track circuit based on Levenberg-Marquardt algorithm and generalized S-transform[J]. Control Theory and Applications，2010，(7)：1612-1617.

[11] Alfredo V.Novel piezoelectric-based power supply for driving piezoelectric actuators designed for active vibration damping applications[J]. Journal of Electroceramics, 2001，(3)：197-210.

[12] Croft D，Sheddand G，Devasia S. Creep hysteresis and vibration compensation for piezo actuators: Atomic force microscopy application[J]. ASME Journal of Dynamic Systems. Measurement and Control，2001，(6)：33-36.

[13] Rifaio ME， Aumond BD， Tomi KY. Imaging at the nano-scale[C]. Proceedings of IEEE ASME International Conference，2003，1197-1200.
[14] Eda HK. In proeess detection of grinding burn by means of utilizing acoustic emission[J]. Annals of the CIRP，1994，43(1)：101-105.
[15] Paros JM，Weisbord L. How to design a flexure hinge[J]. Machine Design，1965，37(11)：151-157.
[16] Wornko A，Huang J，Altintas Y. Piezo electric tool actuator for precision machining on conventional CNC turning centers[J]. Precision Engineering，2003，27(4)：335-345.

STATISTICALLY BASED ON-TARGET OPTIMIZATION IN MICRO-MILLING OF TITANIUM ALLOY FOR BIOMEDICAL APPLICATIONS

Xiang Zhang[1], Yuefeng Li[1], and Guanglin Wang[1]
[1]School of Mechatronics Engineering
Harbin Institute of Technology
Harbin, Heilongjiang Province, P.R. China

INSTRUCTIONS

Micro-milling is a direct and effective manufacturing method for biological implants. Due to the scale effects of micro-milling, controlling the desired surface roughness in micro-milling is more difficult than that of conventional milling. The performance of these biological implants mainly depends on the surface roughness which has a great impact on cell adhesion. Due to the scale effects of micro-milling, controlling the desired surface roughness in micro-milling is more difficult than that of conventional milling. Therefore, in this study an attempt to analyze the optimum milling parameters was carried out. ANOVA was employed to analyze the influences of milling parameters according to spindle speed, feed per tooth, axial depth of cut and milling area in micro-milling of Ti6Al4V titanium alloy. The milling parameters were optimized via Taguchi method for osteoblasts and fibroblasts adhesion in up milling area, middle milling area and down milling area respectively. This optimum method was verified in the additional experiments for getting the objective surface roughness.

INTRODUCTION

Biomedical titanium alloy has a high technical content and economic value, which is widely used in treating and replacing human tissues and organs. It is a new developing field of material science and technology, and has become the preferred material for artificial joint, artificial bone, artificial dental implant and other hard tissue replacement or repair of medical equipment products [1]. Since the 1930s, metal materials have been used in the medical field. Then, pure titanium has been confirmed the feasibility of clinical application. In the late 1970s, Ti6Al4V titanium alloy came into use in the medical field. Subsequently, Ti6Al7Nb, Ti5Al2.5Fe, Ti13Nb13Zr, Ti12Mo6Zr2Fe and other new titanium alloy appeared, became useful in a small range of applications in the field of biological materials [2].

Because of its excellent bio-compatibility and comprehensive mechanical properties, Ti6Al4V is still the largest amount of biomedical titanium alloy for biological implants. As the surface roughness of biological implants has a great impact on cell adhesion, too large or too small surface roughness is not conducive to biological cell adhesion and growth, surface roughness of biological implants need be controlled strictly [3]. Micro-milling is a direct and effective manufacturing method for biological implants which could manufacture micro-structure with complex three-dimensional shape. For its high rate of material removal, micro-milling has become one of the most promising approaches to rapid manufacture of medical devices and implants.

Due to the scale effect of micro-milling, quality control of the milled surface is more difficult than conventional milling. Furthermore, the chemical reaction between titanium alloy and the tool material in milling process could result in rapid tool wear and high surface roughness. In addition, as the thermal conductivity of Ti6Al4V titanium alloy is quite low, the shear region temperature rises quickly in high-speed milling. The combination of high temperature, high strain and high strain rate promotes the dynamic re-crystallization softening effect, and reduces the internal stress which prevents the material from continuing deforming. These effects lead to the formation of adiabatic shear bands which makes a big challenge in micro-milling of titanium alloy [4,5]. Compared with conventional milling, surface quality control in micro-milling is more difficult. The researches on milled surface morphology and quality have always been one of the hotspots in micro-milling. Many techniques have been applied to optimizing the process parameters in micro-milling such as Taguchi method [6], response surface method [7], multi-objective optimization [8,9], regression analysis [10], analysis of variance[11-13], modeling and simulation [14-16] and other methods [17,18].

These researches based on the average surface roughness aim to reduce the milled surface roughness. Due to the effect of the scale effects in micro-milling, when the actual uncut chip thickness is smaller than the minimum chip

thickness, workpiece elastically deforms under the interaction with the milling cutter, and no material is removed from the workpiece; when the actual uncut chip thickness is larger than the minimum chip thickness, the interaction forces of the workpiece with the cutter are mainly dominated by shearing forces, and the material as thick as the actual engagement is removed as a chip [19]. Taking into account the characteristics of the cutter trajectory, the actual uncut chip thickness in the side areas of the feed direction is much smaller than the middle area, which results in higher elastically deformation rate and surface roughness. So the average surface roughness cannot reflect the whole surface quality of the workpiece. In addition, as the surface roughness of biomedical materials influence cell adhesion, the surface roughness needs to be controlled within a certain range strictly [3].

In this study, milled surface is divided into up milling area, middle milling area and down milling area. The average surface roughness is measured in those three areas. Taguchi method is used to on-target optimize the process parameters in micro-milling of Ti6Al4V titanium alloy, so that a suitable surface roughness can be provided for osteoblasts (OST) and fibroblasts (FIB) adhesion.

MATERIAL AND METHODS

Milling experiments were carried on a developed 5-axis micro-milling machine tool, as shown in FIGURE 1. The surface of the workpiece is ground to insure flatness. A carbide two-flute micro-end milling cutter with the diameter of 1 mm, helix angle of 30 deg, length of cut of 2 mm was used. The cutter was clamped in a high speed precision spindle with the tool overhand of 19 mm.

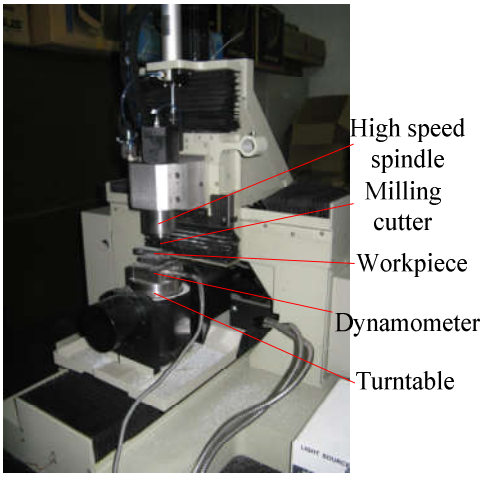

FIGURE 1. The experimental set-up

The workpiece was a rectangular block Ti6Al4V titanium alloy, which is still the most widely used titanium alloy for biomedical applications. The full-immersion slot end milling without cutting fluid was conducted. The milled surface was divided into up milling area, middle milling area and down milling, as shown in FIGURE 2.

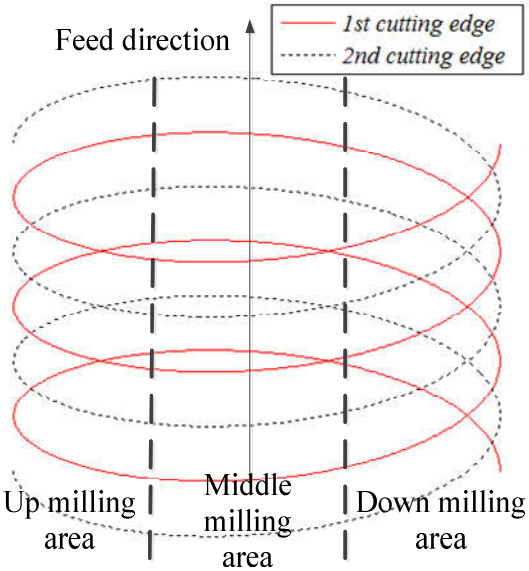

FIGURE 2. The schematic of slot end milling

In order to highlight the scale effects of micro-milling, spindle speed, feed per tooth and axial depth of cut were chosen as the main influencing factors coded as *α*, *β* and *γ* respectively. TABLE 1 illustrates the levels and values of those influencing factors.

TABLE 1. The levels and values of the main influencing factors

Factor	Code	Level		
		1	2	3
Spindle speed (r/min)	*α*	20000	40000	60000
Feed per tooth (μm)	*β*	0.2	0.4	0.6
Axial depth of cut (μm)	*γ*	30	60	90

The Taguchi orthogonal array are constructed according to TABLE 1, as shown in TABLE 2. In order to avoid the effect of tool wear on surface roughness, each set of milling test was carried out twice, and the test sequence was arranged in U-type.

The Olympus™ laser scanning confocal microscopy was used to measure the average surface roughness in 3*k* milling areas as show in FIGURE 3. The surface roughness of up milling

area (SRU), middle milling area (SRM) and down milling area (SRD) can be obtained by the following formula:

$$SRU = \sum_{i=1}^{k} Ra_{3i-2} / k$$
$$SRM = \sum_{i=1}^{k} Ra_{3i-1} / k \quad (1)$$
$$SRD = \sum_{i=1}^{k} Ra_{3i} / k$$

TABLE 2. Milling parameters

Run		Code	Spindle speed (r/min)	Feed per tooth (μm)	Axial depth of cut (μm)
1	18	α1β1γ1	20000	0.2	30
2	17	α1β2γ2	20000	0.4	60
3	16	α1β3γ3	20000	0.6	90
4	15	α2β1γ2	40000	0.2	60
5	14	α2β2γ3	40000	0.4	90
6	13	α2β3γ1	40000	0.6	30
7	12	α3β1γ3	60000	0.2	90
8	11	α3β2γ1	60000	0.4	30
9	10	α3β3γ2	60000	0.6	60

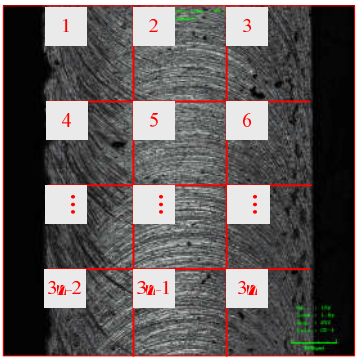

FIGURE 3. Surface roughness measurement

RESULTS

Analysis of variance (ANOVA) of the milled surface roughness was conducted to analyze the influence of spindle speed, feed per tooth, axial depth of cut and milling area. The average surface roughness can be calculated as

$$\overline{Ra} = (Ra_{run(n)} + Ra_{run(19-n)}) / 2 \quad (2)$$

where $Ra_{run}(n)$ is the surface roughness of run n in TABLE 2. The results of ANOVA are shown in TABLE 3.

TABLE 3. ANOVA results

Source	Sum Sq.	d. f.	Mean Sq.	F	Prob>F
Spindle speed	0.19894	2	0.09947	24.74	0.0000
Feed per tooth	0.26042	2	0.13021	32.39	0.0000
Axial depth of cut	0.02346	2	0.01173	2.92	0.0799
Milling area	0.12096	2	0.06048	15.04	0.0001
Error	0.07237	18	0.00402		
Total	0.67615	26			

It can be clearly seen from ANOVA analysis that in milling parameters, feed per tooth and spindle speed have great influences on the surface roughness in micro-milling of Ti6Al4V titanium alloy, and axial depth of cut has little effect. Milling area also has big influence. There are great differences of surface roughness among different milling area. For biomedical applications, such differences of surface roughness will result in uneven cell adhesion.

DISCUSSIONS

Process Optimization

In this paper, Taguchi method was used to optimize milling parameters. According to the target of surface roughness control, on-target signal to noise (*S*/*N*) ratio was used to evaluated milling parameters. The signal to noise ratio is expressed as

$$S/N = -10\lg(\frac{1}{n}\sum_{i=1}^{n}(y_i - m)^2) \quad (3)$$

where y_i is the experiment result, n is the number of experiments, and m is the target value. The suitable surface roughness for OST and FIB adhesion are about 0.85 and 0.55 μm, respectively [21]. Both of the suitable surface roughness are used as the control targets, and the signal-to-noise ratio is calculated by using (3), as shown in TABLE 4.

TABLE 4. Experiment results and signal to noise ratio

No.	SRU (μm)		SRM (μm)		SRD (μm)		*S*/*N* ratio (dB)					
	Run *n*	Run (19-*n*)	Run *n*	Run (19-*n*)	Run *n*	Run (19-*n*)	OST (*m*=0.85 μm)			FIB (*m*=0.55 μm)		
							SRU	SRM	SRD	SRU	SRM	SRD
1	0.976	0.957	0.861	0.792	0.943	0.916	18.64	27.59	21.87	7.61	11.10	8.41
2	0.872	0.890	0.532	0.493	0.857	0.830	29.82	9.42	36.49	9.60	27.48	10.64
3	0.655	0.674	0.420	0.508	0.703	0.651	14.62	8.21	15.14	18.79	20.30	17.75
4	0.734	0.732	0.645	0.606	0.686	0.714	18.64	12.94	16.44	14.75	22.16	16.44
5	0.515	0.579	0.526	0.471	0.497	0.521	10.32	9.06	9.34	29.86	24.67	27.39

6	0.430	0.457	0.417	0.439	0.441	0.423	7.81	7.49	7.57	19.38	18.24	18.54
7	0.727	0.746	0.536	0.540	0.705	0.756	18.87	10.12	18.26	14.58	38.30	14.78
8	0.739	0.742	0.517	0.506	0.723	0.717	19.21	9.41	17.72	14.40	28.20	15.39
9	0.518	0.533	0.466	0.482	0.505	0.522	9.77	8.49	9.46	31.83	22.34	28.52

The mean signal to noise ratios for surface roughness of each milling area are shown in TABLE 5, and plotted as shown in FIGURE 4(a) to 4(c) respectively.

TABLE 5. Mean signal to noise ratio

Parameters		Mean *S/N* ratio (dB)							
		Level 1		Level 2		Level 3		Max-min	
		OST	FIB	OST	FIB	OST	FIB	OST	FIB
SRU	Spindle speed	21.03	12.00	12.26	21.33	15.95	20.27	8.77	9.33
	Feed per tooth	18.72	12.31	19.78	17.95	10.73	23.33	9.05	11.02
	Axial depth of cut	15.22	13.80	19.41	18.73	14.60	21.08	4.81	7.28
SRM	Spindle speed	15.07	19.63	9.83	21.69	9.34	29.61	5.73	9.98
	Feed per tooth	16.88	23.85	9.29	26.78	8.06	20.29	8.82	6.49
	Axial depth of cut	14.83	19.18	10.28	23.99	9.13	27.76	5.70	8.58
SRD	Spindle speed	24.50	12.27	11.12	20.79	15.15	19.56	13.38	8.52
	Feed per tooth	18.86	13.21	21.18	17.81	10.72	21.60	10.46	8.39
	Axial depth of cut	15.72	14.11	20.80	18.53	14.25	19.97	6.55	5.86

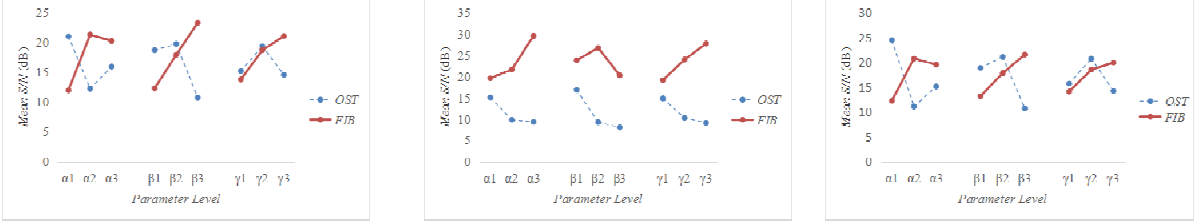

(a) Mean S/N of UMA *(b) Mean S/N of MMA* *(c) Mean S/N of DMA*

FIGURE 4. Mean signal to noise ratios for surface roughness of each milling area.

The graphs clearly show that the mean signal to noise ratios of spindle speed, feed per tooth and axial depth of cut in middle milling area are quite different from side milling area. The process optimization by using the average surface roughness will result in a significant difference of cell adhesion between middle milling area and side milling areas both for OST and FIB.

Spindle speed, feed per tooth and axial depth of cut are not very significant contrast with the controlling target of surface roughness of OST adhesion (m=0.85 μm) in up milling area (FIGURE 4(a)). The low spindle speed (20000 r/min), medium feed per tooth (0.4 μm) and axial depth of cut (60 μm) are favorable for achieving the controlling target of surface roughness for OST adhesion. Based on the graph, the condition to obtain the suitable surface roughness for OST adhesion is $\alpha 1\beta 2\gamma 2$. Feed per tooth significantly affects the control of surface roughness in terms of the controlling target of FIB adhesion (m=0.55 μm). The medium spindle speed (20000 r/min), high feed per tooth (0.6 μm) and axial depth of cut (90 μm) are favorable for achieving the controlling target of surface roughness for FIB adhesion. The condition to obtain the suitable surface roughness for FIB adhesion is $\alpha 2\beta 3\gamma 3$.

The increasing feed rate spindle speed, feed per tooth and axial depth of cut in middle milling area will promote the surface roughness closer to the controlling target of OST adhesion (FIGURE 4(b)). Based on the graph, the condition to obtain the suitable surface roughness for OST adhesion is $\alpha 1\beta 1\gamma 1$ (spindle speed of 20000 r/min, feed per tooth of 0.2 μm, and axial depth of cut of 30 μm). Contrary to the up milling area, spindle speed and axial depth of cut both significantly affect the control of surface roughness according to the controlling target of FIB adhesion. The high spindle speed (60000 r/min), medium feed per tooth (0.4 μm) and high axial depth of cut (90 μm) are favorable for achieving the controlling target of surface roughness for FIB adhesion, and the optimized milling parameters is $\alpha 3\beta 2\gamma 3$.

From FIGURE 4(c) it can be seen that the mean signal to noise ratio of down milling area is same as the up milling area. This indicates that milling method (up milling or down milling) has little effect on surface roughness in micro-milling of Ti6Al4V titanium alloy. Based on the graph, the

conditions to obtain the suitable surface roughness for OST and FIB adhesion are $\alpha1\beta2\gamma2$ and $\alpha2\beta3\gamma3$ respectively.

Optimization Results

Four additional milling experiments were conducted with the optimal condition to verify optimization results. The first two experiments were used to verify the conditions which could respectively obtain the suitable surface roughness for OST and FIB adhesion in up and down milling areas ($\alpha1\beta2\gamma2$ and $\alpha2\beta3\gamma3$). The last two experiments were used to verify the conditions which could respectively obtain the suitable surface roughness for OST and FIB adhesion in middle milling area ($\alpha1\beta1\gamma1$ and $\alpha3\beta2\gamma3$). TABLE 6 shows the optimization results.

TABLE 6. Optimization results.

No.	Objective	Optimal condition	Experimental results (μm)					
			SRU	SRM	SRD	Mean	Std. Dev	Surface
1	SRU & SRD for OST	$\alpha1\beta2\gamma2$	0.881	0.543	0.846	0.757	0.178	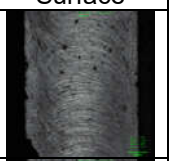
2	SRU & SRD for FIB	$\alpha2\beta3\gamma3$	0.438	0.421	0.425	0.428	0.122	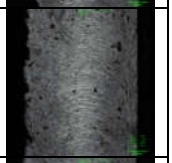
3	SRM for OST	$\alpha1\beta1\gamma1$	0.945	0.811	0.922	0.893	0.072	
4	SRM for FIB	$\alpha3\beta2\gamma3$	0.679	0.565	0.637	0.627	0.090	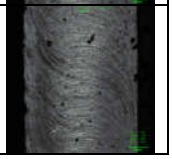

It can be seen from TABLE 6 that in micro-milling of Ti6Al4V titanium alloy, using the optimal condition $\alpha1\beta1\gamma1$ can achieve the suitable surface roughness of 0.893 μm (controlling target is 0.85 μm) for OST adhesion at a spindle speed of 20000 r/min, feed per tooth of 0.2 μm and axial depth of cut of 30 μm. For FIB adhesion, the optimal condition is $\alpha3\beta2\gamma3$ (spindle speed of 60000 r/min, feed per tooth of 0.4 μm and axial depth of cut of 90 μm), and the suitable surface roughness is 0.627 μm (controlling target is 0.55 μm).

CONCLUSIONS

This work focuses on surface roughness control in micro-milling in which Ti6Al4V titanium alloy is used as an example of titanium alloy for biomedical applications. It has evidently shown that how the surface roughness influenced by milling parameters in terms of spindle speed, feed per tooth, axial depth of cut and milling area on surface are analyzed via ANOVA. Furthermore, an on-target optimum method was proved to be efficient in the additional experiments. The following is a summary of other important findings:

Because of scale effects in micro-milling, milling area has great influence on surface roughness. There are great differences of surface roughness among different milling area.

In milling parameters, feed per tooth and spindle speed have great influences on the surface roughness in micro-milling of Ti6Al4V titanium alloy, and axial depth of cut has little effect.

The equalizing milling surface can be obtained when using the on-target optimum method in different milling area, which is suitable for cell adhesion.

ACKBOWLEDGEMENTS

This work is supported by National Natural Science Foundation of China (NSFC, No.51605118) and the Fundamental Research Funds for the Central Universities (Grant No. HIT.NSRIF. 2016042).

REFERENCES

[1] Long M, Rack H J. Titanium alloys in total joint replacement-a materials science

perspective. Biomaterials. 1998; 19: 1621-1639.
[2] Leyens C, Peters M. Titanium and Titanium Alloys. WILEY-VCH Verlag GmbH & Co. KGaA, DE: Weinheim, 2005; 134-147.
[3] Kim H K, Jang J W, Lee C H. Surface modification of implant materials and its effect on attachment and proliferation of bone cells. Journal of Materials Science: Materials in Medicine. 2004; 15: 825-830.
[4] Komanduri R, Turkovich B F V. New observations on the mechanism of chip formation when machining titanium alloys. Wear. 1981; 69: 179-188.
[5] Barry J, Byrne G, Lennon D. Observations on chip formation and acoustic emission in machining Ti-6Al-4V alloy. International Journal of Machine Tools and Manufacture. 2001; 41: 1055-1070.
[6] Kuram E, Ozcelik B. Micro-milling performance of AISI 304 stainless steel using Taguchi method and fuzzy logic modelling. Journal of Intelligent Manufacturing. 2016; 27: 817-830.
[7] Gao Q, Gong Y D, Zhou Y G, Wen X L. Experimental study of micro-milling mechanism and surface quality of a nickel-based single crystal superalloy. Journal of Mechanical Science and Technology. 2017; 31: 171-180.
[8] Venkata R R, Dhiraj P R, Joze B. A multi-objective algorithm for optimization of modern machining processes. Engineering Applications of Artificial Intelligence. 2017; 61: 103-125.
[9] Thepsonthi T, Özel T. Multi-objective process optimization for micro-end milling of Ti-6Al-4V titanium alloy. International Journal of Advanced Manufacturing Technology. 2012; 63: 903-914.
[10] Yu H D, Yuan H T, Xu J K, Hou W W, Qi Y. Study on surface quality in micro milling stainless steel 06Cr17Ni12Mo2 processing. in IEEE 3M-NANO - IEEE Int. Conf. Manip., Manuf. Meas. Nanoscale, Chongqing, 2016; 352-356.
[11] Shi Z Y, Liu Z Q, Li Y C, Qiao Y. Swept mechanism of micro-milling tool geometry effect on machined oxygen free high conductivity copper (OFHC) surface roughness. Materials. 2017; 10:1-20.
[12] Vipindas K, Kuriachen B, Mathew J. Investigations into the effect of process parameters on surface roughness and burr formation during micro end milling of TI-6Al-4V", International Journal of Advanced Manufacturing Technology. 2016; 1-16.
[13] Jing X B, Li H Z, Wang J, Yuan Y J, Zhang D W, Kwok N, Nguyen T. An investigation of surface roughness in micro-end-milling of metals. Australian Journal of Mechanical Engineering. 2017; 15: 166-174.
[14] Lu X H, Jia Z Y, Wang H, Si L K, Wang X X. Surface roughness prediction model of micro-milling Inconel 718 with consideration of tool wear. International Journal of Nanomanufacturing. 2016; 12: 93-108.
[15] Sun Y Z, Liang Y C, Du R X. Micro-milling: simulation of surface generation and experimental analysis of surface roughness. Wseas Transactions on Circuits and Systems. 2006; 5: 1293-1300.
[16] Zhang X, Han Z Y, Fu H Y, Sun Y Z. Modeling and simulation of machined surface error in micro-ball-end milling. Journal of Computer-Aided Design and Computer Graphics. 2010; 22: 2177-2181.
[17] Özel T, Thepsonthi T, Ulutan D, Kaftanoğlu B. Experiments and finite element simulations on micro-milling of Ti-6Al-4V alloy with uncoated and cBN coated micro-tools. CIRP Annals-Manufacturing Technology. 2011; 60: 85-88.
[18] Marcon A, Melkote S, Kalaitzidou K, DeBra D. An experimental evaluation of graphite nanoplatelet based lubricant in micro-milling. CIRP Annals-Manufacturing Technology. 2010; 59: 141-144.
[19] Li C F, Lai X M, Li H T, Ni J. Modeling of three-dimensional cutting forces in micro-end-milling. Journal of Micromechanics and Microengineering. 2007; 17: 671-678.
[20] Germain G, Morel A, Bouchnak T B. Identification of material constitutive laws representative of machining conditions for two titanium alloys: Ti6Al4V and Ti555-3. Journal of Engineering Materials and Technology. 2013; 135: 1-11.
[21] Liang Y C, Song D P, Chen M J, Bai Q S. New development on effect of surface roughness of Ti-material for biomedical applications on cell adhesion. Chinese Journal of Mechanical Engineering. 2008; 44:6-15.

ADVANCED VIBRATION CONTROL FOR ULTRA PRECISION MACHINING TECHNOLOGY

Takeshi Hashimoto[1], Ayman M. Kamal[1], Ben H. Jacobs[1], Jeff W. Roblee[1], and Jeffrey L. Worthey[2]
[1]Ametek Precitech, Inc.
Keene, NH, USA
[2]Ametek TMC
Peabody, MA, USA

INTRODUCTION

Single point diamond turning (SPDT) using ultra-precision machine tools has long been an effective technology for creating optical surfaces on infrared and non-ferrous metals. To push the performance of an ultra-precision machine tool to its full capability, special attention should be spent on environmental conditions. Ideally, such a machine should be placed in a room free of floor vibration, temperature variation, and acoustic noise. These perfect conditions are impossible to achieve, but a reasonable attempt to approach these conditions is desirable. In this study, we focus on the application of floor vibration control to our ultra-precision machine tool, Nanoform X, using two stages of isolation – active cancellation of low-frequency floor vibration with the Technical Manufacturing Corporation (TMC™) Quiet-Base™ and high-frequency passive isolation with TMC™ UltraDamp™ isolators.

Motivation

The first goal is to demonstrate the capabilities of ultra-precision diamond turning for visible, infrared, and optical molding for the ophthalmic and precision mechanical component markets while subjected to vibration from adjacent traffic, construction, other machines…etc influencing the SPDT machine tool.

The second goal is to show the potential for diamond turning mobile phone and smart device camera molds with no diffractive color or tool marks and minimizing surface roughness through the application of advanced vibration control techniques.

Even in the ideal case, the SPDT process creates a periodic surface structure that forms a diffractive grating for specific optical wavelengths. To create a no-color surface, the spatial frequency of this surface structure must be small enough not to diffract light at visible wavelengths. Unfortunately, it is impossible to achieve the ideal case in the picometer regime. In particular, outside vibration sources often create additional periodic surface structures that diffract light. Recent developments by Precitech including the use of active vibration cancellation, low vibration auxiliary equipment and advanced vibration analysis techniques have made the process of producing no-color surfaces more repeatable and deterministic.

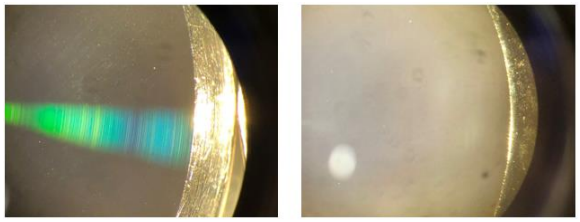

FIGURE 1. Left: Mold cut on a typical ultra-precision machine with standard cutting conditions, diffractive colors exist. Right: Mold cut with Nanoform X with TMC™ UltraDamp™ isolators on TMC™ Quiet-Base™ with Precitech No-color cutting conditions, no diffractive colors exist.

VIBRATION ISOLATION

Pneumatic Air Isolators

A passive isolator is characterized by its natural frequency, f_n, and level of damping. When driven at frequencies higher than f_n, structures separated by the isolator become progressively more decoupled with increasing frequency. At or near f_n, however, the passive isolator will amplify motion. The amount of amplification is dictated by damping and can range from negligible to a factor of 10x or more. Below f_n, motion is transferred at a scale of one-to-one.

In the case of pneumatic isolators, f_n is typically lower than 4 Hz. As shown in Fig. 2, high frequency isolation is a function of both damping and natural frequency. The plot shows

transmissibility curves for three isolators from TMC™ with different levels of damping: Gimbal Piston®, MaxDamp™, and UltraDamp™. A pneumatic spring incorporating pneumatic damping, such as the Gimbal Piston®, will provide outstanding high frequency attenuation at the expense of amplification near its 2 Hz resonant peak. The MaxDamp™ isolator balances isolation performance with a smaller resonant peak at 3 Hz while maintaining favorable high frequency roll off. The UltraDamp™ isolator provides aggressive damping to maximize stability under high acceleration conditions. This stiffens the pneumatic spring overall, shifting f_n closer to 3.5 Hz.

In addition to vibration isolation, f_n and the level of damping also directly determine the settling time of a system. For applications with moving payloads, sensitive measurements or processes must be delayed until residual motion has subsided. In these cases, a more damped response is often preferred.

To take advantage of rapid settling and minimal resonant amplification, the No-color technology includes UltraDamp™ isolators. To further address low-frequency floor vibration and maximize performance, an active isolation solution was added in series with the pneumatic isolators for the Nanaform X No-color system.

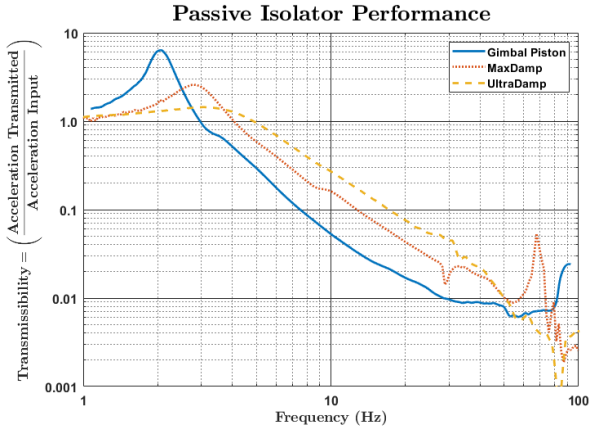

FIGURE 2. Transmissibility of pneumatic isolators with increasing levels of damping.

Serial-Type Quiet-Base™ System

In general, active isolation systems require sensors to observe undesired motion and actuators to correct for it. As shown in Fig. 3, the architecture can be either serial or parallel. While both aim to minimize disturbances experienced by precision equipment, each type has distinct characteristics that are advantageous to different applications.

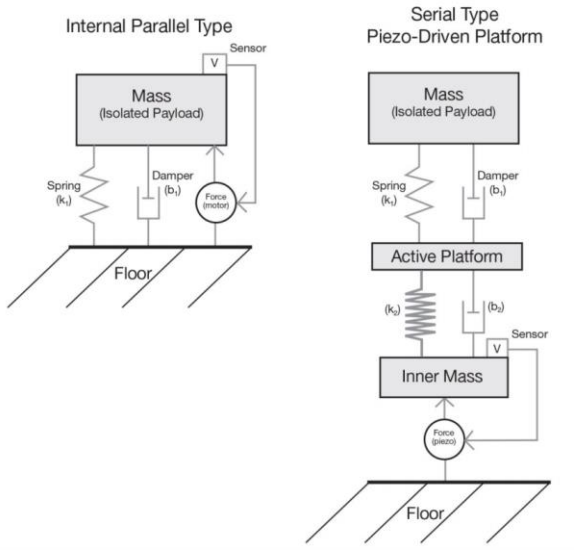

FIGURE 3. Internal parallel type active system vs. serial type active platform.

Parallel type designs sense motion directly on the isolated payload and correct errant motion with a restorative force applied parallel to the supporting isolator. In this configuration, a feedback loop can sense the resonance of the spring element and reduce amplification, even to the point of adding isolation at low frequencies. The amount of reduction depends on the initial level of amplification and the maximum gain achievable by the feedback system. Placing the sensor on the payload, however, introduces payload dynamics and variation into the feedback loop. This limits robustness and could require dedicated system-level tuning. The parallel arrangement is well suited to high force moving stages.

Serial type designs instead place sensors on an intermediate platform. High force actuators, such as piezoelectric ceramics, support the system weight and keep this inner mass stationary. The high stiffness of the isolators results in higher control bandwidth, so that vibrations propagating from the floor are significantly reduced over a broad frequency range. Another well-damped, passive spring element decouples the active payload from the feedback system. The resonant frequency of this stage is intentionally shifted higher to avoid interference with the softer pneumatic springs that comprise the second stage of isolation. This

decoupling allows for independent tuning of the feedback system regardless of payload.

The entire Precitech Nanoform X is supported by a piezo-driven active vibration platform, the QUIET-Base™ from TMC™. With this system, the piezoelectric actuators are in series with elastomer springs that support the payload. The QUIET-Base™ alone starts isolating at frequencies as low as 0.5 Hz. Combined with UltraDamp™ passive isolator in series, the total system achieves 90% reduction at 2.5 Hz and 99% at 10 Hz. As shown in Fig. 4, this is a considerable improvement over passive isolators and typical parallel type active systems.

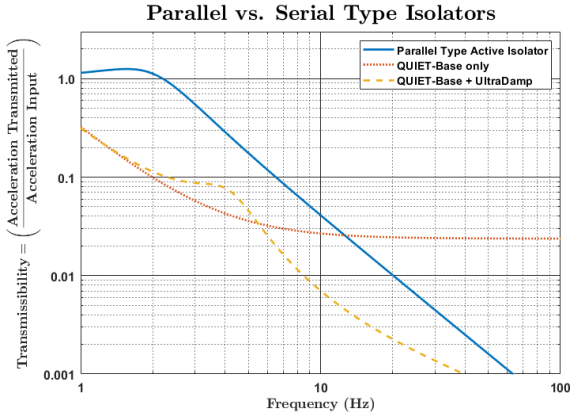

FIGURE 4. Transmissibility of serial and parallel type actuators.

VIBRATION MEASURMENTS

A setup using three seismic accelerometers is used to test and qualify vibration isolation as well as diagnose sources and path of vibration transmitted to the machine. The three accelerometers are mounted on (1) the floor adjacent to the machine, (2) on the Quiet-Base™ active vibration cancellation platform, and (3) on the machine spindle.

Measurements are performed with peak-hold to capture transient events. A Hanning window with 50% overlap is used with 15-averages frames.

Fig.7 shows a comparison between accelerometer response (in rms m/s velocity units) between cases of Quiet-Base™ on and off.

The pneumatic air isolators passively isolate vibrations >10 Hz from being transmitted to the spindle. Below 10 Hz, vibration from the floor is obviously seen on the spindle. When the active Quiet-Base™ is turned on, vibration on the spindle is greatly reduced.

With Quiet-Base™ off, peak vibrations are observed between 1-8 Hz up to 90 nm/s rms. That was reduced to below 30 nm/s rms, with Quiet-Base™ on.

SURFACE CUT AND FINISH

Two axis or XZC diamond turning on Nanoform X is used with TMC/Precitech Quiet-Base™. Slide types are dovetail slides. Bearing types are water-cooled hydraulic oil slides and an air-bearing spindle, also water cooled. X-axis following error is 1.6 nm and Z-axis following error is 1.1 nm (Fig. 5).

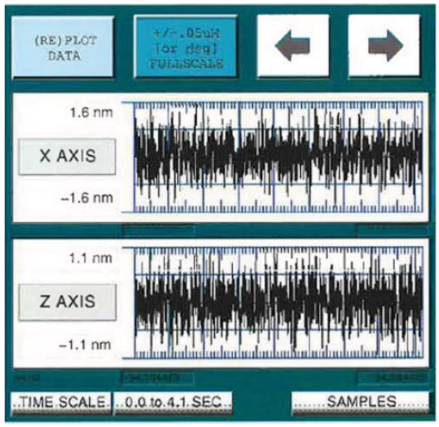

FIGURE 5. Position error plot sampled at 2 kHz with no filtering over 4 seconds.

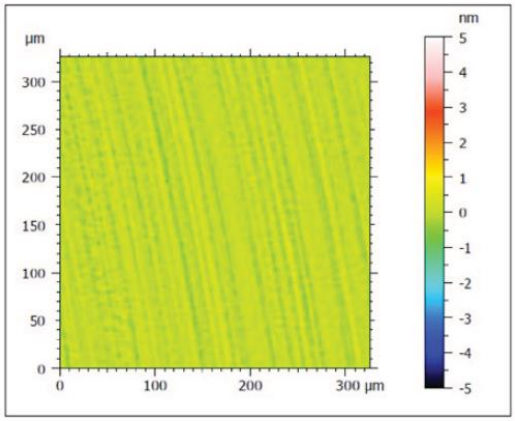

Roughness (Gaussian filter, 25 µm)

ISO 25178		
Height Parameters		
Sa	0.15035	nm
Sq	0.18782	nm

FIGURE 6. Observed surface finish on the test cut part.

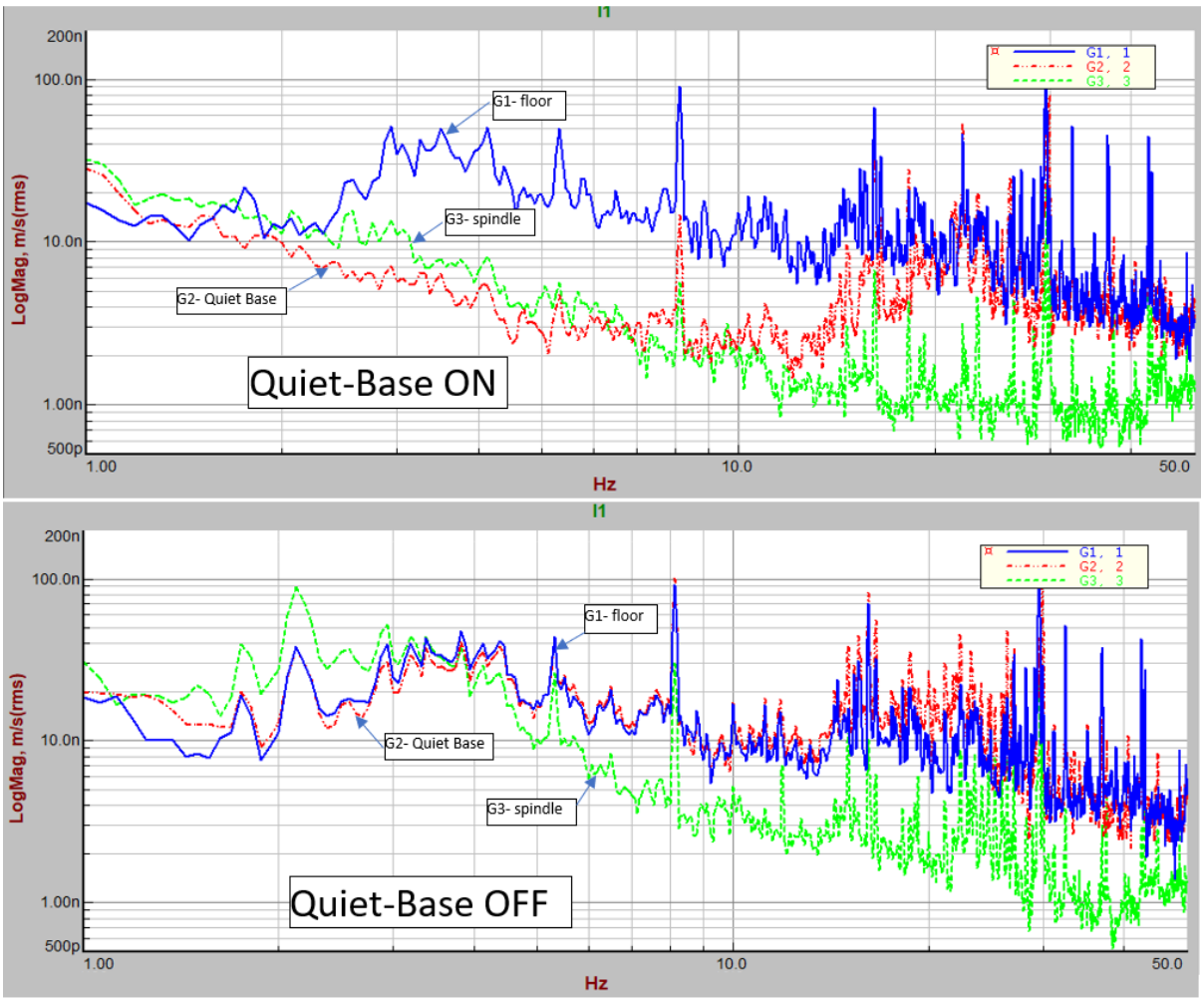

FIGURE 7. Comparison between accelerometer response (in rms m/s velocity units) on floor, on Quiet-Base™ and on machine spindle with Quiet-Base™ on and off.

Process conditions are optimized to minimize surface roughness and to eliminate diffractive color and tool marks. Feed rate is up to 1.8 mm/min. Tool radius is < 100 μm. The test part is a 12.7 mm diameter, with 254 mm convex spherical radius nickel plated steel test part.
Observed surface finish was 0.15 nm Sa, measured halfway between the center and the edge (Fig.6). A 25 μm filter us used with form error removal using 12th order polynomial.

SUMMARY

Recent developments by Precitech including the use of active vibration cancellation from TMC™, the use of low vibration auxiliary equipment and advanced vibration techniques have made the process of producing no-color surfaces more repeatable and deterministic.

A two-stage system of vibration isolation including UltraDamp™ passive pneumatic air isolators and a Quiet-Base™ serial type piezoelectric active vibration platform is employed to control the vibration of surface structures that create diffractive gratings.
Vibration is controlled to within 10 nm/s between 10-50 Hz, and higher vibration amplitudes at lower frequencies, down to the sub-hertz range are reduced to 30 nm/s from 90 nm/s using the Quiet-Base™ active vibration cancellation platform.
Z-axis position following error is controlled to less than ± 2 nm and observed surface finish on the part is 0.15 nm Sa.

REFERENCES

[1] TMC Vibration Control technical section www.techmfg.com.
[2] Precitech Ultra-Precision Technologies https://www.precitech.com/

PROCESS CHAINS FOR THE MASS PRODUCTION OF FUNCTIONAL STRUCTURED SURFACES

Lars Schönemann[1,2], Ann-Katrin Holthusen[1], and Oltmann Riemer[1]
[1]LFM Laboratory for Precision Machining of the Leibniz-IWT and
[2]MAPEX Center for Materials and Processes
University of Bremen
Germany

INTRODUCTION

Micro- and nano-structuring is a viable means to enhance a surface with additional functionality [1]. This can be observed in many cases in nature, for instance on a lotus leaf (hydrophobic), on gecko feet (adhesive), on shark skin (drag-reducing), or moth eyes (anti-reflective) [2]. This concept of nature has also been successfully transferred to technical products, e.g. for improved tribological behavior of molds, dust repellent surfaces, anti-reflection optics, or micro-lens arrays [3].

For the mass-production of polymer parts with functional surfaces, replication is the method of choice. Moreover, molding processes also find increasing usage in replicating ceramic components. Nonetheless, adding such functionality to a technical component is in most cases introduced as one of the last processing steps in the production sequence (or "process chain"). For instance, applying an anti-reflective coating on an optical lens is done after the required shape and surface finish has been achieved by grinding and polishing. Directly applying a micro- or nano-structure of similar functionality to the mold, however, would lead to a far more economic process chain, because the structuring only has to be done once and not repeatedly for every individual part [4].

THE PROSURF PROJECT

In this context, the European project "ProSurf —High Precision Production Technologies for the Mass Production of Functional Structured Surfaces" aims to transfer a selection of advanced methods for surface modification into industrial mass-production lines that use replication processes. The objectives are:

1. Development of modeling tools to translate a desired functionality into geometrical surface structures.
2. Establishing methods for surface modification up to technology readiness level 6.
3. Mass-producing complex products by highly precise plastic and ceramic replication technologies.
4. Implementing a strategy for process and quality control, including in-line and off-line measurements.
5. Validation of the developed tools and process chains in product demonstrators.

To ensure that the developed methods can be easily implemented, in particular if several surface modifying methods are to be combined, the entire production process has to be considered, including handshakes between different stages, off-line and in-line quality monitoring, and modeling. In consequence, the results will cover a broad scope of applications and have a vast potential to trigger further innovations. To showcase the performance of the developed solutions, demonstration studies improving actual products will be carried out, focusing on optical functional surfaces as well as on tribological functional surfaces. As for the latter, these are targeted towards improving powder injection molding processes for the replication of ceramic parts by introduction drag reducing structures to the mold surface.

The optical micro-structures will be generated primarily by fast tool servo assisted diamond machining processes. For instance, holographic safety features, that shall be utilized for anti-counterfeiting and batch tracking of replicated polymer parts, will be machined into specified areas of the molding insert using the nano Fast Tool Servo (nFTS) diamond turning process that has been previously developed at the LFM [5]. Now, the challenge lies in the density of the data that may be inscribed onto the lens and in adapting the nFTS process to machine on a freeform base geometry. Other optical structures will be applied to the demonstrators for generating anti-reflective,

self-cleaning and anti-fogging functionality or to visually enhance a product by adding a holographic effect to it. The respective structures are machinable by nanoimprinting lithography (see [6]) or, in a more flexible fashion, by the so-called Virtual Spindle Fast Tool Servo (VSTS) turning technique [7].

EXEMPLARY PROCESS CHAIN: MANUFACTURING FREEFORM HOLOGRAMS

In this section, general thoughts and design considerations for manufacturing holograms on a freeform base geometry will be presented. The typical process chain consists of a) the design of the holograhic structure, b) the mold machining by nFTS turning, c) the replication into the polymer product and d) the accompanying metrology and quality control (Figure 1).

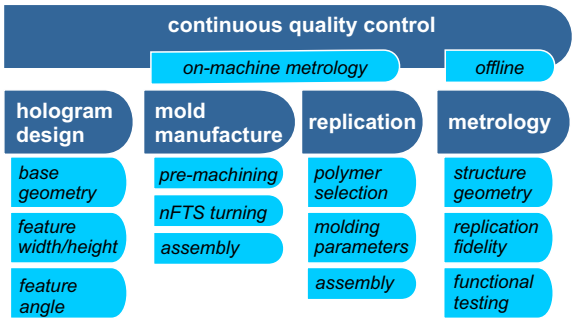

FIGURE 1. Process chain for manufacturing plastic components with diffractive elements

Freeform hologram design

Holographic images rely on introducing phase differences to incident light in order to obtain selective constructive and destructive interference. These are introduced by different height levels of the holographic structure, all below the wavelength of the incident light. On planar surfaces, these differences are solely caused by the height of the inscribed structure, whereas on freeform surfaces, the local height levels have to be considered in the calculation of the hologram.

nFTS turning on freeform surfaces

Diffractive pattern are generated by modulating the cutting depth of a diamond turning process with a high speed actuator, the nano Fast Tool Servo, according to the angular and radial position of the tool, i.e. utilizing $a_{p,nFTS}(\varphi, x)$. One particular challenge of manufacturing holographic structures on arbitrary products is the adaption of the machining process to the underlying freeform geometry. Previously, nFTS turning has only been conducted on planar and circular workpieces, with the process being initialized manually after reaching the outer diameter of the workpiece, regardless of its angular orientation. From then, the structure generation simply had to be synchronized with the rotation of the spindle to generate the desired diffractive pattern.

With freeform surfaces, however, it is essential to consider angular orientation of the workpiece to compensate for local slope and height changes. This requires are more sophisticated synchronization of machine tool and the nFTS control system, ensuring that the hologram generation exactly starts at the specified angular and radial position (cf. Figure 2). Furthermore, the infeed has to be adapted according to the local height level by a slow tool servo (STS), i.e. by superimposing $a_{p,STS}(\varphi, x)$ and $a_{p,nFTS}(\varphi, x)$.

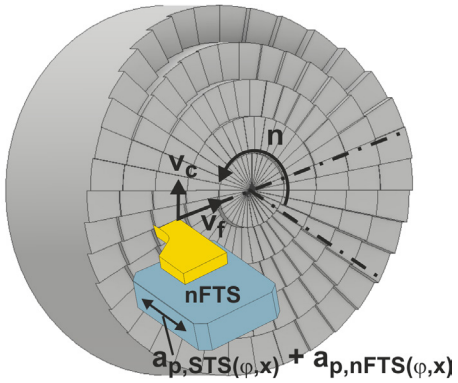

FIGURE 2. nFTS turning of a diffractive pattern on a freeform surface

In the past diamond knife tools have been used for nFTS turning that feature an intrinsic knife angle equivalent to the generated blaze structures. Thus, only the feed was the decisive factor for pattern size and height. Generating freeform holograms, however, requires more flexibility in pattern generation, as the angle of the structures needs to be adapted to the local slope and curvature of the freeform. Therefore, trapezoid diamond tools with a small cutting edge width have to be used in nFTS turning, whose inclination angle to the surface may be changed during machining by an additional rotation axis (B-axis, see Figure 3). This, in turn, requires a more sophisticated tool setting to align the cutting edge to the rotational center of the B-axis mechanically or to compensate a para-

sitic tool shift by numerically shifting the working coordinate system upon rotation.

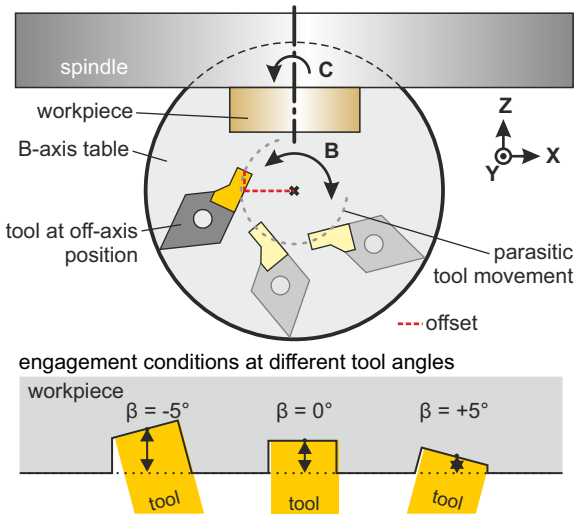

FIGURE 3. Parasitic tool movement upon rotation and effect on cutting depth at the respective angle

The numerical compensation has been successfully applied with different processes for machining optical microstructures, e.g. for Diamond Micro Chiseling on curved surfaces [8]. However, with diffractive pattern feature sizes are much smaller and thus tighter tolerances in tool setting have to be met.

Replication of diffractive pattern

Previous studies have shown that the fine geometric features of holographic planar surfaces may successfully be transferred from the molding insert to the plastic product, cf. [9]. There is, however, a considerable edge rounding of the blaze structures which reduces the optically effective area of the pattern and thereby has an impact on the appearance of the hologram, e.g. by blurring the image or by causing unwanted stray light. The magnitude of the edge rounding effect depends on the choice of molding parameters as well as the utilized polymer and thus can be fine-tuned to maximize the size of the optical effective area. On a laboratory scale, good results have already been achieved with the replication of nanostructures. Now, this has to be scaled-up to production use.

Characterization of nano-structures

The nano-structures of a diffractive pattern are so small and numerous that a full characterization of a pattern is feasible. Hence, only a small proportion of the surface may be checked by atomic force microscopy (AFM) or white light interferometry (WLI) after machining (Figure 4).

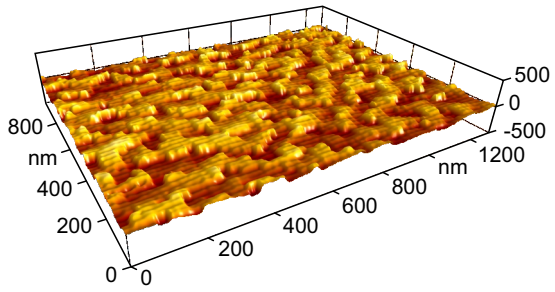

FIGURE 4. WLI image of nFTS-turned diffractive nanostructure (metal mirror)

With the increasing complexity of the machining process, however, it is desirable to check the structure generation directly on the machine tool. A huge potential to do so is seen in the on-machine application of dispersed reference interferometry (DRI), as this technique features a high axial resolution and robustness to discontinuous and structured surfaces [10].

For the final inspection of the holographic structure, its optical functionality has to be evaluated. This is done in an optical test setup (Figure 5) in which the diffractive pattern is illuminated by monochromatic light and the reflected light is projected onto a screen or sensor array (e.g. a CCD camera). By recording the image and comparing the intensity distribution to the source image, the quality of the hologram may be assessed.

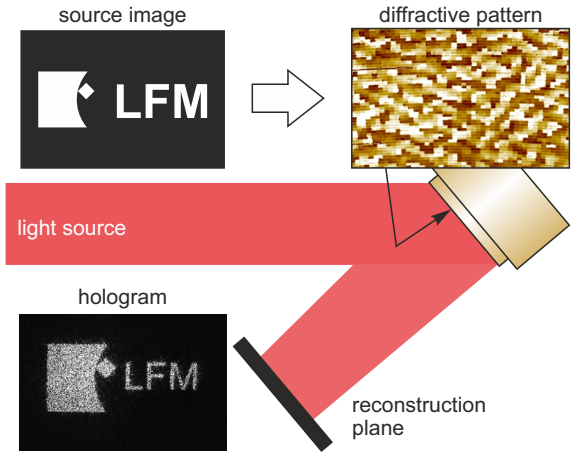

FIGURE 5. Optical setup for evaluating diamond turned holograms

SUMMARY AND OUTLOOK

Establishing process chains for the mass production of polmer parts with functional surfaces requires an investigation of all relevant steps in the production sequence. In this paper, the considerations for adapting the nano Fast Tool Servo turning technique to enable the generation of arbitrary holographic patterns on freeform surfaces are presented. Such holograms may be used as anti-counterfeiting measures or for batch tracking of polymer parts. The freeform base geometry has to be considered in the design phase of the structures and also required further effort in setting up the nFTS turning process. As for replication, particular attention has to be given to the precise reproduction of the diffractive pattern by adapting the molding parameters accordingly. Furthermore, intermediate checking of the structure fidelity by on-machine metrology is vital. The ongoing research work concentrates on implementing the complete process chain as part of the demonstration work in the European project “ProSurf”.

ACKNOWLEDGMENTS

This project has received funding from the European Union’s Horizon 2020 research and innovation programme under grant agreement No 767589. Further information may be found at www.prosurf-project.eu.

REFERENCES

[1] Evans CJ, Bryan JB. "Structured", "Textured" or "Engineered" Surfaces. CIRP Ann. 1999;48(2):541–556.

[2] Malshe A, Rajurkar K, Samant A, Hansen HN, Bapat S, Jiang W. Bio-inspired functional surfaces for advanced applications. CIRP Ann. 2013;62(2):607–628.

[3] Bruzzone AAG, Costa HL, Lonardo PM, Lucca DA. Advances in engineered surfaces for functional performance. CIRP Ann. 2008;57(2):750–769.

[4] Schönemann L, Preuss W. Mold Structuring by Diamond Machining. In: Brinksmeier E, Gläbe R, Riemer O, editors. Fabrication of Complex Optical Components. Lect. Notes Prod. Engin.. Berlin Heidelberg: Springer; 2013. p. 53–66.

[5] Meier A. Diamond turning of diffractive microstructures. Precis Eng. 2015;42:253–260.

[6] Fernández A, Francone A, Thamdrup LH, Johansson A, Bilenberg B, Nielsen T, et al. Hierarchical surfaces for enhanced self-cleaning applications. J Micromech Microeng. 2017;27(4):045020.

[7] To S, Zhu Z, Wang H. Virtual spindle based tool servo diamond turning of discontinuously structured microoptics arrays. CIRP Ann. 2016;65(1):475–478.

[8] Dörgeloh T, Schönemann L, Riemer O, Brinksmeier E. Diamond Micro Chiseling of retroreflective arrays on curved surfaces. In: 17th euspen International Conference & Exhibition; 2017. p. 125–126.

[9] Holthusen AK, Riemer O, Schmütz J, Meier A. Mold machining and injection molding of diffractive microstructures. J Manuf Processes. 2017;26:290–294.

[10] Martin H, Jiang X. Dispersed reference interferometry. CIRP Ann. 2013;62(1):551–554.

MACHINED SURFACE QUALITY IMPROVEMENT FOR CFRP HOLE MAKING PROCESS USING ULTRASONICALLY ASSISTED DRILLING

Tae-Gon Kim, Kangwoo Shin, An-Mok Jeong, Jong-Wook An, Hyo-Young Kim, Cheol-Ho Kim and Seok-Woo Lee
Manufacturing system group
Korea Institute of industrial Technology (KITECH)
Cheon-an, South Korea

INTRODUCTION

Carbon Fiber Reinforced Plastics (CFRP) is composite materials which composed carbon fibers and polymer matrix.[1] Due to its lightweight and high strength properties, CFRP is widely used for lightweight parts in aerospace and automotive industries.[2] CFRP is made of stacking structure of several unidirectional layers to compensate fiber orientation effects.[3] When CFRP is drilled, thrust force pushes carbon fiber laminates and excessive thrust force causes delamination between laminate layers.[4] Therefore, thrust force is one of constrain in CFRP drilling process to improve machining quality. However, limited thrust force becomes obstacles to increase feed rate because high feed rate causes high thrust force.[5] Ultrasonic assisted machining (UAM) has been used for method to reduce thrust force.[6] In CFRP drilling process, reduced thrust force causes lower tool wear and higher machining quality. When number of drilled hole is increased, thrust force and delamination factor are increased because tool is worn and push out force on laminated layer.

In this study, UAM is applied in CFRP drilling process to improve machining quality. Ultrasonic drilling unit have been developed for CFRP drilling process. Thrust force in drilling process was compared with conventional drilling and UAM. Also, delamination factor and surface roughness were measured to analysis the machinability of CFRP.

EXPERIMENT SETUP

Table 1 shows the experimental conditions for ultrasonic drilling. As a workpiece, CFRP which used for aerospace parts is machined. The thickness of CFRP is 16mm, and the CFRP is composed of T1000 graded fiber and epoxy polymer matrix. The stacking sequence is [Woven / -45° / 90° / -45° / 0° / 45° / 90° / 45° / 0° / 0° / 45° / -45° / 90° / -45°…]s. The drilling cutter is SSD060 model of WIDIN. The diameter is 6 mm and the tool is made of tungsten carbide material. The spindle speed are 4,000, 8,000, 12,000 rpm and feed conditions are 0.01, 0.05, 0.1 mm/rev. The feed conditions are designed by considering vibration amplitude of ultrasonic actuating on tool tip. Ultrasonic actuator has 34 kHz frequency and 15 μm amplitude. When the feed is 0.01 mm/rev, the cutting edge of tool is move down 15 μm per 1 revolution because the

TABLE 1. Experimental conditions.

Component		Value
CFRP material	Staking Sequence	[Woven / -45° / 90° / -45° / 0° / 45° / 90° / 45° / 0° / 0° / 45° / -45° / 90° / -45°...]s
	Carbon fiber	T1000
	Thickness	16 mm
Cutting tool	Model	SSD060, WIDIN
	Diameter	6 mm
	Material	Uncoated Tungsten Carbide
	Point angle	118
	Number of flute	2
Machining condition	Feed	0.01, 0.03, 0.05, 0.1 mm/rev
	Spindle speed	4,000, 8,000, 12,000 rpm
Ultrasonic vibration condition	Frequency	34 kHz
	Amplitude	15 μm

tool has two cutting edges. Therefore, the feed conditions are 0.01, 0.05, 0.1 mm/rev to analysis from the low feed speed to the high feed speed. The drilling thrust force, delamination factors and surface roughness are measured in drilling process

CUTTING FORCE MEASUREMENT

Each thrust force is calculated by averaging the force value during one hole making process at fully engaged status which means the drilling tool is fully entered in drilled hole. The thrust force is measured using tool dynamometer for drilling process (KISTLER 9272). When the machined hole number is increased, the thrust force is increased because the tool is worn. Moreover, when the feed rate is increased, the thrust force increased because chip removal volume is increased in high feed speed. For 20 holes machining process for various machining conditions, the cutting force is increased by proceeding the process, and ultrasonic assisted machining reduced the cutting force.

In this study, the thrust force is measured for 20 holes making procedure at each drilling condition. The thrust forces on each machining condition were compared using the average thrust force of 20 holes. Figure 1 shows thrust forces for various spindle speed in conventional dry process and ultrasonic assisted drilling process at 0.05mm/rev feed condition. Thrust forces were decreased at every spindle speed conditions. At 4,000 rpm and 0.05 mm/rev feed, the average cutting force in conventional hole making process is 79.09 N and ultrasonic assisted drilling process is 66.19 N, so the cutting force is reduced around 17%. At 8,000 rpm and 0.05 mm/rev feed, the cutting force in conventional process is 81.7 N and ultrasonic process reduces cutting force to 72.3 N, 12%. At high spindle speed (12,000 rpm), the thrust force is decreased 7% by ultrasonic assisted machining. When the spindle speed is lower, the ultrasonic machining is more effective, because the vibration number during one revolution is larger at low cutting speed condition.

Figure 2 shows thrust forces for various feed conditions in conventional dry process and ultrasonic assisted drilling process at 8,000 rpm. As shown in figure, the cutting force is decreased by ultrasonically assisted effect at every cutting condition. The reducing rate is more effective when the feed is low because when ultrasonically vibration amplitude is smaller than feeding length during 1 revolution,

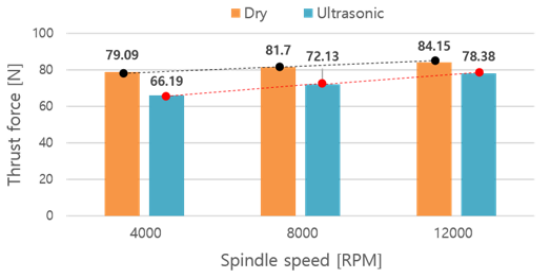

FIGURE 1. Thrust force variation w.r.t the spindle speed in conventional and ultrasonic assisted drilling.

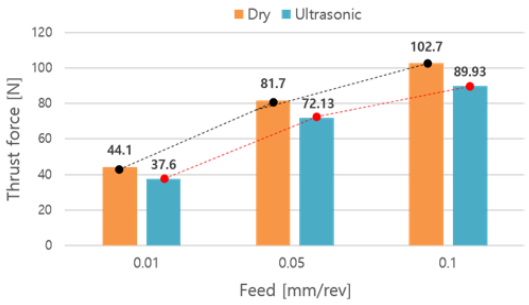

FIGURE 2. Thrust force variation w.r.t the feed in conventional and ultrasonic assisted drilling.

cutting edge and workpiece are detached for an instant. In conventional drilling process, cutting point movement at cutting tool edge is defined by tool diameter, spindle speed and feed rate in axial direction. When cutting point is separated instantly, impact of ultrasonic vibration is transferred to workpiece.

Ultrasonic vibration effect can be observed in cutting force signal during short time such as one radiation time. At 6,000 rpm spindle speed, the tool is rotated 1 revolution for 0.015 sec, therefore 0.02 second can analyze cutting force behavior during one rotation time. Measuring time of two signal is synchronized based on cutting force signal shape to compare same moments. In CFRP drilling process, cutting force signal has short period vibration due to stacking structure. If the stacking layer thickness is small, vibration period can be shorter. The short period vibration can be measured at ultrasonic assisted drilling process.

DELAMINATION FACTOR MEASUREMENT

Delamination factor is widely used parameter to evaluate hole surface quality. Figure 3 shows definition of delamination factor. In this study, delamination factor is measured a microscope

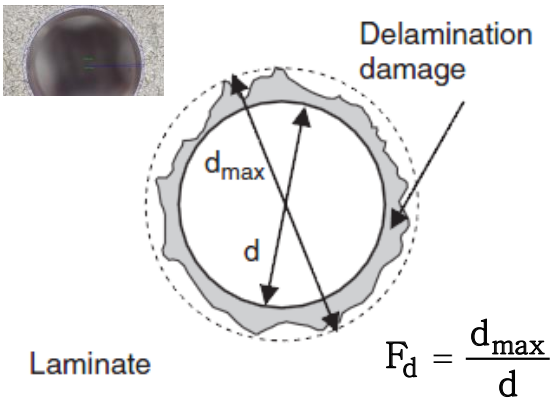

FIGURE 3. Delamination factor of CFRP hole

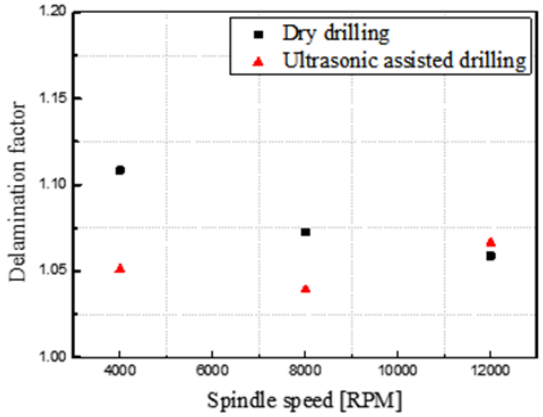

FIGURE 4. Delamination factor w.r.t the spindle speed in conventional and ultrasonic assisted drilling.

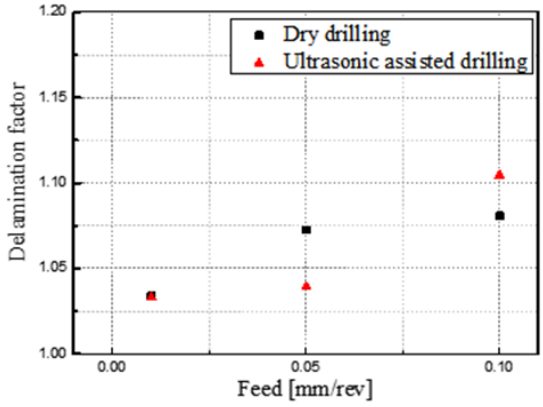

FIGURE 5. Delamination factor w.r.t the feed in conventional and ultrasonic assisted drilling.

image of CFRP hole. The hole diameter (d) and the diameter of delamination damage (d_{max}) is measured using microscope image. Fig. 4

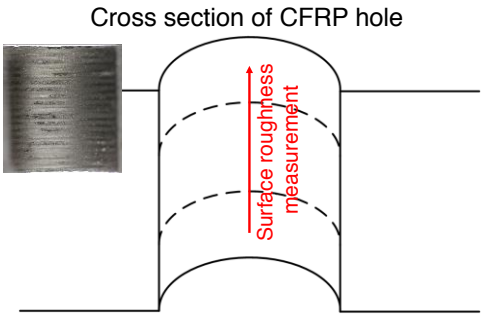

FIGURE 6. Surface roughness measurement on cross section surface of CFRP hole.

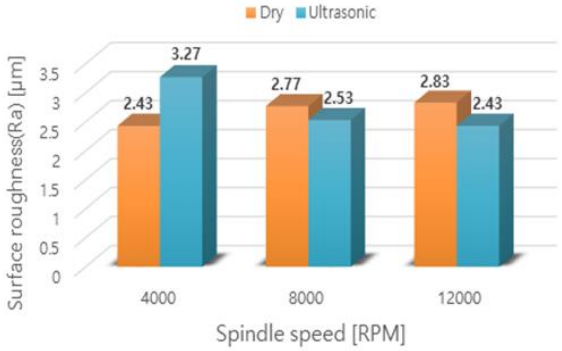

FIGURE 7. Surface roughness w.r.t the spindle speed in conventional and ultrasonic assisted drilling.

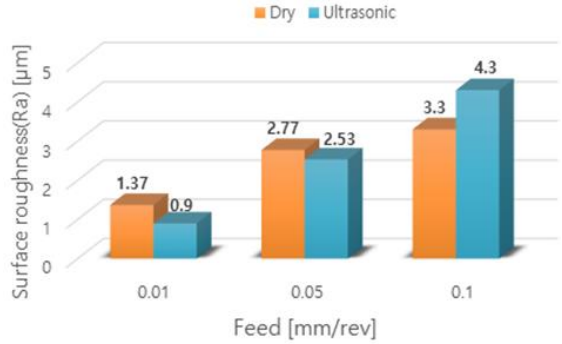

FIGURE 8. Surface roughness w.r.t the feed in conventional and ultrasonic assisted drilling.

shows delamination factor for spindle speed. As shown in fig., ultrasonic assisted drilling contribute low delamination factor comparing conventional dry process. At low spindle speed, delamination factor is reduced effectively.
However, at the high spindle speed, delamination factor is similar. In conventional dry process, delamination factor is more sensitive to spindle speed than ultrasonic assisted drilling

process because ultrasonic vibration increase relative cutting speed by instant impact. Fig. 5 shows delamination factor for feed condition. At 0.05 mm/rev, ultrasonic is more effective, but at high feed (0.1 mm/rev) ultrasonic increases the delamination factor because instant impact is less effective at high feed. However, in the region which ultrasonic impact is effective, delamination factor can be reduced by ultrasonic effect.

SURFACE ROUGHNESS MEASUREMENT

Surface roughness of hole wall is one of the important factor for hole making process because hole wall is contact surface with fastener such as bolt or rivet. If surface quality is low, the fastener can be broken by contact damage. Figure 7 and fig. 8 show surface roughness measurement on wall of CFRP hole w.r.t. the spindle speed and feed, respectively. In conventional dry process, surface roughness is slightly increased by the cutting speed. However, at the ultrasonic assisted process, the surface roughness is decreased from 3.27 to 2.43 by increasing cutting speed.

Surface roughness of CFRP hole wall is influenced by fiber pull-out defect on hole wall. Fiber pull-out defect is related on fiber cutting angle. For example, when the cutting angle is 45 degree, the fiber is cut by shearing, but if the cutting angle is 135 degree, the fiber is cut by bending. [5] Ultrasonic vibration can be change the fiber cutting angle, so the fiber pull-out defect can be decreased at the ultrasonic vibration assisted machining.

As shown in fig. 8, surface roughness is decreased at the low feed condition. At the low feed, ultrasonic vibration affects the machining quality because vibration amplitude is larger than feeding distance during one rotation. Therefore, the surface roughness is improved from 1.37 μm to 0.9 μm at the 0.01mm/rev condition.

CONCLUSION

Various feed condition were compared for CFRP in conventional drilling process and ultrasonic assisted machining. The feed conditions were selected by considering ultrasonic vibrating amplitude. The cutting force was measured for feed condition and ultrasonic. The cutting force was decreased by assisting ultrasonic vibration. When the vibration amplitude and drilling down speed are similar, cutting force was most decreased to 40%. The vibration on cutting motion was helpful to reduce cutting force. By reducing cutting force, delamination was decreased to 25%. The surface roughness on hole wall is improved 34% at low feed condition.

ACKNOWLEDGEMENT

This work was supported by the Technology Innovation Program (10053248, Development of Manufacturing System for CFRP (Carbon Fiber Reinforced Plastics) Machining) funded By the Ministry of Trade, industry & Energy(MOTIE, Korea).

REFERENCES

[1] M. Perner, S. Algermissen, R. Keimer, H.P. Monner, Avoiding defects in manufacturing processes: A review for automated CFRP production, Robotics and Computer-Integrated Manufacturing. 2016; 38: 82-92.

[2] Franck Girot Pr., Frédéric Dau, Mª Esther Gutiérrez-Orrantia, New analytical model for delamination of CFRP during drilling, Journal of Materials Processing Technology. 2017; 240: 332-343.

[3] J. Fernández-Pérez, J.L. Cantero, J. Díaz-Álvarez, M.H. Miguélez, Influence of cutting parameters on tool wear and hole quality in composite aerospace components drilling, Composite Structures. 2017; 178: 157-161.

[4] N. Feito, J. López-Puente, C. Santiuste, M. H. Miguélez, Numerical prediction of delamination in CFRP drilling, Composite Structures. 2014; 108: 677-683.

[5] Demeng Che, Ishan Saxena, Peidong Han, Ping Guo, Kornel F. Ehmann, Machining of carbon fiber reinforced plastics/polymers: A literature review, Journal of Manufacturing Science and Engineering, Transactions of the ASME. 2014; 136: 677-683.

[6] Weixing Xu, Liangchi Zhang, Mechanics of fibre deformation and fracture in vibration-assisted cutting of unidirectional fibre-reinforced polymer composites, International Journal of Machine Tools and Manufacture. 2016; 103: 40-52.

PREPARING AND REPAIRING PRECISION GROUND SURFACES USING FLATSTONES

Henry Arneson
Professional Instruments Company
Hopkins, Minnesota, USA

ABSTRACT
Precision flatstones are an essential tool for use with precision surfaces. When a flatstone is rubbed on such a surface, small asperities and high spots are caught in the porous cavities of the flatstone and are sheared off. The rest of the surface remains largely unchanged. For that reason, flatstones are essential for repairing or preparing precision ground surfaces. They remove localized swelling that occurs from surface damage such as nicks and dents. These small swellings from seemingly insignificant accidents can severely inhibit precision assemblies of these parts. The process of removing the surface damage with flatstones is also self-limiting; as the high spots wear down, material removal decreases until there is full contact of the stone to the surface. This process is demonstrated and results are shown for various common examples of surface damage imaged by the a laser scanning microscope.

FIGURE 1. A pair of flatstones used to prepare a soft iron magnetic chuck before mounting a part.

BACKGROUND

Professional Instruments has been manufacturing and using flatstones to prepare and repair precision ground flat surfaces for over 50 years. The first flatstones were ground by Harold Arneson for his precision assembly work on air bearing spindles. Although the manufacturing process has become more efficient, the original stoning principle still remains the same. Flatstones today are sold commercially and used as a critical component in almost every high precision process employed at Professional Instruments.

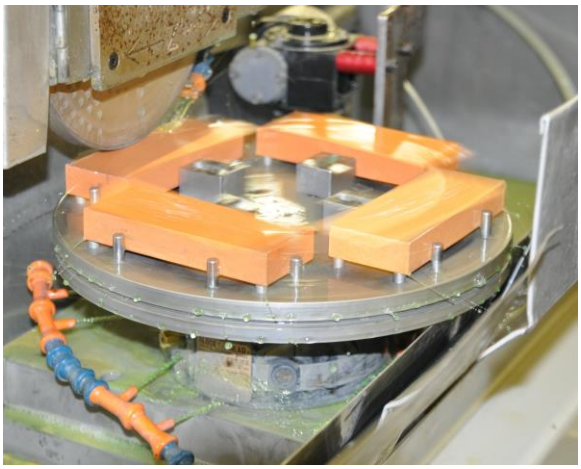

FIGURE 2. Flatstones being roto-ground on a 4R Blockhead airbearing spindle as a batch.

FLATSTONES TODAY

The stones start as untreated knife sharpening stones, very rough and aggressive and unsuitable for work on a ground workpiece. Made of aluminum oxide (with a Mohs hardness of 9) and have a grit of 150-300, which is unimportant because the gritty surface becomes a porous flat surface (pores ranging from 0.001 to 0.005 inches). Faces and edges are ground to tight flatness and perpendicularity requirements (this permits stoning up to an edge). Another important innovation is the packaging of stones as a pair. Before stoning a surface, the stones should first be rubbed against each other to ensure that there is no material protruding from the surface of the

stone. When the stones are used, they shear off material from the surface being stoned and sometimes that sheared off material can stick out proudly from the stone. Rubbing the stones together ensures that the work surface of the stone is clean and won't scratch.

SURFACE TREATMENT WITH FLATSTONES

Precision ground flat surfaces are prone to small damages that will ruin their functionality. Small accidents such as dropping a hex wrench can create a divot which will displace some material above the functional plane of the surface. The high spot is hard to detect with the naked eye, but will interfere when it is being mated with another flat surface. When a flatstone is rubbed on a surface, small defects and high spots are caught in the porous cavities of the flatstones and are sheared off. The rest of the undamaged surface will remain unaffected. This process is self-limiting because once a flat surface loses its imperfections, the cutting action stops. Bearing down by the user on the stone starts as a relatively high force over a small area forcing the high spots into the porous structure of the flatstone to be sheared off by the rubbing action. As defects become less prominent, the applied force of the user becomes distributed across the whole face of the stone. When there are no localized asperities left, the cutting action stops and the user is left with two flat surfaces smoothly moving across each other. This stage of treatment is easily discerned as there is a distinct decrease in resistance and difference in the feedback of the stone when the surface is sufficiently treated. The former high spot will also take on a mirror like quality. It is important to remember that this is not a lapping process. When it is determined that the stone can smoothly operate across the surface, then the surface is ready to be mated or used in a precision assembly. This principle is demonstrated in Figure 3.

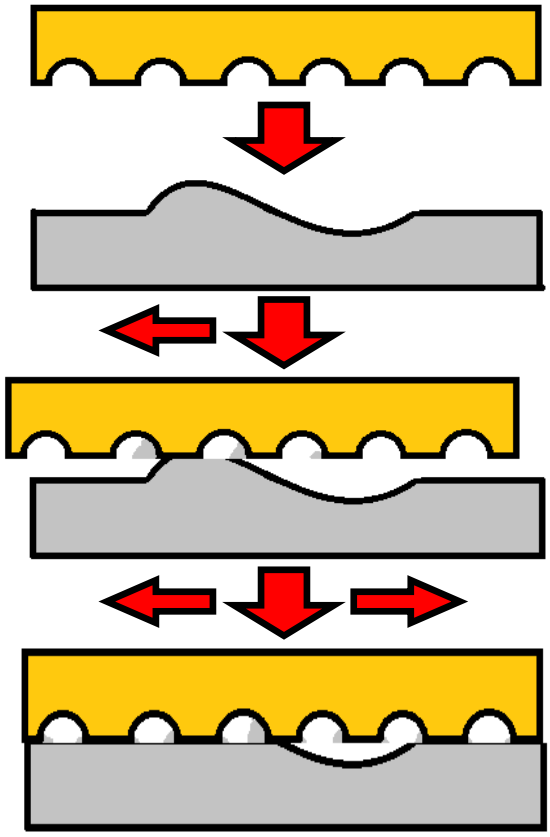

FIGURE 3. Sketch of a flatstone being used on a dent in an otherwise flat ground surface.[Top] Unused flatstone approaching a dented surface. [Middle] First engagement of the flatstone to the damaged surface; notice the high spot being sheared and absorbed into the porous stone's structure. [Bottom] The high spot has been completely sheared away, leaving a flat surface and a small dent from the original damage.

STONING MEASUREMENT

To demonstrate the effectiveness of flatstones, a part is deliberately damaged and then repaired back to functional quality. These results are repeated on a flat ground mild steel part. The first example is a divot created by a sharp tool. This is representative of dropping a tool on the part. Figure 4 and Figure 5 show the defect before and after stoning, respectively.

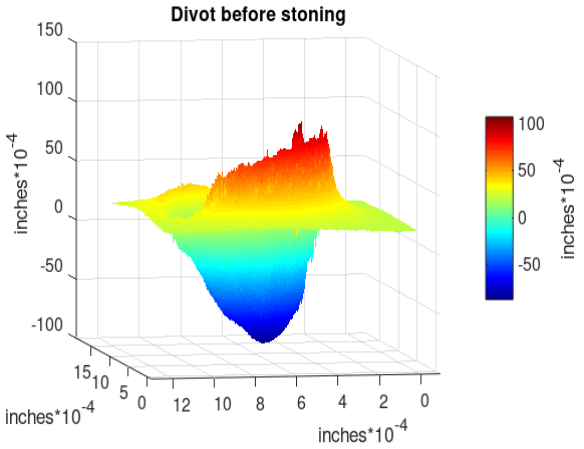

FIGURE 4. Surface plot of a divot caused by a sharp tool. It is clearly shown that the damage extends above the surface because of the displaced material.

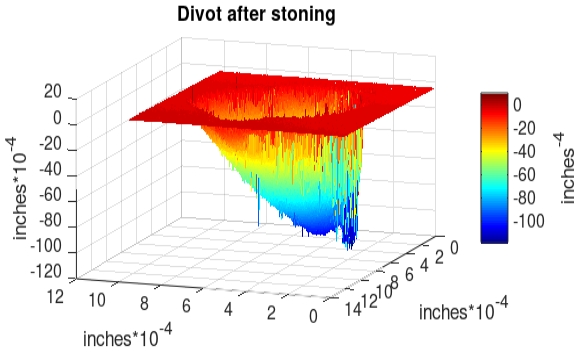

FIGURE 5. Surface plot of the same divot after stoning. The displaced material is removed and the top surface is now flat.

Before stoning, edges around the divot are raised because of the displaced material from the hole. This displaced material rises well above the functional plane of the flat ground part. After stoning, the raised edges around the divot have been sheared down to flats illustrated in Figure 5. The next example of damage that can be repaired with a flatstone is a shallow scratch, shown in Figure 6 and Figure 7.

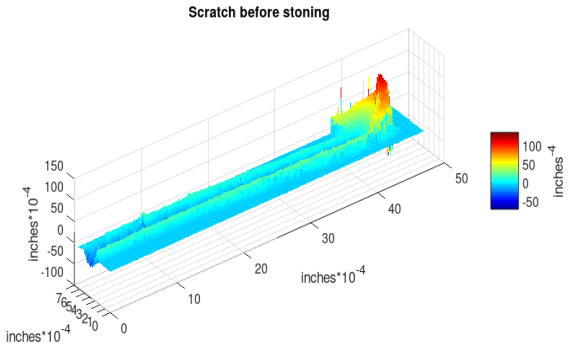

FIGURE 6. Surface plot of a scratch caused by a sharp tool. The scratch not only creates a trench, but also raised areas on the sides of the scratch.

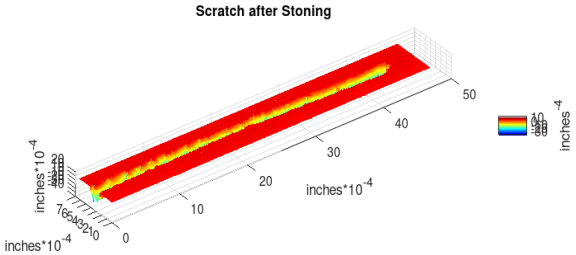

FIGURE 7. Surface plot of the same scratch after stoning. The displaced material is removed and the top surface is now flat.

Even the light scratch showed a significant deformation above the plane of the flat surface. Again after the treatment with the flat stones, the raised spots are replaced with a flat. Figure 8 shows a section of the same scratch before and after stoning. The raised edges of the scratch are sheared and smoother than the rest of the ground surface.

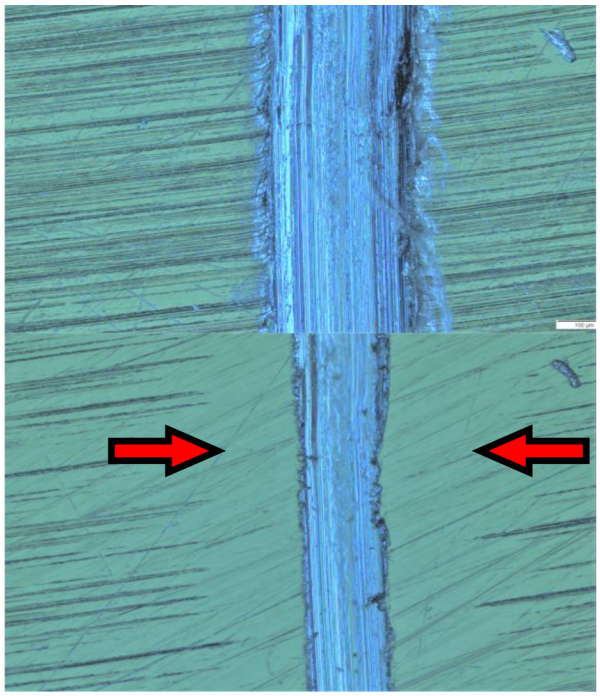

FIGURE 8. The same scratch from a detailed image. The raised areas, indicated by the arrows on the sides of the scratch are smoother than the rest of the ground surface.

The principle of shearing high spots is also demonstrated Figure 9. A profilometer reading is taken on a flat precision ground mild steel plate before and after stoning. Here the small variability in the ground surface is clearly visible and the surface roughness is 8.6 µin. After stoning, the peaks in the surface trace have been sheared off leaving only the low spots under the flat top surface. The surface finish also improved to 6.2 µin.

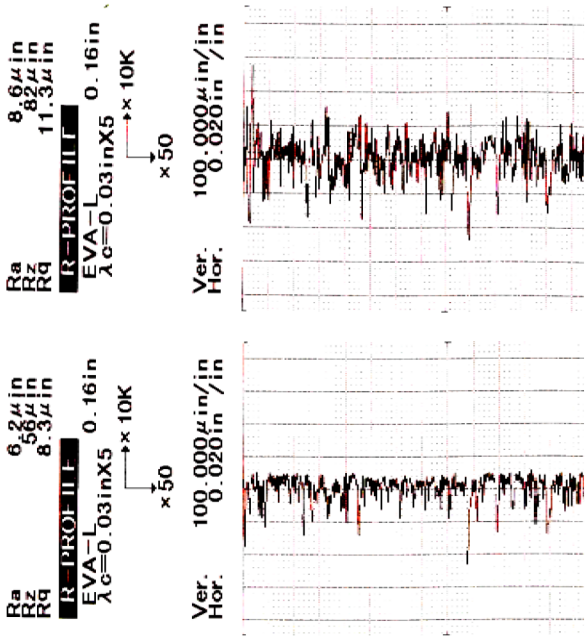

FIGURE 9. Profilometer reading of a flat ground plate before [top] and after [bottom] stoning.

CONCLUSION

Flatstones are essential for repair or preparing precision ground flat surfaces. Damage to a surface results in raised areas which degrade its functional quality. In the worst case, this can lead to the failure of a precision assembly and the end product, such as an air bearing, will not function. Use of a flatstone is an easy manual process that removes these defects and cleans the surface. This is demonstrated and measured on examples of common workplace damage.

REFERENCES

[1] GF-5 Precision-Ground Flatstones. Professional Instruments Company. Available from: http://www.airbearings.com/flatstones

[2] Carl Zeiss. Surfcom: Surface Finish Parameters. [poster] IMT Corporation

[3] Marsh, Eric. Repairing a Damaged Part with Flat Stones. PennState University. Available from: http://mdrl.mne.psu.edu/docs/flatstones.pdf

CHARACTERIZING CHEMICAL WEAR OF SINGLE CRYSTAL DIAMOND TOOLS IN CUTTING ALLOYS

Alexander Blum[1], Kristen Venditti[1], Radha Patel[1]and Chris Evans[1]
[1]Department of Mechanical Engineering and Engineering Science
University of North Carolina at Charlotte
Charlotte, NC 28223, US

ABSTRACT
Interferometric measurement of plunge cuts made in a copper plated reference sample between repeated facing cuts of a Monel wear sample allow for detailed measurement of edge recession without removing the cutting tool from the machine. This allows the progression of tool wear to be evaluated with a resolution of less than 5 nm. The method described in [1,2] was used to evaluate the effect of crystallographic orientation on the rate of tool edge recession when cutting Monel, demonstrated previously to give chemical wear.

INTRODUCTION
Single point diamond turning (SPDT) uses highly polished SCD tools in conjunction with precision machinery to produce optical surfaces. In the 1970s and 80s, diamond turning evolved into the mainstream and began to be commonly used to manufacture optics [6]. The use of “diamond turnable” materials is important in this context, due to the cost of single crystal tools [7]. Wear rates on the diamond tool must be low enough so that it is economically feasible to produce an optical surface.

Additionally, diamond tool wear can occur even in materials considered “diamond turnable,” leading to surface form errors, high cutting forces, and surface roughness [2]. Techniques such as ultrasonic machining have been developed to reduce wear when cutting titanium and steels [8], but diamond tool wear for alloys has not been quantified generally . That is the focus of this research. Diamond tool wear is still a fundamental limitation when micro-machining with SCD tools, despite eight decades of research on the topic.

Wear mechanisms can be classified under four broad categories: abrasion, adhesion, tribothermal, and tribochemical. The importance of chemical mechanisms has been emphasized repeatedly, and the role of unpaired d-shell electrons has been identified [1], [2].

The work described here is part of a larger project to characterize chemical wear rates in diamond turning. The project objectives are:

- Measure single crystal diamond tool (SCD) temperatures during orthogonal finish machining to compare measured edge temperatures to FEM models.
- Quantify how oxygen partial pressure during single point diamond turning (SPDT) affects the diamond tool wear.
- Determine activation energies for chemical wear while SPDT under varying cutting conditions, using temperatures from the validated models and from experimentally varying process conditions.

Anisotropic etching of diamonds by reactive ion etching and inductively coupled plasma etching has been demonstrated in commercially available systems. It has also been demonstrated in molten cerium [3] and molten nickel [4]. Both cerium and nickel [1,5], cause diamond tool wear as predicted for metals with unpaired d-shell electrons; Ce has one unpaired d-shell electron and Ni two.

For the single crystal diamond tools used here, the rake face is nominally (110), so the chip sliding across the rake interacts, nominally, with the same areal density of “dangling bonds” (or hydrocarbon terminated bonds) suggesting that crater wear should be independent of rotation angle of the tool with respect to the nose. At the nose of the tool, the clearance is 6 degrees off 100, with the crystallographic orientation varying around the leading edge. If the tool is rotated, the sampled crystallographic orientations of the diamond at the edge/clearance in the leading edge changes.

The hypothesis tested in this experiment is that edge recession rates will vary with diamond crystallographic orientation but that crater wear

will not. Future work will test the hypothesis that the presence of oxygen facilitates carbon-carbon bond breaking at high temperatures [5], increasing wear rates. This hypothesis will be tested by building an enclosure around the diamond turning work volume similar to that described in [5]. This volume will be flooded with helium, reducing the oxygen partial pressure. The relationship between oxygen partial pressure and tool edge recession will be evaluated.

Measurement of Diamond Tool Wear

Quantification of tool wear in SPDT is difficult. Research often uses indirect measures, such as cutting force and surface finish, to describe wear. This provides a relevant metric but does not allow for detailed analysis of the mechanisms involved. Evans et al. provide a detailed overview of how quantitative approaches have been refined, and of the approach used to measure plunges in this experiment [1], [2].

Previous research has investigated copper-nickel alloys. They are interesting because copper causes negligible tool wear, while nickel provides extremely high rates of wear and all alloy compositions are single phased. Monel (~65% Ni) was used for this experiment.

EXPERIMENTAL METHOD

A concentric copper ring and Monel sample is mounted to the spindle of a Precitech Nanoform 350 diamond turning machine. The wear sample is faced in a series of passes from the edge towards the center of the part. In between each facing pass the diamond tool is plunged into the witness sample. Surface replications of the Monel were taken between each pass, and force was measured during the facing cuts and plunges.

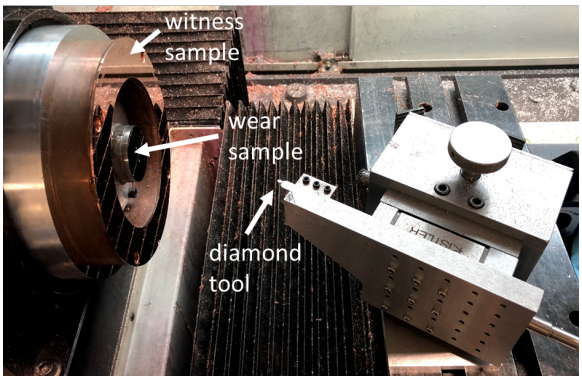

FIGURE 1: Experimental setup showing copper wear ring, Monel wear sample, diamond tool, and Kistler dynamometer.

All diamond tools used are fabricated by Edge Technologies. All tools are new or relapped before being used. Nominal tool geometry is 0.5 mm nose radius, 0° rake angle, and 6° conical clearance. In these experiments, "0°" refers to the nominal alignment of the diamond in the fabricated tool. +/- N° describes rotation of the tool post such that the "nose" of the cutting tool is rotated N degrees from nominal.

For each crystallographic orientation the following steps are performed. First, the new tool is plunged into the copper ring to replicate the unworn edge. Then the Monel sample is faced and the tool is plunged into the copper ring again. This process is repeated until the Monel is faced five times, and six plunges have been cut into the copper ring. Oil mist lubrication is used during all tests.

TABLE 1: Experiment parameters.

No. Facing Passes	**Facing Distance (mm)**	**Facing DOC (µm)**	**Feed Rate (mm/min)**
5	6	0.5	2.0
Plunge DOC (µm)	**Plunge Feed Rate (nm/rev)**	**No. Plunge Cuts**	
12	500	6	

The process described above is repeated for three crystallographic orientations. The reference orientation, 0°, is with the tool parallel to the centerline of the spindle. Plunges are taken at 0°, 15°, and 30° orientations.

Plunge Cut Analysis

Each plunge is measured using a Zygo ZeGage Scanning White Light Interferometer with 20x objective; data is exported to Matlab for processing.

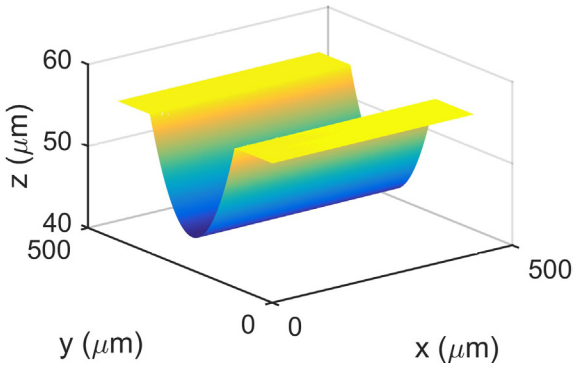

FIGURE 2: Imported plunge in Matlab, before processing.

The data processing algorithm is as follows:

1. Import data to Matlab as 2-D phase maps, axis convention shown above.
2. Rotate about z-axis so that plunge edges are parallel to x-axis.
3. Remove piston and tilt, using the flat surface to sides of plunge as reference.
4. Column average the phase map to create 1-D vector representing plunge, create corresponding x-vector. Deviation of plunge from a straight line in the field of view of the interferometer is approximately 0.02 pixels, introducing a negligible "blur" due to column averaging.
5. Interpolate vectors from previous step over finer spacing.
6. Repeat steps (2)-(5) for all six plunges.
7. Center the initial plunge at x=0.
8. Align all plunges with the initial, unworn plunge, as shown in Figure 3, using the unworn portions of the tool edge.
9. Subtract each plunge from the initial, unworn plunge
10. Plot results of previous step (Figure 4)

The original tool tip is centered at zero. Positive values correspond to the leading edge, negative values correspond to the trailing edge.

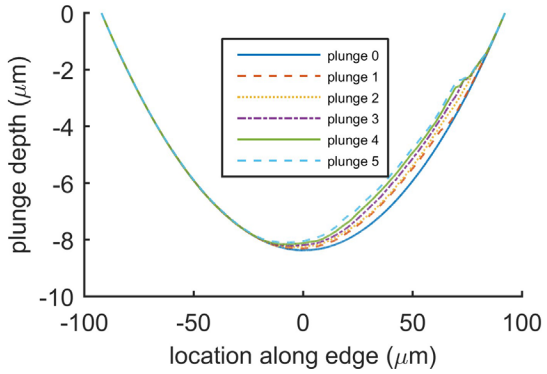

FIGURE 3: Aligned plunges from 0° test.

RESULTS

For the 0° (reference) case there is approximately 400 nm of edge recession at the nose on pass one. Subsequent passes do not noticeably increase the nose recession. Leading edge wear is small on pass one, but increases with each subsequent pass. Under similar conditions Browy [3] showed both nose and leading edge wear, although the magnitudes of edge recession differ. The composition (specifically interstitial nitrogen content and hence thermal conductivity and local temperatures) differs between the tools used in [3] and those used here. The edge preparation method is also different. These factors will be evaluated in future work

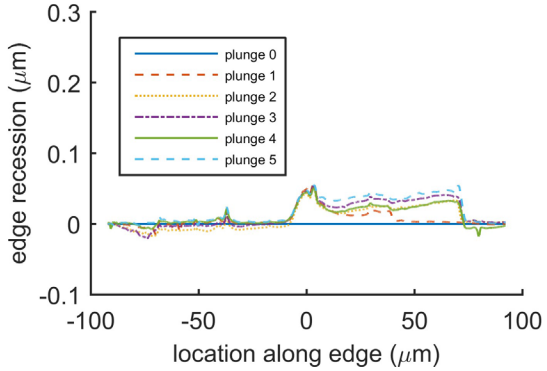

FIGURE 4: 0° (reference) residual.

The 15° residual shows a similar magnitude of nose wear when compared to the reference case. However, leading edge wear has increased by at least factor of ten. There appears to be a periodic structure to the nose wear that is not present in the leading edge wear.

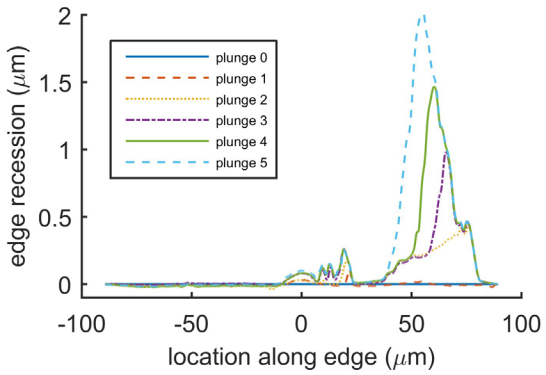

FIGURE 5: 15° residual

Comparing both of these results to those obtained at 30° shows a dramatic increase in the rate of tool wear, under otherwise identical cutting conditions. The wear is primarily along the leading edge, and appears to grow at a linear rate between passes. The 15° case shows a higher 'spike' along the leading edge (see plunge 5), but the total area under the curve is greater for the 30° plunges.

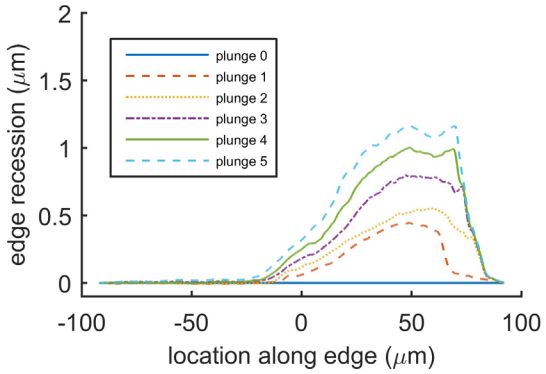

FIGURE 6: 30° residual.

The maximum cutting force during plunge six was 0.16 N for the 0° case and 0.8 N for the 30° case, for a five-fold increase in cutting force.

CONCLUSION

Edge recession measurements and cutting forces support the hypothesis that chemical wear rates are a function of the diamond orientation. Both depth of cut and crystallographic orientation wary around the leading edge. More data are required to separate these and other effects such as diamond chemistry and thermal conductivity.

Acknowledgement: This work is supported in part by NSF CMMI Grant 1728554

REFERENCES

[1] Evans C. J., Browy E.C., Childs T.H.C., and Paul E."Interferometric measurements of single crystal diamond tool wear," CIRP Annals, **64** (2015) pp125-8

[2] Browy, E.C. "The evaluation of chemical wear on single crystal diamond tools while diamond turning a binary Cu-Ni alloy system," MS thesis, UNC Charlotte, 2014

[3] Jin S., Zhu W., Siegrist T., Tiefel T. H., Kammlott G. W., Graebner J. E., and McCormack M., *Applied Physics Letters* **65**, 2675 (1994)

[4] W. Smirnova, J. J. Hees, D. Brink, W. Müller-Sebert, A. Kriele, O. A. Williams, and C. E. Nebel "Anisotropic etching of diamond by molten Ni particles" Appl. Phys. Lett. **97**, 073117 (2010

[5] Paul, E., Evans C. J., Mangamelli, A., McGlauflin M. L., and Polvani R. S. "Chemical aspects of tool wear in single point diamond turning," Precision Engineering 1996; 18:4-19.

[6] Evans, C.J. Precision Engineering: An Evolutionary View. Cranfield, UK: Cranfield Press, 1989

[7] Evans, C.J. "Cryogenic diamond turning of stainless steel," Annals CIRP, 1991 40, 571-5.

[8] Shi, M. and Lane, B. et al. "Diamond tool wear measurements by electron-beam-induced deposition," Precision Engineering 34, 718-721, 2010.

Diamond Turning of Plastic Optics

Charan Bodlapati[1], Thomas Dow[1], Anthony Wong[1], Ken Garrard[1] and Alex Sohn[2]
[1]Precision Engineering Consortium
Department of Mechanical and Aerospace Engineering
North Carolina State University
Raleigh, NC, USA
[2]Facebook Reality Labs
Seattle, WA, USA

INTRODUCTION

Optical devices are extremely important since they play a critical role in optical recording and display. Single point diamond turning is one of the most common methods used to create plastic optics. Diamond turning of plastics is influenced by a wide variety of factors such as glass transition temperature of the polymer, material properties and operator controlled cutting conditions. Since diamond is one of the hardest materials in nature and polymers are relatively soft, little tool wear is expected. However, industry has identified that tool wear is a major problem in diamond turning of polymers. Most of the optical industry uses Polymethyl methacrylate (PMMA) and Polycarbonate (PC) for creating optics. Prior work on diamond turning of plastics was performed by Gubbels [1] and Carr et al. [2], but information on parameters that can optimize the surface finish and minimize diamond tool wear is lacking. The main objective of this research is to optimize machining parameters (such as feed, tool radius, depth of cut, cutting speed and rake angle) to produce optical quality surface while minimizing tool wear while cutting PMMA and PC. A wide range of experiments were performed on these two materials by varying the machining parameters and measuring tool wear using the Electron Beam Induced Deposition (EBID) technique [3] in a Scanning Electron Microscope (SEM).

SURFACE FINISH STUDY

Experimental Setup

The machining experiments were performed on a Pneumo ASG 2500 diamond turning machine (DTM). The experimental setup shown in Figure 1 is a typical turning operation. The setup consists of a 50 mm diameter plastic rod attached to the spindle and a mono-crystalline diamond tool is attached to the tool post. A chip management system is employed which includes an Electrostatics Inc., HPN AC ionizer and a chip suction system. An air ionizer consists of an air nozzle and a 5000 V Herbert static power supply, connected via a shielded high voltage cable. The ionizer creates a vertical air flow past the chip exiting from the workpiece. The vertical flow of air guides the chip to the vacuum flow and removes it from the cutting zone.

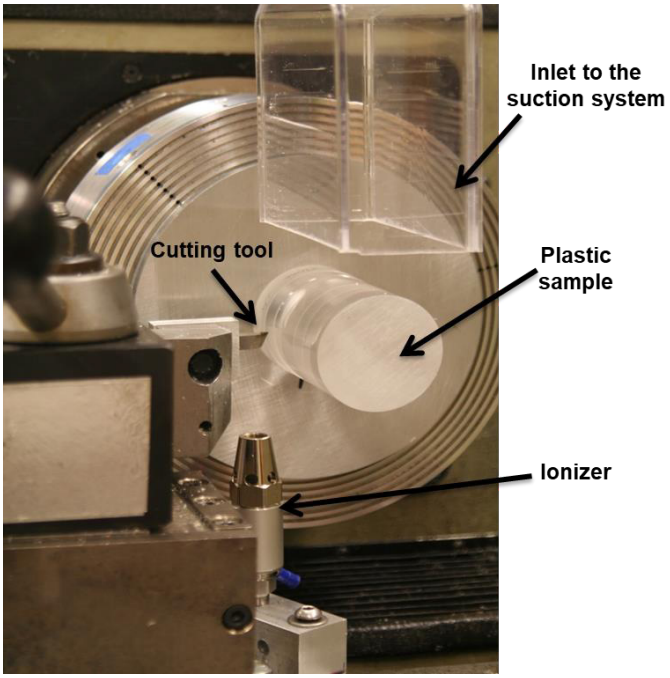

FIGURE 1. Experimental setup

Poly (methyl methacrylate) (PMMA)

PMMA is a transparent thermoplastic with a high refractive index, light transmission qualities and high scratch resistance, which makes it favorable to be used as an optical material. Many overlapping feed experiments were performed on PMMA to study the effects of machining parameters – feed rate, depth of cut, cutting speed, tool radius, tool rake angle, and

chip management on surface finish and tool wear.

Surface finish and feed rate are geometrically related using a parabolic approximation [4] as shown in Equation 1.

$$\text{Theoretical RMS surface finish} = \frac{f^2}{26.6\ R} \qquad (1)$$

Where f is feed rate in μm/rev and R is nose radius of the tool in μm. RMS finish is in μm.

According to equation 1, the relation between the feed rate and surface finish is parabolic for a given tool radius, but this relation was found not to hold at very small feed rates or small theoretical roughness. Figure 2 shows the variation of RMS roughness with feed rate. According to Lucas Lamonds [5], the surface finish at finer feeds also depends on asynchronous spindle rotation and machine vibration. When the amplitude of machine vibration is more than the height of grooves created due to the feed rate, then the geometric relation between surface finish and feed rate (equation 1) will not hold.

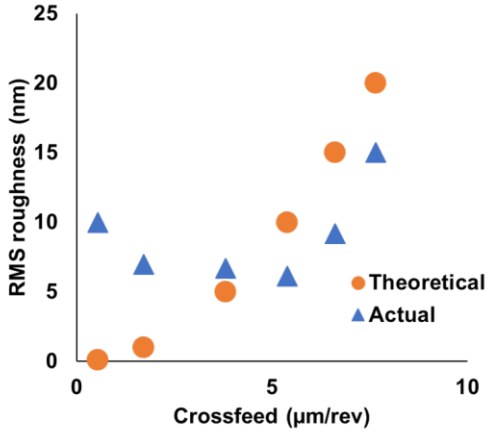

FIGURE 2. Effect of cross feed on RMS roughness of PMMA when machined with a 100 μm nose radius tool at 1450 rpm and 10 μm depth of cut (DOC)

Figure 3 shows the effect of tool radius on RMS roughness when machining PMMA. Figure 3 shows that smaller radius tools generate better surface finish for the same theoretical RMS roughness. Figure 4 shows the variation of RMS roughness with the rake angle of the tool on PMMA. -5^0 rake angle was found to be better than 0^0 and 5^0 rake angles. A similar kind of variation was observed by Gubbels [1] and is predicted since PMMA is a brittle material [6].

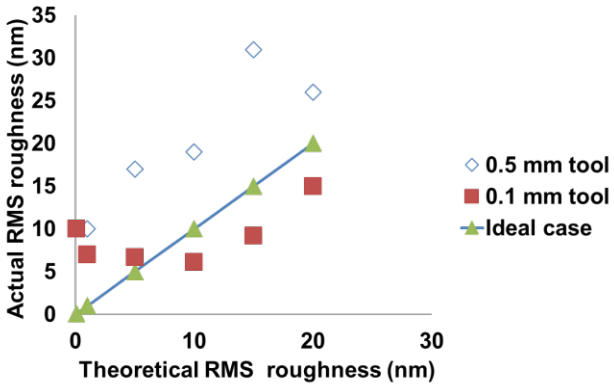

FIGURE 3. Effect of tool radius on RMS roughness of PMMA when machined with a 100 μm and 500 μm nose radius tools at 1450 rpm and 10 μm depth of cut (DOC)

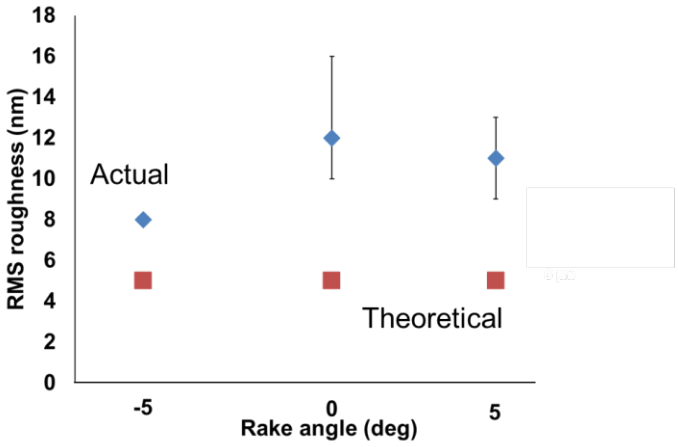

FIGURE 4. Effect of rake angle on RMS roughness on PMMA when machined with a 250 μm and nose radius tool at 1450 rpm and 10 μm depth of cut (DOC)

No effect of cutting speed, depth of cut and air ionization on RMS surface finish were found when PMMA was machined.

Polycarbonate (PC)

Polycarbonate is a transparent thermoplastic and is a high impact strength polymer. Dry turning of polycarbonate to obtain optical quality surface finishes was difficult. Polycarbonate chips were found to ball up on the diamond tool during cutting and strike the machined surface. This degraded surface finish. Figure 5 shows streakiness on the surface of polycarbonate sample after diamond turning.

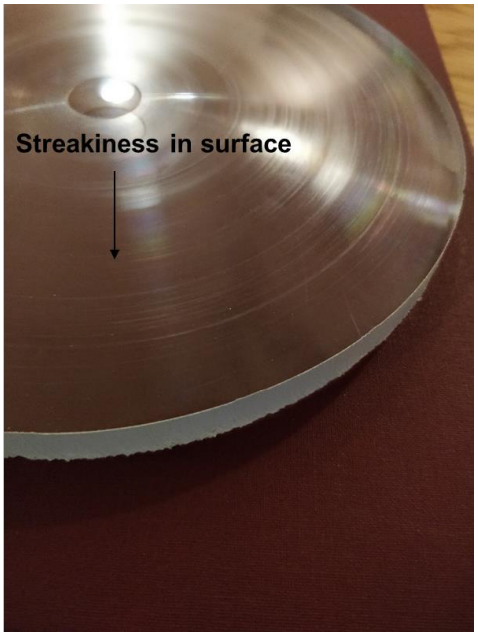

FIGURE 5. Polycarbonate sample after machining without any chip control

To manage chips when machining polycarbonate, the experimental setup shown in Figure 1 was employed. Experimental flow analysis on chips generated using setup 1 showed that the air pressure from the ionizer at 0.5 Pa and suction of 400 feet per minute (fpm) was optimum for managing chips.

Figure 6 shows the effect of crossfeed on RMS surface finish achieved. It is clear from Figure 6 that surface finish on PMMA was better than that of PC under similar cutting conditions.

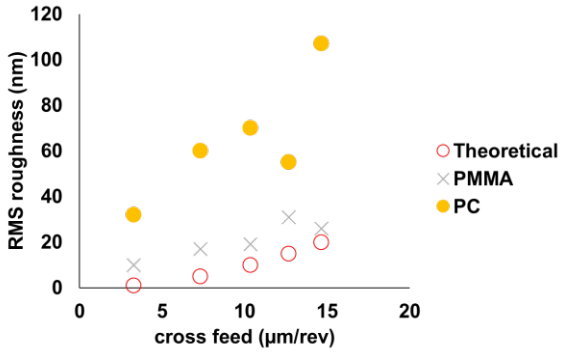

FIGURE 6. Effect of cross feed on RMS surface finish on PC when machined with a 400 µm nose radius tool at 20 µm depth of cut

Figure 7 shows the effect of depth of cut on RMS surface finish. Higher depths of cut were found to give better surface finish on polycarbonate.

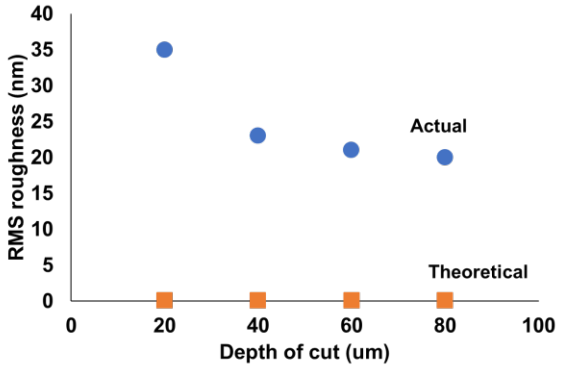

FIGURE 7. Effect of depth on RMS surface finish of PC when machined with a 100 µm nose radius tool

It was found that there exists a critical stiffness of the chip for a given tool radius and feed rate to get good surface finish on PC. The chip can be easily entrained into the vertical flow created by the ionizer. For a 100 µm radius tool and 0.6 µm/rev feed rate, the critical stiffness was found to be achieved at depths of cut greater than 40 µm.

However, the surface finish was found to be limited by buildup on the tool. Figure 8 shows the PC surface and a theoretical tool profile after machining with a 400 µm nose radius tool and 14 µm/rev cross feed. PC surface in Figure 8 was measured using Keyence confocal VKX-1000 microscope. Theoretical grooves in Figure 8 are smaller than the measured grooves, which could be due to the buildup on the diamond tool.

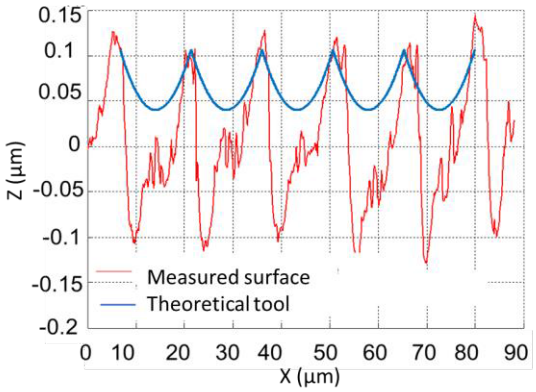

FIGURE 8. Evidence of Build up edge (BUE) on the PC surface

Figure 9 shows the effect of rake angle on PC surface finish. $+5^0$ rake angle was found to be better than zero. The surface finish data generated by $+5^0$ rake angle was found to have a relatively small standard deviation compared to zero rake. No effect of cutting speed on surface finish was found after machining PC.

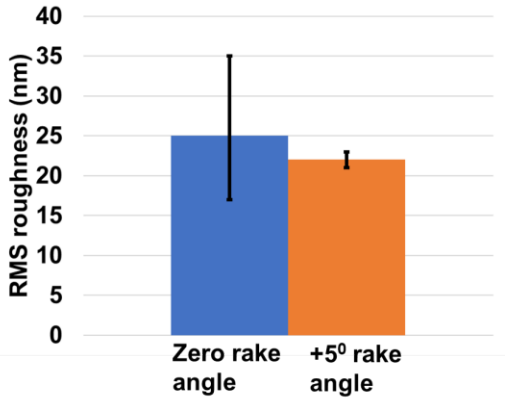

FIGURE 9. Effect of rake angle on RMS surface finish on PC when machined with a 250 µm nose radius tool at 20 µm depth of cut

TOOL WEAR STUDY

Variable Chip Thickness Experiments

Variable chip thickness experiments to investigate tool wear used the experimental setup shown in Figure 1. Figure 10 shows the tool after cutting PMMA and PC. Wear on the tool that was used to cut PC was more prominent than on the tool that cut PMMA. It was also found that damage on the tool is not constant along nose radius of the diamond tool. This is due to the variable chip thickness during the cutting process. Figure 11 shows the comparison of the two tool profiles after machining.

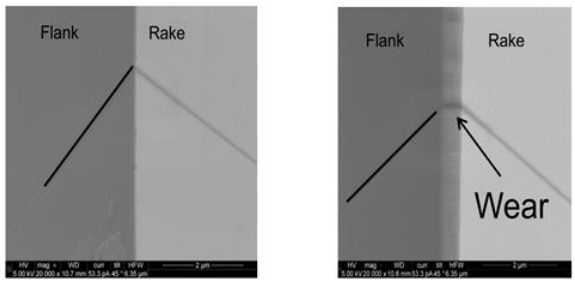

FIGURE 10. SEM images with EBID [3] line at the center line of the tool (a) PMMA after 8 km of cutting (b) PC after 3 km of cutting (20,000X mag) under same cutting conditions

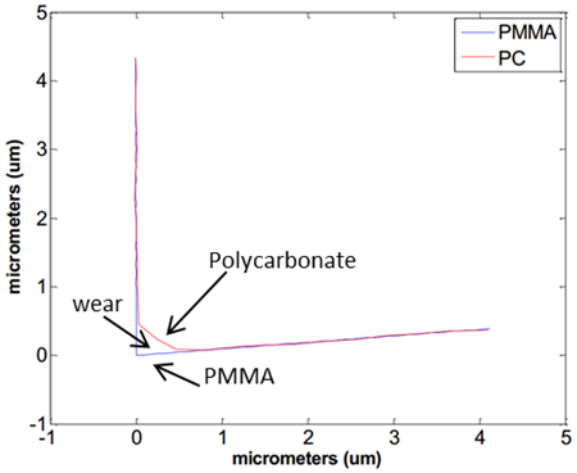

FIGURE 11. Tool profiles from Figure 2 after cutting PMMA (8 km of cutting) and PC (3 km of cutting) under similar cutting conditions

Constant Chip Thickness Experiments

Constant chip thickness experiments were believed to give a better idea of tool wear, since uncut chip thickness is constant across entire width of chip. The setup used for performing constant chip thickness experiments is shown in Figure 12. A 3.5 mm wide square diamond tool was plunged from the outside diameter of 0.5 mm thick plastic disk, towards the center.

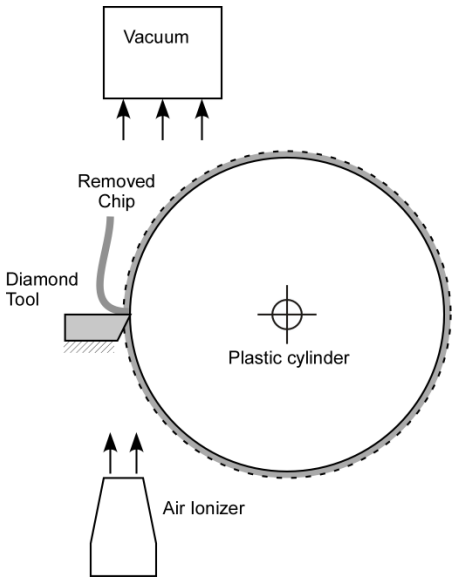

FIGURE 12. Schematic of the plunge cutting setup

Chip thickness was found to be the critical parameter that effects tool wear in variable chip thickness experiments. Plunge cutting

experiments on PC with different uncut chip thickness – 2 µm, 3 µm and 10 µm were performed.

The images of tools after cutting are shown in Figure 13. An unknown material was found on the rake face after cutting PC at 2 μm/rev, shown in Figure 13 (a). Chemicals like Dichloro-methane, chloroform, Keller's reagent and acetone could not remove the material from the tool. 3 µm/rev and 10 µm/rev feed rates resulted in damage of clearance face of the tool. This is shown in Figure 13 (b) and 13 (c). At 10 µm/rev, a series of holes from clearance face through to the rake face of the tool were observed. A reason for this could be that a large static electric field was developed during cutting, since both PC and diamond are insulators. Figure 14 shows one of the possible configurations of charge developed while cutting PC with diamond [1]. The positive ions from the ionizer want to travel to the negative ions on the lower side of the chip. If this static electric field developed during cutting was greater than bond dissociation energy of carbon, then the ions from the ionized air would rip through the diamond and make through holes in the diamond [1] as shown in Figure 13 (c).

CONCLUSIONS

Diamond turning PMMA is found to give better surface finish than PC. Smaller nose radius tools were found to produce surface finish on both PMMA and PC. -5^0 rake angle gave better surface finish on PMMA, and $+5^0$ rake angle gave consistent surface finish on PC. Higher depths of cut were found to generated better surface finishes on PC. Surface finish on PC was found to be affected by chip management and build up on the tool while cutting. PC wears tools more than PMMA under similar cutting conditions. Tool wear after machining PC is affected by the maximum chip thickness.

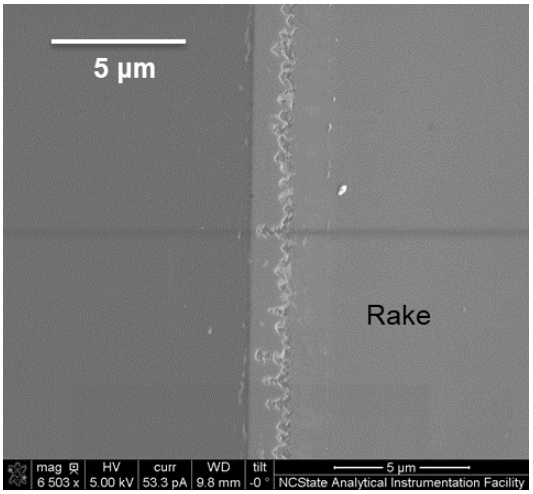

(a) 2 μm/rev, 6500X magnification

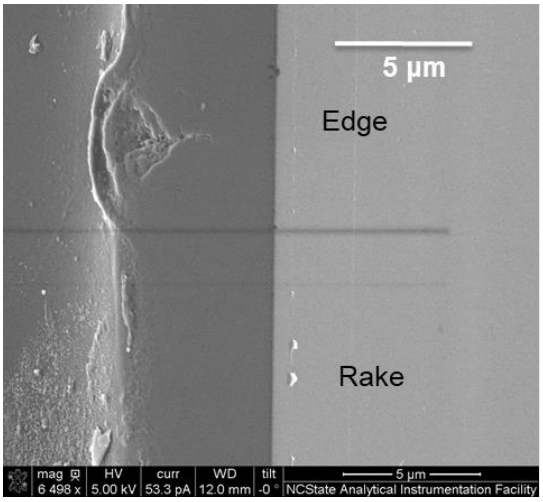

(b) 3 μm/rev, 6500X magnification

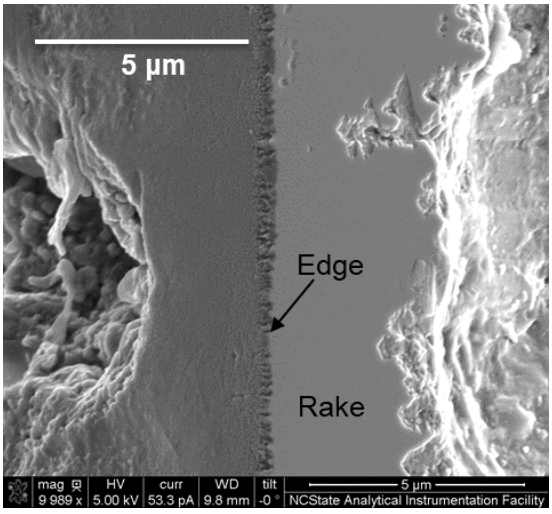

(c) 10 μm/rev, 6500X magnification

FIGURE 13. Tool damage after cutting PC for 4 km

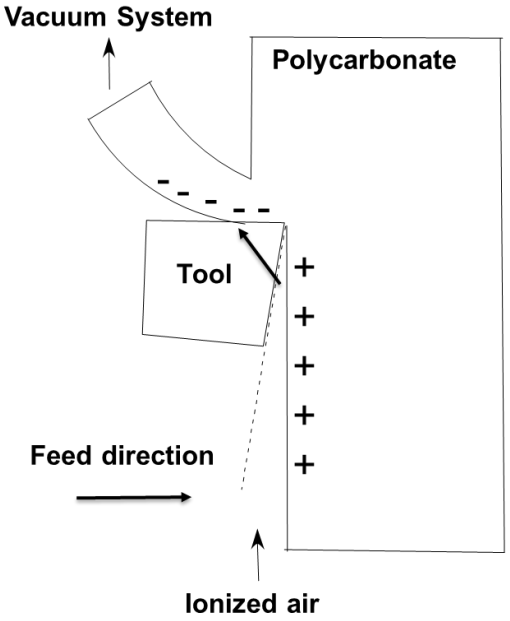

FIGURE 14. Schematic of possible charge configuration during PC cutting [1]

REFERENCES

[1] Gubbels GPH. Diamond turning of glassy polymers[dissertation]. Eindhoven University; 2006.
[2] Carr JW, Feger C. Ultraprecision machining of polymers. Precision Engineering. 1993;15(4):221-37.
[3] Drescher J. Scanning electron microscopic technique for imaging a diamond tool edge. Precision Engineering. 1993;15(2):112-4.
[4] Boothroyd G. Fundamentals of metal machining and machine tools. Crc Press; 1988 Nov 15.
[5] Lamonds DL. Surface Finish and Form Fidelity in Diamond Turning[dissertation]. North Carolina State University; 2008.

Poster Sessions 2

AXIALLY FORCE LIMITED GRINDING SPINDLE FOR ROBOTIC GRINDING

Austin Brown, Alexander Slocum
MIT Department of Mechanical Engineering
Cambridge, Massachusetts

Abstract

Grinding and Polishing of small parts is often easily performed by human hands, yet is challenging to automate. The grinding and polishing process is best done using a force-control scheme, which human hands perform naturally. Heavy robotic arms, which favor a position-control scheme, are difficult to control precisely, and trajectory errors can cause excessive grinding force which leads to burning of the part or destruction of the grinding wheel. Prior art of direct force control on a large robot arm requires the end-effector to have a 6-axis dynamometer, which is unwieldy, costly, and greatly limits the speed/precision of the process. We will discuss a new type of grinding spindle which is axially compliant, allowing the position-control robot arm to be used in a force-control nature. The spindle has a disjoint force-displacement curve, effectively operating in two modes: position-control mode at first, until a critical force is exceeded, when the spindle transitions into force-mode, keeping constant grinding force on the part though a certain range of travel. This limits the amount of force which can be imparted during grinding to a safe amount. The spindle is very simple and mechanically robust. We have built this hybrid position-force control spindle and tested it. The spindle was shown to perform correctly and successfully completed the test grind.

Introduction

Today's world demands increasing automation. Nearly every field is turning towards automation to produce products at higher volumes with lower costs. Manufacturing is a sector which is moving increasingly towards full automation. However, new technology presents new problems. One manufacturing area which is looking towards increased automation is the grinding and polishing of watches. Watch grinding requires high dexterity and skill. The workforce is aging without being replaced. One promising option for automation is to replace the humans with robot arms. Robot arms are incredibly versatile, meaning that a large number of operations can be performed by a single arm, and that the arm can be repurposed for other operations if products change.

However, robot arms are generally not very precise when they most fast: robot arms have very low control bandwidth compared to other machining machine types, and therefore at high path speeds precision suffers greatly. A robot arm's low bandwidth is due to the high moving mass and cantilevered nature of the robot arms. Robots have versatility at the cost of accuracy and control bandwidth. This means that any motion will have small trajectory errors, with the problems becoming worse at higher speeds. In the case of grinding, the grinding wheel is usually rigid, and so small trajectory errors

can cause huge forces to arise. Huge forces result in many problems, most likely destruction of the grinding disk. Compliant grinding media, such as belts, can be used to polish, but have difficulty achieving accurate parts.

Ideally, a hybrid force-position control scheme could be implemented for robotic grinding. A final shape of workpiece is desired, which requires position-mode control, but grinding cannot be done with excessive forces, which requires force control. Prior art of force-control bolt grinding was done with a 6-axis dynamometer mounted to the end of the robot arm, between the end of the arm and the workpiece [1]. This solution is effective, but very costly and requires changing the robot controller. The robot arm can still not operate at very high speed, because even with force feedback, the robot arm is too heavy to quickly react. One solution is just to just slow the entire process down, but then the robot can no longer compete with a human.

Background

Grinding is the process of machining using an abrasive wheel to remove material. The workpiece is brought into contact with the abrasive wheel and the workpiece is slowly eroded away. Grinding can be used to achieve micron precision. Polishing is a variant on grinding, where the goal is to smooth the surface of the workpiece, usually for aesthetic reasons. Both processes can be done easily by machines. Force-control is a control scheme in which a force is controlled to be the desired parameter, in this case force control can be used to keep constant grinding force between the part and the surface of the grinder. In force control, the position is allowed to be whatever it needs to be to achieve the desired force. In position control, the precisely the opposite is true: the force is commanded to whatever it needs to be to achieve the desired position. In the case of the discussed grinding problem, the ideal control scheme is position-mode control with force control built in to ensure forces to not become too high.

Conventionally, grinding is done with incredibly precise position-control to circumvent this force-control problem. An example of this is a surface grinder, where the grinding wheel is lowered with micron precision until it touches the part, where then a precise amount of material is removed. The incredible precision of the surface grinder does not experience excessive forces because material removal is so tightly controlled. However, with a robot arm doing the grinding, the problem that arises is that inaccurate position-control on robot arms dictates a force which is too high for the grinding process to safely undertake. Even with prior art of a six-axis dynamometer mounted to a robot arm, the robot arm does not have high enough bandwidth to grind parts accurately at high speed while keeping limits on the desired force.

High forces arise in this situation because there is no compliance in the structural loop of the whole system. We have solved this problem by allowing a precise amount of compliance in the structural loop. We have introduced compliance at the grinding spindle, and ideal place to add compliance as the robot arm is left unchanged, and the bandwidth of the system can be high as moving mass is low.

Functional Requirements

The first functional requirement for the hybrid position-force control grinder is

that the grinder must function as a grinder. The unit must possess an abrasive cutting surface which moves past the workpiece at a high speed. The grinding wheel must stay relatively flat to grind the workpiece precisely. The grinder must resist sudden shock loads, as the environment it is operated in is rough-and-tough. The grinder must implement the novel hybrid position/force control scheme: it must maintain a precise position for any force between zero force and the breakaway force, with high stiffness, but when the breakaway force is exceeded, the device must maintain a constant grinding force for a range of positions. The grinding force in the force-control regime must be relatively linear. The moving mass of the grinder must be kept relatively low, to ensure high force control bandwidth. From a usability standpoint, the grinding abrasive must be easy to attach and replace. The abrasive must also be firmly mounted, as compliance in the grinding abrasive will cause strange effects in the position-control mode. The mechanism must be relatively simple to build and service. The grinder must use components that are impervious to grinding dust.

Concepts, Strategy, and Solution

Several strategies were proposed to implement the hybrid position-force control scheme on the grinder. The solution must satisfy the functional requirements. The largest design decision was how to simply implement hybrid position-force control without ungainly complexity. This control scheme could be implemented either electronically with sensors and actuators, or entirely mechanically. A mechanical approach was selected, with the electronic approach being saved for future work. Several concepts were proposed to create the mechanical position-force control scheme. The basic layout for all concepts proposed is the same: A disk covered in abrasive media is preloaded forward against a hard stop. The disk will stay against the hard stop until the preload force is exceeded, causing the disk to move back away from the workpiece.

The first concept involved an axially-compliant flexure on top of a rotating spindle. This method separates the linear motion and the rotary motion, compartmentalizing the modules. An adhesive-backed sanding disk would be attached to the face of the disk. The flexure mechanism allows for axial compliance with rotational stiffness. This solution was ultimately not selected due to greater complexity than other solutions.

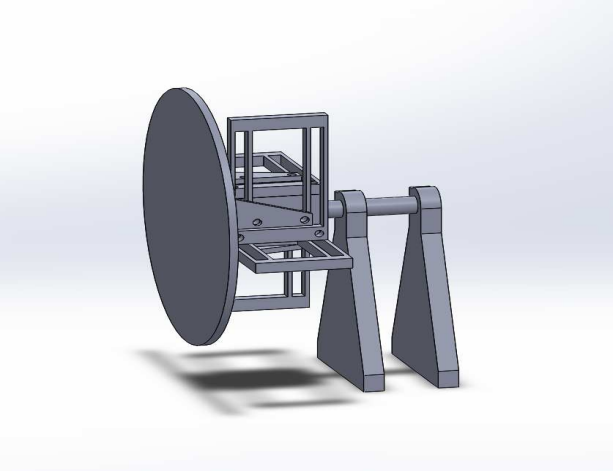

Figure 1: Flexure-base Axially Compliant Grinder, side view.

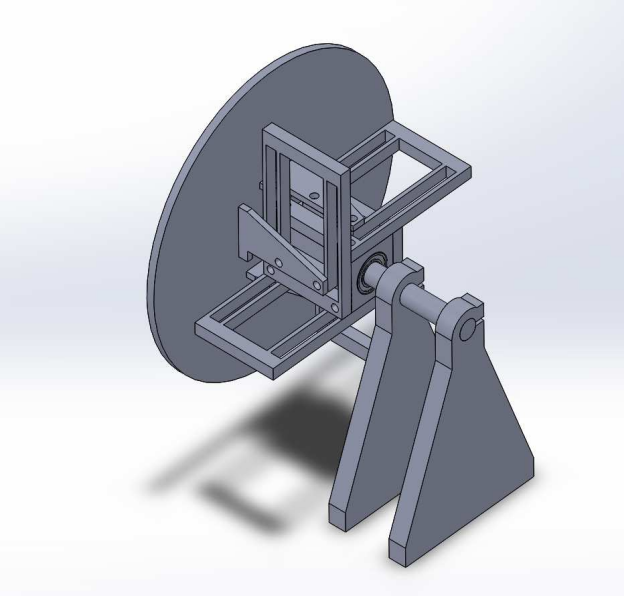

Figure 2: Flexure-base Axially Compliant Grinder, rear view.

The second concept involved an axially-compliant shaft supported by three air bearings. Two air bearings of identical ID would fit around a precision shaft, enabling rotation without axial constraint. The third air bearing is a doughnut-shaped thrust air bearing, which prevents motion in one direction by abutting a precision surface on the back of the main shaft. This surface also serves as the drive pulley for driving the rotary motion. A precise preload force is applied to keep the thrust flange against the thrust air bearing. When the preload force is exceeded, the pad simply lifts off the air bearing. This finely allows for the two modes of operation: position-mode when the thrust flange is in contact with the air bearing, and force mode when the flange is not in contact and only being forced with the preload force.

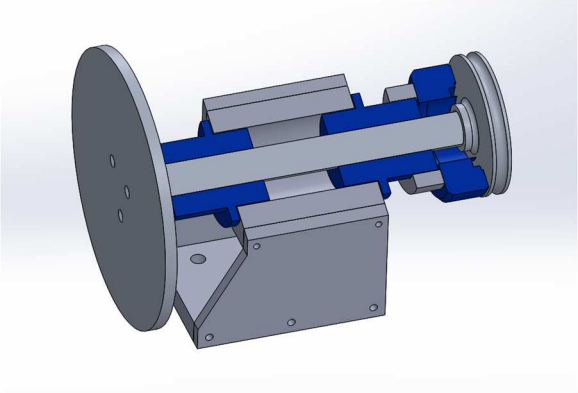

Figure 3: Cutaway of grinder with three separate air bearings. Air bearings colored blue.

The third strategy involved a simplification of the second strategy, combining the back rotary air bearing with the thrust bearing into a combined radial-thrust bearing. This would have been a very nice and elegant solution. Ultimately this solution proved infeasible as off-the-shelf air bearings do not come in the same size radial and combined radial-thrust.

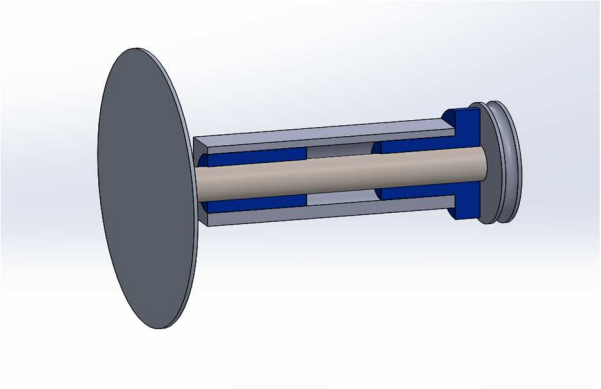

Figure 4: Cutaway of grinder with combined radial-thrust bearing. Air bearings colored blue.

The second strategy for hybrid position-force control was selected going forward.

The next step was to determine the preload mechanism, to preload the grinder up against the thrust air bearing. Two

options were floated: a very light grinder with spring preload, or a heavier grinder with gravity preload.

The first option involved a grinder with very light moving mass and a spring preload, with the goal of keeping as high axial bandwidth motion as possible. This would allow for very high-speed axial acceleration, satisfying the functional requirement of keeping constant force under many operating regimes. The light-mass grinder would be particularly beneficial for grinding as fast as possible. One way to implement this spring preload mechanism was through the use of a flat piece of spring steel pressing on a tooling ball. The tooling ball was mounted to the end of the shaft and the piece of spring steel was mounted to the frame. Below is a model of what such a grinder could look like. Note the pocketed disks to reduce the moving mass.

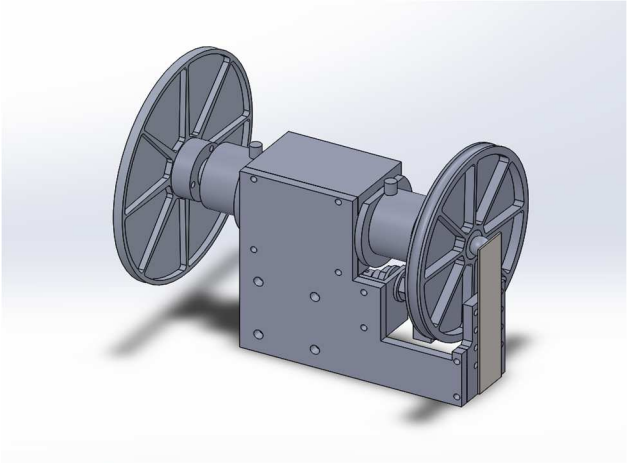

Figure 5: Design of spring preloaded spindle. Spring mechanism made of tooling ball and flat plate of spring steel.

The second strategy for preload was a simple gravity preload. Instead of using a spring to preload the mechanism axially, the whole grinder could simply be mounted at an angle, such that a component of gravity would preload the mechanism. The downside to this strategy was that the bandwidth of the device suffers heavily compared to the lighter spring-based design, as the device must be heavy enough to preload itself. However, gravity preload was ultimately selected as it is much simpler than a spring-based mechanism.

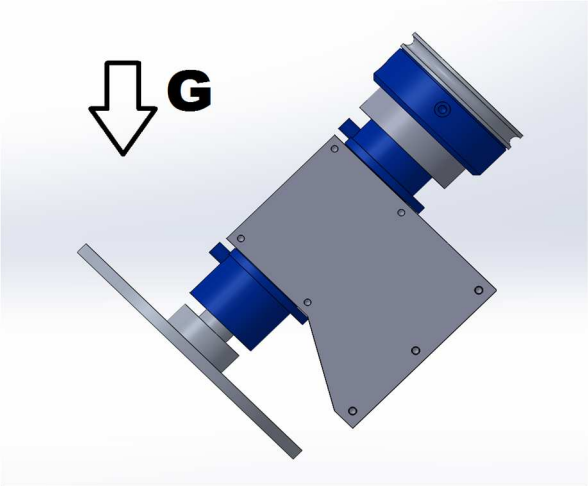

Figure 6: Gravity preloaded grinder spindle.

Ultimately the second strategy (gravity preload) was chosen due to simpler construction.

The final CAD model of the grinder is pictured below. The grinder frame is made from a solid billet of aluminum. The two radial air bearings are secured into the block with epoxy. The thrust air bearing mounts on a small spacer plate, again through epoxy. The motor selected to drive the unit is an Andymark, Inc. CIM motor, commonly found in FIRST robotics kits. Power is transmitted to the main shaft through a belt on two pulleys. It must be noted that the grinder shaft pulley will move in and out, as this shaft moves axially. A circular belt profile was chosen as this is very tolerant of misalignment. The grooves on the pulleys are large, further helping

tolerate misalignment. A simple rubber O-ring will be used as a belt. The pulley and the thrust bearing surface are the same piece. The grinding disk is held to the front of this shaft through the use of a screw-on clamping coupling, so that the grinding disk could easily be removed. The rotation direction was set to tighten this coupling during operation.

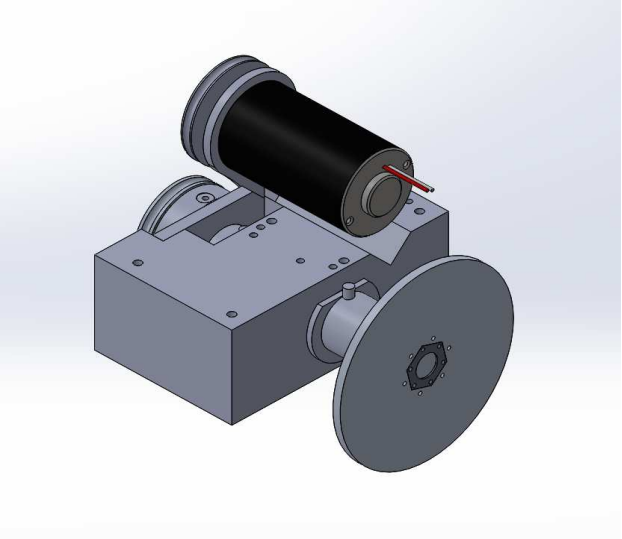

Figure 7: Design of final grinder, front view.

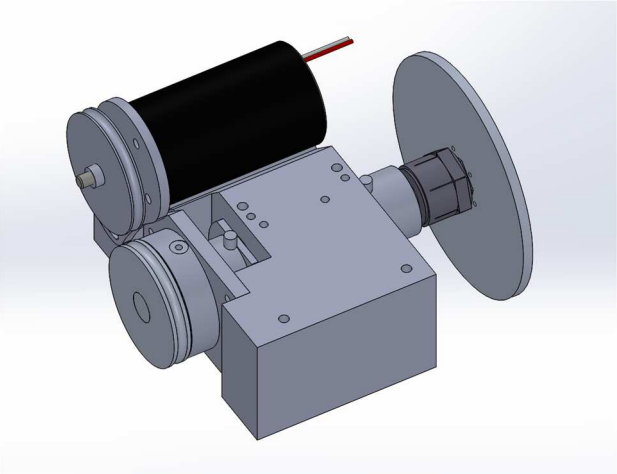

Figure 8: Design of final grinder, side view.

CFRP Drilled Hole Inspection System with Reaction Force Compensation

Chang-Hoon Seo[1,2], JaeHoon Jo[1], TaeGon Kim[1], CheolHo Kim[1], SeokWoo Lee[1], Moon G. Lee[2], HyoYoung Kim[1*],

[1]Manufacturing system R&D Group,
Korea Institute of Industrial Technology (KITECH), South Korea
[2]Department of Mechanical Engineering
Ajou University, South Korea

INTRODUCTION

In recent years, concerns regarding the environment have been increasing owing to global warming and the exhaustion of the Earth's resources. Simultaneously, a demand for lightweight materials has emerged in the aerospace and automotive industries. Carbon-fiber-reinforced plastic (CFRP) is a composite material with great formability and high strength of carbon fiber. Although CFRP is advantageous in terms of strength, its machining process is a drawback. In particular, numerous holes exist in automotive and aircraft parts. A defect in the drilled holes in CFRP leads to safety problems. In the aerospace and automotive industries, safety is the most important factor. CFRP parts require high-quality machining but many machining defects exist such as delamination. In fact, during the final assembly in aircraft, drilling defects such as delamination account for 60% of all rejections. Defects related to drilled holes in CFRP have a negative effect on the system stability. It is very important to detect defects with high accuracy because the safety of cars and airplanes is linked to human life. This research discusses the development of CFRP drilled hole inspection system with a reaction force compensation mechanism. The gantry stage developed in this study requires fast point-to-point motion to examine numerous drilled holes in the CFRP unit in a short time. For precise inspection, measurements must be recorded after the system has become completely stable. Generally, the precision stage is mounted on a precision granite with air dampers that negate ground vibration. When the linear motor is driven, the reaction force is transmitted to the system base, and this force causes the vibration into the total stage system. Figure 1 illustrates the concept of generating reaction forces. When the stage system moves at a high acceleration to improve the productivity, the reaction force increases.

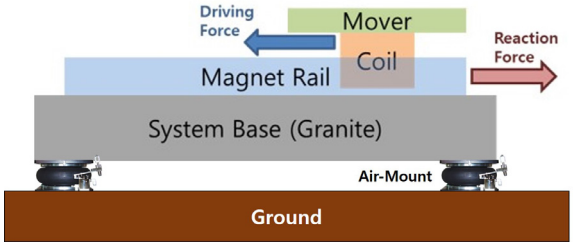

FIGURE 1. Concept of reaction force in the stage system

CONCEPT DESIGN OF THREE-DOF REACTION FORCE COMPENSATION

The vibration caused by the reaction force is the primary factor that degrades the life and productivity of precision manufacturing and inspection equipment. Methods for minimizing the reaction force to remove vibrations due to the reaction force were studied [1-3]. Most studies reported the compensation of the reaction force to balance the forces and offset the reaction force using counterbalance. The reaction force compensation using the counterbalance reduced the vibration of the base by 80%–90%. However, this counterbalance system is disadvantageous in that the system becomes larger and the control becomes complicated. To overcome these problems, a method of reducing the reaction force by installing internal voice coil motor (VCM) actuators at both ends of the granite was proposed [4]. The method of using an external VCM actuator is advantageous in that it is small and enables precise vibration control. We herein propose a new type of reaction force compensation mechanism using an external actuator.

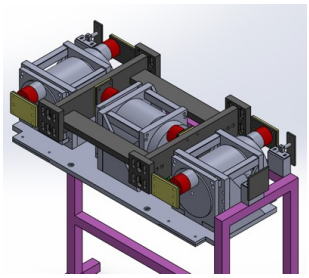

FIGURE 2. Proposed three-DOF reaction force compensation mechanism

Figure 2 presents the proposed residual vibration attenuation system. Three VCMs and three capacitive sensors are used in the reaction force compensation mechanism. A vibration attenuation system for reaction force compensation was incorporated in the system to decrease the settling time of residual vibration. The VCM generates a force that compensates for residual vibration. The residual vibration increases as the system generates a high-speed point-to-point motion during the inspection process. A longer settling time reduces the system performance, especially in the proposed H-type gantry stage, which has a high center of mass. Figure 3 shows the overall CFRP drilling holes inspection system including the proposed reaction force compensation mechanism. The developed CFRP drilling holes inspection system will contribute significantly to improving the quality of CFRP drilled holes.

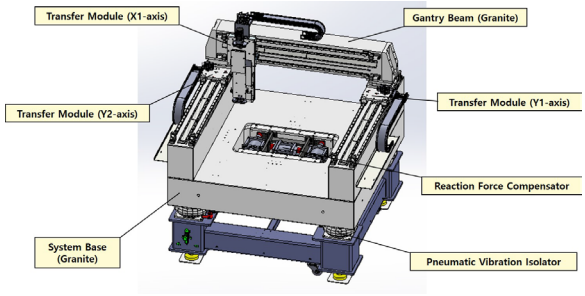

FIGURE 3. Gantry stage, including reaction force compensation mechanism

DESIGN OF H-TYPE GANTRY STAGE

The newly developed CFRP inspection system should exhibit a 3 m × 5 m operating range to inspect the standard sedan car frame hole. However, in this study, a small test bed type was designed for the performance test of the new concept reaction force compensation mechanism. The prototype H-type gantry stage was designed for a small CFRP component inspection. The primary specifications are summarized in Table 1. The prototype stage is the typical H-type gantry stage with three-DOF using linear motors and linear encoders. The steel frame is fixed on the ground. The base granite is placed on four air mounts to reduce the vibration from the ground. The x-axis is driven by one linear motor and the y-axis is driven by two linear motors. The z-axis is driven by a servo motor. Of special consideration is the installation space of the reaction force compensation mechanism, which is located in the middle of the base granite and coincides with the center of gravity of the inspection system, which is advantageous in reducing the reaction force.

TABLE 1. The primary performance of prototype H-type gantry stage.

	units	X (Cross)	Y (Gantry)	Z (Vertical)
Outer Size	mm	1800 × 2100 × 2300		
Payload	kg	30 @ Z-slide		
Max. Travel	mm	930	1,000	300
Max. Acceleration	G	0.6	0.6	0.05
Max. Velocity	mm/s	1,000	1,000	50
Rated Force	N	280	1120	-
Peak Force	N	600	2400	-
Straightness	μm	± 20	± 20	± 20
Flatness	mm	± 20	± 20	± 20
Orthogonality	arcsec	± 10 (X to Y)		-
Control Resolution	μm	0.4	0.4	0.1

DESIGN OF REACTION FORCE COMPENSATION MECHANISM

Three VCM actuators were used for reducing the reaction force of the gantry stage. The fixed part of the VCM is fixed to the steel frame, and the moving part of the VCM is in point contact with the base granite. Figure 4 shows the detailed components of the proposed reaction force compensation mechanism. A ball caster with five DOF was attached to the end of the VCM. EVA foam was used to prevent damage due to impact. The VCM is installed in an LM guide mechanism. Therefore, the VCM actuator always exhibits a one-DOF linear motion. The VCM power was selected to match the linear motor output power of the gantry stage. Each VCM actuator mechanism is designed to transmit forces in both directions.

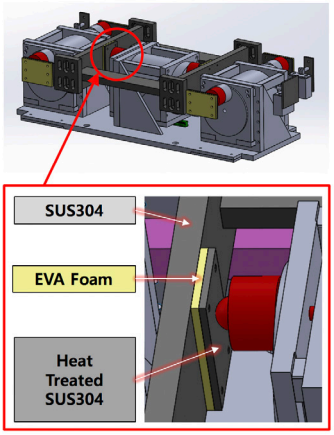

FIGURE 4. Detailed components of the proposed reaction force compensation mechanism.

The sensor for the feedback control of the VCM actuator uses a capacitor sensor. The fixed supports of the capacitor sensors are fixed to the steel base frame that is fixed on the ground. Therefore, the sensor measures the displacement of the base granite movement by the reaction force. Table 2 shows the more detailed specifications of the actuators and sensors.

TABLE 2. The specification of VCM actuator and sensor.

Specifications of Actuator	AVM150		
	Stroke	mm	5.00
	Conti. Force	N	585.77
	Peak Force	N	1757.30
	Resistance	Ω	4.40
	Inductance	mH	2.60
	Conti. Current	Arms	6.00
	Peak Current	Arms	18.00
Specifications of sensor	LION Precision		
	Range	mm	2.00
	Resolution	nm	30
	Linearity	%F.S	0.2
	Bandwidth	kHz	15

DYNAMIC CHARACTERISTICS OF THE PRECISION STAGE

To control the gantry stage and the reaction force compensation mechanism, the dynamic characteristics of the H-type gantry system were experimentally confirmed. The VCM actuator inside the gantry stage was used to vibrate the granite at various frequencies. Figure 5 shows the time response and force-position relation of the system base. When the force excitation is performed using three VCMs, the X and Y axes are partially coupled. In addition, the displacement and force relationship graphs show that the system has nonlinear characteristics. It is estimated that the nonlinearity is due to the granite being placed on the air mount. The first natural frequency of the system is less than 1 Hz, and the second natural frequency is observed at 13 Hz.

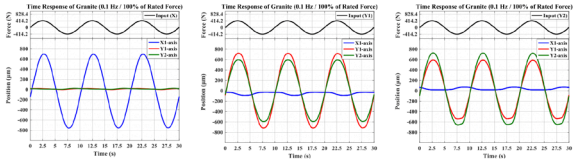

(a) Time response of system base

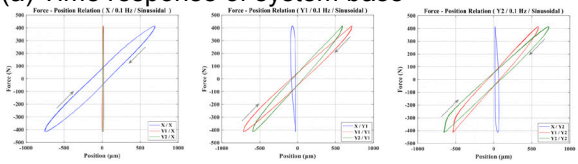

(b) Force–position relation of system base

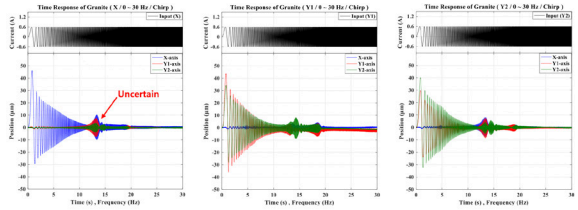

(c) Frequency response of system base

FIGURE 5. Dynamic characteristics of the system

The mathematical modeling of the system is compared with the experimental results above. Hence, the steel base frame, air mount, and granite were simplified to a two-DOF system and mathematical modeling was performed in the state space. Figure 6 compares the mathematical model with the actual experimental model and shows a good agreement.

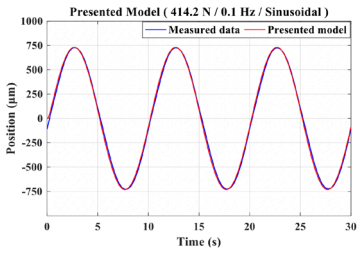

FIGURE 6. Comparison of mathematical model and experimental model

CONTROL

The prototype system is primarily driven by two control algorithms: the gantry stage control algorithm, and the reaction force compensation control algorithm. These two algorithms operate on the system simultaneously, not separately. Figure 7 shows the PID-based control algorithm of the prototype system. In the gantry control, variable gains were applied to compensate for the nonlinear friction based on the two-DOF mathematical modeling. Velocity control and position control were simultaneously applied to control the nonlinearity of the guide. In the reaction force compensation mechanism control, the input signal of the motor is used as the feed forward control. Simultaneously, the position the PID control of the granite was applied using the three capacitor sensors.

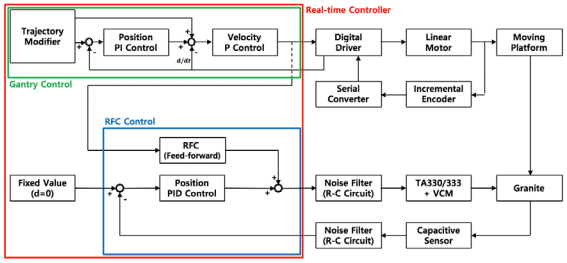

FIGURE 7. Schematic diagram of integrated control algorithm

EXPERIMENTS

To verify the effectiveness of the reaction force compensation system, the system was fabricated and tested. Figure 8 shows the experimental results of the proposed prototype system. The experimental results show that the speed and position of both the X and Y axes are accurately controlled within a predetermined range. To verify the performance of the reaction force compensation mechanism, the granite displacement before and after the control is compared. The results show that most of the reaction force on the x-axis and y-axis is effectively reduced.

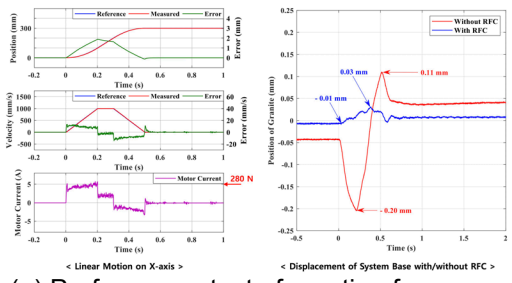

(a) Performance test of reaction force compensation for x-axis

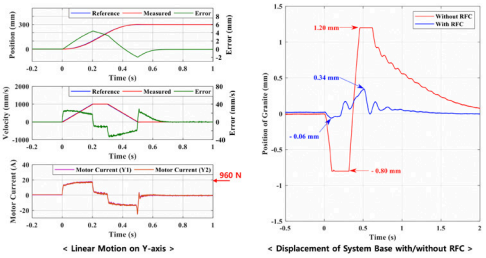

(b) Performance test of reaction force compensation for y-axis

FIGURE 8. Experimental results

CONCLUSIONS

We proposed a new type of reaction force compensation mechanism. A prototype reaction force compensation mechanism that removed the reaction force at the center of the gantry stage was designed and manufactured. The H-type gantry stage was designed and manufactured for the performance evaluation of the reaction force compensation mechanism. The experimental results showed that the proposed reaction force compensation system could effectively reduce the reaction force of the stage.

ACKNOWLEDGEMENTS

This work was supported by the Technology Innovation Program (10053248, Development of Manufacturing System for CFRP (Carbon Fiber Reinforced Plastics) Machining), and funded by the Ministry of Trade, Industry & Energy (MOTIE, Korea).

REFERENCES

[1] Arakelian VH, Smith MR. Shaking force and shaking moment balancing of mechanisms: A historical review with new examples. Journal of Mechanical Design, 2005; 127: 334-339.

[2] Nguyen DC, Ahn H-J. Semi-active reaction force compensation for a linear motor motion stage. International Journal of Precision Engineering and Manufacturing. 2016; 17: 857-862.

[3] Nguyen DC, Ahn H-J. Semi-active reaction force compensation for a linear motor motion stage. International Journal of Precision Engineering and Manufacturing. 2016; 17: 857-862.

[4] Seo CH, Lee H, Kim H, Lee MG. Reaction force compensator for high speed precision stage of laser direct imaging process. Shock and Vibration. 2018.

FREQUENCY RESPONSE FUNCTIONS FOR SLIDING FRICTION CONTACTS

Christoph Kossack, John Ziegert, and Tony L. Schmitz
Department of Mechanical Engineering and Engineering Science
University of North Carolina at Charlotte, Charlotte, NC

INTRODUCTION

In the study of dynamic systems, the frequency response function, or FRF, is a powerful analytical and experimental analysis tool. It defines the complex-valued frequency domain behavior, typically represented as the magnitude and phase or, alternately, the real and imaginary parts versus excitation frequency [1]. Modal testing provides a common experimental approach for identifying structural dynamics in the form of the FRF [2]. The application of impact testing, where an instrumented hammer is used to excite the structure over a sufficient bandwidth and a linear transducer is used to measure the corresponding vibratory response, is widespread in both industry and academia. While impact testing for flexible structures is commonplace, its use for measuring the dynamic response of systems with sliding contact is largely unexplored.

In this paper, an experimental platform (the friction measuring machine, or FMM) is described that enables transient, linear sliding motion between friction contact pairs under constant normal force loading [3-4]. Using the FMM, impact tests are completed with a hammer and laser vibrometer. The hammer provides the input energy in the form of a short duration impact and the system oscillates until it comes to rest (typically not at its starting position). The vibrometer measures the velocity during the decaying response as energy is dissipated in the friction contact. These experimental results are combined with simulation of a dynamic oscillator with sliding (Coulomb) friction [5] in order to parameterize idealized dynamic models that include friction.

BACKGROUND

Friction, which can be defined as the resistance to relative sliding between two bodies in contact under a normal load [6], is ubiquitous in manufacturing, metrology, mechanical design, and control. For manufacturing processes such as forging, rolling, extrusion, drawing, sheet metal forming, machining, and grinding, friction tends to increase the required force and power; therefore, the associated cost is significant. In forging, for example, friction forces at the die-workpiece interface can cause barreling, which yields inhomogeneous deformation patterns within the workpiece. It also leads to the familiar "friction hill" pressure distribution at the die-workpiece interface. In metal cutting, a high friction force is developed between the sheared chip and the rake face of the cutting tool in the secondary shear zone [6-10]. This, in turn, generates heat which tends to increase tool wear rates. For these and other reasons, the synthesis and testing of new lubricants and coatings to be used in manufacturing processes is an important, and continuous, research objective. Friction is also a necessary phenomenon, however. Without it, rolling, or reducing workpiece thickness using compressive forces applied by opposing rolls, would not be possible because the workpiece would not be pulled into the gap between the rolls.

Friction must also be considered in the control of manufacturing and metrology equipment. Servo-controlled, multi-axis positioning systems are widely used in: conventional and ultra-high precision machine tools; coordinate measuring machines; semi-conductor lithography equipment; micro- and nano-manufacturing systems; satellite imaging systems; and others. In many applications, axis positioning accuracies on the order of one part in 10^6 (or less) of the range of motion is required. For these high accuracy applications, motion velocities and accelerations are typically small, with the result that friction is often the dominant force in the system. This is true even when efforts are made to use very low friction interfaces, such as hydrostatic, aerostatic, or rolling contact bearings. Despite the use of tribological elements designed to reduce friction, it can still play a significant role in the system's positioning repeatability and accuracy [11].

Modeling and measurement of friction behavior is a critical research topic for both engineering and the physical sciences. Friction models, such as those based on adhesion or other mechanisms, relate surface condition, normal load, sliding velocity, temperature, and environment, for example, to friction forces. Traditional friction measurement attempts to assign known operating conditions, while recording the resulting friction forces. In this way, friction models may be validated (or modified) and the performance of new lubricants and coatings may be assessed. In this research, this traditional force-based (Newtonian) friction measurement paradigm is replaced by a displacement-based (Lagrangian) strategy. In prior work, the measurement uncertainty for the force-based approach was evaluated and it was

determined that its accuracy, particularly at low friction conditions, is limited [12]. This motivates the alternate Lagrangian measurement technique implemented here.

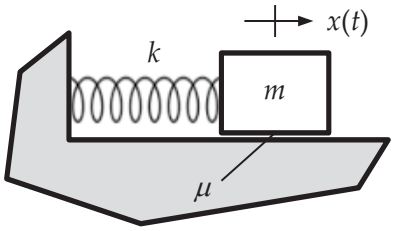

Figure 1. Spring-mass oscillator with Coulomb friction.

SLIDING CONTACT MODEL

In this work a dynamic oscillator is used to model sliding friction (Fig. 1). When the mass is given an initial displacement from its equilibrium position, for example, this displacement characterizes the initial energy input to the system. The system is then released and allowed to oscillate until motion ceases. If the final rest position differs from the equilibrium position, energy remains in the system. During the decaying oscillation, the time dependent displacement and velocity describe the transient response. This characterizes the energy dissipation in a continuous time record. The dissipation describes the friction behavior at the interface over a range of sliding velocities from near-zero to the maximum. Alternately, the input energy can be imposed in the form of an impulsive force. Again, the system oscillates until the motion stops due to frictional energy loss.

A numerical simulation is detailed that includes an impulsive force input to initiate the oscillatory motion. The differential equation of motion is provided in Eq. 1, where f is the impulsive force input, m is the mass, k is the linear spring constant, and F_f is the friction force. For the Coulomb model, the friction force is equal to the product of the friction coefficient, μ, and the normal force, $N = mg$. Given the time domain force input and corresponding response output (displacement or velocity), the FRF is determined by calculating:

1. the discrete Fourier transform of the time domain force input to convert to the frequency domain
2. the discrete Fourier transform of the time domain displacement or velocity output
3. their complex-valued, frequency domain ratio.

If displacement is selected, the receptance FRF, $\frac{X}{F}(\omega)$, is obtained, where ω is the excitation frequency in rad/s. For velocity, the mobility FRF, $\frac{V}{F}(\omega)$, is obtained, where V is the complex-valued velocity in the frequency domain.

$$\begin{aligned} m\ddot{x} + kx + F_f &= f, \dot{x} > 0 \\ m\ddot{x} + kx &= f, \dot{x} = 0 \\ m\ddot{x} + kx - F_f &= f, \dot{x} < 0 \end{aligned} \quad (1)$$

To demonstrate the numerical simulation, a rectangular force input with a short duration, Δt, was selected; its magnitude was constant over Δt and zero otherwise. The time domain input force and output displacement signals are presented in Fig. 2 for three Δt values: {2.5, 5, and 10} ms. Note the linear decay in the oscillating displacement peaks. This is indicative of friction energy dissipation and contrary to the exponential decay observed for viscous damping [5]. The corresponding receptance FRFs are shown in Fig. 3. These results demonstrate that the response changes with the amount of energy input into the system (i.e., the area under the force curve).

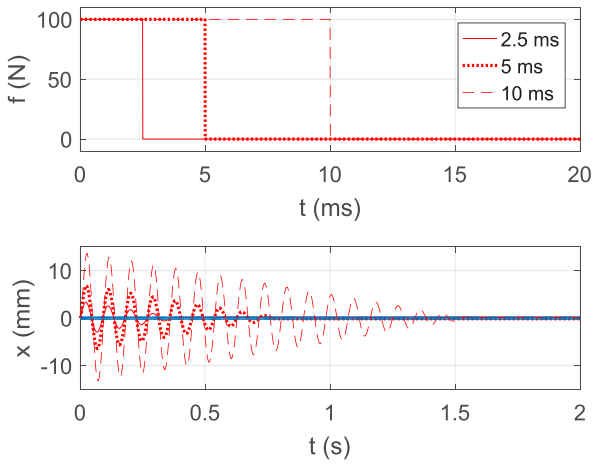

Figure 2. (Top) Impulse force input for three Δt values; (bottom) displacement output. Note the change in range for the time axes between the top and bottom panels.

In addition to the impulse value, changes in the friction force magnitude also modify the system response. In a second numerical study, F_f in Equation 1 was varied for a constant impulsive force input (Δt = 10 ms with a magnitude of 100 N). In the Fig. 1 model, the normal force is fixed by the mass so the friction force can only be changed by increasing or decreasing the friction coefficient. In the experimental setup used in this research (i.e., the FMM), the normal force was set independently so this restriction was

avoided. For the purposes of this numerical examination, however, the mass was kept constant and three friction coefficients were selected: μ = 0.05, 0.1, and 0.2. These results are displayed in Figs. 4-5.

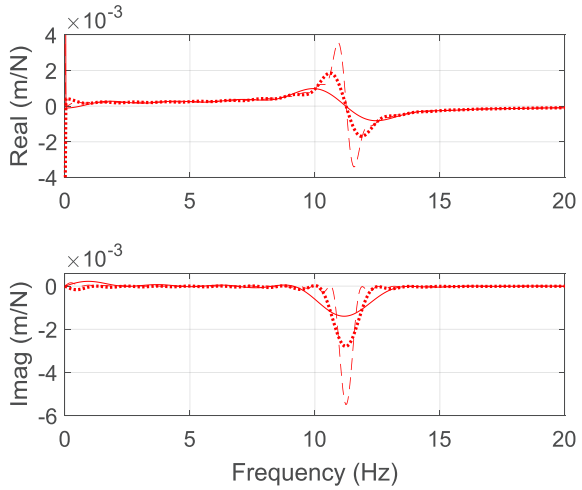

Figure 3. (Top) Real part of the receptance FRF for three Δt values (same legend as Fig. 2). (Bottom) Imaginary part of the receptance FRF.

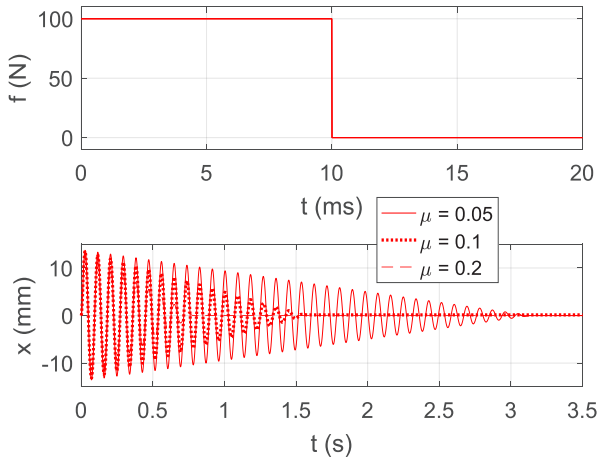

Figure 4. (Top) Impulse force input. (Bottom) Displacement output for three friction coefficient values.

EXPERIMENTAL SETUP

The FMM provides relative linear motion between a friction contact pair (pin and flat counterface) using a parallelogram, leaf-type flexure. Figure 6 displays the four leaf spring arrangement, where one end of each spring is clamped to a rigid base and the other is clamped to a faceplate which carries the motion platform. For this study, the input energy was supplied by the hammer impact which was applied to the motion platform at the middle of the leaf spring length to minimize platform rotation. A capacitance sensor (not shown) was used to monitor parasitic motion (i.e., arc motion perpendicular to the desired motion direction) of the platform. It was negligible when compared to the linear motion magnitude.

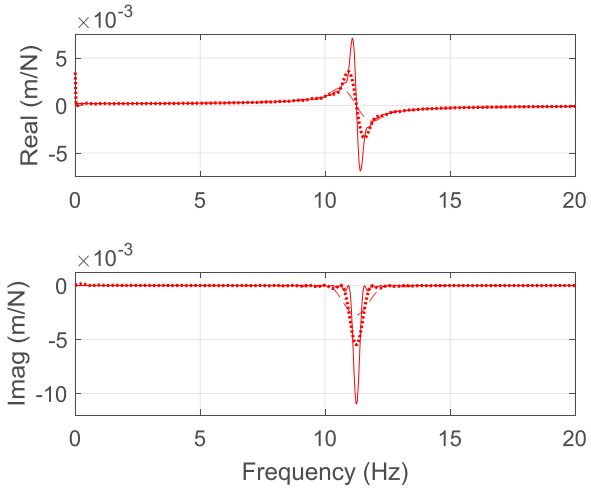

Figure 5. (Top) Real part of the receptance FRF for three friction coefficient values (same legend as Fig. 4). (Bottom) Imaginary part of the receptance FRF.

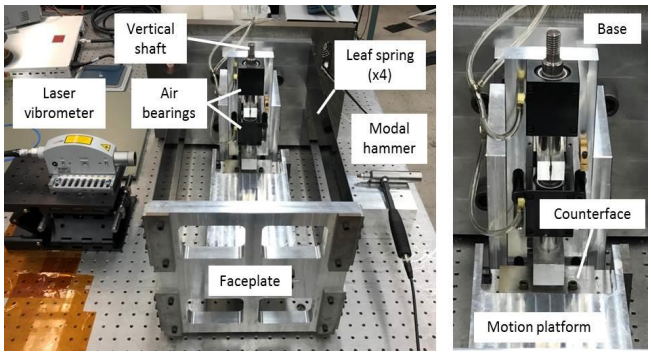

Figure 6. Photograph of FMM. They key components are identified.

The FMM dynamics with no friction contact were determined by: 1) imposing an initial displacement to the motion platform with a linear stage and electromagnet (not shown in Fig. 6); 2) measuring the corresponding free vibration velocity after release; and 3) using a nonlinear least squares optimization function in MATLAB (*lsqnonlin*) to solve for the mass, damping, and spring constants that minimized the difference between the measured velocity and the solution to the damped oscillator's second order differential equation of motion, $m\ddot{x} + c\dot{x} + kx = 0$, where c is the viscous damping constant that was included to account for the small energy dissipation during the flexure motion. The results were: m =

10.391 kg, c = 0.275 N-s/m, and k = 1982 N/m. The corresponding undamped natural frequency and viscous damping ratio were: $f_n = \frac{1}{2\pi}\sqrt{\frac{1982}{10.391}} = 2.20$ Hz and $\zeta = \frac{c}{2\sqrt{km}} = \frac{0.275}{2\sqrt{1982(10.391)}} = 0.00096 = 0.096\%$.

The FMM friction contact for FRF testing is produced between the pin and counterface. The pin is clamped into a holder and then attached to the vertical shaft shown in Fig. 6. The shaft is supported by a pair of air bearings, which are rigidly attached to the base. The normal force between the pin and counterface is provided by a mass attached to the top of the vertical shaft. The mass for the tests completed in this study was 0.680 kg (normal force of 6.67 N).

After the pin is clamped to the vertical shaft, it is lowered onto sandpaper which is attached by adhesive tape to the counterface. The sample is then moved back and forth for several interations to ensure that the contacting surfaces are flat and parallel. This is repeated for a range of increasing grit numbers to leave a smooth pin face. For the tests performed here, the contact pair consisted of a polytetrafluouroethylene (PTFE) pin on a polished steel counterface. The interface was lubricated using CRC Ultra Lite 3-36 Ultra Thin Non Staining Lubricant. The lubrication was applied to ensure that each impact force level selected for testing would result in a sufficient number of oscillations during the decaying motion.

Three impact force ranges were applied to the FMM using the impact hammer. Since the impact hammer is a manual device and repeating the same force level with each impact is not possible, a tolerance of ±50 N was selected for impact acceptance. The nominal impact force levels were 450 N (low), 1000 N (medium), and 1450 N (high). The impact force was applied using a PCB 086D05 modally tuned hammer with added mass and a rubber tip. The corresponding velocity was measured using a Polytec OFV-534 laser vibrometer head and OFV-5000 controller. The sampling time for each test was selected to be 33 s to ensure adequate frequency resolution for the FRFs. The sampling frequency was 10 kHz. The FMM was impacted by the hammer 10 times for each nominal force level. Between each impact, the CRC Ultra Lite 3-36 was reapplied to the counterface to ensure a consistent lubrication condition.

RESULTS

The measured time domain force and velocity signals were imported into MATLAB for analysis. Figure 7 displays the impact force and velocity data for 10 trials at the medium impact level.

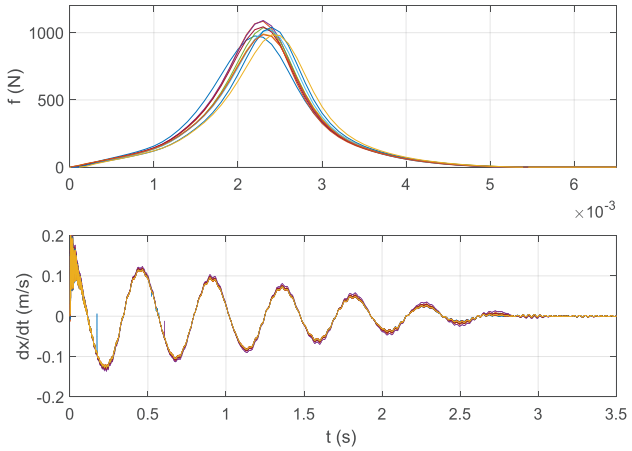

Figure 7. (Top) Time domain force, f, for 1000 N (medium) level. (Bottom) Time domain velocity, $\dot{x}$, due to force input. Note the change in time scale between the top and bottom panels.

The FRFs for the three force levels were determined by converting the time domain force and velocity signals into the frequency domain using the discrete Fourier transform. The mobility for each data set was then calculated by dividing the frequency domain velocity by the frequency domain force. To convert to receptance, the mobility FRF was divided by $i\omega$. This follows from an assumption of harmonic motion, where $x = Xe^{i\omega t}$ and $\dot{x} = i\omega Xe^{i\omega t}$. Figure 8 displays the real and imaginary parts of the corresponding receptance for 10 trials at the medium force level.

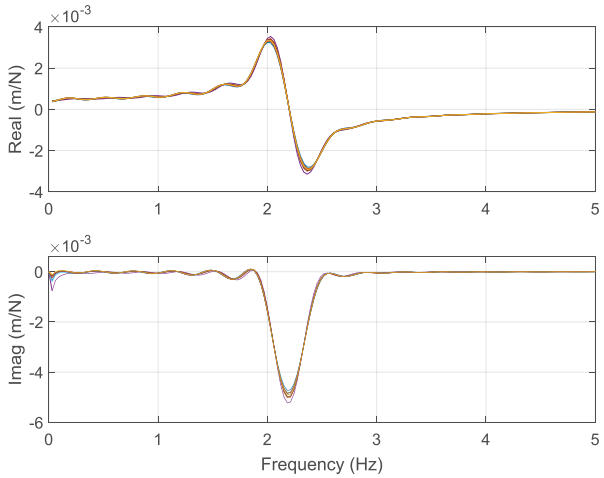

Figure 8. (Top) Real part of receptance FRF for 10 trials at the 1000 N (medium) force level. (Bottom) Imaginary part of receptance FRF for 10 trials.

The receptances are next compared for the three force levels. Figure 9 displays the mean FRF

magnitudes for the low, medium, and high levels (10 trials each, averaged in the frequency domain). Figure 10 shows the impulse versus receptance magnitude for the three force levels (mean impulse values of 0.98 N-s, 1.42 N-s and 1.64 N-s), where the + symbol identifies the mean of 10 trials at each level. A linear trend is observed with an R^2 value very close to unity.

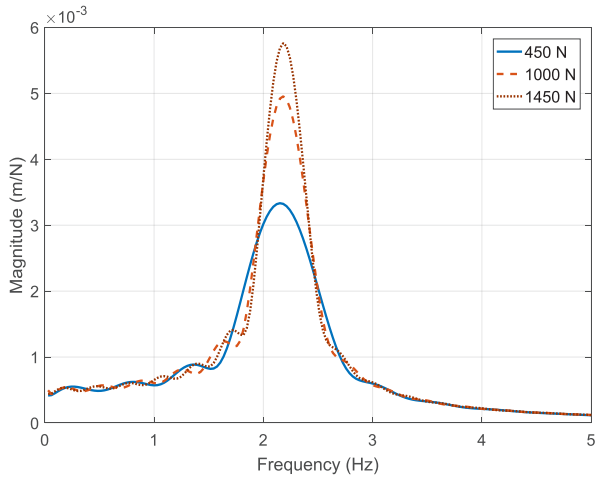

Figure 9. Mean FRF magnitude at three force levels. The magnitude increases with force for the FMM with friction contact.

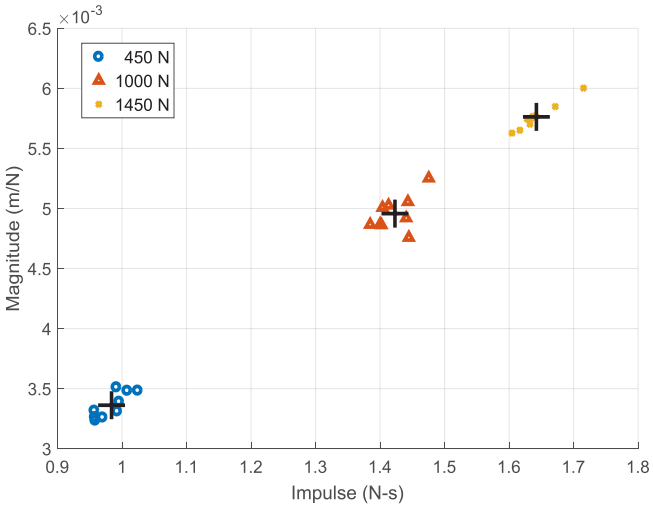

Figure 10. Impulse versus receptance magnitude for the three force levels.

Next, Eq. 1 was modified to include both sliding friction and viscous damping. This equation was solved by fixed time step numerical integration and the friction coefficient was identified to provide a best fit to the measured mobility FRFs. The measured force from the impact hammer, f, was used as input to avoid introducing errors due to approximations of the excitation force. Because the sampling frequency for the measured force was 10 kHz, the numerical integration time step was 1×10^{-4} s.

A result for the 450 N (low) force level is shown in Fig. 11. The measured force is displayed in the top panel, while the simulated (solid line) and measured (dotted line) velocity are displayed in the bottom panel. The friction coefficient is 0.113. Figure 12 shows the corresponding mobility FRF. The 1000 N (medium) force levels results are provided in Figure 13. The 1450 N (high) force level results are shown in Figure 14. The friction coefficient is 0.113 in all cases.

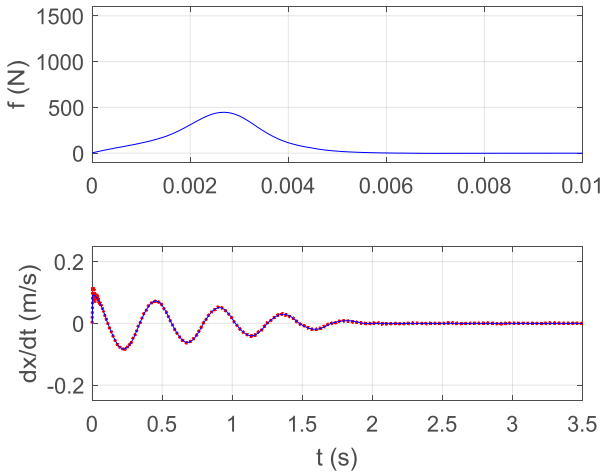

Figure 11. (Top) Low force level (450 N) input. (Bottom) Simulated (solid) and measured (dotted) velocity for 0.113 friction coefficient. Note that the top and bottom panels have different time scales.

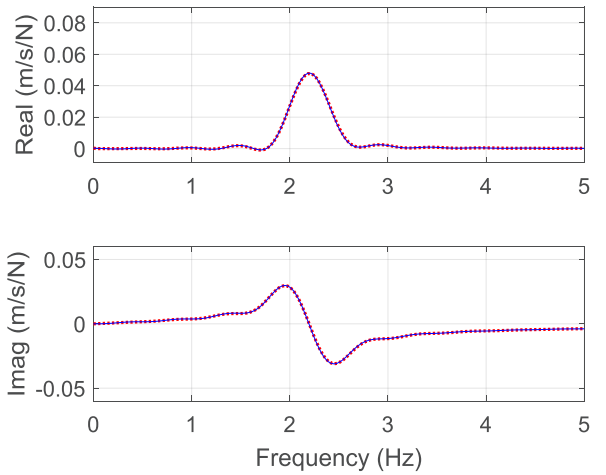

Figure 12. (Top) Real part of simulated (solid) and measured (dotted) mobility FRF for the low (450 N) force level with a friction coefficient of 0.113. (Bottom) Imaginary part of simulated and measured mobility FRFs.

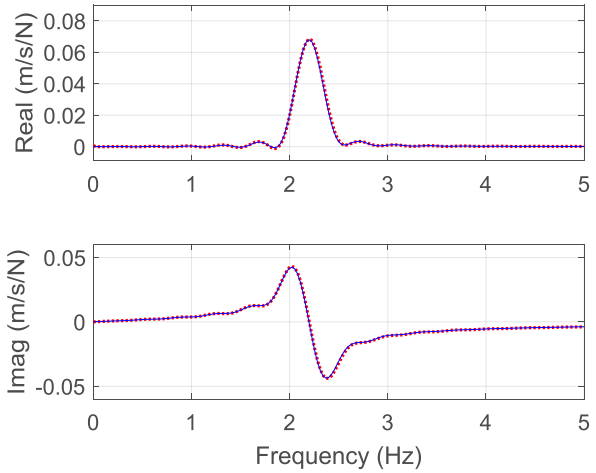

Figure 13. (Top) Real part of simulated (solid) and measured (dotted) mobility FRF for the medium (1000 N) force level with a friction coefficient of 0.113. (Bottom) Imaginary part of simulated and measured mobility FRFs.

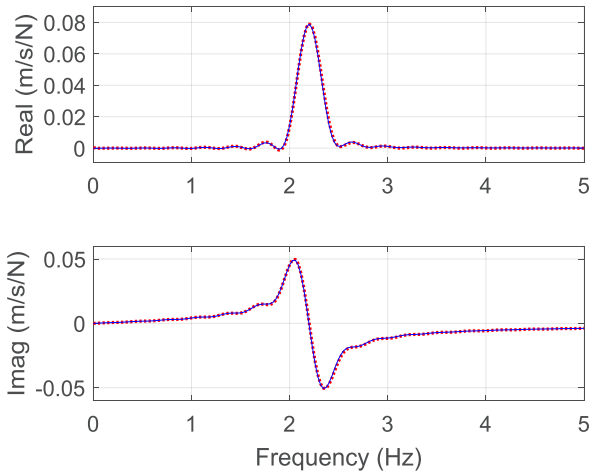

Figure 14. (Top) Real part of simulated (solid) and measured (dotted) mobility FRF for the high (1450 N) force level with a friction coefficient of 0.113. (Bottom) Imaginary part of simulated and measured mobility FRFs.

CONCLUSIONS

This paper described frequency response function (FRF) measurement and simulation for a damped oscillator with a sliding (Coulomb) friction contact. The dynamic system was realized using the parallelogram leaf-type flexure-based friction measuring machine (FMM). The FMM enabled linear motion between a pin-counterface friction contact with impact force input. The corresponding velocity was measured to characterize the energy dissipation. Results were presented for a lubricated polytetrafluouroethylene-polished steel contact. It was observed that the FRF magnitude increased linearly with impulse (i.e., the area under the time domain force profile). It was also seen that a single friction coefficient was sufficient to describe the response under three force levels (450 N, 1000 N, and 1450 N).

REFERENCES

[1] Schmitz, T. and Smith, K.S., 2012, Mechanical Vibrations: Modeling and Measurement, Springer, New York, NY, 2012.

[2] Ewins, D.J., 1984, Modal Testing: Theory and Practice, Vol. 15, Research studies Press, Letchworth.

[3] Lomascolo, C., Ziegert, J., and Schmitz, T., 2016, Displacement-based measurement of static and dynamic coefficients of friction, American Society for Precision Engineering Annual Meeting, October 23-28, Portland, OR.

[4] Kossack, C., Schmitz, T., and Ziegert, J., 2017, Identification of friction energy dissipation using free vibration velocity: Measurement and modeling, American Society for Precision Engineering Annual Meeting, October 29-November 3, Charlotte, NC.

[5] Inman, D.J., 2008, Engineering Vibration, Vol. 3, Prentice Hall, New Jersey.

[6] Kalpakjian, S. and Schmid, S., 2008, Manufacturing Processes for Engineering Materials, 5th Ed., Prentice Hall, Upper Saddle River, NJ.

[7] Astakhov, V., 2006, Tribology of Metal Cutting, Elsevier Science and Technology, Oxford, UK.

[8] Astakhov, V., 1998, Metal Cutting Mechanics, CRC Press, Boca Raton, FL.

[9] Tlusty, G., 1999, Manufacturing Processes and Equipment, Prentice Hall, Upper Saddle River, NJ.

[10] Yang, X. and Liu, C.R., 2002, A new stress-based model of friction behavior in machining and its significant impact on residual stresses computed by finite element method, International Journal of Mechanical Sciences, 44: 703-723.

[11] Olsson, H., Åström, K.J., Canudas de Wit, C., Gäfvert, M., and Lischinsky, P., 1998, Friction models and friction compensation, European Journal of Control, 4/3: 176-195.

[12] Schmitz, T., Action, J., Ziegert, J., and Sawyer, W.G., 2005, On the difficulty at measuring low friction: Uncertainty analysis for friction coefficient measurements, Journal of Tribology, 127: 673-678.

OPTIMALLY LOCATING MULTIPLE TUNED-MASS-DAMPERS FOR VIBRATION REDUCTION IN MACHINE TOOL STRUCTURE

Jihyun Lee[1], Chang-Ju Kim[1], Changho Lee[2] and Kangjae Lee[2]
[1]Department of Ultra-Precision Machines and Systems
Korea Institute of Machinery & Materials, Daejeon, South Korea
[2]Doosan Machine Tools Co., Ltd, Changwon, South Korea

OVERVIEW

The objective of this paper is to optimally locate multiple tuned-mass-dampers (multiple TMDs) on a machine tool structure with dynamic variation by the change of tool position for the reduction of vibrations. The effect of TMDs' location on the torsional vibration of the ram structure is investigated using a rigid planar model. The analysis reveals that their locations have an influence on increasing the effective frequency range, like the effect of mass ratio. In order to quickly search optimal locations of multiple TMDs in the system varying its dynamics, Linear-Time-Invariant (LTI) control framework is developed and then multi-model H_∞ optimization is applied. Simulation results of a double column machining center show that multiple TMDs which locate at optimal positions could provide more vibration reduction in the system varying dynamics than by multi-TMDs whose locations are not optimized and to single TMD whose location is optimized. A genetic algorithm is used to compare the simulation time. It presents that the application of control theory helps reduce simulation time drastically. Experiments are planned for future work.

INTRODUCTION

The usage of a tuned-mass-damper (TMD) is a classical solution to reduce vibrations in machine tool structure because it is simple and cost-effective. Traditional analysis method proposed by Den Hartog[1] is commonly used to tune parameters of single TMD. A major problem is that it is suitable only when the natural frequency of the structure is not variable to the natural frequency of single TMD. Multiple tuned mass dampers (multiple TMDs)[2] or multi-mass dampers (MMD)[3] is a solution to overcome poor performance outside a narrow frequency band. Optimal stiffness and damping coefficients of multiple TMDs[2,3] are able to increase robustness and widen effective frequency range. Iterative adjustment of individual mass is a common solution to tune its frequency to the target mode after the design of stiffness and damping coefficients.

In general, the TMDs are attached near the tooltip in the machine tool structure to suppress vibrations directly[3]. It is, however, not practical in industries because of space restriction and interfering with the machining process. Brecher[4] points out that an optimal MMD location within a structure for a single target mode shape could help dissipate kinematic energy. In his paper, an equivalent kinetic mass at discrete points is iteratively evaluated, which requires lots of computation time for the system varying its dynamic. In order to reduce the computation time and expand design conditions, there is a need to provide a systematic approach to optimize continuous placements of TMDs that provide the best reduction of vibrations in machine tool structure.

This paper investigates the effect of multiple TMDs' placements on the reduction of a torsional vibration on ram structure with varying dynamics. The control theoretic application technique proposed by the author[5] is applied to quickly search their optimal position. Stiffness and damping coefficients of each TMD are assumed to be known[1]. The equation of motion of the system is re-formulated as LTI control framework such that locations of TMD are defined as a static feedback gain matrix. The multi-model H_∞ command in MATLAB is then used to find the optimal static feedback gain matrix such that the torsional vibration of the ram structure is minimized. The outline of this paper is as follows: Section 2 describes problems in 3-axis large double-column type machining center and then motivates the study of the optimal location of multiple TMDs. In Section 3, the machine is modeled by a planar system and formulated for applying a control theoretic approach. Its simulation results are described in Section 4. Conclusions and future work are discussed in Section 5 and 6.

PROBLEM DESCRIPTION

Consider the 3-axis double column machining center represented in Fig. 1. The machine has its *x*-axis on the table, its *y*-axis on the cross beam which supports loads from saddle and ram structures and its *z*-axis on the ram structure equipped with a tool. The double column structure has the advantage of high dynamic stiffness and small thermal deformation.

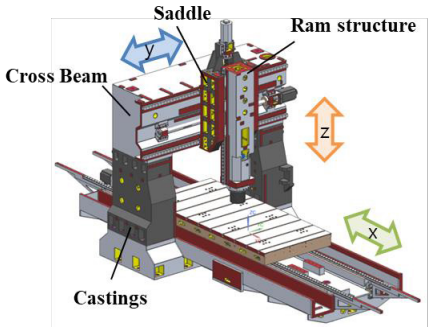

FIGURE 1: Schematic of Doosan Machine Tools' BM 1530M double column machining center

By design, this machining center experiences large vibrations in the combined saddle and ram structure about the *y*-axis due to low stiffness of LM guideways about the *y*-axis on the cross beam. CAE of the machine at tool position *z* =[−400, −200, 0, 200, 400]*mm* is generated and used to analyze mode shapes and vibrations, which is described in Fig. 2. The analysis shows that rolling motion of the structure combined with saddle and ram (i.e., red-dot circle in Fig. 2) is dominant at *z* =[−400, −200, 0]*mm*, which is the main tool location for processing a workpiece. Its resonant frequency is varying according to the change of tool position. Therefore, it is necessary to determine the optimal location of multiple TMDs that can minimize the torsional vibration about the *x*-axis varying its resonant frequency depending on the structure's tool position *z*.

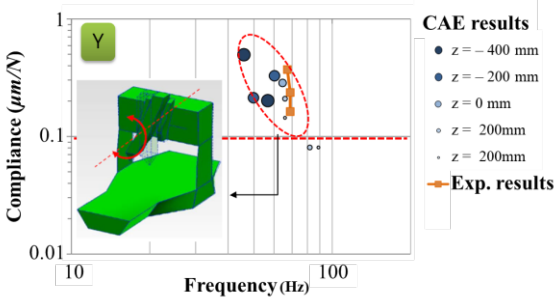

FIGURE 2: Dynamic stiffness variation of BM 1530M depending on tool position (z)

MODELING AND OPTIMIZATION APPROACH

The structure combined saddle and ram equipped with multiple TMDs is modeled as a planar system consisting of a rigid mass connected by a torsional spring, as shown in Fig. 3, to study the torsional vibration in its *y*-*z* plane.

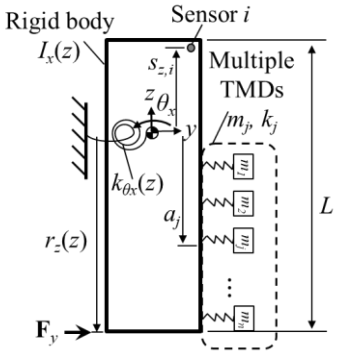

FIGURE 3: Schematic of simplified ram structure

The system dynamics variation by the change of tool position can be realized by $I_x(z)$, $k_{\theta x}(z)$ and $r_z(z)$ as a function of *z*, which are determined by using a curve fitting two FRFs measured at different positions of the ram structure without TMD. $I_x(z)$ is a centroidal moment of inertia about the *x*-axis. $k_{\theta x}(z)$ attached at the center of gravity(CG) of the structure is a torsional stiffness of the structure in the θ_x direction. Assume that a tool acting the force F_y is attached at distance $r_z(z)$ from the CG. Each TMD in *n* numbers TMDs consists of stiffness k_j and mass m_j at the distance a_j from the CG in the *z*-axis. Assuming, for theoretical convenience, that the system in Fig. 3 is modally damped. The equation of motion of the system can be written as

$$\mathbf{M}(z)\ddot{\mathbf{u}} + \mathbf{K}(z)\mathbf{u} = \mathbf{F}(z)$$

where

$$\mathbf{u} = \begin{bmatrix}\theta_x & y_1 & \cdots & y_n\end{bmatrix}^{\mathrm{T}}, \mathbf{F} = \begin{bmatrix}r_z(z)F_y & 0 & \cdots & 0\end{bmatrix}^{\mathrm{T}},$$

$$\mathbf{M} = \mathrm{diag}\left(\begin{bmatrix}I_x(z) & m_1 & \cdots & m_n\end{bmatrix}\right), \quad (1)$$

$$\mathbf{K} = \begin{bmatrix} k_{\theta x}(z) + \sum_{j=1}^{n} k_j a_j & -\mathbf{k}_{\mathbf{v}} \\ -\mathbf{k}_{\mathbf{v}}^{\mathrm{T}} & \mathrm{diag}([k_1, \cdots, k_n]) \end{bmatrix}$$

where $k_v = \{k_1 a_1, \cdots, k_n a_n\}$. The effect of TMD location on spreading distance between resonant frequencies by a TMD is derived in Eq. (2) from Eq. (1). The farther the TMD position is, the wider the distance between resonant frequencies is, which is described in Fig. 4.

$$\frac{\omega}{\omega_{sys}} = \sqrt{\left(1+\frac{\mu}{2}\right) \pm \sqrt{\mu+\left(\frac{\mu}{2}\right)^2}}, \qquad (2)$$

where $\mu = m_j a_j^2 / I_x$ and $\omega_a = \sqrt{(k_j/m_j)}$.

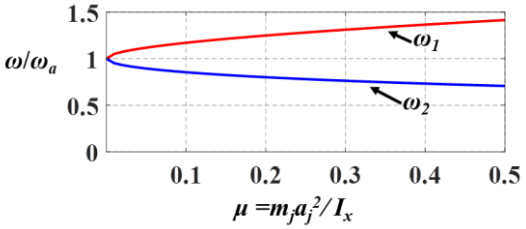

FIGURE 4: The two resonant frequencies of a TMD as a function of the μ[1]

The vibration of this model measured at a sensor s_z can be quantified by the H_∞ norm of the frequency response function (FRF) from F_y to $s_z\theta_x$; it is expressed as

$$\|G(j\omega)\|_\infty = \left\| \frac{s_z \theta_x}{F_y} \right\|_\infty, \qquad (3)$$

where ω represents excitation frequencies in rad/s and j is the unit imaginary number. The H_∞ norm represents the peak magnitude of its FRF. Figure 5 shows the variation of $\|G(j\omega)\|_\infty$ depending on the location of single TMD at z = −200*mm*. The result presents that single TMD has an optimal position to minimize the torsional vibration, which means that the optimal position does not have to be the tooltip position.

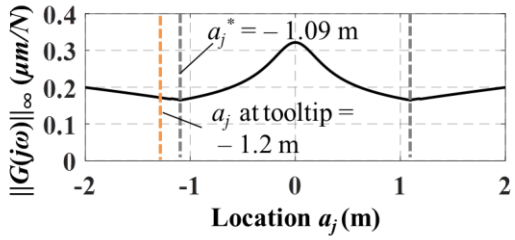

FIGURE 5: Plot of $\|G(j\omega)\|_\infty$ as a function of a_j showing local optimum at a_j^* =−1.09mm

Given the multiple TMDs, we want to find $a_j = a_j^*$ such that $\|G(j\omega)\|_\infty$ is minimized. A multi-model H_∞ synthesis[6] based on LTI control framework as shown in Fig. 6 is applied to search the optimal location. The machine can be controlled via the same structured controller, a_j. Control gain matrix is defined as each TMD's location $F_d = [a_1 \cdots a_n]$. Multi-model H_∞-optimization provides optimal location a_j^* to minimize vibration of the system most vulnerable to the vibration. The detailed procedure to develop the control framework is described in the author's paper[5].

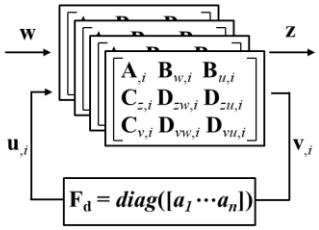

(i =the number of plants generated by changing tool location)

FIGURE 6: LTI Control Framework for multi-model H_∞ synthesis

SIMULATION RESULTS

Simulations are carried out based on the parameters of the 3-axis machine described in Table 1.

TABLE 1. System parameters

Parameter	Values
$l_x(z)$ [*kg-m²*]	$-7.5\times10^3z^3+5.3\times10^3z^2+347z+625$
$k_{\theta x}(z)$ [*Nm*]	$4.11\times10^8z^2+5.27\times10^7z+1.14\times10^8$
$r_z(z)$ [*m*]	$-19z^4+3.7z^3+1.6z^2+0.23z-1.2$
L [*m*]	2.38
n	6

Single TMD (m_{total} = 20kg) is divided into six multiple TMDs(m_j = 3.33kg). The stiffness of each TMD is calculated by the conventional method[1]. Since the machine desires to minimize its vibration at the tooltip, the sensor location s_z is defined as r_z. The optimal location for each TMD, a_j^*, can be determined from the framework presented in the preceding section by employing multi-model H_∞ optimal control theory to determine the optimal gain matrix $\mathbf{F}_d$. MATLAB provides a command, *hinfstruct*, for this purpose. Accordingly, a_j^* for each TMD described in Tab. 2 is achieved using MATLAB's *hinfstruct* function with an initial condition of $a_j \approx 0$, a maximum boundary of $r_z(z)+L$ and a minimum boundary of $r_z(z)$ for z = [−400:10:400]*mm*.

TABLE 2. Optimized multiple TMDs specification(standard at z = −400mm)

Parameter	Value	Parameter	Value
k_1 [*N/mm*]	484.2	a_1^* [*mm*]	627(head)
k_2 [*N/mm*]	443.8	a_2^* [*mm*]	627(head)
k_3 [*N/mm*]	521.5	a_3^* [*mm*]	627(head)
k_4 [*N/mm*]	410.3	a_4^* [*mm*]	–1750(tooltip)
k_5 [*N/mm*]	457.6	a_5^* [*mm*]	–1750(tooltip)
k_6 [*N/mm*]	497	a_6^* [*mm*]	627(head)

The multi-model H_∞ synthesis takes 64 *second* simulation time, whereas a genetic algorithm takes 2216 *second*. It confirms that the H_∞ synthesis can greatly reduce it simulation time. Figure 7 shows the comparison of the maximum singular value of $G(j\omega)$ at z =[−400, −200, 0, 200, 400]*mm* obtained from the system (a) without TMD, (b) with single TMDs attached at the optimal location a_j^* = –1.75m(tooltip), (c) with multiple TMDs attached at tooltip and (d) at the optimal location described in Tab. 2. Multiple TMDs suppress H_∞ norms of the system over the frequency range where the target frequency of BM 1530M (i.e., the resonant frequency of torsional mode) moves according to the change of tool location in the *z*-axis. Figure 8 shows that the multiple TMDs attached at their optimized location have an advantage of reducing the torsional vibration of the ram structure over the tool locations *z* more than that attached at the tooltip. For all tool locations, the average reductions of H_∞ norm for the structure with optimized multiple TMDs, non-optimized multiple TMDs and single TMD are 34%, 32%, and 28%, which is described in Fig. 9. That means distributed multiple TMDs at the optimal location improve the vibration reduction 6% more than single TMD in the structure whose dynamic is changed according to the change of tool location.

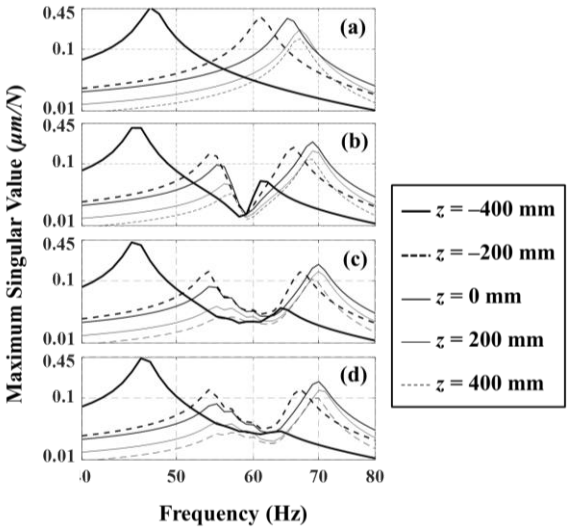

FIGURE 7: FRFs of the system with (a)no TMD, (b)single TMD attached at a_j^*, (c)multiple TMDs attached at tooltip and (d) at a_j^*

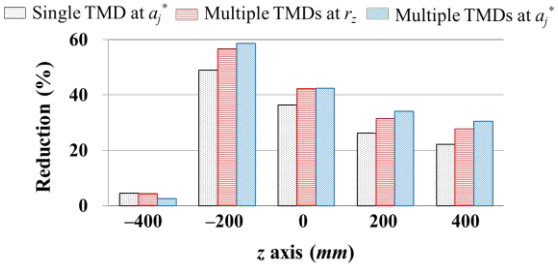

FIGURE 8: Comparison of FRF magnitudes of $|H(\omega)|$

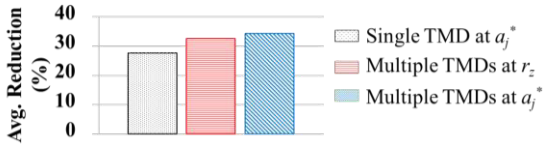

FIGURE 9: Comparison of average reduction of H_∞ norm: TMD< MTMD at r_z< MTMD at a_j^*

CONCLUSION

This paper investigates that the effect of location of multiple TMDs on the torsional vibration of the ram type machine tool structure with dynamic variation by the change of tool position. The analysis from a simplified planar system with multiple TMDs shows that when the TMD position is farther from the CG, the distance between resonant frequencies is wider. The TMD is commonly attached at the tooltip but this paper shows that it is not an optimal position. Control theoretic framework[5] is re-formulated from the analytic model and then multi-model H_∞-optimization is applied to search optimal locations of the multiple TMDs. The results verify that multiple TMDs located at optimal locations allow 6% vibration reduction more than single TMD and 2% vibration reduction more than multiple TMDs attached at the tooltip. Simulation time by H_∞-optimization confirms that the application of control theory has a benefit in the design of TMD.

FUTURE WORK

Design of multiple TMDs and experimental set up is currently being built collaborating with Doosan Machine Tools Corporation to validate the findings of this paper. Moreover, some questions remain in this paper: How to optimize the stiffnesses and locations of multiple TMDs together by using the control theoretic framework? How to design the optimal locations while considering manufacturing design constraints? How much robustness of the optimized TMD? These questions would be answered as future work.

REFERENCES

[1] Hartog D. Mechanical Vibrations. Courier Corporation.1985.

[2] Yang Y, Munoa J, Altintas Y. Optimization of Multiple Tuned Mass Dampers to Suppress Machine Tool Chatter. Int. J. Machine Tools and Manufacture. 2010; 50: 834-842.

[3] Brecher C, Schmidt S, Fey M. Analytic Tuning of Robust Multi-Mass Dampers. CIRP Annals. 2016; 65: 365-368.

[4] Brecher C, Schmidt S, Fey M. On the Integration of Tuned Multi-Mass Dampers into a Topology Optimization Method for Machine Tool Structural Dynamics. 2015; 11th world congress on structural and multidisciplinary optimization. Sydney.

[5] Lee J, Ghasemi A H, Okwudire C E, Scruggs J. A Linear Feedback Control Framework for Optimally Locating Passive Vibration Isolators with Known Stiffness and Damping Parameters. J. Vibration and Acoustics. 2017; 139; 011006.

[6] Apkarian P, Noll D. The H∞ control problem is solved. AerospaceLab Journal. 2017; 13:1.

CONTROL OF SEMI-ACTIVE SUSPENSION IN HIGH SPEED CAPSULE TRAIN BY USING HARDWARE-IN-THE-LOOP SIMULATION EXPERIMENT

Jin-Ho Lee[1], Won-Hee You[1], Jungyoul Lim[1] and Kwan-Sup Lee[1]
[1] New Transportation Innovative Research Center, Korea Railroad Research Institute
Uiwang-si, Kyunggi-do, Republic of Korea

INTRODUCTION

Recently, as new generation of transportation system, the high speed capsule train is attracting attention in the world. The capsule train runs inside the tube whose pressure is under 0.001 atm. Since the amount of air is rare inside tube with this pressure, the air-resistance, the major obstacle to higher speed can be drastically reduced. Moreover, the capsule train is levitated from the tube surface by using electrodynamic suspension(EDS) method, which makes frictionless smooth running. Theoretically, the capsule train characterized by sub-vacuum tube and frictionless levitation could run with over 1,000km/h speed[1].

The capsule train especially utilizes the superconducting magnet for EDS levitation. In EDS levitation, the interaction between superconducting magnet in capsule train and ground coil installed in guideway generates the levitation and guidance force, and resultantly the magnetic stiffness and damping between capsule train and guideway are determined[2]. Many studies to determine the magnetic stiffness and damping coefficient in EDS levitation have been conducted and general conclusions from studies indicate that the magnetic damping coefficient in EDS levitation is very small or becomes even negative[3,4,5]. This is very unfavorable in capsule train's dynamic aspect, since the vibration caused from outer disturbance such as guideway irregularity can be directly transferred to the bogie without any absorbing of vibration, which results the degradation of ride comfort in carbody. To improve the ride comfort in capsule train, the semi-actively operated suspension system between bogie and carbody is suggested in this study. Firstly, through the dynamic analysis based on the simulation, the performance of suggested suspension is examined. Then, by using the hardware-in-the-loop simulation(HILS) system composed with the capsule train dynamic model and the real actuator as semi-active suspension, the performance of semi-active suspension is experimentally confirmed. The results shows the effectiveness of suggested semi-active suspension in the capsule train.

CONCEPT OF THE CAPSULE TRAIN

The configuration of capsule train is shown in Figure 1. The capsule train is composed with 3 parts such as the front motor car, the middle passenger cabin and the rear motor car. Each motor car has one bogie(Figure 2) composed with superconducting magnet for levitation, guidance and propulsion, air spring for suspension and wheels for running and guiding. The overall specification of capsule train is described in Table 1.

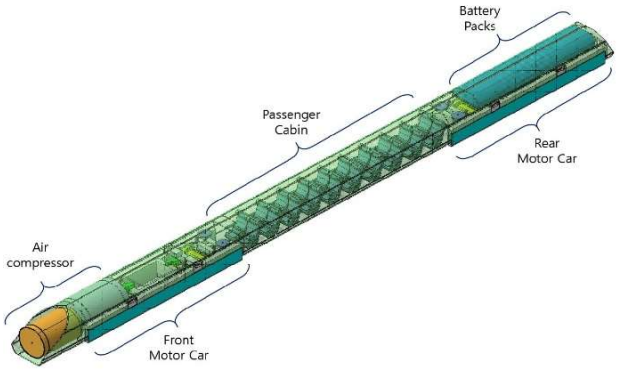

FIGURE 1. The configuration of the capsule train.

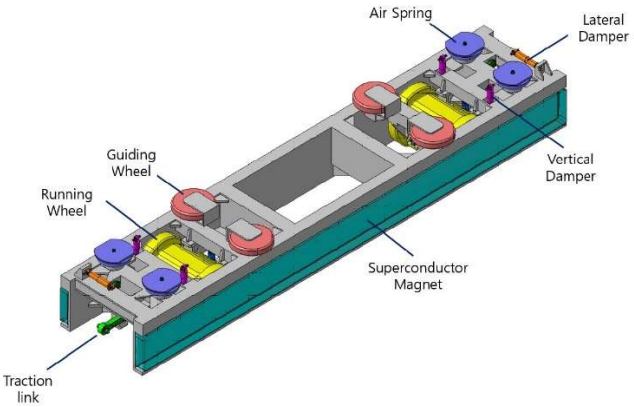

FIGURE 2. The configuration of the bogie.

TABLE 1. Overall specification of capsule train.

Height X Width X Length	1.46 X 1.4 X 26(m)
Weight	25.9(ton)
Number of passengers	20

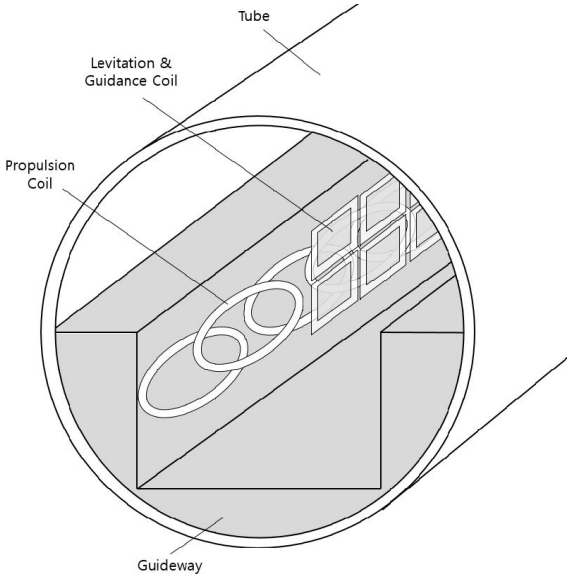

FIGURE 3. The configuration of the guideway.

The guideway to support the capsule train is placed inside the tube as shown in Figure 3. The sides of the guideway contains the series of 3 phase coil for propulsion and null flux coil for levitation and guidance. The propulsion is based on the linear synchronous motor(LSM) which uses the interaction between the stator(3 phase coil in the guideway) and rotor(superconductor magnet in the capsule train). The levitation and guidance is based on the null flux typed electrodynamic suspension(EDS) method.

DYNAMIC ANALYSIS OF THE CAPSULE TRAIN

The analytical model to analyze the lateral and roll dynamic analysis of the capsule train can be developed as shown in Figure 4. In this paper, only lateral and roll motion of dynamics are investigated, however, the vertical and pitch motion dynamics could be easily extended. Major parameters for this model are listed in Table 2.
To drive the lateral(x), vertical(y) and roll(θ) motion of bogie(b) and car body(c), 12 state variables are chosen like,

$$x = [\dot{x_b}, x_b, \dot{y_b}, y_b, \dot{\theta_b}, \theta_b, \dot{x_c}, x_c, \dot{y_c}, y_c, \dot{\theta_c}, \theta_c]^T. \quad (1)$$

Then, the system equation representing lateral, vertical and roll dynamics is expressed as follows.

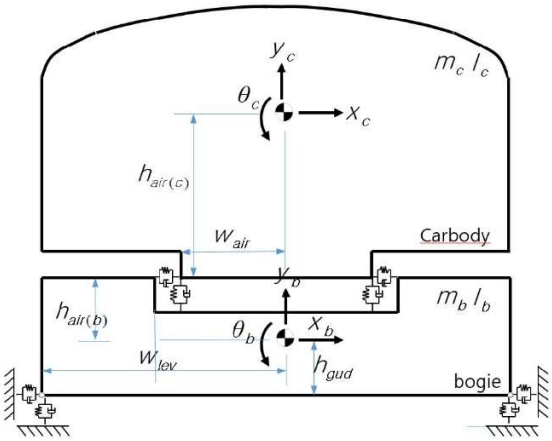

FIGURE 4. Analytical model for lateral and rolling motion.

TABLE 2. Parameters for analytical model.

Bogie mass	2093kg
Car body mass	16361kg
Bogie moment of inertia	10000kgm^2
Car body moment of inertia	16700kgm^2
Magnetic spring constant in guidance	1.56×10^{6}N/m
Magnetic spring constant in levitation	2.67×10^{6}N/m

$$\dot{x} = Ax + Bu,\ z = Cx \quad (2)$$

In equation (2), A, B, C and u represent state matrix, input matrix, output matrix and input vector respectively. The detail description for elements of matrix A and B is skipped. As disturbance input to the capsule train model, the guideway irregularity of lateral direction shown in Figure 5 is used.
Figure 6 shows the lateral acceleration of carbody in time and frequency domain, when the capsule train is running with 1,000km/h speed. As shown in this figure, the first and second mode of vibration is noticeable, which could mainly affect the passenger ride comfort.

VIBRATION REDUCTION BY USING SEMI-ACTIVE SUSPENSION

To reduce the lateral vibration of the capsule train, the MR(Magnetorheological) damper as semi-active secondary suspension between bogie and carbody is considered. MR damper(Figure 7) is consisted with MR grease whose damping characteristic is changed according to the applied current which can be adjustable. MR damper has also unique characteristics such as bilinear and hysteresis as shown in Figure 8. To model the

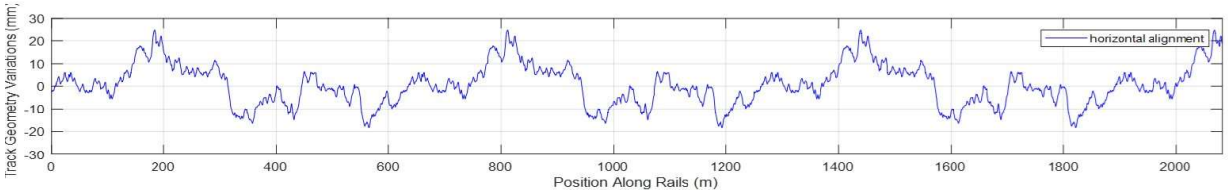

FIGURE 5. Guideway irregularity for simulation.

MR damper, amplitude function can be established like following equation.

$$A_{mr}(I) = \sum_{i=0}^{n} a_i I^i \quad (3)$$

And backbone-shape function to realize the bilinear characteristic is used as follows.

$$S_b(I,V) = \tanh[(b_1 I + b_2)V]$$
$$F_s = A_{mr}(I) S_b(I,V) \quad (4)$$

Lastly, by using the delay function as following equation, the hysteresis behavior of MR damper can be modeled.

$$\begin{cases} \dot{x} = -Ax + BF_s \\ F_h = Ax + CF_s \end{cases} \quad (5)$$

The modeling of MR damper based on the previous equation is realized by using MATLAB Simulink as shown in Figure 9 and this can be combined with the capsule train dynamic model for full simulation as shown in Figure 10.
To control the MR damper, the sky-hook control as semi active control strategy is used. In the sky-hook control system, the damping coefficient of MR damper is controlled according to the carbody velocity for only one direction, which is described in the following equation.

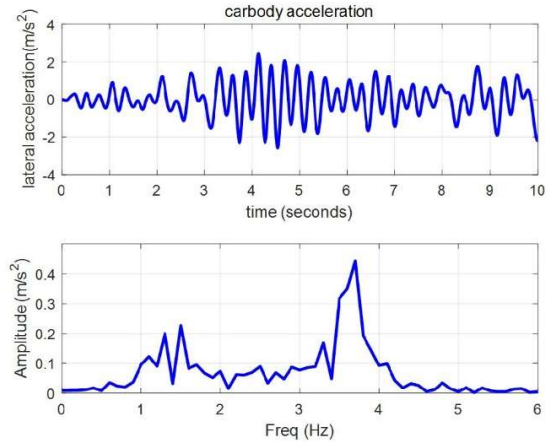

FIGURE 6. Lateral acceleration of carbody in time domain and frequency domain.

$$C_{skyhook} = \begin{cases} G\dot{y}_1 & \dot{y}_1\dot{y}_{12} \geq 0 \\ 0 & otherwise \end{cases} \quad (6)$$

Here, G is skyhook control gain, $\dot{y}_1$ is carbody velocity and $\dot{y}_{12}$ is relative velocity between carbody and bogie.
Figure 11 shows the simulation results indicating the lateral vibration of the carbody is reduced by applying the MR damper as semi active suspension in the capsule train.

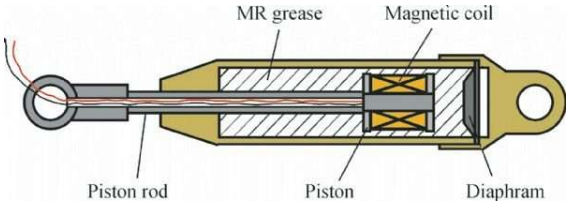

FIGURE 7. MR damper[6].

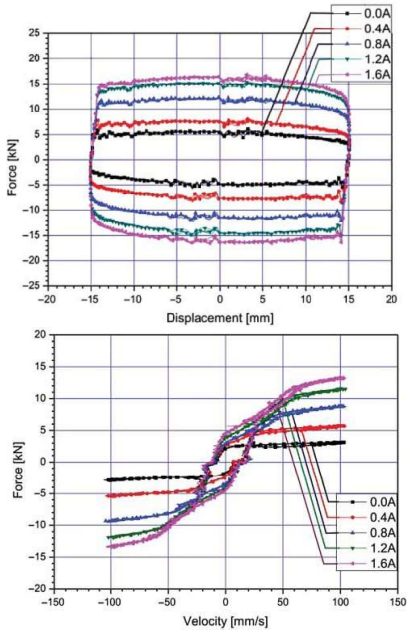

FIGURE 8. Characteristics of MR damper[7].

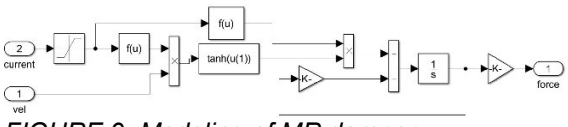

FIGURE 9. Modeling of MR damper.

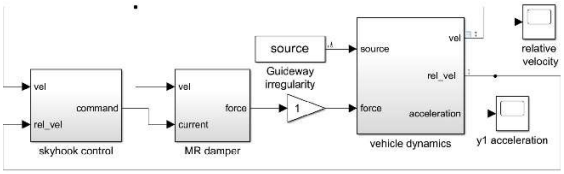

FIGURE 10. Simulation model for the semi-active suspension in capsule train.

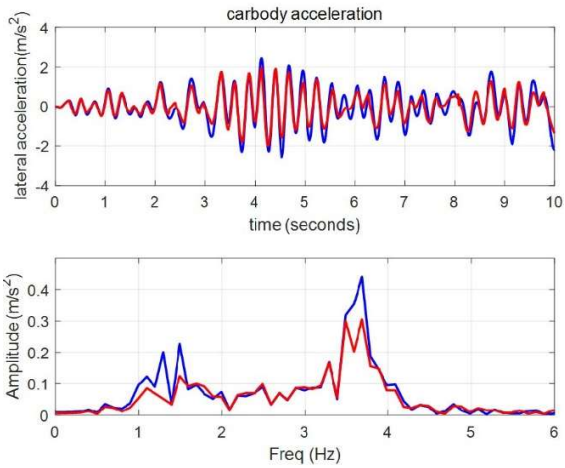

FIGURE 11. Lateral vibration reduction due to the MR damper application as semi-active suspension(red: after MR damper application).

HARDWARE IN THE LOOP EXPERIMENT

To validate the previous simulation results, the HILS(Hardware-in-the-loop) system is manufactured as shown in Figure 12. In this system, the MR damper whose specification is shown in Table 3 is used as hardware. The previously developed dynamic model of capsule train is used for simulation and the guideway irregularity input to the capsule train is realized by using the AC servo motor.

Figure 13 shows the HILS experimental result indicating the effectiveness of MR damper as semi-active suspension in the capsule train.

ACKNOWLEDGEMENT

This research was supported by a grant from R&D Program of the Korea Railroad Research Institute, Republic of Korea.

TABLE 3. Specification of MR damper.

Length, Diameter	700, 200mm
Stroke	60mm
Max. damping force	5kN
Dynamic range	3

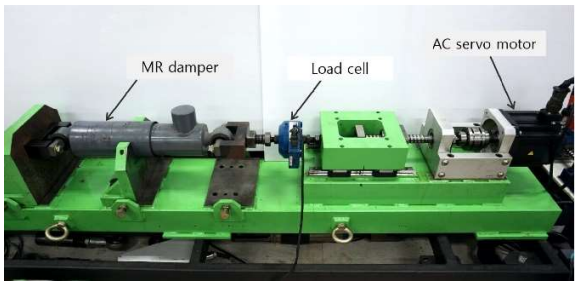

FIGURE 12. HILS(Hardware-in-the-loop) system.

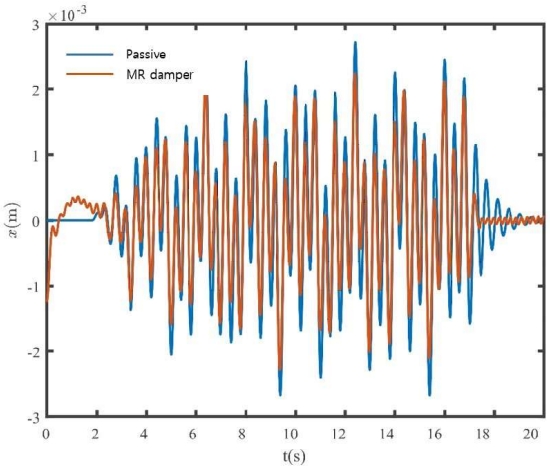

FIGURE 13. Experimental results of HILS system.

REFERENCES

[1] Musk, E. Hyperloop Alpha. 2013.

[2] He, J.L., Rote, D.M. and Coffey, H.T. *Electrodynamic forces of the cross-connected figure-eight null-flux coil suspension system*. Maglev conference, 1993.

[3] Moon, Francis C. *Superconducting Levitation*. John Wiley & Sons, Inc., 1944.

[4] He, J. and Coffey, H. Magnetic damping forces in figure-eight-shaped null-flux coil suspension systems, article, August 1, 1997

[5] Higashi, K. Ohashi, S. Ohsaki, H. and Masada, E. Magnetic damping of the electrodynamic suspension-type superconducting levitation system. Electrical Engineering in Japan, Vol. 127, No. 2, 1999.

[6] Sugiyama, S., Sakurai, T. and Morishita, S. *Vibration control of a structure using Magneto-Rheological grease damper*. Front. Mech. Eng. 8: 261, 2013.

[7] Kwak, M.K., Lee, J.H., Yang, D.H. and You, W.H. *Hardware-in-the-loop simulation experiment for semi-active vibration control of lateral vibrations of railway vehicle by magneto-rheological fluid damper,* Vehicle System Dynamics, 52:7, 891-908, 2014.

DESIGN of MOBILE MACHINE TOOLS with WHEELS

Sungcheul Lee[1], Hyunsoo Kim[1], and Seung-Kook Ro[1]
[1]Department of Ultra-Precision Machines and Systems
Korea Institute of Machinery and Materials
Daejeon, Republic of Korea

OVERVIEW

At present, large machine tool systems are very expensive owing to the guide and machine frame. In addition, the space and energy consumption for their operation is high. To overcome this problem, a mobile machining platform is proposed that can machine a large complex product on a workpiece without a guide-based machine tool frame. Applying the mobile machining system to the machining and maintenance of large parts such as plants can lower transportation costs and reduce the risk of damage to large structures. In this paper, we introduce a mobile moving platform that freely moves on the workpiece, which is a key element of the mobile machining system. The conceptual design was rendered based on a design methodology, a prototype was built, and a need motion was carried out.

INSTRUCTIONS

The current machine tool systems for the processing of large complex products such as high-tech aerospace, energy plant, and green transportation industry are expensive due to large guide and machine frame. As the cost is more than several billion won per unit, the new processing methodology has become necessary. In order to do this, a mobile machining method capable of machining a large complex product on a workpiece without a guide-based machine tool frame has been proposed [1]. As an alternative, a mobile based machining system technology has been proposed.

The existing mobile machine platform has a multi-axis articulated robot mounted on a moving platform, and has a structure for assembling, painting, welding, and polishing an aircraft or a ship [2-12]. Such a structure moves on the floor by its own weight, and therefore is not suitable as a mechanism for transferring over an existing workpiece. Therefore, we propose a mechanism that can move continuously using wheels and move freely in a desired direction.

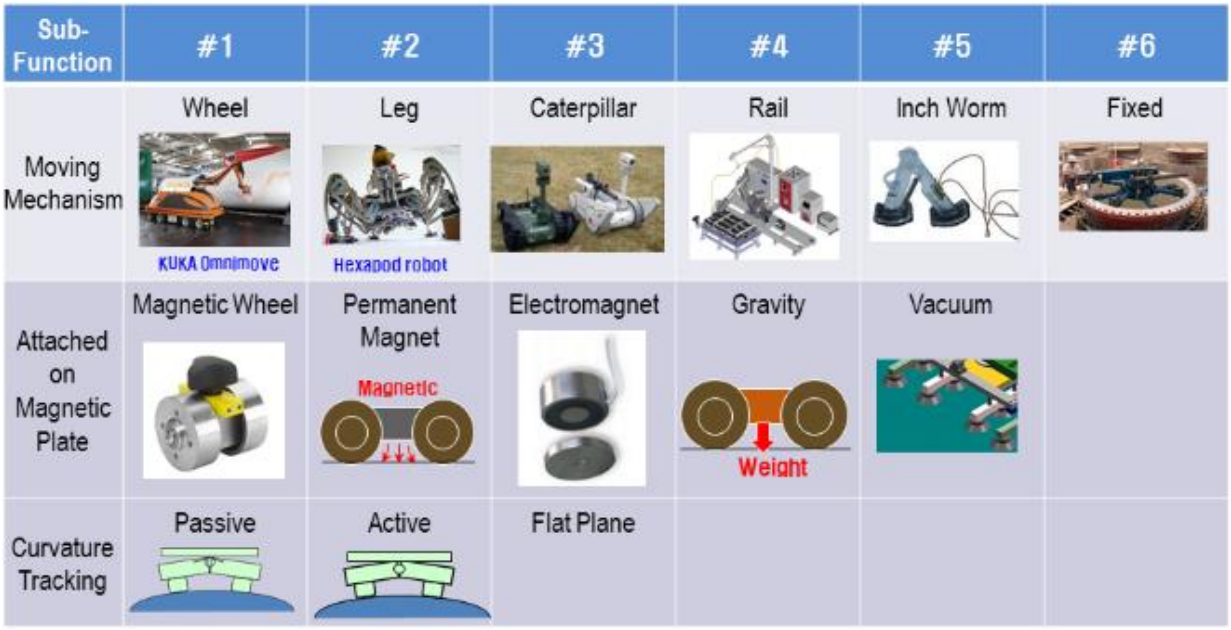

Figure 1. Design methodology for mobile machine tools

(a) Crawling type mobile robot *(b) Mobile machine tools with wheels*

Figure 2. Design alternatives for mobile machine tools

DESIGN ALTERNATIVES

The core module for developing a mobile machining system is a mobile transport platform. In this paper, we describe the development of the wheel-based mobile moving mechanism technology for surface conditions. We have developed a wheel - based mobile moving mechanism technology capable of curved surface and attached on steel plates. First, the principles of operation are divided into three categories using the design methodology. The conceptual design was carried out by listing the operation principle corresponding to the moving part on the steel plate, the part fixed to the steel plate, and the principle of tracking the curved surface. Among the operating principles shown in Figure 1, mechanism design was carried out using a wheel-driven mechanism, a magnet wheel, and a method of actively tracking the curved surface.

Based on the operating principles given above, one design alternative can be made by selecting and combining one operating principle in each category. For example, a crawling type mobile robot [9] can be designed by combining an inch worm type, an air adsorption type, and a flat transfer type (Figure 2 (a)). Figure 2(b) shows a method of attaching and driving a wheel using permanent magnets and actively tracking the curved surface. This design enables continuous movement of the plane with two axes of linearity and three degrees of freedom of rotation, and enables the transfer from the vertical wall of the steel plate. It is also possible to change the platform so that it can be mounted on curved surfaces.

MECHANICAL DESIGN

The mobile platform is configured as shown in Figure 3, and the configuration and conditions are as follows. It is driven by four wheels, and each wheel has a steering device, which can realize a plane three degree of freedom motion. It is possible to cope with plane driving and curved surface driving, and designed to be able to climb slope.

The mobile platform is divided into three bodies. There are one main body for performing machining in the center and two drive bodies for controlling the drive. It is designed to correspond to curved surface by controlling angle of three bodies.

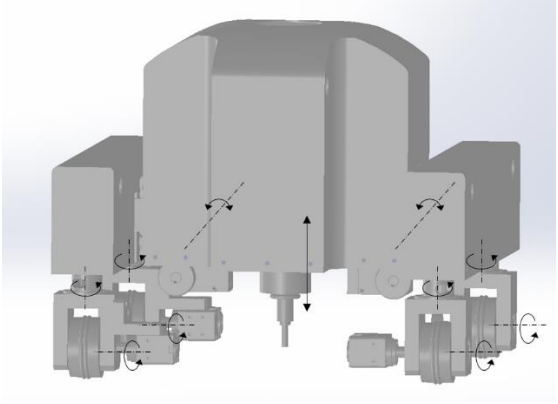

Figure 3. Overview of Wheel-based mobile machine tools

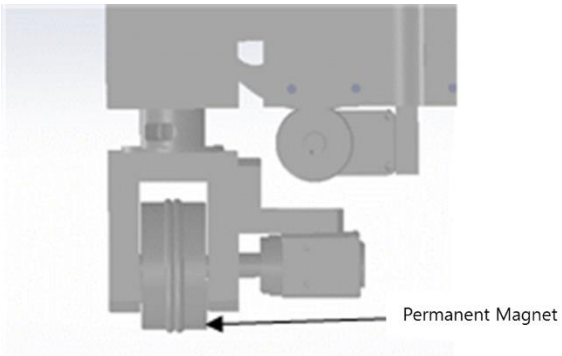

Figure 4. Design of the permanent magnet

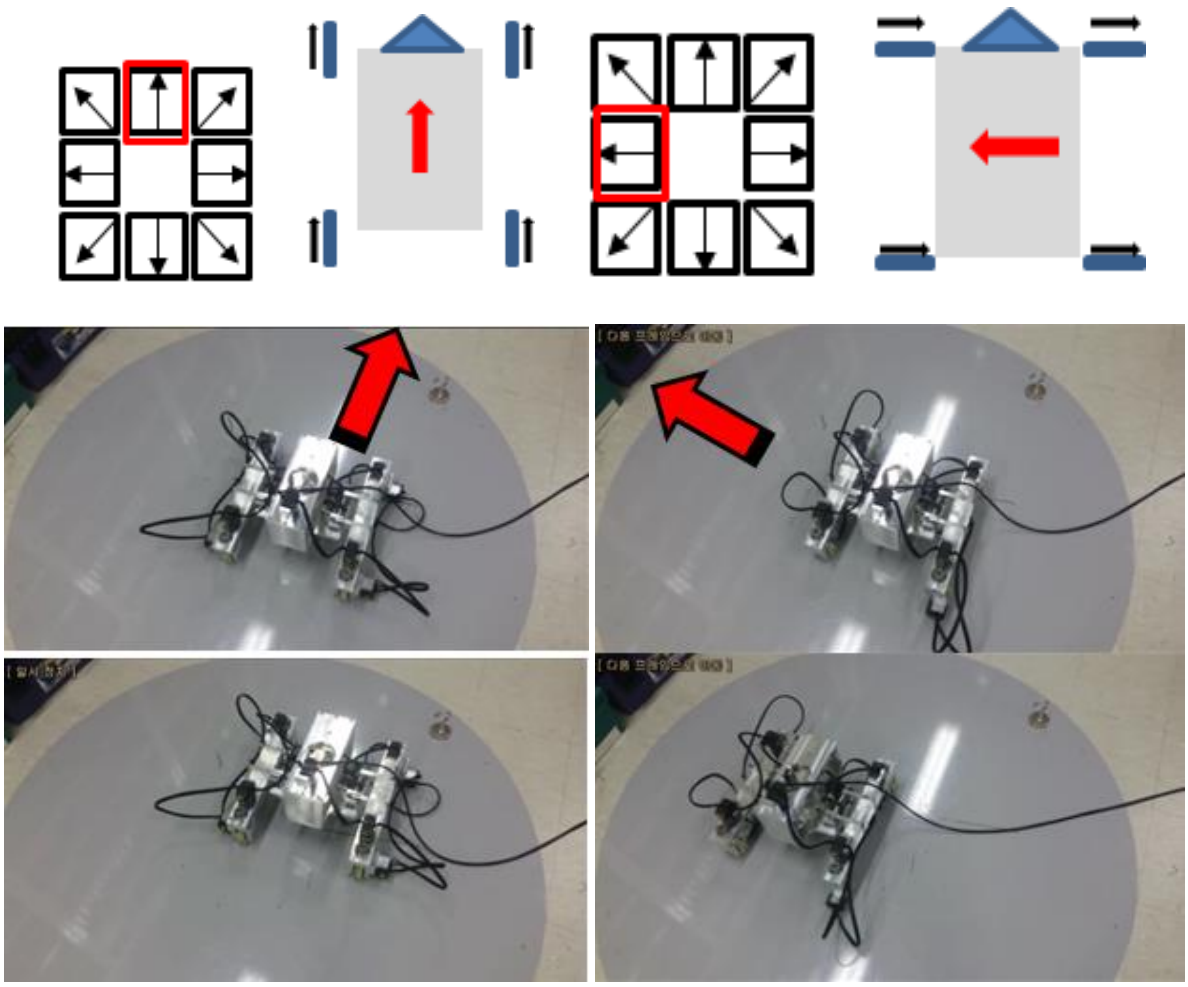

(a) Move forward *(b) Move left*

Figure 5. Motion of wheel-based mobile machine platform

Total 11 revolving motors were used. The motor is a Robotis XM430-W350 model. Each motor is a reducer-integrated type with a reduction ratio of 353.5 to 1, and is a motor capable of RS-485 serial communication. A total of four driving motors were used to drive the four wheels. Four motors were used to steer each motor. Two motors were used to adjust the relative angles of the three bodies for curved surfaces. In order to move the spindle up and down, one motor was used as lead screw type.

In the first design, a rubber wheel and a spaced magnet are used to fix to a magnet surface. Then, there was a phenomenon that one side of the wheel touches the surfaces, and the design is changed in the form of a wheel as a magnet (Figure 4).

The design of the moving platform for the mobile machine was performed. We used a magnet to move the vertical wall of the steel plate and complete the design to adapt it to the curved surface.

MOBILE PLATFORM PRODUCTION

The manufactured moving platform is capable of simultaneous uniaxial motion and multiple axle motion through external input from driving software. We have implemented 3-DOF planar motion (X-axis straight line, Y-axis straight line, θ-axis rotation) on the current horizontal plane, respectively. When forward driving is performed, the wheel moves to a predetermined position (Figure 5(a)). When moving left and right, first rotate four wheels at 90 degrees and then move to the desired position using the driving wheel (Figure 5(b)).

CONCLUSION

The design of the moving platform for the mobile machine was performed. We used a magnet to move the vertical wall of the steel plate and complete the design to adapt it to the curved surface. And we made the robot based on the design. We demonstrated the movement of the moving platform on the 90 degree wall.

REFERENCES

[1] Kim CJ, Yun JW, Ro SK., Design of an Inch-worm Type Moving Mechanism for Mobile Machining Systems. KSMTE Annual Autumn Conference. 2015; 144-144.

[2] Yang H, Baradat C, Krut S, Pierrot F. An Agile Manufacturing System for Large Workspace Applications. Robotics in Smart Manufacturing. 2013; 57-70.

[3] Schlosser C, Schüpstuhl T. Numerical Controlled Robot Crawler: New Resource for Industries with Large Scale Products. Production Engineering. 2014; 8:6: 719-725.

[4] Neugebauer R, Priber U, Rentzsch H, Ihlenfeldt S, Hoffmann D. Mobile Systems for Machining Large Work Pieces. CARV2011. 2011; 135-140.

[5] Ro SK. Development of Core Technologies for Mobile Machining Platform. Proceeding of KSMTE Annual Autumn Conference. 2017; 72-72.

[6] Bostelman R, Hong T, Marvel J. Survey of Research for Performance Measurement of Mobile Manipulators. Journal of Research of the National Institute of Standards and Technology. 2016;121: 342-366.

[7] Cho G, Chu B. Performance Evaluation of Concrete Polishing Robot with Omnidirectional Mobile Mechanism. Journal of the Korean Society of Manufacturing Technology Engineers. 2016; 25:2: 112-117.

[8] Olarra A, Axinte D, Uriarte L, Bueno R. Machining with the WalkingHex: A Walking Parallel Kinematic Machine Tool for in Situ Operations. CIRP Annals - Manufacturing Technology. 2017; 66: 361-364.

[9] Kim CJ, Yun JW, Ro SK. Performance Evaluation of a Inch-worm Type Moving Mechanism for Mobile Machining Systems. Proceeding of KSMTE Annual Spring Conference. 2016; 18-18.

[10] Pahl G, Beitz W. Engineering Design: A Systematic Approach. Springer-Verlag London, London. 2013.

[11] DMG MORI, n.d., viewed 30 November <http://us.dmgmori.com/blob/269958/b23d8087fc832744d806746a7d7bcae4/pu0usultrasonic-pdf-data.pdf>. 2017.

[12] Kim M J, Kang BH, Kim OS, Seo KW, Kim JY. Design and Control of a Wearable Robot for Stair-Climbing Assistance. Journal of the KSMTE. 2017; 26:1: 89-99.

DEVELOPMENT OF DYNAMIC MODEL FOR THE SPECIAL PROTOTYPE OF FOUR-AXIS MACHINE USING COORDINATE TRANSFORMATION METHOD

Chang Kyu Song[1], Pham Van Dinh[1], and Chan Hong Lee[1]
[1]Department of Ultra Precision Machines & Systems
Korea Institute of Machinery and Materials
Daejeon, South Korea

INTRODUCTION

The virtual machine tools are being developed extensively in recent decades. Especially, they have been applied in high-tech fields such as semiconductor, display, smartphone equipment, etc. To increase the accuracy in manufacturing and machining, the machine tools are designed and optimized through the virtual machine [1, 2]. The machine tool is assembled from various mechanical components by kinematic joints and fixed joints. Hence, the rigidity and stability of the machine tool must be obtained through the finite element method (FEM) to optimize the structure and materials [3]. The spindle is analyzed through frequency response function (FRF) by reacceptance coupling substructure analysis (RCSA) [4]. The dynamic characteristics of bearings and guide-way are invested to reduce the vibration and friction force, this role improves the accuracy and increases the performance of machine [5, 6]. Otherwise, dynamic model of machine tool for stage is developed to optimize the control systems by coordinate transformation method (CTM) [7] to analyze the dynamics. This method has the advantages of allowing dynamic analysis of multi-axis machine tools and increasing the speed calculation due to applying directly mathematical method, but these methods have some disadvantages such as without supports for special configurations of machine tool.

To overcome the disadvantages of the conventional methods, this research develops the dynamic model for special configurations using Coordinate Transformation Method (CTM). This method combines the energy method with Lagrange's Equation to establish the six degrees of freedom (DOF) motion equations for each axis of machine tool. The dynamic analysis results of the entire system were then established through the transformation matrix. This method transfers the complex multi-axis machine into the some multiple one-axis machines to analyze the dynamic easier. The accuracy of this method was tested through simulation results in Matlab environment with good agreement.

DEVELOPMET OF DYNAMIC MODEL FOR FOUR-AXIS MACHINE.

The four-axis machine tool in Fig. 1 is designed to manufacture the high precision instruments. This machine has two linear Z-axis carrying cutting tool Z_1Z_2 and XY carrying workpieces. This research applies the CTM method to build the dynamic model and using to analyze the control signals of multi-axis machine. The CTM method will be applied to separate this machine into the two parts: the cutting tool Z_1Z_2 and workpieces XY.

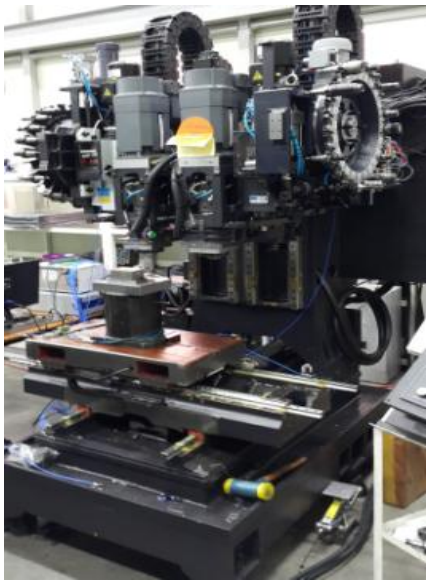

FIGURE 1. Prototype of four-axis machine tool

Considering the workpieces XY in figure 2: The forces acting on the X-axis include the driving force of the motor (F_{m1}) and the disturbance force from the Y-axis (F_{d21}). Seminally, the forces acting on the Y-axis also include the driving force of the motor (F_{m2}) and the inertial moment force from the X-axis (F_{d12}). The motion equations of the workpiece XY can be obtained by the CTM method [7] as follows:

$$\begin{aligned}[M_1]\ddot{q}_1+[C_1]\dot{q}_1+[K_1]q_1&=[G_{m1}]F_{m1}+F_{d21}\\ [M_2]\ddot{q}_2+[C_1]\dot{q}_2+[K_2]q_2&=[G_{m2}]F_{m2}+F_{d12}\end{aligned} \quad (1)$$

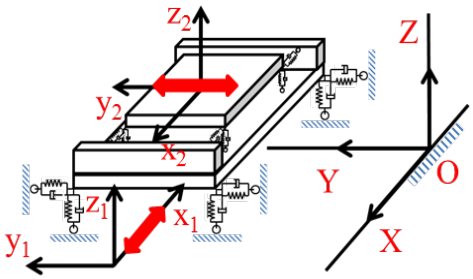

FIGURE 2. Dynamic analysis of workpiece XY

where M_1 , M_2, are mass matrix of tables of X, Y-axis respectively, K_1 , K_2 are stiffness matrix and C_1 , C_2 are damping matrix of bearings, F_{m1} , F_{m2} is the driving motor forces of X, Y-axis, F_{d21} , F_{d12} is disturbance forces from Y-axis acting to X-axis and X-axis acting to Y-axis, G_{m1} , G_{m2} is the force positions along each axis.

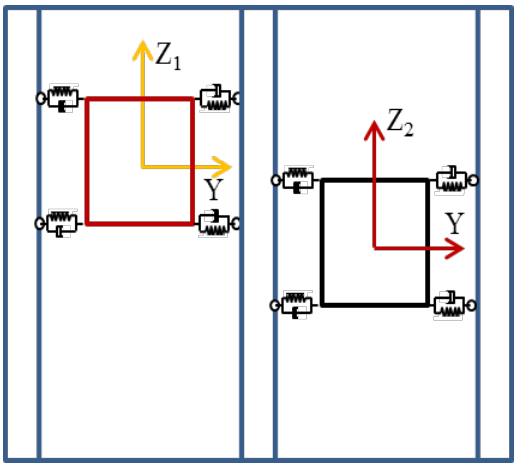

FIGURE 3. Dynamic analysis of cutting tool Z_1Z_2

Considering the cutting tool Z_1Z_2 in figure 3: Figure 3 shows two-axis Z_1Z_2 which are arranged in Z-direction. Hence, the forces acting on the Z_1Z_2-axis include the driving force of the motor (F_{m3}, F_{m4}) and without the disturbance force acting on the Z_1 stage and Z_2 stage due to these axes are arranged independently on a base. The motion equations of the cutting tool Z_1Z_2 – stages can be obtained as follows:

$$\begin{aligned}[M_3]\ddot{q}_3+[C_3]\dot{q}_3+[K_3]q_3&=[G_{m3}]F_{m3}\\ [M_4]\ddot{q}_4+[C_4]\dot{q}_4+[K_4]q_4&=[G_{m4}]F_{m4}\end{aligned} \quad (2)$$

where M_3 , M_4, are mass matrix of tables of Z_1Z_2--axis respectively in *Kg*, K_3 , K_4 are stiffness matrix in Nm^{-1} , and C_3 , C_4 are damping matrix of bearings, F_{m3} , F_{m4} is the driving motor forces of Z_1, Z_2 –axis in *N*, G_{m3} , G_{m4} is the force positions on Z_1, Z_2-axis respectively.

$$q=[x \quad y \quad z \quad \theta_x \quad \theta_y \quad \theta_z]$$

where x, y, z is position of stage in X, Y, Z-direction respectively in *m*, $\theta_x, \theta_y, \theta_z$ is rotation angles of stage around X, Y, Z –axis in *rad*.

The driving force of the motor acts on the machine table (Fig. 4). $F=\left[f_x \quad f_y \quad f_z \quad \tau_x \quad \tau_y \quad \tau_z\right]^T$

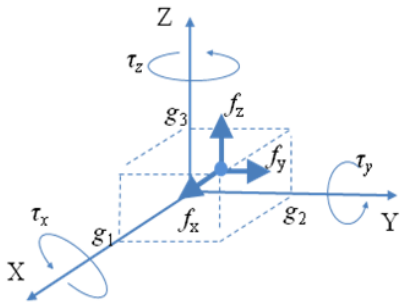

FIGURE *4. Driving force set point coordinates.*

The disturbance forces can be obtained as follows:

$$\begin{aligned}F_{d21}&=[C_2]\dot{q}_2+[K_2]q_2\\ F_{d12}&=[M_2]\ddot{q}_1\end{aligned} \quad (3)$$

The dynamic equation of 4-axis machine can be obtained from Eq. (1) to Eq. (3) as follows:

$$[M]\ddot{q}+[C]\dot{q}+[K]q=[G]F \quad (4)$$

The mass, stiffness, damping, and position matrix for each axis can be obtained as described in [7].

$$[M]=\begin{bmatrix} M_1 & 0 & 0 & 0 \\ 0 & M_2 & 0 & 0 \\ 0 & 0 & M_3 & 0 \\ 0 & 0 & 0 & M_4 \end{bmatrix},[C]=\begin{bmatrix} C_1+C_2 & -C_2 & 0 & 0 \\ -C_2 & C_2 & 0 & 0 \\ 0 & 0 & C_3 & 0 \\ 0 & 0 & 0 & C_4 \end{bmatrix}$$

$$[K]=\begin{bmatrix} K_1+K_2 & -K_2 & 0 & 0 \\ -K_2 & K_2 & 0 & 0 \\ 0 & 0 & K_3 & 0 \\ 0 & 0 & 0 & K_4 \end{bmatrix},[G]=\begin{bmatrix} G_1 & 0 & 0 & 0 \\ 0 & G_2 & 0 & 0 \\ 0 & 0 & G_3 & 0 \\ 0 & 0 & 0 & G_4 \end{bmatrix}$$

$$F=\begin{bmatrix} F_{m1} \\ F_{m2} \\ F_{m3} \\ F_{m4} \end{bmatrix},q=\begin{bmatrix} q_1 \\ q_2 \\ q_3 \\ q_4 \end{bmatrix}$$

Equation (4) is converted into Eq. (5), and the state-space model can be used to solve the dynamic problem in the Simulink environment such as Fig. 5.

$$\begin{cases} \dot{X}=AX+BU \\ Y=C'X \end{cases} \quad (5)$$

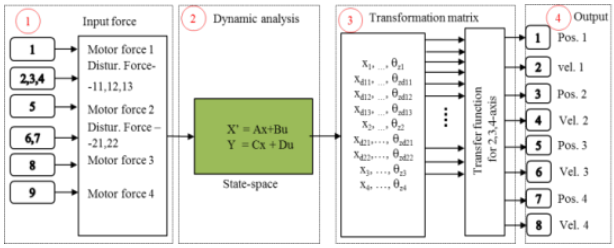

FIGURE 5. Dynamic modeling of the four-axis machine tool

in which $X=\begin{bmatrix} \dot{q} \\ q \end{bmatrix}$; $A=\begin{bmatrix} -M^{-1}C & -M^{-1}K \\ I & 0 \end{bmatrix}$;

$$B=\begin{bmatrix} M^{-1}[G] \\ 0 \end{bmatrix}$$

To account for the case where the desired output is not just the states but is some linear combination of the states, an output matrix C' is defined to relate the outputs to the states. The output matrix C' has as many rows as outputs required and as many columns as states. In this case, if we want to get the displacement of the X-axis, output matrix C' is represented as follows:

$$C'=\begin{bmatrix} 0 & 0 & 0 & 0 & 0 & 0 & 1 & 0 & 0 & 0 & B_{i30} & -B_{i20} \end{bmatrix}$$

where B_i is the displacement from the measurement point to the center of mass, as shown in Fig. 6

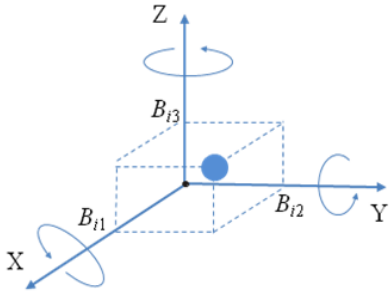

FIGURE. *6. Sensor measurement point coordinates.*

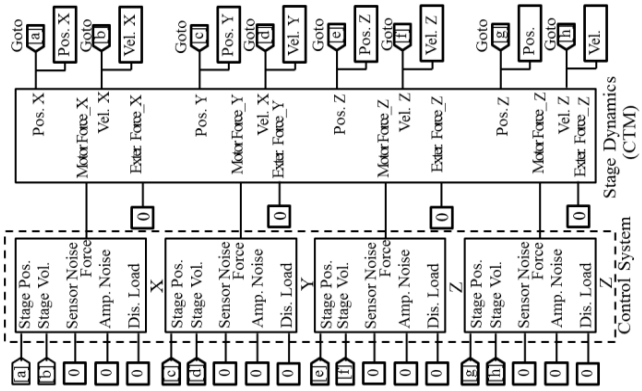

FIGURE *7. Control modeling for SMEC machine tool.*

RESULTS

The dynamic modeling of the four-axis machine is described as Fig.5. This dynamic model was combined with the control system of Mitsubishi to simulate the control signals such as Fig. 7. The simulation and simulation results were described in Fig. 8.

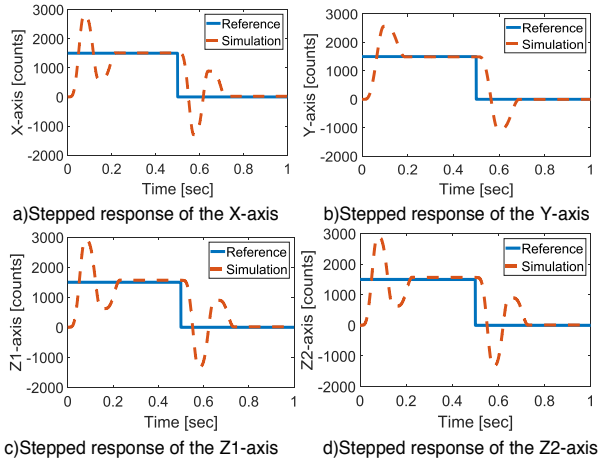

FIGURE 8.Comparison between Simulation and reference results

The simulation results are quite good but the response time is slow because the control gain is not optimal.

CONCLUSIONS

This research developed the dynamic model and the motion equations for special configuration of four-axis machine tool with two Z-axis using coordinate transformation method.

This method can be used to support designers and machine tool manufacturers in selecting optimal motors, design parameters, materials, and control parameters without the need for practical experimentation. Additional, it can be used to analyze the dynamic of almost configurations in machine tool field to find out an optimal configuration.

The simulation results need to be further improved in the future researches to decrease the response time in simulation process.

REFERENCES

[1] Y. Altintas, C. Brecher, M. Weck, S. Witt, 2005. Virtual Machine Tool. CIRP- Manufacturing Technology, 54(2), 115-138.

[2] Y. Altintas, Y. Cao, 2005. Virtual Design and Optimization of Machine Tool Spindles. CIRP Annals - Manufacturing Technology, 54 (1), 379-382.

[3] Huijie Zhang,Wanhua Zhao, Chao Du, Hui Liu and Jun Zhang, 2015. Dynamic modeling and analysis for gantry-type machine tools considering the effect of axis coupling force on the slider–guide joints' stiffness. Journal of Mechanical Engineers, 230(11), 2036-2046.

[4] Uttara V. Kumar, Tony L. Schmitz. Spindle dynamics identification for Receptance Coupling Substructure Analysis. Precision Engineering, 36(3), 435-443.

[5] H. Ohta, G. Hanaoka and Y. Ueki, 2017. Sticking of a Linear-Guideway Type Recirculating Ball Bearing, 139(3).

[6] B. R. Jorgensen, Y. C. Shin, 1997. Dynamics of Machine Tool Spindle/ bearing Systems Under Thermal Growth. Journal of Tribology, 119(4), 875-882.

[7] P. V. Dinh, Chang K. Song, 2017. A novel dynamic model for multiple configurations of machine tools using a coordinate transformation method, IJAMT, 95(1-4), 27-42.

[8] Kwon S, Song C, Kim B, Lee H, 2013. Physical Modeling and Experimental Verification for Multi-Axis Machinery Equipment. KSPE Conference, (in Korean).

REFERENCE TRAJECTORY GENERATION OF DECOUPLABLE COARSE-FINE STAGE FOR POINT-TO-POINT POSITIONING APPLICATIONS

Deokkyun Yoon and Chinedum E. Okwudire
Department of Mechanical Engineering
The University of Michigan
Ann Arbor, MI

OVERVIEW

Reference trajectory generation algorithm for a decouplable coarse-fine stage for rapid point-to-point positioning applications is investigated in this study. The investigated algorithm only needs limited preview of the fine stage's reference, thus rendering the implementation of the algorithm inside a real-time controller possible. Using the previewed fine stage's reference, the coarse stage's reference is generated with appropriately selected finite impulse response filters. Preliminary results show that the investigated approach can generate faster coupling motions than an offline B-Spline-based full-trajectory optimization approach developed in prior work. Experimental results demonstrate reductions in residual vibration, tracking error, and linear motor control effort for sufficiently large stepping sizes.

BACKGROUND AND MOTIVATION

A decouplable coarse-fine (DCFS) linear stage design approach that enables improved precision and energy efficiency during rapid point-to-point positioning (i.e., stepping motion) was presented by the authors [1]. Figure 1 shows the schematic of the DCFS design [1]. The table of fine stage (FS), mounted on the isolated base, is driven by linear motor (LM) force (u_{FS}), while the position (x_{FS}) is measured relative to the base. Due to the presence of low-stiffness vibration isolators, u_{FS} creates residual vibration of the base. The coarse stage (CS) is mounted on the machine ground and driven by the geared rotary motor (RM) force (u_{CS}), with higher efficiency than the LM.

During rapid point-to-point positioning, the CS directly drives the FS table. The two stages become coupled with physical contact between them. When coupled, the CS either pushes or stops the FS during the acceleration/deceleration (acc/dec) portions of motion trajectories. The bumpers mounted in-between the CS and FS ensure smooth (de)coupling of the stages. This acc/dec based coupling strategy is chosen because actuation force requirements are high and vibration isolation is not needed during the rapid acc/dec. Once the table approaches the target position, the CS becomes physically decoupled from the FS table and the LM takes over to complete the final portion of the motion, when force requirements are low and positioning precision and vibration isolation requirements are high. With the negligible isolated base displacement (x_B), the FS and CS are decoupled when $d = x_{CS} - x_{FS} > -\delta$ or $d < \delta$, where δ is the nominal gap between the FS and CS, and the FS is effectively isolated from the ground vibration. Note that the kinematic limits of the two stages are designed to be similar, such that the CS and FS can travel together in parallel [1].

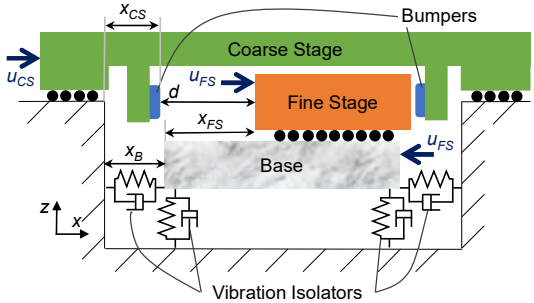

FIGURE 1. Schematic of DCFS design.

The idea of a DCFS is not new (e.g., see [2]). However, the unique features of the presented stage concept in [1] are: (1) when coupled, the CS and FS are driven in parallel not in series as in [2]; and (2) the CS is mounted on the ground while the FS is mounted on the isolated base, which is different from [2] where both stages are mounted on the isolated base. In prior work, the reference trajectory of the CS was generated based on the known FS trajectory using an offline B-Spline fitting approach [1]. The B-Spline fitting approach, considering the kinematic limits of the CS, required the entire FS reference to be known. Therefore, when the reference trajectory becomes long, the B-Spline approach can be computationally expensive for both trajectory generation and controller memory requirement points of view. In order to generate the CS

reference trajectory with less computational cost, finite impulse response (FIR) filtering (i.e., central moving averaging) with the knowledge of required motion types is considered in this investigation. For this approach, a limited length of FS reference preview is made available to the trajectory generation algorithm, facilitating online implementation of the investigated approach.

COARSE STAGE REFERENCE GENERATION WITH FINE STAGE REFERENCE PREVIEW

Desired displacement between FS and CS

During operation of the DCFS, the maximum relative distance the CS needs to travel is 2δ when it needs to traverse from the left bumper coupling to the right bumper coupling (see Figure 1). Because the reference for d (d_{ref}) before and after the (de)coupling event are constant, its time derivatives are 0. In addition, δ is very small for the decouplable coarse-fine stage application; therefore, the CS needs to make the coupling motion with the maximum acceleration, followed immediately by the maximum deceleration (i.e., there is no constant velocity travel). Thus, the minimum time (T_m) required for relative CS travel distance of 2δ with a finite acceleration is

$$T_m = \sqrt{2\delta / a} \tag{1}$$

where a is the acceleration limit of the CS. Note that the axis acceleration limit of the CS can be used to calculate T_m, because the time derivatives of d_{ref} should have different signs than those of the FS reference during the relative motion (see Figures 5 and 6). In fact, T_m given in Eq. 1 is a conservative estimate since under most cases, the relative motion is only by δ (i.e., the DCFS transitions from the coupled state to the de-coupled state or vice versa). In addition, the FS reference acceleration is not always at its maximum /minimum when the FS and CS are coupled.

Figure 2 shows the coupling motion types, where d_{des} is the desired displacement difference between the FS and CS references for (de)coupling and t is time. The following logic is used to generate d_{des},

$$d_{des} = \begin{cases} \delta & \text{if } a_{FS,ref} < 0 \\ -\delta & \text{if } a_{FS,ref} > 0 \\ 0 & \text{otherwise} \end{cases} \tag{2}$$

where $a_{FS,ref}$ is the reference acceleration of the FS. The motion types described with Figure 2 (a), (b), (c), and (d) are for cases with the relative motion by δ, while Figure 2 (e) and (f) describe the cases for relative motions by 2δ.

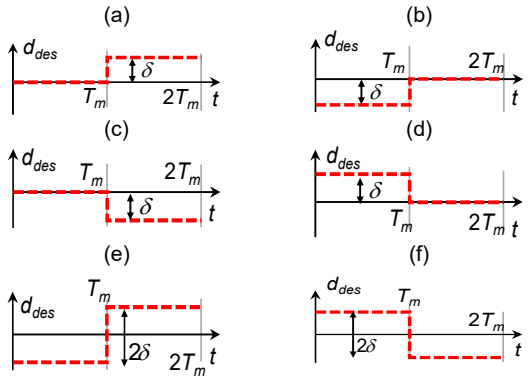

FIGURE 2. Desired displacement between the FS and CS reference for (de)coupling. (a) – (d): transition from coupled to decoupled or decoupled to coupled cases, (e) and (f): transition from one coupled state to the other coupled state cases.

Based on d_{des}, the coupling motion reference trajectory (d_{ref}) considering the kinematic (e.g., velocity and acceleration) limits of the stage is generated by filtering the signal with an FIR filter [3]. Based on motion types, two FIR filters are switched back-and-forth to generate d_{ref}, as will be shown in the following sections.

Finite impulse response (FIR) filters for trajectory generation

For the relative motion by δ, the minimum time steps for preview is

$$k_{a,1} = \left\lceil \frac{\sqrt{\delta / a}}{T_s} \right\rceil \tag{3}$$

where T_s is the sampling interval of a real-time controller and $\lceil\ \rceil$ denotes the ceiling function. Using this, the modified acceleration and velocity for trajectory become

$$a_{\text{mod},1} = \frac{\delta}{\left(k_{a,1}T_s\right)^2};\ v_{\text{mod},1} = \frac{\delta}{k_{a,1}T_s} \tag{4}$$

The FIR filters for generating velocity and acceleration profiles ($MA_{v,1}$ and $MA_{a,1}$) are

$$MA_{v,1} = \left[\frac{1}{k_{v,1}} \cdots \frac{1}{k_{v,1}}\right];\ MA_{a,1} = \left[\frac{1}{k_{a,1}} \cdots \frac{1}{k_{a,1}}\right] \tag{5}$$

where

$$k_{v,1} = \left\lceil \frac{\delta}{v_{\text{mod},1}T_s} \right\rceil \tag{6}$$

The two FIR filters shown in Eq. 5 are combined by convolving each other to create the FIR filter (MA_1) to be applied to the d_{des} signal.

$$MA_1 = \left(MA_{v,1} * MA_{a,1}\right) \tag{7}$$

Similarly, the FIR filter for the relative motion with 2δ (MA_2) can be computed following the equations shown below.

$$k_{a,2} = \left\lceil \frac{\sqrt{2\delta / a}}{T_s} \right\rceil;\ a_{\mathrm{mod},2} = \frac{2\delta}{\left(k_{a,2}T_s\right)^2} \tag{8}$$

$$v_{\mathrm{mod},2} = a_{\mathrm{mod},2}k_{a,2}T_s;\ k_{v,2} = \left\lceil \frac{2\delta}{v_{\mathrm{mod},2}T_s} \right\rceil \tag{9}$$

$$MA_{v,2} = \left[\frac{1}{k_{v,2}} \cdots \frac{1}{k_{v,2}}\right];\ MA_{a,2} = \left[\frac{1}{k_{a,2}} \cdots \frac{1}{k_{a,2}}\right] \tag{10}$$

$$MA_2 = \left(MA_{v,2} * MA_{a,2}\right)$$

Because the FIR filter with a longer length must be taken for preview, the preview length needed by the real-time controller is

$$k_m = k_{a,2} = \left\lceil \frac{\sqrt{2\delta / a}}{T_s} \right\rceil \tag{11}$$

Note that regulation of higher order derivatives (e.g., jerk and snap) of d_{ref} can be accomplished by stacking more FIR filters in series and broadening the preview length accordingly.

As an illustrative example, a = 10 m/s^2, δ = 0.4 mm, and T_s = 0.1 ms are used to generate the two FIR filters (MA_1 and MA_2) shown in Figure 3. Here, the length of MA_1 is extended by padding 0's before and after the actual filter, so that the two filters have the equal length. In Figure 3, i = 0 is used to describe the present (i.e., current) time frame.

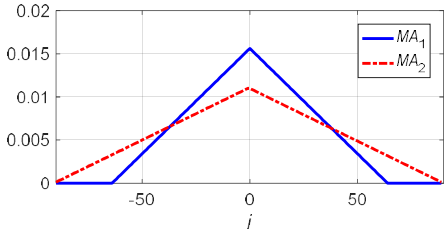

FIGURE 3. FIR filters used to generate d_{ref}. MA_1 and MA_2 are used for relative motions of δ and 2δ, respectively.

Selection of FIR filters

The two FIR filters (MA_1 and MA_2) are switched back-and-forth depending on the d_{des} signal. Since MA_2 is a more conservative approach of the two, it serves as the default filter. To determine which filter needs to be applied, the decision logic presented with the flowchart shown in Figure 4 is used. With the presented logic, the more aggressive filter (MA_1) is applied only when the desired displacement for coupling motion is δ and there has been no relative motion between the CS and FS for the last ½ length of the filter. The latter condition serves as the trajectory continuity constraint when the FIR filter switch occurs.

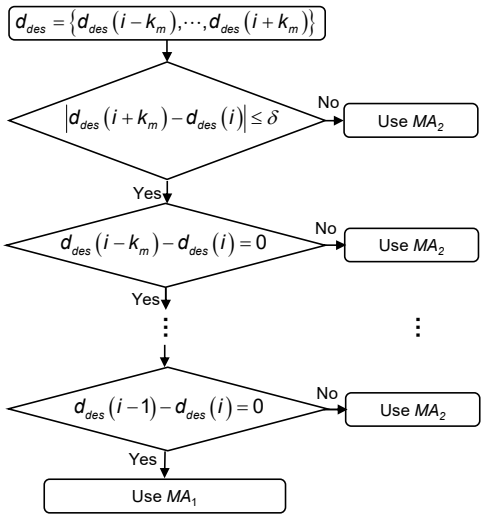

FIGURE 4. Flow chart for selecting which FIR filter to be applied to the d_{des} signal.

Compared to the B-Spline fitting [1], the FIR filtering based approach achieves faster coupling motion as shown in Figure 5, when a 50 mm point-to-point positioning is used as example. Because the B-splines' control points are sparser than the actual trajectory points, the B-Spline-based approach requires more time for the relative motion. The time derivatives of reference trajectory in Figure 6 show that the FIR filtering approach does not fully exploit the useable acceleration, but it is a more efficient use of given time than the prior work. The CS reference ($x_{CS,ref}$) is

$$x_{CS,ref} = x_{FS,ref} + d_{ref} \tag{12}$$

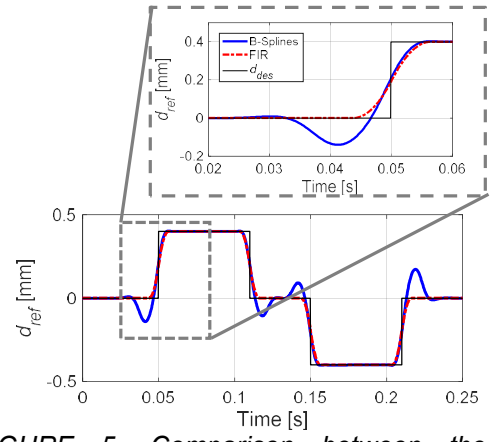

FIGURE 5. Comparison between the d_{ref} generation methods.

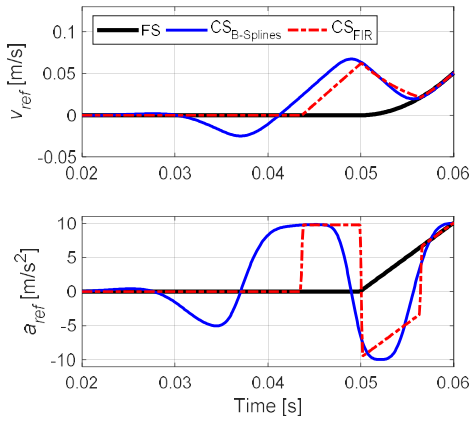

FIGURE 6. Comparisons of velocity (v_{ref}) and acceleration (a_{ref}) references for FS and CS.

DECOUPLABLE COARSE-FINE STAGE

A decouplable coarse-fine stage (DCFS), whose CAD model is shown in Figure 7 [1], is used for experimental validation of the FIR filtering-based reference trajectory generation algorithm.

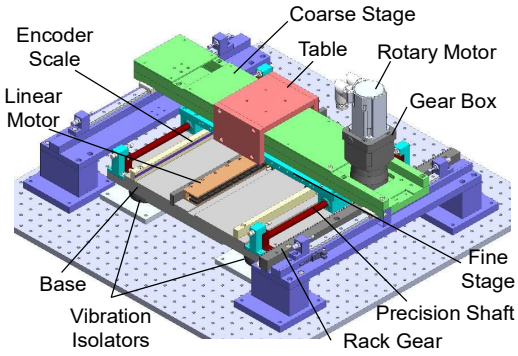

FIGURE 7. CAD model of decouplable coarse-fine stage used for experiment.

An air-core linear motor (Aerotech, BLMUC-95) drives the FS, guided by air bushings (New Way, S8013E02) riding on precision ground shafts. The FS position is measured by a linear encoder (Renishaw, T1000 readhead with 20 μm pitch scale) with 4.88 nm post-interpolation resolution (dSPACE, DS3002). A table for mounting substrates is attached to the FS. The FS is mounted on a 400 mm × 400 mm × 33 mm steel base, which is isolated from the ground via rubber vibration isolators (Vibra Systems, LF6045). A rotary servo motor (Kollmorgen, AKM21C) with a gear reducer with the 10:1 speed ratio (Stöber, PE series) drives the CS, which is riding on linear bearings (Misumi, SE2BLV16) attached to the machine ground. To convert from rotary motion to linear motion, rack and pinion gears (Atlanta Drive Systems, Module 2 Class 10) are installed for the CS. PWM amplifiers (Aerotech, Soloist CP10 and Kollmorgen, AKD P00606) power the motors with the 47 N and 1,059 N (equivalent) force limits, respectively. The CS and FS become coupled when δ = 0.4 mm. The bumpers are made of Shore A70 hardness urethane.

The stage's specifications are summarized in Table 1 [1]. For analysis of the stage performance, the isolated base vibration is measured by a laser displacement sensor (Keyence, LK-G10). Note that the measured base displacement is not used for control. A real-time controller (dSPACE, DS1007 and DS5203 with sampling time T_s = 0.1 ms) is used to control the stage.

TABLE 1. Specifications of decouplable coarse-fine stage.

FS Moving Mass (m_{FS})	3.4 kg
CS Moving Mass (m_{CS})	17.3 kg equivalent
Stage Travel	0.15 m
Natural Frequency of Isolated Base	7.9 Hz
FS Feedback Controller Bandwidth	240 Hz
CS Feedback Controller Bandwidth	70 Hz

EXPERIMENTAL RESULT

Rapid point-to-point positioning experiments are conducted with stepping sizes ranging from 1 mm to 100 mm. The kinematic limits imposed on the $x_{FS,ref}$ generation are 0.5 m/s, 10 m/s^2, and 1,000 m/s^3, respectively. The same control scheme as the prior work [1] is used, meaning the feedback controller of FS becomes active only when $|a_{FS,ref}| < 5$ m/s^2.

The stage performance comparison between the decoupled throughout the trajectory (i.e., $x_{CS,ref} = x_{FS,ref}$) and the coupled (i.e., $x_{CS,ref} = x_{FS,ref} + d_{ref}$) cases using the 3 mm and 50 mm stepping size reference trajectories are shown in Figures 8 and 9. For both cases, the base vibration displacement (x_B) is reduced, but the reduction is much greater with the 50 mm stepping size due to the large inertial load required for acceleration. The FS tracking error, and motor control input (u_{FS}) reductions are achieved with the coupled case for the 50 mm stepping size, which are similar to the result of prior work [1]. On the other hand, the 3 mm stepping size with the coupled case show increased tracking error and u_{FS}, when compared to the decoupled case. This is attributed to the large tracking error when the stages become decoupled (i.e., the FS feedback controller becomes active again) as

the reference approaches the target position. Because of the low inertial load from the 3 mm stepping case, small residual vibration and tracking error are observed. In this case, the FS alone can provide good tracking performance.

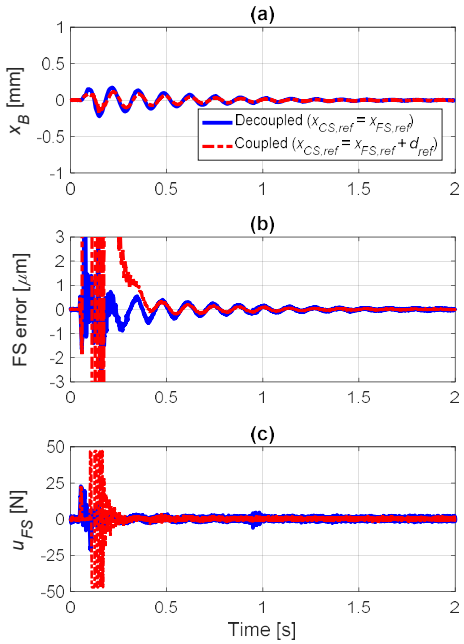

FIGURE 8. Comparison of (a) base vibration, (b) FS tracking error, and (c) FS control input for rapid 3 mm point-to-point positioning.

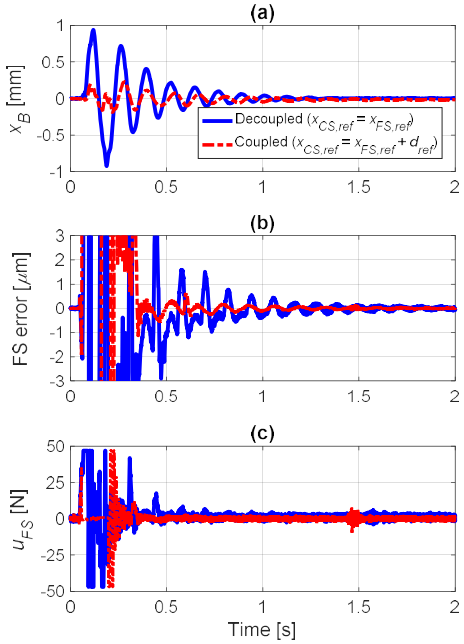

FIGURE 9. Comparison of (a) base vibration, (b) FS tracking error, and (c) FS control input for rapid 50 mm point-to-point positioning.

The RMS base vibration and FS control input over the range of stepping sizes tested are compared in Figure 10. For all stepping sizes tested, reduction in residual vibration is achieved. The FS control input reduction is only observed for stepping sizes > 10 mm. The increased FS control input for stepping sizes < 10 mm is attributed to the large initial error when the feedback controller for FS is re-activated after the acc/dec (see Figure 8 as an example). Thus, if the stepping distance is small, the decoupled approach ($x_{CS,ref}$ = $x_{FS,ref}$) should be used as both the tracking error and motor control input are smaller.

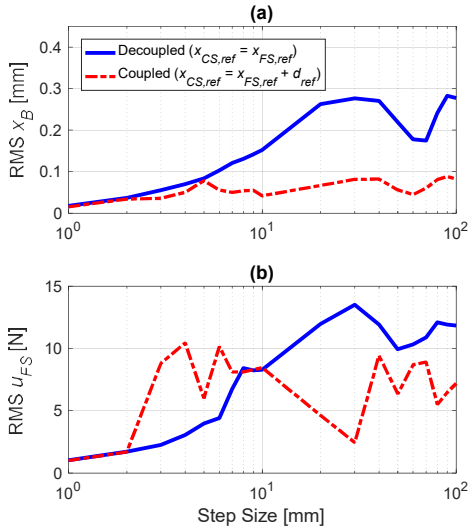

FIGURE 10. Comparison of (a) RMS base vibration displacement and (b) RMS FS control input over the stepping sizes tested (1 – 100 mm).

The cost of reducing the residual vibration of base is u_{CS} in DCFS. Therefore, the efficiency of both actuators must be compared across the cases tested. The copper loss (L_c) of motor is assessed by

$$L_c = \left(u_{RMS} / k_m\right)^2 \tag{13}$$

where u_{RMS} is the RMS force of motor over the motion duration and k_m is the motor constant. The motor constants of the stage are $k_{m,CS}$ = 39.95 N/W$^{0.5}$ and $k_{m,FS}$ = 3.35 N/W$^{0.5}$, respectively for the CS and FS [1]. Notice the large efficiency gain for the CS from the mechanical advantage. The control input for CS is shown in Figure 11 (a) and the copper loss comparisons for the 2 s long stepping motions are provided in Figure 11 (b). The coupling approach returns less copper loss from the FS actuator ($L_{c,FS}$) when stepping sizes are larger than 10 mm. Even if the copper loss at the CS

($L_{c,CS}$) is accounted for, the coupling approach still performs better for most cases. Note that copper loss at the CS does not directly influence the thermal errors of FS, because the two stages are physically separated.

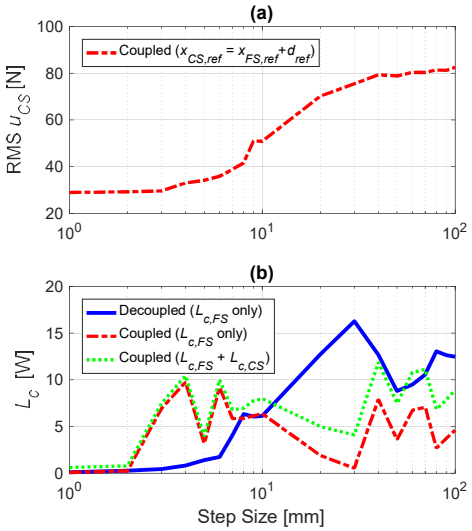

FIGURE 11. (a) CS control input and (b) comparison of measured copper loss over the stepping sizes tested (1 – 100 mm).

CONCLUSION

Reference trajectory generation algorithm using finite impulse response (FIR) filter for de-couplable coarse-fine stage (DCFS) for point-to-point positioning (i.e., stepping) applications is presented. The presented FIR filter-based trajectory generation approach requires a limited preview of the fine stage's reference to determine the required coupling motion and enforce kinematic limits on the coarse stage's trajectory. The computational requirement for the FIR filter-based algorithm is low, such that the algorithm can be implemented inside a real-time controller, eliminating the need for offline B-spline-based optimization of prior work [1]. The experimental results with the DCFS show that significant reductions in residual vibration of isolated base, fine stage tracking error, and linear motor control effort are achieved simultaneously, if the stepping size is sufficiently large. For short distance stepping motions, it is more advantageous to have the stage decoupled throughout the trajectory as the residual vibration reduction benefit is marginal and tracking error and control effort can be overly sacrificed.

ACKNOWLEDGEMENT

This work is funded by the National Science Foundation's CAREER Award #1350202: Dynamically Adaptive Feed Drives for Smart and Sustainable Manufacturing and Rackham Graduate Student Research Grant and Center for Entrepreneurship Engineering Prototyping Fund of the University of Michigan.

REFERENCES

[1] Yoon D, Zeng B, Okwudire C. Decouplable Coarse-fine Stage for Improved Precision and Efficiency in Point-to-point Positioning. 32nd American Society for Precision Engineering Annual Meeting. 2017; 67: 483-488.

[2] Yazaki Y, Fujimoto H, Hori Y, Sakata K, Hara A, Saiki K. Method of Shortening Settling Time Using Final State Control for High-Precision Stage with Decouplable Structure of Fine and Coarse Parts. Electrical Engineering in Japan. 2016; 195: 39-49.

[3] Suh S, Kang S, Chung D, Stroud I. Theory and design of CNC systems. Springer Science & Business Media. 2008.

ENERGY-EFFICIENT ELECTROMAGNETIC TEETER-TOTTER ACTUATOR WITH MAGNET FLUX-BIASING AND LATCHING

Jun Young Yoon, Brij M. Bhushan, David L. Trumper
Department of Mechanical Engineering
Massachusetts Institute of Technology
Cambridge, MA, USA

INTRODUCTION

This paper presents a bi-stable teeter-totter electromagnetic actuator which has a low energy consumption of 1.3 mJ/stroke, with a latching force of 4.5 N. The switching takes place within 3 ms, which results in a low average power consumption, especially at lower actuation frequencies. This actuator can be used as a bi-stable switching device, shifting between two latched states, as well as a precision positioning device. The potential applications of this actuator include diaphragm micro-pumps [1, 2], valves to switch between pressure and vacuum [3], relays, and micro-mirror positioners.

ACTUATOR OPERATING PRINCIPLE

Figure 1 shows a picture of our teeter-totter actuator with the materials used for various components. The actuator consists of 1) a low-carbon steel stator, 2) coils wrapped around the stator waist, 3) neodymium permanent magnets attached inside the stator legs, 4) a low-carbon steel rotor, which we refer to as a teeter-totter, and 5) a poly-carbonate notch-flexure to provide the bearing and pivot for the rotation of the rotor. Note that the poly-carbonate insert with a notch flexure inside the stator also brings the stator and rotor together as a compact stand-alone piece and sets the nominal air-gap distance of 200 μm for both sides at the neutral rotor position while resisting against the maximum attractive force of about 4 N.

By placing the magnets inside the stator legs with their magnetization vectors toward opposite directions, we create unidirectional bias fluxes in both air-gaps. At the neutral rotor position, there is zero net torque on the rotor since the moment due to the reluctance force on each pole face is balanced. Energizing the winding coil with current creates a net torque on the rotor. The coil-driven magnetic flux strengthens the magnetic field on one side while weakening it on the other side, creating a force difference between the two sides. Beyond a certain level of Ampere-turns (power to the winding coil), this net torque overcomes the magnet latching force and makes the rotor switch to the other latched position. The switching direction of the rotor can be reversed by changing the current direction in the coil wire.

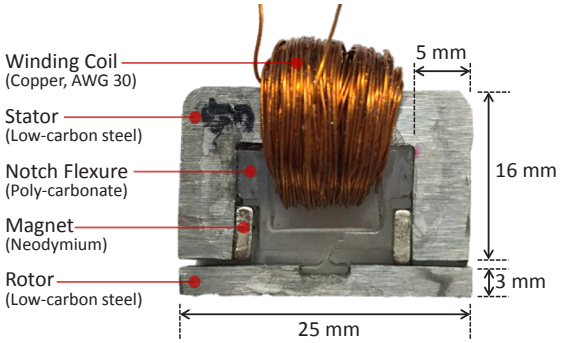

FIGURE 1. Electromagnetic teeter-totter actuator module showing various parts, materials used, and dimensions.

Note that this flux-biasing is also possible by placing the magnets directly on the stator pole faces. However, the magnetic air-gap would then be significantly larger, requiring more power to switch the rotor. We can have a larger working air-gap and hence a larger travel range for a given power input by re-locating the magnets to the inside of the stator legs. Another advantage of having the magnets inside the legs is that we can avoid the direct mechanical impact caused by the rotor flipping, which might damage the brittle magnets if they were on the pole faces [4].

PERFORMANCE PREDICTION

In order to predict the performance of our teeter-totter actuator, we simulate the magnetic force and resultant torque on the rotor using the ANSYS Maxwell 3D FEA package. Figure 2b shows the simulated reluctance force difference $F_{net} = F_{right} - F_{left}$ for various Ampere-turns (AT), where F_{right} and F_{left} are the reluctance forces on the right and left sides, respectively, as shown in Figure 2a. Note that the air-gap is 200 μm at the neutral rotor position, and when

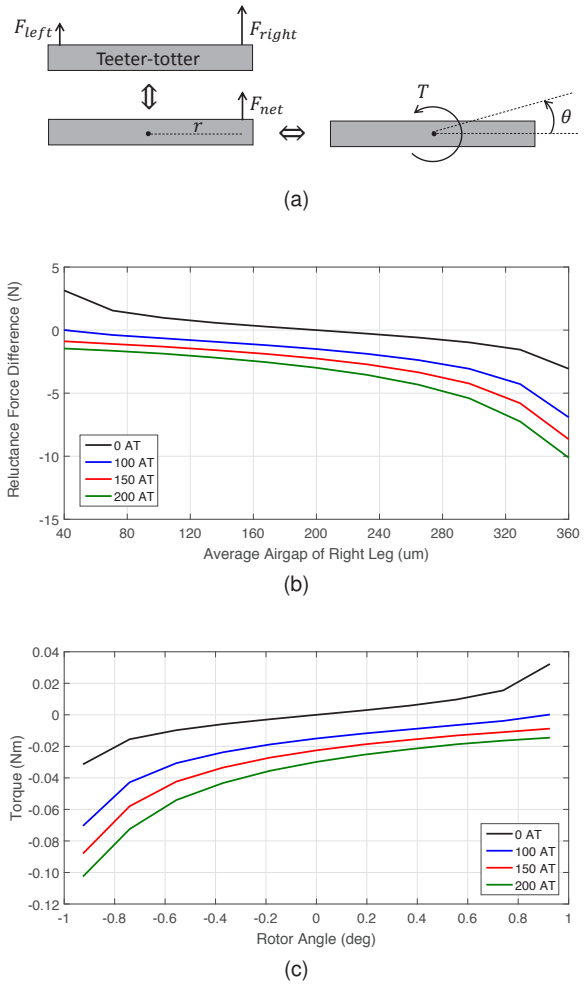

FIGURE 2. Simulated force and torque performance of teeter-totter actuator for different Ampere-turns (AT). (a) Schematic showing force and torque on the teeter-totter rotor. (b) Reluctance force difference versus average air-gap distance of stator right leg. (c) Resultant toque versus rotor angle.

the rotor is latched to the right-side stator leg, the average air-gap is about 40 μm rather than zero. The simulation result in Figure 2b predicts the latching force to be 3.2 N for both sides. This force is referred to a position at the center of the actuator legs, at a radius of $r = 10$ mm from the pivot point. Figure 2c shows the resultant torque by the reluctance force difference on the teeter-totter rotor versus the rotor angle in degrees. With a nominal air-gap of 200 μm and a radius of 10 mm, our teeter-totter actuator has a rotational range of $\pm 1^\circ$. Note that the negative torsional stiffness in a linear range about the neutral rotor position is predicted to be 1.8 Nm/rad, which makes the equilibrium state unstable in

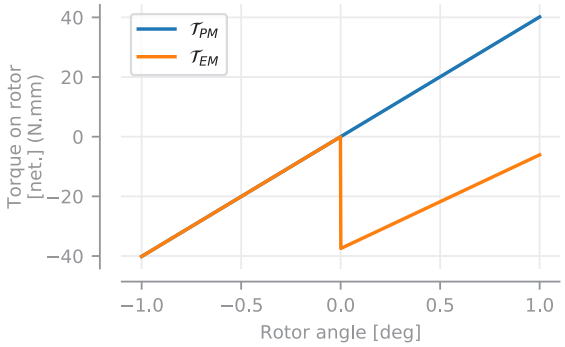

FIGURE 3. Linearized torque versus rotor angle curves with permanent magnet only ($\mathcal{T}_{PM}$) and with the MMF of 150 AT in the winding ($\mathcal{T}_{EM}$). The $\mathcal{T}_{PM}$ curve corresponds to a negative stiffness of about -2.3 Nm/rad. The $\mathcal{T}_{EM}$ curve has a slope of -1.8 Nm/rad with -8 N mm torque at the $+1^\circ$ position due to the winding current. The discontinuity in the $\mathcal{T}_{EM}$ curve is due to turning off the winding current when the rotor is past the neutral position. The linearized curves are obtained from FEA analysis shown in Figure 2c.

open-loop, but helps the rotor flipping and latching for our purpose [4].

From the simulated result, a minimum of 100 AT is expected to be required to overcome the latching force, beyond which the rotor flips to the other side. Note that these expected values are nominal, and can be different considering practical factors. A simplified model to predict the order of the switching time is discussed in the modeling section and the measured performance of the fabricated teeter-totter actuator is discussed subsequently.

FLIPPING TIME ESTIMATION

To estimate the switching time of our teeter-totter actuator, we use negative torsional stiffness value of -2.3 Nm/rad obtained by joining the torque at the two latched positions, from the 0 AT plot in Figure 2c, passing through 0 at the neutral position. We assume that we start with the rotor latched at the right position of 1° and flip to the left position of -1°. The torque due to the winding MMF of 150 AT is modeled as a straight line with a negative stiffness of -1.8 Nm/rad and with a value of of -0.008 Nm at $+1^\circ$ angle. When the rotor reaches the neutral position of 0°, we turn the current off to minimize the energy consumption, as shown in Figure 3. The inertia of the rotor and the force from the permanent magnet continue the rotor motion to latch onto the left side (-1°).

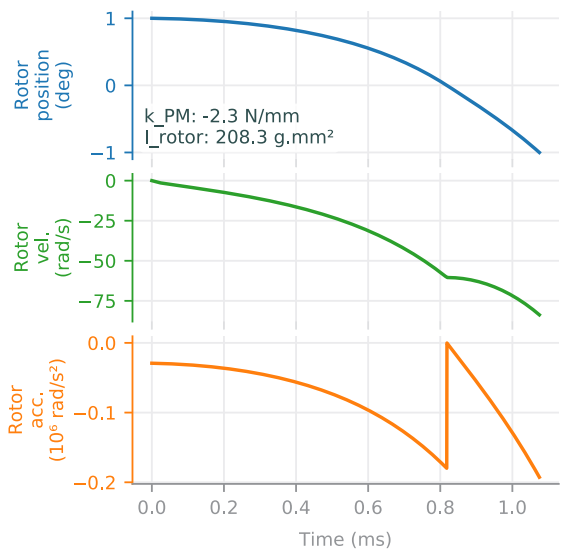

FIGURE 4. Trajectory of the rotor showing the position, velocity, and acceleration of the rotor when pulsed with an MMF of 150 AT for 0.82 ms. At 0.82 ms, the net torque on the rotor changes from being on the $\mathcal{T}_{EM}$ curve to the $\mathcal{T}_{EM}$ curve which is shown as a discontinuity in the acceleration. The velocity is continuous throughout and the position changes smoothly till it latches onto the other side, which takes about 1.1 ms.

This is shown in Figure 3 as a discontinuity in the $\mathcal{T}_{EM}$ curve beyond which it joins the $\mathcal{T}_{PM}$ curve.

Once we have the net torque on the rotor at each angular position, we can calculate the corresponding acceleration of the rotor at those points. From the accelerations, we calculate the velocities versus position, and then, the elapsed time to reach each position. Figure 4 shows the modeled position, velocity, and acceleration curves with time. Winding current is turned off once the rotor reaches the neutral position which occurs at about 0.82 ms which causes a discontinuity in the acceleration as shown in the figure. The velocity is continuous and the rotor position varies smoothly till the rotor latches to the other side. The total time predicted for the flipping itself is 1.1 ms [4].

Note that we experimentally observed switching time is 2.8 ms, with 1 ms for current rise by a voltage pulse of 7 V and 1.8 ms for the flipping itself, as discussed in the following section. The modeling underestimates the flipping time, and it is primarily due to neglecting the effects of back-emf generated by the changing magnet flux as the rotor rotates past the neutral position. In addition, winding current above the threshold for the voltage pulse and secondary effects due to fringe-fields and leakage are not modeled.

EXPERIMENTAL TEST-BED

We use a National Instruments Compact RIO module (NI cRIO-9076 with NI 9263 analog output card), running at 1 kHz, to generate the actuation signal. A power amplifier amplifies the voltage signal to drive the winding coil. In order to test the performance of our teeter-totter actuator, we secure the stator using toe-clamps on the stator legs with the rotor free to rotate.

The latching force is measured by pushing on the air-gap rotor side with a force meter, slowly increasing the force until the rotor flips. For measuring the minimum flipping current, we gradually increase the voltage across the winding until the rotor flips, and measure the corresponding current using a current probe (TM502A by Tektronix).

EXPERIMENTAL RESULTS

The actuator winding has 450 turns of AWG 30 wire. The measured resistance (R) is 6.0 Ω, with inductance (L) measured to be 23 mH (at 20 Hz with 100 mA) using an Agilent 4284A Precision LCR Meter. Using three identical teeter-totter actuator prototypes, the average latching force is measured to be 4.55 N, and it requires an average 150 Ampere-turns (AT) to flip the rotor. These measured performance values are slightly different from our prediction by FEM discussed in the previous section, but still on the same order of magnitude. We speculate that the discrepancy comes from practical factors such as friction, and manufacturing and assembly tolerances.

The flipping time is dependent on how quickly the threshold current of 0.3 A (=450 turns/150 AT), can be crossed. Once the rotor starts accelerating and crosses the neutral position, it latches to the other side even with zero current in the winding coil. Such behavior is utilized to minimize the energy consumption per stroke by adjusting the actuation voltage on-time duration and amplitude.

Figure 5 shows the measured time response of the current in the winding coil to a 1-Hz voltage pulse input of $\pm$7 V with on-time of 2 ms. The current crosses the measured threshold of 0.3 A in 1 ms, and it takes about 1.8 ms after that for the rotor to flip to the other side. The flipping point can be seen as a slight bump in the decreasing

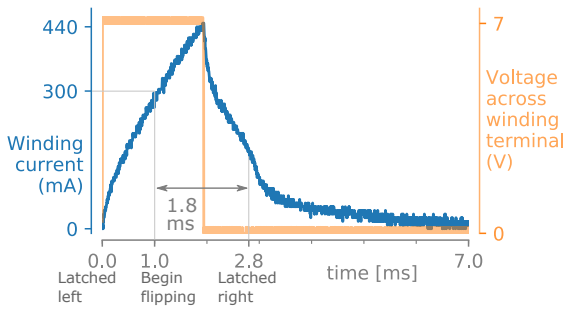

FIGURE 5. Time response of current through the actuator winding to a voltage step of 7 V with on-time of 2 ms. The overall switching time from one side to the other is about 2.8 ms. The latching point can be seen as a slight bump due to the back-emf in the decreasing current waveform.

current curve due to the sudden increase in the flux linkage caused by the rotor making contact with the pole face on the other side. From the measured current waveform, we obtain an RMS current of 21 mA. With the winding coil resistance of 6 Ω, the average power is calculated to be

$$P_{avg} = I_{RMS}^2 R \simeq 2.6 \text{ mW}.$$

In our experiments, we found the temperature rise to be low, of about $0.2\,^{\circ}\text{C}$ at an average operating power level of $2.6\,\text{mW}$. Therefore, this actuator is beneficial for low frequency, temperature sensitive applications such as in micro-fluidic pumping and valving for biological applications [5].

With the bidirectional voltage excitation at 1 Hz, we have a mechanical switching frequency of two strokes per second. The energy consumption of our teeter-tooter actuator per stroke is then

$$\begin{aligned} E_{avg} &= 2.6\,\text{mW} \times 1\,s/2\,\text{stroke} \\ &= 1.3\ \text{mJ/stroke}. \end{aligned}$$

Our teeter-totter actuator is tested up to the switching frequency of 100 Hz, and is capable of achieving such high-frequency operation given the short switching time of 2.8 ms.

CONCLUSION

We presented, in this paper, the design and testing of our bi-stable energy-efficient teeter-totter electromagnetic actuator. Using permanent magnets inside the stator legs to bias the magnetic flux in the air-gaps, we achieved a significant reduction on the power consumption, resulting in a low energy consumption of 1.3 mJ/stroke. The magnet flux-biasing also helps latch the teeter-totter rotor to the stable end positions with the measured average latching force of 4.55 N. Our energy-efficient teeter-totter actuator can be used for micro-pumps, valves, and relays as a switching device, and also for micro-mirror positioners as a precision positioning system with a position controller. Since it exhibits a low temperature rise due to a lower power dissipation, such actuator can also be used for temperature-sensitive applications such as in micro-fluidic pumping system for biological experiments conducted in a temperature-controlled incubator.

ACKNOWLEDGMENTS

We would like to appreciate Prof. Linda Griffith and her research group at MIT for insight in applications related to biological fluid handling. We also thank Daniel Rathbone for his input on manufacturing and assembly, and Dr. Minkyun Noh for fruitful discussions on magnetic design ideas at the precision motion control lab at MIT.

REFERENCES

[1] Iverson BD, Garimella SV. Recent advances in microscale pumping technologies: a review and evaluation. Microfluidics and Nanofluidics. 2008;5(2):145–174. Available from: http://link.springer.com/10.1007/s10404-008-0266-8.

[2] Au AK, Lai H, Utela BR, Folch A. Microvalves and Micropumps for BioMEMS. Micromachines. 2011 may;2(4):179–220. Available from: http://www.mdpi.com/2072-666X/2/2/179/.

[3] Oh KW, Ahn CH. A review of microvalves. Journal of Micromechanics and Microengineering. 2006 may;16(5):R13–R39. Available from: http://iopscience.iop.org/article/10.1088/0960-1317/16/5/R01.

[4] Bhushan BM. Electromagnetic pump and hardware development for organs-on-chips. Massachusetts Institute of Technology; 2018. Available from: https://dspace.mit.edu/handle/1721.1/117299.

[5] Nguyen NT, Huang X, Chuan TK. MEMS-Micropumps: A Review. Journal of Fluids Engineering. 2002 jun;124(2):384. Available from: http://dx.doi.org/10.1115/1.1459075.

Transfer Function Identification Using Controller With Limited Internal Memory

Thomas Haase and Eric Köhler
PIMag® Magnetic Drives
Physik Instrumente (PI) GmbH & Co.KG
Karlsruhe, Germany

INSTRUCTIONS

In production of a wide variety of micro- and nanopositioning stages, PI (Physik Instrumente GmbH & Co. KG) uses a wide variety of different piezo and electromagnetic actuators. Defining optimal and task specific control parameter for different stages is always time-consuming and requires a thorough understanding of system identification and control technology. In particular if robustness and control stability have to be verified analytical, simple tools to identify the transfer function of a stage or system are essential.

STATE OF THE ART

Different approches of how to identify and measure open loop and closed loop transfer functions of an unknown system are state of the art. With respect to control engineering, stimulating the system using a step function should be enough. Unfortunately, system properties like friction, damping and the always limited controller recording bandwidth reduce the resolution of the system response. Thus, step functions are still an admissible means but not advisable for higher frequencies.

Sine sweeps are a very popular approach to stimulate unknown systems. A major advantage of using sine sweeps is its ability to go through resonance frequencies due to the fact, that the temporal stimulation on each frequency is short. A second advantage is its time-saving concept. Predefining sine sweep signals are not a challenge. However, basis of this approach is sufficiently large internal data storage or a high speed (real-time) user interface due to the amount of incoming and outgoing data, in particular for higher frequencies. Additionally, predefined sine sweeps as shown in Figure 1 oscillate the system but do not relate to natural frequencies. A lot of motion controller offer such high speed servo cycle frequencies f with $f \leq 50kHz$, but at the same time the customer interface is not real time capable or too slow. Thus, the amount of recordable data points with servo cycle time resolution is limited due to the available internal memory. This paper analyses an approach of how to use punctual sinusoidal signals and an adapting mechanism to identify transfer functions (TFI) with controllers that offer only limited internal memory and non-real-time user interfaces, Figure 2.

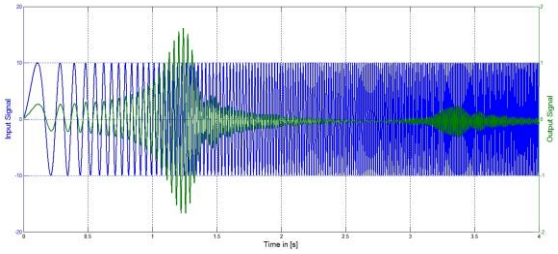

FIGURE 1. Transfer function identification using a sine sweep input signal to identify a system

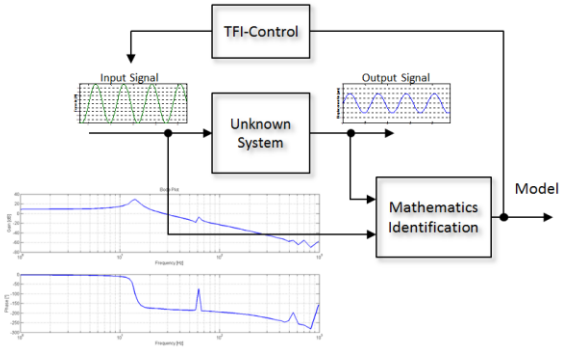

FIGURE 2. Transfer function identification using a TFI-Control feedback

TFI CONTROL

The identification algorithm of Figure 2 determines punctual gain and phase of the system and therewith the transfer function. The TFI control feedback improves the resolution and quality of transfer functions particular in higher frequency regions by adapting the input signal amplitude. Therefore and independent of the control algorithm, its structure and design a

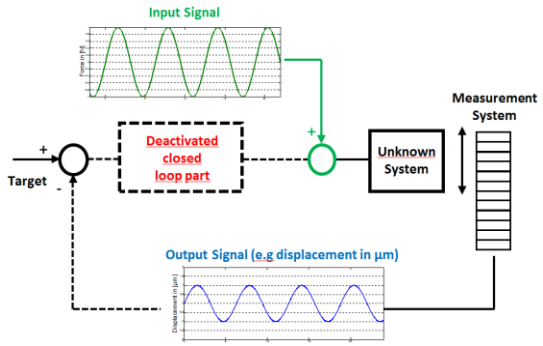

FIGURE 3. Open loop stimulation

predefined sine signal is added to the system as kind of interfering signal in open-loop mode, Figure 3. Typically, the input signal has a well-known physical unit. In motion systems, in which the output of the control algorithm is used to control an actuator, the physical unit might be the motor current in [A] or the desired force in [N]. The same applies also for the output signal. In motion systems, the physical dimension might be a distance, e.g. measured in [μm]. The knowledge about both units is important to gauge the resulting transfer function. It is admissible, that the so called unknown system of Figure 3 also contains closed loop components (e.g. of the controller). As an example, an analog current control loop which is implemented in hardware can be part of the unknown system. However, everything between the input and the output signal will be identified as one common transfer function. It can also mean that the identified TF is only valid in combination with the driving controller due to special power drivers, current control loops or e.g. analog filters of the controller.

Basic Principle

The basic idea of the TFI is to design individual sine input signals with constant frequencies to generate predictable sine output signals. The output signals are recorded with the limited internal memory of the controller and transferred to an external PC for further evaluations. This approach is performed for any interesting frequency to identify a full TF. In each step, the input signal is adapted in relation to the last output signal. For instance, a flexure based motion stage as shown in Figure 4 has an integrated voice coil actuator with a nominal force of $F_N = 5N$. It was defined, that the customer interface shall oscillate with a desired amplitude A_D of $A_D = 50\mu m$. A_D is fully user-defined. This amplitude can be measured in high-resolution with the internal sensor and is simultaneously small enough with regard to higher frequencies. So, the physical unit of the gain will be given in $\left[\frac{\mu m}{N}\right]$. To initially create oscillations, open-loop sine input signals in [N] for each frequency are required and performed repeatedly, Figure 3 and 8.

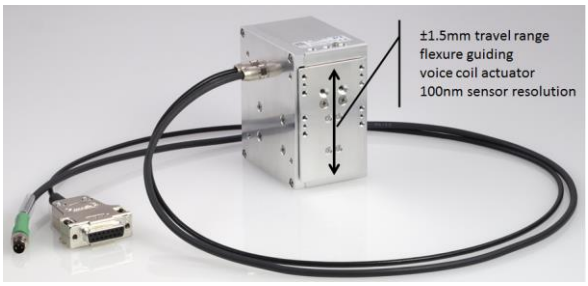

FIGURE 4. V-900K014: a flexure based voice coil actuator. The identified transfer function is shown in Figure 5.

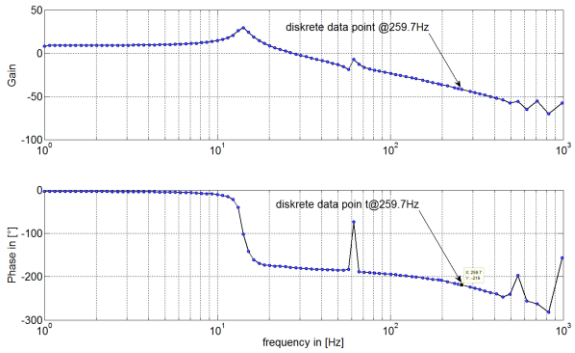

FIGURE 5. Identified discrete transfer function.

Input and output signals are compared to determine punctual the corresponding gain and phase of the transfer function, Figure 5 and 6. Data analysis is done in frequency domain as shwon in Figure 10. Furthermore, the comparison will examine whether the desired amplitude A_D was achieved. If not, the amplitude of the input signal of the next (higher) frequency is adjusted. If the amplitude A_o of the output signal is smaller than the desired amplitude A_D, the amplitude of the input (force) signal increase. If the amplitude of the output is too high – maybe close to resonance frequencies – the amplitude of the input signal is decreased. Figure 7 shows the development of the normalized input signal (upper graph) as well as the resulting amplitude A_o by the example of the linear stage of Figure 4.

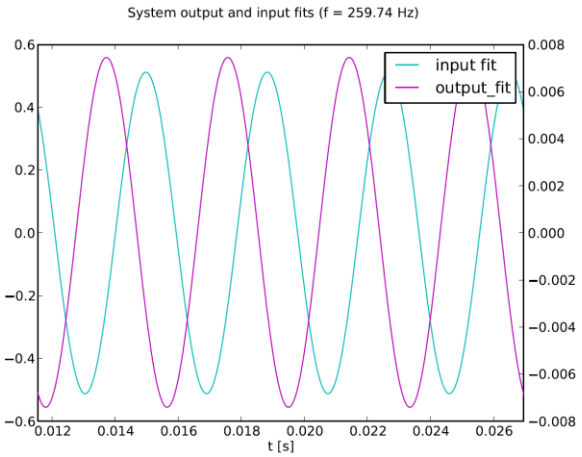

FIGURE 6. Optimal frequencies fit to f_s to avoid nonlinearities

TFI CONTROL OPTIMIZATION

Frequency Selection

The approach, to stimulate with individual frequencies is based on the fact, that most controller offer too little memory to execute and measure full and high-resolution sine sweep signals. To avoid this problem, only one single frequency is written into the controller memory and sent to the external, unknown system as input signal, Figure 3. In Figure 5, all frequencies f are spaced evenly on a log scale. A linear spaced interval might also be possible. To create a continuous oscillation, the actual stored input frequency is chained together and played repeatedly.

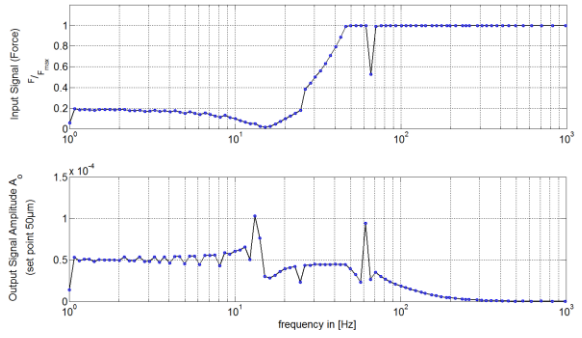

FIGURE 7. TFI Control: adjusting the input signal (Force in [N]) to control the amplitude A_o of the output signal and securely pass through resonance frequencies

This execution requires optimal adjusted frequencies f_{opt} with regard to the controller servo clock frequency f_s. Otherwise, linked frequencies include nonlinearities at the transition of two sine waves. This means that not each frequency f can be used as input signal. Depending on the servo rate (e.g. $f_s = 20kHz$) only certain frequencies f_{opt} can be mapped perfectly. Following formula can be used to identify optimal frequencies:

$$f_{opt} = \frac{f_s}{round\left(\frac{f_s}{f}\right)}$$

As an example it will be verified, whether the frequency $f_{expl.} = 260Hz$ can be mapped into the memory of a controller running with $f_s = 20kHz$:

$$f_{opt} = \frac{20kHz}{round\left(\frac{20.000\ \frac{1}{s}}{260\frac{1}{s}}\right)} = \frac{20kHz}{77} = 259.74Hz$$

It can be seen, that only $f_{opt} = 259.7Hz$ fits into the $f_s = 20kHz$ - resolution of the controller, see Figure 6.

Resonance Frequencies

The comparison between the desired and received output signal amplitude A_o is used to adapt the input signal. Figure 7 shows the development of the amplitude of the output signal A_o as well as the force amplitude of the input signal. This PI stage has two main resonance frequencies. The first resonance frequency is close to 13Hz. Figure 7 illustrates that the amplitude of the output signal increase close to 13Hz and the TFI controller reduce the input signal for the next step. After passing the resonance, the gain of the input signal needs to increase to reach the desired amplitude (here: $A_D = 50\mu m$). Exactly the same happens while running through the 2nd eigenfrequency in the range of 61Hz. A very simple approach is chosen to adapt the gain of the input signal:

$$P_G = \frac{A_D}{A_o}$$

Figure 7 demonstrates that the maximal output amplitude A_o even within a resonance frequency is only in a range of $A_{max}{\sim}100\mu m$. Taking a maximum force F_{max} of the actuator into account, the new amplitude F^i of the input signal in [N] for the stage of Figure 4 is calculated to:

$$F^i = \min\left(F_{max}, P_G^i \cdot F^{i-1}\right)$$

$$F^i = \min\left(F_{max}, \frac{A_D^{i-1}}{A_o^{i-1}} \cdot F^{i-1}\right)$$

Resolution Improvement

The TFI control feedback can be used to gain higher resolution and accuracy in higher frequency regions. This is realized by adapting the amplitude of the input signal depending on the previous output signal. On the one hand, the gain P_G that is used to calculate the new input amplitude can minimize the signal particular close to resonance frequencies and keeps the resulting motion within limits. On the other hand and especially in higher frequency regions in which the system might not be able to fulfill the requested output amplitude the gain P_G is useful to intensify the input signal up to a predefined limit. In a motion system as shown in Figure 4 amplitude limits might be a maximal motor current or the motor force F_{max}. Such a full powered system offers highest output signal dimensions and therewith highest resolution and analysis quality. Due to the fact that the algorithm handles individual frequencies, additional and individual planned pause times between two different oscillations are feasible. Particularly when the desired output amplitude cannot be reached and the input signal is driven with maximal amplitude (e.g. nominal force F_{max}, Figure 7) stages might get warm. To avoid this and potentially temperature depending errors, sufficient break times between two frequency steps are recommended.

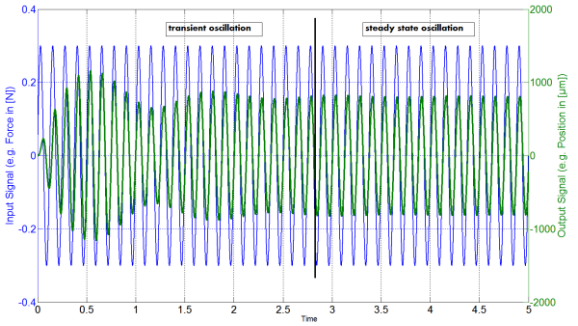

FIGURE 8. Transient vs. steady state oscillation

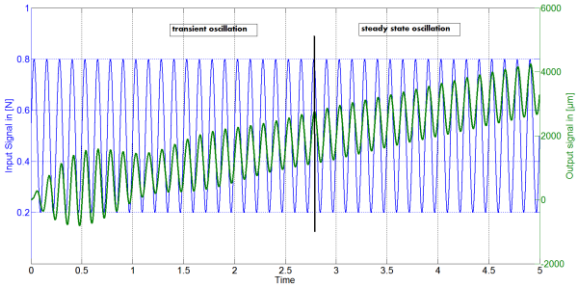

FIGURE 9.Optimized signals to minimize the influence of friction

Observe Transient Response and Friction

Friction and nonlinear transient response might distort or downgrade the quality of the transfer function identification. Steady state oscillation is required to determine the correct gain. In order to achieve this it is meaningful to separate the transient from the steady state oszillation, Figure 8. This means that the data is not recorded at the beginning of the oscillation but after a predefined number of cycles. Additionally, if the unknown system is a linear or rotary stage, it is possible to reduce the influence of friction by adding a constant offset to the input signal. This offset ensures a constant motion of the stage in one direction and eliminates static friction, Figure 9. Before analysing this data it has to be detrended to eliminate the inital offset and constant velocity. All data is analysed in the frequency domain as shown in Figure 10. Prior to any further frequency analysis, the stage has to move back into its initial position. Alternatively it is necessary to ensure that the stage will not move into any limits.

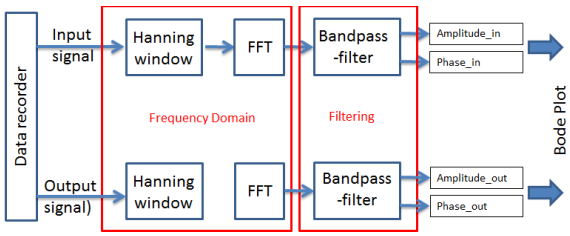

FIGURE 10. Data processing

CONCLUSION

This paper presented a simple TFI control concept to identify transfer functions. Single sine waves were written to the limited memory of a controller and used to determine punctual gain and phase. It was shown how to adapt the input signal based on the last output signal to receive maximal resolution and how the TFI control handles resonance frequencies. Different optimization criteria and further advantages were discussed. At the same time, it must be clear that the time effort is much higher. Depending on the frequency resolution, the communication interface, pause times, the number of settling sine waves and some more parameters a transfer identification process with this method offers high quality but might need much more time than using sine sweep. In this context one should consider whether high frequency resolution is required and which identification method might be optimal.

OVERVIEW OF AN ACTIVELY DAMPED VIBRATION ISOLATION SYSTEM FOR ULTRA HIGH VACUUM OPTICAL EXPERIMENTS

Álvaro Fernández Galiana[1], and Fabrice Matichard[1,2]
[1]LIGO Laboratory
Massachusetts Institute of Technology
Cambridge, Massachusetts, USA
[2]LIGO Laboratory
California Institute of Technology
Pasadena, California, USA

INTRODUCTION

We present a Ultra-High Vacuum (UHV) compatible tabletop 6-axis vibration isolation system, with integrated active damping control, able to provide a factor of 60 dB isolation above 100 Hz. While this isolation platform has been preliminary designed to support optics in Advanced LIGO detectors [1], it features characteristics that make it suitable for a variety of applications. The system has been engineered to facilitate the construction and assembly process, while minimizing the production costs. The platform provides six degrees of freedom of passive isolation with a combination of vertical springs and a horizontal pendulum. It is instrumented with voice-coil actuators and optical shadow sensors to damp the resonances. All materials are compatible with stringent vacuum requirements. The architecture of this system maximizes the optical table dimensions with respect of the space available. Three units are currently operating for Advanced LIGO. The paper presents the system design, controls principles, and experimental results.

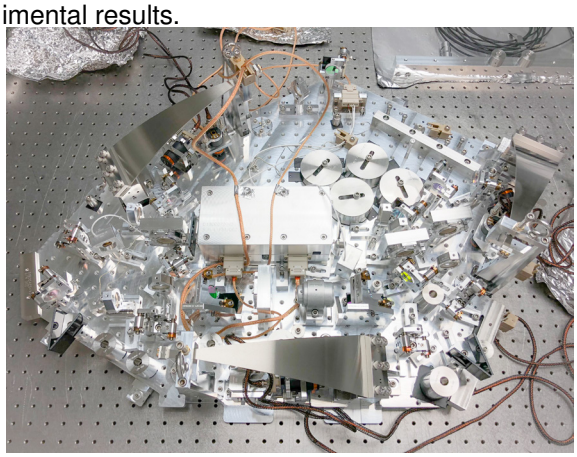

FIGURE 1. ***UHV COMPATIBILITY.*** *Picture of the isolation platform at the LIGO Livingston Observatory. All the materials have been selected to fulfill the aLIGO vacuum requirements [2].*

MECHANICAL DESIGN

This system provides seismic isolation and active damping control in all 6 degrees of freedom. It is a compact mono-stage suspension where the suspended stage (stage 1) is mechanically isolated from the ground (stage 0) (see Figure 2). It behaves as a single spring-mass system in all the degrees of freedom.

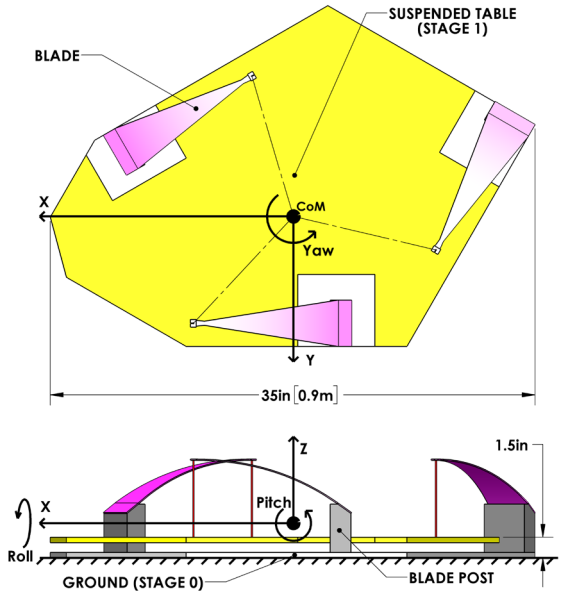

FIGURE 2. ***COMPACTNESS.*** *Schematics of the isolation platform. The optical table is suspended from three blade posts that keep it only 1.5 in. above the ground level. Its footprint matches the available space in the aLIGO chambers.*

A key element is that stage 1 is suspended with independent blade posts (see Figure 3), which are responsible for the passive isolation. They are bolted to stage 0 and reduce the overall cost, weight, and dimensions compared to a welded structure. This technique maximizes the optical table dimensions with respect of the space available (see Figure 1) and makes it adaptable to dif-

ht!]

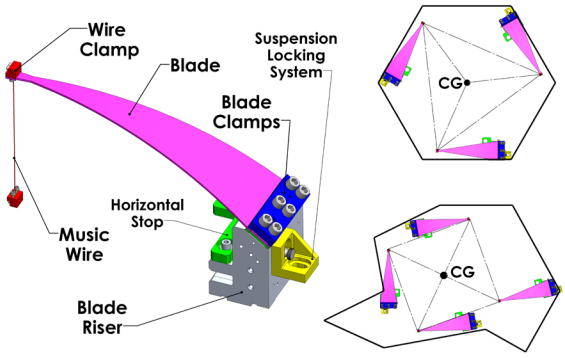

FIGURE 3. ***SHAPE ADAPTABILITY.*** *Suspension Blade Post (left). The blade riser is clamped to the ground and the suspended stage is attached to the tip of the table. The blade is clamped to the post at a specific angle and the wire is clamped to the tip of the blade. In addition, the blade post has built-in hard stops that limit the range of motion of the optical table. Using independent blade posts to suspend the optical table makes this design adaptable to different requirements. As an illustration, two potential optical tables shapes that could be isolated using this concept (right).*

TABLE 1. Basic isolation platform mechanical parameters.

Parameter	Value
Total dimensions	0.94 x 0.67 m
Total height	0.21 m
Total mass	31.5 kg
Suspended stage	
Table surface	0.34 m^2
Table height	0.38 m
Mass	36 kg
Wire length l	145.6 $\times 10^{-3}$ m
Wire diameter d	0.61 $\times 10^{-3}$ m

ferent optical table shapes (see Figure 3). The number, position, and characteristic features of these blade posts are selected according to the payload and required performance.

There are two types of resonances that are critical to the design of this type of seismic isolator: the suspension modes and the structural modes. The first are the rigid mode frequencies for each degree of freedom. The structural modes are the resonances of the elements that compose the system, such as the blade posts or blade guards (see Figure 4). The isolation bandwidth can be defined as the range between the highest suspension mode and the lowest structural mode.

For our isolation platform, to meet the aLIGO requirements [1], all the rigid body modes have been kept below 10 Hz, and the first structural modes higher than 200 Hz. At 100 Hz, the suspension provides 60 dB of seismic isolation. The quality factors of the suspension eigenmodes are damped to values less than 100, reducing the sensitivity to external motion at frequencies around the resonances. The basic mechanical parameters of the platform are specified in Table 1.

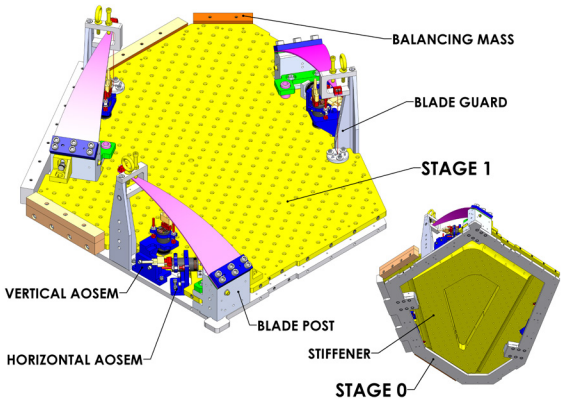

FIGURE 4. ***LARGE EFFECTIVE FOOTPRINT.*** *Rendering of the isolation platform. One of the advantages of this design is that almost the totality of its footprint corresponds to the optical table (useful surface). The isolation platform is has six AOSEM sensor-actuators placed in vertical-horizontal pairs. The blade guards are designed for safety in case of sudden blade release. The optical table is designed with an underneath stiffener to increase its stiffness to mass ratio.*

Ultra-high vacuum compatibility

All the materials of the isolation platform are approved for ultra-high vacuum applications and fulfill the aLIGO vacuum requirements [2], since aLIGO chambers have an air pressure of $10^{-}9$ torr. Hence, before the final assembly all the elements are precision cleaned and vacuum baked. In addition, during the vacuum bake and RGA (Residual Gas Analyzer) scan is performed to provide a direct measure of the outgasing rate and to detect contamination.

Suspended stage

The suspended stage consists of an optical table ($\sim$ 0.34 m^2), the optical components that have to be isolated, and balancing masses. The table's shape and mass are determined by the pay-

load and available space in the aLIGO vacuum chamber[3]. The payloa optics weigh ≈14 kg and, due to the optical path requirements, the available space is limited, which explains the irregular heptagonal shape of the suspension (see Figure 1).

For this type of mono-stage suspension, the first structural mode corresponds to the bending resonance of the suspended stage (Figure 5). To enlarge the bandwidth, this frequency must be as high as possible, which is the purpose of the table's stiffener (see Figure 4). The shape of this stiffener has been optimized to find a good mass-stiffness compromise. This optimization is done iteratively using Finite Element Analysis (FEA) of the loaded optical table. The result is presented in Figure 5 and shows that the benefit of this optimization is up to 20 Hz increase of the bandwidth. The table weights ∼18 kg and has its first resonance at around 225 Hz.

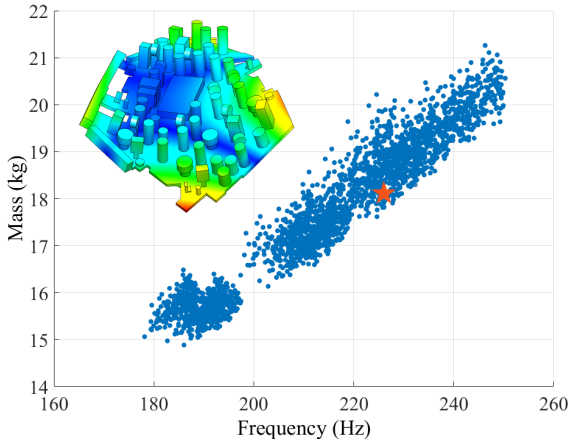

FIGURE 5. ***HIGH ISOLATION BANDWIDTH.*** *Result of the bench stiffener optimization and loaded bench first resonant mode. Using iterative finite element analysis on the optical table for different stiffener shapes and sizes we can increases the isolation system's bandwidth by up to 20 Hz. The selected dimension (star) was chosen for its total mass (∼ 18 kg) and center of mass position.*

Horizontal isolation

Horizontal isolation (X-Y axis in Figure 2) is achieved by suspending stage 1 from three wires. The pendulum a simple and effective way to provide passive horizontal isolation. The wires are clamped using a metallic clamp that guarantees low friction loss. The horizontal modes frequency can be calculated using Equation 3.

$$z_z = \sqrt{\frac{EI}{mg}}\,\tanh\frac{mgl}{2EI} \tag{1}$$

$$k_{xx}(=k_{zz}) = \frac{mg}{l-2z_z} \tag{2}$$

$$f_{xx}(=f_{yy}) = \frac{1}{2\pi}\sqrt{\frac{k_{xx}}{m}} \tag{3}$$

where E is the wire Young's modulus, I is the area moment of inertia and area of the wire, m is the mass supported by each wire, d and l are the diameter and length of the wires, and z_z is the vertical distance from the wire tip to the Zero Moment Point (ZMP), the point where a force would not produce any moment.

The isolation platform wires are 145.6 mm long and therefore the horizontal resonance frequency is 1.34 Hz. They are 0.61 mm diameter stainless steel music wires. This value is large enough to guarantee the minimum Factor of Safety (FoS), which is 3 for our design and can be calculated using the following equations

$$\tau_{max} = \frac{mg\delta}{A(l-2z_z)};\ \sigma_{max} = \frac{mg}{A} + \frac{mgz_z d\delta}{2I(l-2z_z)} \tag{4}$$

$$\sigma_{VM} = \sqrt{\sigma_{max}^2 + \tau_{max}^2} \qquad FoS = \frac{\sigma_{VM}}{\sigma_{yield}} \tag{5}$$

where δ is the maximum allowed lateral displacement of the wire ends (1 mm for this isolation platform), A is the area of the wire, τ_{max} and σ_{max} are, respectively, the maximum shear and normal stress at the wire for the displacement δ, σ_{VM} is the equivalent Von Mises stress, and σ_{yield} is the yield strength of the wire. Note that these general formulas take into account the normal (both axial and from bending) and shear stresses of the wire, but in our case it could be simplified, since the contribution of bending is orders of magnitude higher.

On the other hand, the wire diameter must also be small enough to guarantee that the violin frequencies (∼763 Hz in the presented system) are much higher than the blade vertical mode.

The rotational stiffness of the isolation system is estimated using the translation stiffness and the number and distribution of the blade posts. Equations 6 and 7 provide these rotational stiffness for

an equilateral triangular distribution, such as the one used in our system.

$$k_{roll}(= k_{pitch}) = \frac{3}{2}k_{zz}R^2 + 3k_{yy}h_z^2 - Mgh_z \quad (6)$$

$$k_{yaw} = \frac{3}{2}(k_{xx} + k_{yy})R^2 + 3\frac{GI}{l} \quad (7)$$

where h_z is the vertical offset between the center of gravity (CG) and the ZMP, and G and I correspond, respectively, to the shear modulus and the moment of inertia of the music wire. In addition some cross couplings must be considered mainly due to the offset h_z and to the fact that the blades are not flat when the suspension is floated (Figure 3), which makes their tip motion not vertical around the equilibrium. Their values can be approximated with an analytical expression but the derivation is out of the scope of this overview paper.

Vertical isolation

The vertical isolation is provided by three triangular stainless steel cantilever blade springs. This shape guarantees an homogeneous stress distribution (theoretically, assuming small deformation), approximated by equation 11.

$$k_{zz} = \sqrt{\frac{Eah^3}{6l^3}} \quad (8)$$

$$f_z = \frac{1}{2\pi}\sqrt{\frac{k_{zz}}{m}} \quad (9)$$

$$\omega_{tip} = \frac{6mgl^3}{Eah^3} \qquad \omega'_{tip} = \frac{12mgl^2}{Eah^3} \quad (10)$$

$$\sigma_{xx_{max}}^{blade} = \frac{6mgl}{ah^2} \qquad FoS = \frac{\sigma_{XX_{max}}}{\sigma_{yield}} \quad (11)$$

where E is the blade Young's modulus, a is the width of the blade at the base, h is the blade thickness, m is the mass supported by each blade, and l is the length of the blade. Since there are three design parameters (a, l, and h) and only two constraints (from equations 9 and 11), the design has one degree of freedom. For our suspension we defined the length l such that it was well suited to the overall dimensions of the instrument. The selected parameters and the design performance are given in Table 2.

Steel (grade 440C stainless steel) has been used for the blades, which are also manufactured flat.

TABLE 2. Basic isolation platform mechanical parameters.

Parameter	Value
Design paramenters	
Blade base width a	85 $\times 10^{-3}$ m
Blade thickness h	2.11 $\times 10^{-3}$ m
Blade length l	280 $\times 10^{-3}$ m
Young's modullus E	2.1 $\times 10^{11}$ Pa
Modeled results	
Vertical resonance f_z	1.64 Hz
Spring constant k_{zz}	1273.1 $\frac{N}{m}$
Tip deflection	92.5 $\times 10^{-3}$ m
Tip rotation	0.66 rad
FoS	3.44

The blade expected performance is ultimately checked with Finite Element Analysis. Nevertheless, the preliminary calculations were made using equations 10 and 11, which assume classical infinitesimal strain beam theory. In our system, the error of the preliminary calculation is around 1 % in deflection and 7 % in stress.

As previously discussed, a key element of this design is the blade post. It has two main purposes: connect the blade to the ground and set the vertical position of the suspended stage. The height and angle of the base of the post are determined using FEA to accurately predict the deformation of the blade.

Due to its annular shape, stage 0 has low torsional stiffness and relies on being well clamped to a ground structure.

ACTIVE DAMPING CONTROL

Since the system has low loss, i.e. high Q, the suspension modes must be damped to avoid poor performance close to the resonances. We use low noise ultra-high vacuum compatible sensor-actuator produced by the LIGO Scientific Collaboration, named AOSEMs. They use a coil-magnet pair to generate an actuation strength of 0.0309 N/A and a shadow sensor to monitor relative motion.

Control noise

The main sources of noise of our platform, besides the ground seismic motion (X_0), are the AOSEM sensor noise (N_s) [4] and the analog-to-digital (ADC) and digital-to-analog (DAC) converters noises (N_{dac}, N_{adc})[5, 6]. Each source of noise N_i generates a motion to the suspended

TABLE 3. Basic isolation platform modeled and measured eigenmodes.

Degree-of-freedom	Measured (Modeled)
Longitudinal-X	1.33 (1.35) Hz
Transverse-Y	1.43 (1.35) Hz
Vertical-Z	1.74 (1.63) Hz
Roll	2.47 (2.10) Hz
Pitch	1.74 (1.62) Hz
Yaw	1.57 (1.53) Hz

stage (X_{N_i}). Therefore, the motion of the optical table (X_1) is consequence of ground seismic noise and electronic noise from the damping controls. Assuming that they are all incoherent, the displacement noise of the optical table can be estimated as:

$$|X_1|^2 \sim |X_{N_{ELEC}}|^2 + |X_{X_0}|^2 \quad (12)$$

where,

$$|X_{N_{ELEC}}|^2 \sim |X_{N_{DAC}}|^2 + |X_{N_{ADC}}|^2 + |X_{N_S}|^2 \quad (13)$$

PERFORMANCE

A proptotype of the platform was tested at the MIT LIGO facilities and two units have been installed at the aLIGO observatories in Livingston, LA (LLO) and Hanford, WA (LHO). The results presented in this section are from the testing of these three units.

Transfer functions

The transfer functions were obtained by driving the coils and reading out the shadow sensors in the AOSEMs. Figure 6 shows the roll (RX) transfer function of the suspension. The coils were diagonalized to account for the different dc and frequency dependent gains of the individual current drivers and fundamental mechanical resonances. The frequencies and quality factors of each resonance, summarized in Table 3, are obtained by fitting the data with second order functions.

Structural modes

One of the advantages of this suspension is that its structure is slender and light. These two factors reduce the impact of our system' resonances onto neighboring elements. Additionally, the structural modes can be kept higher than 200 Hz. The modal response of the platform was measured with an impact hammer and it is consistent with the FEA predictions.

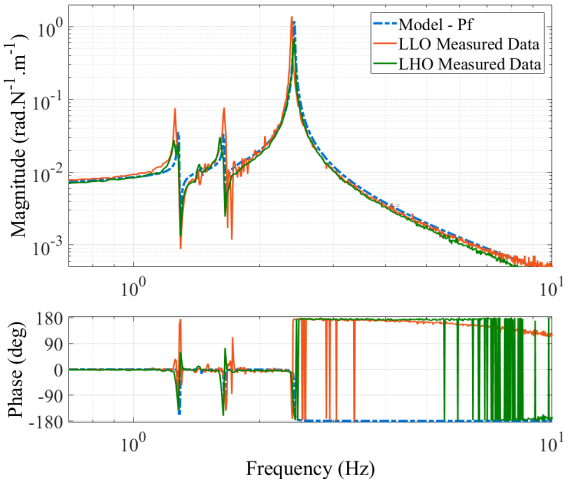

*FIGURE 6. f^2 **ISOLATION.** Measured transfer functions at both the LIGO Livingston Observatory (LLO) and the LIGO Handford Observatory (LHO) for the Roll (RX) degree of freedom, calibrated to match the dynamical model (P_f). This data matches f^2 isolation after the resonances and shows that the rigid mode frequencies were well predicted.*

Active Damping

For our isolation platform, the controller (C) is a simple band-pass filter with one zero and two poles p_1 and p_2. This simple controller is sufficient to bring the Q values to less that 100 without without degrading the passive isolation (see Figure 7).

For the simple band-pass filters, the estimated total displacement noise of the suspended stage due to electronic noise can be found in Figure 8. This noise is orders of magnitude lower than the residual seismic noise (motion of stage 1 due to ground motion) if the suspension was mounted directly on the ground. However, when the suspension is in-chamber, the electronic noise becomes predominant at frequencies above 3 Hz. The solution is to increase the roll-off of the filter, for example adding an elliptic filter close to UGF.

In future work we intend to find better controllers that maximize the performance of our system.

CONCLUSION

We present the design and measured performance of the isolation platform that is going to be used in Advanced LIGO. The suspension provides vibration isolation in all 6 degrees of freedom to a set of optics and all the eigenmodes are kept below 10 Hz. The suspension is also actively

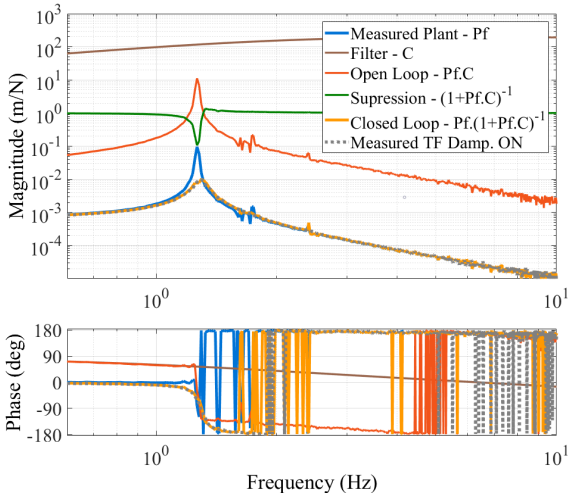

FIGURE 7. ***Q-VALUE REDUCTION.*** *Numerical model of the performance of the damping control for the longitudinal (X) degree of freedom. Using a simple band-pass filter (brown), the Q is reduced from ≈250 (blue) to ≈30 (orange) without degradation of the high frequency isolation. The phase margin of the controller is ∼ 53 deg (red). The damped transfer function was measured (grey) and matches the damping model.*

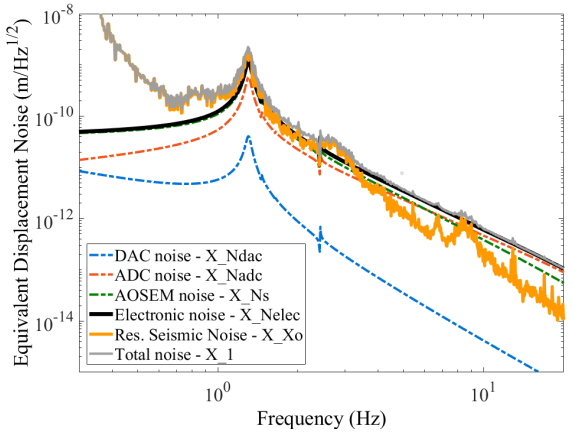

FIGURE 8. ***LOW CONTROL NOISE.*** *Noise budget for the transverse (Y) degree of freedom. The total electronic noise produced by the damping control electronics (dashed black) is compared with the estimated residual seismic noise (orange). For our current controller, the electronic noise is the predominant source of noise above 3 Hz.*

damped with voice-coil actuators such that the quality factors are all well below 100. Two units of the presented isolation platform have been installed in the aLIGO observatories.

Due to its simple and flexible design, low cost of production, and rapid procurement time, this isolation system can easily be deployed in many other potential applications.

ACKNOWLEDGMENTS

We wish to thank Lee McCuller, Lisa Barsotti, Matthew Evans, Maggie Tse, Peter Fritschel, and Nergis Mavalvala from LIGO-MIT, as well as Norna Robertson and Calum Torrie from LIGO-Caltech for their help in designing this isolation platform. Also thank Stuart M. Aston, Jeff Kissel, Arnaud Pele, TJ Shaffer, Janeen H. Romie, and Betsy Weaver from the aLIGO observatories for their contribution during the testing and installation. LIGO was constructed by the California Institute of Technology and Massachusetts Institute of Technology with funding from the National Science Foundation (NSF) and operates under cooperative Agreement No. PHY- 0107417. This paper has LIGO Document No. LIGO-P1800182.

REFERENCES

[1] Aasi J, Abbott B, Abbott R, Abbott T, Abernathy M, Ackley K, et al. Advanced LIGO. Classical and quantum gravity. 2015;32(7):074001.

[2] Coyne D, et al. LIGO vacuum compatible materials list. LIGO Laboratory; 2013. LIGO-E960050-v12.

[3] Matichard F, Lantz B, Mason K, Mittleman R, Abbott B, Abbott S, et al. Advanced LIGO two-stage twelve-axis vibration isolation and positioning platform. Part 1: Design and production overview. Precision Engineering. 2015;40:273–286.

[4] Aston S. Advanced LIGO BOSEM Noise Measurement Report. LIGO Laboratory; 2011. LIGO-T0900496-v4.

[5] Heefner J. Preliminary Noise Measurements of the General Standards PCI66-16AI64SSA-64-50M ADCs. LIGO Laboratory; 2006. LIGO-T060158-x0.

[6] Mittleman R. 16 Bit Low Frequency DAC noise measurement. LIGO Laboratory; 2015. LIGO-T1500007-v1.

SURFACE METROLOGY USING EXTENDED-RANGE PARTITIONED APERTURE WAVEFRONT SENSING

Devin R. Beaulieu[1] and Thomas G. Bifano[2]
[1]Department of Electrical and Computer Engineering
Boston University
Boston, MA
[2]Photonics Center
Boston University
Boston, MA

INTRODUCTION

Partitioned Aperture Wavefront (PAW) sensing is a recently developed technique for precision optical surface metrology [1]. This latest work describes and implements methods to computationally extend the range of measurable surface gradients without modifying the optical setup. In addition, application of PAW surface measurement to relatively large objects (approximately 60 mm in diameter) is experimentally demonstrated for the first time.

THE PARTITIONED APERTURE APPROACH

The PAW sensor fundamentally uses a photometric technique to measure local surface tilts, and then integrates these tilt measurements to reconstruct topography. PAW sensing is an achromatic variant of the pyramid sensor [2] (commonly used for wavefront sensing in astronomy), and offers advantages over traditional optical surface metrology techniques (e.g. interferometry, Shack-Hartman.) The key, unique optical element is the PAW lens, which consists of four ordinary lenses cut and cemented together to form a quatrefoil shape. This lens creates four separate sub-images of the object on the camera which contain tilt information. There is no need to oscillate the lens as is done when wavefront sensing with pyramid sensors.

Measurement of an object's surface can be made by comparing relative intensities between the four sub-images formed by the PAW lens, as depicted in FIGURE 1. To achieve this, the entire object is illuminated by light with a numerical aperture (NA) set by a square aperture. If the object is perfectly flat, light from all points passes centered through the PAW lens, with equal intensity in each quadrant. This forms four, equal-intensity sub-images of the object. However, local tilts at a given point on the object will shift where the reflected falls light on the PAW lens, altering the relative intensities of corresponding pixels in the four sub-images. For example, a local upwards tilt of the object will cause that point to become brighter in the top images, and dimmer in the

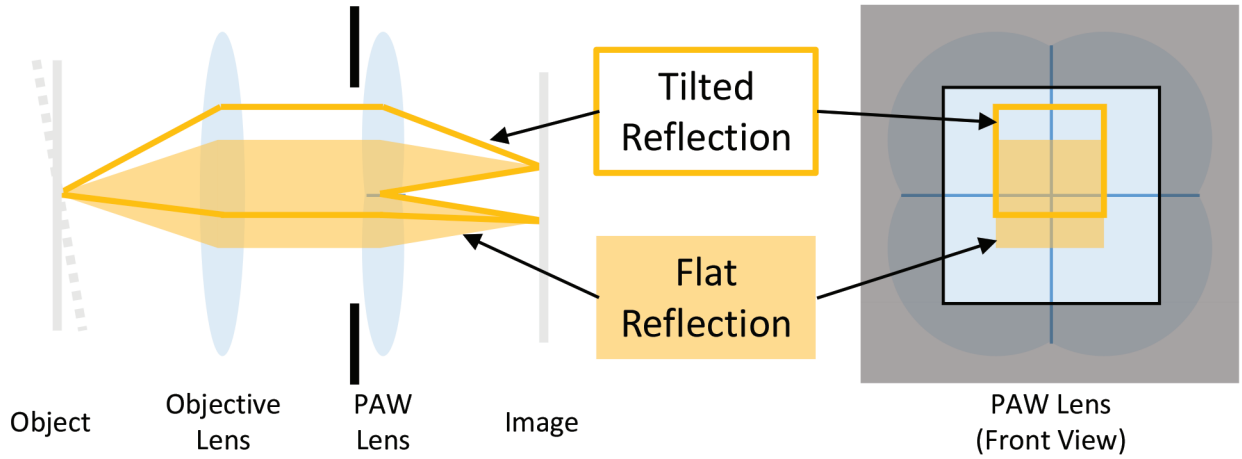

FIGURE 1. Side and front view of a simplified PAW setup. Path of illumination light reflected by a single example point on the object is shown for both flat and tilted surfaces. The local tilt modulates the intensity of the four points formed on the image plane.

bottom images. By measuring the relative intensities, it is possible to back out the horizontal and vertical surface gradients, and from there calculate a precise surface topography.

This approach enables collection of high-resolution surface maps at high speed, limited primarily by the camera resolution and rate. Each surface measurement is made based on a single camera frame, at the full resolution of each sub-image (i.e. half the camera resolution.)

The maximum tilt angle (or dynamic range) which can be measured by PAW is driven by the NA of light collected by the optics. Prior demonstrations of the PAW sensor were limited to tilts equal to the NA of the illumination, which is half the NA of the collection optics [3]. Beyond this range, the light tilts far enough that it no longer enters all four quadrants of the PAW, breaking a prior assumption.

EXTENSION OF DYNAMIC RANGE

This most recent work introduces an improved processing method, increasing the range of measurable surface tilts for objects with uniform reflectivity without altering the optical design of the sensor.

While maximum tilt in previous implementations was limited to be half the collection NA, there is unexploited information for larger tilt angles: up to

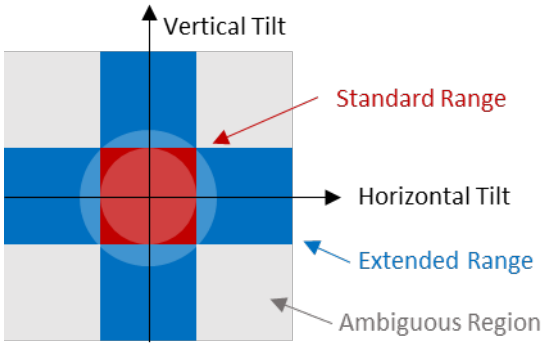

FIGURE 2. Dynamic range of angles which can be measured by PAW using standard- and extended-range processing methods.

1.5 times the NA in the principal directions, shown as “Extended Range” in FIGURE 2. Utilizing this information greatly increases the dynamic range but requires changes to the processing approach.

In the standard tilt range, the quadrants’ intensities increase and decrease linearly with changes in tilt angle, with total intensity conserved. This is the relationship exploited by prior PAW sensing demonstrations. Outside this range, the light shifts far enough that it passes through only two quadrants instead of all four, leaving the far side dark. A square aperture on the PAW lens is used to start blocking the light as it shifts further, such that the bright side begins decreasing in intensity, while the far side remains

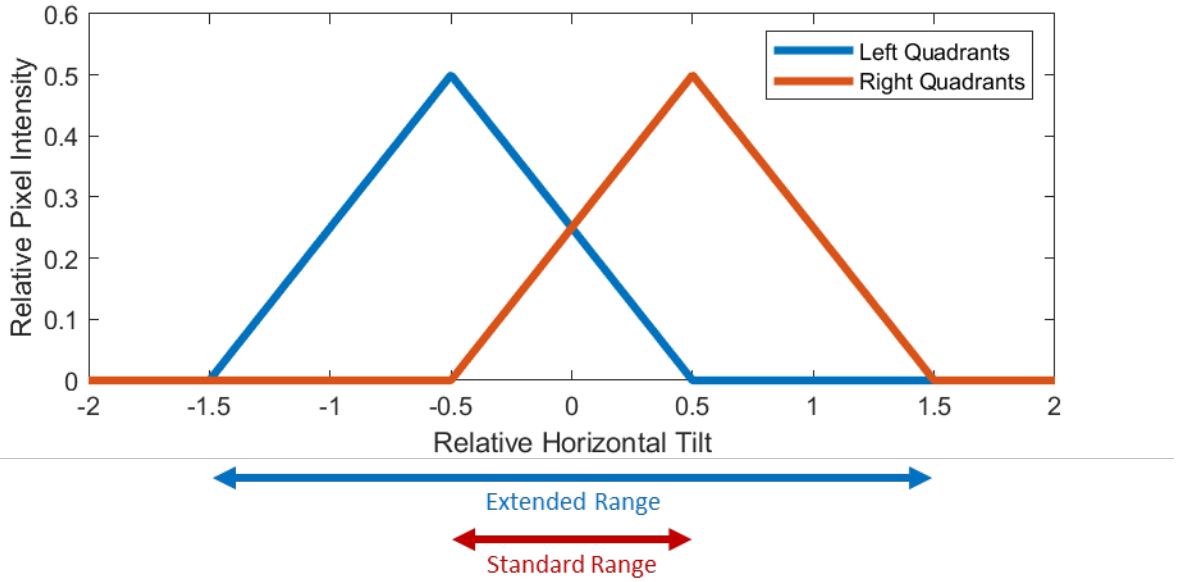

FIGURE 3. This diagram shows the relationship between horizontal tilts and the intensity in each quadrant on the PAW lens. The standard range only covers the linear region is in the middle, while the extended range covers additional tilts where light starts being blocked by the aperture.

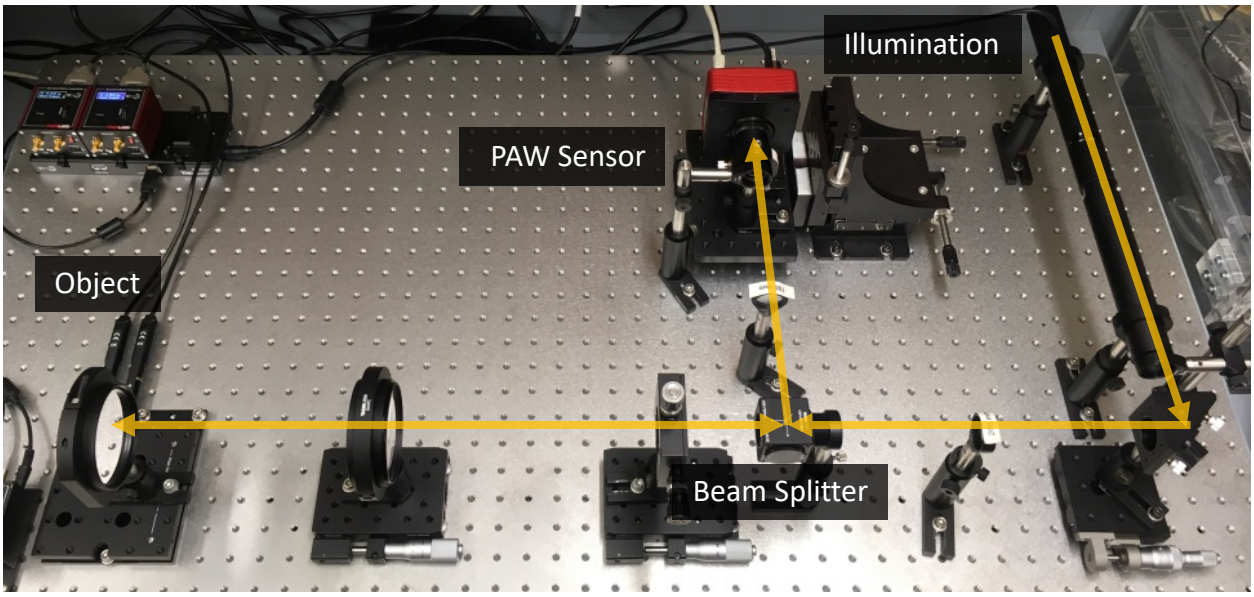

FIGURE 4: Experimental setup.

dark. This relationship is depicted in FIGURE 3, and gives a method of extracting angles up to 1.5 times the collection NA. Large off-axis tilts (as seen in FIGURE 2) are ambiguous: light only passes through one PAW quadrant, so while the amplitude of tilt can be measured, direction is ambiguous.

Processing in the extended range requires a new computation strategy and must be fast enough to maintain a high frame-rate. A 4-D lookup table was precomputed based on the sensor response, with each dimension corresponding to the relative pixel intensity measured in each quadrant. The tilt in each dimension is then linearly interpolated from the table. As total intensity is no longer conserved in the extended range, it is necessary to assume a uniform intensity object, (or to separately measure the intensity of the object,) so that relative (normalized) intensities can be calculated.

EXPERIMENTAL TESTING

To demonstrate the feasibility of utilizing this extended range, we assembled a PAW camera setup, shown in FIGURE 4, to observe objects as large as 60 mm in diameter with tilts on the order of ±3 mrad. The intended use of this setup is to make surface measurements of deformable mirrors, but we envision utility in a broader set of surface metrology applications.

The setup consists of two primary optical paths, with an illumination arm and imaging arm joined with a beamsplitter. The illumination optics provide light with an NA of 0.0025 set by a square aperture. A large (75 mm diameter) doublet lens is needed to project this light onto the object, and then collect the reflected light while minimizing aberrations. The rest of the relaying optics are 1" in diameter. The collection path supports double the NA (0.005), so that light tilted by the surface is still collected. The beamsplitter splits off the returning light, which is imaged by the PAW lens onto a camera (1392x1020 resolution) with 20x demagnification (3 mm subimages.) This permits

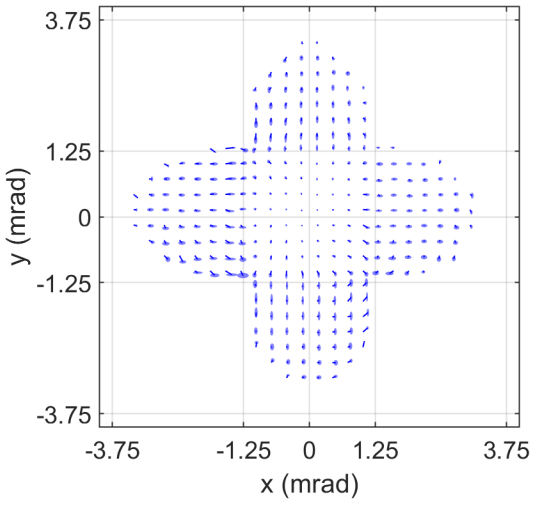

FIGURE 5: Accuracy of PAW measurements for full range of angles. Line shows average measurement error over the object, while ellipse depicts standard deviation.

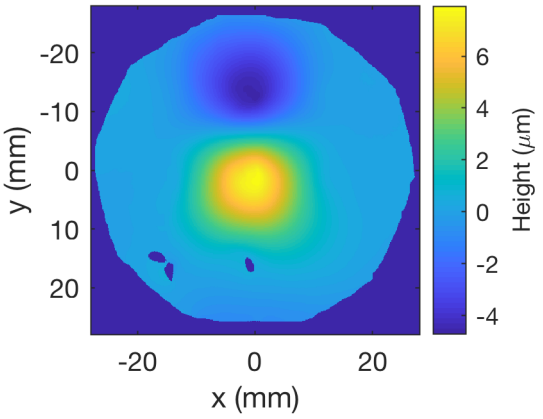

FIGURE 6: DM surface with upwards and downwards actuated pixels as measured by the PAW sensor.

510x510 pixel surface measurements of 60 mm diameter objects with maximum tilts in x and y theoretically up to ±3.75 mrad (±1.25 mrad in the standard range). Note that a slightly undersized collection aperture reduces the dynamic range actually achieved in the experimental results.

The sensor was evaluated in two ways, first with a flat mirror to validate sensor measurements with a known input, and then with a DM mock-up to show reconstruction of a more complex surface.

The results from the flat mirror can be seen in FIGURE 5. Here a 75 mm reference mirror is sequentially adjusted to a grid of x and y tilts spanning the measurement range. A calibrated stage is used to achieve known input angles. At each position, a PAW image is captured and x and y angle measurements are calculated across the mirror's surface. As the mirror is flat, these are expected to be uniform over the surface; variance is due to measurement error. In the plot, average offset over the mirror surface is represented by a solid line while the standard deviation is shown by the ellipse. The results reveal a successful extension in measurement range from about ±1.1 to ±3.3 mrad by use of the new processing techniques.

Finally, a DM mock-up is used to demonstrate the reconstruction of a more complex surface, as seen in FIGURE 6. This measurement is made by integrating the x and y tilts over the mirror into a surface. In this plot the pair of actuated pixels are apparent, with one pushed up and one pulled down. Note that this measurement represents a single camera frame, making it possible to monitor an object's dynamic response at standard camera rates.

CONCLUSION

PAW sensing represents a cost-effective approach for high-frame rate surface metrology which can scale to a wide range of object dimensions. This work represents the first demonstration of nonlinear processing to extend the angle range of the PAW sensing approach. The measurable tilts in the principle directions increases from 0.5 to 1.5 times the collection NA of the system. Simultaneously it is shown that, with appropriate optics, PAW techniques can extend beyond the initial demonstrations in microscopy to macro-scale objects.

REFERENCES

[1] Barankov R, Mertz J. Single-exposure surface profilometry using partitioned aperture wavefront imaging. Opt. Let. 2013;38:3961-3964.

[2] Ragazzoni R. Pupil plane wavefront sensing with an oscillating prism. J. Mod. Opt. 1996;43:289-293.

[3] Barankov R, Baritaux J, Mertz J. High-resolution 3D phase imaging using a partitioned detection aperture: a wave-optic analysis. J. Opt. Soc. Am. A 2015;32(11):2123-2135.

AN INVESTIGATION OF COSINE ERROR FOR SCANNING PROBE MEASUREMENTS OF FREEFORM SURFACES

ChaBum Lee[1], Joshua Tarbutton[2], and Tony L. Schmitz[2]
[1]Department of Mechanical Engineering
Texas A&M University, College Station, TX
[2]Department of Mechanical Engineering and Engineering Science
University of North Carolina at Charlotte, Charlotte, NC

INTRODUCTION

Freeform optics represent geometries that are, in general, neither planar nor spherical and remove the traditional requirement of rotational symmetry from optical designs. Freeform surfaces introduce radical new design freedom into optical assemblies. However, they also generate inherent manufacturing and measurement challenges. For example, the traditional Fizeau interferometer that relies on planar and spherical reference wavefronts to compare against the surface under test is not well suited to freeforms with significant departures from these traditional geometries.

Surface measurement by point probe scanning instruments, whether the instrument transduction scheme is mechanical or optical, is ultimately a convolution of the measuring machine error motions, the point probe geometry (e.g., roundness of a nominally spherical tip), and the desired surface under test. While these are critical considerations that have been extensively explored in the literature, in this paper, the specific measurement issue to be examined is the cosine error that is introduced by a non-normal direction of the (linear) probe axis with respect to the surface under test.

This study introduces a novel methodology for the machined optical surface metrology that integrates a displacement probe in a precision spindle. To eliminate cosine error, the displacement probe is always placed normal to the measurement target surface by rotating the probe. Spindle rotational error measured by a reversal method [1-3] was compensated for in the surface profile measurement. The optical concave and convex mirror surfaces and bearing bore and outer surfaces are measured by the proposed method, and the uncertainty sources associated with the proposed measurement method are discussed. The paper is organized as follows. First, the cosine error is defined. Second, a measurement strategy is presented to highlight cosine error for a simple artifact geometry. Third, an experimental validation of the proposed measurement method is presented with artifacts. Fourth, conclusions are presented.

COSINE ERROR

Cosine error is a well understood phenomenon in displacement measurement. In a displacement measuring interferometry (DMI), for example, the DMI axis is not, in general, exactly aligned with the motion axis direction; see Fig. 1. The misalignment angle, θ, represents a cone of possible angular misalignments. This introduces uncertainty into the displacement measurement, but perhaps more importantly, it also results in a measurement bias. Regardless of the θ value, the measured displacement is always less than the (unknown) actual displacement. Cosine error can be modeled as shown in Eq. 1, where d_m is the measured displacement and d is the actual displacement.

$$d_m = d\cos\theta \tag{1}$$

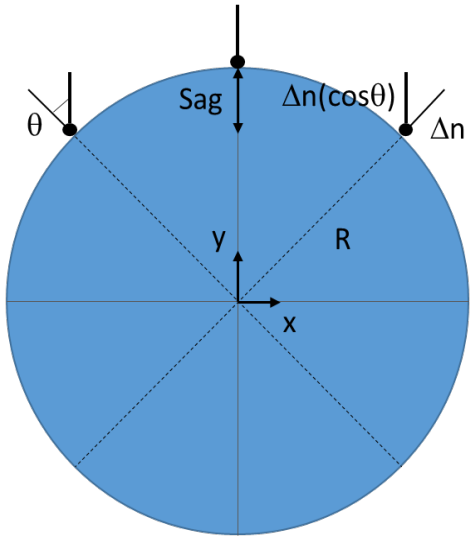

Figure 1. Cylinder measurement using a probe axis oriented in the y direction.

Cosine error also exists for point probe scanning measurements of non-planar, including freeform, surfaces. The situation is described by the surface measurement of a cylinder shown in Fig. 1. Here, the linear probe axis direction is fixed in the *y* direction. As the probe scans the surface, the angle between

the probe (measurement) axis and the surface normal varies. The angle, θ, is large at the extreme x locations (left and right) and zero in the middle at the cylinder apex. The angle value is $\sin\theta = x/R$, where R is the cylinder radius. Consider a Δn "bump" on the surface at any circumferential location. The deviation measured by the linear probe, Δy, depends on θ and is always less than the actual deviation (except at the apex). See Eq. 2.

$$\Delta y = \Delta n \cos\theta \qquad (2)$$

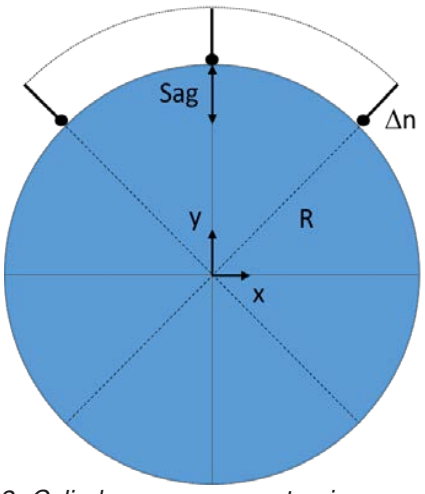

Figure 2. Cylinder measurement using a probe axis oriented in the surface normal direction.

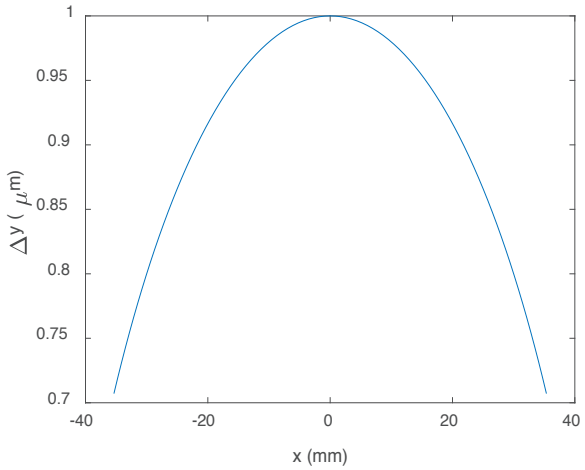

Figure 3. Probe "bump" height as a function of the scanning position, x, for the Fig. 1 orientation.

To eliminate this cosine error and corresponding bias, the linear probe direction can be maintained along the surface normal. This requires rotation about the z axis (i.e., the C rotary axis) in addition to the x and y scanning motions. The new measurement path is depicted in Fig. 2. Here the probe's displacement axis is always normal to the cylinder's surface.

Consider an example of a 50 mm radius and a θ variation of -45 deg to +45 deg (left to right in Fig. 1, x = -35.355 mm to 35.355 mm). If the "bump" size is Δn = 1 μm, the corresponding probe value for the Fig. 1 y direction orientation is provided in Fig. 3. It is observed that that error varies from 29.3% to zero and back to 29.3%. If the Fig. 2 measurement path is selected, on the other hand, the cosine error contribution is eliminated. The sag for this example is $R - (R^2 - x^2)^{0.5}$ = 16.645 mm.

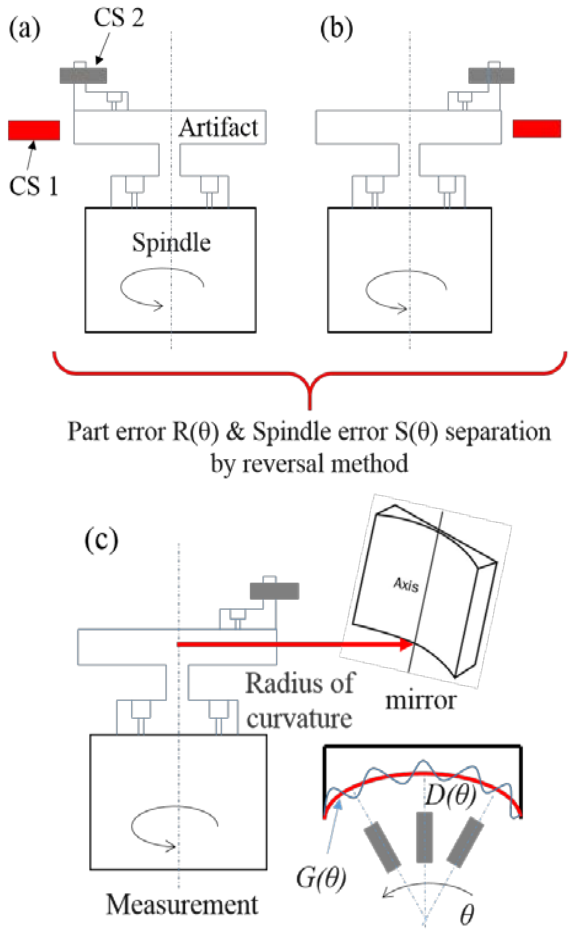

Figure 4. Reversal method: (a) measurement at θ = 0 deg, and (b) measurement at θ = 180 deg; (c) the proposed surface profile measurement method: angular displacement θ, part error R(θ), spindle error S(θ), sensor output D(θ), and surface profile G(θ).

MEASUREMENT METHOD

The proposed measurement system illustrated in Figure 4 consists of an aerostatic bearing spindle, two capacitive sensors (CS), a sensor holder, and an

artifact attached on the spindle shaft. Because the rotating accuracy of a spindle directly affects the CS 2 output, the spindle error S(θ) was separated from the part (artifact) error R(θ) by a reversal method proposed by Brian and Donaldson [4-5]. First, the artifact is positioned at an arbitrary angular position on the spindle, and a roundness trace is acquired from CS 1. Then, the CS 1 and the artifact are rotated by 180 deg. A new roundness trace is then acquired. Figure 4a and b show the two reversal positions. In position 1 (Figure 4(a)), the CS 1 reads a measured signal $m_1(\theta)$ given by:

$$m_1(\theta) = R(\theta)+S(\theta). \quad (3)$$

In position 2 (Figure 4b), the CS 1 reads a measured signal $m_2(\theta)$ given by

$$m_2(\theta) = R(\theta)-S(\theta). \quad (4)$$

Then, the part and spindle errors can easily be obtained as:

$$R(\theta) = (m_1(\theta)+m_2(\theta))/2, \quad (5a)$$

$$S(\theta) = (m_1(\theta)-m_2(\theta))/2. \quad (5b)$$

After separating spindle error from the part error, the measurement target (mirror surface with a radius of curvature, R_o) is placed with the offset distance from the spindle rotational axis that is the same as a radius of curvature of the measurement target and its surface profile can be obtained by rotating the spindle. This measurement enables the measurement probe to be always placed toward to the measurement target surface at a right angle. However, because this surface profile information includes spindle error, the corrected surface profile can be expressed as:

$$G(\theta) = R_o+\Delta D(\theta)-S(\theta),\ \Delta D(\theta)= D(\theta)- D_o, \quad (6)$$

where R_o is the radius of curvature of the measurement target and D_o is the initial offset distance of CS 2 at the beginning of the measurement. See Figure 4c.

SETUP AND MEASUREMENT RESULTS

The experimental setup is shown in Figure 5. The measurement was performed in a vibration-controlled lab environment. An aerostatic bearing spindle (Dover Instrument) and two identical capacitive sensors (Capacitec, 10 nm resolution, effective sensing diameter of 5 mm) are employed for the experiment. To eliminate the spindle dynamic effects and brushless DC motor effects, the measurement data was discretely collected from the equally spaced points of the target surface and was averaged. Surface profiles of the concave (R_o 95 mm) cylindrical lens were measured by the proposed measurement system.

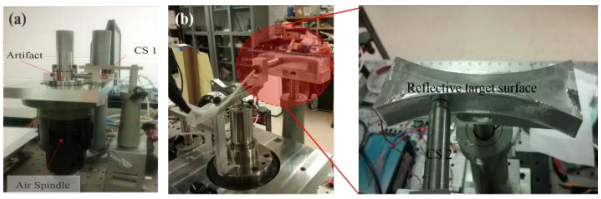

Figure 5. Experimental setup: (a) spindle and CS 1 only, and (b) full setup and detailed image.

The spindle error was separated by the reversal method; the results are shown in Figure 6. The spindle motion was measured in 10 deg intervals twice. From Equation 4, the spindle error S(θ) was 0.081 μm and its peak-to-valley (PV) value was 0.298 μm. Also, the part error R(θ) was 0.217 µm and its PV value was 0.786 μm.

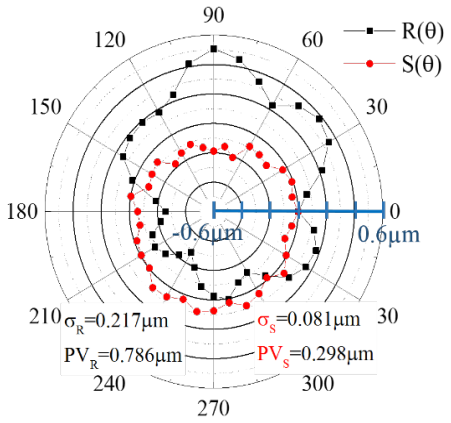

Figure 6. Results of spindle error separation.

As shown in Figure 4, after separating the spindle error from the part error, the displacement probe scans the cylindrical mirror and, then, the surface profile ΔG(θ) that subtracts R_0 from G(θ) can be calculated from Equation 5. The aluminum foil tapes were adhered to the acrylic cylindrical concave and convex lenses to make it conductive for capacitance measurement between the probe and target surfaces. Concave and convex target surfaces were placed 95 mm and 100 mm away from the center of the spindle rotational axis for each measurement, respectively. By rotating the spindle axis to always orient the measurement probe normal to the target surface, each target surface was measured three times with at equal intervals of 5 mm over 87 mm. From the results shown in Figure 7, the PV value for the concave surface profile was approximately 27 μm and the measurement standard deviation (from three measurement results) was 0.24 μm (Figure 7b).

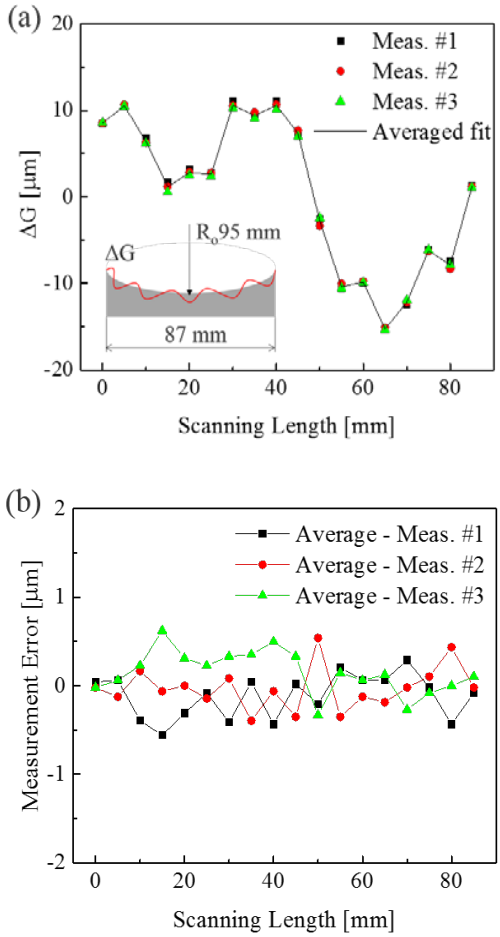

Figure 7. Surface profile measurement results of concave lens R_o 95 mm: (a) surface profile and (b) measurement deviation.

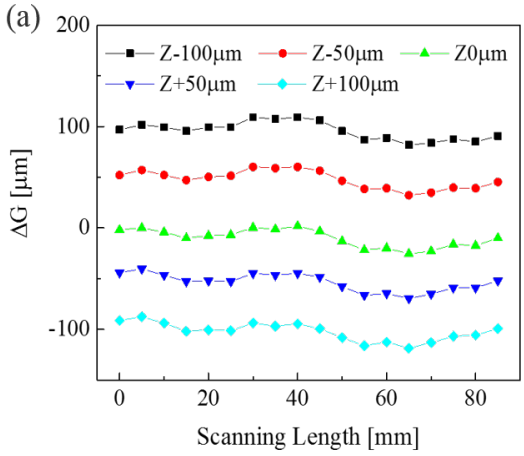

Figure 8. Measurement target surface positioning effects on surface profiles.

In the proposed measurement method, placing the target surface at the correct position (the same as the radius of curvature of each target) from the spindle rotation axis is critical to the surface profile measurement. Because there may exist spindle rotation axis-to-target surface positioning error, the effects of positioning error on surface profile measurement were investigated by measuring the surface profile at various positions along the Z-axis. The offset distance between spindle rotation axis and target surface varies from -100 μm to +100 μm (at a given distance R_o) and the manual linear stage with the micrometer was used to move the target surface forward and backward. The offset distance from -100 μm to +100 μm was selected because such positioning accuracy of the target surface can be easily achieved, even manually, in measurement alignment processes. Similarly to the previous measurements in Figure 7, each target surface was measured at equal intervals of 5 mm over 87 mm. Also, the measurement data was discretely collected from the equally spaced points of the target surface and was averaged to eliminate the spindle dynamic effects and brushless DC motor effects. From the result of Figure 8, at a given offset distance (±100 μm), the measured surface profiles showed trends over the offset distances for both concave and convex surfaces. These results indicate that the proposed measurement method is effective for measuring both the concave and convex surfaces and is not significantly sensitive to the offset distance between the spindle rotation axis and the measurement target surface.

As a part of measurement uncertainty estimation of the proposed system, the surface profile error could result from four alignment errors: (a) probe offset error, (b) probe angular alignment error, (c) probe distance error along the radial direction and (d) target positioning error. In this study, the probe with an effective sensing diameter of 5 mm was used, so the probe offset error and probe angular alignment error can be neglected. However, as the sensing area of the probes gets smaller, those errors could be significant to the surface profile measurement. The probe distance effect along the radial direction be neglected because the probe only picks up the constant gap distance between the probe and target surface. However, depending on the probe type, such as a laser-based displacement sensor, eddy current sensor, or LVDT (linear variable differential transformer), and its effective sensing area, this error can be significant. Measurement uncertainty of the proposed system depending on the probe type will be investigated in future work.

CONCLUSIONS

A measurement method that eliminates cosine error, particularly for optical surface metrology, was proposed. Cosine error can be eliminated through always aligning the probe normal to the target surface by rotating the probe attached on the spindle axis. Spindle rotation error was compensated in the surface profile data using a reversal method. The proof of the concept was tested and it was confirmed that the proposed measurement system can be applied for measuring both concave and convex surface profiles. As a result, the measurement method can both eliminate cosine error and scan the large area quickly. In addition, the proposed measurement system can be used for freeform surface measurement by integration with precision machine tools for on machine measurement applications.

ACKNOWLEDGEMENTS

The research was supported by the National Science Foundation (Award Number: CMMI 1663210) through Texas A&M University and (Award Number: CMMI 1663405) through University of North Carolina at Charlotte.

REFERENCES

1. Donaldson, R.R., A simple method for separating spindle error from test ball roundness error, Annals of the CIRP, 21, 125–126, (1972).
2. Eric R. Marsh, Precision Spindle Metrology, DEStech Publication Inc., 2010.
3. Bala Muralikrishnan and Jay Raja, Computational Surface and Roundness Metrology, (Springer, 2009).
4. Yadong Li, Peihua Gu, Free-form surface inspection technique state of the art review, Computer-Aided Design, 36(13), 1395-1417 (2004).
5. Jin-Ho Kang, ChaBum Lee, Jae-Young Joo, and Sun-Kyu Lee, Phase-locked loop based on machine surface topography measurement using lensed fibers, Applied Optics, 50(4), 460-467 (2011).

SUBWAVELENGTH FIBER-OPTIC DISPLACEMENT SENSING BASED ON NON-CONTACT NEAR-FIELD SPECKLEGRAMS

Wang Chen, Fu Feng, Wei Lin, Dihan Chen and Shih-Chi Chen*
Mechanical and Automation Engineering
The Chinese University of Hong Kong
Shatin, N.T., Hong Kong
*Email: scchen@mae.cuhk.edu.hk

INTRODUCTION

In this paper, we present a low-cost non-contact displacement sensor based on fiber specklegrams, achieving a precision of 10 nm, speed of 100 Hz, and a detection range of 3 - 10 micrometers. By collimating the incident laser and reflected light from the sample surface in a flexible fiber, the interference among the different eigenmodes propagating in the multimode fiber (MMF) forms unique specklegram images at different sample positions in space. Accordingly, precise and repeatable noncontact displacement detection can be realized by comparing the recorded specklegrams with the calibrated specklegram database through imaging processing algorithms.

NONCONTACT DISPLACEMENT SENSING

Subwavelength non-contact displacement sensing has a wide range of engineering applications, e.g., multi-axis positioning, or nano-fabrication systems. Although existing methods, e.g., capacitance probes or laser interferometry, may achieve tens to hundred nm precision, they are usually prohibitively expensive and difficult to be applied to a small object or work envelope [1]. Fiber-optic sensors have been proved as a reliable device to monitor various physical parameters, e.g., displacement, temperature, and pressure etc. Previous fiber-optic displacement sensors based on spectroscopy measurements have achieved micrometer to millimeter level precision [2] with the advantages of small envelope, low-cost and insensitivity to target materials. The precision is, however, limited by the poor-quality factor of the optical resonator [3]. Meanwhile, Fiber-optic sensors using interferometric methods, e.g., Fabray-Perot, typically provide higher sensitivity and dynamics. Among them, fiber specklegram analysis is a technique that exploits the interference among the different eigenmodes propagating in an MMF to extract and monitor subwavelength displacement around the waveguide. This works well as the phase difference of different eigenmodes in an MMF varies rapidly with the environment around the fiber. Although the interference among the different eigenmodes in an MMF is complex and difficult to model, recent advancement in computation methods and hardware presents a great opportunity to perform fast image processing to extract useful information stored in specklegrams.

OPERATION PRINCIPLE

To achieve displacement sensing based on fiber specklegrams, we compare the correlation coefficients between the target position and the reference position. This works because the interference among the different eigenmodes propagating in the MMF forms unique specklegrams at the proximal end of the fiber for each target position. And once the reflected light varies slightly as the sample surface moves, the coupling ratio (amplitude and phase) between the reflected light and the fiber eigenmodes will be influenced consequently. By exploiting this physical phenomenon, precise position estimation can be realized by calculating the coupling ratio which strongly depends on the distance between the sample surface and the sensor head.

Specifically, the amplitude varies rapidly in the near field region, where the evanescent wave dominates. Accordingly, the laser intensity varies as a function of the distance between the fiber tip and the target surface, since the coupling phase varies rapidly as the wavelength of the laser is short. A small variation during beam propagation can significantly influence the phase, i.e., $\Delta\varphi = d/\lambda \cdot 2\pi$, where $\Delta\varphi$ is the phase difference, d is the displacement, and λ is the laser wavelength.

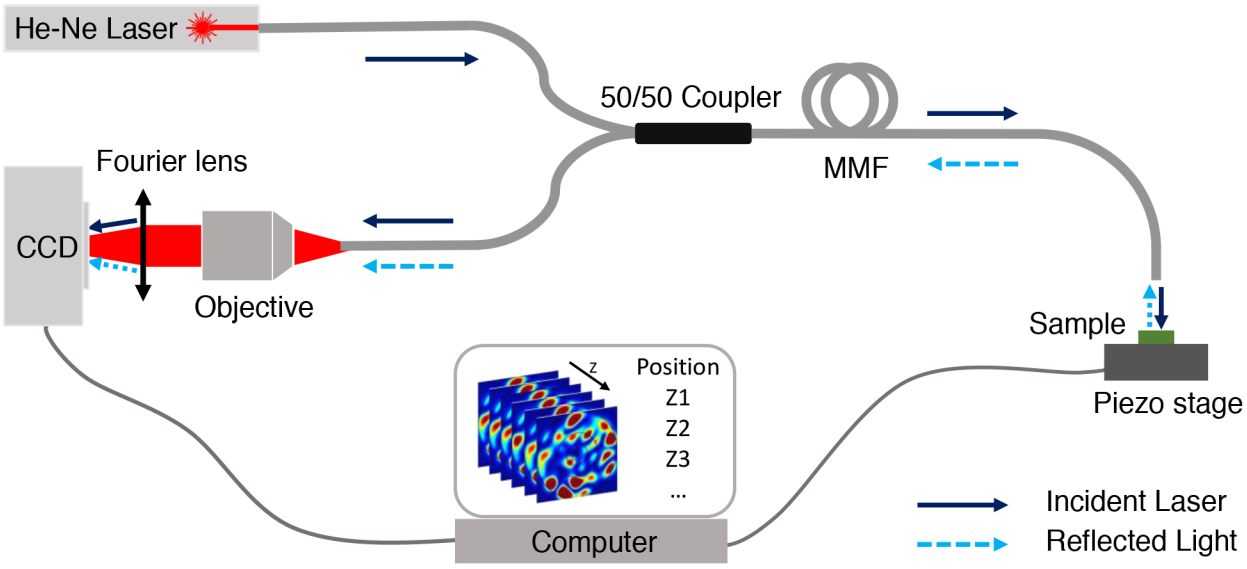

FIGURE 1. Optical configuration of the fiber-optic displacement sensing system

The far field speckle pattern intensity distribution of an MMF fiber can be mathematically described in Eq. (1):

$$A_0(x,y) = \sum_{m=0}^{M} a_m(x,y) exp[i\varphi_m(x,y)] \qquad (1)$$

where M is the modal number of the fiber; $a_m(x,y)$ and $\varphi_m(x,y)$ are the amplitude and phase distribution of the m[th] mode.

The intensity distribution of the speckle pattern can thus be mathematically expressed in Eq. (2):

$$I_0(x,y) = |A_0(x,y)|^2 = \sum_{m=0}^{M}\sum_{n=0}^{N} a_m a_n \, exp[i(\varphi_m - \varphi_n)] \qquad (2)$$

In order to quantitatively compare each recorded specklegram and determine the exact displacement. The 2-D correlation coefficient (r) is utilized to indicate the relevance, which is expressed in Eq. (3):

$$r = \frac{\sum_m \sum_n (A_{mn} - \bar{A})(B_{mn} - \bar{B})}{\sqrt{(\sum_m \sum_n (A_{mn} - \bar{A})^2)(\sum_m \sum_n (B_{mn} - \bar{B})^2)}} \qquad (3)$$

where A_{mn} and B_{mn} represent the values of individual pixels on the CCD camera (i.e., $m \times n$ pixels) of two images A and B; $\bar{A}$ and $\bar{B}$ denote the mean values of matrix A and B respectively. The 2-D correlation coefficient is a number that represents the similarity between the two images in relation with their respective pixel intensity.

To achieve displacement sensing, a database of specklegram images needs to be constructed and carefully calibrated. In our experiment, a commercial piezoelectric positioner is used to record the specklegram database by moving the sample surface away from the selected reference surface with 2 nm steps. To determine the exact location of a sample that is arbitrarily positioned in space, one then compares the specklegram recorded at that specific position with the specklegram database; when the correlation coefficient reaches the maximum value, it indicates that the two specklegram images are recorded at the same position; hence the position of the sample is determined.

EXPERIMENT CONFIGURATION

Figure 1 presents the optical configuration of the fiber-optic sensing system. The sensor consists of a He-Ne laser (632.8 nm; R-30988, REO) with an output power of 5 mW; a 2 × 1 step index multimode fused fiber coupler (50/150 μm step index; numerical aperture (NA) = 0.22); and a charge-coupled device (CCD) camera (Zyla sCOMS, Andor). During a measurement, the laser is first coupled into the top fiber. After the 50/50 fiber coupler, the laser beam is transmitted to the remote fiber detection head, which is placed 2 - 5 micrometers away from the sample surface, i.e., a silicon chip, mounted on a piezoelectric XYZ stage. Lastly, the reflected light is collected by the sensor head and propagates back to the bottom fiber; and the interference pattern, i.e., specklegram, among the different eigenmodes in the MMF is projected to the CCD

camera for data acquisition and position estimation.

EXPERIMENTAL RESULTS

In this section, we devise and perform experiments to validate the operation principle and characterize the precision and range of displacement detection. Figure 2 presents the specklegram images recorded at different sample positions, i.e., 150, 300, 450, 600, 750, 900, 1050, 1200, and 1350 nanometers. As can be observed in Fig. 2, the specklegram images are distinctively different at different positions.

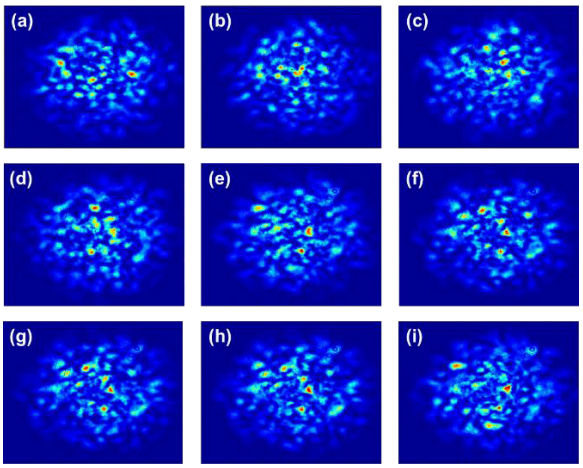

FIGURE 2. Recorded specklegram images when the sample moves away from the fiber detection head (d = 0); d = 150, 300, 450, 600, 750, 900, 1050, 1200, and 1350 nm for (a) – (i) respectively.

By calculating the correlation coefficients, we characterize and quantify the correlation between the recorded specklegrams and the reference image. Figure 3 plots the calculated correlation coefficients (*r*) between the specklegram images recorded at the initial reference position and the rest of the scanning positions. A sample is placed near the fiber (i.e., within 1 μm) and subsequently scans away from the fiber head in 2 nm steps. For each position, a specklegram is recorded by the CCD camera, which forms the reference specklegram database. From the result, the maximum *r* value occurs at the 0 position, which agrees with the prediction. Over the near field regime (< 3.5 μm), the correlation coefficient then decreases rapidly. The decreasing trend is mainly attributed to the inhomogeneous intensity variation of different eigenmodes when the sample moves away from the fiber scanning head. It is worth noting that the correlation coefficient slightly increases in some regions. This is due to the phase delay and amplitude change of different eigenmodes. From the experiment, it is confirmed that the specklegrams are highly sensitive to displacements in the near field region with a detection range of ~3.5 micrometers, which will be later verified in the positioning experiments.

For the far field regime (> 4 μm), as shown in Fig. 3, the initial position of the sample is set to be 2 micrometers away from the fiber detection head, and slowly scans away in 2 nm steps. From the results, we find that the *r* value oscillates with little attenuation. This is because in the far field regime the intensity decreases slowly with the increasing distance between the fiber head and the sample. The slow attenuation makes it difficult to choose the position of the maximal *r* value. For example, when the displacement is n*λ/2 (i.e., the reflected photons experience a 2nπ phase change), the correlation coefficients show little differences, leading to a small detection range, i.e., λ/4 ~ 158 nm.

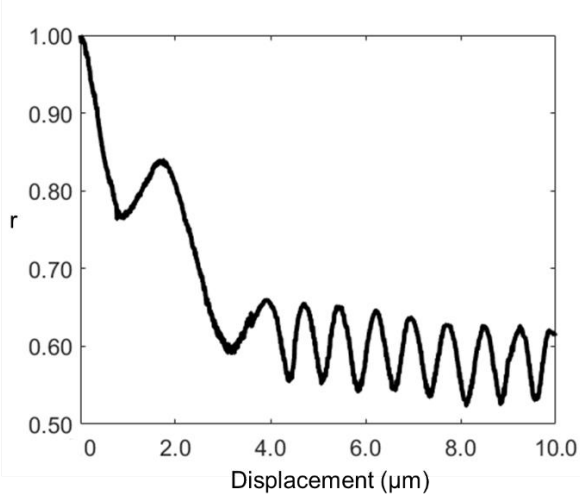

FIGURE 3. Correlation coefficients between the specklegrams recorded at the initial reference position and the rest of the scanning positions including near field regime, i.e., the distance between the sample and fiber < 3.5 micrometer; and far field regime, i.e., d > 4 micrometers.

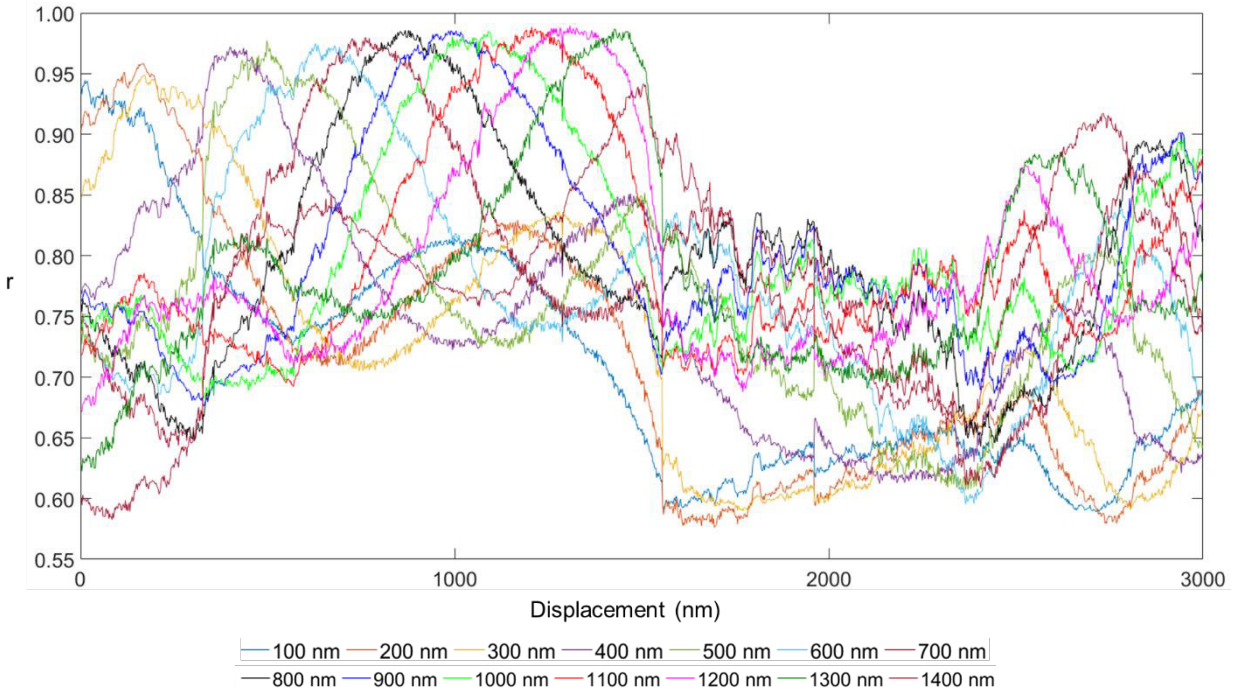

FIGURE 4. Correlation coefficients between the specklegrams recorded at the measured position and the calibrated specklegram database

With the calibrated specklegram database, positioning experiments are devised and performed to verify the sensor precision in the near field regime. Figure 4 plots the correlation coefficient curves for specklegrams recorded at 14 different positions. Each color-coded curve has a known position from the piezoelectric positioner. By observing the curves, one may find their maximum value precisely registers to the known position on the horizontal axis with ~10 nm precision. Next, we place the sample on the piezoelectric positioner, and command the stage to move forward at a speed of 100 nm/s over a range of 1.4 micrometers. During the process, the CCD camera records the fiber specklegrams at 1 Hz. By comparing the recorded specklegrams with the database, the position of the sample at each time point is determined. The results are presented in Fig. 5. From the results, one may observe that the measured positions (red dots) well overlap with the command position (black line). These experiments confirm feasibility and precision of the new fiber sensor system.

To examine the repeatability of the fiber-optic sensor, the sample is repeatedly moved to a second position (1000 nm from the reference plane) for six times. Figure 6 plots the correlation coefficient curves. From the zoom-in view, one can observe that although in different experiments the curves slightly shift, their maximum values occur at the same position, i.e., the correlation coefficients can be used to detect the sample surface position with tens of nanometer precision.

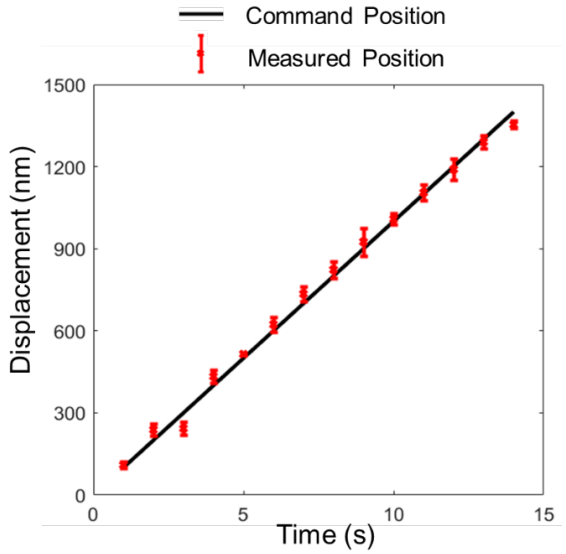

FIGURE 5. Positioning experiment. The sample is moved at a constant speed (100 nm/s) and the fiber-optic sensor records the specklegram images at 1 Hz from t = 1s to 14s.

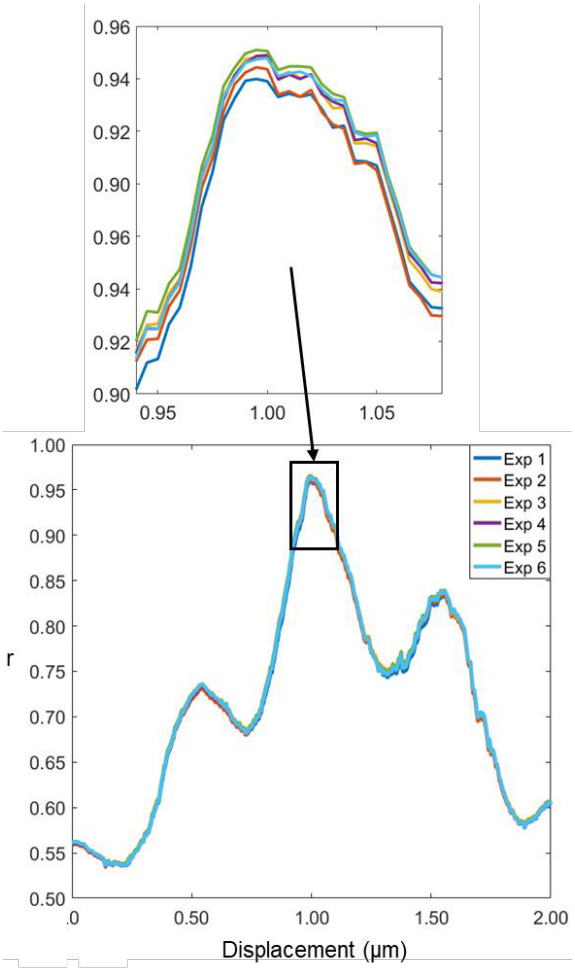

FIGURE 6. Examination of sensor repeatability: Comparison of correlation coefficient curves among six independent experiments

From the experiment, we can conclude that the fiber-optic sensor achieves a precision and repeatability of ~10 nm even it is subjected to electronic noises or external disturbances, e.g., temperature variation. Note that the experiment is performed within a duration of 2 hours, where the speckle patterns remain stable. For long experiments, the speckle pattern may be influenced by environmental disturbances, e.g., temperature or humidity variation. In this case, one can use a reference fiber channel to compensate the measurement errors induced by external disturbances [4].

CONCLUSION

In conclusion, we have reported a high-precision fiber-optic displacement sensor based on specklegram analysis. The new fiber sensor achieves non-contact displacement sensing with ~10 nm precision and a detection range of 3 -10 microns. The fiber sensor has a bandwidth of ~5 Hz and can precisely record the target position at 100 Hz, which is only limited by the speed of the CCD camera. The high precision and repeatability are realized by exploiting the sensibility of fiber specklegram and the fast-electric field variation in near field regime. The new fiber-optic displacement sensor has the advantages of (1) low-cost, (2) compact device envelope, (3) high precision, and (4) insensitivity to sample/target materials, and may find important applications in metrology and nanofabrication, e.g., near field plasmonic lithography [5], and probe-based nano-manufacturing [6].

REFERENCES

[1] Xia S, Schieveen Van, Nihtianov S, and Spronck J. High-resolution Low-latency Capacitive Displacement Sensor. Annu. J. Electron. 2009; 117-120.

[2] Wang X, Zhao C, Wang Y, Shen C, and Dong X. A Highly Sensitive Fibre-optic Nano-displacement Sensor Based on Surface Plasmon Resonance. J. Light. Technol. 2016; 34(9): 2324-2330.

[3] Götzinger S, Benson O, and Sandoghdar V. Influence of a Sharp Fiber Tip on High-Q Modes of a Microsphere Resonator. Optics Letters. 2002; 27(2): 80-82.

[4] Feng F, Chen W, Chen D, Lin W, and Chen S. In-situ Ultrasensitive Label-free DNA Hybridization Detection using Optical Fiber Specklegram. Sensors and Actuators: B. Chemical. 2018; 272:160-165.

[5] W. Srituravanich, Pan L, Wang Y, Sun C, Bogy D, and Zhang X. Flying Plasmonic Lens in the Near Field for High-speed Nanolithography. Nature Nanotechnology 2008; 3(12): 733-737.

[6] Li C, Wang J, and Chen S. Flexure-based Dynamic-tunable Five-axis Nanopositioner for Parallel Nanomanufacturing. Precision Engineering. 2016; 45: 423-434.

GEOMETRIC ERROR MEASUREMENT OF THE LINEAR AXIS OF CNC MACHINE TOOLS BY MULTILATERATION USING FOUR LASER TRACERS

Lin Han, Jun Zha, and Yaolong Chen
State Key Laboratory for Manufacturing Systems Engineering
Xi'an Jiaotong University
Xi'an, Shaanxi, China

INTRODUCTION

Linear axes are key components of CNC machine tools and coordinate measuring machines, of which the accuracy plays a very important role on the machining and measuring performance. The geometric error is one of the most important factors that seriously deteriorates the system accuracy of a linear axis [1]. The measurement and identification of geometric errors are indispensable for the manufacturing of a precision linear axis.

As shown in Figure 1, when a linear axis moves, six position-dependent geometric errors (*PDGEs*) occur in three directions (*X, Y, Z*). The six *PDGEs* which are defined in the ISO 230-1:2012 especially for the *Y* axis are three linear error motions: the linear positioning error motion, E_{YY}, the straightness error motions in the *X* and *Z* directions, E_{XY} and E_{ZY}, as well as three angular error motions: E_{AY}, E_{BY} and E_{CY} around the *X*, *Y*, and *Z* directions [2].

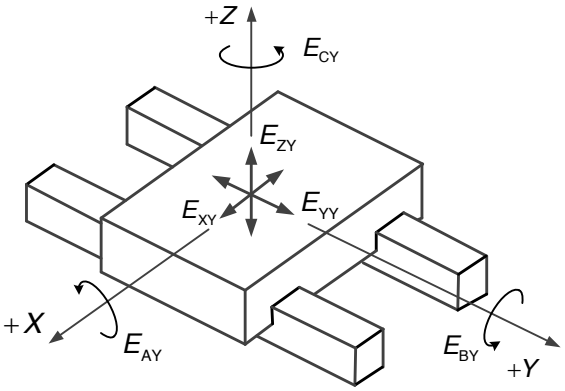

FIGURE 1. Geometric error components of Y axis

Current commercial laser interferometers are widely used in the measurement of the six *PDGEs.* However, most of them can only measure one geometric error at a time and increase high requirements for the operator which make it time consuming. Many scholars do research on the simultaneous geometric error measurement after realizing this. Feng et al. developed a system which can simultaneously measure the six *PDGEs* [3], while the optical path design for each geometric error measurement is complicated and the system hasn't been widely used. Zhang et al. used one laser tracker to realize the measurement and identification of geometric errors of a linear axis based on the multilateration measurement [4]. However, the multilateration measurement using a single laser tracer must repeat four or more tests at different laser tracer positions to measure the geometric errors of a machine tool which need more than two hours and is sensitive to thermal. In this case, it is urgent to rapidly measure and identify the six geometric errors of the linear axis.

In this paper, a new method which can simultaneously measure and identify the 6 geometric errors of the linear axis of CNC machine tools based on multilateration using four laser tracers is proposed. Four laser tracers are used to increase the measurement redundancy and accuracy and to realize the simultaneous measurement. The efficiency is highly promoted by 50% compared with single laser tracer measurement and 80% compared with the commercial laser interferometer measurement.

MULTILATERATION MEASUREMENT OF 3D POINTS USING FOUR LASER TRACERS

Multilateration technology is firstly used to accurately locate an aircraft using three to five stations on the ground. In this paper, four laser tracers are used to realize the multilateration measurement. Only the relative displacements measured by laser tracers are used to realize the precision positioning of the targets. The measurement schematic is shown in Figure 2.

The equations of the measurement based on multilateration can be determined by the distance between each laser tracer and the retroreflector as:

$$\boldsymbol{F}(d)=0 \tag{1}$$

Each of the nonlinear equations can be written in the form:

$$F_{ij}=\sqrt{\left(x_j-x_{pi}\right)^2+\left(y_j-y_{pi}\right)^2+\left(z_j-z_{pi}\right)^2}-\left(l_i+l_{ij}\right)=0 \tag{2}$$

where (x_j,y_j,z_j) is the *j-th* position of the retroreflector; (x_{pi}, y_{pi}, z_{pi}) is the position of the *i-th* laser tracer; l_{ij} is the length measured by the *i-th* laser tracer to *j-th* position of the retroreflector and l_i is the dead length of the measurement by the *i-th* laser tracer.

Six parameters can be constrained to zero by the coordinate system (X_L,Y_L,Z_L) formed by four laser tracers shown in Figure 2. At least 10 positions of the retroreflector should be measured using four laser tracers based on multilateration so that the equations can be solved using iterative methods like Levenberg-Marquardt algorithm. Finally, the volumetric errors of the commanded positions can be got after solving the nonlinear equations for the preparation of geometric error identification.

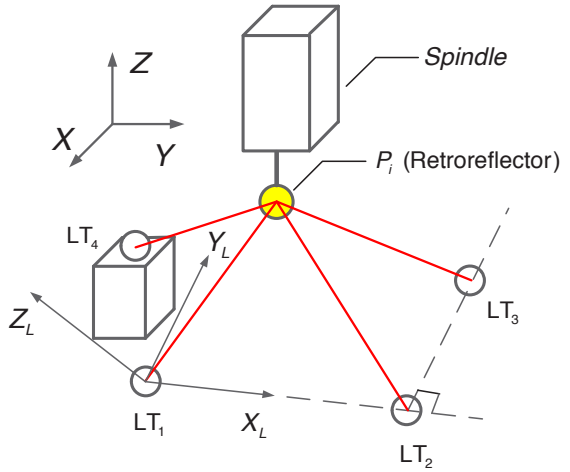

FIGURE 2. Geometric error measurement based on multilateration ((X,Y,Z) is the coordinate system of the machine tool; (X_L,Y_L,Z_L) is the coordinate system formed by four laser tracers; LT_1-LT_4 are four laser tracers)

GEOMETRIC ERROR MODEL OF THE LINEAR AXIS

The screw theory is wildly used in the geometric error modeling of CNC machine tools because of its high computational efficiency and concise description with clear physical meaning for geometric errors. Before establishing the geometric error model, some specifications are set as follows: the coordinate system is the right-hand Cartesian coordinate system; the positive linear error motions are along the axes directions of the coordinate system and the positive angular error motions meet the right-hand rule. Hence the actual pose g_{FY} of *Y* axis can be described by the product of its six error motions based on the screw theory as:

$$g_{FY}=e^{\hat{\xi}_y\theta_y}e^{\hat{\xi}_{EYY}\theta_{EYY}}e^{\hat{\xi}_{EXY}\theta_{EXY}}e^{\hat{\xi}_{EZY}\theta_{EZY}}e^{\hat{\xi}_{EAY}\theta_{EAY}}\bullet e^{\hat{\xi}_{EBY}\theta_{EBY}}e^{\hat{\xi}_{ECY}\theta_{ECY}}g_{FY}(\mathbf{0}) \tag{3}$$

And the geometric error model can be obtained:

$$\Delta g_{FY}=g_{FY}-e^{\hat{\xi}_y\theta_y}g_{FY}(\mathbf{0})=\begin{bmatrix}R_E & P_E\\ \mathbf{0} & 1\end{bmatrix} \tag{4}$$

where y is the command movement of the *Y* axis; and $\hat{\xi},\theta$ are twist and motion of the movement of Y axis or the six *PDGE*s described in Figure 1; $g_{FY}(\mathbf{0})$ is the initial pose of the retroflector relative to the coordinate system of the machine tool which can be determined by the following matrix and the position (x_t, y_t, z_t) is the nominal position of the retroreflector in the tool coordinate system; R_E is the attitude error of the retroreflector; P_E is the position error of the retroreflector.

$$g_{FY}(\mathbf{0})=\begin{bmatrix}1 & 0 & 0 & x_t\\ 0 & 1 & 0 & y_t\\ 0 & 0 & 1 & z_t\\ 0 & 0 & 0 & 1\end{bmatrix} \tag{5}$$

The equation can be simplified by the products of matrix and the attitude error R_E and position error P_E can be determined as follows:

$$R_E=\begin{bmatrix}1 & -E_{CY} & E_{BY}\\ E_{CY} & 1 & -E_{AY}\\ -E_{BY} & E_{AY} & 1\end{bmatrix} \tag{6}$$

$$P_E = \begin{bmatrix} -y_t E_{CY} + z_t E_{BY} + E_{XY} \\ x_t E_{CY} - z_t E_{AY} + E_{YY} \\ -x_t E_{BY} + y_t E_{AY} + E_{ZY} \end{bmatrix} \quad (7)$$

In order to identify the attitude errors and the position errors, the retroflector must be positioned in three directions with different offsets in the coordinate system of *Y* axis shown in Figure 3. Firstly, the angular error motions are identified from the measurement of the three positions of the retroflector by the linear least square method. Then the linear error motions can be identified through one of the position errors of the linear axis. Note that if the retroflector is positioned very closely to the tool tip position, the calculation will be greatly simplified because of the little effect of angular error motions on the position errors of the retroreflector. Boundary conditions that all geometric parameters should start from zero also should be considered in the geometric error identification.

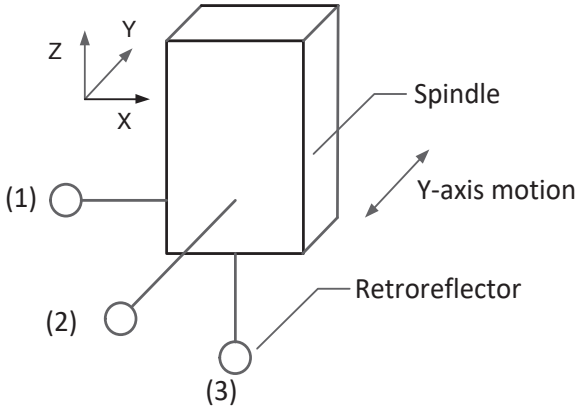

FIGURE 3. Arrangement of the retroreflector. ((1), (2) and (3): three points of the retroreflector positioned in X, Y and Z directions of a machine tool)

GEOMETRIC ERROR MEASUREMENT AND IDENTIFICATION EXPERIMENT OF THE Y AXIS

The six *PDGE*s measurement and identification experiments of Y-axis were conducted on a three-axis gantry-type high speed milling machine tool using four Etalon laser tracers. The experimental setup was shown in Figure 4. In the experiments, the positions of X axis and Z axis were set to 0mm. The measurement travel of Y axis was set to (-800mm, 0mm). The measurement interval was set to 80mm and the moving speed of Y axis was 2m/min. The machine tool was set to pause 3s at each commanded position of Y axis. The machine tool was warmed up for 2 hours before the measurement. And the temperature range during the measurement process was under 20±1˚C. And the measurement took about half an hour.

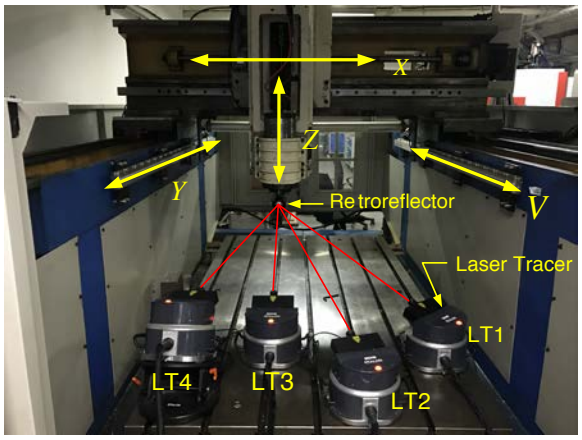

FIGURE 4. Three-axis milling machine tool experimental setup

The six *PDGE*s of Y axis are identified after the measurement shown in Figure 5.

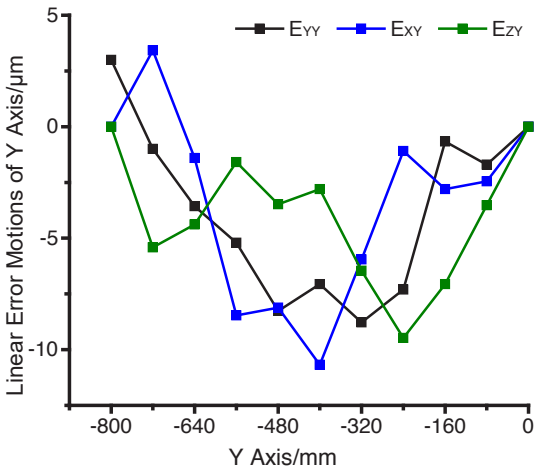

(a)

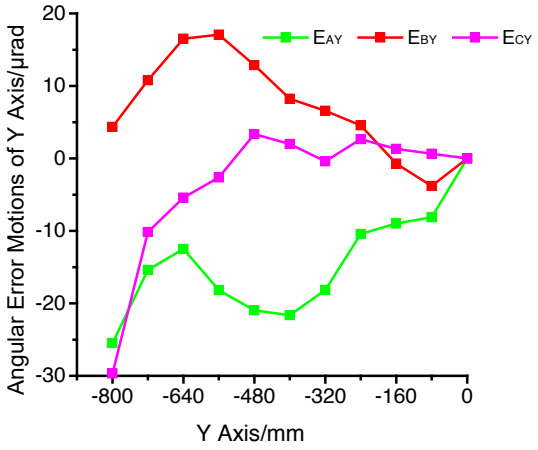

(b)

FIGURE 5. Geometric error components of Y Axis ((a):Linear Error Motions of Y Axis; (b): Angular Error Motions of Y Axis)

A comparison experiment in the same condition with the measurement mentioned between the multilateration method proposed in this paper and the conventional method using a commercial laser interferometer was carried out to verify the effectiveness of the multilateration measurement. The results for E_{YY} and E_{AY} are shown in Figure 6. It shows that two results of *PDGE*s are very close. And the measurement proposed in this paper are more effective and the measurement efficiency can be increased by more than 80% compared with the measurement by the laser interferometer which took about one hour and a half.

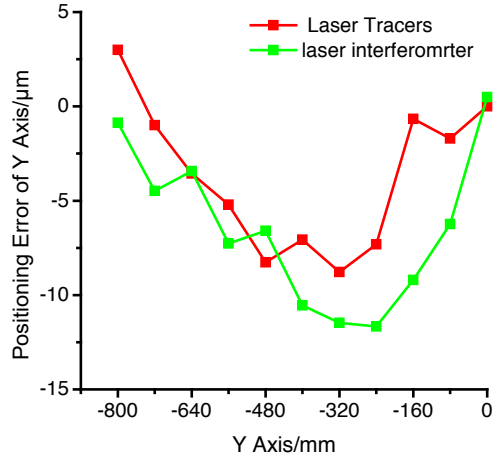

(a)

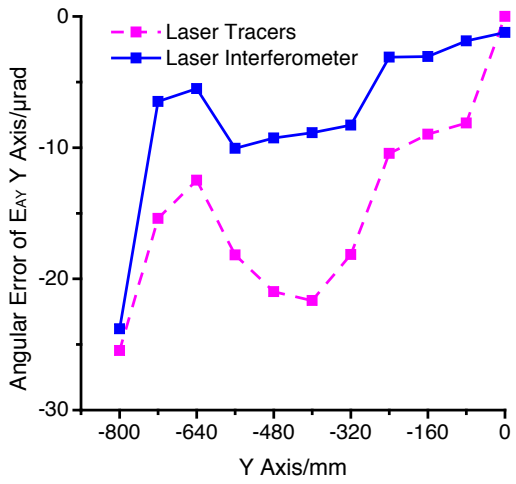

(b)

FIGURE 6. Geometric error components Comparison of Y Axis ((a):Linear Error Motion Comparison of Y Axis; (b): Angular Error Motion Comparison of Y Axis)

ACKNOWLEDGEMENTS

This work was funded by the following fund: National Science and Technology Major Project of China (2017ZX04013001).

REFERENCES

[1] H. Schwenke, W. Knapp, H. Haitjema, et al, Geometric error measurement and compensation of machines-An update. CIRP Ann.-Manuf.Technol. 57 (2) (2008) 660-675.

[2] ISO 230-1:2012, Test code for machine tools-part 1: Geometric accuracy of machines operating under no-load or quasi-static conditions. International Organization for Standardization.

[3] F. Qibo, Z. Bin, C. Cunxing, K. Cuifang, et al, Development of a simple system for simultaneously measuring 6DOF geometric motion errors of a linear guide. Opt. Express. 21(22) (2013) 25805-25819.

[4] Zhang, Z. & Hu, H. Three-point method for measuring the geometric error components of linear and rotary axes based on sequential multilateration. J. Mech. Sci. Technol. 27(9) (2013) 2801-2811.

NEW 3D FIGURE MEASUREMENT SYSTEM BY ANGLE INTEGRATION

Takashi Miyawaki[1], Takahiro Yamamoto[1], and Eiji Sawaya[1]
[1]Department or Division
Nikon Corporation
2-15-3 Konan Minato-ku, Tokyo, Japan

INSTRUCTIONS

Techniques for measuring surface shapes of optical elements such as lenses and mirrors with high accuracy are research topics in which technological innovation is progressing constantly. Lenses and mirrors that are large and require high precision are required in the fields of gigantic mirrors of astronomical telescopes, X-ray mirrors and exposure systems. In addition, compact high precision optical elements are required in the fields of smart phones, microscopes, endoscopes and the like. A wave front interferometer with very high measurement reproducibility is effective for high accuracy measurement. However, since the measurement is based on the reference surface, it is necessary to guarantee the accuracy of the reference surface, and the shape guarantee method of the reference surface has been researched variously. In the three-dimensional shape measurement (CMM), the reference surface is unnecessary, but calibration of the system is indispensable in order to perform highly accurate measurement, and various calibration methods such as stage driving and length measuring mechanism It has been proposed [1]. It can be said that it is a very difficult task to guarantee measurement accuracy by either method. Development of highly accurate shape measurement technology using angle information has been developed for a long time, but further developments are becoming more active in recent years. Helmholtz Zentrum Berlin has developed the Nanometer Optical Component Measuring Machine (MON) and realized high accuracy measurement [2]. For high-precision measurement Nanoprofiler is under development at Osaka University, and high-precision measurement is realized by converting the inclination of the surface into a shape [3, 4]. Therefore, we newly developed a contactless three-dimensional shape measuring device PSM. This device aims to correspond to highly accurate measurement and a wide range of measurement objects. In order to measure a large measurement object with high accuracy, it is characterized by using various correction mechanisms.

PRINCIPLE OF MEASUREMENT

PSM calculates the shape profile by the integration from the angle profile data of the measurement object. Before the measurement, the angle profile of the measurement surface is calculated by the surface information such as an aspherical expression. Using the angle profile information, the angle sensor is scanned by the drive stage along the measurement target so that the angle sensor is always perpendicular to the measurement surface. At the each point, angle profile is measured by the sensor. And at the same time, the drive information of the stage is acquired by various correction sensors. Finally, the relative positional relationship between the angle sensor and the measurement object is calculated from each acquired value. This makes it possible to correct the value of the angle profile of the measurement surface and obtain a highly accurate value. A shape profile is obtained by integrating and calculating the measured angle profile. The object to be measured has a rotationally symmetrical shape, and the cross section is scanned in a spoke shape when the object is viewed from directly above. Measurement in the cross section direction is set as one set, and the cross sectional shape is calculated from the sectional angle profile. As shown in Fig. 1, it is possible to calculate the shape profile of the surface by repeating the cross section measurement a plurality of times.

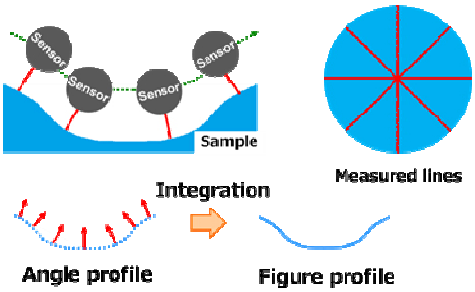

FIGURE 1. Angle profile scanning and integration form angle profile to figure profile

MAIN SENSOR AND METROLOGY LOOP

In PSM, a sensor that measures angle and a sensor that measures distance are installed in the main sensor. In both the angle sensor and the distance sensor, the inputted light passes through the lenses and is focused on the object to be measured. And the reflected light is further introduced into the quadrant sensor through the lenses. In the quadrant sensor, the positional change of the light is acquired, and the optical system is designed so that the angle change can be measured by the distance change on the quadrant sensor.

Based on the result measured by the main sensor, the relationship between the relative angle and position of the main sensor and the object to be measured is calculated. In the main sensor, it is possible to calculate the relationship between the distance and the angle with respect to the object to be measured.

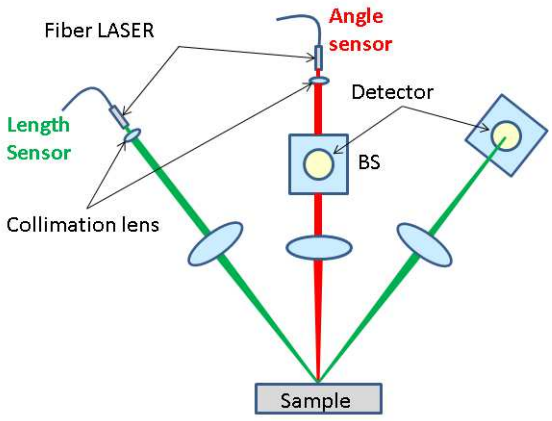

FIGURE 2. Main sensor schematic Measure angle and distance simultaneously

Furthermore, in the PSM, the positional relationship between the main sensor and the object to be measured is corrected by the metrology loop configuration. If there is an error in the relative position between the main sensor and the object to be measured, the position where the measurement light is irradiated shifts according to the shape (mainly the radius of curvature) of the object to be measured, and the angle of the reflected light is shifted. In order to correct this value, it is necessary to accurately measure and correct the relative position. As shown in FIGURE 3, the position of the main sensor is measured by a distance sensor with reference to a highly rigid structure called a Metrology Frame. By connecting with the object to be measured by distance sensor measurement, the reference frame and measurement surface are connected. Measure the position and angle of the moving mirror installed on the optical component table on the XYZ stage from the measuring interferometer installed in the reference frame. As a result, the driving position of the stage is measured from the Metrology Frame as a starting point, and the Metrology Frame and the object are connected by measuring the relationship between the driving position of the stage and the object to be measured by the distance sensor. This makes it possible for the angle sensor and the object to be connected to connect the measurement loop via the Metrology Frame, and the relative position and angle are measured.

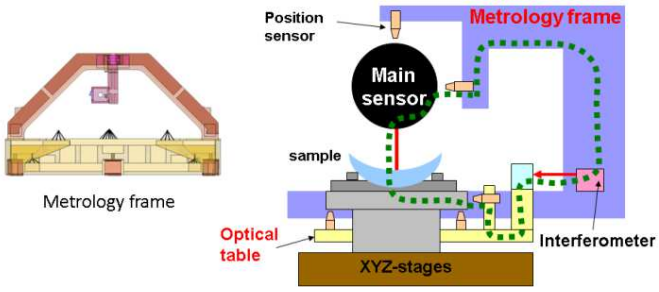

FIGURE 3. Metrology Frame and Loop By several sensors, relative angle and position between Main sensor and measured object is monitored.

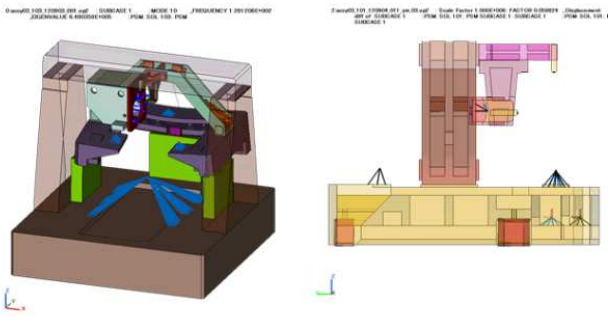

FIGURE 4. Evaluation of deformation Metrology Frame and Whole system has been evaluated by deformation simulation

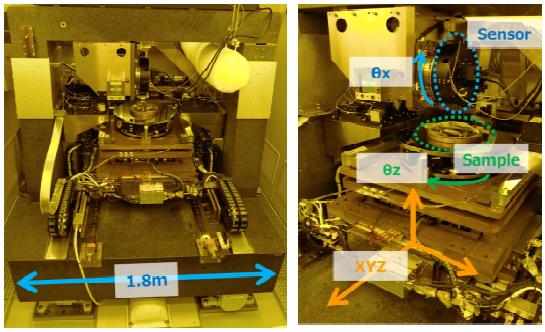

FIGURE 5. System overview and stage configuration

In order to realize Metrology Loop with high precision, it is necessary to minimize the deformation of Metrology Frame. For the deformation of Metrology Frame we performed preliminary assessment on weight balance and thermal deformation. As a result, it was confirmed that even when all the deformations were included, it was a deformation of 5 nm or less. Based on this result, we designed the actual Metrology Frame and optimized the structure.

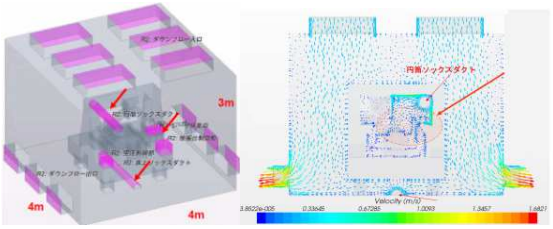

FIGURE 6. Chamber is specially designed for this system. All air flow is simulated.

SYSTEM SPECIFICATION

It has a device configuration as shown in FIG. 4, and the measurable sample has a maximum diameter of 430 mm and a thickness of 100 mm. However, the measurable size varies depending on the shape of the measurement object. The measurable shape has a rotationally symmetrical shape, and the measurable radius of curvature is 10 mm or more.

As a specific configuration, the main sensor is mounted on the Theta-X axis, and the object to be measured is mounted on the X, Y, Z, Theta-z axes below it. By driving these five axes it becomes possible to scan the surface of the object to be measured.

In order to further improve the stability of the measurement, we developed a chamber to minimize temperature change. By analyzing the air flow around the main sensor and the whole device, the air flow is controlled to create a more stable environment for measurement.

EVALUATION

As an evaluation, we measured small radius sphere sample. Sample's radius of curvature is concave 50mm and measured diameter is 30mm. To evaluate simple repeatability, we measured sample 2 times consecutively. And we calculate subtracted data which is subtraction between pixel data sets. We defined this data as a repeatability data. Repeatability data was 0.34 nm in RMS and 1.6 nm in PV.

In previous evaluation, we have measured repeatability of 173mm radius's convex lens. This repeatability was 0.46 nm in RMS and 2.5 nm in PV. From two evaluations, we conclude that the difference of radius and figure which is concave or convex does not effect to the measurement.

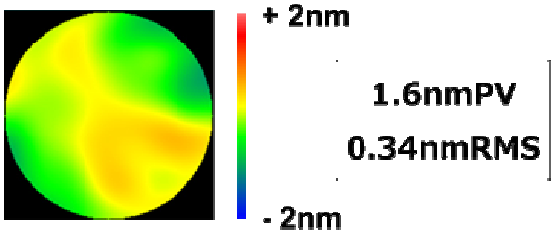

FIGURE 7. Repeatability evaluation results This data is fitted Zernike polynomials. Lower than 10th order Equation is used.

CONCLUSION

We developed new 3D figure measurement system by angle. In this report, we described system configuration and evaluation results. Especially from evaluation, we could reveal that PSM has good same repeatability in different radius and figure which is concave or convex.
As a next step, we will expand evaluation target and evaluation method. And final target is evaluation for accuracy. To confirm accuracy, we start from round robin test at first.

REFERENCES

[1] H.Takeuchi,K.Yosizumi, H. Tsutsumi, “Ultrahigh accurate 3-D profilometer using atomic force probe of measuring nanometer, Winter topical meeting 4-5 February, north Carolina,USA.(2004)

[2] F. Siewert, H.Lammert, T. Zeschke, “The nanometer optical component measuring machine,” Modern Developments in X-ray and Neutron Optics, Springer,(2008)

[3] High-accuracy three-dimensional aspheric mirror measurement with nanoprofiler based on normal vector tracing method, *R. Kudo, T. Kitayama, Y. Tokuta, H. Shiraji, M. Nakano, K. Yamamura, K. Endo, (2017) Optics and Lasers in Engineering 98 (2017) 159-162

[4] Measurement of aspheric mirror by nanoprofiler using normal vector tracing, K. Kitayama, H. Shiraji, K. Yamamura, K. Endo, SPIE Optics+Photonics, 9962-10, (2016)August San Diego, CA, USA

High-resolution non-fluorescent imaging with low-coherence interference structured illumination microscopy

Shin Usuki[1], Gaku Shibata[2], and Kenjiro T. Miura[2]
[1] Research Institute of Electronics
Shizuoka University
Hamamatsu, Shizuoka, Japan
[2] Graduate School of Engineering
Shizuoka University
Hamamatsu, Shizuoka, Japan

INTRODUCTION

In recent years, high-resolution optical microscopy using structured illumination [1] has been developed and used in fluorescent bio-imaging applications [2-5]. Since structured illumination can be generated over the entire observation area, the technique enables high-speed and high-resolution imaging through parallel image processing. Therefore, it is expected to be applicable not only to fluorescent bio-imaging but also to non-fluorescent imaging in industrial fields. However, there are two critical problems for achieving high performance. Speckle noise affects the reflected light image, because the structured illumination is typically generated by laser interference. Since imaging in industrial fields is based on coherent image formation, it is difficult to use structured illumination effectively. Although random speckle noise can be suppressed by using a laser-beam homogenizer or by using a series of images for reconstruction [6], suppressing noise from the observed sample pattern is difficult. In particular, speckle noise critically affects defect inspection of optically transparent (or semi-transparent) substrate surfaces and causes artifacts that can raise false detections during reconstruction. In addition, there is a requirement for employing high-precision positioning stages for determining the illumination phase-shift value because structured illumination microscopy theoretically requires several images with phase-shifted illumination. Furthermore, prospective use in an industrial setting requires the consideration of special circumstances, such as vibration, under which conventional laboratory systems may not function properly. Hence, this high-resolution imaging technique cannot be effectively used in practical, industrial applications. In this study, we attempted to detect the phase of the structured illumination as a fringe signal with another interferometric measurement system, which is employed by structured illumination microscopy as originally developed; it uses a low-coherence light source for high-resolution and low-speckle imaging. We constructed an optical system consisting of Michelson interferometers, which allow the low-coherence interference fringes to be manipulated on a sample and the phase to be detected on another image sensor. Feeding back the phase of structured illumination through super-resolution processing allows robust imaging despite vibrations, drifting, and environmental changes. Moreover, because high-precision positioning of structured illumination is unnecessary in the proposed system, we can replace piezoelectric actuators with low-cost and high-speed stepping motors. We report the effectiveness of our system as verified by experiments.

METHOD

We attempted to detect the phase of the structured illumination as a fringe signal with another interferometric measurement system, which is installed in originally developed structured illumination microscopy [7]. This system employs a super-luminescent diode (SLD) as a low-coherence light source for high-resolution and low-speckle imaging. Using an SLD allows speckle noise to be suppressed because speckle noise is produced by highly coherent light sources. Also we constructed an optical system consisting of Michelson interferometers, which allow the low-coherence interference fringes to be manipulated on a sample and the phase to be detected on another image sensor. We can calculate the displacement from the contrast of the fringe signal and the phase-shift value of the structured illumination from the displacement of the fringe signal. When an observation is performed under environmental disturbance or by using a low-precision stage, such as the commonly used

stepping motor stage, the phase-shift value cannot be determined precisely. However, in such a situation, our proposed method can determine the phase-shift value from the fringe signal image without performing a quantity-of-stage operation. Furthermore, since highly specific instrumentation is not required, structured illumination using an SLD offers the same attractive features as optical microscopy—high-speed and low-cost observation.

DEVELOPMENT

In the development of the system, we employs a Michelson interferometer to realize the stringent demand for adjustment of the difference in optical path length needed to achieve and precisely control the two-beam low-coherence interference pattern. Figure 1 shows a schematic of the low-coherence interference structured illumination microscopy with the fringe measurement system. It shows top view of the overall system. The beam emitted from SLD passes single-mode fiber and collimating lens. A first beam splitter divides the beam in two arms. The structured illumination is generated by two-beam interference and can be shifted by controlling a mirror on one optical path with a positioning stage. It allows that samples need not be manipulated. We add another Michelson interferometer which acts as a fringe measurement system to obtain phase-shift value of the structured illumination on the sample. The bottom in the Figure 1 shows side view of the microscope part. The incident light to the microscopic imaging system is scattered (diffracted) by sample with the structured illumination. This is a sort of dark-field imaging system. The reflected light which is corresponding to the 0th order diffracted light is controlled by mirrors on a beam steering. Using the polarization pickup system, only the directions of the lights reflected on the sample are bend with the polarizing beam splitters. And then the fringe signal is detected on another image sensor. The optical path length is controlled by a mirror on one arm with a stepping-motor stage.

RESULT AND DISCUSSION

The experimental specifications of the developed system are listed in Table 1. In a series of experiments, a line and space pattern was employed as a sample for a resolution evaluation. Figure 2 shows a schematic of the sample. This sample has three types of pitches: 0.2 μm, 0.4 μm and 0.6 μm. However, because

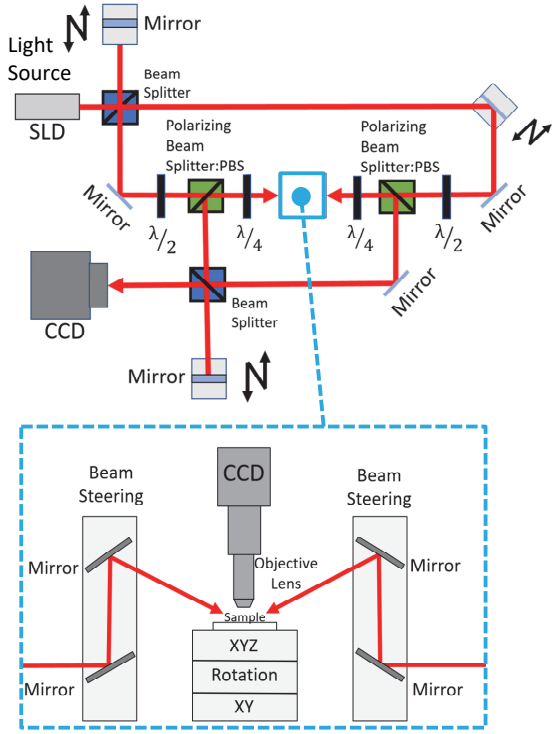

FIGURE 1. Low-coherence interference structured illumination microscopy with a fringe measurement system: top view of the overall system and side view of the microscope part.

TABLE 1. Experimental specifications of the developed system

SLD-as-light-source wavelength λ	0.67 μm
Structured illumination pitch P	0.47 μm
Observation magnification M	100
Numerical aperture of objective NA	0.55
Diffraction limit under the SLD DL	0.74 μm

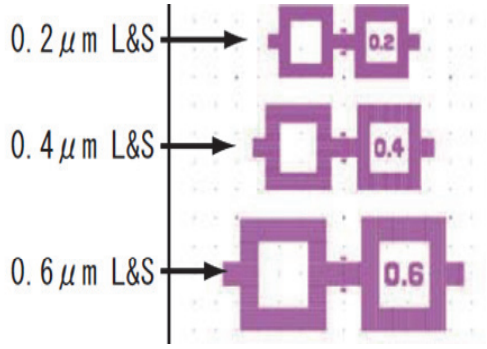

FIGURE 2. Line and space sample with the pitch of 0.2 μm, *0.4* μm and *0.6* μm

the diffraction limit is 0.74 μm, even when using a white light source, a conventional optical microscope cannot resolve a pitch of 0.2 μm and 0.4 μm. In this study, we acquire three images with shifted phases of the structured illumination in the transverse direction, which are generated by two-beam interference of the SLD source. Then we seek to obtain high frequency information through the image reconstruction computation. Figure 3 shows acquired images of the part of the line and space sample with the pitch of 0.4μm under the structured illumination by low-coherence interference. Figure 4 presents an observation using conventional microscopy with the same SLD as the uniform illumination. This image does not show improved resolution. In this image, the pitch of 0.4 μm on the sample was not resolved because it was still diffraction-limited. As the result of the mathematical computation in the spatial frequency domain, three spectra provide three solutions, which correspond to the origin, spatial-frequency-shifted by structured illumination, and shifted in the opposite direction symmetrically in spatial frequency domain, respectively. Finally, computations base on structured illumination microscopy is performed by summing up these images with appropriate weights and inverse Fourier transforms to the spatial domain. Figure 5 shows high-resolution image of the line and space as the results of resolution improvement computation. Although intensity unevenness is apparent in the resulting image, the 0.4 μm pitch, which is smaller than the diffraction limit, is surely resolved because of the spatial resolution improvement with structured illumination microscopy.

CONCLUSION

In order to achieve high-resolution non-fluorescent optical imaging for use in industrial fields, we proposed low-coherence interference structured illumination microscopy with a fringe measurement system to feedback phase of the structured illumination into computation. We achieved high-resolution imaging beyond the diffraction limit without high precision stages and verified its effectiveness through experiments. In future prospect, we will try to optimize the system including computation settings and to evaluate the maximum resolution of the developed system. We shall also consider applications for pattern-height detection using absolute optical path length difference measurements, which is a feature of low-coherence interference.

FIGURE 3. Acquired images of the part of the line and space sample with the pitch of 0.4μm under the structured illumination by low-coherence interference

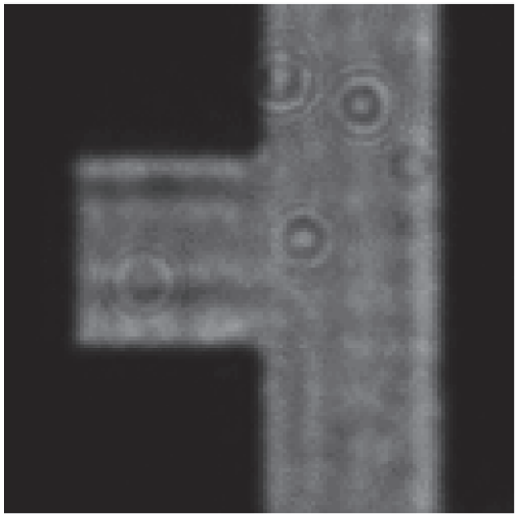

FIGURE 4. Diffraction-limited image acquired by conventional microscopy with the same SLD as the uniform illumination

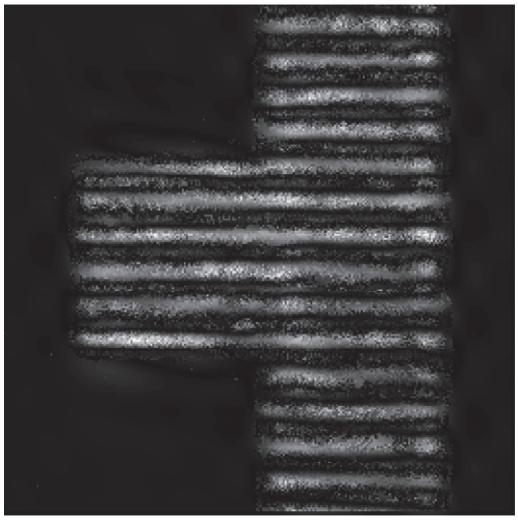

FIGURE 5. Structured illumination microscopy image of the line and space with improved resolution

ACKNOWLEDGEMENT
This work was supported by JSPS KAKENHI Grant-in-Aid for Young Scientists (A), Grant Number 16H06063.

REFERENCES
[1] M.G.L. Gustafsson, Surpassing the lateral resolution limit by a factor of two using structured illumination microscopy, J. Microsc. 198 (2) (2000) 82–87.
[2] Nikon Super Resolution Fluorescent Microscope N-SIM, <http://www.nikon.com/products/instruments/lineup/bi oscience/s-resolution/nsim/>.
[3] M.G.L. Gustafsson, D.A. Agard, J.W. Sedat, I5M: 3D widefield light microscopy with better than 100 nm axial resolution, J. Microsc. 195 (Pt. 1) (1999) 10–16.
[4] Lin Shao, Berith Isaac, Satoru Uzawa, David A. Agard, John W. Sedat, Mats G.L. Gustafsson, I5S: Wide-field light microscopy with 100-nmscale resolution in three dimensions, Biophys. J. 94 (June) (2008) 4971–4983.
[5] Diane S. Lidke, Keith A. Lidke, Advances in high-resolution imagingtechniques for three-dimensional imaging of cellular structures, J. Cell Sci. 125 (2012) 2571–2580.
[6] S. Usuki, H. Nishioka, S. Takahashi, K. Takamasu, Experimental verification of super-resolution optical inspection for semiconductor defect by using standing wave illumination shift, Int. J. Adv. Manuf. Technol. 46 (9) (2010) 863–875.
[7] S. Usuki, T. Takada and K. T. Miura, Optical Microscopy with Improved Resolution Using Two-beam Interference of Low-coherence Light, Measurement, 78, (2016)373-380.

CMM INTERIM PERFORMANCE CHECK PART 1: DESIGN CRITERIA

Lucas M. Valdez[1], Joshua D. Montano[2] and Mario O. Valdez[3]
[1] Pit Technologies
[2] Prototype Fabrication
[3] Production Agency Quality
Los Alamos National Laboratory (LANL)
Los Alamos, NM, USA

INTRODUCTION

The international standard for Coordinate Measuring Machines (CMM) verification is the *ISO 10360* series. Specifically, *ISO 10360-2*, states "*It is strongly recommended that the CMM be checked with regularity during the periods between periodic reverification* [1]."

Los Alamos National Laboratory (LANL) has a number of CMMs site-wide where calibrations are completed on an annual basis [2]. Customers rely upon accurate results to ensure product specifications are met, thus maintaining each CMM's performance is critical through the use of interim checks. With a variety of interim checks and artifacts available, task-specific checks and artifacts are highly recommended to mimic a production-type of measurement process. For LANL's applications, the use of a Machine Checking Gage (MCG) by Renishaw mimics a typical part's measurement volume well. In pursuing an interim check on a weekly basis between calibration cycles, assurance is obtained that each CMM is meeting the stated levels of accuracy in addition to allowing for spot-checks of each subsystem of the CMM.

The work described in this paper covers how the MCG is used to potentially single-out certain geometry errors. First a design strategy describes the tolerances limits, sampling size, as well as pattern, and geometrical error calculations. The novelty is that dynamic scanning of the MCG is used for data collection, which will be used in Part two of the research: *CMM Interim Performance Check Part 2: Case Study,* to study machine capability, Analysis of Variance (ANOVA) statistics and Monte Carlo simulations for validating the sample size accuracy.

DESIGN STRATEGY

The design strategy revolves around tolerance limit estimation(s) using manufacture specifications. For the tolerance limit estimations, it is assumed that the maximum permissible errors (MPEs) for size, probing and scanning are independent of one another, (i.e. their product is zero) so quadrature is used to quantify the estimates.

Tolerance Limit Calculations

For estimating each CMM's tolerance limit, the manufacture's specifications and a review of internally published literature [3], [4], [5], [6], [7], [8], [9] are utilized in the evaluations. Estimation of the tolerance limits for the MPEs of length, probing and scanning given by the manufacturer (per the *ISO 10360* series), are used as well as the manufacturer's specification for repeatability (per the *B89* standard [10]). The maximum permissible error for length, MPE_L is calculated from Eq. (1).

$$MPE_L = A + \frac{L}{K}(\mu m) \tag{1}$$

A is the variance resulting from repeated sampling on a final dimension, K is the length-dependent measurement deviation and L is the length measured in millimeters. For probing and scanning, MPE_P and MPE_S are the designations used, respectively, and the pivot repeatability test is MPE_{PR}.

The first tolerance limit, form of the measurement sphere (T_S), is generated by calculating a root-sum-square (RSS) of two times the size (since the equation is plus or minus) and the probing, as shown in Eq. (2).

$$\begin{aligned} T_S &= \sqrt{Size^2 + Probing^2} \\ &= \sqrt{(2 \cdot MPE_L)^2 + {MPE_P}^2} \end{aligned} \tag{2}$$

Similarly, to estimate the tolerance limit of a scanned diameter (T_D), Eq. (1) is used with the scanning error instead of the probing, from Eq. (2).

$$T_D = \sqrt{Size^2 + Scanning^2} = \sqrt{(2 \cdot MPE_L)^2 + {MPE_S}^2} \quad (3)$$

Finally, the pivot repeatability (T_{PR}), is taken from the *B89* standard for repeatability estimated by Eq. (4).

$$\mathrm{T_{PR}} = \mathrm{FS} \cdot \mathrm{MPE_{PR}} \quad (4)$$

The factor of safety, $FS = 2$, is used and determined based on engineering judgment knowing there is additional CMM movement and time between the pivot measurements not included in the *B89* test.

Using Eq. (1) thru (4), the results for the limit calculations can be seen in TABLE 1. (NOTE: Only the B&S Global Image will be used for testing.)

TABLE 1. Manufacturer Machine Specifications and Limit Calculations

Machine	MPE_P (µm)	MPE_S (µm)	MPE_L (±µm)	*Arm Radius (mm)*	*B89 (µm)*	T_S (µm)	T_D (µm)	T_{PR} (µm)
B&S Chameleon	3.0	3.8	2.1 + L/355	226	2.0	7.4	7.7	4.0
B&S Chameleon	3.0	3.8	2.1 + L/355	226	2.0	7.4	7.7	4.0
Leitz PMM-C	0.6	1.5	0.6 + L/600	380	^	3.8	4.0	2.6
Leitz PMM-C (Expanded)	1.0	1.5	1.0 + L/400	380	^	5.9	6.0	2.6
Leitz Reference	0.9	1.9	0.9 + L/350	380	^	6.2	6.4	2.8
Leitz Reference (Expanded)	0.9	1.9	1.5 + L/350	380	^	7.4	7.6	2.8
B&S Chameleon	3.0	3.8	2.1 + L/355	226	2.0	7.4	7.7	4.0
Leitz PMM	0.8	1.7	1.2+ L/300	226	^	5.5	5.7	2.6
B&S Global Performance	1.6	2.9	1.5 + L/333	226	1.7	5.9	6.4	3.4
B&S Xcel	3.5	4.5	4.5 + L/250	226	3.5	13.1	11.4	7.0
B&S Xcel	3.5	4.5	4.5 + L/250	226	3.5	13.1	13.4	7.0
B&S Global Image	1.7	3.4	1.7 + L/333	226	1.5	6.3	2.4	3.0
Tesa MicroHite	3.5	NA	3.0 + L/250	151	2.0	9.1	NA	4.0
Tesa MicroHite (Expanded)	5.0	NA	5.0 + L/250	151	2.0	34.5	NA	4.0

^No B89 specifications for Leitz [9]. Assumed PMM = 1.3um, Reference = 1.4um

DATA SAMPLING AND SIZE DETERIMINATION

For the data collection effort, a sampling strategy and sample size need to be determined. The following subsections define each.

Sampling Strategy

The point distribution strategy, or sampling strategy, for point-to-point probing is eight individual points collected azimuthally at three levels, along the polar direction for a total of 24 measurement points, as shown in FIGURE 1.

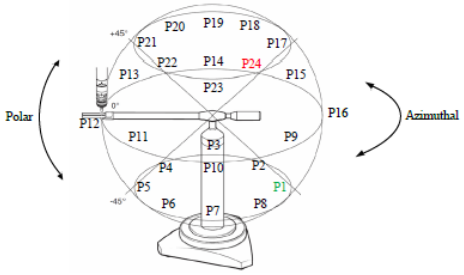

FIGURE 1. MCG Sampling Strategy (source: Renishaw).

Sample Size

Determination of the sample size needed for a specified margin of error, requires a standard deviation from the measurement process. A standard deviation is determined from a preliminary MCG experiment using a B&S Global Image CMM. From the 24 measurements taken, a standard deviation of 0.0014 mm is determined. Using the standard deviation, the sample size for the desired margin of error can be calculated using Eq. (5),

$$n = \left(\frac{Z \cdot \sigma}{m}\right)^2 \quad (5)$$

where Z is the z-score for a specific confidence interval (based on standard normal z-tables), σ is the standard deviation of the MCG measurement process and m is the margin of error. The sample size calculations can be seen in TABLE 2.

TABLE 2. Sample Size as a Function of Margin of Error

		Confidence Interval	
		$Z = 1.96$ @ 95%	$Z = 2.576$ @ 99%
Margin of Error	$m = \pm 0.001\ mm$	$n = \left(\frac{(1.96)(0.0014)}{0.001}\right)^2$ $n = 8.1$ $n = 9$ *measurements*	$n = \left(\frac{(2.576)(0.0014)}{0.001}\right)^2$ $n = 13.9$ $n = 14$ *measurements*
	$m = \pm 0.0005\ mm$	$n = \left(\frac{(1.96)(0.0014)}{0.0005}\right)^2$ $n = 32.2$ $n = 33$ *measurements*	$n = \left(\frac{(2.576)(0.0014)}{0.0005}\right)^2$ $n = 55.7$ $n = 56$ *measurements*

Examining the estimated margin of error, the sample size varies significantly. The margin of error is used to express the random sampling error of the MCG measurement process, for

example, for the 24 points of the MCG measurement process, the margin of error at 95% confidence is 0.00056 mm and at 99% confidence 0.00061 mm, respectively. Both are acceptable for the MCG process tolerance, therefore, the authors have chosen a sample size of 20 measurements, which produces, based on the previous process standard deviation, a margin of error at 95% confidence of 0.00074 mm and a margin of error at 99% confidence of 0.00081 mm. These margin of errors will ensure that the results will have a high-level of confidence. Furthermore, with this sample size, there is enough information to determine what the distribution of the data will be. Additionally, the chosen sample size will be compared to a baseline and a Monte Carlo simulation in *CMM Interim Performance Check Part 2: Case Study.*

MACHINE ERRORS

Data is collected over the course of weeks to ensure that environmental effects are inherent in the measurement data, along with the measurement process errors. Analysis of the measurement data covers machine geometry errors and summary statistics of the measurement process.

Geometry and Statistical Calculations

The machine geometry errors are calculated using the *ISO 10360* standards [1], [11] , as well as published work by Hocken, *et al.* [12] and available Hexagon Metrology literature [13]. The machine parameter sources and formulae are listed in TABLE 3 and can be seen in FIGURE 2.

TABLE 3. Geometric Parameters and Summary Statistics

Source	*Formulae*	*Comment*
Probing Form	$R_{max,point} - R_{min,point}$	MCG result
Scanning Form (THP, TLP, THN, TLN)	$R_{max,scan} - R_{min,scan}$	*ISO 10360-4*
XY Squareness*^	$\left(\frac{2(L_B - L_A)}{L_A + L_B}\right)_{XY} * radian$	$L_{A,B}$- Positions of arm, Machine Geometry Error
XZ Squareness*^	$\left(\frac{2(L_B - L_A)}{L_A + L_B}\right)_{XZ} * radian$	$L_{A,B}$- Positions of arm, Machine Geometry Error
YZ Squareness*^	$\left(\frac{2(L_B - L_A)}{L_A + L_B}\right)_{YZ} * radian$	$L_{A,B}$- Positions of arm, Machine Geometry Error
X Linear**x	$X_i + X_f$	*ISO 10360-2*, i – initial point, f – final point
Y Linear**x	$Y_i + Y_f$	*ISO 10360-2*, i – initial point, f – final point
Z Linear**	Not available	*ISO 10360-2*, Not available
Spatial 1**o	$(-X_1, -Y_1, -Z_1) + (X_7, Y_7, Z_7)$	*ISO 10360-2*
Spatial 2**o	$(X_2, -Y_2, -Z_2) + (-X_8, Y_8, Z_8)$	*ISO 10360-2*
Spatial 3**o	$(X_3, -Y_3, Z_3) + (-X_5, Y_5, -Z_5)$	*ISO 10360-2*
Spatial 4**o	$(-X_4, -Y_4, Z_4) + (X_6, Y_6, -Z_6)$	*ISO 10360-2*
Average Radius	$\bar{R} = \frac{1}{n}\sum_{i=1}^{n} R_i$	MCG health report.
Pivot Location	$O_i - O_f = (x_i, y_i, z_i) - (x_f, y_f, z_f) = \sqrt{x^2 + y^2 + z^2}$	Quality check.
Temperature	Environment (All data collected at 20 ± 1°C)	Extrinsic effect.

*Radial – tangential. Radial is defined as direction with similar signs (plus/plus or minus/minus)
^ Refer to FIGURE 2A below.
x Refer to FIGURE 2B below.
o Refer to FIGURE 2C below.
** *ISO 10360-2* data collection Strategy [1].

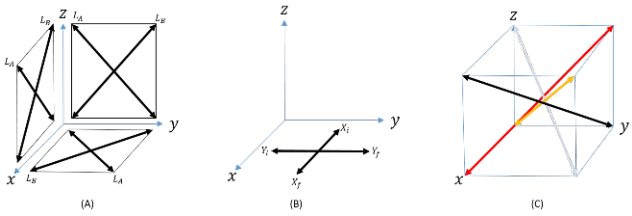

FIGURE 2. CMM Geometric Errors: (A) Squareness: (B) Linear; and (C) Spatial.

The geometry errors, as well as the summary statistics, are calculated from the sample size of 20, previously determined and are shown below in TABLE 4.

TABLE 4. Geometrical and Summary Statistics from 20 B&S Global Image MCG Measurements

Sources (units)	*20 Measurements*
Average Radius (mm)	*226.553*
Form Error (µm)	*5.000*
Pivot X (µm)	*0.400*
Pivot Y(µm)	*0.300*
Pivot Z(µm)	*-0.300*
Pivot XYZ (µm)	*0.800*
XY Squareness (arcsec)	*1.213*
XZ Squareness (arcsec)	*-0.059*
YZ Squareness (arcsec)	*1.713*
X Linear (mm)	*453.106*
Y Linear (mm)	*453.109*
Spatial 1 (mm)	*453.108*
Spatial 2 (mm)	*453.107*
Spatial 3 (mm)	*453.106*
Spatial 4 (mm)	*453.104*
C_p (form)	*2.11*
C_{pk}(form)	*1.98*
% over (form)	*0.0*
C_p (pivot)	*1.41*
C_{pk} (pivot)	*2.09*
% over (pivot)	*0.0*

The values from TABLE 4 will be used as the baseline for the Monte Carlo Simulation and compared to an additional 141, legacy MCG measurements which were taken over an extended period of time.

CONCLUSION

In conclusion, the MCG interim check has been implemented preliminarily on CMMs at LANL. The design strategy for testing provided a matrix with appropriate MCG arm lengths needed for the different sizes (measuring volumes) of CMMs. Machine specifications are used to determine the MCG limits of the CMMs. From these limits, error tolerance estimations are determined for probing, scanning and pivot repeatability where they provide threshold values for determining if the CMMs under test are in need of recalibration or adjusted for certain parameters.

The usefulness of this research aided in the determining how an interim check on a CMM can be beneficial during calibration cycles and help forecast if there could be any potential for

excursion from the specifications of the machines. It also lays out the required formulae, to conduct more experiments with the variety of machines listed in TABLE 1.

This work is the basis for part two of the research: *CMM Interim Performance Check Part 2: Case Study,* which will also include machine capability and Monte Carlo simulation for sample size uncertainty.

ACKNOWLEDGMENTS
The authors would like to thank the following management for their support in this research: Pit Technologies, Production Agency Quality & Prototype Fabrication. The authors would also like to thank Pit Sustainment for funding this research.

REFERENCES

[1] I. 10260-2, ""Geometrical Product Specification (GPS) - Acceptance and reverification tests for coordinate measuring machines (CMM) - Part 2: CMMs used for measuring linear dimensions," 2009.

[2] LANL, "Calibration Intervals," Los Alamos.

[3] T. Spepan, "LANL Performance Testing & Calibration Requirements for MQ-2 Coordinate," Los Alamos National Laboratory, Los Alamos, 2007.

[4] Leitz, "Leitz Reference 600/700/900 Technical Data_ M42-230-004-203," 2008. [Online].

[5] One, "ONE Next Gen. Specifications_72-95028," 2006. [Online].

[6] Lietz, "Leitz PMM-C Line_ M42-205-004-203," 2012. [Online].

[7] B. &. Sharpe, ""Global Performance Coordinate Measuring Machine_ 575-2011-04-28-ST-LANL," 2011. [Online].

[8] B. &. Sharpe, ""Global B Image Specification_62-95099," 2001. [Online].

[9] Tesa, "Tesa Micro-Hite DCC User Manual_3912.172.0512," 2005. [Online].

[10] ASME, "Methods for Performance Evaluation of Coordinate Measuring Machines - B89.4," ASME, 2001.

[11] ASME, ""Geometrical Product Specification (GPS) – Acceptance and reverification tests for coordinate measuring machines (CMM) – Part 4: CMMs used in scanning measuring mode," ASME, 2000.

[12] R. Hocken, Coordinate Measuring Machines and Systems, CRC Press, 2012.

[13] S. Holland, Hexagon Service Utilities Workbook, Hexagon Metrology, 2006.

CMM INTERIM PERFORMANCE CHECK PART 2: CASE STUDY

Lucas M. Valdez[1], Mario O. Valdez[2] and Joshua D. Montano[3]
[1] Pit Technologies
[2]Production Agency Quality
[3] Prototype Fabrication
Los Alamos National Laboratory (LANL)
Los Alamos, NM, USA

INTRODUCTION

The international standard for Coordinate Measuring Machines (CMM) verification is the *ISO 10360* series. Specifically, *ISO 10360-2*, states "*It is strongly recommended that the CMM be checked with regularity during the periods between periodic reverification* [1]."

Los Alamos National Laboratory (LANL) has a number of CMMs site-wide where calibrations are completed on an annual basis [2]. Customers rely upon accurate results to ensure product specifications are met thus, maintaining each CMM's performance is critical through the use of interim checks. With a variety of interim checks and artifacts available, task-specific checks and artifacts are highly recommended to mimic a production-type of measurement process. For LANL's applications, the use of a Machine Checking Gage (MCG), by Renishaw mimics a typical part's measurement volume well. In pursuing an interim check on a weekly basis between calibration cycles, assurance is obtained that each CMM is meeting the stated levels of accuracy in addition to allowing for spot-checks of each subsystem of the CMM.

The work described in this paper covers how the MCG is utilized in a case study for determining machine process capability and sample size. First the CMM used for this study will be detailed and how the data from part one of the research: *CMM Interim Performance Check Part 1: Design Criteria*, is used to study machine capability, Analysis of Variance (ANOVA) statistics and Monte Carlo simulations for validating the sample size accuracy.

CMM

As an example for determining MCG arm length a B&S Global Image has a measuring volume of 900 mm x 900 mm x 800 mm, where the coordinates are XYZ, respectively. From the measuring volume, a recommended MCG arm length was determined to be 380 mm.

MACHINE CAPABILITY

Data is collected over the course of weeks, to ensure that environmental effects are inherent in the measurement data, along with the measurement process errors. Analysis of the measurement data covers a gauge repeatability and reproducibility study (GR&R study), process capability metrics and a Monte Carlo simulation of the measurement process for sample size validation.

Gage Repeatability and Reproducibility Study

To certify the machine process capabilities, a GR&R study is conducted. Specific to this study, discrete measurement results from the CMM are utilized via deviations from the nominal data, where the percent contribution of the GR&R study sources are tabulated. Additionally, this study shows the process tolerance as the amount of deviation the MCG can have and still meet process requirements (i.e. the difference between the upper and lower specification limits). TABLE 1 identifies the GR&R sources, standard deviation (i.e. VarComp) and standard deviation percent contribution (i.e. % Contribution of VarComp), as well as the process tolerance.

TABLE 1. GR&R Study Percent Contributions with Process Tolerance

GR&R Study		
Sources	*VarComp (µm)*	*% Contribution of VarComp*
Total GR&R	*1.90*	*29.04*
Repeatability	*1.90*	*28.40*
Reproducibility	*0.02*	*0.65*
Operator	*0.02*	*0.65*
Part-To-Part	*4.60*	*70.96*
Total Variation	*6.50*	*100.00*
Process tolerance = *6.30 µm*		

Each source has a standard deviation which quantifies the source, effectively showing the sensitivity of each source on the process. It is shown that the part-to-part variation is the most significant error source for the process, which implies that the setup of the MCG was inconsistent. The operator has the least

influence, thus the smallest deviation which is logical since the MCG measurement processes is direct computer controlled (DCC). The total process variation is 0.0065 mm where the process tolerance (i.e. maximum bounding measurement error) is 0.0063 mm, a 0.0002 mm difference. This difference implies that the process lacks robust capability, yet with a submicron deviation acceptability can be reasoned through engineering judgment about what adjustments should be made to the measurement process and machine.

Furthermore, with the standard deviation at 95% confidence, the percent study variation and the precision-to-tolerance (P/T) ratio of the sources are tabulated. The (P/T) ratio is:

$$\frac{P}{T} = \frac{6\sigma}{USL - LSL} \qquad (1)$$

where 6σ (or ±3σ) is for 95% confidence. σ, is the standard deviation of the process and *USL* and *LSL* are the upper and lower specification limits, or tolerance, of the processes, respectively. The P/T ratio requirement is less than 10% for critical processes and less than 30% for non-critical processes where anything above 30% needs attention. TABLE 2 shows the results.

TABLE 2. GR&R Standard Deviation, 95% Confidence Standard Deviation, Percent Study Variation and P/T Ratio

	GR&R Study			
Source	*Standard Deviation (μm)*	*K× Standard Deviation (μm)*	*% Study Variation*	*P/T Ratio (%)*
Total GR&R	*1.3759*	*8.2553*	*53.89*	*131.04*
Repeatability	*1.3605*	*8.1629*	*53.29*	*129.57*
Reproducibility	*0.2053*	*1.2321*	*8.04*	*19.56*
Operator	*0.2053*	*1.2321*	*8.04*	*19.56*
Par-To-Part	*2.1506*	*12.9037*	*84.24*	*204.82*
Total Variation	*2.5531*	*15.3185*	*100.00*	*243.15*

FIGURE 1, provides a graphical representation of the tabulated values in TABLE 2. Furthermore, the total variation is larger than the process variation, suggesting that the measurement process of the CMM needs maintenance. Additionally, the largest source of variation is part-to-part and the smallest is operator. These results entail that the actual measurement process can identify significant irregularities in the data for each machine such as identifying systematic errors in need of correction. The operator variation is low since the operator only places/removes the MCG on the pivot point and the CMM stylus before and after the MCG run. Overall, the MCG has proven to be a good interim check for identifying machine geometry errors and measurement process variation sources.

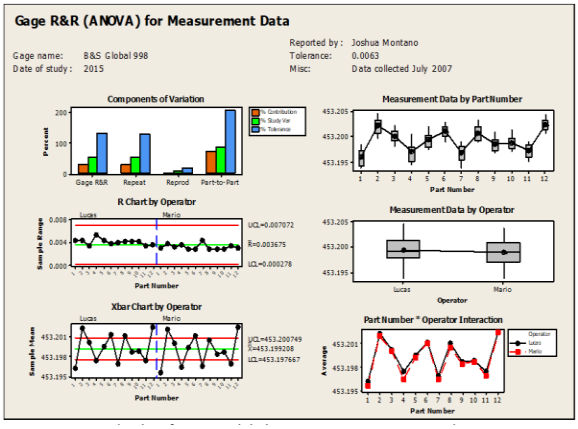
Gage R&R (ANOVA) for Measurement Data
Components of Variation
Measurement Data by Part Number
R Chart by Operator
Measurement Data by Operator
Xbar Chart by Operator
Part Number * Operator Interaction

FIGURE 1. GR&R Study Plots for B&S Global Image CMM Measurement Data

SAMPLE SIZE UNCERTAINTY

To validate the sample size determination, a Monte Carlo simulation of the MCG process is conducted.

Monte Carlo

Previously mentioned in the design strategy is a sample size needs to be determined to govern if the data is sufficient for data analysis purposes. However, to ensure that the sample size is adequate, a Monte Carlo simulation is performed with 10^5 trials [3], [4] for verification. The sample size uncertainty is used to validate the determined sample size and legacy data from a previous study of 141 MCG runs. The metrics for these simulations will be machine errors, specifically those of the geometry, summary statistics and process capability values.

Initially, the Monte Carlo simulation utilized a Gaussian (Normal) distribution in the random number generator, however, after running the simulation, the data presented itself being skewed-left. With the ill-fitting data to the chosen distribution, it proved that the results from the simulation would be an inaccurate representation of the measurement processes. This led to the decision for investigation and determination of the correct statistical distribution.

After numerous trials, the data determined that a lognormal distribution is the best statistical representation. To ensure that a lognormal distribution is accurate, a fit was set. FIGURE 2 below shows the results of the Monte Carlo run and a theoretical lognormal fit where the

threshold value in the upper-right legend shows that data-to-fit is less than 1% in error.

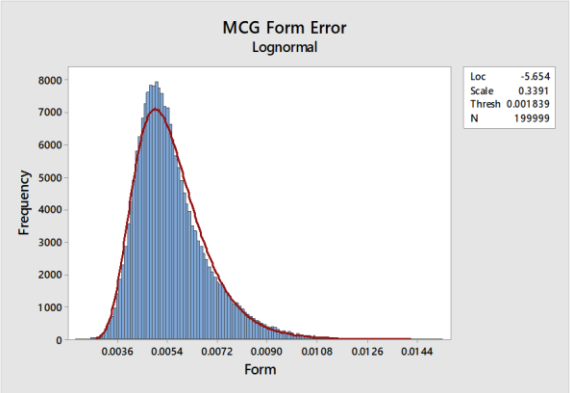

FIGURE 2. Monte Carlo Simulation of First 20 MCG Form Error Measurements

With the distribution now identified, the Monte Carlo simulation was then re-run with the same model, where maximum and minimum values for each MCG measurement are used as bounding parameters. Values for the MCG summary statistics, geometrical errors and measurement process capability, were determined and compared to the 20 initial MCG measurements and 141 legacy MCG measurements where TABLE 3 shows the results of the three sample sizes for the summary statistics, the machine geometry errors and process capability. The comparisons between the three sample sizes agree well with a majority of the machine parameters

TABLE 3. Comparison between the Determined, Simulated and Legacy Sample Size

Sources (units)	*20 Measurements*	*Monte Carlo*	*141 Measurements*
Average Radius (mm)	*226.553*	*226.554*	*226.552*
Form Error (µm)	*5.000*	*6.300*	*6.100*
Pivot *X* (µm)	*0.400*	*0.300*	*0.200*
Pivot *Y*(µm)	*0.300*	*0.300*	*0.400*
Pivot Z(µm)	*-0.300*	*-0.500*	*-0.400*
Pivot *XYZ* (µm)	*0.800*	*1.00*	*1.10*
XY Squareness (arcsec)	*1.213*	*1.223*	*0.782*
XZ Squareness (arcsec)	*-0.059*	*-0.229*	*-0.331*
YZ Squareness (arcsec)	*1.713*	*1.317*	*1.472*
X Linear (mm)	*453.106*	*453.106*	*453.104*
Y Linear (mm)	*453.109*	*453.111*	*453.107*
Spatial 1 (mm)	*453.108*	*453.109*	*453.104*
Spatial 2 (mm)	*453.107*	*453.107*	*453.103*
Spatial 3 (mm)	*453.106*	*453.107*	*453.103*
Spatial 4 (mm)	*453.104*	*453.105*	*453.101*
C_p (form)	*2.11*	*1.96*	*1.03*
C_{pk}(form)	*1.98*	*1.30*	*0.72*
% over (form)	*0.0*	*0.0*	*1.6*
C_p (pivot)	*1.41*	*1.50*	*0.96*
C_{pk} (pivot)	*2.09*	*2.06*	*1.29*
% over (pivot)	*0.0*	*0.0*	*0.0*

An additional comparison is between the measured and simulated measurement. To do this, the differences between the sets are calculated for each one of the sources listed in TABLE 4. The results between these comparisons are small for most of the sources tested. The largest differences are from the *XY* squareness, C_p and C_{pk} of the form error from the MCG.

TABLE 4. Difference between Measured and Simulated Measurement Sets

Sources (units)	*20 vs. Monte Carlo*	*141 vs. Monte Carlo*
Average Radius (µm)	*-0.500*	*-2.100*
Form Error (µm)	*-1.300*	*-0.200*
Pivot *X* (µm)	*0.1000*	*-0.100*
Pivot *Y* (µm)	*0.100*	*0.100*
Pivot *Z* (µm)	*0.200*	*0.100*
Pivot *XYZ* (µm)	*-0.200*	*0.100*
XY Squareness (arcsec)	*-0.010*	*-0.441*
XZ Squareness (arcsec)	*0.170*	*-0.102*
YZ Squareness (arcsec)	*0.396*	*0.155*
X Linear (µm)	*-0.300*	*-2.300*
Y Linear (µm)	*-1.800*	*-3.900*
Spatial 1 (µm)	*-1.000*	*-4.900*
Spatial 2 (µm)	*-0.500*	*-4.300*
Spatial 3 (µm)	*-1.000*	*-4.400*
Spatial 4 (µm)	*-0.600*	*-3.800*
C_p (form)	*0.150*	*-0.930*
C_{pk}(form)	*0.680*	*-0.580*
% over (form)	*0.000*	*1.600*
C_p (pivot)	*-0.090*	*-0.540*
C_{pk} (pivot)	*0.030*	*-0.770*
% over (pivot)	*0.000*	*0.000*

A Monte Carlo simulation is also performed on the summary statistics of the form error, pivot error and average radius of the MCG. TABLE **5** shows the results.

TABLE 5. Comparison of the Summary Statistics for the From, Pivot Repeatability and Average Radius of both the Measured and Simulated Results

Statistics	*Form (20) (mm)*	*Pivot (20) (mm)*	*Ave. Radius (20) (mm)*	*Form (Sim) (mm)*	*Pivot (Sim) (mm)*	*Ave. Radius (Sim) (mm)*	*Form (141) (mm)*	*Pivot (141) (mm)*	*Ave. Radius (141) (mm)*
Ave.	*0.005*	*0.001*	*226.553*	*0.006*	*0.001*	*226.554*	*0.006*	*0.001*	*226.552*
Std. Dev	*0.001*	*0.001*	*0.001*	*0.001*	*0.001*	*0.0001*	*0.002*	*0.001*	*0.001*
Skew.	*-0.049*	*0.539*	*2.381*	*-0.235*	*-0.078*	*0.003*	*0.770*	*1.528*	*0.562*
Kurt.	*-1.084*	*-0.689*	*8.549*	*-0.139*	*-0.579*	*-0.071*	*0.846*	*3.171*	*0.316*
Min.	*0.004*	*0.000*	*226.552*	*0.003*	*0.0000*	*226.553*	*0.003*	*0.000*	*226.548*
Q1	*0.004*	*0.001*	*226.553*	*0.006*	*0.001*	*226.554*	*0.005*	*0.001*	*226.551*
Med.	*0.005*	*0.001*	*226.553*	*0.006*	*0.001*	*226.554*	*0.006*	*0.001*	*226.551*
Q3	*0.006*	*0.001*	*226.553*	*0.007*	*0.001*	*226.554*	*0.007*	*0.001*	*226.553*
Max.	*0.006*	*0.002*	*226.555*	*0.009*	*0.002*	*226.555*	*0.011*	*0.003*	*226.556*

From TABLE 5 the difference between measurement samples and simulations are small for most of the sources tested. The largest differences are from the skewness and kurtosis of the form error, pivot repeatability and average radius of the measurements. These results show that our sample size of 20 measurements is adequate for the MCG measurement process, thus large uncertainty in the measurement results are unlikely. In addition to TABLE 5, TABLE 6 is the resulting difference between the measurement sample sizes and the Monte Carlo simulation.

TABLE 6. Difference between the Sample Sizes and Monte Carlo Simulation

Statistics	*20 vs. Monte Carlo (mm)*	*141 vs. Monte Carlo (mm)*
Form		
Ave.	*-0.0013*	*-0.0002*
Std. Dev	*-0.0001*	*0.0007*
Skew.	*0.1859*	*1.0051*
Kurt.	*-0.9440*	*0.9853*
Min.	*0.0007*	*0.0002*
Q1	*-0.0014*	*-0.0007*
Med.	*-0.0013*	*-0.0003*
Q3	*-0.0014*	*0.0000*
Max.	*-0.0023*	*0.0027*
Pivot		
Ave.	*-0.0002*	*0.0001*
Std. Dev	*0.0000*	*0.0002*
Skew.	*0.6175*	*1.6065*
Kurt.	*-0.1094*	*3.7513*
Min.	*0.0003*	*0.0002*
Q1	*-0.0002*	*0.0000*
Med.	*-0.0002*	*0.0000*
Q3	*-0.0002*	*-0.0001*
Max.	*-0.0004*	*0.0011*
Radius		
Ave.	*-0.0005*	*-0.0021*
Std. Dev	*0.0003*	*0.0010*
Skew.	*2.3782*	*0.5590*
Kurt.	*8.6207*	*0.3871*
Min.	*-0.0002*	*-0.0042*
Q1	*-0.0005*	*-0.0028*
Med.	*-0.0006*	*-0.0023*
Q3	*-0.0005*	*-0.0014*
Max.	*0.0005*	*0.0014*

CONCLUSION

The measurement results provided useful statistics to aid in the determination of potential errors using the MCG. Additional information is gained about the machine geometry errors, thus aiding in the determination if these errors are too large to ignore. The measurement data also provided machine capability statistics to determine if the MCG process is capable on the CMMs under test. These results showed that the CMMs under test are capable of measuring accurately but do influence the measurement results. The GR&R study results indicate low contributions from reproducibility. This is a positive indication that operator influence is minimal and most of the error is coming from the MCG and the CMM. The Monte Carlo simulation compared very well with the 20 measurements and the 141 measurements, therefore proving the sample size of 20 measurements is adequate for our testing.

Overall, the MCG provided to be a very beneficial tool for interim checking of the CMMs. This interim check will help lower the potential for nonconformance reporting and minimizes risk for passing bad parts when the CMM is out of specification. The MCG also helps with determining potential errors associated with the CMM geometry and also provides useful data to calculate the necessary statistics needed for machine capability testing.

ACKNOWLEDGMENTS

The authors would like to thank the following management for their support in this research: Pit Technologies, Production Agency Quality & Prototype Fabrication. The authors would also like to thank Pit Sustainment for funding this research.

REFERENCES

[1] I. 10260-2, ""Geometrical Product Specification (GPS) - Acceptance and reverification tests for coordinate measuring machines (CMM) - Part 2: CMMs used for measuring linear dimensions," 2009.

[2] L. A. N. Laboratory, "Calibration Intervals," Los Alamos.

[3] A. Steele and R. Douglas, "Simplifications from Simulations: Monte Carlo Methods for Uncertainties," NCSLI Measure, 2016.

[4] R. Jeges, "Monte Carlo simulation in MS Excel-Project Smart," 2007. [Online]. Available: https://www.projectsmart.co.uk/docs/monte-carlo-simulation.pdf.

PERFORMANCE INVESTIGATION OF A LARGE-SCALE ROTARY TABLE UNDER LOADS

Qichang Wang[1], Gert Goch[1], Axel von Freyberg[2], Frank Horn[2], Norbert Steffens[3] and Andreas Fischer[2]
[1] Center for Precision Metrology,
University of North Carolina at Charlotte,
Charlotte, NC, USA
[2] Bremen Institute for Metrology Automation and Quality Science,
University of Bremen,
Bremen, Germany
[3] Hexagon Manufacturing Intelligence,
Wetzlar, Germany

1. INSTRUCTIONS

Geometric inspections of large-scale parts, at affordable costs and within reasonable measuring time, are necessary in manufacturing industries. For example, to improve the reliability and safety of wind energy system (WES) over the lifetime of 20 years, WES manufacturers need to inspect a variety of components such as main bearings, gears and pitch bearings [1]. Multi-axis measuring devices including coordinate measuring machines (CMMs), gear measuring instruments (GMI), form testers, etc. are versatile instruments for these applications. As key components of multi-axis measuring devices, rotary tables provide a quick rotary positioning of components to assess measurands.

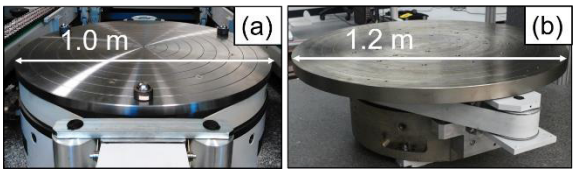

FIGURE 1. Large-scale rotary tables with external pressurized bearings: (a) Zollern ZHRT 1000.0340.0550 hydrostatic rotary table (b) Zollern ZART 1200.0390.0 aerostatic rotary table.

To keep pace with the increasing demands on the measuring volume and load capacity, large-scale rotary tables are designed and built (Figure 1). Complicated aerostatic and hydrostatic bearing systems are implemented to provide very smooth rotational motion under various maximum loads up to several metric tons.

Although the performances of rotary tables have been improved by numerous efforts in design and production, there still exist non-trivial and undesired error motions, originating from the drive train, bearings, etc. Commonly, error maps are produced at non-load situations and are used for all loading scenarios. However, this strategy needs to be reconsidered when large workpieces with masses up to several tons become the measuring objects. Different loads may deviate the operation conditions of bearings and drive train components by varying different amounts. It is also not clear whether and how the error motions change in asymmetric loading scenarios. In real applications, gravity centers of non-rotationally symmetric parts may be eccentric to the rotary axis. Rotationally symmetric parts might also not be centered very precisely, because large-scale parts are loaded onto rotary tables by traveling overhead cranes, fork lifters or lift carriages [2].

Because of the complicated and nonflexible setup, the traditional calibration methods [3] are not suitable for cases when the rotary tables are under load. This paper applies a calibration method, which only requires a simple, quick and flexible setup [4]. This method is able to separate the deviations of rotary table, artifact (circular ball plate) and measuring device (3-axis CMM) simultaneously. Error motions of rotary tables under symmetric and asymmetric loads were investigated experimentally. Section 2 describes experimental setups. Section 3 reports and discusses experimental results.

2. EXPERIMENTAL SETUPS

2.1 Workpiece delivery system

A Zollern ZHRT 1000.0340.0550 hydrostatic rotary table at the Bremen Institute for Metrology, Automation and Quality Science (BIMAQ), University of Bremen, was investigated. This table and a Leitz PMM-F 30.20.07 form a 4-axis CMM for large scale metrology applications. A delivery system was designed and installed to facilitate the handling of large and heavy parts (Figure 2). Workpieces are loaded onto a steel or granite measuring palette using a traveling overhead crane or fork lifter at the loading gate. Then, the measuring palette is transported to and loaded on the rotary table. The unloading process is performed in the reverse way. Kinematic coupling between the rotary table and the palette assures positioning repeatability.

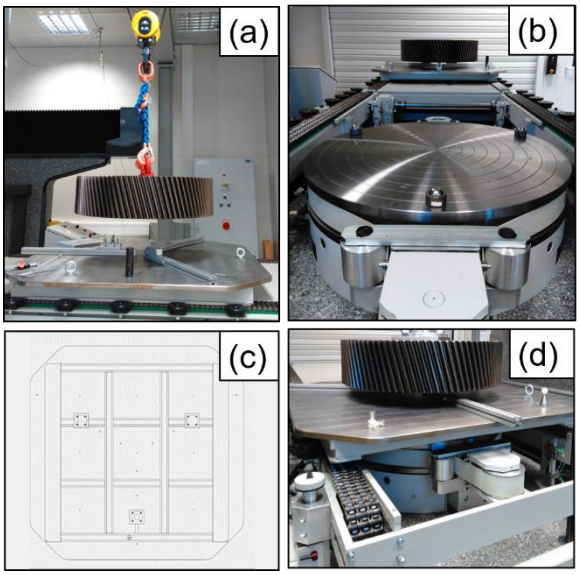

FIGURE 2. Loading procedure of a heavy gear onto hydrostatic rotary table: (a) preparation and placement of a helical gear on a measuring palette using traveling overhead crane; (b) transportation of the measuring palette from loading gate to rotary table, with three hemisphere components for kinematic coupling; (c) schematic of the steel palette (bottom view); (d) loading the measuring palette on rotary table.

2.2 Symmetric and asymmetric loads

Two sets of experiments were carried out to investigate the performances of this rotary table under symmetric and slightly asymmetric loads with eccentricity *X*. The load configurations are illustrated in Figure 3.

In the first set of experiments, five symmetric loads up to $F = 33.8$ kN were designed (Figure 4): (1) non-load (2) palette only (3) palette and a helical external gear as measuring object (4) palette, a helical gear and 4 spur gears as additional load (5) palette, a helical gear and 8 spur gears. From case 3 to case 5, multiple points were measured on the top lands of gears to determine the coordinates of their gravity centers. Then, the overall eccentricities were calculated. Since the eccentricities were less than 5.0 mm, the rotary table was considered as symmetrically loaded.

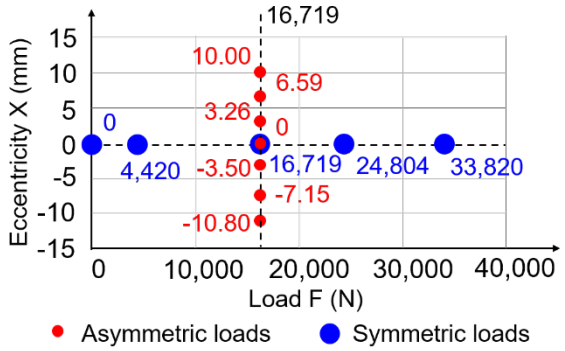

FIGURE 3. Load configurations in two sets of experiments with 5 symmetric loading cases between non-load and $F = 33.8$ kN (blue dots), and 7 asymmetric loading cases between $X = -10.80$ mm and $X = 10.0$ mm at $F = 16.7$ kN (red dots).

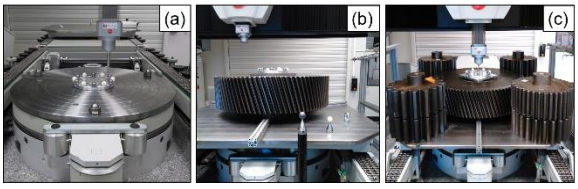

FIGURE 4. Experimental setup for rotary table under symmetric loads: (a) case 1: non-load; (b) case 3: measuring palette and a helical gear; (c) case 5: palette, a helical gear and 8 spur gears as additional load.

In the second set of experiments, the ring gear was shifted off-center intentionally to create seven slight asymmetric loading cases. These sets of experiments mimicked measuring tasks, where positioning accuracies of heavy parts are limited.

Figure 5 illustrates the positioning process of a helical ring gear. The gear was placed on the blocks of three linear motions guides, which were

fixed on the measuring palette. Three short pins inserted into the blocks had contact with the inner cylindrical surface of the gear. By calculating and adjusting the position of short pins and blocks before loading the ring gear, the eccentricity value of the ring gear can be defined with an uncertainty below 1 mm. The inner cylindrical surface was measured to calculate the overall eccentricity.

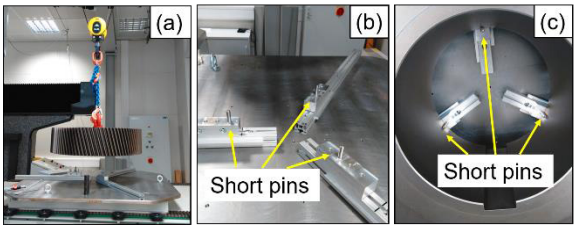

FIGURE 5. Experimental setup for rotary table under slightly asymmetric loads: (a) loading the ring gear onto the linear motions guides; (b) three linear motion guides and accessories; (c) preset the positions of three blocks and three short pins to constraint the position of the gear.

2.4 Fixture of artifact

The circular ball plate artifact consists of a base plate, 6 tungsten carbide spheres and 6 ceramic spheres (Figure 6).

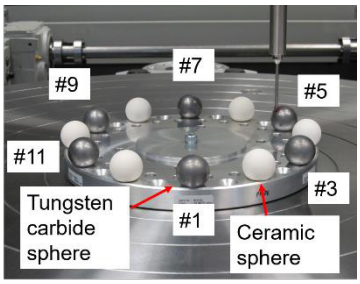

FIGURE 6. Circular ball plate artifact with six tungsten carbide spheres and six ceramic spheres.

The base plate has a tapered hole at the center, which matches the shape and size of a cylindrical fixturing component. In case 1 and 2 of symmetrically loading experiments, the artifact was fixed on the rotary table or the measuring palette, respectively. Figure 7 illustrates how the artifact was clamped on the measuring palette.

In the other cases, the artifact was moved up to the top of the helical gear for good accessibility. However, the artifact had a smaller diameter than the inner cylindrical surface of the gear. To solve this problem, the artifact was put on a rectangular plate, which was placed on top of the gear (Figure 8).

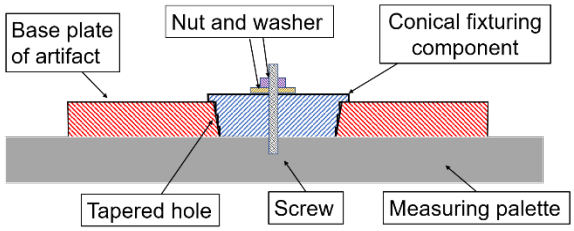

FIGURE 7. Schematic of clamping method for the artifact on measuring palette.

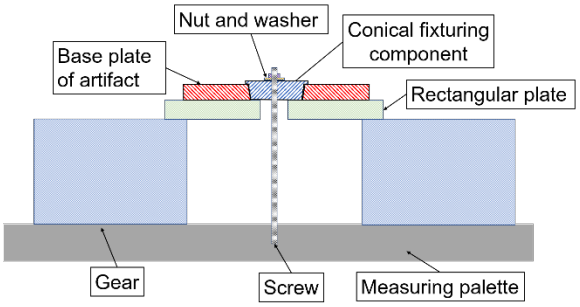

FIGURE 8. Schematic of clamping method for artifact on top of helical gear.

3. EXPERIMENTAL RESULTS

3.1 Calibration procedure

In all experiments, the rotary table was rotated by four cycles in the counter-clock-wise (CCW) direction in steps of 7.5°. At each step, 15 points were probed on every tungsten carbide sphere (#1, #3, #5, #7, #9 and #11).

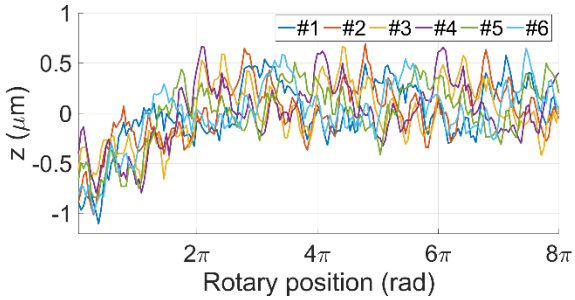

FIGURE 9. Measured z coordinates of six sphere centers in four cycles in non-load case. No warm-up routine was executed.

Figure 9 demonstrates measured *z* coordinates of six sphere centers in four cycles. As a uniform warm-up routine was not found and executed before the experiments, the rotary table took the first cycle to reach a stable operating condition.

Therefore, only data from cycle 2 to cycle 4 was used for analysis.

3.3 Experimental results

A rotary table has three translational error motions δ_x, δ_y and δ_z, two tilt error motions ε_x and ε_y, and one angular positioning deviation ε_z (Figure 10).

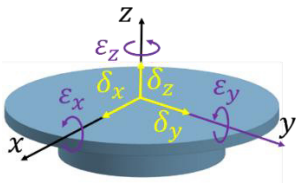

FIGURE 10. Six error motions of rotary tables.

As presented in [4], all error motions except δ_z had periods of 2π in the non-load case. δ_z did not have a fully repeatable pattern in three cycles, which may result from the thickness variation of the oil film used for the hydrostatic bearing, because temperature control of an oil film in a closed system is very challenging. Similar phenomena existed in the other tested loading scenarios.

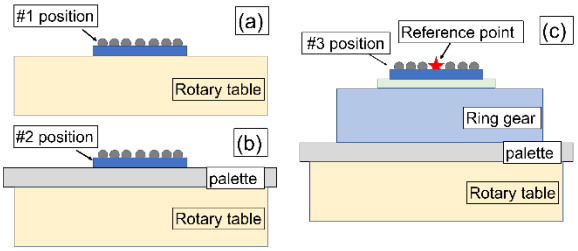

FIGURE 11. Illustration of three artifact positions in the experiments, with a reference point defined as the enter of approximated wokpiece coordinate system at the #3 position.

In first set of experiments, the artifact was positioned at three different heights (Figure 11). The center of the approximated wokpiece coordinate system at the #3 position is defined as the reference point. Separated error motions of case 1 and case 2 were tranformed to the refence point to be compared with results of the other cases. δ_x and δ_y were recalculated according to Equation 1:

$$\begin{bmatrix}\delta_x\\ \delta_y\end{bmatrix}_{AW,new} = \begin{bmatrix}\delta_x\\ \delta_y\end{bmatrix}_{AW} + H\begin{bmatrix}\varepsilon_y\\ -\varepsilon_x\end{bmatrix}_{AW} \quad (1)$$

H is the height difference between the #1 (or #2) position and the #3 position of the artifact. Subscript *AW* denotes the approximated workpiece coordinate system (WCS) at the #1 or #2 position. Subscript *AW*, new denotes the transformed approximated WCS.

Figure 12 shows the approximated error motions in symmetric loading cases from non-load to *F* = 33.82 kN. In most metrology tasks, the measuring palette is loaded onto the rotary table together with workpieces. Case 2 to case 5 had similar ε_x, ε_y and ε_z, which showed that changing values of symmetric loads had negligible influence on the tilt error motions and angular positioning deviations of the rotary table. The error motions of the non-load case were different from the ones of other cases. Further investigation is needed to investigate the causes.

This rotary table had consistent δ_x and δ_y from medium load (case 3) to heavy load (case 5). However, δ_x and δ_y under non-load and light load (case 2) were different from heavy loads. Presumably, this is partially due to the transformation of the coordinate system of first two cases to the #3 position. Recalculated curves of δ_x and δ_y were influenced by the uncertainty of the tilt error motions. Because δ_z was not repeatable in multiple cycles, the approximated curves in five cases are different.

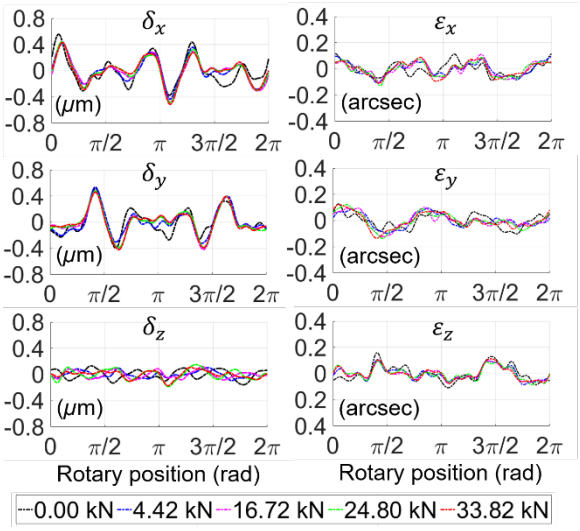

FIGURE 12. Separated error motions of a hydrostatic rotary table under symmetric loads from F = 0.00 kN to F = 33.82 kN.

Figure 13 shows the approximated error motions in the asymmetric loading cases when *F* = 16.7 kN load was shifted along the *x*-axis from with an eccentricity *X* = -10.80 mm to

$X = 10.00$ mm. No significant differences in all seven cases were found. This set of experiments confirms that the performances of rotary tables are not significantly affected, when a symmetric medium load is placed with an eccentricity in the millimeter range. This is meaningful because the positioning accuracies of workpieces in many applications are limited due to large size and heavy weight.

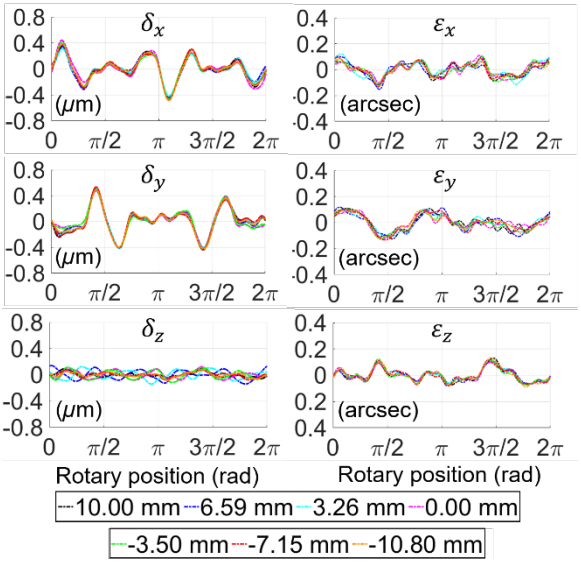

FIGURE 13. Separated error motions of a hydrostatic rotary table under seven asymmetric loads of F = 16.7 kN.

4. SUMMARY

This paper reports the performances of a heavy-duty hydrostatic rotary table under symmetric and slightly asymmetric loads, when the table was rotated in the CCW direction. Error motions of the rotary table under loads were separated using a 3-axis CMM and a circular ball plate artifact. This rotary table demonstrates consistent performances in most tested loading scenarios. As a result, load eccentricities to the rotational axis of a few millimeter do not significantly influence its error motions.

5. ACKNOWLEDGEMENT

The authors are grateful to the Center for Precision Metrology and Hexagon Metrology for financial support.

6. REFERENCES

[1] Goch, G., Knapp, W., Härtig, F. (2012). Precision engineering for wind energy systems. *CIRP Annals*, *61*(2), 611-634.

[2] Schmitt, R. H., Peterek, M., Morse, E., Knapp, W., Galetto, M., Härtig, F., Goch, G., Hughes, B., Forbes, A., Estler, W. T. (2016). Advances in large-scale metrology–review and future trends. *CIRP Annals*, *65*(2), 643-665.

[3] Suh, S. H., Lee, E. S., Jung, S. Y. (1998). Error modelling and measurement for the rotary table of five-axis machine tools. *The International Journal of Advanced Manufacturing Technology*, *14*(9), 656-663.

[4] Wang, Q., Miller, J., Von Freyberg, A., Steffens, N., Fischer, A., Goch, G. (2018). Error mapping of rotary tables in 4-axis measuring devices using a ball plate artifact. *CIRP Annals*, 67(1), 559-562.

The Effect of Suqareness on the Performance of the Ultra-Precision Machine

Tao Lai[1,2], Xiaoqiang Peng[1,2], Guipeng Tie[1,2] ,Feng Shi[1,2], Lin Zhou[1,2]and Ye Tian[1,2]
[1] College of Artificial Intelligence
National University of Defense Technology
Changsha, Hu'nan, China
[2] Hu'nan Key Laboratory of Ultra-precision Machining Technology
Changsha, Hu'nan, China

INSTRUCTIONS

To achieve a measuring uncertainty of less than ultra-precision level, it is generally necessary to analyze the effect of squareness on machine, such as CMMs and profilometer [1]. These squareness of the movement axis of high-precision platforms require more accuracy. The accurate error measurement of the precision motion platform is the prerequisite for the implementation of the motion platform operations [2].

For squareness measurement method, in literature three fundamentally three category method are used to measure the squareness in a metrology system. The first category includes parametric modeling methods, such as the integrated geometric error modeling method [3] and the product of exponential modeling method [4][5]. The disadvantage of this category is introduced the model assumptions (e.g. neglecting crosstalk between the slides).The second category uses standard to measure squareness. The standards such as L-square [6] and dial gauges [7]. But the measurement accuracy is limited by the standards. The third category measure the sqaureness based on error separation [8,9,10,11]. This technique may also use the standards, but the accuracy is not limited by the standards. Therefore, a small uncertainty can be obtained by the error separation.

For effect model of squareness on measurement, there are few literatures about the effect model. Jian Z. et.al.[12] studied the influence of 21 geometrical errors of machine tools on precision of on-line measuring. Qiu G. et.al. [13] investigated the mathematical model of contacting aspheric surface contour measurement. The effect of squareness on micro-aspheric surface profile measurement is introduced by A. Shibuya.et al [14].
The ability and uncertainty of the geometric calibration and compensation of the metrology system should be very important design consideration, especially if a calibration uncertainty in the ultra-precision range is required. And the squarenesss of geometric error is main error to affect the measurement. Therefore, the effect model of squareness is necessary to obtain with an accurate way.

EFFECT OF SQUARENESS ON CURVED SURFACE MEASUREMENT

The effect of three squareness on measuring artifact is shown in Fig.1. The ideal point A is ideal point without squareness between the axes. The measurement point A' is actual measurement point with squareness between the axes. As shown in Fig.1 (a), the ideal point A is transferred to measurement A' due to squareness S_{xy} between the axis X and axis Y from the view I. The coordinate relationship between the point A and the point A' is obtained by

$$\begin{cases} x = x' + y' \tan S_{xy} \\ y = y' / \cos S_{xy} \\ z = f(x, y) \end{cases} \quad (1)$$

As shown in Fig.1(b), the ideal point A is transferred to measurement A' due to squareness S_{yz} between the axis Z and axis Y from the view H. The coordinate relationship between the point A and the point A' is obtained by

$$\begin{cases} x = x' \\ y = y' + z' \tan S_{yz} \\ z = f(x, y) \end{cases} \quad (2)$$

As shown in Fig.1(c), the ideal point A is transferred to measurement point A' due to squareness S_{xz} between the axis Z and axis X from the view J. The coordinate relationship between the point A and the point A' is obtained by

$$\begin{cases} x = x' + z'\tan S_{xz} \\ y = y' \\ z = f(x,y) \end{cases} \quad (3)$$

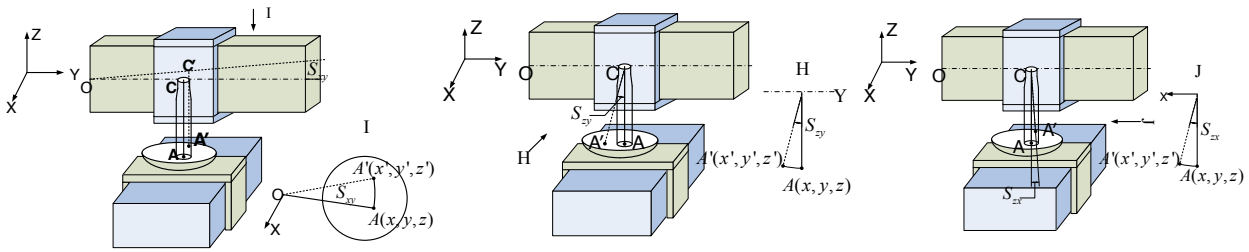

(a) squareness Sxy between the axis X and axis Y (b) squareness Szy between the axis Z and axis Y (c) squareness Szx between the axis Z and axis X

Figure 1. Effect of three suqareness on measuring artifact

Summation of equation(1)-(3) yield

$$\begin{cases} x = x' + y'\tan S_{xy} + z'\tan S_{xz} \\ y = y'/\cos S_{xy} + z'\tan S_{yz} \\ z = f(x,y) \end{cases} \quad (4)$$

The measurement point A is affected by three squareness and relationship between the point A and A' is described by equation (4).

SIMULATION

The artifacts Sphere and Bicubic Curved Surface are applied to calculate the measurement error distribution with the squareness 0.1arcsec. The aperture of the Sphere is 75mm and the curvature radius is 289mm as shown in Fig.2(a). The aperture of Bicubic Curved Surface is also 75mm ,and the curved surface equation is z=0.0025[(x/10)^3+(y/10)^3] as shown in Fig.2(b). Therefore, the measurement error is generated by the sqaureness at 0.1 arcsec when artifact Sphere is measured. The measurement error distribution is shown in Fig.3, actually, the distribution is the difference between the measurement point A and A'. The peak value 5nm is emerged at the edge of the Sphere with the squareness S_{xy} at 0.1 arcsec as shown in Fig.3(a). Similarly, the peak value 40nm is obtained at the edge of the Sphere with the squareness S_{zy} and S_{zx} at 0.1 arcsec as shown in Fig.3(b) and (c). The two error distributions due to the S_{zy} and S_{zx} are symmetric. The measurement error distribution is shown in Fig.4 when the artifact Bicubic Curved Surface is measured. The measurement error of Bicubic Curved Surface is smaller than error of Sphere, and the peak values are generated at 2nm, 0.05nm and 0.05nm by the squareness S_{xy} , S_{zy} and S_{zx} respectively.

(a) Sphere *(b) Bicubic Curved Surface*

Figure.2 Artifact Sphere and Bicubic Curved Surface

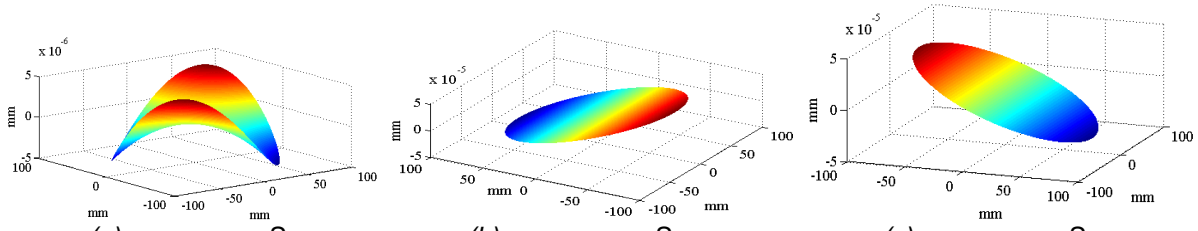

(a)squareness Sxy *(b) squareness Szy* *(c) squareness Szx*

Figure. 3 Difference between measurement point A and A' on Sphere due to squareness

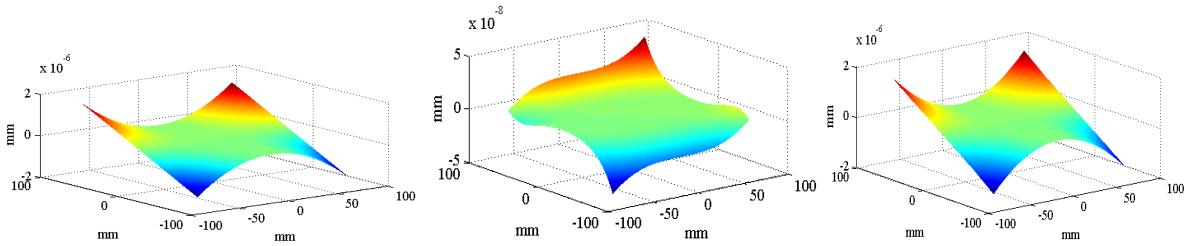

(a)squareness S_{xy} *(b) squareness S_{zy}* *(c) squareness S_{zx}*

Figure. 4 Difference between measurement point A and A' on Bicubic Curved Surface due to squareness

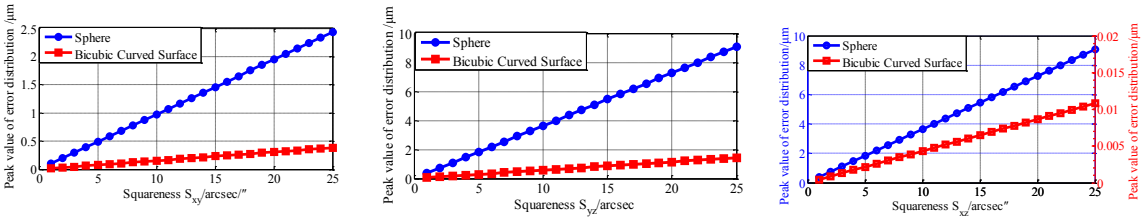

(a)squareness S_{xy} *(b) squareness Szy* *(c) squareness Szx*

Figure.5 Relationship between the peak value and the squareness

Actually, the squareness is greater than 0.1 arcsec. For precision measurement machine, the squareness is varied form 1 arcsec to 30 arcsecs or even larger. Therefore, the relationship between the peak value and the squareness is shown in Fig.5. As shown in Fig.5(a),(b) and (c), there is a linearity relationship between the peak value and the squarenss. At a same squareness, the peak value of Sphere is larger than the peak value of Bicubic Curved Surface. For measuring the Sphere, the squareness S_{xy} between the axis X and Y is weak error compared with the other two squareness But for measuring the Bicubic Curved Surface, the squareness S_{xy} is main error compared with the other two squareness. Therefore, the measurement error is differently affected by three squareness when the machine measures different curved surfaces.

According to the equation (4), the effect of three squareness on measurement curved surface.is obtained as shown in figure 6. Similarity, the peak value of Sphere is larger than the peak value of Bicubic Curved Surface at any squareness value. And it is a linearity relationship between the peak value and the squareness. Therefore, the effect of suqareness on measurement curved surface is related to aperture and the curvature radius.

CONCLUSION

In this paper, the effect model of squareness on measuring curved surface is independently built on ultra-precision cartesian coordinate measurement machine. The relationship between ideal point and actual measurement point under the affection of squareness is obtained. For a single squareness at 0.1 arcsec, the difference between measurement ideal point and actual measurement point on Sphere and Bicubic Curved Surface is calculated. The peak values of the error distribution of Sphere and Bicubic Curved Surface are 5nm/2nm 、 40nm/0.05 nm and 40nm/0.05nm due to the squarenes Sxy , Szy and Szx respectively. For three squareness 0.1 arcsec, the measurement errors of Sphere and Bicubic Curved Surface are 50nm and 2nm respectively. Therefore, the measurement error is differently affected by three squareness when the machine measures different curved surfaces. At last, with the value of squareness increased, the peak value of measurement error is increased. There is a linearity relationship between the peak value and the squareness.

ACKNOWLEDGEMENT

This work is financially supported by the Science Challenge Project (TZ2018006), Key Research and Development Plan (2016YFB1102304), National Natural Science Foundation of China. (No.51405151)

REFERENCES

[1] Theo Ruijl, Ultra Precision Coordinate Measuring Machine, the Technology University Delft, the Netherlands, 2001:107-102.

[2] Henselmans R., Cacace L.A., Kramer G.F.Y., Rosielle P.C.J.N., Steinbuch M, The NANOMEFOS non-contact measurement machine for freeform optics,. Precision Engineering 2011, 35 : 607–624

[3] Zhu S, Ding G, Qin S. Integrated geometric error modeling, identification and compensation of CNC machine tools. Int J Mach Tools Manuf 2012;52(1):24–9.

[4] Fu G, Fu J, Xu Y. Product of exponential model for geometric error integration of multi-axis machinetools. Int J Adv Manuf Technol 2014;71(9/12):1653–67.

[5] Yu Qiao, Youping Chen, Jixiang Yang, Bing Chen, a five-axis geometric errors calibration model based on the common perpendicular line (CPL) transformation using the product of exponentials (POE) formula. Int J Mach Tools Manuf 2017;118-119:49-60.

[6] Jie, Wang SJ, Sun YB. A way of squareness measurement on heavy numerical control machine tool with laser interferometer. Meas Technol 2009;5(7), 072011-1-072011-5.

[7] Wang X. The squareness between the motions parts of machine are measured by a square. Machinist 1994; 6:15–6.

[8] Lai T, Peng X, Tie G, et al. A novel way of squareness measurement on ultra-precision motion stage basing on the error separation[C].SPIE: Eighth International Symposium on Advanced Optical Manufacturing and Testing Technology. 2016:96840D. IDS:BG2JX

[9] Lai T, Peng X, Tie G, et al. High Accurate Squareness Measurement Squareness Method for Ultra-Precision Machine Based on Error Separation. Precision Engineering, 2017. IDS: EW4AI

[10] Lai T, Liu J, Shan Y, et al. Out-of-Squareness Measurement on Ultra-Precision Machine Based on the Error Separation SPIE: Modeling Aspects in Optical Metrology VI,. 2017, Vol: 10330, DOI: 10.1117/12.2270171.

[11] Lai T, Peng X, Junfeng L, Tie G, et al. High accurate measurement and calibration of the squareness on ultra-precision machine based on error separation. Proceedings of Mechanical Engineers Part B: Journal of Engineering Manufacture, 2017(4):095440541773757

[12] Jian Zhen, Study on Influence of Geometrical Error of Machine Tools on Precision of On-line Measuring. Nanjing University of Aeronautics and Astronautics, 2008.

[13] Qiu G , Guo P , Xie B , Yang X, Wang Y. Mathematical model of contacting aspheric surface contour measurement. Optics and Precision Engineering, 2007,15(4):492-498.

[14] A. Shibuya, Y. Nagaike, A spiral scanning probe system for micro-aspheric surface profile measurement, Int J Adv Manuf Technol (2010) 46:845–862.

USING ERROR SEPARATION TO TEST ULTRA HIGH ACCURACY SPINDLES

Dave Arneson, Henry Arneson, and Dan Oss
Professional Instruments Company
Hopkins, Minnesota, USA

ABSTRACT
To test the accuracy of a modern ultra-precise air bearing spindle for a diamond turning machine you need to use some sort of error separation technique. But more than just deciding to perform a reversal or a multi-probe test, you need to do a careful assessment of whether or not your test hardware is up to the task. This paper looks at what we at Professional Instruments are doing to test our ISO 5.5 spindle, which needs to have axial and radial accuracies of better than 12.5 nm at speeds from 500 to 10,000 rpm.

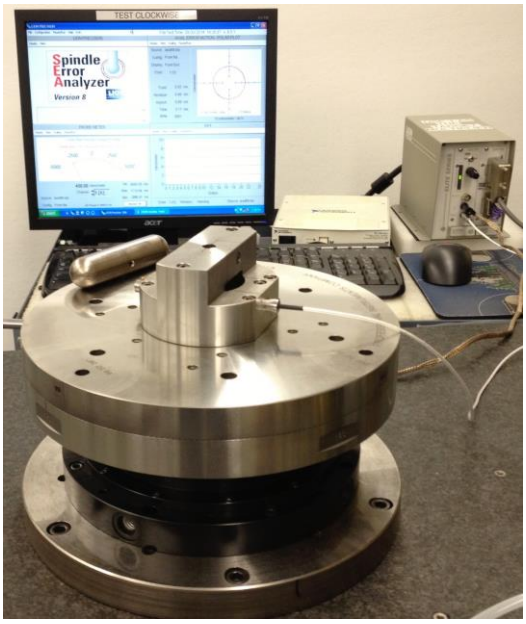

FIGURE 1. Error separation test of a Professional Instruments ISO 5.5 air bearing spindle.

INTRODUCTION
The ASME B89.3.4 Standard Axes of Rotation provides a comprehensive description of modern spindle error motion terms [1]. Marsh describes the procedures to accurately capture error motion of a spindle according to this standard [2].

Before advances in computers, data acquisition, capacitive sensors and encoders enabled the development of modern spindle error analyzers, error motion measurements were costly, time consuming, and limited to low speeds. After careful consideration, we chose to use a modified multiprobe technique with an indexing plate that rotates a single probe for our testing. This requires calibration of only a single probe and, more importantly, it doesn't require indexing the ball during our tests.
Error separation is important because two-lobe errors tend to be the largest spindle and testball errors. Two-lobe errors in the ball and in the spindle can cancel each other, leaving you with a result much better than the true spindle error.
A one-piece 440 stainless steel testball was designed and built specifically for this test, because any non-uniform bending of the artifact will end up looking just like a spindle error. A flange-mount is the best way to attach a testball to a spindle because tapers or sleeves allow it to rock while rotating.

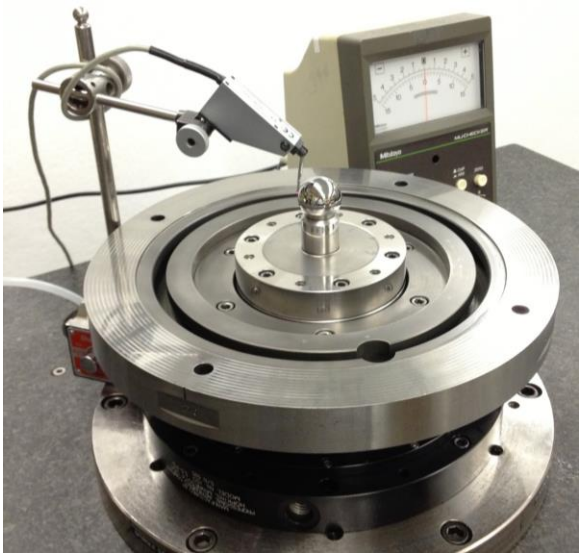

FIGURE 2. Dialing in the flange-mount test ball.

METHODOLOGY

Professor Marsh made us a Matlab executable program that takes three individual test results from our Lion Spindle Analyzer and separates the ball error from the synchronous spindle error. The result is filtered (typically to 150 upr) and the asynchronous error from the zero degree angle test is added back in.

FIGURE 3. Test apparatus with a single probe indexed to the 3 angles: 0°, 99.84375°, 202.5°.

We have experimented with reversal, but that has proved to be cumbersome and complicated. In 2007 we built test equipment to allow us to do error separation using the multiprobe method with a single probe. Since building this test hardware, we have tested hundreds of spindles and verified our results with cutting tests.

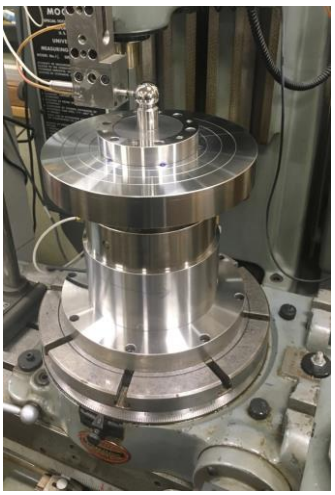

FIGURE 4. Test ball being inspected during manufacturing to ensure it is round to better than the required 10 nanometers at the equator.

RESULTS

It is important to test spindles at speeds they are to be used at. There are many factors that go into what the accuracy of your spindle will be and the speed you run at is one of them. Note the total radial error of the spindle in Table 1. It measures less than 3 nanometers at 1,500 rpm, but more than 10 nanometers at 10,000.

TABLE 1. Error motion summary of a recent spindle.

2. ERROR MOTION Inspected By: MO Date: 6/26/2018

Spindle Speed (rpm)		500	1,500	3,000	5,000	7,500	10,000
Radial	Synchronous	0.14 µ" **3.46 nm**	0.07 µ" **1.80 nm**	0.11 µ" **2.72 nm**	0.13 µ" **3.31 nm**	0.13 µ" **3.28 nm**	0.24 µ" **6.08 nm**
	Asynchronous	0.10 µ" **2.63 nm**	0.05 µ" **1.37 nm**	0.05 µ" **1.37 nm**	0.08 µ" **2.12 nm**	0.17 µ" **4.42 nm**	0.19 µ" **4.95 nm**
	Total	0.21 µ" **5.32 nm**	0.11 µ" **2.87 nm**	0.14 µ" **3.57 nm**	0.20 µ" **5.12 nm**	0.25 µ" **6.44 nm**	0.41 µ" **10.43 nm**
Axial	Fundamental	0.04 µ" **1.02 nm**	0.03 µ" **0.73 nm**	0.02 µ" **0.48 nm**	0.01 µ" **0.30 nm**	0.02 µ" **0.55 nm**	0.05 µ" **1.26 nm**
	Residual	0.03 µ" **0.81 nm**	0.02 µ" **0.47 nm**	0.02 µ" **0.43 nm**	0.03 µ" **0.86 nm**	0.04 µ" **0.93 nm**	0.06 µ" **1.48 nm**
	Asynchronous	0.09 µ" **2.38 nm**	0.06 µ" **1.42 nm**	0.05 µ" **1.23 nm**	0.09 µ" **2.20 nm**	0.10 µ" **2.58 nm**	0.13 µ" **3.28 nm**
	Total	0.18 µ" **4.45 nm**	0.10 µ" **2.47 nm**	0.09 µ" **2.29 nm**	0.16 µ" **3.99 nm**	0.22 µ" **5.69 nm**	0.28 µ" **7.09 nm**

Fundamental axial error motions are extremely important for diamond turning machines. The probe mount hardware we developed positions the probe coaxially with the axis of rotation. That's important because fundamental axial error motion tests are influenced by how close you line up the center of the probe to the center of the spindle. You can actually get results that give you a spurious lower fundamental axial error result if you aren't on center.

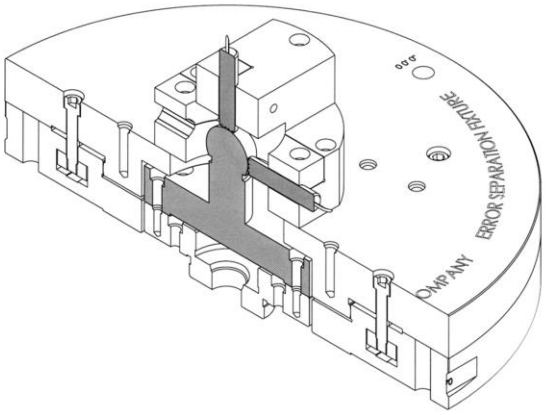

FIGURE 5. Cutaway of the error separation hardware.

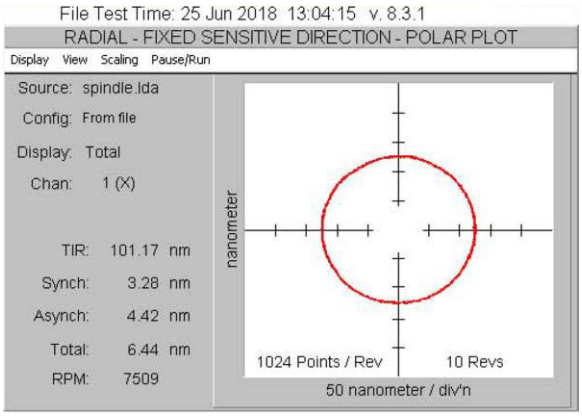

FIGURE 5. Typical error motion result at 7,500 rpm.

CONCLUSION

You're still going to need that shiny object. Measuring spindle error motions to nanometers takes a combination of specialized hardware, technique and software. Whilst error separation techniques are a valuable tool, they have their limits. A rule of thumb is don't expect to get more than a 10X improvement in accuracy, so if you have a ball that is round to 10 nanometers you should be able to trust your results to 1 nanometer resolution, but not down to an angstrom. Each Professional Instruments model 5.5 spindle is put through a rigorous battery of tests before it is allowed to ship, and it doesn't ship unless it measures under 12.5 nanometers on every one of those tests.

REFERENCES

[1] 2010 ASME B89.3.4-2010. Axes of Rotation: Methods for Specifying and Testing (New York, NY: ASME)
[2] Marsh E 2010 Precision Spindle Metrology Second Edition (Lancaster, PA: Destech Publications, Inc)
[3] Grejda RD 2002 Use and calibration of ultraprecision axes of rotation with nanometer level metrology (University Park, PA: Pennsylvania State University)
[4] Marsh ER, Arneson DA, Martin DL 2010 A comparison of reversal and multiprobe error separation. Precision Engineering 34:85-91

USING GREJDA OPTIMIZATION TO DETERMINE THE BEST ORIENTATION OF A SPINDLE

Byron Knapp, Dave Arneson, and Dan Oss
Professional Instruments Company
Hopkins, Minnesota, USA

ABSTRACT

The most demanding machine tool and form metrology applications require spindles with nanometer-level spindle error motion. Achieving this level of accuracy requires continued advances in metrology, artifacts, sensors, and fixturing. However, many are unaware of a simple solution for improved error motion using the optimum orientation angle. While the concept was introduced in the B89.3.4 Standard [1], the benefit was first demonstrated by Grejda using Donaldson reversal [2]. This paper discusses spindle metrology using multiprobe error separation and Grejda optimization to determine the orientation angle which yields the lowest fixed sensitive direction radial error motion.

BACKGROUND

Schlesinger is credited with developing the first systematic approach to the testing of machine tools—including spindle testing. In his book *Testing Machine Tools*, he was the first to describe a method to measure spindle accuracy using contact displacement indicators and a cylindrical test mandrel or testball [3]. Schlesinger pointed out that artifact out-of-roundness and spindle error motions are measured simultaneously so the artifact form error should be minimized.

Bryan, Clouser and Holland extended this approach to measure lathes with fixed sensitive direction error motions [4]. Bryan et al. suggest a check for the problem of artifact out-of-roundness by orienting the sphere in several angular positions relative to the spindle rotor and observing changes in the measurement. They point out that as the spindle and artifact accuracies approach one another, efforts must be made to distinguish and separate each error.

In theory, the reversal technique described by Donaldson provides the simplest method for separating spindle error motion from artifact form error [5]. In practice, measurement accuracy of reversal suffers from the difficulty of repositioning the artifact and the sensor [6]. Whitehouse developed a multiprobe technique which eliminated the artifact repositioning but this method requires accurate positioning and alignment of the sensor [7]. Grejda was the first to implement error separation a precision rotary table [2]. The rotary table rotates the stator of the spindle eliminating the repositioning and handling of the sensor. The combination of these two techniques (Whitehouse and Grejda), results in an implementation of error separation suitable for nanometer-level testing in a production environment.

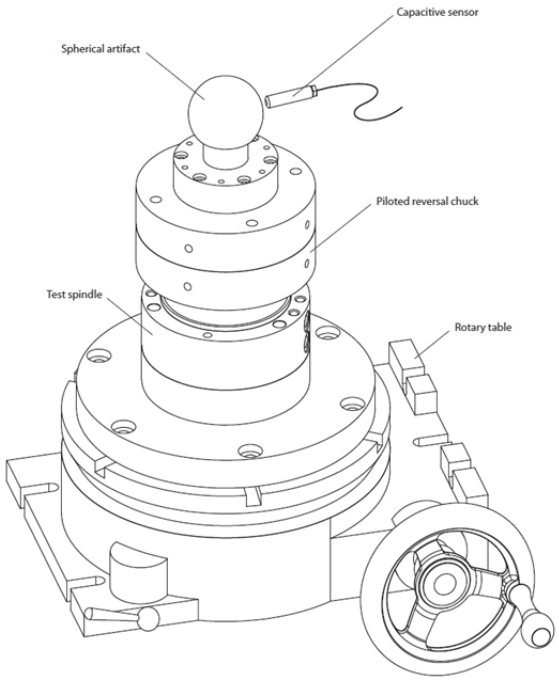

FIGURE 1. Spindle mounted to rotary table for error separation using Grejda's approach [2].

The novelty of this work is in combining the techniques of Whitehouse and Grejda to find the orientation angle with minimum fixed sensitive direction radial spindle error motion using multiprobe error separation. The orientation angle is defined as the angle from the sensor to a known fiducial on the spindle stator. With two orthogonal measurements in a plane normal to the axis of rotation, the fixed sensitive direction error at any orientation can be calculated using Equation 1.

$$R(\theta) = \Delta X(\theta)cos\phi + \Delta Y(\theta)sin\phi \quad (1)$$

Where $R(\theta)$ is fixed sensitive error motion at an orientation angle ϕ, θ is angular position of the axis of rotation, $\Delta X(\theta)$ and $\Delta Y(\theta)$ are the two orthogonal separated spindle error results at orientation angles 0° and 90°.

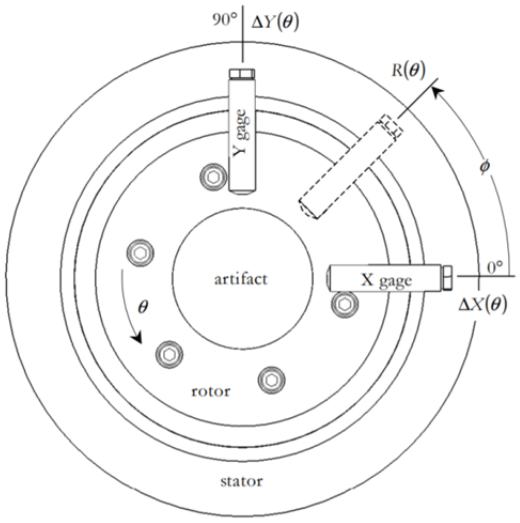

FIGURE 2. Calculating fixed sensitive direction spindle error for any orientation angle ϕ [2].

Multiprobe error separation is used to obtain the separated spindle error components necessary to solve Equation 1. Illustrated in Figure 3, Equations 2-4 are solved for the artifact form error, $F(\theta)$, and spindle errors $\Delta X(\theta)$ and $\Delta Y(\theta)$ using the technique described by Marsh [8].

$$m_A(\theta) = F(\theta) + \Delta X(\theta)sin\phi \quad (2)$$

$$m_B(\theta) = F(\theta - \phi) + \Delta X(\theta)cos\phi + \Delta Y(\theta)sin\phi \quad (3)$$

$$m_C(\theta) = F(\theta - \psi) + \Delta X(\theta)cos\psi + \Delta Y(\theta)sin\psi \quad (4)$$

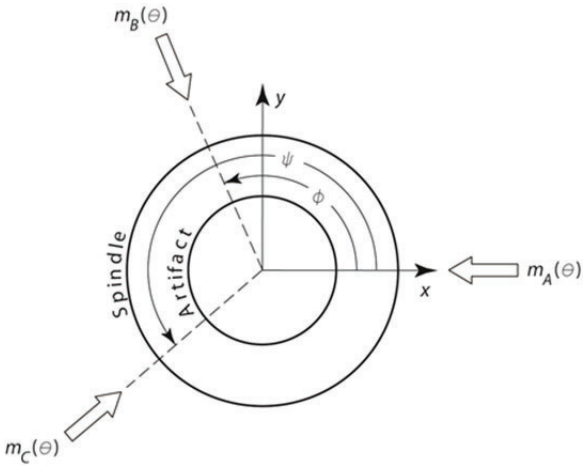

FIGURE 3. Multiprobe error separation used to obtain artifact form error $F(\theta)$ and spindle error components $\Delta X(\theta)$ and $\Delta Y(\theta)$ after Marsh [8].

METHODOLOGY

In this work, fixed sensitive direction error motion is predicted for any orientation angle using multiprobe error separation and Grejda optimization. The spindle under test is used in a roundness tester for calibrating spindle metrology testballs. It is a 4R Blockhead air bearing spindle with a 512-line encoder mounted to an ultra-precision rotary table (Moore Tool Company Special LRT) as shown in Figure 4. The diamond-tipped air bearing contact sensor (Lion Precision C-LVDT) is attached to the quill of a manual measuring machine (Moore Tool Company No. 3 UMM). Measurement results are low-pass filtered to 15 UPR (Undulations Per Revolution).

Despite the possibility to perform error mapping of the target, an error separation is performed for each test. On the nanometer-level, it is critical to verify artifact out-of-roundness after each test as a feedback mechanism to detect invalid measurements from noise and other disturbances. The spindle stator is rotated via the rotary table to three positions for separation. The asymmetrically spaced stator orientations of 0°0’0”, 99°50’37.5”, and 202°30’0” are chosen to avoid harmonic suppression. This approach provides results comparable to Donaldson reversal while being better suited to a production environment [6].

FIGURE 4. Setup to find the Grejda optimum for a precision roundness measuring machine.

RESULTS

Three typical multiprobe measurements at 0°0’0”, 99°50’37.5”, and 202°30’0” are shown in Figures 5-7. The synchronous error, which includes the artifact form error, ranges from 8.8 nm at 202°30’0” to 16.3 nm at 0°0’0”. The asynchronous error ranges from 1.9 nm to 3.1 nm. These three measurements are separated into spindle and artifact error as shown in Figure 8. The synchronous spindle error is 10.7 nm and the artifact form error 7.8 nm. Using Equation 1, the predicted spindle error as a function of orientation angle is generated in Figure 9. The error motions at the best and worst orientation angle are shown in Figure 10. Furthermore, the prediction was verified with measurements at orientation angles 20°, 50°, 80°, 110°, and 170° with results summarized in Table 1.

TABLE 1. Summary of predicted and measured error using Grejda optimization.

Orientation angle	0	20	50	80	90	110	170
Predicted (nm)	10.7	10.8	9.5	7.9	7.5	6.7	10.4
Measured (nm)	10.7	10.7	9.4	8.9	7.5	6.4	10.2
Error (nm)	0.0	0.1	0.1	-1.0	0.0	0.3	0.2

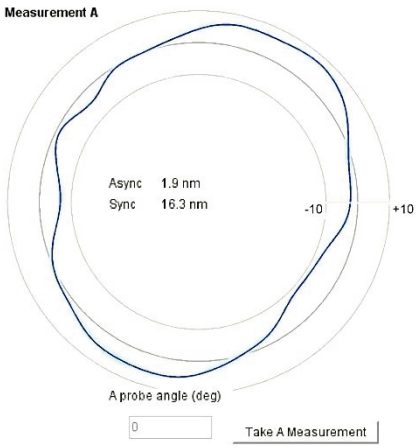

FIGURE 5. Measurement A at orientation angle 0°0’0” (spindle and artifact error).

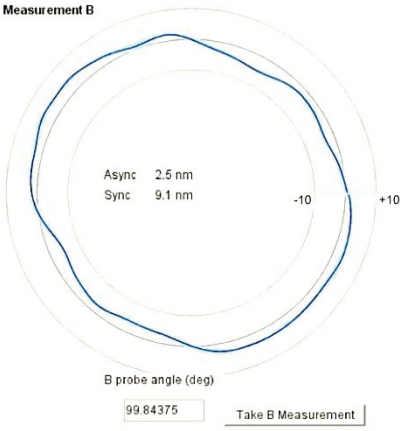

FIGURE 6. Measurement B at orientation angle 99°50’37.5” (spindle and artifact error).

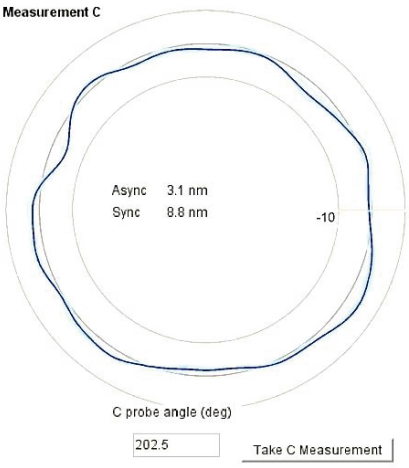

FIGURE 7. Measurement C at orientation angle 202°30’0” (spindle and artifact error).

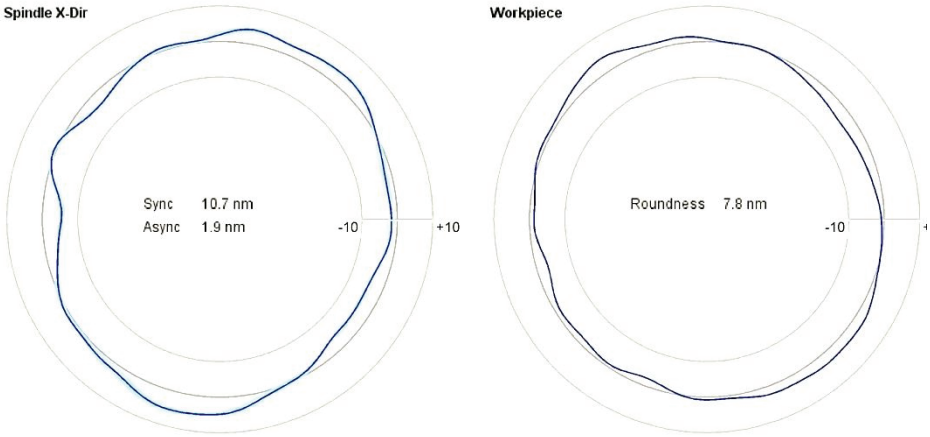

FIGURE 8. Multiprobe error separation result from the measurements in Figures 5-7. The spindle error is 10.7 nm at orientation angle 0° (left) and the artifact form error is 7.8 nm (right).

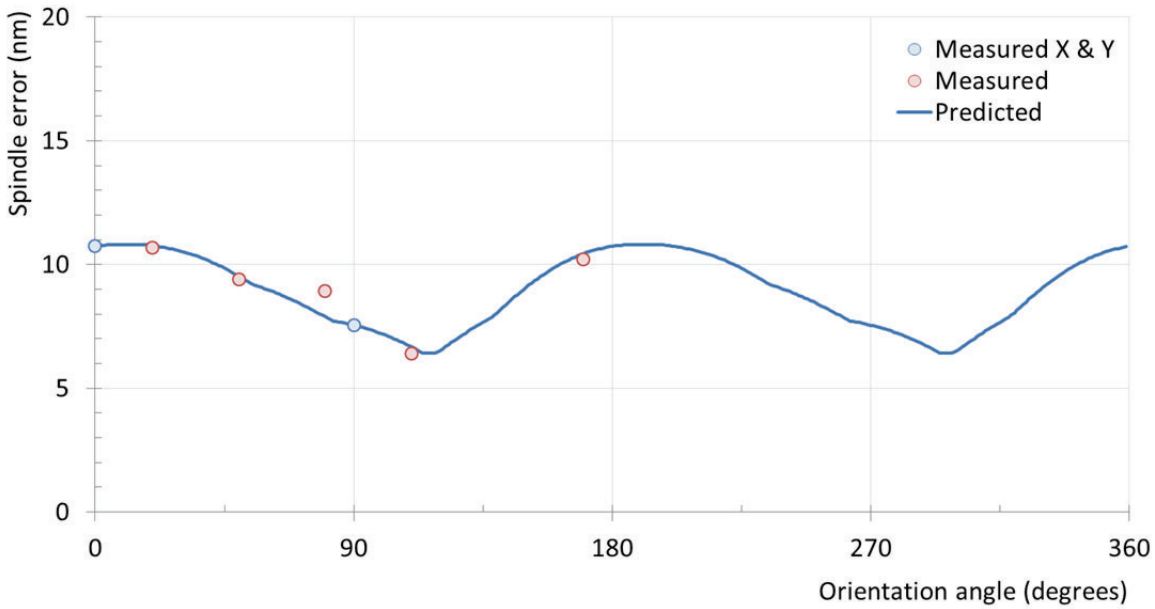

FIGURE 9. The preferred orientation angle reveals itself at 115° using Grejda optimization.

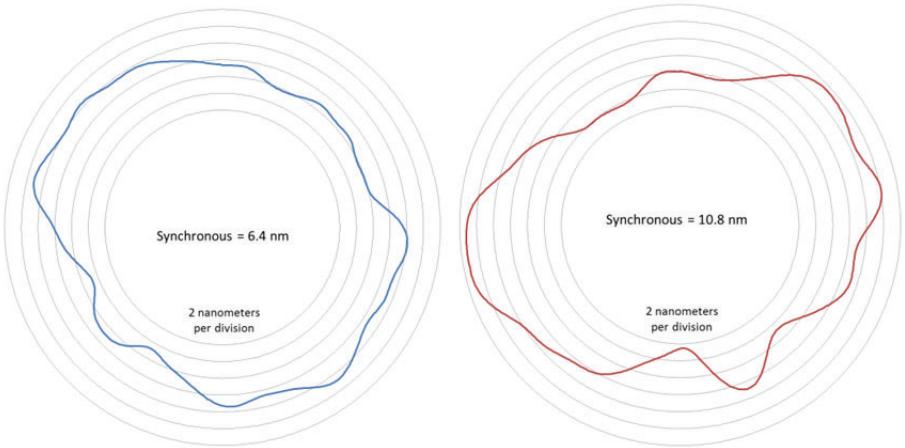

FIGURE 10. The optimum orientation angle is 115° (left) and the worst orientation angle is 10° (right). Selecting the Grejda optimum orientation provides greater than 40% improvement.

CONCLUSIONS

For fixed sensitive direction applications that require spindles with nanometer-level accuracy, the stator orientation can be selected for lowest possible error motion. This Grejda optimum orientation angle can be found for radial or tilt error motion given two orthogonal spindle error results. In this work, the multiprobe method is used to separate the spindle and artifact error to obtain two orthogonal components of radial spindle error. These error components are used to predict the fixed sensitive direction radial spindle error at every orientation angle. In this case, the spindle error is predicted to vary from a minimum of 6.4 nm to a maximum of 10.8 nm. The Grejda optimum orientation angle with the minimum error provides a 40% improvement in error motion compared to the maximum. This improvement in error motion can be realized simply by correctly positioning the spindle stator during machine tool assembly.

REFERENCES

[1] ANSI/ASME B89.3.4-2010. Axes of Rotation; Methods for Specifying and Testing. ASME New York: 2010.

[2] Grejda RD Use and calibration of ultraprecision axes of rotation with nanometer level metrology (University Park, PA: Pennsylvania State University). 2002.

[3] Schlesinger G Testing Machine Tools: For the use of Machine Tool Makers, Users, Inspectors and Plant Engineers, Sixth Edition. The Machinery Publishing Co. London: 1961.

[4] Bryan J, Clouser R, Holland E Spindle Accuracy. American Machinist, 111(25):149-164, 1967.

[5] Donaldson RR A simple method for separating spindle error from test ball roundness error. Annals of CIRP, 21(1):125-126, 1972.

[6] Marsh ER, Arneson DA, Martin DL A Comparison of Reversal and Multiprobe Error Separation. Precision Engineering. 34:85-91, 2010.

[7] Whitehouse DJ Some Theoretical Aspects of Error Separation Techniques in Surface Metrology. J. of Phys. E: Sci. Inst. 9:531-536, 1976.

[8] E Marsh ER Precision Spindle Metrology, Second Edition. Destech Publications, Inc. Lancaster, PA: 2010.

DEVELOPMENT OF A FLEXURE-BASED MODAL HAMMER

Michael F. Gomez, Ryan W. Copenhaver, T. Michael Stokes, Emma D. Betters, and Tony L. Schmitz
Department of Mechanical Engineering and Engineering Science
University of North Carolina at Charlotte, Charlotte, NC

INTRODUCTION

Impact testing is a widely used method for the determination of structural frequency response functions (FRF) [1]. Typically, an impact hammer is used to excite a structure and the corresponding response is measured. Currently, impact hammers measure forces through piezoelectric based sensors. Alternatively, force measurements can be inferred from displacement measurements using a flexure. This deconvolution of the force from the displacement response using the known structural dynamics is presented here.

WORKING PRINCIPLE

The force from a modal hammer is a short duration impact which excites a structure over a range of frequencies depending on the force profile. The flexural hammer proposed here has a single degree of freedom (SDOF) flexure which is compliant only in the direction of impact. The applied force excites the SDOF flexure and produces a vibratory response.

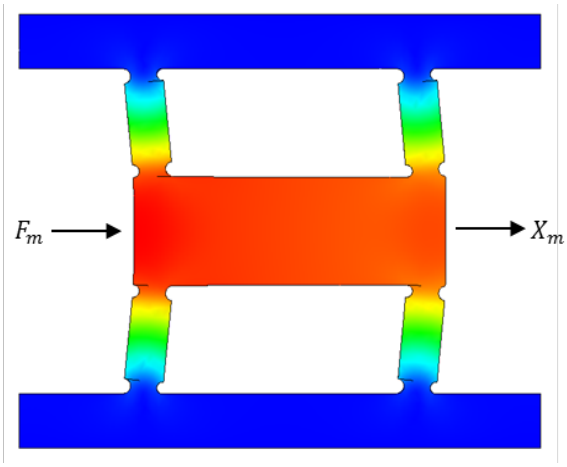

Figure 1. Working principle of the flexural hammer. An impact force, F_m, is applied to the flexure and the displacement, X_m, is measured.

The resulting flexure displacement is measured and converted to the frequency domain using the discrete Fourier transform. The frequency dependent displacement and SDOF flexure FRF are deconvolved using the inverted flexure FRF. The frequency domain impact force is obtained using Eq. 1.

$$F_m(\omega) = \left(\frac{X}{F}(\omega)\right)^{-1} \cdot X_m(\omega) \tag{1}$$

where, $X_m(\omega)$ is the frequency domain displacement, $\left(\frac{X}{F}(\omega)\right)^{-1}$ is the inverted flexure FRF, and $F_m(\omega)$ is the frequency domain impact force. Note that the inverted flexure FRF is low pass filtered to attenuate unwanted high frequency content.

IMPACT TESTING SIMULATION

A time domain simulation was programmed in MATLAB® which calculates the displacement of a SDOF system excited by an impact force using numerical integration [1]. The impact force was modeled using a triangular profile with a magnitude of 500 N over 1 ms (Fig. 2).

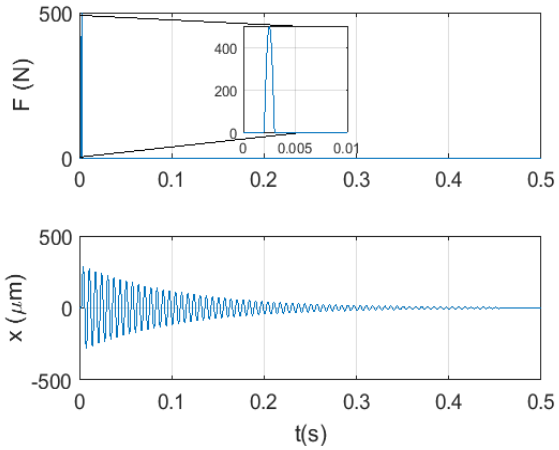

Figure 2. Time domain simulation for a SDOF flexure response (bottom) from an impact force profile (top).

Once the deconvolution is completed using Eq. 1, the frequency domain excitation force is obtained. The force content of the excitation is in good agreement with the input force up to approximately 1500 Hz; see Fig. 3. Note that the natural frequency, f_n, of the SDOF flexure shown is 200 Hz.

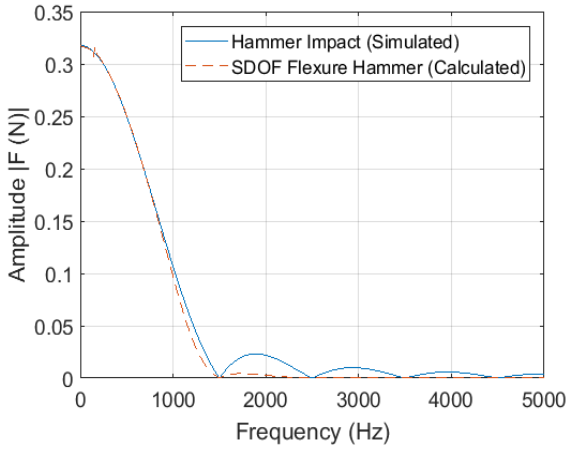

Figure 3. Comparison of the force frequency content for the simulated (input) and calculated (Eq. 1 deconvolution) impact forces.

As an additional analysis, the time domain force profiles of the simulated (input) and calculated (Eq. 1) impact forces were observed. The time response for the calculated force was obtained using the inverse Fourier transform. It is seen in Fig. 4 that the two time domain force signals are similar. The discrepancy in force magnitude is a byproduct the low pass filter applied to the inverse FRF and, therefore, the calculated force content.

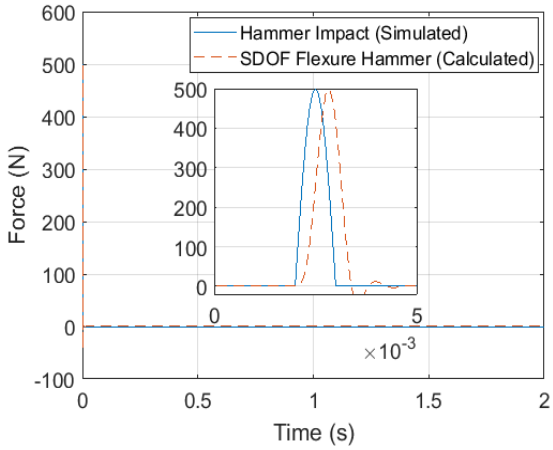

Figure 4. Time domain comparison of force profiles for the simulated (input) and calculated (Eq. 1) hammer impacts

DESIGN PARAMETER CASE STUDY

The feasibility of a flexure-modal hammer was explored through a series of simulations which were used to investigate the constraints necessary for the hammer design and development. The SDOF flexure dynamics used in the simulation are provided in Table 1.

Table 1. SDOF flexure dynamics.

f_n [Hz]	Damping ratio	Stiffness [N/m]
200.0	0.01	1.0×10^6

The first set of tests were performed to assess the effect of flexure dynamics on excitation bandwidth. During modal testing, the excitation bandwidth of the force is dependent on the structural mass and tip stiffness of the hammer. A stiff tip excites a wide frequency range with relatively low energy input. A soft tip, on the other hand, excites a lower frequency range with a higher energy input into this range [1].

To illustrate this concept, soft and stiff tip hammer impulses were simulated. The frequency domain response is displayed in Figs. 5 and 6, respectively.

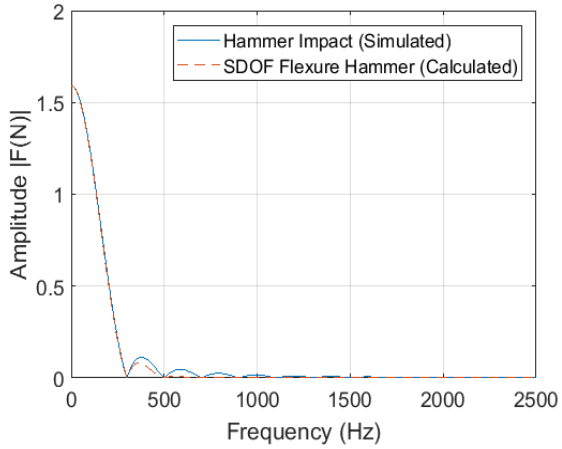

Figure 5. Frequency domain comparison of an excitation force indicative of a soft tip hammer impulse.

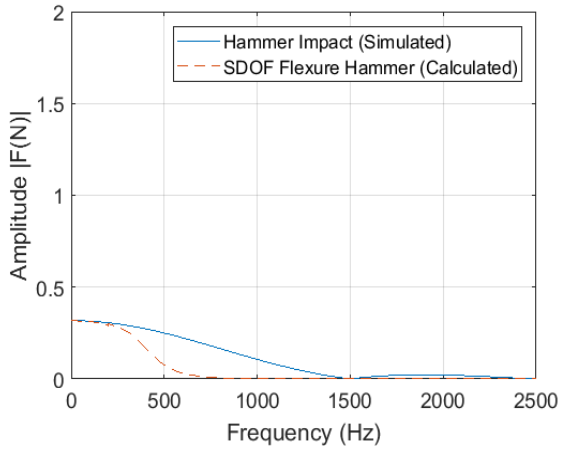

Figure 6. Frequency domain comparison of an excitation force indicative of a stiff tip hammer impulse. Note that frequency content is lost at the higher frequencies due to the low pass filter cut-off frequency.

To operate at a wide frequency range, the flexural natural frequency should correspond to the desired measurement bandwidth. Due to the low natural frequency of the flexure, force content is lost for the stiff hammer impulse, Fig. 7.

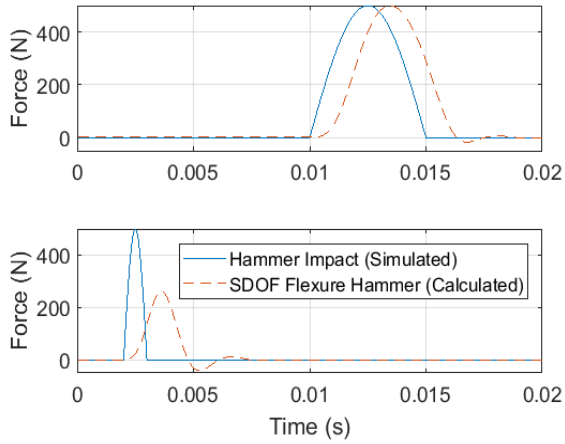

Figure 7. Time domain comparison of soft tip (top panel) and stiff tip (bottom panel) hammer impacts.

Incrementally increasing the flexure natural frequency (and low pass filter cut-off frequency) improves the ability to reproduce the impact excitation. At measurement intervals which cover a large bandwidth of excitation frequencies, a relatively high natural frequency is needed to successfully deconvolve the structural dynamics.

It is shown by Fig. 8 that low frequency excitations are less sensitive to the flexure frequency. A 4th order lowpass Butterworth filter was applied to the inverse flexure FRF with a cut-off frequency equal to the two times the natural frequency.

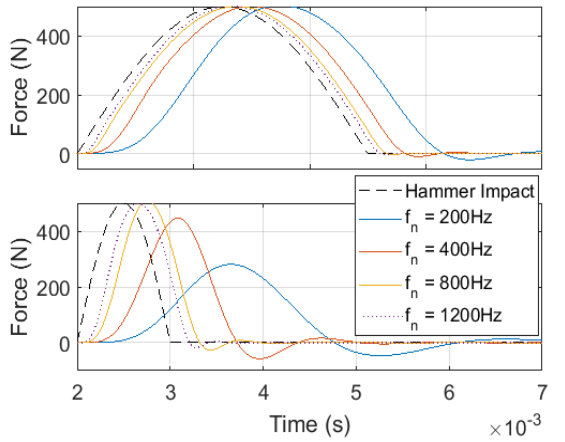

Figure 8. Time domain comparison of simulated and calculated forces at varying natural frequencies.

The effects of noise on the structural deconvolution method is demonstrated in Figs. 9 and 10. A 5% noise level was added to the displacement signal which was subsequently smoothed using a moving average filter. For the purposes of this simulation, the flexure natural frequency was 1200 Hz (based on the results presented in Fig. 8).

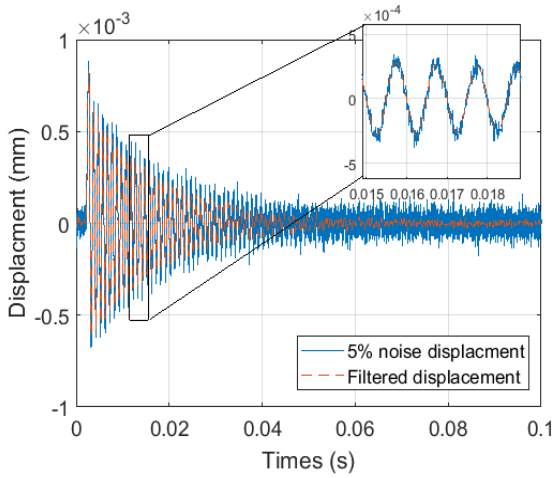

Figure 9. Time domain response of the SDOF system to a hammer impulse. A 5% noise level and a moving average filter was applied to the displacement signal.

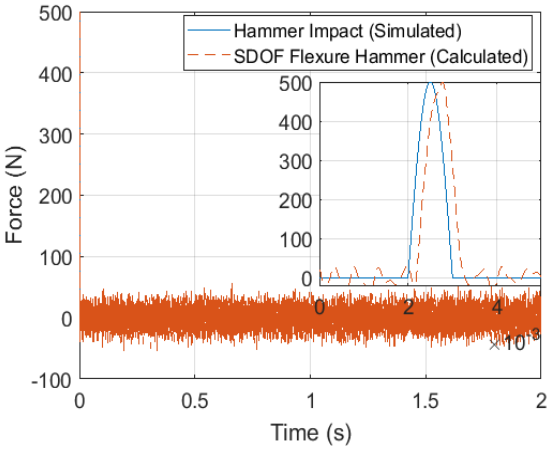

Figure 10. Time domain comparison of the simulated and calculated hammer impulse using the displacement signal shown in Fig. 9.

A low sampling frequency may also have an adverse effect on the structural deconvolution. To investigate, the simulation sampling frequency was adjusted to {5, 10, and 100) kHz. The results are shown in Fig. 11.

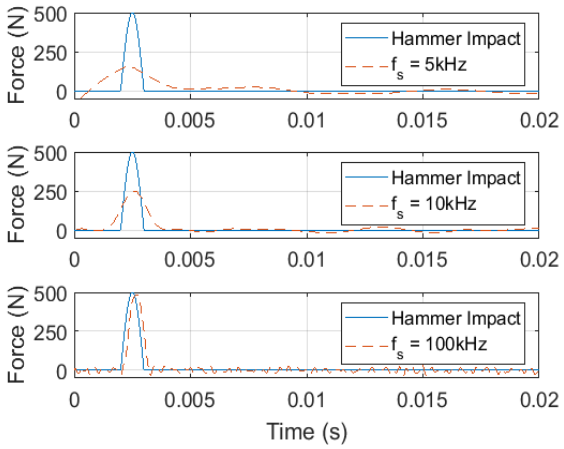

Figure 11. Time domain comparison of simulated and calculated forces with a varying sampling rate. As the sampling rate increases, the resolution and accuracy of the reproduced impact also increases.

CONCLUSIONS

It has been shown through a series of simulations that it is possible to accurately reconstruct a hammer impulse through structural deconvolution. Design constraints were developed for the use of SDOF flexure displacement measurement to reconstruct the impulse excitation force. It was shown that flexure natural frequency, signal-to-noise ratio, and sampling frequency have a considerable effect on the resulting force signal accuracy. The flexure natural frequency is an important factor which must be considered when designing and manufacturing the flexure needed for modal testing. Furthermore, a low noise vibration transducer is required to accurately reconstruct the excitation impulse. The flexure dynamics can be adjusted to excite various bandwidths depending on the measurement application.

It has been shown that knife edge [2] and curved edge sensors can be used for dynamic displacement measurements [3]. When used in combination with a SDOF flexure, this will provide a low cost alternative to traditional piezoelectric dynamic displacement devices. To continue this research, a flexure-knife edge modal hammer will be designed, constructed, and tested. A comparison with commercially available piezoelectric hammers will be performed.

ACKNOWLEDGEMENTS

The research was supported by the National Science Foundation through award number CMMI 1663405.

REFERENCES

[1] Schmitz T. L. and Smith K. S. (2012). Mechanical Vibrations: Modeling and Measurement. Springer, New York, NY.

[2] Lee C., Jeon S., Stepanick C. K., Zolfaghari A., Tarbutton J. A. (2017). Investigation of optical knife edge sensor for low-cost, large-range and dual-axis nanopositioning stages. Journal of the International Measurement Confederation 103: 157-164.

[3] Lee C., Zhaeo R., and Jeon S. (2017). A simple optical system for miniature spindle runout monitoring. Journal of the International Measurement Confederation 102: 45-46.

A 3-D NONLINEAR ANALYTICAL STIFFNESS MODEL FOR DEFLECTED LEAF SPRINGS

Marijn Nijenhuis, J.P. Meijaard, Dannis M. Brouwer
Precision Engineering
Faculty of Engineering Technology
University of Twente
Enschede, The Netherlands

INTRODUCTION

Leaf springs in precision flexure mechanisms are used for guiding motion. Their motion guiding performance is governed by the leaf spring stiffness. For a typical range of motion, the stiffness varies due to geometrically nonlinear effects. Current methods that characterize the stiffness behavior of leaf springs have limitations:

- finite element methods (FEM) are accurate, but parameter-specific, making it computationally expensive to evaluate designs for a range of design parameters, especially for large deformations;
- analytical methods that do offer parametric insight are either inaccurate, because of linearization, or restricted in applicability, because of 2-D analysis [1].

To parametrically predict the performance characteristics such as 3-D stiffness variations and error motions of flexure mechanisms, we have developed an accurate analytical leaf spring model for moderate deformations, captured in a compact format.

This work presents a new closed-form parametric model that

1. describes the stiffness of the typical leaf spring in all directions under deflection due to a general 3-D loading condition;
2. is accurate, with respect to FEM, because it includes the nonlinear effects of elongation, bending, torsion, and shear;
3. quantifies flexure design concepts, such as
   - support (off-axis) stiffness decreasing with deflection and loading,
   - actuation stiffness changing with loading (load-stiffening and load-softening),
   - stiffness changing due to overconstraints, and
   - parasitic (error) motions;
4. is also formulated as a scalar potential energy expression, to help future generalization of this model (to e.g. multi-leaf spring systems and the numeric implementation as an efficient finite element).

METHOD

The starting point is Timoshenko-Vlasov beam theory with nonlinear strain–displacement relations in order to capture not just bending and shear deformation, but also (the nonlinearity-inducing effects of) elongation, non-uniform torsion and warping deformation [2, 3].

Since the governing differential equations admit no exact solution, an approximating analytical solution is obtained by means of a variational equilibrium principle instead. By choosing interpolation (also called trial or test) functions with undetermined coefficients, application of the variational principle yields a system of algebraic equations in the coefficients that is typically easier to solve than the differential equations. The accuracy of the solution depends on the choice and number of interpolation functions.

We have observed that the common principle of minimum potential energy (in which variations of the displacement fields are allowed) works well for solutions to the linear problem, but not for the nonlinear problem of the current investigation: the rationale for choosing an appropriate refinement of the displacement interpolation functions is lacking. Inspired by the results of previous work [4], we have selected a different variational equilibrium principle, named after Hellinger and Reissner, that allows simultaneous variations of displacement (and rotation) fields and moment (and force) fields [5]. The strength of this approach lies in the observations that

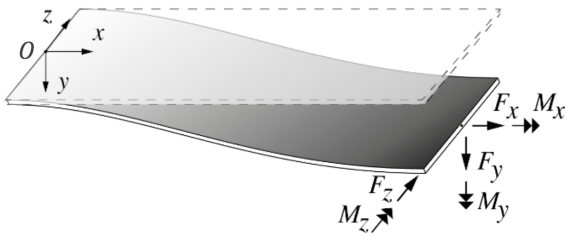

FIGURE 1. Fixed–free leaf spring subject to a general force and moment vector.

1. there is a good rationale for the moment interpolation: given the configuration of a *deformed* beam, the distribution of moments is known explicitly from force and moment balance equations;

2. this separate moment interpolation, combined with displacement interpolation based on only the solution to the *linear* problem yields a nonlinear model with sufficient accuracy for leaf springs that are used in practice.

The construction of the interpolation functions is based on three basic assumptions for the leaf spring under consideration:

1. the width has the same order of magnitude as the length,

2. the maximum transverse displacement is 15% of the length (we define $\alpha := 0.15$), and

3. the maximum allowable strain is $\alpha^3 = 0.003$.

Upon imposing that the maximum deflection is limited by the yield stress $E\alpha^3$ (for Young's modulus E) and the critical buckling loads, these assumptions lead to order of magnitude estimates of all physical quantities involved in terms of powers of α. The various interpolation functions are then constructed by consistently retaining leading order terms.

RESULTS

The leaf spring in figure 1 is fixed on one end and loaded by a general force F and moment M on the other. The corresponding displacements and rotations are u and ϕ. Owing to their relatively low associated stiffness, we classify ϕ_x, u_y, ϕ_z as the three kinematic degrees of freedom (DOFs). Loads in the direction of the degrees of freedom, M_x, F_y, M_z, are the actuation loads. Owing to their relatively high associated stiffness, we classify u_x, ϕ_y, u_z as the error motions. Loads in the direction of the error motions, F_x, M_y, F_z, are the applied loads.

The six model equations can be displayed in various ways; a particularly interesting format is obtained by choosing the three DOFs and the three applied loads as the independent variables. The six model equations then represent the three error motions and three actuation loads of the leaf spring.

For brevity's sake, the effects of constrained warping are omitted in the equations shown here (the equation structure stays the same, only the coefficients change; they become dependent on the ratio GJL^2/EI_w, where G is the shear modulus, J Saint-Venant's constant, L the leaf spring length, E Young's modulus, and I_w Vlasov's warping constant).

Flexure performance: error motions

The expressions for the three error motions are given by

$$\begin{aligned} u_x/L = {} & F_x \frac{1}{EA} \\ & + \begin{bmatrix} \phi_z & u_y/L \end{bmatrix} \begin{bmatrix} -1/15 & 1/20 \\ 1/20 & -3/5 \end{bmatrix} \begin{pmatrix} \phi_z \\ u_y/L \end{pmatrix} \\ & + F_x \frac{L^2}{EI_z} \begin{bmatrix} \phi_z & u_y/L \end{bmatrix} \begin{bmatrix} 11/6300 & -1/1400 \\ -1/1400 & 1/700 \end{bmatrix} \begin{pmatrix} \phi_z \\ u_y/L \end{pmatrix} \\ & - \frac{1}{360} F_z \frac{L^2}{EI_z} \phi_x \phi_z, \end{aligned} \tag{1}$$

$$\begin{aligned} \phi_y = {} & -\frac{1}{2} F_z \frac{L^2}{EI_y} + M_y \frac{L}{EI_y} \\ & - \phi_x \phi_z + \phi_x u_y/L \\ & + F_z \frac{L^2}{GJ} \begin{bmatrix} \phi_z & u_y/L \end{bmatrix} \begin{bmatrix} -1/30 & 1/60 \\ 1/60 & -1/10 \end{bmatrix} \begin{pmatrix} \phi_z \\ u_y/L \end{pmatrix} \\ & + M_y \frac{L}{GJ} \begin{bmatrix} \phi_z & u_y/L \end{bmatrix} \begin{bmatrix} 2/15 & -1/10 \\ -1/10 & 1/5 \end{bmatrix} \begin{pmatrix} \phi_z \\ u_y/L \end{pmatrix}, \end{aligned} \tag{2}$$

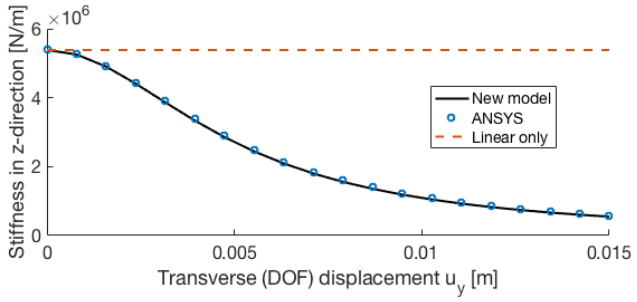

FIGURE 2. Accurate description of the nonlinear decrease in support stiffness.

$$
\begin{aligned}
u_z/L = {} & \frac{1}{3}F_z\frac{L^2}{EI_y} - \frac{1}{2}M_y\frac{L}{EI_y} + F_z\frac{L}{kGA} \\
& + \frac{1}{6}\phi_x\phi_z \\
& + \frac{1}{180}F_z\frac{L^2}{EI_z}\phi_x^2 - \frac{1}{360}F_x\frac{L^2}{EI_z}\phi_x\phi_z \\
& + F_z\frac{L^2}{GJ}\begin{bmatrix}\phi_z & u_y/L\end{bmatrix}\begin{bmatrix}13/1260 & -1/105 \\ -1/105 & 3/35\end{bmatrix}\begin{pmatrix}\phi_z \\ u_y/L\end{pmatrix} \\
& + M_y\frac{L}{GJ}\begin{bmatrix}\phi_z & u_y/L\end{bmatrix}\begin{bmatrix}-1/30 & 1/60 \\ 1/60 & -1/10\end{bmatrix}\begin{pmatrix}\phi_z \\ u_y/L\end{pmatrix}.
\end{aligned}
\tag{3}
$$

Various contributions from bending (stiffness EI_y, EI_z), shear (stiffness kGA) and torsion (stiffness GJ) can be identified.

The three error motions Eqs. (1)–(3) all have the same structure, which can be summarized as:

error motion =	
elastic terms	(linear in *applied loads*)
+ **kinematic** terms	(quadratic in *DOFs*)
+ **elastokinematic** terms	(linear in *applied loads*, quadratic in *DOFs*)

Since the error motions are ideally zero, the expressions highlight the various sources of unwanted compliance: the common linear elastic effect, and the nonlinear kinematic and elastokinematic effect. (Awtar et al. identified these sources in the 2-D analysis for a different error motion [1].) While the common linear terms are constant and independent of DOF motion, the new nonlinear terms describe how the error motion changes with DOF motion. Also, the elastokinematic terms capture the important effect that the support stiffness decreases with increasing motion in the DOF. This is indicated in figure 2 for the lateral support stiffness $\partial F_z/\partial u_z$ of a steel leaf spring with length 100 mm, width 50 mm and thickness 1 mm. The figure shows 1) the inadequacy of using just the linear terms and 2) the good match with Shell181 finite elements in ANSYS (for an error of 2.37% at $u_y = 0.15L$).

Flexure performance: actuation loads

The three expressions for the actuation loads are given by

$$
\begin{aligned}
F_y\frac{L^2}{EI_z} = {} & \begin{bmatrix}-6 & 12\end{bmatrix}\begin{pmatrix}\phi_z \\ u_y/L\end{pmatrix} \\
& + F_x\frac{L^2}{EI_z}\begin{bmatrix}-1/10 & 6/5\end{bmatrix}\begin{pmatrix}\phi_z \\ u_y/L\end{pmatrix} \\
& - M_y\frac{L}{EI_z}\phi_x,
\end{aligned}
\tag{4}
$$

$$
\begin{aligned}
M_z\frac{L}{EI_z} = {} & \begin{bmatrix}4 & -6\end{bmatrix}\begin{pmatrix}\phi_z \\ u_y/L\end{pmatrix} \\
& + F_x\frac{L^2}{EI_z}\begin{bmatrix}2/15 & -1/10\end{bmatrix}\begin{pmatrix}\phi_z \\ u_y/L\end{pmatrix} \\
& - \frac{1}{6}F_z\frac{L^2}{EI_z}\phi_x,
\end{aligned}
\tag{5}
$$

$$
\begin{aligned}
M_x\frac{L}{GJ} = {} & \phi_x \\
& - M_y\frac{L}{GJ}u_y/L \\
& - \frac{1}{6}F_z\frac{L^2}{GJ}\phi_z.
\end{aligned}
\tag{6}
$$

The actuation loads Eqs. (4)–(6) all share the following structure:

$$
\begin{aligned}
\text{actuation load} = {} & \begin{matrix}\text{linear} \\ \text{stiffness} \\ \text{coefficient}\end{matrix} \times \textit{DOFs} \\
& + \begin{matrix}\text{geometric} \\ \text{stiffness} \\ \text{coefficient}\end{matrix} \times \textit{applied loads} \times \textit{DOFs}
\end{aligned}
$$

The expressions convey that the actuation load is not just dependent on the DOF motion, but also on the applied loads. This captures parametrically how the actuation stiffness changes due to applied loads (i.e. the load-stiffening effect or load-softening and eventually buckling effect due to e.g. overconstraints).

Potential energy expression

A scalar expression for the total potential energy is also obtained as part of the model derivation. It

is given by

$$
\begin{aligned}
P = \int_0^l \Bigg[& \hat{M}_z \hat{u}_y'' - \frac{\hat{M}_z^2}{2EI_z} \\
& + \hat{M}_x \hat{\phi}_x' - \frac{\hat{M}_x^2}{2GJ} \\
& + \hat{F}_z \left(\hat{u}_z' + \hat{\phi}_y \right) - \frac{\hat{F}_z^2}{2kGA} \\
& + \hat{F}_x \left(\hat{u}_x' + \hat{u}_y'^2/2 \right) - \frac{\hat{F}_x^2}{2EA} \\
& + \hat{M}_y \left(\hat{\phi}_y' + \hat{\phi}_x \hat{u}_y'' \right) - \frac{\hat{M}_y^2}{2EI_y} \Bigg] ds \\
& - M_x \phi_x - M_y \phi_y - M_z \phi_z \\
& - F_x u_x - F_y u_y - F_z u_z
\end{aligned}
\tag{7}
$$

in conjunction with the displacement and moment interpolation functions Eqs. (8)–(9), given in the appendix. This expression shows clear contributions (on each line in the integrand) of strain energy due bending about the z-axis, torsion, shear, elongation, and bending about the y-axis, resp. It also shows that the order of magnitude estimate truncation scheme has led to geometrically nonlinear terms (viz. $\hat{u}_y'^2/2$ and $\hat{\phi}_x \hat{u}_y''$) in the strain and curvature relations for the deformations that are associated with high stiffness: elongation and bending about the y-axis.

By means of energy methods, this expression can be used for e.g. treating multi-leaf spring mechanisms and creating a finite-element-like implementation. The benefit of this formulation as basis for the construction of elements is that it yields an element that is sufficiently accurate to describe an entire leaf spring (so, no need for meshing into multiple elements), and with only 12 degrees of freedom (like a 3-D spatial beam element). The reduction in computation time facilitates the simulation and optimization of more complex flexure mechanisms.

CONCLUSIONS

The contribution of this work is a parametric force–displacement model tailored to leaf springs typically used in precision mechanism design. This paper treats the relevant nonlinear effects due to bending, elongation, shear and torsion, under general 3-D loading conditions, whilst being sufficiently simple and compact to provide parametric insight. The upcoming journal publication will detail a model for all relevant nonlinear effects by also including warping.

REFERENCES

[1] Awtar S, Slocum AH, Sevincer E. Characteristics of Beam-Based Flexure Modules. Journal of Mechanical Design. 2007;129(6):625–639.

[2] Timoshenko S, Gere JM. Theory of Elastic Stability. 2nd ed. New York: McGraw-Hill; 1961.

[3] Vlasov VZ. Thin-walled elastic beams. Jerusalem: Israel program for scientific translations; 1961.

[4] Nijenhuis M, Meijaard JP, Mariappan D, Herder JL, Brouwer DM, Awtar S. An Analytical Formulation for the Lateral Support Stiffness of a Spatial Flexure Strip. Journal of Mechanical Design. 2017;139(5):051401:1–11.

[5] Washizu K. Variational Methods in Elasticity and Plasticity. 3rd ed. Oxford, New York: Pergamon Press; 1982.

APPENDIX

The moment (and force) interpolation functions are given by

$$
\begin{aligned}
\hat{M}_x(s) &= M_x + F_z \left[u_y - u_y(s) \right] + u_y' \left[M_y - F_z(L-s) \right], \\
\hat{M}_y(s) &= M_y - F_z(L-s), \\
\hat{M}_z(s) &= M_z - F_x \left[u_y - u_y(s) \right] + F_y(L-s) \\
&\quad - \phi_x(s) \left[M_y - F_z(L-s) \right], \\
\hat{F}_x(s) &= F_x, \\
\hat{F}_z(s) &= F_z.
\end{aligned}
\tag{8}
$$

The displacement (and rotation) interpolation functions are given by

$$
\begin{aligned}
\hat{\phi}_x(\xi) &= \phi_x \xi, \\
\hat{\phi}_y(\xi) &= \frac{1}{1+\Phi} \left[u_z/L \left(-6\xi + 6\xi^2 \right) + \phi_y \left(-2\xi + 3\xi^2 \right) \right. \\
&\quad \left. + \xi \phi_y \Phi \right], \\
\hat{u}_x(\xi) &= u_x \xi, \\
\hat{u}_y(\xi) &= u_y \left(3\xi^2 - 2\xi^3 \right) + L\phi_z \left(-\xi^2 + \xi^3 \right), \\
\hat{u}_z(\xi) &= \frac{1}{1+\Phi} \left[u_z \left(3\xi^2 - 2\xi^3 \right) - L\phi_y \left(-\xi^2 + \xi^3 \right) \right. \\
&\quad \left. + L\phi_y \Phi \left(\xi/2 - \xi^2/2 \right) + \xi u_z \Phi \right],
\end{aligned}
\tag{9}
$$

where $\xi = s/L$ and $\Phi = 12EI_y/kGAL^2$.

SELF-ALIGNMENT OF KINEMATIC COUPLINGS: EFFECTS OF DEFORMATIONS

Francesco Patti, J.M. Vogels
VDL ETG
Eindhoven, The Netherlands

ABSTRACT
This paper contains a study of the kinematic coupling, focusing on the self-aligning property. Such a property expresses how the system is able to overcome the friction forces when reaching the centered position: this is why the characterization of such forces is one of the main subjects that will be analyzed. Normally, friction forces are assumed to be oriented against the possible motion even when motion is not present: an alternative approach will be proposed, that is to consider the deformations of the involved bodies to identify friction orientation. Since a study of the deformations is not always possible due to lack of information (during the concept phase of the design, for instance) it will be proposed a worst case scenario approach: the effect of deformations will be evaluated without studying them in detail. Such approach can be used to estimate the performance of kinematic couplings in the early phase of the design; moreover, it is also useful to easily compare the two analysis (with and without deformations), helping therefore to understand the importance of this phenomenon with respect to self-alignment.

INTRODUCTION
Kinematic couplings are interfaces very commonly used in high precision mechanics: they can connect parts together with high stiffness and repeatability. However, in order to have such performances, it is necessary that the system is self-aligning, meaning that it must have a tendency to spontaneously move to its centered position. This tendency is generated by an external source of energy (gravity in most cases, but also springs, for instance) that will provide forces to move the system. Friction is one of the main factors in the phenomenon of self-alignment: in fact the system will be able to align itself only if the friction coefficient is smaller than a certain value, the so called *limiting coefficient of friction*.
In previous treatments, when looking for the limiting coefficient of friction, the friction forces were assumed to be in the opposite direction of the motion [1,2]. However, when there is no motion, this is not always the case: it will be shown that the direction of friction forces is strictly related to the way the involved bodies deform and in general is not correlated with the possible motion. Intuitively, having the friction forces in the opposite direction of the relative motion works best for preventing the motion: it will be shown that this is not always the case.
Therefore, not only friction orientation is unrelated to the potential motion, but such assumption could lead to underestimate the friction ability to prevent the motion, thus to predict a system to be self-aligning when it actually isn't.

PROBLEM DEFINITION
A kinematic coupling is an interface that connects a system to another in an isostatic way: this is achieved by six contacts, in most cases between three balls and three V-grooves (Figure 1).

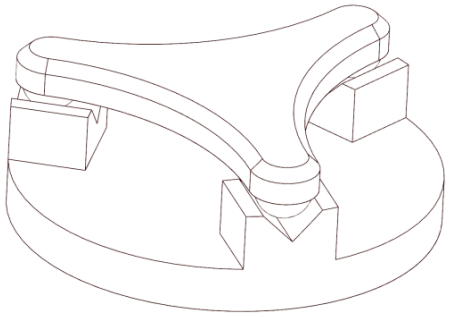

FIGURE 1. An example of conventional kinematic coupling.

When the coupling is put together, at first it will be off-centered, meaning that not all constraints will be in contact. It is assumed that the initial velocity will be zero (worst case scenario). Furthermore, only initial positions close to the centered one will be considered.
The question to be answered is: will the system be able to move towards the centered position? This can be found by studying the equilibrium of the system, in all possible off-centered positions. Thanks to energy based considerations [1], it is

possible to restrict the study to only six cases, the most difficult for the motion. In fact, at the beginning of the positioning phase only few constraints will be in contact. Assuming to have a self-aligning system, the system will move towards the centered position, therefore the number of constraints in contact will increase, until all six constraints will be in contact. The tendency of the system will be to move in a way that the minimum amount of energy will be dissipated; the less the number of active constraints, the more the freedom of the system to follow the less resistive path. So, when only one constraint will be left, the system will be able to move only in one specific path, which in general will be far from being the least resistive.
This line of reasoning brings to the conclusion that if a system is able to move in all of the six paths identified by removing the six constraints one at a time, then it will always be able to move towards the centered position.
Therefore there will be six studies of equilibrium, each one with only five active constraints: the most resistive path will be identified by the smaller limiting coefficient of friction, which will measure the self-aligning property of the coupling.
The state of equilibrium considered will be the so called *incipient motion*: it's a static state such that any reduction of friction coefficient would break the equilibrium. In other words, the system is on the verge of motion.

Model definition: naming convention

As stated before, the study will be limited to a very small area around the centered configuration of the system: this means that it will be possible to consider the contact points coincident with the nominal ones, identified by the position vectors $\vec{r}_i$, where $i = 1,2,\dots,6$ is the index assigned to the six constraints.
Furthermore, every contact will constrain only one direction, identified by the unit vector $\vec{n}_i$, which is defined as the normal of the tangent plane of both faces at the contact point, oriented towards the body to be positioned.
The constraint reactions contain a normal component $\vec{N}_i = N_i\vec{n}_i$ and a tangential component representing friction $\vec{T}_i$.
The external force which provides the energy for the alignment is $\overrightarrow{F_e}$, applied in the point identified by the position vector $\vec{r}_e$.
All these quantities will be expressed in a coordinate system $CS_0(O,x,y,z)$ whose origin and orientation is arbitrary.

Orientation of friction forces

When friction forces are present, the equilibrium problem of a kinematic coupling is undetermined in case of no motion. In fact, the following quantities are unknown:

- 5 normal reactions $\vec{N}_i$ with known direction → 5 variables;
- 5 friction forces $\vec{T}_i$: each force has a known magnitude (μN_i) and is normal to the $\vec{N}_i$ → 10 variables;
- 1 friction coefficient μ → 1 variable.

In total, there are sixteen unknown. The equations available instead are:

- 3 equations for equilibrium of forces;
- 3 equations for equilibrium of moments;
- 5 equations defining the friction coefficient $\mu = \frac{T_i}{N_i}$ $i = 1,2,\dots,6$ except j (the removed face).

This brings to $16 - 11 = 5$ missing equations: the solution belongs to a five dimensional space. To obtain a determined system, five more equations are needed.
An approach that is often followed to solve this indetermination is to assign a specific direction for the five friction forces: it is assumed that friction is oriented as if there were motion. In this way, five more equations become available and the system becomes determined. To know such directions, it is sufficient to evaluate the virtual displacement compatible with the constraints at each contact point.
Although this is often a good approximation as it will be shown later, in reality friction has a different orientation.
A more accurate way to address this problem is to consider the friction forces as normal reactions generated by extra constraints (Figure 2), and follow the usual approach to study hyperstatic (statically undetermined) structures: to introduce the deformations, which will provide extra equations.

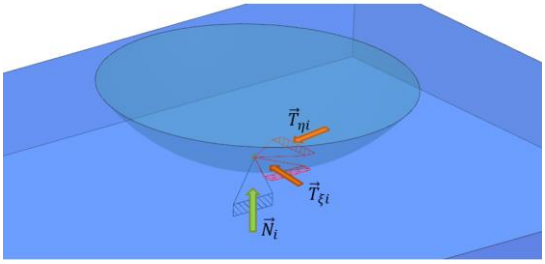

FIGURE 2. Friction force treated as extra constraints.

The five friction forces are replaced by ten normal reactions generated by ten extra constraints, two for each friction force. In fact, every friction force lies on a plane, thus is represented by two simple constraints. By adding these extra constraints, the problem becomes formally overdetermined: therefore it can be solved by considering the body as a solid, which allows to introduce a number of extra equations (the compatibility equations) expressing that the body will deform in a way that the five contact points will not move.
In this case, the unknown variables are:

- 5 normal reactions $\vec{N}_i$ with known direction → 5 variables;
- 10 normal reactions coming from the added constraints: their direction is known → 10 variables.

In total, fifteen unknown variables to be solved. And the equations are:

- 3 equations for equilibrium of forces;
- 3 equations for equilibrium of moments;
- 9 compatibility equations imposing the deformations such that the mutual distances of the five contact points won't change.

Thanks to the added compatibility equations there are in total fifteen equations that will allow to find the fifteen unknown variables: the problem becomes determined.
It is interesting to notice that in this process the possible motion of the system is not involved at all. Moreover, the ratio $\frac{T_i}{N_i} = \mu$ is not part of the equations: these two considerations bring to the following general conclusions:

1. The friction forces will not be oriented against the motion;
2. The friction coefficient required for the equilibrium will be different for each constraint.

Conclusion N.1 shows that assuming the friction forces oriented exactly against the motion is not correct (although in many cases is a good approximation); in some circumstances this could result in underestimating the effectiveness of friction in blocking the motion. In other words, in general there are other directions for which friction forces can be more effective, thus being able to block the motion even with a lower friction coefficient.
Conclusion N.2 instead brings to the following: assuming friction coefficient equal for all constraints, the condition of incipient motion is characterized by only one constraint where the reaction lies on the cone of friction, and not all of them.
The just explained approach shows that when in equilibrium problems friction forces are involved, and there is no relative motion, the deformations of the bodies play an important role: the orientation of friction forces depends on the internal deformations and it influences the efficiency of friction in preventing the motion.
This behavior can be visualized as follows: when a coupling is put together, at some point the moving body starts touching the counterpart in a number of points, which will generate constraint reactions: the body will deform under this load. Assuming these deformations so small that there won't be relative displacements at any contact point, these deformations will generate friction forces that will oppose the deformation itself in order to prevent sliding. Friction forces therefore will be oriented against such sliding, which is not provoked by rigid movement, but merely by local deformations of the bodies.
To see the effect of friction orientation in reaching equilibrium, a simple case in 2D is shown (see below Figure *3*): the problem is studied with the graphical method explained in [2].

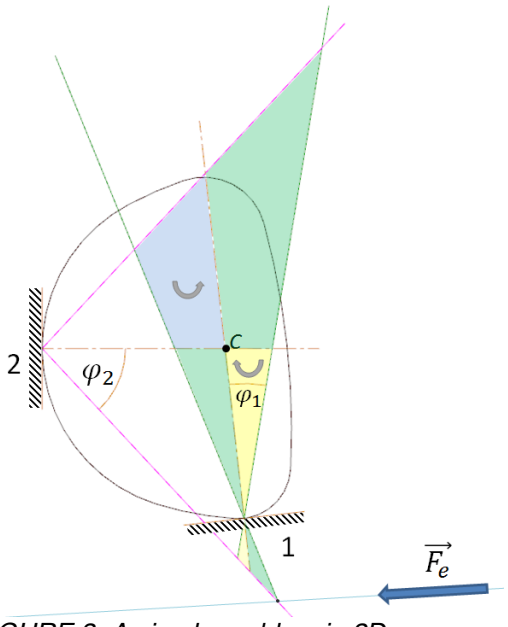

FIGURE 3. A simple problem in 2D.

A body is constrained in two points, having therefore one degree of freedom. Will the external force be able to move it? Considering the hypothesis of friction against the direction of the motion, since the motion will be a clockwise rotation around C, the intersection to be considered between the friction angles is the one in yellow: the system could be in equilibrium only if the external force would intersect the yellow area. Since this is not the case with the friction coefficients represented, equilibrium cannot be verified. But if friction forces are allowed to be oriented towards the relative motion (as a result of a certain deformation of the body), the three areas in green must be added. Thanks to this extension, the conditions for equilibrium are met. In this particular case, the friction force of constraint 1 is pointing towards the motion, and yet this situation is more efficient in terms of preventing the motion than the case of friction against it (yellow areas).

EVALUATING THE LIMITING COEFFICIENT OF FRICTION

In this paragraph the equations of equilibrium will be obtained, in order to find the limiting coefficient of friction. This will be done in two ways: assuming friction forces oriented against the incipient motion, and considering the effects of deformations. In both cases it will be assumed that the incipient motion is characterized by all friction forces lying on their cone of friction.

Analysis with friction oriented against the relative motion

The first steps consist in studying the displacements of each contact point i when one constraint j is removed. Defining $\Delta\vec{\theta}$ as the rotation of the body and $\Delta\vec{s}_O$ the displacement of the origin O, the following system expresses the compatibility equations of the five active constraints (the 6th equation for $i = j$ is only needed to assign a specific value for the displacement):

$$\left(\Delta\vec{s_0} + \Delta\vec{\theta} \times \vec{r}_i\right) \cdot \vec{n}_i = -\delta_{i,j} \qquad i = 1, 2, \dots, 6 \quad (1)$$

where $\Delta\vec{s_0} + \Delta\vec{\theta} \times \vec{r}_i = \Delta\vec{s}_i$ is the displacement of point i and $\delta_{i,j}$ is the delta of Kronecker. The solution of this system gives the displacement $\Delta\vec{s}_i$ of each contact point, which is needed to express the direction of the friction forces. The equations of equilibrium are:

$$\begin{cases} \vec{F}_e + \sum_{i \neq j} \left(N_i \vec{n}_i - \mu N_i \dfrac{\Delta\vec{s}_i}{|\Delta\vec{s}_i|} \right) = 0 \\ \vec{r}_e \times \vec{F}_e + \sum_{i \neq j} \vec{r}_i \times \left(N_i \vec{n}_i - \mu N_i \dfrac{\Delta\vec{s}_i}{|\Delta\vec{s}_i|} \right) = 0 \end{cases} \quad (2)$$

It can be demonstrated that the above system has five solutions, thus five values of μ. The smallest positive value represents the limiting coefficient of friction for the constraint j removed; the limiting coefficient of friction of the system is the smallest of these six values.

Analysis considering deformations

To consider the effect of deformations, the knowledge about the elastic behavior of the involved bodies is needed. Such information is normally not available at the moment of concept definition of the kinematic coupling. To overcome this problem, it is followed a worst case scenario with respect to self-alignment: the coefficient of friction is expressed as a function of the friction forces orientations, which are considered not related anymore to the motion; such a function is then minimized by using a computer algebra program. This way allows to

find the worst case scenario, without getting into the details of internal deformations.

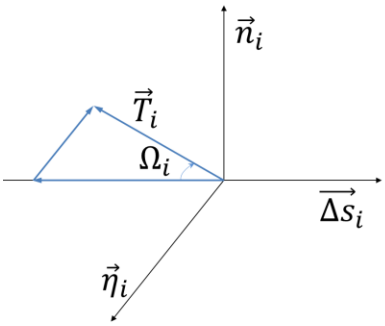

FIGURE 4. Definition of angles Ω_i.

Figure 4 shows the definitions of the six angles Ω_i that define the orientations of friction forces. The force applied to the generic contact point can be expressed as follows:

$$\vec{F}_i = N_i\vec{n}_i - \mu N_i \frac{\Delta\vec{s}_i}{|\Delta\vec{s}_i|}\cos\Omega_i - \mu N_i \frac{\Delta\vec{s}_i}{|\Delta\vec{s}_i|}\times\vec{n}_i \sin\Omega_i \qquad (3)$$

where $i = 1,2,\dots,6\ except\ j$
The equilibrium equations (2) become therefore:

$$\begin{cases} \vec{F}_e + \sum_{i\neq j}\left(N_i\vec{n}_i - \mu N_i \frac{\Delta\vec{s}_i}{|\Delta\vec{s}_i|}\cos\Omega_i - \mu N_i \frac{\Delta\vec{s}_i}{|\Delta\vec{s}_i|}\times\vec{n}_i \sin\Omega_i\right) = 0 \\ \vec{r}_e\times\vec{F}_e + \sum_{i\neq j}\vec{r}_i\times\left(N_i\vec{n}_i - \mu N_i \frac{\Delta\vec{s}_i}{|\Delta\vec{s}_i|}\cos\Omega_i - \mu N_i \frac{\Delta\vec{s}_i}{|\Delta\vec{s}_i|}\times\vec{n}_i \sin\Omega_i\right) = 0 \end{cases} \qquad (4)$$

This system of equations has, like the system (2), five solutions of which the one with the smallest positive value of μ is the one with physical meaning: such value in this case is function of five angles Ω_i. It is relatively easy to minimize this function by using a computer algebra program. The result is a set of friction orientations together with the smallest coefficient of friction associated: it expresses the case where a certain elastic behavior of the bodies brings to a particular set of friction orientations such that equilibrium can be reached with the smallest coefficient of friction.

COMPARISON OF THE TWO RESULTS

The two approaches are now applied to the common case of kinematic coupling with three grooves at 120°, keeping β, the half angle of the V, variable (see Figure 5); the external force is vertical, applied at the center of the system.

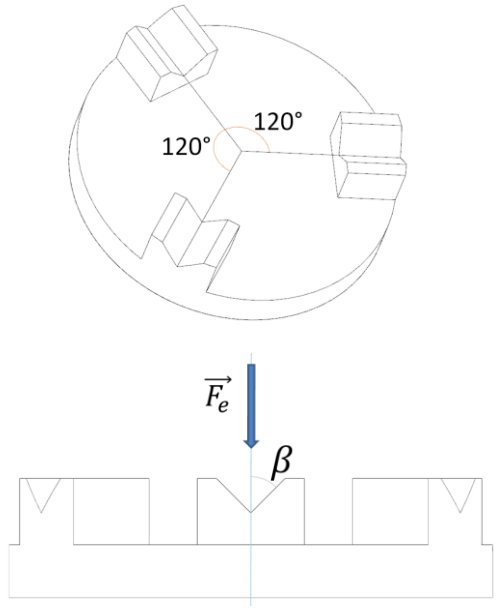

Figure 5. Standard Kinematic Coupling.

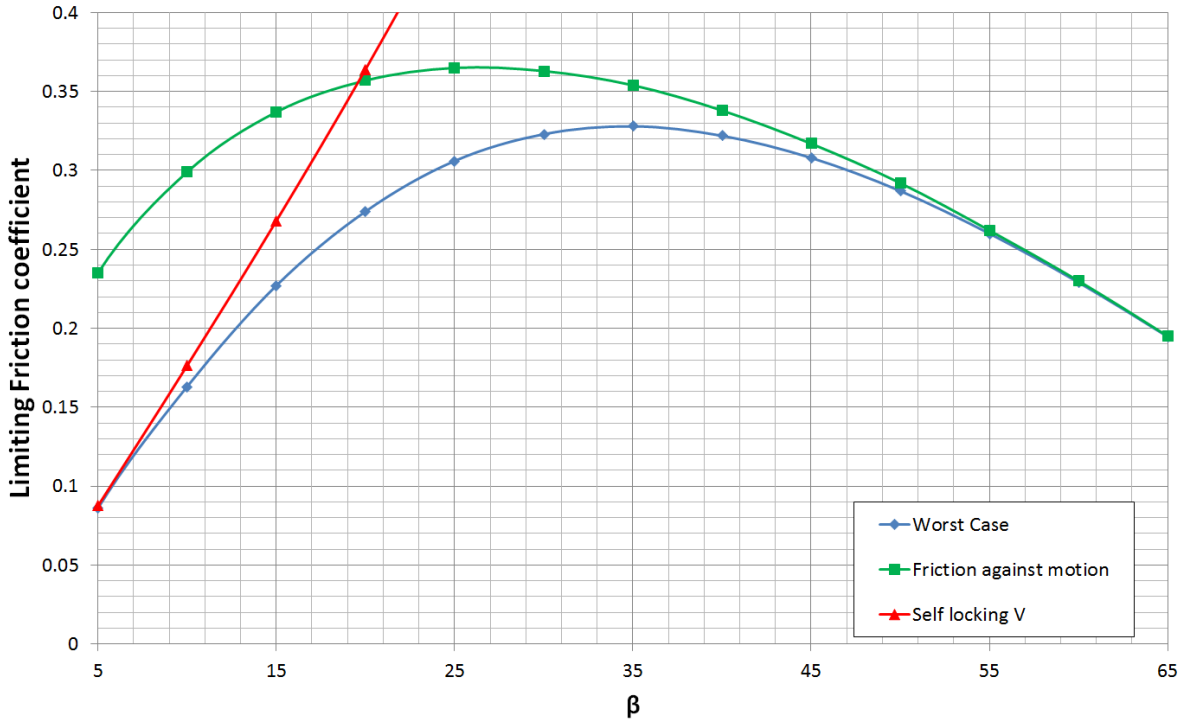

Figure 6 Comparison of worst case analysis and friction against motion approach.

Figure 6 shows the limiting coefficient of friction evaluated in case of friction forces oriented against the relative motion, and oriented in a way that the friction has the best efficiency in preventing the motion.
Around the standard configuration β=45° the two approaches give almost the same result, therefore it is safe to use the green line. When instead the angle gets smaller, the difference is not negligible any more: the green line underestimates the efficiency of friction.
Moreover, it's interesting to note the green line doesn't take into account the phenomenon of self-locking, which is instead included in the blue line: this is because self-locking is caused by the deformations of the bodies in contact, which are taken into account only by the blue line.

CONCLUSIONS

This study has shown that evaluating the self-aligning property of kinematic couplings by considering friction oriented as if there were motion is a good approximation for the standard kinematic coupling of Figure 1, but it might not be accurate in other situations: deformations can change the direction or friction forces, making friction more efficient in preventing the motion. In such cases it is possible to have a first evaluation of the limiting coefficient of friction with the worst case approach: however, more detailed analysis and/or experiments are needed to validate the first results.

REFERENCES

[1] L. C. Hale and A. H. Slocum. Optimal design techniques for kinematic couplings. Precision Engineering – Journal of the International Societies for Precision Engineering and Nanotechnology, 2000.
[2] M. Koster. Constuctieprincipes voor het nauwkeuring bewegen en positioneren. Uitgeverij Universiteit Twente: 335-337. Dutch.

ON THE DESIGN OF LONG RANGE MULTIAXIAL NANOFABRICATION MACHINES BASED ON CARTESIAN NANOPOSITIONING SYSTEMS WITH ADDITIONAL ULTRA PRECISION ROTATIONS

Ralf Schienbein[1], Florian Fern[2], David Jorda[1], René Theska[1], Roland Füßl[2]
[1] Institute of Design and Precision Engineering, Precision Engineering Group, Department of Mechanical Engineering, Technische Universität Ilmenau, Germany
[2] Institute of Process Measurement and Sensor Technology, Department of Mechanical Engineering, Technische Universität Ilmenau, Germany

INTRODUCTION

As result of a comprehensive literature survey, the majority of nanopositioning and nano-measuring machines (NPMMs) are based on three independent linear movements in a Cartesian coordinate system with a repeatability in the nanometer range. This in combination with the specific nature of sensors and tools (further on summarized as tool) limits the addressable part geometries. Depending on the tool in use, spherical and aspherical geometries as well as free-form surfaces cannot be measured or only to a certain limit. This article contributes to the enhancement of multiaxial machine structures by the implementation of rotational movements while keeping the precision untouched. Approaches are known, which allow the movement with a degree of freedom of four or five, which is required for addressing freeform surfaces orthogonal to the surface [1-3]. In comparison to this, our aim is the extension of NPMMs with additional degrees of rotational freedom for multitool concepts and freeform manufacturing [4]. Suitable concepts of the overall machine structure were investigated. A parameter based evaluation system was created to identify solution concepts fulfilling given requirements [5]. The rotation of the tool in use showed a high application potential. This article contributes to the systematic development of multiaxial machine structures based on existing NPMMs [4, 6] in the early design state. An evaluation system is developed which supports the user in the selection of sub structures (positioning and measuring systems) fulfilling given requirements in the best possible manner. This paper presents derived exemplary solutions based on chosen requirements, a summary and an outlook for further developments.

EVALUATION OF MULTIAXIAL NPMMS

To support the selection of machine structures for the development of a multiaxial nanopositioning machine, an evaluation system was developed. This is based on modular arrangement variants of basic components, a dynamic evaluation system and indications of the characteristics to be considered for the design process. The fundamental structures of nanopositioning and nanomeasuring machines are based on three modes of movement, the Sample Scanning Mode (SSM), the Mixed Scanning Mode (MSM) and the Scanning Probe Mode (SPM). Suitable concepts of the extension of Cartesian scanning modes to overall machine structures with additional degrees of rotational

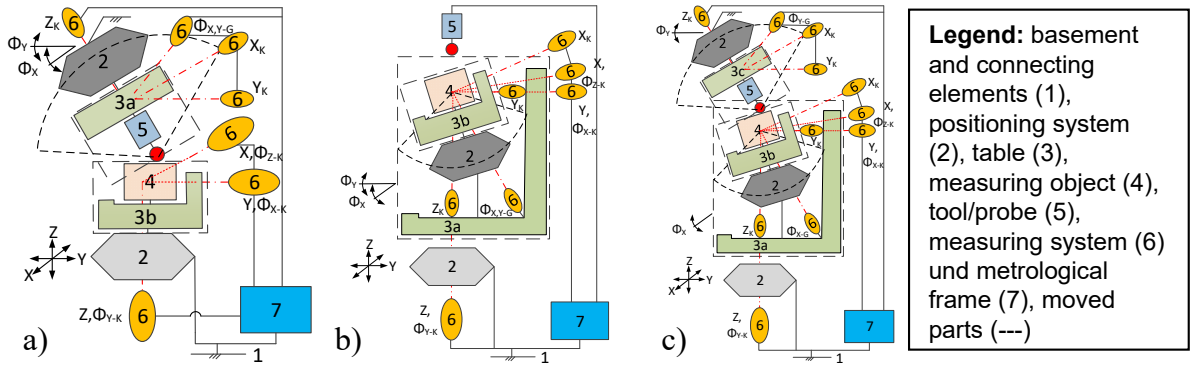
a)
b)
c)
Legend: basement and connecting elements (1), positioning system (2), table (3), measuring object (4), tool/probe (5), measuring system (6) und metrological frame (7), moved parts (---)

FIGURE 1. System configurations for the Sample Scanning Mode with additional rotations of the tool (a), the object (b), or tool and object (c)

freedom were investigated [7]. First evaluations for the overall structure show the highest degree of fulfilment for a SSM with additional rotations of the tool (figure 1a). Alternatively, rotations of the sample or of the sample and the tool should be considered, as shown in figure 1.

SAMPLE SCANNING MODE WITH TOOL ROTATIONS

In a first step, the rotation of tools with a maximum mass of 2 kg and an overall extension in the measuring direction of 50 mm is considered. For this purpose, a total of 23 suitable kinematic variants for addressing a hemisphere orthogonally to its surface are determined by means of a structural synthesis, by varying the position of the instantaneous center of rotation and the number of joints.
In the following, kinematic variants are selected by use of a parameter-based evaluation system. The evaluation criteria deploid are mainly based on quantitative characteristics in order to minimize subjective influences. To achieve this, typical values of positioning systems are derived from comprehensive design catalogs [7] and software-supported [8] parameter studies of the geometries and motion ranges. The design catalogs contain currently commercially available positioning systems for ultra-precise rotations including multiaxial solutions such as hexapods. Figure 2 shows the kinematics with the highest degree of fulfilment.

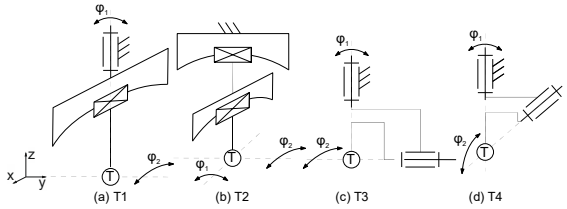

FIGURE 2. Suitable kinematics for tool rotations

These variants T1-T3 describe rotations of the tool center point (T) around the main axes of the Cartesian coordinate system of the NPMM.
In addition, the angular position of the individual rotary axes to the main axes of the NPMM can be varied. Figure 3 shows that variation in 45° steps. The large number of new variants of axis orientation can be summarized to two basic principles per choosen kinematic (a and b in figure 3). Figure 4 shows this for the kinematic T1 (named V1 and V2).

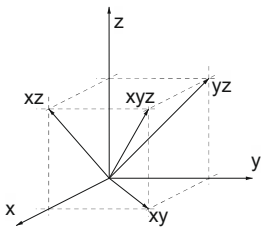

Orientation of rotation axis φ_2	Orientation of rotation axis φ_1							
	x	y	z	xy	xz	yz	xyz
x	-	a	a	b	b	a	b
y	a	-	a	b	a	b	b
z	a	a	-	a	b	b	b
xy	b	b	a	-	b	b	b
xz	b	a	b	b	-	b	b
yz	a	b	b	b	b	-	b
xyz	b	b	b	b	b	b	-

FIGURE 3. Variation of the axis orientation
The parameter based evaluation system is extended by these variants and used for the selection of suitable kinematics.

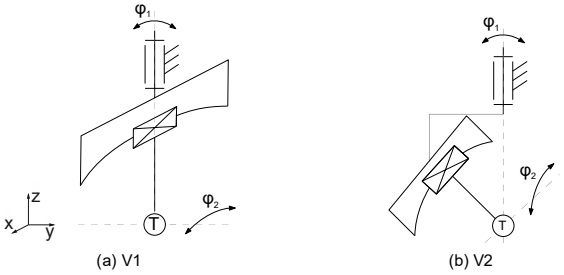

FIGURE 4. Variants of the axis orientation of T1

For the integration of additional tool rotations in NPMMs with Sample Scanning Mode, the variants T3, T1, as well as T4 and V2 are particularly recommended. These allow the construction of multiaxial nanopositioning systems based on commercially available ultra-precision rotary positioning systems.

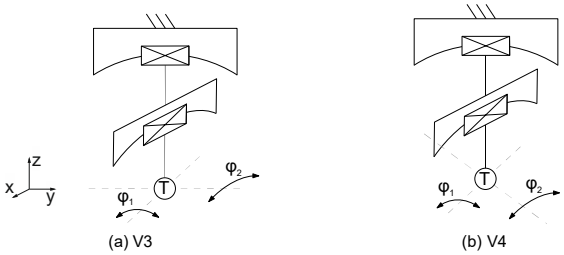

FIGURE 5. Variants of the axis orientation of T2

In general, kinematics with a high degree of fulfilment consider a common instantaneous center of rotation in the tool center (T).
This results in maximum rotation angles of 90° for Φy and 360° for Φz as well as minimized mass and no required linear correction movement. In addition, they are in compliance to the Abbe Comparator Principle, thus avoiding first order positioning errors.

SAMPLE SCANNING MODE WITH SAMPLE ROTATIONS

In analogy to the rotation of the tool, possible kinematic variants are determined and evaluated for the rotation of the sample by use of the parameter based evaluation system. The solution variants for the rotation of the tool show in comparison the higher degree of fulfilment. However, different arrangement sequences must be selected for addressing a hemisphere orthogonally to its surface for rotations of samples. Since the sample has an unknown structure, linear correction movements are necessary to address the whole sample surface. As a result, the addressable sample points or the angle of rotation of the positioning system used, are considerably restricted. With additional rotations, the sample dimensions are restricted to a part of the Cartesian volume. Depending on the kinematic variants, characteristic addressable volumes were calculated showing the limits for the hemispherical and orthogonal surface contact for a given rotation kinematic (figure 6). If the sample fits to the dimensions derived from the given Cartesian volume, any hemisphere within the characteristic volume can be measured.

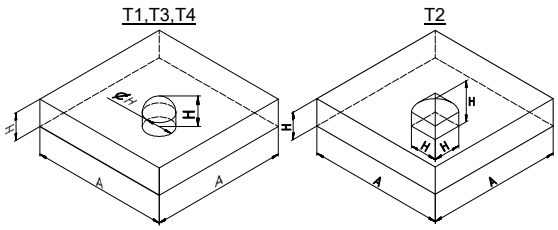

FIGURE 6. Restrictions of object geometries due to the concept of object rotation

SAMPLE SCANNING MODE WITH SAMPLE AND TOOL ROTATIONS

The restrictions of object geometries can be avoided, if rotations of the tool are implemented in addition to the object movements.

Figure 7 shows the kinematics with the highest degree of fulfilment for the combined object and tool rotation with decreasing degree of fulfilment from a) to c). A higher degree of freedom influences the achievable uncertainty of the NPMM [6]. If the exact position of the tool center point (T) is not measured directly, the displacement as a consequence of the error motion can be calculated by geometric dimensions of the substructures. There are three translational and three rotational errors for every stage of rotation, which are dependent on the

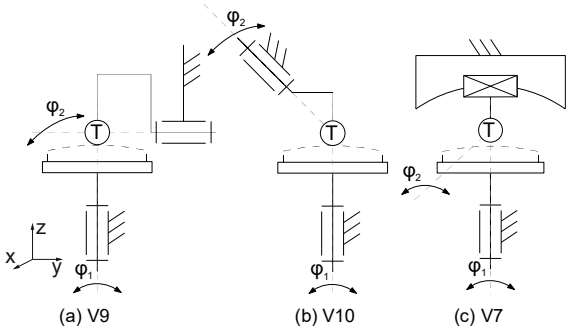

FIGURE 7. Suitable kinematics for combined object and tool rotation

actuation angle. The movement of (T) can be calculated by a superposition of the components resulting from those error motions. For tool rotation principles with an instantaneous center of rotation in (T) the resolution and measurement uncertainty of the rotation measurement system does not affect the position of (T). The sample rotation can be described in the same manner as for the tool rotation. Since (T) is fixed, the error motion of the positioning system now affects the position of the sample. Due to the dimension of the sample, the sample position is not independent from the properties of the angular measurement system. Although the characteristic lengths are much smaller for the sample rotation the described systematic error leads to a comparable uncertainty for both approaches [9].

One approach to reduce the measurement uncertainty of the overall system is the in situ measurement of the respective translation and rotation errors of the rotation systems. This is simplified by the separation of the rotations to the object and tool, since only one positioning system has to be measured.

If this is not possible caused by the complexity of the overall structure due to rotations around more than one axis, the movements of the tool or the object needs to have a high reproducibility.

COMPARISON OF THE REPRODUCIBILITY OF ROTATIONEL AXES

As shown in previous studies [9], the measurement uncertainties of the NPMMs increase in general significantly if additional rotational axes are integrated. Caused by the fact that data of commercially available rotation units are only rudimentary or not existing at all, they must be estimated as described in [9] or measured accordingly before the integration of

the rotary axes. For the implementation of the variant T1 of figure 2 to a NPMM [10], corresponding test series were carried out to determine the reproducibility of different arrangements of two positioning systems. Based on the evaluation system described in the previous chapters, a rotation stage [11] and a goniometer [12] were selected for the tool rotation of the NPMM. Both positioning systems were measured separately and combined in arrangement according to principle T1 with a universal autocollimator Elcomat 3000 [13] and a flat mirror reflector in the rotational center.

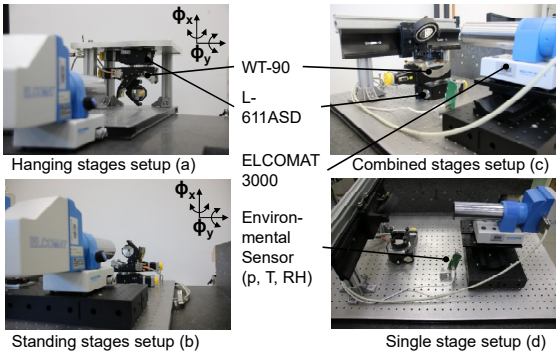

FIGURE 8. Setups for the measurements of the rotation reproducibility

In addition, the influence of the arrangement in standing and hanging construction with or against the direction of gravity was investigated (figure 8). This corresponds to an application for tool or object rotation in the chosen NPMM. For each measurement setup, the parameters positioning speed and unidirectional or alternating direction of movement were varied.
Figure 9 shows exemplarily the raw data of the measurement of the setup number 1-1 for v = 1 °/s and ϕ_x and ϕ_y respectively. Since the repeatability of the positioning is particularly important for the integration into the NPMM.

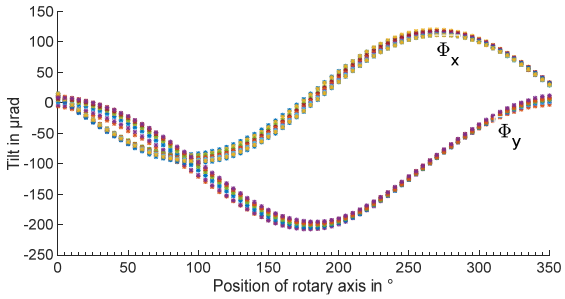

FIGURE 9. Position-dependent Tilt of L-611

It was determined as the standard deviation of the mean value for the corresponding angular position of the rotary axis. Table 1 contains the respective maxima and minima over the full range of motion for unidirectional movement.

Table 1. Range of Tilt-repeatability for different stage setups

setup number	1-1	1-2	1-3	2-1	2-2	2-3
stage setup	hanging			standing		
first stage	L-611	L-611	L-611	L-611	L-611	L-611
second stage	-	WT-90	WT-90	-	WT-90	WT-90
measured stage	L-611	L-611	WT-90	L-611	L-611	WT-90
max. repeatability of ϕ_x in ± *µrad*	10,210	2,800	9,140	6,150	2,600	9,310
min. repeatability of ϕ_x in ± *µrad*	2,250	2,050	1,300	2,970	2,130	1,055
max. repeatability of ϕ_y in ± *µrad*	12,930	7,700	6,695	14,420	8,700	17,952
min. repeatability of ϕ_y in ± *µrad*	2,615	5,100	2,025	7,275	5,850	1,000

DEFORMATIONS DUE TO THE ROTATION OF THE TOOL

The integration of additional positioning systems for the rotation of objects according to Figure 1c corresponds to additional masses, which must be moved by the existing linear positioning systems, if the permissible parameters of the objects are not to be restricted. Simultaneously a direct temperature input and direct static and dynamic deformation of the supporting structure, in this case the reflectors for the ultra-precise length and angle measuring systems, is introduced. In NPMMs, these are generally mirror corners of the highest thermal and geometric stability. A deformation between the reflection surface and the object thus has a direct influence on the NPMMs measurement uncertainty. In general, the distance between the rotation axes and the existing measuring systems for the X, Y and Z movements is larger for structures according to Figure 1a.
At the same time, the supporting structures are used as a static coupling between the tool and the metrological frame that is as thermally and geometrically stable as possible. Rotation axes for the tool result in additional and complex deformations. The deflection of the cuboidal cover plate of the NMM1 (PI) supported at three corners due to the additional mass of the positioning system (Po), for example, cannot be completely solved analytically. The static Ritz-procedure offers a possible solution approach [14]:

$$\omega(x,y) = xya_1 + x^2y^2a_2 \qquad (1)$$

with:

$$\begin{pmatrix} a_1 \\ a_2 \end{pmatrix} = \begin{pmatrix} -\dfrac{3a^2 p(20a^4\nu^2 + 28a^4\nu - a^4)}{(15a^4\nu + 41a^4)h^3 E} \\ \dfrac{75}{2}\dfrac{pa^4(\nu^2 - 1)}{(15a^4\nu + 41a^4)h^3 E} \end{pmatrix} \quad (2)$$

The variable deflection due to the variable center of mass, which depends on the positioning angle of the positioning system, can therefore only be calculated to a limited extent and was determined by FEA models using Ansys 19 (figure 10). Simulations of tool rotations were evaluated using the selected positioning systems (L611 and WT90) within the NMM1.

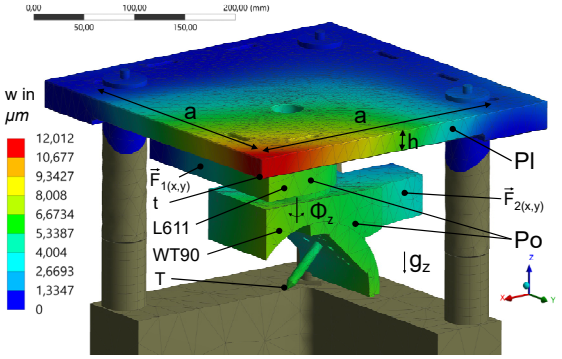

FIGURE 10. FEA model of the upper NMM1 frame with additional rotary axes L611 and WT90

The corresponding values for the deflection ω of the toolcenterpoint (T) and the free end of the cover plate (t) are shown in figure 11.

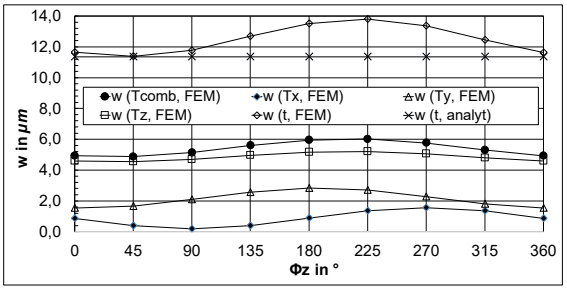

FIGURE 11. Deflection of (T) and (t) due to the variable center of mass

A reduction of the deflection is effectively possible by a material change or by increasing the plate cross section (h), as shown by the FEA results for the combined shift of T (T_{comb}) for ϕ_z=225° (table 3). Due to a minimal coefficient of thermal expansion, the materials used for the simulation are generally used for the metrological frame (table 2).

Table 2. Materiel properties for the FEA

Values of structural properties used in FEA studies						
Property	Material					Unit
	Al (EN AW 7075)	Zerodur	SiC	Pyrex	Invar 36	
Density (ρ)	2,77	2,53	3,20	2,23	8,00	$10^3 kgm^{-3}$
Young's modulus (E)	71	90,3	414	64	145	$10^9 Pa$
Poisson's ratio (υ)	0,33	0,24	0,14	0,2	0,29	-
edge length of plate (a)	245					mm
mass of positioning system (Po)	6,6					kg

However, the increase of the plate cross section (h) causes a significant increase in mass and thus in the pressure load on the metrological frame. This in turn increases the creep of these structures, as an additional deformation ε(t), relative to the elastic start deformation ε_0. For ULE and quartz glass, for example, after t=500h values of ε(t) of ≤ 0,1%, for Invar36 ≤ 0,039% and for Zerodur ≤ 0,7% are realistic [15]. Furthermore, the additional rotation axes lead to a direct vibration input at the too. This influences the dynamics of the measurement, since the additional oscillation has to be considered. The frequencies of the vibrations introduced by the positioning systems are investigated by comprehensive measurements using a Laser Vibrometer [16]. Typical frequencies are in the range of 10 ≤ f ≤ 550 Hz, which is in accordance with the literature [17]. FEA-based topology optimization was therefore carried out to adapt the structure. The objective was to increase the stiffness of the cover plate and the first natural frequency while simultaneously maintaining a constant or reduced mass (table 3).

Table 3. Variants of the topology optimized top plate of the NMM1 for additional rotation axes

Variant	**V0**	**V1**	**V2**	**V3**	**V4**
	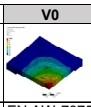	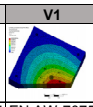	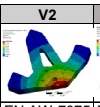	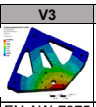	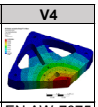
Material	EN AW 7075	EN AW 7075	EN AW 7075	EN AW 7075	EN AW 7075
plate height (h) in *mm*	21	48	48	48	48
plate mass (m_{Pl}) in *kg*	7,7127	9,8783	6,6042	7,2721	6,8101
T_{comb} in *µm*	3,2273	0,59794	0,70658	0,70231	0,68581
1.eigen-frequency (f_1) in *Hz*	282,01	714,01	646,56	648,85	655,34
2. eigen-frequency (f_2) in *Hz*	694,26	2171,9	1832,9	1887,1	1910,3
max. amplitude in T_z (at f1 and 1% damping) in *µm*	34,395	6,0541	7,6761	7,6302	7,4713

For the analysis of the amplitudes of (T), forces of ($F_{1,2} \leq 20N$) were considered in the area of the motors of the rotation axes and thus the greatest possible unbalance excitations for the frequency response analysis (figure 10).

CONCLUSION

A systematic parameter based dynamic evaluation approach was developed for the creation and selection of adequate machine structures for multiaxial nanopositioning systems (DOF>3). To support the selection, detailed parameter sets are generated containing explicit moving ranges, uncertainties, resolutions, reproducibilities and costs. The parameter sets are further detailed with derived characteristics such as deformations, vibrations or thermal influences due to the additional rotations based on FEA-models and verified experimental data. This approach is also applied to the rotation of the sample. The results are compared to those of the tool rotation and mixed versions. After all, the knowledge gained, is formed into general rules for the verification and optimization of design solutions for multiaxial nanopositioning machines.

Out of these investigations, a rotation of the tool is a favourable solution. Kinematics with a high degree of fulfilment consider a common instantaneous center of rotation in the tool center point (T). Compared to a fixed tool position this leads to shifting deviations of (T) due to deformations of the frame depending on the actual mass distribution. In addition, deviations of (T) are caused by vibrations and thermal influences of the positioning system.

The strict separation of the force frame and the metrology frame, thermal shielding and direct measuring systems for the deviation of (T) can compensate the effects that are dependent on the selected overall structure and positioning system.

ACKNOWLEDGMENTS

The authors gratefully acknowledge the support by the Deutsche Forschungsgemeinschaft (DFG) in the framework of Research Training Group “Tip- and laser-based 3D-Nanofabrication in extended macroscopic working areas” (GRK 2182) at the Technische Universiät Ilmenau, Germany.

REFERENCES

[1] Henselmans R: Non-contact Measurement Machine for freeform optics. Eindhoven: Technische Universiteit Eindhoven; 2009

[2] Taylor Hobson, Ametek: LuphoScan; 2015

[3] Schuler A, Weckenmann A, Hausotte T. Setup and evaluation of a sensor tilting system for dimensional micro- and nanometrology. J. Meas. Sci.Tech. 2014. 25(6):064010

[4] Manske E, Jäger G. Multi-sensor approach for multivalent applications in nanometrology. Int. J. of automation and smart technology: AUSMT. 2. 2012. p. 141-145

[5] Schienbein R, Theska R. A contribution to the development of multiaxial nanopositioning machines. Proceedings of the 17th International Conference EUSPEN; 29th May – 2nd June; Hannover, Germany. p.113-114.

[6] Jäger G, Manske E, Hausotte T, Büchner H.-J. The metrological basis and operation of nanopositioning and nanomeasuring machine NMM-1 tm - Technisches Messen. 2009. 76(5):524

[7] Schienbein R, Theska R, Weigert F. A contribution to the implementation of ultraprecision rotations for multiaxial nanopositioning machines. Proceedings of the 59th Ilmenau Scientific Colloquium; 2017 Sep 11-15; Ilmenau, Germany; 1.1.03

[8] ARTAS - Engineering Software: SAM 6.1.

[9] Schienbein R, Fern F, Weigert F, Theska R, Füßl R. The implementation of ultra precision rotations to multiaxial nanofabrication machines: challenges and solution concepts. Proceedings of the 18th International Conference EUSPEN; 2018 June 4-8, Venice, Italy; p 65-66

[10] SIOS Meßtechnik GmbH 2018: NMM1

[11] Physik Instrumente (PI) GmbH & Co. KG 2018: L-611.9ASD

[12] Physik Instrumente (PI) GmbH & Co. KG 2018: WT-90 (65509201)

[13] MÖLLER-WEDEL OPTICAL GmbH 2018: ELCOMAT 3000

[14] Fern F. Analytische und numerische Untersuchungen zu Durchbiegungen und Schwingungen von 2d-Kontinua. Ilmenau: TU Ilmenau; 2016

[15] Hausotte T. Nanopositionier- und Nanomessmaschinen: Geräte für hochpräzise makro- bis nanoskalige Oberflächen- und Koordinatenmessungen. Ilmenau; 2011

[16] SIOS Meßtechnik GmbH 2018: Laser Vibrometer SP-S Series

[17] Naumann H. Handbuch Bauelemente der Optik; 7th ed. Hanser: München; 2014

ON THE EFFICIENT SIMULATION OF THE FLEXIBLE MULTIBODY DYNAMICS OF FLEXURE BASED PRECISION MECHANISMS USING SUPERELEMENTS

Jurnan Schilder, Mieke van den Belt
Faculty of Engineering Technology
University of Twente
Enschede, The Netherlands

INTRODUCTION

In precision engineering, flexure hinges are commonly used for the absence of friction, hysteresis and backlash. These hinges require high compliance in their driving directions and high stiffness in supporting directions. Because many modern applications require the flexure hinges to be well-behaved in a large range of motion, the hinge should maintain its support stiffness even for deformations far outside of its linear stroke. As the support stiffness of standard hinges dramatically drops with deflection, shape and topology optimization is used to design more sophisticated flexure hinges that meet the stiffness requirement. For this purpose, it is common to develop finite element models of the flexure hinges.

However, for the analysis and optimization of flexure based precision mechanisms, it is of importance to study the static and dynamic behavior of the mechanism as a whole. For this purpose, flexible multibody dynamics models of these mechanisms are needed. In order to keep computational costs of advanced optimizations within acceptable bounds, model order reduction techniques are required. In recent work [1], the authors developed a new flexible multibody formulation in which reduced order models of flexible bodies can be efficiently included. This formulation is based on the commonly used floating frame formulation. In this work, it is explained how the new formulation can be used for the analysis and optimization of flexure based precision mechanisms, by reducing individual flexure hinges to so-called superelements.

FLOATING FRAME FORMULATION

In the floating frame formulation, rigid body motion and elastic deformation are described by separate generalized coordinates. Rigid body motion is described by the absolute coordinates of the floating frame; a coordinate system that moves along with the body. Elastic deformation is described locally, relative to the floating frame by a combination of deformation shapes. These deformation shapes can be interpreted as the reduction basis for the body's local finite element model. In this work, it is assumed that the Craig-Bampton method [2] is used to reduce a body's finite element model. Different bodies are connected together or to the fixed world in their interface points. The kinematic constraint equations corresponding to these connections are typically expressed in terms of the absolute interface coordinates. Figure 1 shows a graphical representation of how the absolute interface coordinates are expressed in terms of the absolute floating frame coordinates and the local interface coordinates. Since the absolute interface coordinates are not part of the generalized coordinates in the floating frame formulation, Lagrange multipliers are required to enforce the kinematic constraints. Because this increases the number of unknowns, this is an important disadvantage of the floating frame formulation. Further details on the floating frame formulation can be found in standard textbooks on flexible multibody dynamics, such as [3].

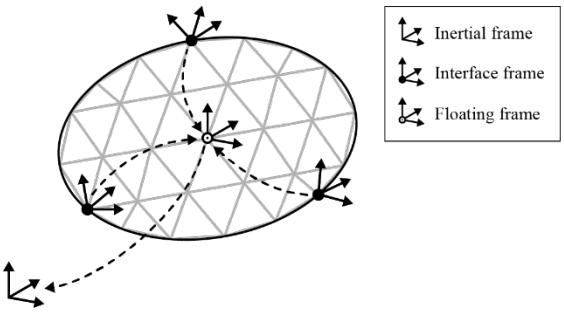

FIGURE 1. In the floating frame formulation the absolute floating frame coordinates describe rigid body motion and elastic deformation is described locally, relative to the floating frame.

SUPERELEMENT FORMULATIONS

In order to develop a more efficient formulation, it is desired to combine the floating frame formulation's possibility to apply model order reduction of a body's finite element model with a possibility to enforce kinematic constraints directly. To this end, the Lagrange multipliers need to be eliminated from the floating frame formulation. This can be done if the absolute interface coordinates uniquely describe the body's kinematics. In other words, if it is possible to express both the floating frame coordinates and the generalized coordinates corresponding to local elastic mode shapes in terms of the absolute interface coordinates, the Lagrange multipliers can be eliminated. One could say that in this case a superelement is created: the motion of a flexible body is described entirely by the motion of its interface points. The term superelement refers to the similar way in which the displacement field of a finite element is described uniquely by the displacements of its nodes.

In literature, multiple methods are described with which superelements can be created. The most straightforward possibility is to locate the floating frame at an interface point and to not take the Craig-Bampton modes of that specific interface point into account [4]. An important disadvantage of this method is that simulation results become dependent on which interface point is chosen. Moreover, a better accuracy can be expected when the floating frame is located close to the body's center of mass. Therefore, it is possible to introduce an auxiliary interface point at the center of mass and locate the floating frame there [5]. However, in this case 6 additional degrees of freedom are introduced.

The method presented in [1] eliminates the Lagrange multipliers from the formulation by applying a coordinate transformation on a flexible body's equations of motion. With this transformation, the absolute floating frame coordinates and generalized coordinates corresponding to the elastic deformation shapes can be expressed in terms of the absolute interface coordinates. This method allows to locate the floating frame at the center of mass of the undeformed body, without introducing 6 additional degrees of freedom. Figure 2 shows a graphical representation of the result of this coordinate transformation.

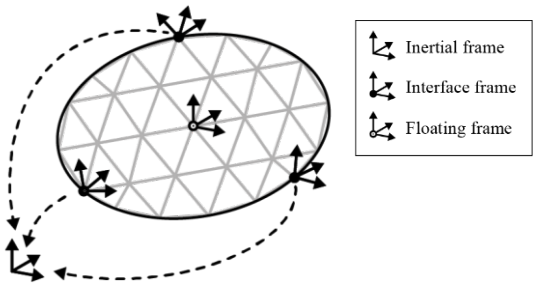

FIGURE 2. In the new superelement formulation, the absolute interface coordinates are the degrees of freedom. The floating frame is located in the center of mass of the undeformed body, which does not need to be an interface point.

Because the Craig-Bampton modes are able to describe 6 rigid body motions, their use allows for the demand of 6 additional constraints. In [1], these are that any linear combination of the Craig-Bampton modes should not result in elastic deformation at the location of the floating frame. In general, this is a nonlinear constraint in the configuration space. However, in its tangent space it can be used to express the variation of the absolute floating frame coordinates $\delta\mathbf{q}_{FF}$ and the variation of the local interface coordinates $\delta\mathbf{q}_{LI}$ in terms of the variation of the absolute interface coordinates $\delta\mathbf{q}_{AI}$:

$$\begin{bmatrix}\delta\mathbf{q}_{FF}\\ \delta\mathbf{q}_{LI}\end{bmatrix} = [\mathbf{A}]\delta\mathbf{q}_{AI} \qquad (1)$$

where $[\mathbf{A}]$ denotes the kinematic transformation matrix. At this point the equation of motion of a flexible body in the floating frame formulation can be considered. Because the equation of motion is solved for numerical increments, the coordinate transformation (1) can be applied within each increment. In this way, the equations of motion of the entire multibody system can be solved in terms of the absolute interface coordinates. The equations of motion of the entire multibody system can then be assembled and solved without Lagrange multipliers.

LARGE DEFORMATIONS WITHIN A BODY: MODAL DERIVATIVES

In [1], it was assumed that within a flexible body, elastic deformations remain sufficiently small, such that linear theory of elasticity can be used locally. However, in order to create superelements for large stroke flexure hinges, it is necessary to include geometric nonlinear effects. In [6], Wu et al. have explained how

modal derivatives can be applied to augment a linear reduction basis of Craig-Bampton modes by their modal derivatives. This method was applied successfully to reduce several structural dynamics problems. Since the new superelement formulation presented in this work uses Craig-Bampton modes to describe a body's local elastic behavior, it is suggested to apply the method in [6] to create a model order reduction method suitable for flexible multibody systems in which each body may be subjected to large deformations.

Consider a flexible body of which its linear elastic behavior is described with sufficient accuracy by the Craig-Bampton modes. The modal derivative $\boldsymbol{\theta}_{ij}$ denotes the sensitivity of Craig-Bampton mode $\boldsymbol{\phi}_i$ with respect to an elastic deformation in Craig-Bampton degree of freedom q_j. The modal derivatives are computed as:

$$\boldsymbol{\theta}_{ij} = \frac{\partial \boldsymbol{\phi}_i}{\partial q_j} = -\mathbf{K}^{-1} \frac{\partial \mathbf{K}}{\partial q_j} \boldsymbol{\phi}_i \qquad (2)$$

where $\mathbf{K} = \mathbf{K}(\mathbf{q})$ should be interpreted as the nonlinear finite element model's stiffness matrix of the body with all interface coordinates fixed, except for all coordinates of the interface point of which q_i is a generalized coordinate.

As an example, consider a two-dimensional beam. Figure 3 shows the Craig-Bampton modes related to the bending deformation of the right interface point (ϕ_1, ϕ_2) and the three corresponding modal derivatives $(\theta_{11}, \theta_{12}, \theta_{22})$. Note that the Craig-Bampton modes describe a deformation in the transverse direction $v(x)$, whereas the modal derivatives describe a deformation in the axial direction $u(x)$. Hence, the modal derivatives describe the shortening of the beam, that occurs when it is subjected to bending. From Figure 3, θ_{11} should be interpreted as the shortening of the beam, when the beam is subjected to a transverse displacement according to ϕ_1. Similarly, θ_{22} is the shortening of the beam when the beam is subjected to a transverse displacement according to ϕ_2.

It is important to mention that the modal derivatives have a nonzero deflection at the interface points. Consequently, motion of the interface points causes excitation of both the local interface coordinates corresponding to the Craig-Bampton modes as well as the generalized coordinates corresponding to the modal derivatives. However, it is possible to modify the basis of the modal derivatives by subtracting the component that is already present in the static Craig-Bampton modes. As the modified reduction basis is obtained simply column operations, they span the same reduced space [6].

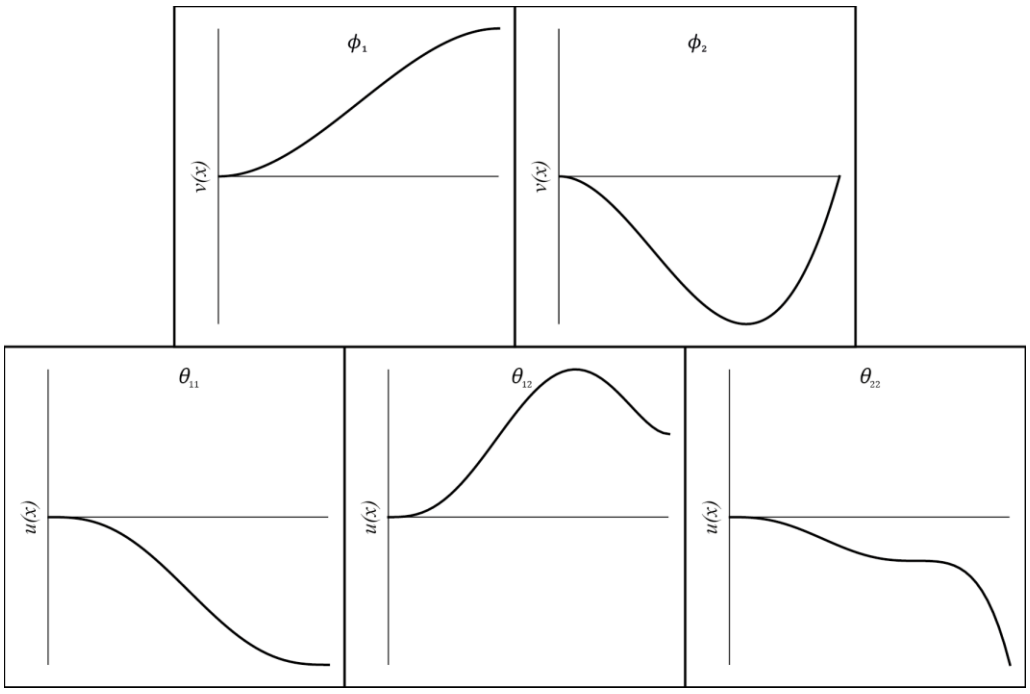

FIGURE 3. Craig-Bampton modes and modal derivatives related to a 2D beam's right interface point.

Let $\mathbf{q}$ denote all generalized coordinates corresponding to the local finite element model of the body. It can be partitioned in the boundary nodes $\mathbf{q}^b$ at the body's interface points and internal nodes $\mathbf{q}^i$. The proposed local reduction is as follows:

$$\mathbf{q} = \begin{bmatrix} \mathbf{q}^b \\ \mathbf{q}^i \end{bmatrix} = \begin{bmatrix} \mathbf{1} & \mathbf{0} \\ \mathbf{\Phi} & \mathbf{\Theta} \end{bmatrix} \begin{bmatrix} \mathbf{q}^b \\ \boldsymbol{\zeta} \end{bmatrix} \tag{3}$$

where $\mathbf{\Phi}$ is the set of Craig-Bampton modes, $\mathbf{\Theta}$ is the set of all modified modal derivatives and here $\boldsymbol{\zeta}$ denote their generalized coordinates. In this way, an efficient description of a body's local deformation is obtained. The strategy for establishing the coordinate transformation from local interface coordinates to absolute interface coordinates is the same as before. However, it should be anticipated that as a consequence of the geometric nonlinearities, the calculation of the elastic forces may require additional Newton-Raphson iterations in the solution procedure.

NUMERICAL EXAMPLES

In [7], the authors have validated the proposed solution strategy with the equilibrium analysis of two commonly used flexure mechanisms: a parallel leaf spring mechanisms and a cross flexure mechanism. These mechanisms are subjected to a static load that deforms the mechanisms beyond the linear range. A nonlinear finite element model of each leaf spring is created using 10 beam elements and is reduced subsequently using Craig-Bampton modes and their model derivatives. As a comparison, an equilibrium analysis of both flexure hinges is performed using the nonlinear finite element formulation of Ansys using nonlinear beam elements. It was observed that for moderate deflections, the modal derivatives are capable of properly describing higher order effects such as shortening and geometric stiffening, which are typically important effects for flexure mechanisms. However, it was found that when the applied external load increases such that the mechanism's deformation becomes exceedingly large, the reduction basis is no longer successful. In such extreme circumstances, additional higher order terms should be included. For the purpose of illustration, the results of the equilibrium analysis of the cross flexure mechanisms are reproduced here from [7] and shown in Figure 4. It can be seen that when 2 Craig-Bampton modes (CBs) and the 3 associated modal derivatives (MDs) are used as a reduction basis, the equilibrium configuration is very close to the results obtained with the unreduced model and Ansys.

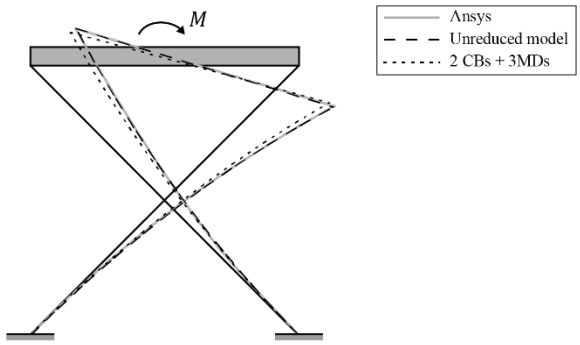

FIGURE 4. Equilibrium analysis of a cross flexure mechanisms subjected to a bending moment.

CONCLUSION: MODELING STRATEGY FOR MULTIBODY FLEXURE BASED PRECISION MECHANISMS

Based on the above considerations, the authors propose the following innovative strategy for the efficient simulation of the flexible multibody dynamics of flexure based precision mechanisms: For each flexure hinge within the mechanism, a geometrically nonlinear finite element model is created. Then, the flexure hinge's natural modes and modal derivatives are determined, as described in this work. The combined number of natural modes and modal derivatives should be equal or larger than the number of interface coordinates. In this way, it is always possible to express the generalized coordinates corresponding to this reduction basis in terms of the absolute interface coordinates, at least in the coordinates' tangent space. Now, a flexure hinge's superelement is obtained that is able to describe large elastic deformations. All superelements are assembled in the equations of motion of the whole mechanism, which can be solved conveniently using the new floating frame formulation described in [1]. In this way, no Lagrange multipliers are required to solve the equations of motion of the entire multibody system. The use of modal derivatives if found an efficient way to include geometrically nonlinear effects within a body, which is commonly the case for flexure based precision mechanisms.

REFERENCES

[1] Ellenbroek M, Schilder J. On the use of absolute interface coordinates in the floating frame of reference formulation for flexible multibody systems. Multibody System Dynamics. 2017 https://doi.org/10.1007/s11044-017-9606-3

[2] Craig R, Bampton M. Coupling of substructures for dynamic analysis. AIAA Journal, 6(7), 1313-1319, 1968

[3] Shabana A. Dynamics of Multibody ystems. Cambridge, Cambridge University Press. 1998

[4] Cardona A, Géradin M. Modeling of superelements in mechanism analysis. International Journal for Numerical Methods in Engineering, Vol 32, 1565-1593. 1991

[5] Cardona A. Superelements Modelling in Flexible Multibody Dynamics. Multibody System Dynamics, Vol 4, 245-266. 2000

[6] Wu L, Tiso P, Van Keulen F. A modal derivatives enhanced Craig-Bampton method for geometrically nonlinear structural dynamics. ISMA, Leuven, Belgium. 2016

[7] Schilder J, Segeth F, Ellenbroek M, Van den Belt M, De Boer A. Model order reduction of large stroke flexure hinges using modal derivatives. ISMA, Leuven, Belgium. 2018

A THREE-DIMENSIONAL BEAM RAY TRACING OF LASER TRANSPORTATION SYSTEM

Hongliang Shi, Daniele Spiga, Joseph Robinson,
Kai Nicholas Lafortune, Michael Greenberg, Lin Zhang, Alan Fry
SLAC National Accelerator Laboratory
Stanford University
Menlo Park, CA 94025

ABSTRACT

In this work, we present an analytical model of 3-dimensional (3D) beam ray tracing of the reflected beam in multi-mirror system. It features module of reflected beam from a single mirror considering the spatial position in 6 Degree of Freedom (DOF). A 3D beam ray tracing of multiple mirrors in serial chain is further developed based on the module method.

INTRODUCTION

The vast majority of pump/probe experiments explore timescales of femtoseconds to picoseconds, requiring optical sources to have a well-defined spatial overlap. Currently in Linac Coherent Light Source at SLAC National Accelerator Laboratory, a beam transportation system is under development for transferring the pump laser to the end stations. Considering the various sources of positioning errors, eg. vibration and thermal drift, the pump laser is required to spatially overlap with a probe soft X-ray after about 20-meter transportation. In order to deeply understand and develop the transportation system to meet the various requirements, we analyze the beam ray tracing with respects to the mechanical system design.

Considerable work has been done in the beam ray tracing modeling[1, 2]. Knudsen et al.[3] proposed a Monte Carlo method based software package for simulating X-ray optics. Warr and Howard [4] developed a ray tracing program for 3D laser beam analysis. Spiga et al. developed the analytical modeling for X-ray mirror system[5, 6]. While several programs are still available to perform ray tracing computations in a beamline (XRT and McXTrace), in this work we focus on developing a general analytical method to trace a fast ray tracing in discrete steps, by computing the direction vector of a reflected laser beam. The method is based on coordinate transformation of beam directions and of the normal vectors of the mirrors. Furthermore, the analytical modeling of a single mirror serves as a module for a mirror system beam tracing, which is obtained by following a sequential iteration of the module.

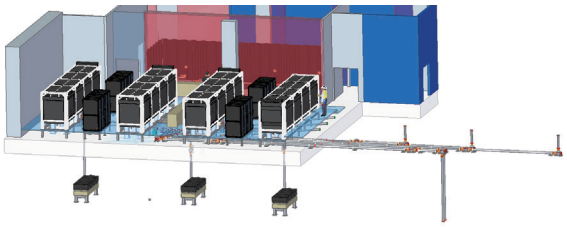

FIGURE 1. Laser system overview.

REFLECTED BEAM BY A SINGLE MIRROR

In this section, we present an analytical modeling of 3D ray tracing of a single beam ray for a mirror-based optical system. As shown in Fig. 2, a mirror surface is implicitly defined by an equation $F(x, y, z) = 0$. Due to rotations and space displacements, it is changed into a new position by a transformation matrix $[T]$. Our goal is to analytically trace the reflected beam ray from the mirror at the new (roto-translated) position.

In order to locate the mirror position in 3D space, we use six variables to define the DOF: three variables $\theta_x, \theta_y, \theta_z$ for Euler angles and $\delta_x, \delta_y, \delta_z$ for translational displacements. In the 3D space, the rotational matrix for the Euler angles and the displacement vector are denoted as

$$[R]_{3\times3} = [R(\theta_y)][R(\theta_z)], \mathbf{d} = \begin{bmatrix} \delta_x \\ \delta_y \\ \delta_z \end{bmatrix}, \quad (1)$$

where we assume $\theta_x = 0$, because the mirror we study here is symmetric about the axis of the

[0]The Publisher, by accepting this article for publication, acknowledges the U.S. Government's right to retain a nonexclusive, royalty-free license in and to any copyright covering.

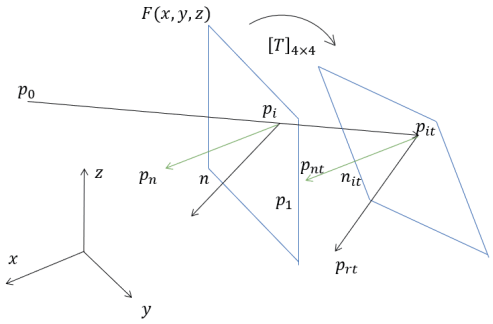

FIGURE 2. Ray reflection from a single mirror. The surface normal at the impact point p_i is dubbed as n. The subscripts 't' are used to label the same vectors after roto-translation.

beam propagation, and

$$[R(\theta_y)] = \begin{bmatrix} \cos\theta_y & 0 & \sin\theta_y \\ 0 & 1 & 0 \\ -\sin\theta_y & 0 & \cos\theta_y \end{bmatrix}, \quad (2)$$

$$[R(\theta_z)] = \begin{bmatrix} \cos\theta_z & \sin\theta_z & 0 \\ -\sin\theta_z & \cos\theta_z & 0 \\ 0 & 0 & 1 \end{bmatrix}.$$

A location of the mirror surface is obtained, in the global reference frame, by multiplication into $[R]_{3\times3}$ and adding $\mathbf{d}$ (Eq. 1). We can briefly rewrite this transformation as a plain multiplication of the mirror coordinate vector into a 4×4 matrix.

The new matrix is defined as:

$$[T]_{4\times4} = \begin{bmatrix} [R]_{3\times3} & \mathbf{d} \\ 000 & 1 \end{bmatrix}. \quad (3)$$

We now trace the incident beam. Any point in an incident beam ray is defined by the equation

$$\mathbf{p_i} = \mathbf{p_0} + \mathbf{k}t, \quad (4)$$

where $\mathbf{p_0}$ is the origin point of the ray, $\mathbf{k}$ is the direction vector of the beam ray, normalized to unity, and t defines the distance from $\mathbf{p_0}$. They can be specified in the 3D space, as

$$\mathbf{p_i} = \begin{bmatrix} p_{ix} \\ p_{iy} \\ p_{iz} \end{bmatrix}, \mathbf{p_0} = \begin{bmatrix} p_{0x} \\ p_{0y} \\ p_{0z} \end{bmatrix}, \mathbf{k} = \begin{bmatrix} k_x \\ k_y \\ k_z \end{bmatrix}. \quad (5)$$

Here and throughout the text, we keep denoting 3D vectors in boldface. In order to clearly present the coordinate transformation, we denote a 4D position vector as follows:

$$\widetilde{\mathbf{p}}_\mathbf{0} = \begin{bmatrix} \mathbf{p_0} \\ 1 \end{bmatrix} = \begin{bmatrix} p_{0x} \\ p_{0y} \\ p_{0z} \\ 1 \end{bmatrix}, \quad (6)$$

while for the 4D direction vectors, the definition is

$$\widetilde{\mathbf{k}}_\mathbf{0} = \begin{bmatrix} \mathbf{k} \\ 0 \end{bmatrix} = \begin{bmatrix} k_x \\ k_y \\ k_z \\ 0 \end{bmatrix}. \quad (7)$$

Using 4D vectors, we can briefly perform the coordinate transformation of $\mathbf{p_0}$ and $\mathbf{k}$ into the non-rotated mirror reference frame (primed) as

$$\widetilde{\mathbf{p}}'_\mathbf{0} = [T]^{-1}\widetilde{\mathbf{p}}_\mathbf{0}, \quad (8)$$

$$\widetilde{\mathbf{k}}' = [T]^{-1}\widetilde{\mathbf{k}}. \quad (9)$$

Figure 3 shows, for example, how $\mathbf{p_0}$ turns into $\mathbf{p_0}'$ by $[T]^{-1}$ in the case of a simple transformation.

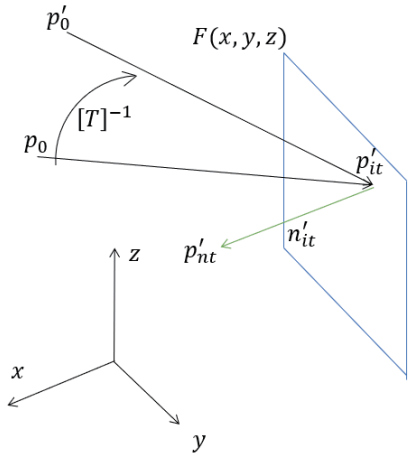

FIGURE 3. Ray reflection from a single mirror: n'_{it} denotes the outer normal to the reflecting surface at the incidence point p'_{it}. Primes denote the non-transformed mirror reference frame. The transformation matrix operates on the ray direction rather than on the surface.

We can rewrite the transformed ray equation (Eq. 4), with $t' = t$ as distances are unaffected by roto-translations:

$$\mathbf{p'_i} = \mathbf{p'_0} + \mathbf{k}'t. \quad (10)$$

This transformation allows us to find the ray incidence in the reference frame where the mirror surface has the simplest possible expression $F(x, y, z) = 0$: a flat mirror is, e.g., defined as

$$F(x, y, z) = x, \tag{11}$$

while for a parabolic mirror with the focus in the origin of the reference frame we have

$$F(x, y, z) = x - a(y^2 + z^2) + \frac{1}{4a}, \tag{12}$$

where $a = 1/2R_c$ is a parameter related to the mirror's radius of curvature in its vertex, R_c.

As shown in Fig. 3, the intersection point of the ray (Eq. 4) with the surface $F(x, y, z) = 0$ is usually easy to compute. After substituting $p'_{ix}, p'_{iy}, p'_{iz}$ into the equation $F(x, y, z) = 0$, we obtain an algebraic equation of unknown t. Depending on the expression of $F(x, y, z)$, we may get multiple solutions of t. For example, there is a single solution for a flat mirror, while there are two solutions for a parabolic mirror equation, of which only one – usually the one with smallest value of t – has physical meaning.

Now, with the value of t in hand, we obtain the intersection point, p'_{it} from Eq. 10. Moreover, the normal vector of the surface $F(x, y, z) = 0$ at the point $\mathbf{p'_{it}}$ could be derived as

$$\mathbf{n'_{it}} = \frac{\nabla F(x, y, z)}{\|\nabla F(x, y, z)\|}, \text{where} \begin{bmatrix} x \\ y \\ z \end{bmatrix} \rightarrow \mathbf{p'_{it}}. \tag{13}$$

For example, the normal vector of a flat mirror is

$$\mathbf{n'_{it}} = \begin{bmatrix} 1 \\ 0 \\ 0 \end{bmatrix}, \tag{14}$$

while the inward-pointing normal vector of a parabolic mirror at the point $\mathbf{p'_{it}}$ can be derived from Eq. 13 as

$$\mathbf{n'_{it}} = \begin{bmatrix} \frac{1}{\sqrt{1+4a^2(p'_{ity}+p'_{itz})}} \\ \frac{-2a\mathbf{p'_{ity}}}{\sqrt{1+4a^2(p'_{ity}+p'_{itz})}} \\ \frac{-2a\mathbf{p'_{itz}}}{\sqrt{1+4a^2(p'_{ity}+p'_{itz})}} \end{bmatrix}. \tag{15}$$

After we have the derived points in the transformed coordinate, we could transform the points

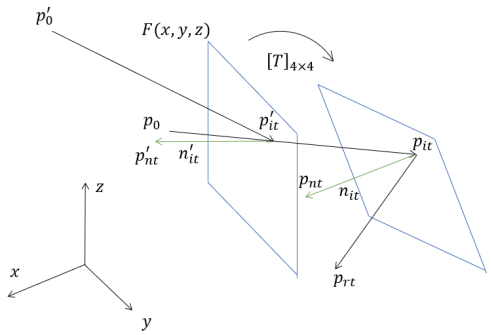

FIGURE 4. Laser system overview.

and vectors back to the original coordinate as

$$\widetilde{\mathbf{n}}_{\mathbf{it}} = [T]\widetilde{\mathbf{n}}'_{\mathbf{it}}, \tag{16}$$

$$\widetilde{\mathbf{p}}_{it} = [T]\widetilde{\mathbf{p}}'_{\mathbf{it}}. \tag{17}$$

With the derived normal vector $\mathbf{n_{it}}$ from the point $\mathbf{p_{it}}$, we could further obtain the point of $\mathbf{p_{nt}}$ as

$$\mathbf{p_{nt}} = \mathbf{p_{it}} + \mathbf{n_{it}} \tag{18}$$

Based on the normal vector $\mathbf{n_{it}}$ in the original frame and the direction vector of the incident beam $\mathbf{k}$, we obtain the vector of the reflected ray[5] as

$$\mathbf{k_r} = \mathbf{k} - \mathbf{2}(\mathbf{n_{it}} \cdot \mathbf{k})\mathbf{n_{it}}, \tag{19}$$

where the dot denotes a scalar product. Furthermore, the point on the reflected beam from the point $\mathbf{p_{it}}$ is derived as

$$\mathbf{p}_{rt} = \mathbf{p}_{it} + \mathbf{k}_r. \tag{20}$$

As shown in Fig. 5, a mirror is to be placed at a target position, Plane 1, from the original position Plane 0, where the global coordinate is defined. Plane 1' is denoted as the real position of the mirror. The difference between real position and target position is due to several position error sources, including static and dynamic sources. The static errors include machining tolerance of mechanical part, assembly error, etc. The dynamic errors include vibration, thermal drift, etc. The transformation from Plane 1 to Plane 1' is modeled with 6DOF in the local coordinates of Plane 1. Further, the real reflected beam o' and ideally-reflected beam o is derived from the incident beam in the original coordinate frame.

Thus, the transformation matrix $[T]$ could be derived as the product of two matrices: $[T_p]$ and $[T_j]$

$$[T] = [T_p][T_j], \tag{21}$$

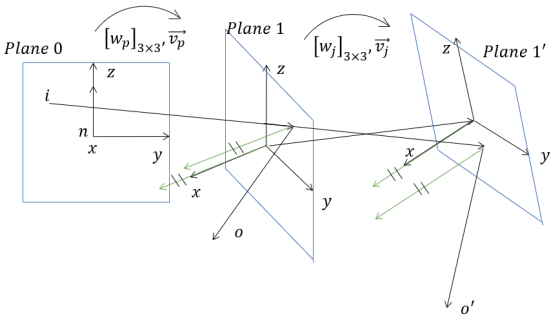

FIGURE 5. The beam ray tracing of mirror from global and local coordinate transformation.

where $[T_p]$ represents the nominal roto-translation in space, and $[T_j]$ accounts for misalignment and misplacing errors.

MIRROR SYSTEM

In this section, as an application example of the proposed method, we analyze a mirror system under development. The layout of the transportation is illustrated in Fig. 6, in which there are a lot of beam pipes in vacuum. Multiple mirrors are used to change the beam directions through the beam pipe. Here, we model the mirrors through one beam line as an example.

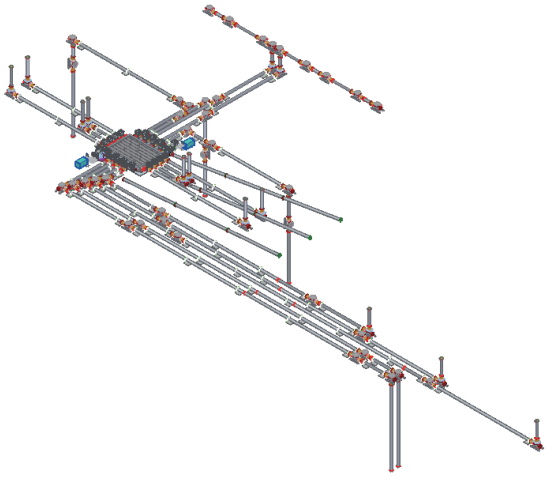

FIGURE 6. Beam transport of the laser system.

Based on the proposed module method, the 3D beam ray tracing is derived for multi-mirror reflection in space, and it is shown in Fig. 7. As shown in the modeling, four lasers with radius of 7.5 mm are transferred in parallel. With the positioning of the mirrors in 3D space, the beam ray-trace is demonstrated. One issue we are interested is whether the 4 laser beams could be successfully

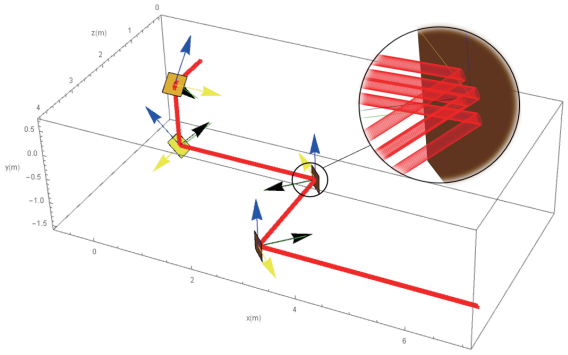

FIGURE 7. 3D beam ray tracing of four mirrors.

transferred through the pipes. This requires the beam not to hit the pipe and stay within the mirror area, which is 4 inches in diameter. Firstly, we assume the system is already aligned perfectly in the space. Then, the 1st, 2nd, and 4th mirrors are fixed in the installation process. However, the 3rd mirror is mounted on a stack of stages, which has 3DOF: goniometer, rotational stage, and linear stage. The stages allow enough mobilities for alignment, however, the workspace also needs to be defined.

There are two requirements here for the workspace. First of all, at the downstream of the 3rd mirror, the beams are required to hit the 4th mirror. Fig. 8 (a) shows that beams' location on the 4th mirrors when steering the 3rd mirror. The results show that 0.06 degrees in 2DOF are the maximum allowed tip and tilt angle of the 3rd mirror. Secondly, the downstream beams of the 4th mirror are transferred in the pipe, so the beams are required to have no interference with the pipe. Fig. 8 (b) shows that 0.06 degrees are also the maximum value in 2DOF for the 3rd mirror.

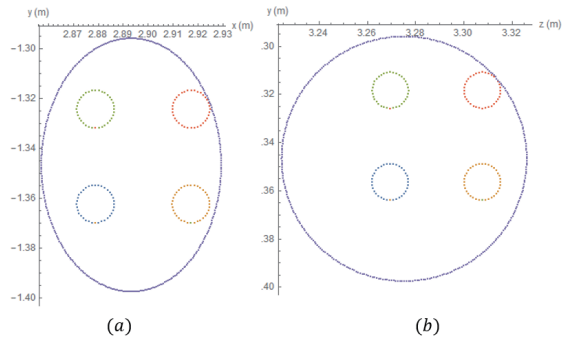

FIGURE 8. The section view of beam ray tracing at the 4th mirror of Fig. 7. (a) The beam position vs mirror area. (b) The beam position vs pipe area

CONCLUSION

In this manuscript, we proposed an analytical modeling method of 3D beam ray tracing of mirror system. The method features modeling the reflected beam from single mirror as a module, and then applying the module to modeling the mirror system. Both global and local coordinate systems can be used in the modeling, and this makes the proposed method practical in analysis for various conditions.

ACKNOWLEDGMENT

The reported work is conducted at the Linac Coherent Light Source (LCLS), SLAC National Accelerator Laboratory, which is supported by the U.S. Department of Energy, Office of Science, Office of Basic Energy Sciences under Contract No. DE-AC02-76SF00515.

REFERENCES

[1] Estabrook K, Kruer WL, Bailey DS. Twodimensional raytrace calculations of thermal whole beam selffocusing. The Physics of Fluids. 1985;28(1):19–21.

[2] Konstantin Klementiev RC. Powerful scriptable ray tracing package xrt; 2014.

[3] Bergbck Knudsen E, Prodi A, Baltser J, Thomsen M, Kjr Willendrup P, Sanchez del Rio M, et al. McXtrace: a Monte Carlo software package for simulating X-ray optics, beamlines and experiments. Journal of Applied Crystallography;46(3):679–696.

[4] Warr GB, Howard J. A three-dimensional Gaussian-beam ray-tracing program for designing interferometer/polarimeter plasma diagnostics. Review of Scientific Instruments. 2001;72(5):2305–2309.

[5] Spiga, D , Cotroneo, V , Basso, S , Conconi, P . Analytical computation of the off-axis effective area of grazing incidence X-ray mirrors. A&A. 2009;505(1):373–384.

[6] Spiga, D . Optics for X-ray telescopes: analytical treatment of the off-axis effective area of mirrors in optical modules. A&A. 2011;529:A18.

DESIGN OF COMPACT LINEAR NANOPOSITIONING FLEXURE STAGES WITH CENTIMETER TRAVEL RANGE FOR X-RAY INSTRUMENTATION

Deming Shu[1], Barry Lai[1], Steven Kearney[1], Jayson Anton[1,2], Wenjun Liu[1], Jorg Maser[1], Christian Roehrig[1], and Jonathan Z. Tischler[1]

[1]Advanced Photon Source, Argonne National Laboratory, Argonne, IL 60439, U.S.A.
[2]University of Illinois at Chicago, Chicago, IL 60607, U.S.A

INTRODUCTION

To overcome the performance limitations of precision ball-bearing-based or roller-bearing-based linear stage systems, the first flexural linear stage system T8-52 using deformation-compensated flexural pivot mechanisms was designed and constructed at the Advanced Photon Source (APS) at Argonne National Laboratory (ANL) in 2011 [1,2]. The T8-52 flexure stage maintained the travel range of typical linear stages of 10 - 12 mm, maintained similar load capacities (1 - 2 kg), and while allowing steps sizes of five nanometers [2].

As shown in Figure 1, the basic parallel mechanism of the prototype horizontal flexure stage includes seven elements linked by eight commercial flexural pivots: four I-link bars; two parallel bars; and one U-shaped middle bar. With the fine tuning, pairing, and optimizing of the orientation of each flexural pivot, the precision linear motion is approached [2].

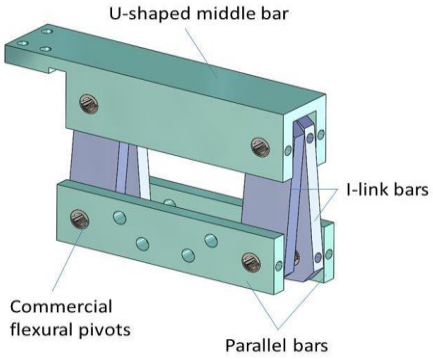

Figure 1. 3-D model of the basic parallel mechanism of the prototype horizontal flexure stage.

In 2014, the APS T8-54 linear flexure stage is designed to perform a precision wire scan as a differential aperture for the 3-D diffraction microscope at the APS sector 34 [3]. The operation experiences gained from the T8-54 flexure stage led to a novel middle-bar relative position control mechanism, developed at the APS in 2016, to enhance the stiffness of the parallel flexure linear guiding mechanism [4]. The middle-bar relative position control mechanism provides a 1:2 ratio relative position control between the middle-bar and the stage carriage as shown in Figure 2. It was successfully applied to the APS T8-56 linear flexure stage for a horizontal sample scanning stage for a hard x-ray microscope at the APS sector 2.

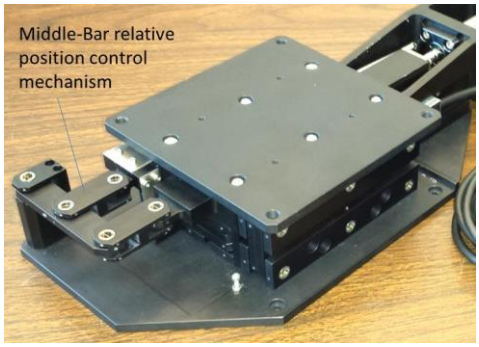

Figure 2. Photograph of the T8-56 linear flexure stage with middle-bar relative position control mechanism.

In 2016, the vertical linear flexural stage APS T8-55 was designed and constructed for the hard x-ray microscope at the APS sector 2 as a vertical sample scanning stage [5-8]. Table 1 and 2 summarize the design specifications of the APS T8-55 and T8-56 vertical and horizontal linear flexural stage system. Figure 3 shows a photograph of the T8-55 and T8-56 flexural stage system installed in the x-ray microscope instrument at the APS sector 2 experimental station.

The APS Upgrade project will massively increase the coherence of the x-ray source [9]. With the upgraded APS, more beamlines will be

equipped with advanced x-ray nanofocusing optics and will have the capability to perform as an x-ray nanoprobe associated with cutting edge techniques. More specific nanopositioning instruments will be developed to support the challenging scientific research goals. In this paper, we present the new design and development of the APS T8-57 and T8-58 horizontal and vertical linear flexure stage system with more compact overall dimensions for point to point nanopositioning applications.

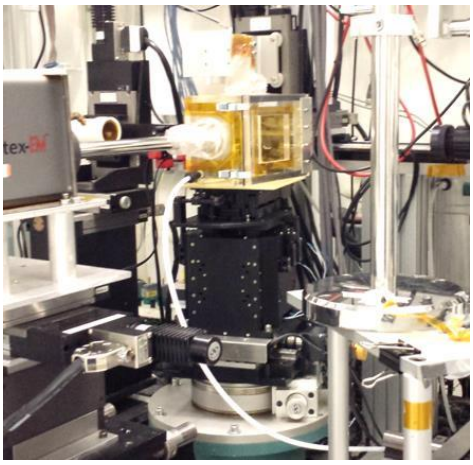

Figure 3. Photograph of the T8-55 and T8-56 flexural stage system installed in the x-ray microscope instrument at the APS sector 2 experimental station.

THE HORIZONTAL LINEAR FLEXURE NANOPOSITIONING STAGE APS T8-57

The APS T8-57 horizontal linear flexure stage is designed to be mounted on the top of the APS T8-58 vertical stage. The combination of the APS T8-57 and T8-58 flexure stages will perform as a pair of sample scanning stages for a hard x-ray scanning microscope with point to point nanopositioning applications. Figure 4 shows a 3-D model of the APS T8-57 horizontal linear flexure stage.

The design of the APS T8-57 horizontal linear flexural stage is a scale-down version of the APS T8-56 horizontal linear flexural stage driving by a combination of PI™ P-841.10 PZT linear actuator and Newport™ PZA-12 piezo motor driven actuator [10,11]. Same as the T8-56 stage, it consists three sets of deformation-compensated flexural linear guiding mechanisms. Two sets of the linear guiding mechanisms are mounted vertically between the stage base and carriage. The third set of the linear guiding mechanism links the stage base and carriage horizontally. The symmetrically arranged middle-bar relative position control mechanism integrates the three sets of the guiding mechanisms into a united guiding system. Table 3 summarizes the design specifications of the APS T8-57 horizontal linear flexural stage system.

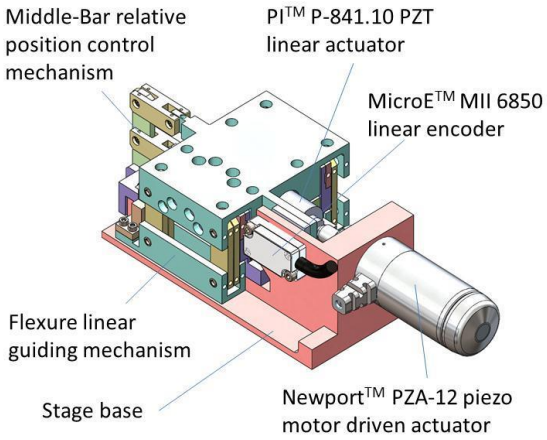
Middle-Bar relative position control mechanism
PI™ P-841.10 PZT linear actuator
MicroE™ MII 6850 linear encoder
Flexure linear guiding mechanism
Stage base
Newport™ PZA-12 piezo motor driven actuator

Figure 4. 3-D model of the APS T8-57 horizontal linear flexure nanopositioning stage.

THE VERTICAL LINEAR FLEXURE NANOPOSITIONING STAGE APS T8-58

The design of the APS T8-58 vertical linear flexural stage is a scale-down version of the APS T8-55 vertical linear flexural stage driving by combination of PI™ P-841.10 PZT linear actuator and Newport™ PZA-12 piezo motor driven actuator [10,11].

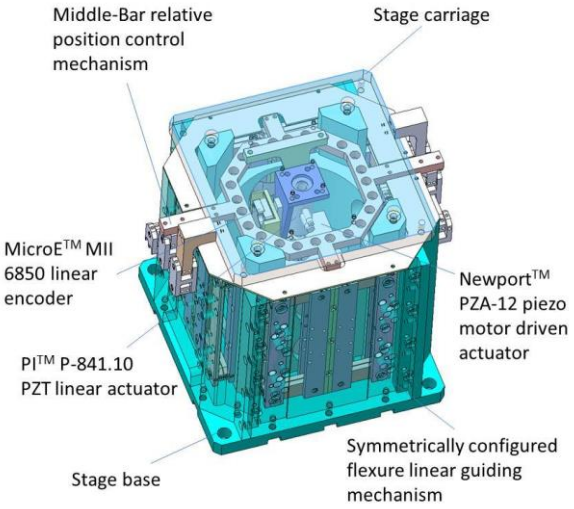
Middle-Bar relative position control mechanism
Stage carriage
MicroE™ MII 6850 linear encoder
Newport™ PZA-12 piezo motor driven actuator
PI™ P-841.10 PZT linear actuator
Symmetrically configured flexure linear guiding mechanism
Stage base

Figure 5. 3-D model of the APS T8-58 vertical linear flexure nanopositioning stage.

Same as the T8-55 stage, the T8-58 stage consists of a symmetrically configured vertical flexure linear guiding mechanism with middle-bar relative position control mechanism, a stage base, and a decoupled linear driving mechanism as show in figure 5. The vertical flexure linear guiding mechanism has four vertical guiding panels. Each guiding panel includes two sets of

the deformation-compensated flexural-pivots-based linear guiding mechanism. They are mounted vertically between the stage base and carriage to provide a precision frictionless vertical motion guiding. The APS T8-58 vertical stage has a total of eight sets of flexural guiding mechanisms.

To compensate transversal relative motions between the middle-bars, special flexural mechanisms are designed to link the middle-bars with a motion synchronizing linkage for middle-bar relative position control mechanism, which integrates the eight sets of guiding mechanisms into a united guiding system. Table 4 summarizes the design specifications of the APS T8-58 vertical linear flexural stage system.

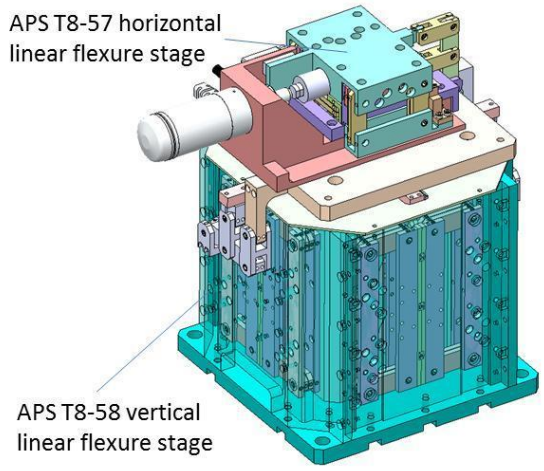

Figure 6. 3-D model of combination of the APS T8-57 and T8-58 flexure stages.

SUMMARY

Based on the deformation compensated compact linear guiding mechanism using commercial flexural pivots, prototypes of vertical and horizontal linear nanopositioning flexure stages APS T8-54, T8-55 and T8-56, with centimeter-level travel range, have been designed and tested at the Advanced Photon Source (APS) for x-ray instrumentation applications. Recently, new version of the vertical and horizontal linear nanopositioning flexure stages T8-57 and T8-58, with similar guiding mechanism and further improved compact designs, have been developed at the APS to overcome the performance limitations of precision ball-bearing-based or roller-bearing-based linear stage systems. The mechanical design and its preliminary test results with laser interferometers are described in this paper. Figure 6 shows a 3-D model of combination of the APS T8-57 and T8-58 flexure stages for hard x-ray microprobe and nanoprobe applications.

Table 1. Design specifications of the APS T8-55 vertical linear nanopositioning flexure stage

T8-55 Vertical linear nanopositioning flexure stage	
Overall dimensions (mm)	185 (L) x 146 (W) x 160 (H)
Normal load capacity (kg)	4
Driving system	Oriental Motor™ stepper motor w/harmonic gearhead and timing belt
Linear encoder	MicroE™ MII 6850
Encoder resolution	10 nm
Travel range (mm)	12 – 16 mm (vary with types of flexural pivots installed)
Min. incremental motion (nm)	2
Max. driving speed (mm/sec)	0.5
Vacuum compatibility	UHV Flexure mechanism

Table 2. Design specifications of the APS T8-56 horizontal linear nanopositioning flexure stage

T8-56 Horizontal linear nanopositioning flexure stage	
Overall dimensions (mm)	347 (L) x 125 (W) x 52 (H)
Normal load capacity (kg)	2
Driving system	Oriental Motor™ stepper motor w/harmonic gearhead
Linear encoder	MicroE™ MII 6850
Encoder resolution	10 nm
Travel range (mm)	12 – 16 mm (vary with types of flexural pivots installed)
Min. incremental motion (nm)	2
Max. driving speed (mm/sec)	1
Vacuum compatibility	UHV Flexure mechanism

Table 3. Design specifications of the APS T8-57 horizontal linear nanopositioning flexure stage

T8-57 Horizontal linear nanopositioning flexure stage	
Overall dimensions (mm)	178 (L) x 57 (W) x 38 (H) (with closed-loop coarse and fine drivers)
Overall dimensions (mm)	160 (L) x 57 (W) x 38 (H) (with closed-loop voice-coil driver)
Normal load capacity (kg)	0.5
Coarse driver type	Newport™ PZA-12 linear actuator
Coarse driver encoder type	MicroE™ MII 6850
Fine driver type	PI 841.10V PZT actuator
Fine driver encoder type	Strain gage sensor
Voice coil driver type	BEI LAS-13
Voice coil encoder type	Hall effect sensor
Coarse travel range (mm)	12 (3-mm with voice-coil)
Fine travel range (micron)	15
Coarse min. incremental (nm)	50
Fine min. incremental (nm)	2
Vacuum compatibility	UHV Flexure mechanism

Table 4. Design specifications of the APS T8-58 vertical linear nanopositioning flexure stage

T8-58 Vertical linear nanopositioning flexure stage	
Overall dimensions (mm)	139 (L) x 115 (W) x 132 (H) (with closed-loop coarse and fine drivers)
Normal load capacity (kg)	1.5
Coarse driver type	Newport™ PZA-12 linear actuator
Coarse driver encoder type	MicroE™ MII 6850
Fine driver type	PI 841.10V PZT actuator
Fine driver encoder type	Strain gage sensor
Coarse travel range (mm)	12
Fine travel range (micron)	15
Coarse min. incremental (nm)	50
Fine min. incremental (nm)	2
Vacuum compatibility	UHV Flexure mechanism

ACKNOWLEDGEMENTS

The authors would like to acknowledge Patricia Fernandez and Dean Haeffner for their management support. This work was supported by the U.S. Department of Energy, Office of Science, Office of Basic Energy Sciences, under Contract No. DE-AC02-06CH11357.

REFERENCES

[1] U.S. Patent granted No. 8,957,567, D. Shu, S. Kearney, and C. Preissner, 2015.
[2] D Shu, S Kearney, and C Preissner, "Design of a precision flexural linear stage system with sub-nanometer resolution and 12-mm travel range," J. Phys. Conf. Ser. 425 212011(2013).
[3] D. Shu, W. Liu, S. Kearney, J. Anton, and J. Z. Tischler, Proceedings of SPIE-2015, "Mechanical design of a precision linear flexural stage for 3-D x-ray diffraction microscope at the Advanced Photon Source," Optomechanical Engineering conference, 9573-28, San Diego, CA, Aug. 2015.
[4] D. Shu, W. Liu, S. Kearney, J. Anton, B. Lai, J. Maser, C. Roehrig, and J. Z. Tischler, "Mechanical design and development of compact linear nanopositioning flexure stages with centimeter-level travel range and nanometer-level resolution," Proceedings of MEDSI-2016, TUBA04, Sept. 11-16, 2016, Barcelona, Spain.
[5] S. Kearney and D. Shu, "Trajectory Error Analysis of a Flexure Pivot Type Guide for Linear Nanopositioning," Proceedings of SPIE 2017, Optomechanical Engineering conference, Vol. 10371-14, San Diego, CA, Aug. 2017.
[6] D. Shu, B. Lai, S. Kearney, J. Anton, W. Liu, J. Maser, C. Roehrig, and J. Z. Tischler, U.S. Patent application in progress for ANL-IN-16-125 and ANL-IN-16-150, 2016.
[7] D. Shu, J. Anton, S. Kearney, B. Lai, W. Liu, J. A. Maser, C. Roehrig, and J. Tischler, "Mechanical Design of Compact Vertical and Horizontal Linear Nanopositioning Flexure Stages With Centimeter-Level Travel Range for X-Ray Beamline Instrumentation," Proceedings of 8th Int. Particle Accelerator Conference, pp. 4096–4099, Copenhagen, Denmark, May 2017.
[8] D. Shu, B. Lai, S. Kearney, J. Anton, W. Liu, J. Maser, C. Roehrig, and J. Z. Tischler, "Design and test of precision vertical and horizontal linear nanopositioning flexure stages with centimeter-level travel range for x-ray instrumentation," Proceedings of SPIE 2017, Optomechanical Engineering conference, Vol. 10371-13, San Diego, CA, Aug. 2017.
[9] http://www.aps.anl.gov
[10] https://www.physikinstrumente.com
[11] http://www.newport.com/Picomotor-Piezo-Linear-Actuators/

The submitted manuscript has been created by UChicago Argonne, LLC, Operator of Argonne National Laboratory ("Argonne"). Argonne, a U.S. Department of Energy Office of Science laboratory, is operated under Contract No. DE-AC02-06CH11357. The U.S. Government retains for itself, and others acting on its behalf, a paid-up nonexclusive, irrevocable worldwide license in said article to reproduce, prepare derivative works, distribute copies to the public, and perform publicly and display publicly, by or on behalf of the Government.

EFFICIENT MODELLING OF SHORT AND WIDE LEAF SPRINGS USING A SUPERELEMENT FORMULATION

Mieke van den Belt, Jurnan Schilder, Dannis Brouwer
Faculty of Engineering Technology
University of Twente
Enschede, The Netherlands

ABSTRACT
In this work, a recently developed superelement in the floating frame of reference formulation will be applied to plate elements. It is shown that for applications in which short and wide leaf springs are required, currently used flexible multibody models using beam elements do not provide sufficient accuracy. Relevance of the new formulation for the efficient modelling of flexure mechanisms will be shown.

INTRODUCTION
Flexure hinges are frequently used in precision engineering for their deterministic behavior, due to the absence of friction, hysteresis and backlash [1]. For most of their applications, flexure hinges allow motion by being compliant in driving directions, while constraining motion in their supporting directions (Figure 1). However, flexure hinges typically have a reduced performance in their deflected state, as the support stiffness rapidly decreases with deflection [1].

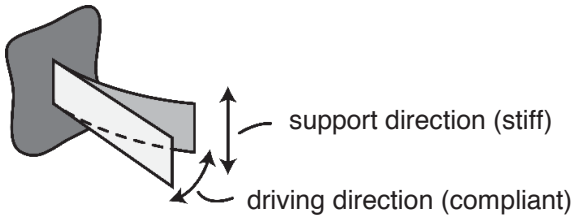

FIGURE 1. Single leaf spring flexure.

Shape and topology optimization is used to design sophisticated mechanisms, for which the flexure mechanisms are included in geometrically nonlinear multibody analyses. Due to the low aspect-ratio (defined as height/length) of many flexures, they can be simplified as flexible multibody systems using nonlinear beam elements. By doing so, full nonlinear finite element meshes using solid or plate elements can be avoided. This way, large deformations can still be included, while computational costs are reduced significantly.

In several precision machines, balance masses are used to remove vibrations from the frame. Recent development is aimed at suspending these balance masses by flexure mechanisms. Therefore, optimizations are aimed at flexure mechanisms with a high support stiffness while heavily loaded in supporting direction, whereas state-of-the-art optimizations are mostly aimed at high support stiffness during large range of motion [2]. This shifts the focus of design optimizations significantly. However, for flexure mechanisms loaded in their supporting direction, the typical high aspect-ratio of the leaf springs has to be taken into account. This aspect-ratio implies that mechanisms can no longer be modelled as beam elements and that the current approach no longer provides sufficient accuracy.

In order to obtain sufficient accuracy, plate elements need to be used, however, this increases the number of degrees of freedom and therefore computational costs significantly. These high computational costs ask for reduction techniques that are suitable for geometrically nonlinear problems.

The floating frame of reference formulation is a commonly used formulation for these geometrically nonlinear problems [3]. In this formulation, a floating frame describes a body's large rigid body motions, and a linear combination of mode shapes is used to describe local elastic deformations. Because local deformations remain small, these mode shapes can be obtained by applying powerful model order reduction techniques on a body's linear finite element model. Compared to nonlinear finite element formulations, a large disadvantage of the floating frame formulation is that Lagrange multipliers are required to satisfy kinematic constraints, increasing the number of unknowns.

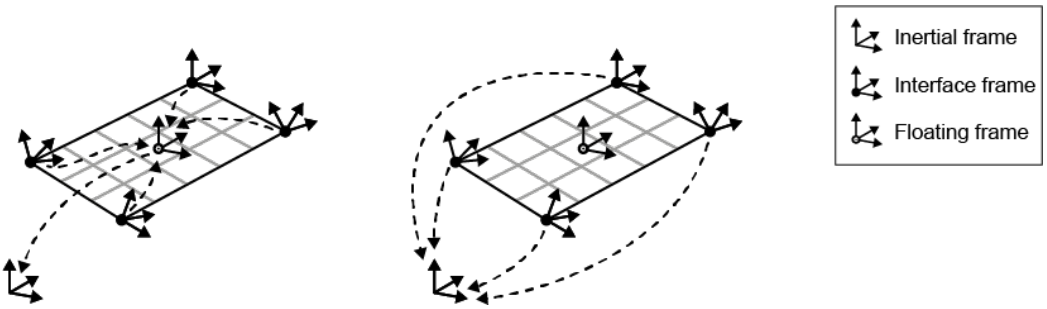

FIGURE 2. Meshed leaf spring. Left: floating frame formulation, both the absolute floating frame coordinates and the local interface coordinates are the degrees of freedom. Right: superelement formulation, only the absolute interface coordinates are the degrees of freedom.

Recently, Ellenbroek and Schilder [4] presented a method that overcomes this problem. By using Craig-Bampton modes [5], a coordinate transformation from the absolute floating frame coordinates and local interface coordinates to the absolute interface coordinates is established. This coordinate transformation can be used to create superelements in the floating frame formulation. Figure 2 shows a graphical representation of both the original floating frame of reference formulation and the superelement formulation, for a floating frame model of a leaf spring.

In contrast to state-of-the-art optimizations, problems involving high aspect-ratio leaf springs do not necessarily consider a large range of motion, and the local elastic deformations thus remain small. Therefore, superelements in the floating frame formulation offer a suitable reduction method. Although the method is applicable for the reduction of arbitrarily shaped bodies, the original work [4] only presented validation problems with beams. In previous work [6], the authors have successfully implemented superelements in the floating frame formulation for plates.

This work presents a detailed comparison of the corotational frame formulation of Spacar [7], the inertial frame formulation of Ansys, and the superelement formulation, specifically for high aspect-ratio leaf springs under high load. For demonstration purposes, the method is used to determine the stiffness in supporting direction for a single leaf spring that is loaded in supporting direction while deflected in driving direction. The main contribution of this work will thus be showing the relevance of superelements in the floating frame formulation for efficient modelling of flexure mechanisms including high aspect-ratio leaf springs.

ABSOLUTE INTERFACE COORDINATES IN THE FLOATING FRAME FORMULATION

To describe the kinematics of a plate in the regular floating frame formulation, the coordinates of each interface point are expressed in terms of the absolute floating frame coordinates and the local interface coordinates. This is shown graphically in the left part of Figure 2.

Describing the local elastic deformations can be done in various ways. In this work, the Craig-Bampton modes [5] are used. By using these, the coordinate transformation towards absolute interface coordinates can easily be established. However, since both the Craig-Bampton modes and the floating frame coordinates are able to describe 6 rigid body modes, these 6 modes need to be eliminated from the set of Craig-Bampton modes. This is realized by demanding zero elastic deformation at the location of the floating frame. This way, a coordinate transformation can be established, as is described in detail in [4].

As the coordinate transformation cannot be applied on the position level, as the constraints may not be solved analytically because of possible nonlinearities. Therefore, the transformation has to be applied on either velocity level or the virtual displacements. The coordinate transformation on the virtual displacements is then given by

$$\begin{bmatrix} \delta \mathbf{q}_{FF} \\ \delta \mathbf{q}_{LI} \end{bmatrix} = [\mathbf{A}] \delta \mathbf{q}_{AI} \tag{1}$$

In this, $\delta\mathbf{q}_{FF}$, $\delta\mathbf{q}_{LI}$ and $\delta\mathbf{q}_{AI}$ are the variation in respectively the floating frame coordinates, the local interface coordinates, and the absolute interface coordinates. $[\mathbf{A}]$ represents the transformation matrix which is a combination of rotation matrices and two other transformation matrices, $[\mathbf{Z}]$ and $[\mathbf{T}]$. $[\mathbf{T}]$ is a transformation matrix that removes the rigid body motion of the floating frame from the expression and is given by

$$[\mathbf{T}] = \mathbf{1} - \left[\boldsymbol{\Phi}_{rig}\right][\mathbf{Z}] \tag{2}$$

$[\boldsymbol{\Phi}_{rig}]$ contains the displacement of all interface coordinates when the body is subjected to a rigid body motion with respect to the floating frame. The matrix $[\mathbf{Z}]$ is given by:

$$[\mathbf{Z}] = \left([\boldsymbol{\Phi}_{CB}]\left[\boldsymbol{\Phi}_{rig}\right]\right)^{-1}[\boldsymbol{\Phi}_{CB}] \tag{3}$$

where $[\boldsymbol{\Phi}_{CB}]$ consists of the Craig-Bampton mode shapes evaluated at the floating frame.

Using the coordinate transformation, we can now rewrite the equation of motion and the equilibrium equation. The equilibrium equation is given by:

$$[\mathbf{R}][\mathbf{T}]^T\mathbf{K}_{CB}\mathbf{q}_{LI} = \mathbf{F} \tag{4}$$

where $[\mathbf{R}]$ contains the rotation matrices that relate the floating frame to the inertial frame. $\mathbf{K}_{CB}$ is the stiffness matrix that is obtained by model order reduction of the body's finite element model using the Craig-Bampton modes, and $\mathbf{q}_{LI}$ are the local interface coordinates. The rewritten equilibrium equation (4) is the basis of the examples discussed later on.

NUMERICAL EXAMPLE

To show the relevance of superelements in the floating frame formulation for efficient modelling of flexure mechanisms including high aspect-ratio leaf springs, leaf springs in various dimensions are modelled. In these simulations, the length and thickness of the leaf spring remain constant, namely 45 and 1.5 mm, respectively. The height is varied from 4.5 to 450 mm, that is, the leaf springs have aspect ratios varying from 1/10 to 10. The leaf spring is shown in Figure 3 and has a Young's modulus of $E = 210\,GPa$ and a Poisson ratio of $\nu = 0.3$.

For each aspect ratio, the load in driving direction ($F_{driving}$) is determined such that the end node has an angle of 5°. The load in supporting direction is based on the critical buckling load, which is determined in undeflected position. $F_{supporting}$ equals one tenth of this critical buckling load. Loads for all aspect-ratios are shown in Table 1.

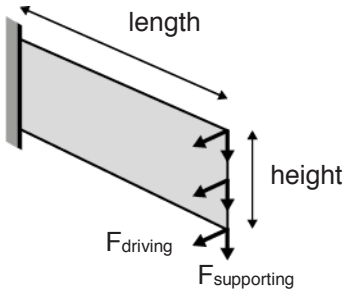

FIGURE 3. Leaf spring loaded in driving and supporting direction.

TABLE 1. Loads in driving and supporting direction for all aspect-ratios.

Aspect-ratio	$F_{driving}$ (N)	$F_{supporting}$ (N)
0.1	22.972	65.7
0.2	45.944	131.4
0.5	114.86	328.5
1	229.72	657
2	459.44	1314
5	1148.6	3285
10	2297.2	6570

The stiffness in driving and supporting direction is simply determined by the linear definition F = k*u. The stiffness in a given direction thus equals the deflection in that direction divided by the load in that direction:

$$k_{driving} = \frac{u_{driving}}{F_{driving}} \tag{5}$$

$$k_{supporting} = \frac{u_{supporting}}{F_{supporting}} \tag{6}$$

For both $u_{driving}$ and $u_{supporting}$, the deflection of the node at the center of the free end is used. The leaf springs are modelled using the superelement formulation and compared to two other formulations.

Figure 4 shows the deflected shape of the leaf spring, when loaded by both a force in driving direction and in supporting direction. The aspect-ratio of the presented leaf spring is 5.

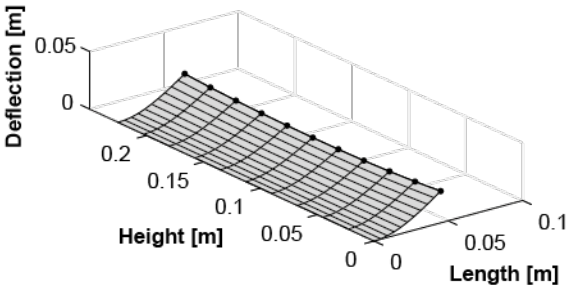

FIGURE 4. Deflected leaf spring with an aspect-ratio of 5 (displacement scale = 10).

The results for the stiffness in driving and supporting direction are shown in Figure 5 and 6, respectively. For clarity, the horizontal axis is presented on a logarithmic scale. The small rectangles on the horizontal axis represent the shape of the leaf spring.

The results for the superelement formulation implemented for plates are represented by the black solid line in Figure 5 and 6. The grey dashed line represents the results from Spacar [7], which uses the corotational formulation using nonlinear beam elements. The solid grey line represents the results from using shell elements (shell181) in Ansys. Ansys uses a nonlinear finite element formulation based on the full nonlinear Green-Lagrange strain expression [8]. Figure 5 shows the stiffness in driving direction, Figure 6 shows the stiffness in supporting direction. Both figures show a clear resemblance between the superelement formulation and the results from Ansys using shell elements, while Spacar is far off.

Furthermore, Figure 6 clearly shows that beam elements do not provide sufficient accuracy to describe leaf springs with a high aspect ratio, especially when the leaf springs are loaded in-plane. The supporting stiffness is underestimated by over 60% when using beam elements, whereas the superelement formulation slightly overestimates the stiffness, but only by around 10%.

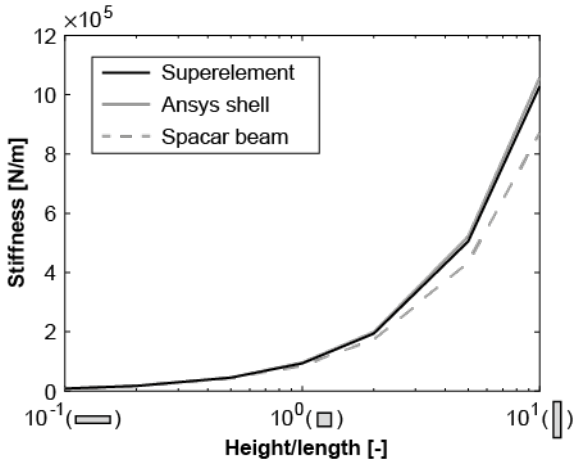

FIGURE 5. Stiffness in driving direction of a leaf spring that is loaded in both driving and supporting direction.

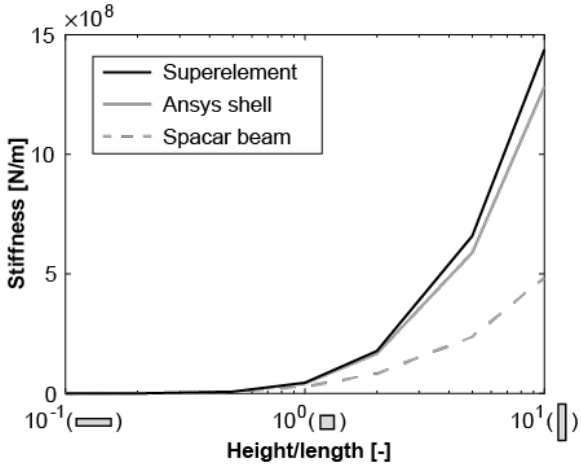

FIGURE 6. Stiffness in supporting direction of a leaf spring that is loaded in both driving and supporting direction.

The final remark that can be made, is about the shape of the deformation. Figure 7 shows the displacement of the free end of the leaf spring (indicated by the dots in Figure 4). The aspect-ratio of the presented leaf spring is 5. As can be seen in this figure, results from the superelement formulation and Ansys show that the tips of the leaf spring deflect more than the middle part. This effect can only be seen when more than one element in height-direction is used, therefore the results from Spacar, using beam elements, do not show this.

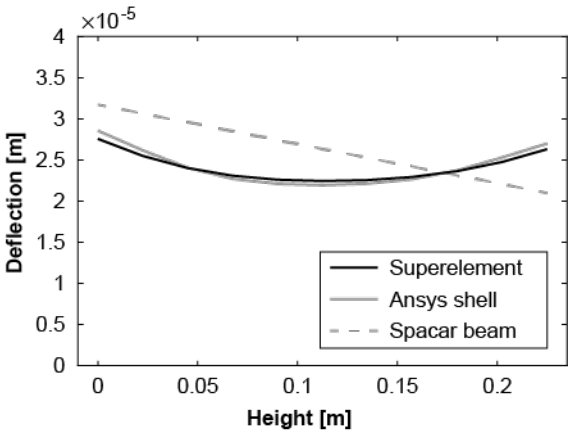

FIGURE 7. Deflection of free end.

Spacar thus is not only far less accurate when considering the supporting stiffness, but also fails to describe the correct shape. The new superelement formulation shows better results on both aspects.

CONCLUSIONS

Previous work [6] showed that the method can successfully be used for the efficient description of plates in flexible multibody systems. However, this work only showed examples with out-of-plane bending.

This work extends the validation for plate elements, by also addressing plates that are loaded both in-plane and out-of-plane. Results show that the new superelement formulation is in good agreement with well-established plate-formulations such as the nonlinear finite element formulation of for example Ansys. Both the supporting stiffness and the shape of the deformation show realistic and accurate results. Therefore, the superelement formulation can indeed be used for the efficient modelling of short and wide leaf springs.

In future work, the superelement formulation will be used as an actual reduction method, whereas current examples only show results for the unreduced model. This way, not only accuracy but also efficiency of the method can be evaluated.

ACKNOWLEDGEMENTS

This research was funded by the Netherlands Organisation for Scientific Research (14665 NWO TTW) of the Ministry of Education, Culture and Science of the Netherlands.

REFERENCES

[1] Gunnink K, Aarts RGKM, Brouwer DM. Performance optimization of large stroke flexure hinges for high stiffness and eigenfrequency. Proceedings of the 28th Annual Meeting of the American Society for Precision Engineering (ASPE). Saint Paul, Minnesota: American Society for Precision Engineering.

[7] Jonker JB, Meijaard JP. A geometrically non-linear formulation of a three-dimensional beam element for solving large deflection multibody system problems. International journal of non-linear mechanics. 2013; 53, 63-74. DOI: 10.1016/j.ijnonlinmec.2013.01.012

[2] Naves M, Brouwer DM, Aarts RGKM. Building block based spatial topology synthesis method for large stroke flexure hinges. Journal of mechanisms and robotics. 2017; 9(4), [041006].

[3] Nada AA, Hussein BA, Megahed SM, Shabana AA. Use of the floating frame of reference formulation in large deformation analysis: experimental and numerical validation. Proceedings of the Institution of Mechanical Engineers, Part K: Journal of Multi-body Dynamics. 2010; 224(1), 45-58.

[5] Craig RR, Bampton MCC. Coupling of substructures for dynamic analysis. AIAA Journal. 1968; 6(7), 1313-1319.

[4] Ellenbroek MHM, Schilder JP. On the use of absolute interface coordinates in the floating frame of reference formulation for flexible multibody dynamics. Multibody system dynamics. DOI: 10.1007/s11044-017-9606-3

[6] Van den Belt M, Schilder JP, Brouwer DM. An absolute interface coordinates floating frame of reference formulation for plates. ISMA, Leuven, Belgium. 2018.

[8] De Borst R, Crisfield MA, Remmers JJC, Verhoosel CV. Non-Linear Finite Element Analysis of Solids and Structures, 2nd edn. John Wiley & Sons, Ltd, New York. 2012.

6-DOF FORCE MEASUREMENT PLATFORM USED FOR MAPPING FUNCTIONS IN MAGNETIC LEVITATION SYSTEMS

Rainer Gloess, Alexander Goos
Central Innovation, Advanced Mechatronics
Physik Instrumente (PI) GmbH &Co.KG
Karlsruhe, Germany

INTRUDUCTION

The theory for the development of magnetically levitated positioning stages is based on the calculation of magnetic flux density, Lorenz forces or reluctance forces and parasitic forces.
In the design phase of magnetic levitation systems for industrial applications, a couple of simplified magnetic structures and sensors were used. All of these simplifications were not used in the modelling procedure. Therefore, it is highly recommended to verify the theoretical concept with the real measurement data.
Extremely accurate magnetic levitation systems are used for example, in the semiconductor industry for fine positioning of wafers. High-load maglev systems are used for example, in a cleanroom environment for transportation of large flat panels. Magnetic levitation technology opens new application fields for extremely accurate scanning procedures and can combine scanning and surface tracking features in one system. [1] [2]

The main advantage in relation to “standard” air bearing systems or mechanical guided systems is that magnetic levitation provides perfect cleanroom conditions with no abrasion during its lifetime, while nonlinearities or wobble from the guiding system do not exist.

The article describes a measuring method for six degrees of freedom (Forces Fx, Fy, Fz, Torque Tx, Ty, Tz). This method can be used during the design and development phase to correlate theoretical and real-world measuring methods for the design. It guarantees the correlation between theory and the real measurement on the design. The measuring device uses a passive 6 DOF hexapod structure with optoelectronic sensors in the struts for measuring the force. This hexapod structure allows a simple matrix calculation for all three forces and three torques from the forces of the six struts.

6 DOF FORCE / TORQUE MEASUREMENT DEVICE

The 6 DOF force platform was designed as a very low-cost object with a minimum number of parts. Only three different parts and 12 joints are used:

- 3-D printed flexures for the struts
- 3-D printed aperture for photo interrupter
- Base plate and top platform have the same shape

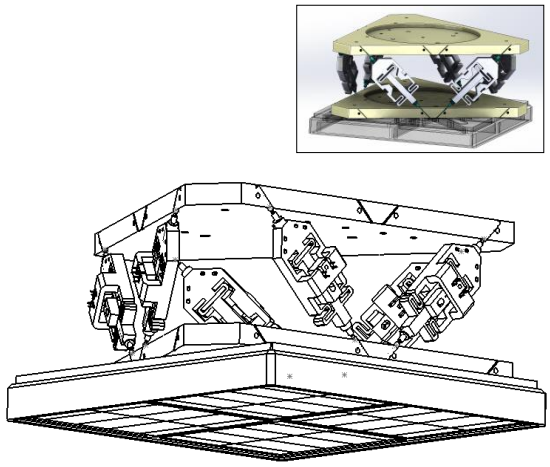

FIGURE 1: 6 DOF Force measuring platform with magnetic levitation platform facing downwards

A super-elastic titanium material is used for the joint wires. That material allows a huge stress in the short bending area. The wires are crimped into screws.
Photo interrupters are used for detecting the deformation in the struts, respectively the force in the struts. An adjustable aperture is mounted at one end of the struts while the other segment is slightly deformed by the load (force). Even if that photo interrupter does not provide a very linear characteristic curve, it is linear enough in the middle zone to use it for mapping functions.

MEASUREMENT SETUP

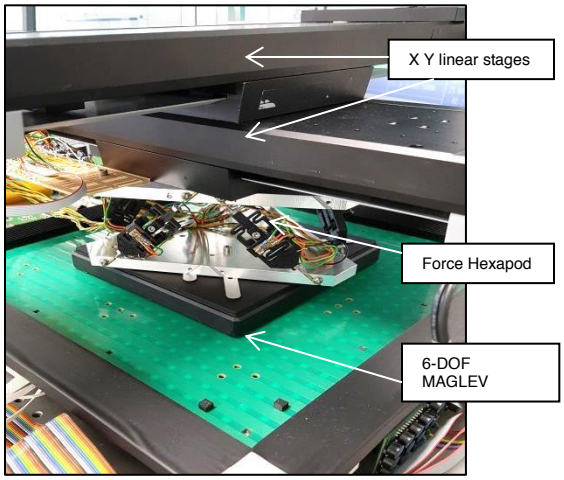

FIGURE 2: Measuring setup for a planar magnetic levitation stage

The setup of the upper section shows two cross coupled precision linear stages. These stages are used to move the force platform together with the magnetic levitation positioning stage over the 6 DOF planar maglev system in 2D. The stages can be controlled in the micrometer range.

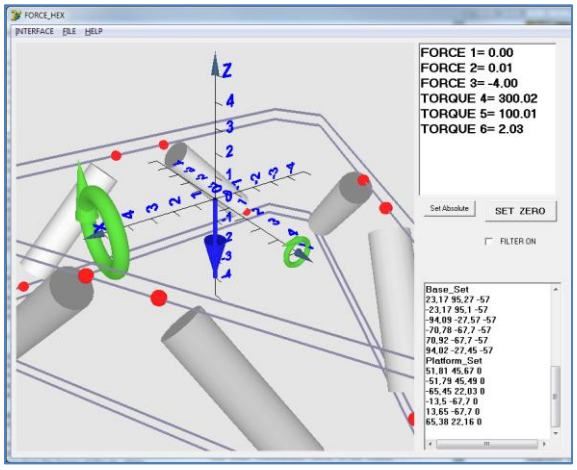

FIGURE 3: Graphic interface for the 6 DOF force measurement platform (Fz=-4N, Tx=300mNm,Ty=100mNm)

For online visualization and control of the two linear stages, a graphical software tool was developed to show the force vector and all three torque components around the defined axes. Because of the weakness of the simple 3-D printed struts, an update rate of 20Hz was used.

For the data interface to the computer, a simple 8-channel A/D USB module from Meilhaus Electronic with 12bit resolution was used. The material costs of the force hexapod including sensors and the A/D converter is less than $200. No additional amplifiers are necessary.

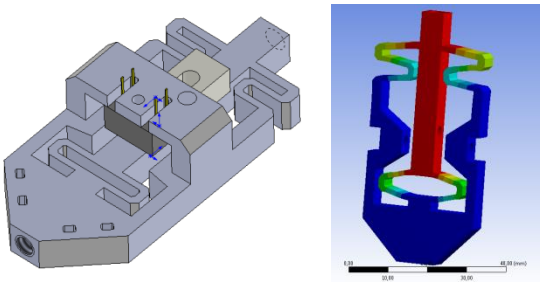

FIGURE 4: left: Flexure-strut design, photo-interrupter for detecting the deflection of the strut, right: FEM calculation of the deformation

Figure 4 shows the strut design with an adjustable aperture and the photo interrupter placed in the middle section of the strut. The sensitivity curve (movement of the aperture in the light gap) of the photo interrupter can be slightly linear.

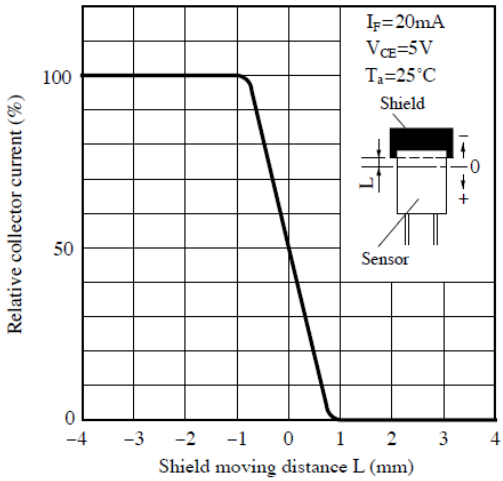

FIGURE 5: Relative collector current vs. position of the aperture for a photo interrupter (data sheet GP1S56T Sharp)

With +/- 10 V operation voltage at each photo interrupter no additional amplifier needs to be used. The scaling of the voltage to the applied force for each strut is calibrated (mapped) in the software tool.

TRANSFORMATION OF STRUT FORCES

To calculate the three force components and three torque components, a matrix operation has to be performed. The following configuration matrix was determind from our geometry:

config=

0.354	-0.614	0.705	32.216	-36.547	-47.989
-0.354	-0.614	0.705	32.089	36.533	47.909
0.354	0.614	0.705	15.540	46.169	-47.983
0.709	0.000	0.705	-47.754	9.523	47.988
-0.709	0.000	0.705	-47.758	-9.629	-47.984
-0.354	0.614	0.705	15.631	-46.116	47.991

The configuration matrix is defined by the geometry of the hexapod. The torque arm values are calculated by a vector product of the direction vector of the strut and the joint distance at the force platform.

$$\begin{bmatrix} c_{11} & c_{12} & \cdots & c_{16} \\ c_{21} & & & \\ \vdots & & \ddots & \vdots \\ c_{61} & & \cdots & c_{66} \end{bmatrix} \cdot \begin{bmatrix} F1 \\ F2 \\ F3 \\ F4 \\ F5 \\ F6 \end{bmatrix} = \begin{bmatrix} Fx \\ Fy \\ Fz \\ Tx \\ Ty \\ Tz \end{bmatrix} \quad (1)$$

Because the geometry of the force hexapod is nearly constant, the calculation can be done without a new definition of the configuration matrix. F1…F6 are the forces in the struts, Fx…Tz are the force and torque at the platform.

USING THE FORCE PLATFORM ON A PLANAR MAGLEV SYSTEM

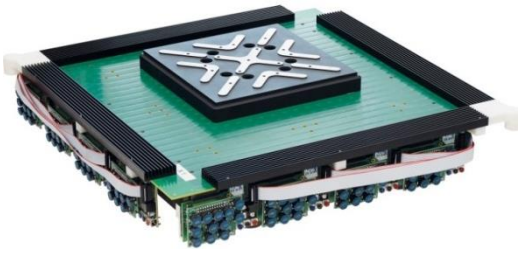

Figure 6: MAG 6-D system without cover, the driver and cables for digital interface are on the side

In this paper, we show the use of the 6 DOF force sensor for measuring on the planar maglev system shown in figure 6. The passive stage carries the Halbach arrays and a 2-D grid. All drivers are mounted in connectors directly on the PCB.

COIL DESIGN

The coils for both directions are placed on the PCB board. The coils are designed in a three-phase architecture, placed rectangularly onto the upper and lower side of each single layer. Buried vias are used to allow the cross section of the coil structure on each PCB layer.

.

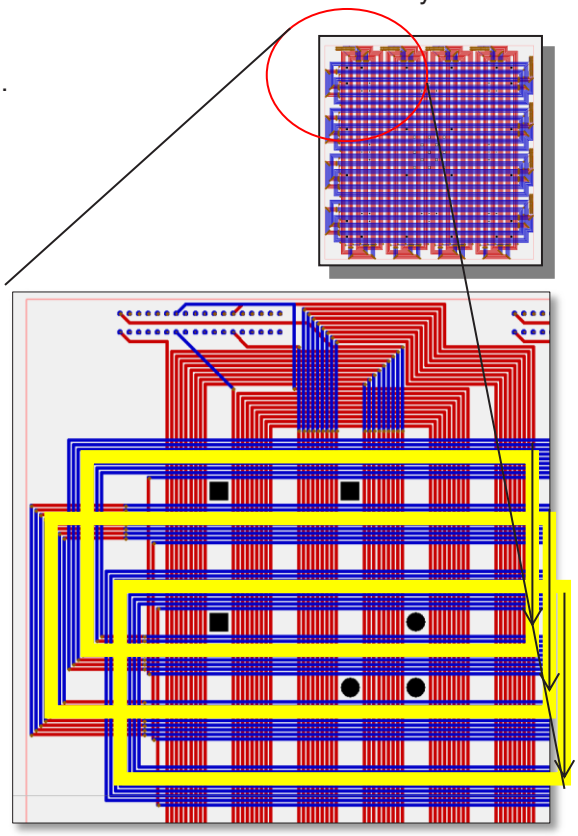

Figure 7: Coil board design, a section of the board show the 3 phase structure of the driving coils

The structure is described in [4]. The principle board design was used from X. Lu in [5].
In our new design, we have gaps between the 3 phase coils. These gaps are necessary to allow access to the sensor head from the bottom through the coil board to the flying stage, where the grid and the reflective layer are placed.
The disadvantage is that the linear properties of force generation are disturbed a little and the efficiency is lower than without these gaps.

DECOUPLING OF LIFTING AND X/Y FORCES

The idea is to use a thin incremental encoder glass below the movable stage and above the coils, small gaps have to be placed between the

driving coil layout for access to the sensor heads. However, the gaps cause distortions in linear force generation.

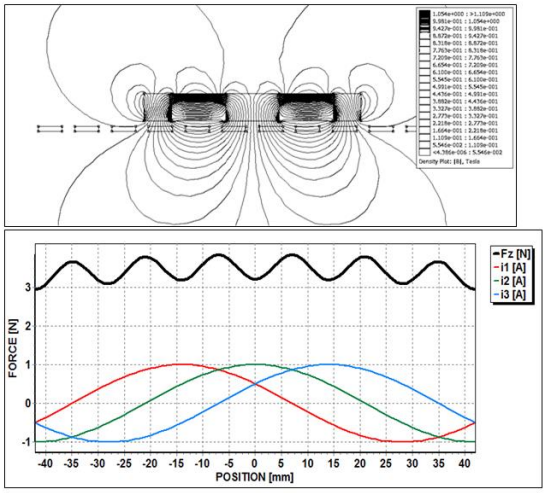

Figure 8: Gaps of 4 mm are between the 3-phase coil structure, 2-D view on a cut of only one the Halbach array and the corresponding coils. (i1=phase1… i3=phase3)

$$phase1(x) = ampl \cdot \cos\left(\pi \cdot \frac{x}{42} - \frac{\pi}{3}\right) \qquad (2)$$

$$phase2(x) = ampl \cdot \cos\left(\pi \cdot \frac{x}{42}\right) \qquad (3)$$

$$phase3(x) = ampl \cdot \cos\left(\pi \cdot \frac{x}{42} + \frac{\pi}{3}\right) \qquad (4)$$

The simple 2-D model of a section of the halbach arrays, the coil board with gaps, the driving current ditribution, and calculation results are shown in figure 9. As a result, the lifting force (Z force) has harmonics above the motion range. This should be decoupled to make control easier.
It was shown in [4] that a superposition of the 3-phase current with a spatial amplitude modulation cancels the nonlinearities.

MEASURING RESULTS

The simple model reduces cross coupling but does not eliminate it. There are some reasons for more dependencies:

- The model was only in 2 D
- The 4 Halbach arrays are mounted from 8 Halbach parts.
- The Halbach arrays are not perfectly magnetized

With a moderate current of only 1.5A in the clusters of the coil assembly, the stage can be driven by more than 40 N in a vertical and horizontal direction. The coil structure (in 12 layers on a PCB) does not need additional wiring and is connected with highly efficient PWM drivers placed directly on the main board.
The drivers are controlled by digital serial SPI channels – the digital connection to the controller.

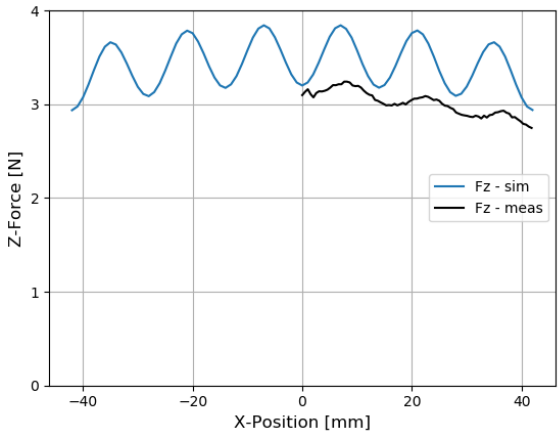

Figure 9: Comparison between simulation and measured force Fz

Figure 9 shows the measurement result with the force hexapod platform for a small lifting force of 3N. The same order of harmonics can be seen as we get in the 2-D magnetic field calculations for Lorentz force Fz. The period of the measured distortions is 14 mm as the calculation desires.
The measured distortions are smaller than the 2D calculation shows.

DECOUPLING OF LIFTING AND X/Y FORCES

It can be shown that the horizontal component can also be decoupled and linearized by using a spatial frequency phase shift between two phases. [6]

$$ampl(x) = 1 + 0.09 * \cos\left(\pi * \frac{x}{7}\right) \qquad (5)$$

Using this amplitude spatial frequency (5) the distortions are canceled caused by the gaps in the PCB.
With this feed forward term, the control function can be linearized despite the fact that the gaps in the coil structure distort the linear properties.

Current distribution

For levitating the stage, it is necessary to know which coil needs which current to decouple the forces and torques.

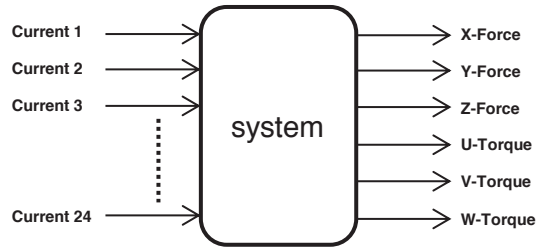

Figure 11: Coupled system

In [6], it was shown how to reduce the cross coupling of the 24 current sources, e.g., how we can decouple torque from force generation. Inducing a curtain force but not generating parasitic force isn't that easy. For example, by rotating the stage around the Z axis, all of the four Halbach array blocks must have a different force direction.

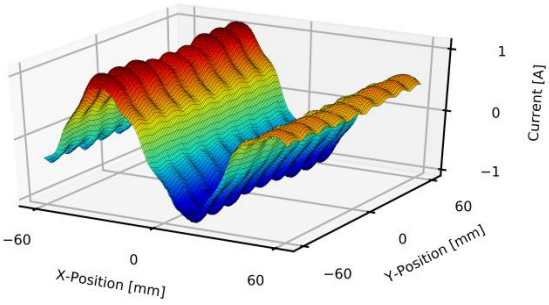

Figure 12: Current distribution of one phase of the drivers over the motion range of the planar stage

The Lorentz force is calculated with J as current density and B as magnetic flux density:

$$F = \int (J \times B) dv \qquad (6)$$

$$T = \int r \times (J \times B) dv \qquad (7)$$

To find a solution for decoupled torques, offline optimization was done. With the measured 3-D flux density of the stage in the XY plane for different distances, the current distribution and the geometry of the coil board, the forces F, and torques T of the stage can be calculated.

With the force sensor system, we can verify the calculation and the implementation into the control algorithm. The precalculated current distributions are used as mapping function and as feed forward terms in the controller.

SUMMARY

6 DOF force and torque analysis of high precision magnetic levitation systems is very helpful in the design phase. [7] It opens the way to mapping of nonlinearities, compensation curves, and feed forward function into the digital controller.
We have shown a very simple and low cost design of a 6 DOF force and torque sensor based on a hexapod structure, which makes it easy to adapt to the mechanical requirements.
Using that type of sensor makes the correlation of control current and real measured forces clear. It also saves time during the implementation of complex mapping and feed forward algorithms.

REFERENCES

[1] Frissen,J.Compter, M.Renkens,G.Fockert, R.Coolen, US Patent 6,847,134, Displacement device, Jan.25,2005

[2] W.Kim, D. Trumper, High-precision magnetic levitation stage for photolithography PrecisionEng. 22 2, 1998, pp. 66-77

[3] R.Gloess, Ch.Mock, Ch.Rudolf, C.Walenda, Ch.Schaeffel, M.Katzschmann, H.-U. Mohr, Magnetic Levitation in 6- DOF with Halbach Array Configuration, ACTUATOR 2010, Bremen

[4] R.Gloess,A.Goos, Nanometer Resolution of Magnetic Levitation Stages for Planar and Linear Scan Applications, ISMB16 conference ID129, Beijing 2018

[5] X.Lu, I.Usmann, A Novel Long-Stroke Planar Motor, Proc. ASPE, 3313, Nov. 2011

[6] A.Goos, R.Gloess, Sensor Array and Algorithms for Current Control in a 6-DOF Magnetic Levitation Actuator, ACTUATOR 2018, Bremen

[7] J.de Boeij,E.Lomonova, Look-Up Table Based Real-Time Commutation of 6-DOF Planar Actuators, IEEE Conference, Singapore 2007

A NOVEL SEMI-ACTIVE JOINT FOR SIMULTANEOUSLY ACHIEVING FAST SETTLING AND EXCELLENT IN-POSITION STABILITY IN POINT-TO-POINT POSITIONING

Xin Dong[1], Chinedum E. Okwudire[1]
[1]Smart and Sustainable Automation Research Lab
Department of Mechanical Engineering, University of Michigan
Ann Arbor, MI, USA

OVERVIEW

The design of a novel semi-active joint for connecting mechanical bearings to a precision motion stage is presented. The semi-active joint enables the benefits of bearing friction on in-position stability to be achieved while avoiding its adverse effects on settling time in point-to-point positioning. To achieve this goal, the joint is equipped with solenoid actuators that switch its stiffness from low, during settling, to high once the stage gets into position. Simulation results, using the semi-active joint, show 51% and 55% improvements in settling time and in-position stability, compared to the case with rigid joint and compliant joint, respectively. Preliminary experiments on an in-house built motion stage equipped with the designed semi-active joint show that the proposed method has excellent in-position stability, while potentially achieving large reductions of settling time. However, the associated impact force, when the semi-active joint switches its stiffness, excites high frequency dynamics of the system, severely jeopardizing the settling performance. Ongoing work is focused on mitigating the adverse effects of switching using both mechanical design and control methods.

BACKGROUND AND MOTIVATION

Mechanical bearings (i.e., sliding, and especially rolling bearings) are used for motion guidance in most precision and some ultra-precision motion stages due to their low cost, large motion range, high off-axis stiffness and vacuum compatibility [1]. They are also preferable over other bearing types for their excellent in-position stability due to the presence of pre-motion (i.e., 'static') friction caused by mechanical contact. However, the presence of pre-motion friction causes the stages to take a long time to settle into position during point-to-point motions [2]-[4]. To address this issue, model-based compensation methods are most commonly used to predict and cancel out the friction experienced by the stage [2][3]. However, accurate compensation of pre-motion friction often requires the use of complex models which are not robust to changes in on-machine friction [4]-[6].

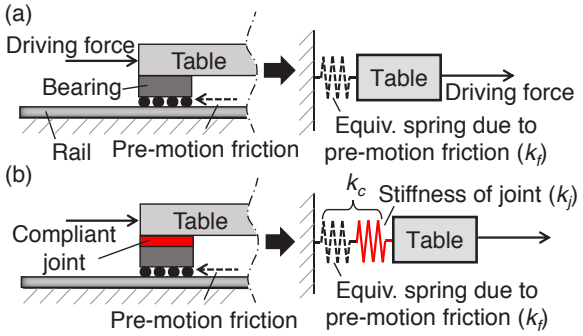

Fig. 1 Schematic and spring model of motion stage with mechanical bearing attached to the table: (a) rigidly, and (b) using the compliant joint.

Prior work [4][5] done by the present authors has demonstrated that undesirable effects of pre-motion friction can be effectively mitigated by attaching the bearing to the moving table of the stage using a joint that is very compliant in the motion direction. Fig. 1(a) shows a typical mechanical-bearing-guided stage in which pre-motion friction is modeled as an equivalent nonlinear spring of stiffness k_f connecting the table to the ground [4][5][7]. At the start of the motion, k_f is very large; but as more driving force is applied to counteract friction, k_f rapidly reduces and eventually becomes zero. Standard feedback controllers often encounter difficulties when trying to overcome the high initial stiffness of pre-motion friction, resulting sluggish settling during point-to-point positioning. Fig. 1(b) illustrates the concept of the compliant joint method [4][5]: rather than being rigidly attached to the moving table, the bearing is attached using a joint of stiffness k_j in the motion direction. Accordingly, the stage with the compliant joint is modeled as a series combination of k_f and k_j, with combined stiffness $k_c = k_f k_j/(k_f + k_j)$. A very small k_j dominates the combined stiffness felt by the stage when k_f is very large in the pre-motion regime. Using the compliant joint, accurate and robust compensation of pre-motion friction, and

large reductions in settling time have been experimentally demonstrated [4][5].

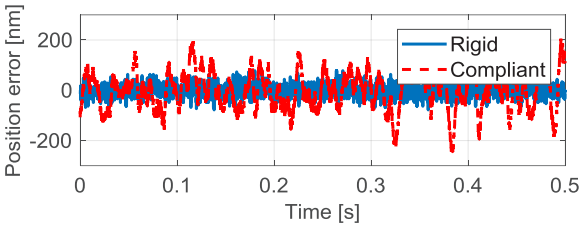

Fig. 2 Measured in-position error of rigid and compliant stages presented in [4][5] when a PWM amplifier is used.

While the adverse effects of pre-motion friction during motion transients (e.g., settling) are mitigated by introducing the compliant joint, the benefits of friction during in-position are also diminished. Due to the initially very large k_f, mechanical-bearing-guided stages often have excellent in-position stability compared to, e.g., air bearing stages (which have zero stiffness in the motion direction). The compliant joint replaces the stiff k_f with a much softer stiffness k_c (since $k_j << k_f$), leading to increased susceptibility of stage's position to disturbances. As a result, the stage with the compliant joint (i.e., compliant stage) has significantly larger errors during in-position, compared to that of the stage without it (i.e., rigid stage), when a PWM amplifier (which is known to have relatively large noise) is used to drive the motor – see Fig. 2. This issue can be mitigated by switching to a linear amplifier which has much less noise level; however, this causes increased cost and reduced energy efficiency.

SEMI-ACTIVE JOINT

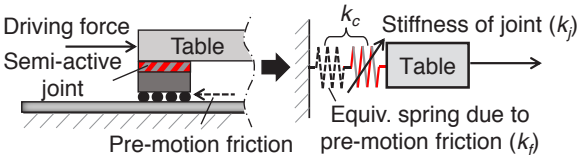

Fig. 3 Schematic and spring model of a mechanical-bearing-guided stage equipped with the semi-active joint.

Fig. 3 shows the proposed method for mitigating the undesirable effects of pre-motion friction during motion transients while maintaining excellent in-position performance. The bearing is attached to the table using a joint that can be switched between two modes (stiff or compliant). The joint is very stiff ($k_j >> k_f$) when the stage is at rest (e.g., while it is in position) such that the combined stiffness approaches the high frictional stiffness (i.e., $k_c \rightarrow k_f$); the joint becomes compliant ($k_j << k_f$) during motion transients such that the combined stiffness is dominated by the much softer k_j (i.e., $k_c \rightarrow k_j$).

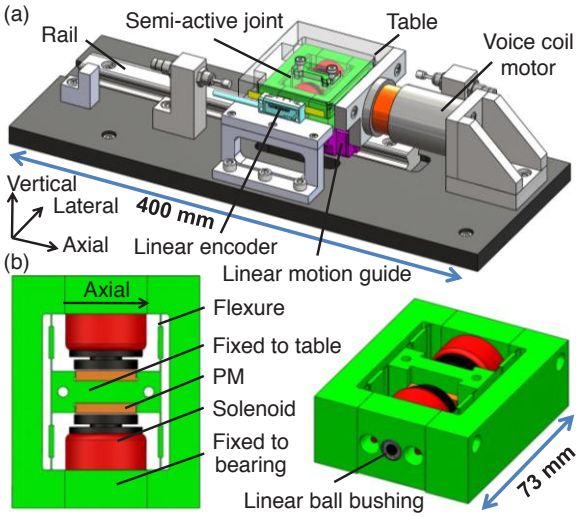

Fig. 4 CAD model of (a) a motion stage equipped with (b) the designed semi-active joint prototype.

Table 1. Stiffness values of flexure, bearing and their combination [N/m].

	Axial	Vertical	Lateral
Flexure	5×10^4	5×10^7	1×10^8
Bearing	$\sim 10^6$	3×10^7	4×10^7
Combined	$\sim 5 \times 10^4$	2×10^7	3×10^7

Fig. 4(a) shows the CAD model of a single-axis mechanical-bearing-guided motion stage equipped with the proposed semi-active joint. The stage has 1.35 kg moving mass and 25 mm travel range. It is guided by a high-rigidity pre-loaded linear motion guide with end seals (THK, SR-25TB), riding on a super-precision grade rail, lubricated using grease (THK, AFB-LF). A voice coil motor (Moticont, LVCM-044) is used to drive the stage. The table's position is measured using a linear encoder system (Renishaw, T1000 read head and RGSZ20 scale) with post interpolation resolution of 4.88 nm.

A semi-active joint prototype (see Fig. 4(b)) is used to attach the bearing to the table. A flexure (made of Aluminum 7075-T6) with four leaf springs is adopted in the semi-active joint design due to its non-contact and friction-free nature. The outer platform of it is connected to the bearing and the center platform is connected to the moving table. Table 1 summarizes the stiffness values of the designed flexure (obtained via finite element analysis using SolidWorks®). Note that the flexure achieves orders of

magnitude less stiffness (in the axial direction) than the initial stiffness of pre-motion friction experienced by the bearing. It also maintains the same order of magnitude of off-axis stiffness as the bearing, so as not to unduly compromise the rigidity in lateral and vertical directions. The stiffness of the semi-active joint is switched through two solenoid actuators and permanent magnets (PMs) which are attached to the outer and center platforms of the flexure, respectively. When no power is applied, the PMs attract the armatures of solenoids such that the center platform of flexure is locked (through contact friction) to the outer platform (i.e., the joint is stiff); when power is applied, the solenoid actuators pull the armatures away from the PMs to allow relative motion between the bearing and the table (i.e., the joint is compliant). Note that linear ball bushings are added between armatures and coils of the solenoid actuators to increase the axial stiffness of the semi-active joint when it is switched to stiff mode.

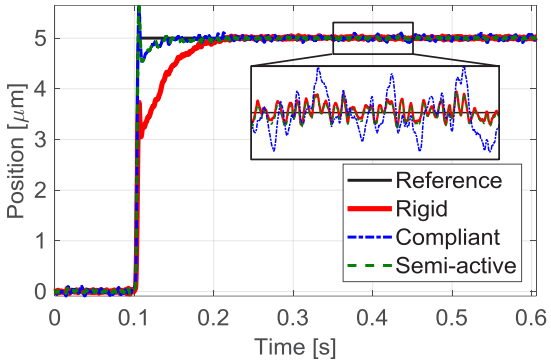

Fig. 5 Simulated settling performance of the stage with rigid joint, compliant joint and semi-active joint (which is switched to compliant mode only from 0.1 s to 0.15 s).

Table 2. Simulated settling time and in-position error (RMS).

	Settling time	In-position error
Rigid	91 [ms]	17 [nm]
Compliant	45 [ms]	38 [nm]
Semi-active	45 [ms]	17 [nm]

Fig. 5 shows the simulated settling performance using the stage of Fig. 4(a) equipped with the rigid joint, compliant joint [4][5] and proposed semi-active joint during a 5 μm point-to-point motion. As seen from Table 2, the compliant stage reduces the settling time by 51%, however, at a cost of more than doubling the root-mean-square (RMS) error during in-position, compared to the rigid stage. Using the proposed semi-active joint (which is switched to compliant mode from 0.1 s to 0.15 s), the stage achieves the same settling time as the compliant stage while maintaining the same in-position performance as the rigid stage.

POINT-TO-POINT POSITIONING TESTS

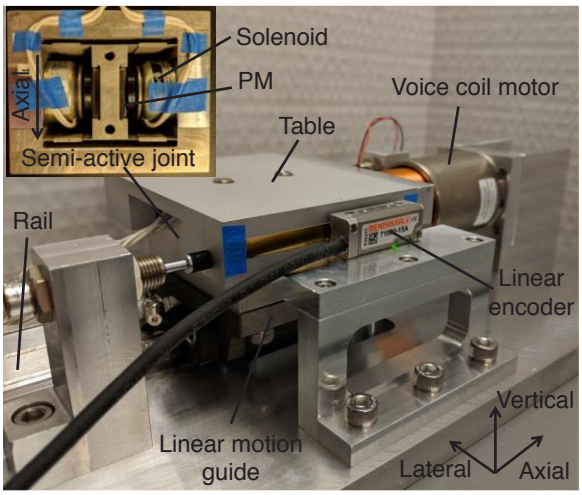

Fig. 6 Assembled in-house built stage equipped with the designed semi-active joint prototype.

Fig. 6 shows the in-house built mechanical-bearing-guided motion stage equipped with the designed semi-active joint prototype. A cascaded P/PI controller with velocity and acceleration feedforward is used for feedback control of the stage. It is tuned to 150 Hz closed loop bandwidth based on the identified dynamics of the rigid stage using loop shaping; the exact same controller gains are used for controlling the stage with compliant joint and semi-active joint. The controller is implemented using a real-time control board (dSPACE, DS1007), running at 10 kHz sampling frequency. A linear amplifier (Trust Automation, TA-115) is used to power the voice coil motor. The solenoid actuators are controlled through two relay modules for switching the semi-active joint between its two modes.

Experiments are carried out using the in-house built stage shown in Fig. 6 for evaluating the settling performance of the proposed method. Point-to-point motion profiles with step sizes of 5 μm and 5 mm are used as the reference trajectory [4]. The time taken for the stage to settle into a ±25 nm window after each step is evaluated. Fig. 7(a) compares the typical settling performance of the stage with rigid joint, compliant joint and semi-active joint during point-to-point motions with 5 μm step size. The rigid stage takes 150 ms to settle while the compliant stage settles within 14 ms, i.e., 91% faster. However, the in-position

error of the compliant stage is 5.4 nm, which is more than two times larger than that of the rigid stage (i.e., 2.3 nm). Using the proposed semi-active joint, which is switched to compliant mode before the start of the motion and switched back to stiff mode when the reference command reaches the target position, the stage is able to achieve an in-position error of 2.3 nm. However, switching of the joint introduces large motion errors during settling, followed by severe oscillations. As a result, the stage with the semi-active joint takes 110 ms to settle which is faster than the rigid stage, but significantly slower than the compliant stage. As seen from the frequency spectrum of position error signal after switching (see Fig. 7(b)), several high frequency modes are excited due to the impact force; since the feedback controller has limited bandwidth, the oscillation takes a very long time to settle. However, observe that the transient dynamics of the stage with semi-active joint is very similar to that of the compliant stage. Therefore, the proposed method can potentially achieve similar settling performance as the compliant stage if the adverse effects of switching are mitigated.

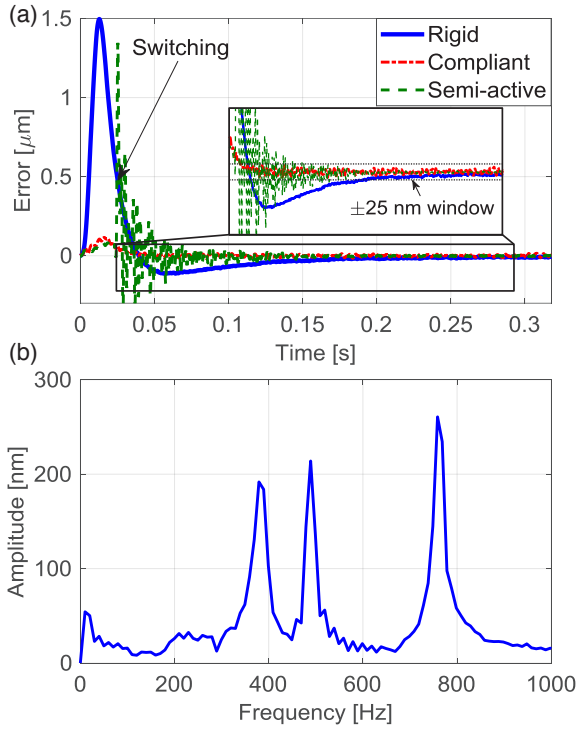

Fig. 7 (a) Typical positioning performance of the stage into the ±25 nm window during point-to-point motions with 5 μm step size; (b) frequency spectrum of position error signal for the semi-active joint case after switching.

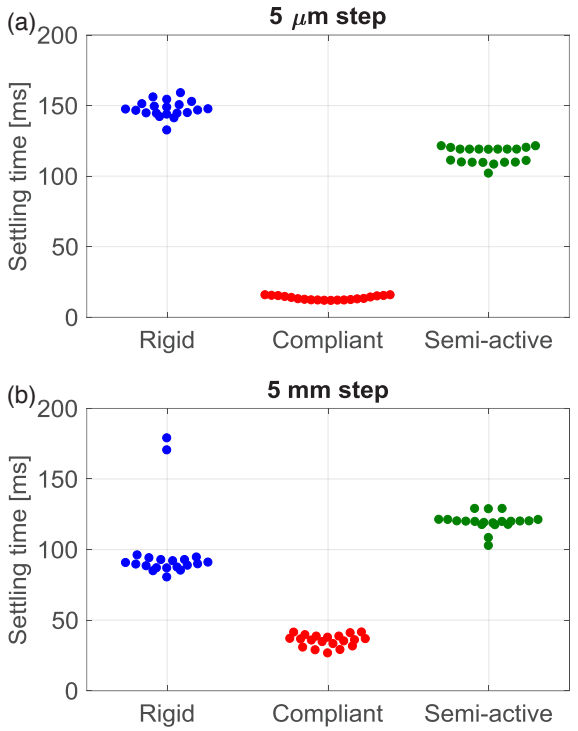

Fig. 8 Comparison of settling times into the ±25 nm window during point-to-point motions with (a) 5 μm and (b) 5 mm step size.

Table 3. Mean settling time and in-position error (RMS) during point-to-point positioning tests.

	Settling time	In-position error
5 μm step		
Rigid	147 [ms]	2.4 [nm]
Compliant	13 [ms]	5.5 [nm]
Semi-active	115 [ms]	2.4 [nm]
5 mm step		
Rigid	98 [ms]	2.7 [nm]
Compliant	35 [ms]	5.9 [nm]
Semi-active	119 [ms]	2.8 [nm]

Fig. 8 compares the settling performance during point-to-point positioning tests with 5 μm and 5 mm step size, based on 20 trials at random positions of the table and Table 3 summarizes the mean settling time and RMS errors during in-position. Note that mean settling times of the rigid stage are 147 ms and 98 ms for the 5 μm and 5 mm cases, respectively. The compliant stage is able to achieve 91% and 64% reductions in the mean settling times (i.e.,13 ms and 35 ms), at a cost of more than doubling the in-position errors compared to the rigid stage. Using the proposed semi-active joint, the stage is able to achieve almost the same in-position stability as the rigid stage. However, due to the large motion errors and the associated residual vibrations (that are

caused by the impact force during switching), the stage with the semi-active joint only achieves slightly faster (22% improvement) settling time during the 5 μm step motion, and has even worse performance during the 5 mm case, compared to the rigid stage. In order to improve the settling performance of the proposed method to similar levels as the compliant stage, ongoing work is focused on mitigating the undesirable effects of switching dynamics using both mechanical design and control methods. For example, damping materials will be implemented to prevent the excitation of high frequency modes. Similarly, electrical low-pass filter (through RC circuits) will be added to slow down the solenoid actuators during switching which will consequently reduce the impact force. From the control side, advanced control techniques, such as disturbance observer and harmonic cancelling controller, will be investigated.

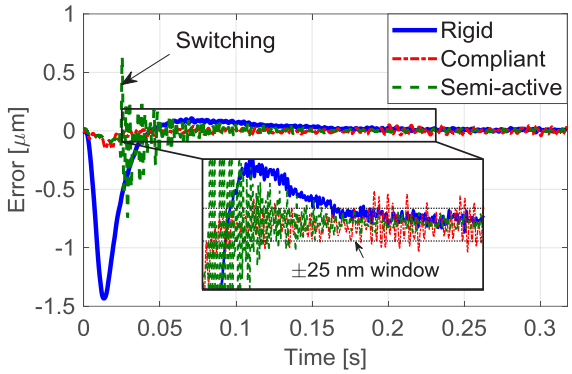

Fig. 9 Typical positioning performance of the stage into the ±25 nm window during point-to-point motion with 5 μm step size. (Note: current noise of 0.0025 A RMS value is added to the current outputted by the amplifier)

Note that the linear amplifier used to drive the motor has very small noise level. To simulate the case when a PWM amplifier is used (for its higher force, better energy efficiency and lower cost), normally distributed current noise with 0.0025 A standard deviation (i.e., RMS value) is added to the control command during point-to-point positioning tests. Fig. 9 shows the typical settling performance during the 5 μm step motion. The rigid stage takes 188 ms to settle within the ±25 nm window, with an in-position error of 6 nm. For the compliant stage, the RMS error during in-position increases significantly to 15.8 nm, making it unable to settle into the desired window. Using the proposed semi-active joint, the stage is able to settle within 127 ms with very similar in-position stability (i.e., 6.4 nm) as the rigid stage.

CONCLUSIONS AND FUTURE WORK

In this paper, a novel semi-active joint for simultaneously improving the settling performance of mechanical-bearing-guided motion stages while maintaining excellent in-position stability in point-to-point positioning has been presented. The proposed semi-active joint actively switches its stiffness between two modes: compliant or stiff; the joint is compliant during motion transients such that the undesirable effects of pre-motion friction on the settling time is mitigated through the compliant joint method; the joint becomes very stiff once the stage gets into position such that the benefits of bearing friction on in-position stability is preserved. It has been shown through simulation that the semi-active joint achieves 51% and 55% improvements in settling time and in-position stability, compared to cases with rigid joint and compliant joint, respectively. A semi-active joint prototype has been designed which integrates two solenoid actuators and permanent magnets into a flexure design to realize the switching mechanism. Preliminary experiments on an in-house built mechanical-bearing-guided motion stage equipped with the designed semi-active joint have demonstrated similar transient dynamics as the compliant stage and almost the same in-position stability as the rigid stage. However, the impact force caused by switching introduces large motion errors and excites high frequency modes of the system during settling, significantly increasing the settling time of the stage. Ongoing work is focused on mitigating the adverse effects of switching on the proposed semi-active joint using both mechanical design and control techniques in order to achieve similar settling performance as the compliant joint method.

REFERENCES

[1] Altintas Y, Verl A, Brecher C, Uriarte L, Pritschow G. Machine Tool Feed Drives. Annals of the CIRP 2011; 60(2):779–96.
[2] Maeda Y, Iwasaki M. Rolling friction model-based analyses and compensation for slow settling response in precise positioning. IEEE Trans Ind Electron 2013; 60(12):5841–53.
[3] Bucci B, Vipperman J, Cole D, Ludwick S. Evaluation of a servo settling algorithm. Precis Eng 2013; 37(1):10–22.
[4] Dong X, Okwudire CE. An experimental investigation of the effects of the compliant joint method on feedback compensation of pre-sliding/pre-rolling friction. Prec. Eng. Article in press.

[5] Dong X, Liu X, Yoon D, Okwudire CE. Simple and robust feedforward compensation of quadrant glitches using a compliant joint. Annals of the CIRP 2017; 66(1):353-6.
[6] Reuss M, Dadalau A, Verl A. Friction Variances of Linear Machine Tool Axes. Procedia CIRP 2012; 4:115–9.
[7] Yoon JY, Trumper DL. Friction Modeling, Identification, and Compensation Based on Friction Hysteresis and Dahl Resonance. Mechatronics 2014; 24(6):734–41.

DESIGN OF A META-MATERIAL FOR THE TORSIONAL REINFORCEMENT OF A LEAF SPRING

Deick J. Andree, Marijn Nijenhuis, Dannis M. Brouwer
Precision Engineering
Faculty of Engineering Technology
University of Twente
Enschede, The Netherlands

INTRODUCTION

Meta-materials are engineered materials with physical properties that cannot be found in nature. In this paper, we investigate the ability of meta-materials to improve the performance of flexure mechanisms.

Meta-materials consist of a lattice of cells which have a designed micro-structure with certain desirable physical properties. When decreasing the cell size and increasing the number of cells, the material starts approximating the properties of the cell [1, 2]. Limiting factors in the practical application of meta-materials are the lack of methods for designing the cell based on macro-system requirements, and manufacturing processes and costs. Advances in additive manufacturing have the potential to increase the practical adoption of meta-materials.

Flexure mechanisms are a class of mechanisms that guide and constrain motion by means of purely elastic deformation, resulting in smooth, precise and virtually hysteresis-free operation. For these reasons, flexure mechanisms are used in precision applications that require a high level of determinism. Typical drawbacks include a limited range of motion and insufficient support stiffness (especially in deflected state) [3, 4, 5].

In this work, we investigate the potential of meta-materials in improving the performance of a common flexure element. We have selected a case study for this investigation: a leaf spring is to be manipulated by a lattice of cells specifically designed to increase only the overall torsional stiffness. This way, the manipulated leaf spring, which normally provides relatively low stiffness in three independent motion directions, now only allows two relative motions of low stiffness: a rotation about the y-axis and translation in z-direction of Figure 1. The four remaining motions are associated with relatively high stiffness and can be used to constrain motion when used in a mechanism. The leafspring with meta-material is from now on referred to as the MeMaFlex.

First, we present a systematic design approach for the MeMaFlex. The design goal in terms of macro-structure stiffness is converted to the stiffness requirements of the individual meta-material cells, by analysing the deformation modes of a leaf spring. In meta-material literature, it is common to specify the design goal as some desired mathematical stiffness tensor for the cell; we instead specify the design goal in terms of

1. degrees of freedom (DOFs) between different segments of the cell, and
2. a desired overall increase in torsion stiffness only.

This way the designer has more control on the solution and gets a better insight into the mechanism in the cell, allowing systematic design of the cell structure.

Second, a stiffness and mass model for the MeMaFlex is created to predict the performance of the design. Since meta-materials essentially consist of a large number of repeated structures, a finite element model is created by first modeling a single cell (with 3-D Timoshenko beam elements) and then using sub-structuring techniques to describe the entire MeMaFlex. An optimization routine is used to find design parameters that yield optimal performance.

Third, an experiment is conducted for validation. The MeMaFlex is manufactured using an additive manufacturing (SLS 3-D printing) technique. A modal analysis is performed to measure the natural frequencies (which serve as a representative stiffness measure given the constant mass) and compare them with the numerically predicted performance.

CELL DESIGN

The MeMaFlex consists of a normal leaf spring with its longitudinal direction in x-direction; on the top and bottom face of the leaf spring, meta-material is added in a cylindrical volume, as shown in Figure 1. The indicated coordinate frame is maintained in the rest of this paper.

The leaf spring has three DOFs (relative motions associated with low stiffness), namely x-axis rotation (Rx), y-axis rotation (Ry), and z-axis translation (Tz).

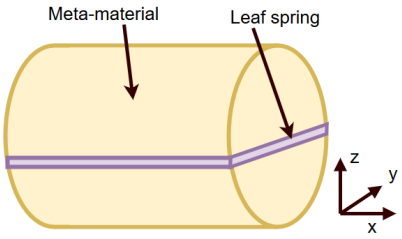

FIGURE 1. Schematic shape and orientation of the MeMaFlex

The function of the meta-material is to constrain the Rx direction and to gain a flexure element with four constrained directions and only two DOFs. To convert this stiffness objective to a stiffness requirement for the cell micro-structure, the deformation modes of the leaf spring are analyzed: motion in the original three DOFs is due to (a combination of) bending in the x, z-plane and torsion deformation.

For pure bending of a beam, there will be neutral planes, as shown in Figure 2. For torsion of a beam, there are neutral planes as well (provided that deformation is small and effects of warping can be neglected), as shown in Figure 3. Because these neutral planes stay undeformed and only move in both situations, one can think of a mechanism between these planes for achieving the design goal. The planes themselves can serve as stiff cross-links between cells. Looking at the movement of the neutral planes in both situations, it can be concluded that for maintaining low bending stiffness between these planes, the Ry and the Tx motions between the planes should be compliant. For obtaining high torsional stiffness, the Ty, Tz and the Rx motions between the planes should be stiff.

These neutral planes can be translated to the front and back (in x-direction) of the meta-material cell. This way, the design goal of the micro-structure of the meta-material cells is formulated: the cells should have two fixed sides that are compliant in Ry and Tx directions, and stiff in Ty, Tz and Rx directions.

Analysis of the neutral planes does not give any information about the Rz direction. The rotation around the z-axis of the meta-material can be either stiff or compliant for the two deformations modes considered. However, considering the complete flexure element, it is also desired to have a stiff rotation around the z-axis, so the meta-material should also be stiff in Rz direction.

A suitable topology for the cell is found by means of the FACT approach, which is a systematic method for designing flexure mechanisms [6, 7]. This method shows the constraint spaces in which trusses can be

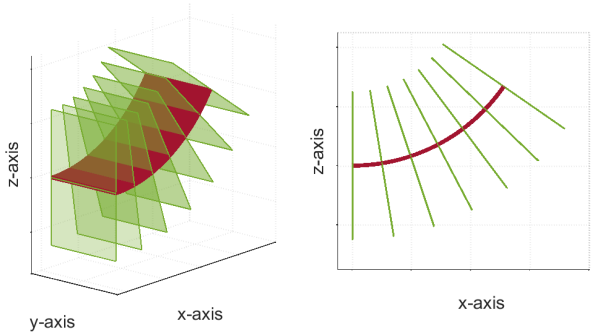

FIGURE 2. Neutral planes in bending deformation.

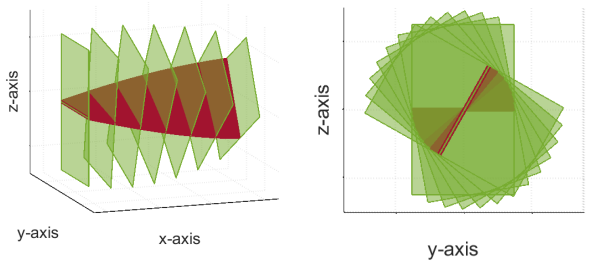

FIGURE 3. Neutral planes in torsion deformation.

placed such that a system with the desired motion is obtained.

Because of the choice of cylindrical volume of the meta-material, the cells will be loaded equally in Ty and Tz directions. To provide equal stiffness in both directions, it is decided to connect a system with one translational DOF and a system with one rotational DOF in series (instead of a single parallel system for both DOF). By series stacking, there is more material in the support direction for providing stiffness, compared to a parallel system for both DOFs. A schematic overview of how the two systems, system A and system B, are placed and what their constraint spaces are is shown in Figure 4.

System A

System A should have one translational DOF; the other degrees of freedom should be constrained. The possible positioning of the constraints is shown in the left constraint space of Figure 4. The most important directions in the cell which contribute to the overall torsional stiffness are Ty, Tz and Rx. These directions can all be constrained by placing beams in the y, z-plane. Therefore, the planar topology of this system is first considered.

The high stiffness in these directions is due to longitudinal stiffness of the beams. The low stiffness in the compliant direction, Tx, is due bending stiffness of the beams. To get a high ration between the de-

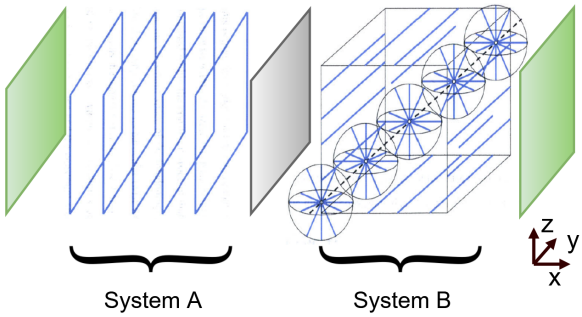

FIGURE 4. The constraint spaces of system A with a Tx DOF and system B with an Ry DOF, placed in series between two neutral planes (edited copy from [6])

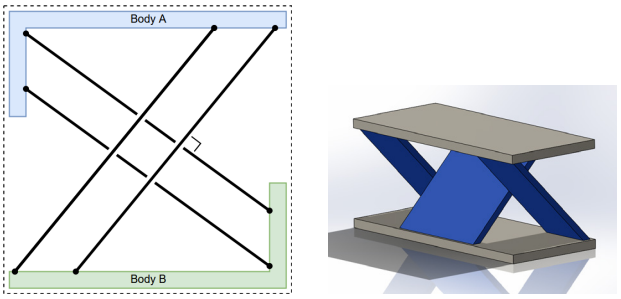

FIGURE 5. Left: beam placement for system A. Right: cross-flexure for system B

sired high longitudinal and low bending stiffness, the length of the beams should be as large as possible. This can be achieved by specific positioning of the beams within the cell.

To provide an equal amount of stiffness to both the Ty and Tz directions, an even number of beams should be placed perpendicular to each other. To add stiffness to the Rx direction, at least two beams should be placed parallel to each other. The design to achieve this is shown in Figure 5 (left).

In this planar situation, the beams lie in a plane and intersect. In the spatial situation, there will be two planes that each have two parallel beams. However, this way the system is not exactly constrained. To ensure only the Tx direction is compliant, this system is placed twice behind each other, such that there are four planes with beams.

System B

The second system should have one DOF, the Ry direction. A common way to achieve this is to cross two leaf springs, creating a cross-flexure, as shown in Figure 5 (right). For the sake of symmetry, one of the leaf springs can be divided in two. This cross flexure is used as system B.

NUMERICAL MODEL

To predict the performance of the MeMaFlex, models for the stiffness and mass are created. These are used for optimization of the design, and for comparison with experiment measurements of the natural frequencies of the system. First, a single cell is modeled using common finite element techniques. Then, the full MeMaFlex is modeled as an assembly of substructured cells.

Stiffness model of cell

3-D Timoshenko beam elements [8] are used to build the structure of the meta-material cell. Because the MeMaFlex consists of multiple cells, the number of degrees of freedom of the model and the associated computational effort will be high. The number of finite element DOFs is reduced by static condensation [9], substructuring the cells into 8-node super elements. The various cells connect to each other at the corners.

Stiffness model of MeMaFlex

The leaf spring of the MeMaFlex is modeled using 3-D Timoshenko beam elements [8]. To the top and bottom face, the cell super elements are attached by means of Lagrange multipliers.

Because compliant mechanisms are affected by gravity, the model is extended with load stiffening effects [10]. Because the leaf spring will carry most of the weight, load stiffening is only applied at the segments of the center leaf spring.

The total stiffness of the MeMaFlex between its two ends is obtained by substructuring the whole system again into a super element of two nodes.

Mass description

A simplified lumped model of the mass of the MeMaFlex is created. To ensure this simplification does not influence the accuracy too much, an additional mass is attached to the end of the MeMaFlex that is dominant with respect to the mass of the cells.

OPTIMIZATION

The global geometry of the MeMaFlex is determined by the limits of the 3D-printer. Minimum dimensions specify the thickness, 0.3 mm, and the distance, 0.6 mm, between the flexible beams. The cell size is chosen to be 20 mm. The MeMaFlex has a length of 160 mm and a diameter of 80 mm. The cells are placed such that they approximate the cylindrical volume, as shown in Figure 6.

Five cell dimensions that influence the cell stiffness are optimized with respect to the stiffness of the MeMaFlex. These dimensions are schematically

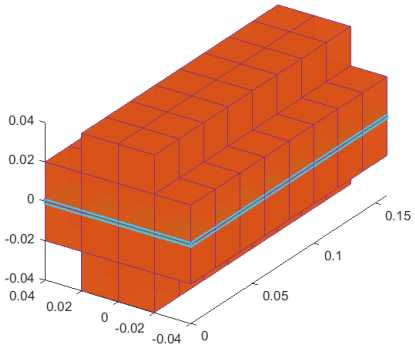

FIGURE 6. Placement of cells on inner leaf spring

shown in Figure 7 as X_1 to X_5.

The first design variable, X_1, determines the width of system A and thus the length of the flexible beams. It also determines the thickness of the support structure, since the outer side of the support frame has fixed distances to the sides of the cell.

The second design variable, X_2, determines the length of system A. A longer system A will fit more beams. However, a longer system A will also result in longer support frames, which results in a lower bending stiffness of these frames.

The other design variables, X_3, X_4 and X_5, determine the dimensions of system B. A compromise needs to be found between a low stiffness of Rx stiffness of the cell and high Ty and Tz stiffnesses. The width of system B is the same as system A.

Notice that the stiffnesses of the support frames and the systems are all in series. This means that the section with the least stiffness is dominant for the total stiffness. For the DOFs which should be compliant this means that only the section which releases this DOF is important. For the DOFs which should be stiff, this means that all the sections should be equally stiff and as stiff as possible.

The objective function Rx/Ry is maximized by means of the fmincon (including globalsearch) function in MATLAB. Figure 8 shows a cutout of a single cell, exposing the parallel beams of system A (on the left) and the cross flexure of system B (on the right behind the transparent separation). A print of the optimized MeMaFlex design is shown in Figure 9.

The torsional stiffness (Rx) increased by a factor of 133 while the bending stiffness (Ry) only increased by a factor of 3.61. The Tz direction increased by a factor of 3.60. The other directions, which are already stiff for a leaf spring increased by a few pro mille. The Rx/Ry ratio for the leaf spring without

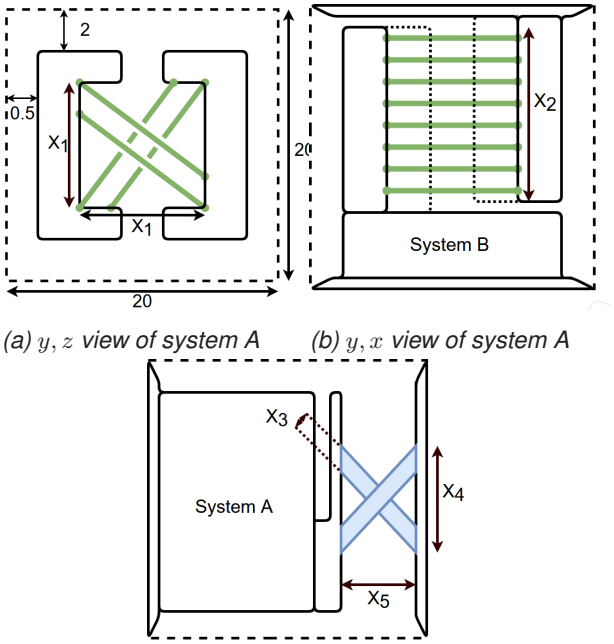

(a) y, z view of system A *(b) y, x view of system A*

(c) x, z view of system B

FIGURE 7. Schematic overview of design parameters for optimization

meta-material is 0.356; with meta-material, it is 13.1. This is an improvement of a factor of 37.

EXPERIMENT

The critical dimensions and masses of the printed MeMaFlex have been measured and corrected in the numerical model (to account for printing tolerances). The MeMaFlex is attached to a frame, clamped on one side and free to vibrate, as shown in Figure 10. The clamping mechanism can be attached in two ways such that the MeMaFlex can be positioned horizontally or vertically, to include or exclude dominant gravity effects. The modal frequencies of the system are measured. For validation of the setup, leaf springs without meta-material have been printed and tested as well.

RESULTS

The predicted and measured frequencies are shown in Table 1. The measured value is the mean value based on the accelerometer data and camera measurement (or whichever one is available in the frequency range).

The errors of the model with respect to the experiment are shown in Figure 11. For each natural mode, there are four measurements: vertical (with gravity), horizontal (without gravity), and for the short and the long dominant end mass. From these results, some conclusions can be made about the different aspects of the model.

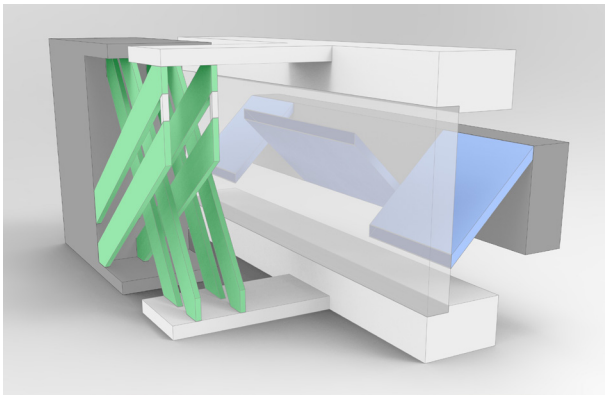

FIGURE 8. A cutout showing the inner parts of a single cell: system A (green) and system B (blue). Grey blocks depict the connections to the next cell. The white body (partly transparent for visualization purposes) is an intermediate rigid body that connects systems A and B.

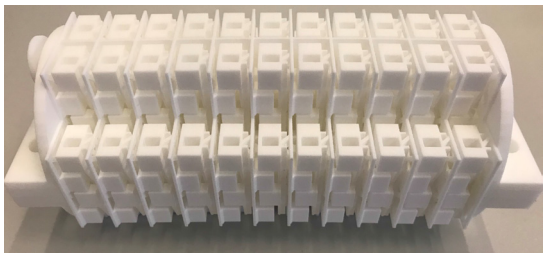

FIGURE 9. Picture of the final design

Load stiffening

Load stiffening due to gravity is present at the vertically conducted experiments. The load stiffening effects have the most influence on the Ry stiffness. The Tz stiffness is hardly affected and the Rx stiffness is not affected at all. It is noticeable that the natural modes to which load stiffening applies the most, have the most variance in error. It is also noticeable that the errors at the vertically conducted experiments are in all measurements worse (a larger negative number) than the errors at the horizontally conducted experiments. From this, it is concluded that the prediction of load stiffening is seems underestimated.

Mass description

Because there is no significant difference between the small and the long dominant end mass, it can concluded that its mass is modeled well. The measurements do not provide information to draw further conclusions specifically about the mass formulation of the MeMaFlex cells.

Stiffness description

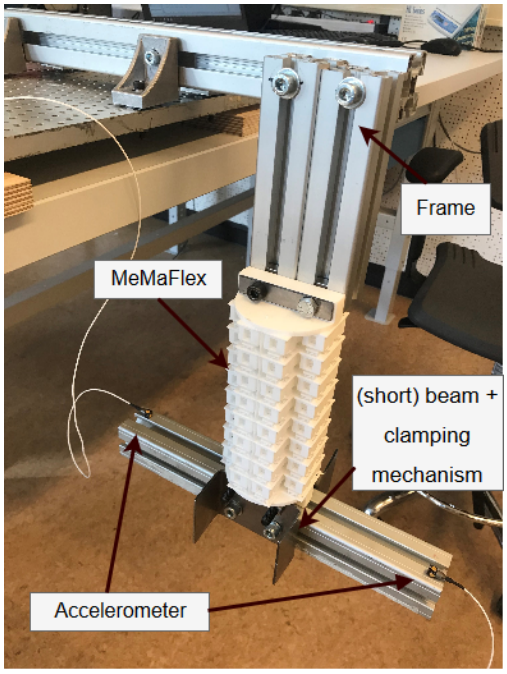

FIGURE 10. Photograph of the set-up of the experiment

In general, the model predicts lower natural frequencies than found in the experiments. Because the mass description seems adequate (i.e. validated for the center leaf spring, and the dominant end mass), it is reasonable to assume that most of the error is due to the stiffness description: in general, the model developed in this paper underestimates the stiffness.

Besides this general error, there is a difference noticeable in the mode shapes. The Ry and Tz modes are underestimated less than the Rx mode. This can be explained by looking at the cell stiffness. The Ry and Tz modes are the desired modes and their stiffness is mostly related to the translational DOF of the cell. The stiffness of this DOF is defined by the stiffness of the frame and the bending of the flexible beams. Since these are in series, the flexible beams are dominant and easy to predict. The Rx mode, however, is not a desired DOF. For this mode, the flexible beams are loaded in longitudinal direction (with a much higher stiffness). This longitudinal beam stiffness is also in series with the overall frame stiffness. Now the frame is the least stiff factor and therefore the dominant factor. The frame is a complicated system of short beams and is not exactly printed the way it is modeled. Therefore this mode is more sensitive to errors due to wrong prediction of the stiffness of the frame.

A benefit of this difference in error, in this particular case, is that the bending/torsion-ratio turns out to

TABLE 1. Measured and predicted natural frequencies in Hertz

Short beam				
	Vertical		Horizontal	
	Model	Measured	Model	Measured
Ry	1.15	1.35	0.65	0.72
Tz	4.12	4.55	3.72	4.45
Rx	9.81	11.98	9.81	12.08
Long beam				
	Vertical		Horizontal	
	Model	Measured	Model	Measured
Ry	0.56	0.73	0.30	0.30
Tz	2.18	2.51	1.66	1.91
Rx	2.52	3.25	2.52	3.25

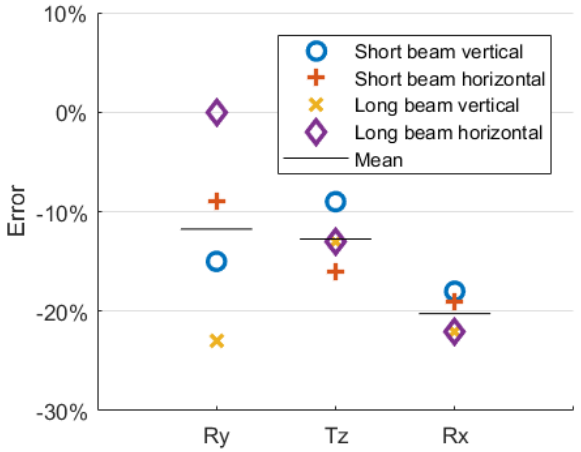

FIGURE 11. Relative error of the predicted natural frequencies with respect to the measurements

be better than predicted by the optimization. Therefore, the actual performance of the MeMaFlex is better than predicted.

CONCLUSION

This paper has presented a case study for the design of a meta-material cell based on the desired mechanical function of the macro-system. Mechanical insight into the deformation modes of the macro-system is converted into design requirements in terms of degrees of freedom of the individual cells. As the case study, the meta-material is used for increasing the torsional stiffness of a leafspring. This way, a new flexure element is created with a translational and rotational DOF. A finite element model for stiffness, mass and gravity is built to predict the performance in terms of modal frequencies. The model incorporates sub-structuring to reduce computational time and make optimization feasible. Experiments are conducted to measure the natural frequencies and validate the models. The compliant modes in the case without gravity are approximated with an accuracy of 18%; in the case with gravity the accuracy is 23%; the stiff modes are approximated with an accuracy of 33%. In general, the measured natural frequencies are higher than predicted by the numerical model, meaning that the actual design performs better than predicted. Potential sources for the discrepancy are identified. The experiment have validated the design and shown that a flexure element with two degrees of freedom has been created.

REFERENCES

[1] Zadpoor AA. Mechanical meta-materials. Mater Horiz. 2016;3:371–381.

[2] Milton G, Cherkaev A. Which elasticity tensors are realizable? Journal of Engineering Materials and Technology, Transactions of the ASME. 1995 10;117(4):483–493.

[3] Slocum AH. Precision Machine Design. Englewood Cliffs, Prentice-Hall; 1992.

[4] Smith ST. Flexures: Elements of Elastic Mechanisms. CRC Press; 2000.

[5] Blanding DL. Exact Constraint: Machine Design Using Kinematic Principles. New York: ASME Press; 1999.

[6] Hopkins JB. Design of parallel flexure systems via Freedom and Constraint Topologies (FACT). Massachusetts Institute of Technology; 2007.

[7] Hopkins JB, Culpepper ML. Synthesis of multi-degree of freedom, parallel flexure system concepts via Freedom and Constraint Topology (FACT) Part I: Principles. Precision Engineering. 2010;34(2):259 – 270.

[8] Przemieniecki JS. Theory of matrix structural analysis. Dover publications; 1968.

[9] Felippa CA. Introduction to Finite Element Methods. University of Colorado; 2004.

[10] Ray DA. Gravity and laboratory suspension effects on the dynamics of controlled flexible spacecraft. Massachusetts Institute of Technology; 1993.

PRECISION SCANNING ONBOARD THE NASA TROPICS MISSION

**Steven Gillmer, Conor McMenamin, Brian Powers, Joseph Racamato,
Michael DiLiberto, Andrew Cunningham, Linda Fuhrman
David Crompton, Steven Michael, Kristin Clark, William Blackwell
Lincoln Laboratory
Massachussetts Institute of Technology
Lexington, MA USA**

INTRODUCTION

Over the past decade, tropical cyclones and severe weather have accounted for an average economic loss of $60 billion per year [1]. In an effort to attenuate the consequences, earth observing satellites drive forecasts by monitoring key environmental variables. Notable forecasting factors include atmospheric temperature, sea surface temperature, sea level, storm intensity, atmospheric water vapor, aerosols, and precipitation. There are a variety of methods that can be used to provide valid forecasting, with microwave sounding providing the most impactful contributions from spacecraft.

The NASA Time-Resolved Observations of Precipitation structure and storm Intensity with a Constellation of Smallsats (TROPICS) mission [2, 3] will be the first demonstration that microwave sounding instruments onboard a constellation of low-cost cubesats can offer reliable weather forecasting. TROPICS will provide rapid revisit - hourly and less - storm evolution predictions. The short timescale fills gaps in our current knowledge of storm evolution due to that fact that current capabilities are an order of magnitude slower. Furthermore, the TROPICS mission provides a significant reduction in cost compared to large billion-dollar class weather forecasting satellites [4].

SCANNING MECHANISM

The TROPICS space vehicle is shown in Figure 2 and includes a microwave sounding radiometer (payload) attached to the spacecraft bus. For wide angle of regard, the payload will spin at a constant 30 RPM rate continuously for the entire lifetime of the mission (1.5 years).

Scanning is accomplished via a scanning mechanism as shown in Figure 3. The scanning mechanism consists of an optical encoder (Celera MicroE), a space-qualified slip ring (Cobham Aeroflex), a 28-pole brushless motor (Blue

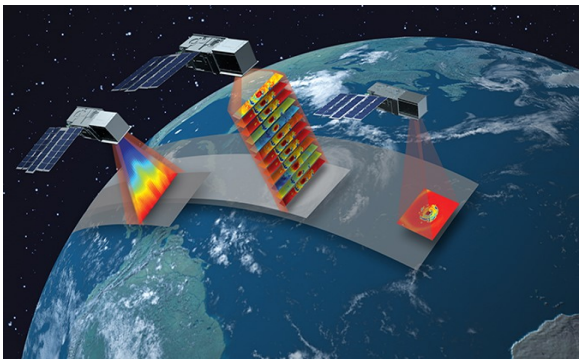

FIGURE 1. The TROPICS mission will provide low-cost weather forecasting. A constellation of identical 3U CubeSats provide sounding with a median revisit rate approaching 30 minutes.

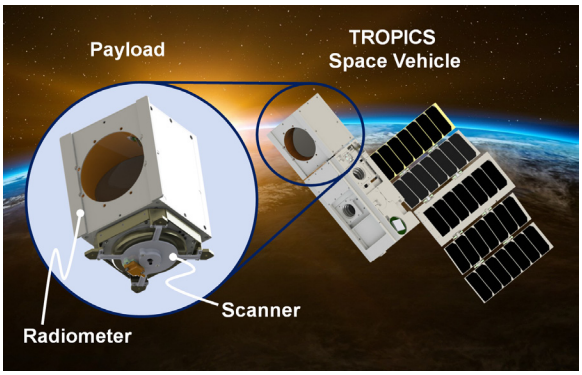

FIGURE 2. The payload will spin at 30 RPM continuously for the lifetime of the mission.

Canyon Technologies) and a back-to-back duplex pair bearing assembly (Kaydon). The scanner is primarily composed of Ti-6Al-4V due to the close thermal expansion match to 440C stainless steel (SS) bearing races and 416 SS motor.

REQUIREMENTS

The operational requirements of the scanner are primarily driven by the need for accurate geolocation of the radiometer pointing vector.

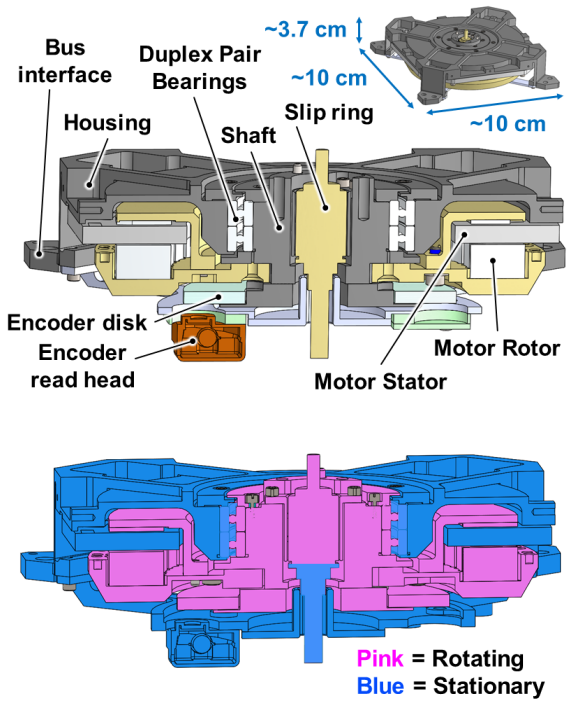

FIGURE 3. Critical components of the scanner.

While spinning, the scanner must maintain a reliable pointing orientation relative to the star trackers and GPS located on the bus portion of the spacecraft. The driving requirements to achieve satisfactory performance can be summarized as follows:

1. Measured angular resolution $\leq$ 170 μrad
2. Pass 12 conductors from stationary bus to rotating payload with 0.75 Amp capacity
3. Operate at $\leq$ 0.5 W (42 mA at 12 V)
4. Rotate with an average angular velocity per cycle of 30 $\pm$ 0.5 RPM
5. Encoder error from sparse spacecraft down-links $\leq$ 870 μrad
6. 20 month operational lifetime spinning at 100% duty cycle
7. Random position wobble of the bearings, cross scan axis $\leq$ 170 μrad

Requirements 1 and 2 are fulfilled with the proper selection of commercial off-the-shelf (COTS) products. The scanner implemented a space-qualified MicroE Mercury 1500V-04 laser encoder

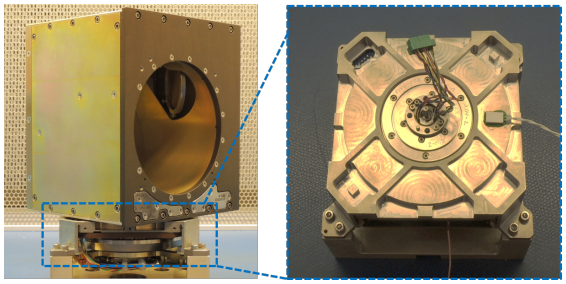

FIGURE 4. The as-built scanning mechanism.

that comes equipped with a 7,200 cycle/rev grating target and 4X interpolation. These specifications translate to a system resolution of $\pm$19μrad – thereby meeting Requirement 1. To pass signals and power from the stationary bus to the rotating payload per Requirement 2, a space qualified slip ring from Cobham Aeroflex (P/N 1001398-500) was incorporated with 12 leads at 1 amp capacity.

Requirements 3–6 are exacerbated by the thermal environment experienced on orbit (low-earth orbit, nominally 550 km). The tested limits of major components are plotted in Figure 5 showing operational (light blue) and survival (grey) ranges. Note that some grey survival ranges are hidden behind operational limits; however, operational limits never exceed survival ranges. Simulations in Thermal Desktop analysis software produce the hot (red) and cold (dark blue) extremes experienced on orbit during operational conditions. In addition to isothermal effects, gradients across the scanner decrease performance on orbit due to increased preload (friction) on the bearings.

GRADIENT ANALYSIS

Gradient simulations have been performed on the scanner to analyze a potential change in preload on the bearings. Those simulations assume the radiometer is hotter or colder than the bus which would cause the Titanium scanner material to differentially expand and increase friction on the SS bearings. Analytical simulations assume the temperature change induces a change in Hertzian contact stress which results in a change in preload. It can be shown that the change in required torque, τ, to spin the motor follows:

$$\Sigma\tau = \left\{2\left[\mu\left(\frac{d}{2}\right)\left(\frac{2N}{\sin C_a}\right) + \frac{\Delta F_H b_a}{\cos C_a}\right]\right\}(2.0\ \mathrm{FS}) + (I\alpha + I_m\alpha)(1.25\ \mathrm{FS}) + (T_f + T_s)(2.0\ \mathrm{FS}), \quad (1)$$

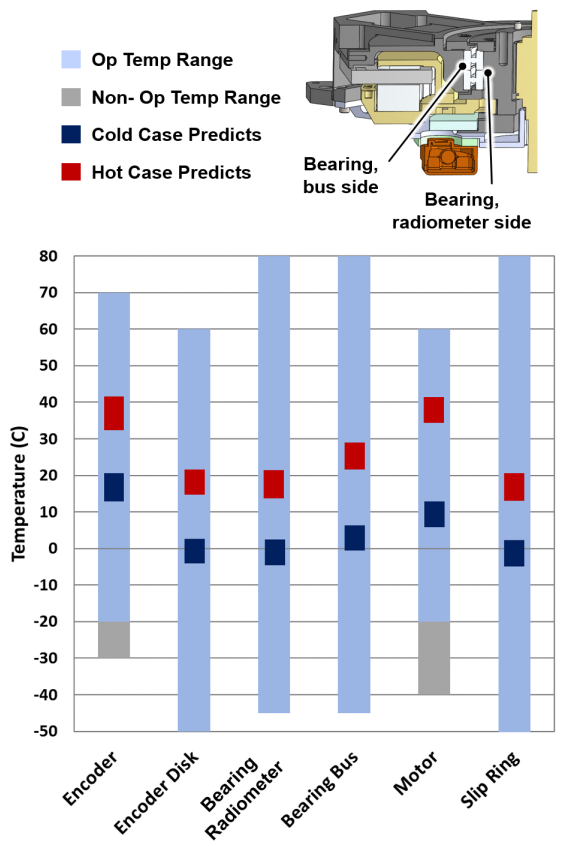

FIGURE 5. Orbital temperature predictions. These plots simulate stacked worst cases for hot (red) and cold (dark blue) through seasonal variations. The simulations take the full spacecraft into account.

where μ is the friction coefficient for precision lubricated ball bearings, d is the nominal bearing diameter, N is the preload at contact angle C_a, ΔF_H is the change in preload due to Hertzian contact stress, b_a is the number of balls, I is the radiometer inertia, I_m is the motor inertia, α is the acceleration, T_f is the motor friction torque, and T_s is the slip ring resistance.

Most of the terms in Equation 1 are readily available from the manufacturers of the various components. An exception is the change in preload due to Hertzian contact stress, ΔF_H, which is non-trivial and the driving component of the gradient analysis. Simulations were conducted using an approximate solution for point contact between objects. Under the "gap bending hypothesis", the effect of two curved surfaces deforming in the Hertzian regime can be reduced to an effective model of a sphere contacting a flat surface [5, 6]. Following this formalism, an equivalent elastic modulus is calculated based on the elastic modulii and Poisson ratios of the two materials in contact:

$$E_e = \frac{1}{\frac{1-\nu_1^2}{E_1} + \frac{1-\nu_2^2}{E_2}}, \tag{2}$$

where subscripts 1 and 2 denote the ball and race materials, respectively. Next, an equivalent radius of the system is found. In the case of a rolling ball bearing, the ball radius has a positive sign convention (since it is convex) and the race radius has a negative sign convention (concave). The equivalent radius is then

$$R_e = \frac{1}{\frac{2}{R_1} + \frac{2}{R_2}}. \tag{3}$$

The deflection of the system in the elastic regime of the bodies at the contact interface is then

$$\Delta\delta = \frac{1}{2}\left(\frac{1}{R_e}\right)^{1/3}\left(\frac{3(\Delta F_H)}{2E_e}\right)^{2/3}. \tag{4}$$

Note that Equation 4 is a function of change in load due to Hertzian contact stress, ΔF_H, and change in deflection, $\Delta\delta$; that is, the equation encapsulates an effective stiffness of a ball bearing under change in preload due to gradients across the scanner. The equation can be rearranged to solve for change in force due to hertzian contact stress, and inserted into Equation 1. For the current analysis, it is assumed that the housing structures of the bearings are infinitely stiff. Therefore, gradients drive enforced deflections, $\Delta\delta$ (assuming linear coefficients of thermal expansion), which produce a change in preload. This assumption can be further refined to account for hoop stress of the bearings and structure; however, for simple calculations, this approximation is considered a conservative estimate.

Safety factors in Equation 1 are incorporated per NASA-STD-5017A. The standard incorporates

TABLE 1. Torque and Force safety factors per NASA-STD-5017A.

Origin of Factor	K_v	K_f
Value Obtained via Theory or Analysis	3.0	1.5
Value Obtained via Test of Flight-Like Hardware	2.0	1.25

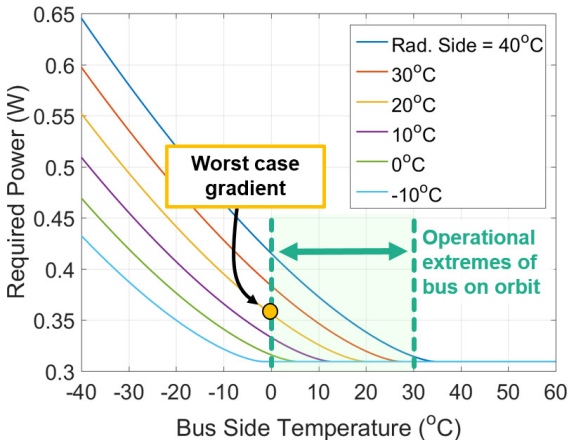

FIGURE 6. Gradients across the scanner bearings were simulated using Equation 1 with safety factors as shown in Table 1.

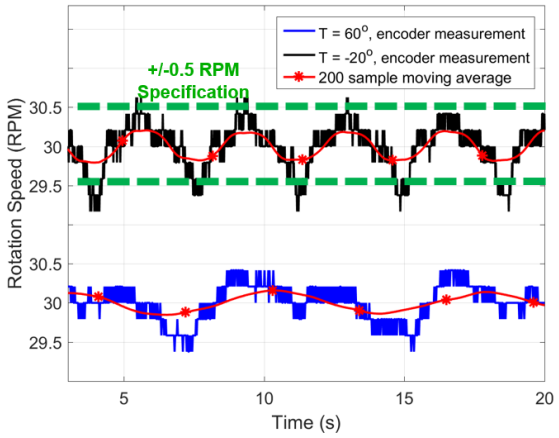

FIGURE 7. The performance of the scanner as measured by the encoder during TVAC testing. The data legend shows the encoder temperature when data was recorded.

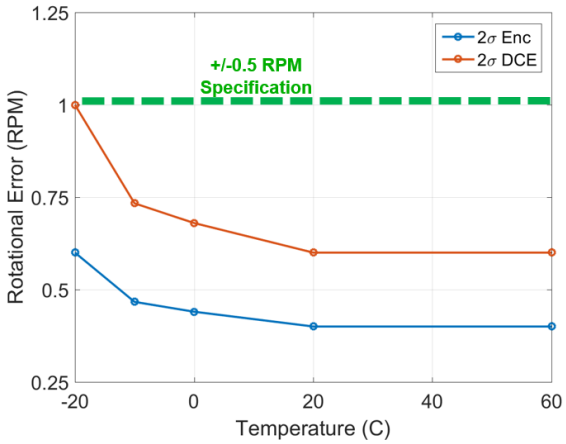

FIGURE 8. Two standard deviations of the error as measured by the encoder and drive control electronics (DCE). The X-axis temperature was the encoder temperature when data was recorded

different safety factors for values that change over the lifetime of the mission, like friction, and values that remain constant, like inertia. These values are represented in Table 1 as K_v and K_f, respectively.

This proceeding presents tests of flight-like hardware; therefore, simulations using Equation 1 are presented in Figure 6 using values obtained using safety factors K_v = 2.0 and K_f = 1.25. The measured torque constant from Blue Canyon Technologies of the motor used in this work was 270 mNm/A. Since the motor was driven with a 12 V commutation voltage, the torque from Equation 6 is converted to Watts in Figure 6 to analyze power consumption. It can be seen that the worst case gradient across the scanner pulls nominally 0.36 W of power.

Referring to Figure 6, the "Bus Side Temperature" refers to the "bus side" of the bearings and "Rad. Side" refers to the "radiometer side" of the bearings as indicated in Figure 5. The only other source power consumption on the scanner is the encoder read head, which nominally pulls 0.125 W. Therefore, these findings validate Requirement 3 through analysis. Experiments will be presented next to validate the requirements through test.

THERMAL-VACUUM TESTING

Operational requirements were validated via ground testing of a qualification (qual) scanner build. The qual scanner was constructed in an identical fashion as the flight scanners that are eventually built. After assembly, testing was carried out in a thermal-vacuum (TVAC) space simulation environment. Temperatures within a bell jar chamber were controlled using heaters and a liquid nitrogen cooled plate. In this fashion, relative amounts of heat and cooling are controlled with a PID controller external to the chamber. The complete thermal test consisted of two TVAC cycles of full operational limits (light blue limits in Figure 5) with an unpowered survival test in between. The survival test was conducted in a nitrogen purge to subject the

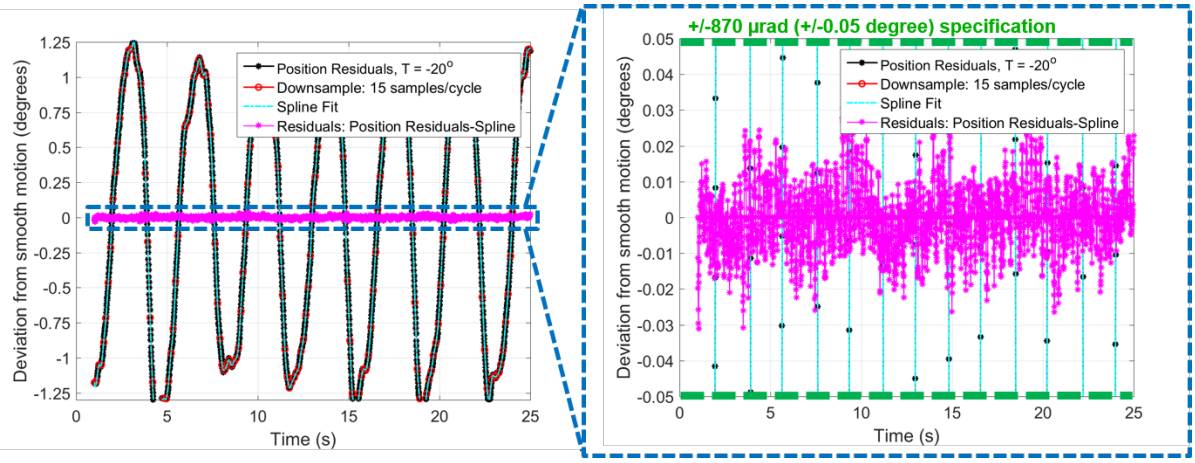

FIGURE 9. The downlinked packets of information from the space vehicle have limited size (nominally 15 samples per revolution at 30 RPM). Therefore, the performance of the scanner must be recoverable to within ± 870 μrad as shown.

scanner components to the grey extremes shown in Figure 5.

Representative data during operational testing is plotted in Figures 7 and 8 as measured by the encoder and drive control electronics (DCE). The drive control electronics operate in closed loop using three hall effect sensors on the the stator for feedback control. The increased errors in the DCE measurement are due to slight eccentricities of the stator/rotor combination. Those systematic errors are not present in encoder data since the encoder grating is actively aligned during assembly to the axis of rotation [7]. It can be seen that as the scanner gets colder, the friction increases due to (a) gradients across the scanner creating increased preload on the bearings, and (b) increased viscosity of the lubrication. The nominal gradient across the bearings during testing at the coldest operational extreme (encoder = -20°C) was 10°C with the rotating shaft warmer than the stator. Requirement 4 states that the average angular velocity *per cycle* must be within $\pm$ 0.5 RPM; therefore, the data is analyzed with a 200 sample moving average (1 cycle is 200 samples due to 100 Hz sampling rate at 30 RPM speed). The data at the extremes successfully validates requirement 4.

Requirement 5 is validated using the worst case performance recorded at an encoder temperature of -20°C as shown in Figure 7. The data can be re-worked in terms of measured angular position and linearly detrended to produce a deviation from smooth motion. During testing, the encoder position was sampled at 100 Hz; however, the size of the data packets that are downlinked on orbit need to be kept as small as possible. Therefore, the downlinked information of angular position is kept to nominally $\sim$15 samples per revolution of the scanner. In post-processing of our measured data, the position is downsampled and then fit with a spline. The spline fit is subtracted from our original data to show that we can reliable recover the true encoder position within $\pm$870 μrad of error.

The final requirement that can be exacerbated with increased preload during thermal excursions is lifetime. All performance specifications must be maintained for 20 months at 100% duty cycle in low earth orbit. Sufficient longevity in most components is achieved with proper selection of COTS parts; however, the primary bearings require increased analysis. Per the manufacturer, Kaydon, the L1 lifetime of the bearings can be calculated as

$$L_1 = a_1 a_L \left(\frac{C}{P_r}\right)^e \left(\frac{1 \times 10^6}{60n}\right). \quad (5)$$

The L1 lifetime gives the ensured survival of 99% of bearings assuming no contamination. The components of the equation include: a_1 which has been set to 0.25 for a 99% survival factor, $a_L = 0.79$ for a grease lubrication factor (Nye Rheolube 2000 grease lubrication), C is the

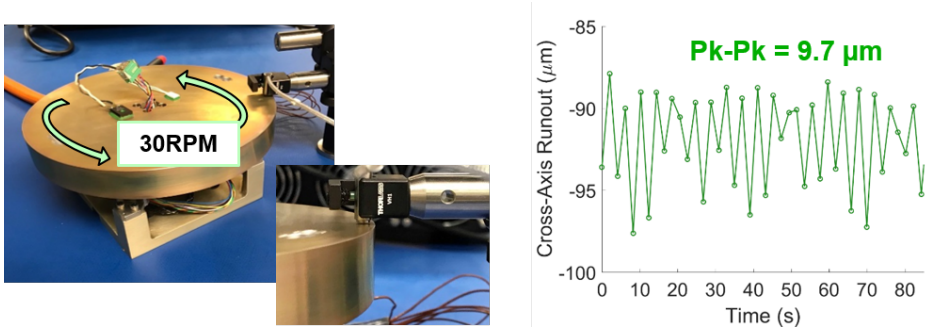

FIGURE 10. The random bearing wobble as measured by a capacitance gauge was approximately 10 μm with a 140 mm lever arm. This translates to 141 μrad of pointing error.

dynamic equivalent load rating, P_r is the dynamic equivalent load rating, $e = 3$ for ball bearings, and n is the speed. Considering these effects with the increased preloads predicted by Equation 4, the L1 lifetime for the bearings in the scanner is calculated as nominally 25 years. The lifetime has significant margin over the required 20 months, thus, lifetime testing was deemed unnecessary.

Requirement 7 is driven by manufacturing tolerances. The bearings chosen for the scanner were ABEC 7 back-to-back duplex pairs with 440C Stainless Steel races and ceramic balls. The bearings are manufactured for high precision, but nevertheless, still perform with some randomness in stability. To measure the wobble, a 140 mm diameter plate was attached to the scanner shaft and measured at the edge with a capacitance gauge. The total wobble while spinning was approximately 10 µm at the edge which translates to approximately 141 µrad of error. Therefore, the requirement is met with significant margin as seen in Figure 10.

CONCLUSIONS

The discussion up to this point has validated seven driving requirements which primarily affect geolocation knowledge. It has been shown that a compact scanner can point with significant precision to achieve mission goals. In addition to this work, survival testing has been completed including random vibration per the NASA General Environmental Verification Standard (GEVS) to ensure robustness during launch. The scanning mechanism of the TROPICS payload has been tested extensively for flight readiness in support of a 2020 launch date.

ACKNOWLEDGEMENTS

This material is based upon work supported by the National Aeronautics and Space Administration under Air Force Contract No. FA8721-05-C-0002 and/or FA8702-15-D-0001. Any opinions, findings, conclusions or recommendations expressed in this material are those of the author(s) and do not necessarily reflect the views of the National Aeronautics and Space Administration.

REFERENCES

[1] Aon Benfield Analytics. Annual Global Climate and Catastrophe Report; 2016.

[2] NASA TROPICS Mission;. https://tropics.ll.mit.edu/CMS/tropics/Mission-Overview.

[3] Blackwell WJ, Braun S, Bennartz R, Velden C, DeMaria M, Atlas R, et al. An Overview of the TROPICS NASA Earth Venture Mission. Quarterly Journal of the Royal Meteorological Society; Accepted Author Manuscript (doi:10.1002/qj.3290).

[4] Hand E. 'David and Goliath' weather eyes set for launch. Science. 2017; 358 (6365).

[5] Slocum AH. Precision Machine Design. Society of Manufacturing Engineers; 1992.

[6] Tripp J. 'Hertzian Contact in Two and Three Dimensions. NASA Technical Report. 1985; 2473.

[7] MicroE Technical Note: Alignment of Rotary Scales;. Retrieved 8/1/2018 from https://www.celeramotion.com/resource/technical-notes.

COMPRESSED AIR SYSTEM FOR ULTRA PRECISION AIR BEARING SPINDLES

Sam Arneson, Dave Arneson, Byron Knapp, and Daniel Oss
Professional Instruments Company
Hopkins, Minnesota, USA

INTRODUCTION

In order to utilize air bearings in any setting it is important to have a proper compressed air supply. Precision air bearing spindles have a small air gap (5μm – 20 μm) and so require a continuous source of clean, dry, oil free air at a constant pressure. Failure to provide any of these leads to crashes and errors in the air bearing spindles. The most common issue in crashed spindles is corrosion inside the spindle due to wet or contaminated air (Figure 1). Repairs to this kind of damage can cost tens of thousands of dollars even before factoring in weeks of downtime in a machine. These repairs are completely avoidable by having an appropriate compressed air system. Therefore, investing in a properly designed compressed air system is essential.

This poster will outline the overall design of a compressed air system for precision air bearing spindles and discuss the individual components of the system.

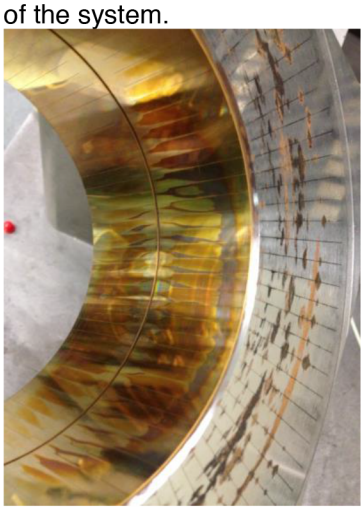

FIGURE 1. Damaged spindle stator from wet air.

SYSTEM DESIGN

The compressed air system at Professional Instruments was designed specifically to support over 100 precision air bearing spindles simultaneously. Other facilities with fewer air bearings may have different components to their compressed air systems; however the process will be similar. The air will be compressed, dried, filtered, and transported. Each part of this process is vital to the performance and longevity of the air bearing spindles.

The notable features of the Professional Instruments compressed air system (Figure 3) are the number of filters and the use of two types of air dryers. These features are critical to reliably provide air that is both sufficiently clean and dry.

The end goal of any compressed air system for air bearings is to provide a continuous source of clean, dry, and oil free air at a constant pressure.

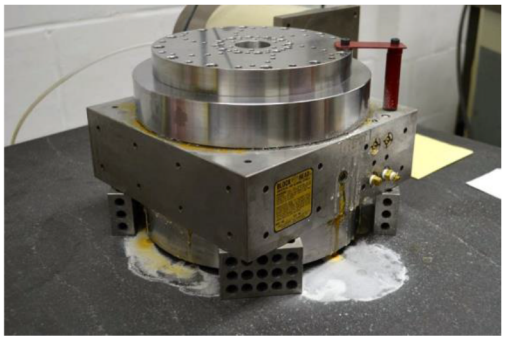

FIGURE 2. Spindle after a catastrophic failure in the air supply.

AIR COMPRESSOR

There are two main types of air compressors; piston (single and multiple stage) and rotary screw. While piston compressors are typically less expensive they have some short comings compared to a rotary screw design when considered as a supply for air bearing spindles. The air from piston compressors is typically hotter (100°+ F above ambient) and dirtier (10+ ppm oil carry over) than air from rotary compressors (15-25°F above ambient and 1-7 ppm respectively) [3] and as a result requires more work to become usable for air bearings. The temperature differential is due to modern rotary screw compressors having built-in aftercoolers for the air. Additionally, piston

compressors have short duty cycles which can cause pressure pulsations in the air lines that can affect air bearing performance.
Air bearing spindles should be kept on air at all times to prevent moisture or other contaminants entering the spindle. This can be done efficiently by lowering the pressure (minimum 40 psi) to the spindle when it is not in use. Professional Instruments uses a day/night valve that enables the air supply to be switched to a lower pressure when the facility is not in operation.

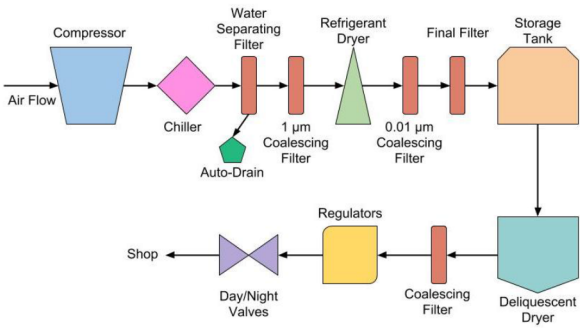

Figure 3. Diagram of compressed air system at Professional Instruments

AIR DRYER

The most important part of an air system for air bearing spindles is ensuring that the air is dry enough to prevent water from condensing inside of the spindles. As a general rule the dew point of the compressed air should be suppressed to at least 10°F below the operating temperature of the spindle.
Professional Instruments utilizes a primary refrigerant air dryer (Zeks HSG) and a backup deliquescent dryer (Van Air D16). Refrigerant dryers are very energy efficient and robust, while also capable of suppressing the dew point to 40°F. The deliquescent dryer is desirable as a backup air dryer since it requires no electrical power and fails at a steady rate. This redundancy increases the overall reliability of the compressed air system.
For point of use setups, Professional Instruments recommends the Kaeser KMM 3 membrane dryer. This dryer is able to suppress the dew point even further and is sufficient to support a small number of air bearing spindles. The unit in Figure 4 is installed at the Zeiss CMMs at one facility as an extra layer of protection.

FIGURE 4. Kaeser KMM 3 Membrane Dryer and humidity alarm.

AIR FILTERS

Oil and other foreign particulates are also detrimental to air bearing spindle performance and need to be removed. To accomplish this, the filters are setup in multiple stages (Figure 3). Each filter is attached to a draining system to prevent liquid from spilling over into the air supply.
The first stage is immediately after compression and consists of two filters: a water separating filter and a 1μm coalescing filter. These together remove the bulk of the moisture and contaminants from the air before it goes through the dryer. The second stage uses two high quality (0.01 μm) coalescing filters to remove any remaining oil in the air before it is moved to the storage tank. After this the air goes through the deliquescent dryer and into the third stage of filters. This final stage involves one coalescing filter immediately after the dryer and activated carbon filters just before each air bearing spindle. These filters act as a final defense against accidental contamination in the air lines or failures in upstream filters.

AIR QUALITY ALARM SYSTEM

A failure in a compressed air system can damage all of the spindles in that system if left unchecked. The system described in this poster has many fail-safes but they are only effective for short periods of time. Therefore, it is important to monitor the system for any abnormalities. Professional Instruments uses multiple humidity sensors (Ohmic Instruments model AMM-10, Figure 5) as an early detection system for fatal contamination inside the compressed air system. Once the alarm is triggered, warning alerts are sent from the DataTaker DT80 unit to all relevant personnel so that the problem can be identified and fixed before any damage is done to the spindles.

FIGURE 5. Compressed air monitoring system.

CONCLUSION

Air bearing spindles are invaluable in many different high precision applications and are intrinsically reliable. The spindles only ever need repair when either a user has overloaded the spindle or the air supply contaminated the spindle. Spindle repairs are expensive and time consuming. But the existence of a good compressed air system drastically reduces the likelihood that an air bearing spindle will ever require a repair.

REFERENCES

[1] McCulloch D, Mac Consulting,. Compressed Air and Gas Handbook. 6th ed. Cleveland: Compressed Air and Gas Institute; 2003

[2] Liebers M, Arneson D, Sanner S. A Shop Air Supply For A Hundred Spindles. ASPE 2012

[3] Chamber M. Piston Versus Rotary Screw Compressors. Kaeser Compressors, inc; 2017

History of the Blockhead Spindle

Christopher D. Arneson, Melvin J. Liebers
Professional Instruments Company
Hopkins, Minnesota, USA

ABSTRACT
In the last half-century, spindle accuracy specifications have gone from tenths to microns to microinches to nanometers.
In the pursuit of precision, the Blockhead air bearing spindle is the gold standard for accuracy and has been the workhorse at Professional Instruments since its inception. “The Blockhead has seen application in a wide variety of fields from basic physics research in the value of the gravitational constant to the fabrication of intraocular lenses for cataract surgery.” [1]
Understanding the history of the Blockhead and how it came to be requires an understanding of the history of Professional Instruments and how two brothers played a key role in the field of precision engineering.

INTRODUCTION
Professional Instruments Company (PICo) was established in 1947, originally as a job shop, by Harold and Ted Arneson (Fig 1), and became known in the precision engineering world with their careful work for Honeywell, fabricating hollow spherical gyroscope rotors in 1960.

Figure 1. Ted (right) and Harold Arneson (middle) observing Al Sanner.

“If it goes around and has to be good, PICo probably had something to do with it”
- Ted Arneson

To meet Honeywell’s specifications, PICo required an accurate spindle. This led Harold to invent the dual-hemisphere “Zeron” air bearing spindle. An interesting problem in measuring spindle accuracy is the need to separate out-of-roundness of the test ball from radial error motion of the spindle. As a result, the development of precision spheres coincided with the development of precision spindles. Having developed his own sphere lapping methods [2] for Honeywell’s gyroscopes, Harold inadvertently constructed an air bearing pivot which inspired the step bearing concept used for the Zeron spindle.
Sphere lapping produced spindles accurate enough to measure the output of the sphere lapping process.
It did not take long before the Zeron spindle could no longer be improved, leading Harold and Ted to a different design, the Blockhead. The Blockhead spindle was produced and patented in 1969 becoming the most widely used ultraprecision air bearing spindle in the world [1].

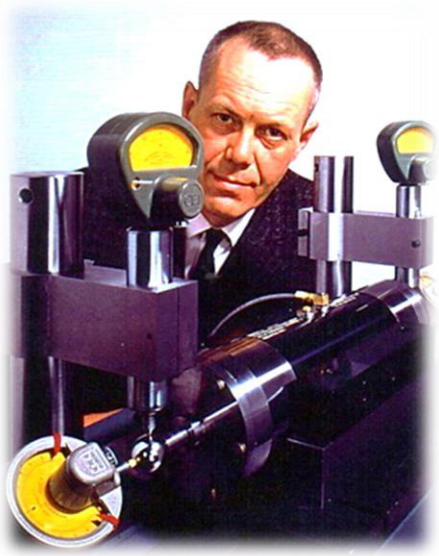

Figure 2. Harold testing an early Zeron spindle, a hydrostatic air bearing capable of sub-microinch accuracy, for radial, axial, and tilt error motion.

A JOB SHOP

PICo started in a rented walk-up with basic tools and a desire to succeed (Fig 3). Harold is shown here watching the assembly of the prototype of a Zeromax stepless transmission – which became an education in precision grinding, metrology, and metallurgy.

Figure 3. Harold (left) in PICo's first shop, located in St. Louis Park, Minnesota.

The invention was intended to be made with just a punch press and a centerless grinder but it wasn't that easy; it turned out to require a high level of skill, requiring between-centers grinding which Harold mastered through careful study of center-lapping, spherical centers, balanced-force drivers, tailstock issues, wheel dressing and balancing, and quirks of the grinder itself.

In the 1950's, Honeywell was in the need of suppliers for difficult-to-make gyroscope parts. They liked what they saw in Ted and Harold and fed them work of increasing difficulty. As a result, PICo acquired indicating mikes, diamond-tipped Mikrokators, and other equipment for working in the sub-tenth world (< 0.0001 inch).

BEARINGS FOR A PERFECT GYRO

Professor Arnold Nordsieck (University of Illinois) had conceived of an electrostatically suspended hollow-ball gyroscope that would allow submarines to remain submerged for longer. Honeywell had taken up the work but needed someone to make the gyroscopes. Ted impressed Nordsieck with PICo's potential and Harold began work on the job of making hollow beryllium balls to an unprecedented level of roundness; lapped to a few microinches, balanced to a 220-second pendulous period, which then spun in a vacuum at 12,000 rpm. [3]

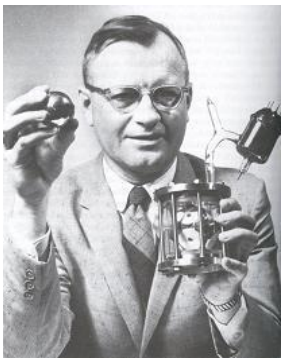

Figure 4. Nordsieck holding an early electrostatically suspended gyroscope ESG. Note the spherical gyro in Arnold's right hand, lapped by Harold. [4]

Figure 5. A U.S. Navy Polaris submarine, the USS Sam Rayburn, which used the ESG to determine its position while submerged.

With inertial electrostatic gyroscopes, the Navy's nuclear-powered submarines could remain submerged for months at a time without requiring inertial navigation resetting.

Due to the high accuracy required in this work it became necessary to develop a spindle that had sub-microinch accuracy. Early efforts took the form of several types of oil lubricated bearings, but it soon became apparent that the spindle needed to be externally pressurized to maintain a fixed position while running or when stopped. Harold's answer to this was the Zeron dual-hemisphere air bearing spindle [5].

Figure 6. An early advertisement for the Zeron hydrostatic bearing, PICo's first air bearing spindle.

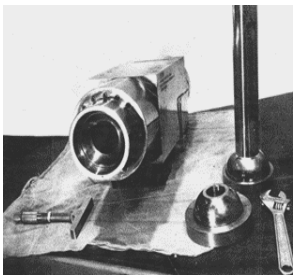

Figure 7. A Zeron bearing with the shaft removed. Note the dual hemisphere thrust surfaces and the long shaft.

However, the Zeron's shaft had to be long to reduce the influence from the rear bearing which greatly limited its stiffness. The resultant reaction on the rear bearing, when a force was applied to the front bearing, caused too much flex. Although it was kinematically correct, the Zeron was not a practical spindle. It was great for measuring, not machining.

TAPERS – STEPS – FLUTES

While working on the gyros, Harold used an air purge to keep coolant out of a pivot bearing that had a honed, barrel-shaped hole. Surprised when it spun freely, he read up on early air bearings in Dudley Fuller's book "Theory and Practice of Lubrication for Engineers" leading to the development of the step bearing.

Taking the next step toward precision, Harold elected for groove compensated bearings, or flutes. A groove compensated bearing has accurate longitudinal grooves distributing air through the bearing which detects off-center conditions, making instant compensating changes in the bearing's air flow to restore the bearing to a centralized condition [5].

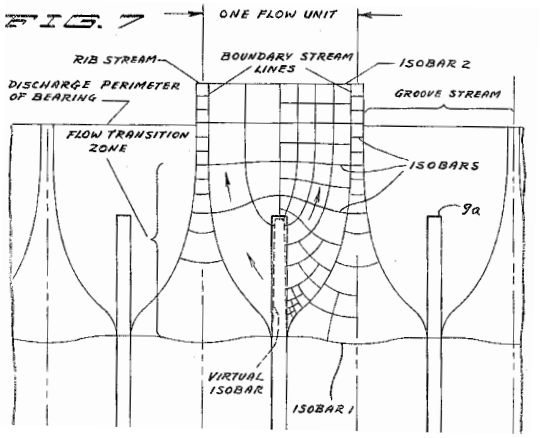

Figure 8. Flute Patent.

THE BLOCKHEAD SPINDLE

Ultimately, the Blockhead [6] was born out of Ted's desire to have an air bearing spindle to sell. The bearing could be used on a grinder, next on a lathe, and then as a highly accurate roundness tester.

For compactness, the shaft became short and stiff, now carrying the radial load, leaving axial and tilt properties to the large-diameter thrust plates. The net result is volumetric efficiency; a lot of load capacity in a compact package.

The first Blockhead sold, S/N 2, was purchased in 1967 by Goddard Space Flight Center. We kept S/N 1 for our own use and it is still grinding parts as the workhead on our Heald 273A internal grinder

Figure 9. A 4B Blockhead Air Bearing.

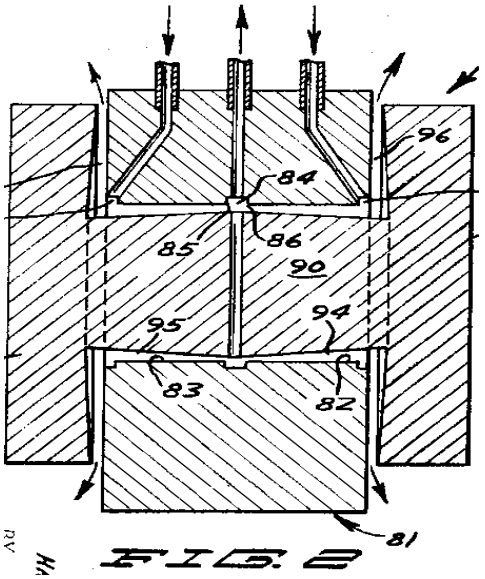

Figure 10. Blockhead Patent Drawing

As Harold described: “What determines the angular stiffness of the bearing as far as the shaft is concerned, is that the flexure of the shaft varies inversely with the cube of the length and directly with the fourth power of the diameter... These advantages all seem to converge on that device which turned out to be the 8 inch Blockhead which I would like to say I designed in some intellectual fashion but just was the result of the impossible conditions that Ted had determined that it had to be.” [7]

CONCLUSION

At the time air bearing spindles were being intensely researched by large companies, universities, and government laboratories around the world, it was a little company in St. Louis Park, Minnesota that ended up making the most accurate spindles in the world.

Professional Instruments air bearing spindles, combined with advanced machine tools enabled the growth of glass grinding exotic shapes for high-end cameras and big lithographic lenses for microcircuits, allowed for high density servotrack writing to dramatically increasing disk drive storage, and have assisted in projects that reach beyond planet Earth.

REFERENCES

[1] Harold E. G. Arneson’s ASPE 1995 Lifetime Achievement Award

[2] U.S. Patent # 3,110,987, Sphere Lapping Apparatus, Harold E. G. Arneson, Nov. 19, 1963

[3] U.S. Patent # 3,136,151, Static Ball Balancing Apparatus and Method, Harold E. G. Arneson, Jun. 9, 1964

[4] MacKenzie, Donald A. Inventing Accuracy: A Historical Sociology of Nuclear Missile Guidance, 1990

[5] U.S. Patent # 3,305,282, Hydrostatic Bearing Structure, Harold E. G. Arneson, Feb. 21, 1967

[6] U.S. Patent # 3,101,224, Externally Pressurized Bearing Structure, Harold E. G. Arneson, Oct. 14, 1969

[7] Harold Arneson & Mel Liebers, Fort Myers Beach, Florida, April 25, 1992 “HOW THE BLOCK-HEAD® CAME TO BE INVENTED”

INVERTED CURVED FLEXURE HINGE WITH TORSIONAL REINFORCEMENTS IN A PRINTED PROSTHETIC FINGER

A.S. (Bas) Boers, M. (Mark) Naves,
L.A. (Luis) Garcia Rodriguez, D.M. (Dannis) Brouwer
Precision Engineering lab
University of Twente
The Netherlands

ABSTRACT

Flexure-based finger joints for prosthetic hands have been studied, but until now they lack stiffness and load capacity. In this paper we present a design which combines large range of motion, stiffness and load capacity, with a torsional overload protection mechanism. Five design considerations which increase grasp force and limit the stress values are presented: (1) Due to the inverted flexure attachment, the flexures are loaded mainly in tension, avoiding buckling of flexures. (2) Curved flexures have been used of which one straightens out at large deflection angles to improve load capacity at large deflections. (3) To achieve high torsional loads, one of the flexures is outfitted with triangular torsional stiffeners, which increase the out-of-plane stiffness significantly, while only slightly increasing the actuation stiffness. (4) The entire joint is rotated by 20˚ so the combination of actuation and contact forces lead to mainly axial forces in the curved leaf spring, avoiding excessive internal bending.

The presented prosthetic flexure-based finger joint is able to achieve 20N of contact force with an additional 5N of out of plane load over the entire 80˚ range of motion, which is a major improvement over existing prosthetic flexure-based finger designs.

INTRODUCTION

Flexure joints applied in prosthetic and robotic hands have been of interest in recent years [1–4]. The main advantages for prosthetic hands are lightweight design, (almost) no assembly needed, reduced cost, and precise grasping force without force feedback. [3–5].

A major challenge for flexure joints in large range of motion applications is the strong decrease of support stiffness in load carrying directions when deflected [6–8]. This loss of support stiffness and accompanying poor load carrying capacity at large rotations currently prevents widespread applicability in robotic and prosthetic hands [3]. Therefore, it is of interest to study the mechanical behavior of monolithic integrated flexure joint designs over the entire range of motion. The decrement of the stiffness in the support direction also leads to loss of load bearing capacity of the hand. Especially when including tendon actuation and high grasping forces, elastic instability of the joint (buckling) can result in reduced load-carrying capacity.

Researchers from the UB Hand compared several flexure topologies for robotic hands by analyzing compliance matrices in undeflected position [4],[9]. Additionally, Tavakoli et al. presented new topologies and analyzed the flexure stresses and deflections for the undeflected state [1]. Although analyzing the stiffness properties of flexure topologies at undeflected state allows the use of simple linear beam equations, it gives no lead to the stiffness properties at larger deflection angles due to the strong non-linear behavior. Furthermore, as critical stiffness and load carrying capacity typically occurs at maximum deflection, , the mechanical properties at maximum deflection angle is of primary interest rather than at the undeflected state.

Kalpathy used a pseudo-rigid-body model with an approximation of Timoshenko beam theory to model leafsprings in a larger range of motion [2]. Although pseudo rigidbody modeling allows for larger deflections, it is limited to simulation of its kinematic behavior and stiffness in the free motion direction. Therefore, evaluation of the support stiffness at large deflection angles is still unavailable.

Odhner presented the “Smooth Curvature model” to calculate compliance matrices in large deflections of planar leafspring designs, as this can be associated with stable grasps [10]. This method allows for evaluation of support stiffness at larger deflections, however, it described the compliance matrix only for the 2-dimensional case. For typical loading-conditions, out-of-plane stiffness and load carrying capacity are important also. Furthermore, it only allows for the evaluation of planar hinge designs.

In this study, a finger is investigated with two finger joints, the MCP (metacarpophalangeal) and PIP (proximal interphalangeal) joint. The DIP (distal interphalangeal) joint is considered rigid. The main focus will be on the design of the PIP joint, which is located in the middle of the finger and is more limited with the available space than the MCP joint. However, the general design considerations still apply to the MCP joint. In Figure 1, the basic geometry of the proposed prosthetic finger is shown, consisting of two joints with two crossing leaf springs each.

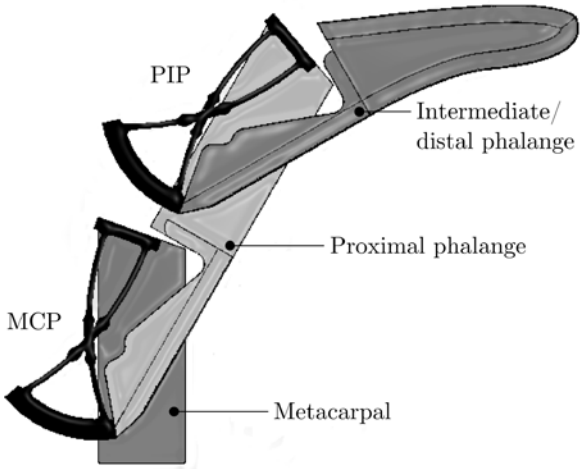

FIGURE 1. Schematic overview of finger design.

Since the working space is limited, an actuation moment cannot be achieved by placing rotational motors in the finger. Therefore, tendons are usually fitted inside the finger, as is the case in a human hand. This tendon only creates flexion (grasping action) of the finger. Extension can be achieved, but only if the finger is pressed against other objects.

REQUIREMENTS

The cylindrical medium power wrap is identified as one of the most commonly used grasps [11], [12] and therefore the main focus of this research. First of all, the flexure joint has to be able to withstand the actuation forces to achieve the required deflection of +/-40˚. Additionally, the finger has to be able to create a contact force F_c acting on the inside of the finger resulting from the medium power wrap, which will have a large contribution to the actuation force. Contact forces in humans can reach up to 60N per finger when evaluating the contact force at a distance of 20 mm from the center of rotation of a human finger joint [13].

In this study, the goal is to design a finger for a hand which allows the user to hold a 2.5kg bottle. When the load is distributed over 5 contact points (four fingers and a thumb), the resulting out-of-plane load (Fs) is approximately 5N per finger. This load combined with an estimated friction coefficient of 0.2 results in a required grasping force (Fc) of approximately 20N. A schematic illustration of the resulting forces when holding a 2.5kg bottle is provided in Figure 2, in which Fa represents the actuation force provided by the tendon. In Table 1 a summary of the requirements is provided.

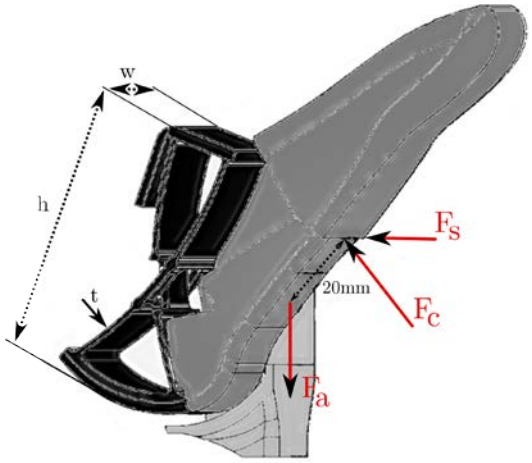

FIGURE 2. Schematic overview of forces acting on the PIP joint with w=15mm and h=40mm. Note: the gravity direction is in the direction of force F_s.

TABLE 1: Boundary conditions

Parameters	Boundary conditions
Joint Height (h)	< 40 mm
Joint width (w)	< 15 mm
Flexure thickness (t)	> 0.8 mm (limit AM)
Deflection angle (θ)	+/- 40˚
Out-of-plane load (Fs)	5N
Contact Force (Fc)	To be maximized
Material	Nylon (PA2200)
Allowable stress	40 MPa
Flexural modulus	1.5 GPa

METHOD

Structural simulations are carried out to investigate the behavior of the finger joint for different load cases. For this simulation, an out-of-plane load (F_s) of 5 N and an contact force (F_c) of 20N is applied to the finger as illustrated in figure 2. Furthermore, action force (F_a) is altered in order to obtain static equilibrium over a

range of motion -40° < θ < +40°. Simulations are conducted with the flexible multibody program SPACAR which uses a series of interconnected nonlinear 3D finite beam elements which includes geometric nonlinearities [14]. Additionally, the results are verified with finite element simulations in SolidWorks.

With the use of these simulations, the shape of the flexures is altered (the values of *w*,*h* and *t*) and the influence of the design considerations described in the next section is analyzed.

DESIGN AND MODELLING

Inverted mounting of the leaf springs

In order to achieve the required high contact and grasping forces, significant actuation forces are required. In its simplest implementation of a cross flexure actuated by a tendon, the leaf springs are loaded in compression. This concept is illustrated in Figure 3. Loading the leaves in compression severely limits the maximum actuation forces, and therefore the contact forces, because of buckling. Especially at large deflection angles, the leaves will be curved and the resistance to buckling will diminish.
A solution is to mount the leaves at the top of the phalanx, such that the leaves are loaded in tension. This creates an 'inverted joint', which is also shown in the finger design in Figure 1.

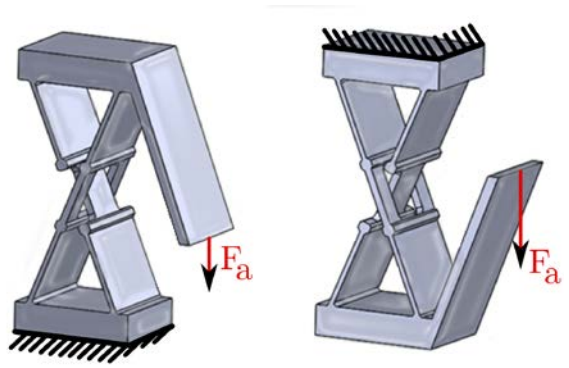

FIGURE 3. Crosshinge loaded in compression and prone to buckle (left), crosshinge loaded in tension due to inversion (right)

Curved Leaf Springs

The curvature of the leaf springs in traditional cross flexures increases as the deflection angle increases. Due to the fact that the maximum loading condition typically occurs at large deflection angles (i.e. a closed hand due to the grasping operation), the highest forces occur when support stiffness and load carrying capacity is at their lowest. In order to compensate for this effect, two flexures which are equally curved and mirrored with respect to each other are used. This way, one of the leaves straightens out in either direction of motion providing high load capacity and support stiffness at larger deflection angles. A schematic illustration is provided in figure 4.

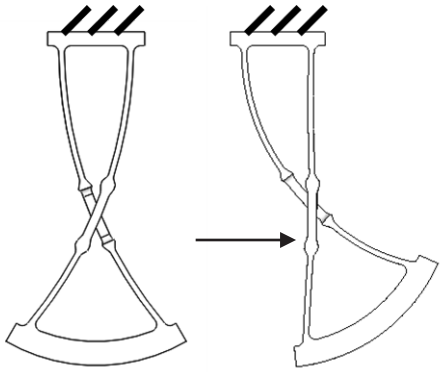

FIGURE 4. Curved Cross Hinge; deflection will result in one of the leafs straightening out.

The joint design is similar to the Curved Hinge presented in [15]. However, due to the possibilities of 3D printing, two crossing leaves can be fabricated. The stiffness of the curved leaf in the direction of the actuation force will be small with respect to the stiffness of the straightened leaf spring. Therefore, the majority of the forces will be fed through the straight leaf, as the leaves are connected in parallel. This means that the strongest leaf is loaded the heaviest, avoiding unwanted stress concentrations in the strongly curved leaf.

A comparison of the stress between a traditional Cross hinge and a Curved Cross Hinge is given 5N of sideways force (Fs) and 20N of contact force (Fc) is presented in figure 5. For the Cross Flexure, the stress at 0˚ (neutral position) when loaded with 20N starts out low (Figure 10). As the deflection angle increases, the stress increases due to both bending and additional internal moments caused by the deflected state of the flexures combined with the external load of 20N. Therefore, stress increases strongly with increasing deflection angle.

For the Curved Cross Hinge the situation is different. At the neutral state, the leaves are curved and therefore initially higher internal moments are present in the flexures, causing

higher stress levels. As the deflection angle increases, bending of the flexures results in an increase of stress. However, as the curvature of the flexure reduces, the internal moments caused by the external load decreases. The combined effect is a rather constant stress profile over the range of motion.

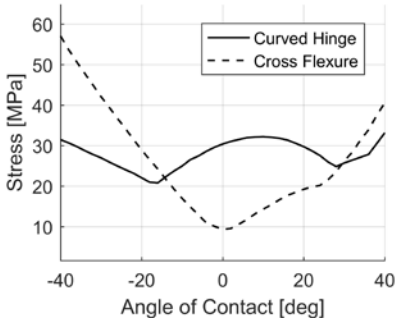

Figure 5: SPACAR results the inverted curved cross hinge with torsion reinforcements and the inverted cross flexure with torsion reinforcements with 20N contact force, 5N side force.

Rotation of the joint

The Curved Hinge is able to withstand the highest forces parallel to the straightened leaf spring. The total applied force to the joint is equal to the sum of the actuation force F_a and the contact force F_c, see Figure 2. To achieve a favorable load case, the Curved Cross Hinge joint as a whole is rotated by an angle of about 20˚ to ensure this favorable loading condition over the range of motion.

Torsion Stiffeners

The resistance of the Curved Cross Hinge to torsion due to lateral forces (F_s) is quite low. In fact, the maximum lateral force at 40˚ deflection angle is just 3N. To prevent large out of plane deflections and to increase load carrying capacity in the transverse direction, triangular torsional reinforcements are used [16]. These triangles allow the main leaf to bend, necessary for flexion, while creating a shape that is stiff in torsion. This is shown in Figure 6. To interfere as little as possible with the rest of the finger, the triangles are placed on the inside of the flexure where possible. The geometry of the triangles is largely bounded by the shape of the flexure, making sure that the reinforcements will not touch the main flexures in all deflected states.

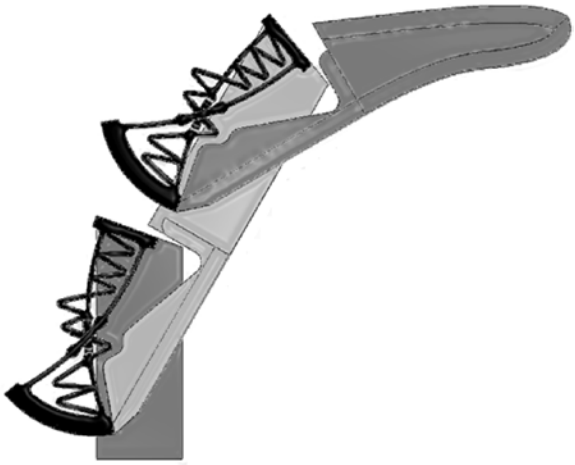

FIGURE 6. Finger design with triangular torsion reinforcements.

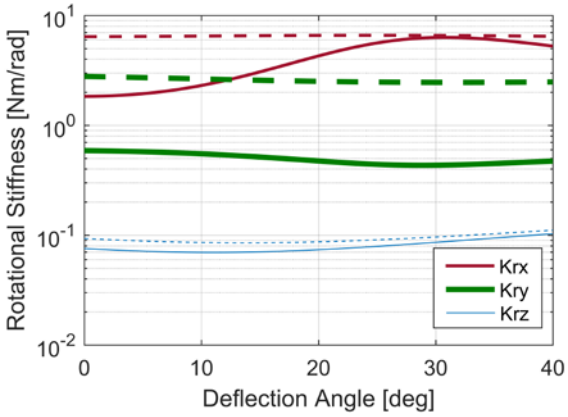

FIGURE 7. Stiffness comparison, reinforced and non-reinforced; Dashed line: Curved Hinge with torsion reinforcements; Solid line: Curved Hinge without torsion reinforcements. See Figure 2 for coordinate system.

In Figure 7 the effect of the torsion reinforcement is shown. An increase in rotational stiffness around the y-axis of a factor 6 is achieved. Additionally the joint is now able to withstand 5N lateral forces, compared to 1.2N without torsion stiffeners. The triangles also give the joint higher and more constant stiffness around the x-axis (K_{rx}). The increase in actuation stiffness (z-axis, K_{rz}) is relatively small so no significantly higher actuation forces are needed.

Overload Protection

Due to the inversion of the leaf springs, the phalanges are crossing. This crossing is conveniently used to create mechanical end stops. The side flanges of the finger prevents the leaves in the joint from excessive twisting.

EXPERIMENTAL VALIDATION

A physical 3D-printed part has been additively manufactured with Selective Laser Sintering (SLS) to test the functionality and verify the obtained grasping/actuation force,. A photograph of the prototype is provided in figure 9.

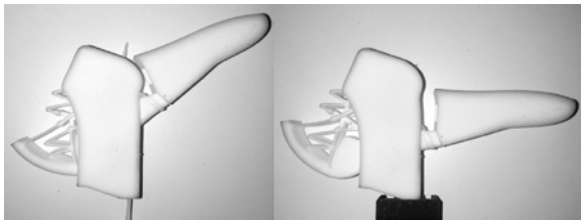

Figure 9. Un-deflected and 40° deflected 3D-printed (SLS) prototype finger.

For validation of the grasping force, the finger is actuated with a tendon with a predefined actuation force and the resulting grasping force is measurement with a force sensor. The experimental setup is pictured in figure 10.

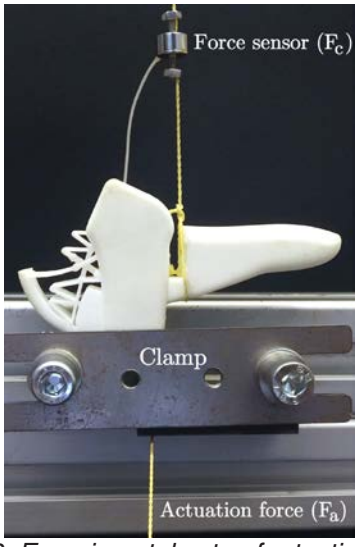

Figure 10. Experimental setup for testing grasping force

The measured actuation and grasping force is provided in figure 10. From these results it can be concluded that the required grasping force of 20N can be obtained without failure/buckling of the flexures. Furthermore, a small offset between the resulting grasping force can be observed under full extension (the user has to push to the fingers to obtain full extension, resulting in initial grasping force of approximately 3N) and full flexion (initial actuation force is required to obtain the required deflection angle).

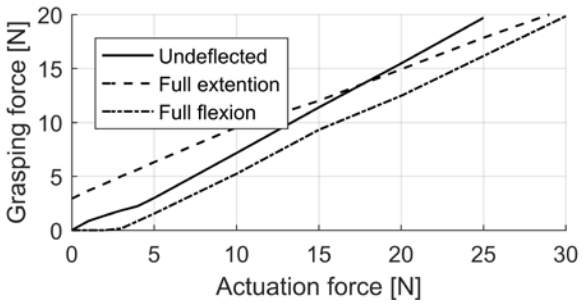

Figure 11. Measured grasping force at undeflected state, full extention and full flexion.

CONCLUSION

The presented prosthetic flexure-based finger joint is able to achieve 20N of contact force with an additional 5N out of plane load over the entire 80˚ range of motion, which is a major improvement over existing prosthetic flexure-based finger designs.

REFERENCES

[1] M. Tavakoli, A. Sayuk, J. Lourenço, and P. Neto, “Anthropomorphic finger for grasping applications: 3D printed endoskeleton in a soft skin,” Int. J. Adv. Manuf. Technol., 2017.

[2] V. Kalpathy and H.-J. Su, “A 3-Spring Pseudo-Rigid-Body Model for Soft Joints with Significant Elongation Effects A 3-Spring Pseudo-Rigid-Body Model for Soft Joints with Significant Elongation Effects,” J. Mech. Robot., 2016.

[3] L. U. Odhner, L. P. Jentoft, M. R. Claffee, N. Corson, Y. Tenzer, R. R. Ma, M. Buehler, R. Kohout, R. D. Howe, and A. M. Dollar, “A compliant, underactuated hand for robust manipulation,” Int. J. Rob. Res., vol. 33, no. 5, pp. 736–752, 2014.

[4] G. Berselli, F. Parvari Rad, R. Vertechy, and V. Parenti Castelli, “Comparative evaluation of straight and curved beam flexures for selectively compliant mechanisms,” 2013 IEEE/ASME Int. Conf. Adv. Intell. Mechatronics Mechatronics Hum. Wellbeing, AIM, 2013.

[5] B. P. Trease, Y.-M. Moon, and S. Kota, “Design of Large-Displacement Compliant Joints,” J. Mech. Des., vol. 127, no. 4, p. 788, 2005.

[6] D. Brouwer, J. Meijaard, and J. B. Jonker, “Large deflection stiffness analysis of parallel prismatic leaf-spring flexures,” Precis. Eng., 2013.

[7] D. Wiersma, S. E. Boer, R. Aarts, and D. Brouwer, “Design and Performance Optimization of Large Stroke Spatial Flexures,” J. Comput. Nonlinear Dyn., vol. 9, no. January 2014, 2013.
[8] S. Awtar, “Analysis of Flexure Mechanisms in the Intermediate Displacement Range,” in Handb. Compliant Mech., L. L. Howell, S. P. Magleby, and B. M. Olsen, Eds. John Wiley & Sons Ltd, 2013.
[9] G. Berselli, A. Guerra, G. Vassura, and A. O. Andrisano, “An engineering method for comparing selectively compliant joints in robotic structures,” IEEE/ASME Trans. Mechatronics, 2014.
[10] L. U. Odhner and A. M. Dollar, “The smooth curvature model: An efficient representation of Euler-Bernoulli flexures as robot joints,” IEEE Trans. Robot., vol. 28, no. 4, pp. 761–772, 2012.
[11] I. M. Bullock, J. Z. Zheng, S. De La Rosa, C. Guertler, and A. M. Dollar, “Grasp frequency and usage in daily household and machine shop tasks,” IEEE Trans. Haptics, vol. 6, no. 3, pp. 296–308, 2013.
[12] C. Cipriani, M. Controzzi, and M. Carrozza, “The SmartHand transradial prosthesis,” J. Neuroeng. Rehabil., 2011.
[13] A.D. Astin, ‘Finger force capability: measurement and prediction using anthropometric and myoelectric measures’, master thesis, Faculty of the Virginia Polytechnic Institute and State University, 1999
[14] Jonker, J.B. and Meijaard, J.P., ‘Spacar – Computer Program for Dynamic Analysis of Flexible Spatial Mechanisms and Manipulators’, Multibody Systems Handbook, W. Schiehlen (eds.), SpringerVerlag, Berlin, pp. 123-143, 1990.
[15] Brouwer, D.M., Meijaard, J.P., Jonker, J.B., ‘Elastic Element Showing Low Stiffness Loss at Large Deflection’, Proceedings of the 24th annual meeting of the American Society of Precision Engineering, Monterey, pp. 30-33, 2009.
[16] M. Naves, D.M. Brouwer, R.G.K.M. Aarts, Building block based spatial topology synthesis method for large stroke flexure hinges, ASME robotics and mechanisms, 2017.

Arthors Index

Authors Index

Abdulkadir, Lukman 321
Abou-El-Hossein, Khaled 321
Abruna, Ernesto 136
Adriaansen, Scott 150
Aguirre, Gorka 26
Allezy, Arnaud 156
An, Jong-Wook 389
An, Zhongyu 364
Anderson, Christopher 156
Andree, Deick J. 563
Anton, Jayson 543
Arima, Kenta 335
Arneson, Dave 505, 508, 575
Arneson, Christopher D. 578
Arneson, Henry 393, 505
Arneson, Sam 575
Arumugam, Kumar 117
Azimi, Farzad 38
Bach, Mathias 59
Badami, Vivek 136
Bartsch, Peter 325
Beaulieu, Devin 462
Behera, Dipankar 93
Berger, Daniel 184
Berselli, Giovanni 174
Betters, Emma 513
Bhushan, Brij 448
Bifano, Thomas 462
Blackwell, William 569
Blaser, Philip 53
Blum, Alexander 397
Bodlapati, Charan 401
Boers, A.S. (Bas) 582
Brackley, Douglas 150
Branson, David 32
Brinksmeier, Ekkard 184
Brouwer, Dannis . . . 174, 517, 547, 563
Brown, Austin 409
Bulla, Benjamin 180
Cayll, David 230
Chabot, Joshua 70
Chalifoux, Brandon 253
Chang, Kao-Der 301
Chang, Yina 201
Chen, Dihan 471
Chen, Shih-Chi 104, 201, 471
Chen, Wang 471
Chen, Yaolong 339, 476
Cheng, Andew 99
Cheung, Chi-Fai 221
Cho, Joon Hyong 230
Choi, Doo-Sun 259, 288
Choi, Seong-Dae 259
Chou, Ta-Hsin 301
Cilla, Julen 26
Clark, Kristin 569
Connolly, Liam 99
Copenhaver, Ryan 263, 513
Cork, Carl 156
Coupland, Jeremy 225
Crompton, David 569
Cullinan, Michael 93, 99, 112, 230
Culpepper, Martin 168
Cunningham, Andrew 569
Dai,Yifan 243
de Groot, Peter 15, 225
Dicke, Clemens 180
Dickinson, Michael 156
DiLiberto, Michael 569
Doig, Allan 150
Doki, Kae 235, 239
Dong, Xin 76, 557
Dow, Thomas 196, 311, 401
Elliott, Kevin 150
Elmadih, Waiel 162
Endo, Katsuyoshi 142
Evans, Chris 397
Fedorynenkp, Dmyro 344
Feng, Fu 471
Fern, Florian 122, 527
Fernandez Galiana, Alvaro 456
Fischer, Andreas 496
Freyberg, Axel 496
Fry, Alan 538

Fuhrman, Linda 569
Furst, Stephen 108
Furushiro, Naomichi 269
Furutani, Katsushi 273
Füßl, Roland 122, 527
Gaines, Geoffrey 156
Galiana, Álváro Fernandez 82
Garcia, James 99
Garrard, Kenneth 401
Geng, Qiang 104
Gillmer, Steven 569
Glavicic, Mike 283
Gloess, Rainer 552
Goch, Gert 21, 496
Gomez, Michael 277, 513
Goos, Alexander 552
Gorges, Stephan 88
Greenberg, Michael 538
Groover, Jesse 21
Gu, Jhen-Nan 301
Guo, Hua 369
Haase, Thomas 452
Haitjema, Han 15
Halbeisen, Leonard 325
Hamer, Tyler 70
Han, Kai 243
Han, Lin 476
Hashimoto, Takeshi 381
Heilmann, Ralf 253
Her, Tsing-Hua 117
Herder, Just 174
Hernandez-Becerro, Pablo 53
Hesse, Steffen 88
Hirooka, Daisuke 269
Hirschmann, Thomas Ch. 249
Holthusen, Ann-Katrin 385
Honeycutt, Andrew 47, 283
Horn, Frank 496
Huang, Lei 136
Idir, Mourad 136
Ihara, Tohru 329
Iñigo, Beñat 26
Inukai, Ryota 273
Jacobs, Ben H. 381
Jagodzinski, Marco 190
Jain, V. K. 357
Je, Tae-Jin 259, 288
Jeon, Eun-Chae 259
Jeong, An-Mok 389
Jeong, Ji-Young 259, 288
Jo, Jae Hoon 415
Jones, Gideon 156
Jorda, David 527
Kajihara, Yusuke 292
Kamal, Ayman M. 381
Kang, Jungmin 142
Karim, Shah 32
Kawai, Kentaro 335
Kawamura, You 297
Kearney, Steven 543
Kim, Chang-Ju 425
Kim, Cheol-Ho 389, 415
Kim, Gyu Ha 146, 350
Kim, Hyo Young 389, 415
Kim, Hyunsoo 434
Kim, Tae-Gon 389, 415
Kimura, Fumihiko 292
Kitayama, Takao 142
Kizaki, Ryo 142
Knapp, Byron 508, 575
Kode, Sai Kumar 38, 215
Köhler, Eric 452
Körner, Lars 127
Kossack, Christoph A. 419
Kühne, Stefan 190
Ladner, Ian S. 230
Lafortune, Kai Nicholas 538
Lai, Barry 543
Lai, Tao 501
Leach, Richard K. 15, 32, 127, 162, 225
Lee, ChaBum 146, 353, 466
Lee, Chan-Hong 438
Lee, Changho 425
Lee, Hiu Hung 201
Lee, Je-Ryung 259, 288
Lee, Jihyun 425
Lee, Jin-Ho 430

Lee, Kangjae 425
Lee, Kwan-Sup 430
Lee, Moongu 415
Lee, Seok Woo 389, 415
Lee, Sungcheul 434
Li, Furen 243
Li, Yipeng 339
Li, Yuefeng 364, 369, 375
Liebers, Melvin J, ... 578
Lim, Jung-Youl 430
Lin, Chun-Ting 301
Lin, Hung-Yi 301
Lin, Wei 201, 471
Liu, Wenjun 543
Liu, Yutao 307
Luo, Chi 243
Malcher, Markus 190
Maser, Jorg 543
Marth, Harry 59
Maskery, Ian 162
Matichard, Fabrice 82, 456
Matsumori, Noboru 269
Maulimov, Mukhtar 43
Mayr, Josef 53
McDonald, Timothy 108
McMenamin, Conor 569
McNutt, Noa 311
Meijaard, Jacob Philippus 517
Michael, Steven 569
Miller, Jimmie A. 21
Miller, Nichole 108
Miura, Kenjiro Takai 484
Miyakawa, Ryan 156
Miyawaki, Takashi 142, 480
Montaño, Joshua D. 488, 492
Moon, Seung-Hwan 259, 288
Morgan, Christopher J. 317
Mototani, Suguru 235, 239
Nakao, Yohichi 344
Nakazato, Ayaka 235, 239
Naples, Neil. J. 350
Naulleau, Patrick 156
Navare, Jayesh Abhay 38, 215
Naves, M. (Marrk) 582
Nijenhuis, Marijn 517, 563
Noh, Minkyun 70
Oberschmidt, Dirk 190
Odedeyi, Peter Babatunde 321
Ohkubo, Yuji 335
Ohue, Hiroyuki 273
Okada, Tatsuaki 273
Okwudire, Chinedum E. . . 76, 442, 557
Onwuka, Goodness Raluchukwu . . 321
Oss, Dan 505, 508, 575
Ouyang, Wenqi 104
Patel, Divyansh S. 357
Patel, Radha 397
Pankow, Mark 196
Patti, Francesco 521
Pawar, Amogh 209
Peng, Xiaoqiang 243, 501
Pham, Van Dinh 438
Piano, Samanta 32
Powers, Brian 569
Qiao, Zheng 307
Racamato, Joseph 569
Ramirez, Aaron E. 168
Ramkumar, J. 357
Ravindra, Deepak 215
Reiser, Jonas 59
Rekawa, Senajith 156
Ren, Mindan 104
Riemer, Oltmann 184, 385
Ro, Seung-Kook 434
Robertson, David 180
Robinson, Joseph 538
Roblee, Jeff W. 381
Roehrig, Christian 543
Roy, Nilabh Kumar 93
Rubeo, Mark A. 317
Saiki, Kazuto 273
Sawaya, Eiji 480
Schattenburg, Mark Lee 253
Schienbein, Ralf 122, 527
Schilder, Jurnan 533, 547
Schindler, Geogor 249
Schmitz, Tony L. . . . 47, 209, 263, 277, 283, 419, 466, 513

Schmuetz, Joerg 325
Schönemann, Lars. 184, 385
Sencer, Burak 43
Seo, Chang Hoon 415
Shahinian, Hossein 38, 215
Sheehan, Brian 150
Shi, Feng 243, 501
Shi, Hongliang 538
Shibata, Gaku 484
Shin, Kangwoo. 389
Shiraji, Hideki (Hiroki) 142
Shu, Deming 543
Slocum, Alexander H. 409
Smith, Stuart T.. . . . . 117, 127
Sohn, Alexander. 401
Song, Chang Kyu. 438
Song, Xiaoqi. 329
Spiga, Daniele 538
Steffens, Norbert 496
Stokes, Michael 513
Stramigioli, Stefano 174
Su, Rong 225
Sun, Rongyan 335
Sun, Xinyao 339
Syam, Wahyudin P. 162
Takahashi, Yukio 329
Takaki, Yushi 235, 239
Takano, Takayoshi 273
Takino, Hideo 297
Tamura, Yuta 292
Tanada, Kenichi 269
Tarbutton, Joshua 466
Thalkar, Mahesh 357
Theska, René. 122, 527
Thomas, Matthew 225
Tian, Ye 243, 501
Tie, Guipeng 501
Tischler, Jpnathan Z. 543
Tolley, Martin 32
Torii, Akihiro 235, 239
Toyoshi, Yui 142
Trumper, David L. 65, 70, 448
Tschiersky, Martin 174
Urreta, Harkaitz 26
Usuki, Shin. 484
Valdez, Lucas M. 488, 492
Valdez, Mario O. 488, 492
van den Belt Mieke 533, 547
Venditti 397
Villarraga-Gómez Herminso. 127
Vogels, John M. 521
Wang. Bo 307
Wang, Guanglin 364, 369, 375
Wang, Qichang 21, 496
Ward, Martin J. 112
Wegener, Konrad 53
Woller, Kevin B. 253
Wong, Anthony R. 196, 401
Wu, Guicheng 364
Wu, Yangong 307
Worthey, Jefrey L. 381
Xue, Jiadai 307
Yamaguchi, Eiji 292
Yamaguchi, Tomomi. 269
Yamamoto, Takahiro 480
Yamamura, Kazuya 142, 335
Yamazaki, Satsuki 344
Yang, Zenghui 369
Yang, Zenghui 364
Yao, Youwei 253
Yi, Allen Y. 350
Yoon, Deokkyun. 442
Yoon, Jun Young 448
You, Won-Hee 430
Zaytsev, Dmytro 38, 215
Zha, Jun 339, 476
Zhang, Lin 350
Zhang, Peng 307
Zhang, Xiang 375
Zhao, Chenyang 221
Zhao, Erxuan 201
Zhong, Yaoyu. 243
Zhou, Lei 65, 70
Zhou, Lin 501
Zhou, Wenchen 350
Ziegert, John C. 419

Volume 70
ISBN 978-1-887706-77-3